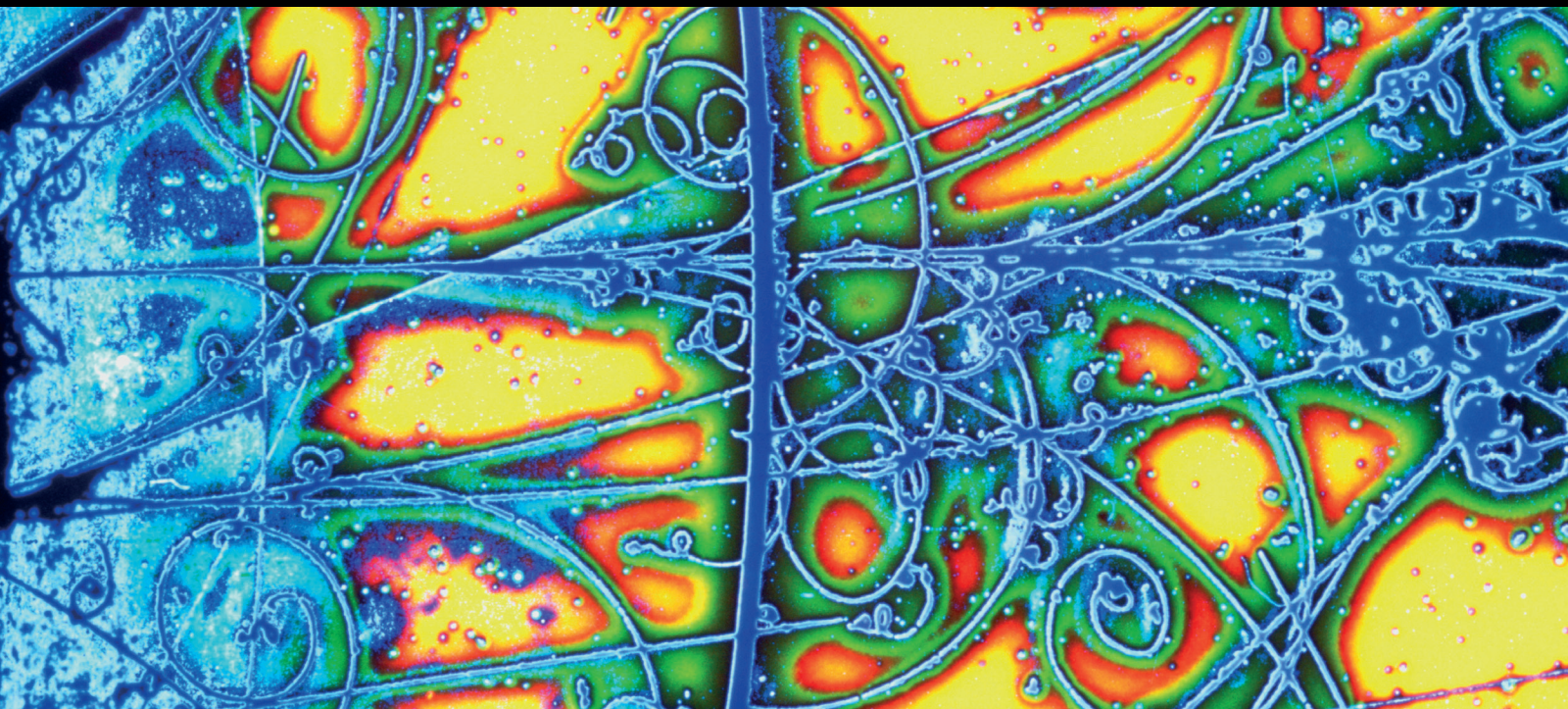


# NEUTRINO Physics

GUEST EDITORS: JOSE BERNABEU, GIAN LUIGI FOGLI,  
ARTHUR B. McDONALD, AND KOICHIRO NISHIKAWA





---

# **Neutrino Physics**



Advances in High Energy Physics

---

## **Neutrino Physics**

Guest Editors: Jose Bernabeu, Gian Luigi Fogli,  
Arthur B. McDonald, and Koichiro Nishikawa



---

Copyright © 2013 Hindawi Publishing Corporation. All rights reserved.

This is a special issue published in "Advances in High Energy Physics." All articles are open access articles distributed under the Creative Commons Attribution License, which permits unrestricted use, distribution, and reproduction in any medium, provided the original work is properly cited.

## Editorial Board

Botio Betev, Switzerland  
P. J. Bussey, UK  
Duncan L. Carlsmith, USA  
Kingman Cheung, Taiwan  
S. H. Dong, Mexico  
Edmond Craig Dukes, USA  
Paula Eerola, Sweden  
Amir H. Fatollahi, Iran  
Frank Filthaut, The Netherlands  
Joseph Formaggio, USA  
Chao-Qiang Geng, Taiwan  
Cecilia Gerber, USA

J. Gracey, UK  
Hong-Jian He, China  
Ian Jack, UK  
Ashutosh V. Kotwal, USA  
Pietro Musumeci, USA  
Piero Nicolini, Germany  
Seog H. Oh, USA  
Dugan O'Neil, Canada  
Sandip Pakvasa, USA  
Manfred Paulini, USA  
Anastasios Petkou, Greece  
Alexey A. Petrov, USA

Ira Rothstein, USA  
Kate Scholberg, USA  
Frederik Scholtz, South Africa  
George Siopsis, USA  
Terry Sloan, UK  
Neil Spooner, UK  
Luca Stanco, Italy  
Elias C. Vagenas, Greece  
Nikos Varelas, USA  
Kadayam Viswanathan, Canada  
Yau W. Wah, USA



# Contents

**Neutrino Physics**, Jose Bernabeu, Gian Luigi Fogli, Arthur B. McDonald, and Koichiro Nishikawa  
Volume 2013, Article ID 943471, 3 pages

**Reactor Neutrinos**, Soo-Bong Kim, Thierry Lasserre, and Yifang Wang  
Volume 2013, Article ID 453816, 34 pages

**The Nature of Massive Neutrinos**, S. T. Petcov  
Volume 2013, Article ID 852987, 20 pages

**Neutrino Propagation in Matter**, Mattias Blennow and Alexei Yu. Smirnov  
Volume 2013, Article ID 972485, 33 pages

**Solar Neutrinos**, V. Antonelli, L. Miramonti, C. Peña Garay, and A. Serenelli  
Volume 2013, Article ID 351926, 34 pages

**Long-Baseline Neutrino Oscillation Experiments**, G. J. Feldman, J. Hartnell, and T. Kobayashi  
Volume 2013, Article ID 475749, 30 pages

**Sterile Neutrino Fits to Short-Baseline Neutrino Oscillation Measurements**, J. M. Conrad, C. M. Ignarra, G. Karagiorgi, M. H. Shaevitz, and J. Spitz  
Volume 2013, Article ID 163897, 26 pages

**Prospects for Neutrino Oscillation Physics**, Silvia Pascoli and Thomas Schwetz  
Volume 2013, Article ID 503401, 29 pages

**Future Long-Baseline Neutrino Facilities and Detectors**, Milind Diwan, Rob Edgecock, Takuya Hasegawa, Thomas Patzak, Masato Shiozawa, and Jim Strait  
Volume 2013, Article ID 460123, 35 pages

**The Era of Kilometer-Scale Neutrino Detectors**, Francis Halzen and Uli Katz  
Volume 2013, Article ID 680584, 20 pages

**Neutrino Yukawa Textures within Type-I Seesaw**, Biswajit Adhikary and Probir Roy  
Volume 2013, Article ID 324756, 14 pages

**Current Direct Neutrino Mass Experiments**, G. Drexlin, V. Hannen, S. Mertens, and C. Weinheimer  
Volume 2013, Article ID 293986, 39 pages

**Geoneutrinos**, Ondřej Šrámek, William F. McDonough, and John G. Learned  
Volume 2012, Article ID 235686, 34 pages

**Search for GeV-Scale Sterile Neutrinos Responsible for Active Neutrino Oscillations and Baryon Asymmetry of the Universe**, S. N. Gninenko, D. S. Gorbunov, and M. E. Shaposhnikov  
Volume 2012, Article ID 718259, 17 pages

**Leptogenesis in the Universe**, Chee Sheng Fong, Enrico Nardi, and Antonio Riotto  
Volume 2012, Article ID 158303, 59 pages



---

**Neutrinos and Big Bang Nucleosynthesis**, Gary Steigman

Volume 2012, Article ID 268321, 24 pages

**Recent Developments in Neutrino/Antineutrino-Nucleus Interactions**, Jorge G. Morfin, Juan Nieves, and Jan T. Sobczyk

Volume 2012, Article ID 934597, 35 pages

**Charged-Current Neutrino-Nucleus Scattering off the Even Molybdenum Isotopes**, E. Ydrefors and J. Suhonen

Volume 2012, Article ID 373946, 15 pages

**Neutrino Mass from Cosmology**, Julien Lesgourgues and Sergio Pastor

Volume 2012, Article ID 608515, 34 pages

**Neutrinoless Double-Beta Decay**, Andrea Giuliani and Alfredo Poves

Volume 2012, Article ID 857016, 38 pages

**A Quantum Sensor for Neutrino Mass Measurements**, Juan Manuel Cornejo and Daniel Rodríguez

Volume 2012, Article ID 849497, 24 pages

**Solar Neutrino Observables Sensitive to Matter Effects**, H. Minakata and C. Peña-Garay

Volume 2012, Article ID 349686, 15 pages

**Atmospheric Neutrinos**, Takaaki Kajita

Volume 2012, Article ID 504715, 24 pages

**Electromagnetic Properties of Neutrinos**, C. Brogini, C. Giunti, and A. Studenikin

Volume 2012, Article ID 459526, 47 pages

**The Results of Search for the Neutrino Magnetic Moment in GEMMA Experiment**, A. G. Beda, V. B. Brudanin, V. G. Egorov, D. V. Medvedev, V. S. Pogosov, M. V. Shirchenko, and A. S. Starostin

Volume 2012, Article ID 350150, 12 pages

## Editorial

# Neutrino Physics

**Jose Bernabeu,<sup>1,2</sup> Gian Luigi Fogli,<sup>3,4</sup> Arthur B. McDonald,<sup>5</sup> and Koichiro Nishikawa<sup>6</sup>**

<sup>1</sup> Department of Physics, University of Valencia, C/Dr. Moliner 50, Burjassot, 46100 Valencia, Spain

<sup>2</sup> Instituto de Física Corpuscular, Universitat de Valencia-Consejo Superior de Investigaciones Científicas (UV-CSIC), C/Catedrático José Beltrán 2, Paterna, 46980 Valencia, Spain

<sup>3</sup> Dipartimento Interateneo di Fisica “Michelangelo Merlin”, Università di Bari, Via Amendola 173, 70126 Bari, Italy

<sup>4</sup> Istituto Nazionale di Fisica Nucleare, Sezione di Bari, Via Orabona 4, 70126 Bari, Italy

<sup>5</sup> Department of Physics, Engineering Physics and Astronomy, Stirling Hall, Queen's University, Kingston, ON, Canada K7L 3N6

<sup>6</sup> Institute of Particle and Nuclear Studies, High Energy Accelerator Research Organization (KEK), 1-1 Oho, Tsukuba 305-0801, Ibaraki, Japan

Correspondence should be addressed to Jose Bernabeu; [jose.bernabeu@uv.es](mailto:jose.bernabeu@uv.es)

Received 20 January 2013; Accepted 20 January 2013

Copyright © 2013 Jose Bernabeu et al. This is an open access article distributed under the Creative Commons Attribution License, which permits unrestricted use, distribution, and reproduction in any medium, provided the original work is properly cited.

Neutrino physics has provided very impressive progress in our understanding of particle physics during recent years. These advances are of primary relevance for a better description of neutrino properties, and presumably they also contain profound implications in the general picture of fundamental interactions and their connections with astrophysics and cosmology. The central role of neutrinos is even more evident when considering that neutrino masses require physics beyond the standard theory. At present, however, we do not have a clear picture of such new physics and its energy scale.

Recently the connecting mixing angle  $\theta_{13}$  between the atmospheric and solar sectors has been determined to be relatively large. This opens exciting possibilities for upcoming neutrino oscillation experiments addressing fundamental questions like the neutrino mass hierarchy and the search for CP violation in the lepton world. The present volume of contributions contains original research articles as well as review papers able to stimulate the continuing advance of knowledge in this field and the prospects and strategies for the next future. These articles describe all facets of this broad field, being experimentally developed with both terrestrial accelerators and astroparticle sources, studies in underground laboratories and including the theoretical scenario.

The paper “*The nature of massive neutrinos*” by S. T. Petcov reviews the compelling experimental evidence for oscillations of solar, reactor, atmospheric, and accelerator neutrinos implying the existence of 3-neutrino mixing in the weak-charged lepton current. The properties of massive

Majorana neutrinos and of their various possible couplings are discussed in detail. Two models of neutrino mass generation with massive Majorana neutrinos, the type I see-saw and the Higgs triplet model, are briefly reviewed. The problem of determining the nature, Dirac or Majorana, of massive neutrinos is considered. The predictions for the effective Majorana mass in neutrinoless double beta decay in the case of 3-neutrino mixing and massive Majorana neutrinos are summarised. The open questions and the main goals of future research in the field of neutrino physics are outlined.

The paper “*Neutrinoless double-beta decay*” by A. Giuliani and A. Poves discusses the current state and future prospects for experiments and theory for measurements of this unique process which has not yet been clearly observed. Neutrinoless double beta decay is energetically allowed for a limited set of nuclei and can only take place if the neutrino is a Majorana particle and has a finite mass. The half life for the process is in excess of  $10^{24}$  years and is very hard to measure. However, a measurement can provide a sensitive determination of an effective mass which is a combination of masses and mixing parameters for the three neutrino mass eigenstates. Combining this with oscillation measurements could provide absolute masses for all three eigenstates.

The paper “*Atmospheric neutrinos*” by T. Kajita discusses production and detection of atmospheric neutrinos. Atmospheric neutrino experiments were the first ones to find neutrino oscillation. The zenith-angle and energy-dependent deficit of muon neutrino events was found in such a way that neutrino oscillations between muon neutrinos and tau



neutrinos explain these data well. This article discusses atmospheric neutrino experiments and the future possibilities of the neutrino oscillation studies with them.

In the paper “*Neutrino propagation in matter*”, by M. Blennow and A. Y. Smirnov, the authors describe in detail the effects of neutrino propagation in the matter of the Earth, relevant for experiments with atmospheric and accelerator neutrinos aiming at the determination of the neutrino mass hierarchy and CP violation. The results of semianalytic descriptions of flavor transitions for the cases of small density perturbations in the limit of large densities and for small density widths are included. In particular the possibility of identifying the neutrino mass hierarchy with atmospheric neutrinos through multimegaton scale detectors having low energy thresholds and with future accelerator experiments is explored.

The paper “*Solar neutrinos*” by V. Antonelli et al. discusses the past history, current status and future prospects for experiment and theory of neutrinos produced by nuclear reactions in the sun. Measurements of these solar neutrinos have provided fundamental information about neutrino properties and about solar models. There are prospects for extending this information in future measurements described in the paper.

The paper “*Solar neutrino observables sensitive to matter effects*” by H. Minakata and C. Peña-Garay discusses the interaction of solar neutrinos with matter in the sun. Such neutrino propagation in matter is described quite well by the Mikheyev-Smirnov-Wolfenstein (MSW) theory and the paper discusses present and future measurements that can test this theory in more detail, as well as providing information on neutrino properties and solar models via matter interactions.

The article “*Reactor neutrinos*” by S.-B. Kim et al. reviews the status and the results of reactor neutrino experiments. Middle and long baseline oscillation experiments provided very recently the most precise determination of the neutrino mixing angle  $\theta_{13}$  and measurements of  $\theta_{12}$  and  $\Delta m^2$ . This paper also provides an overview of the upcoming experiments and of the projects under development, including the determination of the neutrino mass hierarchy and the possible use of neutrinos for society, for non proliferation of nuclear materials and geophysics.

The paper “*Long-baseline neutrino oscillation experiments*” by G. Feldman et al. is a review of long-baseline accelerator neutrino oscillation experiments, including all experiments performed to date and the projected sensitivity of those currently in progress. Accelerator experiments have played a crucial role in the confirmation of the neutrino oscillation phenomenon and in precision measurements of the parameters. Evidence for electron neutrino appearance has recently been obtained, opening the door for determining the mass hierarchy and the CP violating phase: some of the last unknown parameters of the standard model extended to include neutrino mass.

The paper “*Sterile neutrino fits to short baseline neutrino oscillation measurements*” by J. M. Conrad et al. reviews short-baseline oscillation experiments as interpreted within

the context of one, two, and three sterile neutrino models associated with additional neutrino mass states in the 1 eV range. It is shown that while fitting short-baseline data sets to a  $(3 + 3)$  model, defined by three active and three sterile neutrinos, yields the highest quality overall, it still finds inconsistencies with the MiniBooNE appearance data sets. These results motivate the pursuit of further short-baseline experiments, such as those reviewed in this paper.

The interesting subject of sterile neutrinos is discussed for a different energy scale in the article “*Search for GeV-scale sterile neutrinos responsible for active neutrino masses and baryon asymmetry of the universe*” by D. S. Gorbunov et al. In particular, the authors provide a motivation for the existence of three new neutral Majorana particles (sterile neutrinos), associated with simultaneous solution of the problems of neutrino masses and oscillations, of baryon asymmetry of the universe, and of dark matter. A new beam-target experiment is proposed to search for new physics beyond the Standard Model below the Fermi scale, which may lead to discovery of these right-handed partners of the known neutrinos.

The paper “*Current direct neutrino mass experiments*” by G. Drexlin et al. discusses the measurement of neutrino mass through very sensitive experiments examining the distortion of beta decay spectra near the end point via various techniques. The present status and future prospects for techniques using electrostatic retardation or low-temperature bolometers form the principal discussion, with other more unusual techniques included for possible future measurements.

One important input in the determination of the absolute neutrino masses is an accurate Q-value of the beta or electron capture decay. This can be done, from the difference of the masses of the parent and the daughter nuclei, by means of Penning traps. In the paper “*A quantum sensor for neutrino mass measurements*” by J. M. Cornejo and D. Rodriguez, a novel device with unprecedented accuracy and sensitivity is presented. The method can also be applied to the search of the resonant enhancement mechanism for the neutrinoless double electron capture candidates.

In the paper “*Neutrino mass from cosmology*” by J. Lesgourgues and S. Pastor, the authors discuss the important role played by neutrinos in the evolution of the Universe, modifying some of the cosmological observables. In this contribution the main aspects of cosmological relic neutrinos are summarized. The precision of present cosmological data can be used to learn about neutrino properties, in particular their mass, providing complementary information to beta decay and neutrinoless double beta decay experiments. The authors show how the analysis of current cosmological observations, such as the anisotropies of the cosmic microwave background or the distribution of large-scale structure, provide an upper bound on the sum of neutrino masses of order 1 eV or less, with very good perspectives from future cosmological measurements which are expected to be sensitive to neutrino masses well into the sub-eV range.

In “*Neutrinos and Big Bang nucleosynthesis*” by G. Steigman, the major role of neutrinos in the early universe is discussed in detail, including effects on abundances of light elements formed at this time and the relationship of these abundances to the total number of neutrino types.

The paper “*The Era of kilometer-scale neutrino detectors*” by F. Halzen and U. Katz discusses the scientific missions of IceCube and KM3NeT instruments, which include such varied tasks as the search for sources of cosmic rays, the observation of Galactic supernova explosions, the search for dark matter, and the study of the neutrinos themselves. Identifying the accelerators that produce the Galactic and extragalactic cosmic rays has been a priority mission of several generations of high-energy gamma-ray and neutrino telescopes; success has been elusive so far. Detecting the gamma-ray and neutrino fluxes associated with cosmic rays reaches a new watershed with the completion of IceCube, the first neutrino detector with sensitivity to the anticipated fluxes. In this review, the authors first revisit the rationale for constructing kilometer-scale neutrino detectors and subsequently recall the methods for determining the arrival direction, energy, and flavor of neutrinos. The architecture of the IceCube and KM3NeT detectors is described.

The measurement of electron antineutrinos from the decay of Uranium, Thorium and other elements in the earth can be used to determine the abundances of these elements in the crust and mantle and their contribution to the total heat flow in the earth. The past, present, and future experimental and theoretical status is discussed in detail in “*Geoneutrinos*” by O. Šrámek et al., including the importance of these measurements for our understanding of the geophysics of the earth.

The paper “*Neutrino Yukawa textures within type-I see-saw*” by B. Adhikary and P. Roy presents a classification of possible texture zeros in the Dirac neutrino mass matrix of the see-saw mechanism, given the basis where the charged lepton mass matrix and the right-handed Majorana neutrino mass matrix are both diagonal. Such a study is important in view of current experimental progress in determining the active (light) neutrino mixing angles, in particular a relatively large value of  $\theta_{13}$ . Accordingly, the masses and Majorana phases of ultralight neutrinos are predicted within definite ranges and the rate of the neutrinoless double beta decay, though generally below the reach of planned experiments, is seen to approach it in some parametric regions.

In the paper “*Leptogenesis in the Universe*” by C. S. Fong et al., the main aspects of leptogenesis are considered, that is, the class of scenarios in which the cosmic baryon asymmetry originates from an initial lepton asymmetry related to the decay of heavy sterile neutrinos in the early Universe. The authors describe why leptogenesis is an appealing mechanism for baryogenesis, by reviewing motivations, basic ingredients, and specifically related effects. Leptogenesis in supersymmetric scenarios is also addressed, as well as some other popular variations of the basic leptogenesis framework.

In the paper “*Electromagnetic properties of neutrinos*” by C. Brogini et al., the authors discuss the main theoretical aspects and experimental effects of neutrino electromagnetic properties. A general description of the electromagnetic form factors of Dirac and Majorana neutrinos is given. Then, the theory and phenomenology of the magnetic and electric dipole moments is presented, summarizing the experimental results and the theoretical predictions. They discuss also the phenomenology of a neutrino charge radius and radiative

decay. Finally, the theory of neutrino spin and spin-flavor precession in a transverse magnetic field is developed, summarizing its phenomenological applications.

In “*The results of a search for the neutrino magnetic moment in the GEMMA experiment*” by A. Georgievich Beda et al., an upper limit for the neutrino magnetic moment is presented from a measurement at the Kalinin Nuclear Power Plant (KNPP) with the GEMMA spectrometer.

There is a large interest in neutrino interactions in the intermediate energy region, motivated by the need in neutrino oscillation experiments to reduce systematic errors. The subject is reviewed in the paper “*Recent developments in neutrino/antineutrino-nucleus interactions*” by J. G. Morfin et al. They discuss recent inclusive measurements in the lower energy region and then concentrate on exclusive states in the increasing of the mass of the hadronic system, giving in this way an exhaustive review of the current theoretical and experimental situation of neutrino interactions in this energy region.

Neutrinos from supernovae are important probes not only of the currently unknown supernova mechanism but also of neutrino properties. In the paper “*Charged-current neutrino-nucleus scattering off the even molybdenum isotopes*”, E. Ydrefors and J. Suhonen compute the cross-sections of the above processes for an extensive set of neutrino energies, thus obtaining the nuclear responses to supernova neutrinos by folding these cross-sections with a Fermi-Dirac distribution.

The article “*Prospects for neutrino oscillation physics*” by S. Pascoli and T. Schwetz reviews the phenomenology of neutrino oscillations, focusing on subleading effects, which will be the key towards the goals of the determination of the type of the neutrino mass hierarchy and the search for CP violation in the lepton sector. Starting from a discussion of the present determination of three-flavour oscillation parameters, an outlook of the potential of near term oscillation physics is given, as well as on the long-term program towards possible future precision oscillation facilities. Accelerator driven long-baseline experiments as well as nonaccelerator possibilities from atmospheric and reactor neutrinos are discussed.

The article “*Future long-baseline neutrino facilities and detectors*” by M. Diwan et al. discusses the next generation neutrino detectors and neutrino beam facilities. These facilities will address two aspects: the fundamental properties of neutrinos like mass hierarchy, mixing angles, and the CP phase, as well as low-energy neutrino astronomy with solar, atmospheric, and supernova neutrinos. A new detector naturally allows for major improvements in the search for nucleon decay. A next generation neutrino observatory needs a huge detector, which in turn has to be installed in a new international underground laboratory capable of hosting such a huge detector.

Jose Bernabeu  
Gian Luigi Fogli  
Arthur B. McDonald  
Koichiro Nishikawa

## Review Article

# Reactor Neutrinos

Soo-Bong Kim,<sup>1</sup> Thierry Lasserre,<sup>2</sup> and Yifang Wang<sup>3</sup>

<sup>1</sup> KNRC, Department of Physics and Astronomy, Seoul National University, Seoul 151-742, Republic of Korea

<sup>2</sup> CEA, Irfu, SPP, Centre de Saclay, 91191 Gif-sur-Yvette, France and Astroparticule et Cosmologie APC, 10 rue Alice Domon et Léonie Duquet, 75205 Paris Cedex 13, France

<sup>3</sup> Institute of High Energy Physics, Yu-Quan road 19B, Beijing 100049, China

Correspondence should be addressed to Yifang Wang; yfwang@ihep.ac.cn

Received 18 August 2012; Accepted 20 December 2012

Academic Editor: Koichiro Nishikawa

Copyright © 2013 Soo-Bong Kim et al. This is an open access article distributed under the Creative Commons Attribution License, which permits unrestricted use, distribution, and reproduction in any medium, provided the original work is properly cited.

We review the status and the results of reactor neutrino experiments. Short-baseline experiments have provided the measurement of the reactor neutrino spectrum, and their interest has been recently revived by the discovery of the reactor antineutrino anomaly, a discrepancy between the reactor neutrino flux state of the art prediction and the measurements at baselines shorter than one kilometer. Middle and long-baseline oscillation experiments at Daya Bay, Double Chooz, and RENO provided very recently the most precise determination of the neutrino mixing angle  $\theta_{13}$ . This paper provides an overview of the upcoming experiments and of the projects under development, including the determination of the neutrino mass hierarchy and the possible use of neutrinos for society, for nonproliferation of nuclear materials, and geophysics.

### 1. Introduction: 80 Years of Reactor Neutrino Physics

Invented by Pauli [1] in 1930, named by Amaldi in 1934, and later modeled in the Fermi theory of beta decay [2]. The weakly coupling neutrino was first searched for by Reines and Cowan. Starting at the Hanford nuclear reactor (Washington), they later moved to the new Savannah River Plant (South Carolina) to perform their definitive and ground-breaking experimental detection. This breakthrough had two important consequences: resolving and clarifying the unsatisfactory situation of a fundamental particle needed for the consistency of theory, but first thought to be unobservable, and demonstrating the possibility of using neutrinos as a sensitive probe of particle physics. Indeed, several years after the completion of the pioneering, Reines and Cowan's work neutrinos were beginning to be used regularly to investigate the weak interactions, the structure of nucleons, and the properties of their constituent quarks.

In the first crude experiment of 1953 [3], Reines and Cowan's goal was to demonstrate unambiguously a reaction caused in a target by a neutrino produced elsewhere. The experiment pioneered the delayed coincidence technique to search for the reaction:  $\bar{\nu}_e + p \rightarrow e^+ + n$ , where an electron

antineutrino from the Hanford nuclear reactor interacted with a free proton in a large tank filled with cadmium-loaded liquid scintillator. The positron and the resultant annihilation gamma rays are detected as a prompt signal, while the neutron is thermalized in the liquid scintillator and subsequently captured by the cadmium. The excited nucleus then emits gamma radiation which is detected as the delayed signal. The first result, at two standard deviations, was followed in 1956 and 1958 by more precise experiments [4–6], where the significance improved to over four standard deviations. In addition to the detection, the reaction cross-section was measured to be  $11 \pm 2.6 \times 10^{-44} \text{ cm}^2$  [6]. Nowadays, reactor neutrinos like Daya Bay, KamLAND, or Double Chooz are still detected through similar experimental methods.

### 2. Nuclear Reactors and Neutrinos

Nuclear reactors are very intense sources of neutrinos that have been used all along the neutrino's history, from its discovery up to the most recent oscillation studies. With an average energy of about 200 MeV released per fission and 6 neutrinos produced along the  $\beta$ -decay chains of the fission



products, one expects about  $2 \times 10^{20}$   $\nu$ /s emitted in a  $4\pi$  solid angle from a 1 GW reactor (thermal power). Since unstable fission products are neutron-rich nuclei, all  $\beta$  decays are of  $\beta^-$  type, and the neutrino flux is actually pure electronic antineutrinos ( $\bar{\nu}_e$ ).

The neutrino oscillation search at a reactor is always based on a disappearance measurement, using the powerful inverse beta decay (IBD) detection process to discriminate the neutrino signal from backgrounds. The observed neutrino spectrum at a distance  $L$  from a reactor is compared to the expected spectrum. If a deficit is measured, it can be interpreted in terms of the disappearance probability which, in the two neutrino mixing approximation, reduces to

$$P_{ee} = 1 - \sin^2 2\theta \sin^2 \left( \frac{\Delta m^2 L}{4E} \right), \quad (1)$$

where  $\Delta m^2$  is the difference between the squared masses of the two neutrino states and  $\theta$  is the mixing angle fixing the amplitude of the oscillation.

Here, we will especially consider reactor antineutrino detector at short distances below 100 m from the reactor core, in particular ILL-Grenoble, Goesgen, Rovno, Krasnoyarsk, Savannah River, and Bugey [7–15]. These experiments have played an important role in the establishment of neutrino physics, and especially neutrino oscillations, over the last fifty years. Unlike modern long-baseline reactor experiments motivated by the measurement of the last unknown mixing angle  $\theta_{13}$  [16–18], which measure  $P_{ee}$  by comparing the event rate and spectrum in two detectors at different distances, the aforementioned short baseline experiments can only employ one detector and therefore depend on an accurate theoretical prediction for the emitted  $\bar{\nu}_e$  flux and spectrum to measure  $P_{ee}$ .

Until late 2010, all data from reactor neutrino experiments appeared to be fully consistent with the mixing of  $\nu_e$ ,  $\nu_\mu$ , and  $\nu_\tau$  with three mass eigenstates,  $\nu_1$ ,  $\nu_2$ , and  $\nu_3$ , with the squared mass differences  $|\Delta m_{31}^2| \simeq 2.4 \cdot 10^{-3} \text{eV}^2$  and  $\Delta m_{21}^2/|\Delta m_{31}^2| \simeq 0.032$ . The measured rate of  $\bar{\nu}_e$  was found to be in reasonable agreement with that predicted from the “old” reactor antineutrino spectra [19–21], though slightly lower than expected, with the measured/expected ratio at  $0.980 \pm 0.024$ , including recent revisions of the neutron mean lifetime,  $\tau_n = 881.5 \text{ s}$ , in 2011 (PDG).

In preparation for the Double Chooz reactor experiment [16], the Saclay reactor neutrino group reevaluated the specific reactor antineutrino flux for  $^{235}\text{U}$ ,  $^{239}\text{Pu}$ ,  $^{241}\text{Pu}$ , and  $^{238}\text{U}$ . In 2011, they reported their results [22], which correspond to a flux that is a few percent higher than the previous prediction. This also necessitates a reanalysis of the ratio of the observed event rate to the predicted rate for 19 published experiments at reactor-detector distances below 100 m.

**2.1. Reference Antineutrino Spectra.** Fission reactors release about  $10^{20}$   $\bar{\nu}_e$   $\text{GW}^{-1}\text{s}^{-1}$ , which mainly come from the beta

decays of the fission products of  $^{235}\text{U}$ ,  $^{238}\text{U}$ ,  $^{239}\text{Pu}$ , and  $^{241}\text{Pu}$ . The emitted antineutrino spectrum is then given by:

$$S_{\text{tot}}(E_\nu) = \sum_k f_k S_k(E_\nu), \quad (2)$$

where  $f_k$  refers to the contribution of the main fissile nuclei to the total number of fissions of the  $k$ th branch and  $S_k$  to their corresponding neutrino spectrum per fission.

The distribution of the fission products of uranium or plutonium isotopes covers hundreds of nuclei, each of them contributing to  $S_k(E)$  through various  $\beta$  decay chains. At the end the total antineutrino spectrum is a sum of thousands of  $\beta$ -branches weighted by the branching ratio of each transition and the fission yield of the parent nucleus. Despite the impressive amount of data available in nuclear databases, the *ab initio* calculation of the emitted antineutrino spectrum is difficult. Moreover, when looking at the detected spectrum through the IBD process, the 1.806 MeV threshold and the quadratic energy dependence of the cross-section enhance the contribution of transitions with large endpoints ( $E_0 > 4 \text{ MeV}$ ). Systematic errors of the nuclear data and the contribution of poorly known nuclei become a real limitation for the high energy part of the antineutrino spectrum. Uncertainties below the 10% level seem to be out of reach with the *ab initio* approach, preventing any accurate oscillation analysis.

In order to circumvent this issue, measurements of total  $\beta$  spectra of fissile isotopes were performed in the 1980s at ILL [19–21], a high flux research reactor in Grenoble, France. Thin target foils of fissile isotopes  $^{235}\text{U}$ ,  $^{239}\text{Pu}$  and  $^{241}\text{Pu}$ , were exposed to the intense thermal neutron flux of the reactor. A tiny part of the emitted electrons could exit the core through a straight vacuum pipe to be detected by the high resolution magnetic spectrometer BILL [23]. The electron rates were recorded by a pointwise measurement of the spectrum in magnetic field steps of 50 keV, providing an excellent determination of the shape of the electron spectrum with subpercent statistical error. The published data were smoothed over 250 keV. Except for the highest energy bins with poor statistics, the dominant error was the absolute normalization, quoted around 3% (90% CL), with weak energy dependence.

In principle, the conversion of a  $\beta$ -spectrum into an antineutrino spectrum can be done using the energy conservation between the two leptons

$$E_e + E_\nu = E_0, \quad (3)$$

with  $E_0$ , the endpoint of the  $\beta$  transition. However this approach requires to know the contribution of all single branches in the ILL spectra and this information is not accessible from the integral measurement. Therefore a specific conversion procedure was developed using a set of 30 “virtual”  $\beta$ -branches, fitted on the data. The theoretical

expression for the electron spectrum of a virtual branch was of the form

$$S_{\text{virtual}}(Z, A, E_e) = \underbrace{K}_{\text{Norm.}} \times \underbrace{\mathcal{F}(Z, A, E_e)}_{\text{Fermi function}} \times \underbrace{p_e E_e (E_e - E_0)^2}_{\text{Phasespace}} \times \underbrace{(1 + \delta(Z, A, E_e))}_{\text{Correction}}, \quad (4)$$

where  $Z$  and  $A$  are the charge and atomic number of the parent nucleus and  $E_0$  is the endpoint of the transition. The origin of each term is described by the underbraces. The  $\delta$  term contains the corrections to the Fermi theory. In the ILL papers, it included the QED radiative corrections as calculated in [24]. The  $Z$  dependence comes from the Coulomb corrections. Since a virtual branch is not connected to any real nucleus, the choice of the nuclear charge was described by the observed mean dependence of  $Z$  on  $E_0$  in the nuclear databases

$$Z(E_0) = 49.5 - 0.7E_0 - 0.09E_0^2, \quad Z \leq 34. \quad (5)$$

The  $A$  dependence is weaker and linked to the determination of  $Z$  through global nuclear fits.

Once the sum of the 30 virtual branches is fitted to the electron data, each of them is converted to an antineutrino branch by substituting  $E_e$  by  $E_0 - E_\nu$  in (4) and applying the correct radiative corrections. The predicted antineutrino spectrum is the sum of all converted branches. At the end of this procedure, an extra correction term is implemented in an effective way as

$$\Delta S_{\text{branch}}(E_\nu) \approx 0.65 (E_\nu - 4.00) \%. \quad (6)$$

This term is an approximation of the global effect of weak magnetism correction and finite size Coulomb correction [25].

The final error of the conversion procedure was estimated to be 3-4% (90% CL), to be added in quadrature with the electron calibration error which directly propagates to the antineutrino prediction. From these reference spectra, the expected antineutrino spectrum detected at a reactor can be computed. All experiments performed at reactors since then relied on these reference spectra to compute their predicted antineutrino spectrum.

**2.2. New Reference Antineutrino Spectra.** Triggered by the need for an accurate prediction of the reactor antineutrino flux for the first phase of the Double Chooz experiment, with a far detector only, the determination of antineutrino reference spectra has been revisited lately [22]. In a first attempt, a compilation of the most recent nuclear data was performed for an up-to-date *ab initio* calculation of the antineutrino fission spectra. The asset of this approach is the knowledge of each individual  $\beta$  branch, providing a perfect control of the conversion between electron and antineutrino spectra. As a powerful cross-check, the sum of all the branches must match the very accurate electron spectra measured at ILL. Despite the tremendous amount of nuclear data available, this approach failed to meet the required accuracy of few % for two main reasons as follows.

- (i) The majority of the  $\beta$  decays are measured using  $\beta$ - $\gamma$  coincidences, which are sensitive to the so-called pandemonium effect [26]. The net result is an experimental bias of the shape of the energy spectra, with the high energy part being overestimated relative to the low energy part. New measurements are ongoing with dedicated experimental setups to correct for the pandemonium effect, but in the case of the reference spectra many unstable nuclei have to be studied.
- (ii) As mentioned above, an important fraction of the detected neutrinos has a large energy ( $>4$  MeV). The associated  $\beta$  transitions mostly come from very unstable nuclei with a large energy gap between the parent ground state and the nuclear levels of the daughter nucleus. Their decay scheme is often poorly known or even not measured at all.

A reference data set was constituted based on all fission products indexed in the ENSDF database [27]. All nuclei measured separately to correct for the pandemonium effect were substituted when not in agreement with the ENSDF data (67 nuclei from [28] and 29 nuclei from [29]). A dedicated interface, BESTIOLE, reads the relevant information of this set of almost 10000  $\beta$ -branches and computes their energy spectrum based on (4). Then, the total beta spectrum of one fissioning isotope is built as the sum of all fission fragment spectra is weighted by their activity. These activities are determined using a simulation package called MCNP Utility for Reactor Evolution (MURE [30]). Following this procedure, the predicted fission spectrum is about 90% of the reference ILL  $\beta$  spectra, as illustrated in Figure 2 for the  $^{235}\text{U}$  isotope. The missing contribution is the image of all unmeasured decays as well as the remaining experimental biases of the measurements. To fill the gap one can invoke models of the decay scheme of missing fission products. Reaching a good agreement with the ILL electron data remains difficult with this approach.

Another way to fill the gap is to fit the missing contribution in the electron spectrum with few virtual branches. The same ILL procedure can be used except that the virtual branches now rest on the base of physical transitions. This mixed approach combines the assets of *ab initio* and virtual branches methods as follows.

- (i) The prediction still matches accurately the reference electron data from the ILL measurements.
- (ii) 90% of the spectrum is built with measured  $\beta$  transitions with “true” distributions of endpoint, branching ratios, nuclear charges, and so forth. This suppresses the impact of the approximations associated with the use of virtual beta branches.
- (iii) All corrections to the Fermi theory are applied at the branch level, preserving the correspondence between the reference electron data and the predicted antineutrino spectrum.

The new predicted antineutrino spectra are found about 3% above the ILL spectra. This effect is comparable for the 3 isotopes ( $^{235}\text{U}$ ,  $^{239}\text{Pu}$ , and  $^{241}\text{Pu}$ ) with little energy

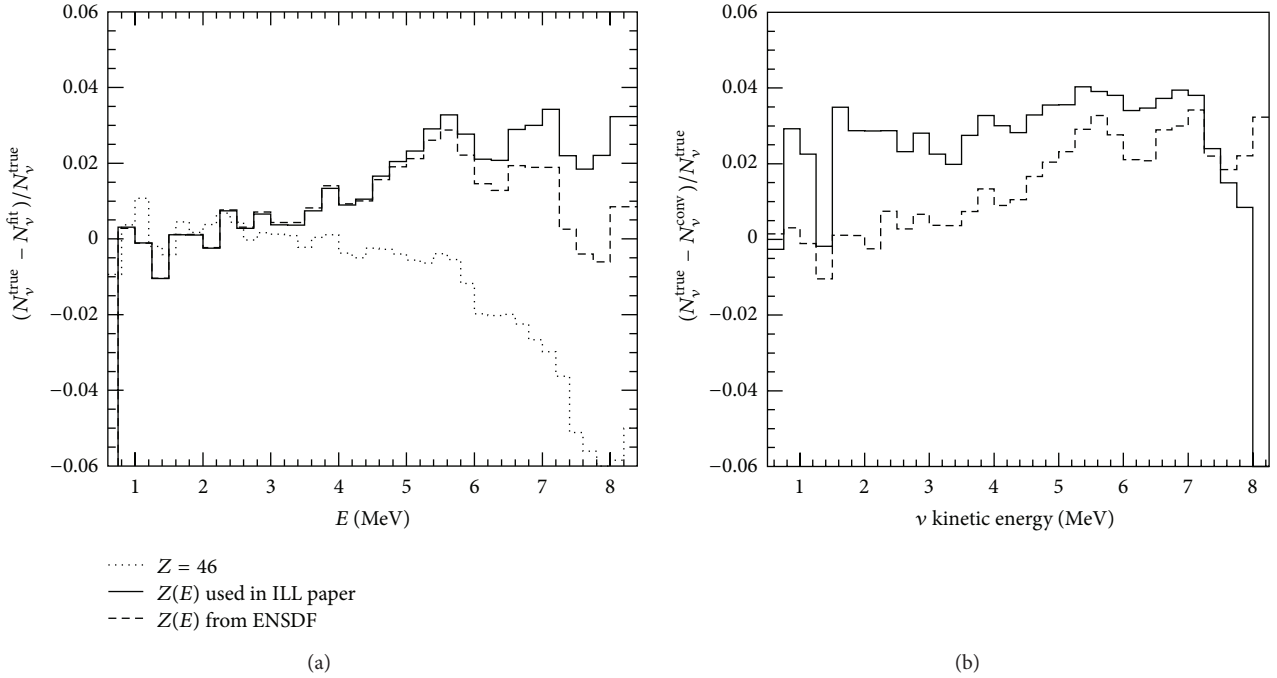


FIGURE 1: Numerical tests of the conversion-induced deviations from a “true” spectrum built from a set of known branches (see text for details). (a) Effect of various  $Z(E)$  polynomials used in the formula of the virtual branches. (b) Deviation of converted spectra with the effective correction of (6) (solid line) or with the correction applied at the branch level.

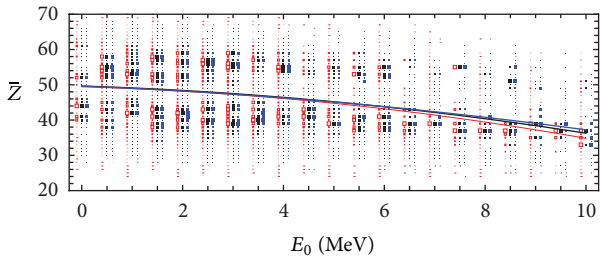


FIGURE 2: The effective nuclear charge  $\bar{Z}$  of the fission fragments of  $^{235}\text{U}$  as a function of  $E_0$ . The area of the each box is proportional to the contribution of that particular  $Z$  to the fission yield in that energy bin. The lines are fits of quadratic polynomials. Black color-ENSDF database; other colors illustrate the small sensitivity to different treatment of the missing isotopes.

dependence. The origin and the amplitude of this bias could be numerically studied in detail following a method initially developed in [31]. A “true” electron spectrum is defined as the sum of all measured branches. Since all the branches are known, the “true” antineutrino spectrum is perfectly defined as well, with no uncertainty from the conversion. Applying the exact same conversion procedure than in the eighties on this new electron reference confirms the 3% shift between the converted antineutrino spectrum and the “true” spectrum.

Further tests have shown that this global 3% shift is actually a combination of two effects. At high energy ( $E > 4$  MeV), the proper distribution of nuclear charges, provided by the dominant contribution of the physical  $\beta$ -branches,

induces a 3% increase of the predicted antineutrino spectrum. On the low energy side, it was shown that the effective linear correction of (6) was not accounting for the cancellations operating between the numerous physical branches when the correction is applied at the branch level (see Figure 1).

Beyond the correction of these above biases, the uncertainty of the new fission antineutrino spectra couldn’t be reduced with respect to the initial predictions. The normalisation of the ILL electron data, a dominant source of error, is inherent to any conversion procedure using the electron reference. Then, a drawback of the extensive use of measured  $\beta$ -branches in the mixed approach is that it brings important constraints on the missing contribution to reach the electron data. In particular, the induced missing shape can be difficult to fit with virtual branches, preventing a perfect match with the electron reference. These electron residuals are unfortunately amplified as spurious oscillations in the predicted antineutrino spectrum leading to comparable conversion uncertainties (see red curve in Figure 3). Finally, the correction of the weak magnetism effect is calculated in a quite crude way, and the same approximations are used since the eighties.

In the light of the above results, the initial conversion procedure of the ILL data was revisited [32]. It was shown that a fit using only virtual branches with a judicious choice of the effective nuclear charge could provide results with minimum bias. A mean fit similar to (5) is still used, but the nuclear charge of all known branches is now weighted by its contribution in the total spectrum, that is, the associated fission yield. As shown in Figure 2, the result is quite stable under various assumptions for the weighting of poorly known



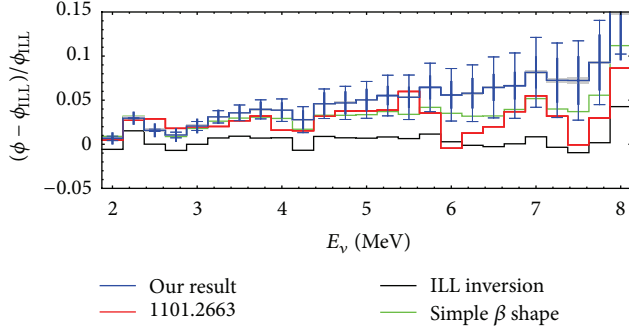


FIGURE 3: Comparison of different conversions of the ILL electron data for  $^{235}\text{U}$ . Black curve: cross-check of results from [19] following the same procedure. Red curve: results from [22]. Green curve: results from [32] using the same description of  $\beta$  decay as in [22]. Blue curve: update of the results from [22], including corrections to the Fermi theory as explained in the text. The thin error bars show the theory errors from the effective nuclear charge  $Z$  and weak magnetism. The thick error bars are the statistical errors.

nuclei. The bias illustrated in the left plot of Figure 1 is corrected.

The second bias (Figure 1(b)) is again corrected by implementing the corrections to the Fermi theory at the branch level rather than using effective corrections as in (6). Using the same expression of these corrections than in [22], the two independent new predictions are in very good agreement (Figure 3), confirming the 3% global shift. Note that the spurious oscillations of the Mueller et al. spectra are flattened out by this new conversion because of the better zeroing of electron residuals.

A detailed review of all corrections to the Fermi theory is provided in [32] including finite size corrections, screening correction, radiative corrections, and weak magnetism. To a good approximation, they all appear as linear correction terms as illustrated in Figure 4 in the case of a 10 MeV endpoint energy. This refined study of all corrections leads to an extra increase of the predicted antineutrino spectra at high energy as illustrated by the blue curve in Figure 3. The net effect is between 1.0% and 1.4% more detected antineutrinos depending on the isotope (see Table 1).

The corrections of Figure 4 are known with a good relative accuracy except for the weak magnetism term. At the present time, a universal slope factor of about 0.5% per MeV is assumed, neglecting any dependence on nuclear structure [25]. Accurate calculation for every fission product is out of reach. Using the conserved vector current hypothesis, it is possible to infer the weak magnetism correction from the electromagnetic decay of isobaric analog states. Examples of the slope factors computed from the available data are shown in Table I of [32]. While most examples are in reasonable agreement with the above universal slope, some nuclei with large value of  $\log ft$  have a very large slope factor. Moreover, a review of the nuclear databases [33] shows that  $\beta$  transitions with  $\log ft > 7$  contribute between 15 and 30% to the total spectrum. Still the data on the weak magnetism slopes are scarce, and none of them corresponds to fission products. At

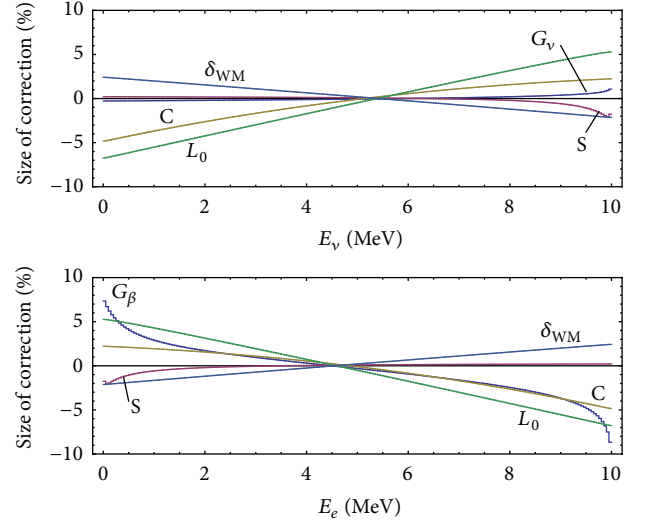


FIGURE 4: Shown is the relative size of the various corrections to the Fermi theory for a hypothetical  $\beta$  decay with  $Z = 46$ ,  $A = 117$ , and  $E_0 = 10$  MeV. The upper panel shows the effect on the antineutrino spectrum, whereas the lower panel shows the effect on the  $\beta$  spectrum.  $\delta_{\text{WM}}$ : weak magnetism correction;  $L_0$ , C: Coulomb and weak interaction finite size corrections; S screening correction;  $G_{\nu,\beta}$ : radiative corrections.

TABLE 1: Relative change of the new predicted events rates with respect to the ILL reference (in %). The relative change of the emitted flux is always close to 3%, dominated by the few first bins because the energy spectra are dropping fast.

$(R_{\text{new}} - R_{\text{ILL}})/R_{\text{ILL}}$	$^{235}\text{U}$	$^{239}\text{Pu}$	$^{241}\text{Pu}$	$^{238}\text{U}$
Values from [22]	2.5	3.1	3.7	9.8
Values from [32]	3.7	4.2	4.7	—

this stage, it is difficult to conclude if the uncertainty of the weak magnetism correction should be inflated or not. The prescription of the ILL analysis, 100%, corresponds to about 1% of the detected neutrino rate. The best constraints could actually come from shape analysis of the reactor neutrino data themselves. The Bugey and Rovno data are accurate although detailed information on the detector response might be missing for such a detailed shape analysis. The combination of the upcoming Daya Bay, Double Chooz, and RENO data should soon set stringent limits on the global slope factor.

The error budget of the predicted spectra remains again comparable to the first ILL analysis. The normalization error of the electron data is a common contribution. The uncertainties of the conversion by virtual branches have been extensively studied and quantified based on the numerical approach. The uncertainty induced by the weak magnetism corrections is, *faute de mieux*, evaluated with the same 100% relative error. The final central values and errors are summarized in table [22].

**2.3. Off-Equilibrium Effects.** For an accurate analysis of reactor antineutrino data, an extra correction to the reference fission spectra has to be applied. It is often of the order of

the percent. It comes from the fact that the ILL spectra were acquired after a relatively short irradiation time, between 12 hours and 1.8 days depending on the isotopes, whereas in a reactor experiment the typical time scale is several months. A nonnegligible fraction of the fission products have a lifetime of several days. Therefore, the antineutrinos associated with their  $\beta$  decay keep accumulating well after the “photograph at 1 day” of the spectra taken at ILL. Very long-lived isotopes correspond to nuclei close to the bottom of the nuclear valley of stability. Hence, one naively expects these  $\beta$  transitions to contribute at low energy. For a quantitative estimate of this effect, the same simulations developed in [22] for the *ab initio* calculation of antineutrino spectra were used. The sensitivity to the nuclear ingredients is suppressed because only the relative changes between the ILL spectra and spectra of longer irradiations at commercial reactors were computed. The corrections to be applied are summarized in [22]. As expected, they concern the low energy part of the detected spectrum and vanish beyond 3.5 MeV. The corrections are larger for the  $^{235}\text{U}$  spectrum because its irradiation time, 12 h, is shorter than the others. The uncertainty was estimated from the comparison between the results of MURE and FISPAC codes as well as from the sensitivity to the simulated core geometry. A safe 30% relative error is recommended.

**2.4.  $^{238}\text{U}$  Reference Spectrum.** The  $^{238}\text{U}$  isotope is contributing to about 8% of the total number of fissions in a standard commercial reactor. These fissions are induced by fast neutrons therefore, their associated  $\beta$ -spectrum could not be measured in the purely thermal flux of ILL. A dedicated measurement in the fast neutron flux of the FRMII reactor in Munich has been completed and should be published in the coming months [34].

Meanwhile the *ab initio* calculation developed in [22] provides a useful prediction since the relatively small contribution of  $^{238}\text{U}$  can accommodate larger uncertainties in the predicted antineutrino spectrum. An optimal set of  $\beta$ -branches was tuned to match the ILL spectra of fissile isotopes as well as possible. The base of this data set consists of the ENSDF branches corrected for the pandemonium effect as described in Section 2.2. Missing  $\beta$  emitters are taken from the JENDL nuclear database [35], where they are calculated using the gross-theory [36]. Finally, the few remaining nuclei were described using a model based on fits of the distributions of the endpoints and branching ratios in the ENSDF database, then extrapolated to the exotic nuclei.

The comparison with the reference  $^{235}\text{U}$  ILL data shows that the predicted spectrum agrees with the reference at the  $\pm 10\%$  level.

Then, this optimal data set is used to predict a  $^{238}\text{U}$  spectrum. Again the activity of each fission product is calculated with the evolution code MURE. The case of an N4 commercial reactor operating for one year was simulated. After such a long irradiation time, the antineutrino spectrum has reached the equilibrium. The results are summarized in [22]. The central values are about 10% higher than the previous prediction proposed in [37]. This discrepancy might be due to the larger amount of nuclei taken into account in the

most recent work. Nevertheless, both results are comparable within the uncertainty of the prediction, roughly estimated from the deviation with respect to the ILL data and the sensitivity to the chosen data set.

**2.5. Summary of the New Reactor Antineutrino Flux Prediction.** In summary, a reevaluation of the reference antineutrino spectra associated to the fission of  $^{235}\text{U}$ ,  $^{239}\text{Pu}$ , and  $^{241}\text{Pu}$  isotopes [22] has revealed some systematic biases in the previously published conversion of the ILL electron data [19–21]. The net result is a  $\approx +3\%$  shift in the predicted emitted spectra. The origin of these biases was not in the principle of the conversion method but in the approximate treatment of nuclear data and corrections to the Fermi theory. A complementary work [32] confirmed the origin of the biases and showed that an extra correction term should be added increasing further the predicted antineutrino spectra at high energy. These most recent spectra are the new reference used for the analysis of the reactor anomaly in the next section. The prediction of the last isotope contributing to the neutrino flux of reactors,  $^{238}\text{U}$ , is also updated by *ab initio* calculations.

The new predicted spectra and their errors are presented in [22]. The deviations with respect to the old reference spectra are given in Table 1.

### 3. Investigating Neutrino Oscillations

**3.1. Exploring the Solar Oscillation.** The sun is a well-defined neutrino source to provide important opportunities of investigating nontrivial neutrino properties because of the wide range of matter density and the great distance from the sun to the earth. Precise measurement of solar neutrinos is a direct test of the standard solar model (SSM) that is developed from the stellar structure and evolution.

Solar neutrinos have been observed by several experiments: Homestake with a chlorine detector, SAGE, GALLEX and GNO with gallium detectors, Kamiokande and Super-Kamiokande with water Cherenkov detectors, and SNO with a heavy water detector. Most recently, Borexino has successfully observed low energy solar neutrinos with their energy spectrum using a liquid scintillator detector of ultra low radioactivity.

The first observation of solar neutrinos by the Homestake experiment demonstrated the significantly smaller measured flux than the SSM prediction, known as “the solar neutrino puzzle” at that time. SAGE, GALLEX, and GNO are sensitive to the most abundant *pp* solar neutrinos, and also observed the deficit. Kamiokande-II and Super-Kamiokande succeeded in real-time and directional measurement of solar neutrinos in a water Cherenkov detector. The solar neutrino problem was solved by SNO through the flavor-dependent measurement using heavy water. In 2001, the initial SNO charged current result combined with the Super-Kamiokande’s high-statistics  $\nu e$  elastic scattering result provided direct evidence for flavor conversion of solar neutrinos. The later SNO neutral current measurements further strengthened the conclusion. These results are consistent with those expected from the large mixing angle (LMA) solution of

solar neutrino oscillation in matter with  $\Delta m_{\text{sol}}^2 \sim 5 \times 10^{-5} \text{ eV}^2$  and  $\tan^2 \theta_{\text{sol}} \sim 0.45$ .

The KamLAND reactor neutrino experiment at a flux-weighted average distance of  $\sim 180 \text{ km}$  obtained a result of reactor antineutrino disappearance consistent with the LMA solar neutrino solution. The current solar neutrino and KamLAND data suggest that  $\Delta m_{21}^2 = (7.50 \pm 0.20) \times 10^{-5} \text{ eV}^2$  with a fractional error of 2.7% and  $\sin^2 2\theta_{12} = 0.857 \pm 0.024$  with a fractional error of 2.8%.

**3.2. Exploring the Atmospheric Oscillation.** The Super-Kamiokande obtained the first convincing evidence for the neutrino oscillation in the observation of the atmospheric neutrinos, in 1998. A clear deficit of atmospheric muon neutrino candidate events was observed in the zenith-angle distribution compared to the no-oscillation expectation. The distance-to-energy  $L/E$  distribution of the Super-Kamiokande data demonstrated  $\nu_\mu \leftrightarrow \nu_\tau$  oscillations and completely ruled out some of exotic explanations of the atmospheric neutrino disappearance such as neutrino decay and quantum decoherence.

Accelerator experiments can better measure the value of  $|\Delta m_{\text{atm}}^2|$  than the atmospheric neutrino observation due to a fixed baseline distance and a well-understood neutrino spectrum. K2K is the first long-baseline experiment to study  $\nu_\mu$  oscillations in the atmospheric  $\Delta m^2$  region with a neutrino path length exceeding hundreds of kilometers. MINOS is the second long-baseline experiment for the atmospheric neutrino oscillation using a  $\nu_\mu$  beam. The MINOS finds the atmospheric oscillation parameters as  $|\Delta m_{\text{atm}}^2| = (2.32^{+0.12}_{-0.08}) \times 10^{-3} \text{ eV}^2$  and  $\sin^2 2\theta_{\text{atm}} > 0.90$  at 90% C.L. OPERA using the CNGS  $\nu_\mu$  beam reported observation of one  $\nu_\tau$  candidate. T2K began a new long-baseline experiment in 2010, and is expected to measure  $|\Delta m_{\text{atm}}^2|$  and  $\sin^2 2\theta_{\text{atm}}$  even more precisely. Nova is expected to be in operation soon for the accurate measurement of atmospheric neutrino oscillation parameters.

The current atmospheric neutrino and accelerator data suggest that  $\Delta m_{32(31)}^2 = (2.32^{+0.12}_{-0.08}) \times 10^{-3} \text{ eV}^2$  with a fractional error of 4.3% and  $\sin^2 2\theta_{23} = 0.97 \pm 0.03$  with a fractional error of 3.1%.

**3.3. Measuring the Last and Smallest Neutrino Mixing Angle  $\theta_{13}$ .** In the presently accepted paradigm to describe the neutrino oscillations, there are three mixing angles ( $\theta_{12}$ ,  $\theta_{23}$ , and  $\theta_{13}$ ) and one phase angle ( $\delta$ ) in the Pontecorvo-Maki-Nakagawa-Sakata matrix [38–40]. It was until 2012 that  $\theta_{13}$  is the most poorly known and smallest mixing angle.

Measurements of  $\theta_{13}$  are possible using reactor neutrinos and accelerator neutrino beams. Reactor measurements have the property of determining  $\theta_{13}$  without the ambiguities associated matter effects and CP violation. In addition, the detector for a reactor measurement is not necessarily large, and the construction of a neutrino beam is not needed. The past reactor measurement had a single detector which was placed about 1 km from the reactors. The new generation reactor experiments, Daya Bay, Double Chooz, and RENO, using two detectors of 10 ~ 40 tons at near (300 ~ 400 m)

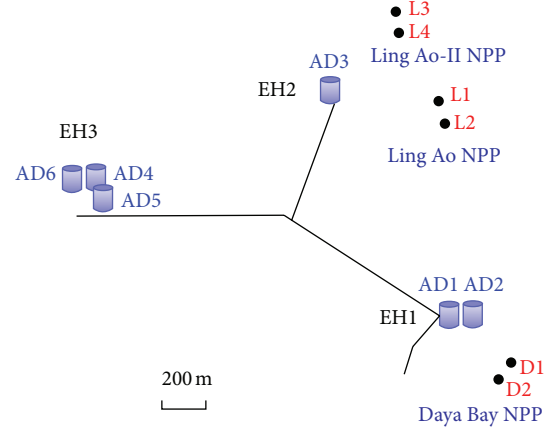


FIGURE 5: Layout of the Daya Bay experiment. The dots represent reactors, labeled as D1, D2, L1, L2, L3 and L4. Six ADs, AD1–AD6, are installed in three EHs.

and far (1 ~ 2 km) locations have significantly improved sensitivity for  $\theta_{13}$  down to the  $\sin^2(2\theta_{13}) \sim 0.01$  level. With  $\theta_{13}$  determined and measurements of  $\nu_\mu \rightarrow \nu_e$  and  $\bar{\nu}_\mu \rightarrow \bar{\nu}_e$  oscillations using accelerator neutrino beams impinging on large detectors at long baselines will improve the knowledge of  $\theta_{13}$  and also allow access to matter or CP violation effects.

Previous attempts at measuring  $\theta_{13}$  via neutrino oscillations have obtained only upper limits [41–43]; the CHOOZ [41, 42] and MINOS [44] experiments set the most stringent limits:  $\sin^2 2\theta_{13} < 0.15$  (90% C.L.). In 2011, indications of a nonzero  $\theta_{13}$  value were reported by two accelerator appearance experiments, T2K [45] and MINOS [46], and by the Double Chooz reactor disappearance experiment [47, 48]. Global analyses of all available neutrino oscillation data have indicated central values of  $\sin^2 2\theta_{13}$  that are between 0.05 and 0.1 (see e.g., [49, 50]). In 2012, Daya Bay and RENO reported definitive measurements of the neutrino oscillation mixing angle,  $\theta_{13}$ , based on the disappearance of electron antineutrinos emitted from reactors. The  $\theta_{13}$  measurements by the three reactor experiments are presented in the following sections.

## 4. Daya Bay

The Daya Bay collaboration announced on March 8, 2012, the discovery of a nonzero value for the last unknown neutrino mixing angle  $\theta_{13}$  [51], based on 55 days of data taking. It is consistent with previous and subsequent measurements [45–48, 52]. An improved analysis using 139 days of data is reported at international conferences, and a paper is now under preparation [53].

**4.1. The Experiment.** The Daya Bay nuclear power complex is located on the Southern coast of China, 55 km to the northeast of Hong Kong and 45 km to the East of Shenzhen. A detailed description of the Daya Bay experiment can be found in [54]. As shown in Figure 5, the nuclear complex consists of six pressurized water reactors grouped into three pairs with each pair referred to as a nuclear power plant (NPP). All six

TABLE 2: Vertical overburden, muon rate  $R_\mu$ , and average muon energy  $E_\mu$  of the three EHs and baselines from antineutrino detectors AD1-6 to reactors D1, D2, and L1-4 in meters.

Halls	Overburden (m.w.e)	$R_\mu$ (Hz/m <sup>2</sup> )	$E_\mu$ (GeV)	ADs	D1	D2	L1	L2	L3	L4
EH1	250	1.27	57	AD1	362	372	903	817	1354	1265
EH1	250	1.27	57	AD2	358	368	903	817	1354	1266
EH2	265	0.95	58	AD3	1332	1358	468	490	558	499
EH3	860	0.056	137	AD4	1920	1894	1533	1534	1551	1525
EH3	860	0.056	137	AD5	1918	1892	1535	1535	1555	1528
EH3	860	0.056	137	AD6	1925	1900	1539	1539	1556	1530

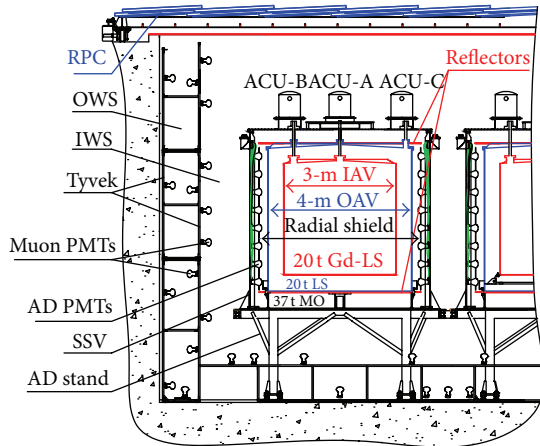


FIGURE 6: Schematic diagram of the Daya Bay detectors.

cores are functionally identical pressurized water reactors of 2.9 GW thermal power [55]. Three underground experimental halls (EHs) are connected with horizontal tunnels. Two antineutrino detectors (ADs) are located in EH1, two (only one installed at this moment) in EH2, and four (only three installed) ADs are positioned near the oscillation maximum in EH3 (the far hall). The baselines from six ADs to six cores are listed in Table 2. They are measured by several different techniques and cross-checked by independent groups, as described in [53]. The overburdens, the simulated muon rate, and average muon energy are also listed in Table 2.

The  $\bar{\nu}_e$ s are detected via the inverse  $\beta$  decay (IBD) reaction,  $\bar{\nu}_e + p \rightarrow e^+ + n$ , in a gadolinium-doped liquid scintillator (Gd-LS) [56–58]. Each AD has three nested cylindrical volumes separated by concentric acrylic vessels as shown in Figure 6. The innermost volume holds 20 t of 0.1% by weight Gd-LS that serves as the antineutrino target. The middle volume is called the gamma catcher and is filled with 21 t of undoped liquid scintillator (LS) for detecting gamma rays that escape the target volume. The outer volume contains 37 t of mineral oil (MO) to provide optical homogeneity and to shield the inner volumes from radiation originating, for example, from the photomultiplier tubes (PMTs) or the stainless steel containment vessel (SSV). There are 192 8-inch PMTs (Hamamatsu R5912) mounted on eight ladders installed along the circumference of the SSV and within the mineral oil volume. To improve uniformity, the PMTs

are recessed in a 3 mm thick black acrylic cylindrical shield located at the equator of the PMT bulb.

Three automated calibration units (ACU-A, ACU-B, and ACU-C) are mounted at the top of each SSV. Each ACU is equipped with a LED, a  $^{68}\text{Ge}$  source, and a combined source of  $^{241}\text{Am}$ - $^{13}\text{C}$  and  $^{60}\text{Co}$ . The Am-C source generates neutrons at a rate of 0.5 Hz. The rates of the  $^{60}\text{Co}$  and  $^{68}\text{Ge}$  sources are about 100 Hz and 15 Hz, respectively.

The muon detection system consists of a resistive plate chamber (RPC) tracker and a high-purity active water shield. The water shield consists of two optically separated regions known as the inner (IWS) and outer (OWS) water shields. Each region operates as an independent water Cherenkov detector. In addition to detecting muons that can produce spallation neutrons or other cosmogenic backgrounds in the ADs, the pool moderates neutrons and attenuates gamma rays produced in the rock or other structural materials in and around the experimental hall. At least 2.5 m of water surround the ADs in every direction. Each pool is outfitted with a light tight cover with dry nitrogen flowing underneath.

Each water pool is covered with an overlapping array of RPC modules [59] each with a size of  $2\text{ m} \times 2\text{ m}$ . There are four layers of bare RPCs inside each module. The strips have a “zigzag” design with an effective width of 25 cm and are stacked in alternating orientations providing a spatial resolution of  $\sim 8\text{ cm}$ .

Each detector unit (AD, IWS, OWS, and RPC) is read out with a separate VME crate. All PMT readout crates are physically identical, differing only in the number of instrumented readout channels. The front-end electronics board (FEE) receives raw signals from up to sixteen PMTs, sums the charge among all input channels, identifies over-threshold channels, records timing information on over-threshold channels, and measures the charge of each over-threshold pulse. The FEE in turn sends the number of channels over threshold and the integrated charge to the trigger system. When a trigger is issued, the FEE reads out the charge and timing information for each over-threshold channel, as well as the average ADC value over a 100 ns time-window immediately preceding the over-threshold condition (pre-ADC).

Triggers are primarily created internally within each PMT readout crate based on the number of over-threshold channels (Nhit) as well as the summed charge (E-Sum) from each FEE. The system is also capable of accepting external trigger requests, for example, from the calibration system.



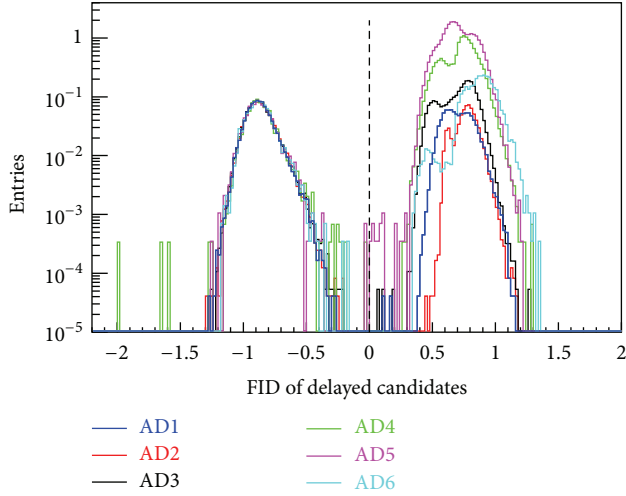


FIGURE 7: Discrimination of flasher events and IBD-delayed signals in the neutron energy region. The delayed signals of IBDs have the same distribution for all six ADs, while the flashers are different.

**4.2. Data, Monte Carlo Simulation, and Event Reconstruction.** The data used in this analysis were collected from December 24, 2011 through May 11, 2012.

The detector halls operated independently, linked only by a common clock and GPS timing system. As such, data from each hall were recorded separately and linked offline. Simultaneous operation of all three detector halls is required to minimize systematic effects associated with potential reactor power excursions.

Triggers were formed based either on the number of PMTs with signals above a  $\sim 0.25$  photoelectron (pe) threshold (Nhit triggers) or the charge sum of the over-threshold PMTs (E-Sum trigger).

A small number of AD PMTs, called flashers, spontaneously emit light, presumably due to a discharge within the base. The visible energy of such events covers a wide range, from sub-MeV to 100 MeV. Two features were typically observed when a PMT flashed. The observed charge for a given PMT was very high with light seen by the surrounding PMTs, and PMTs on the opposite side of the AD saw light from the flasher.

To reject flasher events, a flasher identification variable (FID) was constructed. Figure 7 shows the discrimination of flasher events for the delayed signal of IBD candidates. The inefficiency for selection was estimated to be 0.02%. The uncorrelated uncertainties among ADs were estimated to be 0.01%. The contamination of the IBD selection was evaluated to be  $< 10^{-4}$ .

The AD energy response has a time dependence, a detector spatial dependence (nonuniformity), and a particle species and energy dependence (nonlinearity). The goal of energy reconstruction was to correct these dependences in order to minimize the AD energy scale uncertainty. The LEDs were utilized for PMT gain calibration, while the energy scale was determined with a  $^{60}\text{Co}$  source deployed at the detector center. The sources were deployed once per week to check for and correct any time dependence.

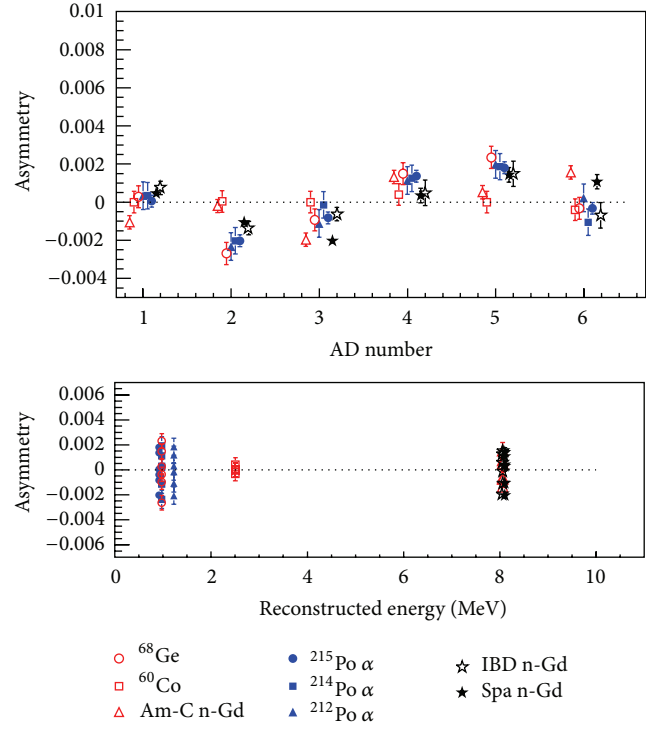


FIGURE 8: Asymmetry values for all six ADs. The sources  $^{68}\text{Ge}$ ,  $^{60}\text{Co}$ , and Am-C were deployed at the detector center. The alphas from polonium decay and neutron capture on gadolinium from IBD and spallation neutrons were uniformly distributed within each detector. Differences between these sources are due to spatial nonuniformity of detector response.

A scan along the  $z$ -axis utilizing the  $^{60}\text{Co}$  source from each of the three ACUs was used to obtain nonuniformity correction functions. The nonuniformity was also studied with spallation neutrons generated by cosmic muons and alphas produced by natural radioactivity present in the liquid scintillator. The neutron energy scale was set by comparing  $^{60}\text{Co}$  events with neutron capture on Gd events from the Am-C source at the detector center. Additional details of energy calibration and reconstruction can be found in [54]. Asymmetries in the mean of the six ADs' response are shown in Figure 8. Asymmetries for all types of events in all the ADs fall within a narrow band, and the uncertainty is estimated to be 0.5%, uncorrelated among ADs.

A Geant4 [60] based computer simulation (Monte Carlo, MC) of the detectors and readout electronics was used to study detector response and consisted of five components: kinematic generator, detector simulation, electronics simulation, trigger simulation, and readout simulation. The MC is carefully tuned, by taking measured parameters of the materials properties, to match observed detector distributions, such as PMT timing, charge response, and energy nonlinearity. An optical model is developed to take into account photon absorption and reemission processes in liquid scintillator.

**4.3. Event Selection, Efficiencies, and Uncertainties.** Two preselections were completed prior to IBD selection. First, flasher



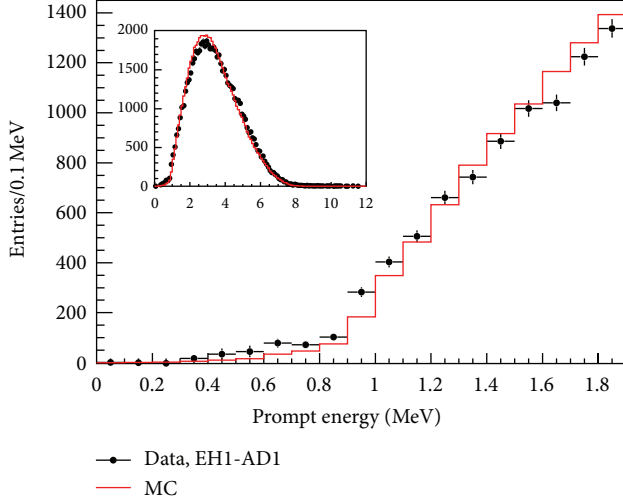


FIGURE 9: The prompt energy spectrum from AD1. IBD selection required  $0.7 < E_p < 12.0$  MeV. Accidental backgrounds were subtracted, where the spectrum of accidental background was estimated from the spectrum of all  $>0.7$  MeV triggers.

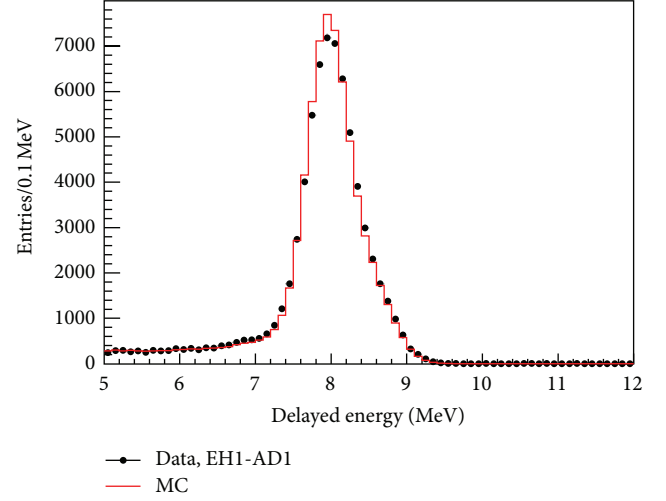


FIGURE 10: The delayed energy spectrum from AD1. IBD selection required  $6.0 < E_d < 12.0$  MeV. Accidental backgrounds were subtracted, where the spectrum of accidental background was estimated from the spectrum of single neutrons.

events were rejected. Second, triggers within a  $(-2\mu\text{s}, 200\mu\text{s})$  window with respect to a water shield muon candidate ( $\mu_{\text{WS}}$ ) were rejected, where a  $\mu_{\text{WS}}$  was defined as any trigger with  $N_{\text{hit}} > 12$  in either the inner or outer water shield. This allowed for the removal of most of the false triggers that followed a muon, as well as triggers associated with the decay of spallation products. Events in an AD within  $\pm 2\mu\text{s}$  of a  $\mu_{\text{WS}}$  with energy  $> 20$  MeV or  $> 2.5$  GeV were classified as AD muons ( $\mu_{\text{AD}}$ ) or showering muons ( $\mu_{\text{sh}}$ ), respectively.

Within an AD, only prompt-delayed pairs separated in time by less than  $200\mu\text{s}$  ( $1 < t_d - t_p < 200\mu\text{s}$ , where  $t_p$  and  $t_d$  are time of the prompt and delayed signal, resp.) with no intervening triggers and no  $E > 0.7$  MeV triggers within  $200\mu\text{s}$  before the prompt signal or  $200\mu\text{s}$  after the delayed signal were selected (referred to as the multiplicity cut). A prompt-delayed pair was vetoed if the delayed signal is in coincidence with a water shield muon ( $-2\mu\text{s} < t_d - t_{\mu_{\text{WS}}} < 600\mu\text{s}$ ) or an AD muon ( $0 < t_d - t_{\mu_{\text{AD}}} < 1000\mu\text{s}$ ) or a showering muon ( $0 < t_d - t_{\mu_{\text{sh}}} < 1\text{s}$ ). The energy of the delayed candidate must be  $6.0\text{ MeV} < E_d < 12.0\text{ MeV}$ , while the energy of the prompt candidate must be  $0.7\text{ MeV} < E_p < 12.0\text{ MeV}$ . The prompt energy, the delayed energy and the capture time distributions for data and MC are shown in Figures 9, 10, and 11, respectively.

The data are generally in good agreement with the MC. The apparent difference between data and MC in the prompt energy spectrum is due to nonlinearity of the detector response; however, the correction to this nonlinearity was not performed in this analysis. Since all ADs had similar nonlinearity (as shown in the bottom panel of Figure 8), and the energy selection cuts cover a larger range than the actual distribution, the discrepancies introduced negligible uncertainties to the rate analysis.

For a relative measurement, the absolute efficiencies and correlated uncertainties do not factor into the error

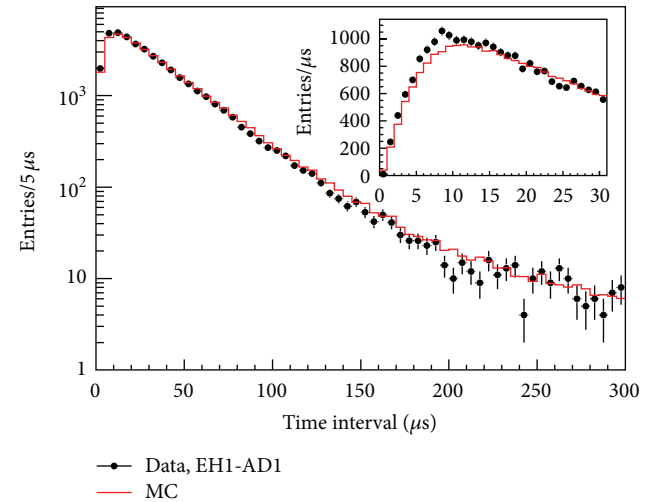


FIGURE 11: The neutron capture time from AD1. IBD selection required  $1 < t_d - t_p < 200\mu\text{s}$ . In order to compare data with MC, a cut on prompt energy ( $E_p > 3$  MeV) was applied to reject accidental backgrounds.

budget. In that regard, only the uncorrelated uncertainties matter. Extracting absolute efficiencies and correlated errors were done in part to better understand our detector, and it was a natural consequence of evaluating the uncorrelated uncertainties. Efficiencies associated with the prompt energy, delayed energy, capture time, Gd capture fraction, and spill-in effects were evaluated with the Monte Carlo. Efficiencies associated with the muon veto, multiplicity cut, and livetime were evaluated using data. In general, the uncorrelated uncertainties were not dependent on the details of our computer simulation.

Table 3 is a summary of the absolute efficiencies and the systematic uncertainties. The uncertainties of the absolute

TABLE 3: Summary of absolute efficiencies and systematic uncertainties. For our relative measurement, only the uncorrelated uncertainties contribute to the final error in our relative measurement.

	Efficiency	Correlated	Uncorrelated
Target protons		0.47%	0.03%
Flasher cut	99.98%	0.01%	0.01%
Delayed energy cut	90.9%	0.6%	0.12%
Prompt energy cut	99.88%	0.10%	0.01%
Multiplicity cut		0.02%	<0.01%
Capture time cut	98.6%	0.12%	0.01%
Gd capture ratio	83.8%	0.8%	<0.1%
Spill-in	105.0%	1.5%	0.02%
Livetime	100.0%	0.002%	<0.01%

efficiencies were correlated among the ADs. No relative efficiency, except  $\epsilon_\mu\epsilon_m$ , was corrected. All differences between the functionally identical ADs were taken as uncorrelated uncertainties. Detailed description of the analysis can be found in [53].

**4.4. Backgrounds.** Backgrounds are actually the main source of systematic uncertainties of this experiment; even though the background to signal ratio is only a few percent. Extensive studies show that cosmic-ray-induced backgrounds are the main component, while AmC neutron sources installed at the top of our neutrino detector for calibration contribute also to a significant portion. Although the random coincidence background is the largest, its uncertainty is well under control. Table 4 lists all the signal and background rates as well as their uncertainties. A detailed study can be found in [53].

The accidental background was defined as any pair of otherwise uncorrelated triggers that happen to satisfy the IBD selection criteria. They can be easily calculated based on textbooks, and their uncertainties are well understood. When calculating the rate of accidental backgrounds listed in Table 4, A correction is needed to account for the muon veto efficiency and the multiplicity cut efficiency. An alternate method, called the off-windows method, was developed to determine accidental backgrounds. This result was also validated by comparing the prompt-delayed distance of accidental coincidences selected by the off-windows method with IBD candidates. The relative differences between off-windows method results and theoretical calculation of 6 ADs were less than 1%.

Energetic neutrons entering an AD aped IBD by recoiling off a proton before being captured on Gd. The number of fast neutron background events in the IBD sample is estimated by extrapolating the prompt energy ( $E_p$ ) distribution between 12 and 100 MeV down to 0.7 MeV. Two different extrapolation methods were used; one is a flat distribution, and the other one is a first-order polynomial function. The fast neutron background in the IBD sample was assigned to be equal to the mean value of the two extrapolation methods, and the systematic error was determined from the sum of their differences and the fitting uncertainties. As a check, the fast

neutrons prompt energy spectrum associated with tagged muons validates our extrapolation method.

The rate of correlated background from the  $\beta$ - $n$  cascade of  ${}^9\text{Li}$ / ${}^8\text{He}$  decays was evaluated from the distribution of the time since the last muon and can be described by a sum of exponential functions with different time constant [61]. To reduce the number of minimum ionizing muons in these data samples, we assumed that most of the  ${}^9\text{Li}$  and  ${}^8\text{He}$  production was accompanied with neutron generation. The muon samples with and without reduction were both prepared for  ${}^9\text{Li}$  and  ${}^8\text{He}$  background estimation. By considering binning effects and differences between results with and without muon reduction, we assigned a 50% systematical error to the final result.

The  ${}^{13}\text{C}$  ( $\alpha n$ )  ${}^{16}\text{O}$  background was determined by measuring alpha decay rates in situ and then by using MC to calculate the neutron yield. We identified four sources of alpha decays, the  ${}^{238}\text{U}$ ,  ${}^{232}\text{Th}$ ,  ${}^{227}\text{Ac}$  decay chains, and  ${}^{210}\text{Po}$  taking into account half lives of their decay chain products, 164.3  $\mu\text{s}$ , 0.3  $\mu\text{s}$ , and 1.781 ms, respectively. Geant4 was used to model the energy deposition process. Based on JENDL [62] ( $\alpha n$ ) cross-sections, the neutron yield as a function of energy was calculated and summed. Finally, with the in-situ measured alpha decay rates and the MC determined neutron yields, the  ${}^{13}\text{C}$ ( $\alpha n$ )  ${}^{16}\text{O}$  rate was calculated.

During data taking, the Am-C sources sat inside the ACUs on top of each AD. Neutrons emitted from these sources would occasionally ape IBD events by scattering inelastically with nuclei in the shielding material (emitting gamma rays) before being captured on a metal nuclei, such as Fe, Cr, Mn, or Ni (releasing more gamma rays). We estimated the neutron-like events from the Am-C sources by subtracting the number of neutron-like singles in the  $Z < 0$  region from the  $Z > 0$  region. The Am-C correlated background rate was estimated by MC simulation normalized using the Am-C neutron-like event rate obtained from data. Even though the agreement between data and MC is excellent for Am-C neutron-like events, we assigned 100% uncertainty to the estimated background due to the Am-C sources to account for any potential uncertainty in the neutron capture cross-sections used by the simulation.

**4.5. Side-By-Side Comparison in EH1.** Relative uncertainties were studied with data by comparing side-by-side antineutrino detectors. A detailed comparison using three months of data from ADs in EH1 has been presented elsewhere [54]. An updated comparison of the prompt energy spectra of IBD events for the ADs in EH1 using 231 days of data (Sep. 23, 2011 to May 11, 2012) is shown in Figure 12 after correcting for efficiencies and subtracting background. A bin-by-bin ratio of the AD1 and AD2 spectra is also shown. The ratio of total IBD rates in AD1 and AD2 was measured to be  $0.987 \pm 0.004$  (stat.)  $\pm 0.003$  (syst.), consistent with the expected ratio of 0.982. The difference in rates was primarily due to differences in baselines of the two ADs in addition to a slight dependence on the individual reactor on/off status. It was known that AD2 has a 0.3% lower energy response than AD1 for uniformly distributed events, resulting in a slight tilt

TABLE 4: Signal and background summary. The background and IBD rates were corrected for the  $\epsilon_\mu \epsilon_m$  efficiency.

	AD1	AD2	AD3	AD4	AD5	AD6
IBD candidates	69121	69714	66473	9788	9669	9452
Expected IBDs	68613	69595	66402	9922.9	9940.2	9837.7
DAQ livetime (days)	127.5470		127.3763		126.2646	
Muon veto time (days)	22.5656	22.9901	18.1426	2.3619	2.3638	2.4040
$\epsilon_\mu \epsilon_m$	0.8015	0.7986	0.8364	0.9555	0.9552	0.9547
Accidentals (per day)	$9.73 \pm 0.10$	$9.61 \pm 0.10$	$7.55 \pm 0.08$	$3.05 \pm 0.04$	$3.04 \pm 0.04$	$2.93 \pm 0.03$
Fast neutron (per day)	$0.77 \pm 0.24$	$0.77 \pm 0.24$	$0.58 \pm 0.33$	$0.05 \pm 0.02$	$0.05 \pm 0.02$	$0.05 \pm 0.02$
$^9\text{Li}/^8\text{He}$ (per AD per day)	$2.9 \pm 1.5$		$2.0 \pm 1.1$		$0.22 \pm 0.12$	
Am-C correlated (per AD per day)	$0.2 \pm 0.2$					
$^{13}\text{C}(\alpha\ n)\ ^{16}\text{O}$ background (per day)	$0.08 \pm 0.04$	$0.07 \pm 0.04$	$0.05 \pm 0.03$	$0.04 \pm 0.02$	$0.04 \pm 0.02$	$0.04 \pm 0.02$
IBD rate (per day)	$662.47 \pm 3.00$	$670.87 \pm 3.01$	$613.53 \pm 2.69$	$77.57 \pm 0.85$	$76.62 \pm 0.85$	$74.97 \pm 0.84$

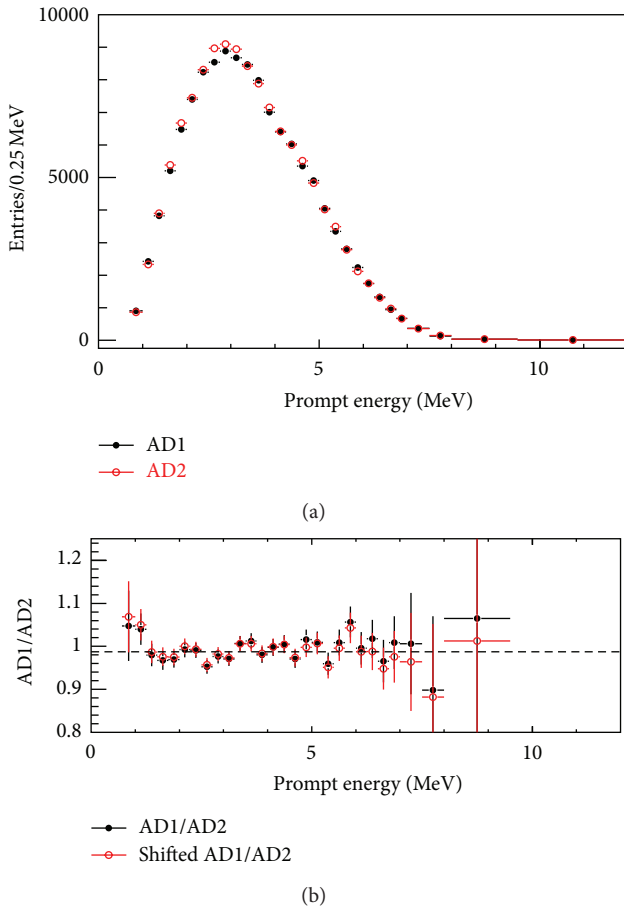


FIGURE 12: The energy spectra for the prompt signal of IBD events in AD1 and AD2 (a) are shown along with the bin-by-bin ratio (b). Within (b), the dashed line represents the ratio of the total rates for the two ADs, and the open circles show the ratio with the AD2 energy scaled by +0.3%.

to the distribution shown in Figure 12(b). The distribution of open circles was created by scaling the AD2 energy by 0.3%. The distribution with scaled AD2 energy agrees well with a flat distribution.

**4.6. Reactor Neutrino Flux.** Reactor antineutrinos result primarily from the beta decay of the fission products of four main isotopes,  $^{235}\text{U}$ ,  $^{239}\text{Pu}$ ,  $^{238}\text{U}$ , and  $^{241}\text{Pu}$ . The  $\bar{\nu}_e$  flux of each reactor ( $S(E)$ ) was predicted from the simulated fission fraction  $f_i$  and the neutrino spectra per fission ( $S_i$ ) [19–22, 32, 37] of each isotope [63],

$$S(E) = \frac{W_{\text{th}}}{\sum_k f_k E_k} \sum_i f_i S_i(E), \quad (7)$$

where  $i$  and  $k$  sum over the four isotopes,  $E_i$  is the energy released per fission, and  $W_{\text{th}}$  is the measured thermal power.

The thermal power data were provided by the power plant. The uncertainties were dominated by the flow rate measurements of feedwater through three parallel cooling loops in each core [63–65]. The correlations between the flow meters were not clearly known. We conservatively assume that they were correlated for a given core but were uncorrelated between cores, giving a maximal uncertainty for the experiment. The assigned uncorrelated uncertainty for thermal power was 0.5%.

A simulation of the reactor cores using commercial software (SCIENCE [66, 67]) provided the fission fraction as a function of burnup. The fission fraction carries a 5% uncertainty set by the validation of the simulation software. The 3D spatial distribution of the isotopes within a core was also provided by the power plant, although simulation indicated that it had a negligible effect on acceptance. A complementary core simulation package was developed based on DRAGON [68] as a cross-check and for systematic studies. The code was validated with the Takahama-3 benchmark [69] and agreed with the fission fraction provided by the power plant to 3%. Correlations among the four isotopes were studied using the DRAGON-based simulation package, and agreed well with the data collected in [70]. Given the constraints of the thermal power and correlations, the uncertainties of the fission fraction simulation translated into a 0.6% uncorrelated uncertainty in the neutrino flux.

The neutrino spectrum per fission is a correlated uncertainty that cancels out for a relative measurement. The reaction cross-section for isotope  $i$  was defined as  $\sigma_i = \int S_i(E_\nu) \sigma(E_\nu) dE_\nu$ , where  $S_i(E_\nu)$  is the neutrino spectra per

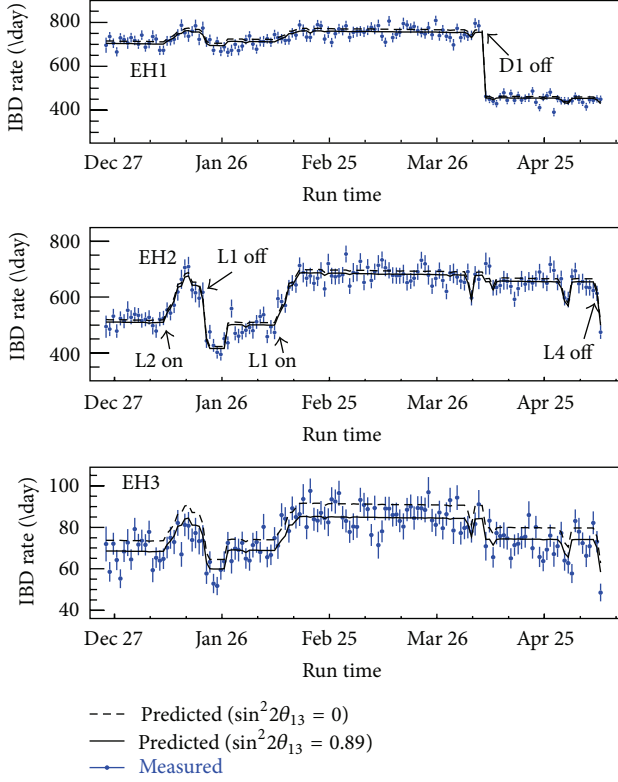


FIGURE 13: The daily average measured IBD rates per AD in the three experimental halls are shown as a function of time along with predictions based on reactor flux analyses and detector simulation.

fission and  $\sigma(E_\mu)$  is the IBD cross-section. We took the reaction cross-section from [10] but substituted the IBD cross-section with that in [71]. The energy released per fission and its uncertainties were taken from [72]. Nonequilibrium corrections for long-lived isotopes were applied following [22]. Contributions from spent fuel [73, 74] ( $\sim 0.3\%$ ) were included as an uncertainty.

The uncertainties in the baseline and the spatial distribution of the fission fractions in the core had a negligible effect to the results.

Figure 13 presents the background-subtracted and efficiency-corrected IBD rates in the three experimental halls. Predicted IBD rate from reactor flux calculation and detector Monte Carlo simulation are shown for comparison. The dashed lines have been corrected with the best-fit normalization parameter  $\varepsilon$  in (10) to get rid of the biases from the absolute reactor flux uncertainty and the absolute detector efficiency uncertainty.

**4.7. Results.** The  $\bar{\nu}_e$  rate in the far hall was predicted with a weighted combination of the two near hall measurements assuming no oscillation. A ratio of measured-to-expected rate is defined as

$$R = \frac{M_f}{\bar{N}_f} = \frac{M_f}{\alpha M_a + \beta M_b}, \quad (8)$$

TABLE 5: Reactor-related uncertainties.

Correlated		Uncorrelated	
Energy/fission	0.2%	Power	0.5%
IBD reaction/fission	3%	Fission fraction	0.6%
		Spent fuel	0.3%
Combined	3%	Combined	0.8%

where  $\bar{N}_f$  and  $M_f$  are the predicted and measured rates in the far hall (sum of AD 4–6) and  $M_a$  and  $M_b$  are the measured IBD rates in EH1 (sum of AD 1–2) and EH2 (AD3), respectively. The values for  $\alpha$  and  $\beta$  were dominated by the baselines and only slightly dependent on the integrated flux of each core. For the analyzed data set,  $\alpha = 0.0439$  and  $\beta = 0.2961$ . The residual reactor-related uncertainty in  $R$  was 5% of the uncorrelated uncertainty of a single core. The deficit observed at the far hall was as follows:

$$R = 0.944 \pm 0.007 \text{ (stat)} \pm 0.003 \text{ (syst)}. \quad (9)$$

The value of  $\sin^2 2\theta_{13}$  was determined with a  $\chi^2$  constructed with pull terms accounting for the correlation of the systematic errors [75] as follows:

$$\chi^2 = \sum_{d=1}^6 \frac{[M_d - T_d(1 + \varepsilon + \sum_r \omega_r^d \alpha_r + \varepsilon_d) + \eta_d]^2}{M_d + B_d} + \sum_r \frac{\alpha_r^2}{\sigma_r^2} + \sum_{d=1}^6 \left( \frac{\varepsilon_d^2}{\sigma_d^2} + \frac{\eta_d^2}{\sigma_B^2} \right), \quad (10)$$

where  $M_d$  is the measured IBD events of the  $d$ th AD with backgrounds subtracted,  $B_d$  is the corresponding background,  $T_d$  is the prediction from neutrino flux, MC, and neutrino oscillations, and  $\omega_r^d$  is the fraction of IBD contribution of the  $r$ th reactor to the  $d$ th AD determined by baselines and reactor fluxes. The uncorrelated reactor uncertainty is  $\sigma_r$  (0.8%), as shown in Table 5.  $\sigma_d$  (0.2%) is the uncorrelated detection uncertainty, listed in Table 8.  $\sigma_B$  is the background uncertainty listed in Table 4. The corresponding pull parameters are  $(\alpha_r, \varepsilon_d, \text{ and } \eta_d)$ . The detector- and reactor-related correlated uncertainties were not included in the analysis; the absolute normalization  $\varepsilon$  was determined from the fit to the data.

The survival probability used in the  $\chi^2$  was

$$P_{\text{sur}} = 1 - \sin^2 2\theta_{13} \sin^2 \left( 1.267 \Delta m_{31}^2 \frac{L}{E} \right) - \cos^4 \theta_{13} \sin^2 2\theta_{12} \sin^2 \left( 1.267 \Delta m_{21}^2 \frac{L}{E} \right), \quad (11)$$

where  $\Delta m_{31}^2 = 2.32 \times 10^{-3} \text{ eV}^2$ ,  $\sin^2 2\theta_{12} = 0.861^{+0.026}_{-0.022}$ , and  $\Delta m_{21}^2 = 7.59^{+0.20}_{-0.21} \times 10^{-5} \text{ eV}^2$ . The uncertainty in  $\Delta m_{31}^2$  had negligible effect and thus was not included in the fit.

The best-fit value is

$$\sin^2 2\theta_{13} = 0.089 \pm 0.010 \text{ (stat.)} \pm 0.005 \text{ (syst.)} \quad (12)$$



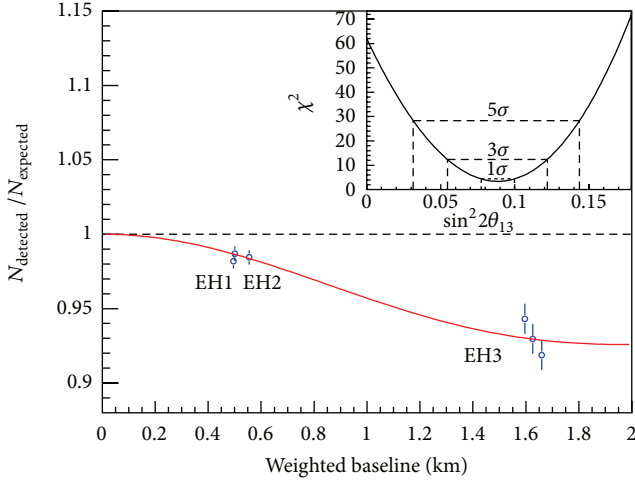


FIGURE 14: Ratio of measured versus expected signal in each detector, assuming no oscillation. The error bar is the uncorrelated uncertainty of each AD. The expected signal was corrected with the best-fit normalization parameter. The oscillation survival probability at the best-fit value is given by the smooth curve. The AD4 and AD6 data points were displaced by  $-30$  and  $+30$  m for visual clarity. The  $\chi^2$  versus  $\sin^2 2\theta_{13}$  is shown in the inset.

with a  $\chi^2/\text{NDF}$  of  $3.4/4$ . All best estimates of pull parameters are within its one standard deviation based on the corresponding systematic uncertainties. The no-oscillation hypothesis is excluded at  $7.7$  standard deviations. Figure 14 shows the measured number of events in each detector, relative to those expected assuming no oscillation. A  $\sim 1.5\%$  oscillation effect appears in the near halls. The oscillation survival probability at the best-fit values is given by the smooth curve. The  $\chi^2$  versus  $\sin^2 2\theta_{13}$  is shown in the inset.

The observed  $\bar{\nu}_e$  spectrum in the far hall was compared to a prediction based on the near hall measurements  $\alpha M_a + \beta M_b$  in Figure 15. The distortion of the spectra is consistent with the expected one calculated with the best-fit  $\theta_{13}$  obtained from the rate-only analysis, providing further evidence of neutrino oscillation.

## 5. Double Chooz

The Double Chooz detector system (Figure 16) consists of a main detector, an outer veto, and calibration devices. The main detector comprises four concentric cylindrical tanks filled with liquid scintillators or mineral oil. The innermost  $8$  mm thick transparent (UV to visible) acrylic vessel houses the  $10\text{ m}^3$   $\nu$ -target liquid, a mixture of n-dodecane, PXE, PPO, bis-MSB, and  $1\text{ g}$  gadolinium/l as a beta-diketonate complex. The scintillator choice emphasizes radiopurity and long-term stability. The  $\nu$ -target volume is surrounded by the  $\gamma$ -catcher, a  $55$  cm thick Gd-free liquid scintillator layer in a second  $12$  mm thick acrylic vessel, used to detect  $\gamma$ -rays escaping from the  $\nu$ -target. The light yield of the  $\gamma$ -catcher was chosen to provide identical photoelectron (pe) yield across these two layers. Outside the  $\gamma$ -catcher is the buffer, a  $105$  cm

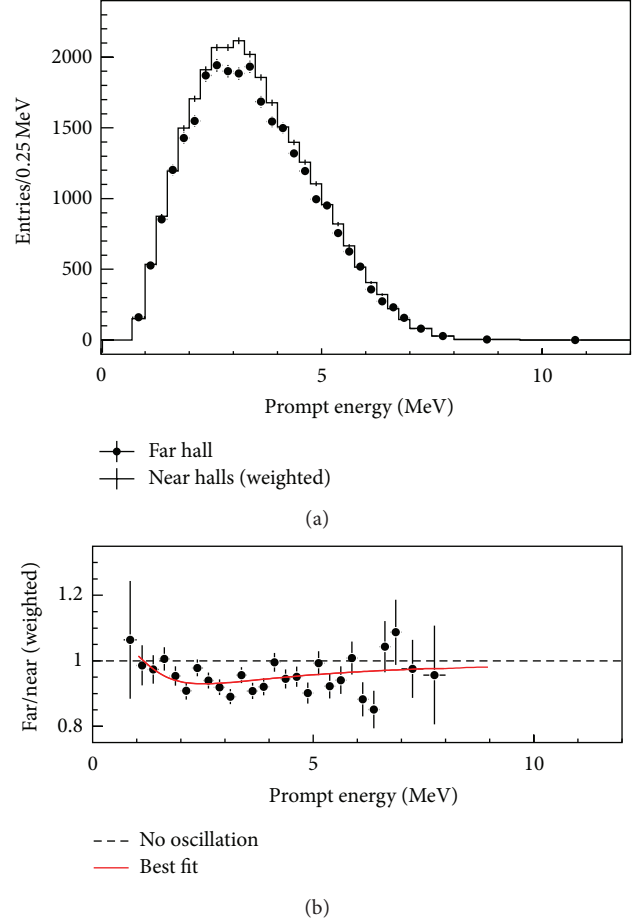


FIGURE 15: (a) Measured prompt energy spectrum of the far hall (sum of three ADs) compared with the no-oscillation prediction from the measurements of the two near halls. Spectra were background subtracted. Uncertainties are statistical only. (b) The ratio of measured and predicted no-oscillation spectra. The red curve is the best-fit solution with  $\sin^2 2\theta_{13} = 0.089$  obtained from the rate-only analysis. The dashed line is the no-oscillation prediction.

thick mineral oil layer. The buffer works as a shield to  $\gamma$ -rays from radioactivity of PMTs and from the surrounding rock and is one of the major improvements over the CHOOZ detector. It shields from radioactivity of photomultipliers (PMTs) and of the surrounding rock, and it is one of the major improvements over the CHOOZ experiment.  $390$   $10$ -inch PMTs are installed on the stainless steel buffer tank inner wall to collect light from the inner volumes. These three volumes and the PMTs constitute the inner detector (ID). Outside the ID, and optically separated from it, is a  $50$  cm thick inner veto liquid scintillator (IV). It is equipped with  $78$   $8$ -inch PMTs and functions as a cosmic muon veto and as a shield to spallation neutrons produced outside the detector. The detector is surrounded by  $15$  cm of demagnetized steel to suppress external  $\gamma$ -rays. The main detector is covered by an outer veto system. The readout is triggered by custom energy sum electronics. The ID PMTs are separated into two groups of  $195$  PMTs uniformly distributed throughout the volume, and the PMT signals in each group are summed.



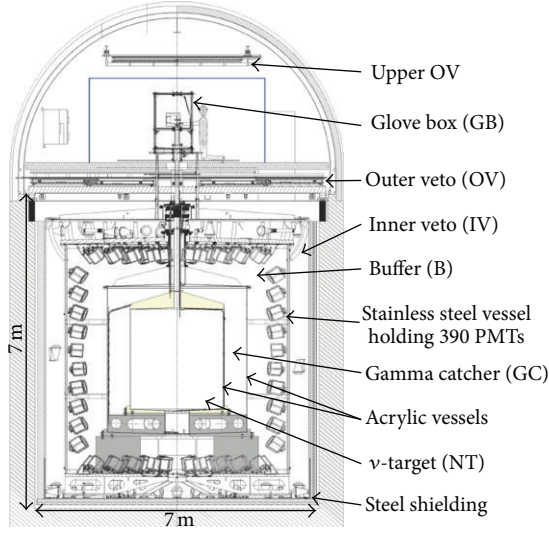


FIGURE 16: A cross-sectional view of the Double Chooz detector system.

The signals of the IV PMTs are also summed. If any of the three sums is above a set energy threshold, the detector is read out with 500 MHz flash-ADC electronics with customized firmware and a dead time-free acquisition system. Upon each trigger, a 256 ns interval of the waveforms of both ID and IV signals is recorded. Having reduced the ambient radioactivity enables us to set a low trigger rate (120 Hz) allowed the ID readout threshold to be set at 350 keV, well below the 1.02 MeV minimum energy of an IBD positron, greatly reducing the threshold systematics. The experiment is calibrated by several methods. A multiwavelength LED-fiber light injection system (LI) produces fast light pulses illuminating the PMTs from fixed positions. Radio-isotopes  $^{137}\text{Cs}$ ,  $^{68}\text{Ge}$ ,  $^{60}\text{Co}$ , and  $^{252}\text{Cf}$  were deployed in the target along the vertical symmetry axis and, in the gamma catcher, through a rigid loop traversing the interior and passing along boundaries with the target and the buffer. The detector was monitored using spallation neutron captures on H and Gd, residual natural radioactivity, and daily LI runs. The energy response was found to be stable within 1% over time.

**5.1. Chooz Reactor Modeling.** Double Chooz's sources of antineutrinos are the reactor cores B1 and B2 at the Électricité de France (EDF) Centrale Nucléaire de Chooz, two N4 type pressurized water reactor (PWR) cores with nominal thermal power outputs of 4.25 GW<sub>th</sub> each. The instantaneous thermal power of each reactor core  $P_{\text{th}}^R$  is provided by EDF as a fraction of the total power. It is derived from the in-core instrumentation with the most important variable being the temperature of the water in the primary loop. The dominant uncertainty on the weekly heat balance at the secondary loops comes from the measurement of the water flow. At the nominal full power of 4250 MW, the final uncertainty is 0.5% (1  $\sigma$  C.L.). Since the amount of data taken with one or two cores at intermediate power is small, this uncertainty is used for the mean power of both cores.

The antineutrino spectrum for each fission isotope is taken from [22, 32], including corrections for off-equilibrium effects. The uncertainty on these spectra is energy dependent but is on the order of 3%. The fractional fission rates  $\alpha_k$  of each isotope are needed in order to calculate the mean cross-section per fission. They are also required for the calculation of the mean energy released per fission for reactor R:

$$\langle E_f \rangle_R = \sum_k \alpha_k \langle E_f \rangle_k. \quad (13)$$

The thermal power one would calculate given a fission is relatively insensitive to the specific fuel composition since the  $\langle E_f \rangle_k$  differ by <6%; however, the difference in the detected number of antineutrinos is amplified by the dependence of the norm and mean energy of  $S_k(E)$  on the fissioning isotope. For this reason, much effort has been expended in developing simulations of the reactor cores to accurately model the evolution of the  $\alpha_k$ .

Double Chooz has chosen two complementary codes for modeling of the reactor cores: MURE and DRAGON [30, 76–78]. These two codes provide the needed flexibility to extract fission rates and their uncertainties. These codes were benchmarked against data from the Takahama-3 reactor [79]. The construction of the reactor model requires detailed information on the geometry and materials comprising the core. The Chooz cores are comprised of 205 fuel assemblies. For every reactor fuel cycle, approximately one year in duration, one-third of the assemblies are replaced with assemblies containing fresh fuel. The other two-thirds of the assemblies are redistributed to obtain a homogeneous neutron flux across the core. The Chooz reactor cores contain four assembly types that differ mainly in their initial  $^{235}\text{U}$  enrichment. These enrichments are 1.8%, 3.4%, and 4%. The data set reported here spans fuel cycle 12 for core B2 and cycle 12 and the beginning of cycle 13 for B1. EDF provides Double Chooz with the locations and initial burnup of each assembly. Based on these maps, a full core simulation was constructed using MURE for each cycle. The uncertainty due to the simulation technique is evaluated by comparing the DRAGON and MURE results for the reference simulation leading to a small 0.2% systematic uncertainty in the fission rate fractions  $\alpha_k$ . Once the initial fuel composition of the assemblies is known, MURE is used to model the evolution of the full core in time steps of 6 to 48 hours. This allows the  $\alpha_k$ 's, and therefore the predicted antineutrino flux, to be calculated. The systematic uncertainties on the  $\alpha_k$ 's are determined by varying the inputs and observing their effect on the fission rate relative to the nominal simulation. The uncertainties considered are those due to the thermal power, boron concentration, moderator temperature and density, initial burnup error, control rod positions, choice of nuclear databases, choice of the energies released per fission, and statistical error of the MURE Monte Carlo. The two largest uncertainties come from the moderator density and control rod positions.

In far-only phase of Double Chooz, the rather large uncertainties in the reference spectra limit the sensitivity to

TABLE 6: The uncertainties in the antineutrino prediction. All uncertainties are assumed to be correlated between the two reactor cores. They are assumed to be normalization and energy (rate and shape) unless noted as normalization only.

Source	Normalization only	Uncertainty (%)
$P_{\text{th}}$	Yes	0.5
$\langle\sigma_f\rangle^{\text{Bugey}}$	Yes	1.4
$S_k(E)\sigma_{\text{IBD}}(E_\nu^{\text{true}})$	No	0.2
$\langle E_f \rangle$	No	0.2
$L_R$	Yes	<0.1
$\alpha_k^R$	No	0.9
Total		1.8

$\theta_{13}$ . To mitigate this effect, the normalization of the cross-section per fission for each reactor is anchored to the Bugey-4 rate measurement at 15 m [10]:

$$\langle\sigma_f\rangle_R = \langle\sigma_f\rangle^{\text{Bugey}} + \sum_k (\alpha_k^R - \alpha_k^{\text{Bugey}}) \langle\sigma_f\rangle_k, \quad (14)$$

where  $R$  stands for each reactor. The second term corrects the difference in fuel composition between Bugey-4 and each of the Chooz cores. This treatment takes advantage of the high accuracy of the Bugey-4 anchor point (1.4%) and suppresses the dependence on the predicted  $\langle\sigma_f\rangle_R$ . At the same time, the analysis becomes insensitive to possible oscillations at shorter baselines due to heavy  $\Delta m^2 \sim 1 \text{ eV}^2$  sterile neutrinos. The expected number of antineutrinos with no oscillation in the  $i$ th energy bin with the Bugey-4 anchor point becomes as follows:

$$N_i^{\text{exp},R} = \frac{\epsilon N_p}{4\pi} \frac{1}{L_R^2} \frac{P_{\text{th}}^R}{\langle E_f \rangle_R} \times \left( \frac{\langle\sigma_f\rangle_R}{(\sum_k \alpha_k^R \langle\sigma_f\rangle_k)} \sum_k \alpha_k^R \langle\sigma_f\rangle_k^i \right), \quad (15)$$

where  $\epsilon$  is the detection efficiency,  $N_p$  is the number of protons in the target,  $L_R$  is the distance to the center of each reactor, and  $P_{\text{th}}^R$  is the thermal power. The variable  $\langle E_f \rangle_R$  is the mean energy released per fission defined in (13), while  $\langle\sigma_f\rangle_R$  is the mean cross-section per fission defined in (14). The three variables  $P_{\text{th}}^R$ ,  $\langle E_f \rangle_R$ , and  $\langle\sigma_f\rangle_R$  are time dependent with  $\langle E_f \rangle_R$  and  $\langle\sigma_f\rangle_R$  depending on the evolution of the fuel composition in the reactor and  $P_{\text{th}}^R$  depending on the operation of the reactor. A covariance matrix  $M_{ij}^{\text{exp}} = \delta N_i^{\text{exp}} \delta N_j^{\text{exp}}$  is constructed using the uncertainties listed in Table 6.

The IBD cross-section used is the simplified form from Vogel and Beacom [71]. The cross-section is inversely proportional to the neutron lifetime. The MAMBO-II measurement of the neutron lifetime [80] is being used, leading to  $K = 0.961 \times 10^{-43} \text{ cm}^2 \text{ MeV}^{-2}$ .

**5.2. Modeling the Double Chooz Detector.** The detector response uses a detailed Geant4 [81, 82] simulation with enhancements to the scintillation process, photocathode

optical surface model, and thermal neutron model. Simulated IBD events are generated with run-by-run correspondence of MC to data, with fluxes and rates calculated as described in the previous paragraph. Radioactive decays in calibration sources and spallation products were simulated using detailed models of nuclear levels, taking into account branching ratios and correct spectra for transitions [83–85]. Optical parameters used in the detector model are based on detailed measurements made by the collaboration. Tuning of the absolute and relative light yield in the simulation was done with calibration data. The scintillator emission spectrum was measured using a Cary Eclipse Fluorometer [86]. The photon emission time probabilities used in the simulation are obtained with a dedicated laboratory setup [87]. For the ionization quenching treatment in our MC, the light output of the scintillators after excitation by electrons [88] and alpha particles [89] of different energies was measured. The nonlinearity in light production in the simulation has been adjusted to match these data. The finetuning of the total attenuation was made using measurements of the complete scintillators [87]. Other measured optical properties include reflectivities of various detector surfaces and indices of refraction of detector materials.

The readout system simulation (RoSS) accounts for the response of elements associated with detector readout, such as from the PMTs, FEE, FADCs, trigger system and DAQ. The simulation relies on the measured probability distribution function (PDF) to empirically characterize the response to each single PE as measured by the full readout channel. The Geant4-based simulation calculates the time at which each PE strikes the photocathode of each PMT. RoSS converts this time per PE into an equivalent waveform as digitized by FADCs. After calibration, the MC and data energies agree within 1%.

A set of Monte Carlo  $\bar{\nu}_e$  events representing the expected signal for the duration of physics data taking is created based on the formalism of (16). The calculated IBD rate is used to determine the rate of interactions. Parent fuel nuclide and neutrino energies are sampled from the calculated neutrino production ratios and corresponding spectra, yielding a properly normalized set of IBD-progenitor neutrinos. Once generated, each event-progenitor neutrino is assigned a random creation point within the originating reactor core. The event is assigned a weighted random interaction point within the detector based on proton density maps of the detector materials. In the center-of-mass frame of the  $\nu$ - $p$  interaction, a random positron direction is chosen, with the positron and neutron of the IBD event given appropriate momenta based on the neutrino energy and decay kinematics. These kinematic values are then boosted into the laboratory frame. The resulting positron and neutron momenta and originating vertex are then available as inputs to the Geant4 detector simulation. Truth information regarding the neutrino origin, baseline, and energy are propagated along with the event, for use later in the oscillation analysis.

**5.3. Event Reconstruction.** The pulse reconstruction provides the signal charge and time in each PMT. The baseline mean ( $B_{\text{mean}}$ ) and rms ( $B_{\text{rms}}$ ) are computed using the full readout

window (256 ns). The integrated charge ( $q$ ) is defined as the sum of digital counts in each waveform sample over the integration window, once the pedestal has been subtracted. For each pulse reconstructed, the start time is computed as the time when the pulse reaches 20% of its maximum. This time is then corrected by the PMT-to-PMT offsets obtained with the light injection system.

Vertex reconstruction in Double Chooz is not used for event selection but is used for event energy reconstruction. It is based on a maximum charge and time likelihood algorithm which utilizes all hit and no-hit information in the detector. The performance of the reconstruction has been evaluated in situ using radioactive sources deployed at known positions along the  $z$ -axis in the target volume, and off-axis in the guide tubes. The sources are reconstructed with a spatial resolution of 32 cm for  $^{137}\text{Cs}$ , 24 cm for  $^{60}\text{Co}$ , and 22 cm for  $^{68}\text{Ge}$ .

Cosmic muons passing through the detector or the nearby rock induce backgrounds which are discussed later. The IV trigger rate is  $46 \text{ s}^{-1}$ . All muons in the ID are tagged by the IV except some stopping muons which enter the chimney. Muons which stop in the ID and their resulting Michel  $e$  can be identified by demanding a large energy deposition (roughly a few tens of MeV) in the ID. An event is tagged as a muon if there is  $>5 \text{ MeV}$  in the IV or  $>30 \text{ MeV}$  in the ID.

The visible energy ( $E_{\text{vis}}$ ) provides the absolute calorimetric estimation of the energy deposited per trigger.  $E_{\text{vis}}$  is a function of the calibrated  $PE$  (total number of photoelectrons):

$$E_{\text{vis}} = PE^m(\rho, z, t) \times f_u^m(\rho, z) \times f_s^m(t) \times f_{\text{MeV}}^m, \quad (16)$$

where  $PE = \sum_i pe_i = \sum_i q_i / \text{gain}_i(q_i)$ . Coordinates in the detector are  $\rho$  and  $z$ ,  $t$  is time,  $m$  refers to data or Monte Carlo (MC), and  $i$  refers to each good channel. The correction factors  $f_u$ ,  $f_s$ , and  $f_{\text{MeV}}$  correspond, respectively, to the spatial uniformity, time stability, and photoelectron per MeV calibrations. Four stages of calibration are carried out to render  $E_{\text{vis}}$  linear, independent of time and position, and consistent between data and MC. Both the MC and data are subjected to the same stages of calibration. The sum over all good channels of the reconstructed raw charge ( $q_i$ ) from the digitized waveforms is the basis of the energy estimation. The  $PE$  response is position dependent for both MC and data. Calibration maps were created such that any  $PE$  response for any event located at any position ( $\rho, z$ ) can be converted into its response as if measured at the center of the detector ( $\rho = 0, z = 0$ ):  $PE_{\odot}^m = PE^m(\rho, z) \times f_u^m(\rho, z)$ . The calibration map's correction for each point is labeled  $f_u^m(\rho, z)$ . Independent uniformity calibration maps  $f_u^m(\rho, z)$  are created for data and MC, such that the uniformity calibration serves to minimize any possible difference in position dependence of the data with respect to MC. The capture peak on H (2.223 MeV) of neutrons from spallation and antineutrino interactions provides a precise and copious calibration source to characterize the response nonuniformity over the full volume (both NT and GC).

The detector response stability was found to vary in time due to two effects, which are accounted for and corrected by the term  $f_s^m(t)$ . First, the detector response can change due to

TABLE 7: Energy scale systematic errors.

	Error (%)
Relative nonuniformity	0.43
Relative instability	0.61
Relative nonlinearity	0.85
Total	1.13

variations in readout gain or scintillator response. This effect has been measured as a  $+2.2\%$  monotonic increase over 1 year using the response of the spallation neutrons capturing on Gd within the NT. Second, few readout channels varying over time are excluded from the calorimetry sum, and the average overall response decreases by  $0.3\%$  per channel excluded. Therefore, any response  $PE_{\odot}(t)$  is converted to the equivalent response at  $t_0$ , as  $PE_{\odot}^m(t_0) = PE_{\odot}^m(t) \times f_s^m(t)$ . The  $t_0$  was defined as the day of the first Cf source deployment, during August 2011. The remaining instability after calibration is used for the stability systematic uncertainty estimation.

The number  $PE_{\odot t_0}$  per MeV is determined by an absolute energy calibration independently, for the data and MC. The response in  $PE_{\odot t_0}$  for H capture as deployed in the center of the NT is used for the absolute energy scale. The absolute energy scales are found to be  $229.9 \text{ } PE_{\odot t_0} / \text{MeV}$  and  $227.7 \text{ } PE_{\odot t_0} / \text{MeV}$ , respectively, for the data and MC, demonstrating agreement within 1% prior to this calibration stage.

Discrepancies in response between the MC and data, after calibration, are used to estimate these uncertainties within the prompt energy range and the NT volume. Table 7 summarizes the systematic uncertainty in terms of the remaining nonuniformity, instability, and nonlinearity. The relative nonuniformity systematic uncertainty was estimated from the calibration maps using neutrons capturing on Gd, after full calibration. The rms deviation of the relative difference between the data and MC calibration maps is used as the estimator of the nonuniformity systematic uncertainty, and is  $0.43\%$ . The relative instability systematic error, discussed above, is  $0.61\%$ . A  $0.85\%$  variation consistent with this nonlinearity was measured with the  $z$ -axis calibration system, and this is used as the systematic error for relative nonlinearity in Table 7. Consistent results were obtained when sampling with the same sources along the GT.

**5.4. Neutrino Data Analysis. Signals and Backgrounds.** The  $\bar{\nu}_e$  candidate selection is as follows. Events with an energy below  $0.5 \text{ MeV}$ , where the trigger efficiency is not  $100\%$ , or identified as light noise ( $Q_{\text{max}}/Q_{\text{tot}} > 0.09$  or  $\text{rms}(t_{\text{start}}) > 40 \text{ ns}$ ), are discarded. Triggers within a  $1 \text{ ms}$  window following a tagged muon are also rejected in order to reduce the correlated and cosmogenic backgrounds. The effective veto time is  $4.4\%$  of the total run time. Defining  $\Delta T \equiv t_{\text{delayed}} - t_{\text{prompt}}$ , further selection consists of 4 cuts:

- (1) time difference between consecutive triggers (prompt and delayed):  $2 \mu\text{s} < \Delta T < 100 \mu\text{s}$ , where the lower cut reduces correlated backgrounds and the upper cut



TABLE 8: Cuts used in the event selection and their efficiency for IBD events. The OV was working for the last 68.9% of the data.

Cut	Efficiency %
$E_{\text{prompt}}$	$100.0 \pm 0.0$
$E_{\text{delayed}}$	$94.1 \pm 0.6$
$\Delta T$	$96.2 \pm 0.5$
Multiplicity	$99.5 \pm 0.0$
Muon veto	$90.8 \pm 0.0$
Outer veto	$99.9 \pm 0.0$

is determined by the approximately 30  $\mu\text{s}$  capture time on Gd;

- (2) prompt trigger:  $0.7 \text{ MeV} < E_{\text{prompt}} < 12.2 \text{ MeV}$ ;
- (3) delayed trigger:  $6.0 \text{ MeV} < E_{\text{delayed}} < 12.0 \text{ MeV}$  and  $Q_{\text{max}}/Q_{\text{tot}} < 0.055$ ;
- (4) multiplicity: no additional triggers from 100  $\mu\text{s}$  preceding the prompt signal to 400  $\mu\text{s}$  after it, with the goal of reducing the correlated background.

The IBD efficiencies for these cuts are listed in Table 8.

A preliminary sample of 9021 candidates is obtained by applying selections (1–4). In order to reduce the background contamination in the sample, candidates are rejected according to two extra cuts. First, candidates within a 0.5 s window after a high energy muon crossing the ID ( $E_{\mu} > 600 \text{ MeV}$ ) are tagged as cosmogenic isotope events and are rejected, increasing the effective veto time to 9.2%. Second, candidates whose prompt signal is coincident with an OV trigger are also excluded as correlated background. Applying the above vetoes yields 8249 candidates or a rate of  $36.2 \pm 0.4$  events/day, uniformly distributed within the target, for an analysis livetime of 227.93 days. Following the same selection procedure on the  $\bar{\nu}_e$  MC sample yields 8439.6 expected events in the absence of oscillation.

The main source of accidental coincidences is the random association of a prompt trigger from natural radioactivity and a later neutron-like candidate. This background is estimated not only by applying the neutrino selection cuts described, but also using coincidence windows shifted by 1 s in order to remove correlations in the time scale of n-captures in H and Gd. The radioactivity rate between 0.7 and 12.2 MeV is  $8.2 \text{ s}^{-1}$ , while the singles rate in 6–12 MeV energy region is  $18 \text{ h}^{-1}$ . Finally, the accidental background rate is found to be  $0.261 \pm 0.002$  events per day.

The radioisotopes  $^8\text{He}$  and  $^9\text{Li}$  are products of spallation processes on  $^{12}\text{C}$  induced by cosmic muons crossing the scintillator volume. The  $\beta$ -n decays of these isotopes constitute a background for the antineutrino search.  $\beta$ -n emitters can be identified from the time and space correlations to their parent muon. Due to their relatively long lifetimes ( $^9\text{Li}$ :  $\tau = 257 \text{ ms}$ ,  $^8\text{He}$ :  $\tau = 172 \text{ ms}$ ), an event-by-event discrimination is not possible. For the muon rates in our detector, vetoing for several isotope lifetimes after each muon would lead to an unacceptably large loss in exposure. Instead, the rate is determined by an exponential fit to the  $\Delta t_{\mu\nu} \equiv t_{\mu} - t_{\nu}$  profile of all possible muon-IBD candidate pairs. The

analysis is performed for three visible energy  $E_{\mu}^{\text{vis}}$  ranges that characterize subsamples of parent muons by their energy deposition, not corrected for energy nonlinearities, in the ID as follows.

- (1) Showering muons crossing the target value are selected by  $E_{\mu}^{\text{vis}} > 600 \text{ MeV}$ , and feature, they an increased probability to produce cosmogenic isotopes. The  $\Delta t_{\mu\nu}$  fit returns a precise result of  $0.95 \pm 0.11$  events/day for the  $\beta$ -n-emitter rate.
- (2) In the  $E_{\mu}^{\text{vis}}$  range from 275 to 600 MeV, muons crossing GC and target still give a sizable contribution to isotope production of  $1.08 \pm 0.44$  events/day. To obtain this result from a  $\Delta t_{\mu\nu}$  fit, the sample of muon-IBD pairs has to be cleaned by a spatial cut on the distance of closest approach from the muon to the IBD candidate of  $d_{\mu\nu} < 80 \text{ cm}$  to remove the majority of uncorrelated pairs. The corresponding cut efficiency is determined from the lateral distance profile obtained for  $E_{\mu}^{\text{vis}} > 600 \text{ MeV}$ . The approach is validated by a comparative study of cosmic neutrons that show an almost congruent profile with very little dependence on  $E_{\mu}^{\text{vis}}$  above 275 MeV.
- (3) The cut  $E_{\mu}^{\text{vis}} < 275 \text{ MeV}$  selects muons crossing only the buffer volume or the rim of the GC. For this sample, no production of  $\beta$ -n emitters inside the target volume is observed. An upper limit of  $< 0.3$  events/day can be established based on a  $\Delta t_{\mu\nu}$  fit for  $d_{\mu\nu} < 80 \text{ cm}$ . Again, the lateral distribution of cosmic neutrons has been used for determining the cut efficiency.

The overall rate of  $\beta n$  decays found is  $2.05^{+0.62}_{-0.52}$  events/day.

Most correlated backgrounds are rejected by the 1 ms veto time after each tagged muon. The remaining events arise from cosmogenic events whose parent muon either misses the detector or deposits an energy low enough to escape the muon tagging. Two contributions have been found: fast neutrons (FNs) and stopping muons (SMs). FNs are created by muons in the inactive regions surrounding the detector. Their large interaction length allows them to cross the detector and capture in the ID, causing both a prompt trigger by recoil protons and a delayed trigger by capture on Gd. An approximately flat prompt energy spectrum is expected; a slope could be introduced by acceptance and scintillator quenching effects. The time and spatial correlations distribution of FN are indistinguishable from those of  $\bar{\nu}_e$  events. The selected SM arise from muons entering through the chimney, stopping in the top of the ID, and eventually decaying. The short muon track mimics the prompt event, and the decay Michel electron mimics the delayed event. SM candidates are localized in space in the top of the ID under the chimney and have a prompt-delayed time distribution following the 2.2  $\mu\text{s}$  muon lifetime. The correlated background has been studied by extending the selection on  $E_{\text{prompt}}$  up to 30 MeV. No IBD events are expected in the interval  $12 \text{ MeV} \leq E_{\text{prompt}} \leq 30 \text{ MeV}$ . FN and SM candidates were separated via their different correlation time distributions. The observed

TABLE 9: Summary of observed IBD candidates, with corresponding signal and background predictions for each integration period before any oscillation fit results have been applied.

	Reactors both on	One reactor $P_{th} < 20\%$	Total
Livetime (days)	139.27	88.66	227.93
IBD candidates	6088	2161	8249
$\nu$ Reactor B1	2910.9	774.6	3685.5
$\nu$ Reactor B2	3422.4	1331.7	4754.1
Cosmogenic isotope	174.1	110.8	284.9
Correlated FN and SM	93.3	59.4	152.7
Accidentals	36.4	23.1	59.5
Total prediction	6637.1	2299.7	8936.8

prompt energy spectrum is consistent with a flat continuum between 12 and 30 MeV, which extrapolated to the IBD selection window providing a first estimation of the correlated background rate of  $\approx 0.75$  events/day. The accuracy of this estimate depends on the validity of the extrapolation of the spectral shape. Several FN and SM analyses were performed using different combinations of IV and OV taggings. The main analysis for the FN estimation relies on IV tagging of the prompt triggers with OV veto applied for the IBD selection. A combined analysis was performed to obtain the total spectrum and the total rate estimation of both FN and SM,  $(0.67 \pm 0.20)$  events/day summarized, in Table 9.

There are four ways that can be utilized to estimate backgrounds. Each independent background component can be measured by isolating samples and subtracting possible correlations. Second, we can measure each independent background component including spectral information when fitting for  $\theta_{13}$  oscillations. Third, the total background rate is measured by comparing the observed and expected rates as a function of reactor power. Fourth, we can use the both-reactor-off data to measure both the rate and spectrum. The latter two methods are used currently as cross-checks for the background measurements due to low statistics and are described here. The measured daily rate of IBD candidates as a function of the no-oscillation expected rate for different reactor power conditions is shown in Figure 17. The extrapolation to zero reactor power of the fit to the data yields  $2.9 \pm 1.1$  events per day, in excellent agreement with our background estimate. The overall rate of correlated background events that pass the IBD cuts is independently verified by analyzing 22.5 hours of both-reactors-off data [48]. The expected neutrino signal is  $< 0.3$  residual  $\bar{\nu}_e$  events.

Calibration data taken with the  $^{252}\text{Cf}$  source were used to check the Monte Carlo prediction for any biases in the neutron selection criteria and estimate their contributions to the systematic uncertainty.

The fraction of neutron captures on gadolinium is evaluated to be 86.5% near the center of the target and to be 1.5% lower than the fraction predicted by simulation. Therefore, the Monte Carlo simulation for the prediction of the number of  $\bar{\nu}_e$  events is reduced by factor of 0.985. After the prediction of the fraction of neutron captures on gadolinium is scaled

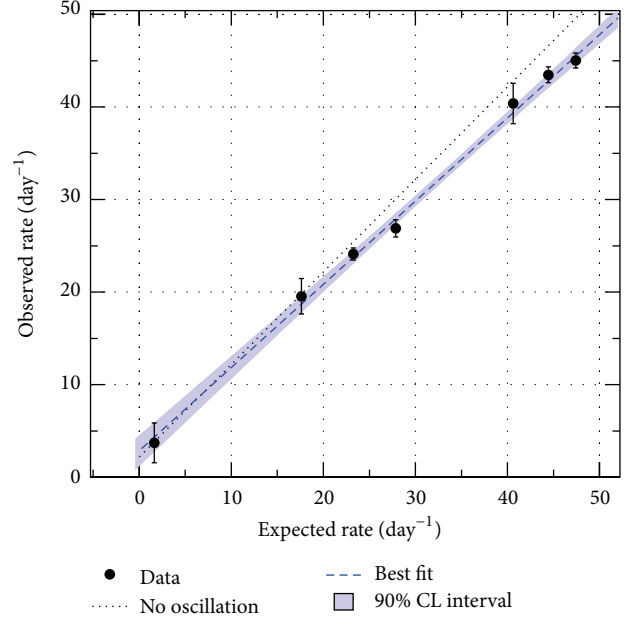


FIGURE 17: Daily number of  $\bar{\nu}_e$  candidates as a function of the expected number of  $\bar{\nu}_e$ . The dashed line shows the fit to the data, along with the 90% C L band. The dotted line shows the expectation in the no-oscillation scenario.

to the data, the prediction reproduces the data within 0.3% under variation of selection criteria.

The  $^{252}\text{Cf}$  is also used to check the neutron capture time,  $\Delta T$ . The simulation reproduces the efficiency (96.2%) of the  $\Delta t_{e+n}$  cut with an uncertainty of 0.5% augmented with sources deployed through the NT and GC.

The efficiency for Gd capture events with visible energy greater than 4 MeV to pass the 6 MeV cut is estimated to be 94.1%. Averaged over the NT, the fraction of neutron captures on Gd accepted by the 6.0 MeV cut is in agreement with calibration data within 0.7%.

The Monte Carlo simulation indicates that the number of IBD events occurring in the GC with the neutron captured in the NT (spill-in) slightly exceeds the number of events occurring in the target with the neutron escaping to the gamma catcher (spill-out), by  $1.35\% \pm 0.04\%$  (stat)  $\pm 0.30\%$  (sys). The spill-in/out effect is already included in the simulation, and therefore no correction for this is needed. The uncertainty of 0.3% assigned to the net spill-in/out current was quantified by varying the parameters affecting the process, such as gadolinium concentration in the target scintillator and hydrogen fraction in the gamma-catcher fluid within its tolerances. Moreover, the parameter variation was performed with multiple Monte Carlo models at low neutron energies.

**5.5. Oscillation Analysis.** The oscillation analysis is based on a combined fit to antineutrino rate and spectral shape. The data are compared to the Monte Carlo signal and background events from high-statistics samples. The same selections are applied to both signal and background, with corrections made to Monte Carlo only when necessary to match detector



performance metrics. The oscillation analysis begins by separating the data into 18 variably sized bins between 0.7 and 12.2 MeV. Two integration periods are used in the fit to help separate background and signal fluxes. One set contains data periods, where one reactor is operating at less than 20% of its nominal thermal power, according to power data provided by EDF, while the other set contains data from all other times, typically when both reactors are running. All data end up in one of the two integration periods. Here, we denote the number of observed IBD candidates in each of the bins as  $N_i$ , where  $i$  runs over the combined 36 bins of both integration periods. The use of multiple periods of data integration takes advantage of the different signal/background ratios in each period, as the signal rate varies with reactor power, while the backgrounds remain constant in time. This technique adds information about background behavior to the fit. The distribution of IBD candidates between the two integration periods is given in Table 9. A prediction of the observed number of signal and background events is constructed for each energy bin, following the same integration period division as the following data:

$$N^{\text{pred}}_i = \sum_{R=1,2}^{\text{Reactors}} N_i^{\gamma,R} + \sum_b^{\text{Bkgnds.}} N_i^b, \quad (17)$$

where  $N_i^{\gamma,R} = P(\bar{\nu}_e \rightarrow \bar{\nu}_e) N_i^{\text{exp},R}$ ,  $P_{\bar{\nu}_e \rightarrow \bar{\nu}_e}$  is the neutrino survival probability from the well-known oscillation formula, and  $N_i^{\text{exp},R}$  is given by (16). The index  $b$  runs over the three backgrounds: cosmogenic isotope; correlated; and accidental. The index  $R$  runs over the two reactors, Chooz B1 and B2. Background populations were calculated based on the measured rates and the livetime of the detector during each integration period. Predicted populations for both null-oscillation signal and backgrounds may be found in Table 9.

Systematic and statistical uncertainties are propagated to the fit by the use of a covariance matrix  $M_{ij}$  in order to properly account for correlations between energy bins. The sources of uncertainty  $A$  are listed in Table 10 as follows:

$$M_{ij} = M_{ij}^{\text{sig.}} + M_{ij}^{\text{det.}} + M_{ij}^{\text{stat.}} + M_{ij}^{\text{eff.}} + \sum_b^{\text{Bkgnds.}} M_{ij}^b. \quad (18)$$

Each term  $M_{ij}^A = \text{cov}(N_i^{\text{pred}}, N_j^{\text{pred}})_A$  on the right-hand side of (18) represents the covariance of  $N_i^{\text{pred}}$  and  $N_j^{\text{pred}}$  due to uncertainty  $A$ . The normalization uncertainty associated with each of the matrix contributions may be found from the sum of each matrix; these are summarized in Table 10. Many sources of uncertainty contain spectral shape components which do not directly contribute to the normalization error but do provide for correlated uncertainties between the energy bins. The signal covariance matrix  $M_{ij}^{\text{sig.}}$  is calculated taking into account knowledge about the predicted neutrino spectra. The  ${}^9\text{Li}$  matrix contribution contains spectral shape uncertainties estimated using different Monte Carlo event generation parameters. The slope of the FN/SM spectrum is allowed to vary from a nearly flat spectrum. Since accidental background uncertainties are measured to a high

TABLE 10: Summary of signal and background normalization uncertainties in this analysis relative to the total prediction.

Source	Uncertainty (%)
Reactor flux	1.67%
Detector response	0.32%
Statistics	1.06%
Efficiency	0.95%
Cosmogenic isotope background	1.38%
FN/SM	0.51%
Accidental background	0.01%
Total	2.66%

precision from many off-time windows, they are included as a diagonal covariance matrix. The elements of the covariance matrix contributions are recalculated as a function of the oscillation and other parameters (see below) at each step of the minimization. This maintains the fractional systematic uncertainties as the bin populations vary from the changes in the oscillation and fit parameters.

A fit of the binned signal and background data to a two-neutrino oscillation hypothesis was performed by minimizing a standard  $\chi^2$  function:

$$\chi^2 = \sum_{i,j}^{36} (N_i - N_i^{\text{pred}}) \times (M_{ij})^{-1} (N_j - N_j^{\text{pred}})^T + \frac{(\epsilon_{\text{FN/SM}} - 1)^2}{\sigma_{\text{FN/SM}}^2} + \frac{(\epsilon_{{}^9\text{Li}} - 1)^2}{\sigma_{{}^9\text{Li}}^2} + \frac{(\alpha_E - 1)^2}{\sigma_{\alpha_E}^2} + \frac{(\Delta m_{31}^2 - (\Delta m_{31}^2)_{\text{MINOS}})^2}{\sigma_{\text{MINOS}}^2}. \quad (19)$$

The use of energy spectrum information in this analysis allows additional information on background rates to be gained from the fit, in particular because of the small number of IBD events between 8 and 12 MeV. The two fit parameters  $\epsilon_{\text{FN/SM}}$  and  $\epsilon_{{}^9\text{Li}}$  are allowed to vary as part of the fit, and they scale the rates of the two backgrounds (correlated and cosmogenic isotopes). The rate of accidentals is not allowed to vary since its initial uncertainty is precisely determined in-situ. The energy scale for predicted signal and  ${}^9\text{Li}$  events is allowed to vary linearly according to the  $\alpha_E$  parameter with an uncertainty  $\sigma_{\alpha_E} = 1.13\%$ . A final parameter constrains the mass splitting  $\Delta m_{31}^2$  using the MINOS measurement [90] of  $\Delta m_{31}^2 = (2.32 \pm 0.12) \times 10^{-3} \text{ eV}^2$ , where we have symmetrized the error. This error includes the uncertainty introduced by relating the effective mass-squared difference observed in a  $\nu_\mu$  disappearance experiment to the one relevant for reactor experiments and the ambiguity due to the type of the neutrino mass hierarchy; see for example [91]. Uncertainties for these parameters,  $\sigma_{\text{FN/SM}}$ ,  $\sigma_{{}^9\text{Li}}$ , and  $\sigma_{\text{MINOS}}$ , are listed as the initial values in Table 11. The best fit gives  $\sin^2 2\theta_{13} = 0.109 \pm 0.030(\text{stat.}) \pm 0.025(\text{syst})$  at  $\Delta m_{31}^2 = 2.32 \times 10^{-3} \text{ eV}^2$ , with a  $\chi^2/\text{NDF} = 42.1/35$ . Table 11 gives the resulting values of the fit parameters and their uncertainties. Comparing the

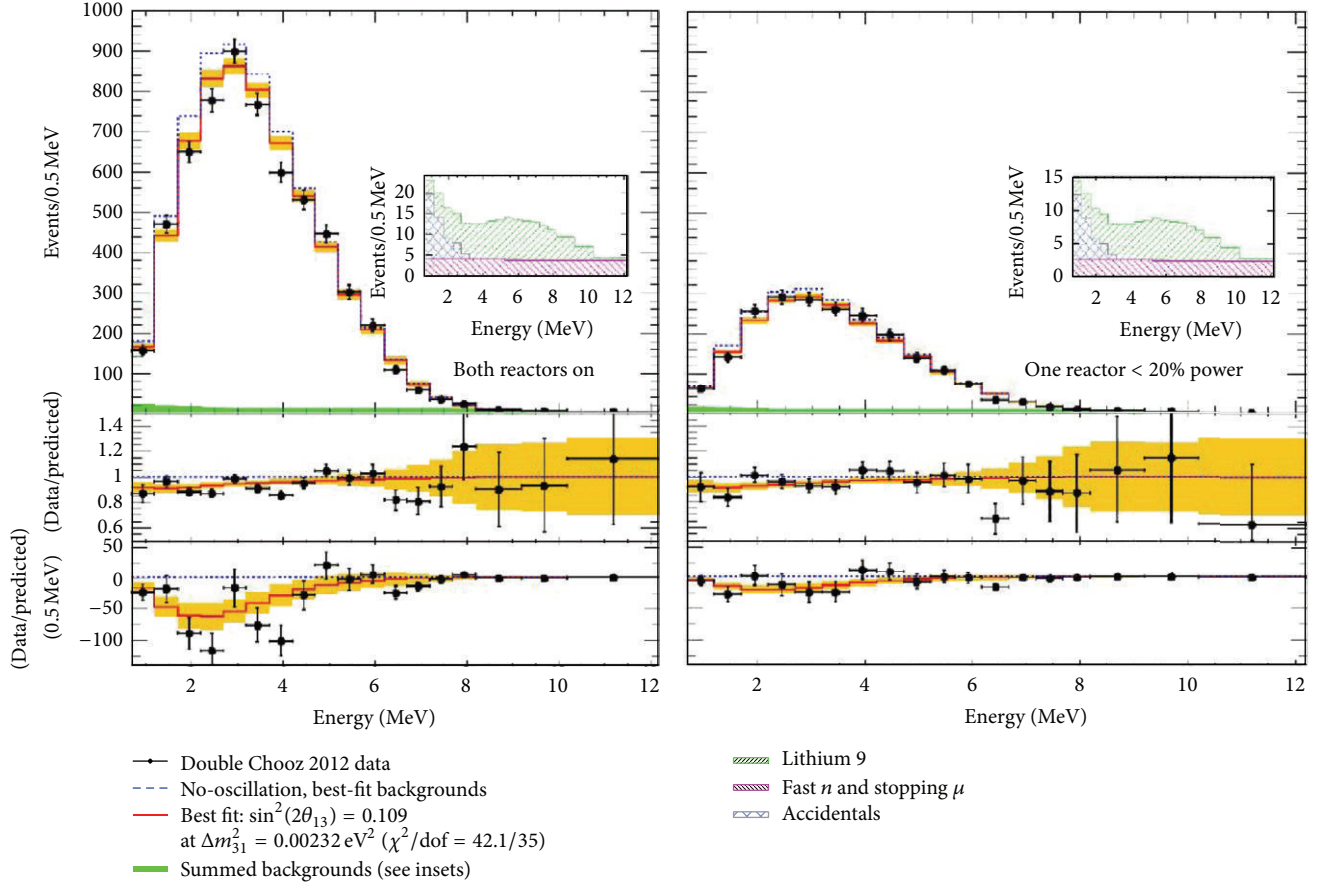


FIGURE 18: Measured prompt energy spectrum for each integration period (data points) superimposed on the expected prompt energy spectrum, including backgrounds (green region), for the no-oscillation (blue dotted curve) and best-fit (red solid curve), backgrounds at  $\sin^2 2\theta_{13} = 0.109$  and  $\Delta m_{31}^2 = 2.32 \times 10^{-3} \text{eV}^2$ . Inset: stacked spectra of backgrounds. Bottom: differences between data and no-oscillation prediction (data points) and differences between best-fit prediction and no-oscillation prediction (red curve). The orange band represents the systematic uncertainties on the best-fit prediction.

TABLE 11: Parameters in the oscillation fit. Initial values are determined by measurements of background rates or detector calibration data. Best-fit values are outputs of the minimization procedure.

Fit parameter	Initial value	Best-fit value
$^9\text{Li}$ Bkg. $\epsilon_{\text{Li}}$	$(1.25 \pm 0.54) \text{d}^{-1}$	$(1.00 \pm 0.29) \text{d}^{-1}$
FN/SM Bkg. $\epsilon_{\text{FN/SM}}$	$(0.67 \pm 0.20) \text{d}^{-1}$	$(0.64 \pm 0.13) \text{d}^{-1}$
Energy scale $\alpha_E$	$1.000 \pm 0.011$	$0.986 \pm 0.007$
$\Delta m_{31}^2$ ( $10^{-3} \text{eV}^2$ )	$2.32 \pm 0.12$	$2.32 \pm 0.12$

values with the ones used as input to the fit in Table 9, we conclude that the background rate and uncertainties are further constrained in the fit, as well as the energy scale.

The final measured spectrum and the best-fit spectrum are shown in Figure 18 for the new and old data sets, and for both together in Figure 19.

An analysis comparing only the total observed number of IBD candidates in each integration period to the expectations produces a best fit of  $\sin^2 2\theta_{13} = 0.170 \pm 0.052$  at  $\chi^2/\text{NDF} = 0.50/1$ . The compatibility probability for the rate-only and rate+shape measurements is about 30% depe-

nding on how the correlated errors are handled between the two measurements.

Confidence intervals for the standard analysis were determined using a frequentist technique [92]. This approach accommodates the fact that the true  $\chi^2$  distributions may not be Gaussian and is useful for calculating the probability of excluding the no-oscillation hypothesis. This study compared the data to 10,000 simulations generated at each of 21 test points in the range  $0 \leq \sin^2 2\theta_{13} \leq 0.25$ . A  $\Delta\chi^2$  statistic, equal to the difference between the  $\chi^2$  at the test point and the  $\chi^2$  at the best fit, was used to determine the region in  $\sin^2 2\theta_{13}$  where the  $\Delta\chi^2$  of the data was within the given confidence probability. The allowed region at 68% (90%) CL is  $0.068$  ( $0.044$ )  $< \sin^2 2\theta_{13} < 0.15$  ( $0.17$ ). An analogous technique shows that the data exclude the no-oscillation hypothesis at 99.9% ( $3.1\sigma$ ).

## 6. RENO

The reactor experiment for neutrino oscillation (RENO) has obtained a definitive measurement of the smallest neutrino

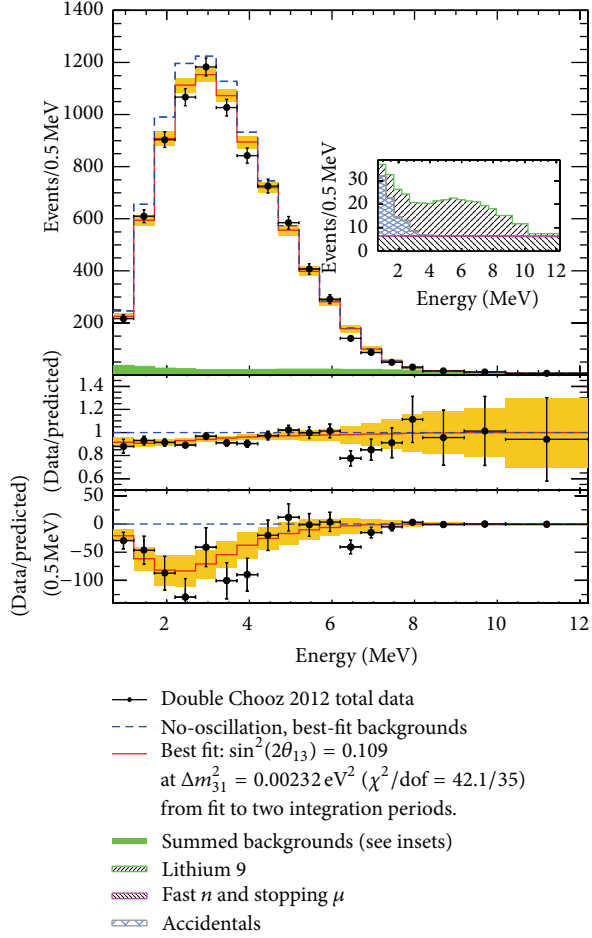


FIGURE 19: Sum of both integration periods plotted in the same manner as Figure 18.

mixing angle of  $\theta_{13}$  by observing the disappearance of electron antineutrinos emitted from a nuclear reactor, excluding the no-oscillation hypothesis at  $4.9\sigma$ . From the deficit, the best-fit value of  $\sin^2 2\theta_{13}$  is obtained as  $0.113 \pm 0.013(\text{stat.}) \pm 0.019(\text{syst.})$  based on a rate-only analysis.

Consideration of RENO began in early 2004, and its proposal was approved by the Ministry of Science and Technology in Korea in May 2005. The company operating the Yonggwang nuclear power plant, KHNP, has allowed us to carry out the experiment in a restricted area. The project started in March 2006. Geological survey was completed in 2007. Civil construction began in middle 2008 and was completed in early 2009. Both near and far detectors are completed in early 2011, and data taking began in early August 2011. RENO is the first experiment to measure  $\theta_{13}$  with two identical detectors in operation.

**6.1. Experimental Setup and Detection Method.** RENO detects antineutrinos from six reactors at Yonggwang Nuclear Power Plant in Korea. A symmetric arrangement of the reactors and the detectors, as shown in Figure 20, is useful for minimizing the complexity of the measurement. The

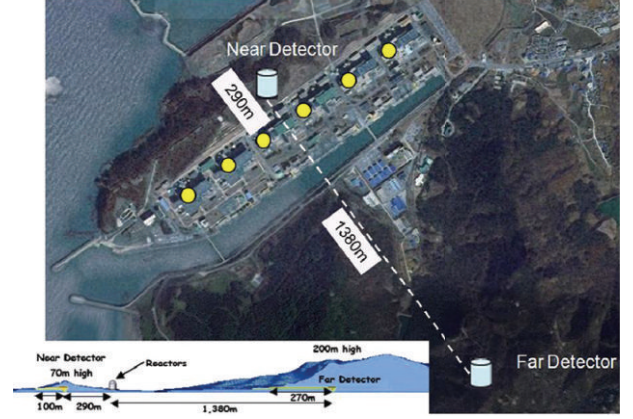


FIGURE 20: A schematic setup of the RENO experiment.

six pressurized water reactors with each maximum thermal output of  $2.8 \text{ GW}_{\text{th}}$  (reactors 3, 4, 5, and 6) or  $2.66 \text{ GW}_{\text{th}}$  (reactors 1 and 2) are lined up in roughly equal distances and span  $\sim 1.3 \text{ km}$ .

Two identical antineutrino detectors are located at 294 m and 1383 m, respectively, from the center of reactor array to allow a relative measurement through a comparison of the observed neutrino rates. The near detector is located inside a restricted area of the nuclear power plant, quite close to the reactors to make an accurate measurement of the antineutrino fluxes before their oscillations. The far (near) detector is beneath a hill that provides 450 m (120 m) of water-equivalent rock overburden to reduce the cosmic backgrounds.

The measured far-to-near ratio of antineutrino fluxes can considerably reduce systematic errors coming from uncertainties in the reactor neutrino flux, target mass, and detection efficiency. The relative measurement is independent of correlated uncertainties and helps to minimize uncorrelated reactor uncertainties.

The positions of two detectors and six reactors are surveyed with GPS and total station to determine the baseline distances between detector and reactor to an accuracy of less than 10 cm. The accurate measurement of the baseline distances finds the reduction of reactor neutrino fluxes at detector to a precision of much better than 0.1%. The reactor-flux-weighted baseline is 408.56 m for the near detector and 1443.99 m for the far detector.

**6.2. Detector.** Each RENO detector (Figure 21) consists of a main inner detector (ID) and an outer veto detector (OD). The main detector is contained in a cylindrical stainless steel vessel that houses two nested cylindrical acrylic vessels. The innermost acrylic vessel holds  $18.6 \text{ m}^3$  (16.5 t)  $\sim 0.1\%$  Gadolinium-(Gd-) doped liquid scintillator (LS) as a neutrino target. An electron antineutrino can interact with a free proton in LS,  $\bar{\nu}_e + p \rightarrow e^+ + n$ . The coincidence of a prompt positron signal and a delayed signal from neutron capture by Gd provides the distinctive signature of inverse  $\beta$  decay.



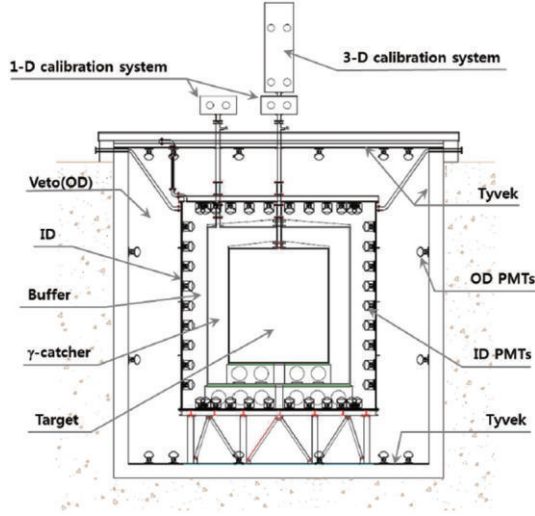


FIGURE 21: A schematic view of the RENO detector. The near and far detectors are identical.

The central target volume is surrounded by a 60 cm thick layer of LS without Gd, useful for catching  $\gamma$ -rays escaping from the target region and thus increasing the detection efficiency. Outside this  $\gamma$ -catcher, a 70 cm thick buffer layer of mineral oil provides shielding from radioactivity in the surrounding rocks and in the 354 10-inch photomultipliers (PMTs) that are mounted on the inner wall of the stainless steel container.

The outermost veto layer of OD consists of 1.5 m of highly purified water in order to identify events coming from outside by their Cherenkov radiation and to shield against ambient  $\gamma$ -rays and neutrons from the surrounding rocks.

The LS is developed and produced as a mixture of linear alkyl benzene (LAB), PPO, and bis-MSB. A Gd-carboxylate complex using TMHA was developed for the best Gd loading efficiency into LS and its long-term stability. Gd-LS and LS are made and filled into the detectors carefully to ensure that the near and far detectors are identical.

**6.3. Data Sample.** In the 229 day data-taking period between 11 August 2011 to 26 March 2012, the far (near) detector observed 17102 (154088) electron antineutrino candidate events or  $77.02 \pm 0.59$  ( $800.8 \pm 2.0$ ) events/day with a background fraction of 5.5% (2.7%). During this period, all six reactors were mostly on at full power, and reactors 1 and 2 were off for a month each because of fuel replacement.

Event triggers are formed by the number of PMTs with signals above a  $\sim 0.3$  photoelectron (pe) threshold (NHIT). An event is triggered and recorded if the ID NHIT is larger than 90, corresponding to 0.5–0.6 MeV well below the 1.02 MeV as the minimum energy of an IBD positron signal or if the OD NHIT is larger than 10.

The event energy is measured based on the total charge ( $Q_{\text{tot}}$ ) in pe, collected by the PMTs and corrected for gain variation. The energy calibration constant of 250 pe per MeV is determined by the peak energies of various radioactive sources deployed at the center of the target.

TABLE 12: Event rates of the observed candidates and the estimated background.

Detector	Near	Far
Selected events	154088	17102
Total background rate (per day)	$21.75 \pm 5.93$	$4.24 \pm 0.75$
IBD rate after background subtraction (per day)	$779.05 \pm 6.26$	$72.78 \pm 0.95$
DAQ Livetime (days)	192.42	222.06
Detection efficiency ( $\epsilon$ )	$0.647 \pm 0.014$	$0.745 \pm 0.014$
Accidental rate (per day)	$4.30 \pm 0.06$	$0.68 \pm 0.03$
${}^9\text{Li}/{}^8\text{He}$ rate (per day)	$12.45 \pm 5.93$	$2.59 \pm 0.75$
Fast neutron rate (per day)	$5.00 \pm 0.13$	$0.97 \pm 0.06$

**6.4. Background.** In the final data samples, uncorrelated (accidentals) and correlated (fast neutrons from outside of ID, stopping muon followers and  $\beta$ - $n$  emitters from  ${}^9\text{Li}/{}^8\text{He}$ ) background events survive selection requirements. The total background rate is estimated to be  $21.75 \pm 5.93$  (near) or  $4.24 \pm 0.75$  (far) events per day and summarized in Table 12.

The uncorrelated background is due to accidental coincidences from random association of a prompt-like event due to radioactivity and a delayed-like neutron capture. The remaining rate in the final sample is estimated to be  $4.30 \pm 0.06$  (near) or  $0.68 \pm 0.03$  (far) events per day.

The  ${}^9\text{Li}/{}^8\text{He}$   $\beta$ - $n$  emitters are mostly produced by energetic muons because their production cross-sections in carbon increase with muon energy. The background rate in the final sample is obtained as  $12.45 \pm 5.93$  (near) or  $2.59 \pm 0.75$  (far) events per day from a fit to the delay time distribution with an observed mean decay time of  $\sim 250$  ms.

An energetic neutron entering the ID can interact in the target to produce a recoil proton before being captured on Gd. Fast neutrons are produced by cosmic muons traversing the surrounding rock and the detector. The estimated fast neutron background is  $5.00 \pm 0.13$  (near) or  $0.97 \pm 0.06$  (far) events per day.

**6.5. Systematic Uncertainty.** The combined absolute uncertainty of the detection efficiency is correlated between the two detectors and estimated to be 1.5%. Uncorrelated relative detection uncertainties are estimated by comparing the two identical detectors. They come from relative differences between the detectors in energy scale, target protons, Gd capture ratio, and others. The combined uncorrelated detection uncertainty is estimated to be 0.2%.

The uncertainties associated with thermal power and relative fission fraction contribute to 0.9% of the  $\bar{\nu}_e$  yield per core to the uncorrelated uncertainty. The uncertainties associated with  $\bar{\nu}_e$  yield per fission, fission spectra, and thermal energy released per fission result in a 2.0% correlated uncertainty. We assume a negligible contribution of the spent fuel to the uncorrelated uncertainty.

**6.6. Results.** All reactors were mostly in steady operation at the full power during the data-taking period, except for reactor 2 (R2), which was off for the month of September 2011,

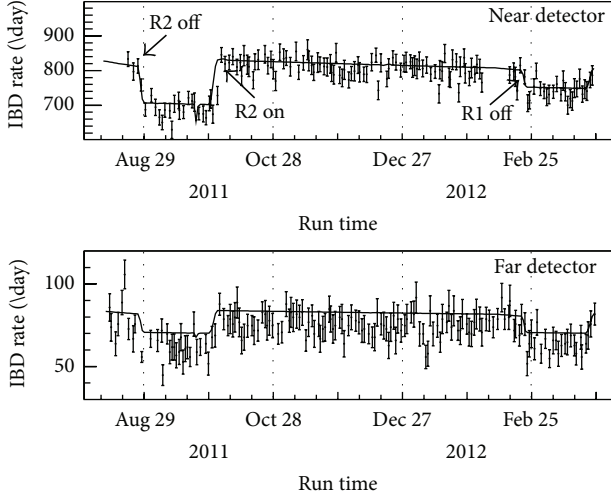


FIGURE 22: Measured daily-average rates of reactor neutrinos after background subtraction in the near and far detectors as a function of running time. The solid curves are the predicted rates for no oscillation.

and reactor 1 (R1), which was off from February 23 2012 for fuel replacement. Figure 22 presents the measured daily rates of IBD candidates after background subtraction in the near and far detectors. The expected rates assuming no oscillation, obtained from the weighted fluxes by the thermal power and the fission fractions of each reactor and its baseline to each detector, are shown for comparison.

Based on the number of events at the near detector and assuming no oscillation, RENO finds a clear deficit, with a far-to-near ratio

$$R = 0.920 \pm 0.009 \text{ (stat.)} \pm 0.014 \text{ (syst.)}. \quad (20)$$

The value of  $\sin^2 2\theta_{13}$  is determined from a  $\chi^2$  fit with pull terms on the uncorrelated systematic uncertainties. The number of events in each detector after the background subtraction has been compared with the expected number of events, based on the reactor neutrino flux, detection efficiency, neutrino oscillations, and contribution from the reactors to each detector determined by the baselines and reactor fluxes.

The best-fit value thus obtained is

$$\sin^2 2\theta_{13} = 0.113 \pm 0.013 \text{ (stat.)} \pm 0.019 \text{ (syst.)}, \quad (21)$$

and it excludes the no-oscillation hypothesis at the 4.9 standard deviation level.

RENO has observed a clear deficit of 8.0% for the far detector and of 1.2% for the near detector, concluding a definitive observation of reactor antineutrino disappearance consistent with neutrino oscillations. The observed spectrum of IBD prompt signals in the far detector is compared to the non oscillation expectations based on measurements in the near detector in Figure 23. The spectra of prompt signals are obtained after subtracting backgrounds shown in the inset. The disagreement of the spectra provides further evidence of neutrino oscillation.

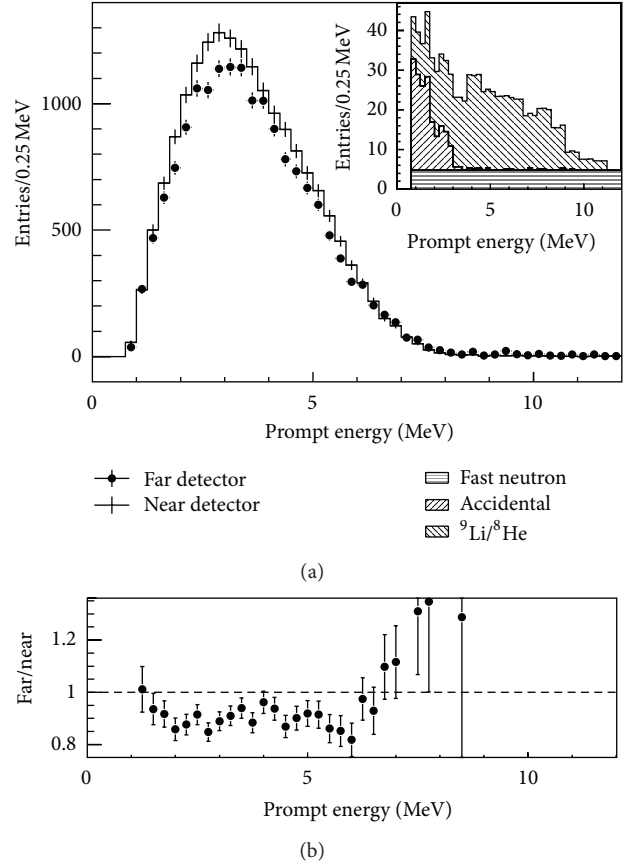


FIGURE 23: Observed spectrum of the prompt signals in the far detector compared with the nonoscillation predictions from the measurements in the near detector. The backgrounds shown in the inset are subtracted for the far spectrum. The background fraction is 5.5% (2.7%) for far (near) detector. Errors are statistical uncertainties only. (b) The ratio of the measured spectrum of far detector to the non-oscillation prediction.

In summary, RENO has observed reactor antineutrinos using two identical detectors each with 16 tons of Gd-loaded liquid scintillator and a 229 day exposure to six reactors with total thermal energy of  $16.5 \text{ GW}_{\text{th}}$ . In the far detector, a clear deficit of 8.0% is found by comparing a total of 17102 observed events with an expectation based on the near detector measurement assuming no oscillation. From this deficit, a rate-only analysis obtains  $\sin^2 2\theta_{13} = 0.113 \pm 0.013 \text{ (stat.)} \pm 0.019 \text{ (syst.)}$ . The neutrino mixing angle  $\theta_{13}$  is measured with a significance of 4.9 standard deviation.

**6.7. Future Prospects and Plan.** RENO has measured the value of  $\sin^2 2\theta_{13}$  with a total error of  $\pm 0.023$ . The expected sensitivity of RENO is to obtain  $\pm 0.01$  for the error based on the three years of data, leading to a statistical error of 0.006 and a systematic error of  $\sim 0.005$ .

The fast neutron and  $^9\text{Li}/^8\text{He}$  backgrounds produced by cosmic muons depend on the detector sites having different overburdens. Therefore, their uncertainties are the largest



contribution to the uncorrelated error in the current result, and change the systematic error by 0.017 at the best-fit value.

RENO makes efforts on further reduction of backgrounds, especially by removing the  $^9\text{Li}/^8\text{He}$  background by a tighter muon veto requirement and a spectral shape analysis to improve the systematic error. A longer-term effort will be made to reduce the systematic uncertainties of reactor neutrino flux and detector efficiency.

## 7. The Reactor Antineutrino Anomaly-Thierry

**7.1. New Predicted Cross-Section per Fission.** Fission reactors release about  $10^{20} \bar{\nu}_e \text{ GW}^{-1} \text{ s}^{-1}$ , which mainly come from the beta decays of the fission products of  $^{235}\text{U}$ ,  $^{238}\text{U}$ ,  $^{239}\text{Pu}$ , and  $^{241}\text{Pu}$ . The emitted antineutrino spectrum is then given by  $S_{\text{tot}}(E_\nu) = \sum_k f_k S_k(E_\nu)$ , where  $f_k$  refers to the contribution of the  $k$ th branch and  $S_k$  to their corresponding neutrino spectrum per fission. Antineutrino detection is achieved via the inverse beta-decay (IBD) reaction  $\bar{\nu}_e + {}^1\text{H} \rightarrow e^+ + n$ . Experiments at baselines below 100 m reported either the ratios ( $R$ ) of the measured to predicted cross-section per fission, or the observed event rate to the predicted rate.

The event rate at a detector is predicted based on the following formula:

$$N_\nu^{\text{Pred}} (\text{s}^{-1}) = \frac{1}{4\pi L^2} N_p \frac{P_{\text{th}}}{\langle E_f \rangle} \sigma_f^{\text{pred}}, \quad (22)$$

where the first term stands for the mean solid angle and  $N_p$  is the number of target protons for the inverse beta-decay process of detection. These two detector-related quantities are usually known with very good accuracy. The last two terms come from the reactor side. The ratio of  $P_{\text{th}}$ , the thermal power of the reactor, over  $\langle E_f \rangle$ , the mean energy per fission, provide the mean number of fissions in the core.  $P_{\text{th}}$  can be known at the subpercent level in commercial reactors, somewhat less accurately at research reactors. The mean energy per fission is computed as the average over the four main fissioning isotopes, accounting for 99.5% of the fissions

$$\langle E_f \rangle = \sum_k \langle E_k \rangle, \quad k = {}^{235}\text{U}, {}^{238}\text{U}, {}^{239}\text{Pu}, {}^{241}\text{Pu}. \quad (23)$$

It is accurately known from the nuclear databases and study of all decays and neutron captures subsequent to a fission [72]. Finally, the dominant source of uncertainty and by far the most complex quantity to compute is the mean cross-section per fission defined as

$$\sigma_f^{\text{pred}} = \int_0^\infty S_{\text{tot}}(E_\nu) \sigma_{V-A}(E_\nu) dE_\nu = \sum_k f_k \sigma_{f,k}^{\text{pred}}, \quad (24)$$

where the  $\sigma_{f,k}^{\text{pred}}$  is the predicted cross-sections for each fissile isotope,  $S_{\text{tot}}$  is the model dependent reactor neutrino

spectrum for a given average fuel composition ( $f_k$ ), and  $\sigma_{V-A}$  is the theoretical cross-section of the IBD reaction:

$$\sigma_{V-A}(E_e) [\text{cm}^2] = \frac{857 \times 10^{-43}}{\tau_n [\text{s}]} p_e [\text{MeV}] \times E_e [\text{MeV}] (1 + \delta_{\text{rec}} + \delta_{\text{wm}} + \delta_{\text{rad}}), \quad (25)$$

where  $\delta_{\text{rec}}$ ,  $\delta_{\text{wm}}$ , and  $\delta_{\text{rad}}$  are, respectively, the nucleon recoil, weak magnetism, and radiative corrections to the cross-section (see [22, 93] for details). The fraction of fissions undergone by the  $k$ th isotope,  $f_k$ , can be computed at the few percent level with reactor evolution codes (see for instance [79]), but their impact in the final error is well reduced by the sum rule of the total thermal power, accurately known from independent measurements

Accounting for new reactor antineutrino spectra [32] the normalization of predicted antineutrino rates,  $\sigma_{f,k}^{\text{pred}}$ , is shifted by +3.7%, +4.2%, +4.7%, and +9.8% for  $k = {}^{235}\text{U}$ ,  $^{239}\text{Pu}$ ,  $^{241}\text{Pu}$ , and  $^{238}\text{U}$ , respectively. In the case of  $^{238}\text{U}$ , the completeness of nuclear databases over the years largely explains the +9.8% shift from the reference computations [22].

The new predicted cross-section for any fuel composition can be computed from (24). By default, the new computation takes into account the so-called off-equilibrium correction [22] of the antineutrino fluxes (increase in fluxes caused by the decay of long-lived fission products). Individual cross-sections per fission per fissile isotope are slightly different, by +1.25% for the averaged composition of Bugey-4 [10], with respect to the original publication of the reactor antineutrino anomaly [93] because of the slight upward shift of the antineutrino flux consecutive to the work of [32] (see Section 2.2 for details).

**7.2. Impact of the New Reactor Neutrino Spectra on Past Short-Baseline (<100 m) Experimental Results.** In the eighties and nineties, experiments were performed with detectors located a few tens of meters from nuclear reactor cores at ILL, Goesgen, Rovno, Krasnoyarsk, Bugey (phases 3 and 4), and Savannah River [7–15]. In the context of the search of  $\mathcal{O}(\text{eV})$  sterile neutrinos, these experiments, with baselines below 100 m, have the advantage that they are not sensitive to a possible  $\theta_{13}$ ,  $\Delta m_{31}^2$ -driven oscillation effect (unlike the Palo Verde and CHOOZ experiments, for instance).

The ratios of observed event rates to predicted event rates (or cross-section per fission),  $R = N_{\text{obs}}/N_{\text{pred}}$ , are summarized in Table 13. The observed event rates and their associated errors are unchanged with respect to the publications; the predicted rates are reevaluated separately in each experimental case. One can observe a general systematic shift more or less significantly below unity. These reevaluations unveil a new *reactor antineutrino anomaly* ([http://irfu.cea.fr/en/Phoce/Vie\\_des\\_labos/Ast/ast\\_visu.php?id\\_ast=3045](http://irfu.cea.fr/en/Phoce/Vie_des_labos/Ast/ast_visu.php?id_ast=3045)) [93], clearly illustrated in Figure 24. In order to quantify the statistical significance of the anomaly, one can compute the weighted average of the ratios of expected-over-predicted rates, for all short-baseline



Gaussian, but with slightly longer tails, which were taken into account in the calculations (in contours that appear later, error bars are enlarged). With the old antineutrino spectra, the mean ratio is  $\mu = 0.980 \pm 0.024$ .

With the new antineutrino spectra, one obtains  $\mu = 0.927 \pm 0.023$ , and the fraction of simple Monte Carlo experiments with  $r \geq 1$  is 0.3%, corresponding to a  $-2.9\sigma$  effect (while a simple calculation assuming normality would lead to  $-3.2\sigma$ ). Clearly, the new spectra induce a statistically significant deviation from the expectation. This motivates the definition of an experimental cross-section  $\sigma_f^{\text{ano},2012} = 0.927 \times \sigma_f^{\text{pred,new}}$ . With the new antineutrino spectra, the minimum  $\chi^2$  for the data sample is  $\chi_{\text{min,data}}^2 = 18.4$ . The fraction of simple Monte Carlo experiments with  $\chi_{\text{min}}^2 < \chi_{\text{min,data}}^2$  is 50%, showing that the distribution of experimental ratios in  $\vec{R}$  around the mean value is representative given the correlations.

Assuming the correctness of  $\sigma_f^{\text{pred,new}}$ , the anomaly could be explained by a common bias in all reactor neutrino experiments. The measurements used different detection techniques (scintillator counters and integral detectors). Neutrons were tagged either by their capture in metal-loaded scintillator, or in proportional counters, thus leading to two distinct systematics. As far as the neutron detection efficiency calibration is concerned, note that different types of radioactive sources emitting MeV or sub-MeV neutrons were used (Am-Be,  $^{252}\text{Cf}$ , Sb-Pu, and Pu-Be). It should be mentioned that the Krasnoyarsk, ILL, and SRP experiments operated with nuclear fuel such that the difference between the real antineutrino spectrum and that of pure  $^{235}\text{U}$  was less than 1.5%. They reported similar deficits to those observed at other reactors operating with a mixed fuel. Hence, the anomaly can be associated neither with a single fissile isotope nor with a single detection technique. All these elements argue against a trivial bias in the experiments, but a detailed analysis of the most sensitive of them, involving experts, would certainly improve the quantification of the anomaly.

The other possible explanation of the anomaly is based on a real physical effect and is detailed in the next section. In that analysis, shape information from the Bugey-3 and ILL-published data [7, 8] is used. From the analysis of the shape of their energy spectra at different source-detector distances [8, 9], the Goesgen and Bugey-3 measurements exclude oscillations with  $0.06 < \Delta m^2 < 1 \text{ eV}^2$  for  $\sin^2(2\theta) > 0.05$ . Bugey-3's 40 m/15 m ratio data from [8] is used as it provides the best limit. As already noted in [94], the data from ILL showed a spectral deformation compatible with an oscillation pattern in their ratio of measured over predicted events. It should be mentioned that the parameters best fitting the data reported by the authors of [94] were  $\Delta m^2 = 2.2 \text{ eV}^2$  and  $\sin^2(2\theta) = 0.3$ . A reanalysis of the data of [94] was carried out in order to include the ILL shape-only information in the analysis of the reactor antineutrino anomaly. The contour in Figure 14 of [7] was reproduced for the shape-only analysis (while for the rate-only analysis discussed above that of [94] was reproduced, excluding the no-oscillation hypothesis at  $2\sigma$ ).

### 7.3. The Fourth Neutrino Hypothesis (3 + 1 Scenario)

**7.3.1. Reactor Rate-Only Analysis.** The reactor antineutrino anomaly could be explained through the existence of a fourth nonstandard neutrino, corresponding in the flavor basis to a sterile neutrino  $\nu_s$  with a large  $\Delta m_{\text{new}}^2$  value.

For simplicity, the analysis presented here is restricted to the 3 + 1 four-neutrino scheme in which there is a group of three active neutrino masses separated from an isolated neutrino mass, such that  $|\Delta m_{\text{new}}^2| \gg 10^{-2} \text{ eV}^2$ . The latter would be responsible for very short-baseline reactor neutrino oscillations. For energies above the IBD threshold and baselines below 100 m, the approximated oscillation formula

$$P_{ee} = 1 - \sin^2(2\theta_{\text{new}}) \sin^2\left(\frac{\Delta m_{\text{new}}^2 L}{4E_{\bar{\nu}_e}}\right) \quad (26)$$

is adopted, where active neutrino oscillation effects are neglected at these short baselines. In such a framework, the mixing angle is related to the  $U$  matrix element by the relation:

$$\sin^2(2\theta_{\text{new}}) = 4|U_{e4}|^2(1 - |U_{e4}|^2). \quad (27)$$

One can now fit the sterile neutrino hypothesis to the data (baselines below 100 m) by minimizing the least-squares function

$$(P_{ee} - \vec{R})^T W^{-1} (P_{ee} - \vec{R}), \quad (28)$$

assuming  $\sin^2(2\theta_{13}) = 0$ . Figure 25 provides the results of the fit in the  $\sin^2(2\theta_{\text{new}}) - \Delta m_{\text{new}}^2$  plane, including only the reactor experiment rate information. The fit to the data indicates that  $|\Delta m_{\text{new,R}}^2| > 0.2 \text{ eV}^2$  (99%) and  $\sin^2(2\theta_{\text{new,R}}) \sim 0.14$ . The best-fit point is at  $|\Delta m_{\text{new,R}}^2| = 0.5 \text{ eV}^2$  and  $\sin^2(2\theta_{\text{new,R}}) \sim 0.14$ . The no-oscillation analysis is excluded at 99.8%, corresponding roughly to  $3\sigma$ .

**7.3.2. Reactor Rate+Shape Analysis.** The ILL experiment may have seen a hint of oscillation in their measured positron energy spectrum [7, 94], but Bugey-3's results do not point to any significant spectral distortion more than 15 m away from the antineutrino source. Hence, in a first approximation, hypothetical oscillations could be seen as an energy-independent suppression of the  $\bar{\nu}_e$  rate by a factor of  $(1/2)\sin^2(2\theta_{\text{new,R}})$ , thus leading to  $\Delta m_{\text{new,R}}^2 > 1 \text{ eV}^2$  and accounting for the Bugey-3 and Goesgen shape analyses [8, 9]. Considering the weighted average of all reactor experiments, one obtains an estimate of the mixing angle,  $\sin^2(2\theta_{\text{new,R}}) \sim 0.15$ . The ILL positron spectrum is thus in agreement with the oscillation parameters found independently in the reanalyses mainly based on rate information. Because of the differences in the systematic effects in the rate and shape analyses, this coincidence is in favor of a true physical effect rather than an experimental anomaly. Including the finite spatial extension of the nuclear reactors and the ILL and Bugey-3 detectors, it is found that the small dimensions of the ILL nuclear core lead to small corrections of the oscillation pattern imprinted on the positron spectrum.

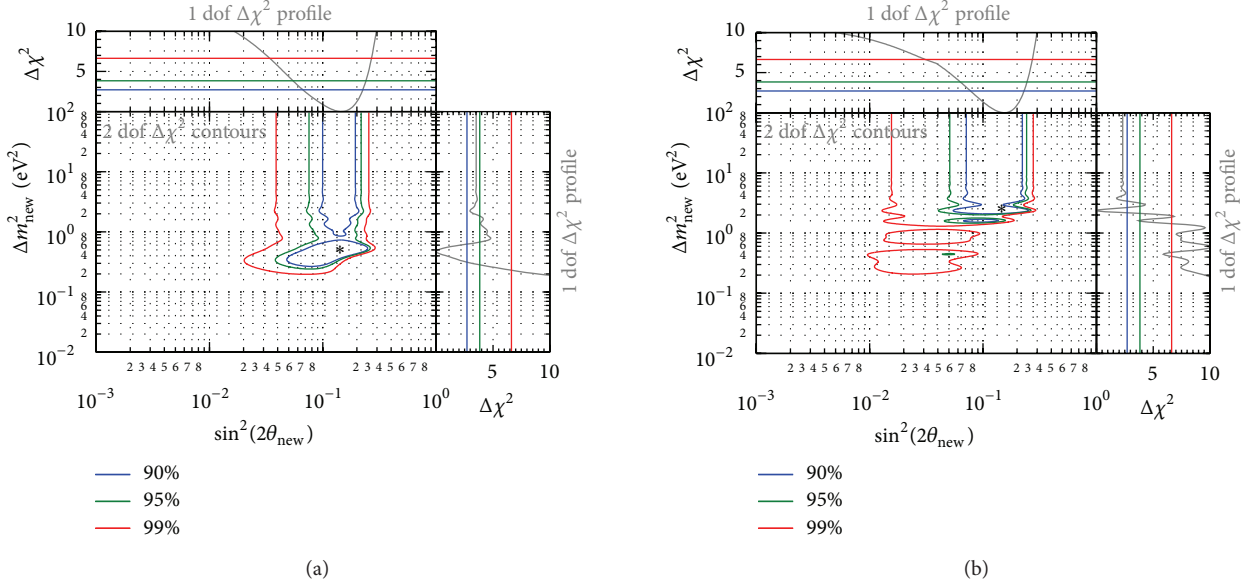


FIGURE 25: (a) Allowed regions in the  $\sin^2(2\theta_{\text{new}}) - \Delta m_{\text{new}}^2$  plane obtained from the fit of the reactor neutrino data, without any energy spectra information, to the 3 + 1 neutrino hypothesis, with  $\sin^2(2\theta_{13}) = 0$ . The best-fit point is indicated by a star. (b) Allowed regions in the  $\sin^2(2\theta_{\text{new}}) - \Delta m_{\text{new}}^2$  plane obtained from the fit of the reactor neutrino data, without ILL-shape information, but with the stringent oscillation constraint of Bugey-3 based on the 40 m/15 m ratios to the 3 + 1 neutrino hypothesis, with  $\sin^2(2\theta_{13}) = 0$ . The best-fit point is indicated by a star.

However, the large extension of the Bugey nuclear core is sufficient to wash out most of the oscillation pattern at 15 m. This explains the absence of shape distortion in the Bugey-3 experiment. We now present results from a fit of the sterile neutrino hypothesis to the data including both Bugey-3 and ILL original results (no-oscillation reported). With respect to the rate only parameters, the solutions at lower  $|\Delta m_{\text{new},R+S}^2|$  are now disfavored at large mixing angle because they would have imprinted a strong oscillation pattern in the energy spectra (or their ratio) measured at Bugey-3 and ILL. The best fit point is moved to  $|\Delta m_{\text{new},R+S}^2| = 2.4 \text{ eV}^2$ , whereas the mixing angle remains almost unchanged, at  $\sin^2(2\theta_{\text{new},R+S}) \sim 0.14$ . The no-oscillation hypothesis is excluded at 99.6%, corresponding roughly to  $2.9\sigma$ . Figure 25 provides the results of the fit in the  $\sin^2(2\theta_{\text{new}}) - \Delta m_{\text{new}}^2$  plane, including both the reactor experiment rate and shape (Bugey-3 and ILL) data.

**7.4. Combination of the Reactor and the Gallium Anomalies.** It is also possible to combine the results on the reactor antineutrino anomaly with the results on the gallium anomaly. The goal is to quantify the compatibility of the reactor and the gallium data.

For the reanalysis of the Gallex and Sage calibration runs with <sup>51</sup>Cr and <sup>37</sup>Ar radioactive sources emitting  $\sim 1 \text{ MeV}$  electron neutrinos [95–100], the methodology developed in [101] is used. However, in the analysis shown here, possible correlations between these four measurements are included. Details are given in [93]. This has the effect of being slightly more conservative, with the no-oscillation hypothesis disfavored at 97.7% C.L. Gallex and Sage observed an average deficit of  $R_G = 0.86 \pm 0.06$  ( $1\sigma$ ). The best-fit point is at

$|\Delta m_{\text{gallium}}^2| = 2.4 \text{ eV}^2$  (poorly defined), whereas the mixing angle is found to be  $\sin^2(2\theta_{\text{gallium}}) \sim 0.27 \pm 0.13$ . Note that the best-fit values are very close to those obtained by the analysis of the rate+shape reactor data.

Combining both the reactor and the gallium data, The no-oscillation hypothesis is disfavored at 99.97% C.L. ( $3.6\sigma$ ). Allowed regions in the  $\sin^2(2\theta_{\text{new}}) - \Delta m_{\text{new}}^2$  plane are displayed in Figure 26, together with the marginal  $\Delta\chi^2$  profiles for  $|\Delta m_{\text{new}}^2|$  and  $\sin^2(2\theta_{\text{new}})$ . The combined fit leads to the following constraints on oscillation parameters:  $|\Delta m_{\text{new}}^2| > 1.5 \text{ eV}^2$  (99% C.L.) and  $\sin^2(2\theta_{\text{new}}) = 0.17 \pm 0.04$  ( $1\sigma$ ). The most probable  $|\Delta m_{\text{new}}^2|$  is now rather better defined with respect to what has been published in [93], at  $|\Delta m_{\text{new}}^2| = 2.3 \pm 0.1 \text{ eV}^2$ .

**7.5. Status of the Reactor Antineutrino Anomaly.** The impact of the new reactor antineutrino spectra has been extensively studied in [93]. The increase of the expected antineutrino rate by about 4.5% combined with revised values of the antineutrino cross-section significantly decreased the normalized ratio of observed-to-expected event rates in all previous reactor experiments performed over the last 30 years at distances below 100 m [7–15]. The new average ratio, updated early 2012, is now  $0.927 \pm 0.023$ , leading to an enhancement of reactor antineutrino anomaly, now significant at the  $3\sigma$  confidence level. The best-fit point is at  $|\Delta m_{\text{new},R+S}^2| = 2.4 \text{ eV}^2$  whereas the mixing angle is at  $\sin^2(2\theta_{\text{new},R+S}) \sim 0.14$ .

This deficit could still be due to some unknown in the reactor physics, but it can also be analyzed in terms of a suppression of the  $\bar{\nu}_e$  rate at short distance as could be



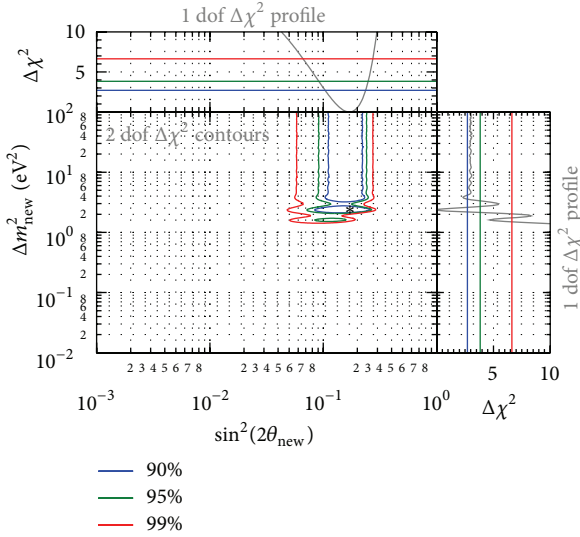


FIGURE 26: Allowed regions in the  $\sin^2(2\theta_{\text{new}}) - \Delta m_{\text{new}}^2$  plane from the combination of reactor neutrino experiments, the Gallex and Sage calibration sources experiments, and the ILL and Bugey-3-energy spectra. The data are well fitted by the  $3 + 1$  neutrino hypothesis, while the no-oscillation hypothesis is disfavored at 99.97% C.L. ( $3.6\sigma$ ).

expected from a sterile neutrino, beyond the standard model, with a large  $|\Delta m_{\text{new}}^2| \gg |\Delta m_{31}^2|$ . Note that hints of such results were already present at the ILL neutrino experiment in 1981 [94].

Considering the reactor  $\bar{\nu}_e$  anomaly and the gallium  $\nu_e$  source experiments [95–101] together, it is interesting to note that in both cases (neutrinos and antineutrinos) comparable deficits are observed at a similar  $L/E$ . Furthermore, it turns out that each experiment fitted separately leads to similar values of  $\sin^2(2\theta_{\text{new}})$  and similar lower bounds for  $|\Delta m_{\text{new}}^2|$  but without a strong significance. A combined global fit of gallium data and of short-baseline reactor data, taking into account the reevaluation of the reactor results discussed here, as well as the existing correlations, leads to a solution for a new neutrino oscillation, such that  $|\Delta m_{\text{new}}^2| > 1.5 \text{ eV}^2$  (99% C.L.) and  $\sin^2(2\theta_{\text{new}}) = 0.17 \pm 0.04$  ( $1\sigma$ ), disfavoring the no-oscillation case at 99.97% C.L. ( $3.6\sigma$ ). The most probable  $|\Delta m_{\text{new}}^2|$  is now at  $|\Delta m_{\text{new}}^2| = 2.3 \pm 0.1 \text{ eV}^2$ . This hypothesis should be checked against systematical effects, either in the prediction of the reactor antineutrino spectra or in the experimental results.

## 8. Reactor Monitoring for Nonproliferation of Nuclear Weapons

In the past, neutrino experiments have only been used for fundamental research, but today, thanks to the extraordinary progress of the field, for example, the measurement of the oscillation parameters, neutrinos could be useful for society.

The International Atomic Energy Agency (IAEA) works with its member states to promote safe, secure, and peaceful nuclear technologies. One of its missions is to verify that

safeguarded nuclear material and activities are not used for military purposes. In a context of international tension, neutrino detectors could help the IAEA to verify the treaty on the non-proliferation of nuclear weapons (NPT), signed by 145 states around the world.

A small neutrino detector located at a few tens of meters from a nuclear core could monitor nuclear reactor cores non-intrusively, robustly, and automatically. Since the antineutrino spectra and relative yields of fissioning isotopes  $^{235}\text{U}$ ,  $^{238}\text{U}$ ,  $^{239}\text{Pu}$ , and  $^{241}\text{Pu}$  depend on the isotopic composition of the core, small changes in composition could be observed without ever directly accessing the core itself. Information from a modest-sized antineutrino detector, coupled with the well-understood principles that govern the core's evolution in time, can be used to determine whether the reactor is being operated in an illegitimate way. Furthermore, such a detector can help to improve the reliability of the operation, by providing an independent and accurate measurement, in real time, of the thermal power and its reactivity at a level of a few percent. The intention is to design an “optimal” monitoring detector by using the experience obtained from neutrino physics experiments and feasibility studies.

Sands is a one cubic meter antineutrino detector located at 25 meters from the core of the San Onofre reactor site in California [102]. The detector has been operating for several months in an automatic and nonintrusive fashion that demonstrates the principles of reactor monitoring. Although the signal-to-noise ratio of the current design is still less than two, it is possible to monitor the thermal power at a level of a few percent in two weeks. At this stage of the work, the study of the evolution of the fuel seems difficult, but this has already been demonstrated by the Bugey and Rovno experiments.

The NUCIFER experiment in France [103], a 850 liters Gd-doped liquid scintillator detector installed at 7 m from the Osiris nuclear reactor core at CEA-Saclay. The goal is the measurement of its thermal power and plutonium content. The design of such a small volume detector has been focused on high detection efficiency and good background rejection. The detector is being operated since May 2012, and first results are expected in 2013.

The near detectors of Daya Bay, RENO, and Double Chooz will be a research detector with a very high sensitivity to study neutrino oscillations. Millions of events are being detected in the near detectors (between 300 and 500 m away from the cores). These huge statistics could be exploited to help the IAEA in its safeguards missions. The potential of neutrinos to detect various reactor diversion scenarios can be tested.

A realistic reactor monitor is likely to be somewhere between the two concepts presented above.

## 9. Future Prospects

Reactors are powerful neutrino sources for free. It is a well understood source since the precision of the neutrino flux and energy spectrum is better than 2%. With a near detector, this uncertainty can be reduced to 0.3%. Clearly, this is much better than usual neutrinos sources such as accelerators, solar, and atmospheric neutrinos. If a detector is placed at different



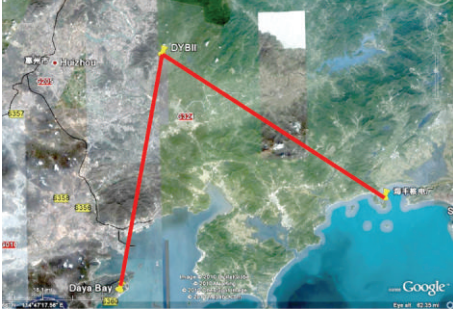


FIGURE 27: The new site for a long-baseline reactor neutrino experiment.

baseline, an experiment with different motivation can be planned.

**9.1. Mass Hierarchy.** With the discovery of the unexpected large  $\theta_{13}$ , mass hierarchy and even the CP phase become accessible with nowadays technologies. A number of new projects are now proposed based on different neutrino sources and different types of detectors.

It is known that neutrino mass hierarchy can be determined by long-baseline (more than 1000 km) accelerator experiment through matter effects. Atmospheric neutrinos may also be used for this purpose using a huge detector. Neutrino mass hierarchy can in fact distort the energy spectrum from reactors [104, 105], and a Fourier transformation of the spectrum can enhance the signature since mass terms appear in the frequency regime of the oscillation probability [106].

It is also shown that by employing a different Fourier transformation as the following:

$$\begin{aligned} \text{FCT}(\omega) &= \int_{t_{\min}}^{t_{\max}} F(t) \cos(\omega t) dt, \\ \text{FST}(\omega) &= \int_{t_{\min}}^{t_{\max}} F(t) \sin(\omega t) dt, \end{aligned} \quad (29)$$

the signature of mass hierarchy is more evident, and it is independent of the precise knowledge of  $\Delta_{23}^2$  [107].

The normal hierarchy and inverted hierarchy have very different shapes of the energy spectrum after the Fourier transformation. A detailed Monte Carlo study [108] shows that if  $\sin^2 2\theta_{13}$  is more than (1-2)%, a (10-50), kt liquid scintillator at a baseline of about 60 km with an energy resolution better than (2-3)% can determine the mass hierarchy at more than 90% C L. In fact, with  $\sin^2 2\theta_{13} = 0.1$ , the mass hierarchy can be determined up to the  $3\sigma$  level with a nominal detector size of 20 kt and a detector energy resolution of 3%.

The group at the Institute of High Energy Physics in Beijing proposed such an experiment in 2008. Fortunately, at a distance of 60 km from Daya Bay, there is a mountain with overburden more than 1500 MWE, where an underground lab can be built. Moreover, this location is 60 km from another nuclear power plant to be built, as shown in Figure 27. The total number of reactors, 6 operational and 6 to be built, may give a total thermal power of more than 35 GW.

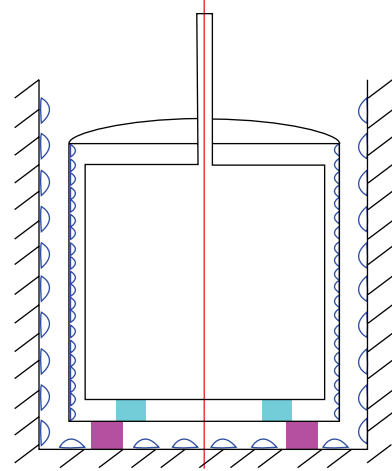


FIGURE 28: A conceptual design of a large liquid scintillator detector.

A conceptual design of the detector is shown in Figure 28. The detector is 30 m in diameter and 30 m high, filled with 20 kt liquid scintillator. The oil buffer will be 6 kt and water buffer is 10 kt. The totally needed number of 20" PMTs is 15000, covering 80% of the surface area.

There are actually two main technical difficulties for such a detector. The attenuation length of the liquid scintillator should be more than 30 m, and the quantum efficiency of PMTs should be more than 40%. R&D efforts are now started at IHEP, and results will be reported in the near future.

There is another proposed project to construct an underground detector of RENO-50 [109]. It consists of 5,000 tons of ultralow-radioactivity liquid scintillator and photomultiplier tubes, located at roughly 50 km away from the Yonggwang nuclear power plant in Korea, where the neutrino oscillation due to  $\theta_{12}$  takes place at maximum. RENO-50 is expected to detect neutrinos from nuclear reactors, the sun, supernova, the earth, any possible stellar object, and a J-PARC neutrino beam. It could be served as a multipurpose and long-term operational detector including a neutrino telescope. The main goal is to measure the most accurate (1%) value of  $\theta_{12}$  and to attempt determination of the neutrino mass hierarchy.

**9.2. Precision Measurement of Mixing Parameters.** A 20 kt liquid scintillator can have a long list of physics goals. In addition to neutrino mass hierarchy, neutrino mixing parameters including  $\theta_{12}$ ,  $\Delta m_{12}^2$  and  $\Delta m_{23}^2$  can be measured at the ideal baseline of 60 km to a precision better than 1%. Combined with results from other experiments for  $\theta_{23}$  and  $\theta_{13}$ , the unitarity of the neutrino mixing matrix can be tested up to 1% level, much better than that in the quark sector for the CKM matrix. This is very important to explore the physics beyond the standard model, and issues like sterile neutrinos can be studied.

In fact, for this purpose, there is no need to require extremely good energy resolution and huge detectors. Some of the current members of the RENO group indeed proposed a 5 kt liquid scintillator detector exactly for this purpose [109].

If funding is approved, they can start right away based on the existing technology.

**9.3. Others.** A large liquid scintillator detector is also ideal for supernova neutrinos since it can determine neutrino energies for different flavors, much better than flavor-blind detectors. Geoneutrinos can be another interesting topic, together with other traditional topics such as atmospheric neutrinos, solar neutrinos, and exotic searches.

## 10. Conclusions and Outlook

Three reactor experiments have definitively measured the value of  $\sin^2 2\theta_{13}$  based on the disappearance of electron antineutrinos. Based on unprecedentedly copious data, Daya Bay and RENO have performed rather precise measurements of the value. Averaging the results of the three reactor experiments with the standard Particle Data Group method, one obtains  $\sin^2 2\theta_{13} = 0.098 \pm 0.013$  [110]. It took 14 years to measure all three mixing angles after the discovery of neutrino oscillation in 1998.

The exciting result of solving the longstanding secret provides a comprehensive picture of neutrino transformation among three kinds of neutrinos and opens the possibility of searching for CP violation in the lepton sector. The surprisingly large value of  $\theta_{13}$  will strongly promote the next round of neutrino experiments to find CP violation effects and determine the neutrino mass hierarchy. The relatively large value has already triggered reconsideration of future long-baseline neutrino oscillation experiments. The successful measurement of  $\theta_{13}$  has made the very first step on the long journey to the complete understanding of the fundamental nature and implications of neutrino masses and mixing parameters.

## References

- [1] W. Pauli Jr., Address to Group on Radioactivity (Tuebingen, 1930) (Unpublished) Septieme conseil de physique Solvay, Bruxelles, 1033 (Gautier-Villars, Paris, France, 1934).
- [2] E. Fermi, "Versuch einer theorie der  $\beta$ -strahlen. I," *Zeitschrift für Physik*, vol. 88, no. 3-4, pp. 161-177, 1934.
- [3] F. Reines and C. L. Cowan Jr., "Detection of the free neutrino," *Physical Review*, vol. 92, no. 3, pp. 830-831, 1953.
- [4] C. L. Cowan Jr., F. Reines, F. B. Harrison, H. W. Kruse, and A. D. McGuire, "Detection of the free neutrino: a confirmation," *Science*, vol. 124, no. 3212, pp. 103-104, 1956.
- [5] F. Reines, C. L. Cowan Jr., F. B. Harrison, A. D. McGuire, and H. W. Kruse, "Detection of the free antineutrino," *Physical Review*, vol. 117, no. 1, pp. 159-173, 1960.
- [6] F. Reines and C. L. Cowan Jr., "Free antineutrino absorption cross section. I. Measurement of the free antineutrino absorption cross section by protons," *Physical Review*, vol. 113, no. 1, pp. 273-279, 1959.
- [7] H. Kwon, F. Boehm, A. A. Hahn et al., "Search for neutrino oscillations at a fission reactor," *Physical Review D*, vol. 24, no. 5, pp. 1097-1111, 1981.
- [8] Y. Declais, R. Aleksanb, M. Avenier et al., "Search for neutrino oscillations at 15, 40 and 95 meters from a nuclear power reactor at Bugey," *Nuclear Physics B*, vol. 434, no. 3, pp. 503-532, 1995.
- [9] G. Zacek, F. V. Feilitzsch, R. L. Mössbauer et al., "Neutrino-oscillation experiments at the Gösigen nuclear power reactor," *Physical Review D*, vol. 34, no. 9, pp. 2621-2636, 1986.
- [10] Y. Declais, H. de Kerret, B. Lefèvre et al., "Study of reactor antineutrino interaction with proton at Bugey nuclear power plant," *Physics Letters B*, vol. 338, no. 2-3, pp. 383-389, 1994.
- [11] A. Afonin et al., *JETP Letters*, vol. 93, p. 1, 1988.
- [12] G. S. Vidyakin, V. N. Vyrodov, Yu. V. Kozlov et al., "Limitations on the characteristics of neutrino oscillations," *JETP Letters*, vol. 59, pp. 390-393, 1994.
- [13] G. Vidyakin et al., *JETP Letters*, vol. 93, p. 424, 1987.
- [14] G. Vidyakin et al., *JETP Letters*, vol. 59, p. 390, 1994.
- [15] Z. Greenwood, W. R. Kropp, M. A. Mandelkern et al., "Results of a two-position reactor neutrino-oscillation experiment," *Physical Review D*, vol. 53, no. 11, pp. 6054-6064, 1996.
- [16] F. Ardellier, I. Barabanov, J. C. Barriere et al., "Double chooz, a search for the neutrino mixing angle theta-13," <http://arxiv.org/abs/hepex/060602>.
- [17] X. Guo, N. Wang, R. Wang et al., "A precision measurement of the neutrino mixing angle theta-13 using reactor Antineutrinos at Daya Bay," <http://arxiv.org/abs/hep-ex/0701029>.
- [18] J. Ahn and Reno Collaboration, "RENO: an experiment for neutrino oscillation parameter theta-13 using reactor neutrinos at Yonggwan," <http://arxiv.org/abs/1003.1391>.
- [19] K. Schreckenbach, G. Colvin, W. Gelletly, and F. von Feilitzsch, "Determination of the antineutrino spectrum from  $^{235}\text{U}$  thermal neutron fission products up to 9.5 MeV," *Physics Letters B*, vol. 160, no. 4-5, pp. 325-330, 1985.
- [20] F. von Feilitzsch, A. A. Hahn, and K. Schreckenbach, "Experimental beta-spectra from  $^{239}\text{Pu}$  and  $^{235}\text{U}$  thermal neutron fission products and their correlated antineutrino spectra," *Physics Letters B*, vol. 118, no. 1-3, pp. 162-166, 1982.
- [21] A. Hahn, K. Schreckenbach, W. Gelletly, F. von Feilitzsch, G. Colvin, and B. Krusche, "Antineutrino spectra from  $^{241}\text{Pu}$  and  $^{239}\text{Pu}$  thermal neutron fission products," *Physics Letters B*, vol. 218, no. 3, pp. 365-368, 1989.
- [22] Th. Mueller, D. Lhuillier, M. Fallot et al., "Improved predictions of reactor antineutrino spectra," *Physical Review C*, vol. 83, no. 5, Article ID 054615, 17 pages, 2011.
- [23] W. Mampe, K. Schreckenbach, P. Jeuch et al., "The double focusing iron-core electron-spectrometer "BILL" for high resolution ( $n, e^-$ ) measurements at the high flux reactor in Grenoble," *Nuclear Instruments and Methods*, vol. 154, no. 1, pp. 127-149, 1978.
- [24] A. Sirlin, "General properties of the electromagnetic corrections to the beta decay of a physical nucleon," *Physical Review*, vol. 164, no. 5, pp. 1767-1775, 1967.
- [25] P. Vogel, "Analysis of the antineutrino capture on protons," *Physical Review D*, vol. 29, no. 9, pp. 1918-1922, 1984.
- [26] J. Hardy, B. Jonson, and P. G. Hansen, "A comment on Pandemonium," *Physics Letters B*, vol. 136, no. 5-6, pp. 331-333, 1984.
- [27] <http://www.nndc.bnl.gov/ensdf>.
- [28] O. Tengblad, K. Aleklett, R. von Dincklage, E. Lund, G. Nyman, and G. Rudstam, "Integral gn-spectra derived from experimental  $\beta$ -spectra of individual fission products," *Nuclear Physics A*, vol. 503, no. 1, pp. 136-160, 1989.

- [29] R. Greenwood, R. G. Helmer, M. A. Lee et al., "Total absorption gamma-ray spectrometer for measurement of beta-decay intensity distributions for fission product radionuclides," *Nuclear Instruments and Methods in Physics Research A*, vol. 314, no. 3, pp. 514–540, 1992.
- [30] O. Meplan, in *Proceeding of the European Nuclear Conference. Nuclear Power for the 21st Century: From Basic Research to High-Tech Industry*, Versailles, France, 2005.
- [31] P. Vogel, "Conversion of electron spectrum associated with fission into the antineutrino spectrum," *Physical Review C*, vol. 76, no. 2, Article ID 025504, 5 pages, 2007.
- [32] P. Huber, "Determination of antineutrino spectra from nuclear reactors," *Physical Review C*, vol. 84, no. 2, Article ID 024617, 16 pages, 2011, Erratum-ibid. vol. 85, Article ID 029901, 2012.
- [33] D. Lhuillier, *Recent re-evaluation of reactor neutrino fluxes, slides of a talk given at Sterile Neutrinos at the Crossroads*, Blacksburg, Va, USA, 2011.
- [34] N. H. Haag, private communication, 2004.
- [35] J. Katakura et al., "JENDL Fission Product Decay Data File," 2000.
- [36] K. Takahashi, "Gross theory of first forbidden  $\beta$ -decay," *Progress of Theoretical Physics*, vol. 45, no. 5, pp. 1466–1492, 1971.
- [37] P. Vogel, G. K. Schenter, F. M. Mann, and R. E. Schenter, "Reactor antineutrino spectra and their application to antineutrino-induced reactions. II," *Physical Review C*, vol. 24, no. 4, pp. 1543–1553, 1981.
- [38] B. Pontecorvo, "Inverse beta processes and nonconservation of lepton charge," *Zhurnal Eksperimentalnoi i Teoreticheskoi Fiziki*, vol. 34, p. 247, 1958.
- [39] B. Pontecorvo, "Inverse beta processes and nonconservation of lepton charge," *Soviet Physics, JETP*, vol. 7, pp. 172–173, 1958.
- [40] Z. Maki, M. Nakagawa, and S. Sakata, "Remarks on the unified model of elementary particles," *Progress of Theoretical Physics*, vol. 28, no. 5, pp. 870–880, 1962.
- [41] M. Apollonio, A. Baldinib, C. Bemporad et al., "Limits on neutrino oscillations from the CHOOZ experiment," *Physics Letters B*, vol. 466, no. 2–4, pp. 415–430, 1999.
- [42] M. Apollonio, A. Baldini, C. Bemporad et al., "Search for neutrino oscillations on a long base-line at the CHOOZ nuclear power station," *The European Physical Journal C*, vol. 27, pp. 331–374, 2003.
- [43] A. Gando, Y. Gando, K. Ichimura et al., "Constraints on  $\theta_{13}$  from a three-flavor oscillation analysis of reactor antineutrinos at KamLAND," *Physical Review D*, vol. 83, no. 5, Article ID 052002, 11 pages, 2011.
- [44] P. Adamson, C. Andreopoulos, D. J. Auty et al., "New constraints on muon-neutrino to electron-neutrino transitions in MINOS," *Physical Review D*, vol. 82, Article ID 051102, 6 pages, 2010.
- [45] K. Abe, N. Abgrall, Y. Ajima et al., "Indication of electron neutrino appearance from an accelerator-produced off-axis Muon neutrino beam," *Physical Review Letters*, vol. 107, no. 4, Article ID 041801, 8 pages, 2011.
- [46] P. Adamson, D. J. Auty, D. S. Ayres et al., "Improved search for Muon-neutrino to electron-neutrino oscillations in MINOS," *Physical Review Letters*, vol. 107, no. 18, Article ID 181802, 6 pages, 2011.
- [47] Y. Abe, C. Aberle, T. Akiri et al., "Indication of reactor  $\bar{\nu}_e$  disappearance in the double chooz experiment," *Physical Review Letters*, vol. 108, no. 13, Article ID 131801, 7 pages, 2012.
- [48] Y. Abe, C. Aberle, J. C. dos Anjos et al., "Reactor electron antineutrino disappearance in the Double Chooz experiment," *Physical Review D*, vol. 86, no. 5, Article ID 052008, 21 pages, 2012.
- [49] G. L. Fogli, E. Lisi, A. Marrone, A. Palazzo, and A. M. Rotunno, "Evidence of  $\theta_{13} > 0$  from global neutrino data analysis," *Physical Review D*, vol. 84, no. 5, Article ID 053007, 7 pages, 2011.
- [50] T. Schwetz, M. Tórtola, and J. W. F. Valle, "Where we are on  $\theta_{13}$ : addendum to 'Global neutrino data and recent reactor fluxes: status of three-flavor oscillation parameters,'" *New Journal of Physics*, vol. 13, Article ID 109401, 5 pages, 2011.
- [51] F. P. An, J. Z. Bai, A. B. Balantekin et al., "Observation of electron-antineutrino disappearance at daya bay," *Physical Review Letters*, vol. 108, Article ID 171803, 7 pages, 2012.
- [52] J. K. Ahn, S. Chebotaryov, J. H. Choi et al., "Observation of reactor electron antineutrinos disappearance in the RENO experiment," *Physical Review Letters*, vol. 108, no. 19, Article ID 191802, 6 pages, 2012.
- [53] F. P. An and Daya Bay Collaboration, "Improved measurement of electron antineutrino disappearance at Daya Bay," *Chin. Phys. C* 37(2013) 011001.
- [54] F. P. An, Q. Anb, J. Z. Bai et al., "A side-by-side comparison of Daya Bay antineutrino detectors," *Nuclear Instruments and Methods in Physics Research A*, vol. 685, pp. 78–97, 2012.
- [55] <http://www.cgnpc.com.cn/n1093/n463576/n463598/>.
- [56] Y. Y. Ding, Z. Y. Zhang, P. J. Zhou, J. C. Liu, Z. M. Wang, and Y. L. Zhao, "Research and development of gadolinium loaded liquid scintillator for Daya Bay neutrino experiment," *Journal of Rare Earths*, vol. 25, pp. 310–313, 2007.
- [57] Y. Y. Ding, Z. Zhang, J. Liu, Z. Wang, P. Zhou, and Y. Zhao, "A new gadolinium-loaded liquid scintillator for reactor neutrino detection," *Nuclear Instruments and Methods in Physics Research A*, vol. 584, no. 1, pp. 238–243, 2008.
- [58] M. Yeh, A. Garnov, and R. L. Hahn, "Gadolinium-loaded liquid scintillator for high-precision measurements of antineutrino oscillations and the mixing angle,  $\theta_{13}$ ," *Nuclear Instruments and Methods in Physics Research A*, vol. 578, no. 1, pp. 329–339, 2007.
- [59] Q. Zhang, Y. Wang, J. Zhang et al., "An underground cosmic-ray detector made of RPC," *Nuclear Instruments and Methods in Physics Research A*, vol. 583, no. 2–3, pp. 278–284, 2007, Erratum-ibid. A, vol. 586, p. 374, 2008.
- [60] <http://geant4.cern.ch/>.
- [61] L. J. Wen, J. Cao, K.-B. Luk, Y. Ma, Y. Wang, and C. Yang, "Measuring cosmogenic  $^9\text{Li}$  background in a reactor neutrino experiment," *Nuclear Instruments and Methods in Physics Research A*, vol. 564, no. 1, pp. 471–474, 2006.
- [62] T. Nakagawa, K. Shibata, S. Chiba et al., "Japanese evaluated nuclear data library version 3 revision-2: JENDL-3.2," *Journal of Nuclear Science and Technology*, vol. 32, no. 12, pp. 1259–1271, 1995.
- [63] J. Cao, "Determining reactor neutrino flux," *Nuclear Physics B—Proceedings Supplements*. In press, <http://arxiv.org/abs/1101.2266>, Proceeding of Neutrino 2010.
- [64] S. F. E. Tournu et al., Tech. Rep. EPRI 2001.1001470, Palo Alto, Calif, USA, 2001.
- [65] C. Xu, X. N. Song, L. M. Chen, and K. Yang, *Chinese Journal of Nuclear Science and Engineering*, vol. 23, p. 26, 2003.
- [66] S. Rauck, "SCIENCE V2 nuclear code package—qualification report (Rev A)," Framatome ANP Document NFPD/DC/89, 14, 2004.
- [67] R. Sanchez, I. Zmijarevi, M. Coste-Delclaux et al., "APOLLO2 YEAR 2010," *Nuclear Engineering and Technology*, vol. 42, no. 5, pp. 474–499, 2010.



- [68] R. R. G. Marleau, A. Hebert, and R. Roy, "A user guide for DRAGON," Tech. Rep. IGE-236 Rev. 1, 2001.
- [69] C. E. Sanders and I. C. Gauld, "ORNL, isotopic analysis of high-burnup PWR spent fuel samples from the takahama-3 reactor," Tech. Rep. NUREG/CR-6798, ORNL/TM-2001/259, 2002.
- [70] Z. Djurcic, J. A. Detwiler, A. Piepke, V. R. Foster, L. Miller, and G. Gratta, "Uncertainties in the anti-neutrino production at nuclear reactors," *Journal of Physics G*, vol. 36, no. 4, Article ID 045002, 2009.
- [71] P. Vogel and J. F. Beacom, "Angular distribution of neutron inverse beta decay,  $\bar{\nu}_e + \bar{p} \rightarrow e^+ + n$ ," *Physical Review D*, vol. 60, no. 5, Article ID 053003, 10 pages, 1999.
- [72] V. I. Kopeikin, L. A. Mikaelyan, and V. V. Sinev, "Reactor as a source of antineutrinos: thermal fission energy," *Physics of Atomic Nuclei*, vol. 67, no. 10, pp. 1892–1899, 2004.
- [73] F. P. An, G. Jie, Z. Xiong-Wei, and L. Da-Zhang, "Simulation study of electron injection into plasma wake fields by colliding laser pulses using OOPIC," *Chinese Physics C*, vol. 33, article 711, 2009.
- [74] B. Zhou, R. Xi-Chao, N. Yang-Bo, Z. Zu-Ying, A. Feng-Peng, and C. Jun, "A study of antineutrino spectra from spent nuclear fuel at Daya Bay," *Chinese Physics C*, vol. 36, no. 1, article 001, 2012.
- [75] D. Stump, J. Pumphlin, R. Brock et al., "Uncertainties of predictions from parton distribution functions. I. The Lagrange multiplier method," *Physical Review D*, vol. 65, no. 1, Article ID 014012, 17 pages, 2001.
- [76] NEA-1845/01, documentation for MURE, 2009.
- [77] G. Marleau et al., Tech. Rep. IGE-157, 1994.
- [78] C. Jones, *Prediction of the reactor antineutrino flux for the double chooz experiment [Ph.D. thesis]*, MIT, Cambridge, Mass, USA, 2012.
- [79] C. Jones, A. Bernstein, J. M. Conrad et al., "Reactor simulation for antineutrino experiments using DRAGON and MURE," <http://arxiv.org/abs/1109.5379>.
- [80] A. Pichlmaier, V. Varlamov, K. Schreckenbach, and P. Geltenbort, "Neutron lifetime measurement with the UCN trap-in-trap MAMBO II," *Physics Letters B*, vol. 693, no. 3, pp. 221–226, 2010.
- [81] J. Allison, K. Amako, J. Apostolakis et al., "Geant4 developments and applications," *IEEE Transactions on Nuclear Science*, vol. 53, no. 1, pp. 270–278, 2006.
- [82] J. S. Agostinelli, J. Allison, K. Amako et al., "Geant4—a simulation toolkit," *Nuclear Instruments and Methods in Physics Research A*, vol. 506, no. 3, pp. 250–303, 2003.
- [83] D. R. Tilley, J. H. Kelley, J. L. Godwin et al., "Energy levels of light nuclei  $A = 8, 9, 10$ ," *Nuclear Physics A*, vol. 745, no. 3–4, pp. 155–362, 2004.
- [84] Y. Prezado, M. J. G. Borge, C. A. Diget et al., "Low-lying resonance states in the  $^9\text{Be}$  continuum," *Physics Letters B*, vol. 618, no. 1–4, pp. 43–50, 2005.
- [85] P. Papka, T. A. D. Brown, B. R. Fulton et al., "Decay path measurements for the 2.429 MeV state in  $^9\text{Be}$ : implications for the astrophysical  $\alpha + \alpha + n$  reaction," *Physical Review C*, vol. 75, no. 4, Article ID 045803, 8 pages, 2007.
- [86] <http://www.chem.agilent.com/en-US/Products/instruments/molecularspectroscopy/fluorescence/systems/caryclipse/pages/default.aspx>.
- [87] C. Aberle, C. Buck, B. Gramlich et al., "Large scale Gd-beta-diketonate based organic liquid scintillator production for anti-neutrino detection," *Journal of Instrumentation*, vol. 7, Article ID P06008, 2012.
- [88] C. Aberle, C. Buck, F. X. Hartmann, S. Schönert, and S. Wagner, "Light output of Double Chooz scintillators for low energy electrons," *Journal of Instrumentation*, vol. 6, Article ID P11006, 2011.
- [89] C. Aberle, [Ph.D. thesis], Universität Heidelberg, Heidelberg, Germany, 2011.
- [90] P. Adamson, C. Andreopoulos, R. Armstrong et al., "Measurement of the neutrino mass splitting and flavor mixing by MINOS," *Physical Review Letters*, vol. 106, no. 18, Article ID 181801, 6 pages, 2011.
- [91] H. Nunokawa, S. Parke, and R. Z. Funchal, "Another possible way to determine the neutrino mass hierarchy," *Physical Review D*, vol. 72, no. 1, Article ID 013009, 6 pages, 2005.
- [92] G. Feldman and R. Cousins, "Unified approach to the classical statistical analysis of small signals," *Physical Review D*, vol. 57, no. 7, pp. 3873–3889, 1998.
- [93] G. Mention, M. Fechner, Th. Lasserre et al., "Reactor antineutrino anomaly," *Physical Review D*, vol. 83, no. 7, Article ID 073006, 20 pages, 2011.
- [94] A. Hoummada and S. Lazrak Mikou, "Neutrino oscillations I.L.L. experiment reanalysis," *Applied Radiation and Isotopes*, vol. 46, no. 6–7, pp. 449–450, 1995.
- [95] P. Anselmann, R. Fockenbrocka, W. Hampel et al., "First results from the  $^{51}\text{Cr}$  neutrino source experiment with the GALLEX detector," *Physics Letters B*, vol. 342, no. 1–4, pp. 440–450, 1995.
- [96] W. Hampel, G. Heusser, J. Kiko et al., "Final results of the  $^{51}\text{Cr}$  neutrino source experiments in GALLEX," *Physics Letters B*, vol. 420, no. 1–2, pp. 114–126, 1998.
- [97] F. Kaether, W. Hampel, G. Heusser, J. Kiko, and T. Kirsten, "Reanalysis of the Gallex solar neutrino flux and source experiments," *Physics Letters B*, vol. 685, no. 2, pp. 47–54, 2010.
- [98] D. Abdurashitov, V. N. Gavrin, S. V. Girin et al., "The Russian-American gallium experiment (SAGE)  $^{51}\text{Cr}$  neutrino source measurement," *Physical Review Letters*, vol. 77, no. 23, pp. 4708–4711, 1996.
- [99] D. Abdurashitov, V. N. Gavrin, S. V. Girin et al., "Measurement of the response of a Ga solar neutrino experiment to neutrinos from a  $^{37}\text{Ar}$  source," *Physical Review C*, vol. 73, no. 4, Article ID 045805, 12 pages, 2006.
- [100] D. Abdurashitov, V. N. Gavrin, V. V. Gorbachev et al., "Measurement of the solar neutrino capture rate with gallium metal. III. Results for the 2002–2007 data-taking period," *Physical Review C*, vol. 80, no. 1, Article ID 015807, 16 pages, 2009.
- [101] C. Giunti and M. Laveder, "Short-baseline electron neutrino disappearance, tritium beta decay, and neutrinoless double-beta decay," *Physical Review D*, vol. 82, no. 5, Article ID 053005, 14 pages, 2010.
- [102] A. Bernstein, in *Proceedings of Neutrinos and Arm Control Workshop*, Honolulu, Hawaii, USA, 2003.
- [103] A. Porta et al., "Reactor neutrino detection for non proliferation with the Nucifer experiment," *Journal of Physics: Conference Series*, vol. 203, no. 1, Article ID 012092, 2010.
- [104] S. T. Petcov and M. Piai, "The LMA MSW solution of the solar neutrino problem, inverted neutrino mass hierarchy and reactor neutrino experiments," *Physics Letters B*, vol. 533, no. 1–2, pp. 94–106, 2002.
- [105] S. Choubey, S. T. Petcov, and M. Piai, "Precision neutrino oscillation physics with an intermediate baseline reactor neutrino experiment," *Physical Review D*, vol. 68, no. 11, Article ID 113006, 19 pages, 2003.



- [106] J. Learned, S. T. Dye, S. Pakvasa, and R. C. Svoboda, “Determination of neutrino mass hierarchy and  $\theta_{13}$  with a remote detector of reactor antineutrinos,” *Physical Review D*, vol. 78, no. 7, Article ID 071302, 5 pages, 2008.
- [107] L. Zhan, Y. Wang, J. Cao, and L. Wen, “Determination of the neutrino mass hierarchy at an intermediate baseline,” *Physical Review D*, vol. 78, no. 11, Article ID 111103, 5 pages, 2008.
- [108] L. Zhan, Y. Wang, J. Cao, and L. Wen, “Experimental requirements to determine the neutrino mass hierarchy using reactor neutrinos,” *Physical Review D*, vol. 79, no. 7, Article ID 073007, 5 pages, 2009.
- [109] S. B. Kim, in *Talk Given at the Conference of Neutrino*, 2012.
- [110] J. Beringer, J.-F. Arguin, R. M. Barnett et al., “Review of particle physics,” *Physical Review D*, vol. 86, no. 1, Article ID 010001, 1528 pages, 2012.

## Review Article

# The Nature of Massive Neutrinos

S. T. Petcov<sup>1,2</sup>

<sup>1</sup> SISSA, INFN, Via Bonomea 265, 34136 Trieste, Italy

<sup>2</sup> Kavli IPMU, University of Tokyo (WPI), Kashiwa 277-8583, Japan

Correspondence should be addressed to S. T. Petcov; petcov@sisssa.it

Received 6 September 2012; Accepted 25 October 2012

Academic Editor: Jose Bernabeu

Copyright © 2013 S. T. Petcov. This is an open access article distributed under the Creative Commons Attribution License, which permits unrestricted use, distribution, and reproduction in any medium, provided the original work is properly cited.

The compelling experimental evidences for oscillations of solar, reactor, atmospheric, and accelerator neutrinos imply the existence of 3-neutrino mixing in the weak charged lepton current. The current data on the 3-neutrino mixing parameters are summarised and the phenomenology of 3- $\nu$  mixing is reviewed. The properties of massive Majorana neutrinos and of their various possible couplings are discussed in detail. Two models of neutrino mass generation with massive Majorana neutrinos—the type I see-saw and the Higgs triplet model—are briefly reviewed. The problem of determining the nature, Dirac or Majorana, of massive neutrinos is considered. The predictions for the effective Majorana mass  $|\langle m \rangle|$  in neutrinoless double-beta- $((\beta\beta)_{0\nu})$  decay in the case of 3-neutrino mixing and massive Majorana neutrinos are summarised. The physics potential of the experiments, searching for  $(\beta\beta)_{0\nu}$ -decay for providing information on the type of the neutrino mass spectrum, on the absolute scale of neutrino masses, and on the Majorana CP-violation phases in the PMNS neutrino mixing matrix, is also briefly discussed. The opened questions and the main goals of future research in the field of neutrino physics are outlined.

## 1. Introduction: The Three Neutrino Mixing—An Overview

It is a well-established experimental fact that the neutrinos and antineutrinos which take part in the standard charged current (CC) and neutral current (NC) weak interaction are of three varieties (types) or flavours: electron,  $\nu_e$  and  $\bar{\nu}_e$ , muon,  $\nu_\mu$  and  $\bar{\nu}_\mu$ , and tauon,  $\nu_\tau$  and  $\bar{\nu}_\tau$ . The notion of neutrino type or flavour is dynamical:  $\nu_e$  is the neutrino which is produced with  $e^+$  or produces an  $e^-$  in CC weak interaction processes;  $\nu_\mu$  is the neutrino which is produced with  $\mu^+$  or produces  $\mu^-$ , and so forth. The flavour of a given neutrino is Lorentz invariant. Among the three different flavour neutrinos and antineutrinos, no two are identical. Correspondingly, the states which describe different flavour neutrinos must be orthogonal (within the precision of the current data):  $\langle \nu_l | \nu_l \rangle = \delta_{ll}$ ,  $\langle \bar{\nu}_l | \bar{\nu}_l \rangle = \delta_{ll}$ ,  $\langle \bar{\nu}_l | \nu_l \rangle = 0$ .

It is also well known from the existing data (all neutrino experiments were done so far with relativistic neutrinos or antineutrinos) that the flavour neutrinos  $\nu_l$  (antineutrinos  $\bar{\nu}_l$ ) are always produced in weak interaction processes in a state that is predominantly left handed (LH) (right handed (RH)). To account for this fact,  $\nu_l$  and  $\bar{\nu}_l$  are described in

the Standard Model (SM) by a chiral LH flavour neutrino field  $\nu_{lL}(x)$ ,  $l = e, \mu, \tau$ . For massless  $\nu_l$ , the state of  $\nu_l$  ( $\bar{\nu}_l$ ), which the field  $\nu_{lL}(x)$  annihilates (creates), is with helicity  $(-1/2)$  (helicity  $+1/2$ ). If  $\nu_l$  has a nonzero mass  $m(\nu_l)$ , the state of  $\nu_l$  ( $\bar{\nu}_l$ ) is a linear superposition of the helicity  $(-1/2)$  and  $(+1/2)$  states, but the helicity  $+1/2$  state (helicity  $-1/2$  state) enters into the superposition with a coefficient  $\propto m(\nu_l)/E$ ,  $E$  being the neutrino energy, and thus is strongly suppressed. Together with the LH charged lepton field  $l_L(x)$ ,  $\nu_{lL}(x)$  forms an  $SU(2)_L$  doublet in the Standard Model. In the absence of neutrino mixing and zero neutrino masses,  $\nu_{lL}(x)$  and  $l_L(x)$  can be assigned one unit of the additive lepton charge  $L_l$  and the three charges  $L_l$ ,  $l = e, \mu, \tau$ , are conserved by the weak interaction.

At present there is no compelling evidence for the existence of states of relativistic neutrinos (antineutrinos), which are predominantly right handed,  $\nu_R$  (left handed,  $\bar{\nu}_L$ ). If RH neutrinos and LH antineutrinos exist, their interaction with matter should be much weaker than the weak interaction of the flavour LH neutrinos  $\nu_l$  and RH antineutrinos  $\bar{\nu}_l$ ; that is,  $\nu_R$  ( $\bar{\nu}_L$ ) should be “sterile” or “inert” neutrinos (antineutrinos) [1]. In the formalism of the Standard Model, the sterile  $\nu_R$  and  $\bar{\nu}_L$  can be described by  $SU(2)_L$  singlet RH

neutrino fields  $\nu_R(x)$ . In this case,  $\nu_R$  and  $\bar{\nu}_L$  will have no gauge interactions, that is, will not couple to the weak  $W^\pm$  and  $Z^0$  bosons. If present in an extension of the Standard Model (even in the minimal one), the RH neutrinos can play a crucial role (i) in the generation of neutrino masses and mixing, (ii) in understanding the remarkable disparity between the magnitudes of neutrino masses and the masses of the charged leptons and quarks, and (iii) in the generation of the observed matter-antimatter asymmetry of the Universe (via the leptogenesis mechanism [2, 3]; see also, e.g., [4, 5]). In this scenario which is based on the see-saw theory [6–9], there is a link between the generation of neutrino masses and the generation of the baryon asymmetry of the Universe. The simplest hypothesis (based on symmetry considerations) is that to each LH flavour neutrino field  $\nu_{lL}(x)$  there corresponds an RH neutrino field  $\nu_{lR}(x)$ ,  $l = e, \mu, \tau$ , although schemes with less (more) than three RH neutrinos are also being considered (see, e.g., [10]).

The experiments with solar, atmospheric, reactor, and accelerator neutrinos (see [11] and the references quoted therein) have provided compelling evidences for flavour neutrino oscillations [1, 12–14]—transitions in flight between the different flavour neutrinos  $\nu_e, \nu_\mu, \nu_\tau$  (antineutrinos  $\bar{\nu}_e, \bar{\nu}_\mu, \bar{\nu}_\tau$ ), caused by nonzero neutrino masses and neutrino mixing. As a consequence of the results of these experiments, the existence of oscillations of the solar  $\nu_e$ , atmospheric  $\nu_\mu$  and  $\bar{\nu}_\mu$ , accelerator  $\nu_\mu$  (at  $L \sim 250$  km,  $L \sim 730$  km, and  $L \sim 295$  km, with  $L$  being the distance traveled by the neutrinos), and reactor  $\bar{\nu}_e$  (at  $L \sim 180$  km and  $L \sim 1$  km), was firmly established. The data imply the presence of neutrino mixing in the weak charged lepton current:

$$\mathcal{L}_{\text{CC}} = -\frac{g}{\sqrt{2}} \sum_{l=e,\mu,\tau} \bar{l}_L(x) \gamma_\alpha \nu_{lL}(x) W^{\alpha\dagger}(x) + \text{h.c.}, \quad (1)$$

$$\nu_{lL}(x) = \sum_{j=1}^n U_{lj} \nu_{jL}(x),$$

where  $\nu_{lL}(x)$  are the flavour neutrino fields,  $\nu_{jL}(x)$  is the left-handed (LH) component of the field of the neutrino  $\nu_j$  having a mass  $m_j$ , and  $U$  is a unitary matrix—the Pontecorvo-Maki-Nakagawa-Sakata (PMNS) neutrino mixing matrix [1, 12–14],  $U \equiv U_{\text{PMNS}}$ . All compelling neutrino oscillation data can be described assuming 3-neutrino mixing in vacuum,  $n = 3$ . The number of massive neutrinos  $n$  can, in general, be bigger than 3 if, for example, there exist right-handed (RH) sterile neutrinos [1] and they mix with the LH flavour neutrinos. It follows from the current data that at least 3 of the neutrinos  $\nu_j$ , say  $\nu_1, \nu_2, \nu_3$ , must be light,  $m_{1,2,3} \lesssim 1$  eV, and must have different masses,  $m_1 \neq m_2 \neq m_3$ . At present there is no compelling experimental evidence for the existence of more than 3 light neutrinos. Certain neutrino oscillation data exhibit anomalies that could be interpreted as being due to the existence of one or two additional (sterile) neutrinos with mass in the eV range, which have a relatively small mixing  $\sim 0.1$  with the active flavour neutrinos (see, e.g., [15] and the references quoted therein).

In the case of 3 light neutrinos on which we will concentrate on in this review, the neutrino mixing matrix  $U$  can

be parametrised by 3 angles and, depending on whether the massive neutrinos  $\nu_j$  are Dirac or Majorana [16] particles, by 1 or 3 CP violation (CPV) phases [17–20]:

$$U = VP, \quad P = \text{diag}\left(1, e^{i(\alpha_{21}/2)}, e^{i(\alpha_{31}/2)}\right), \quad (2)$$

where  $\alpha_{21}$  and  $\alpha_{31}$  are the two Majorana CPV phases and  $V$  is a CKM-like matrix containing the Dirac CPV phase  $\delta$ :

$$V = \begin{pmatrix} c_{12}c_{13} & s_{12}c_{13} & s_{13}e^{-i\delta} \\ -s_{12}c_{23} - c_{12}s_{23}s_{13}e^{i\delta} & c_{12}c_{23} - s_{12}s_{23}s_{13}e^{i\delta} & s_{23}c_{13} \\ s_{12}s_{23} - c_{12}c_{23}s_{13}e^{i\delta} & -c_{12}s_{23} - s_{12}c_{23}s_{13}e^{i\delta} & c_{23}c_{13} \end{pmatrix}. \quad (3)$$

In (3),  $c_{ij} = \cos \theta_{ij}$ ,  $s_{ij} = \sin \theta_{ij}$ , the angles  $\theta_{ij}$  and the Dirac phase  $\delta$  lie in the intervals  $0 \leq \theta_{ij} \leq \pi/2$  and  $0 \leq \delta \leq 2\pi$ , and, in general,  $0 \leq \alpha_{j1}/2 \leq 2\pi$ ,  $j = 2, 3$  [21, 22]. If CP invariance holds, we have  $\delta = 0, \pi$ , and [20, 23–25],  $\alpha_{21(31)} = k^{(l)} \pi$ ,  $k^{(l)} = 0, 1, 2, 3, 4$ .

Thus, in the case of massive Dirac neutrinos, the neutrino mixing matrix  $U$  is similar, in what concerns the number of mixing angles and CPV phases, to the CKM quark mixing matrix. The presence of two additional physical CPV phases in  $U$  if  $\nu_j$  are Majorana particles is a consequence of the special properties of the latter (see, e.g., [17, 26]). On the basis of the existing neutrino data it is impossible to determine whether the massive neutrinos are Dirac or Majorana fermions.

The neutrino oscillation probabilities depend, in general, on the neutrino energy  $E$ , the source-detector distance,  $L$ , on the elements of  $U$ , and, for relativistic neutrinos used in all neutrino experiments performed so far, on the neutrino mass squared differences  $\Delta m_{ij}^2 \equiv (m_i^2 - m_j^2)$ ,  $i \neq j$  (see, e.g., [11, 26]). In the case of 3-neutrino mixing there are only two independent neutrino mass squared differences, say  $\Delta m_{21}^2 \neq 0$  and  $\Delta m_{31}^2 \neq 0$ . The numbering of massive neutrinos  $\nu_j$  is arbitrary. We will employ here the widely used convention of numbering of  $\nu_j$  which allows to associate  $\theta_{13}$  with the smallest mixing angle in the PMNS matrix  $U$ , and  $\theta_{12}$ ,  $\Delta m_{21}^2 > 0$ , and  $\theta_{23}$ ,  $\Delta m_{31(32)}^2$ , with the parameters which drive, respectively, the solar ( $\nu_e$ ) and the dominant atmospheric  $\nu_\mu$  (and  $\bar{\nu}_\mu$ ) (and accelerator  $\nu_\mu$ ) oscillations. Under the assumption of CPT invariance, which we will suppose to hold throughout this article,  $\theta_{12}$  and  $\Delta m_{21}^2$  drive also the reactor  $\bar{\nu}_e$  oscillations at  $L \sim 180$  km (see, e.g., [11]). In this convention  $m_1 < m_2$ ,  $0 < \Delta m_{21}^2 < |\Delta m_{31}^2|$ , and, depending on  $\text{sgn}(\Delta m_{31}^2)$ , we have either  $m_3 < m_1$  or  $m_3 > m_2$  (see further). In the case of  $m_1 < m_2 < m_3$  ( $m_3 < m_1 < m_2$ ), the neutrino mass squared difference  $\Delta m_{21}^2$ , as it follows from the data to be discussed below, is much smaller than  $|\Delta m_{31(32)}^2|$ ,  $\Delta m_{21}^2 \ll |\Delta m_{31(32)}^2|$ . This implies that in each of the two cases  $m_1 < m_2 < m_3$  and  $m_3 < m_1 < m_2$  we have  $|\Delta m_{31}^2 - \Delta m_{32}^2| = \Delta m_{21}^2 \ll |\Delta m_{31(32)}^2|$ . The angles  $\theta_{12}$  and  $\theta_{23}$  are sometimes called “solar” and “atmospheric” neutrino mixing angles and are often denoted as  $\theta_{12} = \theta_\odot$  and  $\theta_{23} = \theta_{\text{atm}}$ , while  $\Delta m_{21}^2$  and  $\Delta m_{31(32)}^2$  are sometimes referred to as the “solar” and “atmospheric” neutrino mass squared differences and correspondingly are denoted as  $\Delta m_{21}^2 \equiv \Delta m_\odot^2$ ,  $\Delta m_{31(32)}^2 \equiv \Delta m_{\text{atm}}^2$ .

TABLE 1: The best-fit values and  $3\sigma$  allowed ranges of the 3-neutrino oscillation parameters, derived in [33] from a global fit of the current neutrino oscillation data. The values (values in brackets) correspond to  $m_1 < m_2 < m_3$  ( $m_3 < m_1 < m_2$ ). The definition of  $\Delta m_A^2$  used is:  $\Delta m_A^2 = m_3^2 - (m_2^2 + m_1^2)/2$ .

Parameter	Best fit ( $\pm 1\sigma$ )	$3\sigma$
$\Delta m_\odot^2$ [ $10^{-5}$ eV $^2$ ]	$7.54^{+0.26}_{-0.22}$	6.99–8.18
$ \Delta m_A^2 $ [ $10^{-3}$ eV $^2$ ]	$2.43^{+0.06}_{-0.10}$ (2.42 $^{+0.07}_{-0.11}$ )	2.19 (2.17)–2.62 (2.61)
$\sin^2\theta_{12}$	$0.307^{+0.018}_{-0.016}$	0.259–0.359
$\sin^2\theta_{23}$	$0.386^{+0.024}_{-0.021}$ (0.392 $^{+0.039}_{-0.022}$ )	0.331 (0.335)–0.637 (0.663)
$\sin^2\theta_{13}$	$0.0241 \pm 0.0025$ (0.0244 $^{+0.0023}_{-0.0025}$ )	0.0169 (0.0171)–0.0313 (0.0315)

Before continuing we would like to note that the preceding discussion is to a large extent based on parts of the text of the review article [11].

The neutrino oscillation data, accumulated over many years, allowed to determine the parameters which drive the solar, reactor, atmospheric, and accelerator neutrino oscillations,  $\Delta m_{21}^2$ ,  $\theta_{12}$ ,  $|\Delta m_{31(32)}^2|$  and  $\theta_{23}$ , with a rather high precision. Furthermore, there were spectacular developments in the period since June 2011 in what concerns the angle  $\theta_{13}$  (see, e.g., [11]). They culminated in March of 2012 in a high precision determination of  $\sin^2 2\theta_{13}$  in the Daya Bay experiment with reactor  $\bar{\nu}_e$  [27, 28]:

$$\sin^2 2\theta_{13} = 0.089 \pm 0.010 \pm 0.005, \quad (4)$$

where we have quoted the latest result of the Daya Bay experiment published in [28]. Subsequently the RENO [29], Double Chooz [30], and T2K [31] (see also [32]) experiments reported, respectively,  $4.9\sigma$ ,  $2.9\sigma$ , and  $3.2\sigma$  evidences for a nonzero value of  $\theta_{13}$ , compatible with the Day Bay result.

A global analysis of the latest neutrino oscillation data presented at the Neutrino 2012 International Conference, held in June of 2012 in Kyoto, Japan, was performed in [33]. We give below the best fit values of  $\Delta m_{21}^2$ ,  $\sin^2\theta_{12}$ ,  $|\Delta m_{31(32)}^2|$ ,  $\sin^2\theta_{23}$ , and  $\sin^2\theta_{13}$ , obtained in [33]:

$$\begin{aligned} \Delta m_{21}^2 &= 7.54 \times 10^{-5} \text{ eV}^2, \\ |\Delta m_{31(32)}^2| &= 2.47 (2.46) \times 10^{-3} \text{ eV}^2, \\ \sin^2\theta_{12} &= 0.307, \quad \sin^2\theta_{23} = 0.39, \\ \sin^2\theta_{13} &= 0.0241 (0.0244), \end{aligned} \quad (5)$$

where the values (the values in brackets) correspond to  $m_1 < m_2 < m_3$  ( $m_3 < m_1 < m_2$ ). The  $1\sigma$  uncertainties and the  $3\sigma$  ranges of the neutrino oscillation parameters found in [33] are given in Table 1 (note that we have quoted the value of  $|\Delta m_{31(32)}^2|$  in (5), while the mass squared difference determined in [33] is  $|\Delta m_A^2| = |\Delta m_{31}^2 - \Delta m_{21}^2/2|$  ( $|\Delta m_A^2| = |\Delta m_{32}^2 + \Delta m_{21}^2/2|$ )).

A few comments are in order. We have  $\Delta m_{21}^2/|\Delta m_{31(32)}^2| \cong 0.031 \ll 1$ , as was indicated earlier. The existing data do not allow to determine the sign of  $\Delta m_{31(32)}^2$ . As we will discuss further, the two possible signs correspond to two different

basic types of neutrino mass spectrum. Maximal solar neutrino mixing, that is,  $\theta_{12} = \pi/4$ , is ruled out at more than  $6\sigma$  by the data. Correspondingly, one has  $\cos 2\theta_{12} \geq 0.28$  at  $3\sigma$ . The results quoted in (6) imply that  $\theta_{23}$  is close to (but can be different from)  $\pi/4$ ,  $\theta_{12} \cong \pi/5.4$  and that  $\theta_{13} \cong \pi/20$ . Thus, the pattern of neutrino mixing is drastically different from the pattern of quark mixing. As we have noticed earlier, the neutrino oscillations experiments are sensitive only to neutrino mass squared differences  $\Delta m_{ij}^2 \equiv (m_i^2 - m_j^2)$ ,  $i \neq j$ , and cannot give information on the absolute values of the neutrino masses, that is, on the absolute neutrino mass scale. They are insensitive also to the nature-Dirac or Majorana, of massive neutrinos  $\nu_j$  and, correspondingly, to the Majorana CPV phases present in the PMNS matrix  $U$  [17, 34].

After the successful measurement of  $\theta_{13}$ , the determination of the absolute neutrino mass scale, of the type of the neutrino mass spectrum, of the nature-Dirac or Majorana, of massive neutrinos, and getting information about the status of CP violation in the lepton sector, are the most pressing and challenging problems and the highest priority goals of the research in the field of neutrino physics.

As was already indicated above, the presently available data do not permit to determine the sign of  $\Delta m_{31(32)}^2$ . In the case of 3-neutrino mixing, the two possible signs of  $\Delta m_{31(32)}^2$  correspond to two types of neutrino mass spectrum. In the widely used convention of numbering the neutrinos with definite mass employed by us, the two spectra read:

- (i) *spectrum with normal ordering (NO)*:  $m_1 < m_2 < m_3$ ,  $\Delta m_{\text{atm}}^2 = \Delta m_{31}^2 > 0$ ,  $\Delta m_\odot^2 \equiv \Delta m_{21}^2 > 0$ ,  $m_{2(3)} = (m_1^2 + \Delta m_{21(31)}^2)^{1/2}$ ;
- (ii) *spectrum with inverted ordering (IO)*:  $m_3 < m_1 < m_2$ ,  $\Delta m_{\text{atm}}^2 = \Delta m_{32}^2 < 0$ ,  $\Delta m_\odot^2 \equiv \Delta m_{21}^2 > 0$ ,  $m_2 = (m_3^2 + \Delta m_{23}^2)^{1/2}$ ,  $m_1 = (m_3^2 + \Delta m_{23}^2 - \Delta m_{21}^2)^{1/2}$ .

Depending on the value of the lightest neutrino mass,  $\min(m_j)$ , the neutrino mass spectrum can be

- (a) *normal hierarchical (NH)*:  $m_1 \ll m_2 < m_3$ ,  $m_2 \cong (\Delta m_\odot^2)^{1/2} \cong 8.68 \times 10^{-3}$  eV,  $m_3 \cong |\Delta m_{\text{atm}}^2|^{1/2} \cong 4.97 \times 10^{-2}$  eV; or
- (b) *inverted hierarchical (IH)*:  $m_3 \ll m_1 < m_2$ , with  $m_{1,2} \cong |\Delta m_{\text{atm}}^2|^{1/2} \cong 4.97 \times 10^{-2}$  eV; or



(c) *quasidegenerate (QD)*:  $m_1 \cong m_2 \cong m_3 \cong m_0$ ,  $m_j^2 \gg |\Delta m_{\text{atm}}^2|$ ,  $m_0 \geq 0.10 \text{ eV}$ .

The type of neutrino mass spectrum (hierarchy), that is, the sign of  $\Delta m_{31(32)}^2$ , can be determined (i) using data from neutrino oscillation experiments at accelerators (NO $\nu$ A, T2K, etc.) (see, e.g., [35]), (ii) in the experiments studying the oscillations of atmospheric neutrinos (see, e.g., [36–39]), and (iii) in experiments with reactor antineutrinos [40–47]. The relatively large value of  $\theta_{13}$  is a favorable factor for the  $\text{sgn}(\Delta m_{31(32)}^2)$  determination in these experiments. If neutrinos with definite mass are Majorana particles, information about the  $\text{sgn}(\Delta m_{31(32)}^2)$  can be obtained also by measuring the effective neutrino Majorana mass in neutrinoless double  $\beta$ -decay experiments [48, 49].

More specifically, in the cases (i) and (ii), the  $\text{sgn}(\Delta m_{31(32)}^2)$  can be determined by studying oscillations of neutrinos and antineutrinos, say,  $\nu_\mu \leftrightarrow \nu_e$  and  $\bar{\nu}_\mu \leftrightarrow \bar{\nu}_e$ , in which matter effects are sufficiently large. This can be done in long base-line oscillation experiments (see, e.g., [35]). For  $\sin^2 2\theta_{13} \geq 0.05$  and  $\sin^2 \theta_{23} \geq 0.50$ , information on  $\text{sgn}(\Delta m_{31(32)}^2)$  might be obtained in atmospheric neutrino experiments by investigating the effects of the subdominant transitions  $\nu_{\mu(e)} \rightarrow \nu_{e(\mu)}$  and  $\bar{\nu}_{\mu(e)} \rightarrow \bar{\nu}_{e(\mu)}$  of atmospheric neutrinos which traverse the Earth (for a detailed discussion see, e.g., [36–39]). For  $\nu_{\mu(e)}$  (or  $\bar{\nu}_{\mu(e)}$ ) crossing the Earth core, new type of resonance-like enhancement of the indicated transitions takes place due to the (*Earth*) *mantle-core constructive interference effect (neutrino oscillation length resonance (NOLR))* [50] (see also [51]). As a consequence of this effect, the corresponding  $\nu_{\mu(e)}$  (or  $\bar{\nu}_{\mu(e)}$ ) transition probabilities can be maximal [52–54] (for the precise conditions of the mantle-core (NOLR) enhancement see [50, 52–54]). It should be noted that the Earth mantle-core (NOLR) enhancement of neutrino transitions differs [50] from the MSW one. It also differs [50, 52–54] from the mechanisms of enhancement discussed, for example, in the articles [55, 56]: the conditions of enhancement considered in [55, 56] cannot be realised for the  $\nu_{\mu(e)} \rightarrow \nu_{e(\mu)}$  or  $\bar{\nu}_{\mu(e)} \rightarrow \bar{\nu}_{e(\mu)}$  transitions of the Earth core crossing neutrinos. For  $\Delta m_{31(32)}^2 > 0$ , the neutrino transitions  $\nu_{\mu(e)} \rightarrow \nu_{e(\mu)}$  are enhanced, while for  $\Delta m_{31(32)}^2 < 0$  the enhancement of antineutrino transitions  $\bar{\nu}_{\mu(e)} \rightarrow \bar{\nu}_{e(\mu)}$  takes place [50] (see also [51–54, 57]), which might allow to determine  $\text{sgn}(\Delta m_{31(32)}^2)$ . Determining the type of neutrino mass spectrum is crucial for understanding the origin of neutrino masses and mixing as well.

All possible types of neutrino mass spectrum we have discussed above are compatible with the existing constraints on the absolute scale of neutrino masses  $m_j$ . Information about the absolute neutrino mass scale can be obtained by measuring the spectrum of electrons near the end point in  $^3\text{H}$   $\beta$ -decay experiments [58–60] and from cosmological and astrophysical data (see, e.g., [61]). The most stringent upper bound on the  $\bar{\nu}_e$  mass was obtained in the Troitzk [62] experiment (see also [63]):

$$m_{\bar{\nu}_e} < 2.05 \text{ eV} \quad \text{at 95\% C.L.} \quad (7)$$

We have  $m_{\bar{\nu}_e} \cong m_{1,2,3} \geq 0.1 \text{ eV}$  in the case of quasidegenerate (QD) spectrum. The KATRIN experiment [63], which is under preparation, is planned to reach sensitivity of  $m_{\bar{\nu}_e} \sim 0.20 \text{ eV}$ ; that is, it will probe the region of the QD spectrum. Information on the type of neutrino mass spectrum can also be obtained in  $\beta$ -decay experiments having a sensitivity to neutrino masses  $\sim \sqrt{|\Delta m_{31(32)}^2|} \cong 5 \times 10^{-2} \text{ eV}$  [64] (i.e., by a factor of  $\sim 4$  better sensitivity than that of the KATRIN experiment [63]). Reaching the indicated sensitivity in electromagnetic spectrometer  $\beta$ -decay experiments of the type of KATRIN does not seem feasible at present. The cosmic microwave background (CMB) data of the WMAP experiment, combined with supernovae data and data on galaxy clustering can be used to derive an upper limit on the sum of neutrinos masses (see, e.g., [61]). Depending on the model complexity and the input data used one obtains [65]  $\sum_j m_j \leq (0.3\text{--}1.3) \text{ eV}$ , 95% C.L. Data on weak lensing of galaxies, combined with data from the WMAP and PLANCK experiments, may allow  $\sum_j m_j$  to be determined with an uncertainty of  $\sigma(\sum_j m_j) = (0.04\text{--}0.07) \text{ eV}$  [66, 67].

Thus, the data on the absolute scale of neutrino masses imply that neutrino masses are much smaller than the masses of the charged leptons and quarks. If we take as an indicative upper limit  $m_j \leq 0.5 \text{ eV}$ ,  $j = 1, 2, 3$ , we have

$$\frac{m_j}{m_{l,q}} \leq 10^{-6}, \quad l = e, \mu, \tau, \quad q = d, sb, u, c, t. \quad (8)$$

It is natural to suppose that the remarkable smallness of neutrino masses is related to the existence of a new fundamental mass scale in particle physics, and thus to new physics beyond that predicted by the Standard Model. A comprehensive theory of the neutrino masses and mixing should be able to explain the indicated enormous disparity between the neutrino masses and the masses of the charged leptons and quarks.

At present no experimental information on the Dirac and Majorana CPV phases in the neutrino mixing matrix is available. Therefore the status of the CP symmetry in the lepton sector is unknown. The importance of getting information about the Dirac and Majorana CPV phases in the neutrino mixing matrix stems, in particular, from the possibility that these phases play a fundamental role in the generation of the observed baryon asymmetry of the Universe. More specifically, the CP violation necessary for the generation of the baryon asymmetry within the “flavoured” leptogenesis scenario [68–70] can be due exclusively to the Dirac and/or Majorana CPV phases in the PMNS matrix [71, 72] and thus can be directly related to the low energy CP-violation in the lepton sector. If the requisite CP violation is due to the Dirac phases  $\delta$ , a necessary condition for a successful (flavoured) leptogenesis is that  $\sin \theta_{13} \geq 0.09$  [72], which is comfortably compatible with the Daya Bay result, (4).

With  $\theta_{13} \neq 0$ , the Dirac phase  $\delta$  can generate CP violating effects in neutrino oscillations [73] (see also [17, 74]), that is, a difference between the probabilities of  $\nu_l \rightarrow \nu_{l'}$  and  $\bar{\nu}_l \rightarrow \bar{\nu}_{l'}$  oscillations in vacuum:  $P(\nu_l \rightarrow \nu_{l'}) \neq P(\bar{\nu}_l \rightarrow \bar{\nu}_{l'})$ ,  $l \neq l' = e, \mu, \tau$ . The magnitude of the CP violating effects of

interest is determined [75] by the rephasing invariant  $J_{\text{CP}}$  associated with the Dirac CPV phase  $\delta$  in  $U$ . It is analogous to the rephasing invariant associated with the Dirac CPV phase in the CKM quark mixing matrix [76, 77]. In the “standard” parametrisation of the PMNS neutrino mixing matrix, (2)-(3), we have

$$\begin{aligned} J_{\text{CP}} &\equiv \text{Im} \left( U_{\mu 3} U_{e 3}^* U_{e 2} U_{\mu 2}^* \right) \\ &= \frac{1}{8} \cos \theta_{13} \sin 2\theta_{12} \sin 2\theta_{23} \sin 2\theta_{13} \sin \delta. \end{aligned} \quad (9)$$

Thus, given the fact that  $\sin \theta_{12}$ ,  $\sin \theta_{23}$ , and  $\sin \theta_{13}$  have been determined experimentally with a relatively good precision, the size of CP violation effects in neutrino oscillations depends essentially only on the magnitude of the currently unknown value of the Dirac phase  $\delta$ . The current data imply  $|J_{\text{CP}}| \lesssim 0.039$ , where we have used (9) and the  $3\sigma$  ranges of  $\sin^2 \theta_{12}$ ,  $\sin^2 \theta_{23}$ , and  $\sin^2 \theta_{13}$  given in Table 1. Data on the Dirac phase  $\delta$  will be obtained in the long baseline neutrino oscillation experiments T2K, NOvA, and other (see, e.g., [78]). Testing the possibility of Dirac CP violation in the lepton sector is one of the major goals of the next generation of neutrino oscillation experiments (see, e.g., [35, 78]). Measuring the magnitude of CP violation effects in neutrino oscillations is at present also the only known feasible method of determining the value of the phase  $\delta$  (see, e.g., [79]).

If  $\nu_j$  are Majorana fermions, getting experimental information about the Majorana CPV phases in the neutrino mixing matrix  $U$  will be remarkably difficult [80–86]. As we will discuss further, the Majorana phases of the PMNS matrix play important role in the phenomenology of neutrinoless double-beta-(( $\beta\beta$ ) $_{0\nu}$ -) decay—the process whose existence is related to the Majorana nature of massive neutrinos [87]:  $(A, Z) \rightarrow (A, Z + 2) + e^- + e^-$ . The phases  $\alpha_{21,31}$  can affect significantly the predictions for the rates of the (LFV) decays  $\mu \rightarrow e + \gamma$ ,  $\tau \rightarrow \mu + \gamma$ , and so forth, in a large class of supersymmetric theories incorporating the see-saw mechanism [88, 89]. As was mentioned earlier, the Majorana phase(s) in the PMNS matrix can be the leptogenesis CP violating parameter(s) at the origin of the baryon asymmetry of the Universe [21, 22, 71, 72].

Establishing whether the neutrinos with definite mass  $\nu_j$  are Dirac fermions possessing distinct antiparticles, or Majorana fermions, that is, spin 1/2 particles that are identical with their antiparticles, is of fundamental importance for understanding the origin of neutrino masses and mixing and the underlying symmetries of particle interactions. Let us recall that the neutrinos  $\nu_j$  with definite mass  $m_j$  will be Dirac fermions if particle interactions conserve some additive lepton number, for example, the total lepton charge  $L = L_e + L_\mu + L_\tau$ . If no lepton charge is conserved, the neutrinos  $\nu_j$  will be Majorana fermions (see, e.g., [26]). The massive neutrinos are predicted to be of Majorana nature by the see-saw mechanism of neutrino mass generation [6–9], which also provides an attractive explanation of the smallness of neutrino masses and, through the leptogenesis theory [2, 3], of the observed baryon asymmetry of the Universe. The observed patterns of neutrino mixing and of neutrino mass squared differences driving the solar and the dominant atmospheric neutrino

oscillations can be related to Majorana massive neutrinos and the existence of an *approximate* symmetry in the lepton sector corresponding to the conservation of the *nonstandard* lepton charge  $L' = L_e - L_\mu - L_\tau$  [90]. They can also be associated with the existence of *approximate* discrete symmetry (or symmetries) of the particle interactions (see, e.g., [91–94]). Determining the nature (Dirac or Majorana) of massive neutrinos is one of the fundamental and most challenging problems in the future studies of neutrino mixing [11].

## 2. The Nature of Massive Neutrinos

**2.1. Majorana versus Dirac Massive Neutrinos (Particles).** The properties of Majorana particles (fields) are very different from those of Dirac particles (fields). A massive Majorana neutrino  $\chi_j$  (or Majorana spin 1/2 particle) with mass  $m_j > 0$  can be described in local quantum field theory which is used to construct, for example, the Standard Model, by 4-component complex spin 1/2 field  $\chi_j(x)$  which satisfies the Dirac equation and the Majorana condition:

$$C(\bar{\chi}_j(x))^T = \xi_k \chi_j(x), \quad |\xi_j|^2 = 1, \quad (10)$$

where  $C$  is the charge conjugation matrix,  $C^{-1} \gamma_\alpha C = -(\gamma_\alpha)^T$  ( $C^T = -C$ ,  $C^{-1} = C^\dagger$ ), and  $\xi_j$  is, in general, an unphysical phase. The Majorana condition is invariant under *proper* Lorentz transformations. It reduces by a factor of 2 the number of independent components in  $\chi_j(x)$ .

The condition (10) is invariant with respect to  $U(1)$  global gauge transformations of the field  $\chi_j(x)$  carrying a  $U(1)$  charge  $Q$ ,  $\chi_j(x) \rightarrow e^{iaQ} \chi_j(x)$ , only if  $Q = 0$ . As a result, (i)  $\chi_j$  cannot carry nonzero additive quantum numbers (lepton charge, etc.), and (ii) the field  $\chi_j(x)$  cannot “absorb” phases. Thus,  $\chi_j(x)$  describes 2 spin states of a spin 1/2, *absolutely neutral particle*, which is identical with its antiparticle,  $\chi_j \equiv \bar{\chi}_j$ . As is well known, spin 1/2 Dirac particles can carry nonzero  $U(1)$  charges: the charged leptons and quarks, for instance, carry nonzero electric charges.

Owing to the fact that the Majorana (neutrino) fields cannot absorb phases, the neutrino mixing matrix  $U$  contains in the general case of  $n$  charged leptons and mixing of  $n$  massive Majorana neutrinos  $\nu_j \equiv \chi_j$ , altogether

$$n_{\text{CPV}}^{(M)} = \frac{n(n-1)}{2}, \quad \text{Majorana } \nu_j, \quad (11)$$

CPV phases [17]. In the case of mixing of  $n$  massive Dirac neutrinos, the number of CPV phases in  $U$ , as is well known, is

$$n_{\text{CPV}}^{(D)} = \frac{(n-1)(n-2)}{2}, \quad \text{Dirac } \nu_j. \quad (12)$$

Thus, if  $\nu_j$  are Majorana particles,  $U$  contains the following number of additional Majorana CP violation phases:  $n_{\text{MCPV}}^{(M)} \equiv n_{\text{CPV}}^{(M)} - n_{\text{CPV}}^{(D)} = (n-1)$ . In the case of  $n$  charged leptons and  $n$  massive Majorana neutrinos, the PMNS matrix  $U$  can be cast in the form [17]

$$U = VP, \quad (13)$$

where the matrix  $V$  contains the  $(n-1)(n-2)/2$  Dirac CP violation phases, while  $P$  is a diagonal matrix with the additional  $(n-1)$  Majorana CP violation phases  $\alpha_{21}, \alpha_{31}, \dots, \alpha_{n1}$ ,

$$P = \text{diag} \left( 1, e^{i(\alpha_{21}/2)}, e^{i(\alpha_{31}/2)}, \dots, e^{i(\alpha_{n1}/2)} \right). \quad (14)$$

As will be discussed further, the Majorana phases will conserve CP if [23–25]  $\alpha_{j1} = \pi q_j$ ,  $q_j = 0, 1, 2$ ,  $j = 2, 3, \dots, n$ . In this case  $\exp(i\alpha_{j1}) = \pm 1$  and  $\exp[i(\alpha_{j1} - \alpha_{k1})] = \pm 1$  have a simple physical interpretation: these are the relative CP-parities of the Majorana neutrinos  $\nu_j$  and  $\nu_1$  and of  $\nu_j$  and  $\nu_k$ , respectively.

It follows from the preceding discussion that the mixing of massive Majorana neutrinos differs, in what concerns the number of CPV phases, from the mixing of massive Dirac neutrinos. For  $n = 3$  of interest, we have one Dirac and two Majorana CPV phases in  $U$ , which is consistent with the expression of  $U$  given in (2). If  $n = 2$ , there is one Majorana CPV phase and no Dirac CPV phases in  $U$ . Correspondingly, in contrast to the Dirac case, there can exist CP violating effects even in the system of two mixed massive Majorana neutrinos (particles).

The Majorana phases do not enter into the expressions of the probabilities of oscillations involving the flavour neutrinos and antineutrinos [17, 34],  $\nu_l \rightarrow \nu_{l'}$  and  $\bar{\nu}_l \rightarrow \bar{\nu}_{l'}$ . Indeed, the probability to find neutrino  $\nu_{l'}$  (antineutrino  $\bar{\nu}_{l'}$ ) at time  $t$  if a neutrino  $\nu_l$  (antineutrino  $\bar{\nu}_l$ ) has been produced at time  $t_0$  and it had traveled a distance  $L \cong t$  in vacuum is given by (see, e.g., [11, 26])

$$P(\nu_l \rightarrow \nu_{l'}) = \left| \sum_j U_{l'j} e^{-i(E_j t - p_j L)} U_{jl}^\dagger \right|^2, \quad (15)$$

$$P(\bar{\nu}_l \rightarrow \bar{\nu}_{l'}) = \left| \sum_j U_{lj} e^{-i(E_j t - p_j L)} U_{j l'}^\dagger \right|^2,$$

where  $E_j$  and  $p_j$  are the energy and momentum of the neutrino  $\nu_j$ . It is easy to show, using the expression for  $U$  in (13), that  $P(\nu_l \rightarrow \nu_{l'})$  and  $P(\bar{\nu}_l \rightarrow \bar{\nu}_{l'})$  do not depend on the Majorana phases present in  $U$  since

$$\sum_j (VP)_{l'j} e^{-i(E_j t - p_j L)} (VP)_{jl}^\dagger = \sum_j V_{l'j} e^{-i(E_j t - p_j L)} V_{jl}^\dagger. \quad (16)$$

The same result holds when the neutrino oscillations take place in matter [34].

If CP-invariance holds, Majorana neutrinos (particles) have definite CP-parity  $\eta_{CP}(\chi_j) = \pm i$ :

$$U_{CP} \chi_j(x) U_{CP}^{-1} = \eta_{CP}(\chi_j) \gamma_0 \chi_j(x_p), \quad (17)$$

$$\eta_{CP}(\chi_j) \equiv i\rho_j = \pm i,$$

where  $x = (x_0, \mathbf{x})$ ,  $x_p = (x_0, -\mathbf{x})$  and  $U_{CP}$  is the unitary CP-transformation operator. In contrast, Dirac particles do not have a definite CP-parity—a Dirac field  $f(x)$  transforms as follows under the CP-symmetry operation:

$$U_{CP} f(x) U_{CP}^{-1} = \eta_f \gamma_0 C(\bar{f}(x_p))^T, \quad |\eta_f|^2 = 1, \quad (18)$$

$\eta_f$  being an unphysical phase factor. In the case of CP invariance, the CP-parities of massive Majorana fermions (neutrinos) can play important role in processes involving real or virtual Majorana particles (see, e.g., [26, 95]).

Using (18) and (17) and the transformation of the  $W^\pm$  boson field under the CP-symmetry operation,

$$U_{CP} W_\alpha(x) U_{CP}^\dagger = \eta_W \kappa_\alpha (W_\alpha(x_p))^\dagger, \quad |\eta_W|^2 = 1, \quad (19)$$

$$\kappa_0 = -1, \quad \kappa_{1,2,3} = +1,$$

where  $\eta_W$  is an unphysical phase, one can derive the constraints on the neutrino mixing matrix  $U$  following from the requirement of CP-invariance of the leptonic CC weak interaction Lagrangian, (1). In the case of massive Dirac neutrinos we obtain  $\eta_{\nu_j}^* \eta_l \eta_W U_{lj}^* = U_{lj}$ ,  $l = e, \mu, \tau$ ,  $j = 1, 2, 3$ . Setting the product of unphysical phases  $\eta_{\nu_j}^* \eta_l \eta_W = 1$ , one obtains the well-known result:

$$\text{CP invariance: } U_{lj}^* = U_{lj}, \quad l = e, \mu, \tau, \quad j = 1, 2, 3, \quad (20)$$

Dirac  $\nu_j$ .

In the case of massive Majorana neutrinos we obtain using (10), (17), (18), and (19):  $\xi_j^*(i\rho_j) \eta_l^* \eta_W U_{lj} = U_{lj}^*$ . It is convenient now to set  $\xi_j = 1$ ,  $\eta_l = i$ , and  $\eta_W = 1$ . In this (commonly used by us) convention we get [26]

$$\text{CP invariance: } U_{lj}^* = \rho_j U_{lj},$$

$$\rho_j = +1 \text{ or } (-1), \quad l = e, \mu, \tau, \quad j = 1, 2, 3, \quad (21)$$

Majorana  $\nu_j$ .

Thus, in the convention used the elements of the PMNS matrix can be either real or purely imaginary if  $\nu_j$  are Majorana fermions. Applying the above conditions to, for example,  $U_{e2}$ ,  $U_{\tau 3}$ , and  $U_{e3}$  elements of the PMNS matrix (2) we obtain the CP conserving values of the phases  $\alpha_{21}$ ,  $\alpha_{31}$ , and  $\delta$ , respectively:  $\alpha_{21} = k\pi$ ,  $k = 0, 1, 2, \dots$ ,  $\alpha_{31} = k'\pi$ ,  $k' = 0, 1, 2, \dots$ ,  $\delta = 0, \pi, 2\pi$ .

One can obtain in a similar way the CP-invariance constraint on the matrix of neutrino Yukawa couplings,  $\lambda_{kl}$ , which plays a fundamental role in the leptogenesis scenario of baryon asymmetry generation, based on the (type I) see-saw mechanism of generation of neutrino masses [2–5, 79]:

$$\mathcal{L}_Y(x) = -\lambda_{kl} \overline{N_{kR}}(x) H^\dagger(x) \psi_{lL}(x) + \text{h.c.}, \quad (22)$$

$$\mathcal{L}_M^N(x) = -\frac{1}{2} M_k \overline{N_k}(x) N_k(x).$$

Here  $N_{kR}(x)$  is the field of a heavy right-handed (RH) sterile Majorana neutrino with mass  $M_k > 0$ ,  $\psi_{lL}$  denotes the Standard Model left-handed (LH) lepton doublet field of flavour  $l = e, \mu, \tau$ ,  $\psi_{lL}^T = (\nu_{lL}^T, l_L^T)$ , and  $H$  is the Standard Model Higgs doublet field whose neutral component has a vacuum expectation value  $v = 174 \text{ GeV}$ . The term  $\mathcal{L}_Y(x) + \mathcal{L}_M^N(x)$  includes all the necessary ingredients of the see-saw mechanism. Assuming the existence of two heavy Majorana



neutrinos, that is, taking  $k = 1, 2$  in (22), and adding the term  $\mathcal{L}_Y(x) + \mathcal{L}_M^N(x)$  to the Standard Model Lagrangian, we obtain the minimal extension of the Standard Model in which the neutrinos have masses and mix and the leptogenesis can be realised. In the leptogenesis formalism it is often convenient to use the so-called orthogonal parametrisation of the matrix of neutrino Yukawa couplings [96]:

$$\lambda_{kl} = \frac{1}{v} \sqrt{M_k R_{kj}} \sqrt{m_j} (U^\dagger)_{jl}, \quad (23)$$

where  $R$  is, in general, a complex orthogonal matrix,  $RR^T = R^T R = 1$ . The CP violation necessary for the generation of the baryon asymmetry of the Universe is provided in the leptogenesis scenario of interest by the matrix of neutrino Yukawa couplings  $\lambda$  (see, e.g., [4, 5, 79]). It follows from (23) that it can be provided either by the neutrino mixing matrix  $U$ , or by the matrix  $R$ , or else by both the matrices  $U$  and  $R$ . It is therefore important to derive the conditions under which  $\lambda$ ,  $R$ , and  $U$  respect the CP symmetry. For the PMNS matrix  $U$  these conditions are given in (21). For the matrices  $\lambda$  and  $R$  in the convention in which (i)  $N_k(x)$  satisfy the Majorana condition with a phase equal to 1 (i.e.,  $\xi_k = 1$ ), (ii)  $\eta_l^I = i$  and  $\eta_l^H = 1$ ,  $\eta_l^I$  and  $\eta_l^H$  being the unphysical phase factors which appear in the CP-transformations of the LH lepton doublet and Higgs doublet fields  $\psi_{lL}(x)$  and  $H(x)$ , respectively (this convention is similar to, and consistent with, the convention about the unphysical phases we have used to derive the CP-invariance constraints on the elements of the PMNS matrix  $U$ ), they read [72]

$$\begin{aligned} \lambda_{kl}^* &= \lambda_{kl} \rho_k^N, \quad \rho_k^N = \pm 1, \quad j = 1, 2, 3, \quad l = e, \mu, \tau, \\ R_{kj}^* &= R_{kj} \rho_j^N, \quad j, k = 1, 2, 3, \end{aligned} \quad (24)$$

where  $i\rho_k^N \equiv \eta_{CP}(N_k) = \pm i$  is the CP-parity of  $N_k$ . Thus, in the case of CP invariance also the elements of  $\lambda$  and  $R$  can be real or purely imaginary. Note that, as it follows from (21) and (24), given which elements are real and which are purely imaginary of any two of the three matrices  $U$ ,  $\lambda$  and  $R$ , determines (in the convention we are using and if CP invariance holds), which elements are real or purely imaginary in the third matrix. If, for instance,  $U_{e2}$  is purely imaginary ( $\rho_2 = -1$ ) and  $\lambda_{1\mu}$  is real ( $\rho_1^N = 1$ ), then  $R_{12}$  must be purely imaginary. Thus, in the example we are considering, a real  $R_{12}$  would signal that the CP symmetry is broken [72].

The currents formed by Majorana fields have special properties, which make them also quite different from the currents formed by Dirac fields. In particular, it follows from the Majorana condition that the following currents of the Majorana field  $\chi_k(x)$  are identically equal to zero (see, e.g., [26]):

$$\bar{\chi}_k(x) \gamma_\alpha \chi_k(x) \equiv 0, \quad (25)$$

$$\bar{\chi}_k(x) \sigma_{\alpha\beta} \chi_k(x) \equiv 0, \quad (26)$$

$$\bar{\chi}_k(x) \sigma_{\alpha\beta} \gamma_5 \chi_k(x) \equiv 0.$$

Equations (25) and (26) imply that Majorana fermions (neutrinos) cannot have nonzero  $U(1)$  charges and intrinsic

magnetic and electric dipole moments, respectively. A Dirac spin 1/2 particle can have nontrivial  $U(1)$  charges, as we have already discussed, and nonzero intrinsic magnetic moment (the electron and the muon, e.g., have it). If CP invariance does not hold, Dirac fermions can have also nonzero electric dipole moments. Equations (26) imply also that the Majorana particles (neutrinos) cannot couple to a real photon. The axial current of a Majorana fermion,  $\bar{\chi}_k(x) \gamma_\alpha \gamma_5 \chi_k(x) \neq 0$ . Correspondingly,  $\chi_k(x)$  can have an effective coupling to a *virtual* photon via the *anapole momentum* term, which has the following form in momentum space:

$$(g_{\alpha\beta} q^2 - q_\alpha q_\beta) \gamma_\beta \gamma_5 F_a^{(k)}(q^2), \quad (27)$$

where  $q$  is the momentum of the virtual photon and  $F_a^{(k)}(q^2)$  is the anapole form factor of  $\chi_k$ . The fact that the vector current of  $\chi_k$  is zero while the axial current is nonzero has important implications in the calculations of the relic density of the lightest and stable neutralino, which is a Majorana particle and the dark matter candidate in many supersymmetric (SUSY) extensions of the Standard Model [97].

In certain cases (e.g., in theories with a keV mass Majorana neutrino (see, e.g., [15]), in the TeV scale type I see-saw model (see, e.g., [98]), in SUSY extensions of the Standard Model) one can have effective interactions involving two different massive Majorana fermions (neutrinos), say  $\chi_1$  and  $\chi_2$ . We will consider two examples. The first is an effective interaction with the photon field, which can be written as

$$\mathcal{L}_{\text{eff}}^{(A)}(x) = \bar{\chi}_1(x) \sigma_{\alpha\beta} (\mu_{12} - d_{12} \gamma_5) \chi_2(x) F^{\alpha\beta}(x) + \text{h.c.}, \quad (28)$$

where  $\mu_{12}$  and  $d_{12}$  are, in general, complex constants,  $F^{\alpha\beta}(x) = \partial^\alpha A^\beta(x) - \partial^\beta A^\alpha(x)$ ,  $A^\mu(x)$  being the 4-vector potential of the photon field. Using the Majorana conditions for  $\chi_1(x)$  and  $\chi_2(x)$  in the convention in which the phases  $\xi_1 = \xi_2 = 1$ , it is not difficult to show that the constants  $\mu_{12}$  and  $d_{12}$  enter into the expression for  $\mathcal{L}_{\text{eff}}^{(A)}(x)$  in the form:  $(\mu_{12} - \mu_{12}^*) = 2i \text{Im}(\mu_{12}) \equiv \tilde{\mu}_{12}$ ,  $(d_{12} + d_{12}^*) = 2 \text{Re}(d_{12}) \equiv \tilde{d}_{12}$ , that is,  $\tilde{\mu}_{12}$  is purely imaginary and  $\tilde{d}_{12}$  is real. In the case of  $\chi_1(x) \equiv \chi_2(x) = \chi(x)$ , the current  $\bar{\chi}(x) \sigma_{\alpha\beta} (\mu_{12} - d_{12} \gamma_5) \chi(x)$  has to be Hermitian, which implies that  $\tilde{\mu}_{12}$  should be real while  $\tilde{d}_{12}$  should be purely imaginary. Combined with constraints on  $\tilde{\mu}_{12}$  and  $\tilde{d}_{12}$  we have just obtained, this leads to  $\tilde{\mu}_{12} = \tilde{d}_{12} = 0$ , which is consistent with (26). In the case of CP invariance of  $\mathcal{L}_{\text{eff}}^{(A)}(x)$ , the constants  $\mu_{12}$  ( $\tilde{\mu}_{12}$ ) and  $d_{12}$  ( $\tilde{d}_{12}$ ) should satisfy

$$\text{CP invariance: } \mu_{12} = -\rho_1 \rho_2 \mu_{12}, \quad d_{12} = +\rho_1 \rho_2 d_{12}. \quad (29)$$

Thus, if  $\rho_1 = \rho_2$ , that is, if  $\chi_1(x)$  and  $\chi_2(x)$  possess the same CP-parity,  $\mu_{12} = 0$  and  $d_{12}$  (and  $\tilde{d}_{12}$ ) can be different from zero. If  $\rho_1 = -\rho_2$ , that is, if  $\chi_1(x)$  and  $\chi_2(x)$  have opposite CP-parities,  $d_{12} = 0$  and  $\mu_{12}$  (and  $\tilde{\mu}_{12}$ ) can be different from zero. If CP invariance does not hold, we can have both  $\mu_{12} \neq 0$  and  $d_{12} \neq 0$  ( $\tilde{\mu}_{12} \neq 0$  and  $\tilde{d}_{12} \neq 0$ ).



As a second example we will consider effective interaction of  $\chi_1$  and  $\chi_2$  with a vector field (current), which for concreteness will be assumed to be the  $Z^0$ -boson field of the Standard Model:

$$\mathcal{L}_{\text{eff}}^{(Z)}(x) = \bar{\chi}_1(x) \gamma_\alpha (v_{12} - a_{12} \gamma_5) \chi_2(x) Z^\alpha(x) + \text{h.c.} \quad (30)$$

Here  $v_{12}$  and  $a_{12}$  are, in general, complex constants. Using the Majorana conditions for  $\chi_1(x)$  and  $\chi_2(x)$  with  $\xi_1 = \xi_2 = 1$ , one can easily show that  $v_{12}$  has to be purely imaginary, while  $a_{12}$  has to be real. In the case of  $\chi_1(x) \equiv \chi_2(x) = \chi(x)$ , the hermiticity of the current  $\bar{\chi}(x) \gamma_\alpha (v_{12} - a_{12} \gamma_5) \chi(x)$  implies that both  $v_{12}$  and  $a_{12}$  have to be real. This, together with constraints on  $v_{12}$  and  $a_{12}$  just derived, leads to  $v_{12} = 0$ , which is consistent with the result given in (25). The requirement of CP invariance of  $\mathcal{L}_{\text{eff}}^{(Z)}(x)$ , as can be shown, leads to ( $\xi_1 = \xi_2 = 1$ ):

$$\text{CP invariance: } v_{12} = -\rho_1 \rho_2 v_{12}, \quad a_{12} = +\rho_1 \rho_2 a_{12}. \quad (31)$$

Thus, we find, similarly to the case considered above, that if  $\chi_1(x)$  and  $\chi_2(x)$  possess the same CP-parity ( $\rho_1 = \rho_2$ ),  $v_{12} = 0$  and  $a_{12}$  can be different from zero; if  $\chi_1(x)$  and  $\chi_2(x)$  have opposite CP-parities ( $\rho_1 = -\rho_2$ ),  $a_{12} = 0$  while  $v_{12}$  can be different from zero. If CP invariance does not hold, we can have both  $v_{12} \neq 0$  and  $a_{12} \neq 0$ .

These results have important implications, in particular, for the phenomenology of the heavy Majorana neutrinos  $N_k$  in the TeV scale (type I) see-saw models, for the neutralino phenomenology in SUSY extensions of the Standard Model, in which the neutralinos are Majorana particles, and more specifically for the processes  $e^- + e^+ \rightarrow \chi_1 + \chi_2$ ,  $\chi_2 \rightarrow \chi_1 + l^+ + l^-$  ( $m(\chi_2) > m(\chi_1)$ ),  $l = e, \mu, \tau$ , where  $\chi_1$  and  $\chi_2$  are, for instance, two neutralinos of, for example, the minimal SUSY extension of the Standard Model (see, e.g., [95, 99]).

Finally, if  $\Psi(x)$  is a Dirac field and we define the standard propagator of  $\Psi(x)$  as

$$\langle 0 | T(\Psi_\alpha(x) \bar{\Psi}_\beta(y)) | 0 \rangle = S_{\alpha\beta}^F(x - y), \quad (32)$$

one has

$$\begin{aligned} \langle 0 | T(\Psi_\alpha(x) \Psi_\beta(y)) | 0 \rangle &= 0, \\ \langle 0 | T(\bar{\Psi}_\alpha(x) \bar{\Psi}_\beta(y)) | 0 \rangle &= 0. \end{aligned} \quad (33)$$

In contrast, a Majorana neutrino field  $\chi_k(x)$  has, in addition to the standard propagator

$$\langle 0 | T(\chi_{k\alpha}(x) \bar{\chi}_{k\beta}(y)) | 0 \rangle = S_{\alpha\beta}^{Fk}(x - y), \quad (34)$$

two nontrivial *nonstandard* (Majorana) propagators

$$\begin{aligned} \langle 0 | T(\chi_{k\alpha}(x) \chi_{k\beta}(y)) | 0 \rangle &= -\xi_k^* S_{\alpha\delta}^{Fk}(x - y) C_{\delta\beta}, \\ \langle 0 | T(\bar{\chi}_{k\alpha}(x) \bar{\chi}_{k\beta}(y)) | 0 \rangle &= \xi_k C_{\alpha\delta}^{-1} S_{\delta\beta}^{Fk}(x - y). \end{aligned} \quad (35)$$

This result implies that if  $\nu_j(x)$  in (1) are massive Majorana neutrinos,  $(\beta\beta)_{0\nu}$ -decay can proceed by exchange of virtual neutrinos  $\nu_j$  since  $\langle 0 | T(\nu_{j\alpha}(x) \nu_{j\beta}(y)) | 0 \rangle \neq 0$ . The Majorana propagators play a crucial role in the calculation of the baryon asymmetry of the Universe in the leptogenesis scenario of the asymmetry generation (see, e.g., [4, 5, 79]).

**2.2. Generating Dirac and Majorana Massive Neutrinos.** The type of massive neutrinos in a given theory is determined by the type of the (effective) mass term  $\mathcal{L}_m^\nu(x)$  neutrinos have, more precisely, by the symmetries of  $\mathcal{L}_m^\nu(x)$  and of the total Lagrangian  $\mathcal{L}(x)$  of the theory. A fermion mass term is bilinear in the fermion fields which is invariant under the proper Lorentz transformations.

Massive Dirac neutrinos arise in theories in which the neutrino mass term conserves some additive quantum number that could be, for example, the (total) lepton charge  $L = L_e + L_\mu + L_\tau$ , which is conserved also by the total Lagrangian  $\mathcal{L}(x)$  of the theory. A well-known example is the Dirac mass term, which can arise in the minimally extended Standard Model to include three RH neutrino fields  $\nu_{lR}$ ,  $l = e, \mu, \tau$ , as  $SU(2)_L$  singlets:

$$\mathcal{L}_D^\nu(x) = -\bar{\nu}_{l'R}(x) M_{Dl'l} \nu_{lL}(x) + \text{h.c.}, \quad (36)$$

where  $M_D$  is a  $3 \times 3$ , in general complex, matrix. The term  $\mathcal{L}_D^\nu(x)$  can be generated after the spontaneous breaking of the Standard Model gauge symmetry by an  $SU(2)_L \times U(1)_{Y_W}$  invariant Yukawa coupling of the lepton doublet, Higgs doublet, and the RH neutrino fields [100]:

$$\mathcal{L}_Y(x) = -Y_{l'l'}^\nu \bar{\nu}_{l'R}(x) H^\dagger(x) \psi_{lL}(x) + \text{h.c.}, \quad (37)$$

$$M_D = v Y^\nu. \quad (38)$$

If the nondiagonal elements of  $M_D$  are different from zero,  $M_{Dl'l} \neq 0$ ,  $l \neq l' = e, \mu, \tau$ , the individual lepton charges  $L_l$ ,  $l = e, \mu, \tau$ , will not be conserved. Nevertheless, the total lepton charge  $L$  is conserved by  $\mathcal{L}_D^\nu(x)$ . As in the case of the charged lepton and quark mass matrices generated via the spontaneous electroweak symmetry breaking by Yukawa type terms in the SM Lagrangian,  $M_D$  is diagonalised by a biunitary transformation:  $M_D = U_R^{\text{lep}} M_D^{\text{diag}} (U_L^{\text{lep}})^\dagger$ , where  $U_R^{\text{lep}}$  and  $U_L^{\text{lep}}$  are  $3 \times 3$  unitary matrices. If the mass term in (36) is written in the basis in which the charged lepton mass matrix is diagonal,  $U_L^{\text{lep}}$  coincides with the PMNS matrix,  $U_L^{\text{lep}} \equiv U_{\text{PMNS}}$ . The neutrinos  $\nu_j$  with definite mass  $m_j > 0$  are Dirac particles: their fields  $\nu_j(x) = (U_L^{\text{lep}})_{jl}^\dagger \nu_{lL}(x) + (U_R^{\text{lep}})_{j'l'}^\dagger \nu_{l'R}(x)$  do not satisfy the Majorana condition,  $C(\bar{\nu}_j(x))^T \neq \xi_j \chi_j(x)$ . Although the scheme we are considering is phenomenologically viable (it does not contain a candidate for a dark matter particle though), it does not provide an insight of why the neutrino masses are much smaller than the charged fermion masses. The only observable “new physics” is that related to the neutrino masses and mixing: apart from the neutrino masses and mixing themselves, this is the phenomenon of neutrino oscillations [100].

Indeed, given the fact that the lepton charges  $L_l$ ,  $l = e, \mu, \tau$ , are not conserved, processes like  $\mu^+ \rightarrow e^+ + \gamma$  decay,  $\mu^- \rightarrow e^- + e^+ + e^-$  decay,  $\tau^- \rightarrow e^- + \gamma$  decay, and so forth are allowed. However, the rates of these processes are suppressed by the factor [100]  $|U_{l'l'} U_{l'j}^* m_j^2 / M_W^2|^2$ ,  $l' \neq l$ ,  $M_W \cong 80$  GeV being the  $W^\pm$ -mass and  $l = \mu$ ,  $l' = e$  for the  $\mu^\pm \rightarrow e^\pm + \gamma$

decay, and so forth, and are unobservably small. For instance, for the  $\mu \rightarrow e + \gamma$  decay branching ratio we have [100]

$$\text{BR}(\mu \rightarrow e + \gamma) = \frac{3\alpha}{32\pi} \left| U_{ej} U_{\mu j}^* \frac{m_j^2}{M_W^2} \right|^2 \quad (39)$$

$$\cong (2.5 - 3.9) \times 10^{-55},$$

where we have used the best fit values of the neutrino oscillation parameters given in (5) and (6) and the two values correspond to  $\delta = \pi$  and 0. The current experimental upper limit reads [101]  $\text{BR}(\mu^+ \rightarrow e^+ + \gamma) < 2.4 \times 10^{-12}$ . Thus, although the predicted branching ratio  $\text{BR}(\mu^+ \rightarrow e^+ + \gamma) \neq 0$ , its value is approximately by 43 orders of magnitude smaller than the sensitivity reached in the experiments searching for the  $\mu \rightarrow e + \gamma$  decay, which renders it unobservable in practice.

As was emphasised already, massive Majorana neutrinos appear in theories with no conserved additive quantum number, and more specifically, in which the total lepton charge  $L$  is not conserved and changes by two units. In the absence of RH singlet neutrino fields in the theory, the flavour neutrinos and antineutrinos  $\nu_l$  and  $\bar{\nu}_l$ ,  $l = e, \mu, \tau$ , can have a mass term of the so-called Majorana type:

$$\mathcal{L}_M^\nu(x) = -\frac{1}{2} \overline{\nu_{l'R}^c}(x) M_{l'l} \nu_{lL}(x) + \text{h.c.}, \quad (40)$$

$$\nu_{l'R}^c \equiv C(\overline{\nu_{l'L}}(x))^T,$$

where  $M$  is a  $3 \times 3$ , in general complex matrix. In the case when all elements of  $M$  are nonzero,  $M_{l'l} \neq 0$ ,  $l, l' = e, \mu, \tau$ , neither the individual lepton charges  $L_l$  nor the total lepton charge  $L$  is conserved:  $L_l \neq \text{const.}$ ,  $L \neq \text{const.}$  As it is possible to show, owing to the fact that  $\nu_{lL}(x)$  are fermion (anticommuting) fields, the matrix  $M$  has to be symmetric (see, e.g., [26]):  $M = M^T$ . A complex symmetric matrix is diagonalised by the congruent transformation:

$$M^{\text{diag}} = U^T M U, \quad U \text{-unitary}, \quad (41)$$

where  $U$  is a  $3 \times 3$  unitary matrix. If  $\mathcal{L}_M^\nu(x)$  is written in the basis in which the charged lepton mass matrix is diagonal,  $U$  coincides with the PMNS matrix:  $U \equiv U_{\text{PMNS}}$ . The fields of neutrinos  $\nu_j$  with definite mass  $m_j$  are expressed in terms of  $\nu_{lL}(x)$  and  $\nu_{lR}^c$ :

$$\mathcal{L}_M^\nu(x) = -\frac{1}{2} \overline{\nu_j}(x) m_j \nu_j(x), \quad (42)$$

$$\nu_j(x) = U_{jl}^\dagger \nu_{lL}(x) + U_{jl}^T \nu_{lR}^c = C(\overline{\nu_j}(x))^T, \quad j = 1, 2, 3. \quad (43)$$

They satisfy the Majorana condition with  $\xi_j = 1$ , as (43) shows.

The Majorana mass term (40) for the LH flavour neutrino fields  $\nu_{lL}$  can be generated

- (i) effectively after the electroweak symmetry (EWS) breaking in the type I see-saw models [6–9],

- (ii) effectively after the EWS breaking in the type III see-saw models [102],
- (iii) directly as a result of the EWS breaking by an  $\text{SU}(2)_L$  triplet Higgs field which carries two units of the weak hypercharge  $Y_W$  and couples in an  $\text{SU}(2)_L \times U_{Y_W}$  invariant manner to two lepton doublets [18, 103, 104] (the Higgs triplet model (HTM) sometimes called also “type II see-saw model”),
- (iv) as a one-loop correction to a Lagrangian which does not contain a neutrino mass term [105, 106] (see also [107]),
- (v) as a two-loop correction in a theory where the neutrino masses are zero at tree and one-loop levels [108, 109] (see also [107]),
- (vi) as a three-loop correction in a theory in which the neutrino masses are zero at tree, one-loop and two-loop levels [107].

In all three types of see-saw models, for instance, the neutrino masses can be generated at the EWS breaking scale and in this case the models predict rich beyond the Standard Model physics at the TeV scale, some of which can be probed at the LHC (see, e.g., [110] and further). We will consider briefly below the neutrino mass generation in the type I see-saw and the Higgs triplet models.

In a theory in which the  $\text{SU}(2)_L$  singlet RH neutrino fields  $\nu_{lR}$ ,  $l = e, \mu, \tau$ , are present (we consider in the present paper the case of three RH sterile neutrinos, but schemes with less than 3 and more than 3 sterile neutrinos are also discussed in the literature, see, e.g., [10, 15]), the most general neutrino mass Lagrangian contains the Dirac mass term (36), the Majorana mass term for the LH flavour neutrino fields (40), and a Majorana mass term for the RH neutrino fields  $\nu_{lR}(x)$  [111]:

$$\mathcal{L}_{D+M}^\nu(x) = -\overline{\nu_{l'R}}(x) M_{D'l} \nu_{lL}(x) - \frac{1}{2} \overline{\nu_{l'R}^c}(x) M_{L'l'} \nu_{lL}(x) - \frac{1}{2} \overline{\nu_{l'R}^c}(x) M_{R'l'} \nu_{lR}(x) + \text{h.c.}, \quad (44)$$

where  $\nu_{l'L}^c \equiv C(\overline{\nu_{l'R}}(x))^T$  and  $M_D$ ,  $M_L$ , and  $M_R$  are  $3 \times 3$ , in general complex matrices. By a simple rearrangement of the neutrino fields this mass term can be cast in the form of a Majorana mass term which is then diagonalised with the help of the congruent transformation [26]. In this case there are six Majorana mass eigenstate neutrinos; that is, the flavour neutrino fields  $\nu_{lL}(x)$  are linear combinations of the fields of six Majorana neutrinos with definite mass. The neutrino mixing matrix in (1) is a  $3 \times 6$  block of a  $6 \times 6$  unitary matrix.

The Dirac-Majorana mass term is at the basis of the type I see-saw mechanism of generation of the neutrino masses and appears in many grand unified theories (GUTs) (see, e.g., [26] for further details). In the see-saw models, some of the six massive Majorana neutrinos typically are too heavy to be produced in the weak processes in which the initial states of the flavour neutrinos and antineutrinos

$\nu_e$  and  $\bar{\nu}_e$ , used in the neutrino oscillation experiments, are being formed. As a consequence, the states of  $\nu_e$  and  $\bar{\nu}_e$  will be coherent superpositions only of the states of the light massive neutrinos  $\nu_j$ , and the elements of the neutrino mixing matrix  $U_{\text{PMNS}}$ , which are determined in experiments studying the oscillations of  $\nu_e$  and  $\bar{\nu}_e$ , will exhibit deviations from unitarity. These deviations can be relatively large and can have observable effects in the TeV scale see-saw models, in which the heavy Majorana neutrinos have masses in the  $\sim (100\text{--}1000)$  GeV range (see, e.g., [112]).

If after the diagonalisation of  $\mathcal{L}_{D+M}^\nu(x)$  more than three neutrinos will turn out to be light, that is, to have masses  $\sim 1$  eV or smaller, active-sterile neutrino oscillations can take place (see, e.g., [15, 26]): an LH (RH) flavour neutrino  $\nu_{lL}$  (antineutrino  $\bar{\nu}_{lR}$ ) can undergo transitions into LH sterile antineutrino(s)  $\bar{\nu}_{l'L} \equiv \bar{\nu}_{l'L}^s$  (RH sterile neutrino(s)  $\nu_{l'R} \equiv \nu_{l'R}^s$ ). As a consequence of this type of oscillations, one would observe a “disappearance” of, for example,  $\nu_e$  and/or  $\nu_\mu$  ( $\bar{\nu}_e$  and/or  $\bar{\nu}_\mu$ ) on the way from the source to the detector.

We would like to discuss next the implications of CP invariance for the neutrino Majorana mass matrix, (40). In the convention we have used to derive (24), in which the unphysical phase factor in the CP transformation of the lepton doublet field  $\Psi_{lL}(x)$ , and thus of  $\nu_{lL}(x)$ ,  $\eta^l = i$ , the requirement of CP invariance leads to the reality condition for  $M$ :

$$\text{CP-invariance: } M^* = M. \quad (45)$$

Thus,  $M$  is real and symmetric and therefore is diagonalised by an orthogonal transformation; that is, if CP invariance holds, the matrix  $U$  in (41) is an orthogonal matrix. The nonzero eigenvalues of a real symmetric matrix can be positive or negative (the absolute value of the difference between the number of positive and number of negative eigenvalues of a real symmetric matrix  $A$  is an invariant of the matrix with respect to transformations  $A' = PAP^T$ , where  $P$  is a real matrix which has an inverse). Consequently,  $M^{\text{diag}}$  in (41) in general has the form

$$M^{\text{diag}} = (m'_1, m'_2, m'_3), \quad m'_j = \rho_j m_j, \quad m_j > 0, \quad \rho_j = \pm 1. \quad (46)$$

Let us denote the neutrino field which has a mass  $m'_j \neq 0$  by  $\nu'_j(x)$ . According to (43), the field  $\nu'_j(x)$  satisfies the Majorana condition:  $\nu'_j(x) = C(\bar{\nu}'_j(x))^T$ . One can work with the fields  $\nu'_j(x)$  remembering that some of them have a negative mass. It is not difficult to show that the CP-parity of the fields  $\nu'_j(x)$  is  $\eta_{\text{CP}}(\nu'_j) = i$ ,  $j = 1, 2, 3$ . The physical meaning of the signs of the masses  $m'_j \neq 0$  of the Majorana neutrinos becomes clear if we change to a “basis” of neutrino fields  $\nu_j(x)$  which have positive masses  $m_j > 0$ . This can be done, for example, by introducing the fields [26]:

$$\begin{aligned} \nu'_j(x) &= (-\gamma_5)^{(1/2)(1-\rho_j)} \nu_j(x) : \nu'_j(x) = \nu_j(x) \quad \text{if } \rho_j = 1; \\ \nu'_j(x) &= -\gamma_5 \nu_j(x) \quad \text{if } \rho_j = -1. \end{aligned} \quad (47)$$

As it is not difficult to show, if  $\nu'_j(x)$  has a mass  $m'_j < 0$ , CP-parity  $\eta_{\text{CP}}(\nu'_j) = i$  and satisfies the Majorana condition  $C(\bar{\nu}'_j(x))^T = \nu'_j(x)$ , the field  $\nu_j(x)$  possesses a mass  $m_j > 0$ , CP-parity  $\eta_{\text{CP}}(\nu_j) = i\rho_j$  and satisfies the Majorana condition  $C(\bar{\nu}_j(x))^T = \rho_j \nu_j(x)$ :

$$\nu_j : m_j > 0, \quad \eta_{\text{CP}}(\nu_j) = i\rho_j, \quad C(\bar{\nu}_j(x))^T = \rho_j \nu_j(x). \quad (48)$$

Thus, in the case of CP invariance, the signs of the nonzero eigenvalues of the neutrino Majorana mass matrix determine the CP-parities of the corresponding positive mass Majorana (mass eigenstate) neutrinos (for further discussion of the properties of massive Majorana neutrinos (fermions) and their couplings, see, e.g., [26]).

**2.3. A Brief Historical Detour.** It is interesting to note that Pontecorvo in his seminal article on neutrino oscillations [13], which was published in 1958 when only one type of neutrino and antineutrino was known, assumed that the state of the neutrino  $\nu$ , emitted in weak interaction processes, is a linear superposition of the states of two Majorana neutrinos  $\nu_1^M$  and  $\nu_2^M$  which have different masses,  $m_1 \neq m_2$ , opposite CP-parities,  $\eta_{\text{CP}}(\nu_1^M) = -\eta_{\text{CP}}(\nu_2^M)$  and are maximally mixed, while the state of the corresponding antineutrino  $\bar{\nu}$  is just the orthogonal superposition of the states of  $\nu_1^M$  and  $\nu_2^M$ :

$$\begin{aligned} |\nu\rangle &= \frac{|\nu_1^M\rangle + |\nu_2^M\rangle}{\sqrt{2}}, \\ |\bar{\nu}\rangle &= \frac{|\nu_1^M\rangle - |\nu_2^M\rangle}{\sqrt{2}}. \end{aligned} \quad (49)$$

Thus, the oscillations are between the neutrino  $\nu$  and the antineutrino  $\bar{\nu}$ , in full analogy with the  $K^0 - \bar{K}^0$  oscillations. From contemporary point of view, Pontecorvo proposed active-sterile neutrino oscillations with maximal mixing and massive Majorana neutrinos. To our knowledge, the article [13] was also the first in which fermion mixing in the weak interaction Lagrangian was introduced.

The article of Maki et al. [14] was inspired, in part, by the discovery of the second type of neutrino—the muon neutrino, in 1962 at Brookhaven. These authors considered a composite model of elementary particles in which the electron and muon neutrino states are superpositions of the states of composite Dirac neutrinos  $\nu_1^D$  and  $\nu_2^D$  which have different masses,  $m_1^D \neq m_2^D$ :

$$\begin{aligned} |\nu_e\rangle &= |\nu_1^D\rangle \cos \theta_c + |\nu_2^D\rangle \sin \theta_c, \\ |\nu_\mu\rangle &= -|\nu_1^D\rangle \sin \theta_c + |\nu_2^D\rangle \cos \theta_c, \end{aligned} \quad (50)$$

where  $\theta_c$  is the neutrino mixing angle. The model proposed in [14] has lepton-hadron symmetry built in and as consequence of this symmetry the neutrino mixing angle coincides with what we call today the Cabibbo angle  $\theta_c \cong 0.22$  (the article by



Maki et al. [14] appeared before the article by Cabibbo [113] in which the “Cabibbo angle”  $\theta_c$  was introduced and the hadron phenomenology related to this angle was discussed, but after the article by Gell-Mann and Lévy [114] in which  $\theta_c$  was also introduced (by the way, in a footnote)). The authors of [14] discuss the possibility of  $\nu_\mu - \nu_e$  oscillations, which they called “virtual transmutations.”

In an article [115] by Katayama et al., published in 1962 somewhat earlier than [14], the authors also introduce two-neutrino mixing. However, this is done purely for model construction purposes and does not have any physical consequences since the neutrinos in the model constructed in [115] are massless particles.

In 1967 Pontecorvo independently considered the possibility of  $\nu_e \leftrightarrow \nu_\mu$  oscillations in the article [1], in which the notion of a “sterile” or “inert” neutrino was introduced. Later in 1969, Gribov and Pontecorvo [116] introduced for the first time a Majorana mass term for the LH flavour neutrinos  $\nu_e$  and  $\nu_\mu$ , the diagonalisation of which leads to two Majorana neutrinos  $\nu_{1,2}^M$  with definite but different masses  $m_{1,2}$ ,  $m_1 \neq m_2$ , and two-neutrino mixing with an arbitrary mixing angle  $\theta$ :

$$\begin{aligned} |\nu_e\rangle &= |\nu_1^M\rangle \cos \theta + |\nu_2^M\rangle \sin \theta, \\ |\nu_\mu\rangle &= -|\nu_1^M\rangle \sin \theta + |\nu_2^M\rangle \cos \theta. \end{aligned} \quad (51)$$

This was the first modern treatment of the problem of neutrino mixing which anticipated the way this problem is addressed in gauge theories of electroweak interactions and in grand unified theories (GUTs). In the same article for the first time the analytic expression for the probability of  $\nu_e \leftrightarrow \nu_\mu$  oscillations was also derived.

#### 2.4. Models of Neutrino Mass Generation: Two Examples

*Type I See-Saw Model.* A natural explanation of the smallness of neutrino masses is provided by the type I see-saw mechanism of neutrino mass generation [6–9]. Integral part of this rather simple mechanism are the RH neutrinos  $\nu_{IR}$  (RH neutrino fields  $\nu_{IR}(x)$ ). The latter are assumed to possess a Majorana mass term  $\mathcal{L}_M^N(x)$  as well as Yukawa type coupling  $\mathcal{L}_Y(x)$  with the Standard Model lepton and Higgs doublets,  $\psi_{IL}(x)$  and  $H(x)$ , given in (37). In the basis in which the Majorana mass matrix of RH neutrinos is diagonal, we have

$$\begin{aligned} \mathcal{L}_{Y,M}(x) &\equiv \mathcal{L}_Y(x) + \mathcal{L}_M^N(x) \\ &= -(\lambda_{kl} \overline{N_{kR}}(x) H^\dagger(x) \psi_{lL}(x) + \text{h.c.}) \\ &\quad - \frac{1}{2} M_k \overline{N_k}(x) N_k(x), \end{aligned} \quad (52)$$

where we have combined the expressions given in (22). When the electroweak symmetry is broken spontaneously, the neutrino Yukawa coupling generates a Dirac mass term:  $m_{kl}^D \overline{N_{kR}}(x) \nu_{lL}(x) + \text{h.c.}$ , with  $m^D = v\lambda$ ,  $v = 174$  GeV being the Higgs doublet v.e.v. In the case when the elements of  $m^D$  are much smaller than  $M_k$ ,  $|m_{il}^D| \ll M_k$ ,  $i, k = 1, 2, 3$ ,  $l = e, \mu, \tau$ ,

the interplay between the Dirac mass term and the mass term of the heavy (RH) Majorana neutrinos  $N_k$  generates an effective Majorana mass (term) for the LH flavour neutrinos [6–9]:

$$M_{l'l} \equiv -(m^D)_{l'k}^T M_k^{-1} m_{kl}^D = -v^2 (\lambda)_{l'k}^T M_k^{-1} \lambda_{kl}. \quad (53)$$

In grand unified theories,  $m^D$  is typically of the order of the charged fermion masses. In SO(10) theories, for instance,  $m^D$  coincides with the up-quark mass matrix. Taking indicatively  $M \sim 0.1$  eV,  $m^D \sim 100$  GeV, one obtains  $M_k \sim M_N \sim 10^{14}$  GeV, which is close to the scale of unification of the electroweak and strong interactions,  $M_{\text{GUT}} \equiv 2 \times 10^{16}$  GeV. In GUT theories with RH neutrinos one finds that indeed the heavy Majorana neutrinos  $N_k$  naturally obtain masses which are by few to several orders of magnitude smaller than  $M_{\text{GUT}}$  (see, e.g., [7, 8]). Thus, the enormous disparity between the neutrino and charged fermion masses is explained effectively in this approach by the huge difference between the electroweak symmetry breaking scale and  $M_{\text{GUT}}$ .

An additional attractive feature of the see-saw scenario under discussion is that the generation and smallness of neutrino masses are related via the leptogenesis mechanism [2, 3] (see also, e.g., [4, 5, 68–70, 79]) to the generation of the baryon asymmetry of the Universe. Indeed, the Yukawa coupling in (52), in general, is not CP conserving. Due to this CP-nonconserving coupling, the heavy Majorana neutrinos undergo, for example, the decays  $N_j \rightarrow l^+ + H^{(-)}$ ,  $N_j \rightarrow l^- + H^{(+)}$ , which have different rates:  $\Gamma(N_j \rightarrow l^+ + H^{(-)}) \neq \Gamma(N_j \rightarrow l^- + H^{(+)})$ . When these decays occur in the Early Universe at temperatures somewhat below the mass of, say,  $N_1$ , so that the latter are out of equilibrium with the rest of the particles present at that epoch, CP violating asymmetries in the individual lepton charges  $L_l$  and in the total lepton charge  $L$  of the Universe are generated. These lepton asymmetries are converted into a baryon asymmetry by  $(B - L)$  conserving, but  $(B + L)$  violating, sphaleron processes, which exist in the Standard Model and are effective at temperatures  $T \sim (100 - 10^{12})$  GeV [117]. If the heavy neutrinos  $N_j$  have hierarchical spectrum,  $M_1 \ll M_2 \ll M_3$ , the observed baryon asymmetry can be reproduced provided the mass of the lightest one satisfies  $M_1 \gtrsim 10^9$  GeV [118] (in specific type I see-saw models this bound can be lower by a few orders of magnitude, see, e.g., [119]). Thus, in this scenario, the neutrino masses and mixing and the baryon asymmetry have the same origin—the neutrino Yukawa couplings and the existence of (at least two) heavy Majorana neutrinos. Moreover, quantitative studies based on advances in leptogenesis theory [68–70], in which the importance of the flavour effects in the generation of the baryon asymmetry was understood, have shown that the Dirac and/or Majorana phases in the neutrino mixing matrix  $U$  can provide the CP violation, necessary in leptogenesis for the generation of the observed baryon asymmetry of the Universe [71, 72]. This implies, in particular, that if the CP symmetry is established not to hold in the lepton sector due to the PMNS matrix  $U$ , at least some fraction (if not all) of the observed baryon asymmetry might be due to the Dirac and/or Majorana CP violation present in the neutrino mixing.



In the see-saw scenario considered, the scale at which the new physics manifests itself, which is set by the scale of masses of the RH neutrinos, can, in principle, have an arbitrary large value, up to the GUT scale of  $2 \times 10^{16}$  GeV and even beyond, up to the Planck mass. An interesting possibility, which can also be theoretically well motivated (see, e.g., [120, 121]), is to have the new physics at the TeV scale, that is,  $M_k \sim (100\text{--}1000)$  GeV. Low scale see-saw scenarios usually predict a rich phenomenology at the TeV scale and are constrained by different sets of data, such as, the data on neutrino oscillations, from EW precision tests and on the lepton flavour violating (LFV) processes  $\mu \rightarrow e\gamma$ ,  $\mu \rightarrow 3e$ ,  $\mu^- - e^-$  conversion in nuclei. In the case of the TeV scale type I see-saw scenario of interest, the flavour structure of the couplings of the heavy Majorana neutrinos  $N_k$  to the charged leptons and the  $W^\pm$  bosons, and to the LH flavour neutrinos  $\nu_{lL}$  and the  $Z^0$  boson, are essentially determined by the requirement of reproducing the data on the neutrino oscillation parameters [98]. All present experimental constraints on this scenario still allow (i) for the predicted rates of the  $\mu \rightarrow e + \gamma$  decay,  $\mu \rightarrow 3e$  decay, and  $\mu - e$  conversion in the nuclei to be [122] within the sensitivity range of the currently running MEG experiment on  $\mu \rightarrow e + \gamma$  decay [101] planned to probe values of  $\text{BR}(\mu^+ \rightarrow e^+ + \gamma) \gtrsim 10^{-13}$ , and of the future planned experiments on  $\mu \rightarrow 3e$  decay and  $\mu - e$  conversion [123–127], (ii) for an enhancement of the rate of neutrinoless double-beta-(( $\beta\beta$ )<sub>0ν</sub>-) decay [98], which thus can be in the range of sensitivity of the ( $\beta\beta$ )<sub>0ν</sub>-decay experiments which are taking data or are under preparation (see, e.g., [128]) even when the light Majorana neutrinos possess a normal hierarchical mass spectrum (see further), and (iii) for the possibility of an exotic Higgs decay channel into a light neutrino and a heavy Majorana neutrino with a sizable branching ratio, which can lead to observable effects at the LHC [110] (for further details concerning the low energy phenomenology of the TeV scale type I see-saw model, see, e.g., [98, 120–122]).

Let us add that the role of the experiments searching for lepton flavour violation to test and possibly constrain low scale see-saw models, and more generally, extensions of the Standard Model predicting “new” (lepton flavour violating) physics at the TeV scale, will be significantly strengthened in the next years. Searches for  $\mu - e$  conversion at the planned COMET experiment at KEK [124] and Mu2e experiment at Fermilab [125] aim to reach sensitivity to conversion rates  $\text{CR}(\mu\text{Al} \rightarrow e\text{Al}) \approx 10^{-16}$ , while, in the longer run, the PRISM/PRIME experiment in KEK [126] and the project-X experiment in Fermilab [127] are being designed to probe values of the  $\mu - e$  conversion rate on Ti, which are smaller by 2 orders of magnitude,  $\text{CR}(\mu\text{Ti} \rightarrow e\text{Ti}) \approx 10^{-18}$  [126]. The current upper limit on the  $\mu - e$  conversion rate is  $\text{CR}(\mu\text{Al} \rightarrow e\text{Al}) < 4.3 \times 10^{-12}$  [129]. There are also plans to perform a new search for the  $\mu^+ \rightarrow e^+ e^- e^+$  decay [123], which will probe values of the corresponding branching ratio down to  $\text{BR}(\mu^+ \rightarrow e^+ e^- e^+) \approx 10^{-15}$ , that is, by 3 orders of magnitude smaller than the best current upper limit [130]. Furthermore, searches for tau lepton flavour violation at superB factories aim to reach a sensitivity to  $\text{BR}(\tau \rightarrow (\mu, e)\gamma) \approx 10^{-9}$  (see, e.g., [131]).

*The Higgs Triplet Model (HTM).* In its minimal formulation this model includes one additional  $\text{SU}(2)_L$  triplet Higgs field  $\Delta$ , which has weak hypercharge  $Y_W = 2$  [18, 103, 104]:

$$\Delta = \begin{pmatrix} \frac{\Delta^+}{\sqrt{2}} & \Delta^{++} \\ \Delta^0 & -\frac{\Delta^+}{\sqrt{2}} \end{pmatrix}. \quad (54)$$

The Lagrangian of the Higgs triplet model which is sometimes called also the “type II see-saw model,” reads (we do not give here, for simplicity, all the quadratic and quartic terms present in the scalar potential (see, e.g., [132])):

$$\begin{aligned} \mathcal{L}_{\text{HTM}} = & -M_\Delta^2 \text{Tr}(\Delta^\dagger \Delta) \\ & - \left( h_{\ell\ell'} \bar{\psi}_{\ell L}^C i\tau_2 \Delta \psi_{\ell' L} + \mu_\Delta H^\dagger \Delta^\dagger i\tau_2 H^* + \text{h.c.} \right), \end{aligned} \quad (55)$$

where  $\bar{\psi}_{\ell L}^C \equiv (-\nu_{\ell L}^T C^{-1} - \ell_L^T C^{-1})$ ,  $C$  being the charge conjugation matrix,  $H$  is the SM Higgs doublet, and  $\mu_\Delta$  is a real parameter characterising the soft explicit breaking of the total lepton charge conservation. We will discuss briefly the low energy version of HTM, where the new physics scale  $M_\Delta$  associated with the mass of  $\Delta$  takes values  $100 \text{ GeV} \leq M_\Delta \leq 1 \text{ TeV}$ , which, in principle, can be probed by LHC (see [132, 133] and references quoted therein).

The flavour structure of the Yukawa coupling matrix  $h$  and the size of the lepton charge soft breaking parameter  $\mu_\Delta$  are related to the light neutrino Majorana mass matrix  $M^\nu$ , which is generated when the neutral component of  $\Delta$  develops a “small” vev  $v_\Delta \propto \mu_\Delta$ . Indeed, setting  $\Delta^0 = v_\Delta$  and  $H^T = (v \ 0)^T$  with  $v \approx 174 \text{ GeV}$ , from Lagrangian (55) one obtains

$$M_{\ell\ell'}^\nu \approx 2h_{\ell\ell'} v_\Delta. \quad (56)$$

The matrix of Yukawa couplings  $h_{\ell\ell'}$  is directly related to the PMNS neutrino mixing matrix  $U_{\text{PMNS}} \equiv U$ , which is unitary in this case:

$$h_{\ell\ell'} \equiv \frac{1}{2v_\Delta} (U^* \text{diag}(m_1, m_2, m_3) U^\dagger)_{\ell\ell'}, \quad m_j \geq 0. \quad (57)$$

An upper limit on  $v_\Delta$  can be obtained from considering its effect on the parameter  $\rho = M_W^2/M_Z^2 \cos^2 \theta_W$ . In the SM,  $\rho = 1$  at tree-level, while in the HTM one has

$$\rho \equiv 1 + \delta\rho = \frac{1 + 2x^2}{1 + 4x^2}, \quad x \equiv \frac{v_\Delta}{v}. \quad (58)$$

The measurement  $\rho \approx 1$  leads to the bound  $v_\Delta/v \lesssim 0.03$ , or  $v_\Delta < 5 \text{ GeV}$  (see, e.g., [132]).

For  $M_\Delta \sim (100\text{--}1000) \text{ GeV}$ , the model predicts a plethora of beyond the SM physics phenomena (see, e.g., [132, 134–139]), most of which can be probed at the LHC and in the experiments on charged lepton flavour violation, if the Higgs triplet vacuum expectation value  $v_\Delta$  is relatively small, roughly  $v_\Delta \sim (1\text{--}100) \text{ eV}$ . As can be shown (see, e.g., [132]),

the parameters  $\nu_\Delta$  and  $\mu_\Delta$  are related: for  $M_\Delta \sim \nu = 174 \text{ GeV}$  we have  $\nu_\Delta \equiv \mu_\Delta$ , while if  $M_\Delta^2 \gg \nu^2$ , then  $\nu_\Delta \equiv \mu_\Delta \nu^2 / (2M_\Delta^2)$ . Thus, a relatively small value of  $\nu_\Delta$  in the TeV scale HTM implies that  $\mu_\Delta$  has also to be small, and vice versa. A nonzero but relatively small value of  $\mu_\Delta$  can be generated, for example, at higher orders in perturbation theory [140]. The smallness of the neutrino masses is therefore related to the smallness of the vacuum expectation value  $\nu_\Delta$ , which in turn is related to the smallness of the parameter  $\mu_\Delta$ .

Under the conditions specified above one can have testable predictions of the model in low energy experiments, and in particular, in the ongoing MEG and the planned future experiments on the lepton flavour violating processes  $\mu \rightarrow e\gamma$ ,  $\mu \rightarrow 3e$  and  $\mu + \mathcal{N} \rightarrow e + \mathcal{N}$  (see, e.g., [122]). The HTM has also an extended Higgs sector including neutral, singly charged and doubly charged Higgs particles. The physical singly charged Higgs scalar field (particle) practically coincides with the triplet scalar field  $\Delta^+$ , the admixture of the doublet charged scalar field being suppressed by the factor  $\nu_\Delta/\nu$ . The singly and doubly charged Higgs scalars  $\Delta^+$  and  $\Delta^{++}$  have, in general, different masses [140]:  $m_{\Delta^+} \neq m_{\Delta^{++}}$ . Both cases  $m_{\Delta^+} > m_{\Delta^{++}}$  and  $m_{\Delta^+} < m_{\Delta^{++}}$  are possible. The TeV scale HTM predicts the existence of rich new physics at LHC as well, associated with the presence of the singly and doubly charged Higgs particles  $\Delta^+$  and  $\Delta^{++}$  in the theory (see, e.g., [132, 137–139]).

### 3. Determining the Nature of Massive Neutrinos

The Majorana nature of massive neutrinos typically manifests itself in the existence of processes in which the total lepton charge  $L$  changes by two units:  $K^+ \rightarrow \pi^- + \mu^+ + \mu^+$ ,  $\mu^- + (A, Z) \rightarrow \mu^+ + (A, Z-2)$ , and so forth. Extensive studies have shown that the only feasible experiments having the potential of establishing the Majorana nature of massive neutrinos at present are the  $(\beta\beta)_{0\nu}$ -decay experiments searching for the process  $(A, Z) \rightarrow (A, Z+2) + e^- + e^-$  (for reviews see, e.g., [26, 128, 141, 142]). The observation of  $(\beta\beta)_{0\nu}$ -decay and the measurement of the corresponding half-life with sufficient accuracy not only would be a proof that the total lepton charge is not conserved, but might provide also information (i) on the type of neutrino mass spectrum [48, 49], and (ii) on the absolute scale of neutrino masses (see, e.g., [81]).

The observation of  $(\beta\beta)_{0\nu}$ -decay and the measurement of the corresponding half-life with sufficient accuracy, combined with data on the absolute neutrino mass scale, might provide also information on the Majorana phases in  $U$  [80, 82, 83, 143, 144]. If the neutrino mass spectrum is inverted hierarchical or quasidegenerate, for instance, it would be possible to get information about the phase  $\alpha_{21}$ . However, establishing even in this case that  $\alpha_{21}$  has a CP violating value would be a remarkably challenging problem [83] (see also [84]). Determining experimentally the values of both the Majorana phases  $\alpha_{21}$  and  $\alpha_{31}$  is an exceptionally difficult problem. It requires the knowledge of the type of neutrino mass spectrum and high precision determination of both the absolute neutrino mass scale and of the  $(\beta\beta)_{0\nu}$ -decay effective Majorana mass,  $|\langle m \rangle|$  (see, e.g., [80, 83]).

**3.1. Majorana Neutrinos and  $(\beta\beta)_{0\nu}$ -Decay.** Under the assumptions of 3- $\nu$  mixing, for which we have compelling evidence, of massive neutrinos  $\nu_j$  being Majorana particles and of  $(\beta\beta)_{0\nu}$ -decay generated *only by the (V-A) charged current weak interaction via the exchange of the three Majorana neutrinos  $\nu_j$*  having masses  $m_j \lesssim \text{few MeV}$ , the  $(\beta\beta)_{0\nu}$ -decay amplitude of interest has the form (see, e.g., [80, 141, 142]):  $A(\beta\beta)_{0\nu} \equiv \langle m \rangle M$ , where  $M$  is the corresponding nuclear matrix element (NME) which does not depend on the neutrino mixing parameters, and

$$|\langle m \rangle| = |m_1|U_{e1}|^2 + m_2|U_{e2}|^2 e^{i\alpha_{21}} + m_3|U_{e3}|^2 e^{i(\alpha_{31}-2\delta)}|, \quad (59)$$

is the effective Majorana mass in  $(\beta\beta)_{0\nu}$ -decay,  $|U_{e1}| = c_{12}c_{13}$ ,  $|U_{e2}| = s_{12}c_{13}$ ,  $|U_{e3}| = s_{13}$ . In the case of CP-invariance one has  $2\delta = 0$  or  $2\pi$  and,

$$\eta_{21} \equiv e^{i\alpha_{21}} = \pm 1, \quad \eta_{31} \equiv e^{i\alpha_{31}} = \pm 1, \quad (60)$$

$\eta_{21(31)}$  being the relative CP-parity of the Majorana neutrinos  $\nu_{2(3)}$  and  $\nu_1$ .

It proves convenient to express [145] the three neutrino masses in terms of  $\Delta m_{21}^2$  and  $\Delta m_{31(32)}^2$ , measured in neutrino oscillation experiments, and the absolute neutrino mass scale determined by  $\min(m_j)$  (for a detailed discussion of the relevant formalism, see, e.g., [26, 80, 141, 142]). In both cases of neutrino mass spectrum with normal and inverted ordering one has (in the convention we use):  $\Delta m_{21}^2 > 0$ ,  $m_2 = (m_1^2 + \Delta m_{21}^2)^{1/2}$ . For normal ordering,  $\Delta m_{31}^2 > 0$ , and  $m_3 = (m_1^2 + \Delta m_{31}^2)^{1/2}$ , while if the spectrum is with inverted ordering,  $\min(m_j) = m_3$ ,  $\Delta m_{32}^2 < 0$  and  $m_1 = (m_3^2 + \Delta m_{23}^2 - \Delta m_{21}^2)^{1/2}$ . Thus, given  $\Delta m_{21}^2$ ,  $\Delta m_{31(32)}^2$ ,  $\theta_{12}$ , and  $\theta_{13}$ ,  $|\langle m \rangle|$  depends on  $\min(m_j)$ , the Majorana phases  $\alpha_{21}$ ,  $\alpha_{31}$ , and the type of neutrino mass spectrum.

The problem of obtaining the allowed values of  $|\langle m \rangle|$  given the constraints on the parameters following from  $\nu$ -oscillation data, and more generally of the physics potential of  $(\beta\beta)_{0\nu}$ -decay experiments, was first studied in [145] and subsequently in a large number of papers (see, e.g., [80, 83, 146–153]; extensive list of references on the subject is given in [141, 142]). The results of this analysis are illustrated in Figure 1. The main features of the predictions for  $|\langle m \rangle|$  in the cases of the NH, IH, and QD spectra are summarised below.

(i) NH spectrum:

$$|\langle m \rangle| \equiv \left| \left( \Delta m_{21}^2 \right)^{1/2} s_{12}^2 + \left( \Delta m_{31}^2 \right)^{1/2} s_{13}^2 e^{-i(\alpha_{21}-\alpha_{31}+2\delta)} \right|. \quad (61)$$

Using the  $3\sigma$  allowed ranges of the relevant neutrino oscillation parameters we get

$$4.7 \times 10^{-4} \text{ eV} \lesssim |\langle m \rangle| \lesssim 4.8 \times 10^{-3} \text{ eV}, \quad \text{NH}. \quad (62)$$

(ii) IH spectrum:

$$|\langle m \rangle| \equiv \left( \left| \Delta m_{32}^2 \right| \right)^{1/2} \left( 1 - \sin^2 2\theta_{21} \sin^2 \frac{\alpha_{21}}{2} \right)^{1/2}, \quad (63)$$

$$\left( \left| \Delta m_{32}^2 \right| \right)^{1/2} \cos 2\theta_{12} \lesssim |\langle m \rangle| \lesssim \left( \left| \Delta m_{32}^2 \right| \right)^{1/2}.$$

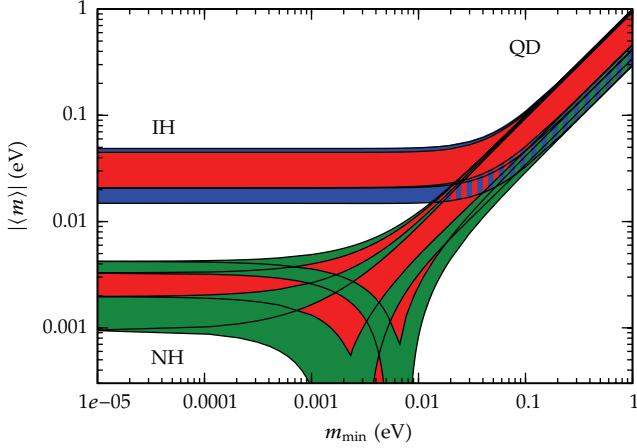


FIGURE 1: The effective Majorana mass  $|\langle m \rangle|$  (including a  $2\sigma$  uncertainty), as a function of  $\min(m_i)$  for  $\sin^2\theta_{13} = 0.0236 \pm 0.0042$  [27, 28] and  $\delta = 0$ . The figure is obtained using also the best fit values and  $1\sigma$  errors of  $\Delta m_{21}^2$ ,  $\sin^2\theta_{12}$ , and  $|\Delta m_{31(32)}^2|$  given in Table 1.7 in [11]. The phases  $\alpha_{21,31}$  are varied in the interval  $[0, \pi]$ . The predictions for the NH, IH, and QD spectra are indicated. The red regions correspond to at least one of the phases  $\alpha_{21,31}$  and  $(\alpha_{31} - \alpha_{21})$  having a CP violating value, while the blue and green areas correspond to  $\alpha_{21,31}$  possessing CP conserving values (from [11]).

Numerically one finds

$$0.014 \text{ eV} \leq |\langle m \rangle| \leq 0.050 \text{ eV}, \quad \text{IH}, \quad (64)$$

the upper and the lower bounds corresponding to the CP-conserving values of  $\alpha_{21} = 0; \pi$ .

(iii) QD spectrum:

$$|\langle m \rangle| \cong m_0 \left( 1 - \sin^2 2\theta_{12} \sin^2 \frac{\alpha_{21}}{2} \right)^{1/2}, \quad (65)$$

$$m_0 \geq |\langle m \rangle| \geq m_0 \cos 2\theta_{12} \geq 0.028 \text{ eV}$$

with  $m_0 \geq 0.1 \text{ eV}$ ,  $m_0 < 2.05 \text{ eV}$  [62] (see also [63]), or  $m_0 \leq (0.3-1.3) \text{ eV}$  [65] (see (7) and the discussion following after it).

For the IH (QD) spectrum we have also [80, 143]

$$\sin^2 \left( \frac{\alpha_{21}}{2} \right) \cong \left( 1 - \frac{|\langle m \rangle|^2}{\bar{m}^2} \right) \frac{1}{\sin^2 2\theta_{12}}, \quad (66)$$

$$\bar{m}^2 \equiv |\Delta m_{32}^2| (m_0^2), \quad \text{IH (QD)}.$$

Thus, a measurement of  $|\langle m \rangle|$  and  $m_0$  ( $|\Delta m_{32}^2|$ ) for QD (IH) spectrum can allow to determine  $\alpha_{21}$ .

The experimental searches for  $(\beta\beta)_{0\nu}$ -decay have a long history (see, e.g., [154, 155]). The most stringent upper limits on  $|\langle m \rangle|$  were set by the IGEX [156] and Heidelberg-Moscow [157], CUORICINO [158], NEMO3 [159], and EXO-200 [160] experiments with  $^{76}\text{Ge}$ ,  $^{130}\text{Te}$ ,  $^{100}\text{Mo}$ , and  $^{136}\text{Xe}$ , respectively (the NEMO3 collaboration has searched for  $(\beta\beta)_{0\nu}$ -decay of  $^{82}\text{Se}$  and other isotopes as well). The IGEX collaboration has obtained for the half-life of  $^{76}\text{Ge}$  that  $T_{1/2}^{0\nu} > 1.57 \times 10^{25} \text{ yr}$

(90% C.L.), from which the limit  $|\langle m \rangle| < (0.33-1.35) \text{ eV}$  was derived [156]. Using the recent more advanced calculations of the corresponding nuclear matrix elements (including the relevant uncertainties) [161] one finds  $|\langle m \rangle| < (0.22-0.35) \text{ eV}$ . The NEMO3 and CUORICINO experiments, designed to reach a sensitivity to  $|\langle m \rangle| \sim (0.2-0.3) \text{ eV}$ , set the limits:  $|\langle m \rangle| < (0.61-1.26) \text{ eV}$  [159] and  $|\langle m \rangle| < (0.19-0.68) \text{ eV}$  [158] (90% C.L.), where estimated uncertainties in the NME are accounted for. The two upper limits were derived from the experimental lower limits on the half-lives of  $^{100}\text{Mo}$  and  $^{130}\text{Te}$ ,  $T_{1/2}^{0\nu} > 5.8 \times 10^{23} \text{ yr}$  (90% C.L.) [159] and  $T_{1/2}^{0\nu} > 3.0 \times 10^{24} \text{ yr}$  (90% C.L.) [158]. With the NMEs and their uncertainties calculated in [161], the NEMO3 and CUORICINO upper limits read, respectively,  $|\langle m \rangle| < (0.50-0.96) \text{ eV}$  and  $|\langle m \rangle| < (0.25-0.43) \text{ eV}$ . A best lower limit on the half-life of  $^{136}\text{Xe}$  was obtained recently in the EXO-200 experiment [160]:  $T_{1/2}^{0\nu} (^{136}\text{Xe}) > 1.6 \times 10^{25} \text{ yr}$  (90% C.L.).

The best lower limit on the half-life of  $^{76}\text{Ge}$ ,  $T_{1/2}^{0\nu} > 1.9 \times 10^{25} \text{ yr}$  (90% C.L.), was found in the Heidelberg-Moscow  $^{76}\text{Ge}$  experiment [157]. It corresponds to the upper limit [161]  $|\langle m \rangle| < (0.20-0.35) \text{ eV}$ . A positive  $(\beta\beta)_{0\nu}$ -decay signal at  $> 3\sigma$ , corresponding to  $T_{1/2}^{0\nu} = (0.69-4.18) \times 10^{25} \text{ yr}$  (99.73% C.L.) and implying  $|\langle m \rangle| = (0.1-0.9) \text{ eV}$ , is claimed to have been observed in [162], while a later analysis reports evidence for  $(\beta\beta)_{0\nu}$ -decay at  $6\sigma$  corresponding to  $|\langle m \rangle| = 0.32 \pm 0.03 \text{ eV}$  [163].

Most importantly, a large number of projects aim at a sensitivity to  $|\langle m \rangle| \sim (0.01-0.05) \text{ eV}$  [128]: CUORE ( $^{130}\text{Te}$ ), GERDA ( $^{76}\text{Ge}$ ), SuperNEMO, EXO ( $^{136}\text{Xe}$ ), MAJORANA ( $^{76}\text{Ge}$ ), MOON ( $^{100}\text{Mo}$ ), COBRA ( $^{116}\text{Cd}$ ), XMASS ( $^{136}\text{Xe}$ ), CANDLES ( $^{48}\text{Ca}$ ), KamLAND-Zen ( $^{136}\text{Xe}$ ), SNO+ ( $^{150}\text{Nd}$ ), and so forth. These experiments, in particular, will test the positive result claimed in [163].

The existence of significant lower bounds on  $|\langle m \rangle|$  in the cases of IH and QD spectra [48, 49], which lie either partially (IH spectrum) or completely (QD spectrum) within the range of sensitivity of the next generation of  $(\beta\beta)_{0\nu}$ -decay experiments, is one of the most important features of the predictions of  $|\langle m \rangle|$ . These minimal values are given, up to small corrections, by  $|\Delta m_{32}^2| \cos 2\theta_{12}$  and  $m_0 \cos 2\theta_{12}$ . According to the combined analysis of the solar and reactor neutrino data [33], (i) the possibility of  $\cos 2\theta_{12} = 0$  is excluded at  $\sim 6\sigma$ , (ii) the best fit value of  $\cos 2\theta_{12}$  is  $\cos 2\theta_{12} \cong 0.39$ , and (iii) at 99.73% C.L. one has  $\cos 2\theta_{12} \geq 0.28$ . The quoted results on  $\cos 2\theta_{12}$  together with the range of possible values of  $|\Delta m_{32}^2|$  and  $m_0$  lead to the conclusion about the existence of significant and robust lower bounds on  $|\langle m \rangle|$  in the cases of IH and QD spectrum. At the same time one can *always* have  $|\langle m \rangle| \ll 10^{-3} \text{ eV}$  in the case of spectrum with normal ordering [81]. As Figure 1 indicates,  $|\langle m \rangle|$  cannot exceed  $\sim 5 \text{ meV}$  for NH neutrino mass spectrum. This implies that  $\max(|\langle m \rangle|)$  in the case of NH spectrum is considerably smaller than  $\min(|\langle m \rangle|)$  for the IH and QD spectrum. This opens the possibility of obtaining information about the type of  $\nu$ -mass spectrum from a measurement of  $|\langle m \rangle| \neq 0$  [48, 49]. In particular, a positive result in the future  $(\beta\beta)_{0\nu}$ -decay experiments with  $|\langle m \rangle| > 0.01 \text{ eV}$  would imply that



the NH spectrum is strongly disfavored (if not excluded). For  $\Delta m_{31(32)}^2 > 0$ , such a result would mean that the neutrino mass spectrum is with normal ordering, but is not hierarchical. If  $\Delta m_{31(32)}^2 < 0$ , the neutrino mass spectrum would be either IH or QD. Prospective experimental errors in the values of oscillation parameters in  $|\langle m \rangle|$  and the sum of neutrino masses, and the uncertainty in the relevant NME, can weaken but do not invalidate these results [82, 83, 86, 164]. Let us note that encouraging results, in what regards the problem of calculation of the NME, were reported at the MEDEX'11 Workshop on Matrix Elements for the Double-beta-decay Experiments [165] (for the bounds on  $|\langle m \rangle|$  obtained using the current results on the NME, see, e.g., [86]).

As Figure 1 indicates, a measurement of  $|\langle m \rangle| \geq 0.01$  eV would either [81] (i) determine a relatively narrow interval of possible values of the lightest neutrino mass  $\min(m_j)$  or (ii) would establish an upper limit on  $\min(m_j)$ . If an upper limit on  $|\langle m \rangle|$  is experimentally obtained below 0.01 eV, this would lead to a significant upper limit on  $\min(m_j)$ .

The possibility of establishing CP-violation in the lepton sector due to Majorana CPV phases has been studied in [81, 84] and in much greater detail in [82, 83]. It was found that it is very challenging: it requires quite accurate measurements of  $|\langle m \rangle|$  (and of  $m_0$  for QD spectrum) and holds only for a limited range of values of the relevant parameters. More specifically [82, 83], establishing at  $2\sigma$  CP-violation associated with Majorana neutrinos in the case of QD spectrum requires for  $\sin^2\theta_\odot = 0.31$ , in particular, a relative experimental error on the measured value of  $|\langle m \rangle|$  and  $m_0$  smaller than 15%, a “theoretical uncertainty”  $F \leq 1.5$  in the value of  $|\langle m \rangle|$  due to an imprecise knowledge of the corresponding NME, and value of the relevant Majorana CPV phase  $\alpha_{21}$  typically within the ranges of  $\sim (\pi/4 - 3\pi/4)$  and  $\sim (5\pi/4 - 7\pi/4)$ .

The knowledge of NME with sufficiently small uncertainty is crucial for obtaining quantitative information on the  $\nu$ -mixing parameters from a measurement of  $(\beta\beta)_{0\nu}$ -decay half-life. The observation of a  $(\beta\beta)_{0\nu}$ -decay of one nucleus is likely to lead to the searches and eventually to observation of the decay of other nuclei. One can expect that such a progress, in particular, will help to solve completely the problem of the sufficiently precise calculation of the nuclear matrix elements for the  $(\beta\beta)_{0\nu}$ -decay [81] (a possible test of the NME calculations is suggested in [81] and is discussed in greater detail in [166]).

If the future  $(\beta\beta)_{0\nu}$ -decay experiments show that  $|\langle m \rangle| < 0.01$  eV, both the IH and the QD spectrum will be ruled out for massive Majorana neutrinos. If in addition it is established in neutrino oscillation experiments that the neutrino mass spectrum is with *inverted ordering*, that is, that  $\Delta m_{31(32)}^2 < 0$ , one would be led to conclude that either the massive neutrinos  $\nu_j$  are Dirac fermions or that  $\nu_j$  are Majorana particles but there are additional contributions to the  $(\beta\beta)_{0\nu}$ -decay amplitude which interfere destructively with that due to the exchange of light massive Majorana neutrinos. The case of more than one mechanism generating the  $(\beta\beta)_{0\nu}$ -decay was discussed recently in, for example, [167, 168], where the possibility to identify the mechanisms inducing the decay was also analysed. If, however,  $\Delta m_{31(32)}^2$  is determined to be

positive in neutrino oscillation experiments, the upper limit  $|\langle m \rangle| < 0.01$  eV would be perfectly compatible with massive Majorana neutrinos possessing NH mass spectrum, or mass spectrum with normal ordering but partial hierarchy, and the quest for  $|\langle m \rangle|$  would still be open.

If indeed in the next generation of  $(\beta\beta)_{0\nu}$ -decay experiments it is found that  $|\langle m \rangle| < 0.01$  eV, while the neutrino oscillation experiments show that  $\Delta m_{31(32)}^2 > 0$ , the next frontier in the searches for  $(\beta\beta)_{0\nu}$ -decay would most probably correspond to values of  $|\langle m \rangle| \sim 0.001$  eV. Taking  $|\langle m \rangle| = 0.001$  eV as a reference value, the conditions under which  $|\langle m \rangle|$  in the case of neutrino mass spectrum with normal ordering would be guaranteed to satisfy  $|\langle m \rangle| \geq 0.001$  eV, were investigated in [146]. In the analysis performed in [146], the specific case of normal hierarchical neutrino mass spectrum and the general case of spectrum with normal ordering, partial hierarchy, and values of  $\theta_{13}$ , including the value measured in the Daya-Bay, RENO, Double Chooz, and T2K experiments, (4), were considered. The ranges of the lightest neutrino mass  $m_1$  and/or of  $\sin^2\theta_{13}$ , for which  $|\langle m \rangle| \geq 0.001$  eV were derived as well, and the phenomenological implications of such scenarios were discussed.

## 4. Outlook

The last 14 years or so witnessed a spectacular experimental progress in the studies of the properties of neutrinos. In this period the existence of neutrino oscillations, caused by nonzero neutrino masses and neutrino mixing, was established and the parameters which drive the oscillations were determined with a relatively high precision. In spite of these remarkable achievements one has to admit that we are still completely ignorant about some of the fundamental aspects of neutrino mixing: the nature, Dirac or Majorana, of massive neutrinos, the type of spectrum the neutrino masses obey, the absolute scale of neutrino masses, and the status of CP symmetry in the lepton sector. Finding out these aspects and understanding the origins of the neutrino masses and mixing and the patterns they and possibly leptonic CP violation exhibit require an extensive and challenging program of research. The main goals of such a research program include the following.

- (i) Determining the nature, Dirac or Majorana, of massive neutrinos  $\nu_j$ . This is of fundamental importance for making progress in our understanding of the origin of neutrino masses and mixing and of the symmetries governing the lepton sector of particle interactions.
- (ii) Determination of the sign of  $\Delta m_{31(32)}^2 (\Delta m_{31}^2)$  and of the type of neutrino mass spectrum.
- (iii) Determining or obtaining significant constraints on the absolute neutrino mass scale.
- (iv) Determining the status of CP symmetry in the lepton sector.
- (v) Understanding at a fundamental level the mechanism giving rise to neutrino masses and mixing and to  $L_I$ -non-conservation. This includes understanding



the origin of the patterns of neutrino mixing and neutrino masses, suggested by the data. Are the observed patterns of  $\nu$ -mixing and of  $\Delta m_{21,31}^2$  related to the existence of a new fundamental symmetry of particle interactions? Is there any relation between quark mixing and neutrino (lepton) mixing? What is the physical origin of CP violation phases in the neutrino mixing matrix  $U$ ? Is there any relation (correlation) between the (values of) CP violation phases and mixing angles in  $U$ ? Progress in the theory of neutrino mixing might also lead to a better understanding of the mechanism of generation of baryon asymmetry of the Universe.

The successful realization of this research program would be a formidable task and would require many years. It already began with the high precision measurement of  $\theta_{13}$  in the Daya Bay and RENO experiments, which showed that  $\sin^2 2\theta_{13}$  has a relatively large value (4). The Double Chooz and T2K experiments also found values of  $\sin^2 2\theta_{13}$ , which are different from zero, respectively, at  $2.9\sigma$  and  $3.2\sigma$  and are compatible with those obtained in the Daya Bay and RENO experiments. These results on  $\theta_{13}$  have far reaching implications. As we have already mentioned or discussed, the measured relatively large value of  $\theta_{13}$  opens up the possibilities, in particular,

- (i) for searching for CP violation effects in neutrino oscillation experiments with high intensity accelerator neutrino beams, like T2K, NO $\nu$ A [169] (the sensitivities of T2K and NO $\nu$ A on CP violation in neutrino oscillations are discussed, e.g., in [78]),
- (ii) for determining the sign of  $\Delta m_{32}^2$ , and thus the type of neutrino mass spectrum, in neutrino oscillation experiments with sufficiently long baselines (see, e.g., [35, 40–47]).

A value of  $\sin \theta_{13} \gtrsim 0.09$  is a necessary condition for a successful “flavoured” leptogenesis with hierarchical heavy Majorana neutrinos when the CP violation required for the generation of the matter-antimatter asymmetry of the Universe is provided entirely by the Dirac CP violating phase in the neutrino mixing matrix [72].

With the measurement of  $\theta_{13}$ , the first steps on the long “road” leading to a comprehensive understanding of the patterns of neutrino masses and mixing, of their origin and implications, were made. The future of neutrino physics is bright.

## Acknowledgments

This research was supported in part by the INFN Program on Astroparticle Physics, by the Italian MIUR Program on Neutrinos, Dark Matter and Dark Energy in the Era of LHC, and by the World Premier International Research Center Initiative (WPI Initiative), MEXT, Japan, and by the European Union FP7-ITN INVISIBLES (Marie Curie Action, PITANGA-2011-289442).

## References

- [1] B. Pontecorvo, “Neutrino experiments and the question of leptonic-charge conservation,” *Zhurnal Eksperimental'noi i Teoreticheskoi Fiziki*, vol. 53, p. 1717, 1967.
- [2] M. Fukugita and T. Yanagida, “Baryogenesis without grand unification,” *Physics Letters B*, vol. 174, pp. 45–47, 1986.
- [3] V. A. Kuzmin, V. A. Rubakov, and M. E. Shaposhnikov, “On anomalous electroweak baryon-number non-conservation in the early universe,” *Physics Letters B*, vol. 155, no. 1-2, pp. 36–42, 1985.
- [4] G. F. Giudice, A. Notari, M. Raidal, A. Riotto, and A. Strumia, “Towards a complete theory of thermal leptogenesis in the SM and MSSM,” *Nuclear Physics B*, vol. 685, no. 1-3, pp. 89–149, 2004.
- [5] W. Buchmüller, P. Di Bari, and M. Plümacher, “Leptogenesis for pedestrians,” *Annals of Physics*, vol. 315, no. 2, pp. 305–351, 2005.
- [6] P. Minkowski, “mu to e gamma at a rate of one out of one billion muon decays?” *Physics Letters B*, vol. 67, pp. 421–428, 1977.
- [7] M. Gell-Mann, P. Ramond, and R. Slansky, “Complex spinors and unified theories,” in *Supergravity*, F. Nieuwenhuizen and D. Friedman, Eds., p. 315, North Holland, Amsterdam, The Netherlands, 1979.
- [8] T. Yanagida, “Baryon number of the Universe,” in *Proceedings of the Workshop on Unified Theories and the Baryon Number of the Universe*, O. Sawada and A. Sugamoto, Eds., KEK, Japan, 1979.
- [9] R. N. Mohapatra and G. Senjanovic, “Neutrino mass and spontaneous parity violation,” *Physical Review Letters*, vol. 44, no. 14, pp. 912–915, 1980.
- [10] R. N. Mohapatra, S. Antusch, K. S. Babu et al., “Theory of neutrinos: a white paper,” *Reports on Progress in Physics*, vol. 70, no. 11, pp. 1757–1867, 2007.
- [11] K. Nakamura and S. T. Petcov, “Neutrino masses, mixing and oscillations”; in J. Beringer et al. (Particle Data Group), ‘Review of particle physics,’ *Physical Review*, vol. D86, Article ID 010001, p. 177, 2012.
- [12] B. Pontecorvo, “Mesonium and Antimesonium,” *Zhurnal Eksperimental'noi i Teoreticheskoi Fiziki*, vol. 33, p. 549, 1957.
- [13] B. Pontecorvo, “Inverse beta processes and nonconservation of Lepton charge,” *Zhurnal Eksperimental'noi i Teoreticheskoi Fiziki*, vol. 34, p. 247, 1958.
- [14] Z. Maki, M. Nakagawa, and S. Sakata, “Remarks on the unified model of elementary particles,” *Progress of Theoretical Physics*, vol. 28, pp. 870–880, 1962.
- [15] K. N. Abazajian, M. A. Acero, S. K. Agarwalla et al., “Light sterile neutrinos: a white paper,” In press, <http://arxiv.org/abs/1204.5379>.
- [16] E. Majorana, “Theory of the symmetry of electrons and positrons,” *Nuovo Cimento*, vol. 14, pp. 171–184, 1937.
- [17] S. M. Bilenky, J. Hosek, and S. T. Petcov, “Oscillations of neutrinos with dirac and Majorana masses,” *Physics Letters B*, vol. 94, no. 4, pp. 495–498, 1980.
- [18] J. Schechter and J. W. F. Valle, “Neutrino masses in  $SU(2) \otimes U(1)$  theories,” *Physical Review D*, vol. 22, pp. 2227–2235, 1980.
- [19] M. Doi, T. Kotani, H. Nishiura, K. Okuda, and E. Takasugi, “CP violation in Majorana neutrinos,” *Physics Letters B*, vol. 102, pp. 323–326, 1981.
- [20] J. Bernabeu and P. Pascual, “CP properties of the Leptonic sector for Majorana neutrinos,” *Nuclear Physics B*, vol. 228, no. 1, pp. 21–30, 1983.

- [21] E. Molinaro and S. T. Petcov, "The interplay between the "low" and "high" energy CP-violation in leptogenesis," *The European Physical Journal C*, vol. 61, no. 1, pp. 93–109, 2009.
- [22] E. Molinaro and S. Petcov, "A case of subdominant/suppressed "high energy" contribution to the baryon asymmetry of the Universe in flavoured leptogenesis," *Physics Letters B*, vol. 671, no. 1, pp. 60–65, 2009.
- [23] L. Wolfenstein, "CP properties of Majorana neutrinos and double beta decay," *Physics Letters B*, vol. 107, no. 1-2, pp. 77–79, 1981.
- [24] S. M. Bilenky, N. P. Nedelcheva, and S. T. Petcov, "Some Implications of CP Conservation for Majorana Neutrinos," *Nuclear Physics B*, vol. 247, pp. 61–69, 1984.
- [25] B. Kayser, "CPT, CP, and C phases and their effects in Majorana particle processes," *Physical Review D*, vol. 30, pp. 1023–1033, 1984.
- [26] S. M. Bilenky and S. T. Petcov, "Massive neutrinos and neutrino oscillations," *Reviews of Modern Physics*, vol. 59, pp. 671–754, 1987.
- [27] F. P. An, J. Z. Bai, A. B. Balantekin et al., "Observation of electron-antineutrino disappearance at Daya Bay," *Physical Review Letters*, vol. 108, Article ID 17803, 2012.
- [28] F. P. An, Q. An, J. Z. Bai et al., "Improved measurement of electron antineutrino disappearance at Daya Bay," *Chinese Physics*, vol. 37, no. 1, 2013.
- [29] J. K. Ahn, S. Chebotaryov, J. H. Choi et al., "Observation of reactor electron antineutrino disappearance in the RENO experiment," *Physical Review Letters*, vol. 108, Article ID 191802, 6 pages, 2012.
- [30] Y. Abe, C. Aberle, J. C. dos Anjos et al., "Reactor  $\bar{\nu}_e$  disappearance in the Double Chooz experiment," *Physical Review D*, vol. 86, Article ID 052008, 21 pages.
- [31] T. Nakaya and T2K Collaboration, "Results from T2K Experiment," in *Proceedings of the 25th International Conference on Neutrino Physics and Astrophysics*, 2012.
- [32] K. Abe, N. Abgrall, Y. Ajima et al., "Indication of electron neutrino appearance from an accelerator-produced off-axis Muon neutrino beam," *Physical Review Letters*, vol. 107, Article ID 041801, 2011.
- [33] G. L. Fogli, E. Lisi, A. Marrone, D. Montanino, A. Palazzo, and A. M. Rotunno, "Global analysis of neutrino masses, mixings and phases: entering the era of leptonic CP violation searches," *Physical Review D*, vol. 86, Article ID 013012, 10 pages, 2012.
- [34] P. Langacker, S. T. Petcov, G. Steigman, and S. Toshev, "Implications of the Mikheyev-Smirnov-Wolfenstein (MSW) mechanism of amplification of neutrino oscillations in matter," *Nuclear Physics, Section B*, vol. 282, no. C, pp. 589–609, 1987.
- [35] A. Bandyopadhyay, S. Choubey, R. Gandhi et al., "Physics at a future neutrino factory and super-beam facility," *Reports on Progress in Physics*, vol. 72, Article ID 106201, 2009.
- [36] J. Bernabu, S. Palomares-Ruiz, and S. T. Petcov, "Atmospheric neutrino oscillations,  $\theta_{13}$  and neutrino mass hierarchy," *Nuclear Physics B*, vol. 669, pp. 255–276, 2003.
- [37] S. Palomares-Ruiz and S. T. Petcov, "Three-neutrino oscillations of atmospheric neutrinos,  $\theta_{13}$ , neutrino mass hierarchy and iron magnetized detectors," *Nuclear Physics B*, vol. 712, no. 1-2, pp. 392–410, 2005.
- [38] S. Petcov and T. Schwetz, "Determining the neutrino mass hierarchy with atmospheric neutrinos," *Nuclear Physics B*, vol. 740, no. 1-2, pp. 1–22, 2006.
- [39] R. Gandhi, P. Ghoshal, S. Goswami, P. Mehta, S. Uma Sankar, and S. Shalgar, "Mass hierarchy determination via future atmospheric neutrino detectors," *Physical Review D*, vol. 76, no. 7, Article ID 073012, 2007.
- [40] S. T. Petcov and M. Piai, "The LMA MSW solution of the solar neutrino problem, inverted neutrino mass hierarchy and reactor neutrino experiments," *Physics Letters, Section B*, vol. 533, no. 1-2, pp. 94–106, 2002.
- [41] S. Choubey, S. T. Petcov, and M. Piai, "Precision neutrino oscillation physics with an intermediate baseline reactor neutrino experiment," *Physical Review D*, vol. 68, no. 11, Article ID 113006, 2003.
- [42] J. G. Learned, S. T. Dye, S. Pakvasa, and R. C. Svoboda, "Determination of neutrino mass hierarchy and  $\theta_{13}$  with a remote detector of reactor antineutrinos," *Physical Review D*, vol. 78, no. 7, Article ID 071302, 2008.
- [43] M. Batygov, S. Dye, J. Learned, S. Matsuno, S. Pakvasa, and G. Varner, "Prospects of neutrino oscillation measurements in the detection of reactor antineutrinos with a medium-baseline experiment," <http://arxiv.org/abs/0810.2580>.
- [44] L. Zhan, Y. Wang, J. Cao, and L. Wen, "Determination of the Neutrino Mass Hierarchy at an Intermediate Baseline," *Physical Review D*, vol. 78, Article ID 111103, 5 pages, 2008.
- [45] L. Zhan, Y. Wang, J. Cao, and L. Wen, "Experimental requirements to determine the neutrino mass hierarchy using reactor neutrino," *Physical Review D*, vol. 79, Article ID 073007, 5 pages, 2009.
- [46] P. Ghoshal and S. T. Petcov, "Neutrino mass hierarchy determination using reactor antineutrinos," *Journal of High Energy Physics*, vol. 2011, article 58, 2011.
- [47] P. Ghoshal and S. T. Petcov, "Addendum: neutrino mass hierarchy determination using reactor antineutrinos," *Journal of High Energy Physics*, vol. 2012, no. 9, article 115, 2012.
- [48] S. Pascoli and S. T. Petcov, "The SNO solar neutrino data, neutrinoless double beta-decay and neutrino mass spectrum," *Physics Letters, Section B*, vol. 544, no. 3-4, pp. 239–250, 2002.
- [49] S. Pascoli and S. T. Petcov, "Addendum: the SNO solar neutrino data, neutrinoless double beta-decay and neutrino mass spectrum," *Physics Letters, Section B*, vol. 580, no. 3-4, pp. 280–289, 2004.
- [50] S. T. Petcov, "Diffractive-like (or parametric-resonance-like?) enhancement of the Earth (day-night) effect for solar neutrinos crossing the Earth core," *Physics Letters, Section B*, vol. 434, no. 3-4, pp. 321–332, 1998.
- [51] M. V. Chizhov, M. Maris, and S. T. Petcov, "On the oscillation length resonance in the transitions of solar and atmospheric neutrinos crossing the earth core," <http://arxiv.org/abs/hep-ph/9810501>.
- [52] M. V. Chizhov and S. T. Petcov, "New conditions for a total neutrino conversion in a medium," *Physical Review Letters*, vol. 83, pp. 1096–1099, 1999.
- [53] M. V. Chizhov and S. T. Petcov, "Chizhov and Petcov reply," *Physical Review Letters*, vol. 85, p. 3979, 2000.
- [54] M. V. Chizhov and S. T. Petcov, "Enhancing mechanisms of neutrino transitions in a medium of nonperiodic constant-density layers and in the Earth," *Physical Review D*, vol. 63, no. 7, Article ID 073003, 2001.
- [55] V. Ermilova, V. Tsarev, and A. Chechin, "Short Notices of the Lebedev Institute," vol. 5, p. 26, 1986.
- [56] E. Kh. Akhmedov, "Neutrino oscillations in inhomogeneous matter," *Yadernaya Fizika*, vol. 47, p. 475, 1988.

- [57] E. K. Akhmedov, M. Maltoni, and A. Y. Smirnov, “1–3 leptonic mixing and the neutrino oscillograms of the Earth,” *Journal of High Energy Physics*, vol. 2007, 51 pages, 2007.
- [58] F. Perrin, *Comptes Rendus*, vol. 197, p. 868, 1933.
- [59] E. Fermi, “Trend to a theory of beta radiation,” *Nuovo Cimento*, vol. 11, pp. 1–19, 1934.
- [60] E. Fermi, “Attempt of a theory of beta radiation,” *Zeitschrift für Physik*, vol. 88, p. 161, 1934.
- [61] O. Lahav and A. R. Liddle, “The cosmological parameters 2010,” <http://arxiv.org/abs/1002.3488>.
- [62] V. N. Aseev, A. I. Belev, A. I. Berlev et al., “Upper limit on the electron antineutrino mass from the Troitsk experiment,” *Physical Review D*, vol. 84, no. 11, Article ID 112003, 2011.
- [63] K. Eitel, “Direct neutrino mass experiments,” *Nuclear Physics B. Proceedings Supplements*, vol. 143, pp. 197–204, 2005.
- [64] S. M. Bilenky, M. D. Mateev, and S. T. Petcov, “A comment on the measurement of neutrino masses in  $\beta$ -decay experiments,” *Physics Letters, Section B*, vol. 639, no. 3–4, pp. 312–317, 2006.
- [65] K. N. Abazajian, E. Calabrese, A. Cooray et al., “Cosmological and astrophysical neutrino mass measurements,” *Astroparticle Physics*, vol. 35, no. 4, pp. 177–184, 2011.
- [66] S. Wang, Z. Haiman, W. Hu, J. Khoury, and M. May, “Weighing neutrinos with galaxy cluster surveys,” *Physical Review Letters*, vol. 95, no. 1, Article ID 011302, 2005.
- [67] S. Hannestad, H. Tu, and Y. Y. Y. Wong, “Measuring neutrino masses and dark energy with weak lensing tomography,” *Journal of Cosmology and Astroparticle Physics*, no. 6, article no. 025, 2006.
- [68] R. Barbieri, P. Creminelli, A. Strumia, and N. Tetradis, “Baryogenesis through leptogenesis,” *Nuclear Physics B*, vol. 575, no. 1–2, pp. 61–77, 2000.
- [69] A. Abada, S. Davidson, F.-X. Josse-Michaux, M. Losada, and A. Riotto, “Flavour issues in leptogenesis,” *Journal of Cosmology and Astroparticle Physics*, no. 4, article no. 004, 2006.
- [70] E. Nardi, Y. Nir, E. Roulet, and J. Racker, “The importance of flavor in leptogenesis,” *Journal of High Energy Physics*, no. 1, pp. 4123–4149, 2006.
- [71] S. Pascoli, S. T. Petcov, and A. Riotto, “Connecting low energy leptonic CP violation to leptogenesis,” *Physical Review D*, vol. 75, no. 8, Article ID 083511, 2007.
- [72] S. Pascoli, S. T. Petcov, and A. Riotto, “Leptogenesis and low energy CP-violation in neutrino physics,” *Nuclear Physics B*, vol. 774, no. 1–3, pp. 1–52, 2007.
- [73] N. Cabibbo, “Time reversal violation in neutrino oscillation,” *Physics Letters B*, vol. 72, no. 3, pp. 333–335, 1978.
- [74] V. Barger, K. Whisnant, and R. J. N. Phillips, “CP nonconservation in three-neutrino oscillations,” *Physical Review Letters*, vol. 45, no. 26, pp. 2084–2088, 1980.
- [75] P. I. Krastev and S. T. Petcov, “Resonance amplification and T-violation effects in three-neutrino oscillations in the earth,” *Physics Letters B*, vol. 205, no. 1, pp. 84–92, 1988.
- [76] C. Jarlskog, “Commutator of the quark mass matrices in the standard electroweak model and a measure of maximal CP nonconservation,” *Physical Review Letters*, vol. 55, no. 10, pp. 1039–1042, 1985.
- [77] C. Jarlskog, “A basis independent formulation of the connection between quark mass matrices, CP violation and experiment,” *Zeitschrift für Physik C*, vol. 29, no. 3, pp. 491–497, 1985.
- [78] J. Bernabeu, M. Blennow, P. Coloma et al., “EURONU WP6 2009 yearly report: update of the physics potential of Nufact, superbeams and betabeams,” <http://arxiv.org/abs/1005.3146>.
- [79] G. Branco, R. Gonzalez Felipe, and F. R. Joaquim, “Leptonic CP Violation,” *Reviews of Modern Physics*. In press, <http://arxiv.org/abs/1111.5332>.
- [80] S. M. Bilenky, S. Pascoli, and S. T. Petcov, “Majorana neutrinos, neutrino mass spectrum, CP-violation and  $\beta\beta_{0\nu}$  decay: the three-neutrino mixing case,” *Physical Review D*, vol. 64, no. 5, Article ID 053010, 2001.
- [81] S. Pascoli, S. T. Petcov, and L. Wolfenstein, “Searching for the CP-violation associated with Majorana neutrinos,” *Physics Letters, Section B*, vol. 524, no. 3–4, pp. 319–331, 2002.
- [82] S. Pascoli, S. T. Petcov, and W. Rodejohann, “On the CP violation associated with Majorana neutrinos and neutrinoless double-beta decay,” *Physics Letters, Section B*, vol. 549, no. 1–2, pp. 177–193, 2002.
- [83] S. Pascoli, S. T. Petcov, and T. Schwetz, “The absolute neutrino mass scale, neutrino mass spectrum, Majorana CP-violation and neutrinoless double-beta decay,” *Nuclear Physics B*, vol. 734, no. 1–2, pp. 24–49, 2006.
- [84] V. Barger, S. L. Glashow, P. Langacker, and D. Marfatia, “No-go for detecting CP violation via neutrinoless double beta decay,” *Physics Letters, Section B*, vol. 540, no. 3–4, pp. 247–251, 2002.
- [85] A. De Gouvêa, B. Kayser, and R. N. Mohapatra, “Manifest CP violation from Majorana phases,” *Physical Review D*, vol. 67, no. 5, Article ID 053004, 2003.
- [86] A. Faessler, G. L. Fogli, E. Lisi, V. Rodin, A. M. Rotunno, and F. Šimkovic, “Quasiparticle random phase approximation uncertainties and their correlations in the analysis of  $0\nu\beta\beta$  decay,” *Physical Review D*, vol. 79, no. 5, Article ID 053001, 2009.
- [87] G. Racah, “On the symmetry of particle and antiparticle,” *Nuovo Cimento*, vol. 14, no. 7, pp. 322–328, 1937.
- [88] S. Pascoli, S. T. Petcov, and C. E. Yaguna, “Quasi-degenerate neutrino mass spectrum,  $\mu \rightarrow e + \gamma$  decay and leptogenesis,” *Physics Letters, Section B*, vol. 564, no. 3–4, pp. 241–254, 2003.
- [89] S. T. Petcov, T. Shindou, and Y. Takanishi, “Majorana CP-violating phases, RG running of neutrino mixing parameters and charged lepton flavour violating decays,” *Nuclear Physics B*, vol. 738, no. 1–2, pp. 219–242, 2006.
- [90] S. T. Petcov, “On pseudo-Dirac neutrinos, neutrino oscillations and neutrinoless double  $\beta$ -decay,” *Physics Letters B*, vol. 110, no. 3–4, pp. 245–249, 1982.
- [91] G. Altarelli and F. Feruglio, “Discrete flavor symmetries and models of neutrino mixing,” *Reviews of Modern Physics*, vol. 82, no. 3, pp. 2701–2729, 2010.
- [92] R. De Adelhart Toorop, F. Feruglio, and C. Hagedorn, “Finite modular groups and lepton mixing,” *Nuclear Physics B*, vol. 858, no. 3, pp. 437–467, 2012.
- [93] H. Ishimori, T. Kobayashi, H. Ohki, H. Okada, Y. Shimizu, and M. Tanimoto, “Non-Abelian discrete symmetries in particle physics,” *Progress of Theoretical Physics Supplement*, no. 183, pp. 1–163, 2010.
- [94] A. Meroni, S. T. Petcov, and M. Spinrath, “A supersymmetric  $SU(5) \times T'$  unified model of flavor with large  $\theta_{13}$ ,” *Physical Review D*, vol. 86, no. 11, Article ID 113003, 2012.
- [95] S. T. Petcov, “CP-violation effect in neutralino pair production in  $e^+e^-$  annihilation and the electric dipole moment of the electron,” *Physics Letters B*, vol. 178, no. 1, pp. 57–64, 1986.
- [96] J. A. Casas and A. Ibarra, “Oscillating neutrinos and  $\mu \rightarrow e, \gamma$ ,” *Nuclear Physics B*, vol. 618, no. 1–2, pp. 171–204, 2001.
- [97] H. Goldberg, “Constraint on the photino mass from cosmology,” *Physical Review Letters*, vol. 50, no. 19, pp. 1419–1422, 1983, Erratum, *Physical Review Letters*, vol. 103, Article ID 099905, 2009.



- [98] A. Ibarra, E. Molinaro, and S. T. Petcov, “Low energy signatures of the TeV scale seesaw mechanism,” *Physical Review D*, vol. 84, no. 1, Article ID 013005, 2011.
- [99] R. Kitano and Y. Nomura, “Supersymmetry, naturalness, and signatures at the CERN LHC,” *Physical Review D*, vol. 73, no. 9, Article ID 095004, 2006.
- [100] S. T. Petcov, “The processes  $\mu \rightarrow e\gamma$ ,  $\mu \rightarrow 3e$ ,  $\nu' \rightarrow \nu\gamma$  decays in the Weinberg-Salam model with neutrino mixing,” *Yadernaya Fizika*, vol. 25, p. 641, 1977, *Soviet Journal of Nuclear Physics*, vol. 25, p. 340, 1977, vol. 25, p. 698, 1977.
- [101] J. Adam, X. Bai, A. M. Baldini et al., “New limit on the lepton-flavor-violating decay  $\mu^+ \rightarrow e^+\gamma$ ,” *Physical Review Letters*, vol. 107, no. 17, Article ID 171801, 2011.
- [102] R. Foot, H. Lew, X. G. He, and G. C. Joshi, “See-saw neutrino masses induced by a triplet of leptons,” *Zeitschrift für Physik C*, vol. 44, pp. 441–444, 1989.
- [103] M. Magg and C. Wetterich, “Neutrino mass problem and gauge hierarchy,” *Physics Letters B*, vol. 94, no. 1, pp. 61–64, 1980.
- [104] R. N. Mohapatra and G. Senjanović, “Neutrino masses and mixings in gauge models with spontaneous parity violation,” *Physical Review D*, vol. 23, no. 1, pp. 165–180, 1981.
- [105] A. Zee, “A theory of lepton number violation and neutrino Majorana masses,” *Physics Letters B*, vol. 93, no. 4, pp. 389–393, 1980.
- [106] S. T. Petcov, “Remarks on the Zee model of neutrino mixing ( $\mu \rightarrow e + \gamma$ ,  $\nu_H \rightarrow \nu_L + \gamma$ , etc.),” *Physics Letters B*, vol. 115, no. 5, pp. 401–406, 1982.
- [107] Y. Farzan, S. Pascoli, and M. A. Schmidt, “Recipes and ingredients for neutrino mass at loop level,” In press, <http://arxiv.org/abs/1208.2732>.
- [108] S. T. Petcov and S. T. Toshev, “Conservation of lepton charges, massive Majorana and massless neutrinos,” *Physics Letters B*, vol. 143, no. 1–3, pp. 175–178, 1984.
- [109] K. S. Babu and E. Ma, “Natural hierarchy of radiatively induced majorana neutrino masses,” *Physical Review Letters*, vol. 61, no. 6, pp. 674–677, 1988.
- [110] C. Garcia Cely, A. Ibarra, E. Molinaro, and S. T. Petcov, “Higgs decays in the low scale type I see-saw model,” *Physics Letters B*, vol. 718, no. 3, pp. 957–964, 2013.
- [111] S. M. Bilenky and B. Pontecorvo, “Again on neutrino oscillations,” *Lettere Al Nuovo Cimento*, vol. 17, no. 17, pp. 569–574, 1976.
- [112] S. Antusch, C. Biggio, E. Fernández-Martínez, M. B. Gavela, and J. López-Pavón, “Unitarity of the leptonic mixing matrix,” *Journal of High Energy Physics*, vol. 2006, no. 10, Article ID 084, 2006.
- [113] N. Cabibbo, “Unitary symmetry and leptonic decays,” *Physical Review Letters*, vol. 10, no. 12, pp. 531–533, 1963.
- [114] M. Gell-Mann and M. Lévy, “The axial vector current in beta decay,” *Il Nuovo Cimento*, vol. 16, no. 4, pp. 705–726, 1960.
- [115] Y. Katayama, K. Matsumoto, S. Tanaka, and E. Yamada, “Possible unified models of elementary particles with two neutrinos,” *Progress of Theoretical Physics*, vol. 28, p. 675, 1962.
- [116] V. Gribov and B. Pontecorvo, “Neutrino astronomy and lepton charge,” *Physics Letters B*, vol. 28, no. 7, pp. 493–496, 1969.
- [117] J. A. Harvey and M. S. Turner, “Cosmological baryon and lepton number in the presence of electroweak fermion number violation,” *Physical Review D*, vol. 42, pp. 3344–3349, 1990.
- [118] S. Davidson and A. Ibarra, “A lower bound on the right-handed neutrino mass from leptogenesis,” *Physics Letters B*, vol. 535, no. 1–4, pp. 25–32, 2002.
- [119] M. Raidal, A. Strumia, and K. Turzyński, “Low-scale standard supersymmetric leptogenesis,” *Physics Letters, Section B*, vol. 609, no. 3–4, pp. 351–359, 2005, Erratum, *Physics Letters, Section B*, vol. 632, p. 752, 2006.
- [120] M. Shaposhnikov, “A possible symmetry of the  $\nu$ MSM,” *Nuclear Physics B*, vol. 763, no. 1–2, pp. 49–59, 2007.
- [121] M. B. Gavela, T. Hambye, D. Hernández, and P. Hernández, “Minimal flavour seesaw models,” *Journal of High Energy Physics*, vol. 2009, no. 9, article no. 038, 2009.
- [122] D. N. Dinh, A. Ibarra, E. Molinaro, and S. T. Petcov, “The  $\mu$ -e conversion in nuclei,  $\mu \rightarrow e\gamma$ ,  $\mu \rightarrow 3e$  decays and TeV scale see-saw scenarios of neutrino mass generation,” In press, <http://arxiv.org/abs/1205.4671>.
- [123] This is part of the program of research planned to be realised with the MuSIC facility at Osaka University, Japan (private communication by Y. Kuno).
- [124] Y. G. Gui, R. Palmer, Y. Arimoto et al., *Conceptual Design Report*, <http://www.hep.ph.ic.ac.uk/muec/documents/comet-cdr-v1.0.pdf>.
- [125] <http://mu2e.fnal.gov/>.
- [126] Y. Mori and The PRIME Working Group, “An experimental search for  $\mu^- \rightarrow e^-$  conversion process at an ultimate sensitivity of the order of  $10^{-18}$  with PRISM,” LOI-25.
- [127] <http://projectx.fnal.gov/>.
- [128] F. Piquemal, “Neutrinoless double beta experiments,” in *Proceedings of the 25th International Conference on Neutrino Physics and Astrophysics*, Kyoto, Japan, 2012.
- [129] C. Dohmen, K. -D. Groth, B. Heer et al., “Test of lepton flavor conservation in  $\mu \rightarrow e$  conversion on titanium,” *Physics Letters B*, vol. 317, no. 4, pp. 631–636, 1993.
- [130] U. Bellgardt, G. Otter, R. Eichler et al., “Search for the decay  $\mu^+ \rightarrow e^+e^+e^-$ ,” *Nuclear Physics B*, vol. 299, no. 1, pp. 1–6, 1988.
- [131] A. G. Akeroyd, W. Bartel, A. Bondar et al., “Physics at super B factory,” <http://arxiv.org/abs/hep-ex/0406071>.
- [132] A. G. Akeroyd, M. Aoki, and H. Sugiyama, “Phenomenology of the Higgs triplet model,” in *The Large Hadron Collider and Higgs Boson Search*, C. J. Hong, Ed., pp. 162–212, 2011.
- [133] F. del Aguila and J. A. Aguilar-Saavedra, “Distinguishing seesaw models at LHC with multi-lepton signals,” *Nuclear Physics B*, vol. 813, no. 1–2, pp. 22–90, 2009.
- [134] E. Ma, M. Raidal, and U. Sarkar, “Phenomenology of the neutrino-mass-giving Higgs triplet and the low-energy seesaw violation of lepton number,” *Nuclear Physics B*, vol. 615, no. 1–3, pp. 313–330, 2001.
- [135] A. G. Akeroyd, M. Aoki, and H. Sugiyama, “Lepton flavor violating decays  $\tau \rightarrow \bar{\mu}\mu$  and  $\mu \rightarrow e\gamma$  in the Higgs triplet model,” *Physical Review D*, vol. 79, no. 11, Article ID 113010, 2009.
- [136] J. Chakraborty, P. Ghosh, and W. Rodejohann, “Lower limits on  $\mu \rightarrow e\gamma$  from new measurements on  $U_{e3}$ ,” *Physical Review D*, vol. 86, no. 7, Article ID 075020, 2012.
- [137] J. Garayoa and T. Schwetz, “Neutrino mass hierarchy and Majorana CP phases within the Higgs triplet model at the LHC,” *Journal of High Energy Physics*, vol. 2008, no. 3, article 009, 2008.
- [138] A. G. Akeroyd, C.-W. Chiang, and N. Gaur, “Leptonic signatures of doubly charged Higgs boson production at the LHC,” *Journal of High Energy Physics*, vol. 2010, no. 11, article no. 005, 2010.
- [139] A. G. Akeroyd and H. Sugiyama, “Production of doubly charged scalars from the decay of singly charged scalars in the Higgs triplet model,” *Physical Review D*, vol. 84, no. 3, Article ID 035010, 2011.



- [140] E. J. Chun, K. Y. Lee, and S. C. Park, "Testing Higgs triplet model and neutrino mass patterns," *Physics Letters, Section B*, vol. 566, no. 1-2, pp. 142–151, 2003.
- [141] W. Rodejohann, "Neutrinoless double beta decay in particle physics," *International Journal of Modern Physics E*, vol. 20, p. 1833, 2011.
- [142] T. Petcov, "Theoretical prospects of neutrinoless double beta decay," *Physica Scripta T*, vol. 121, pp. 94–101, 2005.
- [143] S. M. Bilenky, C. Giunti, C. W. Kim, and S. T. Petcov, "Short-baseline neutrino oscillations and  $(\beta\beta)_{0\nu}$  decay in schemes with an inverted mass spectrum," *Physical Review D*, vol. 54, no. 7, pp. 4432–4444, 1996.
- [144] S. M. Bilenky, S. Pascoli, and S. T. Petcov, "Majorana neutrinos, neutrino mass spectrum, CP violation, and neutrinoless double  $\beta$  decay. II. Mixing of four neutrinos," *Physical Review D*, vol. 64, no. 11, Article ID 113003, 2001.
- [145] S. T. Petcov and A. Yu. Smirnov, "Neutrinoless double beta decay and the solar neutrino problem," *Physics Letters, Section B*, vol. 322, no. 1-2, pp. 109–118, 1994.
- [146] S. Pascoli and S. T. Petcov, "Majorana Neutrinos, Neutrino Mass Spectrum and the  $|< m >| \sim 0.001$  eV frontier in neutrinoless double beta decay," *Physical Review D*, vol. 77, Article ID 113003, 2008.
- [147] F. Vissani, "Signal of neutrinoless double beta decay, neutrino spectrum and oscillation scenarios," *Journal of High Energy Physics*, vol. 1999, article 06, 1999.
- [148] K. Matsuda, N. Takeda, T. Fukuyama, and H. Nishiura, "CP violations in lepton number violation processes and neutrino oscillations," *Physical Review D*, vol. 62, no. 9, Article ID 093001, pp. 1–8, 2000.
- [149] K. Czakon, M. Zralek, and J. Gluza, "Perspectives on finding the neutrino nature," <http://arxiv.org/abs/hep-ph/0003161>.
- [150] H. V. Klapdor-Kleingrothaus, H. Pas, and A. Yu. Smirnov, "Neutrino mass spectrum and neutrinoless double beta decay," *Physical Review D*, vol. 63, Article ID 073005, 2001.
- [151] H. Murayama and C. Peña-Garay, "Neutrinoless double beta decay in light of SNO salt data," *Physical Review D*, vol. 69, no. 3, Article ID 031301, 2004.
- [152] M. Lindner, A. Merle, and W. Rodejohann, "Improved limit on  $\theta_{13}$  and implications for neutrino masses in neutrino-less double beta decay and cosmology," *Physical Review D*, vol. 73, Article ID 053005, 2006.
- [153] M. Duerr, M. Lindner, and A. Merle, "On the quantitative impact of the Schechter-Valle theorem," *Journal of High Energy Physics*, vol. 2011, no. 6, article 091, 2011.
- [154] A. S. Barabash, "Experiment double beta decay: historical review of 75 years of research," *Physics of Atomic Nuclei*, vol. 74, no. 4, pp. 603–613, 2011.
- [155] C. Aalseth, H. Back, L. Dauwe et al., "Neutrinoless double beta decay and direct searches for neutrino mass," <http://arxiv.org/abs/hep-ph/0412300>.
- [156] C. E. Aalseth, F. T. Avignone III, R. L. Brodzinski et al., "IGEX  $^{76}\text{Ge}$  neutrinoless double-beta decay experiment: prospects for next generation experiments," *Physical Review D*, vol. 65, Article ID 092007, 2002.
- [157] H. V. Klapdor-Kleingrothaus, A. Dietz, L. Baudis et al., "Latest results from the HEIDELBERG-MOSCOW double beta decay experiment," *European Physical Journal A*, vol. 12, no. 2, pp. 147–154, 2001.
- [158] C. Arnaboldi, D. R. Artusa, F. T. Avignone III et al., "Results from a search for the  $0\nu\beta\beta$ -decay of  $^{130}\text{Te}$ ," *Physical Review C*, vol. 78, no. 3, Article ID 035502, 2008.
- [159] A. Barabash, "NEMO 3 double beta decay experiment: latest results," *Journal of Physics: Conference Series*, vol. 173, no. 1, Article ID 012008, 2009.
- [160] M. Auger, D. J. Auty, P. S. Barbeau et al., "Search for neutrinoless double-beta decay in  $^{136}\text{Xe}$  with EXO-200," *Physical Review Letters*, vol. 109, Article ID 032505, 6 pages, 2012.
- [161] F. Šimkovic, A. Faessler, H. Mütter, V. Rodin, and M. Stauf, " $0\nu\beta\beta$ -decay nuclear matrix elements with self-consistent short-range correlations," *Physical Review C*, vol. 79, no. 5, Article ID 055501, 2009.
- [162] H. V. Klapdor-Kleingrothaus, A. Dietz, H. L. Harney, and I. V. Krivosheina, "Evidence for neutrinoless double beta decay," *Modern Physics Letters A*, vol. 16, no. 37, pp. 2409–2420, 2001.
- [163] H. V. Klapdor-Kleingrothaus, I. V. Krivosheina, A. Dietz, and O. Chkvorets, "Search for neutrinoless double beta decay with enriched  $^{76}\text{Ge}$  in Gran Sasso 1990–2003," *Physics Letters, Section B*, vol. 586, no. 3-4, pp. 198–212, 2004.
- [164] S. Pascoli, S. T. Petcov, and W. Rodejohann, "On the neutrino mass spectrum and neutrinoless double-beta decay," *Physics Letters B*, vol. 558, no. 3-4, pp. 141–156, 2003.
- [165] The slides of the talks at MEDEX11, <http://medex11.utef.cvut.cz/program.php>.
- [166] S. M. Bilenky and S. T. Petcov, "Nuclear matrix elements of  $0\nu\beta\beta$ -decay: possible test of the calculations," <http://arxiv.org/abs/hep-ph/0405237>.
- [167] A. Faessler, A. Meroni, S. T. Petcov, F. Šimkovic, and J. Vergados, "Uncovering multiple CP-nonconserving mechanisms of  $(\beta\beta)_{0\nu}$  decay," *Physical Review D*, vol. 83, no. 11, Article ID 113003, 2011.
- [168] A. Faessler, G. L. Fogli, E. Lisi, A. M. Rotunno, and F. Šimkovic, "Multi-isotope degeneracy of neutrinoless double beta decay mechanisms in the quasi-particle random phase approximation," *Physical Review D*, vol. 83, Article ID 113015, 2011.
- [169] D. S. Ayres and NOA Collaboration, "NOvA proposal to build a 30 kiloton off-axis detector to study neutrino oscillations in the fermilab NuMI beamline," <http://arxiv.org/abs/hep-ex/0503053>.

## Review Article

# Neutrino Propagation in Matter

Mattias Blennow<sup>1,2</sup> and Alexei Yu. Smirnov<sup>3</sup>

<sup>1</sup> Division of Particle and Astroparticle Physics, Max-Planck-Institut für Kernphysik, Saupfercheckweg 1, 69117 Heidelberg, Germany

<sup>2</sup> Department of Theoretical Physics, KTH Royal Institute of Technology, AlbaNova University Center, Roslagstullsbacken 21, 106 91 Stockholm, Sweden

<sup>3</sup> High Energy, Cosmology and Astroparticle Physics Section, The Abdus Salam International Centre for Theoretical Physics, 34100 Trieste, Italy

Correspondence should be addressed to Mattias Blennow; [emb@kth.se](mailto:emb@kth.se)

Received 3 August 2012; Accepted 21 November 2012

Academic Editor: Gian Luigi Fogli

Copyright © 2013 M. Blennow and A. Yu. Smirnov. This is an open access article distributed under the Creative Commons Attribution License, which permits unrestricted use, distribution, and reproduction in any medium, provided the original work is properly cited.

We describe the effects of neutrino propagation in the matter of the Earth relevant to experiments with atmospheric and accelerator neutrinos and aimed at the determination of the neutrino mass hierarchy and CP violation. These include (i) the resonance enhancement of neutrino oscillations in matter with constant or nearly constant density, (ii) adiabatic conversion in matter with slowly changing density, (iii) parametric enhancement of oscillations in a multilayer medium, and (iv) oscillations in thin layers of matter. We present the results of semianalytic descriptions of flavor transitions for the cases of small density perturbations, in the limit of large densities and for small density widths. Neutrino oscillograms of the Earth and their structure after determination of the 1–3 mixing are described. A possibility to identify the neutrino mass hierarchy with the atmospheric neutrinos and multimeton scale detectors having low energy thresholds is explored. The potential of future accelerator experiments to establish the hierarchy is outlined.

## 1. Introduction

Neutrinos are eternal travelers: once produced (especially at low energies) they have little chance to interact and be absorbed. Properties of neutrino fluxes are flavor compositions, lepton charge asymmetries, and energy spectra of encode information. Detection of the neutrinos brings unique knowledge about their sources, properties of medium, the space-time they propagated as well as about neutrinos themselves.

Neutrino propagation in matter is vast area of research which covers a variety of different aspects: from conceptual ones to applications. This includes propagation in matter (media) with (i) different properties (unpolarized, polarized, moving, turbulent, fluctuating, with neutrino components, etc.), (ii) different density profiles, and (iii) in different energy regions. The applications cover neutrino propagation in matter of the Earth and the Sun, supernova and relativistic jets as well as neutrinos in the early universe.

The impact of matter on neutrino oscillations was first studied by Wolfenstein in 1978 [1]. He marked that matter suppresses oscillations of the solar neutrinos propagating in the Sun and supernova neutrinos inside a star. He considered hypothetical experiments with neutrinos propagating through 1000 km of rock, something that today is no longer only a thought but actual experimental reality. Later Barger et al. [2] have observed that matter can also enhance oscillations at certain energies. The work of Wolfenstein was expanded upon in papers by Mikheev and Smirnov [3–5], in particular, in the context of the solar neutrino problem. Essentially two new effects have been proposed: the resonant enhancement of neutrino oscillations in matter with constant and nearly constant density and the adiabatic flavor conversion in matter with slowly changing density. It was marked that the first effect can be realized for neutrinos crossing the matter of the Earth. The second one can take place in propagation of solar neutrinos from the dense solar core via the resonance region inside the Sun to the surface with negligible density. This

adiabatic flavor transformation, called later the MSW effect, was proposed as a solution of the solar neutrino problem.

Since the appearance of these seminal papers, neutrino flavor evolution in background matter was studied extensively including the treatment of propagation in media which are not consisting simply of matter at rest, but also backgrounds that take on a more general form. For instance, in a thermal field theory approach [6], effects of finite temperature and density can be taken readily into account. If neutrinos are dense enough, new type of effects can arise due to the neutrino background itself, causing a collective behavior in the flavor evolution. This type of effect could have a significant impact on neutrinos in the early universe and in central parts of collapsing stars.

There has been a great progress in treatments of neutrino conversion in matter, both from an analytical and a pure computational points of view. From the analytical side, the description of three-flavor neutrino oscillations in matter is given by a plethora of formulas containing information that may be hard to get a proper grasp of without introducing approximations. Luckily, given the parameter values inferred from experiments, various perturbation theories and series expansions in small parameters can be developed. In this paper we will explain the basic physical effects important for the current and next generation neutrino oscillation experiments and provide the relevant formalism. We present an updated picture of oscillations and conversion given the current knowledge on the neutrino oscillation parameters.

In this paper we focus mainly on aspects related to future experiments with atmospheric and accelerator neutrinos. The main goals of these experiments are to (i) establish the neutrino mass hierarchy, (ii) discover CP violation in the lepton sector and determination of the CP-violating phase, (iii) precisely measure the neutrino parameters, in particular, the deviation of 2-3 mixing from maximal, and (iv) search for sterile neutrinos and new neutrino interactions.

Accelerator and atmospheric neutrinos propagate in the matter of the Earth. Therefore we mainly concentrate on effects of neutrino propagation in the Earth, that is, in usual electrically neutral and nonrelativistic matter. We update existing results on effects of neutrino propagation in view of the recent determination of the 1-3 mixing.

The paper is organized as follows. In Section 2 we consider properties of neutrinos in matter, in particular, mixing in matter and effective masses (eigenvalues of the Hamiltonian); we derive equations which describe the propagation. Section 3 is devoted to various effects relevant to neutrino propagating in the Earth. We consider the properties of the oscillation/conversion probabilities in different channels. In Section 4 we explore the effects of the neutrino mass hierarchy and CP-violating phase on the atmospheric neutrino fluxes and neutrino beams from accelerators. Conclusions and outlook are presented in Section 5.

## 2. Neutrino Properties in Matter

We will consider the system of 3-flavor neutrinos,  $\nu_f^T \equiv (\nu_e, \nu_\mu, \nu_\tau)$ , mixed in vacuum:

$$\nu_f = U_{\text{PMNS}} \nu_m. \quad (1)$$

Here  $U_{\text{PMNS}}$  is the Pontecorvo-Maki-Nakagawa-Sakata (PMNS) mixing matrix [7–9] and  $\nu_m^T \equiv (\nu_1, \nu_2, \nu_3)$  is the vector of mass eigenstates with masses  $m_i$  ( $i = 1, 2, 3$ ). We will use the standard parameterization of the PMNS matrix,

$$U_{\text{PMNS}} = U_{23}(\theta_{23}) I_\delta U_{13}(\theta_{13}) I_\delta^* U_{12}(\theta_{12}), \quad (2)$$

which is the most suitable for describing usual matter effects. In (2)  $U_{ij}(\theta_{ij})$  are the matrices of rotations in the  $ij$ -planes with angles  $\theta_{ij}$  and  $I_\delta \equiv \text{diag}(1, 1, e^\delta)$ .

In vacuum the flavor evolution of these neutrinos is described by the Schrödinger-like equation

$$i \frac{d\nu_f}{dt} = \frac{MM^\dagger}{2E} \nu_f, \quad (3)$$

where  $M$  is the neutrino mass matrix in the flavor basis and  $E$  is the neutrino energy. Equation (3) is essentially a generalization of the equation  $E \approx p + m^2/2E$  for a single ultrarelativistic particle. According to (3), the Hamiltonian in vacuum can be written as

$$H_0 = \frac{1}{2E} U_{\text{PMNS}} M_{\text{diag}}^2 U_{\text{PMNS}}^\dagger, \quad (4)$$

where  $M_{\text{diag}}^2 \equiv M^\dagger M = \text{diag}(m_1^2, m_2^2, m_3^2)$  and we take the masses  $m_i$  to be real (the term  $pI$  is omitted in (4) since it does not produce a phase difference).

**2.1. Refraction and Matter Potentials.** The effective potential for a neutrino in medium  $V_f$  can be computed as a forward scattering matrix element  $V_f = \langle \Psi | H_{\text{int}} | \Psi \rangle$ . Here  $\Psi$  is the wave function of the system of neutrino and medium, and  $H_{\text{int}}$  is the Hamiltonian of interactions.

At low energies, the Hamiltonian  $H_{\text{int}}$  is the effective four-fermion Hamiltonian due to exchange of the  $W$  and  $Z$  bosons:

$$H_{\text{int}} = \frac{G_F}{\sqrt{2}} \bar{\nu} \gamma^\mu (1 - \gamma_5) \nu \times \{ \bar{e} \gamma_\mu (g_V + g_A \gamma_5) e + \bar{p} \gamma_\mu (g_V^p + g_A^p \gamma_5) p + \bar{n} \gamma_\mu (g_V^n + g_A^n \gamma_5) n \}, \quad (5)$$

where  $g_V$  and  $g_A$  are the vector and axial vector coupling constants.

In the Standard Model the matrix of the potentials in the flavor basis is diagonal:  $V_f = \text{diag}(V_e, V_\mu, V_\tau, 0, \dots)$ .

For medium the matrix elements of vectorial components of vector current are proportional to velocity of particles of medium. The matrix elements of the axial vector current are proportional to spin vector. Therefore for nonrelativistic and unpolarized medium (as well as for an isotropic distribution of ultrarelativistic electrons) only the  $\gamma^0$  component of the vector current gives a nonzero result, which is proportional to the number density of the corresponding particles. Furthermore, due to conservation of the vector current (CVC), the couplings  $g_V^p$  and  $g_V^n$  can be computed using the neutral current couplings of quarks. Thus, taking into account that, in the Standard Model, the neutral current couplings of

electrons and protons are equal and of opposite sign, their NC contributions cancel in electrically neutral medium. As a result, the potential for neutrino flavor  $\nu_a$  is

$$V_a = \sqrt{2}G_F \left( \delta_{ae}n_e - \frac{1}{2}n_n \right), \quad (6)$$

where  $n_e$  and  $n_n$  are the densities of electrons and neutrons, respectively.

Only the difference of potentials has a physical meaning. Contribution of the neutral current scattering to  $V$  is the same for all active neutrinos. Since  $V_a$  ( $a = \mu, \tau$ , or a combination thereof) is due to the neutral current scattering, in a normal medium composed of protons neutrons (nuclei) and electrons,  $V_\mu - V_\tau = 0$ . Furthermore, the difference of the potentials for  $\nu_e$  and  $\nu_a$  is due to the charged current scattering of  $\nu_e$  on electrons ( $\nu_e e \rightarrow \nu_e e$ ) [1]:

$$V = V_e - V_a = \sqrt{2}G_F n_e. \quad (7)$$

The difference of potentials leads to the appearance of an additional phase difference in the neutrino system:  $\phi_{\text{matter}} \equiv (V_e - V_a)t \approx Vx$ . This determines the *refraction length*, the distance over which an additional “matter” phase equals  $2\pi$ :

$$l_0 \equiv \frac{2\pi}{V_e - V_a} = \frac{\sqrt{2}\pi}{G_F n_e}. \quad (8)$$

Numerically,

$$l_0 = 1.6 \cdot 10^9 \text{ cm} \frac{1 \text{ g/cm}^3}{n_e m_N}, \quad (9)$$

where  $m_N$  is the nucleon mass. The corresponding column density  $d \equiv l_0 n_e = \sqrt{2}\pi/G_F$  is given by the Fermi coupling constant only.

For antineutrinos the potential has an opposite sign. Being zero in the lowest order the difference of potentials in the  $\nu_\mu$ - $\nu_\tau$  system appears at a level of  $10^{-5}V$  due to the radiative corrections [10]. Thus in the flavor basis in the lowest order in EW interactions the effect of medium on neutrinos is described by  $\widehat{V} = \text{diag}(V_e, 0, 0)$  with  $V_e$  given in (7).

The potential has been computed for neutrinos in different types of media, such as polarized or heavily degenerate electrons, in [11–13].

## 2.2. Evolution Equation, Effective Hamiltonian, and Mixing in Matter

**2.2.1. Wolfenstein Equation.** In the flavor basis, the Hamiltonian in matter can be obtained by adding the interaction term to the vacuum Hamiltonian in vacuum [1, 3–5, 14, 15]:

$$H_f = \frac{1}{2E} U_{\text{PMNS}} M_{\text{diag}}^2 U_{\text{PMNS}}^\dagger + \widehat{V}. \quad (10)$$

In (10) we have omitted irrelevant parts of the Hamiltonian proportional to the unit matrix. The Hamiltonian for antineutrinos can be obtained by the substitution

$$U \longrightarrow U^*, \quad V \longrightarrow -V. \quad (11)$$

There are different derivations of the neutrino evolution equation in matter, in particular, strict derivations starting from the Dirac equation or derivation in the context of quantum field theory (see [16] and references therein).

Although the Hamiltonian  $H_f$  describes evolution in time, with the connection  $x = vt \approx x = ct$ , (12) can be rewritten as  $idv_f/dx = (H_0 + \widehat{V})v_f$  with  $V = V(x)$ , so it can be used as an evolution equation in space.

Due to the strong hierarchy of  $\Delta m^2$  and the smallness of 1–3 mixing, the results can be qualitatively understood and in many cases quantitatively described by reducing  $3\nu$  evolution to  $2\nu$  evolution. The reason is that the third neutrino effectively decouples and its effect can be considered as a perturbation. Of course, there are genuine  $3\nu$  phenomena such as CP violation, but even in this case the dynamics of evolution can be reduced effectively to the dynamics of evolution of  $2\nu$  systems. The evolution equation for two-flavor states,  $v_f^T = (\nu_e, \nu_a)$ , in matter is

$$i \frac{dv_f}{dt} = \left[ \frac{\Delta m^2}{4E} \begin{pmatrix} -\cos 2\theta & \sin 2\theta \\ \sin 2\theta & \cos 2\theta \end{pmatrix} + \begin{pmatrix} \frac{1}{2}V_e & 0 \\ 0 & -\frac{1}{2}V_e \end{pmatrix} \right] v_f, \quad (12)$$

where the Hamiltonian is written in symmetric form.

**2.3. Mixing and Eigenstates in Matter.** The mixing in matter is defined with respect to  $\nu_{im}$ —the eigenstates of the Hamiltonian in matter  $H_f$ .

As usual, the eigenstates are obtained from the equation

$$H_f \nu_{im} = H_{im} \nu_{im}, \quad (13)$$

where  $H_{im}$  are the eigenvalues of  $H_f$ . If the density and therefore  $H_f$  are constant,  $\nu_{im}$  correspond to the eigenstates of propagation. Since  $H_f \neq H_0$ , the states  $\nu_{im}$  differ from the mass states,  $\nu_i$ . For low density  $n \rightarrow 0$ , the vacuum eigenstates are recovered:  $\nu_{im} \rightarrow \nu_i$ . If the density, and thus  $H_f$  change during neutrino propagation,  $\nu_{im}$  and  $H_{im}$  should be considered as the eigenstates and eigenvalues of the instantaneous Hamiltonian:  $H_f = H_f(x)$ ,  $\nu_{im} = \nu_{im}(x)$ , and  $H_{im} = H_{im}(x)$ . For  $n \rightarrow 0$  we have  $H_{im} \rightarrow m_i^2/2E$ .

The mixing in matter is a generalization of the mixing in vacuum (1). Recall that the mixing matrix in vacuum connects the flavor neutrinos,  $\nu_f$ , and the massive neutrinos,  $\nu_{\text{mass}}$ . The latter are the eigenstates of Hamiltonian in vacuum:  $\nu_H = \nu_{\text{mass}}$ . Therefore, the mixing matrix in matter is defined as the matrix which relates the flavor states with the eigenstates of the Hamiltonian in matter  $\nu_H^T = (\nu_{1m}, \nu_{2m}, \nu_{3m})$ :

$$\nu_f = U^m \nu_H. \quad (14)$$

From (13) we find that

$$\nu_{jm}^\dagger H_f \nu_{im} = H_{im} \delta_{ji}. \quad (15)$$

Furthermore, the Hamiltonian can be represented in the flavor basis as

$$H_f = \sum_{\alpha\beta} H_{\alpha\beta} \nu_\alpha \nu_\beta^\dagger. \quad (16)$$



Inserting this expression as well as the relation  $\nu_{jm} = U_{\alpha j}^{m*} \nu_\alpha$ , which follows from (14), into (15) one obtains

$$\sum_{\alpha\beta} U_{\alpha j}^{m*} H_{\alpha\beta} U_{\beta i}^m = H_{im} \delta_{ji} \quad (17)$$

or in matrix form  $U^{m\dagger} H_f U^m = H^{\text{diag}} = \text{diag}(H_{1m}, H_{2m}, H_{3m})$ . Thus, the mixing matrix  $U^m$  can be found diagonalizing the full Hamiltonian. The columns of the mixing matrix,  $U_i \equiv (U_{ei}^m, U_{\mu i}^m, U_{\tau i}^m)$ , are the eigenstates of the Hamiltonian  $H_f$  which correspond to the eigenvalues  $H_{im}$ . Indeed, it follows from (17) that  $H_f U^m = U^m H^{\text{diag}}$ .

Equation (14) can be inverted to  $\nu_H = U^{m\dagger} \nu_f$ , or in components  $\nu_{im} = U_{\alpha i}^{m*} \nu_\alpha$ ,  $\alpha = e, \mu, \tau$ . According to this, the elements of mixing matrix determine the flavor content of the mass eigenstates so that  $|U_{\alpha i}^m|^2$  gives the probability to find  $\nu_\alpha$  in a given eigenstate  $\nu_{im}$ . Correspondingly, the elements of the PMNS matrix determine the flavor composition of the mass eigenstates in vacuum.

**2.4. Mixing in the Two-Neutrino Case.** In the  $2\nu$  case, there is single mixing angle in matter  $\theta_m$  and the relations between the eigenstates in matter and the flavor states read

$$\begin{aligned} \nu_e &= \cos \theta_m \nu_{1m} + \sin \theta_m \nu_{2m}, \\ \nu_\mu &= \sin \theta_m \nu_{1m} - \cos \theta_m \nu_{2m}. \end{aligned} \quad (18)$$

The angle  $\theta_m$  is obtained by diagonalization of the Hamiltonian (12) (see previous section):

$$\begin{aligned} \sin^2 2\theta_m &= \frac{1}{R} \sin^2 2\theta, \\ R &\equiv \left( \cos 2\theta - \frac{2VE}{\Delta m^2} \right)^2 + \sin^2 2\theta, \end{aligned} \quad (19)$$

where  $R$  is the *resonance factor*. In the limit  $V \rightarrow 0$ , the factor  $R \rightarrow 1$  and the vacuum mixing are recovered. The difference of eigenvalues  $H_{im}$  equals

$$\omega_m \equiv H_{2m} - H_{1m} = \frac{\Delta m^2}{2E} \sqrt{R}. \quad (20)$$

This difference is also called the level splitting or oscillation frequency, which determines the oscillation length:  $l_m = 2\pi/\omega_m$  (see Section 3.2).

The matter potential and  $\Delta m^2$  always enter the mixing angle and other dimensionless quantities in the combination

$$\frac{2EV}{\Delta m^2} = \frac{l_\nu}{l_0}, \quad (21)$$

where  $l_0$  is the refraction length. This is the origin of the “scaling” behavior of various characteristics of the flavor conversion probabilities. In terms of the mixing angle in matter the Hamiltonian can be rewritten in the following symmetric form:

$$H_f = \frac{\omega_m}{2} \begin{pmatrix} -\cos 2\theta_m & \sin 2\theta_m \\ \sin 2\theta_m & \cos 2\theta_m \end{pmatrix}. \quad (22)$$

**2.4.1. Resonance and Level Crossing.** According to (19) the effective mixing parameter in matter,  $\sin^2 2\theta_m$ , depends on the electron density and neutrino energy through the ratio (21) of the oscillation and refraction lengths,  $x = l_\nu/l_0 \propto EV$ . The dependence  $\sin^2 2\theta_m(EV)$  for two different values of the vacuum mixing angle, corresponding to angles from the full three-flavor framework, is shown in Figure 1. The dependence of  $\sin^2 2\theta_m$  on  $E$  has a resonant character [3]. At

$$l_\nu = l_0 \cos 2\theta \quad (23)$$

the mixing becomes maximal:  $\sin^2 2\theta_m = 1$  ( $R = \sin^2 2\theta$ ). The equality in (23) is called the *resonance condition* and it can be rewritten as  $2EV = \Delta m^2 \cos 2\theta$ . For small vacuum mixing the condition reads the following: oscillation length  $\approx$  refraction length. The physical meaning of the resonance is that the eigenfrequency, which characterizes a system of mixed neutrinos,  $\omega = 2\pi/l_\nu = \Delta m^2/2E$ , coincides with the eigenfrequency of the medium,  $2\pi/l_0 = 1/V$ . The resonance condition (23) determines the resonance density

$$n_e^R = \frac{\Delta m^2 \cos 2\theta}{2E \sqrt{2} G_F}. \quad (24)$$

The width of resonance on the half of height (in the density scale) is given by  $2\Delta n_e^R = 2n_e^R \tan 2\theta$ . Similarly, for fixed  $n_e$  one can introduce the resonance energy and the width of resonance in the energy scale. The width can be rewritten as  $\Delta n_e^R = n_0 \sin 2\theta$ , where  $n_0 \equiv \Delta m^2/2\sqrt{2}EG_F$ . When the mixing approaches its maximal value:  $\theta \rightarrow \pi/4$ , the resonance shifts to zero density:  $n_e^R \rightarrow 0$ , and the width of the resonance increases converging to the fixed value:  $\Delta n_e^R \rightarrow n_0$ .

In a medium with varying density, the layer in which the density changes in the interval  $n_e^R \pm \Delta n_e^R$  is called the resonance layer. In this layer the angle  $\theta_m$  varies in the interval from  $\pi/8$  to  $3\pi/8$ .

For  $V \ll V_R$ , the mixing angle is close to the vacuum angle:  $\theta_m \approx \theta$ , while for  $V \gg V_R$ , the angle becomes  $\theta_m \approx \pi/2$  and the mixing is strongly suppressed. In the resonance region, the level splitting is minimal [17, 18], therefore the oscillation length, as the function of density, is maximal.

**2.5. Mixing of 3 Neutrinos in Matter.** To a large extent, knowledge of the eigenstates (mixing parameters) and eigenvalues of the instantaneous Hamiltonian in matter allows the determination of flavor evolution in most of the realistic situations (oscillations in matter of constant density, adiabatic conversion, and strong breaking of adiabaticity). The exact expressions for the eigenstates and eigenvalues [19, 20] are rather complicated and difficult to analyze. Therefore approximate expressions for the mixing angles and eigenvalues are usually used. They can be obtained performing an approximate diagonalization of  $H_f$  which relies on the strong hierarchy of the mass squared differences:

$$r_\Delta \equiv \frac{\Delta m_{21}^2}{\Delta m_{31}^2} \approx 0.03. \quad (25)$$

Without changing physics, the factor  $I_{-\delta}$  in the mixing matrix can be eliminated by permuting it with  $U_{12}$  and redefining

the state  $\nu_3$ . Therefore, in what follows, we use  $U_{\text{PMNS}} = U_{23}I_\delta U_{13}U_{12}$ . Here we will describe the case of normal mass hierarchy:  $\Delta m_{31}^2 > 0$ ,  $\Delta m_{32}^2 > 0$ . Subtracting from the Hamiltonian the matrix proportional to the unit matrix  $m_1^2/2E\mathbf{I}$ , we obtain

$$M_{\text{diag}}^2 = \Delta m_{31}^2 \text{diag}(0, r_\Delta, 1). \quad (26)$$

**2.5.1. Propagation Basis.** The propagation basis,  $\tilde{\nu} = (\nu_e, \tilde{\nu}_2, \tilde{\nu}_3)^T$ , which is most suitable for consideration of the neutrino oscillations in matter, is defined through the relation

$$\nu_f = U_{23}I_\delta \tilde{\nu}. \quad (27)$$

Since the potential matrix is invariant under 2-3 rotations, the matrix of the potentials is unchanged and the the Hamiltonian in the propagation basis becomes

$$\tilde{H} = \frac{1}{2E} U_{13} U_{12} M_{\text{diag}}^2 U_{12}^\dagger U_{13}^\dagger + \tilde{V}. \quad (28)$$

It does not depend on the 2-3 mixing or CP violation phase, and so the dynamics of the flavor evolution do not depend on  $\delta$  and  $\theta_{23}$ . These parameters appear in the final amplitudes when projecting the flavor states onto propagation-basis states and back onto (27) the neutrino production and detection.

Explicitly, the Hamiltonian  $\tilde{H}$  can be written as

$$\tilde{H} = \frac{\Delta m_{31}^2}{2E} \times \begin{pmatrix} s_{13}^2 + s_{12}^2 c_{13}^2 r_\Delta + \frac{2V_e E}{\Delta m_{31}^2} & s_{12} c_{12} c_{13} r_\Delta & s_{13} c_{13} (1 - s_{12}^2 r_\Delta) \\ \dots & c_{12}^2 r_\Delta & -s_{12} c_{12} s_{13} r_\Delta \\ \dots & \dots & c_{13}^2 + s_{12}^2 s_{13}^2 r_\Delta \end{pmatrix}. \quad (29)$$

Here all the off-diagonal elements contain small parameters  $r_\Delta$  and/or  $s_{13}$ . Notice that, for the measured oscillation parameters,  $s_{13}^2 \sim r_\Delta$ .

**2.5.2. Mixing Angles in Matter.** The Hamiltonian in (29) can be diagonalized performing several consecutive rotations which correspond to developing the perturbation theory in  $r_\Delta$ . After a 1-3 rotation

$$\tilde{\nu} = U_{13}(\theta_{13}^m) \nu' \quad (30)$$

over the angle  $\theta_{13}^m$  determined by

$$\tan 2\theta_{13}^m = \frac{\sin 2\theta_{13}}{\cos 2\theta_{13} - 2EV'/\Delta m_{31}^2}, \quad (31)$$

$$\text{where } V' = \frac{V}{1 - s_{12}^2 r_\Delta},$$

the 1-3 element of (29) vanishes. The expression (31) differs from that for  $2\nu$  mixing in matter by a factor  $(1 - s_{12}^2 r_\Delta)$ , which increases the potential and deviates from 1 by

$$\xi \equiv s_{12}^2 r_\Delta \approx 10^{-2}. \quad (32)$$

After this rotation the Hamiltonian in the  $\nu'$  basis (30) becomes

$$H' = \frac{\Delta m_{31}^2}{2E} \times \begin{pmatrix} h_{11} & s_{12} c_{12} r_\Delta \cos(\theta_{13}^m - \theta_{13}) & 0 \\ \dots & c_{12}^2 r_\Delta & s_{12} c_{12} r_\Delta \sin(\theta_{13}^m - \theta_{13}) \\ \dots & \dots & h_{33} \end{pmatrix}, \quad (33)$$

where

$$h_{11,33} = \frac{1}{2} \left[ (1 + \xi + x) \mp \sqrt{[\cos 2\theta_{13} (1 - \xi) - x]^2 + \sin^2 2\theta_{13} (1 - \xi)^2} \right], \quad (34)$$

and  $x \equiv 2EV/\Delta m_{31}^2$ . For  $\xi = 0$ , these elements are reduced to the standard  $2\nu$  expressions. In the limit of zero density,  $x \rightarrow 0$ ,  $h_{11} = \xi = s_{12}^2 r_\Delta$ , and consequently the 11-element of the Hamiltonian equals  $H'_{11} = s_{12}^2 \Delta m_{12}^2 / 2E$ .

In the lowest  $r_\Delta$  approximation one can neglect the nonzero 2-3 element in (33). The state  $\nu'_3$  then decouples and the problem is reduced to a two-neutrino problem for  $(\nu'_1, \nu'_2)$ . The eigenvalue of this decoupled state equals

$$H_{3m} \approx \frac{\Delta m_{31}^2}{2E} h_{33}, \quad h_{33} \geq 1. \quad (35)$$

The diagonalization of the remaining 1-2 submatrix is given by rotation

$$\nu' = U_{12}(\theta_{12}^m) \nu_m, \quad (36)$$

where  $\theta_{12}^m$  is determined by

$$\tan 2\theta_{12}^m = \frac{\sin 2\theta_{12} r_\Delta \cos(\theta_{13}^m - \theta_{13})}{c_{12}^2 r_\Delta - h_{11}}. \quad (37)$$

Here  $h_{11}$  and  $\theta_{13}^m$  are defined in (34) and (31), respectively. The eigenvalues equal

$$H_{1m,2m} = \frac{\Delta m_{31}^2}{4E} \left[ c_{12}^2 r_\Delta + h_{11} \mp \sqrt{(c_{12}^2 r_\Delta - h_{11})^2 + \sin^2 2\theta_{12} r_\Delta^2 \cos^2(\theta_{13}^m - \theta_{13})} \right]. \quad (38)$$

According to this diagonalization procedure in the lowest order in  $r_\Delta$  the mixing matrix in matter is given by

$$U^m = U_{23}(\theta_{23}) I_\delta U_{13}(\theta_{13}^m) U_{12}(\theta_{12}^m), \quad (39)$$

where mixing angles  $\theta_{12}^m$  and  $\theta_{13}^m$  are determined in (37) and (31), respectively. The 2-3 angle and the CP violation

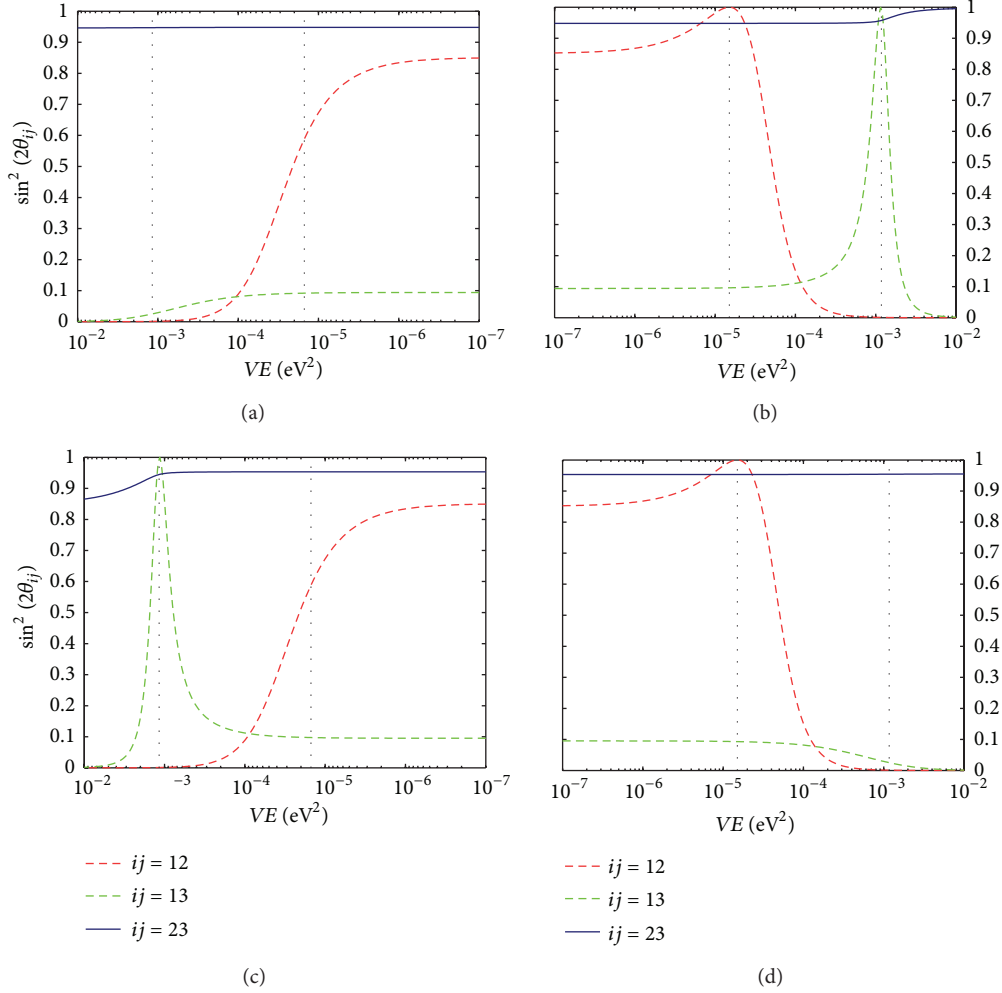


FIGURE 1: Resonance in neutrino mixing. The dependence of  $\sin^2 2\theta_{mij}$  on the product  $VE$  for vacuum mixing:  $\sin^2 2\theta_{12} = 0.851$ ,  $\Delta m_{21}^2 = 7.59 \cdot 10^{-5} \text{ eV}^2$  (red) and  $\sin^2 \theta_{13} = 0.0241$ ,  $\Delta m_{31}^2 = 2.47 \cdot 10^{-3} \text{ eV}^2$  (green). The left semiplane corresponds to antineutrinos. The behavior of  $\theta_{23}$  with vacuum value  $\sin^2 2\theta_{23} = 0.953$  is included for completeness. The dashed lines are the predictions from a strict two-flavor approximation while the solid thin lines are the results of numerical diagonalization of the full three-flavor system. The upper panels show the case of the normal mass hierarchy and the lower panels show the inverted hierarchy.

phase are not modified by matter in this approximation. The eigenvalues  $H_{1m}$  and  $H_{2m}$  are given in (38) and  $H_{3m}$  is determined by (35).

The 2-3 element of matrix (33) vanishes after additional 2-3 rotation by an angle  $\theta'_{23} \sim r_\Delta$ :

$$\tan 2\theta'_{23} = \frac{\sin 2\theta_{12} r_\Delta \sin(\theta_{13}^m - \theta_{13})}{h_{33} - c_{12}^2 r_\Delta}, \quad (40)$$

which produces corrections of the next order in  $r_\Delta$ . With an additional 2-3 rotation the mixing matrix becomes

$$U^m = U_{23}(\theta_{23}) I_\delta U_{13}(\theta_{13}^m) U_{12}(\theta_{12}^m) U_{23}(\theta'_{23}) \quad (41)$$

$$\approx U_{23}(\theta_{23}^m) I_{\delta^m} U_{13}(\theta_{13}^m) U_{12}(\theta_{12}^m),$$

where

$$U_{23}(\theta_{23}^m) I_{\delta^m}^m = U_{23}(\theta_{23}) I_\delta U_{23}(\bar{\theta}_{23}), \quad (42)$$

and the last 2-3 rotation is on the angle  $\bar{\theta}_{23}$  determined through  $\sin \bar{\theta}_{23} = \sin \theta'_{23} / \cos \theta_{13}^m$ . The expression on the RH of (41) is obtained by reducing the expression on the LH side to the standard form by permuting the correction matrix  $U_{23}(\theta'_{23})$ . According to (42), it is this matrix that leads to the modification of 2-3 mixing and CP phase in matter. From (42) one finds

$$\sin \delta^m \sin 2\theta_{23}^m = \sin \delta \sin 2\theta_{23}, \quad (43)$$

that is, the combination  $\sin \delta \sin 2\theta_{23}$  is invariant under inclusion of matter effects. Furthermore,  $\theta_{23}^m \approx \theta_{23}$  and  $\delta^m \approx \delta$  up to corrections of the order  $O(r_\Delta)$ . The results described here allow to understand the behavior of the mixing parameters  $\sin^2 2\theta_{mij}$  in the  $EV$  region of the 1-3 resonance and above it (see Figure 1).

In Figure 2 we present dependence of the flavor content of the neutrino eigenstates on the potential. The energy level

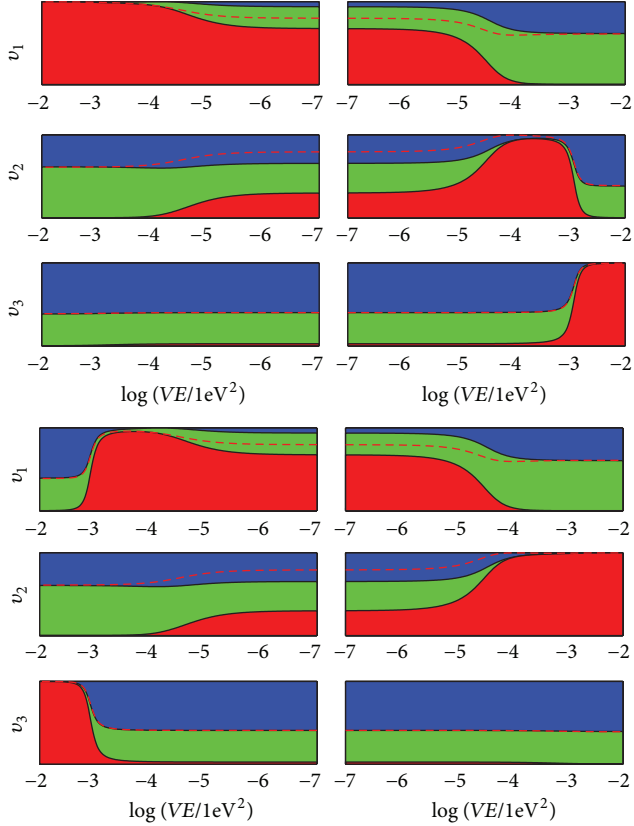


FIGURE 2: The flavor contents of the eigenstates of the Hamiltonian in matter as functions of  $EV$ . The vertical width of the band is taken to be 1, then the vertical sizes of the colored parts give  $|U_{ei}|^2$  (red), and  $|U_{\mu i}|^2$  (green),  $|U_{\tau i}|^2$  (blue). The right and left panels correspond to neutrinos and antineutrinos, respectively. We take the best fit values of [21] with  $\delta = 0$ . Variations of  $\delta$  change the relative  $\nu_\mu$  and  $\nu_\tau$  contents. The dashed red line shows a shift of border between  $\nu_\mu$  and  $\nu_\tau$  flavors for  $\delta = \pi$ . The upper (lower) panel corresponds to normal (inverted) mass ordering.

scheme, the dependence of the eigenvalues  $H_{im}$  on matter density, is shown in Figure 3. The energy levels in matter do not depend on  $\delta$  or  $\theta_{23}$ , but they do depend on the 1–3 and 1–2 mixing.

In the case of normal mass hierarchy, there are two resonances (level crossings) whose location is defined as the density (energy) at which the mixing in a given channel becomes maximal.

- (1) The H resonance, in the  $\nu_e$ - $\nu'_\tau$  channel, is associated to the 1–3 mixing and large mass splitting. According to (31)  $\theta_{13}^m = \pi/4$  at

$$V_{13}^R = \cos 2\theta_{13} (1 - s_{12}^2 r_\Delta) \frac{\Delta m_{31}^2}{2E}. \quad (44)$$

- (2) The L resonance at low densities is associated to the small mass splitting and 1–2 mixing. It appears in the  $\nu'_e$ - $\nu'_\mu$  channel, where  $\nu'_e$  and  $\nu_e$  differ by small (at low densities) rotation given by an angle  $\sim \theta_{13}$  (see (31)).

According to (37) the position of the L-resonance,  $\theta_{12}^m = \pi/4$ , is given by  $c_{12}^2 r_\Delta = h_{11}$ , where  $h_{11}$  is defined in (34). This leads to

$$V_{12}^R = \cos 2\theta_{12} \frac{\Delta m_{21}^2}{2E} \frac{1}{c_{13}^2}. \quad (45)$$

For antineutrinos ( $VE < 0$  in Figure 3), the oscillation parameters in matter can be obtained from the neutrino parameters taking  $V \rightarrow -V$  and  $\delta \rightarrow -\delta$ . The mixing pattern and level scheme for neutrinos and antineutrinos are different both due to the possible fundamental violation of CP invariance and the sign of matter effect. Matter violates CP invariance and the origin of this violation stems from the fact that usual matter is CP asymmetric; in particular, there are electrons in the medium but no positrons.

In the case of normal mass hierarchy there are no antineutrino resonances (level crossings), and with the increase of density (energy) the eigenvalues have the following asymptotic limits:

$$\begin{aligned} H_{1m} &\rightarrow -V, & H_{2m} &\rightarrow \frac{\Delta m_{21}^2 c_{12}^2}{2E_\nu}, \\ H_{3m} &\rightarrow \frac{\Delta m_{31}^2 c_{13}^2}{2E_\nu}. \end{aligned} \quad (46)$$

### 3. Effects of Neutrino Propagation in Different Media

**3.1. The Evolution Matrix.** The evolution matrix,  $S(t, t_0)$ , is defined as the matrix which gives the wave function of the neutrino system  $\nu(t)$  at an arbitrary moment  $t$  once it is known in the initial moment  $t_0$ :

$$\nu(t) = S(t, t_0) \nu(t_0). \quad (47)$$

Inserting this expression in the evolution equation (12), we find that  $S(t, t_0)$  satisfies the same evolution equation as  $\nu(t)$ :

$$i \frac{dS}{dt} = HS. \quad (48)$$

The elements  $S(t, t_0)_{\alpha\beta}$  of this matrix are the amplitudes of  $\nu_\beta \rightarrow \nu_\alpha$  transitions:  $S(t, t_0)_{\alpha\beta} \equiv A(\nu_\beta \rightarrow \nu_\alpha)$ . The transition probability equals  $P_{\alpha\beta} = |S(t, t_0)_{\alpha\beta}|^2$ . The unitarity of the evolution matrix,  $S^\dagger S = I$ , leads to the following relations between the amplitudes (matrix elements):

$$\begin{aligned} |S_{\alpha\alpha}|^2 + |S_{\beta\alpha}|^2 &= 1, \\ |S_{\beta\beta}|^2 + |S_{\alpha\beta}|^2 &= 1, \\ S_{\alpha\alpha}^* S_{\alpha\beta} + S_{\beta\alpha}^* S_{\beta\beta} &= 0, \\ S_{\alpha\beta}^* S_{\alpha\alpha} + S_{\beta\beta}^* S_{\beta\alpha} &= 0. \end{aligned} \quad (49)$$

The first and the second equations express the fact that the total probability of transition of  $\nu_\alpha$  to everything is one, and



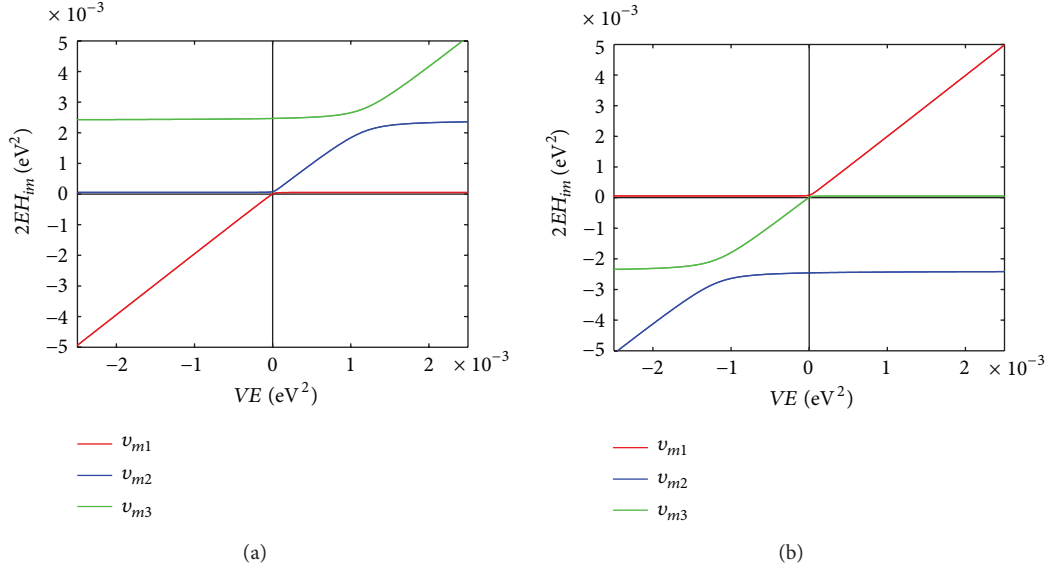


FIGURE 3: The energy level scheme. We here show the dependence of the eigenvalues of the Hamiltonian in matter on  $EV$ . Note that we are plotting  $2EH_{im}$ , which goes to  $\Delta m_{i1}^2$  for low  $VE$ . The left (right) panel corresponds to normal (inverted) mass ordering.

the same holds for  $\nu_\beta$ . The third and fourth equations are satisfied if

$$S_{\alpha\alpha} = S_{\beta\beta}^*, \quad S_{\beta\alpha} = -S_{\alpha\beta}^*. \quad (50)$$

With these relations the evolution matrix can be parametrized as

$$S = \begin{pmatrix} \alpha & \beta \\ -\beta^* & \alpha^* \end{pmatrix}, \quad |\alpha|^2 + |\beta|^2 = 1. \quad (51)$$

The Hamiltonian for a  $2\nu$  system is T symmetric in vacuum as well as in medium with constant density. In medium with varying density the T symmetry is realized if the potential is symmetric. Under T transformations  $S_{\beta\alpha} \rightarrow S_{\alpha\beta}$ , and the diagonal elements  $S_{\alpha\alpha}$  do not change. Therefore according to (50) the T invariance implies that  $S_{\beta\alpha} = -S_{\alpha\beta}^*$ , or  $\text{Re } S_{\beta\alpha} = 0$ ; that is, the off-diagonal elements of the S matrix are pure imaginary.

**3.2. Neutrino Oscillations in Matter with Constant Density.** In a medium with constant density and therefore constant potential the mixing is constant:  $\theta_m(E, n) = \text{const}$ . Consequently, the flavor composition of the eigenstates does not change and the eigenvalues  $H_{im}$  of the full Hamiltonian are constant. The two-neutrino evolution equation in matter of constant density can be written in the matter eigenstate basis as

$$i \frac{d\gamma_m}{dx} = H^{\text{diag}} \gamma_m, \quad (52)$$

where  $H^{\text{diag}} \equiv \text{diag}(H_{1m}, H_{2m})$ . This system of equations splits and the integration is trivial,  $\gamma_{im}(t) = e^{-iH_{im}t} \gamma_{im}(0)$ . The corresponding S matrix is diagonal:

$$\tilde{S}(x, 0) = \begin{pmatrix} e^{i\phi_m(x)} & 0 \\ 0 & e^{-i\phi_m(x)} \end{pmatrix}, \quad (53)$$

where  $\phi_m \equiv (1/2)\omega^m x$  is the half-oscillation phase in matter and a matrix proportional to the unit matrix has been subtracted from the Hamiltonian.

The S matrix in the flavor basis ( $\nu_e, \nu_\mu$ ) is therefore

$$\begin{aligned} S(x, 0) &= U^m \tilde{S}(x, 0) U^{m\dagger} \\ &= \begin{pmatrix} \cos \phi_m + i \cos 2\theta_m \sin \phi_m & -i \sin 2\theta_m \sin \phi_m \\ -i \sin 2\theta_m \sin \phi_m & \cos \phi_m - i \cos 2\theta_m \sin \phi_m \end{pmatrix}. \end{aligned} \quad (54)$$

Then, for the transition probability, we can immediately deduce

$$P_{e\mu} = |S_{e\mu}|^2 = \sin^2 2\theta_m \sin^2 \phi_m, \quad (55)$$

where  $\phi_m = \pi x / l_m$ , with

$$l_m = \frac{2\pi}{H_{2m} - H_{1m}} = \frac{l_\nu}{\sqrt{R}} \quad (56)$$

being the oscillation length in matter. The dependence of  $l_m$  on the neutrino energy is shown in Figure 4. For small energies,  $VE \ll \Delta m^2$ , the length  $l_m \simeq l_\nu$ . It then increases with energy and for small  $\theta$  reaches the maximum  $l_m^{\text{max}} = l_0 / \sin 2\theta$  at  $E^{\text{max}} = E_R / \cos^2 2\theta$ , that is, above the resonance energy. For  $E \rightarrow \infty$  the oscillation length converges to the refraction length  $l_m \rightarrow l_0$ .

A useful representation of the S matrix for a layer with constant density follows from (54):

$$S(x, 0) = \cos \phi_m I - i \sin \phi_m (\sigma \cdot \mathbf{n}), \quad (57)$$

where  $\sigma$  is a vector containing the Pauli matrices and  $\mathbf{n} \equiv (\sin 2\theta_m, 0, -\cos 2\theta_m)$ .

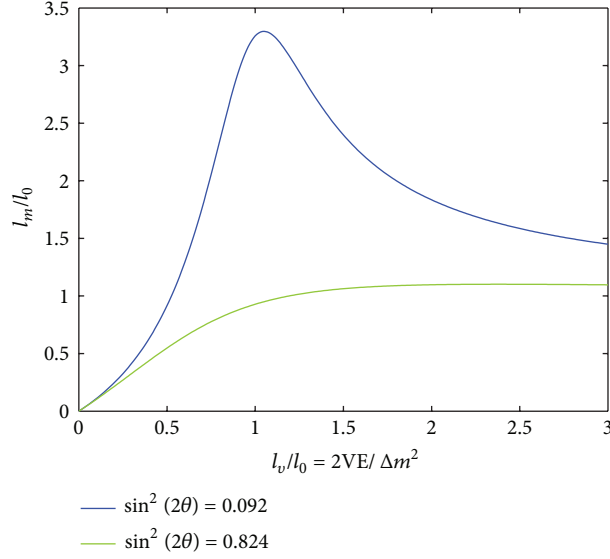


FIGURE 4: Dependence of the oscillation length in matter in units of the refraction length on neutrino energy for two different mixing angles in vacuum.

The dynamics of neutrino flavor evolution in uniform matter are the same as in vacuum, that is, it has a character of oscillations. However, the oscillation parameters (length and depth) differ from those in vacuum. They are now determined by the mixing and effective energy splitting in matter:  $\sin^2 2\theta \rightarrow \sin^2 2\theta_m$ ,  $l_\nu \rightarrow l_m$ .

### 3.3. Neutrino Polarization Vectors and Graphic Representation.

It is illuminating to consider the dynamics of transitions in different media using graphic representation [22–24]. Consider the two-flavor neutrino state,  $\psi^T = (\psi_e, \psi_a)$ . The corresponding Hamiltonian can be written as

$$H = (\mathbf{H} \cdot \boldsymbol{\sigma}), \quad (58)$$

where  $\boldsymbol{\sigma} = (\sigma_1, \sigma_2, \sigma_3)$ ,  $\mathbf{H}$  is the Hamiltonian vector  $\mathbf{H} \equiv (2\pi/l_m) \cdot (\sin 2\theta_m, 0, \cos 2\theta_m)$ , and  $l_m = 2\pi/\Delta H_m$  is the oscillation length. The evolution equation then becomes

$$i\dot{\psi} = (\mathbf{H} \cdot \boldsymbol{\sigma})\psi. \quad (59)$$

Let us define the polarization vector  $\mathbf{P}$

$$\mathbf{P} \equiv \psi^\dagger \frac{\boldsymbol{\sigma}}{2} \psi. \quad (60)$$

In terms of the wave functions, the components of  $\mathbf{P}$  equal

$$\begin{aligned} (P_x, P_y, P_z) \\ = \left( \text{Re } \psi_e^* \psi_a, \text{Im } \psi_e^* \psi_a, \frac{1}{2} (|\psi_e|^2 - |\psi_a|^2) \right). \end{aligned} \quad (61)$$

The  $z$ -component can be rewritten as  $P_z = |\psi_e|^2 - 1/2$ ; therefore  $P_e \equiv |\psi_e|^2 = P_z + 1/2$  and from unitarity  $P_a \equiv |\psi_a|^2 = 1/2 - P_z$ . Hence,  $P_z$  determines the probabilities to find the neutrino in a given flavor state. The flavor evolution of the

neutrino state corresponds to a motion of the polarization vector in the flavor space. The evolution equation for  $\mathbf{P}$  can be obtained by differentiating (60) with respect to time and inserting  $\dot{\psi}$  and  $\dot{\psi}^\dagger$  from evolution equation (59). As a result, one finds that

$$\frac{d}{dt} \mathbf{P} = \mathbf{H} \times \mathbf{P}. \quad (62)$$

If  $\mathbf{H}$  is identified with the strength of a magnetic field, the equation of motion (62) coincides with the equation of motion for the spin of electron in the magnetic field. According to this equation  $\mathbf{P}$  precesses around  $\mathbf{H}$ .

With an increase of the oscillation phase  $\phi$  (see Figure 5) the vector  $\mathbf{P}$  moves on the surface of the cone having axis  $\mathbf{H}$ . The cone angle  $\theta_a$ , the angle between  $\mathbf{P}$  and  $\mathbf{H}$ , depends both on the mixing angle and on the initial state, and, in general, on changes in process of evolution, for example, if the neutrino evolves through several layers of different density. If the initial state is  $\nu_e$ , the angle equals  $\theta_a = 2\theta_m$  in the initial moment.

The components of the polarization vector  $\mathbf{P}$  are nothing but the elements of the density matrix  $\rho = \boldsymbol{\sigma} \cdot \mathbf{P}$ . The evolution equation for  $\rho$  can be obtained from (62)

$$i \frac{d\rho}{dt} = [H, \rho]. \quad (63)$$

The diagonal elements of the density matrix give the probabilities to find the neutrino in the corresponding flavor state.

**3.4. Resonance Enhancement of Oscillations.** Suppose a source produces flux of neutrinos in the flavor state  $\nu_\mu$  with continuous energy spectrum. This flux then traverses a layer of length  $L$  with constant density  $n_e$ . At the end of this layer a detector measures the  $\nu_e$  component of the flux, so that oscillation effect is given by the transition probability  $P_{\mu e}$ . In Figure 6 we show dependence of this probability on

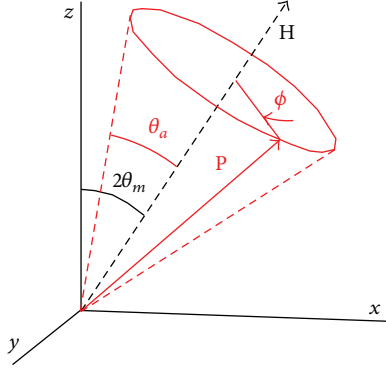


FIGURE 5: Graphic representation of neutrino oscillations. Neutrino polarization vector  $\mathbf{P}$  precesses around the Hamiltonian vector  $\mathbf{H}$  (or the vector of eigenstates of the Hamiltonian). The angle between  $\mathbf{P}$  and  $\mathbf{H}$  is given by the cone angle  $\theta_a$ , and the direction of axis of the cone is determined by the mixing angle in matter  $2\theta_m$ .

energy for thin and thick layers. The oscillatory curves are inscribed in the resonance envelope  $\sin^2 2\theta_m$ . The period of the oscillatory curve decreases with the length  $L$ . At the resonance energy,

$$E_R = \frac{\Delta m^2 \cos 2\theta}{2V} = \frac{\Delta m^2 \cos 2\theta}{2\sqrt{2}G_F n_e}, \quad (64)$$

oscillations proceed with maximal depths. Oscillations are enhanced up to  $P > 1/2$  in the resonance range ( $E_R \pm \Delta E_R$ ) where  $\Delta E_R = \tan 2\theta_R$  (see Section 2.4). This effect was called the resonance enhancement of oscillations.

**3.5. Three-Neutrino Oscillations in Matter with Constant Density.** The oscillation probabilities in matter with constant density have the same form as oscillation probabilities in vacuum and the generalization of (53) is straightforward. In the basis of the eigenstates of the Hamiltonian the evolution matrix equals

$$\tilde{S}(x, 0) = \begin{pmatrix} e^{-2i\phi_{1m}(x)} & 0 & 0 \\ 0 & e^{-2i\phi_{2m}(x)} & 0 \\ 0 & 0 & e^{-2i\phi_{3m}(x)} \end{pmatrix}, \quad (65)$$

and for the elements of the  $S$  matrix in the flavor basis we obtain  $S_{\alpha\beta} = \sum_i U_{\alpha i}^{m*} U_{\beta i}^m e^{-2i\phi_i^m(x)}$ . Removing  $e^{-2i\phi_{2m}}$  and using the unitarity of the mixing matrix in matter we have

$$S_{\alpha\beta} = \delta_{\alpha\beta} + 2ie^{\phi_{21}^m(x)} U_{\alpha 2}^{m*} U_{\beta 2}^m \sin \phi_{21}^m(x) - 2ie^{-i\phi_{32}^m(x)} U_{\alpha 3}^{m*} U_{\beta 3}^m \sin \phi_{32}^m(x). \quad (66)$$

In particular, for the amplitudes in matter involving only  $\nu_e$  and  $\nu_\mu$ , we obtain

$$\begin{aligned} S_{e\mu}^{\text{cst}} &= 2ie^{i\phi_{21}^m} [U_{e1}^m U_{\mu 1}^{m*} \sin \phi_{21}^m - e^{-i\phi_{31}^m} U_{e3}^m U_{\mu 3}^{m*} \sin \phi_{32}^m], \\ S_{\mu\mu}^{\text{cst}} &= 1 + 2ie^{i\phi_{21}^m} |U_{\mu 1}^m|^2 \sin \phi_{21}^m - 2ie^{-i\phi_{32}^m} |U_{\mu 3}^m|^2 \sin \phi_{32}^m, \\ S_{ee}^{\text{cst}} &= 1 + 2ie^{i\phi_{21}^m} \cos^2 \theta_{13}^m \cos^2 \theta_{12}^m \sin \phi_{21}^m - 2ie^{-i\phi_{32}^m} \sin^2 \theta_{13}^m \sin \phi_{32}^m. \end{aligned} \quad (67)$$

### 3.6. Propagation in a Medium with Varying Density and the MSW Effect

**3.6.1. Equation for the Instantaneous Eigenvalues and the Adiabaticity Condition.** In nonuniform media, the density changes along neutrino trajectory:  $n_e = n_e(t)$ . Correspondingly, the Hamiltonian of system depends on time,  $H = H(t)$ , and therefore the mixing angle changes during neutrino propagation:  $\theta_m = \theta_m(n_e(t))$ . Furthermore, the eigenstates of the instantaneous Hamiltonian,  $\nu_{1m}$  and  $\nu_{2m}$ , are no longer the “eigenstates” of propagation. Indeed, inserting  $\nu_f = U(\theta_m)\nu_m$  in the equation for the flavor states (c.f., (3)) we obtain the evolution equation for eigenstates  $\nu_{im}$ :

$$i \frac{d\nu_m}{dt} = \begin{pmatrix} H_{1m} & -i\dot{\theta}_m \\ i\dot{\theta}_m & H_{2m} \end{pmatrix} \nu_m, \quad (68)$$

where  $\dot{\theta}_m \equiv d\theta_m/dt$ . The Hamiltonian for  $\nu_{im}$  (68) is nondiagonal and, consequently, the transitions  $\nu_{1m} \leftrightarrow \nu_{2m}$  occur. The rate of these transitions is given by the speed with which the mixing angle changes with time. According to (68) [3, 25],  $|\dot{\theta}_m|$  determines the energy of transition  $\nu_{1m} \leftrightarrow \nu_{2m}$  and  $|H_{2m} - H_{1m}|$  gives the energy gap between the levels.

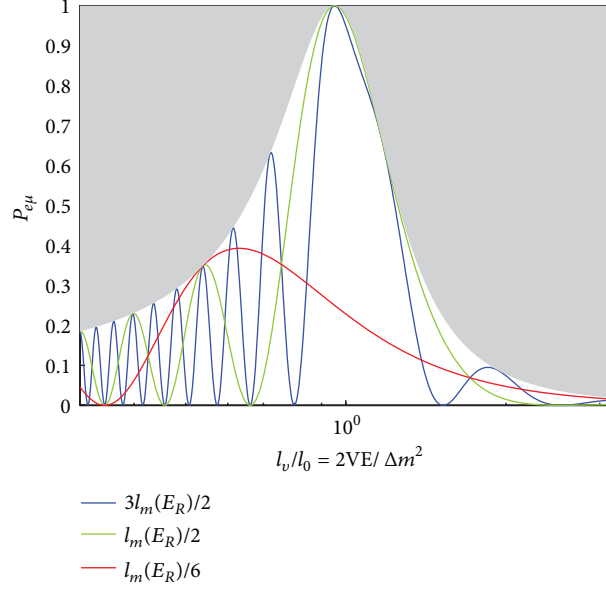


FIGURE 6: Resonance enhancement of neutrino oscillations in matter with constant density. Shown is the dependence of the transition probability  $\nu_e \rightarrow \nu_\mu$  on energy for  $\sin^2 \theta_{13} = 0.0241$  for three different sizes of layers:  $L = 3l_m(E_R)/2$ ,  $l_m(E_R)/2$ , and  $l_m(E_R)/6$ . The shaded area shows the resonance envelope:  $\sin^2 2\theta_m(E)$ .

The off-diagonal elements of the evolution equation (68) can be neglected if  $\dot{\theta}_m$  is much smaller than other energy scales in the system. The difference of the diagonal elements of the Hamiltonian is, in fact, the only other energy quantity and therefore the criterion for smallness of  $\dot{\theta}_m$  is

$$\dot{\theta}_m \ll H_{2m} - H_{1m}. \quad (69)$$

This inequality implies a slow enough change of density and is called the *adiabaticity condition*. Defining the adiabaticity parameter [22, 25] as

$$\gamma \equiv \left| \frac{\dot{\theta}_m}{H_{2m} - H_{1m}} \right|, \quad (70)$$

the adiabaticity condition can be written as  $\gamma \ll 1$ .

For small mixing angle, the adiabaticity condition is most crucial in the resonance layer where the level splitting is small and the mixing angle changes rapidly. In the resonance point, it takes the physically transparent form [3]:  $\Delta r_R > l_m^R$ , where  $l_m^R \equiv l_\nu / \sin 2\theta$  is the oscillation length in resonance, and  $\Delta r_R \equiv (n_e / (dn_e/dr))_R \tan 2\theta$  is the spatial width of the resonance layer. According to this condition at least one oscillation length should be obtained within the resonance layer.

In the case of large vacuum mixing, the point of maximal adiabaticity violation [26, 27] is shifted to density,  $n_e(av)$ , larger than the resonance density:  $n_e(av) \rightarrow n_B > n_R$ . Here  $n_B = \Delta m^2 / 2\sqrt{2}G_F E$  is the density at the border of resonance layer for maximal mixing. Outside the resonance and in the nonresonant channel, the adiabaticity condition has been considered in [28, 29].

**3.7. Adiabatic Conversion and the MSW Effect.** If the adiabaticity condition is fulfilled and  $\dot{\theta}_m$  can be neglected, the Hamiltonian for the eigenstates becomes diagonal. Consequently, the equations for the instantaneous eigenstates  $\nu_{im}$  split as in the constant density case. The instantaneous eigenvalues evolve independently, but the flavor content of the eigenstates changes according to the change of mixing in matter. This is the essence of the adiabatic approximation; we neglect  $\dot{\theta}_m$  in evolution equation but do not neglect the dependence of  $\theta_m$  on density. The solution can be obtained immediately as

$$\tilde{S}(x, 0) = \begin{pmatrix} e^{i\phi_m} & 0 \\ 0 & e^{-i\phi_m} \end{pmatrix}, \quad (71)$$

$$\phi_m = \frac{1}{2} \int_0^x (H_{2m} - H_{1m}) dx',$$

in symmetric form. The only difference from the constant density case is that the eigenvalues now depend on time and therefore integration appears in the phase factors.

The evolution matrix in the flavor basis can be obtained by projecting back from the eigenstate basis to the flavor basis with the mixing matrices corresponding to initial and final densities:

$$\begin{aligned} S_f(x, 0) &= U^m(t) \tilde{S}(x, 0) U^{m\dagger}(0) \\ &= \begin{pmatrix} c_m c_m^0 e^{i\phi_m} + s_m s_m^0 e^{-i\phi_m} & -c_m s_m^0 e^{i\phi_m} + s_m c_m^0 e^{-i\phi_m} \\ -s_m c_m^0 e^{i\phi_m} + c_m s_m^0 e^{-i\phi_m} & s_m s_m^0 e^{i\phi_m} + c_m c_m^0 e^{-i\phi_m} \end{pmatrix}. \end{aligned} \quad (72)$$



From this procedure we find, for example, the probability of  $\nu_e - \nu_e$  transition

$$P_{ee} = |S_f(x, 0)_{ee}|^2 = \frac{1}{2} [1 + \cos 2\theta_m(x) \cos 2\theta_m(0)] + \frac{1}{2} \sin 2\theta_m(x) \sin 2\theta_m(0) \cos 2\phi_m(x). \quad (73)$$

If the initial and final densities coincide, as in the case of neutrinos crossing the Earth, we obtain the same formulas as in constant density case:

$$P_{\alpha\beta} = \left| \sum_i U_{\alpha i}^m(0) U_{\beta i}^{m*}(0) e^{-i\phi_{im}(t, 0)} \right| \quad (74)$$

with the mixing angle taken at the borders (initial or final state). In particular, the survival probability equals  $P_{\alpha\alpha} = 1 - \sin^2 2\theta_m(0) \sin^2 \phi_m(x)$ .

Averaging over the phase, which means that the contributions from  $\nu_1$  and  $\nu_2$  add incoherently, gives

$$P = (\cos \theta_m \cos \theta_m^0)^2 + (\sin \theta_m \sin \theta_m^0)^2 = \sin^2 \theta_m + \cos 2\theta_m \cos^2 \theta_m^0. \quad (75)$$

The mixing in the neutrino production point  $\theta_m^0$  is determined by density in this point,  $n_e^0$ , and the resonance density. Consequently, the picture of the conversion depends on how far from the resonance layer (in the density scale) a neutrino is produced. Strong transitions occur if the initial and final mixings differ substantially, which is realized when the initial density is much above the resonance density and the final one is below the resonance density and therefore neutrinos cross the resonance layer.

According to (73) the oscillation depth equals  $D = |\sin 2\theta_m \sin 2\theta_m^0|$ . Both the averaged probability (75) and the depth (73) are determined by the initial and final densities and do not depend on the density distribution along the neutrino trajectory. Essentially they are determined by the ratios  $\gamma \equiv n/n_R$  in the initial and final moments. This is a manifestation of the universality of the adiabatic approximation result.

In contrast, the phase does depend on the density distribution and the period of oscillations (the latter is given by the oscillation length in matter). So, it is the phase that encodes information about the density distribution.

The probability depends on  $t$  via the phase  $\phi_m(t)$  and also via the mixing angle  $\theta_m(t)$ . Two degrees of freedom are operative and  $P$  dependence on time is an interplay of two effects: oscillations, associated with the phase  $\phi_m(t)$ , and the adiabatic conversion related to change of  $\theta_m$ . Depending on initial condition  $n_e^0$ , the relative importance of the two effects is different. If neutrinos are produced far above the resonance,  $n_e^0 \gg n_e^R$ , the initial mixing is strongly suppressed,  $\theta_m^0 \approx \pi/2$ . Consequently, the neutrino state, for example,  $\nu_e$ , consists mainly of one eigenstate,  $\nu_{2m}$ , and furthermore, one-flavor  $\nu_e$  dominates in  $\nu_{2m}$ . Since the admixture of the second eigenstate is very small, oscillations (interference

effects) are strongly suppressed. Thus, here the nonoscillatory flavor transition occurs when the flavor of whole state (which nearly coincides with  $\nu_{2m}$ ) follows the density change. At zero density  $\nu_{2m} = \nu_2$ , and therefore the probability to find the electron neutrino (survival probability) equals [3]

$$P = |\langle \nu_e | \nu(t) \rangle|^2 \approx |\langle \nu_e | \nu_{2m}(t) \rangle|^2 = |\langle \nu_e | \nu_2 \rangle|^2 \approx \sin^2 \theta. \quad (76)$$

The final probability,  $P = \sin^2 \theta$ , is the feature of the nonoscillatory transition (as pure adiabatic conversion). Deviation from this value indicates the presence of oscillations; see (73).

If neutrinos are produced not too far from resonance, for example, at  $n_e^0 > n_e^R$ , the initial mixing is not suppressed. Although  $\nu_{2m}$  is the main component of the neutrino state, the second eigenstate,  $\nu_{1m}$ , has appreciable admixture; the flavor mixing in the neutrino eigenstates is significant, and the interference effect is not suppressed. Here we deal with the interplay of the adiabatic conversion and oscillations.

Production in the resonance is a special case; if  $\theta_m^0 = 45^\circ$ , the averaged probability equals  $\bar{P} = 1/2$  independently of the final mixing. This feature is important for determining the oscillation parameters. Strong transitions ( $P > 1/2$ ) occur when neutrinos cross resonance layer. These features are realized for solar neutrinos when propagating from their production region inside the Sun to the surface of the Sun. The adiabatic propagation occurs also in a single layer of the Earth (e.g., in the mantle).

**3.8. Adiabaticity Violation.** For most of applications the adiabaticity is either well satisfied (neutrinos in the Sun or supernovae), or maximally broken due to sharp (instantaneous) density change (neutrinos in the Earth, neutrinos crossing the shock wave fronts in supernova). In the former case the evolution is described by the adiabatic formulas. In the latter case description is also simple; one just needs to match the flavor conditions at the borders between layers, find the flavor state before the density jump, and then use it as an initial state for the evolution after the jump. The intermediate case of the adiabaticity breaking can be realized for neutrinos in the mantle of the Earth, for high energy neutrinos propagating in the Sun (neutrinos from annihilation of hypothetical WIMPs) or for sterile neutrinos with very small mixing.

If the density changes rapidly,  $\dot{\theta}_m$  is not negligible in (68) and the adiabaticity condition (70) is not satisfied. The transitions  $\nu_{1m} \leftrightarrow \nu_{2m}$  become noticeable and therefore the admixtures of the eigenstates in a given propagating state change. The  $S$  matrix in the flavor basis is given by

$$S_f(x, 0) = U^m(t) \tilde{S}(x, 0) U^{m\dagger}(0) = U^m(t) \begin{pmatrix} S_{11} & -S_{21}^* \\ S_{21} & S_{11}^* \end{pmatrix} U^{m\dagger}(0), \quad (77)$$

where  $\tilde{S}$  is the evolution matrix in the basis of instantaneous eigenstates. Then the  $\nu_e$ - $\nu_e$  transition probability  $P_{ee} \equiv |S_f(x, 0)_{ee}|^2$  equals

$$P_{ee} = \frac{1}{2} [1 + \cos 2\theta_m(t) \cos 2\theta_m(0)] - P_{21} \cos 2\theta_m(t) \cos 2\theta_m(0) + P_{\text{int}}, \quad (78)$$

where  $P_{21} \equiv |S_{21}|^2$  is the probability of  $\nu_{2m} \rightarrow \nu_{1m}$  transitions and  $P_{\text{int}}$  is an interference term

$$P_{\text{int}} = \frac{1}{4} \sin 2\theta_m(t) \sin 2\theta_m(0) [S_{11}^2 + S_{11}^{*2} + S_{21}^2 + S_{21}^{*2}] + \frac{1}{2} \sin [2\theta_m(0) - 2\theta_m(x)] [S_{11}S_{21}^* + S_{11}^*S_{21}], \quad (79)$$

which depends on the oscillation phase. The averaged probability ( $P_{\text{int}} = 0$ ) equals [30]

$$P_{ee} = \frac{1}{2} + \left(\frac{1}{2} - P_{21}\right) \cos 2\theta_m(t) \cos 2\theta_m(0). \quad (80)$$

If the initial density is much larger than the resonance density, then  $\theta_m(0) \approx \pi/2$  and  $\cos 2\theta_m(0) = -1$ . In this case the averaged probability can be rewritten as

$$P_{ee} = \sin^2 \theta_m(t) + P_{21} \cos 2\theta_m(t). \quad (81)$$

Violation of adiabaticity weakens transitions if  $\cos 2\theta_m(t) > 0$ , thus leading to an increase of the survival probability. In the adiabatic case  $S_{11} = e^{i\phi_m}$ ,  $S_{21} = 0$ , and therefore  $S_{11}^2 + S_{11}^{*2} = 2 \cos 2\phi_m(x)$ , so that (78) is reduced to (73).

In the graphic representation (Figure 5), the neutrino vector moves on the surface of the cone (phase change) and the axis of the cone rotates according to the density change. The cone angle  $\theta_a$  changes as a result of violation of the adiabaticity).

There are different approaches to compute the flop probability  $P_{21}$ . In the adiabatic regime the probability of transition between the eigenstates is exponentially suppressed  $P_{12} \sim \exp(-\pi/2\gamma)$  with  $\gamma$  given in (70) [30, 31]. One can consider such a transition as penetration through a barrier of height  $H_{2m} - H_{1m}$  by a system with the kinetic energy  $d\theta_m/dt$ . This leads to the Landau-Zener probability

$$P_{LZ} = \exp(-\pi^2 \kappa_R) = \exp\left(-\frac{\pi h \Delta m^2}{4E} \frac{\sin^2 2\theta}{\cos 2\theta}\right), \quad (82)$$

where  $h \equiv n(dn/dr)^{-1}$  [32]. In the case of weak adiabaticity violation, one can develop an adiabatic perturbation theory which gives the results as a series expansion in the adiabaticity parameter [33].

### 3.9. Theory of Small Matter Effects

**3.9.1. Minimal Width Condition.** If the vacuum mixing angle is small, there exists a lower limit on the amount of matter needed to induce significant flavor change due to matter

effect. The amount of matter is characterized by the column density of electrons along the neutrino trajectory:

$$d = \int_0^L n_e(x) dx. \quad (83)$$

We can define  $d_{1/2}$  as the column density for which the oscillation transition probability surpasses 1/2 for the first time in the course of propagation. Then it is possible to show that [34]

$$d_{1/2} \geq d_{\min} = \frac{\pi}{2\sqrt{2}G_F \tan 2\theta} \quad (84)$$

for all density profiles. Furthermore, the minimum,  $d_{\min}$ , is realized for oscillations in a medium of constant density equal to the resonance density. The relation (84) is known as the minimal width condition. This condition originates from an interplay between matter effects and vacuum mixing. The acquired matter phase,  $\sqrt{2}G_F d$ , must be large. At the same time, since matter effects by themselves are flavor conserving, also vacuum mixing is required in order to induce flavor conversion. The smaller the vacuum mixing is, the larger the width that is required.

**3.9.2. Vacuum Mimicking.** Vacuum mimicking [35], which states that regardless of the matter density, the initial flavor evolution of neutrino state is similar to that of vacuum oscillations. Consequently for small baselines,  $L$ , it is not possible to see matter effect and any such effect appearing in higher order of  $L$ . Indeed, consider the evolution matrix

$$S = \mathcal{T} \left[ \exp \left( -i \int_0^L H(x) dx \right) \right], \quad (85)$$

where  $\mathcal{T}$  denotes time ordering of the exponential. For small values of  $L$ , it can be expanded as

$$S = 1 - i \int_0^L H(x) dx + \mathcal{O}(L^2). \quad (86)$$

If initial neutrino state has definite flavor, the amplitude of flavor transition is given by the off-diagonal element of  $H(x)$  which does not depend on matter potential. The matter contribution to  $H(x)$  is diagonal. Therefore the flavor transitions depend on the matter density only at higher order in  $L$ . This result holds true as long as  $L \ll l_m$  or when the phase of oscillation is small [36].

This can be seen explicitly in the case of medium with constant density where, expanding the oscillatory factor for small oscillation phase, we have the transition probability

$$P = \sin^2 2\theta_m \sin^2 \phi^m = \frac{1}{R} \sin^2 2\theta \sin^2 \phi \sqrt{R} \approx \phi^2 \sin^2 2\theta. \quad (87)$$

Note that vacuum mimicking only occurs if the initial neutrino state is a flavor eigenstate [36]. If the initial neutrino is in a flavor-mixed state, for example, in a mass eigenstate,

then matter will affect this state already at lowest order in  $L$ . This situation is realized in several settings involving astrophysical neutrinos propagating through the Earth, for example, solar and supernova neutrinos, where the neutrinos arrive at the Earth as mass eigenstates. The mimicking is not valid if there are nonstandard flavor changing interactions, so that matter effect appears in the off-diagonal elements of the Hamiltonian.

**3.9.3. Effects of Small Layers of Matter.** If the minimal width condition is not satisfied, that is  $d = nx \ll G_F^{-1}$ , the matter effect on result of evolution is small. This inequality can be written as  $Vx \ll 1$  which means that the oscillation phase is small. In this case the matter effect can be considered as small perturbation of the vacuum oscillation result even if the MSW resonance condition is satisfied.

The reasons for the smallness of the matter effect are different depending on the energy interval. Consider a layer of constant density with the length  $x$ . There are three possibilities.

- (i)  $E \ll E_R$  ( $E_R$  is the resonance density)—nearly vacuum oscillations in low density medium take place. Matter effect gives small corrections to the oscillation depth and length which are characterized by  $2VE/\Delta m^2 = Vx/2\pi \ll 1$ , here  $x \sim l_\nu$ .
- (ii)  $E \sim E_R$ —modification of oscillation parameters is strong; however  $l_\nu^R \sim l_\nu/\sin 2\theta \sim 2\pi/(V \sin 2\theta)$ . Consequently,  $x/l_\nu^R = xV \sin 2\theta/2\pi \ll 1$ . Oscillations are undeveloped due to smallness of phase.
- (iii)  $E \gg E_R$ —matter suppresses oscillation depth by a factor  $E_R/E \ll 1$ . Since the oscillation length equals  $l_m \approx 2\pi/V$ , one obtains  $x/l_m = xV/2\pi \ll 1$ . Hence in this case the distance is very small and oscillation effect in the layer has double suppression.

### 3.10. Propagation in Multilayer Medium

**3.10.1. Parametric Effects in the Neutrino Oscillations.** The strong transitions discussed in the previous sections require the existence of large effective mixing, either in the entire medium (constant density) or at least in a layer (adiabatic conversion). There is a way to get strong transition without large vacuum or matter mixings. This can be realized with periodically or quasiperiodically changing density [24, 37] when the conditions of parametric resonance are satisfied. Although the flavor conversion in a layer which corresponds to one period is small, strong transitions can build up over several periods. For large mixing even a small number of periods are enough to obtain strong flavor transitions.

The usual condition of parametric resonance is that the period of density change  $T_n$  is an integer times the effective oscillation length  $l_m$  [38]:

$$\int_{l_T} \frac{dx}{l_m} = k, \quad (k = 1, 2, 3, \dots), \quad (88)$$

or  $l_T/\bar{l}_m = k$ . Such an enhancement has been considered first for modulation of the profile by sine function [39]. This

may have some applications for intense neutrino fluxes when neutrino-neutrino interactions become important.

The solvable case, which has simple physical interpretation, is provided by the *castle wall* profile, for which the period  $l_T$  is divided into the two parts  $l_1$  and  $l_2$  ( $l_1 + l_2 = l_T$ ) with the densities  $n_1$  and  $n_2$ , respectively ( $n_1 \neq n_2$  and, in general,  $l_1 \neq l_2$ ). Thus, the medium consists of alternating layers with two different densities [37, 40–45].

For the “castle wall” profile, the simplest realization of the parametric resonance condition is reduced to equality of the oscillation phases acquired by neutrinos over the two parts of the periods [41]:

$$\Phi_1 = \Phi_2 = \pi. \quad (89)$$

The enhancement of transition depends on the number of periods and on the amplitude of perturbation, which determines the swing angle (the difference of the mixing angles in the two layers,  $\Delta\theta \equiv 2\theta_{1m} - 2\theta_{2m}$ ). For small  $\Delta\theta$  a large transition probability can be achieved after many periods. For large “swing” angle, even a small number of periods are sufficient.

**3.10.2. Parametric Enhancement: General Consideration.** In general the condition (89) is not necessary for the enhancement or even for maximal enhancement. First, consider the oscillation effect over one period. The corresponding evolution matrix is given by the product

$$S_T = S_2 S_1, \quad (90)$$

where  $S_k$  ( $k = 1, 2$ ) is the evolution in layer  $k$  given by (57). For brevity we will write it as  $S_k = c_k I - i s_k (\sigma \cdot \mathbf{n}_k)$ ,  $k = 1, 2$ , where  $c_k \equiv \cos \phi_k$ ,  $s_k \equiv \sin \phi_k$ , and  $\phi_k$  is the half phase acquired in layer  $k$ :

$$\phi_k = \frac{1}{2} \Delta H_k l_k = \frac{\Delta m^2}{4E} R(V_k)^{1/2} l_k, \quad (91)$$

$$\mathbf{n}_k \equiv (\sin 2\theta_{mk}, 0, -\cos 2\theta_{mk}).$$

Here  $\theta_{mk}$  is the mixing angle in layer  $k$ .

Insertion of  $S_k$  from (57) into (90) gives [37]

$$S_T = YI - i(\sigma \cdot \mathbf{X}), \quad (92)$$

where

$$Y \equiv c_1 c_2 - s_1 s_2 (\mathbf{n}_1 \cdot \mathbf{n}_2), \quad (93)$$

$$\mathbf{X} = s_1 c_2 \mathbf{n}_1 + s_2 c_1 \mathbf{n}_2 - s_1 s_2 [\mathbf{n}_1 \times \mathbf{n}_2].$$

Explicitly,  $(\mathbf{n}_1 \cdot \mathbf{n}_2) = \cos(2\theta_{m1} - 2\theta_{m2})$  and  $[\mathbf{n}_1 \times \mathbf{n}_2] = \sin(2\theta_{m1} - 2\theta_{m2}) \mathbf{e}_y$ . Using unitarity of  $S_T$ , which gives  $X^2 + Y^2 = 1$ , one can parametrize  $X$  and  $Y$  with a new phase  $\Phi$  as  $Y \equiv \cos \Phi$  and  $X \equiv \sin \Phi$ . Then the evolution matrix  $S_T$  can be written in the form  $S_T = \cos \Phi - i \sin \Phi (\sigma \cdot \widehat{\mathbf{X}}) = e^{-i(\sigma \cdot \widehat{\mathbf{X}})\Phi}$ , where  $\widehat{\mathbf{X}} \equiv \mathbf{X}/X$ . Consequently, the evolution matrix after  $n$  periods equals

$$\begin{aligned} S^n &= (S_T)^n = e^{-i(\sigma \cdot \widehat{\mathbf{X}})n\Phi} \\ &= \cos n\Phi - i(\sigma \cdot \widehat{\mathbf{X}}) \sin n\Phi. \end{aligned} \quad (94)$$

It is simply accounted for by an increase of the phase:  $\Phi \rightarrow n\Phi$ . This is the consequence of the fact that the evolution matrices over all periods are equal and therefore commute. If the evolution ends at some instant  $t$  which does not coincide with the end of a full period, that is,  $t = nT + t'$ , then  $S(t) = S(t')S_n$ .

The transition probability computed with (94) is

$$P_{e\mu}^n = |S_{e\mu}^n|^2 = \frac{X_1^2 + X_2^2}{X^2} \sin^2 n\Phi. \quad (95)$$

It has the form of the usual oscillation probability with phase  $n\Phi$  and depth  $(X_1^2 + X_2^2)/X^2$ . The oscillations described by (95) are called the parametric oscillations. Under condition

$$-X_3 = s_1 c_2 \cos 2\theta_{m1} + s_2 c_1 \cos 2\theta_{m2} = 0, \quad (96)$$

which is called the parametric resonance condition, the depth of oscillations (95) becomes 1 and the transition probability is maximal when  $n\Phi = \pi/2 + \pi k$ , where  $k$  is an integer. There are different realizations of the condition (96) which imply certain correlations among the mixing angles and phases. The simplest one,  $c_1 = c_2 = 0$ , coincides with (89).

**3.10.3. Parametric Enhancement in Three Layers.** For small number of layers an enhancement of flavor transition can occur due to certain relations between the phases and mixing angles in different layers. This in turn imposes certain conditions on the parameters of the layers: their densities and widths. The conditions are similar to the parametric resonance condition and this enhancement is called the *parametric enhancement* of flavor transitions. These conditions can be satisfied for certain energies and baselines for neutrinos propagating in the Earth.

Consider conditions for maximal enhancement of oscillations for a different number of layers. It is possible to show [46] that they are generalizations of the conditions in one layer which require that (i) the depth of oscillations is 1 (we call it the *amplitude condition*) and (ii) the oscillation phase is  $\phi = \pi/2 + \pi k$ —the *phase condition*.

Consider first the case of one layer with (in general) varying density (it can correspond to the mantle crossing trajectories in the Earth). The resonance condition for constant density case,  $\cos 2\theta_m = 0$ , can be written according to (22) and (51) as  $\alpha = \alpha^*$ , that is,  $S_{11}^{(1)} = S_{22}^{(1)}$ , or equivalently,  $\text{Im } S_{11}^{(1)} = 0$ , where the superscript indicates the number of layers. This generalization goes beyond the original MSW resonance condition (even for constant density). The phase condition can be rewritten in terms of the elements of the evolution matrix (c.f., (54)) as  $\text{Re } \alpha \equiv \text{Re } S_{11}^{(1)} = 0$ . The absolute maximum of the transition probability occurs when these conditions are satisfied simultaneously, that is, when  $S_{11}^{(1)} = 0$ .

The parametric resonance condition (96) can be generalized to the case of nonconstant densities in the layers although the generalization is not unique. Indeed, according to (92) the condition  $X_3 = 0$  can be written in terms of the elements of the evolution matrix for the two layers as the equality of the diagonal elements  $S_{11}^{(2)} = S_{22}^{(2)}$ . Let us find the conditions for

extrema for density profiles consisting of two layers. We have  $S^{(2)} = S_2 S_1$ , where  $S_{11}^{(2)} = \alpha_2 \alpha_1 - \beta_2 \beta_1^*$ ,  $S_{12}^{(2)} = \alpha_2 \beta_1 + \beta_2 \alpha_1^*$ , and  $\alpha_i, \beta_i$  for each layer have been defined in (51). The sum of the two complex numbers in the transition amplitude  $S_{12}^{(2)}$  has the largest possible result if they have the same phase:  $\arg(\alpha_2 \beta_1) = \arg(\beta_2 \alpha_1^*)$ , which can also be rewritten as

$$\arg(\alpha_1 \alpha_2 \beta_1) = \arg(\beta_2). \quad (97)$$

This condition is called the *collinearity condition* [46]. It is an extremum condition for the two-layer transition probability under the constraint of fixed transition probabilities in the individual layers. In other words, if the absolute values  $|\beta_i|$  of the transition amplitudes are fixed while their arguments are allowed to vary, then the transition probability reaches an extremum when these arguments satisfy (97).

The conditions for maximal transition probability for three layers can be found in the following way. The 1-2 elements of the evolution matrix  $S^{(3)}$  equal

$$\begin{aligned} S_{12}^{(3)} &= \alpha_3 S_{12}^{(2)} + \beta_3 S_{11}^{(2)*} \\ &= \alpha_3 \alpha_2 \beta_1 + \alpha_3 \beta_2 \alpha_1^* + \beta_3 \alpha_2^* \alpha_1^* - \beta_3 \beta_2^* \beta_1. \end{aligned} \quad (98)$$

In the case of neutrino oscillations in the Earth, the third layer is just the second mantle layer, and its density profile is the reverse of that of the first layer. The evolution matrix for the third layer is therefore the transpose of that for the first one [47]; that is,  $\alpha_3 = \alpha_1$ ,  $\beta_3 = -\beta_1^*$ , and the expression for  $S_{12}^{(3)}$  can be written as

$$S_{12}^{(3)} = \alpha_1 \alpha_2 \beta_1 - \alpha_1^* \alpha_2^* \beta_1^* + |\alpha_1|^2 \beta_2 + |\beta_1|^2 \beta_2^*. \quad (99)$$

Note that  $\beta_2$  is pure imaginary because the core density profile is symmetric. Therefore the amplitude  $S_{12}^{(3)}$  in (99) is also pure imaginary, as it must be because the overall density profile of the Earth is symmetric as well. If the collinearity condition for two layers (97) is satisfied, then not only the full amplitude  $S_{12}^{(3)}$ , but also *each* of the four terms on the right-hand side of (99) is pure imaginary. If the collinearity condition is satisfied for two layers, then it is automatically satisfied for three layers. This is a consequence of the facts that the density profile of the third layer is the reverse of that of the first layer and that the second layer has a symmetric profile. The conditions described here allow reproducing very precisely all the main structures of the oscillograms of the Earth (see Section 4.1).

**3.11. Oscillations of High Energy Neutrinos.** At high energies or in high density medium when  $V > \Delta m^2/2E$ , we can use  $\Delta/V \equiv \Delta m^2/4EV$  as a small parameter and develop a perturbation theory using its smallness. However, in most situations of interest, the neutrino path length in matter  $L$  is so large that  $\Delta \cdot L \gtrsim 1$ . Therefore the vacuum part of the Hamiltonian cannot be considered as a small perturbation in itself and the effect of  $\Delta$  on the neutrino energy level splitting



should be taken into account. For this reason we split the Hamiltonian as  $H = \bar{H}_0 + H_I$  with

$$\begin{aligned}\bar{H}_0 &= \frac{\omega^m}{2} \begin{pmatrix} 1 & 0 \\ 0 & -1 \end{pmatrix}, \\ H_I &= \sin 2\theta \Delta \begin{pmatrix} -\epsilon & 1 \\ 1 & \epsilon \end{pmatrix},\end{aligned}\quad (100)$$

where  $\omega^m$  is the oscillation frequency (20) and  $\epsilon \equiv (2\Delta \cos 2\theta - V + \omega^m)/2\Delta \sin 2\theta \approx (\Delta/V) \sin 2\theta \ll 1$ . The ratio of the second and the first terms in the Hamiltonian (100) is given by the mixing angle in matter  $\theta_m$ :  $2\Delta \sin 2\theta/\omega^m = \sin 2\theta_m$ . Therefore for  $\sin 2\theta_m \ll 1$  the term  $H_I$  can be considered as a perturbation. Furthermore,  $\epsilon \sim \sin 2\theta_m$ , so the diagonal terms in  $H_I$  can be neglected in the lowest approximation.

The solution for  $S$  matrix can be found in the form  $S = S_0 \cdot S_I$ , where  $S_0$  is the solution of the evolution equation with  $H$  replaced by  $H_0$  (see (71)). The matrix  $S_I$  then satisfies the equation

$$i \frac{dS_I}{dx} = S_0^{-1} H_I S_0 S_I = \bar{H}_I S_I, \quad (101)$$

where  $\bar{H}_I \equiv S_0^{-1} H_I S_0$  is the perturbation Hamiltonian in the “interaction” representation. Equation (101) can be solved by iterations:  $S_I = I + S_I^{(1)} + \dots$ , which leads to the standard perturbation series for the  $S$  matrix. For neutrino propagation between  $x = 0$  and  $x = L$  we have, to the lowest non-trivial order,

$$S(L) = S_0(L) \left[ I - i\Delta \sin 2\theta \int_0^L dx \begin{pmatrix} 0 & e^{i2\phi(x)} \\ e^{-i2\phi(x)} & 0 \end{pmatrix} \right]. \quad (102)$$

The  $\nu_e \leftrightarrow \nu_a$  transition probability  $P_2 = [S(L)]_{ae}$  is given by

$$P_2 = \Delta^2 \sin^2 2\theta \left| \int_0^L dx e^{-i2\phi(x)} \right|^2. \quad (103)$$

For density profiles that are symmetric with respect to the center of the neutrino trajectory,  $V(x) = V(L-x)$ , (103) gives

$$P_2 = 4 \left( \frac{\Delta m^2}{4E} \right)^2 \sin^2 2\theta \left[ \int_0^{L/2} dz \cos 2\phi(z) \right]^2, \quad (104)$$

where  $z = x - L/2$  is the distance from the midpoint of the trajectory and  $\phi(z)$  is the phase acquired between this midpoint and the point  $z$ . The transition probability  $P_2$  decreases with the increase of neutrino energy essentially as  $E^{-2}$ . The accuracy of (103) also improves with energy as  $E^{-2}$ .

Inside the Earth, the accuracy of the analytic formula is extremely good already for  $E \gtrsim 8$  GeV. When neutrinos do not cross the Earth's core ( $\cos \Theta > -0.837$ ) and so experience a slowly changing potential  $V(x)$ , the accuracy of the approximation (103) is very good even in the MSW resonance region  $E \sim (5-8)$  GeV.

The above formalism applies in the low energy case as well, with only minor modifications: the sign of  $H_0$  in (100) has to be flipped, and correspondingly one has to replace  $\omega^m \rightarrow -\omega^m$  in the definition of  $\epsilon$ . The expressions for the transition probability in (103) and (104) remain unchanged.

**3.12. Effects of Small Density Perturbations.** Let us consider perturbation around smooth profile for which exact solution is known. The simplest possibility that has implications for the Earth matter profile is the constant density with additional perturbation:  $V(x) = \bar{V} + \Delta V(x)$ . Correspondingly, the Hamiltonian of the system can be written as the sum of two terms:

$$H(x) = \bar{H} + \Delta H(x), \quad (105)$$

where

$$\begin{aligned}\bar{H} &\equiv \bar{\omega} \begin{pmatrix} -\cos 2\bar{\theta} & \sin 2\bar{\theta} \\ \sin 2\bar{\theta} & \cos 2\bar{\theta} \end{pmatrix}, \\ \Delta H &\equiv \frac{\Delta V(x)}{2} \begin{pmatrix} 1 & 0 \\ 0 & -1 \end{pmatrix}.\end{aligned}\quad (106)$$

Here,  $\bar{\theta} = \theta_m(\bar{V})$  is the mixing angle in matter and  $\bar{\omega} = \omega^m(\bar{V})$  is half of the energy splitting (half-frequency) in matter, both with the average potential  $\bar{V}$ . We will denote by  $\bar{S}(x)$  the evolution matrix of the system for the constant density case  $H(x) = \bar{H}$ . The expression for  $\bar{S}(x)$  is given in (54) with  $\theta_m = \bar{\theta}$  and  $\phi_m(x) = \phi(x) \equiv \bar{\omega}x$ ,  $\bar{\omega} = \omega^m(\bar{V})$ .

The solution of the evolution equation with Hamiltonian (105) [46] is of the form

$$\begin{aligned}S(x) &= \bar{S}(x) + \Delta S(x), \\ \Delta S(x) &= -i\bar{S}(x) K_1(x),\end{aligned}\quad (107)$$

where  $K_1(x)$  satisfies  $|K_1(x)_{ab}| \ll 1$ . Inserting (107) into the evolution equation, one finds the following equation for  $K_1(x)$  to the first order in  $\Delta H(x)$  and  $K_1(x)$ :

$$\begin{aligned}\frac{dK_1(x)}{dx} &= \bar{S}^\dagger \Delta H(x) \bar{S} \\ &= \frac{\Delta V}{2} \left[ -\cos 2\bar{\theta} \begin{pmatrix} -\cos 2\bar{\theta} & \sin 2\bar{\theta} \\ \sin 2\bar{\theta} & \cos 2\bar{\theta} \end{pmatrix} \right. \\ &\quad \left. + \sin 2\bar{\theta} \cos 2\phi G(\bar{\theta}) + \sin 2\bar{\theta} \sin 2\phi \sigma_2 \right],\end{aligned}\quad (108)$$

where  $G(\bar{\theta}) \equiv \cos 2\bar{\theta} \sigma_1 + \sin 2\bar{\theta} \sigma_3$ . The first term in (108) does not contribute to  $S \equiv S(L)$  since  $\langle \Delta V \rangle \equiv \int \Delta V(x) dx = 0$ , and (108) can be immediately integrated:

$$\begin{aligned}K_1(L) &= \frac{1}{2} \sin 2\bar{\theta} \left[ G(\bar{\theta}) \int_0^L \Delta V(x) \cos 2\phi(x) dx \right. \\ &\quad \left. + \sigma_2 \int_0^L \Delta V(x) \sin 2\phi(x) dx \right].\end{aligned}\quad (109)$$

Introducing the distance from the midpoint of the neutrino trajectory  $z \equiv x - L/2$ , one obtains from (109)

$$\Delta S \equiv \Delta S(L) = -i \sin 2\bar{\theta} \left[ G(\bar{\theta}) \Delta I + \sigma_2 \Delta J \right], \quad (110)$$

where  $\Delta I \equiv (1/2) \int_{-L/2}^{L/2} \Delta V(z) \cos(2\bar{\omega}z) dz$ ,  $\Delta J \equiv (1/2) \int_{-L/2}^{L/2} \Delta V(z) \sin(2\bar{\omega}z) dz$ . In these integrals,  $\Delta V(z) \equiv \Delta V(x(z))$  and  $x(z) = z - L/2$ . The integral  $\Delta J$  vanishes if the perturbation  $\Delta V(z)$  is symmetric with respect to the midpoint of the trajectory. Analogously,  $\Delta I$  vanishes if  $\Delta V(z)$  is antisymmetric. The expression for  $S$  defined in (107) is equivalent to (13)–(16) obtained in [48] in the context of solar neutrino oscillations.

For practical purposes it is useful to have an expression for  $S$  which is *exactly* unitary regardless of the size of the perturbation. For this we rewrite (110) as follows:

$$\begin{aligned} \Delta S &= \epsilon S', \\ S' &= -i \left[ G(\bar{\theta}) \cos \xi + \sigma_2 \sin \xi \right], \end{aligned} \quad (111)$$

where  $\sin \xi = \Delta J / \sqrt{(\Delta J)^2 + (\Delta I)^2}$  and  $\epsilon = \sin 2\bar{\theta} \cdot \sqrt{(\Delta J)^2 + (\Delta I)^2}$ . Thus,  $S = \bar{S} + \epsilon S'$  and we replace it by

$$S = \cos \epsilon \bar{S} + \sin \epsilon S'. \quad (112)$$

Here both  $S'$  and  $\bar{S}$  are unitary matrices, and due to their specific form the combination on the right-hand side of (112) is exactly unitary.

For a symmetric density profile with respect to the midpoint of the trajectory, the term  $\Delta J$  is absent. From (54), (110), and (112) we immediately get the transition probability

$$\begin{aligned} P &= \left[ \cos \epsilon \sin 2\bar{\theta} \sin \phi + \sin \epsilon \cos 2\bar{\theta} \right]^2 \\ &\approx \sin^2 2\bar{\theta} \left[ \sin \phi + \Delta I \cos 2\bar{\theta} \right]^2, \end{aligned} \quad (113)$$

where  $\epsilon \equiv \sin 2\bar{\theta} \Delta I$  and  $\phi \equiv \phi(L) = \bar{\omega}L$ . Here the first term in the square brackets describes oscillations in constant density matter with average potential  $\bar{V}_1$ .

**3.13. Oscillation Probabilities and Their Properties.** It is convenient to consider the neutrino flavor evolution in the propagation basis  $\tilde{\nu} = (\nu_e, \tilde{\nu}_2, \tilde{\nu}_3)^T$ , defined in (27). In this basis propagation is not affected by the 2-3 mixing and CP violation. The dependence on these parameters appears when one projects the initial flavor state on the propagation basis and the final state back onto the original flavor basis. The propagation-basis states are related to the mass states as

$$\tilde{\nu} = U_{13} I_\delta U_{12} \nu. \quad (114)$$

Since the transformations, which connect  $\tilde{\nu}$  and  $\nu_f$ , do not depend on matter potential and therefore distance, the states  $\tilde{\nu}$  satisfy the evolution equation  $i(d\tilde{\nu}/dt) = \tilde{H}\tilde{\nu}$ , with the Hamiltonian  $\tilde{H}$  defined in (28).

**3.13.1. S Matrix and Oscillation Amplitudes.** A number of properties of the oscillation probabilities can be obtained from general consideration of matrix of the oscillation amplitudes. We introduce the evolution matrix (the matrix of amplitudes) in the propagation basis as

$$\tilde{S} = \begin{pmatrix} A_{ee} & A_{e\tilde{2}} & A_{e\tilde{3}} \\ A_{\tilde{2}e} & A_{\tilde{2}\tilde{2}} & A_{\tilde{2}\tilde{3}} \\ A_{\tilde{3}e} & A_{\tilde{3}\tilde{2}} & A_{\tilde{3}\tilde{3}} \end{pmatrix}. \quad (115)$$

Then according to (27) the  $S$  matrix in the flavor basis equals

$$\begin{aligned} S &= \tilde{U} \tilde{S} \tilde{U}^\dagger, \\ \tilde{U} &\equiv U_{23} I_\delta. \end{aligned} \quad (116)$$

In this part, we use the notation  $A_{ij}$  for the amplitudes in the propagation basis and  $S_{ij}$  for the amplitudes in the flavor basis. In terms of the propagation-basis amplitudes (115) the  $S$  matrix in the flavor basis can be written as

$$S = \begin{pmatrix} A_{ee} & c_{23} A_{e\tilde{2}} + s_{23} e^{-i\delta} A_{e\tilde{3}} & -s_{23} A_{e\tilde{2}} + c_{23} e^{-i\delta} A_{e\tilde{3}} \\ c_{23} A_{\tilde{2}e} + s_{23} e^{i\delta} A_{\tilde{3}e} & c_{23}^2 A_{\tilde{2}\tilde{2}} + s_{23}^2 A_{\tilde{3}\tilde{3}} + K_{\mu\mu} & -s_{23} c_{23} (A_{\tilde{2}\tilde{2}} - A_{\tilde{3}\tilde{3}}) + K_{\mu\tau} \\ -s_{23} A_{\tilde{2}e} + c_{23} e^{i\delta} A_{\tilde{3}e} & -s_{23} c_{23} (A_{\tilde{2}\tilde{2}} - A_{\tilde{3}\tilde{3}}) + K_{\tau\mu} & s_{23}^2 A_{\tilde{2}\tilde{2}} + c_{23}^2 A_{\tilde{3}\tilde{3}} + K_{\tau\tau} \end{pmatrix}, \quad (117)$$

where

$$\begin{aligned} K_{\mu\mu} &\equiv s_{23} c_{23} (e^{-i\delta} A_{\tilde{2}\tilde{3}} + e^{i\delta} A_{\tilde{3}\tilde{2}}), \\ K_{\mu\tau} &\equiv c_{23}^2 e^{-i\delta} A_{\tilde{2}\tilde{3}} - s_{23}^2 e^{i\delta} A_{\tilde{3}\tilde{2}}, \\ K_{\tau\mu} &= K_{\mu\tau} (\delta \rightarrow -\delta, \tilde{2} \leftrightarrow \tilde{3}), \\ K_{\tau\tau} &= -K_{\mu\mu}. \end{aligned} \quad (118)$$

The scheme of transitions is shown in Figure 7. There is certain hierarchy of the amplitudes which can be obtained immediately from the form of the Hamiltonian in the propagation basis (29):

$$\begin{aligned} A_{e\tilde{3}}, A_{\tilde{3}e} &\sim s_{13}, \\ A_{e\tilde{2}}, A_{\tilde{2}e} &\sim r_\Delta \sim s_{13}^2, \\ A_{\tilde{3}\tilde{2}}, A_{\tilde{2}\tilde{3}} &\sim s_{13} r_\Delta \sim s_{13}^3, \end{aligned} \quad (119)$$

that is,  $A_{\bar{2}\bar{3}}$  and  $A_{\bar{3}\bar{2}}$  are the smallest amplitudes. In the propagation basis there is no fundamental CP or T violation. Therefore for a symmetric density profile with respect to the middle point of trajectory (as in the case of the Earth) the neutrino evolution is T invariant which yields

$$\begin{aligned} A_{\bar{2}e} &= A_{e\bar{2}}, \\ A_{\bar{3}e} &= A_{e\bar{3}}, \\ A_{\bar{3}\bar{2}} &= A_{\bar{2}\bar{3}}. \end{aligned} \quad (120)$$

Consequently, for  $K_{\alpha\beta}$  we obtain

$$\begin{aligned} K_{\mu\tau} &= A_{\bar{2}\bar{3}} (\cos 2\theta_{23} \cos \delta - i \sin \delta), \\ K_{\tau\mu} &= K_{\mu\tau} (\delta \rightarrow -\delta), \\ K_{\mu\mu} &= -K_{\tau\tau} = A_{\bar{2}\bar{3}} \sin 2\theta_{23} \cos \delta. \end{aligned} \quad (121)$$

These terms proportional to small amplitudes  $A_{\bar{2}\bar{3}}$  and  $A_{\bar{3}\bar{2}}$  are of the order  $O(s_{13}^2)$ .

For a symmetric density profile, from (117), (120), and (121) one finds for the probabilities  $P_{\alpha\beta} \equiv |S_{\beta\alpha}|^2$ :

$$P_{ee} = |A_{ee}|^2 = 1 - |A_{e\bar{2}}|^2 - |A_{e\bar{3}}|^2, \quad (122)$$

$$\begin{aligned} P_{\mu e} &= c_{23}^2 |A_{e\bar{2}}|^2 + s_{23}^2 |A_{e\bar{3}}|^2 \\ &\quad + 2s_{23}c_{23} \operatorname{Re}(e^{-i\delta} A_{e\bar{2}}^* A_{e\bar{3}}), \end{aligned} \quad (123)$$

$$\begin{aligned} P_{\tau e} &= s_{23}^2 |A_{e\bar{2}}|^2 + c_{23}^2 |A_{e\bar{3}}|^2 \\ &\quad - 2s_{23}c_{23} \operatorname{Re}(e^{-i\delta} A_{e\bar{2}}^* A_{e\bar{3}}), \end{aligned} \quad (124)$$

$$\begin{aligned} P_{\mu\mu} &= |c_{23}^2 A_{\bar{2}\bar{2}} + s_{23}^2 A_{\bar{3}\bar{3}} \\ &\quad + 2s_{23}c_{23} \cos \delta A_{\bar{2}\bar{3}}|^2, \end{aligned} \quad (125)$$

$$\begin{aligned} P_{\mu\tau} &= |s_{23}c_{23} (A_{\bar{3}\bar{3}} - A_{\bar{2}\bar{2}}) \\ &\quad + (\cos 2\theta_{23} \cos \delta + i \sin \delta) A_{\bar{2}\bar{3}}|^2. \end{aligned} \quad (126)$$

For antineutrinos the amplitudes can be obtained from the results presented above substituting

$$\begin{aligned} \delta &\rightarrow -\delta, \quad A_{ij} \rightarrow \bar{A}_{ij}, \\ \text{where } \bar{A}_{ij} &\equiv A_{ij} (V \rightarrow -V). \end{aligned} \quad (127)$$

Notice that the amplitudes of transitions (123) and (124), that involve  $\nu_e$ , are given by linear combinations of two propagation-basis amplitudes. The other flavor amplitudes depend on three propagation-basis amplitudes.

**3.13.2. Factorization Approximation and Amplitudes for Constant Density.** As follows immediately from the form of the Hamiltonian  $\tilde{H}$  in (29), in the limits  $\Delta m_{21}^2 \rightarrow 0$  or/and  $s_{12} \rightarrow 0$  the state  $\tilde{\nu}_2$  decouples from the rest of the system, and consequently, the amplitude  $A_{e\bar{2}}$  vanishes. In this limit,  $A_{e\bar{3}}$

(as well as  $A_{\bar{3}\bar{3}}$  and  $S_{ee}$ ) is reduced to a  $2\nu$  amplitude which depends on the parameters  $\Delta m_{31}^2$  and  $\theta_{13}$ :  $A_A(\Delta m_{31}^2, \theta_{13}) \equiv A_{e\bar{3}}(\Delta m_{21}^2 = 0)$ . The corresponding probability equals  $P_A \equiv |A_A|^2$ .

In the limit  $s_{13} \rightarrow 0$  the state  $\tilde{\nu}_3$  decouples while the amplitude  $A_{e\bar{3}}$  vanishes and the amplitude  $A_{e\bar{2}}$  reduces to a  $2\nu$  amplitude depending on the parameters of the 1-2 sector,  $\Delta m_{21}^2$  and  $\theta_{12}$ . Denoting this amplitude by  $A_S$  we have  $A_S(\Delta m_{21}^2, \theta_{12}) \equiv A_{e\bar{2}}(\theta_{13} = 0)$ . We will use the notation  $P_S \equiv |A_S|^2$ .

This consideration implies that to the leading nontrivial order in the small parameters  $s_{13}$  and  $r_\Delta$  the amplitudes  $A_{e\bar{2}}$  and  $A_{\bar{2}e}$  are reduced to two neutrino probabilities and depend only on the ‘‘solar’’ parameters, whereas the amplitudes  $A_{e\bar{3}}$  and  $A_{\bar{3}e}$  only on the ‘‘atmospheric’’ parameters:

$$\begin{aligned} A_{e\bar{2}} &\simeq A_{\bar{2}e} \simeq A_S(\Delta m_{21}^2, \theta_{12}), \\ A_{e\bar{3}} &\simeq A_{\bar{3}e} \simeq A_A(\Delta m_{31}^2, \theta_{13}). \end{aligned} \quad (128)$$

The approximate equalities in (128) are called the factorization approximation.

Due to the level crossing phenomenon the factorization approximation (128) is not valid in the energy range of the 1–3 resonance where the 1–3 mixing in matter is enhanced. In the case of a matter with an arbitrary density profile, one can show, using simple power counting arguments, that the corrections to the factorization approximation for the amplitude  $A_{e\bar{2}}$  are of order  $s_{13}^2$ , whereas the corrections to the ‘‘atmospheric’’ amplitude  $A_{e\bar{3}}$  are of order  $r_\Delta$  [49], in agreement with our consideration for constant density. The amplitude  $A_{e\bar{3}}$  does not in general have a 2-flavor form, once the corrections to the factorization approximation are taken into account.

Using the expressions for  $U_{ei}^m$  and  $U_{\mu i}^m$  in terms of the mixing angles in the standard parametrization, we can rewrite (67) as

$$S_{e\mu}^{\text{cst}} = \cos \theta_{23}^m A_{e\bar{2}}^{\text{cst}} + \sin \theta_{23}^m e^{-i\delta^m} A_{e\bar{3}}^{\text{cst}}, \quad (129)$$

where

$$\begin{aligned} A_{e\bar{2}}^{\text{cst}} &\equiv -ie^{i\phi_{21}^m} \cos \theta_{13}^m \sin 2\theta_{12}^m \sin \phi_{21}^m, \\ A_{e\bar{3}}^{\text{cst}} &\equiv -ie^{i\phi_{21}^m} \sin 2\theta_{13}^m [\sin \phi_{32}^m e^{-i\phi_{31}^m} + \cos^2 \theta_{12}^m \sin \phi_{21}^m]. \end{aligned} \quad (130)$$

Here  $\phi_{31}^m = \phi_{32}^m + \phi_{21}^m$ . Since to a good approximation  $\theta_{23}^m \approx \theta_{23}$  and  $\delta^m \approx \delta$  (see Section 2.5) [20, 50], the amplitudes  $A_{e\bar{2}}^{\text{cst}}$  and  $A_{e\bar{3}}^{\text{cst}}$  can be identified with  $A_{e\bar{2}}$  and  $A_{e\bar{3}}$  in (123) and (124).

In terms of mixing angles,  $U_{\mu 1}^m = -s_{12}^m c_{23}^m - c_{12}^m s_{13}^m s_{23}^m e^{i\delta^m}$ ,  $U_{\mu 3}^m = c_{13}^m s_{23}^m$ , the amplitude  $S_{\mu\mu}^{\text{cst}}$  can be rewritten as

$$\begin{aligned} S_{\mu\mu}^{\text{cst}} &= \cos^2 \theta_{23}^m A_{\bar{2}\bar{2}}^{\text{cst}} \\ &\quad + \sin^2 \theta_{23}^m A_{\bar{3}\bar{3}}^{\text{cst}} + \sin 2\theta_{23}^m \cos \delta^m A_{\bar{2}\bar{3}}^{\text{cst}}, \end{aligned} \quad (131)$$

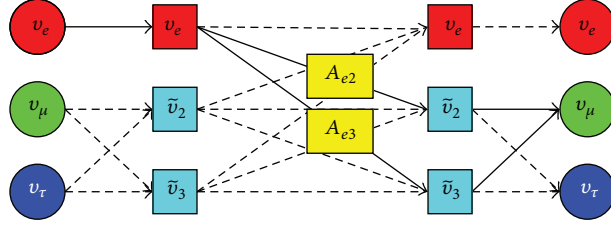


FIGURE 7: Scheme of transitions between the flavor states. Evolution is considered in the propagation basis  $\tilde{\nu}$ . The lines which connect the flavor states and the propagation-basis states indicated projection of one basis onto another. The lines connecting the states of propagation basis  $\tilde{\nu}$  show transitions between them.

where

$$\begin{aligned} A_{\bar{2}\bar{2}}^{\text{cst}} &\equiv 1 + 2ie^{i\phi_{21}^m} \sin^2 \theta_{12}^m \sin \phi_{21}^m, \\ A_{\bar{3}\bar{3}}^{\text{cst}} &\equiv 1 - 2ie^{-i\phi_{32}^m} \cos^2 \theta_{13}^m \sin \phi_{32}^m \\ &\quad + 2ie^{i\phi_{21}^m} \sin^2 \theta_{13}^m \cos^2 \theta_{12}^m \sin \phi_{21}^m, \\ A_{\bar{2}\bar{3}}^{\text{cst}} &\equiv ie^{i\phi_{21}^m} \sin \theta_{13}^m \sin 2\theta_{12}^m \sin \phi_{21}^m. \end{aligned} \quad (132)$$

Notice that  $A_{\bar{2}\bar{2}}^{\text{cst}}$  has exactly the form of the corresponding  $2\nu$  amplitude driven by the solar parameters. The amplitude  $A_{\bar{3}\bar{3}}^{\text{cst}}$  also coincides to a very good approximation with the corresponding  $2\nu$  amplitude driven by the atmospheric parameters. In the approximation  $\theta_{23}^m \approx \theta_{23}$  and  $\delta^m \approx \delta$  the amplitudes (132) can be identified with the corresponding amplitudes in the propagation basis.

### 3.13.3. Properties of the Flavor Oscillation Probabilities

- (1)  $\nu_e$ - $\nu_e$  channel: the total probability of the  $\nu_e$  disappearance equals

$$1 - P_{ee} = P_{e\mu} + P_{e\tau} = P_{e\bar{2}} + P_{e\bar{3}}. \quad (133)$$

The probability  $P_{ee}$  does not depend on the CP-violating phase and the 2-3 mixing in the standard parametrization. The interference of the solar and atmospheric modes in  $P_{ee}$  originates mainly from  $P_{e\bar{3}} \equiv |A_{e\bar{3}}|^2$ . The survival probability then equals  $P_{ee} = 1 - P_{e\mu} - P_{e\tau} = 1 - P_A - P_S$ . At high energies, where the effects of the 1-2 mixing and mass splitting in  $P$  are suppressed, the probability is  $P_{ee} \approx 1 - P_{e\tau} \approx 1 - P_A$ .

- (2)  $\nu_e$ - $\nu_\mu$  and  $\nu_e$ - $\nu_\tau$  channels: the transition probability  $P_{\mu e} \equiv P(\nu_\mu \rightarrow \nu_e)$  (see (123)) can be rewritten as

$$\begin{aligned} P_{\mu e} &= c_{23}^2 |A_{e\bar{2}}|^2 + s_{23}^2 |A_{e\bar{3}}|^2 \\ &\quad + \sin 2\theta_{23} |A_{e\bar{2}}^* A_{e\bar{3}}| \cos(\phi - \delta), \end{aligned} \quad (134)$$

where  $\phi \equiv \arg(A_{e\bar{2}}^* A_{e\bar{3}})$ . Unlike  $1 - P_{ee}$ , this probability contains the interference term between  $A_{e\bar{2}}$  and  $A_{e\bar{3}}$  which depends on the CP violation phase. Since the amplitude  $A_{e\bar{2}}$  is suppressed at high energies due to

the smallness of the 1-2 mixing in matter, in the lowest approximation we have

$$P_{\mu e} \approx \sin^2 \theta_{23} |A_{e\bar{3}}|^2 \approx \sin^2 \theta_{23} |A_A|^2. \quad (135)$$

The maximal value of the probability equals  $P_{\mu e} \approx s_{23}^2$ . According to (123) and (124) the oscillation probabilities  $P_{\tau e}$  and  $P_{e\tau}$  can be obtained from the corresponding probabilities  $P_{\mu e}$  and  $P_{e\mu}$  through the substitution  $s_{23} \rightarrow c_{23}$ ,  $c_{23} \rightarrow -s_{23}$  [51]. The interference term has the opposite signs for channels including  $\nu_\tau$  as compared with those with  $\nu_\mu$ , which can be obtained from the unitarity condition  $P_{ee} + P_{\mu e} + P_{\tau e} = 1$  and the fact that  $P_{ee}$  does not depend on  $\delta$ .

- (3) The  $\nu_\mu$  survival probability,  $P_{\mu\mu}$ , for symmetric density profiles, (125), can be rewritten as

$$\begin{aligned} P_{\mu\mu} &= |c_{23}^2 A_{\bar{2}\bar{2}} + s_{23}^2 A_{\bar{3}\bar{3}}|^2 \\ &\quad + 2 \sin 2\theta_{23} \cos \delta \operatorname{Re} [A_{\bar{2}\bar{3}}^* (c_{23}^2 A_{\bar{2}\bar{2}} + s_{23}^2 A_{\bar{3}\bar{3}})] \\ &\quad + \sin^2 2\theta_{23} \cos^2 \delta |A_{\bar{2}\bar{3}}|^2. \end{aligned} \quad (136)$$

Since  $A_{\bar{2}\bar{3}} = \mathcal{O}(r_\Delta s_{13})$  is a small quantity, to a good approximation one can neglect the term  $\sim \cos^2 \delta$  in (125), which is proportional to  $|A_{\bar{2}\bar{3}}|^2$ . For high energies in the limit  $\Delta m_{21}^2 \rightarrow 0$  we have  $A_{\bar{2}\bar{2}} = 1$ ,  $A_{\bar{2}\bar{3}} = 0$ . Then, parameterizing the 33-amplitude as  $A_{\bar{3}\bar{3}} = \sqrt{1 - P_A} e^{-i\phi_{33}^m}$  we obtain from (136)

$$\begin{aligned} P_{\mu\mu} (\Delta m_{21}^2 = 0) &= 1 - \sin^2 2\theta_{23} \sin^2 \phi_x - s_{23}^4 P_A \\ &\quad - 0.5 \sin^2 2\theta_{23} \cos 2\phi_x \left(1 - \sqrt{1 - P_A}\right), \end{aligned} \quad (137)$$

where  $\phi_x = 0.5 \arg[A_{\bar{3}\bar{3}}^* A_{\bar{2}\bar{2}}] = \phi_{22}^m - \phi_{33}^m$ . The probability can be rewritten as

$$\begin{aligned} P_{\mu\mu} &= 1 - 0.5 \sin^2 2\theta_{23} - s_{23}^4 P_A \\ &\quad + 0.5 \sin^2 2\theta_{23} \left(\sqrt{1 - P_A}\right) \cos 2\phi_x. \end{aligned} \quad (138)$$



- (4)  $\nu_\mu$ - $\nu_\tau$  channel: for symmetric matter density profiles the probability of  $\nu_\mu \rightarrow \nu_\tau$  oscillations is given in (126). It can be rewritten as

$$P_{\mu\tau} = \frac{1}{4} \sin^2 2\theta_{23} |A_{22} - A_{33}|^2 + \sin 2\theta_{23} \cos 2\theta_{23} \cos \delta \operatorname{Re} [(A_{33}^* - A_{22}^*) A_{23}] - \sin 2\theta_{23} \sin \delta \operatorname{Im} [A_{e2}^* A_{e3}] + (1 - \sin^2 2\theta_{23} \cos^2 \delta) |A_{23}|^2. \quad (139)$$

The amplitude depends on  $\delta$  through the terms proportional to  $\cos \delta$  and  $\sin \delta$ , and therefore  $P_{\mu\tau}$  contains both CP- and T-even and -odd terms. One can show that the  $\delta$ -dependent interference terms, which are proportional to  $\sin \delta$  and  $\cos \delta$ , satisfy the relation  $P_{\mu\tau}^\delta = -P_{\mu e}^\delta - P_{\mu\mu}^\delta$ . In the limit  $\Delta m_{21}^2 \rightarrow 0$  we obtain

$$P_{\mu\tau} = 0.5 \sin^2 2\theta_{23} - s_{23}^2 c_{23}^2 P_A - 0.5 \sin^2 2\theta_{23} \left( \sqrt{1 - P_A} \right) \cos 2\phi_X. \quad (140)$$

#### 4. Matter Effects and Determination of Neutrino Mass Hierarchy

4.1. *Propagation of Neutrinos through the Earth.* Flavor neutrino evolution in the Earth is essentially oscillations in a multi-layer medium with slowly changing density in the individual layers and sharp density change on the borders of layers. For energies  $E > 0.1$  GeV, possible short-scale inhomogeneities of the matter distribution can be neglected and the density profile experienced by neutrinos is symmetric with respect to the midpoint of the trajectory:

$$V(x) = V(L - x). \quad (141)$$

Here  $L = 2R_\oplus |\cos \theta_z|$  is the length of the trajectory inside the Earth,  $R_\oplus = 6371$  km is the Earth radius, and  $\theta_z$  is the zenith angle related to the nadir angle as  $\Theta_\nu = \pi - \theta_z$ . For  $0 \leq \Theta_\nu \leq 33.1^\circ$  neutrinos cross both the mantle and the core of the Earth, whereas for larger values of the nadir angle they only cross the Earth's mantle. The column density of the Earth along the diameter equals  $d_{\text{Earth}} = \int n(x) dx$ , which is bigger than the minimal width; the size of the Earth is comparable with the neutrino refraction length.

For the 1-2 channel, the adiabaticity is well satisfied for all energies. We can therefore use the adiabatic approximation. The results of the evolution are determined by the mixing at the surface of the Earth and by the adiabatic phase. In the 1-3 channel the adiabaticity is broken at the resonance. Thus, the constant density approximation with the average density works well in this regime. For energies below the resonance the matter effect becomes small and the constant density approximation and the adiabatic approximation give very similar results.

For the core-crossing trajectories, the profile consists of three layers in the first approximation: (i) mantle (with

increasing density), (ii) core (with a symmetric profile), and (iii) second mantle layer (with decreasing density). This second mantle layer is T-inverted with respect to the first. In this approximation the profile can be considered as three layers of constant effective densities. As such, it looks like a part (1.5 period) of the castle wall profile. Consequently, the parametric enhancement of oscillations, and in particular, the parametric resonance can be realized.

4.1.1. *Neutrino Oscillograms of the Earth.* A comprehensive description of effects of neutrino passage through the Earth can be obtained in terms of neutrino oscillograms. The oscillograms are defined as lines of equal probabilities (or certain combinations of probabilities) in the  $E_\nu$ - $\cos \theta_z$  plane. In Figure 8, we show the oscillograms for the oscillation probabilities  $P_{e\mu}$  and  $P_{\mu\mu}$ , as well as the corresponding probabilities for antineutrinos [43, 46, 52–55].

The structure of the oscillograms is well defined and unique and reflects the structure of the Earth as well as the properties of the neutrinos themselves. In a sense, the oscillograms are the neutrino images of the Earth. In contrast to usual light, there are several different images in different flavors as well as in neutrinos and antineutrinos.

The positions of all main structures of the oscillograms are determined by different realizations of the amplitude condition and the phase condition. These are generalizations of the condition for maximal flavor transitions in the case of vacuum oscillations or oscillation in uniform matter. Recall that, in the latter case,  $P = 1$  requires

- (i)  $\sin^2 2\theta_m = 1$ , the amplitude condition, which is nothing but the MSW resonance condition, and
- (ii)  $\phi = \pi/2 + \pi k$ , the phase condition.

At  $E > 1$  GeV the main structures of oscillograms are generated by the 1–3 mixing. They include the following.

- (1) The MSW resonance pattern (resonance enhancement of the oscillations) for trajectories crossing only the mantle, with the main peak at  $E_\nu \sim (5\text{--}7)$  GeV. The position of the maximum is given by the MSW resonance condition:

$$E_\nu = E_R(\Theta_\nu) = \frac{\Delta m_{31}^2 \cos 2\theta_{13}}{2\bar{V}_1(\Theta_\nu)}, \quad (142)$$

where  $\bar{V}_1(\Theta_\nu)$  is the average value of the potential along the trajectory characterized by  $\Theta_\nu$ . The phase condition becomes  $2\phi(E_\nu, \Theta_\nu) = 2\omega(\bar{V}, E_\nu)L(\Theta_\nu) = \pi$  and the intersection of the resonance and the phase condition lines gives the absolute maximum of  $P_A$ . Combining these conditions gives the coordinates of the peak:  $\cos \Theta_\nu = 0.77$  and  $E_R = 6$  GeV.

- (2) Three parametric ridges in the domain of core-crossing trajectories  $|\cos \theta_z| > 0.87$  and  $E_\nu > 3$  GeV. The parametric ridges differ by the oscillation phase acquired in the core,  $\phi_2$ .

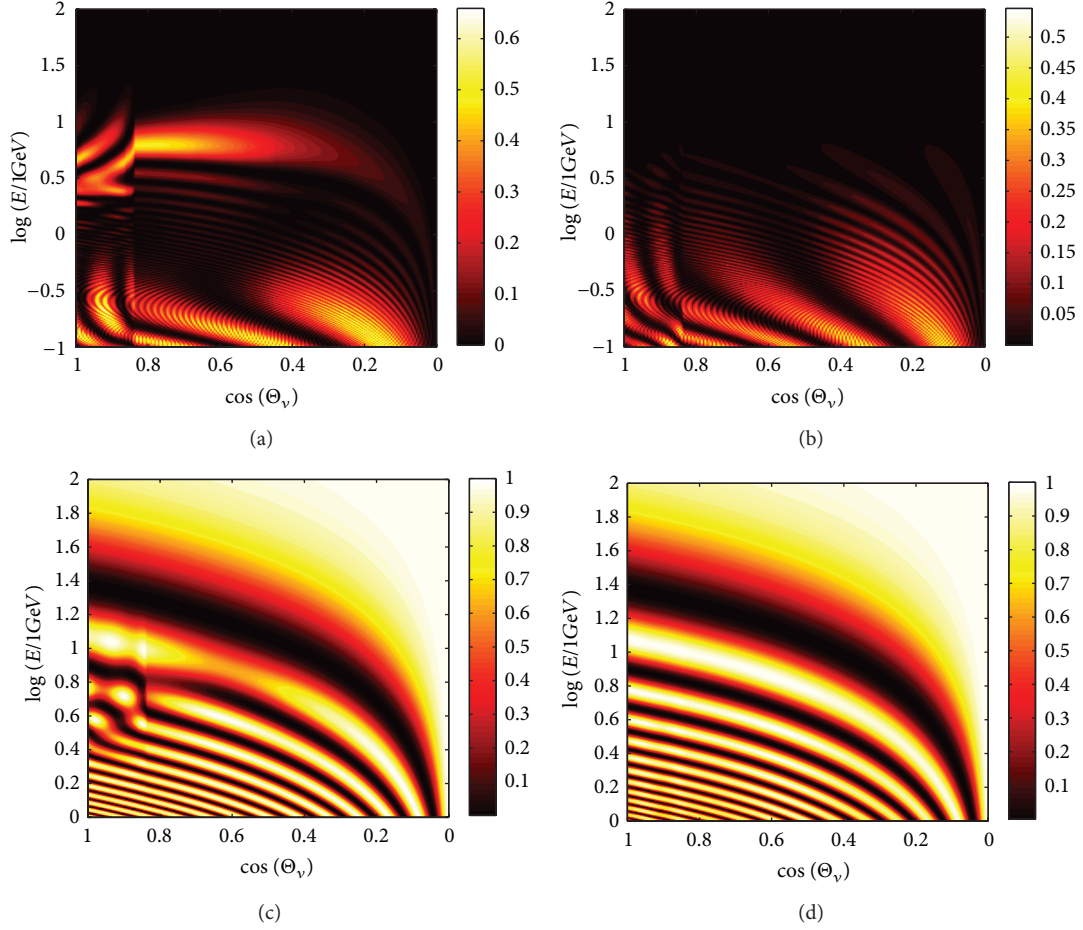


FIGURE 8: Neutrino oscillograms of the Earth. Shown are the lines of equal flavor conversion probability in the  $E_\nu$ - $\cos\Theta_\nu$  plane. Upper panels:  $\nu_e \rightarrow \nu_\mu$  (left) and  $\bar{\nu}_e \rightarrow \bar{\nu}_\mu$  (right); bottom panels:  $\nu_\mu \rightarrow \nu_\mu$  (left) and  $\bar{\nu}_\mu \rightarrow \bar{\nu}_\mu$  (right). Normal hierarchy is assumed.

- (i) *Ridge A* lies between the core resonance (at  $\Theta_\nu \sim 0^\circ$ ) and the mantle resonance regions,  $E_\nu \approx 3$ – $6$  GeV. The phase in the core is  $\phi_2 \leq \pi$ . This ridge merges with the MSW resonance peak in the mantle.
  - (ii) *Ridge B* is situated at  $E_\nu \geq 5$  GeV. For the lowest energies in the ridge and  $\Theta_\nu \sim 0$ , the half phase in the core equals  $\phi_2 \sim (1.2\text{--}1.3)\pi$ .
  - (iii) *Ridge C* is located at  $E_\nu > 11$  GeV in the matter dominated region, where the mixing and, consequently, oscillation depth are suppressed.
- (3) The MSW resonance peak in core located at  $E_\nu \sim 2.5$ – $2.8$  GeV.
  - (4) The regular oscillatory pattern at low energies with “valleys” of zero probability and ridges in the mantle domain and a more complicated pattern with local maxima and saddle points in the core domain.

In Figure 9, we show graphic representations of oscillations which correspond to salient features of the oscillograms.

For energies  $E_\nu < 1$  GeV the main structures are induced by the 1-2 mixing with small corrections due to 1-3 vacuum

oscillations. Neglecting effect of  $\theta_{13}$  we have  $1 - P_{ee} = |A_{e\bar{2}}|^2 \equiv P_S$ . The probabilities of the modes including  $\nu_e$  are expressed in terms of a unique probability  $P_S$ .

The 1-2 pattern differs from the pattern for the 1-3 mixing due to the large value of the 1-2 mixing. The oscillation length at the resonance is smaller than that for the 1-3 mixing,  $l_m^R = l_\nu / \sin 2\theta_{12} \sim l_\nu$ . The resonance energy is shifted to smaller values both due to  $\Delta m_{21}^2 \ll \Delta m_{31}^2$  and because of the factor  $\cos 2\theta_{12} \approx 0.4$ :  $E_{12}^R = (\Delta m_{21}^2 / 2\bar{V}) \cos 2\theta_{12}$ . Here  $\bar{V}$  is the average value of the potential. The adiabaticity is better satisfied than for the 1-3 mixing case and therefore the oscillation probability in the mantle is determined by the potential near the surface of the Earth  $\bar{V}$  averaged over a distance of the order of the first oscillation length. The oscillation length in matter  $l_m$  monotonically increases with energy, approaching the refraction length  $l_0 \equiv 2\pi/\bar{V}$  (c.f. Figure 4). The jump of the mixing angle at the mantle-core boundary is small. Thus, the sudden distortion of the oscillation patterns at  $\Theta_\nu = 33^\circ$  is not as significant as it is for the 1-3 mixing, in particular below the 1-2 resonance energy. These features allow understanding the structure of the oscillograms. In the mantle domain ( $\Theta_\nu > 33^\circ$ )

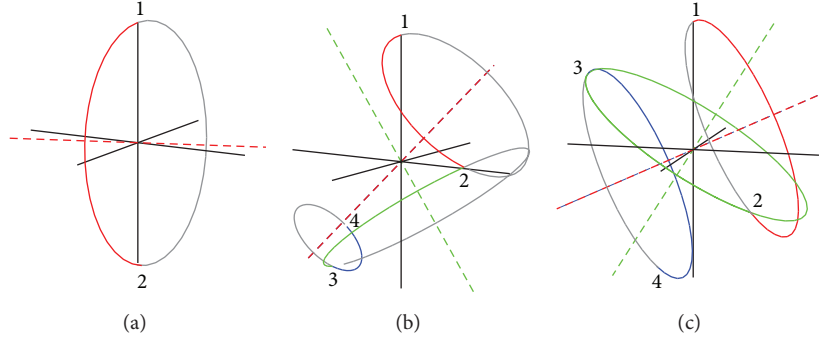


FIGURE 9: Graphic representation of transition in different points of oscillogram: peak due to MSW resonance in the mantle (left), peak due to parametric enhancement of transition driven by 1–3 mixing (middle), and peak due to parametric enhancement of transition driven by 1–2 mixing (right). In the left panel, neutrinos traverse only the mantle layer. In the right panel, neutrinos traverse the mantle (red), the core (green), and again the mantle (blue). The dashed lines correspond to the Hamiltonian vector  $\mathbf{H}$  for the mantle (red) and core (green), respectively.

the oscillation pattern for neutrinos is determined by the resonance enhancement of oscillations. There are three MSW resonance peaks above 0.1 GeV, which differ from each other by value of the total oscillation phase. The outer peak ( $\Theta_\nu \approx 82^\circ$ ) corresponds to  $\phi \approx \pi/2$ , the middle ( $\Theta_\nu = 60^\circ$ ) to  $\phi \approx 3\pi/2$ , and the inner ( $\Theta_\nu \approx 40^\circ$ ) to  $\phi = 5\pi/2$ . Recall that such a large phase can be acquired due to the smaller resonance oscillation length in comparison to that of the 1–3 mixing case, for which only one peak with  $\phi = \pi/2$  can be realized. The resonance energy is given by (45), and for the surface potential we find

$$E_{12}^R \approx 0.12 \text{ GeV}. \quad (143)$$

The ratio of the 1–2 and 1–3 resonance energies equals  $E_{12}^R/E_{13}^R \approx 1/50$ . The estimate (143) is valid for the two outer peaks. For the peak at  $\Theta_\nu = 40^\circ$ ,  $\bar{V}$  is larger and, accordingly, the resonance energy is slightly smaller. The width of the 1–2 resonance is large and therefore the regions of sizable oscillation probability are more extended in the  $E_\nu$  direction as compared to the oscillations governed by the 1–3 mixing and splitting.

The resonance energy in the core is  $E_{12}^R \approx 0.04 \text{ GeV}$ . Therefore for  $E_\nu > (0.10\text{--}0.15) \text{ GeV}$  the 1–2 mixing in the core is substantially suppressed by matter. The peak at  $E_\nu \approx 0.2 \text{ GeV}$  and  $\Theta_\nu \approx 25^\circ$  is due to the parametric enhancement of the oscillations. It corresponds to the realization of the parametric resonance condition when the oscillation half phases equal approximately  $\phi_{\text{mantle}} \approx \pi/2$  and  $\phi_{\text{core}} \approx 3\pi/2$  (note that the total phase is  $\approx 5\pi/2$  and this parametric ridge is attached to the  $5\pi/2$  MSW peak in the mantle domain).

**4.1.2. Oscillograms for the Inverted Mass Hierarchy.** The main change compared to the normal hierarchy is that the 1–3 resonance structure now appears in the antineutrino channel. The level crossing scheme is modified in comparison to NH. In the neutrino channel there is only the 1–2 resonance.

In the approximation of  $\Delta m_{21}^2 = 0$ , the neutrino oscillograms for the inverted hierarchy coincide with the antineutrino oscillograms for the normal hierarchy and vice

versa, provided that  $\Delta m_{31}^2$  is taken to be the same in both cases [56]:  $P_A^{IH} = \bar{P}_A^{NH}$ ,  $\phi_X^{IH} = -\bar{\phi}_X^{NH}$ . Therefore  $P_{\alpha\beta}^{IH} = \bar{P}_{\alpha\beta}^{NH}$ ,  $\bar{P}_{\alpha\beta}^{IH} = P_{\alpha\beta}^{NH}$ . The inclusion of the 1–2 mixing and mass splitting breaks this symmetry.

## 4.2. CP Violation Effects

**4.2.1. Interference and CP Violation.** The survival probability  $P_{ee}$  does not depend on the CP-violating phase  $\delta$  neither for oscillations in vacuum nor in matter [57, 58]. This is the consequence of the facts that  $\delta$  can be removed by transforming to the propagation basis and that  $\nu_e$  is not affected by this transformation. For oscillations in vacuum, or in matter with symmetric density profiles, the other two survival probabilities,  $P_{\mu\mu}$  and  $P_{\tau\tau}$ , are T-even quantities dependent on  $\delta$  only through terms proportional to  $\cos \delta$  and  $\cos 2\delta$  [59]. In contrast to this, for oscillations in a matter with nonsymmetric density profiles, these probabilities also acquire terms proportional to  $\sin \delta$  and  $\sin 2\delta$ .

Introducing the phase  $\phi \equiv \arg(A_{e\bar{2}}^* A_{e\bar{3}})$  and omitting small terms proportional to  $|A_{\bar{2}\bar{3}}|^2 = \mathcal{O}(s_{13}^6)$  we obtain

$$P_{\mu e}^\delta = \sin 2\theta_{23} \cos(\phi - \delta) |A_{e\bar{2}} A_{e\bar{3}}|, \quad (144)$$

$$P_{\mu\mu}^\delta = -\sin 2\theta_{23} \cos \delta \cos \phi |A_{e\bar{2}} A_{e\bar{3}}| - D_{23}, \quad (145)$$

$$P_{\mu\tau}^\delta = -\sin 2\theta_{23} \sin \delta \sin \phi |A_{e\bar{2}} A_{e\bar{3}}| + D_{23}, \quad (146)$$

where  $D_{23} \equiv (1/2) \sin 4\theta_{23} \cos \delta \text{Re}[A_{e\bar{2}\bar{3}}^* (A_{\bar{3}\bar{3}} - A_{\bar{2}\bar{2}})]$  is proportional to the small deviation of the 2–3 mixing from maximal one. Notice that  $D_{23}$  enters  $P_{\mu\mu}^\delta$  and  $P_{\mu\tau}^\delta$  with opposite signs while  $P_{\mu e}^\delta$  does not depend on  $D_{23}$  at all.  $D_{23}$  is CP even. The sum of these interference terms is zero.

For the other channels,  $P_{\alpha\beta}^\delta = P_{\beta\alpha}^{-\delta}$ . For antineutrinos, according to (127), the probabilities have the same form as the corresponding probabilities derived above with a changed sign of  $\delta$  and the amplitudes computed with the opposite sign of the potential. Thus, the  $\delta$ -dependent parts in all the

channels are expressed in terms of two combinations of the propagation-basis amplitudes,  $|A_{e\bar{2}}A_{e\bar{3}}|$  and  $D_{23}$ .

**4.2.2. Magic Lines and CP Domains.** To better assess the effect of  $\delta$ , one can consider the difference of the oscillation probabilities for two different values of the CP phase  $\Delta P_{\alpha\beta}^{\text{CP}}(\delta) \equiv P_{\alpha\beta}(\delta) - P_{\alpha\beta}(\delta_0)$ . In practice, this quantifies how well the phase  $\delta$  fits with some assumed true value  $\delta_0$ . The structure of the oscillograms for  $\Delta P_{\alpha\beta}^{\text{CP}}(\delta)$  can be understood in terms of the grids of magic lines and interference phase lines along which  $\Delta P_{\alpha\beta}^{\text{CP}}(\delta) \approx 0$ .

For the  $\nu_\mu \rightarrow \nu_e$  oscillation probability, the equality

$$\begin{aligned} \Delta P_{\mu e}^{\text{CP}}(\delta) &\equiv P_{\mu e}(\delta) - P_{\mu e}(\delta_0) \\ &= P_{\mu e}^\delta(\delta) - P_{\mu e}^\delta(\delta_0) \end{aligned} \quad (147)$$

is exact and the condition  $\Delta P_{\mu e}^{\text{CP}} = 0$  is equivalent to

$$\begin{aligned} |A_{e\bar{2}}A_{e\bar{3}}| \cos(\phi - \delta) \\ = |A_{e\bar{2}}A_{e\bar{3}}| \cos(\phi - \delta_0). \end{aligned} \quad (148)$$

This equality is satisfied if at least one of the following three conditions is fulfilled:

$$\begin{aligned} A_{e\bar{2}}(E_\nu, \Theta_\nu) &= 0, \\ A_{e\bar{3}}(E_\nu, \Theta_\nu) &= 0, \\ \phi(E_\nu, \Theta_\nu) - \delta_0 &= -[\phi(E_\nu, \Theta_\nu) - \delta] + 2\pi l. \end{aligned} \quad (149)$$

The last condition implies

$$\phi(E_\nu, \Theta_\nu) = \frac{(\delta + \delta_0)}{2} + \pi l. \quad (150)$$

Under the conditions (149), the equality (148) is satisfied identically for all values of  $\delta$ . In these cases the transition probability does not depend on the CP phase. Since the amplitudes  $A_{e\bar{2}}$  and  $A_{e\bar{3}}$  are complex quantities, these conditions can be satisfied in isolated points of the  $(\Theta_\nu, E_\nu)$  plane only. In contrast to this, in the factorization approximation  $A_{e\bar{2}} = A_S$  and  $A_{e\bar{3}} = A_A$  both the conditions are fulfilled along certain lines in the oscillograms. This occurs because the amplitudes  $A_S$  and  $A_A$  take a 2-flavor form. On the basis of neutrino states where the corresponding  $2 \times 2$  Hamiltonians are traceless, both  $A_A$  and  $A_S$  are pure imaginary because of the symmetry of the Earth's density profile [47].

Let us consider the equalities  $A_S = 0$  and  $A_A = 0$  using the constant density approximation.

- (1) The condition  $A_S(E_\nu, \Theta_\nu) = 0$  is satisfied when  $\sin \phi_S(E_\nu, \Theta_\nu) = 0$ , which leads to

$$L(\Theta_\nu) \approx \frac{2\pi n}{\omega_{21}^m}, \quad n = 1, 2, \dots \quad (151)$$

At energies  $E_\nu \gtrsim 0.5$  GeV which are much higher than the 1-2 mixing MSW resonance in the mantle and in the core of the Earth one has  $\omega_{21}^m \approx V$  and the condition (151) becomes

$$L(\Theta_\nu) \approx \frac{2\pi n}{V}. \quad (152)$$

This expression is energy independent and determines the baselines for which the “solar” contribution to the probability vanishes [61]. In the plane  $(\Theta_\nu, E_\nu)$  it represents nearly vertical lines at fixed  $\Theta_\nu$ . There are three solar magic lines which correspond to  $n = 1$  (in the mantle domain)  $\Theta_\nu \approx 54^\circ$  and  $n = 2, 3$  (in the core domain) [61]  $\Theta_\nu \approx 30^\circ$  and  $12^\circ$ . The existence of a baseline ( $L \approx 7600$  km) for which the probability of  $\nu_e \leftrightarrow \nu_\mu$  oscillations in the Earth is approximately independent of the “solar” parameters ( $\Delta m_{21}^2, \theta_{12}$ ) and of the CP phase  $\delta$  was first pointed out in [62] and later discussed in, for example, [61, 63–68]. This baseline was dubbed “magic” in [63].

- (2) The atmospheric magic lines are determined by the condition  $A_A(E_\nu, \Theta_\nu) = 0$  [61]. Along these lines, the “atmospheric” contribution to the amplitudes of  $\nu_\mu \leftrightarrow \nu_e$  and  $\nu_\tau \leftrightarrow \nu_e$  transitions vanishes and the probabilities of oscillations involving  $\nu_e$  or  $\bar{\nu}_e$  do not depend on CP phase. In the constant density approximation, the condition  $A_A = 0$  is satisfied when  $\sin \phi_A = 0$  ( $\phi_A = \pi k, k = 1, 2, \dots$ ) or explicitly

$$L(\Theta_\nu) \approx \frac{2\pi k}{\omega_{31}^m}, \quad k = 1, 2, \dots \quad (153)$$

For energies which are not too close to the 1–3 MSW resonance, it reduces to

$$E_\nu \approx \frac{\Delta m_{31}^2 L(\Theta_\nu)}{|4\pi k \pm 2VL(\Theta_\nu)|}, \quad (154)$$

which corresponds to the bent curves in the  $(\Theta_\nu, E_\nu)$  plane. For very large energies, where  $\Delta m_{31}^2/2E \ll V$ , the atmospheric lines approach the same vertical lines as the solar magic lines (152).

- (3) The condition (150) determines the interference phase lines in the  $(\Theta_\nu, E_\nu)$  plane. In the constant density approximation  $\phi \approx -\phi_{31}^m$ . Consequently in the energy range between the two resonances we have

$$\phi_{31}^m \approx \frac{\Delta m_{31}^2 L}{4E_\nu} = \phi_A^0, \quad (155)$$



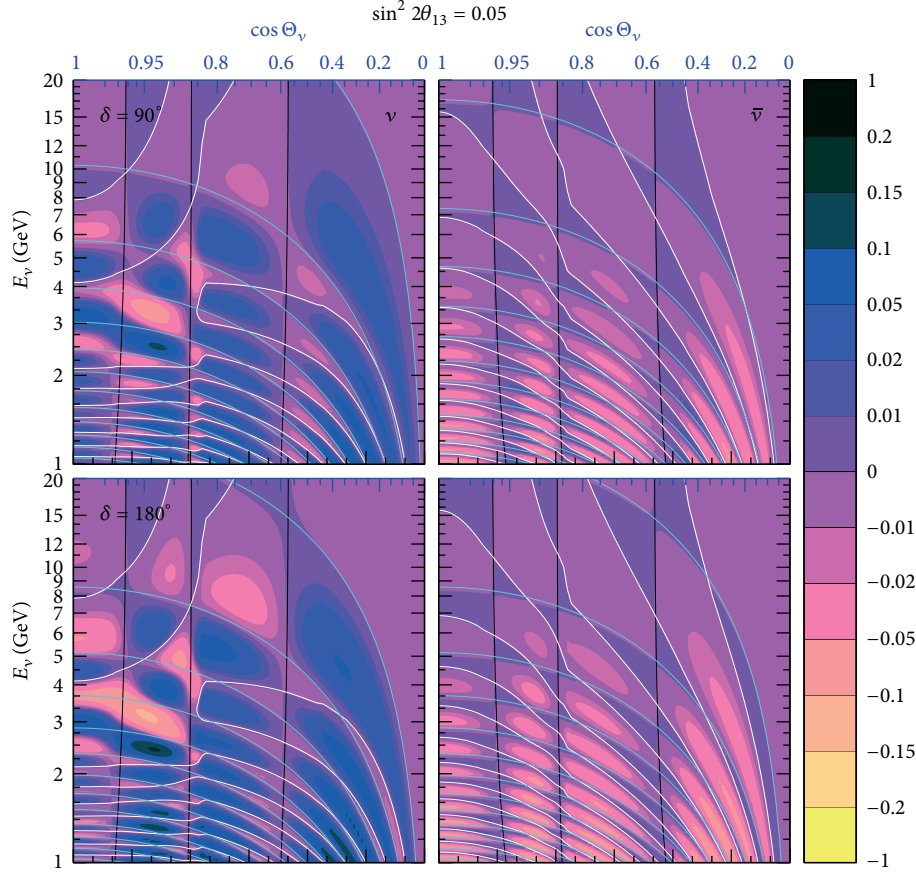


FIGURE 10: Oscillograms for the difference of probabilities  $\Delta P_{\mu e}^{\text{CP}}(\delta) = P_{\mu e}(\delta) - P_{\mu e}(\delta_0)$  with  $\delta_0 = 0^\circ$ . Shown are the solar (black), atmospheric (white), and interference phase condition (cyan) curves from [60].

that is, in the first approximation  $\phi$  does not depend on the matter density. From (150) we then obtain

$$E_\nu = \frac{\Delta m_{31}^2 L(\Theta_\nu)}{4\pi l - 2(\delta + \delta_0)}. \quad (156)$$

Thus, in the factorization approximation, the conditions (149) and (150) define three sets of lines (grid of magic lines) in the oscillograms (see Figure 10), which play crucial roles in understanding the CP violation effects. Along the lines, the probabilities  $P_{\mu e}$ ,  $P_{e\mu}$ ,  $P_{\tau e}$ , and  $P_{e\tau}$  do not depend on the CP phase in the first order approximation. The other probabilities depend on the phase weakly.

From Figure 10, we can see that the magic lines described above do not coincide exactly with the lines of  $\Delta P_{\mu e}^{\text{CP}} = 0$  which bound the CP-domains. Furthermore, interconnections of the latter occur. This is due to the breakdown of the factorization approximation.

**4.3. Determination of Hierarchy with Accelerator Experiments.** An accelerator neutrino experiment has a fixed baseline which corresponds to a vertical line with the length determined by the available energy spectrum. In the oscillogram of Figure 11 we have included such lines for a handful of

accelerator experiments. Furthermore, this energy spectrum is usually peaked at certain energy (or narrow energy range) resulting in the experiment being most sensitive to the oscillation probability at that specific energy. An accelerator neutrino experiment would typically run for several years in neutrinos or antineutrinos before switching polarity and therefore getting information both on  $P_{\alpha\beta}$  and  $\bar{P}_{\alpha\beta}$ . The goal of such a search is to observe in which channel the oscillation probability is suppressed and in which it is enhanced. If a neutrino experiment could run at energy similar to the resonant one and at a baseline of several thousand kilometers, then this determination would be quite simple. However, as can be seen from the oscillogram, accelerator neutrino experiments are confined to relatively shallow trajectories with rather poor oscillatory pattern, and this severely limits their capabilities leading to various degeneracies. In particular, lack of knowledge of the mass hierarchy is part of the famous eightfold degeneracy, which arises as follows. Assume we have access to the values of oscillation probabilities  $P_{\mu e}$  and  $\bar{P}_{\mu e}$  at a given baseline  $L$  and energy  $E$  only. Then there exist three types of ambiguities that give rise to the same values of the probabilities in different parts of the parameter space (mixing angles, CP phase, and signs of mass differences).

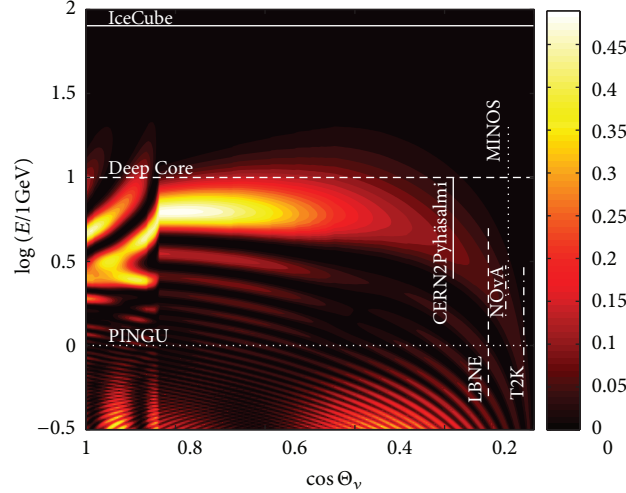


FIGURE 11: Physics reach of the accelerator and atmospheric neutrino experiments. Shown are areas in the oscillogram for  $\nu_e \rightarrow \nu_\mu$  channel which can be covered by different accelerator (vertical sections) and atmospheric neutrino experiments (sensitive to the area above the corresponding horizontal lines).

- (1) *Sign (hierarchy) degeneracy*: this is the degeneracy due to the unknown neutrino mass hierarchy. Changing the mass hierarchy, it is often possible to find a point in parameter space that predicts the same oscillation probabilities.
- (2) *Intrinsic  $(\theta_{13}, \delta)$  degeneracy*: for any combination of  $(\theta_{13}, \delta)$ , there exists a different combination  $(\hat{\theta}_{13}, \hat{\delta})$  that also predicts the same oscillation probabilities.
- (3) *Octant  $(\theta_{23})$  degeneracy*: changing the octant of  $\theta_{23}$  also leads to a degeneracy due to  $\mu$ - $\tau$  symmetry. If  $\theta_{23}$  is close to maximal, the effects of this degeneracy are less pronounced.

Since each of these degeneracies is twofold, an overall degeneracy is eightfold:  $2^3 = 8$ . The first two of these degeneracies can be illustrated in a biprobability plot of Figure 12. As follows from this figure, even if both the probabilities (for a given neutrino energy) are known with infinite accuracy, we cannot identify the hierarchy within the pink region.

For known mass hierarchy (e.g., normal one) a given value of  $\theta_{13}$  fixes ellipse in the plot along which the CP phase varies. Increasing  $\theta_{13}$  moves the ellipse up and to the right in the plot. Therefore for every point on an ellipse, there will be another ellipse corresponding another value  $\theta_{13}^{\text{prime}}$ , which crosses this point and therefore  $\theta_{13}^{\text{prime}}$  reproduces the same oscillation probabilities. For example, in the left intersection of the black and white ellipse (Figure 12) both combinations of  $\theta_{13}$  and  $\delta$  correspond to those precise oscillation probabilities and there are also values of  $\theta_{13}$  and  $\delta$  that will reproduce them in the inverted hierarchy. For the right intersection, the intrinsic degeneracy is still present, while the sign degeneracy is resolved. It should be remembered that this type of figure is just an illustration. In real experiment the neutrino energy spans over wide range, the oscillation probabilities would

not be exactly known, and strictly this type of consideration becomes invalid.

In order to see how these degeneracies manifest themselves in an experimental setup, we show the oscillation probability  $P_{\mu e}$  as a function of the baseline length in Figure 13. While the 295 km baseline is too short for matter effects to be very significant, as the baseline increases matter effects start being more and more important. In particular, when the oscillation phase maximum occurs at an energy similar to that of the matter resonance, as is the case of 7500 km baseline, we can see the enhancement of the transition probability in the neutrino channel for the normal hierarchy and the suppression in the inverted. In a simple two-flavor scenario, the amplitude of  $P_{\mu e}$  at the resonance is one by definition in the normal mass hierarchy case. At the same time, the oscillation amplitude in the inverted hierarchy at the same energy is given by

$$\sin^2 2\tilde{\theta} = \frac{\sin^2 2\theta}{1 + 3\cos^2 2\theta} \approx \frac{1}{4} \sin^2 2\theta, \quad (157)$$

where the last equality holds for small  $\theta$ . On the other hand, if the neutrino energy is far below the resonance in order to accumulate a significant oscillation phase, such as in the left and middle panels, then the oscillation amplitude will be effectively given by

$$\sin^2 2\tilde{\theta} \approx \sin^2 2\theta \left[ 1 + \frac{4VE}{\Delta m^2} \cos 2\theta \right]. \quad (158)$$

The reason that the 810 km baseline separates the hierarchies better than the 295 km one is based mainly on the fact that the oscillation maximum can be reached for higher energies due to the longer baseline, and thus, the relative difference between probabilities for the two hierarchies increases. Also note that the oscillation probabilities for the 7500 km baseline are not very dependent on the CP-violating phase  $\delta$ . This is

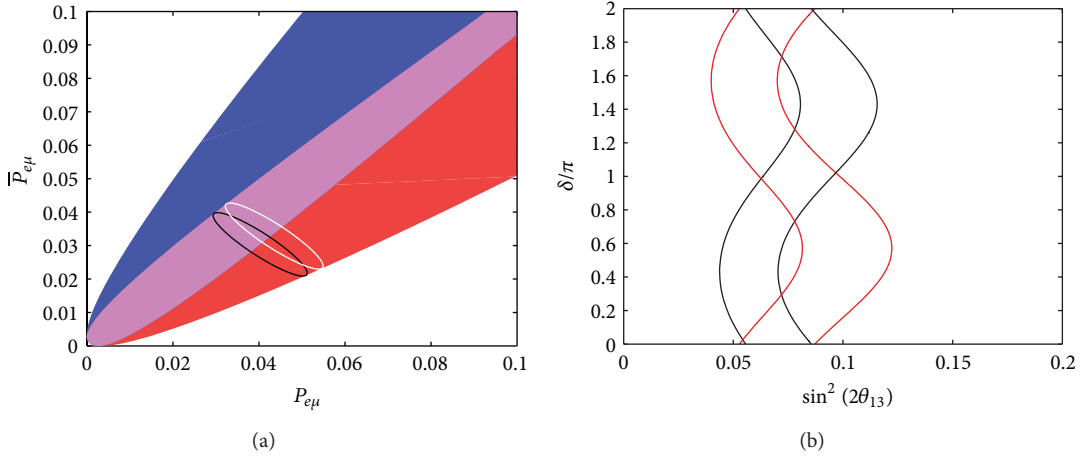


FIGURE 12: Two different illustrations of parameter space degeneracies. Left panel: biprobability plot for  $L = 295$  km and  $E = 0.65$  GeV. The red band indicates the possible values of the probabilities for normal hierarchy, the blue for inverted, and the pink for the intersection of the two. The black and white ellipses represent the possible values of the probabilities for two different fixed values of  $\theta_{13}$ . Right panel: probability isocontours of  $P_{\mu e}$  (black) and  $\bar{P}_{\mu e}$  (red). The values of the probabilities correspond to those of the intersections between the black and white ellipses in the left panel (with the thick lines representing the upper left intersection). The intersections are where the parameter values reproduce the oscillation probabilities for both neutrinos and antineutrinos.

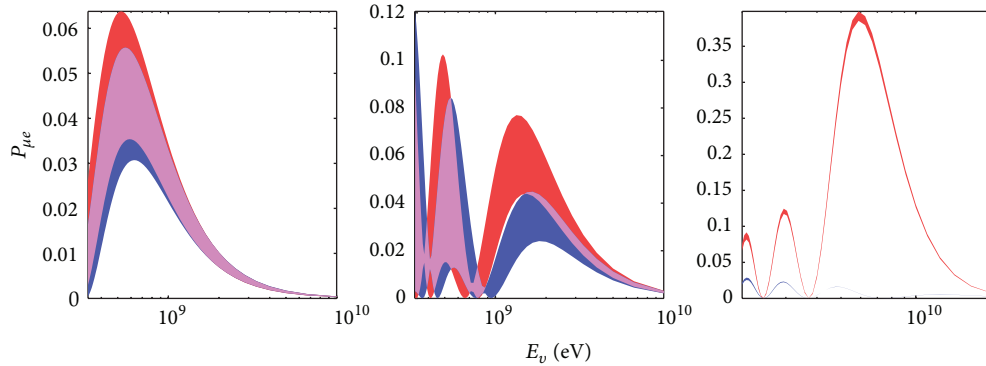


FIGURE 13: The neutrino oscillation probability  $P_{\mu e}$  at baselines of 295 (left), 810 (middle), and 7500 km (right) as a function of the neutrino energy. The red (blue) band corresponds to the normal (inverted) mass hierarchy and the band width is obtained by varying the value of  $\delta$ . The probabilities for  $\bar{P}_{\mu e}$  look similar with the hierarchies interchanged. Note the different scales of the axes.

due to the so-called magic baseline effect, which has been discussed before.

In order to successfully determine the neutrino mass hierarchy in a single accelerator experiment, two conditions are of major importance. (1) The baseline must be long enough to allow for a significant value of  $VE$  in order to separate the neutrino and antineutrino oscillation probabilities. To separate the mass hierarchy determination from the effects of the CP phase, this separation must be large enough to avoid overlap of the probabilities within the experimental uncertainties. (2) The statistics must be high enough and the systematics low enough in order to make the split statistically significant. The literature contains several proposals for long baseline experiments with baselines of several thousands of

kilometers in order to satisfy these conditions. However, as we will discuss later, the large value of  $\theta_{13}$  also provides us with an opportunity to pin down the value of  $\delta$ . Such measurements require the presence of interference terms which will be small at the very long baselines, and instead medium long baselines around 1000 km, such as the 810 km baseline shown in Figure 13, may be preferable due to the significant  $\delta$  dependence of probabilities.

**4.3.1. CP Violation Effects and the Mass Hierarchy.** Figure 13 shows a significant dependence of the probabilities on the CP-violating phase  $\delta$ , especially at small baselines. We are mainly interested in the oscillation probability at the first or second oscillation maximum, where an experiment would typically

be placed. In these baselines  $L$  the  $\nu_\mu$ - $\nu_e$  oscillation probability (the “golden channel”) can be expanded in the small quantity  $\Delta m_{21}^2 L/2E$  which gives [69]

$$P_{e\mu} \approx s_{23}^2 P^{2f} + c_{13} \sin 2\theta_{13} \sin 2\theta_{12} \sin 2\theta_{23} \frac{\Delta m_{21}^2}{2EV} \times \sin\left(\frac{VL}{2}\right) \sin\left(\frac{\Delta m_{31}^2 L}{4E}\right) \cos\left(\delta - \frac{\Delta m_{31}^2 L}{4E}\right), \quad (159)$$

where  $P^{2f}$  is the two-flavor oscillation probability discussed earlier. In (159) we have neglected terms of the second (and higher) order in  $\Delta m_{21}^2 L/2E$  (while the first neglected term is not suppressed by  $\theta_{13}$ , for the value of  $\theta_{13}$  measured by reactor experiments the suppression by the solar mass square splitting is about 6 times stronger) as well as the matter effect on  $\Delta m_{31}^2$ . It is the second term that is responsible for creating the band of different oscillation probabilities displayed in Figure 13, and hence, for creating the sign degeneracy in accelerator neutrino experiments. The appearance of the  $\sin(VL/2)$  term is an inheritance from the magic baseline oscillations and will vanish the  $\delta$ -dependent term when  $VL = 2\pi$ . Furthermore, we can observe that this term contains all of the mixing angles in the same way as the Jarlskog invariant, which is expected due to the CP dependence of the term.

#### 4.4. Determination of Hierarchy with Atmospheric Neutrinos

**4.4.1. Neutrino Fluxes.** The original flux of atmospheric neutrinos contains incoherent components of  $\nu_e$ ,  $\nu_\mu$  and the corresponding antineutrinos, while the original  $\nu_\tau$  flux is negligible. We introduce  $\Phi_e^0$  and  $\Phi_\mu^0$ , the electron and muon neutrino fluxes, as well as  $\bar{\Phi}_e^0$  and  $\bar{\Phi}_\mu^0$ , the electron and muon antineutrino fluxes, at the detector in the absence of oscillations. The flavor ratios

$$r \equiv \frac{\Phi_\mu^0}{\Phi_e^0}, \quad \bar{r} \equiv \frac{\bar{\Phi}_\mu^0}{\bar{\Phi}_e^0} \quad (160)$$

increase with energy.

There is a small neutrino-antineutrino asymmetry: the neutrino flux  $\bar{\Phi}_\mu^0/\Phi_\mu^0 \approx 0.8$ -0.9. All the fluxes (at  $E > 1$  GeV) decrease rapidly with energy  $\Phi_\alpha^0 \propto E^{-k}$ ,  $k = k(E) = 3$ -5, and an azimuthal dependence shows up at low energies.

The flux of neutrinos of flavor  $\nu_\alpha$  at a detector, with oscillations taken into account, is given by

$$\Phi_\alpha = \Phi_e^0 P_{e\alpha} + \Phi_\mu^0 P_{\mu\alpha} = \Phi_e^0 [P_{e\alpha} + r(E, \Theta_\nu) P_{\mu\alpha}], \quad \alpha = e, \mu, \tau. \quad (161)$$

Similar expressions hold for the antineutrino fluxes. Inserting the analytic expressions for the probabilities (122)–(126), one finds

$$\begin{aligned} \frac{\Phi_e}{\Phi_e^0} &= 1 + (rs_{23}^2 - 1) P_{e\bar{3}} + (rc_{23}^2 - 1) P_{e\bar{2}} + rP_{\mu e}^\delta, \\ \frac{\Phi_\mu}{\Phi_\mu^0} &\approx 1 - 2s_{23}^2 c_{23}^2 [1 - \text{Re}(A_{\bar{2}\bar{2}}^* A_{\bar{3}\bar{3}})] \\ &\quad - \frac{s_{23}^2}{r} (rs_{23}^2 - 1) P_{e\bar{3}} - \frac{c_{23}^2}{r} (rc_{23}^2 - 1) P_{e\bar{2}} + P_{\mu\mu}^\delta + \frac{1}{r} P_{e\mu}^\delta, \\ \frac{\Phi_\tau}{\Phi_\mu^0} &\approx 2s_{23}^2 c_{23}^2 [1 - \text{Re}(A_{\bar{2}\bar{2}}^* A_{\bar{3}\bar{3}})] \\ &\quad - \frac{c_{23}^2}{r} (rs_{23}^2 - 1) P_{e\bar{3}} - \frac{s_{23}^2}{r} (rc_{23}^2 - 1) P_{e\bar{2}} + P_{\mu\tau}^\delta + \frac{1}{r} P_{e\tau}^\delta, \end{aligned} \quad (162)$$

where  $P_{e\bar{3}} \equiv |A_{e\bar{3}}|^2$  and  $P_{e\bar{2}} \equiv |A_{e\bar{2}}|^2$  are defined in Section 3.13. In the factorization approximation they correspond to the atmospheric and solar oscillation modes. The  $\delta$ -dependent terms have been introduced in (144).

Using unitarity relations

$$\begin{aligned} |A_{\bar{2}\bar{2}}|^2 &= 1 - |A_{\bar{2}e}|^2 - |A_{\bar{2}\bar{3}}|^2 \\ &\approx 1 - |A_{\bar{2}e}|^2 = 1 - P_{e\bar{2}}, \end{aligned} \quad (163)$$

where the terms proportional to  $|A_{\bar{3}\bar{2}}|^2$  have been neglected we can approximate

$$\text{Re}(A_{\bar{2}\bar{2}}^* A_{\bar{3}\bar{3}}) \approx \sqrt{(1 - P_{e\bar{3}})(1 - P_{e\bar{2}})} \cos \psi. \quad (164)$$

Here  $\psi \equiv \arg A_{33} A_{22}^*$  is the relative phase between the two amplitudes. For the  $\nu_e$  flux, we then obtain

$$\begin{aligned} \frac{\Phi_e}{\Phi_e^0} &\approx 1 + (rs_{23}^2 - 1) P_{e\bar{3}} + (rc_{23}^2 - 1) P_{e\bar{2}} \\ &\quad + r \sin 2\theta_{23} \sqrt{P_{e\bar{3}} P_{e\bar{2}}} \cos(\phi - \delta). \end{aligned} \quad (165)$$

The oscillated fluxes satisfy the sum rule

$$\Phi_e + \Phi_\mu + \Phi_\tau = \Phi_e^0 + \Phi_\mu^0, \quad (166)$$

which simply reflects the unitarity of transitions and, consequently, conservation of the total flux in oscillations.

The formulas (161) also show the screening effect. Terms with oscillation probabilities driven by the 1-2 and 1-3 mixings appear with the “screening” factors [70, 71]:  $P_{e\bar{3}}$  with  $(rs_{23}^2 - 1)$  and  $P_{e\bar{2}}$  with  $(rc_{23}^2 - 1)$ . The contribution of the “atmospheric mode” vanishes along the line  $r(E, \Theta_\nu) = 1/s_{23}^2$ , whereas the contribution of the “solar mode” vanishes along  $r(E, \Theta_\nu) = 1/c_{23}^2$ . For maximal mixing both contributions vanish along the same line,  $r(E, \Theta_\nu) = 2$ . For the neutrino energies above 0.1 GeV,  $r > 1.8$ -1.9, and only one of these



contributions can vanish for substantial deviation of the 2-3 mixing from maximal:  $s_{23}^2$  or  $c_{23}^2 < 0.45$ . Thus, both the effects of 1-2 and 1-3 mixing turn out to be subleading and the oscillation effects are well described by the first order approximation of 2-3 vacuum oscillations.

In the  $\nu_\mu$  flux, the contributions of the 1-2 and 1-3 modes are suppressed by additional factors  $s_{23}^2/r$  and  $c_{23}^2/r$ , respectively. There is no suppression of the interference terms, which depend on the CP violation phase. Furthermore, in the  $\nu_e$  flux the interference term is enhanced by the flux ratio  $r$ . There is no suppression of the interference terms of the 1-2 and 1-3 modes in the  $\mu$ - $\tau$  mode.

**4.4.2. Sensitivity to Mass Hierarchy.** Let us discuss the sensitivity of large water or ice detectors of atmospheric neutrinos to the neutrino mass hierarchy. The  $\nu_\mu$ -like events correspond to interactions  $\nu_\mu + N \rightarrow \mu + X$ ,  $\bar{\nu}_\mu + N \rightarrow \mu^+ + X$  and can be observed as events with muon tracks and hadron cascades. There are also some contributions from  $\nu_\tau$  which produce  $\tau$  with subsequent decay into  $\mu$ . The number of  $\nu_\mu$ -like events in the  $ij$ -bin in the  $E_\nu$ - $\cos\theta_z$  plane equals

$$N_{ij,\mu}^{NH} = 2\pi N_A \rho T \int_{\Delta_i \cos\theta_z} d\cos\theta_z \times \int_{\Delta_j E_\nu} dE_\nu V_{\text{eff}}(E_\nu) D_\mu(E_\nu, \theta_z), \quad (167)$$

where  $T$  is the exposure time,  $N_A$  is the Avogadro number,  $\rho$  is the density of ice,  $V_{\text{eff}}(E_\nu, \theta_z)$  is the effective volume of the detector, and the number density of events per unit time per target nucleon is given by

$$D_\mu(E_\nu, \theta_z) = \left[ \sigma^{CC} \left( \Phi_\mu^0 P_{\mu\mu} + \Phi_e^0 P_{e\mu} \right) + \bar{\sigma}^{CC} \left( \bar{\Phi}_\mu^0 \bar{P}_{\mu\mu} + \bar{\Phi}_e^0 \bar{P}_{e\mu} \right) \right]. \quad (168)$$

It is assumed here that experiments do not distinguish the neutrino and antineutrino events and corresponding signals are summed up.

The fine-binned distribution of events (166) is shown in Figure 14. For illustration we use the effective volume of PINGU with 22 additional strings [72], which increases from  $\sim 2$  Mt at  $E_\nu = 2$  GeV to 20 Mt at  $E_\nu = 20$  GeV. The pattern of the event number distribution follows the oscillatory picture due to the  $\nu_\mu$ - $\nu_\mu$  mode of oscillations with a certain distortion in the resonance region. The maxima and minima are approximately along the lines of equal oscillation phases  $E_\nu \sim \phi_{32} \Delta m_{32}^2 |\cos\theta_z| R_\oplus$  (where  $R_\oplus$  is the Earth radius), with distortion in the resonance region  $E_\nu = (4-10)$  GeV. In the high density bins, the number of events reaches 200 and the total number of events is about  $10^5$ .

The expression for the density of events (168) can be written as

$$D_\mu^{NH} = \sigma^{CC}(E_\nu) \Phi_\mu^0 \left[ \left( P_{\mu\mu} + \frac{1}{r} P_{e\mu} \right) + \kappa_\mu \left( \bar{P}_{\mu\mu} + \frac{1}{\bar{r}} \bar{P}_{e\mu} \right) \right], \quad (169)$$

where

$$\kappa_\mu \equiv \frac{\bar{\sigma}^{CC} \bar{\Phi}_\mu^0}{\sigma^{CC} \Phi_\mu^0}. \quad (170)$$

Similarly one can determine the number of events for inverted mass hierarchy. Let us introduce the  $N$ - $I$  hierarchy asymmetry for the  $ij$ -bin in the  $(E_\nu, \cos\theta_z)$  plane as

$$A_{ij}^{N-I} \equiv \frac{N_{ij}^{IH} - N_{ij}^{NH}}{\sqrt{N_{ij}^{NH}}}. \quad (171)$$

The moduli of the asymmetry (171) are the measures of statistical significance of the difference of the number of events for the normal and inverted mass hierarchies:  $S_{ij} = |A_{ij}|$ .

The strongest effect of hierarchy change is in the strips along the constant phase lines in the energy interval  $E_\nu = (4-12)$  GeV, where these lines are distorted by the matter effect. Here the asymmetry changes sign with the zenith angle, and the number of intervals with the same sign asymmetry increases with the decrease of energy. The  $\nu_\tau \rightarrow \tau \rightarrow \mu$  events can be considered as background events and treated within  $\sim 5\%$  systematic errors.

**4.4.3. Measurements.** According to Figure 14, the hierarchy asymmetry of the  $\nu_\mu$  events has opposite signs in different parts of the oscillogram. Thus, the integration over  $E_\nu$  and  $\cos\theta_z$  substantially reduces the sensitivity to the hierarchy. Due to this, a relatively good reconstruction of the neutrino energy and direction is required to identify the hierarchy. The uncertainties of the reconstruction of energy  $\sigma_E$  and angle  $\sigma_\theta$  should be comparable to or smaller than the sizes of the domains with the same sign of the asymmetry. The oscillograms for the reconstructed neutrino energy  $E_\nu^r$  and angle  $\theta_z^r$  can be obtained by smearing of the  $E_\nu$ - $\cos\theta_z$  oscillograms with the reconstruction functions of the width  $\sigma_E$  and angle  $\sigma_\theta$ .

Small uncertainties  $\sigma_E$  and  $\sigma_\theta$  require rather precise measurements of the energy  $E_\mu$  and direction  $\theta_\mu$  of the muon, as well as energy of the accompanying hadron cascade  $E_h$ . Then the neutrino energy equals  $E_\nu^r = E_\mu + E_h$ . The reconstruction of the neutrino direction is more involved. In the first approximation, one can use  $\theta_\nu \approx \theta_\mu$  with a spread which decreases with energy:  $\sigma_\theta \sim A \sqrt{m_p/E_\nu}$  ( $A = O(1)$ ). Knowledge of the hadron cascade energy allows reducing this uncertainty. Further improvements could be possible if some information about geometry of the cascade is available. A possibility to separate (at least partially) the neutrino and antineutrino samples would significantly improve sensitivity to the mass hierarchy, as well as to CP violation.

All this imposes conditions on the detector characteristics. According to Figure 14, the most sensitive region to the hierarchy is around the resonance and above:  $E = (5-15)$  GeV. The number of events in Super-Kamiokande is too small, but (upgraded) ice and underwater detectors of the multimeton ( $\sim 10$  Mt) scale could collect around the order

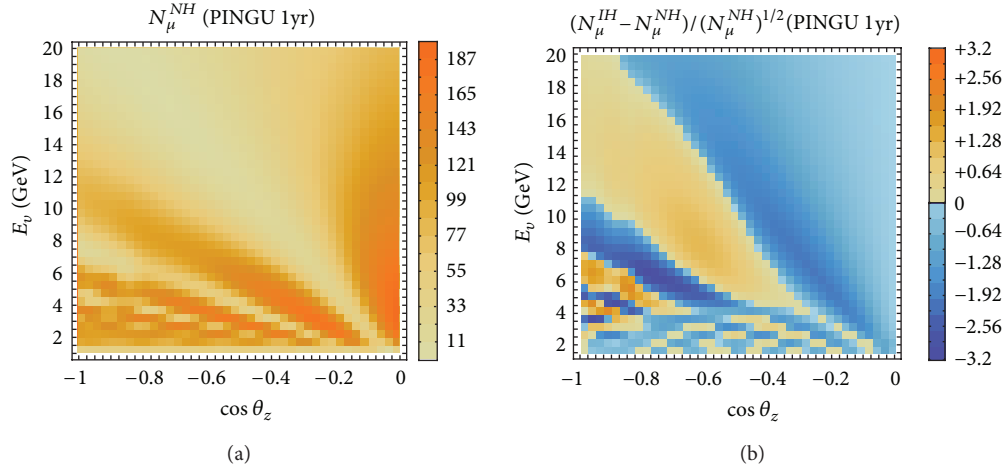


FIGURE 14: Left: the binned distribution of the number of  $\mu$  events in PINGU after 1 year under the assumption that the neutrino hierarchy is normal. Right: the  $N$ - $I$  hierarchy asymmetry of  $\nu_\mu$  events in the  $E_\nu$ - $\cos\theta_z$  plane. The absolute value of the asymmetry in a given bin determines the statistical significance of the difference of the numbers of events for the inverted and normal mass hierarchies. Both figures from [56].

of  $10^5 \nu_\mu$  events a year in this range so that a high statistics study becomes possible.

A small enough spacing between the PMTs ( $\sim 10$ – $20$  m between strings and  $3$ – $5$  m in the vertical direction) will allow the reduction of the threshold down to a few GeV and perform reasonably good measurements of the muon and hadron cascade characteristics. Very high statistics will also allow resolving the problem of parameter degeneracy; effects qualitatively similar to the mass hierarchy effect can be obtained by small (within  $1\sigma$  interval) variations of  $\Delta m_{32}^2$  and  $\theta_{23}$ . The effect of an unknown CP phase is small.

High statistics would allow resolving the degeneracy problem by selecting specific regions in the  $E_\nu$ - $\cos\theta_z$  for the analysis, where effects of  $\Delta m_{32}^2$  are suppressed in comparison to the hierarchy effects or averaged out as a result of specific integration. High statistics also allow performing an analysis of the data using  $\Delta m_{32}^2$  and  $\theta_{23}$  as fit parameters. This will open a possibility to determine the mass hierarchy and measure these parameters simultaneously.

Note that other experimental techniques using atmospheric neutrinos may also prove valuable for determination of the mass hierarchy. In particular, experiments that can separate neutrinos from antineutrinos on an event basis need a significantly lower number of events to obtain the same sensitivity. Thus, such detectors can be smaller in size as compared to the neutrino telescopes. In this context, a magnetized iron calorimeter, such as the India-based Neutrino Observatory [73], could also provide an important contribution to the determination of mass hierarchy. The capabilities of detectors using charge identification were studied in [74].

**4.4.4. Interplay between Accelerator and Atmospheric Neutrinos.** The atmospheric neutrino data can also be used to complement the data from accelerator neutrino experiments in order to extract the most information possible.

As was demonstrated in [74], the atmospheric neutrino determination of the neutrino mass hierarchy can be significantly affected by the addition of external priors and, in particular, may lead to different sensitivity to the neutrino mass hierarchy in the cases of true normal or inverted hierarchy. However, once external input on the neutrino oscillation parameters is included by considering also other experiments, the room to mimic the true oscillation pattern in the wrong hierarchy becomes much more restricted and the sensitivity to the hierarchy increases. Adding the accelerator experiments' own sensitivity to the mass hierarchy, a measurement may be possible even for the current generation of accelerator experiments by the addition of detector capable of lepton charge identification. This has been discussed in [75] and the prospects of using a magnetized iron calorimeter detector to augment the current generation of accelerator experiments are a  $2$ – $4\sigma$  determination of the mass hierarchy within 10 years of data taking, depending on the true value of the oscillation parameters and the characteristics of the detector.

## 5. Discussion and Conclusions

In this paper, we have described the effects of neutrino propagation in matter relevant to experiments with atmospheric and accelerator neutrinos and aimed at the determination of the neutrino mass hierarchy and CP violation. Thus, to a large extent, we have focused on neutrino propagation in the Earth matter.

- (1) At relatively low energies, the dominant effect of neutrino interactions with matter is the elastic forward scattering, which is described by an effective potential. Neutrino evolution in matter is then described by a Schrödinger-like equation including this effective potential. The potential differences for neutrinos of different types influence the flavor evolution of the system of mixed neutrinos. In the majority of realistic

situations, neutrinos propagate in normal (unpolarized nonrelativistic) matter with nearly constant or slowly changing density.

- (2) Matter modifies the neutrino flavor mixing and changes the eigenvalues of the Hamiltonian of propagation. This is equivalent to a modification of the dispersion relations of neutrinos. The influence of matter on mixing of neutrinos has a resonance character. At energies or densities for which the eigenfrequency of the neutrino system with mixing  $\omega_{ij} = \Delta m_{ij}^2/2E$  equals approximately the eigenfrequency of the medium  $2\pi/l_0$ , the mixing in matter becomes maximal. Large mixing shifts the position of the resonance to lower values of the potential. At usual densities, there are two resonances related to the two mass squared differences  $\Delta m_{21}^2$  and  $\Delta m_{31}^2$  between the neutrino mass eigenstates. The resonances are realized in oscillation channels involving electron neutrinos.
- (3) In many practical situations, knowledge of neutrino mixing in matter and the eigenstates of the Hamiltonian in matter allows finding the results of the neutrino flavor evolution immediately. This includes neutrino oscillations in matter with constant density and also adiabatic conversion of neutrinos, where the averaged oscillation results can be written down immediately. In the nonaveraged case, the problem is reduced to finding the oscillation phase (integrating the energy splittings over distance). In this sense the Nature has implemented the most (computationally) simple setups. The very convenient presentation of mixing in matter can be obtained as series expansion in the ratio of the two mass squared differences,  $r_\Delta$  (perturbative diagonalization of the effective Hamiltonian), which allows to understanding a number of subtle results. The simplest and physically transparent description of dynamics of neutrino flavor evolution can be obtained in the propagation basis (in the case of the standard parameterization). In this basis, the CP-violating phase and 2-3 mixing do not influence the evolution and the amplitudes of transitions do not depend on  $\delta$  or  $\theta_{23}$ . The dependence on these parameters appears as a result of projecting the states of the propagation basis back to the flavor states at production and detection. In many practical cases the  $3\nu$  evolution can be reduced to evolution of two neutrino systems with certain corrections.
- (4) There are two practically important cases: (i) neutrino propagation in matter with constant or nearly constant density and (ii) neutrino propagation in matter with slowly (adiabatically) changing density.
- (5) In the case of constant density, flavor evolution has a character of oscillations with parameters determined by mixing and mass splitting in matter. The oscillations are an effect of a phase difference increase in the course of neutrino propagation. The resonance enhancement of oscillations is realized in an energy

region around  $E_R$ . If the density is approximately constant, then the results can be obtained by using perturbation theory in the deviation of the density distribution from a constant one. The accuracy improves if the density profile is symmetric with respect to the middle point of the neutrino trajectory, as is realized for neutrinos crossing the Earth. A simple and rather precise semianalytical description of neutrino oscillations in matter with varying density can be obtained in the limits of small density,  $V < \Delta m_{ij}^2/2E$ , and high density,  $V \gg \Delta m_{ij}^2/2E$ . The latter gives a very accurate description of neutrino flavor evolution in the Earth at  $E > (8-10)$  GeV.

- (6) In a medium with slowly changing density, adiabatic conversion takes place. This effect is related to the change of mixing in matter due to density change. Adiabaticity implies that there are no transitions among the eigenstates of the instantaneous Hamiltonian during propagation. The strongest flavor transformation is realized when the initial density is much larger, and the final one is much lower than the resonance density. In this case, the initial state (and due to adiabaticity, the state at any other moment of evolution) practically coincides with one of the eigenstates. Therefore, oscillation effects are absent and nonoscillatory flavor conversion takes place. This is realized for supernova neutrinos and approximately for high energy solar neutrinos. In general, if the initial mixing is not strongly suppressed, an interplay of adiabatic conversion and oscillations occurs. Adiabatic transformations are also realized for neutrinos with energy  $\leq 1$  GeV propagating in the mantle of the Earth. In particular, this means that the oscillation depth at the detector is determined by mixing at the surface of the Earth and not by mixing at average density. Until now, the matter effects have been observed in solar neutrinos and, indirectly, in atmospheric neutrinos and there is good chance that they will be observed by new generation of the accelerator and atmospheric neutrino experiments.
- (7) Strong flavor transition can be realized without enhancement of mixing. This occurs in matter with periodic or quasiperiodic density change when the parametric resonance condition is fulfilled. For small mixing strong transition requires a large number of periods. A similar enhancement can take place in matter with several layers of different densities. Here the enhancement occurs when a certain correlation between the oscillation phases in each layer and amplitudes of oscillations determined by mixing is present. The case of a medium with 3 layers (1.5 periods) is of practical interest for neutrinos crossing both the mantle and the core of the Earth. For a multilayer medium two conditions must be satisfied to have strong transitions: the amplitude (collinearity) and the phase conditions.
- (8) For neutrinos crossing a small amount of matter, such as accelerator experiments with baselines up to

$(1-2) \cdot 10^3$  km, the column density of matter is small and, according to the minimal width condition, the matter effect on oscillations is small regardless of energy, vacuum mass splitting, and neutrino mixing. Furthermore, if the oscillation phase is small, then mimicking of vacuum oscillations occurs.

- (9) A comprehensive description of the neutrino flavor transitions in the Earth is given in terms of neutrino oscillograms of the Earth. After the recent determination of the 1–3 mixing, the structure of oscillograms is well fixed. The salient features of oscillograms at high energies (due to 1–3 mixing) are the MSW resonance peak in the mantle domain, three parametric ridges, and the MSW peak in the core domain. At low energies (due to 1–2 mixing), there are three peaks, due to the MSW resonance, and the parametric ridge. The positions of all these and other structures are determined by the generalized phase and amplitude conditions. In the case of normal mass hierarchy, the resonance peaks induced by the 1–3 mixing are in the neutrino channels. For inverted mass hierarchy they are in the antineutrino channels. This is the foundation for determining the neutrino mass hierarchy. The resonance structures due to the 1–2 mixing are always in the neutrino channels, since the sign of the small mass square difference has been fixed.
- (10) The CP properties of the oscillograms (their dependence on CP phase) are determined by the CP domains, areas in which the CP violation effect has the same sign. The borders of these domains are approximately determined by the grids of the magic lines (solar and atmospheric magic lines) and the lines where the oscillation phase condition is fulfilled.
- (11) Measurements of matter effects in neutrino oscillations provide a good opportunity to determine the neutrino mass hierarchy. The 1–2 ordering has been determined due to the matter effect of solar neutrinos. The 1–3 ordering can be identified by studying the matter effects in accelerator and atmospheric neutrino experiments. There is a good chance that future studies of the atmospheric neutrinos with multi-megaton underwater (ice) detectors will be able to establish the mass hierarchy. With a threshold of a few GeV, these detectors will be sensitive to the resonance region ( $\sim 6$ – $10$ ) GeV, where the difference of probabilities for the normal and inverted mass hierarchies is maximal. The challenges here are the accuracy of reconstruction of the neutrino energies and directions. Integration over the energy and angle, as well as summation of neutrino and antineutrino signals, diminishes the sensitivity to the hierarchy. Another problem is the degeneracy of the hierarchy effects with the effects of other neutrino parameters, in particular with  $\Delta m_{32}^2$  and  $\theta_{32}$ .
- (12) In accelerator experiments, many of the problems mentioned above are absent. However, existing and

proposed accelerator experiments will cover only peripheral regions of oscillograms where enhancement of oscillations is very weak and oscillatory structures are rather poor. As a consequence the problem of degeneracy here is even more severe.

## References

- [1] L. Wolfenstein, "Neutrino oscillations in matter," *Physical Review D*, vol. 17, no. 9, pp. 2369–2374, 1978.
- [2] V. Barger, K. Whisnant, S. Pakvasa, and R. J. N. Phillips, "Matter effects on three-neutrino oscillations," *Physical Review D*, vol. 22, no. 11, pp. 2718–2726, 1980.
- [3] S. Mikheev and A. Y. Smirnov, "Resonance amplification of oscillations in matter and spectroscopy of solar neutrinos," *Soviet Journal of Nuclear Physics*, vol. 42, pp. 913–917, 1985.
- [4] S. P. Mikheyev and A. Y. Smirnov, "Resonant amplification of  $\nu$  oscillations in matter and solar-neutrino spectroscopy," *Il Nuovo Cimento C*, vol. 9, no. 1, pp. 17–26, 1986.
- [5] S. Mikheev and A. Y. Smirnov, "Neutrino oscillations in a variable density medium and neutrino bursts due to gravitational collapse of stars," *Soviet Physics—JETP*, vol. 64, pp. 4–7, 1986.
- [6] D. Notzold and G. Raffelt, "Neutrino dispersion at finite temperature and density," *Nuclear Physics*, vol. B307, pp. 924–936, 1988.
- [7] B. Pontecorvo, "Mesonium and anti-mesonium," *Soviet Physics—JETP*, vol. 6, p. 429, 1957.
- [8] Z. Maki, M. Nakagawa, and S. Sakata, "Remarks on the unified model of elementary particles," *Progress of Theoretical Physics*, vol. 28, no. 5, pp. 870–880, 1962.
- [9] B. Pontecorvo, "Neutrino experiments and the problem of conservation of leptonic charge," *Soviet Physics—JETP*, vol. 26, pp. 984–988, 1968.
- [10] F. J. Botella, C. S. Lim, and W. J. Marciano, "Radiative corrections to neutrino indices of refraction," *Physical Review D*, vol. 35, no. 3, pp. 896–901, 1987.
- [11] S. Esposito and G. Capone, "Neutrino propagation in a medium with a magnetic field," *Zeitschrift für Physik*, vol. C70, pp. 55–64, 1996.
- [12] H. Nunokawa, V. B. Semikoz, A. Y. Smirnov, and J. W. F. Valle, "Neutrino conversions in a polarized medium," *Nuclear Physics B*, vol. 501, no. 1, pp. 17–40, 1997.
- [13] A. Lobanov and A. Studenikin, "Neutrino oscillations in moving and polarized matter under the influence of electromagnetic fields," *Physics Letters B*, vol. 515, no. 1–2, pp. 94–98, 2001.
- [14] L. Wolfenstein, "Effects of matter on neutrino oscillations," in *Proceedings of the Long-Distance Neutrino Detection (Neutrinos '78)*, West Lafayette, Ind, USA, 1978.
- [15] L. Wolfenstein, "Neutrino oscillations and stellar collapse," *Physical Review D*, vol. 20, no. 10, pp. 2634–2635, 1979.
- [16] E. K. Akhmedov and A. Wilhelm, "Quantum field theoretic approach to neutrino oscillations in matter," *Journal of High Energy Physics*, <http://arxiv.org/abs/1205.6231>.
- [17] N. Cabibbo, "Summary talk," in *Proceedings of the 10th International Workshop on Weak Interactions and Neutrinos*, 1985.
- [18] H. A. Bethe, "Possible explanation of the solar-neutrino puzzle," *Physical Review Letters*, vol. 56, no. 12, pp. 1305–1308, 1986.
- [19] A. Bueno, M. Campanelli, and A. Rubbia, "Physics potential at a neutrino factory: can we benefit from more than just detecting muons?" *Nuclear Physics B*, vol. 589, no. 3, pp. 577–608, 2000.



- [20] M. Freund, "Analytic approximations for three neutrino oscillation parameters and probabilities in matter," *Physical Review D*, vol. 64, no. 5, Article ID 053003, 2001.
- [21] G. L. Fogli, E. Lisi, A. Marrone, D. Montanino, A. Palazzo, and A. M. Rotunno, "Global analysis of neutrino masses, mixings, and phases: entering the era of leptonic CP violation searches," *Physical Review D*, vol. 86, no. 1, Article ID 013012, 10 pages, 2012.
- [22] A. Y. Smirnov and S. Mikheev, "Neutrino oscillations in matter with varying density," in *Quarks '86: Proceedings of the Seminar Tbilisi*, 1986.
- [23] J. Bouchez, M. Cribier, W. Hampel, J. Rich, M. Spiro, and D. Vignaud, "Matter effects for solar neutrino oscillations," *Zeitschrift für Physik C*, vol. 32, no. 4, pp. 499–511, 1986.
- [24] V. K. Ermilova, V. A. Tsarev, and V. A. Chechin, "Parametric enhancement of neutrino oscillations in matter," *Fiz. [Short Notices of the Lebedev Institute]*, vol. 5, p. 26, 1986.
- [25] A. Messiah, "Treatment of electron-neutrino oscillations in solar matter: the MSW effect," in *Proceedings of the Moriond Workshop, Massive Neutrinos*, 1986.
- [26] E. Lisi, A. Marrone, D. Montanino, A. Palazzo, and S. T. Petcov, "Analytical description of quasivacuum oscillations of solar neutrinos," *Physical Review D*, vol. 63, Article ID 093002, 2001.
- [27] A. Friedland, "On the evolution of the neutrino state inside the sun," *Physical Review D*, vol. 64, Article ID 013008, 2001.
- [28] A. Y. Smirnov, D. N. Spergel, and J. N. Bahcall, "Is large lepton mixing excluded?" *Physical Review D*, vol. 49, no. 3, pp. 1389–1397, 1994.
- [29] H. Minakata and H. Nunokawa, "Inverted hierarchy of neutrino masses disfavored by supernova 1987A," *Physics Letters B*, vol. 504, no. 4, pp. 301–308, 2001.
- [30] S. J. Parke, "Nonadiabatic level crossing in resonant neutrino oscillations," *Physical Review Letters*, vol. 57, no. 10, pp. 1275–1278, 1986.
- [31] W. C. Haxton, "Analytic treatments of matter-enhanced solar-neutrino oscillations," *Physical Review D*, vol. 35, no. 8, pp. 2352–2364, 1987.
- [32] S. T. Petcov, "On the non-adiabatic neutrino oscillations in matter," *Physics Letters B*, vol. 191, no. 3, pp. 299–303, 1987.
- [33] P. C. de Holanda, W. Liao, and A. Y. Smirnov, "Toward precision measurements in solar neutrinos," *Nuclear Physics B*, vol. 702, no. 1-2, pp. 307–332, 2004.
- [34] C. Lunardini and A. Y. Smirnov, "The minimum width condition for neutrino conversion in matter," *Nuclear Physics B*, vol. 583, no. 1-2, pp. 260–290, 2000.
- [35] H. Minakata and H. Nunokawa, "Measuring leptonic CP violation by low energy neutrino oscillation experiments," *Physics Letters B*, vol. 495, no. 3-4, pp. 369–377, 2000.
- [36] E. K. Akhmedov, "Matter effects in oscillations of neutrinos traveling short distances in matter," *Physics Letters*, vol. 503, pp. 133–139, 2001.
- [37] E. K. Akhmedov, "Resonance enhancement of the neutrino spin precession in matter and the solar neutrino problem," *Soviet Journal of Nuclear Physics*, vol. 48, pp. 382–383, 1988.
- [38] P. I. Krastev and A. Y. Smirnov, "Parametric effects in neutrino oscillations," *Physics Letters B*, vol. 226, no. 3-4, pp. 341–346, 1989.
- [39] V. Ermilova, V. Tsarev, and V. Chechin, "Buildup of neutrino oscillations in the earth," *Letters to Journal of Experimental and Theoretical Physics*, vol. 43, p. 453, 1986.
- [40] Q. Y. Liu and A. Y. Smirnov, "Neutrino mass spectrum with  $\nu\mu \rightarrow \nu s$  oscillations of atmospheric neutrinos," *Nuclear Physics B*, vol. 524, no. 3, pp. 505–523, 1998.
- [41] Q. Liu, S. Mikheyev, and A. Y. Smirnov, "Parametric resonance in oscillations of atmospheric neutrinos?" *Physics Letters B*, vol. 440, pp. 319–326, 1998.
- [42] S. T. Petcov, "Diffractive-like (or parametric-resonance-like?) enhancement of the Earth (day-night) effect for solar neutrinos crossing the Earth core," *Physics Letters B*, vol. 434, no. 3-4, pp. 321–332, 1998.
- [43] M. Chizhov, M. Maris, and S. Petcov, "On the oscillation length resonance in the transitions of solar and atmospheric neutrinos crossing the earth core," <http://arxiv.org/abs/hep-ph/9810501>.
- [44] M. V. Chizhov and S. T. Petcov, "New conditions for a total neutrino conversion in a medium," *Physical Review Letters*, vol. 83, no. 6, pp. 1096–1099, 1999.
- [45] M. V. Chizhov and S. T. Petcov, "Enhancing mechanisms of neutrino transitions in a medium of nonperiodic constant-density layers and in the Earth," *Physical Review D*, vol. 63, no. 7, Article ID 073003, 2001.
- [46] E. K. Akhmedov, M. Maltoni, and A. Y. Smirnov, "1–3 leptonic mixing and the neutrino oscillograms of the Earth," *Journal of High Energy Physics*, vol. 0705, p. 077, 2007.
- [47] E. Akhmedov, P. Huber, M. Lindner, and T. Ohlsson, "T violation in neutrino oscillations in matter," *Nuclear Physics B*, vol. 608, no. 1-2, pp. 394–422, 2001.
- [48] E. Lisi and D. Montanino, "Earth regeneration effect in solar neutrino oscillations: an analytic approach," *Physical Review D*, vol. 56, no. 3, pp. 1792–1802, 1997.
- [49] A. Takamura and K. Kimura, "Large non-perturbative effects of small on neutrino oscillation and CP violation in matter," *Journal of High Energy Physics*, vol. 0601, p. 053, 2006.
- [50] S. Toshev, "On T violation in matter neutrino oscillations," *Modern Physics Letters A*, vol. 6, p. 455, 1991.
- [51] E. K. Akhmedov, R. Johansson, M. Lindner, T. Ohlsson, and T. Schwetz, "Series expansions for three flavor neutrino oscillation probabilities in matter," *Journal of High Energy Physics*, vol. 0404, p. 078, 2004.
- [52] P. Lipari, unpublished, 1998.
- [53] T. Ohlsson and H. Snellman, "Neutrino oscillations with three flavors in matter: applications to neutrinos traversing the Earth," *Physics Letters B*, vol. 474, no. 1-2, pp. 153–162, 2000.
- [54] M. Jacobson and T. Ohlsson, "Extrinsic CPT violation in neutrino oscillations in matter," *Physical Review D*, vol. 69, Article ID 013003, 2004.
- [55] T. Kajita, "Atmospheric neutrinos," *New Journal of Physics*, vol. 6, pp. 1–34, 2004.
- [56] E. K. Akhmedov, S. Razzaque, and A. Y. Smirnov, "Mass hierarchy, 2-3 mixing and CP-phase with Huge Atmospheric Neutrino Detectors," <http://arxiv.org/abs/1205.7071>.
- [57] T.-K. Kuo and J. T. Pantaleone, "T nonconservation in three neutrino oscillations," *Physics Letters B*, vol. 198, p. 406, 1987.
- [58] H. Minakata and S. Watanabe, "Solar neutrinos and leptonic CP violation," *Physics Letters B*, vol. 468, no. 3-4, pp. 256–260, 1999.
- [59] H. Yokomakura, K. Kimura, and A. Takamura, "Overall feature of CP dependence for neutrino oscillation probability in arbitrary matter profile," *Physics Letters B*, vol. 544, no. 3-4, pp. 286–294, 2002.
- [60] E. Kh. Akhmedov, M. Maltoni, and A. Yu. Smirnov, "Neutrino oscillograms of the Earth: effects of 1-2 mixing and CP-violation," *Journal of High Energy Physics*, vol. 2008, no. 6, article 072, 2008.

- [61] A. Y. Smirnov, “Neutrino oscillations: what is “magic” about the magic baseline?” <http://arxiv.org/abs/hep-ph/0610198>.
- [62] V. Barger, D. Marfatia, and K. Whisnant, “Breaking eight fold degeneracies in neutrino CP violation, mixing, and mass hierarchy,” *Physical Review D*, vol. 65, Article ID 073023, 2002.
- [63] P. Huber, “CP, T and CPT violation in future long baseline experiments,” *Journal of Physics G*, vol. 29, no. 8, pp. 1853–1856, 2003.
- [64] P. Huber and W. Winter, “Neutrino factories and the “magic” baseline,” *Physical Review D*, vol. 68, no. 3, Article ID 037301, 2003.
- [65] R. Gandhi, P. Ghoshal, S. Goswami, P. Mehta, and S. U. Sankar, “Earth matter effects at very long baselines and the neutrino mass hierarchy,” *Physical Review D*, vol. 73, no. 5, Article ID 053001, 2006.
- [66] A. Blondel, “Future neutrino oscillation facilities: physics priorities and open issues,” *Acta Physica Polonica B*, vol. 37, no. 7, pp. 2077–2113, 2006.
- [67] P. Huber, M. Lindner, M. Rolinec, and W. Winter, “Optimization of a neutrino factory oscillation experiment,” *Physical Review D*, vol. 74, no. 7, Article ID 073003, 2006.
- [68] S. K. Agarwalla, S. Choubey, and A. Raychaudhuri, “Unraveling neutrino parameters with a magical beta-beam experiment at INO,” *Nuclear Physics B*, vol. 798, no. 1-2, pp. 124–145, 2008.
- [69] A. Cervera, A. Donini, M. B. Gavela et al., “Golden measurements at a neutrino factory,” *Nuclear Physics B*, vol. 579, no. 1-2, pp. 17–55, 2000.
- [70] O. L. G. Peres and A. Yu. Smirnov, “Testing the solar neutrino conversion with atmospheric neutrinos,” *Physics Letters B*, vol. 456, no. 2-4, pp. 204–213, 1999.
- [71] E. K. Akhmedov, A. Dighe, P. Lipari, and A. Y. Smirnov, “Atmospheric neutrinos at super-Kamiokande and parametric resonance in neutrino oscillations,” *Nuclear Physics B*, vol. 542, no. 1-2, pp. 3–30, 1999.
- [72] D.F. Cowen and D. Grants, *Private communications*.
- [73] INO, India-Based Neutrino Observatory, <http://www.ino.tifr.res.in/ino/>.
- [74] S. T. Petcov and T. Schwetz, “Determining the neutrino mass hierarchy with atmospheric neutrinos,” *Nuclear Physics B*, vol. 740, no. 1-2, pp. 1–22, 2006.
- [75] M. Blennow and T. Schwetz, “Identifying the neutrino mass ordering with INO and NOvA,” *Journal of High Energy Physics*, <http://arxiv.org/abs/1203.3388>.

## Review Article

# Solar Neutrinos

**V. Antonelli,<sup>1</sup> L. Miramonti,<sup>1</sup> C. Peña Garay,<sup>2</sup> and A. Serenelli<sup>3</sup>**

<sup>1</sup> *Dipartimento di Fisica, Università degli Studi di Milano and INFN Milano, Via Celoria 16, 20133 Milano, Italy*

<sup>2</sup> *Instituto de Fisica Corpuscular, CSIC-UVEG, 46071 Valencia, Spain*

<sup>3</sup> *Instituto de Ciencias del Espacio (CSIC-IEEC), Facultad de Ciencias, Campus UAB, 08193 Bellaterra, Spain*

Correspondence should be addressed to V. Antonelli; [vito.antonelli@mi.infn.it](mailto:vito.antonelli@mi.infn.it)

Received 13 July 2012; Accepted 9 October 2012

Academic Editor: Arthur B. McDonald

Copyright © 2013 V. Antonelli et al. This is an open access article distributed under the Creative Commons Attribution License, which permits unrestricted use, distribution, and reproduction in any medium, provided the original work is properly cited.

The study of solar neutrinos has given a fundamental contribution both to astroparticle and to elementary particle physics, offering an ideal test of solar models and offering at the same time relevant indications on the fundamental interactions among particles. After reviewing the striking results of the last two decades, which were determinant to solve the long standing solar neutrino puzzle and refine the Standard Solar Model, we focus our attention on the more recent results in this field and on the experiments presently running or planned for the near future. The main focus at the moment is to improve the knowledge of the mass and mixing pattern and especially to study in detail the lowest energy part of the spectrum, which represents most of the solar neutrino spectrum but is still a partially unexplored realm. We discuss this research project and the way in which present and future experiments could contribute to make the theoretical framework more complete and stable, understanding the origin of some “anomalies” that seem to emerge from the data and contributing to answer some present questions, like the exact mechanism of the vacuum to matter transition and the solution of the so-called solar metallicity problem.

### 1. Motivations for the Solar Neutrino Study

The analysis of neutrinos emitted in the fusion processes inside the Sun is one of most significant examples of the relevant role played by the study of neutrino properties in elementary particle physics and astrophysics and in creating a link between these two sectors [1–13]. The pioneering work in the sixties [14–16] had the main goal of understanding better the way in which our star shines and to test solar models. But the surprising result of an apparent deficit in the electron neutrino flux reaching the detector marked the raise of the so-called solar neutrino puzzle and opened a whole new field of research, that has been central in elementary particle physics for many decades.

The experimental results obtained using different techniques in more than thirty years [17] and the parallel theoretical advancements confirmed at the end the validity of Pontecorvo’s revolutionary idea of neutrino oscillation [18, 19], proving in a crystal clear way that neutrinos are massive and oscillating particles. This is one of the first pieces of clear evidence of the need to go beyond the standard model of

electroweak interactions and the attempt to accommodate the experimental results about neutrino masses and mixing is a test that every theory “beyond the Standard Model” has to pass. Therefore, it is clear why these results had a great impact on elementary particle physics and also on cosmological models. At the same time, the possibility of measuring directly at least some components of the solar neutrino spectrum and of recovering in an indirect way the value of total solar neutrino flux have been fundamental for the progressive refinement of the standard solar model (SSM), which evolved during these years and is now in a general good agreement with the solar neutrino experiments.

Despite the fundamental steps forward made in the last decades, many questions are still open about the real nature and the main properties of neutrinos and the exact mixing mechanism, for example are neutrinos Majorana or Dirac fermions, the determination of mass hierarchy and exact mass values, accurate determination of the mixing angles, and presence of CP violation. The solar neutrino experiments presently running or planned for the future can contribute to solve at least some of these puzzles. The new frontier in this

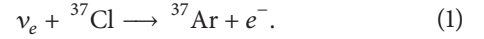
field is the study of the low energy part of the solar neutrino spectrum, which represents the great majority of the spectrum and is still an almost unexplored realm. Some of the challenges ahead are reducing significantly the indetermination on *pep* and CNO neutrinos and attaching the *pp* solar neutrino measurement. This would be essential to test the stability and consistency of the standard explanation of the oscillation mechanism, confirming or definitely disproving the presence of discrepancies between theory and experiments, which has lately stimulated a flourishing of models introducing the so-called “Non Standard Interactions” (Section 6.1). Once more, these results would be of great interest to improve the knowledge both of elementary particle properties and interactions and of the astrophysical models of the Sun. They could help also to discriminate between different versions of the solar models, for instance, for what concerns the so-called “solar abundance problem,” and to deepen the comparison with the results coming from other studies of solar properties, for example, from helioseismology. These studies would of course imply a further improvement of the already known detection techniques and the introduction of new ones (see, for instance, Section 7). Also from this point of view, solar neutrino physics will continue to give a stimulating contribution both to elementary particle physics and to astrophysics.

In the present paper we are going to treat all of these topics, focusing our attention on the important advancements of the last years, on the main open questions, and the future perspectives of solar neutrino physics. In Section 2, the interested reader can find a short review of the history of the so-called “solar neutrino puzzle,” from the the radiochemical experiments results up to the first data obtained by SNO and the reactor experiment KamLAND, that solved this puzzle. The following section is devoted to the standard solar model, its main input parameters (with the relative uncertainties) and predictions, the helioseismology, and the “metallicity problem.” The other ingredient essential for the calculation of the expected neutrino signal, the neutrino flavor conversion probability (in vacuum and matter), is discussed in Section 4. In Section 5, we report and discuss the important advancements which took place after 2002: from the results of the different phases of SNO and Super-Kamiokande to the discussion of the impact on solar neutrino physics of the data obtained by the reactor experiment KamLAND and finally to the first real-time measurements of the low energy solar neutrinos performed by Borexino. The discussion on the present phenomenological situation is completed in Section 6, with a particular attention to three flavors and to free fluxes analyses. We close the paper turning our attention to the near and far future, discussing the experimental and the theoretical challenges in Sections 7, 8, and 9.

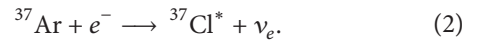
## 2. Brief History and Solution of the Solar Neutrino Problem

**2.1. From Homestake to Super-Kamiokande.** The first experiment built to detect solar neutrinos took place in the Homestake gold mine in South Dakota [14–16]. The detector

consisted of a large tank containing 615 metric tons of liquid perchloroethylene, chosen because it is rich in chlorine and the experiment operated continuously from 1970 until 1994. Neutrinos were detected via the reaction:



The energy threshold of this reaction,  $E_{\text{th}} = 814 \text{ keV}$ , allowed the detection of  ${}^7\text{Be}$  and  ${}^8\text{B}$  (and a small signal from the CNO and *pep*) but not that of *pp* neutrinos, because of their low maximal energy of 0.42 MeV. The radioactive  ${}^{37}\text{Ar}$  isotopes decay by the electron capture with a  $\tau_{1/2}$  of about 35 days into  ${}^{37}\text{Cl}^*$ :



Once a month, after bubbling helium through the tank, the  ${}^{37}\text{Ar}$  atoms were extracted and counted. The number of atoms created was only about 5 atoms of  ${}^{37}\text{Ar}$  per month in 615 metric tons  $\text{C}_2\text{Cl}_4$ . The number of detected neutrinos was lower (about 1/3) than the value expected by the Solar Standard Model. This discrepancy is the essence of the solar neutrino problem, which has been for many years an important puzzle among physicists.

There were three possible explanations to the solar neutrino problem. The first one was to consider that Homestake could be wrong, that is, the Homestake detector could be inefficient and, in this case, its reactions would not have been predicted correctly. After all, to detect a handful of atoms per week in more than 600 metric tons of material is not an easy task (the science that studies the interior of the Sun by looking at its vibration modes). The second one was to consider that the SSM was not correct, but as helioseismology started to provide independent tests of solar models, the SSM passed all tests. Indeed, nonstandard solar models constructed ad hoc to resolve the solar neutrino problem seemed very unlikely when scrutinized under the light of helioseismology. The third one, and the strangest hypothesis, was to consider that something happens to the neutrinos while traveling from the core of the Sun to the Earth.

The first real-time solar neutrino detector, Kamiokande, was built in Japan in 1982–1983 [20]. It consisted of a large water Čerenkov detector with a total mass of 3048 metric tons of pure water. In real-time neutrino experiments, scientists study the bluish light produced by the electrons scattered by an impinging neutrino according to the following equation:



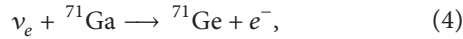
In the Kamiokande detector, light is recorded by 1000 photomultiplier tubes (PMT) and the energy threshold of the reaction is  $E_{\text{th}} = 7.5 \text{ MeV}$ ; therefore, only  ${}^8\text{B}$  and *hep* neutrinos are detected (Here and in the rest of the paper, following the convention commonly adopted in the literature, we use the term “energy threshold” to indicate the lowest observable neutrino energy also for Čerenkov’s detector experiments. However, it is important to bear in mind that for these experiments, differently from the radiochemical ones, there is not a real energy threshold for the reaction and the lowest limit on



the detectable energy is, instead, mainly due to the difficulty of separating the signal from the radioactive background due to natural sources and impurities.). At the beginning of the 90s, a much larger version of the detector was built, Super-Kamiokande, where the active mass was more than 50000 metric tons of pure water viewed by about 11200 PMTs. In Super-Kamiokande, the energy threshold was lowered to  $E_{\text{th}} = 5.5 \text{ MeV}$  [21].

Radiochemical experiments integrate in time and in energy because they are slow and need time to produce measurable results. This causes the loss of information about single individual energy values. In real-time experiments, instead, it is possible to obtain single values and therefore a spectrum energy to distinguish the different neutrino contributions. Furthermore, given that the scattered electron maintains the same direction of the impinging neutrino, it is possible to infer the direction of the incoming neutrino and therefore to point at its source. This proved that the detected neutrinos actually came from the Sun. The number of detected neutrinos was about 1/2 lower than the number of expected ones, aggravating the solar neutrino problem.

Until 1990, there were no observations of the initial reaction in the nuclear fusion chain, that is, the detection of  $pp$  neutrinos, which are less model dependent and hence more significant to test the hypothesis that fusion of hydrogen powers the Sun. Two radiochemical experiments were built in order to detect solar  $pp$  neutrinos, both employing the reaction



which has a threshold of  $E_{\text{th}} = 233 \text{ keV}$ .

In the Gallex experiment, located at the Gran Sasso underground laboratory in Italy, 30 metric tons of natural gallium were employed [22, 23], while in the Soviet-American experiment (SAGE), located in the Baksan underground laboratory, there were more than 50 metric tons of metallic gallium [24]. Calibration tests with an artificial neutrino source,  ${}^{51}\text{Cr}$ , confirmed the efficiency of both detectors. Once again, the measured neutrino signal was smaller than predicted by the SSM ( $\approx 60\%$ ).

All experiments detected fewer neutrinos than expected from the SSM. Table 1 summarizes the ratios between the observed and the expected neutrino interaction rates for all the experiments before SNO.

**2.2. The Advent of SNO and KamLAND: The Solution of the Solar Neutrino Problem.** The real breakthrough in solar neutrino physics was due to the advent of the SNO (Sudbury Neutrino Observatory) experiment. It had the peculiarity to measure simultaneously, by means of a deuterium Čerenkov detector, three different interaction channels for neutrinos: the neutral current (NC:  $\nu_X + d \rightarrow \nu_X + p^+ + n$ ), receiving contributions from all active flavors, the elastic scattering (ES:  $\nu_X + e^- \rightarrow \nu_X + e^-$ ), and the charged current (CC:  $\nu_e + d \rightarrow e^- + p^+ + p^+$ ), that is, sensitive only to electronic neutrinos. In this way, it has been possible to prove in a clear and direct way that the measured total neutrino flux was in a very good agreement with the SSM predictions, but only a fraction of

TABLE 1: Ratios of the observed versus expected neutrino rates in the four solar neutrino experiments (before SNO, see later).

Homestake	$0.34 \pm 0.03$
Super-K	$0.46 \pm 0.02$
SAGE	$0.59 \pm 0.06$
Gallex and GNO	$0.58 \pm 0.05$

these neutrinos had conserved its flavor during their way from the production point in the Sun to the detector.

The first SNO data [25], including elastic scattering and charged current analysis, published in 2001, confirmed the results obtained by previous solar neutrino experiments, mainly by Super-Kamiokande [26], providing a significant evidence (at the  $3.3\sigma$  level) of the presence of a nonelectronic active neutrino component in the solar flux. For the first time, it was possible to indicate the large mixing angle (LMA) as the preferred solution of the solar neutrino puzzle, even if different alternative possibilities (and in particular the low probability, low mass —LOW— solution) were still surviving [27, 28]. In the following years, the SNO experiment measured also the neutral current channel, using different techniques. The data of these different “phases” of the experiment are usually reported as SNO I [29], SNO II [30] (characterized by the addition of salt to improve the efficiency of neutral current detection) and SNO III [31] (with the use of helium chamber proportional counters).

The year 2002 is very often denoted as the “annus mirabilis” of solar neutrino physics: in April the first SNO results including neutral current detection [29, 32] marked a turning point in the history of the solar neutrino problem, in October the Nobel prize for physics was awarded to Davis [33] and Koshiba (for their pioneering work on the detection of cosmic neutrinos), and in December of the same year the first results of the Kamiokande Liquid scintillator antineutrino detector (KamLAND) [34] offered the first clear terrestrial confirmation of the validity of the oscillation solution to the solar neutrino problem.

The total  ${}^8\text{B}$  neutrino flux,  $\phi_{\text{NC}} = 5.09^{+0.44}_{-0.43} (\text{stat})^{+0.46}_{-0.43} \times (\text{syst}) \times 10^6 \text{ cm}^{-2} \text{ s}^{-1}$ , measured by SNO with neutral currents was in a very good agreement with the SSM [35]. Assuming the standard shape for the component of the solar neutrino flux (undistorted spectrum hypothesis), the SNO collaboration recovered also a value of the nonelectronic component of the flux which was  $5.3\sigma$  different from zero, providing a direct proof of the validity of the oscillation hypothesis. These data were also decisive to indicate the LMA region as the solution to the solar neutrino puzzle.

Looking at the oscillation probability, it is apparent that the reactor experiments that run before KamLAND, and used neutrino energy beams of the order of the MeV with a baseline of the order of 1 km, could test only values of  $\Delta m^2$  above  $10^{-3} \text{ eV}^2$  (For instance, in a simple 2-flavor analysis, the flavor transition probability is given by the expression  $P_{12} = \sin^2(2\theta_{12})\sin^2(\Delta m_{12}^2 (\text{eV}^2)L(\text{km})/4E(\text{GeV}))$ , where  $\theta_{12}$  is the mixing angle between the two flavors,  $\Delta m_{ij}^2 \equiv m_1^2 - m_2^2$  the difference of the masses squared,  $L$  the distance traveled,

and  $E$  the neutrino energy.). The KamLAND experiment, instead, with an average baseline of about 180 km, was ideal to probe the LMA region, which corresponds to values of  $\Delta m^2$  of the order  $10^{-5}$ – $10^{-4}$  eV<sup>2</sup> [36–38]. The KamLAND experiment studied the ratio of the number of inverse  $\beta$  decay events (due to reactor  $\bar{\nu}_e$  with an energy threshold of 3.4 MeV) to the expected number of events without disappearance and also the spectrum shape [34]. The observed deficit of events was inconsistent with the expected rate in absence of oscillation at the 99.95% confidence level.

Since one would expect a negligible reduction of the  $\bar{\nu}_e$  flux from the SMA, LOW, and vacuum solar neutrino solutions, the LMA was the only oscillation solution compatible with KamLAND results and CPT invariance. This evidence was further reinforced by the data published by the collaboration in the following years (with greater statistical precisions and reduced systematic errors), which showed also a spectral distortion in a very good agreement with the oscillation solution [39–41]. KamLAND data also restricted the allowed LMA region in a significant way. The preferred values for  $\Delta m_{12}^2$  and  $\theta_{12}$  are slightly higher than the ones corresponding to the best fit solution of the solar neutrino experiments, but this small tension can be explained by taking into account the experimental uncertainties. Moreover, the difference on the  $\Delta m_{12}^2$  parameter has been reduced by the more recent solar neutrino data.

### 3. Standard Solar Model

SSMs have to be understood, primarily, as a framework within which solar models can be constructed and clear predictions can be made with respect to the properties of the solar interior, including the production of solar neutrinos. The defining characteristics are simple: the SSM is the result of the evolution of a  $1 M_\odot$  star since its formation and the evolutionary models have to include the physical ingredients considered *standard* in stellar structure and evolution models (here, *standard* also implies trying to keep to a minimum the number of free tunable parameters—knobs—in the model). SSMs are therefore progressively refined as our understanding of stellar physics progresses.

In practice, an SSM is constructed as follows. An initial chemically homogeneous model of a  $1 M_\odot$  stellar model on the pre-main sequence is constructed with a composition determined by a guess (educated one) for the initial mass fractions of hydrogen  $X_{\text{ini}}$ , helium  $Y_{\text{ini}}$ , and metals  $Z_{\text{ini}}$  ( $X_{\text{ini}} + Y_{\text{ini}} + Z_{\text{ini}} = 1$ ); additionally, a third free parameter has to be specified, the mixing length parameter  $\alpha_{\text{MLT}}$  of convection. This model is then evolved up to the solar system age  $\tau_\odot = 4.57$  Gyr [42, 43]. At this age, the model is required to match the present-day solar luminosity  $L_\odot$  and radius  $R_\odot$ , as well as the surface metal-to-hydrogen abundance ratio  $(Z/X)_\odot$ . The initial and final surface metal-to-hydrogen ratios differ by about 10% to 15% due to the effects of gravitational settling. In general, the SSM constructed with the first set of guesses for  $\alpha_{\text{MLT}}$ ,  $Y_{\text{ini}}$ , and  $Z_{\text{ini}}$  will not lead to a satisfactory agreement with the surface constraints, and an iterative procedure is used to refine the free parameters until the right surface

conditions are achieved at  $\tau_\odot$ . In general, surface conditions are matched to one part in  $10^5$  or  $10^6$  within two or three iterations. It is important to keep in mind that the SSM is not just a snapshot aimed at representing the present-day structure of the Sun, but actually the result of taking into account all its previous history. There are alternative ways to construct a model of the present-day solar structure using, for example, helioseismic constraints. This kind of models is constructed “ad-hoc” to match helioseismic data and is, therefore, a limited predictive power.

The internal structure of an SSM depends on the values adopted for the three constraints mentioned above and, of course, on the physical inputs of the models such as the radiative opacities, cross-sections of nuclear reactions, and others. Next, we describe the changes/updates that have occurred during the last decade that impact predictions of solar models.

#### 3.1. Input Physics and Parameters

**3.1.1. Solar Surface Composition.** The constraint imposed by the surface metallicity of the Sun or, more precisely, the surface metal-to-hydrogen ratio  $(Z/X)_\odot$  is critical in the construction of solar models. The reason is that, aside from the 10 to 15% change in this value due to the action of gravitational settling,  $(Z/X)_\odot$  determines almost directly the metallicity of solar models. As for any other star, the metal content in the Sun has a fundamental role in its structure through its contribution to the radiative opacity  $\kappa$ , which determines, in turn, the temperature gradient in the radiative solar interior. It is important, in fact, that the abundance of individual metals are accurately determined, because different elements contribute to the radiative opacities in different regions of the Sun.

The abundance of metals in the solar surface has to be determined or inferred from a variety of sources: photospheric abundances from solar spectra, chemical analysis of primitive meteorites, emission lines from the solar corona, and composition of the solar wind [44]. While meteoritic abundances are the most precisely determined, at 2/3 of the solar metallicity is composed by the volatile elements C, N, and O and can only be determined from the analysis of the solar spectrum.

Over the last decade, the development of three-dimensional radiation hydrodynamic (3D RHD) models of the solar atmosphere has prompted a thorough revision of the solar composition determined from the solar spectrum. These 3D RHD models of the solar atmosphere capture the dynamics of convection and its interaction with the radiation field and are able to reproduce features such as the solar granulation pattern, observed limb-darkening, and asymmetries in the shapes of spectral lines [45]. The structure of the solar model atmospheres derived by different groups are nicely consistent with each other, adding to the credibility of the models. Newly derived spectroscopic abundances rely on the 3D atmosphere model or more appropriately on a one-dimensional model obtained from a suitably averaged 3D model, as the background on top of which detailed radiative transfer and line formation calculations are performed *a posteriori*. It is this

second step that leads, finally, to the determination of the abundances of the different elements. The most thorough and consistent determination of the solar photospheric abundances based on 3D model atmospheres has been presented by Asplund and collaborators [46, 47], although the revision on key elements like oxygen was initially published already in 2001 [48]. In addition to using 3D RHD atmosphere models, nonlocal thermodynamic equilibrium has been taken into account when computing the line formation for some key elements such as C, N, and O. Also, and this is of particular importance for oxygen, blends in the solar spectrum that had been previously unnoticed were identified and taken into account in the determination of abundances. The most relevant result in the context of solar models and neutrinos is that abundances of CNO elements (also Ne, but this is mostly because its abundance ratio to oxygen is assumed fixed) have been revised down by 30% to 40%. Combining the abundance of all metals, the present-day metal-to-hydrogen ratio that has been obtained is  $(Z/X)_{\odot} = 0.0178$  [46]. This represents a large decrease in comparison with previously accepted values, 0.0245 [49] and 0.0229 [50], that have been widely used in solar modeling. We note, however, that results by Asplund have not been unchallenged. In fact, also based on 3D RHD model solar atmospheres, larger CNO abundances have been derived [51] to yield  $(Z/X)_{\odot} = 0.0209$ , much closer to older determinations. Discrepancies between authors seem to have their origin at the preferred set of spectral lines each group uses and on using either a spectral synthesis or equivalent width techniques to determine the final abundances.

In the last decade, there have been two flavors in SSM calculations. In one case, a *high* solar metallicity from older determinations [49, 50] is adopted; we will generically refer to these models as *high-Z* solar models. In the other case, a *low*  $(Z/X)_{\odot}$  [46, 47] is taken from and we refer to these, not surprisingly, as the *low-Z* solar models. Differences in the structure of *high-Z* and *low-Z* models are readily noticeable in quantities such as the internal sound speed and density profiles, the depth of the solar convective envelope, and the surface helium abundance among others. The deficit that *low-Z* models have in matching helioseismic constraints has been named the solar abundance problem in the literature, in clear analogy to the solar neutrino problem. We discuss it in some detail in Section 3.2.

**3.1.2. Radiative Opacities.** The most widely used calculations of atomic radiative opacities, appropriate for solar interiors, are those from OPAL [52]. However, the opacity project (OP) released in 2005 a completely independent set of atomic radiative opacities for stellar interiors [53]. In the case of the solar radiative interior, differences between OPAL and OP Rosseland mean opacities are of the order of a few percent, with OP being larger by about 3% at the base of the convective zone and 1% to 2% smaller in the central regions (see Figure 7 in [53]). At low temperatures neither OP nor OPAL atomic opacities are adequate, because the possible formation of molecules have to be taken into account and, therefore, they have to be complemented by low-temperature opacities [54]. However, due to the relatively high solar temperature, their influence in the properties of solar models is rather limited.

**3.1.3. Nuclear Reactions Cross-Sections.** Experimental and theoretical work on the determination of nuclear cross-sections have been very active fields with a strong impact on solar model predictions of solar neutrino fluxes (A nonresonant charged-particle induced reaction cross-section can be written as  $\sigma(E) = (S(E)/E) \exp[-2\pi\eta(E)]$  where  $\eta(E) = Z_1 Z_2 \alpha / v$  is the Sommerfeld parameters,  $v = \sqrt{2E/\mu}$ ,  $\alpha$  the fine structure constant in natural units, and  $\mu$  the reduced mass of the interacting nuclei. The nuclear physics is isolated in  $S(E)$ , the astrophysical or S-factor, a slowly varying function of energy that can be more accurately extrapolated from experimental data down to the energy of the Gamow peak.). Recently, a set of recommended rates and uncertainties, expressed through the S-factor, for all the reactions both in the pp-chains and CNO-bicycle that are relevant to solar modeling and neutrino production, has been published (Solar Fusion II, [55], hereafter SFII). The results presented in SFII reflect the progress made in laboratory and theoretical nuclear astrophysics over the last decade, since the publication of the seminal Solar Fusion I (SFI) article [56]. Unfortunately, for reasons of space, here we cannot review in detail every reaction. Instead, we provide in Table 2 the standard S-factors at zero energy,  $S(0)$ , and the uncertainties recommended in SFII for the most relevant reactions. For comparison, with results from SFI are also shown. The impact of changes in key reactions on the production of neutrino fluxes is discussed in Section 3.3. The reader is referred to the SFII paper and references therein for details on the experimental and theoretical developments in nuclear astrophysics related to the Sun during the last decade.

**3.2. Solar Models: Helioseismology.** Helioseismology, the study of the natural oscillations of the Sun, provides a unique tool to determine the structure of the solar interior. The 90s witnessed a rapid development of helioseismic observations and analysis techniques, which led, in very few years, to an accurate characterization of the solar interior [57]. The agreement between SSMs and helioseismic inferences of the solar structure [35, 58] provided a strong support to the accuracy with which SSMs could predict the  $^8\text{B}$  neutrino flux and, therefore, a strong indication, before Kamland and SNO results found evidence of neutrino flavor oscillations, that the solution to the solar neutrino problem had to be found in the realm of particle physics.

In the context of the present paper, the most relevant results from helioseismology are the following (The Sun is characterized by an outer region where energy is transported by convection. The boundary between this region, located at  $R_{\text{CZ}}$ , and the radiative interior can be accurately located by helioseismology because the discontinuity in the slope of the temperature gradient across this boundary leaves its imprint in the solar sound speed profile. The depth of the envelope can be located by helioseismology because properties of solar oscillations are sensitive to the derivative of the sound speed as a function of depth.). The depth of the convective envelope is  $R_{\text{CZ}} = 0.713 \pm 0.001 R_{\odot}$  [59] and the surface helium abundance  $Y_{\text{S}} = 0.2485 \pm 0.0034$  [60]. The sound speed differences between the Sun and a reference solar model can



TABLE 2: Standard astrophysical factors and uncertainties for key nuclear reactions in the  $pp$ -chains and CNO-bicycle. SFII represents the state-of-the-art [55]; SFI [56] shows, for comparison, the situation around 1998.

Reaction		SFII S(0) [keV b]	SFI S(0) [keV b]
$S_{11}$	$p(p, e^+ \nu_e) d$	$4.01 \times 10^{-22} (1 \pm 0.010)$	$4.00 \times 10^{-22} (1 \pm 0.005)$
$S_{33}$	${}^3\text{He}({}^3\text{He}, 2p){}^4\text{He}$	$5.21 \times 10^3 (1 \pm 0.052)$	$5.4 \times 10^3 (1 \pm 0.074)$
$S_{34}$	${}^3\text{He}({}^4\text{He}, \gamma){}^7\text{Be}$	$5.6 \times 10^{-1} (1 \pm 0.054)$	$5.3 \times 10^{-1} (1 \pm 0.094)$
$S_{\text{hep}}$	${}^3\text{He}(p, e^+ \nu_e){}^4\text{He}$	$8.6 \times 10^{-20} (1 \pm 0.30)$	$2.3 \times 10^{-20}$
$S_{17}$	${}^7\text{Be}(p, \gamma){}^8\text{B}$	$2.08 \times 10^{-2} (1 \pm 0.077)$	$1.9 \times 10^{-2} (1^{+0.20}_{-0.10})$
$S_{1,14}$	${}^{14}\text{N}(p, \gamma){}^{15}\text{O}$	$1.66 (1 \pm 0.072)$	$3.5 (1^{+0.11}_{-0.46})$

be obtained by inversion from the oscillation frequencies with a formal error of a few parts per  $10^{-4}$  for most of the solar interior  $0.07 \leq R/R_\odot \leq 0.95$  [61, 62]. Most recently, using a time series 4752 days long from the Birmingham Solar Oscillation Network, improved results on the sound speed in the solar core have been obtained [63]. The density profile can also be determined from the inversion of frequencies, but with worse precision than for the sound speed, and we therefore assign to it a secondary role in constraining the solar structure.

As mentioned previously, metals determine to a large extent the radiative opacity in the solar interior and, in this way, define the temperature stratification from below of the convective envelope inwards, to the solar center. At the base of the convective zone, for example, metals are responsible for about 70% of the total radiative opacity with O, Fe, and Ne being the main contributors. In the solar core, where light metals are completely ionized, the contribution from Fe and, to a lesser extent Ni, Si, and S, is still above 30%. In view of this, it is not surprising that the low CNO and Ne abundances determined from 3D model atmospheres have a strong impact on the structure of the solar interior.

It has been clear since initial works where  $low$ -Z SSMs were presented that low  $(Z/X)_\odot$  values posed a problem, later named the solar abundance problem, for solar modeling [60, 67–69]. In short, all helioseismic predictions of these models are in disagreement with observations. On the other hand,  $high$ -Z SSMs have consistently reproduced earlier success [58]. The solar abundance problem represents the incompatibility between the best solar atmosphere and interior models available [70]. In this paper, we will base the presentation and discussion of results on the most up-to-date standard solar models that we identify as SFII-GS98 and SFII-AGSS09 [64], representative of  $high$ -Z and  $low$ -Z SSM families defined in Section 3.1, respectively. With the exception made on small quantitative variations, results based on these models are extensible to results for all SSMs available in the literature corresponding to each of the two families.

The most important characteristics of the SFII-GS98 and SFII-AGSS09 models are summarized in Table 3. Helioseismic constraints are also included for comparison when appropriate. The disagreement between SFII-AGSS09 and helioseismic data is evident in the surface metallicity and helium abundances,  $Z_s$  and  $Y_s$ , and in the depth of the convective envelope  $R_{CZ}$ . A similar conclusion could be drawn from comparing  $Y_{\text{ini}}$ ; however, the determination of the solar

value of  $Y_{\text{ini}}$  [71] depends strongly on the seismic value for  $Y_s$  and, therefore, it is not an independent constraint. When model uncertainties are included, the discrepancy between SFII-AGSS09 and seismic results are, for each of the quantities mentioned above, of the order 3 to  $4-\sigma$  [72]. On the contrary, the SFII-GS98 model performs very well, within  $1-\sigma$ , when model uncertainties are accounted for.

Very explicit manifestations of the solar abundance problem are shown in the plots in Figure 1, where degradation in the sound speed and density profiles found in  $low$ -Z SSMs are clearly evident. Particularly the peak in the sound speed profile differences found right below the convective zone is 4 times larger in the  $low$ -Z SFII-AGSS09 than in the  $high$ -Z SFII-GS98 model. The reason is the wrong location of  $R_{CZ}$  in the model, caused by the lower opacity which, in turn, is due to the low abundance of metals. The density profile also shows very large discrepancies, but they are less telling. Density inversions include as a constraint the known value of the solar mass and for this reason small differences in the core, where density is large, translate into the large difference seen in the outer envelope. The average rms in the sound speed and density differences,  $\langle \delta c/c \rangle$  and  $\langle \delta \rho/\rho \rangle$ , also show that  $low$ -Z models are about 4 times worse than  $high$ -Z models.

Low-degree helioseismology provides useful information about the solar innermost regions. Specific combinations of mode frequencies enhance the signal that the structure of the solar core imprints on the oscillation pattern [73]. This has been used to determine the mean molecular weight averaged over the innermost 20% solar core [66],  $\langle \mu_C \rangle$  in Table 3. Comparison with SSMs results shows that  $\langle \mu_C \rangle$  is too low in  $low$ -Z models as a result of the lower helium abundance ( $Y_C$ ). This is due to the lower temperature in the solar core and the constraint imposed by the solar luminosity. The decreased nuclear energy production originated by a smaller core temperature has to be compensated by an increased hydrogen mass fraction, therefore leading to a lower molecular weight. It is interesting to note this puts a stringent constraint in the amount of rotational mixing that can take place in the solar core if the  $low$ -Z abundances are correct, since any mixing would lower the molecular weight even more, by bringing fresh hydrogen from outer regions, and make the agreement with helioseismic data worse.

The current situation regarding SSMs and their performance against helioseismic inferences on the solar structure can be summarized as follows. SSMs that use solar abundances derived from 1D model atmospheres [49, 50], that



TABLE 3: Main characteristics of SSMs representative of *high-Z* (GS98) and *low-Z* (AGSS09) solar compositions. Models have been computed including the most up-to-date input physics [64]. Helioseismic constraints are given when available. See text for details.

	SFII-GS98	SFII-AGSS09	Helioseismology
$(Z/X)_\odot$	0.0229	0.0178	—
$Z_\odot$	0.0170	0.0134	$0.0172 \pm 0.002$ [65]
$Y_\odot$	0.2429	0.2319	$0.2485 \pm 0.0034$ [60]
$R_{CZ}/R_\odot$	0.7124	0.7231	$0.713 \pm 0.001$ [59]
$\langle \delta c/c \rangle$	0.0009	0.0037	—
$\langle \delta \rho/\rho \rangle$	0.011	0.040	—
$Z_C$	0.0200	0.0159	—
$Y_C$	0.6333	0.6222	—
$\langle \mu_C \rangle$	0.7200	0.7136	$0.7225 \pm 0.0014$ [66]
$Z_{\text{ini}}$	0.0187	0.0149	—
$Y_{\text{ini}}$	0.2724	0.2620	—

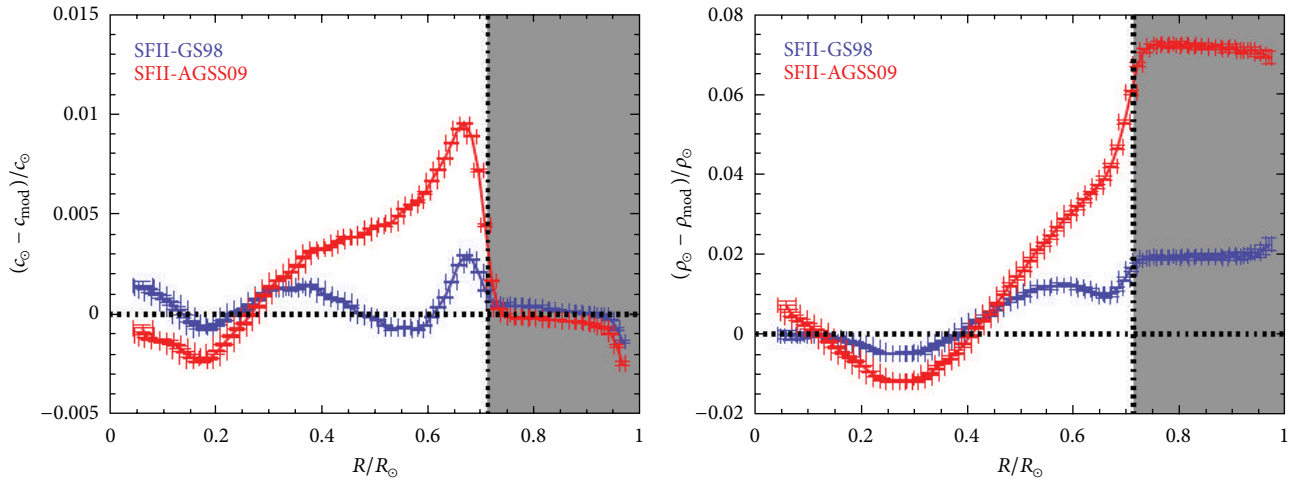


FIGURE 1: Sound speed and density relative differences between solar models and the Sun as determined from helioseismic inversions [72]. The convective envelope is depicted by the grey area.

is, *high-Z* models, reproduce overall the most important seismic constraints. Improvements in the input physics, for example, radiative opacities and nuclear reaction rates, that have occurred over the last 10 years introduce only small changes to the solar structure as seen by helioseismology. On the other hand, the solar abundance problem arises if the solar surface composition used to construct SSMs are derived from the most sophisticated 3D RHD solar model atmospheres. The family of *low-Z* SSMs does not match any helioseismic constraint.

Have we reached the limit where the paradigm of the SSM is not good enough as a model of the solar interior? Are the 3D-based determinations of solar abundances systematically underestimating the metallicity of the solar surface? Does the microscopic input physics in solar models, for example, radiative opacities, need to be thoroughly revised? It is not possible to advance answers to these questions, but solar neutrino experiments can play an important role in guiding the research towards the solution of the solar abundance problem. In the next section, we discuss the current status on the theoretical predictions of solar neutrino fluxes and the prospects of using solar neutrinos to constraint the properties of the solar core.

### 3.3. Solar Models: Neutrino Fluxes

**3.3.1. Production.** Based on theoretical arguments and indirect evidence, it has long been believed that the source of energy of the Sun is the conversion of protons into helium,  $4p \rightarrow {}^4\text{He} + 2e^+ + 2\nu_e + \gamma$ . The original quest for solar neutrinos was indeed the search for the experimental confirmation of this hypothesis (Under peculiar conditions reached in advanced phases of stellar evolution, hydrogen can be converted into helium by other cycles like the NaMg-cycle. While important for nucleosynthesis or intermediate mass elements, these processes are not energetically relevant.). In more detail, hydrogen burning in the Sun (and in all other hydrogen-burning stars) takes place either through the pp-chains or the CNO-bicycle [43, 75]. Proton fusion through the pp-chains is a primary process because only protons need to be present in the star. On the contrary, the CNO-bicycle is secondary because the proton fusion relies on, and is regulated by, the abundance of C, N, and O which act as catalyzers. This qualitative difference is very important, since it renders neutrino fluxes from the CNO-bicycle a very good diagnostic tool to study properties of the solar core, particularly its composition, as it will be discussed below. A general discussion

TABLE 4: SSM predictions for solar neutrino fluxes (second and third columns) and solar neutrino fluxes (fourth column) inferred from all available neutrino data. Units are, in  $\text{cm}^{-2} \text{s}^{-1}$ , as usual:  $10^{10}$  (*pp*),  $10^9$  ( ${}^7\text{Be}$ ),  $10^8$  (*pep*,  ${}^{13}\text{N}$ ,  ${}^{15}\text{O}$ )  $10^6$  ( ${}^8\text{B}$ ,  ${}^{17}\text{F}$ ), and  $10^3$  (*hep*). Note that the limit on the fluxes relative to the CNO cycle do not contain yet the information coming from recent Borexino result [74]. A revised analysis including these data is in progress.

Flux	SFII-GS98	SFII-AGSS09	Solar	BP04
<i>pp</i>	5.98 ( $1 \pm 0.006$ )	6.03 ( $1 \pm 0.006$ )	6.05 ( $1^{+0.003}_{-0.011}$ )	5.94 ( $1 \pm 0.01$ )
<i>pep</i>	1.44 ( $1 \pm 0.012$ )	1.47 ( $1 \pm 0.012$ )	1.46 ( $1^{+0.010}_{-0.014}$ )	1.40 ( $1 \pm 0.02$ )
<i>hep</i>	8.04 ( $1 \pm 0.30$ )	8.31 ( $1 \pm 0.30$ )	18 ( $1^{+0.4}_{-0.5}$ )	7.8 ( $1 \pm 0.16$ )
${}^7\text{Be}$	5.00 ( $1 \pm 0.07$ )	4.56 ( $1 \pm 0.07$ )	4.82 ( $1^{+0.05}_{-0.04}$ )	4.86 ( $1 \pm 0.12$ )
${}^8\text{B}$	5.58 ( $1 \pm 0.13$ )	4.59 ( $1 \pm 0.13$ )	5.00 ( $1 \pm 0.03$ )	5.79 ( $1 \pm 0.23$ )
${}^{13}\text{N}$	2.96 ( $1 \pm 0.15$ )	2.17 ( $1 \pm 0.13$ )	$\leq 6.7$	5.71 ( $1 \pm 0.36$ )
${}^{15}\text{O}$	2.23 ( $1 \pm 0.16$ )	1.56 ( $1 \pm 0.15$ )	$\leq 3.2$	5.03 ( $1 \pm 0.41$ )
${}^{17}\text{F}$	5.52 ( $1 \pm 0.18$ )	3.40 ( $1 \pm 0.16$ )	$\leq 5.9$	5.91 ( $1 \pm 0.44$ )
$\chi^2/P^{\text{agr}}$	3.5/90%	3.4/90%	—	—

on the production of solar neutrinos is out of the scope of the present paper, but can be found elsewhere [43].

SSM calculations of neutrino fluxes have been affected by developments in the input physics discussed in previous sections. The two areas that have the strongest impact on the neutrino fluxes predicted by models are changes in nuclear cross-sections and the new solar composition. In Table 4, we list the results for neutrino fluxes for the up-to-date SSMs SFII-GS98 and SFII-AGSS09. For comparison, we include, in the last column, results from the BP04 SSM [76].

The most striking difference is the large reduction in the  ${}^{13}\text{N}$  and  ${}^{15}\text{O}$  fluxes between the SFII-GS98 and BP04 models, which use the same solar composition. This reduction comes as a result of the new determination of  $S_{1,14}$ , mostly by the LUNA experiment [77, 78], that has halved its value with respect to previous results (Table 2). If correct, the new expectation value of the combined  ${}^{13}\text{N} + {}^{15}\text{O}$  fluxes poses an even more challenging task for neutrino experiments to detect CNO fluxes. By comparing fluxes in Table 4 for models computed with the same solar composition (SFII-GS98 and BP04), it can be seen that in terms of flux values, those associated with the *pp*-chains have not changed much since 2004, despite improvements in the input physics entering solar model calculations. Few percent changes are present and are the result of changes in the nuclear cross-sections discussed before and also of the new OP radiative opacities. This is an encouraging situation; it implies that neutrino fluxes are robust predictions of solar models and, as experimental data on solar neutrinos accumulate, it will be possible to start fulfilling the initial goal posed by Davis and Bahcall: to use solar neutrinos to learn about the solar interior.

In Figure 2, we show the distribution of the solar neutrino fluxes as a function of solar radius. Together with the electron density profile, provided also by solar models (and neutron density profiles for sterile neutrino studies), these quantities are of fundamental importance for neutrino oscillation studies. It is worth noting that the  ${}^{13}\text{N}$  flux has two components. The larger one is associated with the operation in quasi-steady state of the CN-cycle in the innermost solar core ( $R < 0.1R_{\odot}$ ), and for this reason coincides with the production region of the  ${}^{15}\text{O}$  flux (Figure 2(b), blue and black curves, resp.). This

component of the  ${}^{13}\text{N}$  flux, as well as the total  ${}^{15}\text{O}$  flux, is linearly dependent on  $S_{1,14}$ . The additional component of the  ${}^{13}\text{N}$  flux comes from the residual burning of  ${}^{12}\text{C}$  by the reactions  ${}^{12}\text{C}(p, \gamma){}^{13}\text{N}(\beta^+){}^{13}\text{C}$  at temperatures not high enough to close the CN-cycle with a proton capture on  ${}^{14}\text{N}$ . This component is completely independent of  $S_{1,14}$ . The careful reader will notice that the ratio of  ${}^{13}\text{N}$  and  ${}^{15}\text{O}$  fluxes is different in the SFII-GS98 and BP04 models, despite having the same solar composition. Whereas the added  ${}^{13}\text{N} + {}^{15}\text{O}$  neutrino flux is linearly proportional to the C + N abundance in the solar core and also linearly proportional to  $S_{1,14}$ , this degeneracy can be broken, at least theoretically, if the two fluxes can be experimentally isolated from one another.

The impact of the *low-Z* solar composition on the production of solar neutrinos can be grasped by comparing results of models SFII-GS98 and SFII-AGSS09 shown in Table 4. As stated before, metals shape the solar structure through the radiative opacity. The lower abundance of metals in the AGSS09 composition is responsible for a reduction of the temperature in the solar core of about 1%. Because of the extreme temperature sensitivity of some of the neutrino fluxes this is enough to produce large changes in the total fluxes. The most extreme case is, of course,  ${}^8\text{B}$ , with the SFII-AGSS09 value being  $\sim 20\%$  smaller. For  ${}^7\text{Be}$  the reduction is of  $\sim 9\%$ .

Given the small uncertainties in the experimental determination of these fluxes, it would be tempting to think these neutrino fluxes have the potential to discriminate between the two flavors of solar composition and contribute, in this way, to the solution of the solar abundance problem. As can be seen in Table 4, unfortunately, the  ${}^7\text{Be}$  and  ${}^8\text{B}$  fluxes determined from experiments lie almost right in between the *high-Z* and *low-Z* models.

In any case, since it is known that *low-Z* solar models do not reproduce well the solar structure as discussed in the previous section, it is dangerous to extract conclusions from comparing neutrino fluxes of this model to experimental results. Regardless of what the solution to the solar abundance problem is, since it will modify the solar interior structure, it will also change the expected values for the neutrino fluxes. In this regard, CNO fluxes are particularly interesting. Although

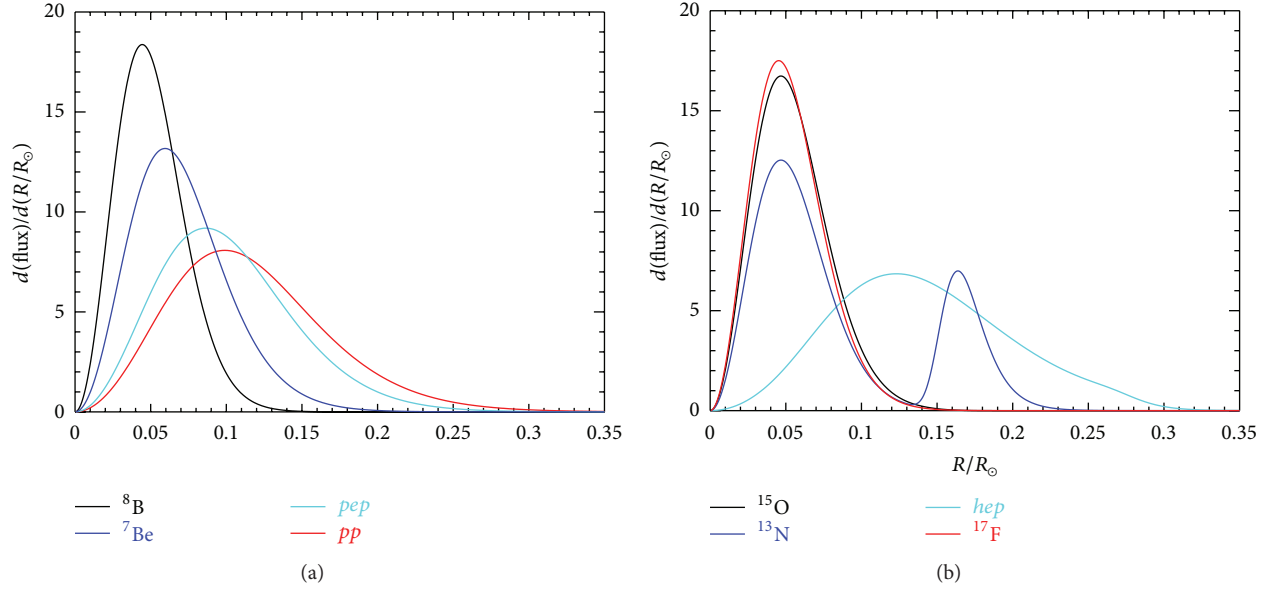


FIGURE 2: Normalized production profiles of solar neutrinos as a function of solar radius.

they are of course affected by temperature variations to a comparable degree as the  $^8\text{B}$  flux is, they carry an extra linear dependence on the solar composition that is not related to temperature variations (The  $^{17}\text{F}$  flux is linearly dependent on O, but unfortunately the flux is too low to be detectable with current experimental capabilities.). Of particular interest is the linear dependence of the  $^{13}\text{N}$  and  $^{15}\text{O}$  fluxes on the combined C + N abundance. It is this dependence that enhances their capability as a diagnostic tool. In fact, differences between SFII-GS98 and SFII-AGSS09 models for these two fluxes are of the order of 30% (taking SFII-GS98 as reference) and, what is more important, a large contribution to these differences does not have an origin on temperature differences between the models.

The last row in Table 4 shows the results of an  $\chi^2$  test for the two models against the solar fluxes also shown in the table. It is clear that both SSMs give a very good agreement with current data. We emphasize again, however, that the four fluxes that are currently well determined from data and the luminosity constraint, depending on the solar composition only in an indirect manner. Experimental determination of the combined  $^{13}\text{N} + ^{15}\text{O}$  flux will therefore provide qualitatively new information on the solar structure and composition. In fact, one can take advantage of the similar response to temperature variations that CNO fluxes and the  $^8\text{B}$  flux has. This has been exploited [79] to develop a very simple method to determine the solar core C + N abundance that minimizes environmental uncertainties in solar models (i.e., sources of uncertainty that affect the solar core temperature). The idea is simple: the temperature dependences are cancelled out by using an appropriate ratio between the  $^8\text{B}$  and the combined  $^{13}\text{N} + ^{15}\text{O}$  fluxes where SSM fluxes only act as normalization values and the overall scale is determined by an actual  $^8\text{B}$  flux measurement. The only additional requirement is that a measurement of the combined  $^{13}\text{N} + ^{15}\text{O}$  flux becomes

available. The current upper limit on this combined flux from Borexino [74] places an upper limit on the C + N central mass fraction of  $X_{\text{C+N}} < 0.072$ . Results for the SFII-GS98 and SFII-AGSS09 models are  $X_{\text{C+N}} = 0.048$  and  $0.039$ , respectively.

**3.3.2. Uncertainties.** Uncertainties in the model predictions of solar neutrino fluxes are given in Table 4. For deriving the total uncertainty basically two approaches can be used. On one hand, all contributions of uncertainty can be treated simultaneously by doing a Monte Carlo simulation [80]. The advantage is that intrinsic nonlinearities are captured in the total error. The disadvantage is that individual contributions to the total uncertainty are hardwired in the final result and cannot be disentangled. Fortunately, for the current level of uncertainties entering SSM calculations, nonlinearities seem to be negligible and the total uncertainty in neutrino fluxes can be obtained (adding quadratically) from individual contributions. To compute the latter, the expansion of fluxes as a product of power laws in the input parameters [43] around central values is a widely used, practical, insightful, and accurate approach. Uncertainties in the model fluxes listed in Table 4 have been obtained in this way.

The most important change introduced in the estimation of uncertainties is related to the treatment of the solar composition. Up until the BP04 model [76], the uncertainty in the solar composition was taken into account by considering variations of the total solar metallicity (to be more precise, changes in the  $(Z/X)_\odot$  value used to construct SSMs). This leads to an overestimation of the neutrino uncertainties. The reason is that metals dominating the error budget in  $(Z/X)_\odot$  (C, N, O, and Ne) have, at most, a moderate impact on the neutrino fluxes because of their small contribution to the radiative opacity, and therefore a rather small impact on temperature, in the region where most neutrinos are produced. On the other hand, elements such as Fe, S, and Si are

second-order in determining  $(Z/X)_\odot$  but play a fundamental role as sources of opacity in the solar core. It is important, therefore, to treat metal uncertainties individually [81]. Of course, in the case of the CNO fluxes the situation is different because CNO elements catalyze the CNO-bicycle and this overimposes an almost linear dependence of the  $^{13}\text{N}$  and  $^{15}\text{O}$  on the C + N content of the solar and a similar dependence of  $^{17}\text{F}$  on the O abundance. The uncertainties in the neutrino fluxes given for the SFII-GS98 and SFII-AGSS09 SSMs have been computed using the uncertainties for each relevant element given in the original publications [46, 50]. As a result, for either family of solar models, that is, *high-Z* or *low-Z* models, the solar composition is not the dominant source of uncertainty for any of the fluxes of the pp-chains. In the case of the CNO fluxes, the linear dependence mentioned above is the dominant source of uncertainty: the combined C + N abundance contributes to a 12% uncertainty for both the  $^{13}\text{N}$  and the  $^{15}\text{O}$  fluxes, and the O abundance to 15% in the  $^{17}\text{F}$  flux.

In the case of the noncomposition uncertainties, the situation has improved in some cases thanks to more precise measurements of nuclear reaction rates. This is the case, in particular, for the  $^3\text{He}(^4\text{He}, \gamma)^7\text{Be}$  reaction, which now contributes only 4.7% and 4.5% of the total uncertainty in the  $^7\text{Be}$  and  $^8\text{B}$  fluxes, respectively. For comparison, the analogous contributions in the BP04 model were 8.0% and 7.5% [76]. Significant progress has also been achieved regarding  $^{14}\text{N}(p, \gamma)^{15}\text{O}$ , which now introduces uncertainties of only 5% and 7% in the  $^{13}\text{N}$  and  $^{15}\text{O}$  fluxes, half the amount it did in 2004. An important contribution to the uncertainty in the  $^8\text{B}$  flux now comes from  $^7\text{Be}(p, \gamma)^8\text{B}$  because the uncertainty of this reaction has been revised upwards [55]. Even if the uncertainty in this rate is now smaller than in SFI (see Table 2), it is larger than that used for the BP04 model, which was taken considering only one experimental result for this reaction.

While progress has been done in some cases, others have not seen much development, particularly diffusion and the delicate issue of radiative opacities. In Table 5, we give the individual contributions to flux uncertainties for the most relevant sources. The reader can compare directly to the situation in 2004 [76].

#### 4. Neutrino Flavor Conversion in Vacuum and Matter

Neutrino flavor conversion has been reviewed by Yu. Smirnov in this volume and we refer the reader for a detailed physics discussion and references to his article. Here we just summarize the basic features and formulae of flavor conversion relevant to solar neutrinos.

We consider mixing of the three flavor neutrinos. The description of flavor conversion of solar neutrinos traveling through a medium is simplified because (a) the hierarchy in mass splittings determined by solar and atmospheric data leads to a reduction of the three neutrino flavor conversion to an effective two-flavor problem and (b) the neutrino parameters, the mixings, and solar mass splitting lead to adiabatic

flavor conversion in solar matter and to cancel the interference term by averaging out. Therefore, the physics of the flavor conversion of solar neutrinos is described by simple expressions with a very good accuracy. In practice, the survival probability is computed numerically to correctly include the number density of scatterers along the trajectory of neutrinos from the production to the detection and to average over the neutrino production region. In solar neutrino flavor conversion,  $\nu_\mu$  and  $\nu_\tau$  are indistinguishable and therefore the survival probability of electron neutrinos is the only function needed to describe the flavor composition of the solar neutrino flux.

Solar neutrino survival or appearance probabilities can be expressed in terms of three oscillation parameters (that can be called the solar oscillation parameters), namely, the mixing angles between the first neutrino mass eigenstate and the two other active mass eigenstates ( $\theta_{12}$  and  $\theta_{13}$ ) and the difference of the squares of the first and second generation mass eigenvalues ( $\Delta m_{21}^2$ ). The survival probability in the absence of Earth-matter effects, that is, during the day, is well described by

$$P_{ee}^D = \cos^4\theta_{13} \left( \frac{1}{2} + \frac{1}{2} \cdot \cos 2\theta_S \cdot \cos 2\theta_{12} \right) + \sin^4\theta_{13}. \quad (5)$$

Here,  $\theta_S$  is the mixing angle at the production point inside the Sun:

$$\cos 2\theta_S \equiv \cos 2\theta_m(\rho_S), \quad (6)$$

where  $\theta_m(\rho)$  is the mixing angle in matter of density  $\rho_S$ ,

$$\cos 2\theta_S = \frac{\cos 2\theta_{12} - \xi_S}{(1 - 2\xi_S \cos 2\theta_{12} + \xi_S^2)^{1/2}}. \quad (7)$$

In (7),  $\xi_S$  is defined as the ratio of the neutrino oscillation length in vacuum,  $l_v$ , to the refraction length in matter,  $l_0$ :

$$\begin{aligned} \xi_S \equiv \frac{l_v}{l_0} &= \frac{2\sqrt{2}G_F\rho_S Y_e \cos^2\theta_{13}}{m_N} \frac{E}{\Delta m^2} \\ &= 0.203 \times \cos^2\theta_{13} \left( \frac{E}{1 \text{ MeV}} \right) \left( \frac{\rho_S Y_e}{100 \text{ g cm}^{-3}} \right), \end{aligned} \quad (8)$$

where

$$l_v \equiv \frac{4\pi E}{\Delta m^2}, \quad l_0 \equiv \frac{2\pi m_N}{\sqrt{2}G_F\rho_S Y_e \cos^2\theta_{13}}. \quad (9)$$

In (8) and (9),  $\rho_S$  is the solar matter density,  $Y_{eS}$  is the number of electrons per nucleon, and  $m_N$  is the nucleon mass. The electron solar density and neutrino production distribution of the neutrino fluxes are derived from solar models as discussed in the previous section. In the last line in (8), we have used the best fit values of the global analysis  $\Delta m^2 = 7.5 \times 10^{-5} \text{ eV}^2$ . The ratio of the parameter  $\rho_S$  to  $\cos 2\theta_{12}$  separates the region where the flavor conversion corresponds to vacuum averaged oscillations from the one of matter dominated conversion.



TABLE 5: Percentage contribution of selected individual sources of uncertainty to the neutrino fluxes.

	$S_{11}$	$S_{33}$	$S_{34}$	$S_{17}$	$S_{1,14}$	Opac	Diff
$pp$	0.1	0.1	0.3	0.0	0.0	0.2	0.2
$pep$	0.2	0.2	0.5	0.0	0.0	0.7	0.2
$hep$	0.1	2.3	0.4	0.0	0.0	1.0	0.5
${}^7\text{Be}$	1.1	2.2	4.7	0.0	0.0	3.2	1.9
${}^8\text{B}$	2.7	2.1	4.5	7.7	0.0	6.9	4.0
${}^{13}\text{N}$	2.1	0.1	0.3	0.0	5.1	3.6	4.9
${}^{15}\text{O}$	2.9	0.1	0.2	0.0	7.2	5.2	5.7
${}^{17}\text{F}$	3.1	0.1	0.2	0.0	0.0	5.8	6.0

The  $\nu_e$  survival probability at night during which solar neutrinos pass through the Earth can be written as

$$P_{ee}^N = P_{ee}^D - \cos 2\theta_s \cos^2 \theta_{13} \langle f_{\text{reg}} \rangle_{\text{zenith}}, \quad (10)$$

where  $P_{ee}^D$  is the one given in (5).  $f_{\text{reg}}$  denotes the regeneration effect in the Earth and is given as  $f_{\text{reg}} = P_{2e} - \sin^2 \theta_{12} \cos^2 \theta_{13}$ , where  $P_{2e}$  is the transition probability of the second mass eigenstate to  $\nu_e$ . Under the constant density approximation in the Earth,  $f_{\text{reg}}$  is given by

$$f_{\text{reg}} = \xi_E \cos^2 \theta_{13} \sin^2 2\theta_E \times \sin^2 \left[ a_E \cos^2 \theta_{13} (1 - 2\xi_E^{-1} \cos^2 \theta_{12} + \xi_E^{-2})^{1/2} \left( \frac{L}{2} \right) \right], \quad (11)$$

for passage of distance  $L$ , where we have introduced  $a_E \equiv \sqrt{2} G_F n_e^{\text{Earth}} = \sqrt{2} G_F \rho_E Y_{eE} / m_N$ .

In (11),  $\theta_E$  and  $\xi_E$  stand for the mixing angle and the  $\xi$  parameter (see (8)) with matter density  $\rho_E$  in the Earth. Within the range of neutrino parameters allowed by the solar neutrino data, the oscillatory term averages to 1/2 in a good approximation when integrated over zenith angle. Then, the equation simplifies to

$$\langle f_{\text{reg}} \rangle_{\text{zenith}} = \frac{1}{2} \cos^2 \theta_{13} \xi_E \sin^2 2\theta_E. \quad (12)$$

At  $E = 7$  MeV, which is a typical energy for  ${}^8\text{B}$  neutrinos,  $\xi_E = 3.98 \times 10^{-2}$  and  $\sin 2\theta_E = 0.940$  for the average density  $\bar{\rho}_E = 5.6 \text{ g/cm}^3$  and the electron fraction  $Y_{eE} = 0.5$  in the Earth. Then,  $\langle f_{\text{reg}} \rangle_{\text{zenith}}$  is given as  $\langle f_{\text{reg}} \rangle_{\text{zenith}} = 1.76 \times 10^{-2}$  for the best fit neutrino parameters. This result is in a reasonable agreement with the computed Earth-matter factor using the best estimates on the Earth-matter density.

## 5. Recent Solar Neutrino Measurements

**5.1. The SNO and SK Legacy.** After the results and analyses from 2002, it was clear that the LMA oscillation was the right solution of the long standing solar neutrino puzzle [82–93], but the activity of the SNO and SK experiments continued in the following years. The data obtained from these experiments were very important in making the LMA solution more

robust and in improving the accuracy and precision of the mixing parameters determination.

The so-called SNO II experiment began in June of 2001 with the addition of 2000 kg of NaCl to the 1000 metric tons of  $\text{D}_2\text{O}$  and ended in October 2003 when the NaCl was removed. The addition of salt significantly increased SNO's efficiency (by a factor  $\sim 3$  with respect to the pure  $\text{D}_2\text{O}$  phase) in the detection of neutrons produced in the neutral current (NC) disintegration of deuterons by solar neutrinos and, by enhancing the energy of the  $\gamma$ -ray coming from neutron capture, allowed a more precise measurement of this interaction channel, well above the low-energy radioactive background. Moreover, the isotropy of the multiple  $\gamma$ -ray emission by neutron capture on  ${}^{35}\text{Cl}$  is different from the one of the Čerenkov light emitted by the single electron of the charged current interaction; therefore, by studying the event isotropy, it has been possible to separate the neutral from the charged current events without any additional assumption on the neutrino energy spectrum. The salt phase results have been reported in two main publications. In [30], referring to the first 254 live days, a global analysis including all the solar and reactor neutrino results rejected the maximal mixing hypothesis at a  $5.4\sigma$  level and gave a value of the  ${}^8\text{B}$  neutrino flux in agreement with previous measurements and with SSMs. These results were essentially confirmed (even if with a small shift towards larger values of the mixing angle) by the second publication [94], which included the full data of the salt phase (391 live days), analyzed in terms of the CC spectra (starting from 5.5 MeV kinetic energy), and NC and ES integrated fluxes separately for day and night. The day-night asymmetry in the neutral current rate, which would be an indication of oscillation to sterile neutrinos or nonstandard interaction with matter in the earth, came out to be consistent with zero.

This result confirmed also the outcome of the study performed for elastic scattering (ES) interaction above 5 MeV by the Super-Kamiokande collaboration [95]. The full SK-I low energy data, corresponding to 1496 live days until July 2001, were investigated analyzing the time variations of the ES rates and fitting them to the variations expected from active two neutrino oscillations. In this kind of study, the zenith angle of the solar neutrinos arriving on the detector is associated to the time variable and the full data are divided in two different time samples from which the day and night rates (D) and (N) are derived. The day-night asymmetry turned out to be  $A_{\text{DN}} = 2(D - N)/(D + N) = -0.021 \pm 0.020(\text{stat.})_{-0.012}^{+0.013}(\text{syst.})$ ,

which is consistent with zero within  $0.9\sigma$ . This value was in a good agreement also with the LMA oscillation solution, which (for the best fit parameter) predicted [95]  $A_{\text{DN}} = -0.018 \pm 0.016(\text{stat.})^{+0.013}_{-0.012}(\text{syst.})$ . The impact of Earth-matter effects on solar neutrino oscillations is an important topic, which has been widely studied in the literature with different techniques (analytical and semianalytical studies and fully numerical analyses)[96–109].

The SK analysis [95, 110] also showed that the energy spectrum of the recoiling electron was consistent with an undistorted solar  $^8\text{B}$  neutrino spectrum and did not find any anomalous periodic time variation of the rates, apart from the expected seasonal variation due to the Earth's orbit eccentricity. The SK best fit point was in quite a good agreement with the SNO results, even if SK would favor slightly larger values of  $\tan^2\theta$ . A SNO-only analysis gave the following best fit parameters [94]:  $\Delta m_{12}^2 = 5.0 \times 10^{-5} \text{ eV}^2$ ,  $\tan^2\theta_{12} = 0.45$ . Including all the other solar neutrino and the KamLAND results, the best fit was obtained for  $\Delta m_{12}^2 = 8.0^{+0.6}_{-0.4} \times 10^{-5} \text{ eV}^2$ ,  $\tan^2\theta_{12} = 0.452^{+0.088}_{-0.070}$ . The effect of KamLAND data was mainly to increase the value of  $\Delta m^2$  and to restrict the allowed region in the mixing parameter plane. The main difference of the global analysis done with the SNO salt phase data with respect to previous studies was the possibility to exclude at 95% CL the secondary region at even larger values of the mass differences (the so-called LMA II solution, with  $\Delta m_{12}^2 > 10^{-4} \text{ eV}^2$ ).

In the third SNO phase (November 2004–November 2006), the neutral current signal neutrons were mainly detected by means of an array of  $^3\text{He}$  proportional counters deployed in the  $\text{D}_2\text{O}$  and looking at the gas ionization induced by neutron capture on  $^3\text{He}$ . In this way, the fluxes correlation was reduced and the accuracy in the mixing angle determination was improved. The total active  $^8\text{B}$  neutrino flux was found [31] to be  $5.54^{+0.33}_{-0.31}(\text{stat.})^{+0.36}_{-0.34}(\text{syst.}) \times 10^6 \text{ cm}^{-2} \text{ s}^{-1}$ , in agreement with previous measurements and SSMs. The ratio of the  $^8\text{B}$  neutrino flux measured with CC and NC reaction was  $\Phi_{\text{CC}}^{\text{SNO}}/\Phi_{\text{NC}}^{\text{SNO}} = 0.301 \pm 0.033$ . The global solar neutrino experiment analysis included, in this case, also the first results coming from the Borexino experiment [111], that we discuss in Section 5.3. The best fit point moved to  $\Delta m_{12}^2 = 4.90 \times 10^{-5} \text{ eV}^2$ ,  $\tan^2\theta_{12} = 0.437$  and the uncertainty in the mixing parameter plane was still quite large. Adding the KamLAND data, the allowed region was significantly restricted (mainly for  $\Delta m^2$ ) and the marginalized  $1\sigma$  regions were  $\Delta m_{12}^2 = 7.59^{+0.19}_{-0.21} \times 10^{-5} \text{ eV}^2$ ,  $\tan^2\theta_{12} = 0.469^{+0.047}_{-0.041}$ .

A subsequent joint reanalysis of SNO I and SNO II data, known as LETA (low energy threshold analysis) [112], succeeded, with improved calibration and analysis techniques, in lowering the energy threshold, with respect to previous analyses [94, 113], down to an effective electron kinetic energy of  $T_{\text{eff}} = 3.5 \text{ MeV}$ . The main effect was to increase the statistics of CC and ES and, above all, of NC events and to increase significantly the precision on both the total  $^8\text{B}$  neutrino flux and the neutrino mixing parameters. The value for the total  $^8\text{B}$  neutrino flux extracted from neutral current was  $\Phi_{\text{NC}} = 5.14^{+0.21}_{-0.20} \times 10^6 \text{ cm}^{-2} \text{ s}^{-1}$ , where the error, obtained by

summing in quadrature the statistic and systematic contributions, was reduced by more than a factor of two with respect to previous publications. For SNO data alone (LETA plus SNO III), the best fit point moved to the LOW region of parameter space, but the significance level was very similar to the one of the usual LMA solution. A global fit, including all the solar and the KamLAND data, essentially confirmed, instead, the previous results [31] for  $\Delta m_{12}^2$  and it made possible a further improvement in the angle determination, giving, in a 2-flavor analysis,  $\tan^2\theta_{12} = 0.457^{+0.041}_{-0.028}$ .

In the last five years, also the Super-Kamiokande collaboration presented new analyses, including the data of the different working phases of this experiment: Super-Kamiokande II [114] (from December 2002 to October 2005) and Super-Kamiokande III (from July 2006 to August 2008) [115]. Due to the 2001 accident, which damaged some of the photomultiplier tubes, the detector sensitivity was reduced with respect to SK-I and therefore it was important to improve the methods adopted for data collection (particularly for vertex event reconstruction, angular resolution, and background reduction) and analysis. In this way, during the 548 days of SK-III a 2.1% systematic uncertainty on the total flux (corresponding roughly to two-thirds of the SK-I value) was reached. The second and third Super-Kamiokande phases essentially confirmed the SK-I results, for what concerns the absence of significant spectral distortion, the total  $^8\text{B}$  measured flux and the day-night asymmetry.

Since September 2008, Super-Kamiokande is running with modernized data acquisition system (DAQ) and electronics, which allow a wider dynamic range in the measured charge and is read out via Ethernet. This phase of the experiment is denoted as Super-Kamiokande IV [116]. Thanks to the fast DAQ every hit can be recorded and the resulting data stream analyzed by an online computer system that finds timing coincidences which are saved as triggers. As a consequence, Super-Kamiokande's energy threshold is now only limited by computing speed and the event reconstruction. The present event reconstruction is able to reconstruct electrons with a total energy of 3 MeV or more. The computing speed limits the energy threshold to 4.2 MeV which is just below the threshold of Super-Kamiokande I and III (4.5 MeV). The same water flow techniques developed during Super-Kamiokande III result in an observed solar neutrino elastic scattering peak between 4 and 4.5 MeV total recoil electron energy. Special techniques are developed to discriminate the signal from the background, taking advantage from the fact that the background is mainly due to  $\beta$  emission from  $^{214}\text{Bi}$  and it is characterized by a larger Coulomb multiple scattering. This makes possible a reduction of about 10–15% of the statistical uncertainty and this method can also be applied to previous phases of the experiment. The additional systematic uncertainty of this method is under investigation.

*5.2. The Impact of KamLAND Results on Solar Neutrino Physics.* Even if it is based on the analysis of a reactor antineutrino beam, the KamLAND experiment played a fundamental role in the solution of the long standing solar

neutrino puzzle. In fact, the first KamLAND data [34] were determinant, in conjunction with the previous solar neutrino experiments (and mainly with SNO) and assuming CPT invariance, to prove the validity of the oscillation hypothesis and to select the LMA solution as the correct one.

Between March 2002 and January 2004, a new set of data were collected and the KamLAND collaboration performed a study including also a reanalysis of the previous data. During the 2002–2004 campaign, important upgrades were done both on the central detector (increasing the photocatode coverage and improving the energy resolution) and in the analysis techniques (reduction of the background with better techniques in the event selection cuts based on the time, position, and geometry of the events). The number of antineutrino events above 2.6 MeV expected in absence of antineutrino disappearance was  $365.2 \pm 23.7(\text{syst})$  and the 258 observed events corresponded to a  $\bar{\nu}_e$  survival probability equal to  $0.658 \pm 0.044(\text{stat.}) \pm 0.047(\text{syst.})$ . The energy spectrum analysis was in disagreement with the no oscillation hypothesis at 99.6% statistical significance. In [39], the KamLAND collaboration, looking at the  $L_0/E$  spectrum dependence (where  $L_0$  is the source-detector distance and  $E$  the  $\bar{\nu}_e$  energy), performed also an interesting study of other alternative hypotheses (like decoherence and decay) for neutrino disappearance. The oscillation hypothesis offered by far the best explanation of the spectrum shape, as one can see from Figure 3.

As shown in Figure 4(a), the best fit obtained from the data analysis was in the so-called LMAI region (with values of  $\Delta m_{12}^2$  around  $8 \cdot 10^{-5} \text{ eV}^2$ ) and the alternative solution at higher  $\Delta m_{12}^2$  (around  $2 \cdot 10^{-4} \text{ eV}^2$ ) was strongly disfavoured, at 98% CL, mainly due to the spectrum distortions. The KamLAND data alone were not sufficient to solve completely the ambiguity on the mixing angle values and to exclude maximal mixing. However, including in the analysis also the results coming from solar neutrino experiments, the allowed values of the angle were significantly restricted (see Figure 4(b)) and the two-flavor combined analysis gave  $\Delta m_{12}^2 = 7.9^{+0.6}_{-0.5} \cdot 10^{-5} \text{ eV}^2$ ,  $\tan^2 \theta_{12} = 0.40^{+0.10}_{-0.07}$  at a  $1\sigma$  level.

The next KamLAND analysis [40] included also, in addition to the one of [34, 39], the new data collected up to May 2007. The increase in data collection was significant (also thanks to enlarging the radius of the fiducial volume from 5.5 to 6 m) and there was a reduction of systematic uncertainties, in the number of target protons and the background. The total uncertainty on  $\Delta m_{21}^2$  was around 2%, mainly due to the distortion of the energy scale in the detector. The total uncertainty, 4.1%, on the expected event rate was due to different sources (above all the definition of the detector fiducial volume and energy threshold, the  $\bar{\nu}_e$  spectra, and the reactor power) and it affected primarily the mixing angle determination. The different background sources were studied and reduced further. The most important one was the  $^{13}\text{C}(\alpha, n)^{16}\text{O}$  reaction made possible by the  $\alpha$  decay of  $^{210}\text{Po}$  (a daughter of  $^{222}\text{Rn}$ ) introduced in the liquid scintillator during the construction, which produces neutrons with energies up to 7.3 MeV.

The results of the statistical analysis are reported in Figure 5, taken from [40]. The allowed oscillation parameter

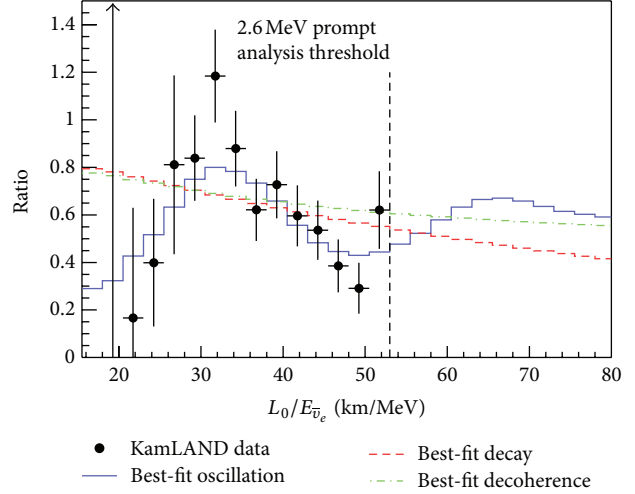


FIGURE 3: Ratio of the observed  $\bar{\nu}_e$  spectrum to the expectation for no oscillation versus  $L_0/E$ . The curves show the expectation for the best-fit oscillation, best-fit decay, and best-fit decoherence models, taking into account the individual time-dependent flux variations of all reactors and detector effects. Taken from [39].

values were  $\Delta m_{21}^2 = 7.58^{+0.14}_{-0.13}(\text{stat.})^{+0.15}_{-0.15}(\text{syst.}) \cdot 10^{-5} \text{ eV}^2$  for the mass eigenvalues and  $\tan^2 \theta_{12} = 0.56^{+0.10}_{-0.07}(\text{stat.})^{+0.10}_{-0.06}(\text{syst.})$ , for  $\tan^2 \theta_{12} < 1$  and the no oscillation hypothesis was excluded at  $5\sigma$ . The extension to the three-neutrino oscillation analysis had the main effect to enlarge the uncertainty on  $\theta_{12}$ , leaving  $\Delta m_{12}^2$  substantially unchanged. Figure 5, taken from [40], shows that the effect of the inclusion in the analysis of the data from SNO [94] and previous solar neutrino experiments was essential to reduce the interval of allowed  $\theta_{12}$  values and also to move the best-fit point towards slightly lower values of the mixing angle.

Figure 6 (taken from [40]) illustrates, instead, the  $\bar{\nu}_e$  survival probability, as a function of the ratio  $L_0/E$  between the average baseline and the antineutrino energies. One can notice that the observed spectrum (after subtraction of background and geoneutrino signals), reproduces correctly the general shape of the expected oscillation cycle, with a slight excess of low energy antineutrinos, that could be interpreted as geoneutrinos.

### 5.3. Toward the Sub-MeV Analysis: The Borexino Detector and Its Measurements.

In the last decade, significant steps forward have been done in the knowledge of solar neutrino properties, thanks mainly to the results obtained by the kiloton scale Čerenkov detectors (SK and SNO) and by advent of the reactor neutrino experiment KamLAND. However, these experiments investigated only the energy part of solar neutrino spectrum above 5 MeV, which represents a small fraction of the full spectrum. The single components of the neutrino spectrum cannot be determined by such techniques at low energies and, therefore, up to the last four years, low energy neutrinos had been observed only via radiochemical methods. A significant change took place with the advent of Borexino, a real-time experiment which opened the way to

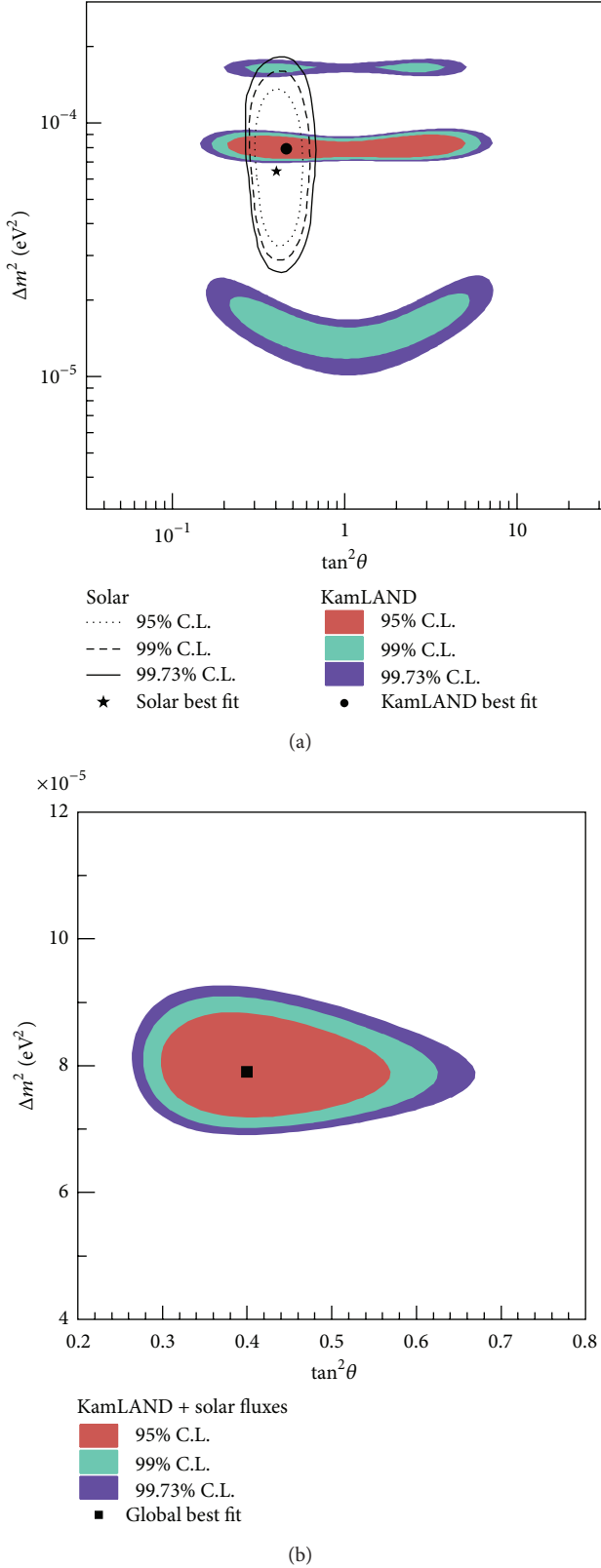


FIGURE 4: (a) Allowed region of the neutrino oscillation parameter from KamLAND antineutrino data (colored regions) and solar neutrino experiments (lines) [30]. (b) the result of a combined two-neutrino oscillation analysis of KamLAND and the observed solar neutrino fluxes under the assumption of CPT invariance. Taken from [39].

the investigation of the sub-MeV region and isolated for the first time the neutrinos corresponding to the monochromatic beryllium line.

**5.3.1. The Borexino Detector.** Borexino is an ultrahigh radio-pure large volume liquid scintillator detector (using pseudocumene—PC (1,2,4-trimethylbenzene)—as aromatic scintillation solvent, and PPO (2,5-diphenyloxazole) as solute at a concentration of 1.5 g/L) located underground at the Italian Gran Sasso National Laboratories (LNGS), under about 1400 m of rock (3800 mwe) [117]. The employment of a liquid scintillator as target mass assures a light production sufficient to observe low energy neutrino events via elastic scattering by electrons. This reaction is sensitive to all neutrino flavors, through the neutral current interaction, but the cross-section for  $\nu_e$  is larger than  $\nu_\mu$  and  $\nu_\tau$  by a factor of 5-6, due to the combination of charged and neutral currents. The main goal of Borexino is the measurement of the monoenergetic (0.862 MeV)  $^7\text{Be}$  neutrinos, which have the basic signature of the Compton-like edge of the recoil electrons at 665 keV (see Figure 7).

The high light yield typical of a liquid scintillator makes it possible to reach a low energy threshold, a good energy resolution of about 5% at 1 MeV, and a pulse shape discrimination between  $\alpha$  and  $\beta$  decays. On the other hand, no directionality is possible and it is also not possible to distinguish neutrino scattered electrons from electrons due to natural radioactivity. For this reason, an extremely low level of radioactive contamination is compulsory and this has been one of the main tasks and technological achievements of the experiment. The background due to the presence of  $\beta$  decay of  $^{14}\text{C}$  ( $\beta_{\text{end-point}}$  156 keV), intrinsic to the scintillator, limits neutrino observation to energies above 200 keV. Techniques for the scintillator purification are based mainly on methods developed and tested in earlier studies with the counting test facility (CTF), a 4-ton prototype of Borexino which demonstrated for the first time the feasibility of achieving the low backgrounds needed to detect solar neutrinos in a large-scale scintillator [120–122]. For Borexino, a larger purification plant was developed similar to the CTF system, but with several improved features including the use of high vacuum and precision cleaning techniques.

The design of Borexino is based on the principle of graded shielding (onion-like structure—see Figure 8).

The scintillator ( $\approx 300$  tons) is contained in a thin nylon inner vessel (IV), of radius 4.25 m, at the center of a set of concentric shells of increasing radiopurity and it is surrounded by an outer vessel (OV), filled with PC and 5.0 g/L DMP (dimethyl phthalate), a material which is able to quench the residual scintillation of PC and acts as a passive shield against radon and other background contaminations originating from the external parts. A third more external vessel is composed of a stainless steel sphere (SSS), enclosing the passive shield (PC-DMP), and the entire detector is contained in a dome-shape structure 16.9 m high with a radius of 9 m, filled with ultrapure water, denominated water tank (WT). The scintillation light is recorded by 2212 8-inches photomultipliers distributed on the inner part of the SSS [123, 124];



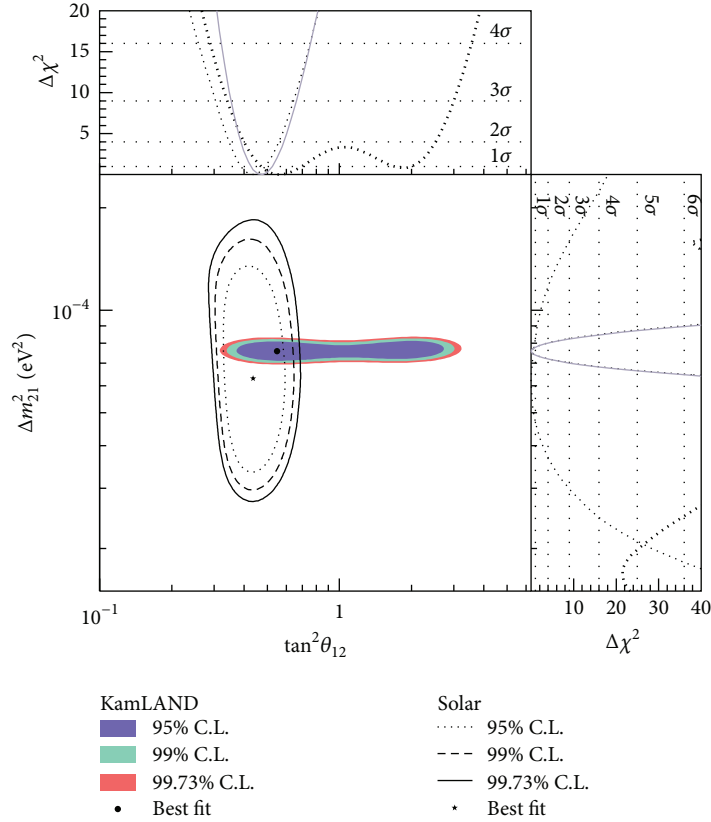


FIGURE 5: Allowed region for neutrino oscillation parameters from KamLAND and solar neutrino experiments. The side-panels show the  $\Delta\chi^2$ -profiles for KamLAND (dashed) and solar experiments (dotted) individually, as well as the combination of the two (solid). Taken from [40].

1828 of them are equipped with aluminum light concentrators designed to increase the light collection efficiency [125]. Čerenkov's light and residual background scintillation in the buffer are thus reduced. The others 384 photomultipliers without concentrators are used to study this background and to identify muons that cross the buffer and not the inner vessel. The water tank is equipped with 208 8-inches photomultipliers and acts as a Čerenkov muon detector. Although the muon flux is reduced by a six-order of magnitude by the 3800 mwe depth of the Gran Sasso Laboratory is still significant ( $1.1 \mu\text{m}^{-2} \text{h}^{-1}$ ). An additional reduction, of the order of about  $10^4$ , has been necessary; for more details see [126].

In order to remove contaminants from dust (U, Th, K), air ( $^{39}\text{Ar}$ ,  $^{85}\text{Kr}$ ), and cosmogenically produced isotopes ( $^7\text{Be}$ ), different purification techniques were applied, such as distillation, water extraction, nitrogen stripping, and ultrafine filtration. The pseudocumene was distilled in-line during the detector filling at 80 mbar and at a temperature of about 90–95°C. Distilled pseudocumene was stripped in an 8 m high (15 cm in diameter) packed column with specially prepared ultralow Ar/Kr nitrogen (0.005 ppm Ar and 0.06 ppt Kr, see [127]). Position reconstruction of the events, as obtained from the photomultipliers timing data via a time-of-flight algorithm, allowed to define a fiducial spherical volume, corresponding approximately to 1/3 (i.e., about 100 tons) of

the scintillator volume in order to reject external  $\gamma$  background. The others 2/3 of the scintillator act as an active shield.

**5.3.2. The Measurement of the  $^7\text{Be}$  Line.** The Borexino collaboration started taking data in May 2007 and after only 3 months (47.4 live days) it was able to extract the  $^7\text{Be}$  signal from the background. The best value estimate for the rate was  $47 \pm 7(\text{stat.}) \pm 12(\text{syst.})$  counts/(day · 100 ton), where the systematic error is mainly due to the fiducial mass determination [119]. An update of the  $^7\text{Be}$  signal was reported after 9 months from an analysis of 192 live days (from May 16 2007 to April 12 2008), corresponding to 41.3 ton · yr fiducial exposure to solar neutrinos.

The severe cuts that had to be passed by the events in order to be selected and enter the analysis were mainly designed to avoid pile up of multiple events and reject the events originated by muons and their daughters and the ones due to radon daughters preceding the  $\alpha - \beta$  Bi-Po delayed coincidences. Moreover, severe cuts (radial and based on the  $z$ -coordinates) were finalized to reduce the external  $\gamma$  background. The remaining fiducial mass was of about 79 metric tons. Important background sources were the fast coincidence decays from the  $^{238}\text{U}$  chain (contamination level of  $(1.6 \pm 0.1) 10^{-17} \text{g/g}$ ) and the  $^{232}\text{Th}$  chain (contamination

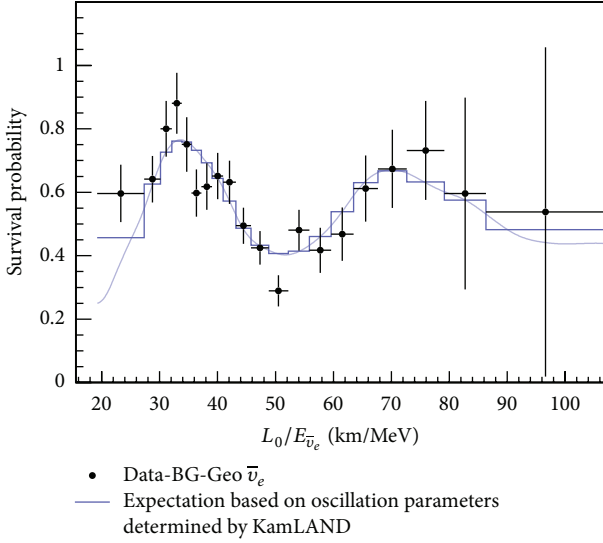


FIGURE 6: Ratio of the background and geo-neutrino-subtracted  $\bar{\nu}_e$  spectrum to the expectation for no oscillation as a function of  $L_0/E$ .  $L_0$  is the effective baseline taken as a flux-weighted average ( $L_0 = 180$  km). The energy bins are equal probability bins of the best fit including all backgrounds. The histogram and curve show the expectation accounting for the distances to the individual reactors, time-dependent flux variations, and efficiencies. The error bars are statistical only and do not include, for example, correlated systematic uncertainties in the energy scale. Taken from [40].

level of  $(6.8 \pm 1.5) \cdot 10^{-18}$  g/g) and the  $^{85}\text{Kr}$  contained in the scintillator that produces the rare decay sequence  $^{85}\text{Kr} \rightarrow ^{85\text{m}}\text{Rb} + e^- + \bar{\nu}_e$ ,  $^{85\text{m}}\text{Rb} \rightarrow ^{85}\text{Rb} + \gamma$ . The total estimated systematic error was 8.5% [111], mainly determined by two sources, introducing an uncertainty of 6% each: the total uncertainty on the fiducial mass and the one on the response function. The best value for the interaction rate of the 0.862 MeV  $^7\text{Be}$  solar neutrinos was  $49 \pm 3(\text{stat.}) \pm 4(\text{syst.})$  counts/(day  $\cdot$  100 ton). This result excludes at the  $4\sigma$  CL the no oscillation hypothesis for  $^7\text{Be}$  solar neutrinos, which in the high metallicity SSM [118, 128] would imply  $74 \pm 4$  counts/(day  $\cdot$  100 ton). The Borexino result is, instead, in a very good agreement with the predictions of the LMA oscillation solution:  $48 \pm 4$  counts/(day  $\cdot$  100 ton).

In order to reduce the systematic uncertainties and to tune the reconstruction algorithm and Monte Carlo simulations, a calibration campaign was performed in 2009 introducing inside the Borexino detector several internal radio sources  $\alpha$ 's,  $\beta$ 's,  $\gamma$ 's, and neutrons, at different energies and in hundreds of different positions, which were determined with a precision better than 2 cm. The previous systematic error on  $^7\text{Be}$  solar neutrino flux was estimated to be [111] at the level of 6% for both the fiducial volume and the energy scale (when thermal neutrons are captured by protons a 2.2 MeV  $\gamma$ -ray is generated.) In the calibration campaign, the detector energy response was studied with eight  $\gamma$  sources and Am-Be neutron source and comparing the calibration data and Monte Carlo simulations at different energies within the solar neutrinos energy region. The energy scale uncertainty,

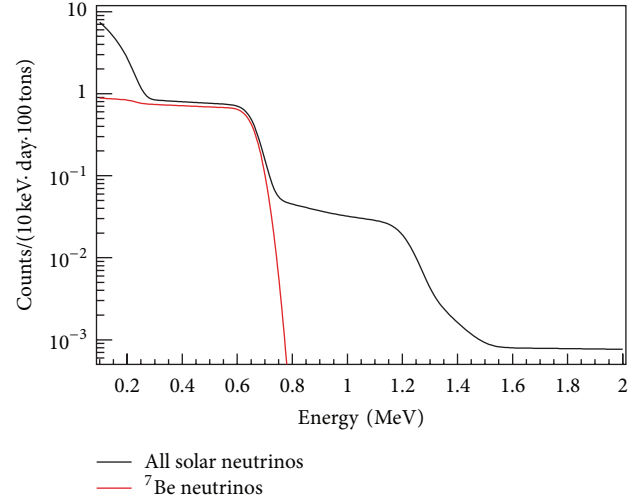


FIGURE 7: Neutrino spectra expected in Borexino (accounting for the detector's energy resolution). The upper line represents the neutrino signal rate in Borexino according to the most recent predictions of the standard solar model [118] including neutrino oscillations with the LMA-MSW parameters. The lower line illustrates the contribution due to  $^7\text{Be}$  neutrinos. The  $pp$  neutrinos contribute to the spectrum below 0.3 MeV and the edge at 1.2 MeV is due to  $pep$  neutrinos (from [119]).

obtained with these studies, was determined to be less than 1.5%.

The inaccuracy of the position (reduced by means of studies with  $\alpha$  and  $\beta$  events) was less than 3 cm, equivalent to a systematic error of 1.3% for the overall fiducial volume in the  $^7\text{Be}$  solar neutrino energy region. The analyzed data set run from May 2007 to May 2010, with a fiducial exposure equivalent to 153.6 ton-year. In order to extract the  $^7\text{Be}$  solar neutrino signal, the spectral fit was applied assuming all the intrinsic background components such as  $^{85}\text{Kr}$ ,  $^{210}\text{Bi}$ ,  $^{14}\text{C}$ , and  $^{11}\text{C}$ . The  $^7\text{Be}$  solar neutrino rate was evaluated to be  $46.0 \pm 1.5(\text{stat.})^{+1.5}_{-1.6}(\text{syst.})$  counts/day  $\cdot$  100 ton [129]. Thanks to the calibration campaign, the systematic error was reduced to 2.7% and the total uncertainty to 4.3%.

**5.4. The  $pep$  and CNO Neutrinos Measurement in Borexino.** In the SSM, due to the solar luminosity constraint and their intimate link to the  $pp$  neutrinos [43, 56], the monoenergetic 1.44 MeV  $pep$  neutrinos have one of the smallest uncertainties (1.2%) [64]. For this reason, after the  $pp$  neutrinos, they constitute the ideal probe to test SSM hypotheses. On the other hand, the detection of neutrinos within the CNO-bicycle is central to probe the solar core metallicity and contribute in this way to the solution of the solar metallicity problem [64, 130]. Also, they are believed to fuel massive stars with mass greater than  $\sim 1.2 M_\odot$  during the main sequence evolution and also stars with lower masses in more advanced stages of evolution. The energy spectrum of neutrinos from the CNO-bicycle is the result of three continuous spectra with end point energies of 1.19 MeV ( $^{13}\text{N}$ ), 1.73 MeV ( $^{15}\text{O}$ ), and

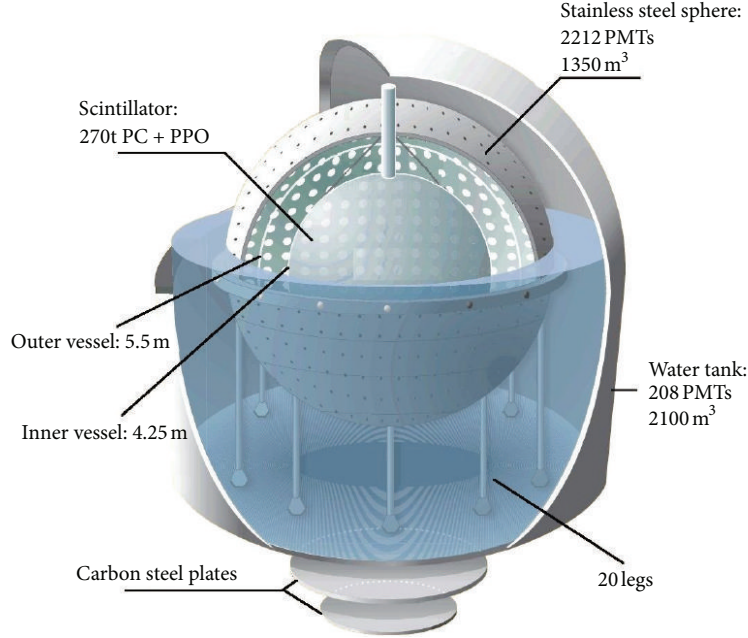


FIGURE 8: Schematic view of the Borexino detector.

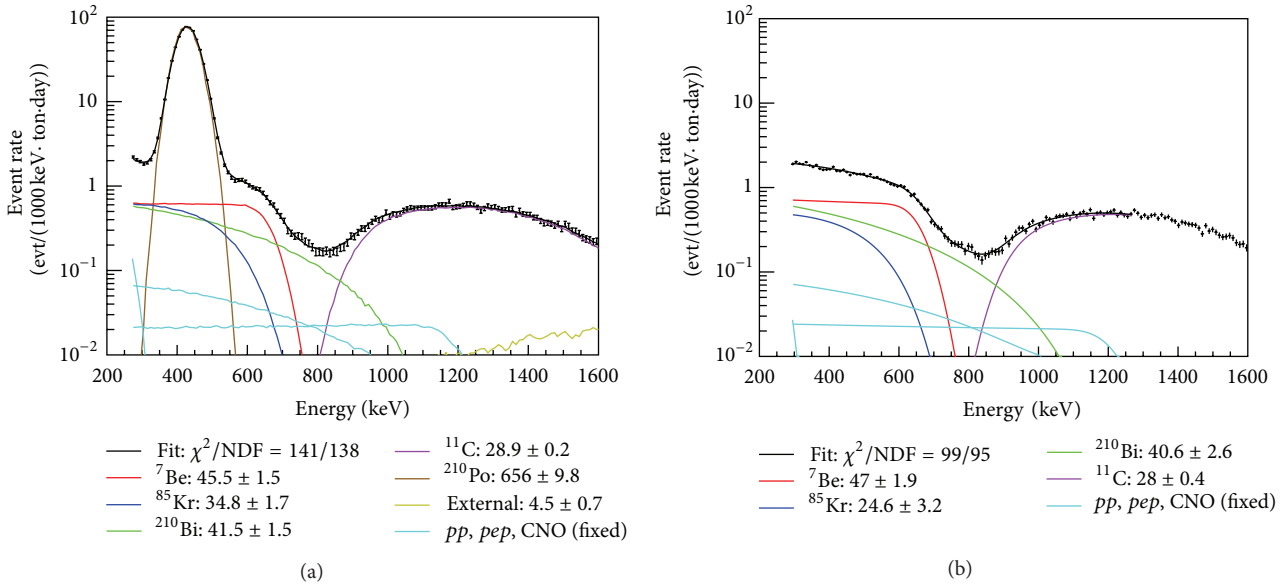


FIGURE 9: Examples of fitted spectra; the fit results in the legends have units [counts/(day · 100 ton)]. (a): A Monte Carlo based fit over the energy region 270–1600 keV to a spectrum from which some, but not all, of the  $\alpha$  events have been removed using a PSA cut, and in which the event energies were estimated using the number of photons detected by the PMT array. (b): An analytic fit over the 290–1270 keV energy region to a spectrum obtained with statistical  $\alpha$  subtraction and in which the event energies were estimated using the total charge collected by the PMT array. In all cases the fitted event rates refer to the total rate of each species, independently from the fit energy window (from [129]).

1.74 MeV ( $^{17}\text{F}$ ). Despite their relevance, until 2011 no *pep* and CNO neutrinos had been detected directly.

The electron recoil energy spectrum from *pep* neutrino interactions in Borexino is a Compton-like shoulder with end point of 1.22 MeV, as one can see from Figures 9 and 10, showing the *pep* and CNO contribution in Borexino.

As already mentioned, very low background levels [111, 119] are required to detect  $^7\text{Be}$  neutrinos; the detection of *pep* and CNO neutrinos is even more challenging, as their expected interaction rates are  $\sim 10$  times lower. The expected rate is on the order of a few counts per day in a 100-ton target. To detect *pep* and CNO neutrinos, the Borexino

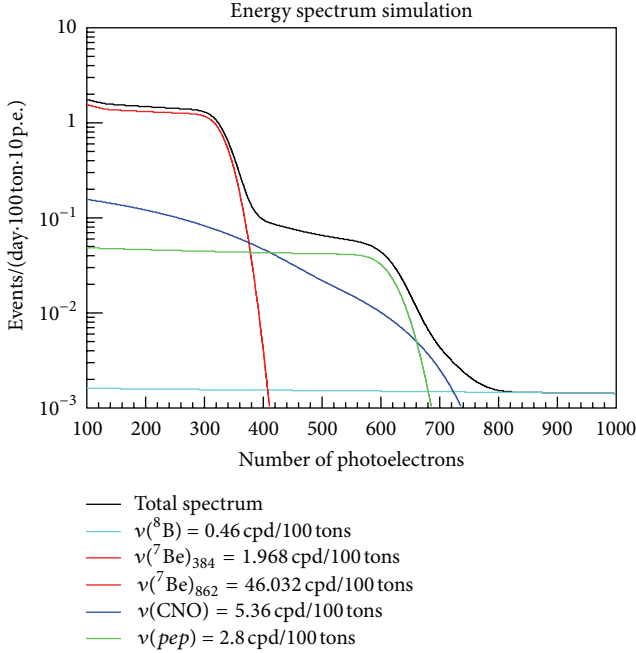


FIGURE 10: The neutrino-induced electron recoil spectra expected in Borexino. The total rates are those predicted by the latest *high-Z* solar model [64]. The *pep* and CNO neutrinos recoil spectra with end points in the region 1.2–1.5 MeV are shown. Also the  $^7\text{Be}$  neutrinos (measured in [129]), with a count rate about 10 times larger, are shown for comparison. Note that the variable on the x-axis is not directly the energy value. Taken from [131].

collaboration adopted a novel analysis procedure to suppress the dominant background in the 1–2 MeV energy range, due to the cosmogenic  $\beta^+$ -emitter  $^{11}\text{C}$  produced within the scintillator by muon interactions with  $^{12}\text{C}$  nuclei. The muon flux crossing the Borexino detector,  $\sim 4300 \mu/\text{day}$ , yields a  $^{11}\text{C}$  production rate of  $\sim 27 \text{ counts}/(\text{day} \cdot 100 \text{ ton})$  (In 95% of the cases at least one free neutron is spalled in the  $^{11}\text{C}$  production process [132], and then captured in the scintillator with a mean time of  $255 \mu\text{s}$  [133].). This background can be reduced by performing a space and time veto following coincidences between signals from the muons and the cosmogenic neutrons [134, 135], discarding exposure that is more likely to contain  $^{11}\text{C}$  due to the correlation between the parent muon, the neutron, and the subsequent  $^{11}\text{C}$  decay (the three-fold coincidence, TFC). The TFC technique is based on the reconstructed track of the muon and the reconstructed position of the neutron-capture  $\gamma$ -ray [133]. The criteria of rejection were applied to obtain the best compromise between  $^{11}\text{C}$  rejection and preservation of fiducial exposure, resulting in a  $^{11}\text{C}$  rate of  $(2.5 \pm 0.3) \text{ count per day}$  and  $(9 \pm 1)\%$  of the original rate, while preserving 48.5% of the initial exposure.

Figure 11 shows the resulting spectrum obtained with data collected between January 2008 and May 2010, corresponding to a fiducial exposure of 20409 ton·day [74]. Despite the TFC veto, the number of  $^{11}\text{C}$  surviving events still constituted a significant background.

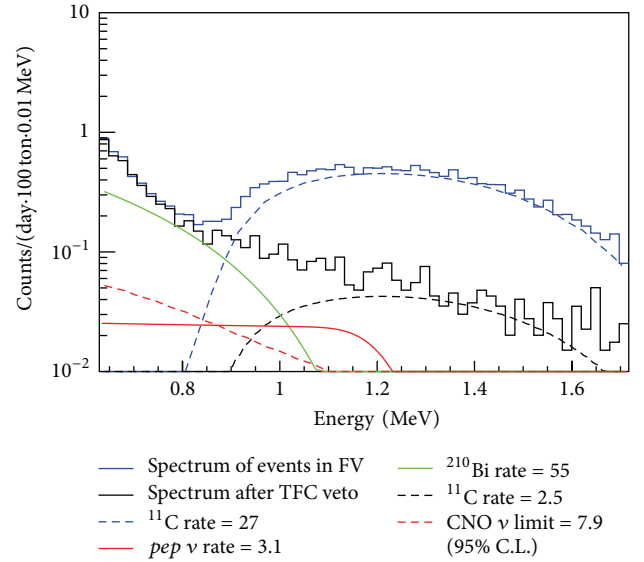


FIGURE 11: Energy spectra of the events in the FV before and after the TFC veto is applied. The solid and dashed blue lines show the data and estimated  $^{11}\text{C}$  rate before any veto is applied. The solid black line shows the data after the procedure, in which the  $^{11}\text{C}$  contribution (dashed) has been greatly suppressed. The next largest background,  $^{210}\text{Bi}$ , and the electron recoil spectra of the best estimate of the *pep* neutrino rate and of the upper limit of CNO neutrino rate are shown for reference. Rate values in the legend are quoted in counts/(day·100 ton) from [74].

To discriminate  $^{11}\text{C} \beta^+$  decays from neutrino-induced  $e^-$  recoils and  $\beta^-$  decays, the pulse shape differences between  $e^-$  and  $e^+$  interactions in organic liquid scintillators [136, 137] were exploited. In fact a small difference in the time distribution of the scintillation signal arises from the finite lifetime of orthopositronium as well as from the presence of annihilation  $\gamma$ -rays, which present a distributed, multisite event topology and a larger average ionization density than electron interactions. The Borexino collaboration employed an optimized pulse shape parameter using a boosted-decision-tree algorithm [138] and trained with a TFC-selected set of  $^{11}\text{C}$  events ( $e^+$ ) and  $^{214}\text{Bi}$  events ( $e^-$ ) selected by the fast  $^{214}\text{Bi}$ – $^{214}\text{Po}$   $\alpha$ – $\beta$  decay sequence (less than 2.8 m from the detector center and with a vertical position relative to the detector center between  $-1.8 \text{ m}$  and  $2.2 \text{ m}$ .) In a work published in 2012 [74], the Borexino collaboration presented the results of an analysis based on a binned likelihood multivariate fit performed on the energy, pulse shape, and spatial distributions of selected scintillation events whose reconstructed position is within the fiducial volume.

The energy spectra and spatial distribution of the external  $\gamma$ -ray backgrounds have been obtained from a full, Geant4-based Monte Carlo simulation and validated with calibration data from a high-activity  $^{228}\text{Th}$  source [139] deployed in the outermost buffer region, outside the active volume.  $\alpha$  events were removed from the energy spectrum by the statistical subtraction method [119]. In the energy region of interest of the fit procedure all background species whose rates were



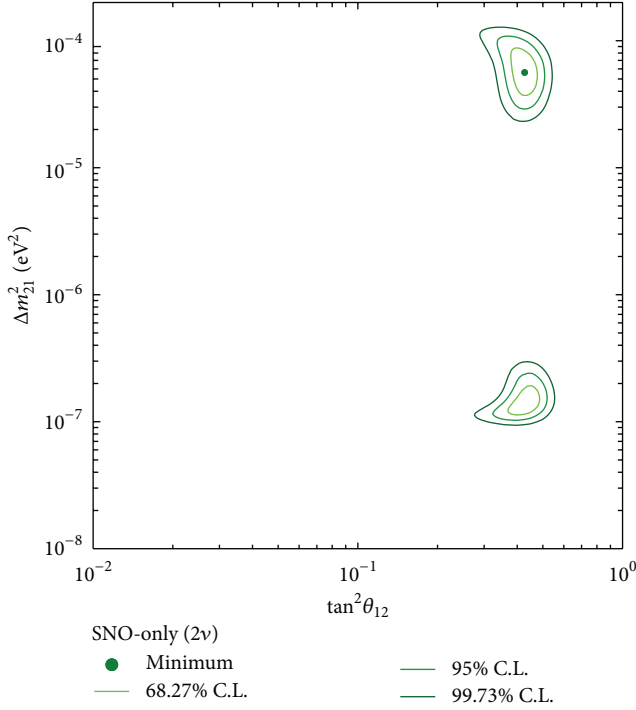


FIGURE 12: Two-flavor neutrino oscillation analysis contour using only SNO data (taken from [147]).

estimated to be less than 5% of the predicted rate from *pep* neutrinos have been excluded (Electron recoils from  ${}^7\text{Be}$ , *pep*, and CNO solar neutrinos, internal radioactive backgrounds  ${}^{210}\text{Bi}$ ,  ${}^{11}\text{C}$ ,  ${}^{10}\text{C}$ ,  ${}^6\text{He}$ ,  ${}^{40}\text{K}$ ,  ${}^{85}\text{Kr}$ , and  ${}^{234\text{m}}\text{Pa}$ , and external  $\gamma$ -rays from  ${}^{208}\text{Tl}$ ,  ${}^{214}\text{Bi}$ , and  ${}^{40}\text{K}$ ). All rates were constrained to positive values and thirteen species were left free in the fit. The rate of the radon daughter  ${}^{214}\text{Pb}$  was fixed using the measured rate of  ${}^{214}\text{Bi}$ - ${}^{214}\text{Po}$  delayed coincidence events. The contribution from *pp* solar neutrinos was fixed to the SSM assuming MSW-LMA [140–145] with  $\tan^2\theta_{12} = 0.47^{+0.05}_{-0.04}$ ,  $\Delta m_{12}^2 = (7.6 \pm 0.2) \cdot 10^{-5} \text{ eV}^2$  [146], and the contribution from  ${}^8\text{B}$  neutrinos to the rate from the measured flux [112, 147].

In Table 6, the results for the *pep* and CNO neutrino interaction rates are shown. The absence of a *pep* neutrino signal was rejected at 98% CL. Concerning the CNO neutrinos flux, its electron-recoil spectrum is similar to the spectral shape of  ${}^{210}\text{Bi}$ , but the last one is about 10 times greater; therefore, it has only been possible to provide an upper limit on the CNO neutrino interaction rate. The 95% CL limit reported in Table 6 has been obtained from a likelihood ratio test with the *pp* neutrino rate fixed to the SSM prediction [64] under the assumption of MSW-LMA,  $(2.80 \pm 0.04) \text{ counts}/(\text{day} \cdot 100 \text{ ton})$ .

## 6. Phenomenological Analysis

**6.1. Status of the Determination of the Mixing Parameters in a 3-Flavor Analysis.** Recently, the SNO collaboration performed a combined analysis of all the three working phases

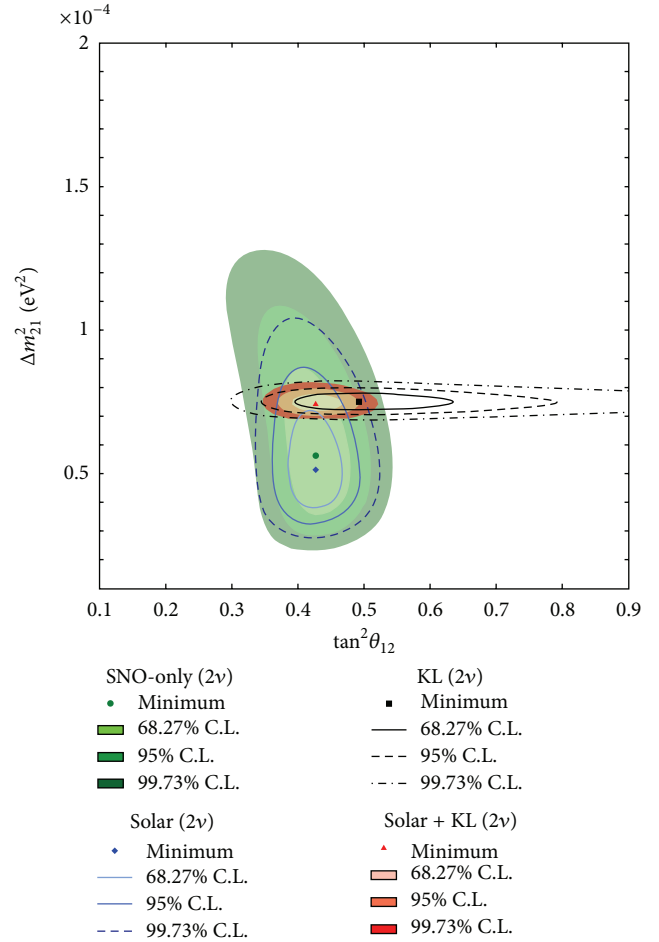


FIGURE 13: Two-flavor neutrino oscillation analysis contour using both solar neutrino and KamLAND results (taken from [147]).

of the experiment [147] based on a fit to Monte Carlo derived probability density functions (PDFs) for each of the possible signals and backgrounds, and also introduced a new way to parametrize the  ${}^8\text{B}$  neutrino signal. Figure 12, reporting the results of the two-flavour (with the assumption  $\theta_{13} = 0$ ) SNO only analysis, shows the further improvement in the mixing parameters accuracy, but, at the same time, it confirms that the SNO results alone would not be sufficient to completely exclude the LOW solution.

This ambiguity was definitely removed, as shown in Figure 13, by including in the analysis the results of all previous solar neutrino experiments [110, 114, 115, 150–153], the  ${}^7\text{Be}$  solar neutrino rate measured by Borexino [129], the  ${}^8\text{B}$  neutrino spectra [154], and the KamLAND data [41] (The KamLAND data were obtained in a completely independent experiment and, therefore, the corresponding  $\chi^2$  values, as functions of the mixing parameters, were directly summed to the  $\chi^2$  values computed by direct solar neutrino analysis.).

The higher values of  $\Delta m_{12}^2$  in the LMA region were excluded, together with the full LOW solution, thanks mainly to the large discrimination power of KamLAND. This experiment, however, did not contribute significantly to improve the mixing angle determination and the accuracy on this

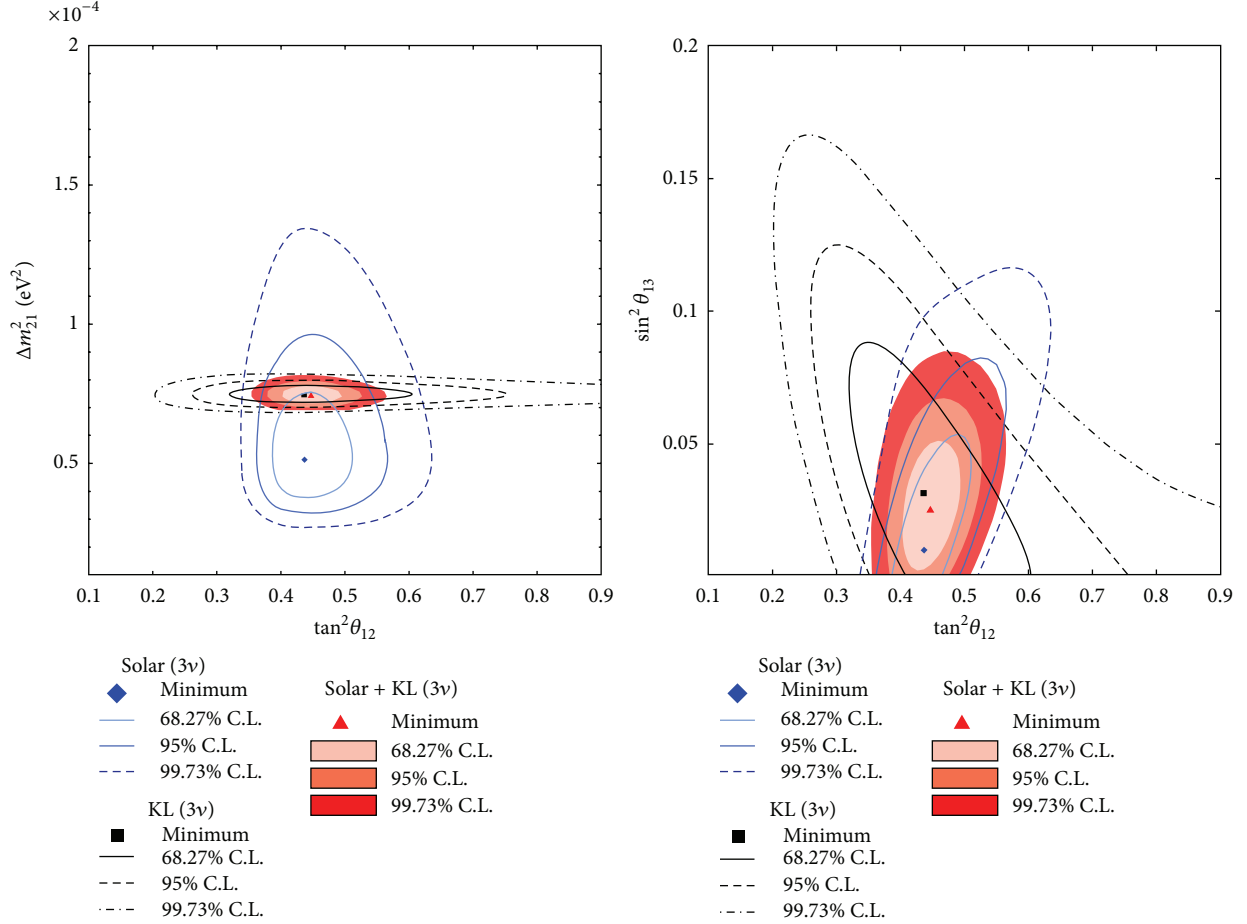


FIGURE 14: Three-flavor neutrino oscillation analysis contour using both solar neutrino and KamLAND results. Taken from [147].

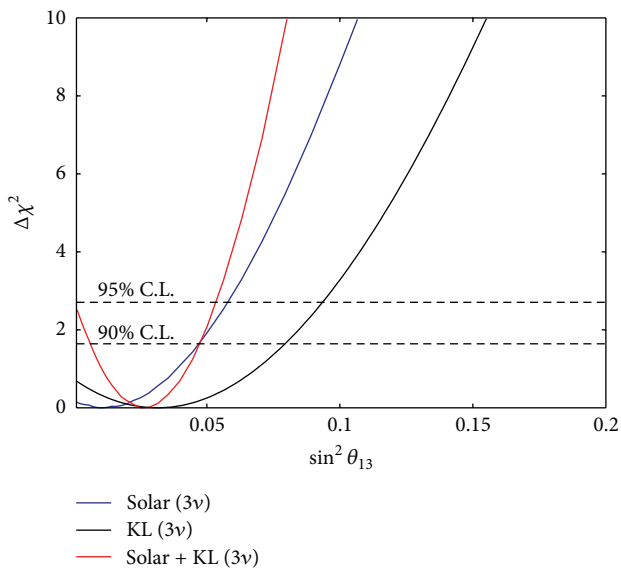


FIGURE 15: Projections of the three-flavor neutrino oscillation parameters. The horizontal lines represent the  $\Delta\chi^2$  for a particular confidence level. Taken from [147].

parameter remained quite high. The results of the two-flavor analysis are reported in Table 7 (taken from [147]).

The slight tension between the solar neutrino experiments and KamLAND was significantly reduced by extending the analysis to the 3 flavor oscillation case as shown in Figure 14, from which it is clear that the best global fit is obtained for values of  $\theta_{13}$  different from zero.

A detailed analysis of the  $\chi^2$  behavior proved also that the combination of solar experiments and KamLAND enables the significant improve of the discriminating power on the  $\theta_{13}$  mixing parameter (see Figure 15 and Table 8).

The indication in favor of  $\theta_{13}$  being different from zero was in agreement with the recent results from the long-baseline experiments T2 K [155] and MINOS [156], and with the combined analysis performed in [157], including also the atmospheric neutrino and the CHOOZ [158] data. Moreover, the validity of this hint has been corroborated by the data obtained this year by the short baseline neutrino reactor experiments [159–162], which established that  $\theta_{13} > 0$  at about  $5\sigma$  (and even more in the Daya Bay case [163]). These experiments found values of  $\sin^2 \theta_{13}$  centered between 0.020 and 0.030, very promising results for future experiments

TABLE 6: Best estimates for the *pep* and CNO solar neutrino interaction rates. For the results in the last two columns both statistical and systematic uncertainties are considered. Total fluxes have been obtained assuming MSW-LMA and using the scattering cross-sections from [146, 148, 149] and a scintillator  $e^-$  density of  $(3.307 \pm 0.003) \cdot 10^{29} \text{ ton}^{-1}$ . The last column gives the ratio between our measurement and the *high-Z* (GS98) SSM [64]. Table taken from [74].

$\nu$	Interaction rate [counts/(day $\cdot$ 100 ton)]	Solar- $\nu$ flux [ $10^8 \text{ cm}^{-2} \text{ s}^{-1}$ ]	Data/SSM ratio
<i>pep</i>	$3.1 \pm 0.6_{\text{stat}} \pm 0.3_{\text{syst}}$	$1.6 \pm 0.3$	$1.1 \pm 0.2$
CNO	$<7.9 (< 7.1_{\text{stat only}})$	$<7.7$	$<1.5$

TABLE 7: Best-fit neutrino oscillation parameters from a two-flavor neutrino oscillation analysis. Uncertainties listed are  $1 \sigma$  after the  $\chi^2$  was minimized with respect to all other parameters (taken from [147]).

Analysis	$\tan^2 \theta_{12}$	$\Delta m_{21}^2 [\text{eV}^2]$	$\chi^2/\text{NDF}$
SNO only (LMA)	$0.427^{+0.033}_{-0.029}$	$5.62^{+1.92}_{-1.36} \times 10^{-5}$	1.39/3
SNO only (LOW)	$0.427^{+0.043}_{-0.035}$	$1.35^{+0.35}_{-0.14} \times 10^{-7}$	1.41/3
Solar	$0.427^{+0.028}_{-0.028}$	$5.13^{+1.29}_{-0.96} \times 10^{-5}$	108.07/129
Solar + KamLAND	$0.427^{+0.027}_{-0.024}$	$7.46^{+0.20}_{-0.19} \times 10^{-5}$	

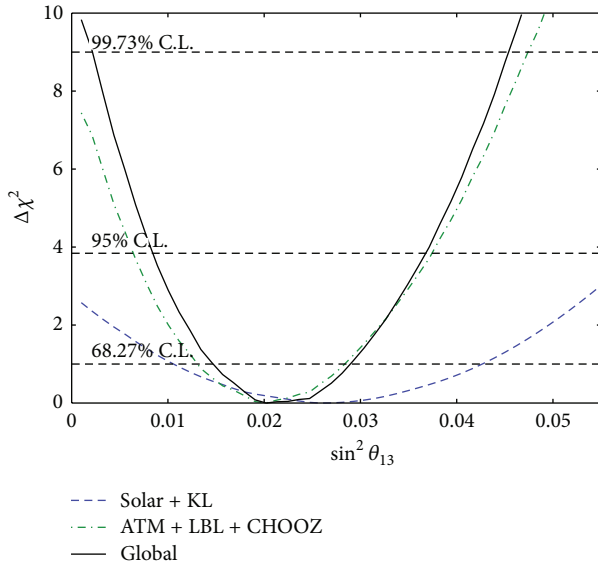


FIGURE 16: Projection over  $\sin^2 \theta_{13}$  combining the projections obtained by analyzing data from all neutrino sources. The data from atmospheric, short-baseline experiments, and long-baseline experiments (ATM + LBL + CHOOZ) was determined from Figure 2 (left panel) in [157] which already includes the latest T2 K [155] and MINOS [156] results.

looking for leptonic CP violation [164]. The impact and the possible consequences of these recent results have been discussed, among the others, in the following papers [164–167]. The different accuracy that can be reached in the determination of the mixing angle between the first and third generation, according to the different kind of neutrino experiments included in the analysis, is represented in Figure 16.

The combined analysis of the different SNO phases was also very useful to obtain a precise determination of the  $^8\text{B}$  solar neutrino flux,  $\Phi_{s_B} = 5.25 \pm 0.16(\text{stat})^{+0.11}_{-0.13}(\text{syst}) \times$

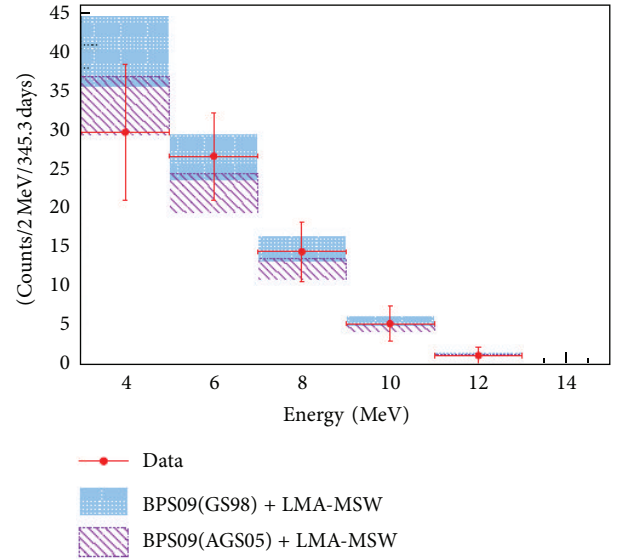


FIGURE 17: In this picture, taken from [154], the final energy spectrum derived from Borexino's analysis (red points) is represented and compared with the Monte Carlo predictions (blue and purple bands) obtained using the MSW-LMA neutrino oscillation model and the standard solar models in the versions corresponding, respectively, to the high metallicity (BPS09(GS98)) and the low metallicity (BPS09 (AGS05)) cases.

$10^6 \text{ cm}^{-2} \text{ s}^{-1}$ , with an important reduction of the systematic uncertainty. This result was consistent with, but more precise than, both the *high-Z* BPS09 (GS),  $\Phi = (5.88 \pm 0.65) \times 10^6 \text{ cm}^{-2} \text{ s}^{-1}$ , and *low-Z* BPS09(AGSS09),  $\Phi = (4.85 \pm 0.58) \times 10^6 \text{ cm}^{-2} \text{ s}^{-1}$ , and solar model predictions [72].

The combination of the LETA analysis by the SNO collaboration [112] and of the Borexino measurements [154] made possible a detailed study of the low energy part of the  $^8\text{B}$  solar neutrino spectrum. Even if characterized by a larger uncertainty (mainly due to a more limited statistics), Borexino

TABLE 8: Best-fit neutrino oscillation parameters from a three-flavor neutrino oscillation analysis. Uncertainties listed are  $\pm 1\sigma$  after the  $\chi^2$  was minimized with respect to all other parameters. The global analysis includes Solar + KL + ATM + LBL + CHOOZ.

Analysis	$\tan^2\theta_{12}^2$	$\Delta m_{12}^2$ [eV <sup>2</sup> ]	$\sin^2\theta_{13} \times 10^{-2}$
Solar	$0.436^{+0.048}_{-0.036}$	$5.13^{+1.49}_{-0.98} \times 10^{-5}$	$<5.8$ (95% C.L.)
Solar + KL	$0.446^{+0.030}_{-0.029}$	$7.41^{+0.21}_{-0.19} \times 10^{-5}$	$2.5^{+1.8}_{-1.5}$ $<5.3$ (95% C.L.)
Global			$2.02^{+0.88}_{-0.55}$

data confirm the LETA indication of low energy data points lower than the theoretical expectations based on matter enhanced oscillation and solar models as shown in Figure 17 (taken from [154]). These results agreed also with the Super-Kamiokande observation [110] of flat spectrum, consistent with the undistorted spectrum hypothesis. The emergence of this slight tension between theory and experiments seems to indicate the presence of new subdominant effects and also suggests the possibility of nonstandard neutrino interactions (like those studied in [168]) or the mixing with a very light sterile neutrino [169]. Future solar neutrino experiments, like SNO+, could shed more light on this subject, by performing precision measurements of lower energies solar neutrinos (like the *pep* neutrinos).

**6.2. Free Flux Analyses.** The increasing data of solar neutrinos allow to independently test the astrophysics of the solar interior and the physics of neutrino propagation. The analysis discussed in previous sections can be modified by also varying the solar neutrino fluxes in order to accommodate all neutrino data, while all the functional dependences are maintained as predicted by the standard model dependences. A key step in this kind of analysis is the imposition of the luminosity constraint [170, 171], which implements in a global way for the Sun the constraint of conservation of energy for nuclear fusion among light elements. Each neutrino flux is associated with a specific amount of energy released to the star and therefore a particular linear combination of the solar neutrino fluxes is equal to the solar luminosity (in appropriate units). One can write the luminosity constraint as

$$\frac{L_{\odot}}{4\pi(\text{A.U.})^2} = \sum_i \alpha_i \Phi_i, \quad (13)$$

where  $L_{\odot}$  is the solar luminosity measured at the Earth's surface, 1 AU is the average Earth-Sun distance, and the coefficient  $\alpha_i$  is the amount of energy provided to the star by nuclear fusion reactions associated with each of the important solar neutrino fluxes,  $\Phi_i$ . The coefficients  $\alpha_i$  are calculated accurately in [171].

The model independent determination of the solar neutrino fluxes [172, 173] shows that present solar neutrino data leads to accurate results for four fluxes and also the correlations between them. This information allows for a consistent global comparison of SSM fluxes with the inferred fluxes by neutrino data. Present data lead to the values for the inferred solar neutrino fluxes reported in the fourth column (labelled as “Solar”) of Table 4 in Section 3. The precision of the  $^7\text{Be}$  and  $^8\text{B}$  neutrino fluxes is driven by the Borexino and SNO

(SK) neutrino experiments, while the precision of the *pp* and *pep* neutrino fluxes mainly comes by the imposition of the luminosity constraint. The neutrino data directly demonstrates that the Sun shines by the *pp* chain. The CNO cycle only contributes to the total luminosity at the percent level.

The reader may wonder how much these inferences are affected by the luminosity constraint. The idea that the Sun shines because of nuclear fusion reactions can be tested accurately by comparing the observed photon luminosity of the Sun with the luminosity inferred from measurements of solar neutrino fluxes. Moreover, this same comparison will test a basic result of the standard solar model, namely, that the Sun is in a quasi-steady state in which the current energy generation in the interior equals the current luminosity at the solar surface. The free flux analysis, without imposing luminosity constraint, permits an estimation of the solar luminosity inferred by neutrino data, which agrees with the directly measured one within 15% ( $1\sigma$ ).

## 7. Future Solar Neutrino Experiments

**7.1. The Near Future: Improvement of *pep* Measurements and CNO Detection.** In the last decades, the intensive study of  $^8\text{B}$  and, more recently,  $^7\text{Be}$  solar neutrinos made possible fundamental steps forward in the solution of the solar neutrino puzzle and the determination of the neutrino mixing parameters. Nevertheless, many key features of the oscillation models (like the transition between the vacuum dominated sub-MeV region and the spectral region between 1 and 3 MeV, where matter effects become relevant) still have to be tested or verified with better accuracy and precision (see Figure 18, taken from [174]).

The apparent partial deficit of events in the low energy part of the  $^8\text{B}$  spectrum suggested the introduction of new theoretical models (as discussed in Section 6). Also for these reasons, the experimental efforts in the last years focused on the detection of neutrinos of ever decreasing energies, to fully confirm the validity of the MSW-LMA solution and verify the fluxes predicted by SSMs, discriminating between different versions of these models. The fluxes of the medium and high energy neutrinos of the *pp* chains ( $^7\text{Be}$ ,  $^8\text{B}$ , and *hep*) are predicted with quite large uncertainties, mainly due to the uncertainties in nuclear cross-sections and solar opacity (Table 5). The *pp* and *pep* fluxes, instead, are strongly correlated between themselves and their values are predicted with the highest precision because SSMs predict that *pp* chain reactions are responsible for more than 99% of the



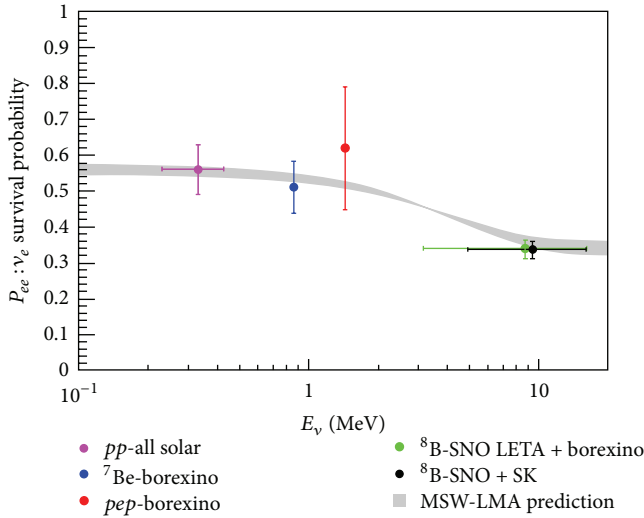


FIGURE 18: The  $\nu_e$  survival probability is represented as a function of neutrino energy. The gray band represents the MSW-LMA prediction. The higher survival probability region at low energies is where vacuum-dominated oscillations occur. As the neutrino energy increases, matter effects become important and the lower survival probability at high energies is due to matter-enhanced oscillations. The reported data correspond to solar neutrino flux measurements performed by different experiments. Taken from [174].

energy powering the Sun [80]. Therefore, the measurements of these components would be the most stringent test of the SSM. The tight correlation between *pep* and *pp* neutrinos is theoretically well established and, therefore, even in the pessimistic hypothesis that *pp* neutrinos could not be measured with the desired accuracy, a significant improvement in the *pep* neutrinos measurement with respect to data presently available would make it possible to reduce significantly the 15% indetermination on the solar luminosity (see Section 6.2) and to test indirectly the SSM's predictions that almost 100% of solar energy is produced by nuclear burning.

As already mentioned, water Čerenkov detectors, which played a fundamental role in the solution of the solar neutrino problem, are characterized by a low photon yield [175, 176] and therefore can detect only the higher part of the spectrum (*hep* and  $^8\text{B}$  neutrinos with a threshold around 3.5 MeV). The radiochemical experiments [153, 177] are limited, instead, by their ability to measure only the integrated neutrino rate above the charge-current interaction threshold (down to 0.23 MeV for the Gallium experiments), without the possibility to discriminate between the different spectrum components. Therefore, an important contribution should come from the present and future organic liquid scintillator detectors, planned to perform low energy solar neutrino spectroscopy. To reach this goal, they will take advantage from the high values of light yield (about  $10^4$  photons per MeV of deposited energy) and from the possibility to assemble very large masses of high purity materials. The excellent levels of radiopurity, reached, for instance, at Borexino, and

the typical geometry of these detectors (which are unsegmented and can be easily adapted to the definition of a fiducial volume) are fundamental to reduce the impact of the background, that is so critical due to the feebleness of the low energy signal.

In the near future, significant contributions are expected from Borexino and SNO+ [178] experiments (the main problem still surviving seems to be the reduction of  $^{210}\text{Pb}$ .) Borexino has already proved its importance in this kind of analysis performing the first measurements of *pep* and CNO neutrinos (even if the level accuracy is not yet the desired one) and further reducing, with the purification campaign started since July 2010, the level of contamination from almost all of the main radioactive background sources. The purification efforts are still ongoing and should make possible a further improvement on the accuracy of the signal extraction. Also, a novel technique [179] would allow to determine the  $^{210}\text{Bi}$  background. Preliminary calculations show that the CNO signal could be extracted from the  $^{210}\text{Bi}$  background with one year of data taking. The SNO+ experiment, that should start taking data soon in the SNOLAB, should take advantage from the location (about two times deeper underground than the Gran Sasso laboratory), with the consequent lower muon flux and a strongly reduced  $^{11}\text{C}$  rate. Moreover, thanks to the detector mass (about three times larger than in Borexino), it should be able to reach a higher counting rate. This could determine a fundamental improvement at least in the case of the *pep* neutrino measurement, where a 5% uncertainty is expected, to a level that should make possible a significant test of the MSW transition region.

In the more optimistic scenarios, it may be also possible to attack the main problem of measuring the lowest energy parts of the solar neutrino spectrum, that is, the *pp* neutrinos and the 0.38 MeV Berillium line. In any case, the presence in organic scintillators of an intrinsic  $^{14}\text{C}$  background will make this very low energy measurements an extremely hard task and they may require the introduction of new techniques, like the ones we are going to describe in the next subsections.

**7.2. The Far Future: Experimental Challenges.** The challenge for all future experiments aimed at measuring the low energy part of solar neutrino spectrum is that of assembling experimental devices with low energy thresholds suitable to detect a low rate signal in a region characterized by different potential sources of radioactive background. This difficult experimental task is common also to the experiments looking for neutrinoless double  $\beta$  decay or for dark matter signals (search for signatures of WIMPs, a stable or long-lived weakly interacting elementary particle, produced in the early Universe, whose existence is predicted in extensions of the standard model). In fact, some of the solar neutrino experiments planned for the future are multipurpose experiments designed also for the other above-quoted topics.

They are all characterized by a very large detector target mass and by the need to reach very high levels of radiopurity. The common feature is that of using scintillator detectors, but they differ for the chosen active scintillator material, which can vary from traditional organic scintillators (developed

with the use of innovative technological devices) to new materials, like the noble gases.

**7.2.1. Noble Liquid Detectors: CLEAN and XMASS.** One of the possible future frontiers is the idea to use scintillation detectors with liquid noble gases, like xenon, argon, and neon. These materials have the advantage of being relatively inexpensive, easy to obtain, and dense and it is not too difficult to build large homogeneous detectors of this kind; moreover, they can be quite easily purified, offer very high scintillation yields (about 30–40 photons/keV), and do not absorb their own scintillation light.

A first example is offered by the CLEAN/DEAP family, a series of detectors based entirely on scintillation in liquid neon (LNe) and liquid argon (LAr). They have been realized using a scalable technology in order to reach increasing sensitivities in the different prototypes realized and installed in the SNOLAB (Pico-CLEAN, Micro-CLEAN, DEAP-I, Mini-CLEAN and CLEAN/DEAP) with the aim to search for dark matter and to perform (through the analysis of elastic neutrino-electron and neutrino-nucleus scattering) a real-time measurement of the  $pp$  solar neutrino flux. The final detector CLEAN (cryogenic low energy astrophysics with noble gases) [180] (see Figure 19) will be made by a stainless steel tank, of about 6 meters of diameter, filled with 135 metric tons of cryogenic liquid neon; only the central part of it, surrounded isotropically by a series of photomultipliers, will constitute the detector fiducial volume. An external tank of water, 10 metres wide and 12 metres high, will act as  $\gamma$ -ray shielding, neutron shielding, and muon veto. According to Monte Carlo simulations, there should be a production of 15000 photons/MeV and it should be possible to reach a 100% photon wavelength shifter efficiency and a statistical uncertainty on the  $pp$  measurements of the order of 1%.

A precise measurement of the  $pp$  component and of the ratio between  $pp$  and  ${}^7\text{Be}$  fluxes would be essential to test the predictions of SSMs. A high accuracy on the  $pp$  neutrino flux would also make possible a better determination of the  $\theta_{12}$  mixing angle, which, complemented with the results from previous solar neutrino experiments and from KamLAND (essential for the  $\Delta m_{12}^2$  measurement), would be fundamental to test the consistency of the LMA solution also in the region of transition between vacuum dominated and matter enhanced oscillations. Finally, CLEAN could in principle try to measure also the CNO neutrino flux, through the analysis of neutrino spectrum from 0.7 to 1.0 MeV, with an estimated accuracy between 10% and 15%.

An interesting alternative to the use of neon is offered by liquid xenon scintillator detectors [181], which take advantage of the fact that among liquid rare gases xenon has the highest stopping power for penetrating radiation (thanks to its high atomic number,  $A \approx 131$ , and density,  $\rho = 3 \text{ g/cm}^3$ ) and also the highest ionization and scintillation yield. The technological improvements of the last twenty to thirty years made possible significant improvements in the cooling and purification techniques of this kind of detectors and in the possibility of assembling large mass detectors, of the order of some

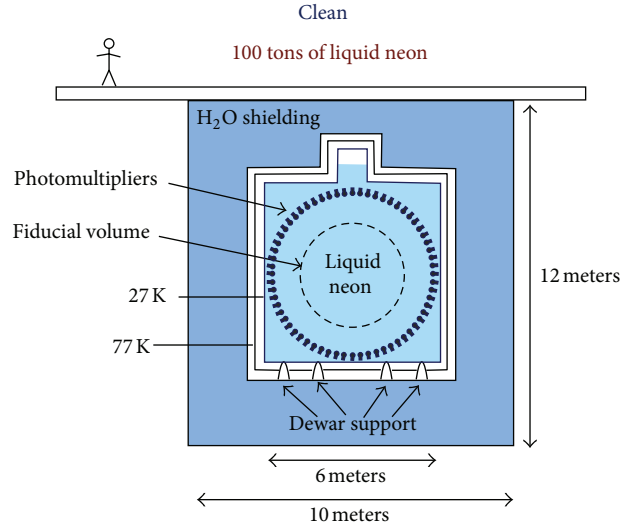


FIGURE 19: Scheme of the CLEAN detector. Taken from [180].

tons (like in the case of MEG [182] experiment, studying the  $\mu \rightarrow e\gamma$  decay).

The XMASS experiment (see Figure 20) is a multipurpose low background and low energy threshold experiment that will use a large massive liquid xenon detector and has been designed to look for WIMPs (dark matter candidates), search for neutrinoless double  $\beta$  decay, and study the  $pp$  and the  ${}^7\text{Be}$  solar neutrinos. After two preliminary phases, during which smaller prototypes have been realized and installed in the Kamioka mine [183], and the first data on double beta decay and dark matter have been taken, the full XMASS detector (that will measure also solar neutrinos) will have a total mass of 20 metric tons, with a fiducial volume of 10 metric tons. Special efforts are required mainly to lower the background, by reducing the radioactive contamination in the parts used for detector construction (with special attention to the photomultipliers and the copper material used for PMT holder), constructing a larger pure water active shield (for muons and mainly neutrons and  $\gamma$  rays), and, above all, developing a distillation system for xenon in order to reduce the contamination by  ${}^{85}\text{Kr}$ , the major source of radioactive background inside the detector.

Another interesting experimental project based on the noble gases liquid scintillator technique is that of DARWIN (dark matter wimp search with noble liquids) [185], which brings together different European and US research groups working on existing experiments and on the study for a future multiton scale LAr and LXe dark matter search facility in Europe. The main goal of the experiment is to look for a WIMP signal and to demonstrate its dark matter nature, taking advantage from the fact of performing the measurement with multiple different targets operating under similar conditions. In this way, it should be possible to estimate the dependence of the rate with the target material and, therefore, to better determine the WIMP candidate mass and to distinguish between spin independent and spin dependent

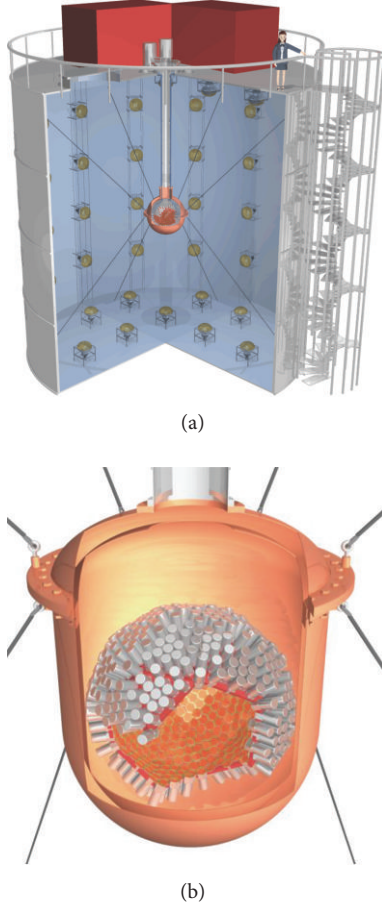


FIGURE 20: Schematic view of the full XMASS facility (a) and details of the inner detector (b) from which one can see the particular configuration of the hexagonal photomultiplier tubes. Taken from [183, 184].

couplings. The energy region of the nuclear recoil spectrum, below 200 keV, that should be investigated by this future experiment is of particular interest also for the study of the  $pp$  solar neutrinos and, in fact, the elastic scattering on electrons by the low energy component of the neutrino spectrum would be one of the main background sources for WIMP searches in liquid xenon detectors, as shown in Figure 21.

DARWIN officially started in 2010; a technical design study should be ready in Spring 2013 and the start of the first physics run is expected by mid-2017.

**7.2.2. Multikiloton Scale Liquid Scintillators: Example LENA.** The Borexino experiment demonstrated the great potential of the liquid-scintillator technique for the detection of low energy solar neutrinos. Thanks to this experience, a next-generation neutrino detector has been proposed: LENA (low energy neutrino astronomy) [186]. LENA is a multipurpose detector aiming to study supernova neutrinos, diffuse supernova neutrino background, proton decay, atmospheric neutrinos, long-baseline neutrino beams, geoneutrinos, and, last but not least, solar neutrinos. The LENA project foresees a cylindrical detector with a diameter of 30 m and a length of

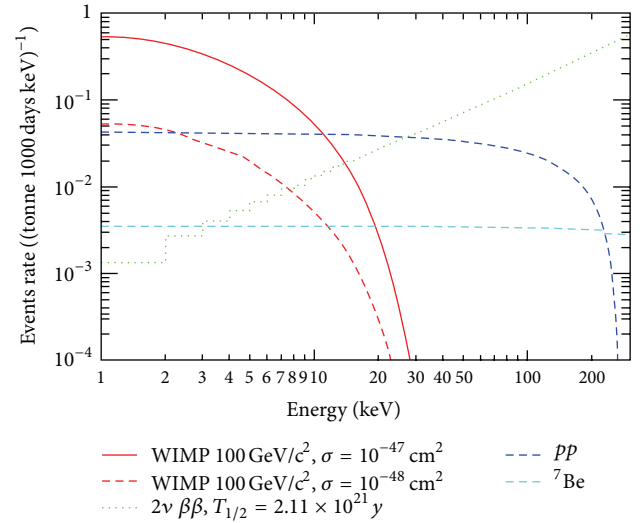


FIGURE 21: Expected nuclear recoil spectrum from WIMP scatters in LXe for a spin-independent WIMP-nucleon cross-section of  $10^{-47} \text{ cm}^2$  (red solid) and  $10^{-48} \text{ cm}^2$  (red dashed) and a WIMP mass of 100  $\text{GeV}/c^2$ , along with the differential energy spectrum for  $pp$  (blue) and  ${}^7\text{Be}$  (cyan) neutrinos, and the electron recoil spectrum from the double beta decay of  ${}^{136}\text{Xe}$  (green). Assumptions are 99.5% discrimination of electronic recoils, 50% acceptance of nuclear recoils, and 80% flat analysis cuts acceptance. Taken from [185].

about 100 m. Inside the detector is foreseen an internal part (with a diameter of about 26 m) containing about 50 kilotons of liquid scintillator, separated from a nonscintillating buffer region by a nylon barrier. Outside, a tank (made in steel or concrete) separates the inner detector from an outer water tank; it is used both for shielding and as an active muon veto. To collect the scintillation light, about 45,000 photomultipliers (with a diameter of 20 cm) are mounted to the internal walls of the detector. To increase the optically active area, the photomultiplier tubes are equipped with conic mirrors, the corresponding surface coverage is about 30%. Figure 22 shows a schematic overview of the current LENA design.

Among the favored solvent for the liquid scintillator in LENA, the LAB (linear alkylbenzene) is currently the preferred one. It has a high light yield and large attenuation length and it has also the advantage of being a nonhazardous liquid. The attenuation lengths is on the order of 10 to 20 m (at a wavelength of 430 nm) and the photoelectron yield could be greater than 200 photoelectrons per MeV (with a scintillator mixture containing 2 g/L PPO and 20 mg/L bisMSB as wavelength shifters). Studies have been carried out to test the large-scale light transport and the differences in scintillator response for  $\alpha$ ,  $\beta$ , and  $\gamma$  particles. An alternative solvent option is the well-studied PXE [187] or a mixture of PXE and dodecane.

As already pointed out, Borexino has splendidly demonstrated the potential of the detection technique with liquid scintillator based detectors for the solar neutrino detection. This technique offers the opportunity for a spectrally resolved measurement of the solar neutrino spectrum in the all energy range.

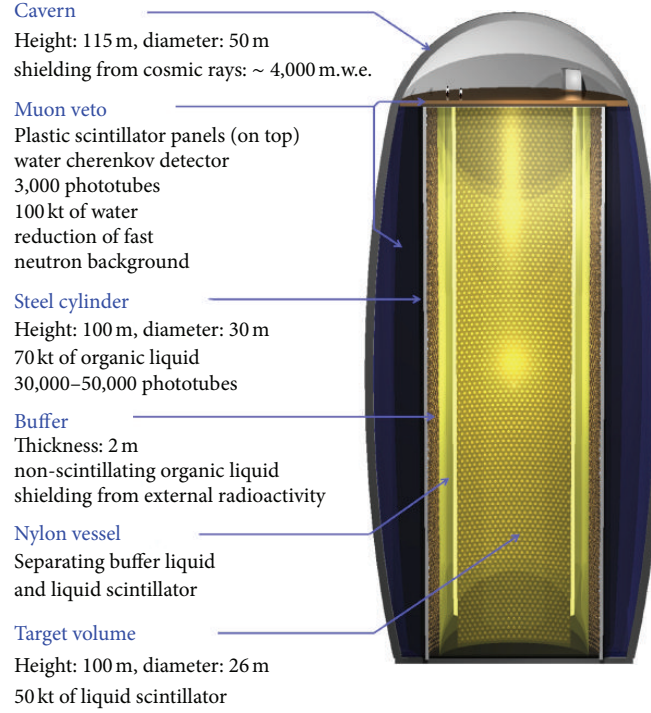


FIGURE 22: Schematical view of the LENA detector. From [186].

TABLE 9: Expected solar neutrino rates in LENA (channel  $\nu e \rightarrow e\nu$ ). The estimates are derived from the existing Borexino analyses [154, 188] as well as expectation values for the respective energy windows (EW) of observation [189–191]. The quoted fiducial masses,  $m_{\text{fid}}$ , in LAB are based on a Monte Carlo simulation of the external  $\gamma$ -ray background in LENA. Table taken and adapted from [186].

Source	EW [MeV]	$m_{\text{fid}}$ [kt]	Rate [cpd]
$pp$	$>0.25$	30	40
$pep$	$0.8\text{--}1.4$	30	$2.8 \times 10^2$
${}^7\text{LiBe}$	$>0.25$	35	$1.0 \times 10^4$
${}^8\text{LiB}$	$>2.8$	35	79
CNO	$0.8\text{--}1.4$	30	$1.9 \times 10^2$

Because the smaller ratio of surface to volume compared to the Borexino detector in LENA it is very likely to reach the excellent background conditions of Borexino (A smaller ratio of surface to volume decreases the chance that the scintillator is contaminated with radioimpurities.) Monte Carlo simulations of the gamma background due to the uranium, thorium, and potassium from the photomultipliers glass show that a fiducial volume of the order of 30 ktons is achievable for solar neutrino studies; LENA will be able to address topics both in neutrino oscillations and in solar physics thanks to its unprecedented statistics. A high statistics can be obtained in short times and in both Pyhsalmi and Frejus underground laboratories, where the detector could be hosted and where the cosmogenic background of  ${}^{11}\text{C}$  will be significantly lower than in Borexino.

Monte Carlo simulations show that for  $pep$ , CNO, and low-energy  ${}^8\text{B}$ -vs detection a fiducial mass of  $\sim 30$  kton is necessary, while the fiducial mass for  ${}^7\text{Be}$ -vs and

high-energy ( $E > 5$  MeV)  ${}^8\text{B}$ -vs could be enlarged to 35 kton or more.

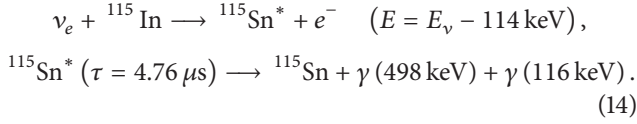
In Table 9 the expected rates in 30 kton for the neutrinos emitted in the  $pp$  chain and the CNO-bicycle are reported, using the most recent solar model predictions. This evaluation refers to a detection threshold set at about 250 keV.

**7.2.3. New Techniques with Organic Scintillators: LENS.** The main goal of the Low Energy Neutrino Spectroscopy (LENS) detector is the real-time measurement of solar neutrinos as a function of their energy, focusing, on particular, in the analysis of the lowest energy neutrinos coming from the proton-proton fusion (i.e., the  $pp$  neutrinos), which represent the main contribution and the less known component of the  $pp$ -chain of fusion reactions inside the Sun.

In order to make an energy spectrum measurement on low energy neutrinos, it is necessary to reach a low threshold for the charged current (CC) process and to be able to



discriminate the background from radioactive decays. The CC process employed in LENS is the neutrino induced transition of  $^{115}\text{In}$  to an excited state of  $^{115}\text{Sn}$ :



Thanks to that it is possible to detect low energy neutrinos with a threshold of 114 keV and measure their energy, following an idea that has been investigated since the 1970s [192].

The primary interaction and the secondary cascade enable a triple coincidence, correlated in space and time. LENS employs as detection medium a liquid scintillator chemically doped with natural indium ( $^{115}\text{In} = 95.7\%$ ). In order to exploit the spatial correlation, the volume of the detector is segmented into cubic cells (7.5 cm) by clear foils (Teflon FEP) that have a lower index of refraction than the liquid scintillator. By internal reflection, the scintillation light produced in a cell is channeled in the directions of the 6-cell faces. The collected channeled light is read out at the edge of the detector by photomultiplier tubes.

LENS should be able to determine the low energy solar neutrino fluxes with an accuracy  $\leq 4\%$ , testing neutrino and solar physics with a global precision better than the present one and also looking for any inconsistency in the LMA conversion mechanism [193].

## 8. Remarks on the Present Status and Future Outlooks

In this paper we went through the main results obtained in the study of solar neutrinos and we focused our attention mainly on the last decade advancements. Since the discovery of neutrino oscillations and the solution to the long standing solar neutrino problem at the dawn of the century, solar neutrino physics has evolved quickly and has become a mature field. It took advantage from the great amount of data of the different working phases of experiments like Super-Kamiokande and SNO, corroborated by the analogous studies of the reactor experiment KamLAND and recently sustained also by the first “low energy” real-time measurements performed by Borexino.

A coherent picture emerges from all of these experimental achievements and from the global analyses performed by the single experimental collaborations and in other parallel theoretical and phenomenological studies and we can say that the basic properties and the values of the parameters driving solar neutrino oscillations,  $\Delta m_{12}^2$ , and  $\theta_{12}$  are now known with quite a satisfactory accuracy (Tables 7 and 8) and the validity of the MSW-LMA solution is well established (Figure 18). Nevertheless, there are still important aspects of the oscillation mechanism on which we would like to shed more light. In particular the vacuum to matter transition regime requires further study (see also Section 9).

Important parallel advancements took place in the study of neutrino oscillations during the very last years; in particular a series of reactor short baseline experiments have confidently established that the mixing angle  $\theta_{13}$  is different from zero, opening interesting opportunities for future experiments looking for leptonic CP violation (the details have been given in Section 6).

From an astrophysical point of view, current solar neutrino data have put us on the verge of fulfilling the original dream of Davies and Bahcall and use solar neutrinos as a probe of the nuclear fusion processes that power the Sun and the vast majority of stars. The four relevant neutrino fluxes produced in the different pp-chains are, thanks to the latest efforts from Borexino, now very well constrained from experimental data ( $^7\text{Be}$  has the largest uncertainty, 4.5%, if the solar luminosity constraint is used in the analysis of the data). Standard solar model predictions are in excellent agreement with solar fluxes, regardless of the solar composition assumed in the construction of the model. In fact, the agreement is so good for both *high-Z* and *low-Z* solar models (Table 4) that it is very unlikely that neutrino fluxes from pp-chains will be able to discriminate between solar compositions. Borexino has also recently established the most stringent upper limit on CNO fluxes which is now only a factor of 1.5 larger than solar model predictions. CNO fluxes carry a wealth of information about the solar core and are, for solar physics, the most coveted prize. The latest developments, both experimentally and in background subtraction techniques, place Borexino at the doors of this momentous measurement. In this regard, potentiality of SNO+ is unmatched, but at present the primary solar neutrino measurements are planned to take place after the double beta decay measurements are carried out for at least 4 years. Some of the possibilities that a measurement of CNO fluxes would offer are discussed in the next section, together with some of the main questions which are still open.

## 9. Open Questions in Solar Neutrino Physics

**9.1. The Metallicity Problem.** The solar abundance or solar metallicity problem has been around for some time now. In analogy with the solar neutrino problem, there have been attempts (although in most cases, it is fair to say, of somewhat less radical nature) to solve it by introducing modifications to the input physics of SSMs. To mention a few of them, we could remember the following:

- (i) large enhancement of Ne abundance [194, 195] is important because of its contribution uncertainty and a weak bond in solar abundances because its abundance is determined rather indirectly [44];
- (ii) increased element diffusion rates [67, 196];
- (iii) accretion of metal-poor materials leading to a “two-zone” solar model in terms of composition [64, 196, 197].

Also solar models including some sort of prescriptions to account for rotation and other dynamical effects have been put forward; however, their performance is quite poor.

So far, all attempts of finding a solution to all the manifestations of the solar abundance problem have failed. In some cases,  $Y_8$  can be brought into agreement with helioseismology, in other cases  $R_{CZ}$  and the sound speed profile, but a simultaneous solution to all the problems has not yet been found.

The exceptions are the two obvious ones: (a) the *low-Z* solar abundances actually underestimate the true metal content of the Sun; (b) an increase of radiative opacities by the right amount (15% to 20% at the base of the convective zone down to about 3% in the solar core) to compensate for the decrease induced by the *low-Z* abundances. The drawback to this idea is that current state-of-the-art radiative opacity calculations differ by only 2 to 3% at the base of the convective envelope, much lower from what would be required by *low-Z* models.

It has indeed been shown that by increasing the radiative opacity in *low-Z* SSMs the agreement with helioseismology can be restored to match results from *high-Z* SSMs [198]. Additionally, the  $^7\text{Be}$  and  $^8\text{B}$  fluxes of a *low-Z* SSMs with increased opacity coincide with those from a *high-Z* model [199]. As good as this may seem, it shows the intrinsic degeneracy between composition and opacities.

Recently, a novel approach, the linear solar models (LSM), that relate changes in solar observables to modifications in the input physics by the calculation of kernels based on SSMs has been developed by [200] (We remark that LSMs offer an efficient way of studying the response of the solar structure to changes in any of the physical ingredients entering solar model calculations that does not require the construction of solar models with the varied physics.). LSMs have been applied in particular to the solar abundance problem and the changes required in the radiative opacity to restore the agreement between *low-Z* models and helioseismology [201] quantitatively, result similar to those quoted above.

By using  $^8\text{B}$  and now  $^7\text{Be}$  as thermometers of the solar core [79], CNO neutrinos represent a unique way to break this degeneracy and provide an independent determination of the CNO abundances, particularly the C + N abundance in the solar core. Keeping in mind the antagonism between solar interior and solar atmosphere models that the solar abundance problem has established, results from CNO fluxes will be of the outmost relevance for solar, and by extension stellar, physics.

**9.2. The Vacuum to Matter Transition?** Solar neutrino experiments already measured the two-extreme-flavor conversion regimes, the vacuum term domination and matter term domination. There is no direct experimental evidence of the transition from one to the other. In fact, the lower energetic  $^8\text{B}$  neutrinos are sensitive to the rise of the spectrum from matter combination towards vacuum, but the data (still very uncertain) seem not to show it. More data coming from Super-Kamiokande, Borexino, and SNO+ experiments will further explore the conversion in this regime.

The precise measurement of low energy neutrinos like pep, exploiting the fact that are more energetic than  $^7\text{Be}$  neutrinos, will also help to see small solar matter effects in the

flavor conversion. This matter effects will be more precisely determined by the comparison of pep and pp neutrino measurements. In fact, the low energy neutrinos that are better suited to test matter effects are the CNO neutrinos. While the CNO neutrinos energy is around the pep neutrinos energy, the former are produced at higher temperatures and therefore at higher densities. The larger matter density where neutrinos are produced leads to larger matter effects for CNO neutrinos than for pep neutrinos. In fact, matter effects produce a significant spectral tilt of CNO neutrinos ( $\sim 10\%$ ), which might be a good handle to separate the signal for background.

The determination of the vacuum to matter transition has a significant impact on the determination of the solar mass splitting derived by solar data, which adds to the implications of Earth-matter effects measured by comparing the neutrino fluxes during the day and night. The good match of the independently determined solar mass splitting by solar neutrino experiments and by reactor experiments leads to the best test on nonstandard neutrino physics to solar neutrinos. There are many possibilities but the two scenarios more studied are the addition of new neutral current interactions [168, 202] which modify the amplitude of matter effects and therefore shift the effective mass splitting and the existence of a sterile neutrino which adds a new state with the appropriate mass splitting [169] to produce deviations of the flavor conversion in the 1–3 MeV range.

**9.3. What Else Can We Learn from CNO Fluxes?** The most fundamental information the CNO fluxes carry is the most obvious one: that the CNO-bicycle operates in stars and it is a viable process for hydrogen fusion. It must not be forgotten that neutrinos are the only direct evidence of nuclear reactions being the source of energy in solar (stellar) interiors. For the Sun, models predict a marginal contribution to the total energy budget from CNO reactions, 0.8% and 0.4% for *high-Z* and *low-Z* solar models. However, CNO becomes the dominant mode for hydrogen burning in stars with masses right above the solar value. Detection of CNO neutrinos will provide direct evidence that CNO reactions actually take place in nature, as originally envisioned by Bethe [203]; it has been a long wait.

The second important aspect of CNO neutrinos is the information they provide about the abundance of metals in the solar core. Knowing the abundance of CNO elements in the solar core is important by itself. In particular, a “perfect” measurement of the combined  $^{13}\text{N} + ^{15}\text{O}$  flux translates into a determination of the solar C + N abundance with  $\sim 10\%$  uncertainty [79], and the dominant sources of uncertainties are experimental and can be potentially reduced. Assuming we know the solar surface abundance of the same elements, that is, let us forget for the time being about the solar abundance problem, we can then put constraints on mixing mechanisms that may have created composition gradients during the evolution of the Sun. SSMs predict that the number density of C + N is enhanced in the solar core, at present day, by  $\sim 16\%$  with respect to the surface due to the effects of the microscopic diffusion. And, although helioseismology shows that models with diffusion work much better than models

without, there is no direct evidence of how efficient diffusion is. In fact, there have been suggestions that the standard prescription [204] may be too efficient in the Sun [205] and that diffusion rates should be lowered by  $\sim 15\%$ . Solar CNO neutrinos could provide a test for the efficiency of the diffusion.

There are other possibilities that might create a contrast between the solar core and surface composition. Recently, it has been shown that the Sun has a peculiar composition when compared to “solar twins,” that is, stars almost identical to the Sun in their surface properties [206, 207]. The authors found that the Sun is enhanced in volatile elements with respect to the solar twins that show no sign of harbouring planets by about 20%. In fact, they have associated this fact to the presence of rocky planets in the solar system, where refractory elements are locked, and the occurrence of an accretion episode of volatile-enriched material [207] after rocky cores is formed in the protoplanetary disk. If this was true, then the Sun would have an envelope that is richer in CNO than its interior. If a measurement of the  $^{13}\text{N} + ^{15}\text{O}$  flux would yield as a result a core composition where the abundance of C + N would be comparable or less than the surface value, then we would have an extremely exciting piece of evidence about the earlier phases of planet formation in the solar system [79].

## Acknowledgments

C. Pena-Garay is supported in part by the Spanish MICINN Grants FPA-2007-60323 and FPA2011-29678, the Generalitat Valenciana Grant PROMETEO/2009/116, and the ITN INVISIBLES (Marie Curie Actions, PITN-GA-2011-289442). A. Serenelli is supported by the European Union International Reintegration Grant PIRG-GA-2009-247732 and the MICINN Grant AYA2011-24704. The authors are all grateful to the editors of this special issue on neutrino physics for their invitation and support.

## References

- [1] S. M. Bilenky, C. Giunti, and W. Grimus, “Phenomenology of neutrino oscillations,” *Progress in Particle and Nuclear Physics*, vol. 43, no. 1, pp. 1–86, 1999.
- [2] G. Altarelli and F. Feruglio, “Models of neutrino masses and mixings,” *New Journal of Physics*, vol. 6, pp. 1–39, 2004.
- [3] A. Strumia and F. Vissani, “Implications of neutrino data circa 2005,” *Nuclear Physics B*, vol. 726, no. 1-2, pp. 294–316, 2005.
- [4] A. Strumia and F. Vissani, “Neutrino masses and mixings and...,” <http://arxiv.org/abs/hep-ph/0606054>.
- [5] R. N. Mohapatra, S. Antusch, K. S. Babu et al., “Theory of neutrinos,” submitted, <http://arxiv.org/abs/hep-ph/0412099>.
- [6] T. Hambye, Y. Lin, A. Notari, M. Papucci, and A. Strumia, “Constraints on neutrino masses from leptogenesis models,” *Nuclear Physics B*, vol. 695, no. 1-2, pp. 169–191, 2004.
- [7] R. N. Mohapatra and A. Y. Smirnov, “Neutrino mass and new physics,” *Annual Review of Nuclear and Particle Science*, vol. 56, pp. 569–628, 2006.
- [8] R. Barbieri, P. Creminelli, and A. Strumia, “Neutrino oscillations and large extra dimensions,” *Nuclear Physics B*, vol. 585, no. 1-2, pp. 28–44, 2000.
- [9] N. Arkani-Hamed, S. Dimopoulos, G. R. Dvali, and J. March-Russell, “Neutrino masses from large extra dimensions,” *Physical Review D*, vol. 65, no. 2, Article ID 024032, 2002.
- [10] G. Altarelli and F. Feruglio, “Tri-bimaximal neutrino mixing from discrete symmetry in extra dimensions,” *Nuclear Physics B*, vol. 720, no. 1-2, pp. 64–88, 2005.
- [11] G. C. Branco, R. González Felipe, F. R. Joaquim, and M. N. Rebelo, “Leptogenesis, CP violation and neutrino data: What can we learn?” *Nuclear Physics B*, vol. 640, no. 1-2, pp. 202–232, 2002.
- [12] E. K. Akhmedov, M. Frigerio, and A. Y. Smirnov, “Probing the seesaw mechanism with neutrino data and leptogenesis,” *Journal of High Energy Physics*, vol. 309, p. 21, 2003.
- [13] T. Hambye, Y. Lin, A. Notari, M. Papucci, and A. Strumia, “Constraints on neutrino masses from leptogenesis models,” *Nuclear Physics B*, vol. 695, no. 1-2, pp. 169–191, 2004.
- [14] J. N. Bahcall, “Solar neutrinos. I. Theoretical,” *Physical Review Letters*, vol. 12, pp. 300–302, 1964.
- [15] R. J. Davis, “Solar neutrinos. II. Experimental,” *Physical Review Letters*, vol. 12, pp. 302–305, 1964.
- [16] R. J. Davis, D. S. Harmer, and K. C. Hoffman, “Search for neutrinos from the sun,” *Physical Review Letters*, vol. 20, pp. 1205–1209, 1968.
- [17] L. Miramonti and F. Reseghetti, “Solar neutrino physics: historical evolution, present status and perspectives,” *Rivista del Nuovo Cimento*, vol. 25, no. 7, pp. 1–128, 2002.
- [18] B. Pontecorvo, “Mesonium and anti-mesonium,” *Journal of Experimental and Theoretical Physics*, vol. 33, p. 549, 1957, Soviet Physics, vol. 6, pp. 429, 1958.
- [19] B. Pontecorvo, “Inverse beta processes and nonconservation of lepton charge,” *Journal of Experimental and Theoretical Physics*, vol. 34, p. 247, 1958, Soviet Physics, vol. 7, pp. 172, 1958.
- [20] K. S. Hirata, T. Kajita, T. Kifune et al., “Observation of  $^8\text{B}$  solar neutrinos in the Kamiokande-II detector,” *Physical Review Letters*, vol. 63, pp. 16–19, 1989.
- [21] Y. Fukuda, T. Hayakawa, E. Ichihara et al., “Measurement of the solar neutrino energy spectrum using neutrino-electron scattering,” *Physical Review Letters*, vol. 82, pp. 2430–2434, 1999.
- [22] W. Hampel, J. Handta, G. Heusser et al., “GALLEX solar neutrino observations: results for GALLEX IV,” *Physics Letters B*, vol. 447, pp. 127–133, 1999.
- [23] M. Altmann, M. Balatab, P. Bellic et al., “Complete results for five years of GNO solar neutrino observations,” *Physics Letters B*, vol. 616, pp. 174–190, 2005.
- [24] J. N. Abdurashitov, T. J. Bowles, M. L. Cherry et al., “Measurement of the solar neutrino capture rate by SAGE and implications for neutrino oscillations in vacuum,” *Physical Review Letters*, vol. 83, pp. 4686–4689, 1999.
- [25] Q. R. Ahmad, R. C. Allen, T. C. Andersen et al., “Measurement of the rate of  $\nu_e + d \rightarrow p + p + e^-$  interactions produced by  $^8\text{B}$  solar neutrinos at the Sudbury neutrino observatory,” *Physical Review Letters*, vol. 87, Article ID 071301, 2001.
- [26] S. Fukuda, Y. Fukuda, M. Ishitsuka et al., “Solar  $^8\text{B}$  and hep neutrino measurements from 1258 days of super-kamiokande data,” *Physical Review Letters*, vol. 86, pp. 5651–5655, 2001.
- [27] J. N. Bahcall, M. C. Gonzalez-Garcia, and C. Peña-Garay, “Global analysis of solar neutrino oscillations including SNO CC measurement,” *Journal of High Energy Physics*, vol. 8, p. 14, 2001.
- [28] G. L. Fogli, E. Lisi, D. Montanino, and A. Palazzo, “Model-dependent and independent implications of the first Sudbury



- Neutrino Observatory results,” *Physical Review D*, vol. 64, Article ID 093007, 2001.
- [29] Q. R. Ahmad, R. C. Allen, T. C. Andersen et al., “Direct evidence for neutrino flavor transformation from neutral-current interactions in the Sudbury Neutrino Observatory,” *Physical Review Letters*, vol. 89, no. 1, Article ID 011301, 6 pages, 2002.
- [30] S. N. Ahmed, A. E. Anthony, E. W. Beier et al., “Measurement of the total active  $^8\text{B}$  solar neutrino flux at the sudbury neutrino observatory with enhanced neutral current sensitivity,” *Physical Review Letters*, vol. 92, no. 18, Article ID 181301, 6 pages, 2004.
- [31] B. Aharmim, S. N. Ahmed, J. F. Amsbaugh et al., “Independent measurement of the total active  $^8\text{B}$  solar neutrino flux using an array of  $^3\text{He}$  proportional counters at the sudbury neutrino observatory,” *Physical Review Letters*, vol. 101, Article ID 111301, 5 pages, 2008.
- [32] Q. R. Ahmad, R. C. Allen, T. C. Andersen et al., “Measurement of day and night neutrino energy spectra at SNO and constraints on neutrino mixing parameters,” *Physical Review Letters*, vol. 89, no. 1, Article ID 011302, 5 pages, 2002.
- [33] R. Davis, “Memories of a Nobel laureate,” *CERN Courier*, vol. 42, no. 10, p. 15, 2002.
- [34] K. Eguchi, S. Enomoto, K. Furuno et al., “First results from KamLAND: evidence for reactor antineutrino disappearance,” *Physical Review Letters*, vol. 90, Article ID 021802, 6 pages, 2003.
- [35] J. N. Bahcall, M. Pinsonneault, and S. Basu, “Solar models: current epoch and time dependences, neutrinos, and helioseismological properties,” *The Astrophysical Journal*, vol. 555, no. 2, p. 990, 2001.
- [36] A. Piepke, “KamLAND: a reactor neutrino experiment testing the solar neutrino anomaly,” *Nuclear Physics B*, vol. 91, pp. 99–104, 2001.
- [37] A. de Gouvea and C. Peña-Garay, “Solving the solar neutrino puzzle with KamLAND and solar data,” *Physical Review D*, vol. 64, Article ID 011301, 8 pages, 2001.
- [38] P. Aliani, V. Antonelli, M. Picariello, and E. Torrente-Lujan, “KamLAND and the determination of neutrino mixing parameters in the post SNO-NC era,” *New Journal of Physics*, vol. 5, p. 2, 2003.
- [39] T. Araki, K. Eguchi, S. Enomoto et al., “Measurement of neutrino oscillation with KamLAND: evidence of spectral distortion,” *Physical Review Letters*, vol. 94, Article ID 081801, 8 pages, 2005.
- [40] S. Abe, T. Ebihara, S. Enomoto et al., “Precision measurement of neutrino oscillation parameters with KamLAND,” *Physical Review Letters*, vol. 100, no. 22, Article ID 221803, 5 pages, 2008.
- [41] A. Gando, Y. Gando, K. Ichimura et al., “Constraints on  $\theta_{13}$  from a three-flavor oscillation analysis of reactor antineutrinos at KamLAND,” *Physical Review D*, vol. 83, Article ID 052002, 11 pages, 2011.
- [42] J. N. Bahcall, W. F. Huebner, S. H. Lubow, P. D. Parker, and R. K. Ulrich, “Standard solar models and the uncertainties in predicted capture rates of solar neutrinos,” *Reviews of Modern Physics*, vol. 54, pp. 767–799, 1982.
- [43] J. N. Bahcall, *Neutrino Astrophysics*, Cambridge University Press, 1989.
- [44] K. Lodders, H. Palme, and H.-P. Gail, “Abundances of the elements in the solar system,” submitted, <http://arxiv.org/abs/0901.1149>.
- [45] B. Beeck, R. Collet, M. Steffen et al., “Simulations of the solar near-surface layers with the CO5BOLD, MURaM, and Stagger codes,” *Astronom & Astrophys*, vol. 539, article 121, 11 pages, 2012.
- [46] M. Asplund, N. Grevesse, A. J. Sauval, and P. Scott, “The chemical composition of the sun,” *Annual Review of Astronomy and Astrophysics*, vol. 47, pp. 481–522, 2009.
- [47] M. Asplund, N. Grevesse, and J. Sauval, “The solar chemical composition,” in *Cosmic Abundances as Records of Stellar Evolution and Nucleosynthesis*, T. G. Barnes III and F. N. Bash, Eds., vol. 336, p. 25, 2005.
- [48] C. Allende Prieto, D. L. Lambert, and M. Asplund, “The forbidden abundance of oxygen in the sun,” *The Astrophysical Journal Letters*, vol. 556, p. L63, 2001.
- [49] N. Grevesse and A. Noels, “Solar composition,” in *Origin and Evolution of Elements*, N. Prantzos, E. Vangioni-Flam, and M. Casse, Eds., p. 15, 1993.
- [50] N. Grevesse and A. J. Sauval, “Standard solar composition,” *Space Science Reviews*, vol. 85, no. 1-2, pp. 161–174, 1998.
- [51] E. Caffau, H. G. Ludwig, M. Steffen, B. Freytag, and P. Bonifacio, “Solar chemical abundances determined with a CO5BOLD 3D model atmosphere,” *Solar Physics*, vol. 268, no. 2, pp. 255–269, 2011.
- [52] C. A. Iglesias and F. J. Rogers, “Updated opal opacities,” *The Astrophysical Journal*, vol. 464, p. 943, 1996.
- [53] N. R. Badnell, M. A. Bautista, K. Butler et al., “Updated opacities from the opacity project,” *Monthly Notices of the Royal Astronomical Society*, vol. 360, no. 2, pp. 458–464, 2005.
- [54] J. W. Ferguson, D. R. Alexander, F. Allard et al., “Low-temperature opacities,” *The Astrophysical Journal*, vol. 623, p. 585, 2005.
- [55] E. G. Adelberger, A. García, R. G. H. Robertson et al., “Solar fusion cross sections. II. The pp chain and CNO cycles,” *Reviews of Modern Physics*, vol. 83, pp. 195–245, 2011.
- [56] E. G. Adelberger, S. M. Austin, J. N. Bahcall et al., “Solar fusion cross sections,” *Reviews of Modern Physics*, vol. 70, pp. 1265–1291, 1998.
- [57] J. Christensen Dalsgaard, “Helioseismology,” *Reviews of Modern Physics*, vol. 74, pp. 1073–1129, 2002.
- [58] J. Christensen Dalsgaard, W. Dappen, S. V. Ajukov et al., “The current state of solar modeling,” *Science*, vol. 272, pp. 1286–1292, 1996.
- [59] S. Basu and H. M. Antia, “Seismic measurement of the depth of the solar convection zone,” *Monthly Notices of the Royal Astronomical Society*, vol. 287, no. 1, pp. 189–198, 1997.
- [60] S. Basu and H. Antia, “Constraining solar abundances using helioseismology,” *The Astrophysical Journal Letters*, vol. 606, no. 1, p. 85L, 2004.
- [61] S. Basu et al. “Solar internal sound speed as inferred from combined BiSON and LOWL oscillation frequencies,” *Monthly Notices of the Royal Astronomical Society*, vol. 292, no. 2, pp. 243–251, 1997.
- [62] A. G. Kosovichev, J. Schou, P. H. Scherrer et al., “Structure and rotation of the solar interior: initial results from the Mdi medium-L program,” *Solar Physics*, vol. 170, no. 1, pp. 43–61, 1997.
- [63] S. Basu, W. J. Chaplin, Y. Elsworth, R. New, and A. M. Serenelli, “Fresh insights on the structure of the solar core,” *Astrophysical Journal Letters*, vol. 699, no. 2, pp. 1403–1417, 2009.
- [64] A. M. Serenelli, W. C. Haxton, and C. Peña-Garay, “Solar models with accretion. I. Application to the solar abundance problem,” *The Astrophysical Journal*, vol. 743, p. 24, 2011.
- [65] H. M. Antia and S. Basu, “Determining solar abundances using helio seismology,” *Astrophysical Journal Letters*, vol. 644, no. 2, pp. 1292–1298, 2006.



- [66] W. J. Chaplin, A. M. Serenelli, S. Basu, Y. Elsworth, R. New, and G. A. Verner, "Solar heavy-element abundance: constraints from frequency separation of low-degree p-modes," *Astrophysical Journal Letters*, vol. 670, no. 1, pp. 872–884, 2007.
- [67] J. Montalbán, A. Miglio, A. Noels, and N. Grevesse, "In SOHO 14 Helio- and asteroseismology: towards a golden future," *ESA Special Publication*, vol. 559, p. 574, 2004.
- [68] S. Turck-Chièze, S. Couvidat, L. Piau et al., "Surprising sun: a new step towards a complete picture?" *Physical Review Letters*, vol. 93, Article ID 211102, 4 pages, 2004.
- [69] J. N. Bahcall, S. Basu, M. H. Pinsonneault, and A. M. Serenelli, "Helioseismological implications of recent solar abundance determinations," *Astrophysical Journal*, vol. 618, no. 2, pp. 1049–1056, 2005.
- [70] F. Delahaye and M. H. Pinsonneault, "The solar heavy-element abundances. I. Constraints from stellar interiors," *Astrophysical Journal*, vol. 649, no. 1, pp. 529–540, 2006.
- [71] A. M. Serenelli and S. Basu, "Determining the initial helium abundance of the sun," *Astrophysical Journal Letters*, vol. 719, no. 1, pp. 865–872, 2010.
- [72] A. M. Serenelli, S. Basu, J. W. Ferguson, and M. Asplund, "New solar composition: the problem with solar models revisited," *Astrophysical Journal Letters*, vol. 705, no. 2, pp. L123–L127, 2009.
- [73] I. W. Roxburgh and S. V. Vorontsov, "The ratio of small to large separations of acoustic oscillations as a diagnostic of the interior of solar-like stars," *Astronomy & Astrophysics*, vol. 411, pp. 215–220, 2003.
- [74] G. Bellini, J. Benziger, D. Bick et al., "First evidence of *pep* solar neutrinos by direct detection in borexino," *Physical Review Letters*, vol. 108, Article ID 051302, 6 pages, 2012.
- [75] D. D. Clayton, *Principles of Stellar Evolution and Nucleosynthesis*, University of Chicago Press, 1984.
- [76] J. N. Bahcall and M. H. Pinsonneault, "What do we (not) know theoretically about solar neutrino fluxes?" *Physical Review Letters*, vol. 92, no. 12, Article ID 121301, 2004.
- [77] A. Formicola, G. Imbriani, H. Costantini et al., "Astrophysical S-factor of  $^{14}\text{N}(p,\gamma)^{15}\text{O}$ ," *Physics Letters B*, vol. 591, pp. 61–68, 2004.
- [78] M. Marta, A. Formicola, Gy. Gyürky et al., "Precision study of ground state capture in the  $^{14}\text{N}(p,\gamma)^{15}\text{O}$  reaction," *Physical Review C*, vol. 78, Article ID 022802, 4 pages, 2008.
- [79] W. C. Haxton and A. M. Serenelli, "CN cycle solar neutrinos and the Sun's primordial core metallicity," *Astrophysical Journal Letters*, vol. 687, no. 1, pp. 678–691, 2008.
- [80] J. N. Bahcall, A. M. Serenelli, and S. Basu, "10,000 Standard solar models: a monte carlo simulation," *Astrophysical Journal, Supplement Series*, vol. 165, no. 1, pp. 400–431, 2006.
- [81] J. N. Bahcall and A. M. Serenelli, "How do uncertainties in the surface chemical composition of the sun affect the predicted solar neutrino fluxes?" *Astrophysical Journal*, vol. 626, no. 1, pp. 530–542, 2005.
- [82] P. C. de Holanda and A. Y. Smirnov, "Solar neutrinos: global analysis with day and night spectra from SNO," *Physical Review D*, vol. 66, Article ID 113005, 10 pages, 2002.
- [83] P. C. de Holanda and A. Y. Smirnov, "LMA MSW solution of the solar neutrino problem and first KamLAND results," *Journal of Cosmology and Astroparticle Physics*, vol. 2003, no. 2, p. 1, 2003.
- [84] J. N. Bahcall, M. C. Gonzalez-Garcia, and C. Peña-Garay, "Before and after: how has the SNO neutral current measurement changed things?" *Journal of High Energy Physics*, vol. 207, p. 54, 2002.
- [85] J. N. Bahcall, M. C. Gonzalez-Garcia, and C. Peña-Garay, "Solar neutrinos before and after KamLAND," *Journal of High Energy Physics*, vol. 302, p. 9, 2003.
- [86] G. L. Fogli, E. Lisi, A. Marrone, D. Montanino, A. Palazzo, and A. M. Rotunno, "Solar neutrino oscillation parameters after first KamLAND results," *Physical Review D*, vol. 67, no. 7, Article ID 073002, 2003.
- [87] S. Pascoli and S. T. Petcov, "The SNO solar neutrino data, neutrinoless double beta-decay and neutrino mass spectrum," *Physics Letters B*, vol. 544, pp. 239–250, 2002.
- [88] M. Maltoni, T. Schwetz, and J. W. F. Valle, "Combining first KamLAND results with solar neutrino data," *Physical Review D*, vol. 67, Article ID 093003, 2003.
- [89] P. Aliani, V. Antonelli, M. Picariello, and E. Torrente-Lujan, "The Neutrino mass matrix after Kamland and SNO salt enhanced results," <http://arxiv.org/abs/hep-ph/0309156>. In press.
- [90] P. Aliani, V. Antonelli, M. Picariello, and E. Torrente-Lujan, "Neutrino mass parameters from Kamland, SNO, and other solar evidence," *Physical Review D*, vol. 69, no. 1, Article ID 013005, 7 pages, 2004.
- [91] A. Bandyopadhyay, S. Choubey, S. Goswami, and D. P. Roy, "Implications of the first neutral current data from SNO for solar neutrino oscillation," *Physics Letters B*, vol. 540, no. 1-2, pp. 14–19, 2002.
- [92] V. Barger, D. Marfatia, K. Whisnant, and B. P. Wood, "Imprint of SNO neutral current data on the solar neutrino problem," *Physics Letters B*, vol. 537, no. 3-4, pp. 179–186, 2002.
- [93] S. M. Bilenky, C. Giunti, J. A. Grifols, and E. Massó, "Absolute values of neutrino masses: status and prospects," *Physics Reports*, vol. 379, no. 2, pp. 69–148, 2003.
- [94] B. Aharmim, S. N. Ahmed, A. E. Anthony et al., "Electron energy spectra, fluxes, and day-night asymmetries of  $^8\text{B}$  solar neutrinos from measurements with NaCl dissolved in the heavy-water detector at the Sudbury Neutrino Observatory," *Physical Review C*, vol. 72, Article ID 055502, 47 pages, 2005.
- [95] M. B. Smy, Y. Ashie, S. Fukuda et al., "Precise measurement of the solar neutrino day-night and seasonal variation in Super-Kamiokande-I," *Physical Review D*, vol. 69, Article ID 011104, 5 pages, 2004.
- [96] P. Langacker, S. T. Petcov, G. Steigman, and S. Toshev, "Implications of the Mikheyev-Smirnov-Wolfenstein (MSW) mechanism of amplification of neutrino oscillations in matter," *Nuclear Physics B*, vol. 282, pp. 589–609, 1987.
- [97] S. T. Petcov, "Exact analytic description of two-neutrino oscillations in matter with exponentially varying density," *Physics Letters B*, vol. 200, pp. 373–379, 1988.
- [98] S. T. Petcov, "Describing analytically the matter-enhanced two-neutrino transitions in a medium," *Physics Letters B*, vol. 406, pp. 355–365, 1997.
- [99] P. I. Krastev and S. T. Petcov, "Resonance amplification and T-violation effects in three-neutrino oscillations in the earth," *Physics Letters B*, vol. 205, pp. 84–92, 1988.
- [100] P. I. Krastev and S. T. Petcov, "Testing the vacuum oscillation and the MSW solutions of the solar neutrino problem," *Nuclear Physics B*, vol. 449, pp. 605–627, 1995.
- [101] M. Chizhov, M. Maris, and S. T. Petcov, "On the oscillation length resonance in the transitions of solar and atmospheric neutrinos crossing the earth core," submitted, <http://arxiv.org/abs/hep-ph/9810501>.
- [102] P. C. de Holanda, W. Liao, and A. Y. Smirnov, "Toward precision measurements in solar neutrinos," *Nuclear Physics B*, vol. 702, no. 1-2, pp. 307–332, 2004.

- [103] A. N. Ioannisian, N. A. Kazarian, A. Y. Smirnov, and D. Wyler, "Precise analytical description of the Earth matter effect on oscillations of low energy neutrinos," *Physical Review D*, vol. 71, no. 3, Article ID 033006, 8 pages, 2005.
- [104] E. K. Akhmedov, M. A. Tortola, and J. W. F. Valle, "A simple analytic three-flavour description of the day-night effect in the solar neutrino flux," *Journal of High Energy Physics*, vol. 405, p. 57, 2004.
- [105] A. Friedland, C. Lunardini, and C. Peña-Garay, "Solar neutrinos as probes of neutrino-matter interactions," *Physics Letters B*, vol. 594, pp. 347–354, 2004.
- [106] W. Liao, "Precise formulation of neutrino oscillation in the earth," *Physical Review D*, vol. 77, Article ID 053002, 11 pages, 2008.
- [107] P. Aliani, V. Antonelli, M. Picariello, and E. Torrente-Lujan, "Global analysis of Solar neutrino oscillation evidence including SNO and implications for Borexino," *Nuclear Physics B*, vol. 634, no. 1-2, pp. 393–409, 2002.
- [108] E. Torrente-Lujan, "Finite dimensional systems with random external fields and neutrino propagation in fluctuating media," *Physical Review D*, vol. 59, Article ID 073001, 7 pages, 1999.
- [109] D. Dooling, C. Giunti, K. Kang, and C. W. Kim, "Matter effects in four-neutrino mixing," *Physical Review D*, vol. 61, Article ID 073011, 18 pages, 2000.
- [110] J. Hosaka, K. Ishihara, J. Kameda et al., "Solar neutrino measurements in Super-Kamiokande-I," *Physical Review D*, vol. 73, Article ID 112001, 33 pages, 2006.
- [111] C. Arpesella, H. O. Back, M. Balata et al., "Direct measurement of the  $^7\text{Be}$  solar neutrino flux with 192 days of Borexino data," *Physical Review Letters*, vol. 101, Article ID 091302, 6 pages, 2008.
- [112] B. Aharmim, S. N. Ahmed, A. E. Anthony et al., "Low-energy-threshold analysis of the Phase I and Phase II data sets of the Sudbury Neutrino Observatory," *Physical Review C*, vol. 81, Article ID 055504, 49 pages, 2010.
- [113] B. Aharmim, Q. R. Ahmad, S. N. Ahmed et al., "Determination of the  $\nu_e$  and total  $^8\text{B}$  solar neutrino fluxes using the Sudbury Neutrino Observatory Phase I data set," *Physical Review C*, vol. 75, Article ID 045502, 69 pages, 2007.
- [114] J. P. Cravens, K. Abe, T. Iida et al., "Solar neutrino measurements in Super-Kamiokande-II," *Physical Review D*, vol. 78, Article ID 032002, 11 pages, 2008.
- [115] K. Abe, Y. Hayato, T. Iida et al., "Solar neutrino results in Super-Kamiokande-III," *Physical Review D*, vol. 83, Article ID 052010, 19 pages, 2011.
- [116] M. Smy, "Low energy neutrino astronomy in super-kamiokande," in *Proceedings of the Meeting of the American Physical Society Division of Particles and Fields at Brown University*, 2011, <http://arxiv.org/abs/1110.0012>.
- [117] G. Alimonti, C. Arpesella, H. Back et al., "The Borexino detector at the Laboratori Nazionali del Gran Sasso," *Nuclear Instruments and Methods in Physics Research A*, vol. 600, pp. 568–593, 2009.
- [118] C. Peña-Garay, "talk at the conference Neutrino Telescopes 2007," March, Venice, Italy, 2007, <http://neutrino.pd.infn.it/conference2007/>.
- [119] C. Arpesella, G. Bellini, J. Benziger et al., "First real time detection of  $^7\text{Be}$  solar neutrinos by Borexino," *Physics Letters B*, vol. 658, pp. 101–108, 2008.
- [120] G. Alimonti, G. Anghloher, C. Arpesella et al., "Ultra-low background measurements in a large volume underground detector," *Astroparticle Physics*, vol. 8, pp. 141–157, 1998.
- [121] G. Alimonti, C. Arpesella, H. Back et al., "Science and technology of Borexino: a real-time detector for low energy solar neutrinos," *Astroparticle Physics*, vol. 16, pp. 205–234, 2002.
- [122] C. Arpesella, H. O. Back, M. Balata et al., "Measurements of extremely low radioactivity levels in BOREXINO," *Astroparticle Physics*, vol. 18, no. 1, pp. 1–25, 2002.
- [123] A. Ianni, P. Lombardi, G. Ranucci, and O. Smirnov, "The measurements of 2200 ETL9351 type photomultipliers for the Borexino experiment with the photomultiplier testing facility at LNGS," *Nuclear Instruments and Methods in Physics Research A*, vol. 537, pp. 683–697, 2005.
- [124] A. Brigatti, A. Ianni, P. Lombardi, G. Ranucci, and O. J. Smirnov, "The photomultiplier tube testing facility for the Borexino experiment at LNGS," *Nuclear Instruments and Methods in Physics Research A*, vol. 537, no. 3, pp. 521–536, 2005.
- [125] L. Oberauer, C. Grieb, F. von Feilitzsch, and I. Manno, "Light concentrators for Borexino and CTF," *Nuclear Instruments and Methods in Physics Research A*, vol. 530, no. 3, pp. 453–462, 2004.
- [126] Borexino Collaboration, "The Borexino detector at the Laboratori Nazionali del Gran Sasso," *Nuclear Instruments and Methods in Physics Research A*, vol. 600, pp. 568–593, 2009.
- [127] H. Simgen and G. Zuzel, "Ultraclean gases—from the production plant to the laboratory," in *Proceedings of the Topical Workshop on Low Radioactivity Techniques (LRT '06)*, P. Loaiza, Ed., vol. 897, pp. 45–50, American Institute of Physics, France, 2006.
- [128] J. N. Bahcall, A. M. Serenelli, and S. Basu, "10,000 Standard solar models: a Monte Carlo simulation," *The Astrophysical Journal Supplement Series*, vol. 165, p. 400, 2006.
- [129] G. Bellini, J. Benziger, D. Bick et al., "Precision measurement of the  $^7\text{Be}$  solar neutrino interaction rate in Borexino," *Physical Review Letters*, vol. 107, Article ID 141302, 5 pages, 2011.
- [130] S. Basu, "Astronomical Society of the Pacific Conference Series," vol. 416, pp. 193, 2009.
- [131] S. Davini, *Measurement of the pep and CNO solar neutrino interaction rates in Borexino [Ph.D. thesis]*, University of Genova, 2012.
- [132] C. Galbiati, A. Pocar, D. Franco, A. Ianni, L. Cadonati, and S. Schönert, "Cosmogenic  $^{11}\text{C}$  production and sensitivity of organic scintillator detectors to pep and CNO neutrinos," *Physical Review C*, vol. 71, Article ID 055805, 11 pages, 2005.
- [133] G. Bellini, J. Benziger, D. Bick et al., "Muon and cosmogenic neutron detection in Borexino," *Journal of Instrumentation*, vol. 6, Article ID P05005, 2011.
- [134] M. Deutsch, *Proposal for a Cosmic Ray Detection System for the Borexino Solar Neutrino Experiment*, Massachusetts Institute of Technology, Cambridge, Mass, USA, 1996.
- [135] H. Back and Borexino Collaboration, "CNO and pep neutrino spectroscopy in Borexino: measurement of the deep-underground production of cosmogenic  $^{11}\text{C}$  in an organic liquid scintillator," *Physical Review C*, vol. 74, Article ID 045805, 6 pages, 2006.
- [136] Y. Kino, *The Journal of Nuclear and Radiochemical Sciences*, vol. 1, pp. 63–68, 2000.
- [137] D. Franco, G. Consolati, and D. Trezzi, "Positronium signature in organic liquid scintillators for neutrino experiments," *Physical Review C*, vol. 83, Article ID 015504, 6 pages, 2011.
- [138] TMVA Users Guide, <http://tmva.sourceforge.net/docu/%20TMVAUsersGuide.pdf>.
- [139] W. Maneschg, L. Baudis, R. Dressler et al., "Production and characterization of a custom-made  $^{228}\text{Th}$  source with reduced

- neutron source strength for the Borexino experiment,” *Nuclear Instruments and Methods in Physics Research A*, vol. 680, pp. 161–167, 2012.
- [140] L. Wolfenstein, “Neutrino oscillations in matter,” *Physical Review D*, vol. 17, pp. 2369–2374, 1978.
- [141] L. Wolfenstein, “Effect of matter on neutrino oscillations,” in *Proceedings of the Neutrino*, pp. C3–C6, Purdue University, 1978.
- [142] S. P. Mikheev and A. Y. Smirnov, “Resonant amplification of neutrino oscillations in matter and solar-neutrino spectroscopy,” *Soviet Journal of Nuclear Physics*, vol. 42, pp. 913–917, 1985.
- [143] S. P. Mikheev and A. Y. Smirnov, “Resonance enhancement of oscillations in matter and solar neutrino spectroscopy,” *Yadernaya Fizika*, vol. 42, pp. 1441–1448, 1985.
- [144] S. P. Mikheev and A. Y. Smirnov, “Resonant amplification of  $\nu$  oscillations in matter and solar-neutrino spectroscopy,” *Nuovo Cimento C*, vol. 9, no. 1, pp. 17–26, 1986.
- [145] V. E. Zakharov and E. A. Kuznetsov, “Quasiclassical theory of three-dimensional wave collapse,” *Soviet Physics, JETP*, vol. 64, no. 4, pp. 773–780, 1986, reprinted in: *Solar neutrinos: the first thirty years*, edited by: J. N. Bahcall.
- [146] K. Nakamura and Particle Data Group, “Review of particle physics,” *Journal of Physics G*, vol. 37, no. 7, Article ID 075021, 2010.
- [147] B. Aharmim, S. N. Ahmed, A. E. Anthony et al., “Combined analysis of all three phases of solar neutrino data from the sudbury neutrino observatory,” In press, <http://arxiv.org/abs/1109.0763>.
- [148] J. N. Bahcall, M. Kamionkowski, and A. Sirlin, “Solar neutrinos: radiative corrections in neutrino-electron scattering experiments,” *Physical Review D*, vol. 51, no. 11, pp. 6146–6158, 1995.
- [149] J. Erler and M. J. Ramsey-Musolf, “The Weak mixing angle at low energies,” *Physical Review D*, vol. 72, Article ID 073003, 2005.
- [150] J. N. Abdurashitov, V. N. Gavrin, V. V. Gorbachev et al., “Measurement of the solar neutrino capture rate with gallium metal. III. Results for the 2002–2007 data-taking period,” *Physical Review C*, vol. 80, Article ID 015807, 16 pages, 2009.
- [151] M. Altmann, M. Balatab, P. Belli et al., “Complete results for five years of GNO solar neutrino observations,” *Physics Letters B*, vol. 616, pp. 174–190, 2005.
- [152] F. Kaether, *Datenanalyse der Sonnenneutrinoexperimente Gallex [Ph.D. thesis]*, Heidelberg, Germany, 2007.
- [153] B. T. Cleveland, T. Daily, R. Davis Jr. et al., “Measurement of the solar electron neutrino flux with the homestake chlorine detector,” *The Astrophysical Journal*, vol. 496, no. 1, p. 505, 1998.
- [154] G. Bellini, J. Benziger, S. Bonetti et al., “Measurement of the solar  $^8\text{B}$  neutrino rate with a liquid scintillator target and 3 MeV energy threshold in the Borexino detector,” *Physical Review D*, vol. 82, Article ID 033006, 10 pages, 2010.
- [155] K. Abe, N. Abgrall, Y. Ajima et al., “Indication of electron neutrino appearance from an accelerator-produced off-axis muon neutrino beam,” *Physical Review Letters*, vol. 107, Article ID 041801, 8 pages, 2011.
- [156] P. Adamson, D. J. Auty, D. S. Ayres et al., “Improved search for muon-neutrino to electron-neutrino oscillations in MINOS,” *Physical Review Letters*, vol. 107, Article ID 181802, 5 pages, 2011.
- [157] G. L. Fogli, E. Lisi, A. Marrone, A. Palazzo, and A. M. Rotunno, “Evidence of  $\theta_{13} > 0$  from global neutrino data analysis,” *Physical Review D*, vol. 84, Article ID 053007, 7 pages, 2011.
- [158] M. Apollonio, A. Baldini, C. Bemporad et al., “Search for neutrino oscillations on a long base-line at the CHOOZ nuclear power station,” *The European Physical Journal C*, vol. 27, pp. 331–374, 2003.
- [159] Y. Abe, C. Aberle, T. Akiri et al., “Indication for the disappearance of reactor electron antineutrinos in the Double Chooz experiment,” *Physical Review Letters*, vol. 108, Article ID 131801, 7 pages, 2012.
- [160] C. Giunti and M. Laveder, “Effect of the reactor antineutrino anomaly on the first Double-Chooz results,” *Physical Review D*, vol. 85, Article ID 031301, 4 pages, 2012.
- [161] F. P. An, J. Z. Bai, A. B. Balantekin et al., “Observation of electron-antineutrino disappearance at daya bay,” *Physical Review Letters*, vol. 108, Article ID 171803, 7 pages, 2012.
- [162] J. K. Ahn, S. Chebotaryov, J. H. Choi et al., “Observation of reactor electron antineutrinos disappearance in the RENO experiment,” *Physical Review Letters*, vol. 108, Article ID 191802, 6 pages, 2012.
- [163] D. Dwyer, for the Daya-Bay Collaboration, talk at Neutrino, 2012.
- [164] G. L. Fogli, E. Lisi, A. Marrone, D. Montanino, A. Palazzo, and A. M. Rotunno, “Global analysis of neutrino masses, mixings, and phases: entering the era of leptonic CP violation searches,” *Physical Review D*, vol. 86, Article ID 013012, 10 pages, 2012.
- [165] D. V. Forero, M. Tortola, and J. W. F. Valle, “Global status of neutrino oscillation parameters after Neutrino-2012,” *Physical Review D*, vol. 86, Article ID 073012, 8 pages, 2012.
- [166] T. Schwetz, “talk at NuTURN 2012,” Workshop on Neutrino at the Turning Point, Laboratori Nazionali del Gran Sasso, Italy, 2012, <http://agenda.infn.it/conferenceDisplay.py?confId=4722>.
- [167] “talk at what is NU ?” Workshop at the Galileo Galilei Institute, Florence, Italy, 2012, <http://www.ggi.fi.infn.it/>.
- [168] A. Friedland, C. Lunardini, and C. Peña-Garay, “Solar neutrinos as probes of neutrino-matter interactions,” *Physics Letters B*, vol. 594, pp. 347–354, 2004.
- [169] P. C. de Holanda and A. Y. Smirnov, “Solar neutrino spectrum, sterile neutrinos, and additional radiation in the Universe,” *Physical Review D*, vol. 83, Article ID 113011, 13 pages, 2011.
- [170] M. Spiro and D. Vignaud, “Solar model independent neutrino oscillation signals in the forthcoming solar neutrino experiments?” *Physics Letters B*, vol. 242, pp. 279–284, 1990.
- [171] J. N. Bahcall, “The luminosity constraint on solar neutrino fluxes,” *Physical Review C*, vol. 65, Article ID 025801, 5 pages, 2002.
- [172] M. C. González-García, M. Maltoni, and J. Salvado, “Updated global fit to three neutrino mixing: status of the hints of  $\theta_{13} > 0$ ,” *Journal of High Energy Physics*, vol. 2010, no. 4, article 56, 2010.
- [173] J. N. Bahcall and C. Peña-Garay, “A road map to solar neutrino fluxes, neutrino oscillation parameters, and tests for new physics,” *Journal of High Energy Physics*, vol. 311, p. 4, 2003.
- [174] A. Chavarria, “Solar neutrinos in 2011,” In press, <http://arxiv.org/abs/1201.6311>.
- [175] J. Boger, R. L. Hahna, J. K. Rowley et al., “The sudbury neutrino observatory,” *Nuclear Instruments and Methods in Physics Research A*, vol. 449, pp. 172–207, 2000.
- [176] S. Fukuda, Y. Fukuda, T. Hayakawa et al., “The Super-Kamio-kande detector,” *Nuclear Instruments and Methods in Physics Research A*, vol. 501, pp. 418–462, 2003.
- [177] J. N. Abdurashitov, V. N. Gavrin, S. V. Girin et al., “Measurement of the solar neutrino capture rate with gallium metal,” *Physical Review C*, vol. 60, Article ID 055801, 32 pages, 1999.



- [178] C. Kraus and S. J. M. Peetersa, "The rich neutrino programme of the SNO+ experiment," *Progress in Particle and Nuclear Physics*, vol. 64, pp. 273–277, 2010.
- [179] F. L. Villante, A. Ianni, F. Lombardi, G. Pagliaroli, and F. Vissani, "A step toward CNO solar neutrino detection in liquid scintillators," *Physics Letters B*, vol. 701, no. 3, pp. 336–341, 2011.
- [180] D. N. McKinsey and K. J. Coakley, "Neutrino detection with CLEAN," *Astroparticle Physics*, vol. 22, no. 5-6, pp. 355–368, 2005.
- [181] E. Aprile and T. Doke, "Liquid xenon detectors for particle physics and astrophysics," *Reviews of Modern Physics*, vol. 82, pp. 2053–2097, 2010.
- [182] A. Baldini, "Research Proposal to INFN, The MEG experiment, search for the  $u \rightarrow e\gamma$  decay at PSI," 2002.
- [183] S. Moriyama, "Status of XMASS experiment," *PoS IDM*, vol. 2011, p. 57, 2010.
- [184] K. Kobayashi, "XMASS experiment, talk given at the TeV Particle Astrophysics 2010," Paris, France, July 2010.
- [185] L. Baudis, "DARWIN: dark matter WIMP search with noble liquids," *Journal of Physics*, vol. 375, part 1, Article ID 012028, 2012.
- [186] M. Wurm, J. F. Beacom, L. B. Bezrukov et al., "The next-generation liquid-scintillator neutrino observatory LENA," *Astroparticle Physics*, vol. 35, pp. 685–732, 2012.
- [187] H. O. Backa, M. Balata, A. de Bari et al., "Study of phenylxylethane (PXE) as scintillator for low energy neutrino experiments," *Nuclear Instruments and Methods in Physics Research A*, vol. 585, no. 12, pp. 48–60, 2008.
- [188] C. Arpesella, H. O. Back, M. Balata et al., "Direct measurement of the  $^7\text{Be}$  solar neutrino flux with 192 days of borexino data," *Physical Review Letters*, vol. 101, Article ID 091302, 6 pages, 2008.
- [189] M. Wurm, *Cosmic background discrimination for the rare neutrino event search in Borexino and LENA [Ph.D. thesis]*, Technische Universität München, 2009.
- [190] D. D'Angelo, *Towards the detection of low energy solar neutrinos in BOREXino: data readout, data reconstruction and background identification [Ph.D. thesis]*, Technische Universität München, 2006.
- [191] A. Ianni, D. Montanino, and F. L. Villante, "How to observe  $^8\text{B}$  solar neutrinos in liquid scintillator detectors," *Physics Letters B*, vol. 627, pp. 38–48, 2005.
- [192] R. S. Raghavan, "Inverse  $\beta$  decay of  $^{115}\text{In} \rightarrow ^{115}\text{Sn}^*$ : a new possibility for detecting solar neutrinos from the Proton-Proton reaction," *Physical Review Letters*, vol. 37, pp. 259–262, 1976.
- [193] R. S. Raghavan, "Discovery potential of low energy solar neutrino experiments," Notes for APSSAWG, March 2004.
- [194] H. Antia and S. Basu, "The discrepancy between solar abundances and helioseismology," *The Astrophysical Journal Letters*, vol. 620, p. L129, 2005.
- [195] J. N. Bahcall, S. Basu, and A. M. Serenelli, "What is the neon abundance of the sun?" *Astrophysical Journal Letters*, vol. 631, no. 2, pp. 1281–1285, 2005.
- [196] J. A. Guzik, L. S. Watson, and A. N. Cox, "Can enhanced diffusion improve helioseismic agreement for solar models with revised abundances?" *Astrophysical Journal*, vol. 627, no. 2, pp. 1049–1056, 2005.
- [197] M. Castro, S. Vauclair, and P. Richard, "Low abundances of heavy elements in the solar outer layers: comparisons of solar models with helioseismic inversions," *Astronomy & Astrophysics*, vol. 463, pp. 755–758, 2007.
- [198] J. Christensen-Dalsgaard, M. P. di Mauro, G. Houdex, and F. Pijpers, "On the opacity change required to compensate for the revised solar composition," *Astronomy & Astrophysics*, vol. 494, pp. 205–208, 2009.
- [199] A. M. Serenelli, "New results on standard solar models," *Astrophysics and Space Science*, vol. 328, pp. 13–21, 2010.
- [200] F. L. Villante and B. Ricci, "Linear solar models," *Astrophysical Journal Letters*, vol. 714, no. 1, pp. 944–959, 2010.
- [201] F. L. Villante, "Constraints on the opacity profile of the sun from helioseismic observables and solar neutrino flux measurements," *The Astrophysical Journal*, vol. 724, p. 98, 2010.
- [202] J. Barranco, O. G. Miranda, C. A. Moura, and J. W. F. Valle, "Constraining nonstandard neutrino-electron interactions," *Physical Review D*, vol. 77, no. 9, Article ID 093014, 10 pages, 2008.
- [203] H. A. Bethe, "Energy production in stars," *Physical Review*, vol. 55, pp. 434–456, 1939.
- [204] A. A. Thoul, J. N. Bahcall, and A. Loeb, "Element diffusion in the solar interior," *Astrophysical Journal Letters*, vol. 421, no. 2, pp. 828–842, 1994.
- [205] F. Delahaye, M. H. Pinsonneault, L. Pinsonneault, and C. J. Zeppen, "Helioseismic constraints on the solar Ne/O ratio and heavy element abundances," submitted, <http://arxiv.org/abs/1005.0423>.
- [206] J. Meléndez, M. Asplund, B. Gustafsson, and D. Yong, "The peculiar solar composition and its possible relation to planet formation," *The Astrophysical Journal Letters*, vol. 704, p. L66, 2009.
- [207] I. Ramírez, M. Asplund, P. Baumann, J. Meléndez, and T. Bensby, "A possible signature of terrestrial planet formation in the chemical composition of solar analogs," *Astronomy & Astrophysics*, vol. 512, p. 33, 2010.



## Review Article

# Long-Baseline Neutrino Oscillation Experiments

G. J. Feldman,<sup>1</sup> J. Hartnell,<sup>2</sup> and T. Kobayashi<sup>3</sup>

<sup>1</sup> Department of Physics, Harvard University, Cambridge, MA 02138, USA

<sup>2</sup> Department of Physics and Astronomy, University of Sussex, Brighton BN1 9QH, UK

<sup>3</sup> Institute of Particle and Nuclear Studies, High Energy Accelerator Research Organization (KEK), 1-1 Oho, Tsukuba 305-0801, Japan

Correspondence should be addressed to J. Hartnell; [jeffhartnell@gmail.com](mailto:jeffhartnell@gmail.com)

Received 27 July 2012; Accepted 8 October 2012

Academic Editor: Koichiro Nishikawa

Copyright © 2013 G. J. Feldman et al. This is an open access article distributed under the Creative Commons Attribution License, which permits unrestricted use, distribution, and reproduction in any medium, provided the original work is properly cited.

A review of accelerator long-baseline neutrino oscillation experiments is provided, including all experiments performed to date and the projected sensitivity of those currently in progress. Accelerator experiments have played a crucial role in the confirmation of the neutrino oscillation phenomenon and in precision measurements of the parameters. With a fixed baseline and detectors providing good energy resolution, precise measurements of the ratio of distance/energy ( $L/E$ ) on the scale of individual events have been made and the expected oscillatory pattern resolved. Evidence for electron neutrino appearance has recently been obtained, opening a door for determining the CP violating phase as well as resolving the mass hierarchy and the octant of  $\theta_{23}$ ; some of the last unknown parameters of the standard model extended to include neutrino mass.

## 1. Introduction

Neutrino oscillation experiments are normally categorized into short-baseline and long-baseline experiments. For experiments using accelerator neutrinos as the source, the long-baseline means that  $E/L \simeq \Delta m^2 \sim 2.5 \times 10^{-3} \text{ eV}^2$ , where  $E$  and  $L$  are the neutrino energy and flight distance, respectively. In this paper, accelerator long-baseline (LBL) neutrino oscillation experiments are reviewed. The recent reactor neutrino experiments to look for nonzero  $\theta_{13}$  at  $\Delta m^2 \sim 2.5 \times 10^{-3} \text{ eV}^2$  and atmospheric neutrino experiments are covered elsewhere in this special issue.

Neutrino beams for the LBL experiments are produced in the “conventional” method where a high-energy proton beam hits a target and the pions that are produced then decay in flight to give muon neutrinos. The typical neutrino energy thus produced is 0.5–10 GeV and that sets the necessary distance to a neutrino detector to be several hundreds of kilometers such that the neutrino oscillation driven by  $\Delta m^2 \sim 2.5 \times 10^{-3} \text{ eV}^2$  can be investigated. This paper describes KEK [1], NuMI [2], CNGS [3], and J-PARC [4] neutrino beams and their associated experiments.

The goals of the first LBL experiments proposed in 1990s, K2K [5], MINOS [6], and CERN to Gran Sasso (CNGS)

experiments OPERA [7] and ICARUS [8] were to clarify the origin of the anomaly observed in the atmospheric neutrino measurements of Kamiokande [9] and IMB [10] and later to confirm the discovery of neutrino oscillations by Super-Kamiokande (SK) in 1998 [11]. Kamiokande observed a deficit of muon neutrinos coming through the earth, which could have been interpreted as muon to tau neutrino oscillation and/or to electron neutrino oscillation. Soon afterwards, the CHOOZ experiment [12] excluded the possibility that muon to electron neutrino oscillation is the dominant mode. Therefore, the goal of the first generation LBL experiments was focused on confirming muon to tau neutrino oscillation. The K2K and MINOS experiments, which used beams with neutrino energies of a few-GeV, focused on detecting muon neutrino disappearance because the energy of the neutrinos was rarely high enough to make  $\nu_\tau$  charged current interactions (threshold energy is about 3.5 GeV). In contrast, the CNGS experiments make use of a higher energy ( $\sim 20 \text{ GeV}$ ) neutrino beam and OPERA is optimized for the detection of tau neutrino appearance.

Soon after the discovery of neutrino oscillation by SK, the importance of the subleading electron neutrino appearance channel was pointed out. In the three flavor mixing picture, the probability of electron neutrino appearance

gives a measure of the mixing angle  $\theta_{13}$ . The existence of electron neutrino appearance at the atmospheric oscillation length means nonzero  $\theta_{13}$ . Only an upper bound of  $\sin^2(2\theta_{13}) = 0.14$  (90% C.L.) from the CHOOZ experiment was known until very recently. Because the CP violating observable, the phase  $\delta$ , appears always in the product with  $\sin(2\theta_{12}) \sin(2\theta_{23}) \sin(2\theta_{13})$  and  $\theta_{23}$  and  $\theta_{12}$  are known to be large, the size of  $\theta_{13}$  is a major factor in the feasibility of the future CP violation search.

With the goal to discover electron neutrino appearance and determine  $\theta_{13}$ , the T2K experiment [4] in Japan started taking data in 2010 and the NOvA experiment [13–15] in the USA is now under construction and will start measurements in 2013. The design of these experiments was optimized for detection of electron neutrino appearance. Both T2K and NOvA adopted a novel “off-axis” beam technique that provides a narrow peak in the energy spectrum, tuned to be at the expected oscillation maximum, while at the same time reducing the unwanted high energy tail. The  $\nu_\mu \rightarrow \nu_e$  transition is a subdominant effect and the oscillation probability to be probed is small. To have enough sensitivity, beam powers of order 1 MW and detector masses of order 10 kilotons are required and as such these experiments are sometimes called “superbeam” experiments.

With evidence of  $\nu_e$  appearance from early T2K results and the recent measurement of  $\bar{\nu}_e$  disappearance by the reactor experiments [16–18], the major focus for the future will be to determine the mass hierarchy and search for evidence of CP violation. NOvA will have the longest baseline of all second-generation experiments at 810 km, which will give enhanced sensitivity to the neutrino mass hierarchy due to the neutrino-matter interaction in the Earth as the neutrinos propagate. Information on the mass hierarchy and the expected precision measurement of  $\theta_{13}$  from the reactor experiments will be crucial to resolve degeneracies in the grand combination of T2K, NOvA, and reactor experiments to reveal information on what nature has chosen for leptonic CP violation.

Beyond oscillations, the provision of intense and relatively well-understood neutrino beams along with the large detectors in these experiments has opened up whole new avenues to look for new physics. This paper provides a concise overview of searches for sterile neutrinos, velocity measurements of neutrinos and searches for violation of Lorentz symmetry. In the future, the MINOS+ experiment [19] will focus on searches for new physics through high-precision, high-statistics measurements with the NuMI beam operating at a peak on-axis energy of 7 GeV.

This paper is structured as follows. Section 2 describes the beams and Section 3 gives an overview of the detectors. The results from long-baseline neutrino oscillation experiments are presented here in three parts. Section 4 describes the measurements made using the dominant  $\nu_\mu \rightarrow \nu_\tau$  oscillation mode. Section 5 details the recent detection of sub-dominant  $\nu_\mu \rightarrow \nu_e$  oscillations. Section 6 describes the results from searches for new physics such as sterile neutrinos. Future sensitivities are described in Section 7 and a conclusion is given in Section 8.

## 2. Neutrino Beams

The accelerator neutrino beams used by the experiments covered in this paper article are described in this section. As in other areas of particle physics, the experiments’ detectors exist in a strongly coupled relationship with the beam and it is important to consider both beam and detector to understand the design and performance of the experiments.

An interesting feature of neutrino beams is that multiple detectors can be simultaneously exposed to the same individual beam spills with no noticeable effect on the beam itself. This is true for Near and Far detectors but also, for example, where there are multiple experiments in the same underground laboratory.

An advantage of accelerator beams is the ability to exploit the pulsed nature of the beams to reject backgrounds from cosmic rays and atmospheric neutrinos. With beam pulses lasting tens of microseconds and accelerator cycle times measured in seconds, a background rejection factor of  $10^5$  is typical.

The beams used in long-baseline experiments are described here in the following order. Section 2.1 describes the beam used by K2K. Section 2.2 describes the NuMI beam used by MINOS and in future NOvA and MINOS+. Section 2.3 describes the CNGS beam used by OPERA and ICARUS. Section 2.4 describes the J-PARC beam used by T2K.

**2.1. KEK Beam.** In this section, the beam for the first LBL experiment K2K in Japan which was in operation from 1999 to 2004 is described [5]. A schematic layout of the K2K beam line is shown in Figure 1. The beam of muon neutrinos was produced with the KEK 12 GeV proton synchrotron (PS) and was sent towards Super-Kamiokande, which is located 250 km from KEK. The central axis of the neutrino beam was aligned to aim at the center of Super-Kamiokande giving an on-axis wideband beam.

The proton beam was extracted from the PS in a single turn with a 2.2 s cycle time. The spill was  $1.1 \mu\text{s}$  long and consisted of nine bunches. The proton beam intensity reached about  $6 \times 10^{12}$  protons/pulse, corresponding to a beam power of about 5 kW.

Initially the target was a 66 cm long, 2 cm diameter Al rod but this was replaced with a wider, 3 cm diameter rod in November 1999. Secondary positive pions were focused by two electromagnetic horns [20]. Both horns had a pulsed current about 1 ms long with a 200 kA peak for the June 1999 run, and that was increased to a 250 kA peak for runs after November 1999. The target was embedded in the first horn and played a role as an inner conductor as shown in Figure 2.

Measurements of the momenta and angular distribution of secondary pions,  $N(p_\pi, \theta_\pi)$ , were made using the pion monitor. This detector was a gas Čerenkov detector occasionally placed just downstream of the second horn in the target station. The results of the pion monitor measurements were used in calculations of the ratio of the flux at SK to the flux at the near detector (ND),  $R_\Phi(E_\nu) \equiv \Phi_{\text{SK}}(E_\nu)/\Phi_{\text{ND}}(E_\nu)$ .

The target region was followed by a 200 m long decay pipe where pions decayed in flight to muon neutrinos and

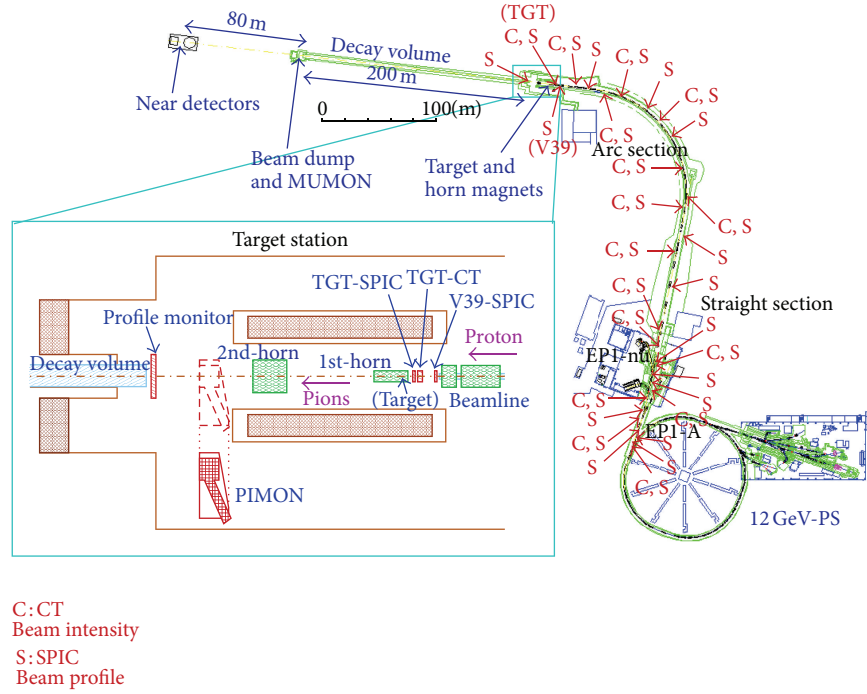


FIGURE 1: A schematic of the K2K beamline that includes the primary proton beamline.

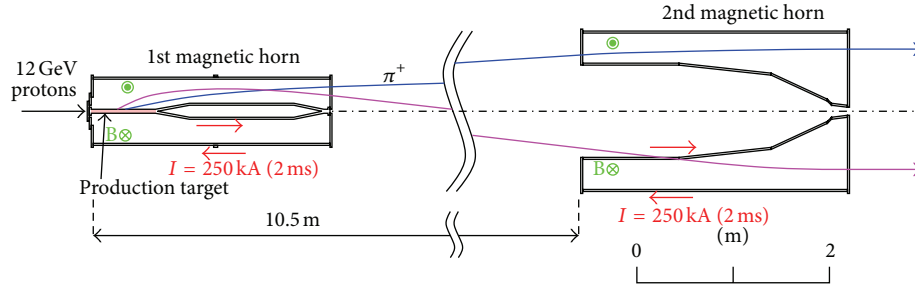


FIGURE 2: A schematic showing the layout and operation of the K2K beamline target and horns.

muons. At the downstream end of the decay pipe, there was a beam dump made of iron 3 m thick and followed by 2 m thick concrete. Muons above 5 GeV could penetrate the beam dump and be detected by the muon monitors installed just behind the beam dump. The muon monitors consisted of  $2\text{ m} \times 2\text{ m}$  segmented ionization chambers along with an array of silicon pad detectors and provided spill-by-spill monitoring of the beam profile and intensity.

Beam line components were aligned with Global Positioning System (GPS) [21]. The alignment uncertainty from the GPS survey was  $\leq 0.01\text{ mrad}$  while that of the civil construction was  $\leq 0.1\text{ mrad}$ , both of which were much better than physics requirement of  $1\text{ mrad}$ .

The expected neutrino spectra at SK are plotted in Figure 3. The average neutrino energy was  $1.3\text{ GeV}$  and the purity of  $\nu_\mu$  in the beam was estimated by Monte Carlo (MC) simulation to be 98.2% and  $\nu_e$  contamination to be 1.3%.

The K2K experiment started physics data taking in June 1999 and finished in November 2004. The total number of

protons on target (POT) delivered was  $1.049 \times 10^{20}$ , of which  $0.922 \times 10^{20}$  POT were used in the final physics analysis.

**2.2. NuMI Beam.** The NuMI beam [2] is located at the Fermi National Accelerator Laboratory in Illinois, USA, and it was initially constructed primarily for the MINOS experiment. In this section a description of NuMI as it was operated for the last 7 years is given first, before going on to discuss the upgrades for the NOvA experiment that are underway at the time of writing. MINOS measured the NuMI flux at distances of 1 km and 735 km from the target and NOvA will have the longest baseline of all such experiments at 810 km.

Protons from the Main Injector (MI) accelerator with a momentum of  $120\text{ GeV}/c$  are used for the production of neutrinos and antineutrinos in the NuMI beamline. Typically, either 9 or 11 slip-stacked batches of protons from the MI are extracted in a single shot onto the NuMI target giving neutrino pulses either 8 or  $10\text{ }\mu\text{s}$  long. Filling the MI with  $8\text{ GeV}/c$  protons from the Booster accelerator takes about

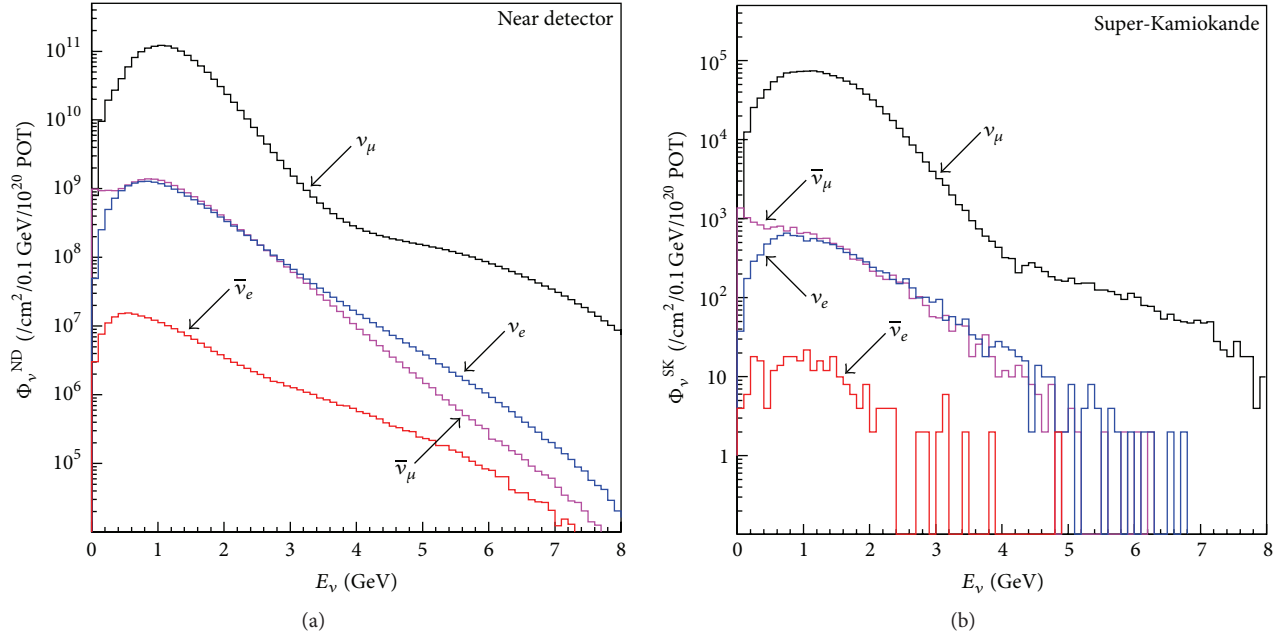


FIGURE 3: Simulated neutrino flux of K2K beam.

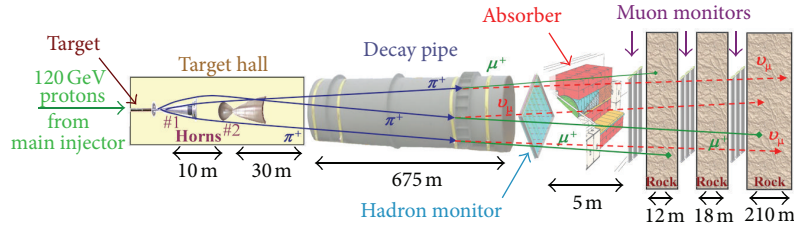


FIGURE 4: A schematic of the NuMI beamline. Protons from the Main Injector strike a graphite target, shown at the far left, and the resulting negatively or positively charged hadrons are focused by two magnetic horns. A 675 m long decay pipe gives the short-lived hadrons and muons time to decay. All hadrons remaining at the end of the decay volume are stopped by the absorber leaving just muons and neutrinos. The remaining muons are stopped by nearly 250 m of rock. Figure from [22].

0.7 s and then acceleration to 120 GeV/c takes a further 1.5 s, giving a total cycle time of about 2.2 s. A single-shot extraction from the MI contains around  $3 \times 10^{13}$  protons and the beam operated at a power of 300–350 kW over the last few years. By the time of the long-shutdown that started on May 1, 2012, NuMI had received nearly  $16 \times 10^{20}$  protons on target.

Figure 4 shows a schematic of the NuMI beamline and the components are described in sequence, starting on the far left with the protons coming from the MI. A water-cooled, segmented graphite target 2.0 interaction lengths long is used to produce the short-lived hadrons that give rise to the neutrinos. Two magnetic horns focus either positively or negatively charged particles towards a 675 m long decay volume, previously evacuated but now filled with helium. At the end of the decay volume a hadron absorber stops any remaining hadrons leaving just neutrinos and muons. Beyond that nearly 250 m of rock attenuates the muons leaving just the neutrinos.

The NuMI beamline was designed to be flexible in its operation with a number of parameters that could be adjusted

to optimise the sensitivity to the physics topics of interest. The position of the target with respect to the first horn, the position of the second horn, the horn current, and polarity could all be adjusted. The vast majority of data were taken in a “low energy” configuration that optimized the sensitivity to the atmospheric mass squared splitting by providing as large a flux as possible at the oscillation maximum for MINOS (around 1.4 GeV). This was achieved by inserting the target as far into the first horn as safely possible and having the second horn close to the first. A horn current of 185 kA was routinely used. Approximately 80% (20%) of the data were taken with the horn current polarity set to focus positively (negatively) charged hadrons enhancing the production of neutrinos (antineutrinos). The energy spectrum measured by MINOS is shown in the results section in Figure 12.

The neutrino flavor composition of the on-axis NuMI beam is as follows: firstly, with the magnetic horn polarity set to focus positive hadrons a neutrino-enhanced beam is produced, giving rise to interactions in the (on-axis) MINOS near detector that are 91.7%  $\nu_\mu$ , 7.0%  $\bar{\nu}_\mu$ , and 1.3%  $\nu_e + \bar{\nu}_e$ ;



secondly, with the opposite polarity an antineutrino-enhanced beam is produced, giving near detector interactions that are 40%  $\bar{\nu}_\mu$ , 58%  $\nu_\mu$ , and 2%  $\nu_e + \bar{\nu}_e$  [23]. However, it should be noted that in the antineutrino-enhanced beam the  $\bar{\nu}_\mu$  component comprises about 80% of the interactions below 6 GeV in the region where the oscillation effect is largest.

On a number of occasions and for relatively short periods the NuMI beamline was operated in nonstandard configurations. These special runs were used to constrain uncertainties in analyses and better understand the beam. Examples include runs with the horn current at 170 kA, 200 kA, and 0 kA; and runs with the target pulled back out of the first horn by up to 2.5 m.

At the time of writing, the long accelerator shutdown to upgrade the NuMI beam for NOvA is underway. With the shutdown of the Tevatron, two relatively straightforward changes will allow the NuMI beam power to be doubled to 700 kW. Previously the Recycler, a fixed field ring in the MI tunnel was used to store antiprotons but now for NOvA it will accumulate protons from the Booster while the MI is ramping. By parallelizing the accumulation and acceleration of protons for NuMI, and with a small increase in the MI ramp rate, the cycle time will be reduced from 2.2 s to 1.33 s. The second change is that the number of batches in the MI ring will be increased from 11 to 12 and the two that were previously used to produce antiprotons will now be used for NuMI.

In addition to the upgrades to the accelerator for NOvA, modifications will also be made to the NuMI beamline. For the NOvA detectors the position of the peak in the energy spectrum will be determined by the off-axis angle and so the flux will be optimized by focusing the maximum number of pions into the decay pipe with energies that allow a substantial fraction of them to decay within the 675 m long decay volume. The optimal configuration of the NuMI beamline for NOvA will be to operate in a so-called “medium energy” configuration with the target sitting a meter or so back from the first horn and with the second horn positioned further downstream. This medium energy beam will have a peak energy of around 7 GeV for the on-axis experiments (e.g., MINOS+) compared to 1.9 GeV for NOvA. The simulated energy spectrum is shown in Figure 5. The NOvA detectors, sitting 14 mrad off-axis, will see a beam flux with significantly higher purity than is obtained on-axis, having only about 1%  $\bar{\nu}_\mu$  contamination of the  $\nu_\mu$ -enhanced beam and about 5%  $\nu_\mu$  contamination of the  $\bar{\nu}_\mu$ -enhanced beam.

The target for the NOvA era has been redesigned since there is no longer the constraint that it should be placed inside the first horn and increased reliability is expected. Beyond the upgrades underway for NOvA, there is the possibility of increasing the beam power further; for example, the first phase of a proton driver could deliver 1.1 MW.

**2.3. CNGS Beam.** The CNGS beam [3, 24] is located at CERN on the border of Switzerland and France and the neutrinos are measured by experiments at the Gran Sasso Laboratory in Italy, 730 km away. CNGS uses 400 GeV/c protons from

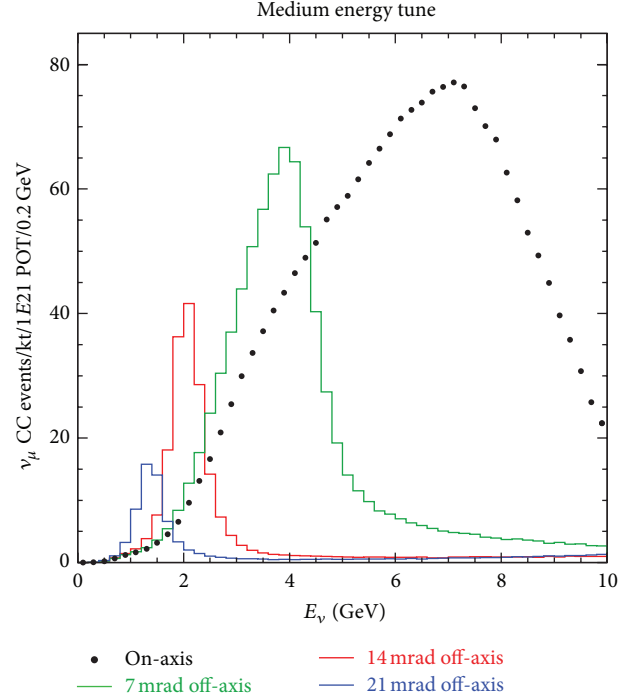


FIGURE 5: The simulated NuMI energy spectrum as it will be in the NOvA-era with the beamline in the “medium energy” configuration. The NOvA detectors will sit 14 mrad off-axis and the energy spectrum at that angle is shown by the red histogram. In contrast, the MINOS+ experiment will sit on-axis and so collect thousands of neutrino interactions per year that will be measured with an  $L/E$  resolution at the 10% level: the on-axis spectrum is shown by the black dots. The green and blue histograms further illustrate how the spectrum changes with the off-axis angle.

CERN’s SPS accelerator that are fast extracted in two 10.5  $\mu$ s spills 50 ms apart every 6 s. Each spill contains typically  $2 \times 10^{13}$  protons to give an average power of around 300 kW. The CNGS beam was commissioned in 2006 and the total exposure is expected to reach  $1.9 \times 10^{20}$  protons on target by the end of the 2012 run.

The CNGS target assembly consists of a magazine containing 5 separate targets, of which one is used at a time and the others are in situ spares. Each target consists of a series of thirteen graphite rods 10 cm long, the first two are 5 cm in diameter and the remainder are 4 cm. The magnetic focusing system consists of a horn and a reflector that are pulsed at 150 kA and 180 kA, respectively. An evacuated decay volume 1000 m long and 2.5 m in diameter allows the short-lived hadrons to decay. At the end of the decay volume there is a graphite and iron hadron stop. Beyond that, two detector stations measure the remaining muons, which are used to derive the intensity and profile of the neutrino beam.

The CNGS beam is operated in a neutrino-enhanced mode and provides a high purity  $\nu_\mu$  source with  $\bar{\nu}_\mu$ -contamination of 2% and  $\nu_e + \bar{\nu}_e$ -contamination of less than 1%. The number of prompt  $\nu_\tau$  in the beam is negligible [25].

At the time of writing, no formal proposal for running the CNGS beam beyond the long LHC-shutdown in 2013 has been made by OPERA or other Gran Sasso experiments.

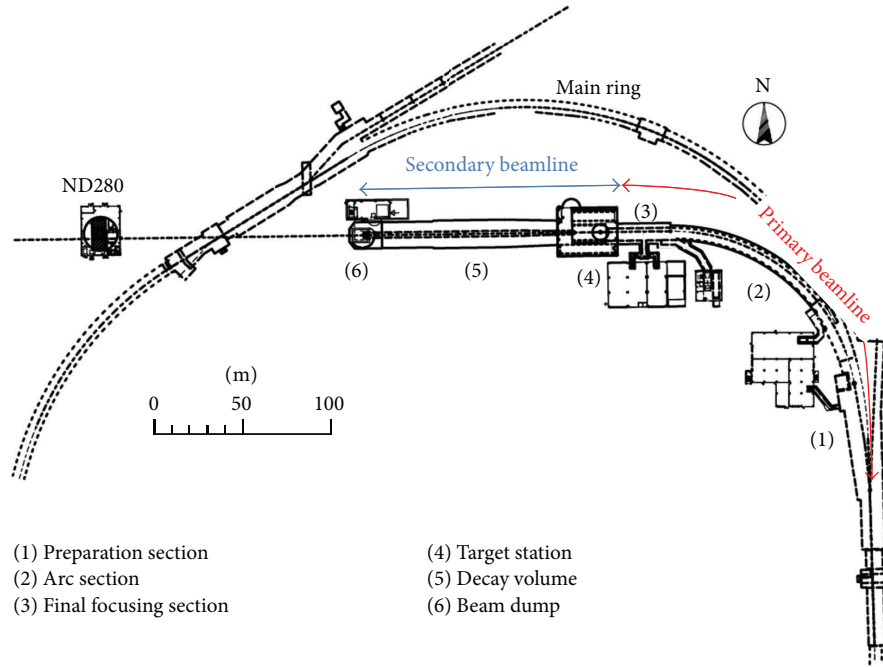


FIGURE 6: A schematic of the overall T2K beam facility showing the primary and secondary beamlines plus the location of the ND280 detector complex.

**2.4. T2K Beam.** The neutrino beam for the Tokai-to-Kamioka (T2K) experiment is produced at the Japan Proton Accelerator Research Complex (J-PARC) and measured by both near detectors locally and by Super-Kamiokande, 295 km from J-PARC. The T2K beam is an off-axis narrow band beam. Details of the experimental apparatus for T2K including the beamline are described in [4].

J-PARC is a high-intensity proton accelerator complex located in Tokai village, Japan, whose construction was completed in 2009. The accelerator chain consists of a 181 MeV LINAC, 3 GeV Rapid Cycling Synchrotron, and a 30 GeV Main Ring (MR). The design beam power of the MR is 750 kW. The proton beam used to produce the neutrino beam is extracted from MR in a single turn (fast extraction) with repetition cycle of 3.52 s at the beginning of operation in 2010 and 2.56 s now in 2012. The beam pulse of the single extraction consist of 8 bunches, 580 ns apart, making the pulse about 5  $\mu$ s long. The beam power achieved for stable operation as of summer 2012 was 200 kW which corresponds to  $1.1 \times 10^{14}$  protons/pulse (ppp) or  $1.3 \times 10^{13}$  protons/bunch (ppb).

The layout of the neutrino beam facility at J-PARC is illustrated in Figure 6. The extracted beam from MR is bent by about 90° to point in the Kamioka direction using 28 superconducting combined function magnets [26–28] and delivered to the production target.

The secondary beamline where the neutrinos are produced is shown in Figure 7. The production target is a 26 mm diameter and 90 cm long graphite rod, corresponding to 2 interaction lengths, in which about 80% of incoming protons interact. The secondary positive pions (and kaons) from the

target are focused by three electromagnetic horns operated at a 250 kA pulsed current.

The target region is followed by a 110 m long decay volume filled with helium gas in which pions and kaons decay in flight into neutrinos. The beam dump, which consists of graphite blocks about 3.15 m thick followed by iron plates 2.5 m thick in total, is placed at the downstream end of the decay volume.

Muon monitors (MUMON) are placed just behind the beam dump to monitor the intensity and the profile of muons which pass through the beam dump on a spill-by-spill basis. High energy muons of >5 GeV can penetrate the beam dump and reach the MUMONs.

The design principle of the J-PARC neutrino facility is that all parts which can never be replaced later, for example, the decay volume shielding and cooling pipes, beam dump cooling capacity, and so forth, are built such that they can be operated with up to 3 MW of beam power from the beginning. Parts that can be replaced are designed to be operated with a beam power up to 750 kW and have a safety factor of 2 to 3.

The neutrino beamline is designed so that the neutrino energy spectrum at Super-Kamiokande can be tuned by changing the off-axis angle down to a minimum of 2.0° from the current (maximum) angle of 2.5°. The unoscillated  $\nu_\mu$  energy spectrum at Super-Kamiokande with a 2.5° off-axis angle is shown in Figure 8.

The construction of the neutrino facility started in 2004 and was completed in 2009. Stable beam production for physics measurements started in January 2010 after careful commissioning. The Great East Japan Earthquake on March 11, 2011 damaged J-PARC and stopped the operation of the accelerators. After recovery work, the accelerator restarted

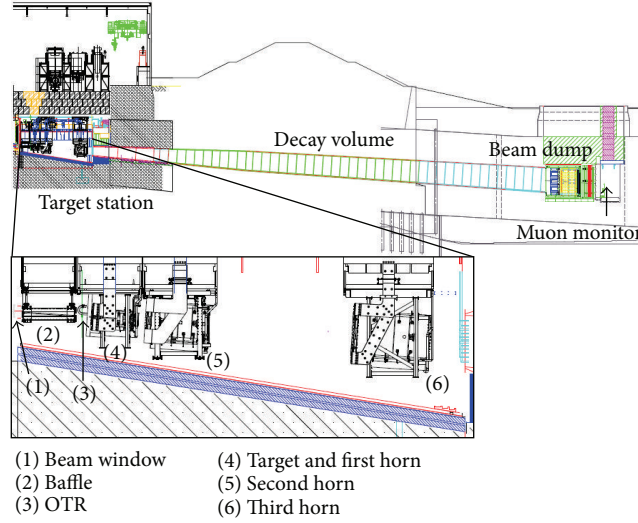
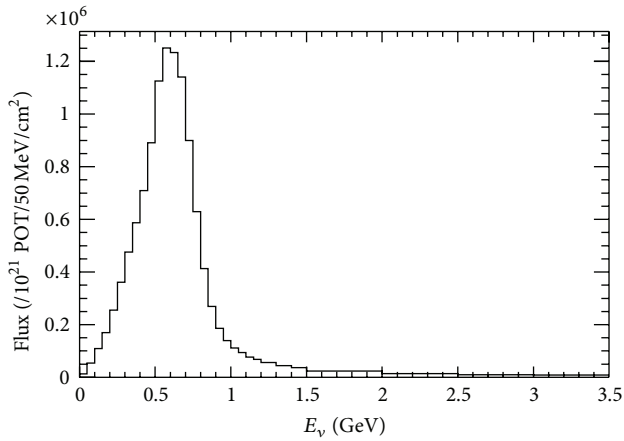


FIGURE 7: Schematic of T2K secondary beam line.

FIGURE 8: The unoscillated  $\nu_\mu$  flux at Super-Kamiokande with an off-axis angle of  $2.5^\circ$  and operation of the electromagnetic horns at 250 kA.

operation in December 2011 and stable beam for T2K data taking was achieved in March 2012.

The J-PARC neutrino facility will provide an integrated number of protons on target of  $7.5 \times 10^{21}$  (equivalent to  $750 \text{ kW} \times 5 \times 10^7 \text{ s}$ ), which is the approved exposure for T2K. With the present power upgrade scenario, this will take about 10 years.

### 3. Detectors

In this section the detectors used by the experiments to achieve their diverse physics goals are described. Design of these detectors took into account multiple factors such as target mass, cost-effectiveness, particle flavor identification purity and efficiency, the beam energy spectrum, and required baseline. The subsections below are time ordered and include K2K Near detectors and Super-Kamiokande

(SK), MINOS, OPERA, ICARUS, the T2K ND280 complex, and NOvA.

**3.1. K2K Near Detectors.** The K2K Near detector complex was located at the KEK laboratory in Japan. The detectors were about 300 m from the beam-target, about 70 m of which was taken up with earth shielding. The detectors were designed to measure the flux and energy spectrum of the beam as it leaves KEK. Their mass composition was chosen to be primarily water so as to largely cancel common systematic uncertainties with Super-Kamiokande. These goals were achieved using a 1 kiloton water Čerenkov detector (the “1 kt”) and fine-grained detectors (FGD). A scintillating fiber detector (SciFi) [29], scintillating counters, a lead glass array (LG), and a muon range detector (MRD) [30] comprised the FGDs. For the second phase of K2K, the LG was replaced by the fully active scintillator-bar detector (SciBar) [31].

The 1 kt used the same technology as the Super-Kamiokande far detector with the same arrangement of photomultiplier tubes and the same 40% coverage. In total, 680 50 cm photomultiplier tubes were used to line an 8.6 m diameter, 8.6 m high cylinder.

The SciFi tracking detector used 20 layers of scintillating fibers, closely packed together in  $2.6 \text{ m} \times 2.6 \text{ m}$  sheets that were separated by 9 cm. These layers were interleaved with 19 layers of water target contained in extruded aluminum boxes and read out using image-intensifier tubes and CCD cameras. The energy and angle of the muons produced in  $\nu_\mu$  CC interactions were measured using the MRD. This detector was designed to be big enough ( $7.6 \text{ m} \times 7.6 \text{ m}$  in the plane transverse to the beam) to measure both the flux and the profile of the beam. The MRD consisted of 12 layers of iron absorber with vertical and horizontal drift tubes in between. The first 4 (upstream) layers were 10 cm thick and the remaining 8 layers were 20 cm thick. With 2.00 m of iron in total, up to 2.8 GeV/c muons could be stopped and their total energy measured.

The SciBar detector was an upgrade to the near detectors designed with the aim of improving the measurement of CC quasi-elastic interactions and was installed in 2003. It was designed with the requirement of high purity and efficiency, with the suppression of inelastic CC interactions involving pions in the final state one of the main goals. The detector was “totally active” and could measure  $dE/dx$  for individual particles such as protons and pions. The SciBar detector consisted of 14,848 extruded scintillator strips (of dimension  $1.3 \times 2.5 \times 300 \text{ cm}^3$ ) packed tightly together to make up the tracker part of the detector. On the downstream side of the tracker was an electromagnetic calorimeter, 11 radiation lengths thick and made of scintillating fibres and lead foils, called the Electron Catcher. This calorimeter was used to aid the measurement of electron showers and  $\pi^0$  produced by neutrino interactions.

**3.2. Super-Kamiokande Detector.** The Super-Kamiokande detector [32] is the world’s largest land-based water Čerenkov detector with a total mass of 50 kilotonnes. SK is a 39 m diameter and 41 m high stainless steel cylindrical tank filled with ultra-pure water that is located 1 km underneath Mt. Ikenoyama in Japan. The water tank is optically separated into a 33.8 m diameter and 36.2 m high cylindrically-shaped inner detector (ID) and outer detector (OD) by opaque black sheets and Tyvek sheets attached to a supporting structure. There are 11,129 inward-facing 50 cm diameter photomultiplier tubes (PMTs) lining the ID giving 40% coverage, and 1885 outward facing 20 cm diameter PMTs on the inner wall of the OD. The ID and OD are optically separated to allow interactions produced within the ID to be distinguished from those entering from outside (e.g., cosmic rays).

A key feature of SK is the ability to separate  $\nu_\mu$  CC events from  $\nu_e$  CC by identifying the electron or muon. The muons, being heavier, produce sharper Čerenkov cones whereas electrons scatter more easily and the resulting “fuzzy” Čerenkov cone is effectively the sum of multiple overlapping cones all pointing in slightly different directions. The vertex for each interaction is reconstructed using the timing from all the hit PMTs and used to define the fiducial volume of 22.5 kilotonnes.

**3.3. MINOS Detectors.** The MINOS detectors [33] are magnetized tracking calorimeters made of steel and plastic scintillator optimized for measurements of muon neutrinos and antineutrinos with energies of a few GeV. The Near Detector at Fermilab has a mass of 0.98 kilotonnes and the Far Detector at the Soudan Underground Laboratory in Minnesota, USA has a mass of 5.4 kilotonnes. The detectors have a planar geometry with the active medium comprised of solid plastic scintillator strips with neighboring planes having their strips orientated in perpendicular directions to give three-dimensional tracking capability. The planes are hung vertically so as to be approximately perpendicular to the path of the beam neutrinos. In the detectors’ fiducial volumes 80% of the target mass is provided by steel planes and they are magnetized to provide average fields of 1.28 T and 1.42 T for the Near and Far detectors, respectively. The

steel planes are 2.54 cm thick (1.45 radiation lengths) and mounted on each one is, at most, a single 1.0 cm thick scintillator plane. Each scintillator plane comprises of up to 192 strips that are 4.1 cm wide and up to 8 m in length. There is an air gap between each plane of 2.4 cm in which the magnetic field is substantially smaller. A schematic of the Near and Far detectors is shown in Figure 9. The Far Detector planes are an 8 m wide octagonal shape and grouped together into two separately magnetized supermodules that are about 15 m in length. The Near Detector planes have a squashed octagon shape that is about 3 m wide and 2 m high. The Near Detector has two main parts: a fully instrumented region used for calorimetry and a muon spectrometer, that is, located downstream in the neutrino beam.

MINOS scintillator is made of polystyrene, doped with the fluors PPO (1%) and POPOP (0.03%), which is coextruded with a thin 0.25 mm  $\text{TiO}_2$  layer. A groove runs along the length of each strip into which a 1.2 mm wavelength-shifting (WLS) fibre optic cable is glued. On exiting the ends of the strips, the WLS fibers run together in a manifold to terminate in a connector. Clear fibre optic cables, with a longer 12 m attenuation length, are used to route the light to multianode photomultiplier tubes.

The Near and Far detectors were designed to be as similar as possible, although due to their different environments it was necessary to use different front-end electronics. On average, several neutrino interactions occur in the Near detector in every beam spill, whereas in the Far detector only a handful of neutrino interactions occur per day. The Near detector electronics digitizes the signal from each PMT pixel continuously during each beam spill at the frequency of the beam RF structure of 53.103 MHz. In contrast, the Far detector electronics has a dead time of at least  $5 \mu\text{s}$  after each PMT dynode trigger. The Far detector self-triggers with high efficiency on neutrino interactions. In addition, the beam spill time is sent over the internet and used to record all detector activity in a  $100 \mu\text{s}$  window around the beam spill. Both Near and Far detectors also record cosmic ray events, and at the Far detector atmospheric neutrino events can be selected.

Neutrino energy reconstruction in MINOS involved both calorimetry of showers (although later analyses also used topological information to improve shower energy resolution) and either range or curvature of muon tracks. The calorimetric energy resolution of the MINOS detectors was determined to be  $21.4\%/\sqrt{E} \oplus 4\%/E$  for electromagnetic showers and  $56\%/\sqrt{E} \oplus 2\%$  for hadronic showers. The accuracy of the simulation of protons, pions, electrons, and muons was determined using a specially constructed calibration detector that was exposed to CERN test-beams [34]. The test-beam data was also used to demonstrate that differences in the Near and Far detector readout systems could be corrected for by the calibration and the detector simulation [35] down to the 1% level.

In the Far detector the optimal fiducial volume of 4.2 kilotonnes included as many events as possible to reduce the statistical uncertainty on the oscillation parameters. Whereas in the Near detector, with millions of events, the fiducial volume was optimized to make the best possible



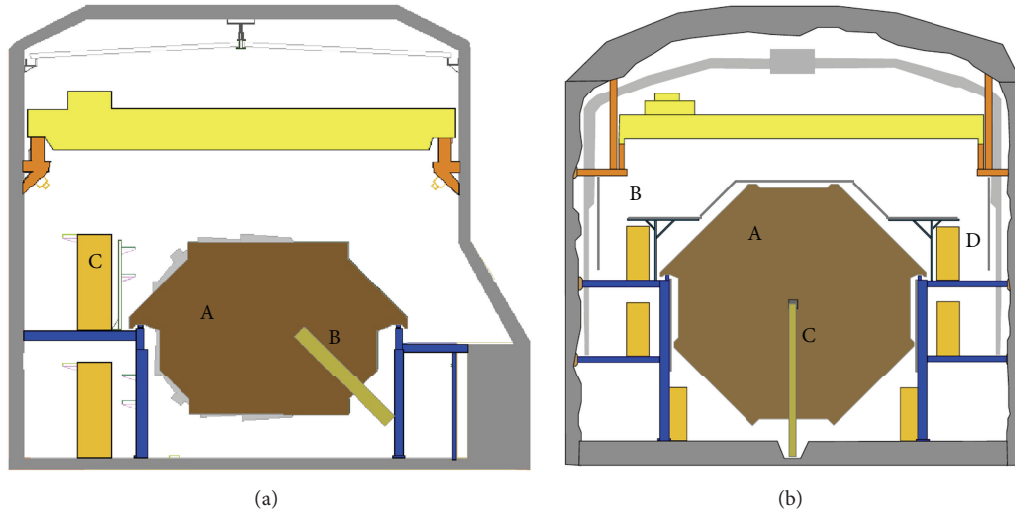


FIGURE 9: Schematics showing the end views of the MINOS Near (a) and Far (b) detectors. For the Near detector the label “A” identifies the upstream steel plate, “B” is the magnet coil, and “C” is an electronic rack. For the Far detector, “A” identifies the steel plane at the end of the second supermodule, the furthest downstream in the beam, “B” is the cosmic ray veto shield, “C” is a magnet coil, and “D” is an electronics rack. The detectors are shown with different scales: the Near detector is 3 m wide compared to 8 m for the Far detector. Figure from [33].

measurement of the neutrino energy spectrum and had a mass of 23.7 tonnes.

**3.4. OPERA Detector.** The OPERA detector is located 1400 m underground in Hall C at the Gran Sasso Laboratory, Italy and is optimized to enable a high-purity selection of tau neutrino interactions on an individual event basis. A key signature of a  $\nu_\tau$  event is the topology of the tau decay. Substantial energy is carried away by the  $\nu_\tau$  produced in tau decay and due to the large tau mass the effect of missing transverse momentum often gives rise to a substantial change in direction (or “kink”) at the point along a track where the tau decays. With a mean lifetime of 0.29 picoseconds, corresponding to  $87 \mu\text{m}$  at the speed of light, directly observing the tau in a necessarily massive detector is an experimental challenge.

The detector used by the OPERA collaboration is a hybrid consisting of a target constructed of fine grained emulsion and electronic detectors. Neutrino events are localized in the target using the scintillator target tracker (TT) detector and a spectrometer is used to measure the momentum and charge of muons. The target is divided into two supermodules with veto planes upstream. Each target region contains 75 000 emulsion cloud chambers (ECC), or “bricks”, which are constructed from 56 lead plates 1 mm thick that are interleaved with 57 nuclear emulsion films. Each ECC weighs 8.3 kg for a total target mass of around 1.25 kilotonnes. An automated system is used to extract the bricks identified by the TT from the detector. Scanning of the emulsion films is performed by automated microscopes located on the surface in Europe and Japan.

**3.5. ICARUS Detector.** The ICARUS T600 detector [36] is located in Hall B of the Gran Sasso Laboratory, Italy and

consists of 760 tonnes of ultra-pure liquid argon (LAr) held at 89 K. The argon provides the target mass and the ionization medium for four time projection chambers (TPCs). These four TPCs come in two pairs, with each pair occupying a volume of  $3.6 \times 3.9 \times 19.6 \text{ m}^3$ . A shared cathode plane runs down the centre of each volume separating the two TPCs, giving a maximum drift path of 1.5 m. This detector provides exquisite electronic imaging of neutrino interactions in three dimensions with a position resolution of around  $1 \text{ mm}^3$  over the whole detector active volume of about  $170 \text{ m}^3$ .

An electric field of 500 V/cm is used to drift ionization electrons towards three parallel planes of wires arranged at  $0^\circ$ ,  $+60^\circ$ , and  $-60^\circ$  to the horizontal. These planes are situated along one side of each TPC and are separated by 3 mm. In total there are 53248 wires that have a pitch of 3 mm and lengths up to 9 m long. The first two planes (Induction-1 and Induction-2) provide signals in a nondestructive way before the charge is finally integrated on the Collection plane. Position information along the drift direction is provided by combining measurement of the absolute time of the ionising event with knowledge of the drift velocity (about  $1.6 \text{ mm}/\mu\text{s}$  at the nominal electric field strength). VUV scintillation light from the liquid argon, measured by PMTs operating at cryogenic temperatures, provides the absolute timing information.

Electronegative impurities such as  $\text{O}_2$ ,  $\text{CO}_2$ , and  $\text{H}_2\text{O}$  were initially reduced by evacuating the detector for 3 months before filling and are generally maintained at below the 0.1 ppb level by recirculating the LAr through purification systems. Full volume recirculation can be accomplished in 6 days. A free electron lifetime of 1 ms corresponds to a 1.5 m drift distance and this has been successfully maintained for the vast majority of the time since the detector started operation in mid-2010.

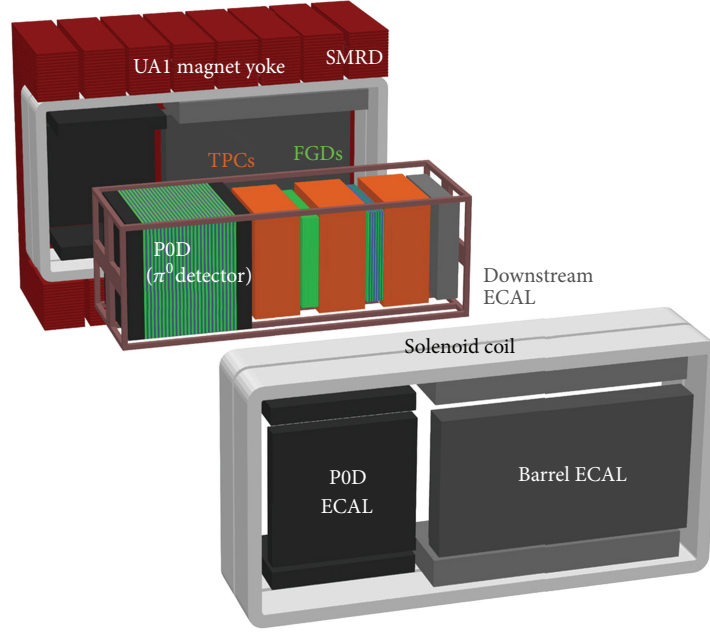


FIGURE 10: An exploded view of the ND280 off-axis near detector for the T2K experiment. The ND280 is a magnetized tracking detector comprising of several subdetectors located inside the UA1 magnet (see the main body of text for detailed descriptions). Figure from [4].

**3.6. T2K ND280 Detectors.** The ND280 detector complex is located on the site of the J-PARC accelerator complex about 280 m downstream of the production target. The T2K experiment is formed of the ND280 detectors, the beamline, and Super-Kamiokande. The ND280 detectors measure the neutrino energy spectrum and flavor content of the beam before it oscillates. Since the far detector is located  $2.5^\circ$  off-axis, the primary near detector is also located off-axis at the same angle. An on-axis near detector, INGRID, measures the neutrino beam profile and intensity.

The off-axis near detector is a magnetized tracking detector comprising of several subdetectors located within the magnet recycled from the UA1 experiment at CERN. Figure 10 shows an exploded view of the off-axis ND280 detector displaying the  $\pi^0$  detector (P0D), the tracker comprising of fine-grained detectors (FGDs) and time projection chambers (TPCs), the electromagnetic calorimeter (ECAL), and side muon range detector (SMRD). The P0D consists of scintillating bars alternating with either a water target or brass or lead foil (to limit the range of any  $\pi^0$ s). The FGDs consist of layers of finely segmented scintillator bars used to measure charged current interactions. These inner detectors are all surrounded by the ECAL to catch any  $\gamma$ -rays that do not convert in the inner detectors. Finally, the SMRD sits in the return yoke of the magnet and measures the range of muons that exit the sides of the detector.

The on-axis INGRID detector consists of 14 identical modules arranged in a cross pattern with two groups: extending 10 m along the horizontal and vertical axes. A further two modules are located at off-axis positions a few meters above the horizontal and to each side of the vertical part of the cross. Each module is constructed from 9 steel plates

6.5 cm thick interleaved with 11 tracking scintillator planes. The planes consist of two sets of 24 scintillator bars measuring  $1.0 \times 5.0 \times 120.3 \text{ cm}^3$ , one set arranged to run vertically and the other horizontally. INGRID measures the center of the beam to a precision of 10 cm, equivalent to 0.4 mrad.

**3.7. NOvA Detectors.** The NOvA [15] far detector will be located 14 m off the NuMI beam axis, 810 km from the NuMI target, off the Ash River Trail in northern Minnesota, USA. The Ash River Trail is the most northern road in the United States near the NuMI beam line. The NOvA near detector will be located on the Fermilab site about 1 km from the NuMI target, also at an angle of 14 mrad to NuMI beam.

The NOvA detectors can be described as totally active, tracking, liquid scintillator calorimeters. The basic cell of the far detector is a column or row of liquid scintillator with approximate transverse dimensions 4 cm by 15.6 m and longitudinal dimension 6 cm encased in a highly-reflective polyvinyl chloride (PVC) container. A module of 32 cells is constructed from two 16-cell PVC extrusions glued together and fitted with appropriate end pieces. Twelve modules make up a plane, and the planes alternate in having their long dimension horizontal and vertical. The far detector will consist of a minimum of 928 planes, corresponding to a mass of approximately 14 kt. Additional planes are possible depending on available funds at the end of the project. Each plane corresponds to 0.15 radiation lengths.

The NOvA near detector will be identical to the far detector except that it will be smaller, 3 modules high by 3 modules wide, with 192 planes. Behind the near detector proper will be a muon ranger, a sandwich of 10 10-cm iron plates each followed by two planes of liquid

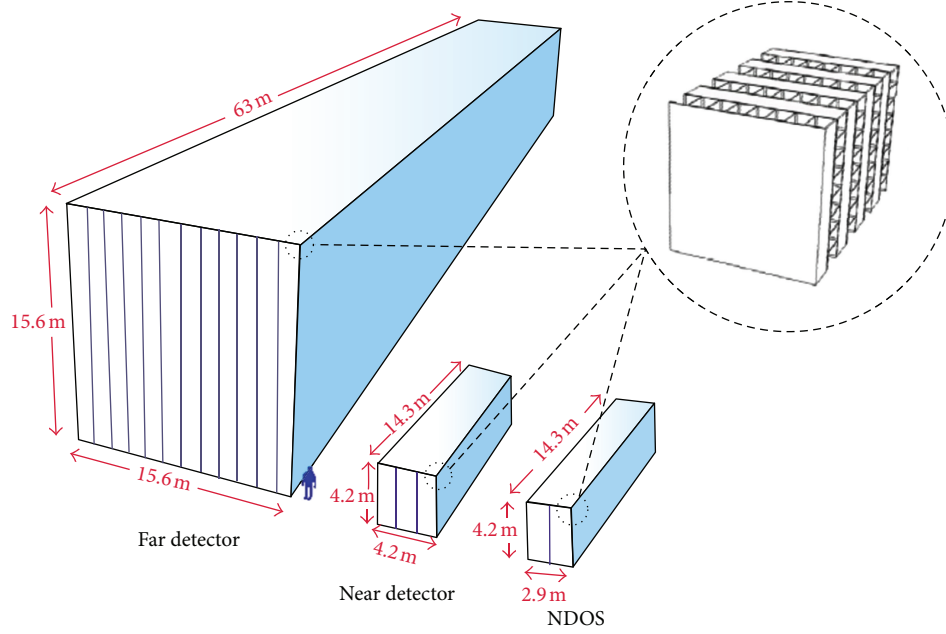


FIGURE 11: Drawings of the NOvA Far and Near detectors. The human figure at the base of the Far detector is for scale.

scintillator detectors. NOvA has also constructed a near detector prototype called the NDOS (Near Detector On the Surface) which has been running since November 2010 on the surface at Fermilab, off axis to both the NuMI and Booster neutrino beams. Figure 11 contains a drawing of the NOvA detectors.

Light is extracted from each liquid scintillator cell by a U-shaped 0.7-mm wavelength-shifting fiber, the ends of which terminate on a pixel of a 32-pixel avalanche photodiode (APD), which is mounted on the module. The APD is custom-made for the NOvA experiment by the Hamamatsu Corporation to optimize the match to the two fiber ends per pixel. Light from the far end of the cell is preferentially attenuated at the lower wavelengths, so that the peak of the spectrum is at about 540 nm. The use of APDs is crucial for the experiment since they have a quantum efficiency of approximately 85% at this wavelength compared to 10% for a photomultiplier with a bialkali photocathode. The system is designed to produce a minimum of 20 photoelectrons from the far end of the cell for the passage of a minimum ionizing particle at normal incidence. The APD is run at a gain of 100, so low noise is required for efficient operation. The APD is cooled to  $-15^{\circ}\text{C}$  by a thermoelectric cooler to reduce the thermal noise of the APD to an acceptable limit.

The NOvA front-end electronics runs in continuous digitization mode at 2 MHz for the far detector and 8 MHz for the near detector. It delivers GPS time-stamped, pedestal subtracted, and zero-suppressed data to the data acquisition system (DAQ). At the far detector, the DAQ buffers the data for up to 20 seconds while awaiting a beam spill time message from Fermilab via Internet. All data within a  $30\text{ }\mu\text{s}$  window around the  $10\text{ }\mu\text{s}$  beam spill will be recorded for offline analysis.

#### 4. Results on $\nu_{\mu} \rightarrow \nu_{\tau}$ : The Dominant Oscillation Mode

The dominant oscillation mode for all long-baseline accelerator experiments performed to date is  $\nu_{\mu} \rightarrow \nu_{\tau}$ . This channel was used by K2K [5, 37] and MINOS [38] to provide essential confirmation of the neutrino oscillations observed by Super-Kamiokande in atmospheric neutrinos [11]. Accelerator experiments with their fixed baselines,  $L$ , and high-energy resolution detectors allow precise measurement of  $L/E$ . In turn, this allows resolution of the oscillatory quantum-mechanical interference pattern and precise measurements of  $|\Delta m^2|$  and  $\sin^2(2\theta)$ ; these results are described here in Section 4.1. The corresponding measurements for muon antineutrinos are described in Section 4.2.

Direct observation of tau appearance by OPERA will further confirm  $\nu_{\mu} \rightarrow \nu_{\tau}$  as the dominant mode of oscillation and the results from the first half of their data set [25, 39] are described in Section 4.3.

**4.1. Precision Measurement of  $|\Delta m^2|$  and  $\sin^2(2\theta)$ .** In an accelerator experiment, measurement of  $|\Delta m^2|$  and  $\sin^2(2\theta)$  is performed by observing the energy-dependent disappearance of muon neutrinos. The fixed baselines,  $L$ , are known to high precision and so contribute a negligible uncertainty to measurement of  $L/E$ , which is dominated by the energy resolution of the detectors. The energy at which the maximum disappearance occurs is a measure of  $|\Delta m^2|$  and the disappearance probability at that point is given by  $\sin^2(2\theta)$ . Figure 12 shows the energy spectrum of muon neutrino candidate events in the MINOS far detector where the energy-dependent deficit can be clearly seen, with the

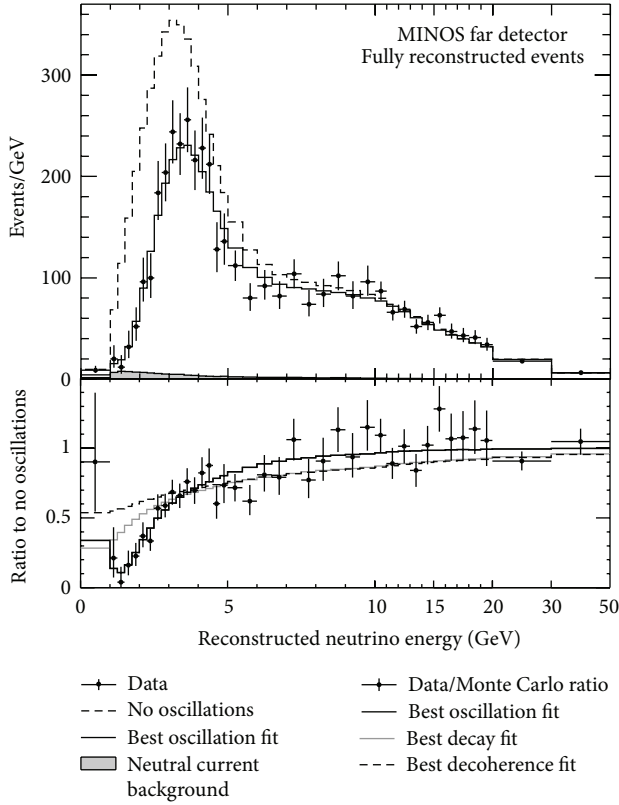


FIGURE 12: The energy spectrum of fully reconstructed muon neutrino candidate events in the MINOS Far detector (a). Both the no oscillation hypothesis and the best oscillation fit are shown. The shaded region shows the expected neutral-current background. The ratio to no oscillations (b) displays the best fits to models of neutrino decay and neutrino decoherence, where they are seen to be disfavored at high significance ( $7\sigma$  and  $9\sigma$ , resp.)

maximum disappearance occurring at around 1.4 GeV for the 735 km baseline.

A crucial ingredient to enabling precise measurements of the oscillation parameters is event-by-event identification of whether the observed interactions are neutral-current (NC) or charged-current (CC) events. In the absence of sterile neutrinos, the spectrum of NC events is unchanged due to oscillations and has to be separated from the muon neutrino CC sample. For the experiments performed to date, identification of the flavor of CC events has been of secondary importance to the separation of NC events since the vast majority of CC events are muon flavor. Given the tau production threshold at a neutrino energy of around 3.5 GeV, this appearance mode is naturally suppressed in K2K, MINOS, T2K, and NOvA due to their lower beam energies and so relatively few  $\nu_\tau$  CC interactions occur. The appearance of electron neutrinos is a subdominant effect (detailed in Section 5) that contributes, for example, only around 1% of the event rate in MINOS. The performance of the different experiments in selecting a  $\nu_\mu$  CC event sample is discussed below.

**4.1.1. K2K  $\nu_\mu$  Disappearance Results.** K2K was the first accelerator long-baseline experiment, taking data from 1999–2004. The neutrino beam was produced and measured

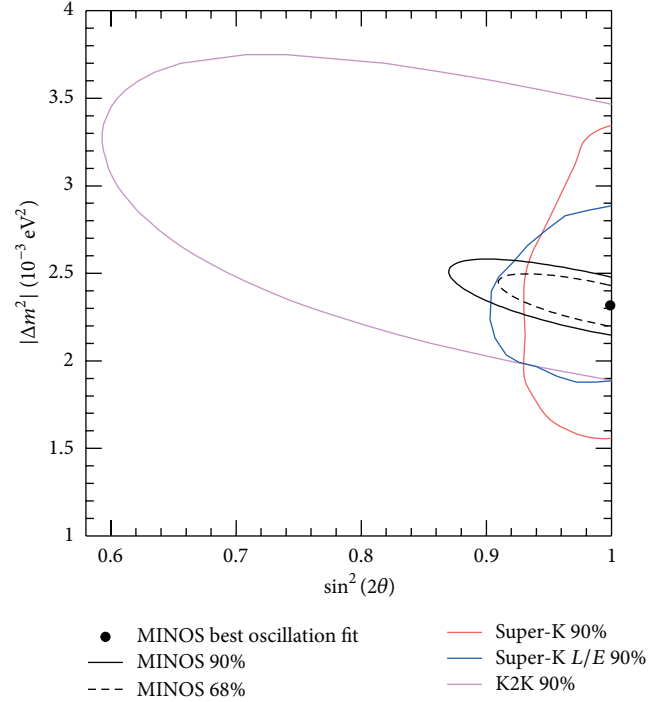


FIGURE 13: The 90% confidence regions for  $|\Delta m^2|$  and  $\sin^2(2\theta)$ . Results shown are published contours from K2K [5], MINOS [40] and Super-Kamiokande [41, 42]. For the latest but still preliminary results see Figure 14.

at KEK in Japan and then observed 250 km away at the Super-Kamiokande detector. K2K saw 112 beam-originated events in the fiducial volume of Super-Kamiokande with an expectation of  $158.1^{+9.2}_{-8.6}$  without oscillation [5]. The water Čerenkov detector allowed separation of 58 single-ring muon-like events in which a distortion of the energy spectrum was seen. At the K2K beam energy these muon-like events contained a high fraction of quasi-elastic events and the incoming neutrino energy was reconstructed using two-body kinematics. Combining information from both the shape of the energy spectrum and the normalization, K2K determined that the probability of obtaining their data in the case of null-oscillations was 0.0015% ( $4.3\sigma$ ) thus confirming the Super-Kamiokande atmospheric neutrino results. The K2K 90% C.L. allowed region in the  $|\Delta m^2|$ - $\sin^2(2\theta)$  plane is shown by the magenta line in Figure 13.

**4.1.2. MINOS  $\nu_\mu$  Disappearance Results.** MINOS started data taking in 2005 and ran for 7 years through April 2012. Around 80% of the data was taken with the beam optimized to produce neutrinos and the remaining 20% antineutrinos (see Section 4.2 for a description of the  $\bar{\nu}_\mu$  disappearance results). The first  $\nu_\mu$  disappearance results from MINOS are given in [38] and detailed in a longer paper [43]. Updated results are given in [44] and those presented here are taken from [40]. Additionally, the results from the preliminary analysis using the full MINOS data set [45] are also summarised here.

The geometry of the MINOS detectors allows three dimensional reconstruction of tracks and showers. Using the



reconstructed vertex information a fiducial volume cut was made that separated incomplete and partially reconstructed events occurring at the edge of the detector from those that were fully reconstructed. As mentioned above, a crucial step in this analysis was the separation of  $\nu_\mu$  CC events from NC events. For the first results a particle identification parameter was constructed using probability density functions for the event length, the fraction of the energy contained in the track, and the average pulse height per plane. The later results used an improved technique based on a k-nearest-neighbor algorithm (kNN). This kNN technique used the energy deposition along a track and its fluctuation to discriminate muons from spurious tracks reconstructed from hadronic activity in NC interactions. For the most recent analysis an overall efficiency for selecting  $\nu_\mu$  CC events of 90% was achieved. The first results made a selection on the charge-sign of the muon but later analyses have included the 7% antineutrino component of the neutrino-enhanced beam, which had a significantly higher average energy [46].

Near detector data was used to substantially reduce systematic effects on this measurement that would otherwise arise from limited knowledge of the neutrino flux and cross-sections. Both the Near and Far Detectors measured a product of flux times cross-section and by doing a relative measurement, the uncertainties on that product canceled to first order. However, the flux was not the same at the Near and Far detectors: one saw a line-source of neutrinos and the other saw what was effectively a point source. The Far Detector flux was populated by neutrinos from more forward decaying pions and so the spectrum was somewhat harder than at the Near detector. The beamline simulation incorporated and was used to estimate these largely geometrical effects.

Due primarily to the flux and cross-section uncertainties, the Near detector data differed from the simulation by up to 20% as a function of energy. An extrapolation procedure used the Near Detector measurements to predict the Far Detector energy spectrum via a number of steps as follows: subtracting the estimated background from the Near Detector energy spectrum; deconvolving the effects of Near detector energy resolution; using a transfer matrix to account for the different flux at the Far Detector; weighting each energy bin according to the oscillation probability; reintroducing the effect of energy resolution at the Far Detector; adding in the estimated Far Detector background. With all these steps complete an oscillated Far Detector prediction was obtained for comparison with the data.

Several sources of systematic uncertainty were accounted for in this measurement. The three largest uncertainties on the measurement of  $|\Delta m^2|$  were on the absolute energy scale of hadronic showers, the absolute energy scale of muons, and the relative normalization of event rates between Near and Far Detectors. Other uncertainties included NC contamination, the relative hadronic energy scale, cross-sections, and beam flux. Overall, the statistical error on the MINOS measurement of  $|\Delta m^2|$  was still more significant than the systematic uncertainty.

The largest three systematic uncertainties on the measurement of  $\sin^2(2\theta)$  were on the NC contamination, cross-sections, and the relative hadronic energy scale. However, the MINOS measurement of  $\sin^2(2\theta)$  was dominated by the statistical uncertainty, with the systematic uncertainty being smaller by more than a factor of four.

Every NuMI beam event with a reconstructed muon was included in the likelihood fit to extract the oscillation parameters. These events were split into 7 event categories to extract the maximum information. Partially reconstructed events, where the neutrino interacted in the rock outside the detector or in the outer edges of the detector, were a separate category and only their reconstructed muon information was used (any shower energy was ignored due to its limited use for this sample). Fully reconstructed  $\nu_\mu$  CC candidate events were separated by the charge-sign of the muon. Positively charged events formed their own single sample but the negatively charged events were divided into 5 categories using their estimated energy resolution (e.g., a highly-elastic CC event where most of the neutrino energy was carried away by the muon was measured more precisely than an inelastic event where shower energy fluctuations smeared the measurement). The four dominant systematic uncertainties were included as nuisance parameters and the mixing angle was constrained by the physical boundary at  $\sin^2(2\theta) = 1$ .

Thousands of beam neutrino interactions have been recorded at the MINOS Far detector and used, as described above, to make the world's most precise measurement of  $|\Delta m^2| = (2.32^{+0.12}_{-0.08}) \times 10^{-3} \text{ eV}^2$  while constraining  $\sin^2(2\theta) < 0.90$  at 90% C.L. [40]. Figure 12 shows the fully reconstructed events recorded by MINOS where the distortion of the energy spectrum expected by oscillations can be seen and contrasts with that expected from alternative models of neutrino disappearance such as neutrino decay or decoherence (they are excluded at 7 and 9  $\sigma$ , resp.). The MINOS contours associated with this published result are shown in Figure 13 (updated but preliminary results from MINOS are shown in Figure 14).

Recently, preliminary MINOS results using the complete data set have been released [45]. The total neutrino-enhanced beam exposure is  $10.7 \times 10^{20}$  POT, 50% more than the previous result given above. Furthermore, two additional data sets are included: firstly, the antineutrino-enhanced beam data ( $3.36 \times 10^{20}$  POT) and secondly, atmospheric neutrinos and antineutrinos (37.9 kiloton-years). While still well within the previous  $1\sigma$  contours, the best fit point for this new analysis has moved slightly away from maximal mixing to  $|\Delta m^2| = (2.39^{+0.09}_{-0.10}) \times 10^{-3} \text{ eV}^2$  and  $\sin^2(2\theta) = 0.96^{+0.04}_{-0.04}$  (the shift in upwards in  $|\Delta m^2|$  being correlated with the shift downward in  $\sin^2(2\theta)$ , due to the required overall normalization being similar to the previous result).

The MINOS preliminary 90% C.L. allowed region in the  $|\Delta m^2|$ - $\sin^2(2\theta)$  plane is shown in Figure 14 by the solid black contour. The latest results from Super-Kamiokande [47] (preliminary) and T2K [48] are shown alongside for comparison. All the results presented here use the 2-flavor approximation.

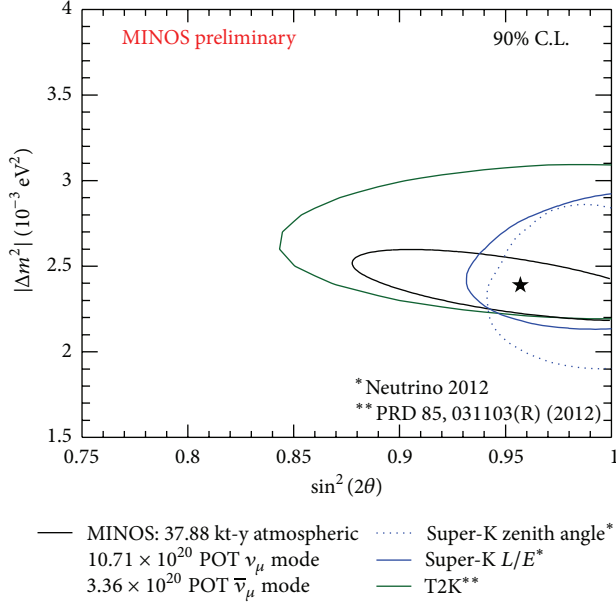


FIGURE 14: Preliminary 90% confidence regions for  $|\Delta m^2|$  and  $\sin^2(2\theta)$  (except for T2K, which is published). Results are shown for MINOS [45], T2K [48], and Super-Kamiokande [47]. The MINOS results shown here are a combination of NuMI beam data and atmospheric neutrino data.

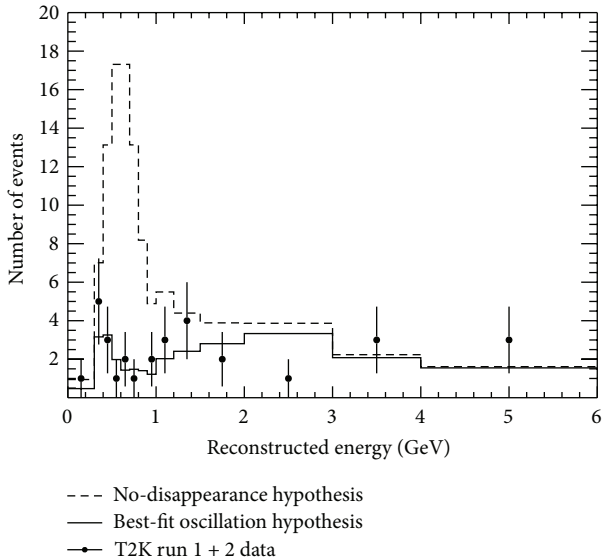


FIGURE 15: Reconstructed neutrino energy spectra of T2K  $\nu_\mu$  disappearance analysis.

**4.1.3. T2K  $\nu_\mu$  Disappearance Results.** T2K started taking data in 2010 and was the first experiment to use an off-axis beam to observe muon neutrino disappearance [48]. The exposure for the first result was  $1.43 \times 10^{20}$  POT and is expected to increase substantially over the next few years. In the Super-Kamiokande far detector, 31 fully contained muon-like ring events were observed against an expectation of  $104 \pm 14$  (syst) without neutrino oscillations. The observed neutrino energy spectrum alongside the predicted spectra with and without oscillation are shown in Figure 15.

The values of the oscillation parameters obtained are consistent with both MINOS results and Super-Kamiokande atmospheric neutrinos. Interestingly, the T2K constraints on  $\sin^2(2\theta)$  already approach the limit set by MINOS. This demonstrates the sensitivity of T2K where the energy peak of the narrow band, off-axis, beam is positioned close to the oscillation maximum and consequently a large fraction of the  $\nu_\mu$  flux disappears. The T2K contours are shown in Figure 14 alongside the latest MINOS results.

**4.2. Measurements of  $|\Delta \bar{m}_{atm}^2|$  and  $\sin^2(2\bar{\theta})$ .** MINOS accumulated 20% of its total exposure with the NuMI beam configured to enhance production of antineutrinos and made the first direct measurement of muon antineutrino disappearance [49]. The CPT theorem, that provides the foundation of the standard model, predicts identical disappearance of neutrinos and antineutrinos in vacuum and the measurements described here allow precision tests of that hypothesis as well as other models of new physics. The first antineutrino result from MINOS reported tension with the neutrino results but with further data the results are now consistent [45, 50]. In addition to these results, the 7% antineutrino component of the neutrino-enhanced beam has also been analyzed [46]; these data provided a higher statistics sample of  $\bar{\nu}_\mu$  events in the 5–15 GeV range, allowing the oscillation probability to be measured with greater precision in that region. The MINOS magnetized detectors were essential to obtaining a high purity sample of  $\bar{\nu}_\mu$  CC events and making the measurements reviewed here.

The antineutrino-enhanced beam flavor composition, described in Section 2, was 40%  $\bar{\nu}_\mu$ , 58%  $\nu_\mu$ , and 2%  $\nu_e + \bar{\nu}_e$  [23]. The reason for the large number of neutrinos was two fold; firstly, the antineutrino cross-section is about 2-3 times lower than for neutrinos; secondly, the yield of negative pions from the beam target was lower than for positive pions. However, the ratio of antineutrinos to neutrinos in the NuMI beam varied strongly as a function of energy and below 6 GeV about 80% of the interactions were antineutrinos (and that is where the oscillation effect was largest for MINOS). Discrimination of muon neutrinos from antineutrinos was performed on an event-by-event basis by analyzing the track curvature in the detector's magnetic field. Efficiency and purity was estimated from the MC simulation at 91.6% and 99.0%, respectively, for the Far Detector.

With the magnetized detectors able to cleanly separate positive and negative muons, the rejection of NC events was an important requirement for this analysis. The  $k$ -nearest-neighbor multivariate technique used for the neutrino analysis (see Section 4.1) was used to separate  $\bar{\nu}_\mu$  CC events from NC. The procedure for extrapolating Near Detector antineutrino data to make a Far Detector prediction was essentially the same as for the neutrino analysis. The detector and beamline simulations were reperformed for antineutrinos to calculate, for example, the required detector resolution deconvolution matrix and flux transfer matrix for  $\bar{\nu}_\mu$ . A slight modification to the oscillation step of the extrapolation was required to allow neutrinos and antineutrinos to oscillate differently in the simulation.

Systematic uncertainties on the measurement of the antineutrino oscillation parameters were similar to those described for neutrinos in Section 4.1.2 above. An additional uncertainty was included on the level of neutrino contamination and the knowledge of the neutrino oscillation parameters. The MINOS measurement of neutrino parameters is not yet systematically limited and given both the factor of 3 lower exposure recorded for antineutrinos ( $3.36 \times 10^{20}$  POT) and the reduced number of  $\bar{\nu}_\mu$  per POT, the antineutrino measurement is dominated by statistical uncertainties.

Recently, a preliminary version of the MINOS measurements of antineutrino oscillation parameters using the full data set have been released [45]. This analysis incorporates three distinct data sets: the antineutrino-enhanced NuMI beam data ( $3.36 \times 10^{20}$  POT); the antineutrinos in the neutrino-enhanced beam ( $10.7 \times 10^{20}$  POT); atmospheric antineutrino data (37.9 kiloton-years). The antineutrino mass splitting was measured to be  $|\Delta\bar{m}_{\text{atm}}^2| = (2.48^{+0.22}_{-0.27}) \times 10^{-3} \text{ eV}^2$  and the mixing angle  $\sin^2(2\bar{\theta}) = 0.97^{+0.03}_{-0.08}$  with  $\sin^2(2\bar{\theta}) > 0.83$  at 90% C.L. The antineutrino contour from MINOS is shown in Figure 16 by the solid black line. Also shown for comparison is the result from the Super-Kamiokande measurement (dashed black) of the combined flux of atmospheric muon neutrinos and antineutrinos [51]. The red contour shows the result from just the NuMI beam data and the blue contour from just the MINOS atmospheric antineutrino data. The MINOS measurements provide the highest precision on the antineutrino mass-squared splitting while Super-Kamiokande measures the antineutrino mixing angle most precisely.

The uncertainty on the difference in the atmospheric mass-squared splittings of neutrinos and antineutrinos is currently dominated by the statistical precision on the antineutrino measurements, by about a factor of 2-3. In the future, NOvA will improve measurement of all the disappearance related parameters for neutrinos and antineutrinos. Importantly for future precision tests of CPT symmetry, several systematic errors on the difference between  $|\Delta m^2|$  and  $|\Delta\bar{m}_{\text{atm}}^2|$  will be significantly smaller than the systematic uncertainty on the two absolute measurements taken separately.

**4.3. Searches for  $\nu_\tau$  Appearance.** The observation of  $\nu_\tau$  appearance with a  $\nu_\mu$  source would directly confirm the hypothesis of  $\nu_\mu \rightarrow \nu_\tau$  oscillations as the cause of the disappearance effect observed by atmospheric and accelerator experiments. This is the goal of the OPERA experiment [7]. Furthermore, there is currently no observation at the 5-sigma level of the appearance of neutrino flavors due to oscillations, only disappearance. The next few years should see the conclusive observation of both  $\nu_\tau$  appearance with OPERA and  $\nu_e$  appearance with T2K and NOvA, demonstrating key aspects of the 3-flavour neutrino oscillation model.

The kinematic threshold for  $\tau$  production from  $\nu_\tau$  interactions is around 3.5 GeV and at that energy the first maximum of the oscillation probability occurs at a baseline of approximately 2500 km. For a fixed baseline, matching the energy

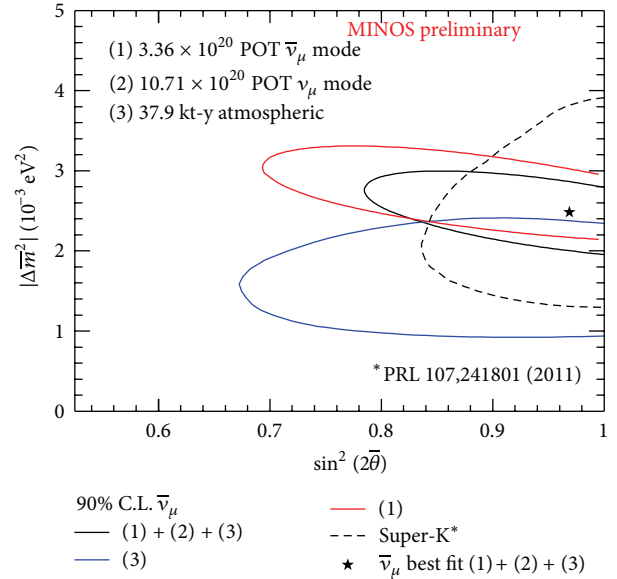


FIGURE 16: The 90% confidence regions for antineutrino parameters  $|\Delta\bar{m}_{\text{atm}}^2|$  and  $\sin^2(2\bar{\theta})$ . Antineutrino results are shown from Super-Kamiokande [51] (dashed black) alongside the latest preliminary results from MINOS [45] (solid black). The MINOS results used three data sets: (1) atmospheric antineutrinos; (2) antineutrinos from the NuMI beam operating in antineutrino-enhanced mode; (3) antineutrinos from the neutrino-enhanced beam. The red contour shows the result from just the NuMI beam data and the blue contour from just the atmospheric antineutrino data.

of the beam with the peak of the product of  $\nu_\tau$  cross-section times oscillation probability maximizes the number of  $\nu_\tau$  interactions in the detector for a given integrated flux: this is largely what the OPERA experiment has done with the CNGS beam. As described in Section 2, the experiments using the CNGS and NuMI beams have very similar baselines, 730 km versus 735 km, respectively, but differ substantially in their average neutrino energies of 17 GeV and 3 GeV, respectively, due to the different physics goals of the experiments.

The OPERA experiment at LNGS started taking data in 2008 with the CNGS beam [3, 24] and in 2010 they published the observation of their first  $\nu_\tau$  candidate event [25]. As described in Section 3, the OPERA detector consists of lead-emulsion bricks with electronic detectors to pinpoint the bricks in which neutrino interactions occurred.

The first candidate  $\nu_\tau$  event observed by OPERA is shown in Figure 17. A detailed description of the likely candidates for each of the numbered tracks is given in [25]. This event is compatible with the decay  $\tau^- \rightarrow \rho^- \nu_\tau$  with the  $\rho(770)$  decaying to a  $\pi^0$  and  $\pi^-$ .

A preliminary analysis of further data has recently been released and a second  $\nu_\tau$  candidate has been observed [52]. This event was seen in the 2010-11 data set and it satisfies the selection criteria for  $\nu_\tau \rightarrow 3$  hadrons. In the data set analyzed to date, the preliminary background estimate was 0.2 events and 2.1 signal events were expected. The Poisson probability of observing 2 or more events given a background expectation of 0.2 is 1.75%.

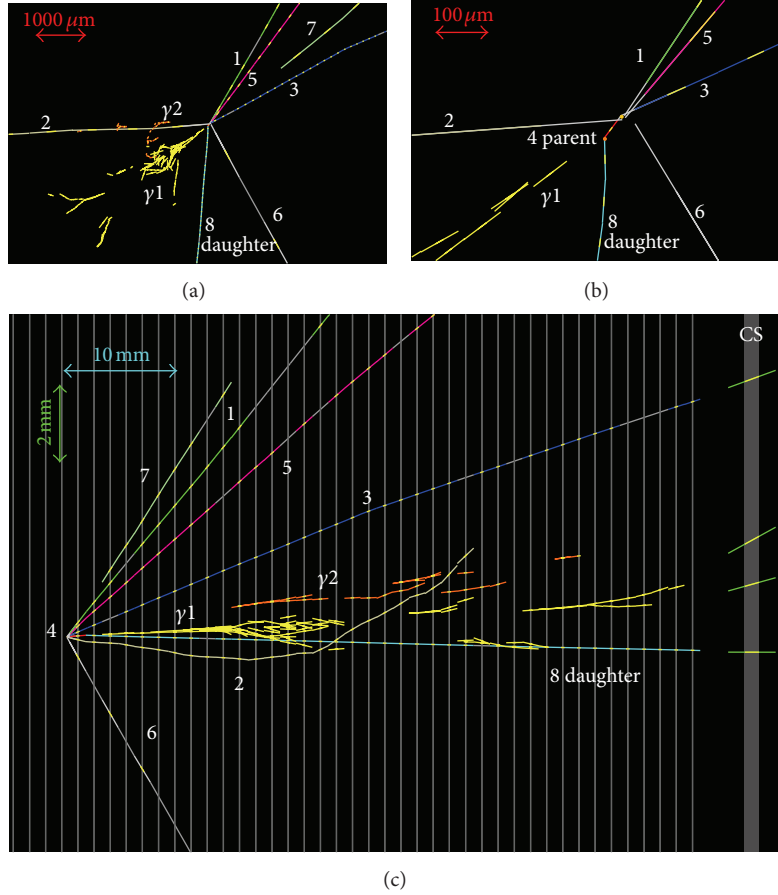


FIGURE 17: The first candidate  $\nu_\tau$  event observed by the OPERA experiment. (a) and (b) show the transverse view with the right plot being a zoom of the left. (c) shows the longitudinal view. The short red track (labeled as “4 parent”) is identified as being due to the  $\tau$  lepton and the track of what is thought to be the tau-daughter is shown in turquoise (labeled as “8 daughter”). A kink is clearly seen, particularly in the zoomed transverse view (b), and demarked by the change in color from red to turquoise along the track. A detailed description of the likely candidates for each of the numbered tracks is given in the OPERA paper [25].

Atmospheric neutrino experiments have a relatively large number of  $\nu_\tau$  events in their data samples, given the broad range of available energies and the Earth’s 13,000 km diameter. Super-Kamiokande has published  $2.4\sigma$  evidence for  $\nu_\tau$  appearance [53] using candidate events selected for the expected shape of  $\nu_\tau$  interactions and characteristics of  $\tau$  leptons. This statistical separation is a complementary approach to OPERA’s goal of directly observing individual  $\nu_\tau$  events. At the time of writing a new SK result was published on the arXiv that provides evidence for  $\nu_\tau$  appearance at the  $3.8\sigma$  confidence level [54]. In the future, MINOS+ will also have a relatively large number of  $\nu_\tau$  events (around 90/year with the  $\nu_\mu$ -enhanced beam) and with sufficient rejection of backgrounds will have sensitivity to this oscillation channel [19].

## 5. Results on $\nu_\mu \rightarrow \nu_e$ : The Subdominant Oscillation Mode

With the baselines and neutrino energies (the  $L/E$ ) used by the experiments described in this paper,  $\nu_\mu \rightarrow \nu_e$  is a subdominant oscillation mode (although at an  $L/E$  25 times

larger, the solar mass splitting would have a significant effect and  $\nu_e$ ’s would then make up the majority of the flux).

Measurements of the subdominant  $\nu_\mu \rightarrow \nu_e$  oscillation mode are of great importance for a number of reasons: firstly, its discovery will demonstrate the full 3-flavor neutrino oscillation model; secondly, with a nonzero value of  $\theta_{13}$  a door is opened to discovering CP violation in the lepton sector; thirdly, by exploiting the neutrino-matter interaction that the neutrinos and antineutrinos experience as they propagate through the Earth, the neutrino mass hierarchy (the sign of  $\Delta m_{32}^2$ ) can also be determined.

Measurements of the subdominant mode made using accelerator neutrino beams are highly complementary to those made using nuclear reactors. The reactor neutrino experiments Double Chooz [16], Daya Bay [18], and RENO [18] have recently observed subdominant neutrino oscillations via the disappearance of  $\bar{\nu}_e$  over a distance of around 1.5 km. This channel is only sensitive to  $\theta_{13}$  and so a direct measurement can be made. In contrast, the accelerator experiments are sensitive to  $\theta_{13}$ , the CP phase, the mass hierarchy, and the octant of  $\theta_{23}$ , enabling a rich set of measurements to be made using a combination of different baselines and energies with neutrinos and/or antineutrinos.



In this section the electron neutrino appearance results from K2K, MINOS, and T2K are presented. A key feature of these experiments is their ability to distinguish the rare occurrence of electron flavor neutrino interactions from among the many more  $\nu_\mu$  CC events and NC events from all neutrino flavors. For example, electron neutrino events in MINOS contribute only around 1% of the event rate. The significant majority of  $\nu_\mu$  CC events are relatively easy to reject due to the presence of the muon. However, in highly inelastic  $\nu_\mu$  CC events the muon can escape detection and should the hadronic shower have a significant electromagnetic component (from, for example,  $\pi^0 \rightarrow \gamma\gamma$ ) then it can be misidentified as an electron neutrino event.

**5.1. K2K  $\nu_e$  Appearance Results.** The first long-baseline accelerator neutrino experiment to search for electron neutrino appearance was K2K [55, 56]. This measurement exploited the ability of the Super-Kamiokande detector to distinguish muons and electrons, which had been well established for the earlier atmospheric neutrino results. As such, the primary background for K2K was events containing a  $\pi^0$  from a NC interaction. This background occurs when one of the two gammas from the  $\pi^0$  decay is not reconstructed, due to highly asymmetric energies or a small opening angle between the two gammas. Beam  $\nu_e$  events are around 1% at the KEK site and the background from such electron neutrinos intrinsic to the beam was estimated to be only 13% of the total background.

At the limit set by the CHOOZ experiment [12] and with an exposure of  $9.2 \times 10^{19}$  protons on target, K2K expected to see only a few events and so it was critical that the background was reduced to a very low level. The basic selection of electron neutrino events is as follows: the first step is to require electron Čerenkov-ring candidates; secondly, any events with electron-equivalent energy below 100 MeV are removed to reject charged pions and electrons from muon decay; thirdly, no candidate may have a muon decay within a  $30 \mu\text{s}$  time window. To improve the rejection of the  $\pi^0$  background a dedicated algorithm to calculate the invariant mass under the assumption that there were two rings was also used. The total background expectation with the above cuts was  $1.7^{+0.6}_{-0.4}$  events (in the case of no oscillation). The overall efficiency for selection of  $\nu_e$  signal events in the simulation is around 50%.

The fraction of the background coming from NC interactions that produce a single  $\pi^0$  (NC  $1\pi^0$ ) was 70% so constraining the associated systematic uncertainty was crucial. To do this a 1 kiloton water Čerenkov Near detector was used to measure the NC  $1\pi^0$ /CC interaction ratio and the uncertainty was constrained to the 12% level. Many other sources of systematic uncertainty were considered and the largest individual one concerned the  $\pi^0$  mass cut and that uncertainty was constrained using atmospheric neutrino data. The other systematics also included the detector efficiency, water properties, neutrino flux at SK, and several neutrino interaction model uncertainties. In total the background uncertainty was between 24 and 39% depending on the run period.

K2K observed 1 event that passed their selection criteria, consistent with the background expectation. These data allowed a 90% C.L. limit to be set on the maximum electron neutrino appearance probability of 0.13, at the oscillation parameters measured by K2K via  $\nu_\mu$  disappearance (see Section 4.1). Such an appearance probability corresponds to an approximate limit of  $\sin^2(2\theta_{13}) < 0.26$ .

**5.2. MINOS  $\nu_e$  Appearance Results.** The first MINOS  $\nu_e$  appearance result was released in 2009 [57] and two further results with more data and analysis improvements have since been published [58, 59]. The MINOS detectors were optimized for measuring muon neutrino interactions at the few-GeV scale. The steel planes are 1.4 radiation lengths thick and the strip width is 4.1 cm (compared to the Molière radius of 3.7 cm) giving a relatively coarse view of an electron shower. Absolutely crucial for controlling the systematic uncertainties on these measurements is the functionally identical design of the Near and Far detectors. As with K2K, the dominant background is from NC interactions. Although,  $\nu_\mu$  CC events also contribute significantly to the background along with intrinsic  $\nu_e$  events in the beam and  $\nu_\tau$  events that have oscillated from  $\nu_\mu$ .

Determining the composition of the background is important for this analysis since at the Far detector a fraction of the  $\nu_\mu$  events have oscillated away and therefore the background from  $\nu_\mu$  CC events is reduced. The other effect of oscillations is to introduce a background from  $\nu_\tau$  in the Far detector that does not exist in the Near detector. In contrast, the NC events do not oscillate away and to first order that background component is the same in the Near and Far detectors. MINOS took a data-driven approach to determining the background composition by comparing the data with the simulation for a number of data sets taken with the NuMI beam in special configurations. For example, with the magnetic horns turned off the peak in the energy spectrum disappears, which drastically changes the CC/NC ratio as a function of energy. Similarly, data taken with the beam configured to produce higher energy neutrinos has an enhanced NC fraction at low energies. A fit to the ND data and MC across all these special data sets was used to estimate the background composition and determine the uncertainties on each component.

The selection of electron neutrino candidate events starts out with fiducial volume cuts and ensuring the event is in time with the low-duty-cycle NuMI beam. Electron showers penetrate only a few (typically 6–12) planes and are transversely compact so any events with tracks longer than 24 planes or with a track extending more than 15 planes beyond the end of a reconstructed shower are rejected. A requirement is also made that events contain at least 5 contiguous planes with an energy deposition at least half that of a minimum ionizing particle. Any events with an energy less than 1 GeV or greater than 8 GeV are also removed. After these preselection cuts 77% of the signal, 39% of NC events, and 8.5% of  $\nu_\mu$  CC events remain.

Further reduction of backgrounds is achieved by a more sophisticated analysis of the energy deposition patterns in

preselected events. The first two MINOS results used an artificial neural network with 11 variables characterizing the transverse and longitudinal profile of events. For the most recent MINOS analyses, a nearest-neighbor “library event matching” (LEM) technique is used. Each data event is compared, one-by-one, to a large library of tens of millions of simulated events. Since the detector is homogeneous, events occurring throughout the volume are translated to a fixed reference location and then compared at the level of individual strips. This approach is computationally intensive and is made more manageable in two notable ways: firstly, fluctuations in the energy deposition of individual strips are allowed for; secondly, library events are shifted by  $\pm 1$  plane in search of a better match. The final LEM discriminant is formed using a neural network that takes as its inputs the event energy along with three variables derived from the 50 best-matched events. A cut of  $\text{LEM} > 0.7$  selects  $(40.4 \pm 2.8)\%$  of signal events.

The predictions for the Far detector signal and backgrounds as a function of energy and LEM uses the Near detector data as the starting point. The simulated ratio of Near and Far detector rates for each background type is used as the conversion factor to translate the Near detector data into a Far detector prediction.

Two data samples provide sidebands that allow many of the procedures developed for this analysis to be tested and the accuracy of the simulation to be probed. Firstly,  $\nu_\mu$  CC events with cleanly identified muons provide a sample of known hadronic showers once the muon hits are removed. These muon-removed events are a lot like NC interactions and the predicted and observed events at the Far detector agree well. The second sideband is the  $\text{LEM} < 0.5$  region that contains almost no  $\nu_e$  appearance events. The Far detector prediction for this  $\text{LEM} < 0.5$  region is obtained in the same way as for the signal region and so all stages of the analysis up to the final signal extraction are exercised, for example, determining the background composition and extrapolating the Near detector data is done in the same way.

A fit to the data, binned as a function of the LEM discriminant and reconstructed energy, was performed using the full 3-flavor oscillation framework including matter effects. The influence of the already measured oscillation parameters was included when constructing the contours.

Updated MINOS results were released this summer for neutrinos, along with the first appearance results for antineutrinos [45]. With an exposure of  $10.6 \times 10^{20}$  POT in the neutrino-enhanced beam and assuming  $\sin^2 2\theta_{13} = 0$  ( $\sin^2 2\theta_{13} = 0.1$ ,  $\delta = 0$ , normal mass hierarchy) MINOS expected to see 128.6 (161.1) events in the Far detector; 152 events were observed.

With an exposure of  $3.3 \times 10^{20}$  POT in the antineutrino-enhanced beam and assuming  $\sin^2 2\theta_{13} = 0$  ( $\sin^2 2\theta_{13} = 0.1$ ,  $\delta = 0$ , normal mass hierarchy) MINOS expected to see 17.5 (21.2) events in the Far detector; 20 events were observed.

The allowed regions as a function of the CP violating phase,  $\delta$ , and  $2\sin^2(2\theta_{13})\sin^2\theta_{23}$  are shown in Figure 18. For  $\delta = 0$  and the normal (inverted) mass hierarchy a best fit of  $2\sin^2(2\theta_{13})\sin^2\theta_{23} = 0.053$  (0.094) is obtained; the 90%

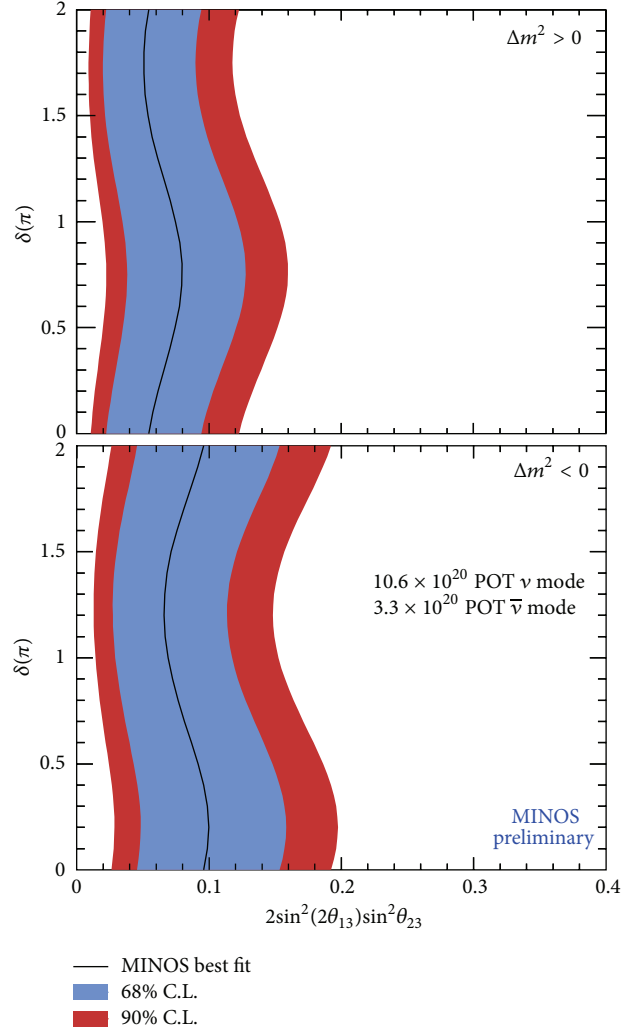


FIGURE 18: MINOS allowed regions for the CP violating phase and  $2\sin^2(2\theta_{13})\sin^2\theta_{23}$ , obtained using the full data set of both neutrinos and antineutrinos. The top (bottom) plot assumes the normal (inverted) mass hierarchy. All values of the CP violating phase are consistent with the data and so the best fit parameters are shown by the black line. The blue (red) band shows the regions allowed at 68% (90%) confidence level. The  $\theta_{13} = 0$  hypothesis is disfavored at the 96% confidence level. These results were preliminary at the time of writing [45].

C.L. allowed range is  $0.01 < 2\sin^2(2\theta_{13})\sin^2\theta_{23} < 0.12$  ( $0.03 < 2\sin^2(2\theta_{13})\sin^2\theta_{23} < 0.19$ ) and the  $\theta_{13} = 0$  hypothesis is disfavored at the 96% confidence level. These results are consistent with both the T2K result described below in Section 5.3 and with the reactor neutrino experiments.

Figure 19 shows the results from the first measurement of electron antineutrino appearance. The data set used for this measurement was obtained with the NuMI beam set to enhance production of antineutrinos. The limits on  $2\sin^2(2\theta_{13})\sin^2\theta_{23}$  are consistent with those from neutrinos. Although, the smaller exposure and lower antineutrino cross-section means that the limits are not as strong as for neutrinos. Significant improvement in measurement of electron antineutrino appearance is not expected until NOvA takes

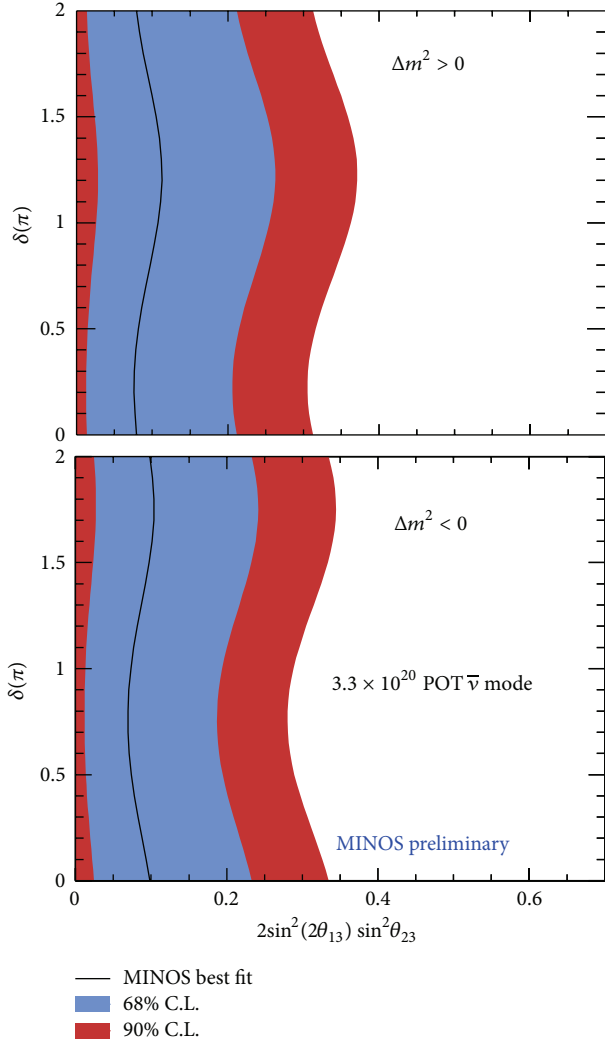


FIGURE 19: MINOS allowed regions for antineutrinos as a function of the CP violating phase and  $2\sin^2(2\theta_{13})\sin^2\theta_{23}$ . See Figure 18 for the full description. These results were preliminary at the time of writing [45].

data using the NuMI beam configured for enhanced  $\bar{\nu}_\mu$  production (see Section 7).

**5.3. T2K  $\nu_e$  Appearance Results.** The primary goal of the T2K experiment is to discover electron neutrino appearance and precisely measure the oscillation probability if it exists. The experimental setup is optimized for this purpose.

T2K reported the first evidence of electron neutrino appearance ( $2.5\sigma$  significance,  $P$ -value = 0.7%) in June 2011 based on  $1.43 \times 10^{20}$  POT data taken before the Great East Japan Earthquake on 11th March 2011 [60].

The goal of the analysis is to select  $\nu_e$  CC interactions at high efficiency and with the background contamination as low as possible. At the peak of the T2K neutrino energy spectrum, around 600 MeV, the interaction of neutrinos is dominated by CC quasi-elastic interaction (CCQE),  $\nu_e + n \rightarrow e^- + p$ , and that was chosen as the target signal interaction. The benefit of CCQE interaction is that with just a measurement

of the momentum of the final lepton, the parent neutrino energy can be reconstructed with a good energy resolution of around 80 MeV.

The signature for signal events in the Super-Kamiokande detector is a single showering (electron-like) ring in the expected energy region. The two major sources of background events are the intrinsic electron neutrino contamination in the beam mainly produced by muon decay in the decay volume and inelastic NC interaction of all flavors that contain a  $\pi^0$  in the final state. The  $\gamma$ s from  $\pi^0$ s are detected in SK by the Čerenkov light from their electromagnetic showers, which can be indistinguishable from the Čerenkov light distribution produced by an electron. For example, if one of the two  $\gamma$ s from the  $\pi^0$  decay is missed, the event topology in SK becomes very similar to that of the signal, that is, a single electron-like ring.

Selection criteria for the signal event are as follows. The “fully contained in fiducial volume” (FCFV) events are selected by requiring: no event activity in either the outer detector or in the 100  $\mu$ s before the event trigger time; at least 30 MeV electron-equivalent energy deposited in the inner detector (defined as visible energy  $E_{\text{vis}}$ ) and the reconstructed vertex to be in the fiducial volume of 22.5 kilotonnes. The event timing is required to be within the range from  $-2\mu$ s to 10  $\mu$ s around the beam trigger time.

Further selection cuts require events with the number of rings equal to 1 and a PID consistent with being electron-like. The visible energy is required to be  $E_{\text{vis}} > 100$  MeV to reduce NC elastic-interactions and decay electron backgrounds. It is also required to have no associated delayed electron signal to reduce the background from invisible  $\pi \rightarrow \mu$  decay. To suppress misidentified  $\pi^0$ , a second electron-like ring is forced to be reconstructed and a cut on the two-ring invariant mass  $M_{\text{inv}} < 105$  MeV/ $c^2$  is imposed. Finally, the neutrino energy  $E_{\nu}^{\text{rec}}$ , computed using the reconstructed momentum and direction of the ring assuming CCQE kinematics and neglecting Fermi motion, is required to be  $E_{\nu}^{\text{rec}} < 1250$  MeV.

The  $\nu_e$  appearance signal efficiency is estimated with MC to be 66% while rejection for  $\nu_\mu + \bar{\nu}_\mu$  CC, beam  $\nu_e$  CC, and NC are  $> 99\%$ ,  $77\%$ , and  $99\%$ , respectively.

The selection is applied to the data and 6 events in SK are selected as signal candidates from all data before the earthquake, corresponding to  $1.43 \times 10^{20}$  POT. The  $E_{\nu}^{\text{rec}}$  distribution of the observed events together with the signal and background expectations are shown in Figure 20.

The expected signal and background events are estimated using the far detector MC simulation with the constraints and inputs from measurements of near detector  $\nu_\mu$  CC events and external data. These external data include hadron production measurements made by the NA61 experiment [61, 62] using 30 GeV protons impinging on the neutrino production target and also neutrino interaction cross-sections measured by previous experiments such as MiniBooNE.

The off-axis near detector measures the number of inclusive  $\nu_\mu$  CC events by selecting events with a single negative muon. The ratio of the observed number of events to that from the MC simulation is  $1.036 \pm 0.028(\text{stat})_{-0.037}^{+0.044}(\text{det.syst}) \pm 0.038(\text{phys.syst})$ . This near detector ratio is multiplied by the

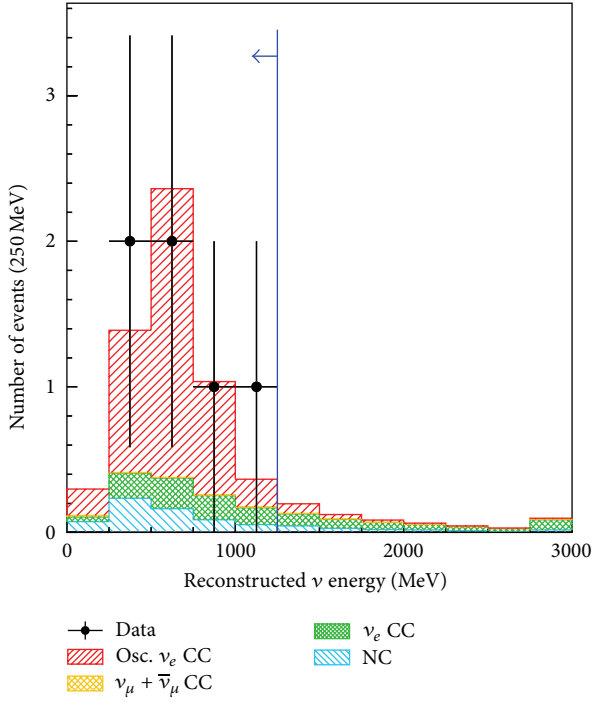


FIGURE 20: Reconstructed neutrino energy  $E_{\nu}^{\text{rec}}$  spectra for T2K  $\nu_e$  appearance search. The black points show the 6 candidate events observed in SK using  $1.43 \times 10^{20}$  POT data. Using  $\sin^2(2\theta_{13}) = 0.1$  the red histogram is the predicted appearance signal, the expected background shown in yellow is for muon neutrinos, green is for the electron neutrinos intrinsic to the beam, and blue is for the NC events.

number of events from the far detector simulation to give the predicted number of events in the far detector data. This method provides partial cancellation of uncertainties in the absolute flux and cross-sections at the far detector.

The number of background events thus obtained when  $\sin^2(2\theta_{13}) = 0$  is estimated to be  $1.5 \pm 0.3(\text{syst})$ . The major contributions to the background systematic error come from the beam flux (8.5%), cross-section (14%), and far detector systematic error (15%). The probability that the observed number of events becomes 6 or larger if  $\sin^2(2\theta_{13}) = 0$  is calculated to be 0.7%, which corresponds to a  $2.5\sigma$  excess.

The constraints on the oscillation parameters are evaluated also by using only the number of events. The confidence intervals are  $0.03(0.04) < \sin^2 2\theta_{13} < 0.28(0.34)$  at 90% C.L. and the best fit parameters are  $\sin^2(2\theta_{13}) = 0.11(0.14)$  for the normal (inverted) hierarchy assuming  $\sin^2(2\theta_{23}) = 1$ ,  $\Delta m_{32}^2 = 2.4 \times 10^{-3} \text{ eV}^2$ , and  $\delta = 0$ . Figure 21 shows the T2K allowed regions of parameters in the  $\sin^2 2\theta_{13}$ - $\delta$  plane.

To summarize the T2K  $\nu_e$  appearance search, 6 signal candidate events are detected while the expected number of background events at  $\sin^2(2\theta_{13}) = 0$  is  $1.5 \pm 0.3$ . The probability to observe 6 or more events without  $\nu_e$  appearance is 0.7%, which corresponds to  $2.5\sigma$  significance (In Summer 2012, T2K updated the results with  $3.01 \times 10^{20}$  POT of data [63]. The observed number of events is 11 while the

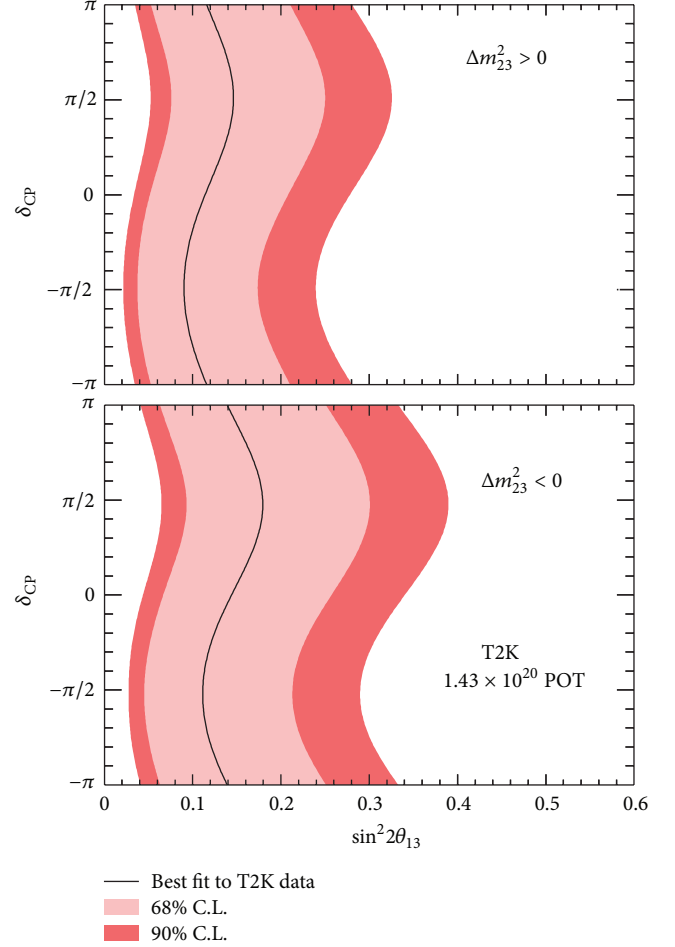


FIGURE 21: Allowed regions in the  $\sin^2 2\theta_{13}$ - $\delta$  plane from the T2K  $\nu_e$  appearance measurement. Light (dark) red areas are 68% C.L. and 90% C.L. regions. Solid black curves are best fit relations.

expected background is  $3.22 \pm 0.43$  at  $\sin^2(2\theta_{13}) = 0$ , which corresponds to  $3.2\sigma$  significance and provides further firm evidence of  $\nu_e$  appearance.). Constraints on the  $\sin^2 2\theta_{13}$ - $\delta$  space are given for both the normal and inverted mass hierarchy.

## 6. Results on New Physics Searches

The provision of intense and relatively well-understood neutrino beams along with large detectors has opened up whole new avenues to look for new physics. Here we focus on three main areas: Section 6.1 describes the searches for sterile neutrinos; Section 6.2 briefly summarizes neutrino velocity measurements; Section 6.3 describes searches for Lorentz symmetry violation.

**6.1. Searches for Sterile Neutrinos.** While the conventional picture of oscillations between three active neutrino flavors is well established, the possibility of mixing with one or more unseen sterile neutrinos is not excluded. Neutral-current (NC) interaction cross-sections are identical for the three active flavors and so no change in the NC event rate would be



observed as a function of  $L/E$  in the standard neutrino model. MINOS provided the first limits on the fraction of mixing to sterile neutrinos allowed at the atmospheric mass splitting in [64], with details given in a longer paper [65]. Earlier, in 2000, Super-Kamiokande had excluded the possibility of maximal  $\nu_\mu \rightarrow \nu_s$  oscillations at 99% C.L. [66] by exploiting the effect such oscillations would have on both the NC event rate and the number of  $\nu_\mu$  and  $\nu_\tau$  candidate events (the difference in the neutrino-matter interaction of  $\nu_\mu$  and  $\nu_\tau$  compared to  $\nu_s$  is significant for atmospheric neutrinos of the energy measured by SK). More recent observations of  $\nu_\tau$  appearance [53, 54] also constrain oscillations to sterile neutrinos, although limits are not directly given in those papers. The current best limits on the fraction of mixing to sterile neutrinos are from MINOS and given in [67].

Selection of NC events in the MINOS detectors requires careful study since the visible energy is relatively low and there is no distinct feature to the events (e.g., missing transverse momentum is not easily observed in the MINOS detectors). NC candidate events can have signal in as few as 4 scintillator strips. The high rate environment of the ND, where there are around 16 events per 10  $\mu$ s beam spill, requires additional selections on timing and topology: events must be separated by at least 40 ns and events that occur within 120 ns of each other must be separated in the beam direction by at least 1 m. To select an NC-candidate event sample the length of the event has to be less than 60 planes and any track in the event must not extend beyond the end of a shower by more than 5 consecutive planes.

An extrapolation procedure similar to that used in the  $\nu_e$  appearance analysis (see Section 5.2) is used to form the Far detector prediction for the NC spectrum. Figure 22 shows the visible energy spectrum of Far detector candidate NC events. The data can be seen to be consistent with no oscillation to sterile neutrinos.

Many sources of systematic uncertainty on the MINOS NC results are similar to the  $\nu_\mu$  disappearance and  $\nu_e$  appearance measurements (see Sections 4.1.2 and 5.2, resp.), for example the absolute and relative energy scale of hadronic showers, and the relative event rate normalization. Uncertainties specific to the NC measurement are in the Near and Far detector selection, and in the CC background. The latest results, given below, are approaching the systematic limit for how much further these measurements can be improved by MINOS.

A straightforward phenomenological approach to presenting the limits on the allowed level of sterile neutrino mixing is to consider the fraction,  $f_s$ , of the disappearing  $\nu_\mu$  flux that could oscillate to  $\nu_s$ . MINOS finds  $f_s < 0.22$  (0.40) at 90% C.L., where the number in brackets is the limit assuming maximal  $\nu_e$  appearance at the CHOOZ limit. The alternative approach to presenting the limits is in the context of a specific model. MINOS has considered two models: firstly, one where the fourth mass eigenstate  $m_4 = m_1$ ; two where  $m_4 \gg m_3$ . The 90% C.L. limits obtained from MINOS data are  $\theta_{24} < 7^\circ$  ( $8^\circ$ ) and  $\theta_{34} < 26^\circ$  ( $37^\circ$ ) in the  $m_4 \gg m_3$  model, and  $\theta_{34} < 26^\circ$  ( $37^\circ$ ) in the  $m_4 = m_1$  model. In the future, the MINOS+ experiment will extend the sensitivity to sterile neutrinos, in particular

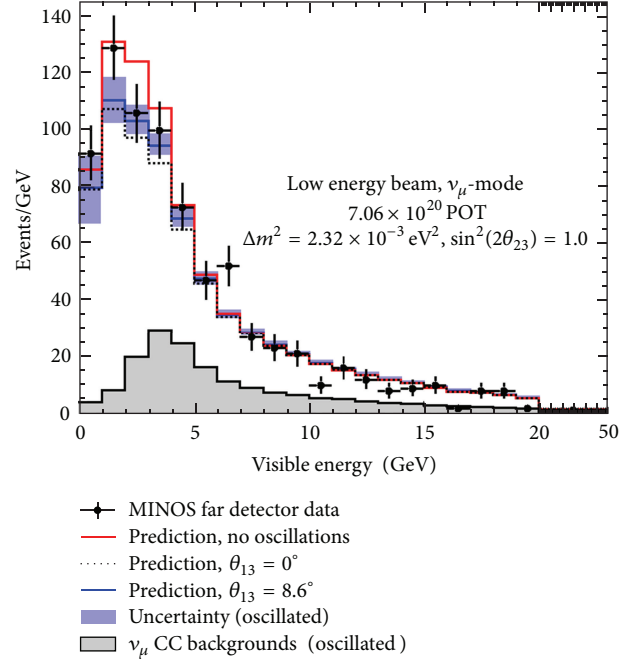


FIGURE 22: Visible energy spectrum of MINOS Far detector neutral-current event candidates [45]. The data are shown by the black points. The prediction obtained from the Near detector data is shown for three cases: no oscillations (red); oscillations with atmospheric parameters and  $\theta_{13} = 8.6^\circ$  (dashed black); oscillations with atmospheric parameters and  $\theta_{13} = 0^\circ$  (dotted black). The contamination of the NC spectrum from  $\nu_\mu$  CC events is shown by the gray histogram.

through also constraining the disappearance of  $\nu_\mu$  and  $\bar{\nu}_\mu$  (see Section 7.2).

**6.2. Neutrino Velocity.** In 2007 MINOS made the first measurement of neutrino velocity in a long-baseline experiment [68]. The time of flight between the Near and Far detectors separated by  $734\,298.6 \pm 0.7$  m was measured to be  $-126 \pm 32(\text{stat}) \pm 64(\text{syst})$  ns w.r.t. the calculated time for light to travel the same distance, which corresponds to  $(v - c)/c = (5.1 \pm 2.9) \times 10^{-5}$ . This result was systematically limited by uncertainties in the timing system and its overall sensitivity comparable with previous neutrino velocity measurements from short-baseline experiments [69].

Dedicated upgrades to the OPERA experiment's timing system along with high statistics neutrino event samples gave substantially improved sensitivity to the neutrino velocity. In September 2011 they released their result  $(v - c)/c = [2.37 \pm 0.32(\text{stat})^{+0.34}_{-0.24}(\text{syst})] \times 10^{-5}$  [70], which generated huge worldwide media interest. However, in February 2012 the OPERA collaboration released a statement, available on their website, saying that two errors in the timing system had been found that could potentially bring the neutrino velocity back into line with expectations from special relativity. This was followed by a measurement from the ICARUS experiment [71], also located in the LNGS laboratory, that was of similar sensitivity to OPERA but consistent with expectations. Around the time of writing OPERA released an updated

result  $(v - c)/c = [0.27 \pm 0.31(\text{stat})_{-0.33}^{+0.34}(\text{syst})] \times 10^{-5}$  [70], confirming that they had understood the anomaly in their first result. Results from Borexino [72] and LVD [73] are also consistent with OPERA and ICARUS. These results from four of the experiments located at Gran Sasso are the world's most precise measurements of the neutrino velocity and they are approaching their ultimate systematic limit. Future measurements that use different beamlines and hence have a lower number of correlated systematic uncertainties will be important. MINOS, and in future MINOS+, will exploit recent investments in their timing systems with the aim of reducing the systematic uncertainties further [74].

**6.3. Searches for Lorentz Symmetry Violation.** MINOS has investigated whether neutrinos have a preferred direction in space and hence violate Lorentz symmetry and consequently also CPT symmetry. This search was performed in the context of the Standard Model Extension theory [75–77] that provides a model-independent framework with coefficients to quantify the various ways Lorentz symmetry could be violated. The experimental observable for these searches is a sidereal variation in the rate of neutrino interactions. MINOS has results for  $\nu_\mu$  and  $\bar{\nu}_\mu$  in the Near detector as well as  $\nu_\mu$  in the Far detector [78–80].

The rotation of the Earth rotates the neutrino beam in the sun-centered inertial reference frame with the sidereal frequency of  $2\pi/23^{\text{h}}56^{\text{m}}04.09053^{\text{s}}$ . The offset of the sidereal frequency from the Earth's rotational frequency of  $2\pi/24^{\text{h}}$  is experimentally advantageous since diurnal effects can potentially average out over the course of a year. The MINOS analysis was performed by examining the data as a function of local sidereal phase (LSP), which is simply the local sidereal time divided by the length of a sidereal day. Each neutrino event was placed in an LSP histogram and the protons on target for each beam spill used in the analysis were placed in a second LSP histogram. The ratio of the two histograms gave the normalized number of neutrino events observed as a function of LSP. Fast Fourier transforms to determine the power associated with sinusoidal functions at the sidereal frequency and its second harmonic were performed. To date, no sidereal variation of the neutrino event rate has been detected.

In addition to long-baseline accelerator experiments, searches for Lorentz symmetry violation have been performed by several other neutrino experiments. This has allowed many of the coefficients in the SME to be constrained over a wide range of directions, baselines, and neutrino energies. A comprehensive summary of experimental limits is given in [81].

## 7. Future Sensitivities

The expected future physics sensitivities of experiments currently running, or about to start taking data, are outlined here. Section 7.1 describes the prospects for measurements of the standard 3-flavor neutrino oscillation parameters and Section 7.2 focuses on models of new physics.

**7.1. Oscillation Physics.** As of 2012, all three mixing angles are known to be nonzero and have been measured to reasonably good accuracy. However, there is no significant information on the mass ordering, the  $\theta_{23}$  octant or CP violation yet. The main goals of long-baseline experiments in the next decade will be to determine or obtain indications of the present unknowns by improving the precision of the measurements as much as possible. Since the CP violation term in the  $\nu_e$  appearance probability depends on all the mixing angles in some way, it is important to improve the precision of  $\theta_{23}$  through  $\nu_\mu$  disappearance measurements as well as  $\nu_e$  appearance. Further, if  $\sin^2(2\theta_{23})$  is not unity, then the determination of the  $\theta_{23}$  octant will tell us whether  $\nu_3$  couples more strongly to  $\nu_\mu$  or  $\nu_\tau$ .

T2K plans to accumulate up to  $750 \text{ kW} \times 5 \times 10^7$  seconds equivalent POT, which is about  $8 \times 10^{21}$  POT and 26 times the exposure so far. The NOvA sensitivities discussed below all assume that NOvA will run for three years in neutrino mode and three years in antineutrino mode, for a total of  $36 \times 10^{20}$  POT. These predicted sensitivities are largely based on analysis techniques that were used by the MINOS experiment. NOvA expects to be able to achieve somewhat better sensitivities as it incorporates additional techniques allowed by NOvA's finer segmentation and greater active fraction.

**7.1.1.  $\nu_\mu$  Disappearance.** The disappearance of  $\nu_\mu$  charged current events measures  $\sin^2(2\theta_{23})$  and  $|\Delta m_{32}^2|$ . The expected statistical precision of the T2K  $\nu_\mu$  disappearance measurements at  $750 \text{ kW} \times 5 \times 10^7$  seconds are plotted in Figure 23 [82]. The statistical precision reaches  $\delta(\sin^2 2\theta_{23}) \sim 1\%$  and  $\delta(|\Delta m_{32}^2|) \sim 0.05 \times 10^{-3} \text{ eV}^2$ . The goal for the systematic uncertainties is to reach the same level as for the statistical errors for both of the parameters.

The latest MINOS measurement of  $\sin^2(2\theta_{23})$  is  $0.96 \pm 0.04$  [45]. For the reasons cited above, NOvA should be able to make a measurement that is about a factor of two to three more sensitive. Figure 24 shows the NOvA sensitivity for three possible values of  $\sin^2(2\theta_{23})$ . NOvA will gain further information about  $\theta_{23}$  from  $\nu_\mu \rightarrow \nu_e$  oscillations, as discussed below.

**7.1.2.  $\nu_\mu \rightarrow \nu_e$  Oscillations.** The parameters for  $\nu_\mu \rightarrow \nu_e$  oscillations are considerably more complex than for  $\nu_\mu$  disappearance. This process is largely proportional to both  $\sin^2(2\theta_{13})$  and  $\sin^2(\theta_{23})$ , with large perturbations caused by the mass ordering (through the matter effect) and by CP violation. A convenient way to see the dependences is through biprobability plots. These plots show the loci of possible NOvA measurements of  $\nu_\mu \rightarrow \nu_e$  and  $\bar{\nu}_\mu \rightarrow \bar{\nu}_e$  oscillation probabilities, given a set of parameters. These parameters include  $\sin^2(2\theta_{13})$ , which is fixed at 0.095, a value consistent with the recent reactor measurements [18, 83, 84], and  $\sin^2(2\theta_{23})$ . Figures 25 and 26 show biprobability plots for  $\sin^2(2\theta_{23}) = 1.00$  and 0.97, respectively. The CP-violating phase  $\delta$  traces out the ovals and the multiplicity of ovals

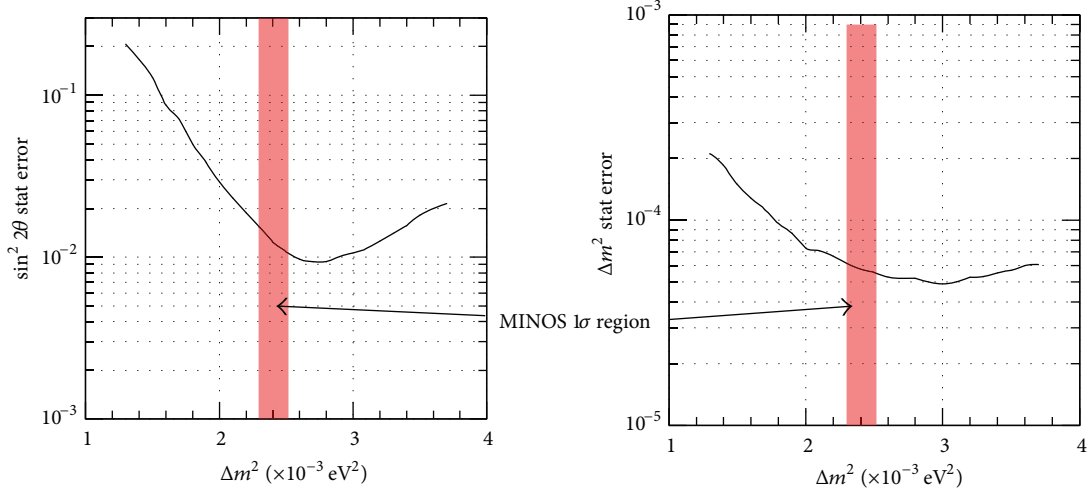


FIGURE 23: T2K expected statistical precision on the oscillation parameters  $\sin^2(2\theta_{23})$  and  $|\Delta m_{32}^2|$  assuming an exposure of  $750 \text{ kW} \times 5 \times 10^7$  seconds as a function of true  $|\Delta m_{32}^2|$  [82]. The  $1\sigma$  confidence intervals for  $|\Delta m_{32}^2|$  from MINOS are indicated by red hatches.

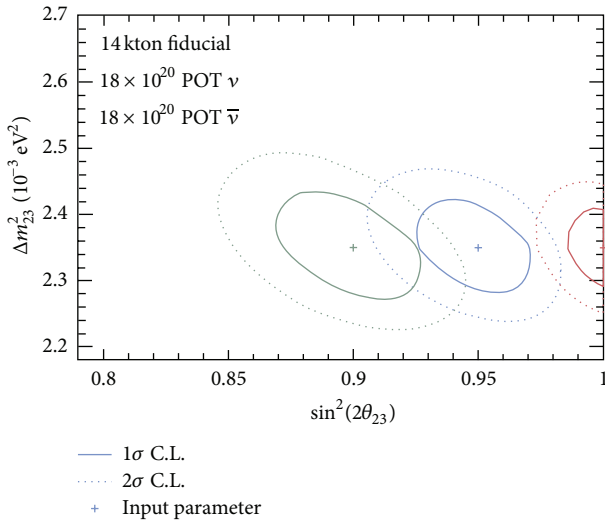


FIGURE 24: One and two standard deviation NOvA sensitivity contours for a joint measurement of  $|\Delta m_{32}^2|$  and  $\sin^2(2\theta_{23})$  for three possible values of these parameters indicated by the plus signs. The single parameter measurement of  $\sin^2(2\theta_{23})$  will be somewhat more sensitive than the extreme limits of the displayed contours.

represents the two possible mass orderings and, for Figure 26, the ambiguity of whether  $\theta_{23}$  is larger or smaller than  $\pi/4$ .

A useful way to visualize what NOvA will be able to do is to superimpose one and two standard deviation contours on the biprobability plots. For example, Figures 27 and 28 show these contours for a favorable set of parameters, normal mass ordering, and  $\delta = 3\pi/2$ . The mass ordering is resolved to more than two standard deviations, the  $\theta_{23}$  ambiguity is resolved to two standard deviations, and CP violation is established to almost two standard deviations. This occurred because the matter effect and the CP-violating effect went in the same direction, so there was no ambiguity.

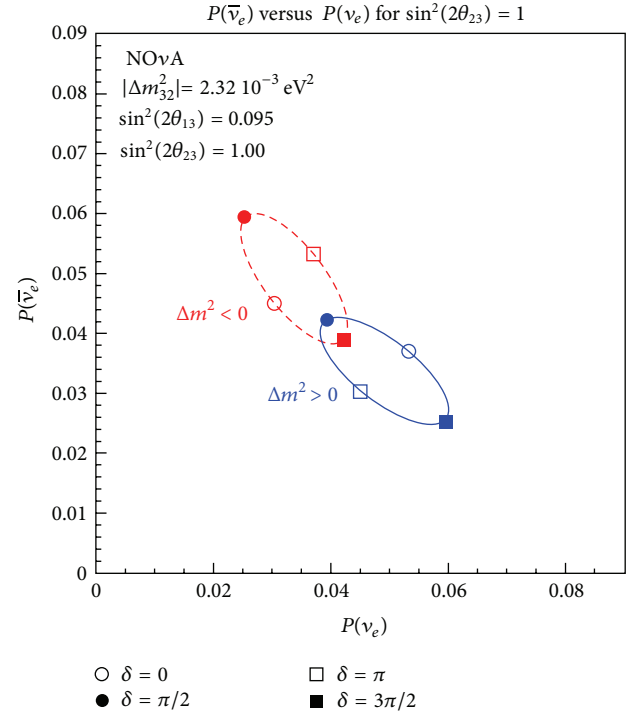


FIGURE 25: Biprobability plot for  $\sin^2(2\theta_{23}) = 1.00$ . See text for explanation.

An unfavorable set of parameters would be one in which the matter effect and the CP-violating effect go in opposite directions so that there is an ambiguity as to which direction each one went. An example of that is shown in Figure 29. The  $\theta_{23}$  ambiguity is resolved, but the mass ordering is not, and therefore there is little information on the CP-violating phase. If nature gives us this situation, then the only way to resolve the mass ordering in the short term is to compare NOvA measurements of  $\nu_\mu \rightarrow \nu_e$  oscillations with those from an experiment with a different baseline. The only experiment

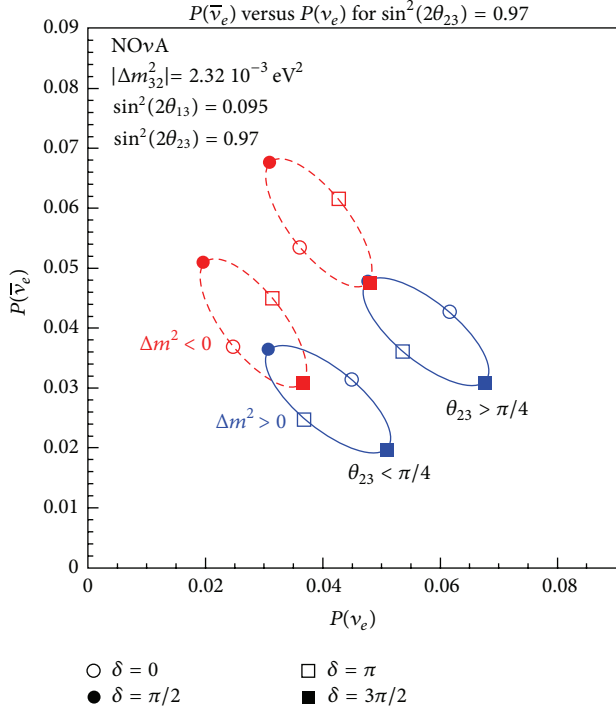


FIGURE 26: Biprobability plot for  $\sin^2(2\theta_{23}) = 0.97$ . See text for explanation.

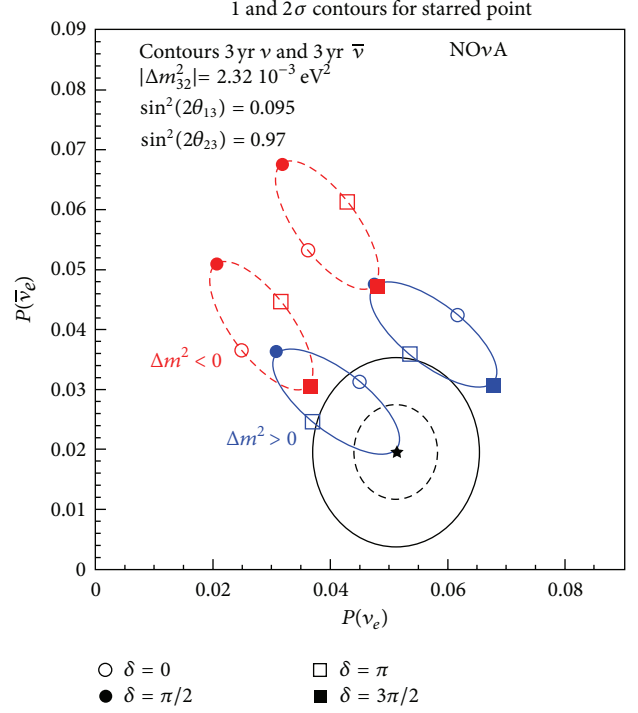


FIGURE 28: Biprobability plot for  $\sin^2(2\theta_{23}) = 0.97$  with NOvA expected 1 and 2 standard deviation contours superimposed on the starred point.

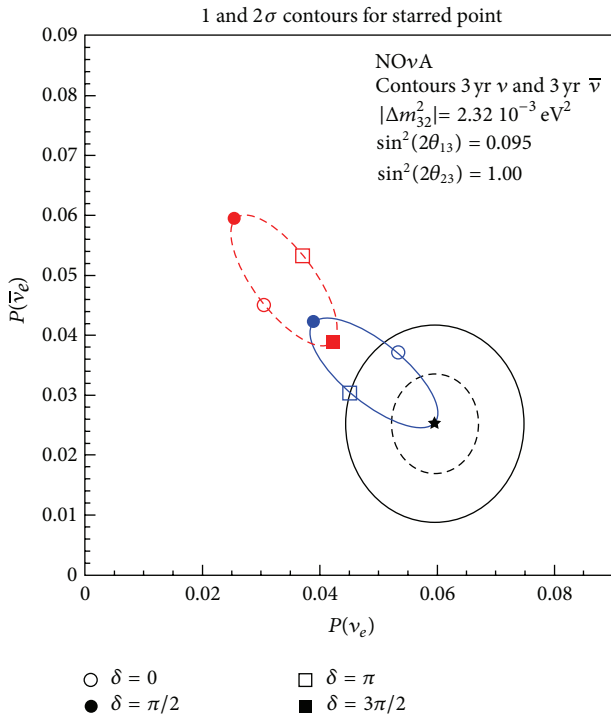


FIGURE 27: Biprobability plot for  $\sin^2(2\theta_{23}) = 1.00$  with NOvA expected 1 and 2 standard deviation contours superimposed on the starred point.

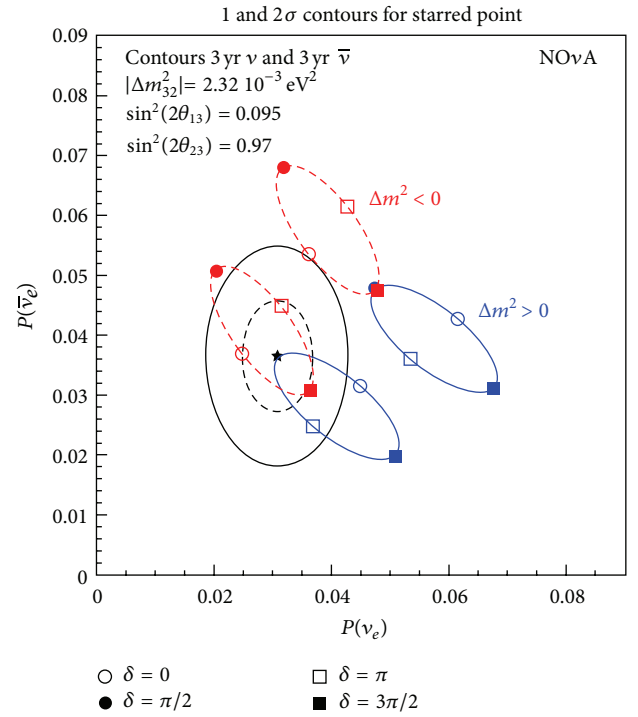


FIGURE 29: Biprobability plot for  $\sin^2(2\theta_{23}) = 0.97$  with NOvA expected 1 and 2 standard deviation contours superimposed on the starred point.



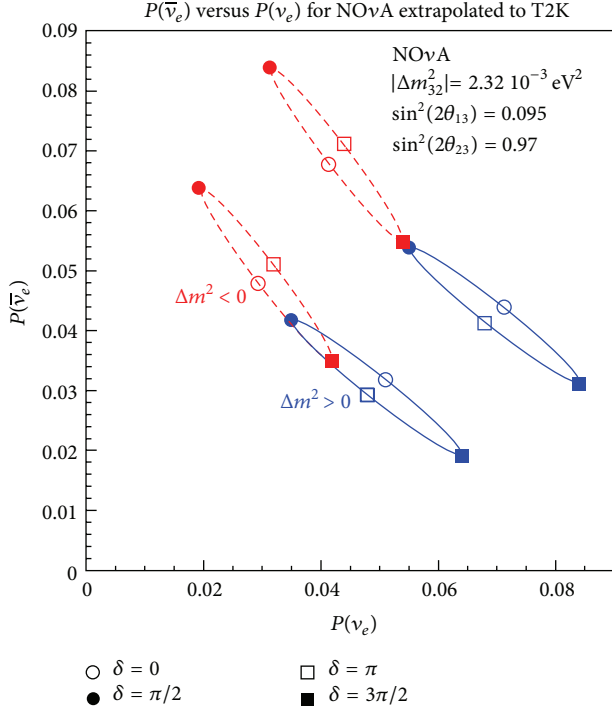


FIGURE 30: Biprobability plot for  $\sin^2(2\theta_{23}) = 0.97$  with NOvA extrapolated to the average oscillation phase of T2K.

that meets that requirement is T2K, which has a 295 km baseline.

The algorithm for resolving the mass ordering is quite simple. If NOvA measures a higher probability of  $\nu_\mu \rightarrow \nu_e$  oscillations than T2K, then the mass ordering is normal; if it is the opposite, it is inverted. That is, because NOvA and T2K will see the identical CP-violation, but T2K will see a much smaller matter effect due to its shorter baseline. The only catch in this algorithm is that the comparison must be done at the same point in the oscillation phase, and the two experiments run at different average oscillation phases. Figures 30 and 31 show the biprobability plots in which the NOvA measurements have been extrapolated to the same oscillation phase as the T2K measurements. A comparison of the two plots shows that the algorithm works for all values of  $\delta$ .

Unfortunately, the combined statistical power of NOvA and T2K at the end of the nominal six-year NOvA run will be insufficient to resolve the mass ordering at the two standard deviation level using this strategy. However, it is unlikely that either the American or the Japanese neutrino program will end at that time. With anticipated improvements in both programs, in the worst case, the mass ordering should be resolved in the next decade. Figures 32 and 34 summarize the NOvA sensitivities for resolving the mass ordering and determining that there is CP violation in the leptonic sector, respectively. These figures are for NOvA alone and use only the total measured oscillation rate. There will be some gain in sensitivity in using the measured energy dependence and, as mentioned previously, improvements in the analysis. Figures 33 and 35 show the same information, but include the

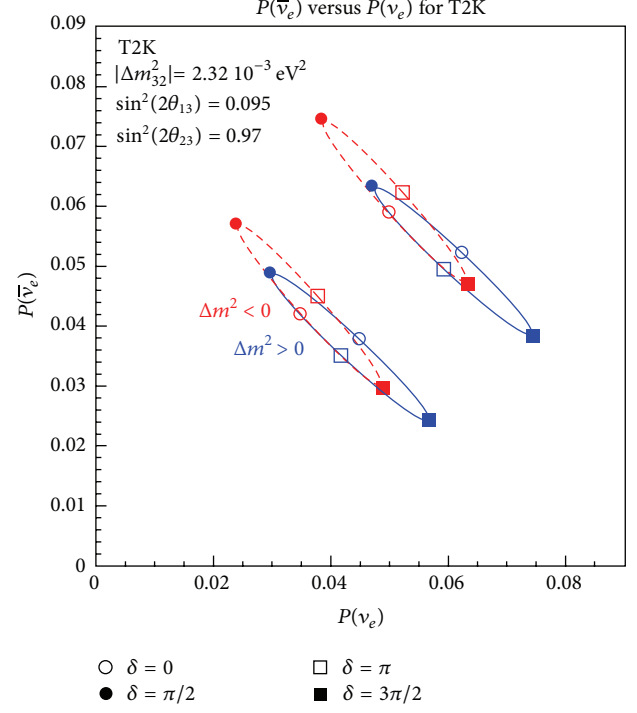


FIGURE 31: Biprobability plot for  $\sin^2(2\theta_{23}) = 0.97$  for T2K.

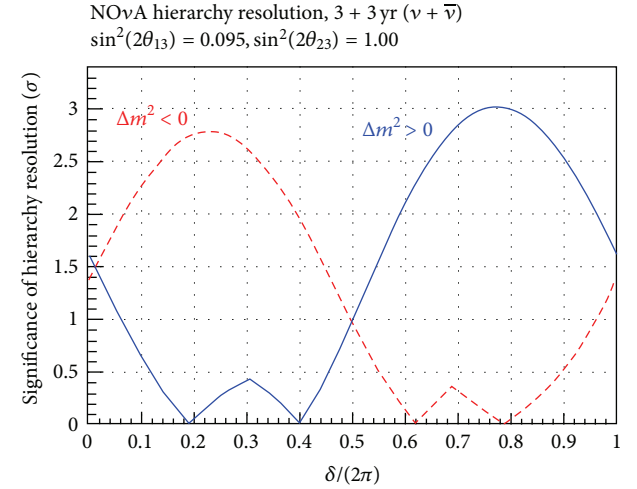


FIGURE 32: Significance of the resolution of the mass ordering as a function of  $\delta$  in standard deviations. These sensitivities are for NOvA alone for the two possible orderings and  $\sin^2(2\theta_{23}) = 1.0$ . The zeros correspond to the crossing of the ovals in Figure 25.

information from T2K that is expected to be available at the end of the nominal six-year NOvA run.

**7.2. Searches for New Physics.** Future data to be accumulated by long-baseline experiments offer novel avenues to search for new physics in several ways. MINOS+ [19] will run with the NuMI beam providing a flux that is least a factor of two higher in energy and power than for MINOS. This wide band beam will yield thousands of interactions a year in the Far detector with well-measured  $L/E$ . In combination

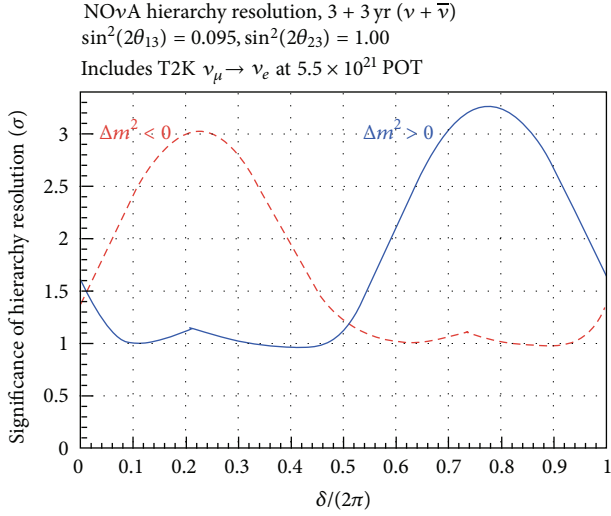


FIGURE 33: Same as Figure 32 except that information from the T2K experiment has been included.

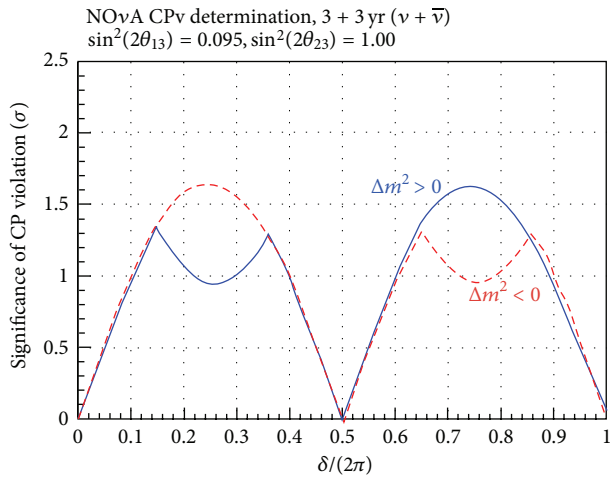


FIGURE 34: Significance of the determination that CP violation occurs in neutrino oscillations as a function of  $\delta$  in standard deviations. These sensitivities are for NOvA alone for the two possible orderings and  $\sin^2(2\theta_{23}) = 1.0$ . The significance goes to zero at  $\delta = 0$  and  $\delta = \pi$  since there is no CP violation at those points. The dips in the peaks occur because the mass ordering has not been resolved for the ordering containing the dips.

with a precise prediction for the spectrum of interactions from the Near detector, precision probes of new physics will be performed. NOvA and T2K experiments will exploit their narrow band beams that have well-defined energies. The NOvA detectors with their fine granular sampling of events (1 plane is 0.15 radiation lengths, see Section 3.7) will provide enhanced ability to distinguish the different neutrino interaction types.

Sterile neutrinos are one of the major areas of interest that will be probed by upcoming experiments. NOvA will improve on the MINOS searches for a deficit in the rate of NC interactions in the Far detector (see Section 6), with significantly better rejection of the dominant background

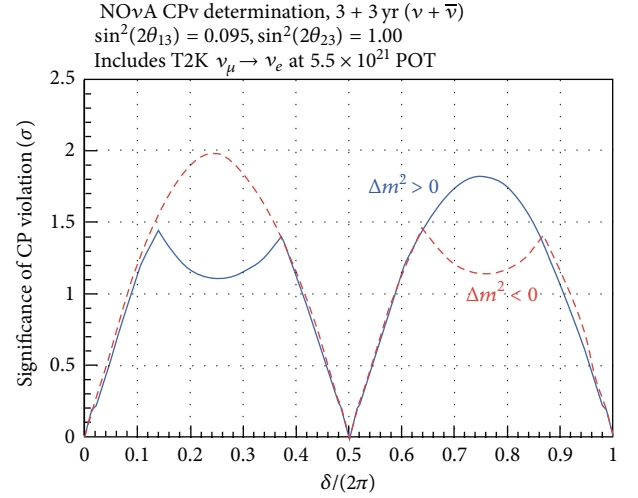


FIGURE 35: Same as Figure 34 except that information from the T2K experiment has been included.

coming from  $\nu_\mu$  CC events. In addition to studies of NC events, MINOS+ will use the complementary approach to looking for sterile neutrinos that involves constraining the disappearance of  $\nu_\mu$  and hence, via unitarity, will constrain the appearance of  $\nu_e$  (that short-baseline experiments are directly sensitive to). Figure 36 shows what MINOS+ expects to add to the world's constraints on muon-electron mixing at mass squared splittings between  $10^{-2} \text{ eV}^2$  and  $10 \text{ eV}^2$  (i.e., larger than the atmospheric and solar mass splittings). The red curve in Figure 36 is the expected combined sensitivity of MINOS+ and the Bugey reactor experiment [85]: Bugey constrains the  $\theta_{14}$  mixing angle with its  $\bar{\nu}_e$  disappearance measurements while MINOS+ aims to constrain  $\theta_{24}$  via the  $\nu_\mu$  disappearance mode. Predicted 90% C.L. sensitivities for MINOS+ combined with Bugey data are shown for exposures of  $1.2 \times 10^{21}$  POT in both neutrino-enhanced (a) and antineutrino-enhanced (b) NuMI beam configurations: these contours show that MINOS+ has the sensitivity to exclude substantial regions of parameter space allowed by MiniBooNE [86] and LSND [87] results.

In addition to searching for sterile neutrinos, MINOS+ will have a rich physics program that includes more precise measurements of  $|\Delta m_{\text{atm}}^2|$  and  $|\Delta \bar{m}_{\text{atm}}^2|$ , a search for tau neutrinos, nonstandard interactions, extra-dimensions, measurements of neutrino time-of-flight, and atmospheric neutrinos.

## 8. Conclusion

Accelerator long-baseline experiments have made many measurements of neutrino oscillations, extracting fundamental neutrino mixing parameters and mass-squared differences. The quantum mechanical interference pattern expected from neutrino oscillations has been observed with high statistics.

The most precise measurements to-date of  $|\Delta m_{\text{atm}}^2|$  for both neutrinos and antineutrinos were made by a long-baseline neutrino oscillation experiment. Measurement of

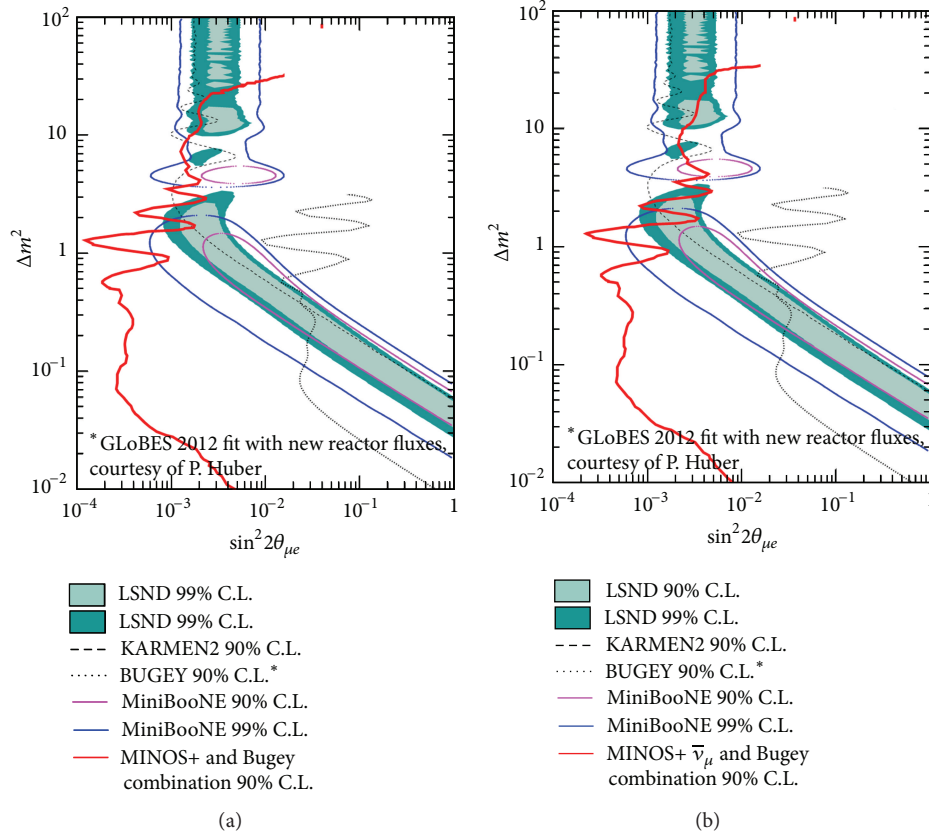


FIGURE 36: Expected sensitivities for MINOS+ combined with Bugey data to  $\sin^2(2\theta_{\mu e})$  as relevant for sterile neutrino searches. 90% C.L. contours are shown for exposures of  $1.2 \times 10^{21}$  POT in both neutrino-enhanced (a) and antineutrino-enhanced (b) NuMI beam configurations [45]. The regions of parameter space allowed by MiniBooNE and LSND experiments along with the limits from KARMEN [88] are also shown.

the largest neutrino mixing angle,  $\theta_{23}$ , has reached the level of precision obtained using atmospheric neutrinos and second generation long-baseline experiments will soon improve the precision considerably further. Evidence for electron neutrino appearance in a beam of muon neutrinos has recently been obtained and is consistent with new results that demonstrate the disappearance of reactor electron antineutrinos due to  $\theta_{13}$ .

Using a dedicated accelerator long-baseline experiment, candidate tau neutrino events have been directly observed in a beam of muon neutrinos and analysis of the complete data set is expected to reveal several more  $\nu_\tau$  candidates. Searches for oscillations into sterile neutrinos have set stringent limits on various models and these will improve further in the future. Long-baseline experiments have also been exploited in searches for Lorentz violation and to make world-leading measurements of the neutrino velocity.

The second generation long-baseline experiments currently taking data, or soon to start, will exploit the relatively large value of  $\theta_{13}$  with the aim of measuring the mass hierarchy, determining the octant of  $\theta_{23}$ , searching for CP violation and exploring models of new physics. Over the next decade, these experiments promise a rich program of research with the sensitivity to make fundamental discoveries.

## References

- [1] M. Ieiri et al., in *Proceedings of the 11th Symposium on Accelerator Science and Technology*, pp. 377–379, SPring-8, Hyogo, Japan, 1997.
- [2] K. Anderson et al., The NuMI Facility Technical Design Report FERMILAB-DESIGN-1998-01, 1998.
- [3] G. Acquistapace et al., The CERN Neutrino Beam to Gran Sasso (NGS) CERN-98-02, INFN-AE-98-05, CERN-YELLOW-98-02, 1998.
- [4] K. Abe, N. Abgrall, H. Aihara et al., “The T2K experiment,” *Nuclear Instruments and Methods in Physics Research, Section A*, vol. 659, no. 1, pp. 106–135, 2011.
- [5] M. H. Ahn, E. Aliu, S. Andringa et al., “Measurement of neutrino oscillation by the K2K experiment,” *Physical Review D*, vol. 74, no. 7, Article ID 072003, 39 pages, 2006.
- [6] I. Ambats et al., (MINOS Collaboration). The MINOS Detectors Technical Design Report, 1998.
- [7] R. Acquafredda, T. Adam, N. Agafonova et al., “The OPERA experiment in the CERN to Gran Sasso neutrino beam,” *Journal of Instrumentation*, vol. 4, no. 4, Article ID P04018, 2009.
- [8] F. Arneodo et al., “(ICARUS). The ICARUS experiment, a second-generation proton decay experiment and neutrino observatory at the Gran Sasso Laboratory,” <http://arxiv.org/abs/hep-ex/0103008>.

- [9] K. S. Hirata, T. Kajita, M. Koshiba et al., "Experimental study of the atmospheric neutrino flux," *Physics Letters B*, vol. 205, no. 2-3, pp. 416–420, 1988.
- [10] T. J. Haines, R. M. Bionta, G. Blewitt et al., "Calculation of atmospheric neutrino-induced backgrounds in a nucleon-decay search," *Physical Review Letters*, vol. 57, no. 16, pp. 1986–1989, 1986.
- [11] Y. Fukuda, T. Hayakawa, E. Ichihara et al., "Evidence for oscillation of atmospheric neutrinos," *Physical Review Letters*, vol. 81, no. 8, pp. 1562–1567, 1998.
- [12] M. Apollonio et al., "Search for neutrino oscillations on a long baseline at the CHOOZ nuclear power station," *European Physical Journal C*, vol. 27, pp. 331–374, 2003.
- [13] D. Ayres et al., "Letter of Intent to build an Off-axis Detector to study  $\nu_{\mu}$  to  $\nu_e$  oscillations with the NuMI Neutrino Beam," <http://arxiv.org/abs/hep-ex/0210005>.
- [14] D. Ayres et al., "NOvA: Proposal to build a 30 kiloton off-axis detector to study  $\nu_{\mu} \rightarrow \nu_e$  oscillations in the NuMI beamline," 2004.
- [15] D. Ayres et al., The NOvA Technical Design Report FERMILAB-DESIGN-2007-01, 2007.
- [16] Y. Abe, C. Aberle, T. Akiri et al., "Indication of reactor  $\bar{\nu}_e$  disappearance in the Double Chooz experiment," *Physical Review Letters*, vol. 108, no. 3, Article ID 131801, 7 pages.
- [17] F. P. An, J. Z. Bai, A. B. Balantekin et al., "Observation of electron-antineutrino disappearance at Daya Bay," *Physical Review Letters*, vol. 108, no. 17, Article ID 171803, 7 pages, 2012.
- [18] J. K. Ahn, S. Chebotaryov, J. H. Choi et al., "Observation of reactor electron antineutrinos disappearance in the RENO experiment," *Physical Review Letters*, vol. 108, no. 19, Article ID 191802, 6 pages, 2012.
- [19] G. Tzanankos et al., MINOS+: A Proposal to FNAL to Run MINOS with the Medium Energy NuMI beam FERMILAB-PROPOSAL-1016, 2011.
- [20] Y. Yamanoi, Y. Suzuki, E. Kusano et al., "Large horn magnets at the KEK neutrino beam line—part 2," *IEEE Transactions on Applied Superconductivity*, vol. 10, no. 1, pp. 252–255, 2000.
- [21] H. Noumi, M. Ieiri, T. Inagaki et al., "GPS survey in long baseline neutrino-oscillation measurement," *IEEE Transactions on Nuclear Science*, vol. 51, no. 5, pp. 2245–2249, 2004.
- [22] R. M. Zwaska, *Accelerator systems and instrumentation for the NuMI neutrino beam [Ph.D. thesis]*, University of Texas at Austin, 2005.
- [23] A. I. Himmel, *Antineutrino oscillations in the atmospheric sector [Ph.D. thesis]*, Caltech, 2011.
- [24] M. Meddahi, K. Cornelis, K. Elsener et al., "Cern Neutrinos to Gran Sasso (CNGS): results from commissioning," in *Proceedings of the IEEE Particle Accelerator Conference (PAC '07)*, pp. 692–694, June 2007.
- [25] N. Agafonova, A. Aleksandrov, O. Altinok et al., "Observation of a first  $\nu_{\tau}$  candidate event in the OPERA experiment in the CNGS beam," *Physics Letters, Section B*, vol. 691, no. 3, pp. 138–145, 2010.
- [26] T. Ogitsu, Y. Makida, T. Kobayashi et al., "Superconducting magnet system at the 50 GeV proton beam line for the J-PARC neutrino experiment," *IEEE Transactions on Applied Superconductivity*, vol. 14, no. 2, pp. 604–607, 2004.
- [27] T. Nakamoto, N. Higashi, T. Ogitsu et al., "Design of superconducting combined function magnets for the 50 GeV proton beam line for the J-PARC neutrino experiment," *IEEE Transactions on Applied Superconductivity*, vol. 14, no. 2, pp. 616–619, 2004.
- [28] T. Ogitsu et al., "Operation of superconducting combined function magnet system for J-PARC neutrino beam line," in *Proceedings of the International Particle Accelerator Conference (IPAC'10)*, Kyoto, Japan, 2010.
- [29] A. Suzuki, H. Park, S. Aoki et al., "Design, construction, and operation of SciFi tracking detector for K2K experiment," *Nuclear Instruments and Methods in Physics Research, Section A*, vol. 453, no. 1-2, pp. 165–176, 2000.
- [30] T. Ishii, T. Inagaki, J. Breault et al., "Near muon range detector for the K2K experiment—construction and performance," *Nuclear Instruments and Methods in Physics Research, Section A*, vol. 481, no. 1-3, pp. 244–253, 2002.
- [31] K. Nitta, E. Aliu, S. Andringa et al., "The K2K SciBar detector," *Nuclear Instruments and Methods in Physics Research, Section A*, vol. 535, no. 1-2, pp. 147–151, 2004.
- [32] S. Fukuda, Y. Fukuda, T. Hayakawa et al., "The Super-Kamiokande detector," *Nuclear Instruments and Methods in Physics Research, Section A*, vol. 501, no. 2-3, pp. 418–462, 2003.
- [33] D. G. Michael, P. Adamson, T. Alexopoulos et al., "The magnetized steel and scintillator calorimeters of the MINOS experiment," *Nuclear Instruments and Methods in Physics Research, Section A*, vol. 596, no. 2, pp. 190–228, 2008.
- [34] P. Adamson, G. Crone, L. Jenner et al., "The MINOS calibration detector," *Nuclear Instruments and Methods in Physics Research, Section A*, vol. 556, no. 1, pp. 119–133, 2006.
- [35] A. Cabrera, P. Adamson, M. Barker et al., "Comparisons of the MINOS near and far detector readout systems at a test beam," *Nuclear Instruments and Methods in Physics Research, Section A*, vol. 609, no. 2-3, pp. 106–113, 2009.
- [36] C. Rubbia, M. Antonello, P. Aprili et al., "Underground operation of the ICARUS T600 LAr-TPC: first results," *Journal of Instrumentation*, vol. 6, no. 7, Article ID P07011, 2011.
- [37] M. H. Ahn, S. Aoki, H. Bhang et al., "Indications of neutrino oscillation in a 250 km long-baseline experiment," *Physical Review Letters*, vol. 90, no. 4, Article ID 041801, 5 pages, 2003.
- [38] D. G. Michael, P. Adamson, T. Alexopoulos, and MINOS Collaboration, "Observation of muon neutrino disappearance with the MINOS detectors in the NuMI neutrino beam," *Physical Review Letters*, vol. 97, no. 19, Article ID 191801, 6 pages, 2006.
- [39] N. Agafonova, A. Aleksandrov, O. Altinok et al., "Search for  $\nu_{\mu} \rightarrow \nu_{\tau}$  oscillation with the OPERA experiment in the CNGS beam," *New Journal of Physics*, vol. 14, Article ID 033017, 2012.
- [40] P. Adamson et al., "Measurement of the neutrino mass splitting and  $\nu_{\mu}$  mixing by MINOS," *Physical Review Letters*, vol. 106, Article ID 181801, 6 pages, 2011.
- [41] Y. Ashie, J. Hosaka, and K. Ishihara, "Evidence for an oscillatory signature in atmospheric neutrino oscillations," *Physical Review Letters*, vol. 93, no. 10, Article ID 101801, 6 pages, 2004.
- [42] Y. Ashie, J. Hosaka, K. Ishihara et al., "A Measurement of atmospheric neutrino oscillation parameters by SUPER-KAMIOKANDE I," *Physical Review D*, vol. 71, Article ID 112005, 35 pages, 2005.
- [43] P. Adamson, C. Andreopoulos, K. E. Arms et al., "Study of muon neutrino disappearance using the Fermilab Main Injector neutrino beam," *Physical Review D*, vol. 77, no. 7, Article ID 072002, 34 pages, 2008.
- [44] P. Adamson, C. Andreopoulos, K. E. Arms et al., "Measurement of neutrino oscillations with the MINOS detectors in the NuMI beam," *Physical Review Letters*, vol. 101, no. 13, Article ID 131802, 5 pages, 2008.



- [45] R. Nichol, "Results from MINOS," in *Neutrino Conference Proceedings*, 2012.
- [46] P. Adamson, D. J. Auty, D. S. Ayres et al., "Search for the disappearance of muon antineutrinos in the NuMI neutrino beam," *Physical Review D*, vol. 84, no. 7, Article ID 071103, 6 pages, 2011.
- [47] Y. Itow, "Atmospheric neutrinos: results from running experiments," in *Neutrino Conference Proceedings*, 2012.
- [48] K. Abe, N. Abgrall, Y. Ajima et al., "First muon-neutrino disappearance study with an off-axis beam," *Physical Review D*, vol. 85, no. 3, Article ID 031103, 8 pages, 2012.
- [49] P. Adamson, C. Andreopoulos, D. J. Auty et al., "First direct observation of Muon antineutrino disappearance," *Physical Review Letters*, vol. 107, no. 2, Article ID 021801, 5 pages, 2011.
- [50] P. Adamson, D. S. Ayres, C. Backhouse et al., "Improved measurement of muon antineutrino disappearance in MINOS," *Physical Review Letters*, vol. 108, no. 19, Article ID 191801, 5 pages, 2012.
- [51] K. Abe, Y. Hayato, and T. Iida, "Search for differences in oscillation parameters for atmospheric neutrinos and antineutrinos at Super-Kamiokande," *Physical Review Letters*, vol. 107, no. 24, Article ID 241801, 6 pages, 2011.
- [52] M. Nakamura, "Results from OPERA," in *Neutrino Conference Proceedings*, 2012.
- [53] K. Abe, Y. Hayato, T. Iida et al., "Measurement of atmospheric neutrino flux consistent with tau neutrino appearance," *Physical Review Letters*, vol. 97, no. 17, Article ID 171801, 6 pages, 2006.
- [54] K. Abe et al., "A measurement of the appearance of atmospheric tau neutrinos by super-kamiokande," <http://arxiv.org/abs/1206.0328>.
- [55] M. H. Ahn, S. Aoki, Y. Ashie et al., "Search for electron neutrino appearance in a 250 km long-baseline experiment," *Physical Review Letters*, vol. 93, no. 5, Article ID 051801, 5 pages, 2004.
- [56] S. Yamamoto, J. Zalipska, E. Aliu et al., "Improved search for  $\nu_\mu \rightarrow \nu_e$  oscillation in a long-baseline accelerator experiment," *Physical Review Letters*, vol. 96, no. 18, Article ID 181801, 5 pages, 2006.
- [57] P. Adamson, C. Andreopoulos, K. E. Arms et al., "Search for muon-Neutrino to electron-Neutrino transitions in MINOS," *Physical Review Letters*, vol. 103, no. 26, Article ID 261802, 5 pages, 2009.
- [58] P. Adamson, C. Andreopoulos, and D. J. Auty, "New constraints on muon-neutrino to electron-neutrino transitions in MINOS," *Physical Review D*, vol. 82, no. 5, Article ID 051102, 6 pages, 2010.
- [59] P. Adamson, D. J. Auty, D. S. Ayres et al., "Improved search for muon-neutrino to electron-neutrino oscillations in MINOS," *Physical Review Letters*, vol. 107, no. 18, Article ID 181802, 6 pages, 2011.
- [60] K. Abe, N. Abgrall, Y. Ajima et al., "Indication of electron neutrino appearance from an accelerator-produced off-axis muon neutrino beam," *Physical Review Letters*, vol. 107, no. 4, Article ID 041801, 8 pages, 2011.
- [61] N. Abgrall, A. Aduszkiewicz, B. Andrieu et al., "Measurements of cross sections and charged pion spectra in proton-carbon interactions at 31 GeV/c," *Physical Review C*, vol. 84, no. 3, Article ID 034604, 26 pages, 2011.
- [62] N. Abgrall, A. Aduszkiewicz, T. Anticic et al., "Measurement of production properties of positively charged kaons in proton-carbon interactions at 31 GeV/c," *Physical Review C*, vol. 85, no. 3, Article ID 035210, 10 pages, 2012.
- [63] T. Nakaya, "Results from T2K," in *Neutrino Conference Proceedings*, 2012.
- [64] N. Abgrall, A. Aduszkiewicz, T. Anticic et al., "Search for active neutrino disappearance using neutral-current interactions in the MINOS long-baseline experiment," *Physical Review Letters*, vol. 101, no. 22, Article ID 221804, 5 pages, 2008.
- [65] P. Adamson, C. Andreopoulos, D. J. Auty et al., "Search for sterile neutrino mixing in the MINOS long-baseline experiment," *Physical Review D*, vol. 81, no. 5, Article ID 052004, 18 pages, 2010.
- [66] S. Fukuda, Y. Fukuda, M. Ishitsuka et al., "Tau neutrinos favored over sterile neutrinos in atmospheric muon neutrino oscillations," *Physical Review Letters*, vol. 85, no. 19, pp. 3999–4003, 2000.
- [67] P. Adamson, D. J. Auty, D. S. Ayres et al., "Active to sterile neutrino mixing limits from neutral-current interactions in MINOS," *Physical Review Letters*, vol. 107, no. 1, Article ID 011802, 5 pages, 2011.
- [68] P. Adamson, C. Andreopoulos, K. E. Arms et al., "Measurement of neutrino velocity with the MINOS detectors and NuMI neutrino beam," *Physical Review D*, vol. 76, no. 7, Article ID 072005, 6 pages, 2007.
- [69] G. R. Kalbfleisch, N. Baggett, E. C. Fowler, and J. Alspector, "Experimental comparison of neutrino, antineutrino, and muon velocities," *Physical Review Letters*, vol. 43, no. 19, pp. 1361–1364, 1979.
- [70] T. Adam, N. Agafonova, A. Aleksandrov et al., "Measurement of the neutrino velocity with the OPERA detector in the CNGS beam," *Journal of High Energy Physics*, vol. 2012, no. 10, article 093, 2012.
- [71] M. Antonello, P. Aprili, B. Baiboussinov et al., "Measurement of the neutrino velocity with the ICARUS detector at the CNGS beam," *Physics Letters, Section B*, vol. 713, no. 1, pp. 17–22, 2012.
- [72] P. Alvarez Sanchez, R. Barzaghi, G. Bellini et al., "Measurement of CNGS muon neutrino speed with Borexino," *Physics Letters, Section B*, vol. 716, no. 3–5, pp. 401–405, 2012.
- [73] N. Yu. Agafonova, M. Aglietta, P. Antonoli et al., "Measurement of the velocity of neutrinos from the CNGS beam with the large volume detector," *Physical Review Letters*, vol. 109, no. 7, Article ID 070801, 5 pages, 2012.
- [74] P. Adamson, "Neutrino speed: results and prospects of experiments at other beamlines," in *Neutrino Conference Proceedings*, 2012.
- [75] D. Colladay and V. A. Kostelecký, "CPT violation and the standard model," *Physical Review D*, vol. 61, no. 3, pp. 6760–6774, 2000.
- [76] D. Colladay and V. A. Kostelecký, "Lorentz-violating extension of the standard model," *Physical Review D*, vol. 58, no. 11, Article ID 116002, 23 pages, 1998.
- [77] V. A. Kostelecký, "Gravity, Lorentz violation, and the standard model," *Physical Review D*, vol. 69, no. 10, Article ID 105009, 20 pages, 2004.
- [78] P. Adamson, C. Andreopoulos, K. E. Arms et al., "Testing Lorentz invariance and CPT conservation with NuMI neutrinos in the MINOS near detector," *Physical Review Letters*, vol. 101, no. 15, Article ID 151601, 5 pages, 2008.
- [79] P. Adamson, D. S. Ayres, and G. Barr, "Search for Lorentz invariance and CPT violation with muon antineutrinos in the MINOS Near Detector," *Physical Review D*, vol. 85, no. 3, Article ID 031101, 6 pages, 2012.

- [80] P. Adamson, D. J. Auty, and D. S. Ayres, "Search for lorentz invariance and  $CPT$  violation with the MINOS Far detector," *Physical Review Letters*, vol. 105, no. 15, Article ID 151601, 15 pages, 2010.
- [81] V. A. Kostelecký and N. Russell, "Data tables for Lorentz and  $CPT$  violation," *Reviews of Modern Physics*, vol. 83, no. 1, pp. 11–31, 2011.
- [82] T. Ajima et al., Tokai-to-Kamioka (T2K) Long Baseline Neutrino Oscillation Experiment Proposal, 2006, [http://j-parc.jp/researcher/Hadron/en/pac\\_0606/pdf/p11-Nishikawa.pdf](http://j-parc.jp/researcher/Hadron/en/pac_0606/pdf/p11-Nishikawa.pdf).
- [83] Y. Abe, C. Aberle, and J. C. Dos Anjos, "Reactor  $\bar{\nu}_e$  disappearance in the Double Chooz experiment," *Physical Review D*, vol. 86, no. 5, Article ID 052008, 21 pages, 2012.
- [84] D. Dwyer, "Improved measurement of electron-antineutrino disappearance at Daya Bay," in *Neutrino Conference Proceedings*, 2012.
- [85] B. Achkar, R. Aleksan, M. Avenier et al., "Search for neutrino oscillations at 15, 40 and 95 meters from a nuclear power reactor at Bugey," *Nuclear Physics B*, vol. 434, no. 3, pp. 503–532, 1995.
- [86] A. A. Aguilar-Arevalo, C. E. Anderson, S. J. Brice et al., "Event excess in the MiniBooNE search for  $\bar{\nu}_\mu \rightarrow \bar{\nu}_e$  oscillations," *Physical Review Letters*, vol. 105, no. 18, Article ID 181801, 5 pages, 2010.
- [87] A. Aguilar, L. B. Auerbach, R. L. Burman et al., "Evidence for neutrino oscillations from the observation of  $\bar{\nu}_e$  appearance in a  $\bar{\nu}_\mu$  beam," *Physical Review D*, vol. 64, no. 11, Article ID 112007, 22 pages, 2001.
- [88] B. Armbruster, I. M. Blair, B. A. Bodmann et al., "Upper limits for neutrino oscillations  $\bar{\nu}_\mu \rightarrow \bar{\nu}_e$  from muon decay at rest," *Physical Review D*, vol. 65, no. 11, Article ID 112001, 16 pages, 2002.

## Review Article

# Sterile Neutrino Fits to Short-Baseline Neutrino Oscillation Measurements

J. M. Conrad,<sup>1</sup> C. M. Ignarra,<sup>1</sup> G. Karagiorgi,<sup>2</sup> M. H. Shaevitz,<sup>2</sup> and J. Spitz<sup>1</sup>

<sup>1</sup> *Massachusetts Institute of Technology, Cambridge, MA 02139, USA*

<sup>2</sup> *Columbia University, New York, NY 10027, USA*

Correspondence should be addressed to C. M. Ignarra; [ignarra@mit.edu](mailto:ignarra@mit.edu)

Received 13 July 2012; Accepted 11 September 2012

Academic Editor: Koichiro Nishikawa

Copyright © 2013 J. M. Conrad et al. This is an open access article distributed under the Creative Commons Attribution License, which permits unrestricted use, distribution, and reproduction in any medium, provided the original work is properly cited.

This paper reviews short-baseline oscillation experiments as interpreted within the context of one, two, and three sterile neutrino models associated with additional neutrino mass states in the  $\sim 1$  eV range. Appearance and disappearance signals and limits are considered. We show that fitting short-baseline datasets to a  $3 + 3$  ( $3 + 2$ ) model, defined by three active and three (two) sterile neutrinos, results in an overall goodness of fit of 67% (69%) and good compatibility between data sets—to be compared to a  $3 + 1$  model with a 55% goodness of fit. While the  $(3 + 3)$  fit yields the highest quality overall, it still finds inconsistencies with the MiniBooNE appearance datasets; in particular, the global fit fails to account for the observed MiniBooNE low-energy excess. Given the overall improvement, we recommend using the results of  $(3 + 2)$  and  $(3 + 3)$  fits, rather than  $(3 + 1)$  fits, for future neutrino oscillation phenomenology. These results motivate the pursuit of further short-baseline experiments, such as those reviewed in this paper.

## 1. Introduction

Over the past 15 years, neutrino oscillations associated with small splittings between the neutrino mass states have become well established [1–16]. Based on this, a phenomenological extension of the Standard Model (SM) has been constructed involving three neutrino mass states, over which the three known flavors of neutrinos ( $\nu_e$ ,  $\nu_\mu$ , and  $\nu_\tau$ ) are distributed. This is a minimal extension of the SM requiring a lepton mixing matrix, analogous to the quark sector and introducing neutrino mass.

Despite its success, the model does not address fundamental questions such as how neutrino masses should be incorporated into an SM Lagrangian or why the neutrino sector has small masses and large mixing angles compared to the quark sector. As a result, while this structure makes successful predictions, one would like to gain a deeper understanding of neutrino phenomenology. This has led to searches for other unexpected properties of neutrinos that might lead to clues towards a more complete theory governing their behavior.

Recalling that the mass splitting is related to the frequency of oscillation, short-baseline (SBL) experiments search for evidence of “rapid” oscillations above the established solar ( $\sim 10^{-5}$  eV<sup>2</sup>) and atmospheric ( $\sim 10^{-3}$  eV<sup>2</sup>) mass splittings that are incorporated into today’s framework. A key motivation is the search for light sterile neutrinos-fermions that do not participate in SM interactions but do participate in mixing with the established SM neutrinos. Indications of oscillations between active and sterile neutrinos have been observed in the LSND [17], MiniBooNE [18], and reactor [19] experiments, though many others have contributed additional probes of the effect, which are of comparable sensitivity and/or complementary to those above.

This paper examines these results within the context of models describing oscillations with sterile neutrinos. An oscillation formalism that introduces multiple sterile neutrinos is described in the next section. Following this, we review the SBL datasets used in the fits presented in this paper, which include both positive signals and stringent limits. We then detail the analysis approach, which we have developed in a series of past papers [20–22]. The global fits are presented

with one, two, and three light sterile neutrinos. While groups [20, 23, 24] have explored fits with two sterile neutrinos in the past, the fits presented here represent an important step forward. In particular, we show that, for the first time, the (3 + 3) model resolves some disagreements between the datasets. Lastly, the future of SBL searches for sterile neutrinos is reviewed.

## 2. Oscillations Involving Sterile Neutrinos

**2.1. Light Sterile States.** Sterile neutrinos are additional states beyond the standard electron, muon, and tau flavors, which do not interact via the exchange of  $W$  or  $Z$  bosons [25] and are thus “sterile” with respect to the weak interaction. These states are motivated by many Beyond Standard Model theories, where they are often introduced as gauge singlets. Traditionally, sterile neutrinos were introduced at very high mass scales within the context of grand unification and leptogenesis. For many years, sterile neutrinos with light masses were regarded as less natural. However, as recent data [17, 19, 26, 27] has indicated the potential existence of light sterile neutrinos, the theoretical view has evolved to accommodate these light mass gauge singlets [28, 29]. At this point, it is generally accepted that the mass scale for sterile neutrinos is not well predicted, and the existence of one or more sterile neutrinos accommodated by introducing extra neutrino mass states at the eV scale is possible. An excellent review of the phenomenology of sterile neutrinos, as well as the data motivating light sterile models, is provided in [23].

Within the expanded oscillation phenomenology, sterile neutrinos are handled as additional noninteracting flavors, which are connected to additional mass states via an extended mixing matrix with extra mixing angles and CP violating phases. These additional mass states must be mostly sterile, with only a small admixture of the active flavors, in order to accommodate the limits on oscillations to sterile neutrinos from the atmospheric and solar neutrino data. Experimental evidence for these additional mass states would come from the disappearance of an active flavor to a sterile neutrino state or additional transitions from one active flavor to another through the sterile neutrino state.

The number of light sterile neutrinos is not predicted by theory. However, a natural tendency is to introduce three sterile states. Depending on how the states are distributed in mass scale, one, two, or all three states may be involved in SBL oscillations. These are referred to as (3 +  $N$ ) models where the “3” refers to the three active flavors and the “ $N$ ” refers to the number of sterile neutrinos.

Introducing sterile neutrinos can have implications in cosmological observations, especially measurements of the radiation density in the early universe. These are compounded if the extra neutrinos have significant mass ( $>1$  eV) and do not decay. Currently, cosmological data allow additional states and in many cases favor light sterile neutrinos [30–36]. Upcoming Planck data [37] is expected to precisely measure  $N_{\text{eff}}$ . This parameter, however, can be considered a model-dependent one. As an example, there are a variety

of classes of theories where the neutrinos do not thermalize in the early universe [23]. In these cases, the cosmological neutrino abundance would substantially decrease, rendering cosmological measurements of  $N_{\text{eff}}$  invalid. Therefore, while the community certainly looks forward to cosmological measurements of  $N_{\text{eff}}$ , we think that SBL experiments are a largely better approach for probing light sterile neutrinos and constraining their mixing properties. We therefore proceed with a study of the SBL data, without further reference to the cosmological results.

**2.2. The Basic Oscillation Formalism.** Before considering the phenomenology of light sterile neutrinos, it is useful to introduce the idea of oscillations within a simpler model. In this section, we first consider the two-neutrino formalism. We then extend these ideas to form the well-established three-active-flavor neutrino model. Based on these concepts, we expand the discussion to include more states in the following section.

Neutrino oscillations require that (1) neutrinos have mass; (2) the difference between the masses is small; (3) the mass eigenstates are rotations of the weak interaction eigenstates. These rotations are given in a simple two-neutrino model as follows:

$$\begin{aligned} \nu_e &= \cos \theta \nu_1 + \sin \theta \nu_2, \\ \nu_\mu &= -\sin \theta \nu_1 + \cos \theta \nu_2, \end{aligned} \quad (1)$$

where  $\nu_i$  ( $i = 1, 2$ ) is the “mass eigenstate,”  $\nu_\alpha$  ( $\alpha = e, \mu$ ) is the “flavor eigenstate,” and  $\theta$  is the “mixing angle.” Under these conditions, a neutrino born in a pure flavor state through a weak decay can oscillate into another flavor as the state propagates in space, due to the fact that the different mass eigenstate components propagate with different frequencies. The mass splitting between the two states is  $\Delta m^2 = |m_2^2 - m_1^2| > 0$ . The oscillation probability for  $\nu_\mu \rightarrow \nu_e$  oscillations is then given by the following:

$$P(\nu_\mu \rightarrow \nu_e) = \sin^2 2\theta \sin^2 \left( \frac{1.27 \Delta m^2 (\text{eV}^2) L (\text{km})}{E (\text{GeV})} \right), \quad (2)$$

where  $L$  is the distance from the source, and  $E$  is the neutrino energy.

From (2), one can see that the probability for observing oscillations is large when  $\Delta m^2 \sim E/L$ . In the discussions below, we will focus on experiments with signals in the  $\Delta m^2 \sim 1 \text{ eV}^2$  range. These experiments are therefore designed with  $E/L \sim 1 \text{ GeV/km}$  (or, alternatively,  $1 \text{ MeV/m}$ ). Typically, neutrino source energies range from a few MeV to a few GeV. Thus, most of the experiments considered are located between a few meters and a few kilometers from the source. This is not absolutely necessary, a very high-energy experiment with a very long baseline is sensitive to oscillations in the  $\Delta m^2 \sim 1 \text{ eV}^2$  range, as long as the ratio  $E/L \sim 1 \text{ GeV/km}$  is maintained. In other words, “short-baseline experiments” is something of a misnomer—what is meant is the experiments with sensitivity to  $\Delta m^2 \sim 1 \text{ eV}^2$  oscillations.



In the case where  $E/L \ll 1 \text{ GeV/km}$ , such as in accelerator-based experiments with long baselines (hundreds of kilometers), one can see from (2) that the oscillations will be rapid. In the case of  $\Delta m^2 \sim 1 \text{ eV}^2$ , sensitivity to the mass splitting is lost because the  $\sin^2(1.27\Delta m^2(L/E))$  term will average to  $1/2$  due to the finite energy and position resolution of the experiment. The oscillation probability becomes  $P = (\sin^2 2\theta)/2$  in this case. Thus, the information from “long-baseline experiments” can be used to constrain the mixing angle, but not the  $\Delta m^2$ .

The exercise of generalizing to a three-neutrino model is useful, since the inclusion of more states follows from this procedure. Within a three-neutrino model, the mixing matrix is written as follows:

$$\begin{pmatrix} \nu_e \\ \nu_\mu \\ \nu_\tau \end{pmatrix} = \begin{pmatrix} U_{e1} & U_{e2} & U_{e3} \\ U_{\mu 1} & U_{\mu 2} & U_{\mu 3} \\ U_{\tau 1} & U_{\tau 2} & U_{\tau 3} \end{pmatrix} \begin{pmatrix} \nu_1 \\ \nu_2 \\ \nu_3 \end{pmatrix}. \quad (3)$$

The matrix elements are parametrized by three mixing angles, analogous to the Euler angles. As in the quark sector, the three-neutrino model can be extended to include an imaginary term that introduces a CP-violating phase. This formalism is analogous to the quark sector, where strong and weak eigenstates are rotated and the resultant mixing is described conventionally by a unitary mixing matrix.

The oscillation probability for three-neutrino oscillations is typically written as the following:

$$P(\nu_\alpha \rightarrow \nu_\beta) = \delta_{\alpha\beta} - 4 \sum_{j>i} U_{\alpha i} U_{\beta i}^* U_{\alpha j}^* U_{\beta j} \sin^2 \left( \frac{1.27 \Delta m_{ij}^2 L}{E} \right), \quad (4)$$

where  $\Delta m_{ij}^2 = m_j^2 - m_i^2$ ,  $\alpha$  and  $\beta$  are flavor-state indices ( $e, \mu, \tau$ ), and  $i$  and  $j$  are mass-state indices (1, 2, 3 in the three-neutrino case, though (4) holds for  $n$ -neutrino oscillations). Although in general there will be mixing among all three flavors of neutrinos, if the mass scales are quite different ( $m_3 \gg m_2 \gg m_1$ ), then the oscillation phenomena tend to decouple and the two-neutrino mixing model is a good approximation in limited regions.

Three different  $\Delta m^2$  parameters appear in (4); however, only two are independent since the two small  $\Delta m^2$  parameters must sum to the largest. If we consider the oscillation data measured at  $>5\sigma$  [1–16], then two  $\Delta m^2$  ranges,  $7 \times 10^{-5} \text{ eV}^2$  (solar) and  $3 \times 10^{-3} \text{ eV}^2$  (atmospheric), are already defined. These constrain the third  $\Delta m^2$ , so that oscillation results at  $\sim 1 \text{ eV}^2$ , such as those discussed in this paper, cannot be accommodated within a three-neutrino model.

**2.3.  $(3 + N)$  Oscillation Formalism.** The sterile neutrino oscillation formalism followed in this paper assumes up to three additional neutrino mass eigenstates, beyond the established three SM neutrino species. We know, from solar and atmospheric oscillation observations, that three of the mass states must be mostly active. Experimental hints point

toward the existence of additional mass states that are mostly sterile, in the range of  $\Delta m^2 = 0.01\text{--}100 \text{ eV}^2$ .

Introducing extra mass states results in a large number of extra parameters in the model. Approximation is required to allow for efficient exploration of the available parameters. To this end, in our model we assume that the three lowest states,  $\nu_1$ ,  $\nu_2$ , and  $\nu_3$ , that are the mostly active states accounting for the solar and atmospheric observations, have masses so small as to be effectively degenerate with equal masses. This is commonly called the “short-baseline approximation” and it reduces the picture to two-, three-, and four-neutrino-mass oscillation models, corresponding to  $(3 + 1)$ ,  $(3 + 2)$ , and  $(3 + 3)$ , respectively.

The active ( $e, \mu, \tau$ ) content of the  $N$  additional mass eigenstates is assumed to be small; specifically, the  $U_{\alpha i}$  elements of the extended  $(3 + N) \times (3 + N)$  mixing matrix for  $i = 4\text{--}6$  and  $\alpha = e, \mu, \tau$ , are restricted to values  $|U_{\alpha i}| \leq 0.5$ , while the following constraints are applied by way of unitarity:

$$\sum_{\alpha=e,\mu,\tau} |U_{\alpha i}|^2 \leq 0.3, \quad (5)$$

for each  $i = 4\text{--}6$ , and

$$\sum_{i=4-6} |U_{\alpha i}|^2 \leq 0.3, \quad (6)$$

for each  $\alpha = e, \mu, \tau$ . In our fits, since the SBL experiments considered have no  $\nu_\tau$  sensitivity, we explicitly assume that  $|U_{\tau i}| = 0$ . The above restrictions therefore apply only for  $\alpha = e, \mu$ , and are consistent with solar and atmospheric neutrino experiments, which indicate that there can only be a small electron and muon flavor content in the fourth, fifth, and sixth mass eigenstates [23].

In this formalism, the probabilities for  $\nu_\alpha \rightarrow \nu_\beta$  oscillations can be deduced from the following equation:

$$\begin{aligned} P(\nu_\alpha \rightarrow \nu_\beta) &= \delta_{\alpha\beta} - \sum_{j<i} \left( 4 \operatorname{Re} \{ U_{\beta i} U_{\alpha i}^* U_{\beta j}^* U_{\alpha j} \} \sin^2 \left( \frac{1.27 \Delta m_{ij}^2 L}{E} \right) \right. \\ &\quad \left. - 2 \operatorname{Im} \{ U_{\beta i} U_{\alpha i}^* U_{\beta j}^* U_{\alpha j} \} \sin \left( \frac{2.53 \Delta m_{ij}^2 L}{E} \right) \right), \end{aligned} \quad (7)$$

where  $\Delta m_{ij}^2 = m_i^2 - m_j^2$  is in  $\text{eV}^2$ ,  $L$  is in m, and  $E$  is in MeV. This formalism conserves CPT, but does not necessarily conserve CP.

To be explicit, for the (3 + 3) scenario, the mixing formalism is extended in the following way:

$$\begin{pmatrix} \nu_e \\ \nu_\mu \\ \nu_\tau \\ \nu_{s_1} \\ \nu_{s_2} \\ \nu_{s_3} \end{pmatrix} = \begin{pmatrix} U_{e1} & U_{e2} & U_{e3} & U_{e4} & U_{e5} & U_{e6} \\ U_{\mu 1} & U_{\mu 2} & U_{\mu 3} & U_{\mu 4} & U_{\mu 5} & U_{\mu 6} \\ U_{\tau 1} & U_{\tau 2} & U_{\tau 3} & U_{\tau 4} & U_{\tau 5} & U_{\tau 6} \\ U_{s_1 1} & U_{s_1 2} & U_{s_1 3} & U_{s_1 4} & U_{s_1 5} & U_{s_1 6} \\ U_{s_2 1} & U_{s_2 2} & U_{s_2 3} & U_{s_2 4} & U_{s_2 5} & U_{s_2 6} \\ U_{s_3 1} & U_{s_3 2} & U_{s_3 3} & U_{s_3 4} & U_{s_3 5} & U_{s_3 6} \end{pmatrix} \begin{pmatrix} \nu_1 \\ \nu_2 \\ \nu_3 \\ \nu_4 \\ \nu_5 \\ \nu_6 \end{pmatrix}. \quad (8)$$

The SBL approximation states that  $m_1 \approx m_2 \approx m_3$ . With this assumption, and for the case of the (3 + 3) scenario, the appearance ( $\alpha \neq \beta$ ) oscillation probability can be rewritten as the following:

$$\begin{aligned} P(\nu_\alpha \rightarrow \nu_\beta) &\simeq -4 |U_{\alpha 5}| |U_{\beta 5}| |U_{\alpha 4}| |U_{\beta 4}| \cos \phi_{54} \sin^2 \left( \frac{1.27 \Delta m_{54}^2 L}{E} \right) \\ &- 4 |U_{\alpha 6}| |U_{\beta 6}| |U_{\alpha 4}| |U_{\beta 4}| \cos \phi_{64} \sin^2 \left( \frac{1.27 \Delta m_{64}^2 L}{E} \right) \\ &- 4 |U_{\alpha 5}| |U_{\beta 5}| |U_{\alpha 6}| |U_{\beta 6}| \cos \phi_{65} \sin^2 \left( \frac{1.27 \Delta m_{65}^2 L}{E} \right) \\ &+ 4 (|U_{\alpha 4}| |U_{\beta 4}| + |U_{\alpha 5}| |U_{\beta 5}| \cos \phi_{54} + |U_{\alpha 6}| |U_{\beta 6}| \cos \phi_{64}) \\ &\times |U_{\alpha 4}| |U_{\beta 4}| \sin^2 \left( \frac{1.27 \Delta m_{41}^2 L}{E} \right) \\ &+ 4 (|U_{\alpha 4}| |U_{\beta 4}| \cos \phi_{54} + |U_{\alpha 5}| |U_{\beta 5}| + |U_{\alpha 6}| |U_{\beta 6}| \cos \phi_{65}) \\ &\times |U_{\alpha 5}| |U_{\beta 5}| \sin^2 \left( \frac{1.27 \Delta m_{51}^2 L}{E} \right) \\ &+ 4 (|U_{\alpha 4}| |U_{\beta 4}| \cos \phi_{64} + |U_{\alpha 5}| |U_{\beta 5}| \cos \phi_{65} + |U_{\alpha 6}| |U_{\beta 6}|) \\ &\times |U_{\alpha 6}| |U_{\beta 6}| \sin^2 \left( \frac{1.27 \Delta m_{61}^2 L}{E} \right) \\ &+ 2 |U_{\beta 5}| |U_{\alpha 5}| |U_{\beta 4}| |U_{\alpha 4}| \sin \phi_{54} \sin \left( \frac{2.53 \Delta m_{54}^2 L}{E} \right) \\ &+ 2 |U_{\beta 6}| |U_{\alpha 6}| |U_{\beta 4}| |U_{\alpha 4}| \sin \phi_{64} \sin \left( \frac{2.53 \Delta m_{64}^2 L}{E} \right) \end{aligned}$$

$$\begin{aligned} &+ 2 |U_{\beta 6}| |U_{\alpha 6}| |U_{\beta 5}| |U_{\alpha 5}| \sin \phi_{65} \sin \left( \frac{2.53 \Delta m_{65}^2 L}{E} \right) \\ &+ 2 (|U_{\alpha 5}| |U_{\beta 5}| \sin \phi_{54} + |U_{\alpha 6}| |U_{\beta 6}| \sin \phi_{64}) \\ &\times |U_{\alpha 4}| |U_{\beta 4}| \sin \left( \frac{2.53 \Delta m_{41}^2 L}{E} \right) \\ &+ 2 (-|U_{\alpha 4}| |U_{\beta 4}| \sin \phi_{54} + |U_{\alpha 6}| |U_{\beta 6}| \sin \phi_{65}) \\ &\times |U_{\alpha 5}| |U_{\beta 5}| \sin \left( \frac{2.53 \Delta m_{51}^2 L}{E} \right) \\ &+ 2 (-|U_{\alpha 4}| |U_{\beta 4}| \sin \phi_{64} - |U_{\alpha 5}| |U_{\beta 5}| \sin \phi_{65}) \\ &\times |U_{\alpha 6}| |U_{\beta 6}| \sin \left( \frac{2.53 \Delta m_{61}^2 L}{E} \right). \end{aligned} \quad (9)$$

CP violation appears in (9) in the form of the three phases defined by

$$\begin{aligned} \phi_{54} &= \arg(U_{e5} U_{\mu 5}^* U_{e4}^* U_{\mu 4}), \\ \phi_{64} &= \arg(U_{e6} U_{\mu 6}^* U_{e4}^* U_{\mu 4}), \\ \phi_{65} &= \arg(U_{e6} U_{\mu 6}^* U_{e5}^* U_{\mu 5}). \end{aligned} \quad (10)$$

In each case,  $\nu \rightarrow \bar{\nu}$  implies  $\phi \rightarrow -\phi$ . In the case of disappearance ( $\alpha = \beta$ ), the survival probability can be rewritten as the following:

$$\begin{aligned} P(\nu_\alpha \rightarrow \nu_\alpha) &\simeq 1 - 4 |U_{\alpha 4}|^2 |U_{\alpha 5}|^2 \sin^2 \left( \frac{1.27 \Delta m_{54}^2 L}{E} \right) \\ &- 4 |U_{\alpha 4}|^2 |U_{\alpha 6}|^2 \sin^2 \left( \frac{1.27 \Delta m_{64}^2 L}{E} \right) \\ &- 4 |U_{\alpha 5}|^2 |U_{\alpha 6}|^2 \sin^2 \left( \frac{1.27 \Delta m_{65}^2 L}{E} \right) \\ &- 4 (1 - |U_{\alpha 4}|^2 - |U_{\alpha 5}|^2 - |U_{\alpha 6}|^2) \\ &\times \left( |U_{\alpha 4}|^2 \sin^2 \left( \frac{1.27 \Delta m_{41}^2 L}{E} \right) + |U_{\alpha 5}|^2 \sin^2 \left( \frac{1.27 \Delta m_{51}^2 L}{E} \right) + |U_{\alpha 6}|^2 \sin^2 \left( \frac{1.27 \Delta m_{61}^2 L}{E} \right) \right). \end{aligned} \quad (11)$$

This formula has no  $\phi_{ij}$  dependencies because CP violation only affects appearance.

We have discussed the formulas for (3 + 1) and (3 + 2) oscillations that arise from (7) in previous papers [20–22]. To reduce to a (3 + 2) model, the parameters  $\Delta m_{61}^2$ ,  $|U_{e6}|$ ,  $|U_{\mu 6}|$ ,  $\phi_{64}$ , and  $\phi_{65}$  are explicitly set to zero; consequently, we have

the following appearance and disappearance formulas for a (3 + 2) model:

$$\begin{aligned}
P(\nu_\alpha \rightarrow \nu_\beta) & \simeq -4 |U_{\alpha 5}| |U_{\beta 5}| |U_{\alpha 4}| |U_{\beta 4}| \cos \phi_{54} \sin^2 \left( \frac{1.27 \Delta m_{54}^2 L}{E} \right) \\
& + 4 (|U_{\alpha 4}| |U_{\beta 4}| + |U_{\alpha 5}| |U_{\beta 5}| \cos \phi_{54}) \\
& \times |U_{\alpha 4}| |U_{\beta 4}| \sin^2 \left( \frac{1.27 \Delta m_{41}^2 L}{E} \right) \\
& + 4 (|U_{\alpha 4}| |U_{\beta 4}| \cos \phi_{54} + |U_{\alpha 5}| |U_{\beta 5}|) \\
& \times |U_{\alpha 5}| |U_{\beta 5}| \sin^2 \left( \frac{1.27 \Delta m_{51}^2 L}{E} \right) \\
& + 2 |U_{\beta 5}| |U_{\alpha 5}| |U_{\beta 4}| |U_{\alpha 4}| \sin \phi_{54} \sin \left( \frac{2.53 \Delta m_{54}^2 L}{E} \right) \\
& + 2 (|U_{\alpha 5}| |U_{\beta 5}| \sin \phi_{54}) |U_{\alpha 4}| |U_{\beta 4}| \sin \left( \frac{2.53 \Delta m_{41}^2 L}{E} \right) \\
& + 2 (-|U_{\alpha 4}| |U_{\beta 4}| \sin \phi_{54}) |U_{\alpha 5}| |U_{\beta 5}| \sin \left( \frac{2.53 \Delta m_{51}^2 L}{E} \right), \\
P(\nu_\alpha \rightarrow \nu_\alpha) & \simeq 1 - 4 |U_{\alpha 4}|^2 |U_{\alpha 5}|^2 \sin^2 \left( \frac{1.27 \Delta m_{54}^2 L}{E} \right) \\
& - 4 (1 - |U_{\alpha 4}|^2 - |U_{\alpha 5}|^2) \\
& \times \left( |U_{\alpha 4}|^2 \sin^2 \left( \frac{1.27 \Delta m_{41}^2 L}{E} \right) \right. \\
& \left. + |U_{\alpha 5}|^2 \sin^2 \left( \frac{1.27 \Delta m_{51}^2 L}{E} \right) \right). \tag{12}
\end{aligned}$$

For a (3 + 1) model,  $\Delta m_{61}^2$ ,  $\Delta m_{51}^2$ ,  $|U_{e6}|$ ,  $|U_{\mu 6}|$ ,  $|U_{e5}|$ ,  $|U_{\mu 5}|$ ,  $\phi_{64}$ ,  $\phi_{65}$ , and  $\phi_{54}$  should be set to zero. This further simplifies the oscillation probabilities, and one recovers the familiar two-neutrino appearance and disappearance probabilities. The appearance and disappearance formulas for a (3 + 1) model are then given by the following:

$$\begin{aligned}
P(\nu_\alpha \rightarrow \nu_\beta) & \simeq 4 |U_{\alpha 4}|^2 |U_{\beta 4}|^2 \sin^2 \left( \frac{1.27 \Delta m_{41}^2 L}{E} \right), \\
P(\nu_\alpha \rightarrow \nu_\alpha) & \simeq 1 - 4 (1 - |U_{\alpha 4}|^2) |U_{\alpha 4}|^2 \sin^2 \left( \frac{1.27 \Delta m_{41}^2 L}{E} \right). \tag{13}
\end{aligned}$$

In principle, the probability for neutrino oscillation is modified in the presence of matter. ‘‘Matter effects’’ arise because the electron neutrino flavor experiences both Charged-Current (CC) and Neutral-Current (NC) elastic forward scattering with electrons as it propagates through matter, while the  $\nu_\mu$  and  $\nu_\tau$  experience only NC forward-scattering. The sterile component experiences no forward-scattering. In practice, SM-inspired matter effects are very small given the short baselines of the experiments, and so we do not consider them further here. Beyond-SM matter effects are beyond the scope of this paper, but are considered in [38].

### 3. Experimental Datasets

This section provides an overview of the various types of past and current neutrino sources and detectors used in SBL experiments. After introducing the experimental concepts, the specific experimental datasets used in this analysis are discussed.

The data fall into two overall categories: disappearance, where the active flavor is assumed to have oscillated into a sterile neutrino and/or another flavor which is kinematically not allowed to interact or leaves no detectable signature, and appearance, where the transition is between active flavors, but with mass splittings corresponding to the mostly sterile states. Appearance and disappearance are natural divisions for testing the compatibility of datasets. If  $|U_{\alpha 4}|^2$  and  $|U_{\beta 4}|^2$  are shown to be small, then the effective mixing angle for appearance,  $4|U_{\alpha 4}|^2 |U_{\beta 4}|^2$ , cannot be large. This constraint that the disappearance experiments place on appearance experiments extends to (3 + 2) and (3 + 3) models also.

CPT conservation, which is assumed in the analysis, demands that neutrino and antineutrino disappearance probabilities are the same after accounting for CP violating effects. To test this, we divide the data into antineutrino and neutrino sets and fit each set separately. If CP violation is already allowed in the oscillation formalism, then any incompatibility found between respective neutrino and antineutrino fits could imply effective CPT violation, as discussed in [22].

Figures 1, 2, and 3 provide summaries of the datasets, showing the constraints they provide in a simple two-neutrino oscillation model, which is functionally equivalent to the (3 + 1) scenario. Figure 1 shows the muon-to-electron flavor datasets in neutrino and antineutrino mode at 95% confidence level (CL). Figures 2 and 3 show results for  $\nu_\mu$  and  $\bar{\nu}_\mu$ , and  $\nu_e$  and  $\bar{\nu}_e$  disappearance, respectively.

**3.1. Sources and Detectors Used in Short-Baseline Neutrino Experiments.** Before considering the datasets in detail, we provide an overview of how SBL experiments are typically designed.

**3.1.1. Sources of Neutrinos for Short-Baseline Experiments.** The neutrino sources used in SBL experiments range in energy from a few MeV to hundreds of GeV and include man-made radioactive sources, reactors, and accelerator-produced beams. While the higher energy accelerator sources are

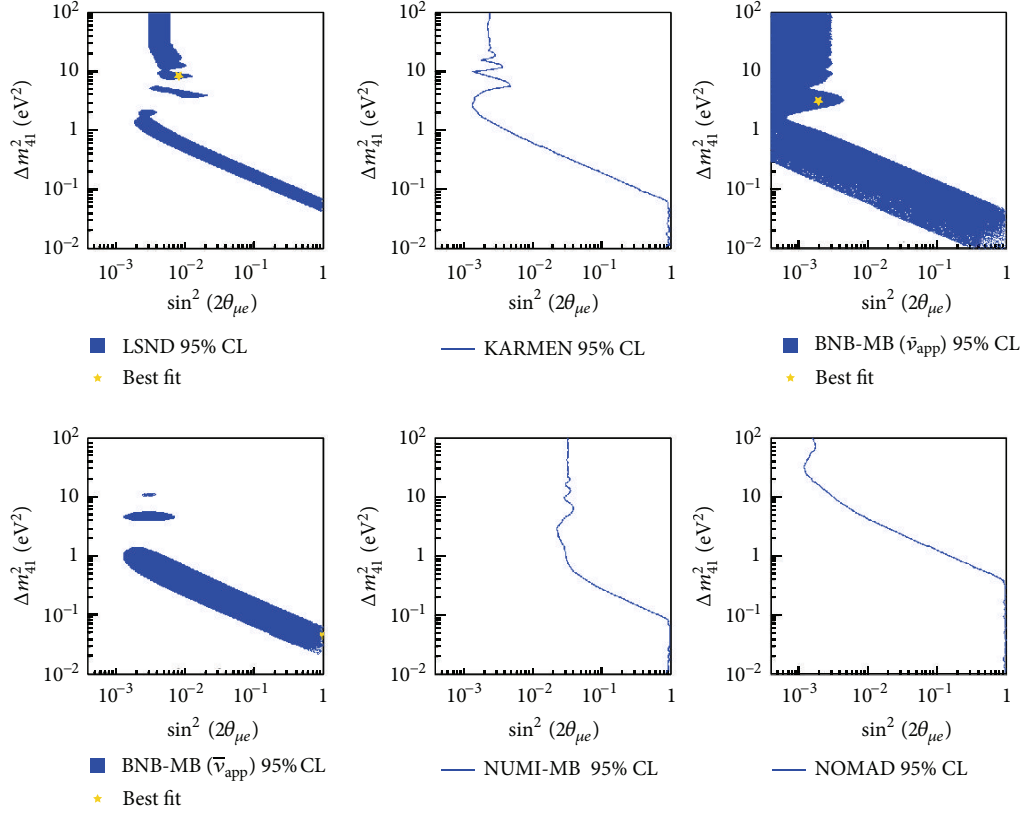


FIGURE 1: Summary of  $\bar{\nu}_\mu \rightarrow \bar{\nu}_e$  and  $\nu_\mu \rightarrow \nu_e$  results, shown at 95% CL. Top row: LSND, KARMEN, BNB-MB( $\nu_{\text{app}}$ ); bottom row: BNB-MB( $\bar{\nu}_{\text{app}}$ ), NuMI-MB( $\nu_{\text{app}}$ ), NOMAD. See Section 3.2 for details and references.

mixtures of different neutrino flavors, the  $<10$  MeV sources rely on beta decay and are thus pure electron neutrino flavor.

At the low-energy end of the spectrum, the rate of electron neutrino interactions from the beta decay of the  $\sim 1$  MCi sources  $^{51}\text{Cr}$  (half-life: 28 days) and  $^{37}\text{Ar}$  (half-life: 35 days) have been studied. These sources were originally produced for the low-energy ( $\sim 1$  MeV) calibration of solar neutrino detectors [39, 40] but have proven themselves interesting as a probe of electron neutrino disappearance.

Moving up in energy by a few MeV, nuclear reactors are powerful sources of  $\sim 2\text{--}8$  MeV  $\bar{\nu}_e$  through the  $\beta^+$ -decaying elements produced primarily in the decay chains of  $^{235}\text{U}$ ,  $^{239}\text{Pu}$ ,  $^{238}\text{U}$ , and  $^{241}\text{Pu}$ . While these four isotopes are the progenitors of most of the reactor flux, modern reactor simulations include all fission sources [41]. Reactor simulations convolute predictions of fission rates over time with neutrino production per fission. Recently, a reanalysis of the production cross-section per fission [23, 42, 43] has led to an increase in the predicted reactor flux. As their energy is too low for an appearance search (the neutrino energy is below the muon production kinematic threshold), reactor source antineutrinos can only be used for  $\bar{\nu}_e$  disappearance searches, where the antineutrinos are detected using CC interactions with an outgoing  $e^+$ .

The lowest neutrino energy (up to 53 MeV) accelerator sources used in existing SBL experiments are based on pion- and muon-decay-at-rest (DAR). The neutrino flux comes

from the stopped pion decay chain:  $\pi^+ \rightarrow \mu^+ \nu_\mu$  and  $\mu^+ \rightarrow e^+ \bar{\nu}_\mu \nu_e$ . Pions are produced in interactions of accelerator protons with, typically, a graphite or water target. The contribution from the decay chain  $\pi^- \rightarrow \mu^- \bar{\nu}_\mu$  is suppressed by designing the target such that the  $\pi^-$  mesons are captured with high probability. The result is a source which has a well-understood neutrino flavor content and energy distribution, with a minimal ( $<10^{-3}$ )  $\bar{\nu}_e$  content [44, 45]. This last point is important as  $\bar{\nu}_\mu \rightarrow \bar{\nu}_e$  is the dominant channel used for oscillation searches by DAR sources.

In a conventional high-energy (from  $\sim 100$  MeV to hundreds of GeV) accelerator-based neutrino beam, protons impinge on a target (beryllium and carbon are typical) to produce secondary mesons. The boosted mesons enter and subsequently decay inside a long, often evacuated, pipe. Neutrinos are primarily produced by  $\pi^+$  and  $\pi^-$  decay in flight (DIF). Pion sign selection, via a large magnet placed directly in the beamlines before the decay pipe, allows for nearly pure neutrino or antineutrino running, with only a few percent “wrong sign” neutrino flux content in the case of neutrino running, and  $\sim 15\%$  [46] in the case of antineutrino running. These beams are generally produced by protons at 8 GeV and above. At these energies, in addition to pion production, kaon production contributes to the flux of both muon and electron neutrino flavors. There is often a substantial muon DIF content as well, contributing both  $\nu_e/\bar{\nu}_e$  and  $\bar{\nu}_\mu/\nu_\mu$  to the beam. The result of the kaon and muon secondary



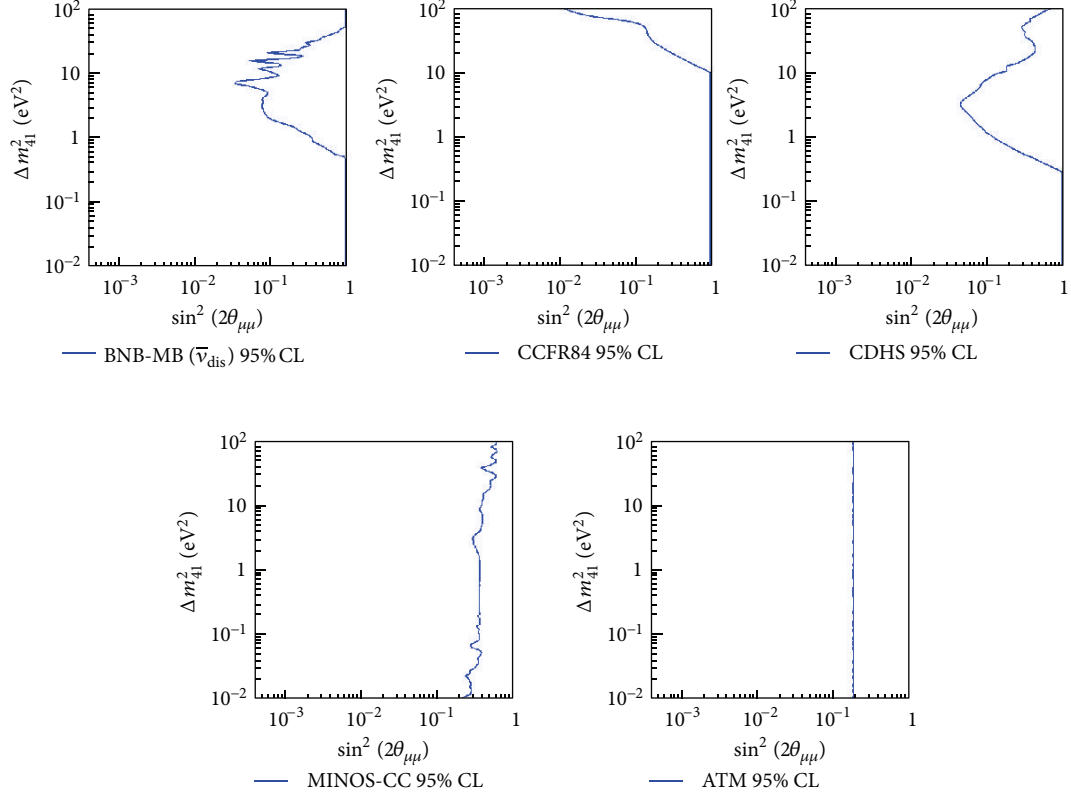


FIGURE 2: Summary of  $\bar{\nu}_\mu \rightarrow \bar{\nu}_\mu$  and  $\nu_\mu \rightarrow \nu_\mu$  results, shown at 95% CL. Top row: BNB-MB( $\nu_{\text{dis}}$ ), CCFR84, CDHS; bottom row: MINOS-CC, ATM. See Section 3.2 for details and references.

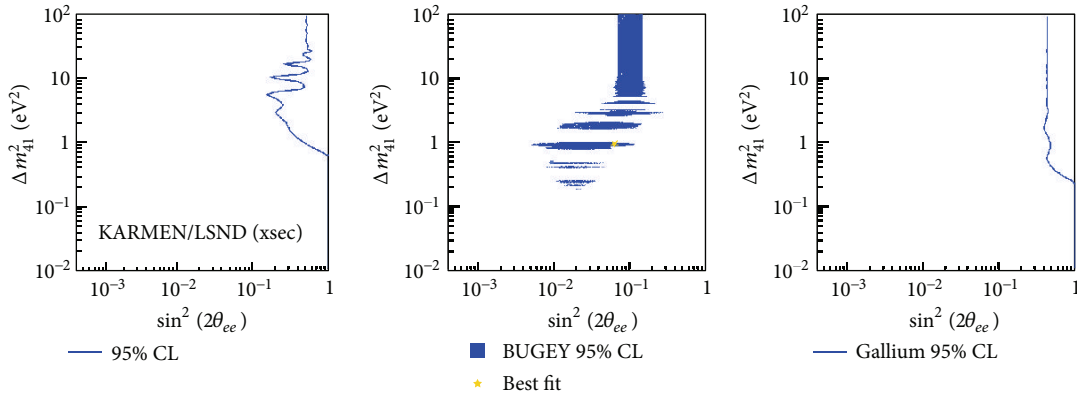


FIGURE 3: Summary of  $\bar{\nu}_e \rightarrow \bar{\nu}_e$  and  $\nu_e \rightarrow \nu_e$  results, shown at 95% CL. From left: KARMEN/LSND(xsec), Bugey, and Gallium. See Section 3.2 for details and references.

content is that, while the neutrinos are predominantly muon flavored, the beam will always have some intrinsic electron flavor neutrino content, usually at the several percent level. Accelerator-based beams are predominantly used for  $\nu_\mu \rightarrow \nu_e$  and  $\bar{\nu}_\mu \rightarrow \bar{\nu}_e$  appearance searches, as well as  $\nu_\mu$  and  $\bar{\nu}_\mu$  disappearance searches. An excellent review of methods in producing accelerator-based neutrino beams can be found in [47].

In contrast to lower-energy neutrino sources (DAR, reactor, and isotope sources), high-energy accelerator-based

neutrino sources are subject to significant energy-dependent neutrino flux uncertainties, often at the level of 10–15%, due to in-target meson production uncertainties. These uncertainties can affect the energy distribution, flavor content, and absolute normalization of a neutrino beam. Typically, meson production systematics are constrained with dedicated measurements by experiments such as HARP [48] and MIPP [49], which use replicated targets (geometry and material) and a wide range of proton beam energies to study meson production cross-sections and kinematics directly. Alternatively,

experiments can employ a two-detector design for comparing near-to-far event rate in energy to effectively reduce these systematics. However, due to the short baselines employed for studying sterile neutrino oscillations, a two-detector search is often impractical. In situ measurements in single-detector experiments can exploit flux (multiplied by cross-section) correlations among different beam components and energies to reduce flux uncertainties, as has been done in the case of the MiniBooNE  $\nu_e$  and  $\bar{\nu}_e$  appearance searches described below.

**3.1.2. Short-Baseline Neutrino Detectors.** Because low-energy neutrino interaction cross-sections are very small, the options for SBL detectors are typically limited to designs which can be constructed on a massive scale. There are several generic neutrino detection methods in use today: unsegmented scintillator detectors, unsegmented Cerenkov detectors, segmented scintillator-and-iron calorimeters, and segmented trackers.

Neutrino oscillation experiments usually require sensitivity to CC neutrino interactions, whereby one can definitively identify the flavor of the interacting neutrino by the presence of a charged lepton in the final state. However, in the case of sterile neutrino oscillation searches, NC interactions can also provide useful information, as they are directly sensitive to the sterile flavor content of the neutrino mass eigenstate,  $|U_{si}|^2 = 1 - |U_{ei}|^2 - |U_{\mu i}|^2 - |U_{\tau i}|^2$ .

Unsegmented scintillator detectors are typically used for few-MeV-scale SBL experiments, which require efficient electron neutrino identification and reconstruction. These detectors consist of large tanks of oil-based ( $C_nH_{2n}$ ) liquid scintillator surrounded by phototubes. The free protons in the oil provide a target for the inverse beta decay interaction,  $\bar{\nu}_e p \rightarrow e^+ n$ . The reaction threshold for this interaction is 1.8 MeV due to the mass difference between the proton and neutron and the mass of the positron. The scintillation light from the  $e^+$ , as well as light from the Compton scattering of the 0.511 MeV annihilation photons provides an initial (“prompt”) signal. This is followed by  $n$  capture on hydrogen and a 2.2 MeV flash of light, as the resulting  $\gamma$  Compton-scatters in the scintillator. This coincidence sequence in time (positron followed by neutron capture) provides a clean, mostly background-free interaction signature. Experiments often dope the liquid scintillator using an element with a high neutron capture cross-section for improved event identification efficiency.

The CC interaction with the carbon in the oil (which produces either nitrogen or boron depending on whether the scatterer is a neutrino or antineutrino) has a significantly higher energy threshold than the free proton target-scattering process. The CC quasielastic interaction  $\nu_e + C \rightarrow e^- + N$  has an energy threshold of 17.3 MeV, which arises from the carbon-nitrogen mass difference and the mass of the electron. In the case of both reactor and radioactive decay sources, the flux cuts off below this energy threshold. However, neutrinos from DAR sources are at sufficiently high energy to produce these carbon scatters.

Unsegmented Cerenkov detectors make use of a target which is a large volume of clear medium (undoped oil or

water is typical) surrounded by, or interspersed with, phototubes. Undoped oil has a larger refractive index, leading to a larger Cerenkov opening angle. Water is the only affordable medium once the detector size surpasses a few kilotons. In this paper, the only unsegmented Cerenkov detector that is considered is the 450-ton oil-based MiniBooNE detector. In such a detector, a track will project a ring with a sharp inner and outer edge onto the phototubes. Consider an electron produced in a  $\nu_e$  CC quasielastic interaction. As the electron is low mass, it will multiple-scatter and easily bremsstrahlung, smearing the light projected on the tubes and producing a “fuzzy” ring. A muon produced by a CC quasielastic  $\nu_\mu$  interaction ( $\nu_\mu n \rightarrow \mu^- p$ ) is heavier and will thus produce a sharper outer edge to the ring. For the same visible energy, the track will also extend farther, filling the interior of the ring and, perhaps, exiting the tank. If the muon stops within the tank and subsequently decays, the resulting electron provides an added tag for particle identification. In the case of the  $\mu^-$ , 18% will capture in water and, thus, have no electron tag, while only 8% will capture in the oil.

Scintillator and iron calorimeters provide an affordable detection technique for  $\sim 1$  GeV and higher  $\nu_\mu$  interactions. At these energies, multiple hadrons may be produced at the interaction vertex and will be observed as hadronic showers. In these devices, the iron provides the target, while the scintillator provides information on energy deposition per unit length. This information allows separation between the hadronic shower, which occurs in both NC and CC events, and the minimum-ionizing track of an outgoing muon, which occurs in CC events. Transverse information can be obtained if segmented scintillator strips are used, or if drift chambers are interspersed. The light from scintillator strips is transported to tubes by wavelength-shifting fibers. Information in the transverse plane improves separation of electromagnetic and hadronic showers. The iron can be magnetized to allow separation of neutrino and antineutrino events based on the charge of the outgoing lepton.

To address the problem of running at  $\sim 1$  GeV, where hadron track reconstruction is desirable, highly segmented tracking designs have been developed. The best resolution comes from stacks of wire chambers, where the material enclosing the gas provides the target. However, a more practical alternative has been stacks of thin extruded scintillator bars that are read out using wavelength-shifting fibers.

**3.2. Data Used in the Sterile Neutrino Fits.** There are many SBL datasets that can be included in this analysis. In this work, we have substantially expanded the number of datasets used beyond those in our past papers [20–22]. In the sections following, we identify and discuss new and updated datasets, as well as provide information on those used in past fits. The fit technique is described in Section 4.2.

**3.2.1. Experimental Results from Decay at Rest Studies.** In past sterile neutrino studies [20–22], we have included the LSND and KARMEN appearance results described below. Since that work, a new study that constrains  $\nu_e$  disappearance from the relative LSND-to-KARMEN cross-section measurements

was published [50]. This new dataset is included in this analysis.

*LSND Appearance.* LSND was a DAR experiment that ran in the 1990s, searching for  $\bar{\nu}_\mu \rightarrow \bar{\nu}_e$ . The beam was produced using 800 MeV protons on target from the LAMPF accelerator at Los Alamos National Laboratory, where a 1 mA beam of protons impinged on a water target. The center of the 8.75 m long, nearly cylindrical detector, was located at 29.8 m from the target, at an angle of  $12^\circ$  from the proton beam direction. This was an unsegmented detector with a fiducial mass of 167 tons of oil ( $\text{CH}_2$ ), lightly doped with b-PBD scintillator. The intrinsic  $\bar{\nu}_e$  content of the beam was  $8 \times 10^{-4}$  of the  $\bar{\nu}_\mu$  content. The experiment observed a  $\bar{\nu}_e$  excess of  $87.9 \pm 22.4 \pm 6.0$  events above background, which was interpreted as oscillations with a probability of  $(0.264 \pm 0.067 \pm 0.045)\%$ . Details are available in [17].

This dataset is referred to as LSND in the analysis below and indicates a signal at 95% CL, as shown in Figure 1. This data covers energies between 20 and 53 MeV and contributes five energy bins to the global fit. Statistical errors are taken into account by using a log-likelihood  $\chi^2$  definition in the fit, while systematic errors on the background prediction are not included because these are small relative to the statistical error. Energy and baseline smearing are taken into account by averaging the oscillation probability over the energy bin width and over the neutrino flight path uncertainty.

*KARMEN Appearance.* KARMEN was another DAR experiment searching for  $\bar{\nu}_\mu \rightarrow \bar{\nu}_e$ . KARMEN ran at the ISIS facility at Rutherford Laboratory, with 200  $\mu\text{A}$  of protons impinging on a copper, tantalum, or uranium target. The neutrino detector was located at an angle of  $100^\circ$  with respect to the targeting protons to reduce background from  $\pi^-$  DIF. The resulting intrinsic  $\bar{\nu}_e$  content was  $6.4 \times 10^{-4}$  of the  $\bar{\nu}_\mu$  content.

The center of the approximately cubic segmented scintillator detector was located at 17.7 m. Thus, this detector was 60% of the distance from the source compared to LSND. The liquid scintillator target volume was 56  $\text{m}^3$  and consisted of 512 optically independent modules (17.4 cm  $\times$  17.8 cm  $\times$  353 cm) wrapped in gadolinium-doped paper. KARMEN saw no signal and set a limit on appearance. More details are available in [51].

This dataset is referred to as KARMEN in the analysis below and indicates a limit at 95% CL, as shown in Figure 1. This dataset contributes nine energy bins, in the range 16 to 50 MeV. As in the case of LSND, statistical errors are taken into account by using a log-likelihood  $\chi^2$  definition in the fit, while systematic errors on the background prediction are not included. Energy and baseline smearing are taken into account by averaging the  $\sin^2(1.27\Delta m^2 L/E)$  and  $\sin(2.53\Delta m^2 L/E)$  term contributions in the total signal prediction over energy bin widths. The limit which is shown here is determined using a  $\Delta\chi^2$ -based raster scan, as discussed in Section 4.2.

*LSND and KARMEN Cross-Section Measurements.* Along with the oscillation searches, LSND and KARMEN measured

$\nu_e + {}^{12}\text{C} \rightarrow {}^{12}\text{N}_{\text{gs}} + e^-$  scattering. In this two-body interaction, with a  $Q$ -value of 17.3 MeV, the neutrino energy can be reconstructed by measuring the outgoing visible energy of the electron. The  ${}^{12}\text{N}$  ground state is identified by the subsequent  $\beta$  decay,  ${}^{12}\text{N}_{\text{gs}} \rightarrow {}^{12}\text{C} + e^+ + \nu_e$ , which has a  $Q$ -value of 16.3 MeV and a lifetime of 15.9 ms.

The cross-section is measured by both experiments under the assumption that the  $\nu_e$  flux has not oscillated, leading to disappearance. The excellent agreement between the two results, as a function of energy, allows a limit to be placed on  $\nu_e$  oscillations. The energy dependence of the cross-section, as well as the normalization, are well predicted and both constraints are used in the analysis [50].

This dataset is referred to as KARMEN/LSND(xsec) in the analysis below, and indicates a limit at 95% CL, as shown in Figure 3. A total of six (for KARMEN) plus five (for LSND) bins are used in the fit, which extend approximately from 28–50 MeV in the case of KARMEN and from 38–50 MeV in the case of LSND. In calculating the oscillation probability, the signal is averaged across the lengths of the detectors. The experiments have correlated systematics arising from the flux normalization due to a shared underlying analysis for pion production in DAR experiments. This is addressed through application of pull terms as described in [50].

*3.2.2. The MiniBooNE Experimental Results.* The MiniBooNE experiment provides multiple results from a single detector. This oil-based 450 t fiducial volume Cerenkov detector was exposed to two conventional beams, the Booster Neutrino Beam (BNB) and the off-axis NuMI beam. The primary goal of MiniBooNE was to search for  $\nu_\mu \rightarrow \nu_e$  and  $\bar{\nu}_\mu \rightarrow \bar{\nu}_e$  appearance, using the BNB, which provides sensitivity to  $\Delta m^2 \sim 0.1\text{--}10 \text{ eV}^2$  oscillations. The NuMI beam also provides some sensitivity to  $\nu_\mu \rightarrow \nu_e$  appearance at a similar  $\Delta m^2$ . In addition to the appearance searches, MiniBooNE also looked for  $\nu_\mu$  and  $\bar{\nu}_\mu$  disappearance using the BNB.

The MiniBooNE datasets included in our analysis have increased throughout the period that our group has been performing fits. Reference [21] used a Monte Carlo prediction for neutrinos and antineutrinos to estimate MiniBooNE's sensitivity to sterile neutrinos. The full BNB neutrino and first published BNB antineutrino datasets from MiniBooNE form the experimental constraints in [22]. Here, we have updated the analysis to include the full BNB antineutrino datasets. A further update has been to employ a log-likelihood method for the BNB neutrino and antineutrino datasets from [18], as this was recently adopted by the MiniBooNE Collaboration [52]. We also use the updated constraints on electron neutrino flux from kaons [18]. A partial dataset from NuMI data taking was presented in [22] and has not been updated, as the result was already systematics limited. In this analysis we also introduce the MiniBooNE disappearance search [53].

In our fits to MiniBooNE appearance data, when drawing allowed regions and calculating compatibilities, which make use of  $\Delta\chi^2$ 's and not absolute  $\chi^2$ 's, we use MiniBooNE's log-likelihood  $\chi^2$  definition, summing over both  $\nu_e$  and  $\nu_\mu$  bins, as described in [52]. For consistency, the absolute MiniBooNE

BNB  $\nu_e$  and  $\bar{\nu}_e$  appearance  $\chi^2$  values quoted in our paper also correspond to the same definition, that is, fitting to both  $\nu_e$  and  $\nu_\mu$  spectra; therefore, they differ from the ones published by MiniBooNE in [18], which are obtained by fitting only to a priori constrained  $\nu_e$  distributions. Note that the two definitions yield consistent allowed regions and compatibility results.

*The Booster Neutrino Beam Appearance Search in Neutrino Running Mode.* The BNB flux composition in neutrino mode consists of  $>90\%\nu_\mu$ ,  $6\%\bar{\nu}_\mu$ , and  $0.06\%\nu_e$  and  $\bar{\nu}_e$  combined [46]. In the MiniBooNE BNB search for  $\nu_e$  appearance, the  $\nu_e$  and  $\bar{\nu}_e$  signal was normalized to the  $\nu_\mu$  and  $\bar{\nu}_\mu$  CC quasielastic events observed in the detector, which peaked at 700 MeV.

The global fits presented here use the full statistics of the MiniBooNE  $\nu_\mu \rightarrow \nu_e$  dataset, representing  $6.46 \times 10^{20}$  protons on target. In this dataset, MiniBooNE has observed an excess of events at 200–1250 MeV, corresponding to  $162.0 \pm 47.8$  electron-like events [18]. The dataset is referred to as BNB-MB( $\nu_{\text{app}}$ ) in the analysis below.

We include the BNB-MB( $\nu_{\text{app}}$ ) dataset in our fits in the form of the full  $\nu_e$  CC reconstructed energy distribution, in 11 energy bins from 200 to 3000 MeV, fit simultaneously with the full  $\nu_\mu$  CC energy distribution, in eight energy bins up to 1900 MeV. We account for statistical and systematic uncertainties in each sample, as well as systematic correlations (from flux and cross-section) among the  $\nu_e$  signal and background and  $\nu_\mu$  background distributions. The systematic correlations are provided in the form of a full 19-bin  $\times$  19-bin fractional covariance matrix. By fitting the  $\nu_e$  and  $\nu_\mu$  spectra simultaneously, we are able to exploit the high-statistics  $\nu_\mu$  CC sample as a constraint on background and signal event rates. This assumes no significant  $\nu_\mu$  disappearance; this simplification could lead to a  $<20\%$  effect on appearance probability obtained in MiniBooNE only fits [18].

The dataset results in a signal at 95% CL, as shown in Figure 1. This has changed slightly from our past analysis [22] now that we are using updated constraints on intrinsic electron neutrinos from kaons and the log-likelihood method, but is in agreement with the equivalent analysis from the MiniBooNE Collaboration [18].

*The Booster Neutrino Beam Appearance Search in Antineutrino Running Mode.* The BNB flux composition in antineutrino mode consists of  $83\%\bar{\nu}_\mu$ ,  $0.6\%\nu_e$  and  $\bar{\nu}_e$  combined, and a significantly larger wrong-sign composition than in neutrino mode, of  $16\%\nu_\mu$ . As in the BNB  $\nu_e$  appearance search, the electron flavor signal was normalized to the muon flavor CC quasielastic events observed in the detector, which peaked at 500 MeV.

The global fits presented here use the full statistics of the MiniBooNE  $\bar{\nu}_\mu$  dataset, representing  $11.27 \times 10^{20}$  protons on target. In this dataset, MiniBooNE has observed an excess of events at 200–1250 MeV, corresponding to  $78.4 \pm 28.5$  electron-like events. The dataset is referred to as BNB-MB( $\bar{\nu}_{\text{app}}$ ) in the analysis below.

As in neutrino mode, we fit the full  $\bar{\nu}_e$  CC energy distribution, in 11 energy bins from 200 to 3000 MeV, simultaneously

with the full  $\bar{\nu}_\mu$  CC energy distribution, in 8 energy bins up to 1900 MeV. The wrong-sign contamination in the beam ( $\nu_\mu$ ) is assumed to not contribute to any oscillations; only  $\bar{\nu}_\mu \rightarrow \bar{\nu}_e$  oscillations are assumed for this dataset. We account for statistical and systematic uncertainties in each sample as well as systematic correlations among the  $\bar{\nu}_e$  and  $\bar{\nu}_\mu$  distributions in the form of a full 19-bin  $\times$  19-bin fractional covariance matrix in each fit. For further information, see [18].

The dataset results in a signal at 95% CL, as shown in Figure 1.

*The NuMI Beam Appearance Search.* The MiniBooNE detector is also exposed to the NuMI neutrino beam, produced from a 120 GeV proton beam impinging on a carbon target. This beam is nominally used for the MINOS long-baseline neutrino oscillation experiment. NuMI events arrive out of time with the BNB-produced events. This 200 MeV to 3 GeV neutrino energy source is dominated by kaon decays near the NuMI target, which is 110 mrad off-axis and located 745 m upstream of the MiniBooNE detector. The beam consists of  $81\%\nu_\mu$ ,  $13\%\bar{\nu}_\mu$ ,  $5\%\nu_e$ , and  $1\%\bar{\nu}_e$ . For more information on this data, see [54].

This dataset is referred to as NuMI-MB( $\nu_{\text{app}}$ ) in the analysis below. As seen in Figure 1, the dataset provides a limit at 95% CL. In the fits presented here, this data is used to constrain electron flavor appearance in neutrino mode, with 10 bins used in the fit. Statistical and systematic errors for this dataset are added in quadrature.

*The Booster Neutrino Beam Disappearance Search.* The MiniBooNE experiment also searched for  $\nu_\mu$  and  $\bar{\nu}_\mu$  disappearance using the BNB. The neutrino (antineutrino) dataset corresponded to  $5.6 \times 10^{20}$  ( $3.4 \times 10^{20}$ ) protons on target, which produced a beam covering the neutrino energy range up to 1.9 GeV. The MiniBooNE  $\nu_\mu$  disappearance result provides restrictions on sterile neutrino oscillations which are comparable to those provided by the CDHS experiment, discussed below. Therefore, we include that dataset in these fits. On the other hand, the  $\bar{\nu}_\mu$  result was weaker due to the combination of fewer protons on target and a lower cross-section. The MINOS  $\bar{\nu}_\mu$  CC constraint, described below, is stronger, and so we do not use the MiniBooNE  $\bar{\nu}_\mu$  dataset.

The fit to the  $\nu_\mu$  dataset uses 16 bins ranging up to 1900 MeV in reconstructed neutrino energy. A shape-only fit is performed, where the predicted spectrum given any set of oscillation parameters is renormalized so that the total number of predicted events, after oscillations, is equal to the total number of observed events. Then the normalized predicted spectrum is compared to the observed spectrum in the form of a  $\chi^2$  which accounts for statistical and shape-only systematic uncertainties and bin-to-bin correlations in the form of a covariance matrix.

This dataset is referred to as BNB-MB( $\nu_{\text{dis}}$ ) in the analysis below. Figure 2 shows that this data sets a limit at 95% CL. It should be noted that the published MiniBooNE analysis used a Pearson  $\chi^2$  method [53], and we are able to reproduce those results. However, to fold these results into our analysis,



we reverted to the  $\Delta\chi^2$  definition used consistently among all datasets included in the fits (see Section 4.2).

**3.2.3. Results from Multi-GeV Conventional Short-Baseline  $\nu_\mu$  Beams.** The set of multi-GeV conventional SBL  $\nu_\mu$  experiments is the same as was used in previous fits. Our overview of these experiments is therefore very brief.

**NOMAD Appearance Search.** The NOMAD experiment [55], which ran at CERN using protons from the 450 GeV SPS accelerator, employed a conventional neutrino beamline to create a wideband 2.5 to 40 GeV neutrino energy source. These neutrinos were created with a carbon-based, low-mass tracking detector located 600 m downstream of the target. This detector had fine spatial resolution and could search for muon-to-electron and muon-to-tau oscillations. No signal was observed in either channel. In this analysis, we use the  $\nu_\mu \rightarrow \nu_e$  constraint.

This dataset is referred to as NOMAD in the analysis below. This dataset contributes 30 energy bins to the global fit. The statistical and systematic errors are added in quadrature. This experiment sets a limit at 95% CL, as seen in Figure 1.

**CCFR Disappearance Search.** The CCFR dataset was taken at Fermilab in 1984 [56] with a narrowband beamline, with meson energies set to 100, 140, 165, 200, and 250 GeV, yielding  $\nu_\mu$  and  $\bar{\nu}_\mu$  beams that ranged from 40 to 230 GeV in energy. This was a two-detector disappearance search, with the near detector at 715 m and the far detector at 1116 m from the center of the 352 m long decay pipe. The calorimetric detectors were constructed of segmented iron with scintillator and spark chambers, and each had a downstream toroid to measure the muon momentum.

This dataset is referred to as CCFR84 in the analysis below. The data were published as the double ratios of the observed-to-expected rates in a near-to-far ratio. For each secondary mean setting, the data are divided into three energy bins. The systematic uncertainty is assumed to be energy independent and fully correlated between the energy bins. Due to the high beam energies and short baselines, this experiment sets a limit at high  $\Delta m^2$  in the muon flavor disappearance search at 95% CL, as shown in Figure 2.

**CDHS Disappearance Search.** The CDHS experiment [57] at CERN searched for  $\nu_\mu$  disappearance with a two-detector design of segmented calorimeters with iron and scintillator. The experiment used 19.2 GeV protons on a beryllium target to produce mesons that were subsequently focused into a 52 m decay channel. The detectors were located 130 m and 885 m downstream of the target.

This dataset is referred to as CDHS in the analysis below. CDHS provides data and errors in 15 bins of muon energy, as seen in Table 1 of [57]. We relate these bins to the neutrino energy distributions using the method described in [20]: the neutrino energy distribution for a given muon energy or range is determined via the NUANCE [58] neutrino event generator. The experiment has a limit at 95% CL and sets constraints that are comparable to the MiniBooNE  $\nu_\mu$

disappearance limit described above, but which extend to slightly lower  $\Delta m^2$ . See Figure 2 for comparison.

**3.2.4. Reactor and Source Experiments.** The reactor experiment dataset has been updated to reflect recent changes in the predicted neutrino fluxes, as discussed below. The source-based experimental datasets are both new to this paper, and have been published since our last set of fits [22].

**Bugey Dataset.** This analysis uses energy-dependent data from the Bugey 3 reactor experiment [59]. The detector consisted of  $^6\text{Li}$ -doped liquid scintillator, with data taken at 15, 45, and 90 m from the 2.8 GW reactor source. The detectors are taken to be pointlike in the analysis.

Recently, a reanalysis of reactor  $\bar{\nu}_e$  flux predictions [23, 42, 43] has led to a reinterpretation of the Bugey data. The data has transitioned from being simply a limit on neutrino disappearance to an allowed region at 95% CL. In this analysis, we adjust the predicted Bugey flux spectra normalization according to the calculations from [23].

There are many other SBL reactor datasets in existence. However, we have chosen to use only Bugey in these fits as the measurement has the lowest combined errors. Also, any global fit to multiple reactor datasets must correctly account for the correlated systematics between them, which is beyond the scope of our fits at present.

This dataset is referred to as Bugey in the analysis below. As shown in Figure 3, this dataset presents a signal at 95% CL. There are 60 bins in this analysis in total, each extending from 1 to 6 MeV in positron energy: the 15 m and 45 m baselines contributing 25 bins each and the 90 m baseline contributing 10 bins. The fit follows the “normalized energy spectra” fit method and  $\chi^2$  definition detailed in [59]. The  $\chi^2$  definition depends not only on the mass and mixing parameters we fit for, but also on five large-scale deformations of the positron spectrum due to systematic effects. Energy resolution and baseline smearing due to the finite reactor core are taken into account. To fold in the flux normalization correction mentioned above, we update the theoretical prediction for the expected ratio by an overall normalization factor of 1.06237, 1.06197, and 1.0627 for the 15 m, 45 m, and 90 m baselines, respectively [23].

**Gallium Calibration Dataset.** Indications of  $\nu_e$  disappearance have recently been published from calibration data taken by the SAGE [39] and GALLEX [40] experiments. These were solar neutrino experiments that used Mega-curie sources of  $^{51}\text{Cr}$  and  $^{37}\text{Ar}$ , which produce  $\nu_e$ , to calibrate the detectors. Each of the two experiments had two calibration periods. The overall rates from these four measurements are consistent and show an overall deficit that has been reported to be consistent with electron flavor disappearance [27, 60]. We use the four ratios of calibration data to expectation, as reported in [27], Table 2:  $1.00 \pm 0.10$ ,  $0.81 \pm 0.10$ ,  $0.95 \pm 0.12$ , and  $0.79 \pm 0.10$ . These correspond to the two periods from GALLEX and the two periods from SAGE, respectively. Our analysis of this dataset, referred to as Gallium below, follows that of [27]; a 4-bin fit to the above measured calibration period rates is used. The predicted rates after oscillations are obtained

by averaging the oscillation probabilities taking into account the detector geometry, the location of the source within the detector, and the neutrino energy distribution for each source (energy line and branching fraction). The neutrino energies are approximately 430 and 750 keV for  $^{51}\text{Cr}$  and 812 keV for  $^{37}\text{Ar}$ . The data result in a limit at 95% CL, as shown in Figure 3.

**3.2.5. Long-Baseline Experimental Results Contributing to the Fits.** While this study concentrates mainly on results from SBL experiments, the data from experiments with baselines of hundreds of kilometers can be valuable. At such long baselines, the ability to identify the  $\Delta m^2$  associated with any observed oscillation has disappeared due to the rapid oscillations. However, these experiments can place strong constraints on the mixing parameters. New to this paper is the inclusion of the MINOS  $\bar{\nu}_\mu$  CC constraint. We have included the atmospheric dataset in our previous fits [20–22].

We note two long-baseline results not included in this analysis. First, we have dropped the Chooz dataset that was included in previous fits [20–22] due to the discovery that  $\sin^2 2\theta_{13}$  is large [12–16], which significantly complicates the use of this data for SBL oscillation searches. Second, the recent muon flavor disappearance results from IceCube [61] were published too late to be included in this iteration of fits. However, the MiniBooNE and MINOS muon flavor disappearance results are more stringent than the IceCube limits, and so we do not expect this to significantly affect the results.

**MINOS  $\bar{\nu}_\mu$  CC Disappearance Search.** MINOS is a muon flavor disappearance experiment featuring two (near and far) iron-scintillator segmented calorimeter-style detectors in the NuMI beamline (described above) at Fermilab. The near detector is located 1 km from the target while the far detector is located 730 km away. The wideband beam peaks at about 4 GeV.

MINOS ran in both neutrino and antineutrino mode. We employ the antineutrino data in our fits as it constrains the allowed region for muon antineutrino disappearance when we divide the datasets into neutrino versus antineutrino fits. The MINOS neutrino mode disappearance limit is not as restrictive as the atmospheric result, and so only the antineutrino dataset is utilized.

This result is referred to as MINOS-CC in the analysis below. The data present a limit at 95% CL as discussed above and shown in Figure 2. In our analysis of MINOS-CC, we fit both the antineutrino (right sign) data published by MINOS in antineutrino mode running [62] and the antineutrino (wrong sign) data published by MINOS in neutrino mode running [63]. The right sign data are considered in 12 bins from 0 to 20 GeV, and the wrong sign in 13 bins from 0 to 50 GeV. We account for possible oscillations in the near detector due to high  $\Delta m^2$  values by using the ratio of the oscillation probabilities at the far and near detectors for each mass and mixing model. As MINOS is sensitive to  $\Delta m^2_{\text{atm}}$ , we add an extra mass state to the oscillation probability using the best-fit atmospheric mass and mixing parameters from

the MINOS experiment [10]. The data points and systematic errors are taken from [62, 63].

**Atmospheric Constraints on  $\nu_\mu$  Disappearance Used in Fits.** Atmospheric neutrinos are produced when cosmic rays interact with nuclei in the atmosphere to produce showers of mesons. The neutrino path length varies from a few to 12,800 km, while neutrino energies range from sub- to few-GeV. Thus, this is a long-baseline source with sensitivity to primarily  $\nu_\mu$  disappearance and effectively no sensitivity to  $\Delta m^2_{ij}$ . The former is a consequence of the atmospheric neutrino flux composition and the detector technology used in atmospheric experiments. Thus, atmospheric neutrino measurements and long-baseline accelerator-based  $\nu_\mu$  disappearance experiments constrain the same parameters and are treated in our fits in a similar way.

As with our past fits, we include atmospheric constraints following the prescription of [64]. We refer to this dataset as ATM. This makes use of two datasets: (1) 1489 days of Super-K muon-like and electron-like events with energies in the sub- to multi-GeV range, taking into account atmospheric flux predictions from [65] and treating systematic uncertainties according to [66]; (2)  $\nu_\mu$  disappearance data from the long-baseline accelerator-based experiment K2K [6, 67, 68]. The atmospheric constraint is implemented in the form of a  $\chi^2$  available as a function of the parameter  $d_\mu$ , which depends on the muon flavor composition of  $m_4$ ,  $m_5$ , and  $m_6$  as follows:

$$d_\mu = \frac{1 - \sqrt{1 - 4A}}{2}, \quad (14)$$

where

$$\begin{aligned} A = & \left(1 - |U_{\mu 4}|^2 - |U_{\mu 5}|^2 - |U_{\mu 6}|^2\right) \\ & \times \left(|U_{\mu 4}|^2 + |U_{\mu 5}|^2 + |U_{\mu 6}|^2\right) \\ & + |U_{\mu 4}|^2 |U_{\mu 5}|^2 + |U_{\mu 4}|^2 |U_{\mu 6}|^2 + |U_{\mu 5}|^2 |U_{\mu 6}|^2. \end{aligned} \quad (15)$$

The atmospheric constraints set a limit at 95% CL as shown in Figure 2.

## 4. Analysis Description

The analysis method follows the formalism described in Section 2.3, and fits are performed to each of the (3+1), (3+2), and (3+3) hypotheses separately.

**4.1. Fit Parameters.** The independent parameters considered in the (3+1) fit are  $\Delta m^2_{41}$ , representing the splitting between the (degenerate) first three mass eigenstates and the fourth mass eigenstate, and  $|U_{e4}|$  and  $|U_{\mu 4}|$ , representing the electron and muon flavor content in the fourth mass eigenstate, which are assumed to be small. The (3+2) model introduces a fifth mass eigenstate (where  $\Delta m^2_{51} \geq \Delta m^2_{41}$ ) two additional mixing parameters”  $|U_{e5}|$  and  $|U_{\mu 5}|$ , and the CP-violating phase  $\phi_{54}$ , defined by (10). The (3+3) model includes all the previous parameters and a sixth mass eigenstate, described by

$\Delta m_{61}^2$ , where  $\Delta m_{61}^2 \geq \Delta m_{51}^2 \geq \Delta m_{41}^2$ , two additional mixing parameters,  $|U_{e6}|$  and  $|U_{\mu 6}|$ , and two more CP-violating phases,  $\phi_{46}$  and  $\phi_{56}$ . The above model parameters are allowed to vary freely within the following ranges:  $\Delta m_{41}^2$ ,  $\Delta m_{51}^2$ , and  $\Delta m_{61}^2$  within 0.01–100 eV<sup>2</sup>;  $|U_{\alpha i}|$  within 0.01–0.5;  $\phi_{ij}$  within 0– $2\pi$ , with the exception that for the  $|U_{\alpha i}|$  there are additional constraints imposed on the mixing parameters in order to conserve unitarity of the full  $(3 + N) \times (3 + N)$  mixing matrix in each scenario, as described in Section 2.3.

**4.2. Fitting Method.** The fitting method closely follows what has been done in [21]. Given an oscillation model,  $(3 + 1)$ ,  $(3 + 2)$ , or  $(3 + 3)$ , the corresponding independent oscillation parameters are randomly generated within their allowed range, and then varied via a Markov Chain  $\chi^2$  minimization procedure [69]. Each independent parameter  $x$  is generated and varied according to

$$x = x_{\text{old}} + s(R - 0.5)(x_{\text{min}} - x_{\text{max}}), \quad (16)$$

where  $x_{\text{old}}$  is the value of parameter  $x$  previously tested in the  $\chi^2$  minimization chain;  $x_{\text{min}}$  and  $x_{\text{max}}$  represent the boundaries on the parameter  $x$  as described in Section 4.1;  $R$  is a random number between 0 and 1, which is varied as one steps from  $x_{\text{old}}$  to  $x$  and  $s$  is the stepsize, a parameter of the Markov Chain. By definition, within the Markov Chain minimization method the point is accepted based only on the point directly preceding it. The acceptance of any new point  $x$  in the chain, where  $x$  is the new point in the oscillation parameter space, is determined by the following:

$$P = \min\left(1, e^{-(\chi^2 - \chi_{\text{old}}^2)/T}\right), \quad (17)$$

where  $T$  is the Markov Chain parameter “temperature.” The stepsize and temperature control how quickly the Markov Chain diffuses toward the minimum  $\chi^2$  value. At every step in the chain, each of which corresponds to a point in the oscillation parameter space, a  $\chi^2$  is calculated by summing together the individual  $\chi_d^2$  contributed from each dataset,  $d$ , included in the fit, where  $d$  denotes a dataset as described in Section 3.2.

In any given fit, we define possible signal indications at 90% and 99% CL by marginalizing over the full parameter space, and looking for closed contours formed about a global minimum,  $\chi_{\text{min}}^2$ , when projected onto any two-dimensional parameter space, assuming only two degrees of freedom. We use the standard two degrees of freedom  $\Delta\chi^2$  cuts of 4.61 for exploring allowed 90% CL regions, 5.99 for exploring allowed 95% CL regions (used only for Figures 1, 2, and 3), and 9.21 for 99% CL regions. If the null point ( $U_{\alpha i}, U_{\beta i} = 0$ ) is allowed at >95% CL, we instead proceed with drawing one-dimensional raster scan limits, obtained with the standard  $\Delta\chi^2$  cuts of 2.70, 3.84, and 6.63 for 90%, 95% (used only for Figures 1, 2, and 3), and 99% CL, respectively.

**4.3. Parameter Goodness-of-Fit Test.** In any given fit, in addition to a standard  $\chi^2$ -probability, which is quoted for the global  $\chi_{\text{min}}^2$  and number of degrees of freedom in the

fit, we also report statistical compatibility comparisons using the parameter goodness-of-fit test (PG test) from [70]. This test reduces the bias imposed toward datasets with a large number of bins in the standard  $\chi^2$ -probability in order to calculate the compatibility between datasets simply on the basis of preferred parameters. The PG (%) can be calculated to quantify compatibility between any two or more datasets, or between combinations of datasets, according to

$$\chi_{\text{PG}}^2 = \chi_{\text{min, combined}}^2 - \sum_i \chi_{\text{min, } d}^2, \quad (18)$$

where  $\chi_{\text{min, combined}}^2$  is the  $\chi^2$ -minimum of the combined fit of the datasets in consideration, and  $\chi_{\text{min, } d}^2$  is the  $\chi^2$ -minimum of each dataset fit individually. When comparing groups of datasets (i.e., appearance experiments versus disappearance experiments), each group is treated as an individual dataset. The number of degrees of freedom ( $\text{ndf}_{\text{PG}}$ ) for the PG test is given by

$$\text{ndf}_{\text{PG}} = \sum_d N_{p_d} - N_{p_{\text{combined}}}. \quad (19)$$

Here,  $N_{p_d}$  represents the number of independent parameters involved in the fit of a particular dataset and  $N_{p_{\text{combined}}}$  represents the number of independent parameters involved in the global fit.

## 5. Results

This section presents the results of the analysis for the  $(3 + 1)$ ,  $(3 + 2)$ , and  $(3 + 3)$  sterile neutrino model fits. For reference, information about the datasets used in the analyses is provided in Table 1. Tables 2 and 3 summarize the results of the fits, which will be described in more detail below. Table 2 gives the fit results for the overall global fits and for various combinations of datasets. When interpreting compatibilities, one should keep in mind that, along with a high compatibility among the individual datasets in a global fit, high compatibility values among groups of datasets is also important. Finally, Table 3 provides the parameters for the best-fit points for each of the models.

**5.1.  $(3 + 1)$  Fit Results.** For a  $(3 + 1)$  model, three parameters are determined:  $\Delta m_{41}^2$ ,  $|U_{e4}|$ , and  $|U_{\mu 4}|$ . A global  $(3 + 1)$  fit of all of the experiments (Figure 4) yields  $\chi^2$ -probability of 55% but a very low compatibility of 0.043%, indicating a low compatibility among all individual datasets. Contrasting the result from the  $\chi^2$  test to the poor compatibility illustrates how the  $\chi^2$  test can be misleading. As discussed above, this is due to some datasets dominating others due to the number of bins in the fit, many of which may not have strong oscillation sensitivity. It is for this reason that most groups fitting for sterile neutrinos now use the PG test as the figure of merit.

In order to understand the source of the poor compatibility, the datasets are subdivided, as shown in Table 2, into separate neutrino and antineutrino results. Within each of these categories, the PG compatibility values are 2.2% and 11% for neutrinos and antineutrinos, respectively. However,

TABLE 1: Datasets used in the fits and their corresponding use in the analysis. Column 1 provides the tag for the data. Column 2 references the description in Section 3.2. Column 3 lists the relevant oscillation process. Column 4 lists which datasets are included in the neutrino versus antineutrino analyses and column 5 lists which datasets are included in the appearance versus disappearance study.

Tag	Section	Process	$\nu$ versus $\bar{\nu}$	App versus Dis
LSND	3.2.1	$\bar{\nu}_\mu \rightarrow \bar{\nu}_e$	$\bar{\nu}$	App
KARMEN	3.2.1	$\bar{\nu}_\mu \rightarrow \bar{\nu}_e$	$\bar{\nu}$	App
KARMEN/LSND(xsec)	3.2.1	$\nu_e \rightarrow \nu_e$	$\nu$	Dis
BNB-MB( $\nu_{\text{app}}$ )	3.2.2	$\nu_\mu \rightarrow \nu_e$	$\nu$	App
BNB-MB( $\bar{\nu}_{\text{app}}$ )	3.2.2	$\bar{\nu}_\mu \rightarrow \bar{\nu}_e$	$\bar{\nu}$	App
NuMI-MB( $\nu_{\text{app}}$ )	3.2.2	$\nu_\mu \rightarrow \nu_e$	$\nu$	App
BNB-MB( $\nu_{\text{dis}}$ )	3.2.2	$\nu_\mu \rightarrow \nu_\mu$	$\nu$	Dis
NOMAD	3.2.3	$\nu_\mu \rightarrow \nu_e$	$\nu$	App
CCFR84	3.2.3	$\nu_\mu \rightarrow \nu_\mu$	$\nu$	Dis
CDHS	3.2.3	$\nu_\mu \rightarrow \nu_\mu$	$\nu$	Dis
Bugey	3.2.4	$\bar{\nu}_e \rightarrow \bar{\nu}_e$	$\bar{\nu}$	Dis
Gallium	3.2.4	$\nu_e \rightarrow \nu_e$	$\nu$	Dis
MINOS-CC	3.2.5	$\bar{\nu}_\mu \rightarrow \bar{\nu}_\mu$	$\bar{\nu}$	Dis
ATM	3.2.5	$\nu_\mu \rightarrow \nu_\mu$	$\nu$	Dis

TABLE 2: The  $\chi^2$  values, degrees of freedom (dof), and probabilities associated with the best-fit and null hypothesis in each scenario. Also shown are the results from the parameter goodness-of-fit tests.  $P_{\text{best}}$  refers to the  $\chi^2$ -probability at the best-fit point and  $P_{\text{null}}$  refers to the  $\chi^2$ -probability at null.

	$\chi^2_{\text{min}}$ (dof)	$\chi^2_{\text{null}}$ (dof)	$P_{\text{best}}$	$P_{\text{null}}$	$\chi^2_{\text{PG}}$ (dof)	PG (%)
3 + 1						
All	233.9 (237)	286.5 (240)	55%	2.1%	54.0 (24)	0.043%
App	87.8 (87)	147.3 (90)	46%	0.013%	14.1 (9)	12%
Dis	128.2 (147)	139.3 (150)	87%	72%	22.1 (19)	28%
$\nu$	123.5 (120)	133.4 (123)	39%	25%	26.6 (14)	2.2%
$\bar{\nu}$	94.8 (114)	153.1 (117)	90%	1.4%	11.8 (7)	11%
App versus Dis	—	—	—	—	17.8 (2)	0.013%
$\nu$ versus $\bar{\nu}$	—	—	—	—	15.6 (3)	0.14%
3 + 2						
All	221.5 (233)	286.5 (240)	69%	2.1%	63.8 (52)	13%
App	75.0 (85)	147.3 (90)	77%	0.013%	16.3 (25)	90%
Dis	122.6 (144)	139.3 (150)	90%	72%	23.6 (23)	43%
$\nu$	116.8 (116)	133.4 (123)	77%	25%	35.0 (29)	21%
$\bar{\nu}$	90.8 (110)	153.1 (117)	90%	1.4%	15.0 (16)	53%
App versus Dis	—	—	—	—	23.9 (4)	0.0082%
$\nu$ versus $\bar{\nu}$	—	—	—	—	13.9 (7)	5.3%
3 + 3						
All	218.2 (228)	286.5 (240)	67%	2.1%	68.9 (85)	90%
App	70.8 (81)	147.3 (90)	78%	0.013%	17.6 (45)	100%
Dis	120.3 (141)	139.3 (150)	90%	72%	24.1 (34)	90%
$\nu$	116.7 (111)	133.4 (123)	34%	25%	39.5 (46)	74%
$\bar{\nu}$	90.6 (105)	153 (117)	84%	1.4%	18.5 (27)	89%
App versus Dis	—	—	—	—	27.1 (6)	0.014%
$\nu$ versus $\bar{\nu}$	—	—	—	—	10.9 (12)	53%



TABLE 3: The oscillation parameter best-fit points in each scenario considered. The values of  $\Delta m^2$  shown are in units of  $\text{eV}^2$ .

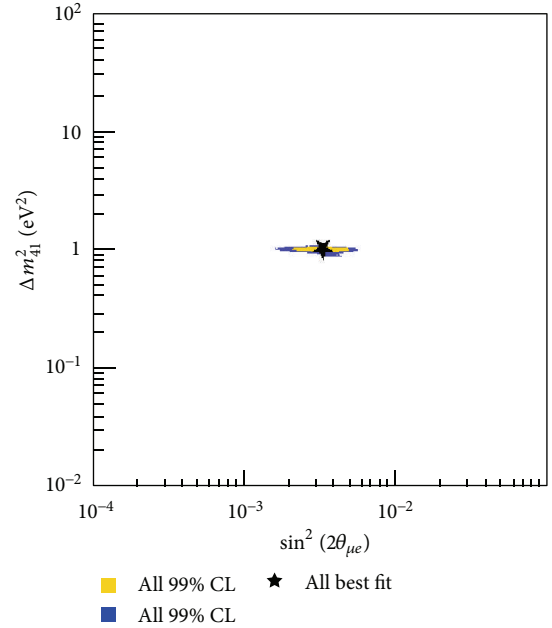
(a)												
3 + 1	$\Delta m_{41}^2$			$ U_{\mu 4} $		$ U_{e 4} $						
All	0.92			0.17		0.15						
App	0.15			0.39		0.39						
Dis	18			0.18		0.18						
$\nu$	7.8			0.059		0.26						
$\bar{\nu}$	0.92			0.23		0.13						
(b)												
3 + 2	$\Delta m_{41}^2$	$\Delta m_{51}^2$	$ U_{\mu 4} $	$ U_{e 4} $	$ U_{\mu 5} $	$ U_{e 5} $	$\phi_{54}$					
All	0.92	17	0.13	0.15	0.16	0.069	$1.8\pi$					
App	0.31	1.0	0.31	0.31	0.17	0.17	$1.1\pi$					
Dis	0.92	18	0.015	0.12	0.17	0.12	N/A					
$\nu$	7.6	17.6	0.05	0.27	0.18	0.052	$1.8\pi$					
$\bar{\nu}$	0.92	3.8	0.25	0.13	0.12	0.079	$0.35\pi$					
(c)												
3 + 3	$\Delta m_{41}^2$	$\Delta m_{51}^2$	$\Delta m_{61}^2$	$ U_{\mu 4} $	$ U_{e 4} $	$ U_{\mu 5} $	$ U_{e 5} $	$ U_{\mu 6} $	$ U_{e 6} $	$\phi_{54}$	$\phi_{64}$	$\phi_{65}$
All	0.90	17	22	0.12	0.11	0.17	0.11	0.14	0.11	$1.6\pi$	$0.28\pi$	$1.4\pi$
App	0.15	1.8	2.7	0.37	0.37	0.12	0.12	0.12	0.12	$1.4\pi$	$0.32\pi$	$0.94\pi$
Dis	0.92	7.2	18	0.013	0.12	0.019	0.16	0.15	0.069	N/A	N/A	N/A
$\nu$	13	17	26	0.076	0.24	0.16	0.067	0.10	0.017	$1.1\pi$	$1.8\pi$	$0.037\pi$
$\bar{\nu}$	7.5	9.1	18	0.024	0.28	0.098	0.11	0.18	0.029	$1.8\pi$	$2.0\pi$	$0.61\pi$

the two datasets favor very different oscillation parameters, as seen in Table 3 and Figure 5. This leads to a very low PG of 0.14% when the neutrino and antineutrino data are compared. The separation of the datasets into appearance and also shows a strong incompatibility, as illustrated in Figure 6, leading to an even lower PG value of 0.013%. These results imply that the (3 + 1) model is not sufficient to describe all datasets simultaneously.

As can be seen in Table 3, two different  $\Delta m_{41}^2$  values are preferred for neutrino versus antineutrino and for appearance versus disappearance. This leads one to suspect that the data would prefer at least two mass splittings between the mostly active and the mostly sterile states and, thus, encourages the consideration of a (3 + 2) interpretation [20]. Moreover, a (3 + 2) model allows the introduction of a CP-violating phase, which can address the differences between neutrino and antineutrino datasets [21]. Therefore, these results lead us to abandon (3 + 1) and move on to testing the (3 + 2) hypothesis. It should be noted that the shortcomings of the (3 + 1) model have now been established by a number of independent analyses [20, 22, 23, 71–73].

**5.2. (3 + 2) Fit Results.** In a (3 + 2) model, there are seven parameters to determine:  $\Delta m_{41}^2$ ,  $\Delta m_{51}^2$ ,  $|U_{e 4}|$ ,  $|U_{\mu 4}|$ ,  $|U_{e 5}|$ ,  $|U_{\mu 5}|$ , and  $\phi_{54}$ . The best-fit values for these parameters from a global fit to all datasets are given in Table 3. The 90% and 99% CL contours in marginalized ( $\Delta m_{41}^2, \Delta m_{51}^2$ ) space can be seen in Figure 7.

Adding a second mass eigenstate reduces the tension seen in the (3 + 1) fits, bringing the overall compatibility to 13%

FIGURE 4: The  $\Delta m_{41}^2$  versus  $\sin^2 2\theta_{\mu e}$  allowed space from fits to all data—neutrino and antineutrino—in a (3 + 1) model.

(see Table 2) and reducing the  $\chi^2$  of the global fit by 12.4 units with four extra parameters introduced in the fit. For this compatibility test, the BNB-MB( $\nu_{\text{app}}$ ) dataset has the worst  $\chi^2$ -probability. When considered by itself, the BNB-MB( $\nu_{\text{app}}$ ) dataset gives a constrained (see Section 3.2.2)  $\chi^2$  (dof) of 19.2

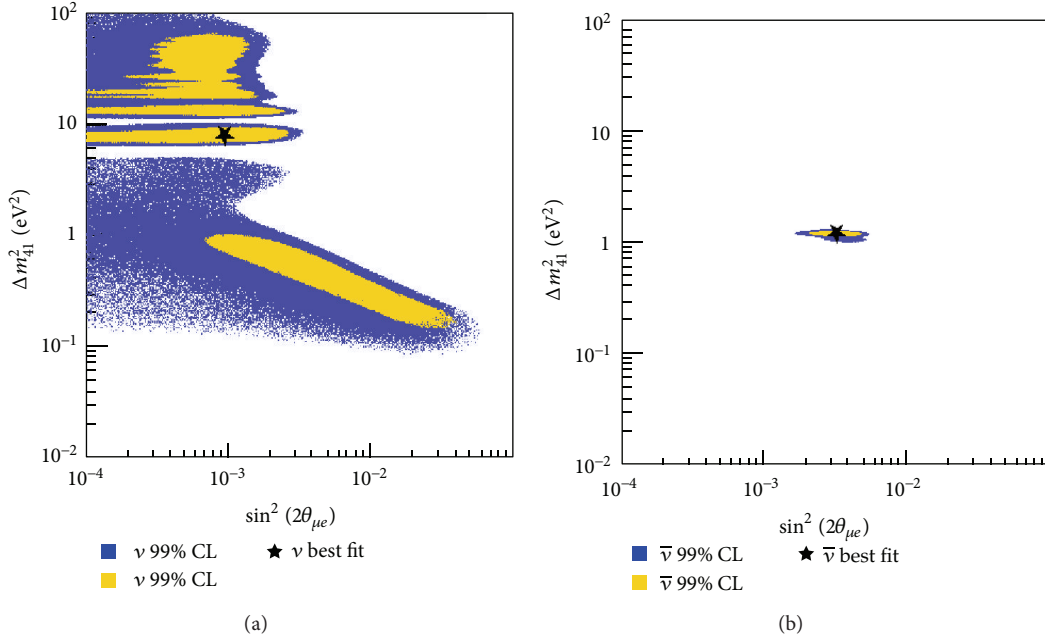


FIGURE 5: The  $\Delta m_{41}^2$  versus  $\sin^2 2\theta_{\mu e}$  allowed space from fits to neutrino (a) and antineutrino (b) data in a  $(3 + 1)$  model.

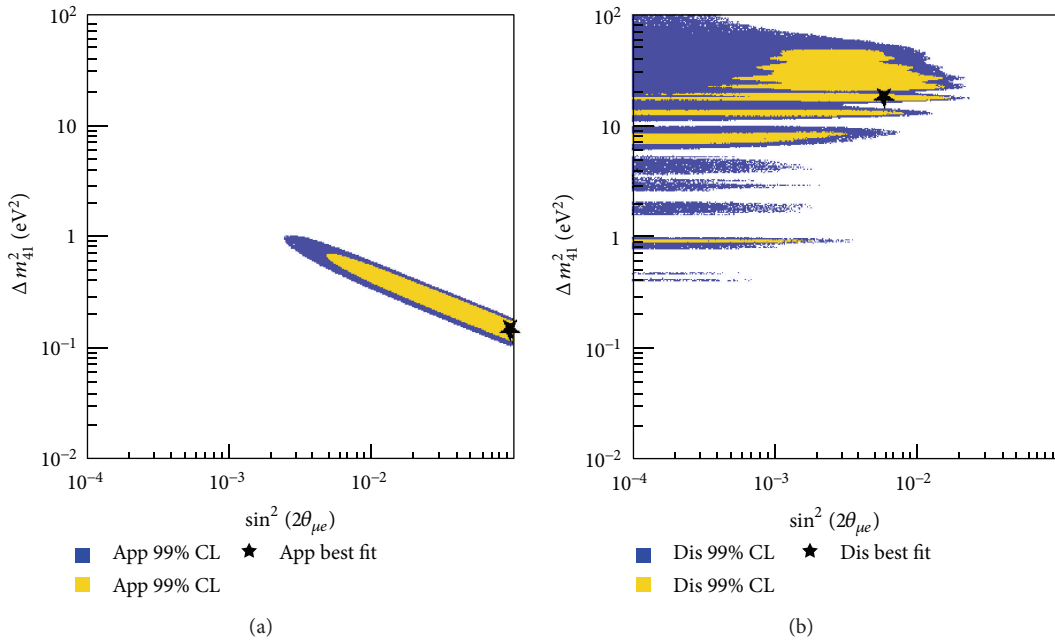


FIGURE 6: The  $\Delta m_{41}^2$  versus  $\sin^2 2\theta_{\mu e}$  allowed space from fits to appearance (a) and disappearance (b) data in a  $(3 + 1)$  model.

(4) for the global best-fit parameters, which corresponds to a  $\chi^2$ -probability of 0.07%. This is one of the first indications that the MiniBooNE neutrino data has some tension with the other datasets.

The need to introduce a CP-violating phase was established in previous studies of global fits [22]. This term affects only fits involving appearance datasets and results in a difference in the oscillation probabilities for  $\nu_\mu \rightarrow \nu_e$

versus  $\bar{\nu}_\mu \rightarrow \bar{\nu}_e$ . In particular, previous studies considered CP-violating fits in an attempt to reconcile the MiniBooNE neutrino appearance results with the MiniBooNE and LSND antineutrino appearance results.

Table 2 gives the fit results in dataset combinations for cross-comparison. We find that the separate neutrino and antineutrino dataset fits remain in good agreement and that the compatibility between them has risen to

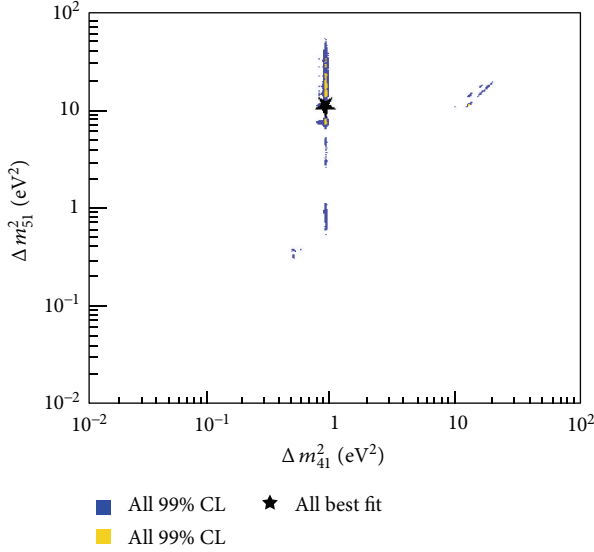


FIGURE 7: The  $\Delta m_{51}^2$  versus  $\Delta m_{41}^2$  allowed space from fits to all data in a (3 + 2) model.

5.3%—a significant improvement over the (3 + 1) result. The best-fit values and allowed regions are shown in Table 3 and in Figure 8, respectively.

While the neutrino versus antineutrino discrepancy has been somewhat reduced, Table 2 points out a second important problem. The appearance and disappearance datasets still have very poor compatibility (0.0082%), even in a (3 + 2) model. The poor compatibility can be partially traced to a discrepancy in the preferred mass splittings for these two datasets. As reported in Table 3, the appearance datasets prefer a low (0.31 eV<sup>2</sup>) and a medium (1.0 eV<sup>2</sup>) mass splitting while the disappearance datasets prefer a medium (0.92 eV<sup>2</sup>) and a high (18 eV<sup>2</sup>) splitting. This is also illustrated in Figure 9. This suggests that three mass splittings may be required to reconcile appearance and disappearance results and motivates the consideration of a (3 + 3) model.

**5.3. (3 + 3) Fit Results.** For a (3 + 3) model, there are 12 model parameters to be determined:  $\Delta m_{41}^2, \Delta m_{51}^2, \Delta m_{61}^2, |U_{e4}|, |U_{\mu 4}|, |U_{e5}|, |U_{\mu 5}|, |U_{e6}|, |U_{\mu 6}|, \phi_{54}, \phi_{64},$  and  $\phi_{65}$ . Adding a third mass eigenstate does not significantly change the global fit  $\chi_{\min}^2$ ; however, the tension between the individual dataset fits is further reduced, raising the compatibility from 13%, in (3 + 2), to 90%. The neutrino and antineutrino compatibility rises by an order of magnitude from the (3 + 2) value to 53%, indicating that the (3 + 3) model can better accommodate the differences in these datasets.

It is interesting to note that the (3 + 3) fit prefers an “inverted hierarchy” among the three mostly sterile states, with  $\Delta m_{54}^2 = m_5^2 - m_4^2 = 16 \text{ eV}^2$  and  $\Delta m_{65}^2 = m_6^2 - m_5^2 = 5.0 \text{ eV}^2$ . The overall splitting relative to the three mostly active states is  $\Delta m_{41}^2 = m_4^2 - m_1^2 = 0.90 \text{ eV}^2$ .

The one puzzling discrepancy for the (3 + 3) fits is the tension still exhibited by the appearance versus disappearance datasets, shown in Figures 10, 11, and 12, where the compatibility remains low, at less than 0.01%. We find

that important sources of this incompatibility are the BNB-MB( $\nu_{\text{app}}$ ) and BNB-MB( $\bar{\nu}_{\text{app}}$ ) datasets. The BNB-MB( $\nu_{\text{app}}$ ) dataset has fairly small statistical and systematic uncertainties and therefore has a large impact on the fits and compatibility calculations. This is shown in Figure 13 where the MiniBooNE data agrees well with the appearance-only fit but disagrees with the overall global fit. Removing both the BNB-MB( $\nu_{\text{app}}$ ) and BNB-MB( $\bar{\nu}_{\text{app}}$ ) sets raises the compatibility to 3.5%, corresponding to an improvement of over two orders of magnitude. It has been known since the first MiniBooNE publication [18] that the BNB-MB( $\nu_{\text{app}}$ ) data was fairly consistent with no oscillations above 475 MeV; however, a significant low-energy excess was present below this energy. The energy dependence of the BNB-MB( $\nu_{\text{app}}$ ) excess does not fit very well with oscillation models extracted from fits to global datasets, unless very low  $\Delta m_{ij}^2$  with large mixing elements  $|U_{ei}|$  and  $|U_{\mu i}|$  are involved in the fit. This may lead to the poor compatibility when included in appearance versus disappearance comparisons. Other possible explanations for this incompatibility include downward fluctuations of the BNB-MB( $\nu_{\text{app}}$ ) data in the higher-energy region or some other process contributing to the low-energy excess such as those suggested in [28, 74].

Statistical issues could be addressed with more MiniBooNE neutrino data that may become available over the next few years. In addition, the MicroBooNE experiment, which is expected to start running in 2014, will provide more information on the low-energy excess events and will answer the question of whether the excess is associated with outgoing electrons or photons [75].

**5.4. Summary of Results.** The sterile neutrino fits to global datasets show that a (3 + 1) model is inadequate; multiple  $\Delta m_{ij}^2$  values are needed along with CP-violating effects to explain the neutrino versus antineutrino differences. A (3 + 2) model improves significantly on the (3 + 1) results but still shows some tension in the neutrino versus antineutrino compatibility and cannot explain the appearance versus disappearance differences. The (3 + 3) model does not seem to further improve the fit and still has poor appearance versus disappearance compatibility. The BNB-MB( $\nu_{\text{app}}$ ) (and BNB-MB( $\bar{\nu}_{\text{app}}$ )) dataset is a prime contributor to this incompatibility and additional experimental information in this region should be available soon. Figure 13 gives a comparison of the BNB-MB( $\nu_{\text{app}}$ ) and BNB-MB( $\bar{\nu}_{\text{app}}$ ) data with the global best-fit predictions and with the appearance-only best-fit predictions for each of the three models, (3 + 1), (3 + 2), and (3 + 3). The global fit prediction is significantly below the data at low energy, which contributes to the poor appearance versus disappearance compatibility.

In summary, out of the three sterile neutrino oscillation hypotheses considered in the analysis, we find that the (3 + 2) and (3 + 3) models provide a better description than the (3 + 1) model, although the MiniBooNE appearance data continue to raise issues within the fits. As has been shown before, (3 + 1) scenarios provide a poor fit to the data, and should not be emphasized. We therefore recommend continued investigations of (3 + 2) and (3 + 3) scenarios.

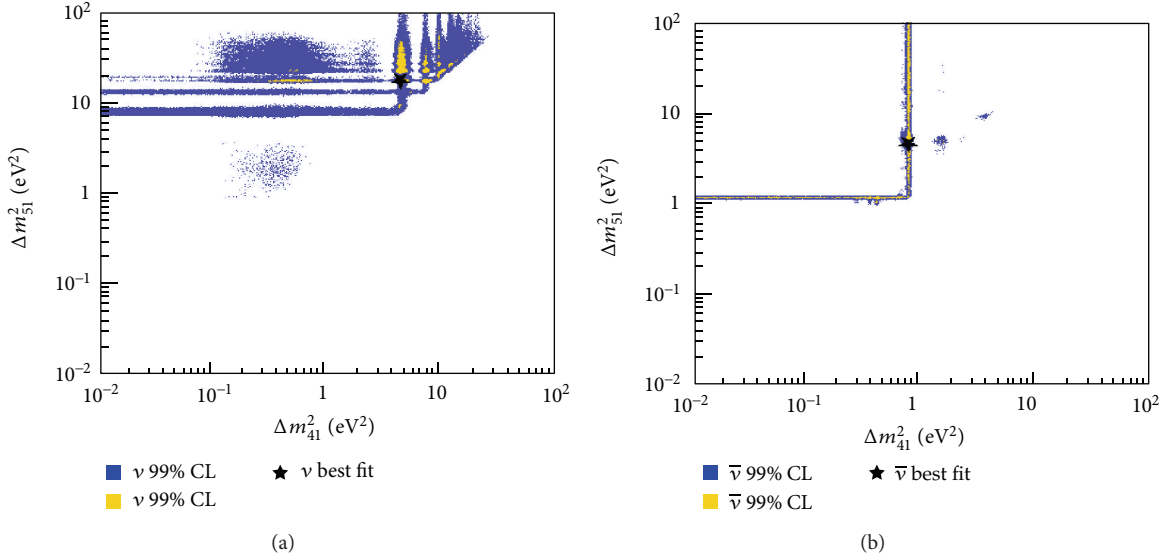


FIGURE 8: The  $\Delta m_{51}^2$  versus  $\Delta m_{41}^2$  allowed space from fits to neutrino (a) and antineutrino (b) data in a (3 + 2) model.

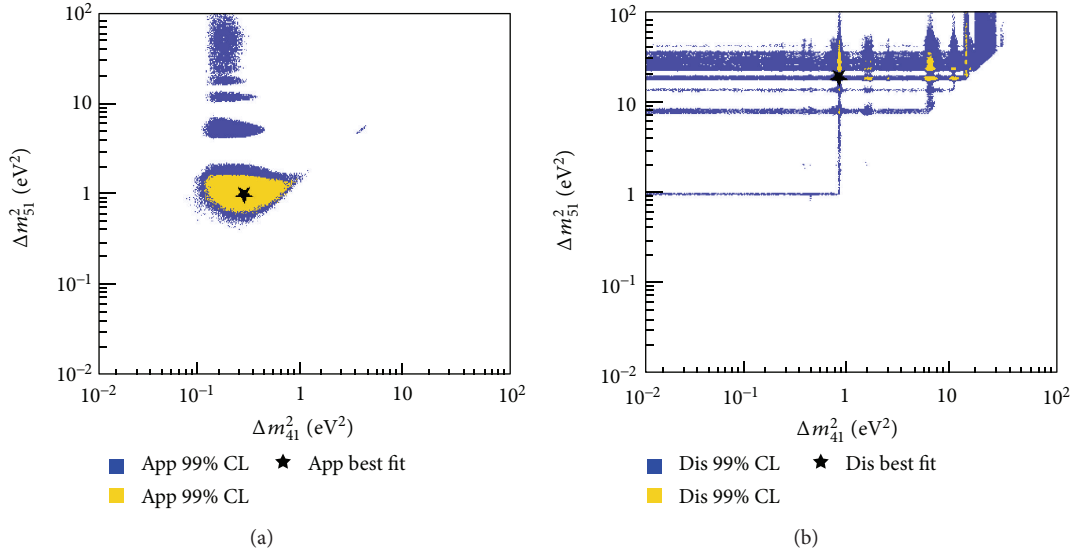


FIGURE 9: The  $\Delta m_{51}^2$  versus  $\Delta m_{41}^2$  allowed space from fits to appearance (a) and disappearance (b) data in a (3 + 2) model.

## 6. The Future

Establishing the existence of sterile neutrinos would have a major impact on particle physics. Motivated by this, there are a number of existing and planned experiments set to probe the parameter space indicative of one or more sterile neutrinos. Such experiments are necessary in order to confirm or refute the observed anomalies in the  $\Delta m^2 \sim 1 \text{ eV}^2$  region. The new experiments are being designed to have improved sensitivity, with the goal of  $5\sigma$  sensitivity and the ability to observe oscillatory behavior in  $L$  and/or  $E$  within single or between multiple detectors. In these experiments, the oscillation signal needs to be clearly separated from any backgrounds.

Sterile neutrino oscillation models are based on oscillations associated with mixing between active and sterile states and demand the presence of both appearance and disappearance. It is therefore imperative that the future program explore both of these oscillation types. Establishing sterile neutrinos will require that both types of measurements are compatible with sterile neutrino oscillation models. Future experiments will search for evidence of sterile neutrino(s) using a variety of neutrino creation sources: (1) pion/muon DIF (e.g., [75–80]), (2) pion or kaon DAR (e.g., [81–86]), (3) unstable isotopes (e.g., [15, 87–90]), and (4) atmospheric (see [23]) and (5) nuclear reactors (e.g., [91, 92]). All of these experiments are under development and the sensitivities are likely to change. Therefore, rather than displaying sensitivity



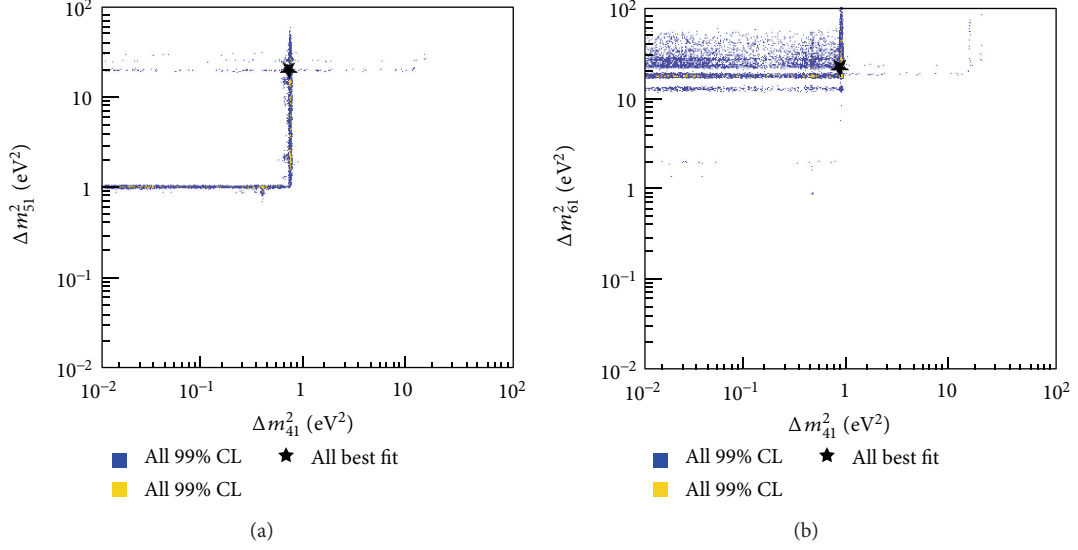


FIGURE 10: The  $\Delta m_{51}^2$  versus  $\Delta m_{41}^2$  and  $\Delta m_{61}^2$  versus  $\Delta m_{41}^2$  correlations from fits to all data in a  $(3 + 3)$  model.

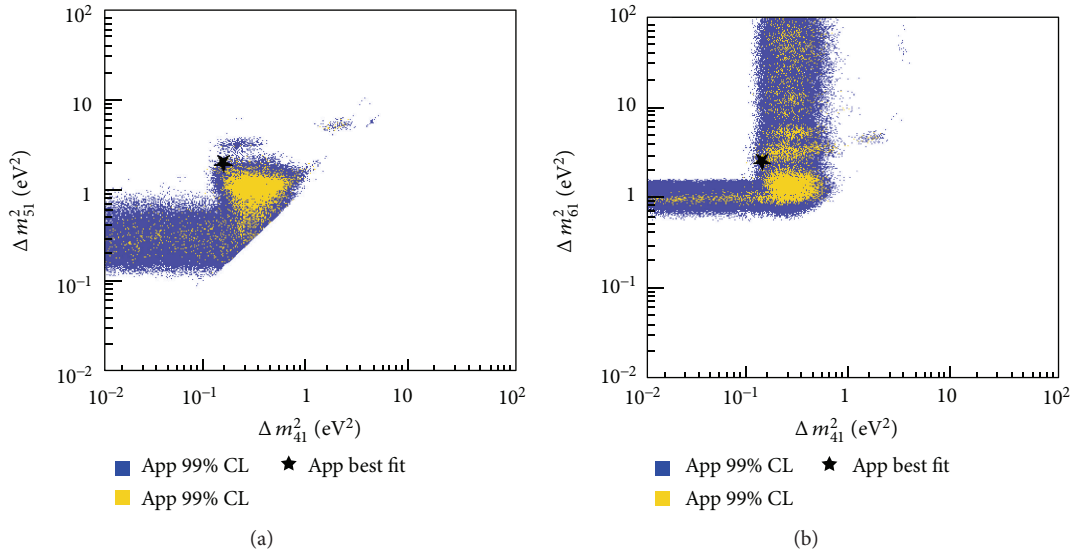


FIGURE 11: The  $\Delta m_{51}^2$  versus  $\Delta m_{41}^2$  and  $\Delta m_{61}^2$  versus  $\Delta m_{41}^2$  correlations from fits to appearance data in a  $(3 + 3)$  model.

curves for each future program, we instead focus on the conceptual ideas behind the experiments. Unless otherwise mentioned, the experiments below will provide “significant” sensitivity to a large portion of the favored sterile neutrino parameter space through searches for neutrino disappearance and/or appearance.

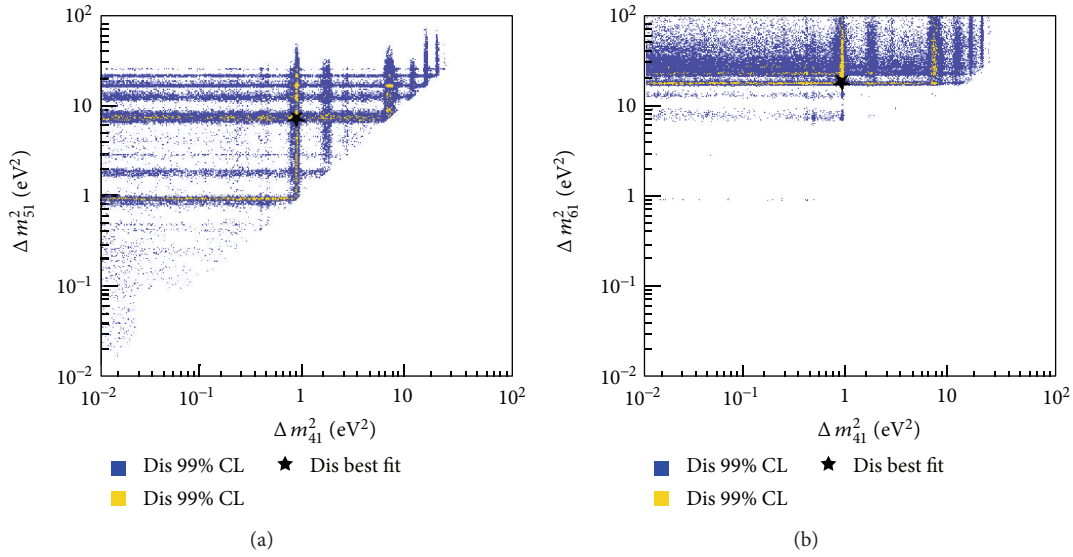
**6.1. The Importance of the  $L/E$  Signature from Multiple Experiments.** Ultimately, in order to determine if there are zero, one, two, or three sterile states contributing to oscillations in SBL experiments, it will be necessary to observe the expected  $L/E$ -dependent oscillation probabilities discussed in Section 2.3. Assuming that the SBL anomalies are confirmed, a consistent  $L/E$  dependence is the only signature which is distinct for oscillations and excludes other

exotic explanations such as CPT violation [22], decays [93], and Lorentz violation [94]. The ideal experiment would reconstruct the oscillation wave as a function of  $L/E$  [95]. The combined information from many experiments, however, is more suitable for covering the widest possible range in  $L/E$  as well as providing valuable flavor and neutrino versus antineutrino information.

The three models,  $(3 + 1)$ ,  $(3 + 2)$ , and  $(3 + 3)$ , have distinct signatures as a function of  $L/E$ . To illustrate this, we consider the case of a hypothetical experiment with 10% resolution in  $L/E$ , assuming the best-fit values presented in Table 3. In the case of  $(3 + 1)$ , as shown in Figure 14, the disappearance (appearance) probabilities shown on the left (right), have maxima and minima that evolve monotonically to  $P = 1/2\sin^2(2\theta)$ , the long-baseline limit discussed in Section 2.2.

TABLE 4: A summary of current and future sterile neutrino oscillation experiments.

Source	App/Dis	Channel	Experiment
Reactor	Dis	$\bar{\nu}_e \rightarrow \bar{\nu}_e$	Nucifer, Stereo, SCRAMM, NIST, Neutrino4, DANSS
Radioactive	Dis	$\nu_e \rightarrow \nu_e, \bar{\nu}_e \rightarrow \bar{\nu}_e$	Baksan, LENS, Borexino, SNO+, Ricochet, CeLAND, Daya Bay
Accelerator-based isotope	Dis	$\bar{\nu}_e \rightarrow \bar{\nu}_e$	IsoDAR
Pion/Kaon DAR	App and Dis	$\bar{\nu}_\mu \rightarrow \bar{\nu}_e, \nu_e \rightarrow \nu_e$	OscSNS, DAEδALUS, KDAR
Accelerator (Pion DIF)	App and Dis	$\nu_\mu \rightarrow \nu_e, \bar{\nu}_\mu \rightarrow \bar{\nu}_e$ $\nu_\mu \rightarrow \nu_\mu, \bar{\nu}_\mu \rightarrow \bar{\nu}_\mu$	MINOS+, MicroBooNE, LArIkton + MicroBooNE, CERN SPS
Low-energy $\nu$ -Factory	App and Dis	$\nu_e \rightarrow \nu_\mu, \bar{\nu}_e \rightarrow \bar{\nu}_\mu$ $\nu_\mu \rightarrow \nu_\mu, \bar{\nu}_\mu \rightarrow \bar{\nu}_\mu$	$\nu$ STORM

FIGURE 12: The  $\Delta m_{51}^2$  versus  $\Delta m_{41}^2$  and  $\Delta m_{61}^2$  versus  $\Delta m_{41}^2$  correlations from fits to disappearance data in a  $(3 + 3)$  model.

This can be contrasted with Figures 15 and 16, where the structure of the oscillation wave, in the approach to the long-baseline limit, is more “chaotic” due to the interference between the various mass splitting terms.

In Figures 14, 15, and 16, the two curves on the disappearance plots on the left refer to muon and electron flavor, respectively. As the theory is CPT-conserving, these disappearance curves should be identical for neutrinos and antineutrinos. The appearance curves on the right also show the importance of neutrino and antineutrino running, which can lead to very different  $L/E$  dependencies for the three models, and constrain CP-violating parameters.

In summary, it seems very unlikely that any *single* future experiment will be able to differentiate between the sterile neutrino models. Multiple experiments looking at different

oscillation channels and covering a wide range of  $L/E$  regions are required. Thus, the consideration of many independent experiments of relatively modest size, such as those listed in Table 4, is essential.

**6.2. Future Experiments.** A summary of future sterile neutrino experiments is provided in Table 4.

**6.2.1. Pion Decay in Flight.** Muon neutrinos (antineutrinos) from positive (negative) pion DIF can be used to search for (anti)neutrino disappearance and electron (anti)neutrino appearance in the sterile neutrino region of interest. Given the usual neutrino energies for these experiments ( $\mathcal{O}(1 \text{ GeV})$ ), the baseline for such an experiment can be considered “short” ( $\mathcal{O}(100\text{--}1000 \text{ m})$ ).

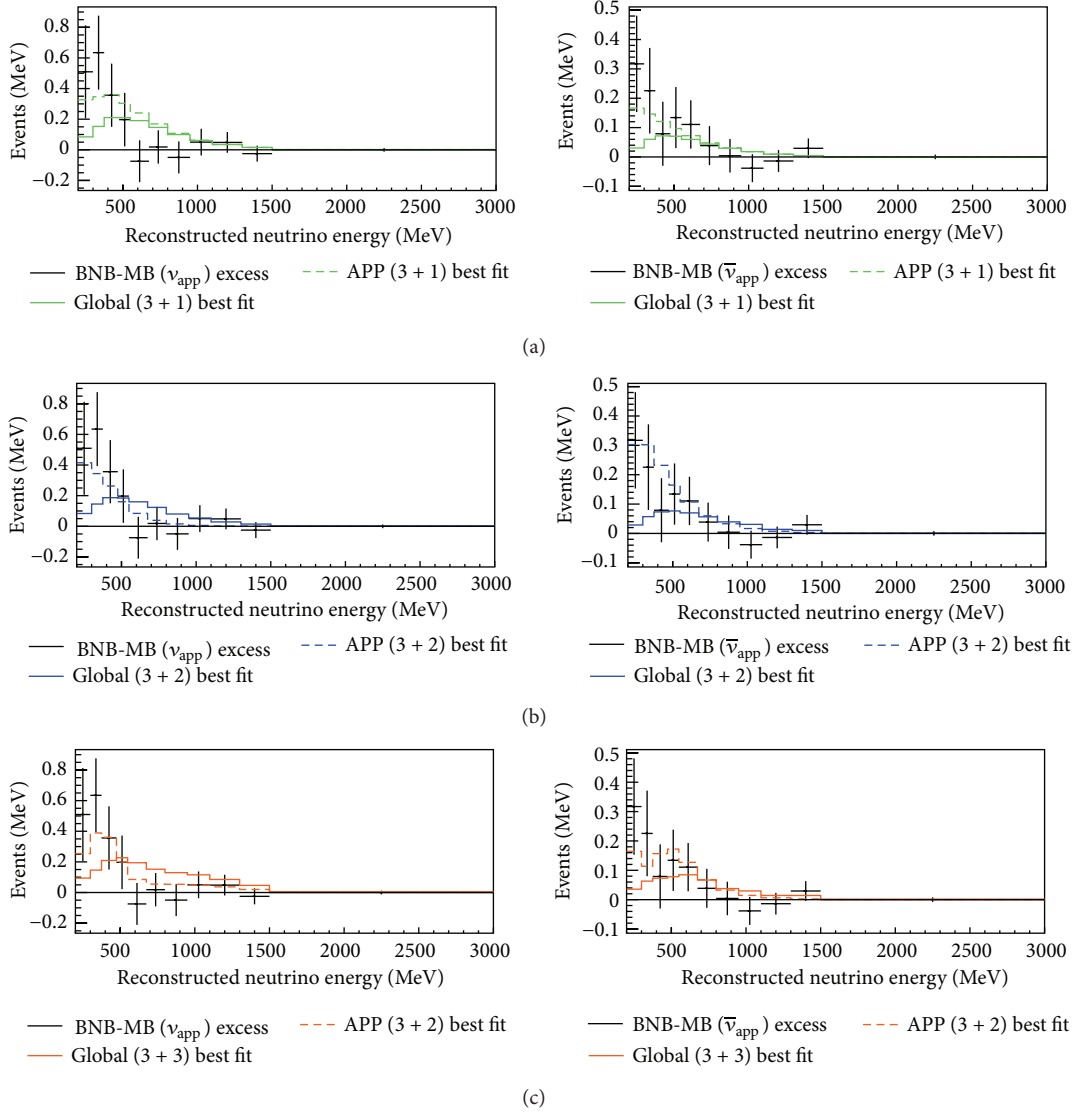


FIGURE 13: A comparison of the BNB-MB( $\nu_{\text{app}}$ ) and BNB-MB( $\bar{\nu}_{\text{app}}$ ) excess data with the global best-fit oscillation signal predictions (solid colored lines) and with the appearance only best-fit predictions (dashed colored lines) for each of the models,  $(3+1)$ ,  $(3+2)$ , and  $(3+3)$ . The error bars on the excess correspond to statistical and unconstrained background systematic errors, added in quadrature.

The BNB at Fermilab will provide pion-induced neutrinos to the MicroBooNE LArTPC-based detector starting in 2014 [75]. MicroBooNE will probe the MiniBooNE low-energy anomaly [96] with a  $\sim 90$  ton active volume about 100 meters closer to the neutrino source than MiniBooNE. Some coverage of the LSND allowed region in neutrino mode is also expected, along with LArTPC development and needed precision neutrino-argon cross-section measurements [97]. A design involving two LArTPC-based detectors in a near/far configuration, with MicroBooNE as the near detector, is also being considered for deployment in the BNB at Fermilab [78]. A similar two-detector configuration in the CERN-SPS neutrino beam has recently been proposed [79]. Two identical LArTPCs, in combination with magnetized spectrometers, would measure the mostly pion DIF-induced muon neutrino composition of the beam as a function of distance (300 m,

1600 m) to probe electron neutrino appearance in the sterile neutrino parameter space.

Another BNB-based idea calls for a significant upgrade to the MiniBooNE experiment in which the current MiniBooNE detector becomes the 540 m baseline far detector in a two detector configuration and a MiniBooNE-like oil-based near detector is installed at a baseline of 200 m [77]. Such a configuration could significantly reduce the now largely irreducible systematics associated with MiniBooNE-far-only, which mainly come from neutral pion background events and flux uncertainty. In conjunction with MicroBooNE, “BooNE” could provide sensitivity to LSND-like electron (anti)neutrino appearance, muon (anti)neutrino disappearance, and the MiniBooNE low-energy anomaly.

A low-energy 3-4 GeV/c muon storage ring could deliver a precisely known flux of electron neutrinos for a muon

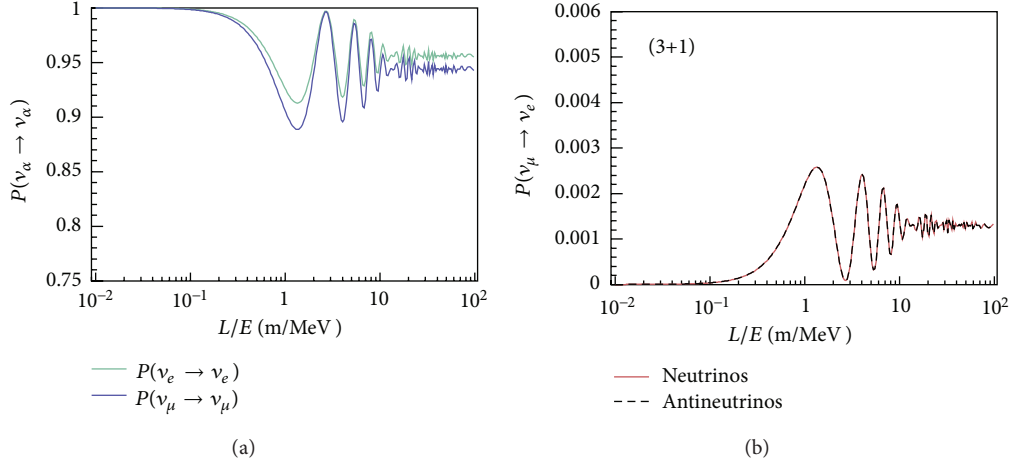


FIGURE 14: The (3 + 1) oscillation probabilities for the global best-fit (“all” datasets) values in Table 3 with 10% resolution in  $L/E$ .

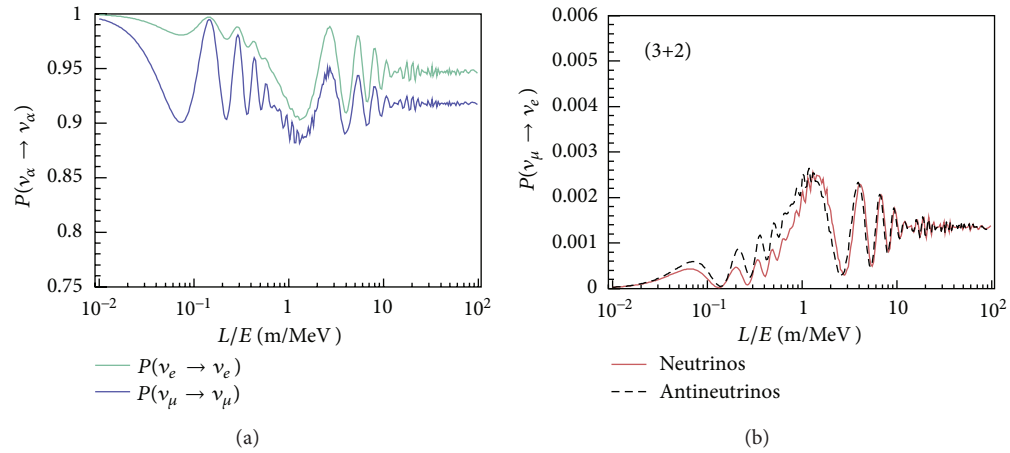


FIGURE 15: The (3 + 2) oscillation probabilities for the global best-fit (“all” datasets) values in Table 3 with 10% resolution in  $L/E$ .

neutrino appearance search in the parameter space of interest for sterile neutrinos [80]. The MINOS-like detectors, envisioned at 20–50 m (near) and  $\sim 2000$  m (far), would need to be magnetized in order to differentiate muon neutrino appearance from intrinsic muon antineutrinos created from the positive muon decay. Similar to most pion DIF beams, the muon storage ring could run in both neutrino mode and antineutrino mode. Such an experiment would also provide a technological demonstration of a muon storage ring with a “simple” neutrino factory [98].

**6.2.2. Pion or Kaon Decay at Rest.** As discussed above, neutrinos from pion DAR and subsequent daughter muon DAR, with their well-known spectrum, provide a source for an oscillation search. Notably, LSND employed muon antineutrinos from the pion daughter’s muon DAR in establishing their  $3.8\sigma$  excess consistent with electron antineutrino appearance.

The 1MW Spallation Neutron Source at Oak Ridge National Laboratory, a pion and muon DAR neutrino source, in combination with an LSND-style detector could directly

probe the LSND excess with a factor of 100 lower steady state background and higher beam power [83, 84]. A 1 MW source at a large liquid scintillator detector is also under consideration [95]. Such an experiment could reconstruct appearance and disappearance oscillation waves across a  $\sim 50$  m length of detector.

If higher energy proton beams are used, then positive kaon DAR and the resulting monoenergetic (235.5 MeV) muon neutrino can also be used to search for sterile neutrinos through an electron neutrino appearance search with a LArTPC-based device [86]. An intense  $>3$  GeV kinetic energy proton beam is required for such an experiment so as to produce an ample number of kaons per incoming proton.

**6.2.3. Unstable Isotopes.** The disappearance of electron antineutrinos from radioactive isotopes is a direct probe of the reactor/gallium anomaly and an indirect probe of the LSND anomaly. As such neutrinos are in the ones-of-MeV range, the baseline for these experiments is generally on the order of tens of meters or so. Oscillation waves within a single detector can



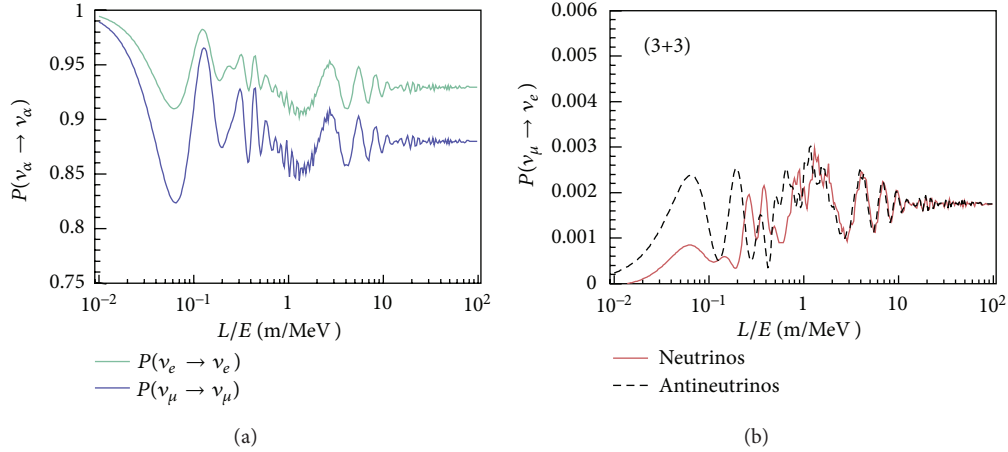


FIGURE 16: The (3 + 3) oscillation probabilities for the global best-fit (“all” datasets) values in Table 3 with 10% resolution in  $L/E$ .

be observed if the neutrinos originate from a localized source, if the oscillation length is short enough, and if the detector has precise enough vertex resolution.

The IsoDAR concept [90] calls for an intense 60 MeV proton source in combination with a kiloton-scale scintillation-based detector for sensitivity to the sterile neutrino. Such a source is being developed concurrently with the DAE $\delta$ ALUS experiment, nominally a search for nonzero  $\delta_{CP}$  [99]. Cyclotron-produced 60 MeV protons impinge on a beryllium-based target, which mainly acts as a copious source of neutrons and is surrounded by an isotopically pure shell of  $^7\text{Li}$ .  $^8\text{Li}$ , created via neutron capture on  $^7\text{Li}$  inside the shell, decays to a 6.4 MeV mean energy electron antineutrino. Placing such an antineutrino source next to an existing detector such as KamLAND [3] could quickly provide discovery-level sensitivity in the reactor anomaly allowed region. Furthermore, IsoDAR has the ability to distinguish between one and multiple sterile neutrinos.

Another unstable-isotope-based idea involves the deployment of a radioactive source inside an existing kiloton-scale detector [89] such as Borexino [100], KamLAND [3], or SNO+ [101]. Electron antineutrinos from a small-extent  $\sim 2 \text{ PBq}$   $^{144}\text{Ce}$  or  $^{106}\text{Ru}$  beta source can be used to probe the sterile neutrino parameter space. For currently favored parameters associated with sterile neutrino(s), such antineutrinos are expected to disappear and reappear as a function of distance and energy inside the detector, much like the IsoDAR concept described above.

**6.2.4. Nuclear Reactor.** A nuclear reactor can be used as a source for an electron antineutrino disappearance experiment with sensitivity to sterile neutrino(s). The Nucifer detector will likely be the first reactor-based detector to test the sterile neutrino hypothesis using antineutrino energy shape rather than just rate [91]. The experiment will take data in 2012/2013. The idea is to place a  $1 \text{ m}^3$  scale Gd-doped liquid scintillator device within a few tens of meters of a small-extent 70 MW research reactor in an attempt to observe antineutrino disappearance as a function of energy.

The observation of an oscillation wave consistent with high  $\Delta m^2$  would be unambiguous evidence for the existence of at least one sterile neutrino. Cosmic ray interactions and their products represent the largest source of background for this class of experiment.

One of the challenges of a reactor-based search is the need for a relatively small reactor size given the baseline required for maximal sensitivity to  $\Delta m_{ij}^2 \sim 1 \text{ eV}^2$ ; a large neutrino source size relative to the neutrino baseline smears  $L$  and reduces  $\Delta m_{ij}^2$  resolution. A sterile search at a GW-scale power reactor is possible, however. The SCRAAM experiment (see [23]) calls for a Gd-doped liquid scintillator detector at the San Onofre Nuclear Generating Station.

**6.2.5. Neutral Current Based Experiments.** All of the future experiments discussed previously involve either disappearance or appearance of neutrinos and antineutrinos detected via the charged current. However, a NC-based disappearance experiment provides unique sensitivity to the sterile neutrino. If neutrino disappearance was observed in a NC experiment, one would know that the active flavor neutrino(s) in question had oscillated into the noninteracting sterile flavor. Particularly, such an experiment would provide a measure of  $|U_{s4}|$ , the sterile flavor composition of the fourth neutrino mass eigenstate, and definitively prove the existence of a sterile flavor neutrino, especially when considered in combination with CC-based experiments. A full understanding of the mixing angles associated with sterile neutrino(s) will require a NC-based experiment. The Ricochet concept [88] calls for oscillometry measurements using NC coherent neutrino-nucleus scattering detected via low temperature bolometers [81, 82, 88]. Both reactor and isotope decay sources are being considered for these measurements, utilizing the as-yet-undetected coherent neutrino-nucleus scattering process. The OscSNS experiment [83, 84] will also have the capability of looking for muon neutrino disappearance via the neutral current channel. Such a measurement would directly probe the sterile neutrino content of possible extra mass eigenstates.

## 7. Conclusions

This paper has presented results of SBL experiments discussed within the context of oscillations involving sterile neutrinos. Fits to  $(3 + 1)$ ,  $(3 + 2)$ , and  $(3 + 3)$  models have been presented. We have examined whether the  $(3 + 3)$  model addresses tensions observed with  $(3 + 1)$  and  $(3 + 2)$  fits.

Several issues arise when comparing datasets in  $(3 + 1)$  and  $(3 + 2)$  models. In a  $(3 + 1)$  model, the compatibility of the neutrino versus antineutrino datasets is poor (0.14%), and the compatibility among all datasets is only 0.043%. In a  $(3 + 2)$  model, there is a striking disagreement between appearance and disappearance datasets, with a compatibility of 0.0082%.

A  $3 + 3$   $(3 + 2)$  model fit has a  $\chi^2$ -probability for the best-fit of 67% (69%), compared to 2.1% for the no oscillation scenario. Though these values are on the order of the  $\chi^2$ -probabilities found for the  $3 + 1$  model, the  $3 + 3$   $(3 + 2)$  fits resolve the incompatibility issues seen in the  $3 + 1$  model, with the exception of the MiniBooNE appearance datasets. Therefore, we argue that the  $3 + 2$  and  $3 + 3$  fits should be the main focus of sterile neutrino phenomenological studies in the future.

While the indications of sterile neutrino oscillations have historically been associated with only appearance-based SBL experiments, the recently realized suppression in observed  $\bar{\nu}_e$  in disappearance reactor experiments provides further motivation for these models. As we have shown, one can consistently fit most results under the  $(3 + 3)$  hypothesis with improved compatibility. However, the need for additional information from both appearance and disappearance experiments provides strong motivation for pursuing the future experiments discussed in this paper.

## Acknowledgments

The authors thank William Louis and Zarko Pavlovic for valuable discussions and the National Science Foundation for its support.

## References

- [1] K. Abe, Y. Hayato, T. Iida et al., “Solar neutrino results in Super-Kamiokande-III,” *Physical Review D*, vol. 83, Article ID 052010, 2011.
- [2] B. Aharmim, S. N. Ahmed, A. E. Anthony et al., “Low energy threshold analysis of the phase I and phase II data sets of the Sudbury Neutrino Observatory,” *Physical Review C*, vol. 81, Article ID 055504, 2010.
- [3] S. Abe, T. Ebihara, S. Enomoto et al., “Precision measurement of neutrino oscillation parameters with KamLAND,” *Physical Review Letters*, vol. 100, Article ID 221803, 2008.
- [4] R. Wendell, C. Ishihara, K. Abe et al., “Atmospheric neutrino oscillation analysis with subleading effects in Super-Kamiokande I, II, and III,” *Physical Review D*, vol. 81, Article ID 092004, 2010.
- [5] W. W. M. Allison, G. J. Alner, D. S. Ayres et al., “Neutrino oscillation effects in Soudan 2 upward-stopping muons,” *Physical Review D*, vol. 72, Article ID 052005, 2005.
- [6] M. H. Ahn, E. Aliu, S. Andringa et al., “Measurement of neutrino oscillation by the K2K experiment,” *Physical Review D*, vol. 74, Article ID 072003, 2006.
- [7] D. G. Michael, P. Adamson, T. Alexopoulos et al., “Observation of muon neutrino disappearance with the MINOS detectors in the NuMI neutrino beam,” *Physical Review Letters*, vol. 97, Article ID 191801, 2006.
- [8] P. Adamson, C. Andreopoulos, K. E. Arms et al., “Study of muon neutrino disappearance using the Fermilab Main Injector neutrino beam,” *Physical Review D*, vol. 77, Article ID 072002, 2008.
- [9] P. Adamson, C. Andreopoulos, K. E. Arms et al., “Measurement of neutrino oscillations with the MINOS detectors in the NuMI beam,” *Physical Review Letters*, vol. 101, Article ID 131802, 2008.
- [10] P. Adamson, C. Andreopoulos, K. E. Arms et al., “Measurement of the neutrino mass splitting and flavor mixing by MINOS,” *Physical Review Letters*, vol. 106, Article ID 181801, 2011.
- [11] P. Adamson, C. Andreopoulos, D. J. Auty et al., “First direct observation of muon antineutrino disappearance,” *Physical Review Letters*, vol. 107, Article ID 021801, 2012.
- [12] P. Adamson, D. J. Auty, D. S. Ayres et al., “Improved search for muon-neutrino to electron-neutrino oscillations in MINOS,” *Physical Review Letters*, vol. 107, Article ID 181802, 2011.
- [13] K. Abe, N. Abgrall, Y. Ajima et al., “Indication of electron neutrino appearance from an accelerator-produced off-axis muon neutrino beam,” *Physical Review Letters*, vol. 107, Article ID 041801, 2011.
- [14] Y. Abe, C. Aberle, T. Akiri et al., “Indication of reactor  $\bar{\nu}_e$  disappearance in the Double Chooz experiment,” *Physical Review Letters*, vol. 108, Article ID 131801, 2012.
- [15] F. P. An, J. Z. Bai, A. B. Balantekin et al., “Observation of electron-antineutrino disappearance at Daya Bay,” *Physical Review Letters*, vol. 108, Article ID 171803, 2012.
- [16] J. K. Ahn, S. Chebotaryov, J. H. Choi et al., “Observation of reactor electron antineutrino disappearance in the RENO experiment,” *Physical Review Letters*, vol. 108, Article ID 191802, 2012.
- [17] A. Aguilar, L. B. Auerbach, R. L. Burman et al., “Evidence for neutrino oscillations from the observation of  $\bar{\nu}_e$  appearance in a  $\bar{\nu}_\mu$  beam,” *Physical Review D*, vol. 64, Article ID 112007, 2001.
- [18] A. Aguilar-Arevalo and MiniBooNE Collaboration, To be submitted to *Physical Review Letters*.
- [19] G. Mention, M. Fechner, T. Lasserre, T. Mueller, and D. Lhuillier, “Reactor antineutrino anomaly,” *Physical Review D*, vol. 83, Article ID 073006, 2011.
- [20] M. Sorel, J. M. Conrad, and M. Shaevitz, “Combined analysis of short-baseline neutrino experiments in the  $(3 + 1)$  and  $(3 + 2)$  sterile neutrino oscillation hypotheses,” *Physical Review D*, vol. 70, Article ID 073004, 2004.
- [21] G. Karagiorgi, A. Aguilar-Arevalo, J. M. Conrad et al., “Leptonic CP violation studies at MiniBooNE in the  $(3 + 2)$  sterile neutrino oscillation hypothesis,” *Physical Review D*, vol. 5, Article ID 013011, 2007.
- [22] G. Karagiorgi, Z. Djuric, J. M. Conrad, M. H. Shaevitz, and M. Sorel, “Viability of  $\Delta m^2 \sim 1 \text{ eV}^2$  sterile neutrino mixing models in light of MiniBooNE electron neutrino and antineutrino data from the Booster and NuMI beamlines,” *Physical Review D*, vol. 80, Article ID 073001, 2009.
- [23] K. N. Abazajian, M. A. Acero, S. K. Agarwalla et al., “Light sterile neutrinos: a white paper,” <http://arxiv.org/abs/1204.5379>.

- [24] M. Maltoni and T. Schwetz, “Sterile neutrino oscillations after first MiniBooNE results,” *Physical Review D*, vol. 76, Article ID 093005, 2007.
- [25] ALEPH Collaboration, DELPHI Collaboration, L3 Collaboration, OPAL Collaboration, SLD Collaboration, LEP Electroweak Working Group, SLD Electroweak and Heavy Flavour Groups, “Precision electroweak measurements on the Z resonance,” *Physics Reports*, vol. 427, pp. 257–454, 2006.
- [26] A. A. Aguilar-Arevalo et al., “Event excess in the MiniBooNE search for  $\bar{\nu}_\mu \rightarrow \bar{\nu}_e$  oscillations,” *Physical Review Letters*, vol. 105, Article ID 181801, 2010.
- [27] M. A. Acero, C. Giunti, and M. Laveder, “Limits on  $\nu_e$  and  $\bar{\nu}_e$  disappearance from Gallium and reactor experiments,” *Physical Review D*, vol. 78, Article ID 073009, 2008.
- [28] M. Martini, M. Ericson, and G. Chanfray, “Neutrino energy reconstruction problems and neutrino oscillations,” *Physical Review D*, vol. 85, no. 9, Article ID 093012, 10 pages, 2012.
- [29] J. Fan and P. Langacker, “Light sterile neutrinos and short baseline neutrino oscillation anomalies,” *Journal of High Energy Physics*, vol. 2012, article 83, 2012.
- [30] J. Dunkley, R. Hlozek, J. Sievers et al., “The Atacama cosmology telescope: cosmological parameters from the 2008 power spectrum,” *The Astrophysical Journal*, vol. 739, article 52, 2011.
- [31] M. C. Gonzalez-Garcia, M. Maltoni, and J. Salvado, “Robust cosmological bounds on neutrinos and their combination with oscillation results,” *Journal of High Energy Physics*, vol. 1008, article 117, 2010.
- [32] E. Giusarma, M. Archidiacono, R. de Putter, A. Melchiorri, and O. Mena, “Sterile neutrino models and nonminimal cosmologies,” *Physical Review D*, vol. 85, Article ID 083522, 2012.
- [33] K. M. Nollett and G. P. Holder, “An analysis of constraints on relativistic species from primordial nucleosynthesis and the cosmic microwave background,” <http://arxiv.org/abs/1112.2683>.
- [34] G. Mangano and P. D. Serpico, “A robust upper limit on  $N_{\text{eff}}$  from BBN, circa 2011,” *Physics Letters B*, vol. 701, pp. 296–299, 2011.
- [35] J. Hamann, S. Hannestad, J. Lesgourgues, C. Rampf, and Y. Y. Y. Wong, “Cosmological parameters from large scale structure—geometric versus shape information,” <http://arxiv.org/abs/1003.3999>.
- [36] A. Smith, M. Archidiacono, A. Cooray et al., “The impact of assuming flatness in the determination of neutrino properties from cosmological data,” <http://arxiv.org/abs/1112.3006>.
- [37] J. Hamann, S. Hannestad, G. G. Raffelt, and Y. Y. Wong, “Sterile neutrinos with eV masses in cosmology—how disfavoured exactly?” *Journal of Cosmology and Astroparticle Physics*, vol. 1109, article 034, 2011.
- [38] G. Karagiorgi, M. H. Shaevitz, and J. M. Conrad, “Confronting the short-baseline oscillation anomalies with a single sterile neutrino and non-standard matter effects,” <http://arxiv.org/abs/1202.1024>.
- [39] J. N. Abdurashitov, V. N. Gavrin, V. V. Gorbachev et al., “Measurement of the solar neutrino capture rate with gallium metal—III. Results for the 2002–2007 data-taking period,” *Physical Review C*, vol. 80, Article ID 015807, 2009.
- [40] F. Kaether, W. Hampel, G. Heusser, J. Kiko, and T. Kirsten, “Reanalysis of the Gallex solar neutrino flux and source experiments,” *Physics Letters B*, vol. 685, no. 1, pp. 47–54, 2010.
- [41] C. Jones, [PhD thesis], Massachusetts Institute of Technology, 2012.
- [42] T. A. Mueller, D. Lhuillier, M. Fallot et al., “Improved predictions of reactor antineutrino spectra,” *Physical Review C*, vol. 83, no. 5, Article ID 054615, 2011.
- [43] P. Huber, “Determination of antineutrino spectra from nuclear reactors,” *Physical Review C*, vol. 84, Article ID 024617, 2011.
- [44] R. Burman et al., *Neutrino Fluxes at KARMEN from Pion Decay in Flight*, FZKA, 1996.
- [45] R. Burman, M. Potter, and E. Smith, “Monte Carlo simulation of neutrino production by medium-energy protons in a beam stop,” *Nuclear Instruments and Methods in Physics Research*, vol. 291, pp. 621–633, 1990.
- [46] A. A. Aguilar-Arevalo, C. E. Anderson, A. O. Bazarko et al., “Neutrino flux prediction at MiniBooNE,” *Physical Review D*, vol. 79, Article ID 072002, 2009.
- [47] S. E. Kopp, “Accelerator neutrino beams,” *Physics Reports*, vol. 439, no. 3, pp. 101–159, 2007.
- [48] M. G. Catanesi, M. T. Muciaccia, E. Radicioni et al., “The HARP detector at the CERN PS,” *Nuclear Instruments and Methods in Physics Research*, vol. 571, pp. 527–561, 2007.
- [49] N. Graf, A. Lebedev, R. J. Abrams et al., “Charged kaon mass measurement using the Cherenkov effect,” *Nuclear Instruments and Methods in Physics Research*, vol. 615, pp. 27–32, 2010.
- [50] J. Conrad and M. Shaevitz, “Limits on electron neutrino disappearance from the KARMEN and LSND  $\nu_e$ -carbon cross section data,” *Physical Review D*, vol. 85, Article ID 013017, 2012.
- [51] B. Armbruster, I. M. Blair, B. A. Bodmann et al., “Upper limits for neutrino oscillations  $\nu_\mu \rightarrow \nu_e$  from muon decay at rest,” *Physical Review D*, vol. 65, Article ID 112001, 2002.
- [52] A. Aguilar-Arevalo et al., “Compatibility of high  $\Delta m^2$   $\nu_e$  and  $\bar{\nu}_e$  neutrino oscillation searches,” *Physical Review D*, vol. 78, Article ID 012007, 2008.
- [53] A. A. Aguilar-Arevalo et al., “A search for muon neutrino and antineutrino disappearance in MiniBooNE,” *Physical Review Letters*, vol. 103, Article ID 061802, 2009.
- [54] P. Adamson et al., “First measurement of  $\nu_\mu$  and  $\nu_e$  events in an off-axis horn-focused neutrino beam,” *Physical Review Letters*, vol. 102, Article ID 211801, 2009.
- [55] P. Astier et al., “Search for  $\nu_\mu \rightarrow \nu_e$  oscillations in the NOMAD experiment,” *Physics Letters B*, vol. 570, p. 19, 2003.
- [56] I. Stockdale, A. Bodek, F. Borchering, N. Giokaris, and K. Lang, “Search for muon neutrino and antineutrino oscillations in the mass range  $15 < \Delta m^2 < 1,000 \text{ eV}^2/c^4$ ,” *Zeitschrift für Physik C*, vol. 27, p. 53, 1985.
- [57] F. Dydak, G. Feldman, C. Guyot, J. Merlo, and H. Meyer, “A search for  $\nu_\mu$  oscillations in the  $\Delta m^2$  range  $0.3\text{--}90 \text{ eV}^2$ ,” *Physics Letters B*, vol. 134, p. 281, 1984.
- [58] D. Casper, “The nuance neutrino simulation, and the future,” *Nuclear Physics*, vol. 112, p. 161, 2002.
- [59] Y. Declais, J. Favier, A. Metref et al., “Search for neutrino oscillations at 15, 40 and 95 meters from a nuclear power reactor at Bugey,” *Nuclear Physics B*, vol. 434, no. 3, pp. 503–532, 1995.
- [60] C. Giunti and M. Laveder, “Statistical significance of the gallium anomaly,” *Physical Review C*, vol. 83, Article ID 065504, 2011.
- [61] A. Esmaili, F. Halzen, and O. Peres, “Constraining sterile neutrinos with AMANDA and IceCube atmospheric neutrino data,” <http://arxiv.org/abs/1206.6903>.
- [62] P. Adamson, D. S. Ayres, C. Backhouse et al., “An improved measurement of muon antineutrino disappearance in MINOS,” <http://arxiv.org/abs/1202.2772>.



- [63] P. Adamson, D. J. Auty, D. S. Ayres et al., "Search for the disappearance of muon antineutrinos in the NuMI neutrino beam," <http://arxiv.org/abs/1108.1509>.
- [64] M. Maltoni, T. Schwetz, M. Tortola, and J. Valle, "Status of global fits to neutrino oscillations," *New Journal of Physics*, vol. 6, p. 122, 2004.
- [65] K. K. M. Honda, T. Kajita, and S. Midorikawa, "A New calculation of the atmospheric neutrino flux in a 3-dimensional scheme," *Physical Review D*, vol. 70, Article ID 043008, 2004.
- [66] M. C. Gonzalez-Garcia and M. Maltoni, "Atmospheric neutrino oscillations and new physics," *Physical Review D*, vol. 70, Article ID 033010, 2004.
- [67] S. H. Ahn et al., "Detection of accelerator-produced neutrinos at a distance of 250 km," *Physics Letters B*, vol. 511, pp. 178–184, 2001.
- [68] M. H. Ahn et al., "Indications of neutrino oscillation in a 250 km long-baseline experiment," *Physical Review Letters*, vol. 90, Article ID 041801, 2003.
- [69] P. Br maud, *Markov Chains: Gibbs Fields, Monte Carlo Simulation, and Queues*, Springer, New York, NY, USA, 1999.
- [70] M. Maltoni and T. Schwetz, "Testing the statistical compatibility of independent data sets," *Physical Review D*, vol. 68, Article ID 033020, 2003.
- [71] J. Kopp, M. Maltoni, and T. Schwetz, "Are there sterile neutrinos at the eV scale?" *Physical Review Letters*, vol. 107, Article ID 091801, 2011.
- [72] C. Giunti and M. Laveder, "Implications of 3 + 1 short-baseline neutrino oscillations," *Physics Letters B*, vol. 706, pp. 200–207, 2011.
- [73] A. Donini, P. Hernandez, J. Lopez-Pavon, M. Maltoni, and T. Schwetz, "The minimal 3 + 2 neutrino model versus oscillation anomalies," *Journal of High Energy Physics*, vol. 2012, no. 7, Article ID 161, 2012.
- [74] J. A. Harvey, C. T. Hill, and R. J. Hill, "Anomaly mediated neutrino-photon interactions at finite baryon density," *Physical Review Letters*, vol. 99, Article ID 261601, 2007.
- [75] H. Chen et al., "Proposal for a New Experiment Using the Booster and NuMI Neutrino Beamlines: MicroBooNE," FERMILAB-PROPOSAL-0974, 2007.
- [76] G. Tzanakos et al., "MINOS+: a Proposal to FNAL to run MINOS with the medium energy NuMI beam," Tech. Rep., 2011.
- [77] I. Stancu et al., "A Proposal to Build a MiniBooNE Near Detector: BooNE," 2011.
- [78] G. Karagiorgi, "MicroBooNE and the road to large liquid argon neutrino detectors," *Physics Procedia*, vol. 37, pp. 1319–1323, 2012.
- [79] C. Rubbia, M. Antonello, D. Bagliani et al., "A comprehensive search for anomalies from neutrino and anti-neutrino oscillations at large mass difference with two LArTPC imaging detectors at different distances from the CERN-PS," Tech. Rep., 2011.
- [80] P. Kyberd, D. R. Smith, L. Coney et al., "nuSTORM: neutrinos from STORed Muons," <http://arxiv.org/abs/1206.0294>.
- [81] A. J. Anderson, J. M. Conrad, E. Figueroa-Feliciano, K. Scholberg, and J. Spitz, "Coherent neutrino scattering in dark matter detectors," *Physical Review D*, vol. 84, no. 1, Article ID 013008, 2011.
- [82] A. J. Anderson, J. M. Conrad, E. Figueroa-Feliciano et al., "Measuring active-to-sterile neutrino oscillations with neutral current coherent neutrino-nucleus scattering," *Physical Review D*, vol. 86, Article ID 013004, 11 pages, 2012.
- [83] I. Stancu and OscSNS Collaboration, "The OscSNS White Paper," 2008.
- [84] G. T. Garvey, A. Green, and C. Green, "Measuring active-sterile neutrino oscillations with a stopped pion neutrino source," *Physical Review D*, vol. 72, Article ID 092001, 2005.
- [85] S. K. Agarwalla and P. Huber, "LSND reloaded," *Physics Letters B*, vol. 696, pp. 359–361, 2011.
- [86] J. Spitz, "Sterile neutrino search with kaon decay at rest," *Physical Review D*, vol. 85, Article ID 093020, 2012.
- [87] C. Grieb, J. Link, and R. S. Raghavan, "Probing active to sterile neutrino oscillations in the LENS detector," *Physical Review*, vol. 75, no. 9, Article ID 093006, 5 pages, 2007.
- [88] J. Formaggio, E. Figueroa-Feliciano, and A. J. Anderson, "Sterile neutrinos, coherent scattering, and oscillometry measurements with low-temperature bolometers," *Physical Review D*, vol. 85, no. 1, Article ID 013009, 14 pages, 2012.
- [89] M. Cribier, M. Fechner, T. Lasserre et al., "Proposed search for a fourth neutrino with a PBq antineutrino source," *Physical Review Letters*, vol. 107, no. 20, Article ID 201801, 4 pages, 2011.
- [90] A. Bungau, A. Adelman, J. R. Alonso et al., "An electron antineutrino disappearance search using high-rate 8Li production and decay," *Physical Review Letters*, vol. 109, Article ID 141802, 5 pages, 2012.
- [91] A. Porta, V. Bui, M. Cribier, M. Fallot, M. Fechner, and L. Giot, "Reactor neutrino detection for non-proliferation with the NUCIFER experiment," *IEEE Transactions on Nuclear Science*, vol. 57, no. 5, pp. 2732–2739, 2010.
- [92] A. P. Serebrov, V. G. Zinoviev, A. K. Fomin et al., "NEUTRINO4 experiment: preparations for search for sterile neutrino at 100 MW reactor SM-3 at 6-12 meters," <http://arxiv.org/abs/1205.2955>.
- [93] S. Gninenko, "Sterile neutrino decay as a common origin for LSND/MiniBooNE and T2K excess events," *Physical Review*, vol. 85, no. 5, Article ID 051702, 5 pages, 2012.
- [94] A. A. Aguilar-Arevalo, C. E. Anderson, A. O. Bazarko et al., "Tests of Lorentz and CPT violation with MiniBooNE neutrino oscillation excesses," <http://arxiv.org/abs/1206.6915>.
- [95] S. K. Agarwalla, J. M. Conrad, and M. H. Shaevitz, "Short-baseline neutrino oscillation waves in ultra-large liquid scintillator detectors," *Journal of High Energy Physics*, vol. 2011, no. 12, article 085, 2011.
- [96] A. A. Aguilar-Arevalo et al., "Unexplained excess of electronlike events from a 1-GeV neutrino beam," *Physical Review Letters*, vol. 102, no. 10, Article ID 101802, 5 pages, 2009.
- [97] C. Anderson et al., "First measurements of inclusive muon neutrino charged current differential cross sections on argon," *Physical Review Letters*, vol. 108, Article ID 161802, 2012.
- [98] S. Geer, "Neutrino beams from muon storage rings: Characteristics and physics potential," *Physical Review D*, vol. 57, pp. 6989–6997, 1998.
- [99] J. M. Conrad and M. H. Shaevitz, "A new method to search for CP violation in the neutrino sector," *Physical Review Letters*, vol. 104, Article ID 141802, 2010.
- [100] G. Alimonti et al., "Science and technology of Borexino: a real-time detector for low energy solar neutrinos," *Astroparticle Physics*, vol. 16, pp. 205–234, 2002.
- [101] M. Chen, "The SNO liquid scintillator project," *Nuclear Physics B*, vol. 145, p. 65, 2005.



## Review Article

# Prospects for Neutrino Oscillation Physics

**Silvia Pascoli<sup>1</sup> and Thomas Schwetz<sup>2</sup>**

<sup>1</sup> *IPPP, Department of Physics, Durham University, Durham DH1 3LE, UK*

<sup>2</sup> *Max-Planck-Institut für Kernphysik, Saupfercheckweg 1, 69117 Heidelberg, Germany*

Correspondence should be addressed to Thomas Schwetz; [schwetz@mpi-hd.mpg.de](mailto:schwetz@mpi-hd.mpg.de)

Received 8 August 2012; Accepted 7 November 2012

Academic Editor: Jose Bernabeu

Copyright © 2013 S. Pascoli and T. Schwetz. This is an open access article distributed under the Creative Commons Attribution License, which permits unrestricted use, distribution, and reproduction in any medium, provided the original work is properly cited.

Recently the last unknown lepton mixing angle  $\theta_{13}$  has been determined to be relatively large, not too far from its previous upper bound. This opens exciting possibilities for upcoming neutrino oscillation experiments towards addressing fundamental questions, among them the type of the neutrino mass hierarchy and the search for CP violation in the lepton sector. In this paper we review the phenomenology of neutrino oscillations, focusing on subleading effects, which will be the key towards these goals. Starting from a discussion of the present determination of three-flavour oscillation parameters, we give an outlook on the potential of near-term oscillation physics as well as on the long-term program towards possible future precision oscillation facilities. We discuss accelerator-driven long-baseline experiments as well as nonaccelerator possibilities from atmospheric and reactor neutrinos.

## 1. Introduction

Over the last 15 years so huge progress has been made in the study of neutrino oscillations [1–4], and with the recent determination of the last unknown mixing angle  $\theta_{13}$  [5–9] a clear first-order picture of the three-flavour lepton mixing matrix has emerged. The results of a global fit [10] to world neutrino oscillation data including data presented at the Neutrino2012 conference are summarized in Figure 1 and Table 1 (for alternative global fits see [11, 12], and combinations of the recent data relevant to the  $\theta_{13}$  determination have been presented in [13, 14]). Global data as of June 2012 disfavour  $\theta_{13} = 0$  with a  $\Delta\chi^2 \approx 100$  and its value are determined as  $\theta_{13} = (8.6^{+0.44}_{-0.46})^\circ$ . (An uncertainty about this number at the level of  $1\sigma$  remains due to a tension between predicted reactor neutrino fluxes and data from reactor experiments with baselines less than 100 m, the so-called reactor anomaly [15].) Establishing such a relatively large value of  $\theta_{13}$ , comparable to the previous bound [16], opens exciting possibilities for neutrino oscillations. There are fundamental open questions in neutrino physics which can be addressed with neutrino oscillations.

- (i) Is there CP violation in the leptonic sector, as in the quark sector? The behaviour under the CP transformation is one of the fundamental properties of

particles and a violation of the CP symmetry might be linked to the baryon asymmetry of the universe.

- (ii) What is the hierarchy of the neutrino mass spectrum, normal or inverted? This information is important phenomenologically for the interpretation of other neutrino experiments, for instance, neutrinoless double beta decay. Moreover, together with the absolute mass scale, it is one of the key pieces of information on neutrino masses.
- (iii) What are the precise values of the neutrino-mixing angles? Do they show an underlying pattern? The answers to these questions are a necessary input in order to solve the flavour problem.

With our current knowledge of  $\theta_{13}$  answering those questions becomes a realistic possibility.

The outline of this work is as follows. In Section 2 we review the current status of neutrino oscillations and discuss the phenomenology of long-baseline (LBL), reactor, and atmospheric neutrino experiments. In Section 3 we discuss the potential of currently operating LBL and reactor facilities in the time frame of about 10 years. In Section 4 some nonaccelerator-based methods to determine the neutrino mass hierarchy are discussed. In Section 5 we give an overview on possible long-term experimental strategies

TABLE 1: Three-flavour oscillation parameters from a fit to global data after the Neutrino2012 conference [10]. The normalization of reactor neutrino fluxes is determined by short-baseline reactor data, which are included in the fit.

	bfp $\pm 1\sigma$	$3\sigma$ range
$\sin^2\theta_{12}$	$0.30 \pm 0.013$	$0.27 \rightarrow 0.34$
$\theta_{12}/^\circ$	$33.3 \pm 0.8$	$31 \rightarrow 36$
$\sin^2\theta_{23}$	$0.41^{+0.037}_{-0.025} \oplus 0.59^{+0.021}_{-0.022}$	$0.34 \rightarrow 0.67$
$\theta_{23}/^\circ$	$40.0^{+2.1}_{-1.5} \oplus 50.4^{+1.2}_{-1.3}$	$36 \rightarrow 55$
$\sin^2\theta_{13}$	$0.023 \pm 0.0023$	$0.016 \rightarrow 0.030$
$\theta_{13}/^\circ$	$8.6^{+0.44}_{-0.46}$	$7.2 \rightarrow 9.5$
$\delta/^\circ$	$300^{+66}_{-138}$	$0 \rightarrow 360$
$\Delta m_{21}^2/10^{-5} \text{ eV}^2$	$7.50 \pm 0.185$	$7.00 \rightarrow 8.09$
$\Delta m_{31}^2/10^{-3} \text{ eV}^2$ (NH)	$2.47^{+0.069}_{-0.067}$	$2.27 \rightarrow 2.69$
$\Delta m_{32}^2/10^{-3} \text{ eV}^2$ (IH)	$-2.43^{+0.042}_{-0.065}$	$-2.65 \rightarrow -2.24$

towards high-precision oscillation facilities. We do not discuss solar, supernova, or other astrophysical neutrinos which are covered in detail in other chapters of this volume.

We will remain within the three-neutrino mixing framework and will not discuss deviations from it such as sterile neutrinos or nonstandard interactions. We use the standard convention for parametrizing the three-flavour lepton-mixing matrix in terms of the three angles,  $\theta_{12}$ ,  $\theta_{23}$ ,  $\theta_{13}$ , and one Dirac-type CP phase  $\delta$  [17]:

$$U = \begin{pmatrix} c_{12}c_{13} & s_{12}c_{13} & s_{13}e^{-i\delta} \\ -s_{12}c_{23} - c_{12}s_{13}s_{23}e^{i\delta} & +c_{12}c_{23} - s_{12}s_{13}s_{23}e^{i\delta} & c_{13}s_{23} \\ +s_{12}s_{23} - c_{12}s_{13}c_{23}e^{i\delta} & -c_{12}c_{23} - s_{12}s_{13}c_{23}e^{i\delta} & c_{13}c_{23} \end{pmatrix}, \quad (1)$$

where  $c_{ij} \equiv \cos\theta_{ij}$  and  $s_{ij} \equiv \sin\theta_{ij}$ . Squared differences of the neutrino masses  $m_i$  are defined as  $\Delta m_{ij}^2 \equiv m_i^2 - m_j^2$ . The neutrino mass hierarchy is determined by the sign of  $\Delta m_{31}^2$ , with  $\Delta m_{31}^2 > 0$  corresponding to normal hierarchy (NH), and  $\Delta m_{31}^2 < 0$  to inverted hierarchy (IH).

## 2. Present Status as Case Study for Oscillation Phenomenology

In this section we introduce the oscillation probabilities relevant to long-baseline accelerator experiments, reactor experiments, as well as atmospheric neutrinos. We use the present data to illustrate the interplay and complementarity of different types of oscillation experiments.

**2.1. The Beam-Reactor Interplay.** Since the advent of data on  $\nu_\mu \rightarrow \nu_e$  searches from T2K [5] and MINOS [6] on the one side, and  $\theta_{13}$  reactor experiments Double Chooz [7], Daya Bay [8], and RENO [9] on the other side, the long anticipated complementarity of beam and reactor experiments [18, 19] is now a reality. In this section we discuss some aspects of that related to deviations of  $\theta_{23}$  from maximal mixing, as well as the dependence of the global fit on the CP phase  $\delta$ .

Recent data seem to indicate a deviation of  $\theta_{23}$  from the maximal mixing value of  $45^\circ$ , roughly at the level of

$1.7\sigma - 2\sigma$ , compare Figure 1 (in [12] a somewhat higher significance is obtained). If confirmed, such a deviation would have profound implications for neutrino mass models based on flavour symmetries. An important contribution to this effect comes from recent MINOS data on  $\nu_\mu$  disappearance. Neglecting effects of  $\Delta m_{21}^2$  and the matter effect, the relevant survival probability is given by

$$P_{\nu_\mu \rightarrow \nu_\mu} = 1 - 4|U_{\mu 3}|^2 \left(1 - |U_{\mu 3}|^2\right) \sin^2 \frac{\Delta m_{31}^2 L}{4E}, \quad (2)$$

$$|U_{\mu 3}|^2 = \sin^2\theta_{23}\cos^2\theta_{13},$$

where  $L$  is the baseline and  $E$  is the neutrino energy. Hence, the probability is symmetric under  $|U_{\mu 3}|^2 \rightarrow (1 - |U_{\mu 3}|^2)$ . In the two-flavour limit of  $\theta_{13} = 0$  this implies that the data is sensitive only to  $\sin^2 2\theta_{23}$ , which for  $\theta_{23} \neq 45^\circ$  leads to a degeneracy between the first and second octants of  $\theta_{23}$  [20]. Indeed, recent data from MINOS [21] have given a best fit point of  $\sin^2 2\theta \approx 0.94$  if analysed in a two-flavour framework.

Since  $\theta_{13}$  is large, one can try to explore a synergy between long-baseline appearance experiments and an independent determination of  $\theta_{13}$  at reactor experiments in order to resolve the degeneracy [18, 20, 22]. Let us look at the appearance probability relevant to the  $\nu_\mu \rightarrow \nu_e$  searches at T2K [5] and MINOS [6]. Expanding to second order in the small parameters  $\sin\theta_{13}$  and  $\alpha \equiv \Delta m_{21}^2/\Delta m_{31}^2$  and assuming a constant matter density that one finds [23–25]:

$$P_{\nu_\mu \rightarrow \nu_e} \approx 4 \sin^2\theta_{13} \sin^2\theta_{23} \frac{\sin^2\Delta(1-A)}{(1-A)^2} + \alpha^2 \sin^2 2\theta_{12} \cos^2\theta_{23} \frac{\sin^2 A \Delta}{A^2} + 2\alpha \sin\theta_{13} \sin 2\theta_{12} \sin 2\theta_{23} \times \cos(\Delta \pm \delta_{\text{CP}}) \frac{\sin \Delta A}{A} \frac{\sin \Delta(1-A)}{1-A}, \quad (3)$$

with the definitions

$$\Delta \equiv \frac{\Delta m_{31}^2 L}{4E}, \quad A \equiv \frac{2EV}{\Delta m_{31}^2}, \quad (4)$$

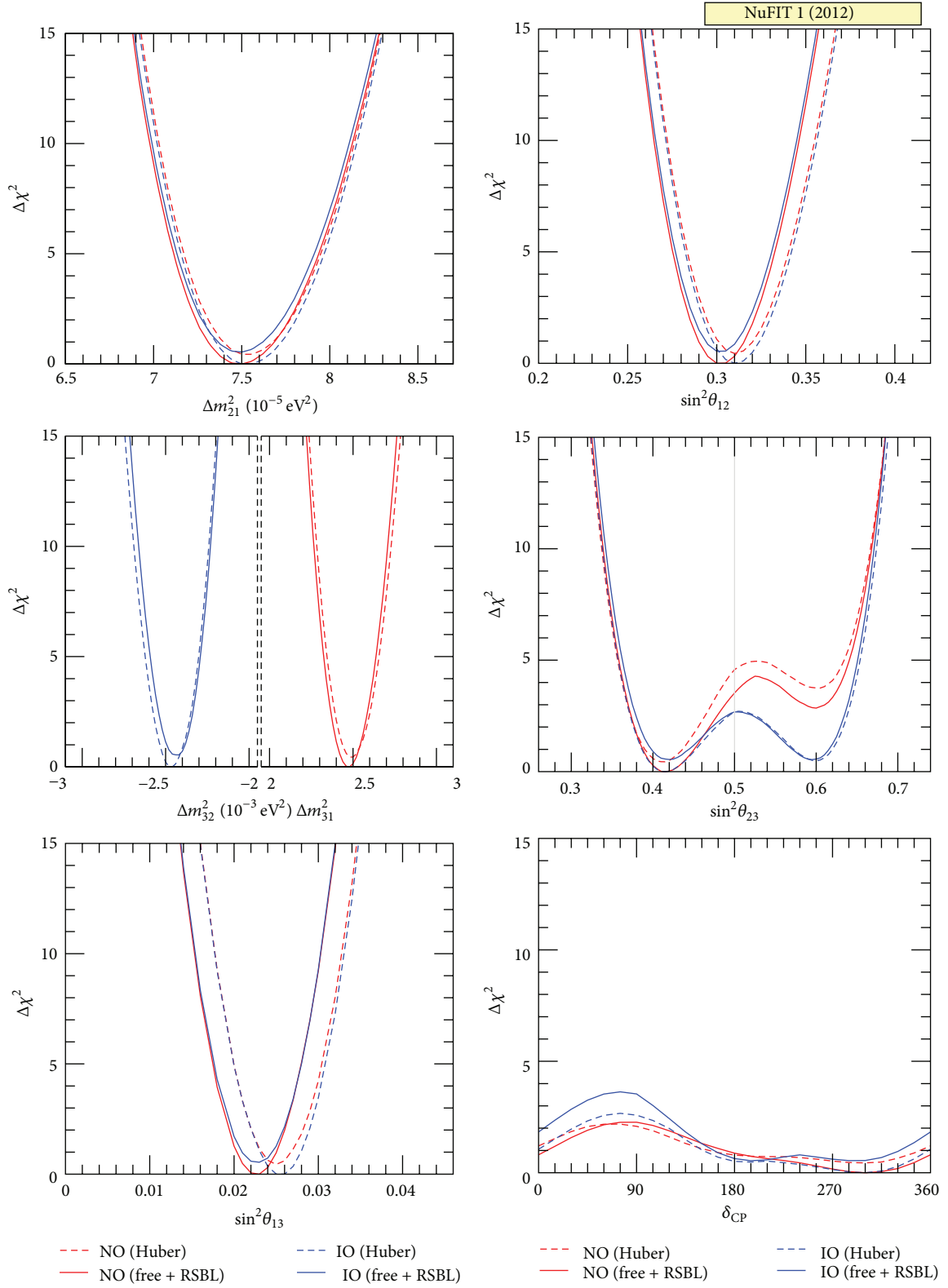


FIGURE 1: Determination of three-flavour oscillation parameters [10]. The red (blue) curves are for NH (IH). Results for different assumptions concerning the analysis of data from reactor experiments are shown: for solid curves the normalization of reactor fluxes is left free, and data from short-baseline (less than 100 m) reactor experiments are included. For dashed curves short-baseline data are not included but reactor fluxes as predicted in [152] are assumed.

where  $L$  is the baseline,  $E$  is the neutrino energy, and  $V$  is the effective matter potential [26]. Note that  $\alpha$ ,  $\Delta$ , and  $A$  are sensitive to the sign of  $\Delta m_{31}^2$  (i.e., the type of the neutrino mass ordering). The plus (minus) sign in (3) applies for neutrinos (antineutrinos), and for antineutrinos  $V \rightarrow -V$ , which implies that  $A \rightarrow -A$ . It is clear from (3) that in the case of large matter effect,  $A \geq 1$ , the terms  $(1 - A)$  depend strongly on the type of the mass hierarchy, and for  $A = 1$  (possible for neutrinos and NH, or antineutrinos and IH) a resonance is encountered [27]. Numerically one finds for a typical matter density of  $3 \text{ g/cm}^3$

$$|A| \approx 0.09 \left( \frac{E}{\text{GeV}} \right) \left( \frac{|\Delta m_{31}^2|}{2.5 \times 10^{-3} \text{ eV}^2} \right)^{-1}. \quad (5)$$

Since, for T2K  $E \sim 0.7 \text{ GeV}$ , matter effects are of order few percent, whereas in experiments like NOvA [28] with  $E \sim 2 \text{ GeV}$  we can have  $|A| \sim 0.2$ . Note that  $\alpha^2 \approx 10^{-3}$ , which implies that the second term in the first line of (3) gives a very small contribution compared to the other terms.

An important observation is that the first term in (3) (which dominates for large  $\theta_{13}$ ) depends on  $\sin^2 \theta_{23}$  and therefore is sensitive to the octant. Reactor experiments with  $L \sim 1 \text{ km}$ , on the other hand, provide a measurement of  $\theta_{13}$  independent of  $\theta_{23}$ . The relevant survival probability is given by

$$P_{\nu_e \rightarrow \nu_e} = 1 - \sin^2 2\theta_{13} \sin^2 \Delta + \mathcal{O}(\alpha^2). \quad (6)$$

Hence, by combining the data from reactor experiments such as Double Chooz [7], Daya Bay [8], and RENO [9] with the appearance data from T2K and MINOS one should be sensitive in principle to the octant of  $\theta_{23}$ . The situation from present data is illustrated in Figure 2, where we show the determination of  $\theta_{13}$  from the beam experiments T2K and MINOS as a function of the CP phase  $\delta$  and the octant of  $\theta_{23}$ , where we have chosen values motivated by the MINOS disappearance result. The resulting regions in  $\sin^2 2\theta_{13}$  are compared to the reactor measurements from DoubleChooz, DayaBay, and RENO. It is clear from that figure that for present data from beams and reactors it is not possible to distinguish between 1st and 2nd  $\theta_{23}$  octants. For both possibilities overlap regions between beams and reactors can be found although they are at different values of  $\delta$ . Therefore, current data from reactor and long-baseline beam experiments are not able to resolve the  $\theta_{23}$  octant degeneracy. The lifting of the degeneracy (at low CL) visible in Figure 1 appears due to atmospheric neutrino data, to be discussed below.

In principle the reactor-beam combination should also offer some sensitivity to the CP phase  $\delta$ . This is shown in the right panels of Figure 2. We see that if the octant of  $\theta_{23}$  and the neutrino mass hierarchy were known, already present data from the beam and reactor experiments used in that figure would show quite sizeable dependence on the CP phase, depending on which of the 4 degenerate solutions is considered. However, it is also clear from the figure that we marginalize over those four solutions,  $\chi^2(\delta)$  becomes very flat, and essentially all values of  $\delta$  would be consistent within  $\Delta\chi^2 \leq 1$ . This is a real-life example of how degeneracies can

seriously spoil the sensitivity of long-baseline data [29]. The somewhat larger  $\delta$  dependence visible in Figure 1 follows again from the global fit including atmospheric neutrinos, as discussed below.

**2.2. Subleading Effects in Atmospheric Neutrino Oscillations.** Atmospheric neutrinos provide a powerful tool to study neutrino oscillations, which is manifest also by the first evidence for oscillations from Super-Kamiokande in 1998 [1]. In this section we briefly discuss subleading oscillation modes, triggered by  $\Delta m_{21}^2$  and/or  $\theta_{13}$ , and comment on using them for addressing some of the open questions in oscillation physics.

An important property of atmospheric neutrinos is the fact that the neutrino source contains  $\nu_e$  and  $\bar{\nu}_\mu$  as well as neutrinos and antineutrinos. Therefore, the contributions to  $e$ -like and  $\mu$ -like event samples can be written schematically as

$$\begin{aligned} N_e &\propto (\Phi_e P_{\nu_e \rightarrow \nu_e} + \Phi_\mu P_{\bar{\nu}_\mu \rightarrow \bar{\nu}_\mu}) \sigma_e \\ &= \Phi_e (P_{\nu_e \rightarrow \nu_e} + r P_{\bar{\nu}_\mu \rightarrow \bar{\nu}_\mu}) \sigma_e \\ N_\mu &\propto (\Phi_e P_{\nu_e \rightarrow \nu_\mu} + \Phi_\mu P_{\bar{\nu}_\mu \rightarrow \bar{\nu}_\mu}) \sigma_\mu \\ &= \Phi_\mu \left( \frac{1}{r} P_{\nu_e \rightarrow \nu_\mu} + P_{\bar{\nu}_\mu \rightarrow \bar{\nu}_\mu} \right) \sigma_\mu, \end{aligned} \quad (7)$$

where  $\Phi_\alpha$  and  $\sigma_\alpha$  are initial flux and detection cross section for neutrino of flavour  $\alpha$ , and we have defined the flux ratio

$$r \equiv \frac{\Phi_\mu}{\Phi_e}, \quad (8)$$

with  $r \approx 2$  in the sub-GeV range and  $r \approx 2.6$ – $4.5$  in the multi-GeV range. In (7) we have suppressed energy and zenith angle dependence, as well as detector resolutions and efficiencies. If the detector cannot identify the charge of the lepton, a sum over neutrino and antineutrinos is implicitly assumed; otherwise, analogous relations hold for neutrinos and antineutrinos separately. Hence, the observation of  $e$ -like and  $\mu$ -like events contains convoluted information on different oscillation channels.

An interesting observable is the excess of  $e$ -like events (relative to the no-oscillation prediction  $N_e^0$ ), since in the two-flavour limit one expects  $N_e = N_e^0$ , and therefore any deviation of the observed number of events from  $N_e^0$  should be due to subleading effects. The excess can be written in the following way; see, for example, [30]:

$$\begin{aligned} \frac{N_e}{N_e^0} - 1 &\approx (r \sin^2 \theta_{23} - 1) P_{2\nu}(\Delta m_{31}^2, \theta_{13}) \\ &+ (r \cos^2 \theta_{23} - 1) P_{2\nu}(\Delta m_{21}^2, \theta_{12}) \\ &- \sin \theta_{13} \sin 2\theta_{23} r \text{Re}(A_{ee}^* A_{\mu e}). \end{aligned} \quad (9)$$

Here  $P_{2\nu}(\Delta m^2, \theta)$  is an effective two-flavour oscillation probability governed by a mass-squared difference  $\Delta m^2$  and a mixing angle  $\theta$ , and  $A_{ee}$  and  $A_{\mu e}$  are elements of a transition amplitude matrix. The three terms appearing in (9) have a



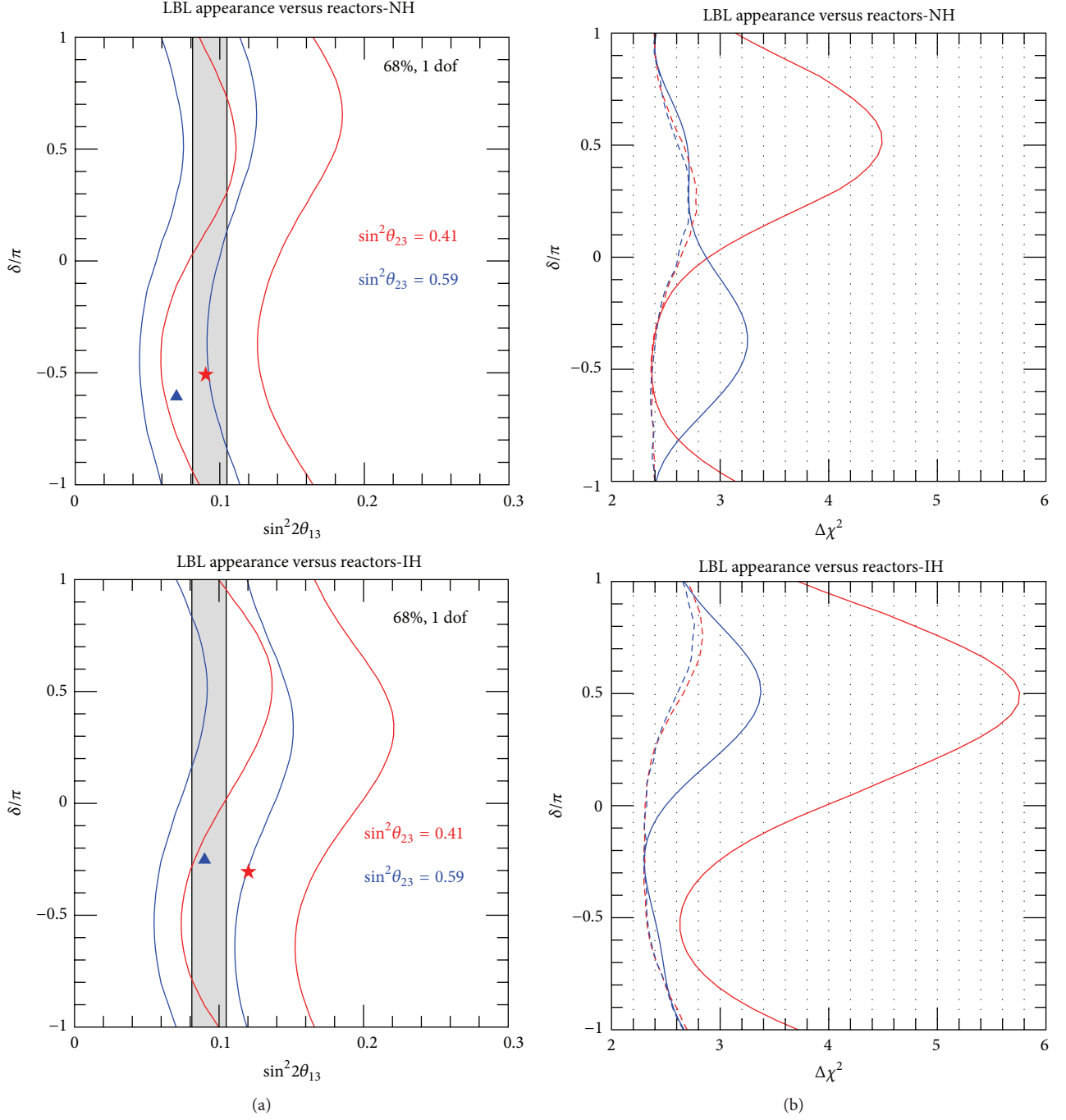


FIGURE 2: (a) Preferred regions in the  $\sin^2 2\theta_{13}$  -  $\delta$  plane. The contour curves correspond to beams T2K + MINOS, where  $\sin^2 \theta_{23}$  is fixed to the two degenerate solutions in the 1st (red) and 2nd (blue) octant. The gray region corresponds to the  $\theta_{13}$  determination from the reactors Double Chooz, Daya Bay, and RENO. (b)  $\Delta\chi^2(\delta)$  for beams (dashed) and beams+reactors (solid) with the same color coding as in the left panels. Upper (lower) panels are for NH (IH).

well-defined physical interpretation. The first term is important in the multi-GeV range and is controlled by the mixing angle  $\theta_{13}$  in  $P_{2\nu}(\Delta m_{31}^2, \theta_{13})$ . This probability can be strongly affected by resonant matter effects [31–36]. Depending on the mass hierarchy the resonance will occur either for neutrinos or antineutrinos. The second term is important for sub-GeV events, and it takes into account the effect of “solar

oscillations” due to  $\Delta m_{21}^2$  and  $\theta_{12}$  [37–40]. Via the prefactor containing the flux ratio  $r$ , both the first and second terms in (9) depend on the octant of  $\theta_{23}$  though, in opposite directions, the multi-GeV (sub-GeV) excess is suppressed (enhanced) for  $\theta_{23} < 45^\circ$ . Finally, the last term in (9) is an interference term between  $\theta_{13}$  and  $\Delta m_{21}^2$  amplitudes, and this term shows also dependence on the CP phase  $\delta$  [30, 40].

Three neutrino effects may also show up in  $\mu$ -like events. This is especially interesting for experiments which can only observe muons, such as: for example, the INO or IceCube experiments. For these types of experiments the multi-GeV region is most interesting, where effects  $\Delta m_{21}^2$  are very small. Hence, we can approximate  $\Delta m_{21}^2 \approx 0$ , and following [41, 42] one can write the excess in  $\mu$ -like events as

$$\frac{N_\mu}{N_\mu^0} - 1 \approx \sin^2 \theta_{23} \left( \frac{1}{r} - \sin^2 \theta_{23} \right) P_{2\nu}(\Delta m_{31}^2, \theta_{13}) - \frac{1}{2} \sin^2 2\theta_{23} [1 - \text{Re}(A_{33})]. \quad (10)$$

The first term is controlled by  $\theta_{13}$  and is subject to resonant matter effects, similar to the first term in (9), though with a different dependence on  $\theta_{23}$  and the flux ratio. In the second term,  $A_{33}$  is a probability amplitude satisfying  $P_{2\nu}(\Delta m_{31}^2, \theta_{13}) = 1 - |A_{33}|^2$ . In the limit  $\theta_{13} = 0$  we have  $\text{Re}(A_{33}) = \cos(\Delta m_{31}^2 L/2E)$ , such that the second term in (10) just describes two-flavour  $\nu_\mu \rightarrow \nu_\mu$  vacuum oscillations.

**2.3. Interplay of Complementary Data Sets in the Present Global Fit.** As mentioned above, while MINOS  $\nu_\mu$  disappearance data prefers a nonmaximal value of  $\theta_{23}$ , we do not observe any sensitivity to the octant of  $\theta_{23}$  from global data without atmospheric neutrinos. In the global analysis of [10] including atmospheric data a weak preference for the 1st octant is obtained in the case of NH; see Figure 1. Similar results are obtained also in [12] with even somewhat higher significance. This can be attributed to a zenith-angle-independent event excess in the sub-GeV  $e$ -like data in SuperKamiokande. Such an excess can be explained by oscillations due to  $\Delta m_{21}^2$  [37–39]. For sub-GeV events the second term in (9) is relevant. In that energy regime  $r \approx 2$  and for  $\sin^2 \theta_{23} \approx 0.5$  the prefactor  $(r \cos^2 \theta_{23} - 1)$  is suppressed, whereas in the 1st octant with  $\sin^2 \theta_{23} < 0.5$  an excess is induced. Let us mention that in an official SuperKamiokande analysis [43] this effect is not clearly observed although one should take into account that there is no combined analysis with MINOS data performed. It can be seen from (9) and (10) that there can be some features in  $e$ -like or  $\mu$ -like data samples which exhibit a different dependence on  $\theta_{23}$ , and which of those subtle effects dominates depends on details of the detector simulation, binning, and treatment of systematic uncertainties. Apparently competing effects become somewhat more important for IH, as in that case the preference for the 1st octant disappears; see Figure 1.

We emphasize the importance of resolving the  $\theta_{23}$  octant degeneracy in order to obtain sensitivity to the CP phase  $\delta$ . This can be seen from Figure 2. By favouring one of the two solution for  $\sin^2 \theta_{23}$  the beam-reactor combination provides a better sensitivity to  $\delta$ , visible in the right panels. With current data this effect is still small, given the final sensitivity to  $\delta$  shown in Figure 1, which is at level of  $\Delta\chi^2 \approx 3$ . We emphasize again the crucial interplay of different data sets necessary for this sensitivity to emerge: MINOS  $\nu_\mu$  disappearance prefers  $\sin^2 2\theta_{23} < 1$ , atmospheric data slightly disfavors  $\sin^2 \theta_{23} > 0.5$ , and the  $\nu_\mu \rightarrow \nu_e$  data from beams

combined with the  $\theta_{13}$  determination from reactors provide sensitivity to  $\delta$ .

### 3. The Current Generation of Long-Baseline Beam and Reactor Experiments

The reactor experiments, Double Chooz [7], DayaBay [8], and RENO [9], have obtained spectacular results already after few weeks of data taking. All of them are still statistics dominated, and the precision of the determination of  $\theta_{13}$  will improve considerably for higher exposures. According to the results of [44] (based on assumptions on systematics from the proposals of the three experiments) the ultimate precision will be dominated by DayaBay. Also T2K [5] is essentially only in the “startup phase” (which unfortunately has been interrupted by the 2011 earthquake in Japan). In addition the NOvA experiment [28] will come online soon and will provide additional data on  $\nu_\mu \rightarrow \nu_e$  appearance. In [45] the expected combined potential of those experiments with their final exposures has been investigated in respect to address the mass hierarchy or a determination of the CP phase  $\delta$ . Here we review the results obtained there in the light of the by now known value of  $\theta_{13}$ . The “nominal” exposures are summarized in Table 2. The experimental configurations are based on official documents as of 2009. As a rough rule of thumb those data might be available around 2020.

Let us first discuss the prospects for the  $\theta_{23}$  measurement, including the determination of the octant in case of a non-maximal value. Figure 3 shows the ability of T2K + NOvA + DayaBay to reconstruct  $\sin^2 \theta_{23}$  as a function of its true value. Data on  $\nu_\mu$  disappearance from T2K and NOvA are mainly sensitive to  $\sin^2 2\theta_{23}$  (see discussion related to (2)), whereas the combination of the  $\nu_\mu \rightarrow \nu_e$  appearance data with the  $\theta_{13}$  reactor measurement provides sensitivity to the octant [18, 20, 22], as discussed above see also Figure 2. While this mechanism does not work for current data, it can be used to identify the right octant at  $3\sigma$  with projected exposures if  $|\sin^2 \theta_{23} - 0.5| > 0.1$ . Note the slight asymmetry of the regions, which is a consequence of the relatively large value of  $\theta_{13}$  and can be understood from (2). We also observe that for large deviations from maximality the accuracy on  $\sin^2 \theta_{23}$  will be quite good, around  $\pm 0.02$  at  $3\sigma$ , whereas close to maximality the determination will be much worse, with a  $3\sigma$  range of about  $0.45 < \sin^2 \theta_{23} < 0.58$ , due to the flatness of  $\sin^2 2\theta$  at  $\theta = 45^\circ$ .

As we have seen above, already with present data a global fit of all experiments shows a slight dependence on the CP phase  $\delta$ . On the other hand the mass hierarchy is undistinguishable with a  $\Delta\chi^2 \leq 1$  between NH and IH, see Figure 1. Now we address the question whether with near-term data from the experiments listed in Table 2 we may be able to say something on the type of the neutrino mass hierarchy or the CP phase  $\delta$ .

Possible outcome of a global fit to data from the final exposure of T2K, NOvA, and DayaBay is shown in Figure 4. Left (right) panel correspond to NH (IH), and we adopt the two exemplary values of  $\delta = \pi/2$  (upper panels) and  $3\pi/2$  (lower panels) corresponding to maximal CP violation. The colored regions would be obtained under the assumption of

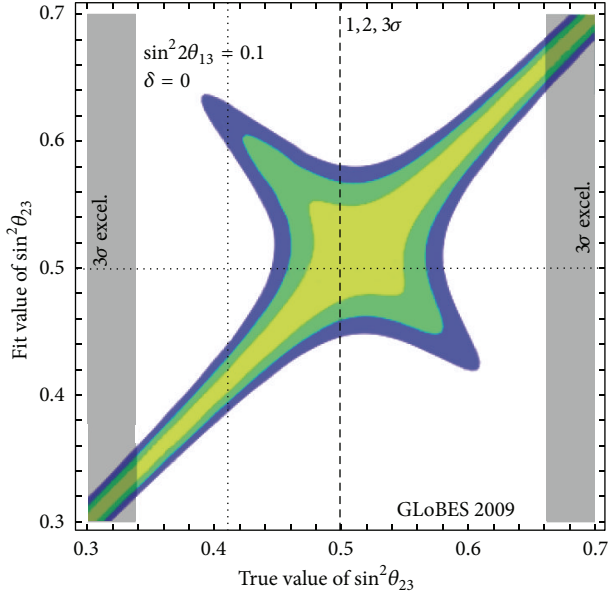


FIGURE 3: Determination of  $\sin^2 \theta_{23}$  at 1, 2, 3 $\sigma$  (1 dof) as a function of the true value from T2K, NOvA, and DayaBay with their final exposures according to Table 2. True values of  $\sin^2 2\theta_{13} = 0.1$  and  $\delta = 0$  have been assumed. The vertical dotted line and the shaded regions indicate the present best fit point and 3 $\sigma$  excluded region, respectively. Figure is based on the results of [45].

known mass hierarchy. In this case some regions of  $\delta$  can be excluded at 3 $\sigma$  although CP-conserving values 0 or  $\pi$  are always contained in the allowed region, indicating that CP violation cannot be established, even under the assumption of known hierarchy. The detailed study performed in [45] shows that only for less than 30% of all possible values of the phase  $\delta$  a hint for CP violation at 90% CL may be obtained. Even for upgraded versions of the beams, with increased beam power, extended running time (up to around 2025), and including antineutrino data from T2K CP violation can be “discovered” at 3 $\sigma$  for about 25% of all possible values of  $\delta$  (see also [46] for related results).

The mass hierarchy determination relies on the matter effect in the  $\nu_\mu \rightarrow \nu_e$  transitions. From the experiments considered here only for the NOvA experiment a notable matter effect is present due to the baseline of 812 km. In Figure 4 we illustrate the combined potential to identify the neutrino mass hierarchy. The black contour curves correspond to the allowed regions obtained by fitting the simulated data with the wrong hierarchy. The local  $\chi^2$  minimum is marked with a black box and the  $\chi^2$  value of the local minimum is given in the figure. It turns out that the four examples shown in the figure correspond approximately to the most optimistic and pessimistic cases for the hierarchy determination. The best possible configuration is obtained for a true NH and  $\delta = 3\pi/2$  (left-lower panel) and a true IH and  $\delta = \pi/2$  (right-upper panel), where the hierarchy can be identified at about 3 $\sigma$ . For the opposite combinations (true NH,  $\delta = \pi/2$  and true IH,  $\delta = 3\pi/2$ ) very poor sensitivity is obtained with  $\chi^2 \approx 2$ . This behaviour

can be understood from (3) by considering the sign of the interference term in the second line. Good sensitivity is obtained when, for the channel which is enhanced by the matter resonance (neutrinos for NH or antineutrinos for IH), the CP phase has such a value that the sign of the interference term is positive (constructive interference), which leads to a maximum enhancement of the event numbers in the resonant channel, see also [47].

Unfortunately a significant determination of the mass hierarchy is only possible for very special points in the parameter space, close to the ones shown in Figure 4, lower-left or upper-right panels. Even for a 90% CL hint for the true hierarchy can be obtained only for about 50% of all possible values of  $\delta$ . With the abovementioned upgrades in beam power and extended running times up to 2025 a 3 $\sigma$  mass hierarchy determination can be reached for about 30–40% of all possible values of  $\delta$  [45] (see also [48] for a recent analysis).

We conclude that with the upcoming experiments as summarized in Table 2 it will be very hard to address CP violation and the mass hierarchy with reasonable significance, and it seems necessary to consider projects beyond those. Before considering high precision long-baseline facilities designed to address those questions in Section 5 we discuss in the next section alternative ways to determine the neutrino mass hierarchy.

#### 4. Alternative Mass Hierarchy Determinations

The fact that  $\theta_{13}$  has been found to be relatively large opens interesting possibilities to identify the mass hierarchy, beyond accelerator-driven long-baseline experiments. In this section we mention some of those possibilities, based on  $\theta_{13}$ -induced matter effects in atmospheric neutrinos as discussed in Section 2.2 by considering different kinds of atmospheric neutrino detectors: magnetized detectors (Section 4.1), huge nonmagnetized detectors using water or liquid argon (Section 4.2), or the IceCube detector (Section 4.3). In Section 4.4 we briefly mention an interesting method based on vacuum oscillations of reactor neutrinos. We do not discuss the possibility to use supernova neutrinos [49–52] or neutrinoless double beta decay [53, 54] to identify the mass hierarchy.

**4.1. Atmospheric Neutrinos—Magnetized.** The determination of the mass hierarchy based on the matter effect relies on the ability to find out whether the resonant enhancement occurs for neutrinos (which would signal NH) or for antineutrinos (IH). Since atmospheric neutrinos contain both neutrinos and antineutrinos, the sensitivity to the hierarchy (for a given total number of events) is much better if neutrino- and antineutrino-induced events can be distinguished, which can be done if the charge of the charged lepton can be identified. In this respect, magnetized iron calorimeters are a promising technology since they offer excellent charge discrimination for muons with few GeV energies. In particular the ICAL experiment at the India-based Neutrino Observatory (INO) [55, 56] aims at the measurement of charge-separated atmospheric neutrino-induced muons. (Sensitivities of a hypothetical magnetized liquid argon detector have been estimated in [57, 58].) In such detectors the identification of

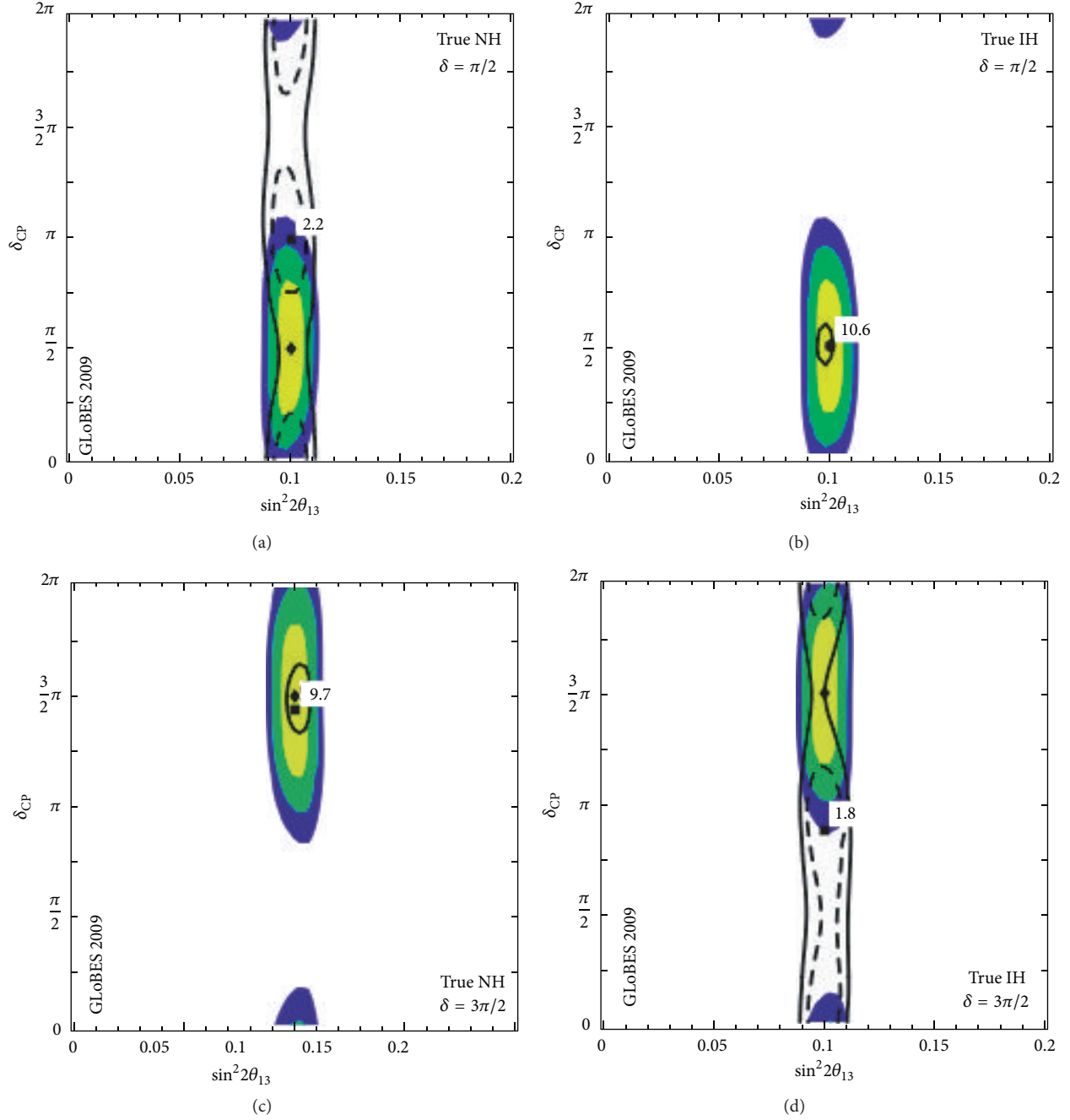


FIGURE 4: Fits in the  $\theta_{13} - \delta$  plane for  $\sin^2 2\theta_{13} = 0.1$ ,  $\theta_{23} = \pi/4$ , and  $\delta = \pi/2$  (upper row) and  $\delta = 3\pi/2$  (lower row) and a true NH (left panels) and IH (right panels), assuming the final exposure from T2K, NOvA, and DayaBay according to Table 2. The contours refer to  $1\sigma$ ,  $2\sigma$ , and  $3\sigma$  (2 dof). The fit contours for the right fit hierarchy are shaded (colored), and the ones for the wrong hierarchy fit are shown as curves. The best-fit values are marked by diamonds and boxes for the right and wrong hierarchy, respectively, where the minimum  $\chi^2$  for the wrong hierarchy is explicitly shown. Figures are based on the results of [45].

electrons is difficult and therefore one relies on signals in  $\mu$ -like events, described by the expression in (10).

Early studies along these lines have been performed in [41, 59]. In Figure 5 we reproduce results obtained recently in [60, 61], where the combined sensitivity of the INO detector with data from T2K, NOvA, and DayaBay has been considered. For other recent studies see, for example, [62, 63].

It has been stressed in [42, 64] that the sensitivity to the mass hierarchy strongly depends on the ability to reconstruct the neutrino energy and direction. The second term in (10) induces characteristic features in the energy and zenith angle distribution of  $\mu$ -like events. If those features can be resolved by the detector, they provide robust sensitivity to the mass hierarchy. The “low” and “high” resolution scenarios referred



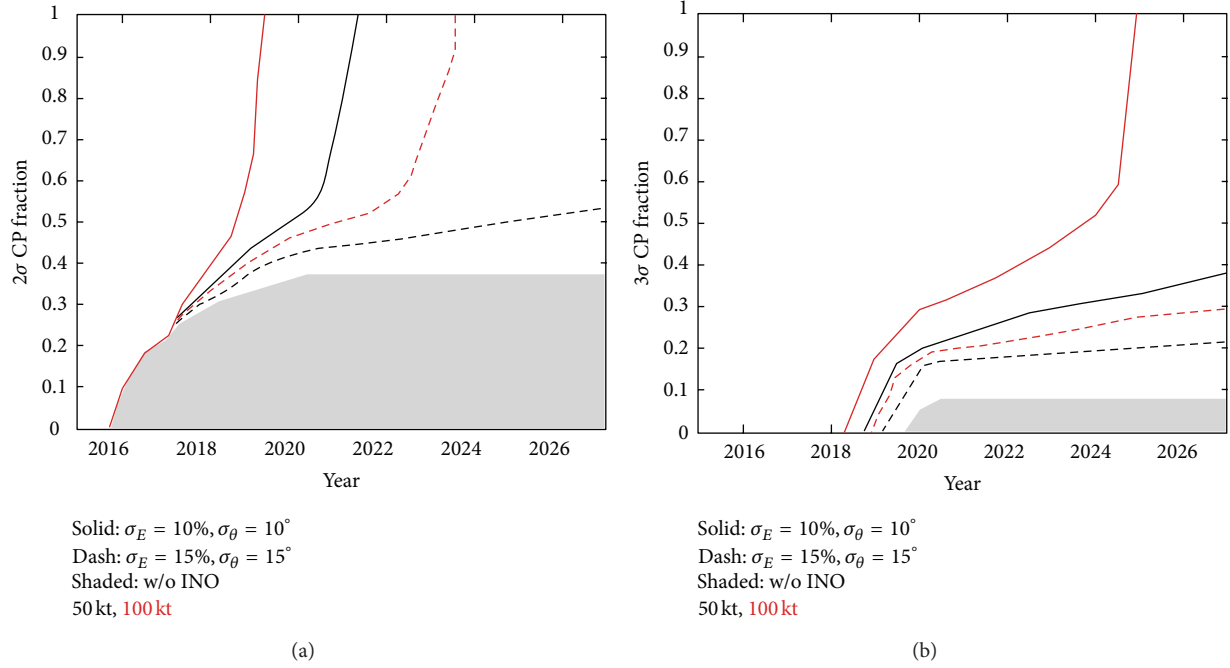


FIGURE 5: The time evolution of the fraction of values of the CP phase  $\delta$  for which the combination of INO, NOvA, T2K, and DayaBay would be sensitive to the mass ordering at  $2\sigma$  (a) and  $3\sigma$  (b). Black (red) curves correspond to INO detector mass of 50 kt (100 kt) and dashed (solid) curves correspond to the low (high) resolution scenario; see text. The shaded area is the corresponding result without atmospheric data from INO. The true value of  $\sin^2 2\theta_{13}$  has been assumed to be 0.09. Figures are based on the results of [60, 61].

to in Figure 5 assume resolutions of  $\sigma_E/E_\nu = 0.15$ ,  $\sigma_\theta = 15^\circ$  (low) and  $\sigma_E/E_\nu = 0.10$ ,  $\sigma_\theta = 10^\circ$  (high). Furthermore the sensitivity for a 50 kt or 100 kt detector is shown, which is supposed to start data taking in 2011 [55]. We observe that the sensitivity to the mass hierarchy is significantly increased compared to NOvA + T2K + DayaBay only. For all but the low resolution 50 kt detector the hierarchy can be identified for all values of  $\delta$  at  $2\sigma$ . However, for a  $3\sigma$  determination with 100% coverage in  $\delta$  the high resolution 100 kt detector seems necessary.

**4.2. Atmospheric Neutrinos—Water/Argon.** If charge identification is not possible (as, for instance, in water Cerenkov detectors) the effect of changing the mass hierarchy is strongly diluted by summing neutrino and antineutrino events. However, the total sample is dominated by neutrinos due to higher fluxes and detection cross-sections. Therefore the cancellation is not complete and a net effect remains between having the resonance in neutrinos or antineutrinos. Furthermore, also a statistical separation of neutrino and antineutrino events may be possible. For example, in SuperKamiokande the fraction of single and multiring events is different for neutrinos and antineutrinos, or the probability to observe a decay electron either from a muon or a pion is different [43]. On the other hand, water Cerenkov detectors can be made very big, possibly at the mega ton scale [65, 66] which may allow to explore those subtle signatures. Since for those detectors electron detection is possible, the impact of the matter effect on multi-GeV  $e$ -like events (see (9)) can be explored.

The left panel of Figure 6 shows the sensitivity to the mass hierarchy of atmospheric neutrino data in a 560 kt water Cerenkov detector, the so-called HyperKamiokande project [66]. Depending on the parameter values, a more than  $3\sigma$  determination of the mass hierarchy seems possible after a few years of exposure. The figure shows that the sensitivity strongly depends on the value of  $\theta_{23}$ . In general the mass hierarchy sensitivity of atmospheric neutrinos is better for larger values of  $\sin^2 \theta_{23}$ . The same behaviour is also observed for magnetized muon detectors such as INO, see, for example, [42]. This follows from the relations given in Section 2.2, where it can be seen that effects of the oscillation probability  $P_{2\nu}(\Delta m_{31}^2, \theta_{13})$ —which encodes the resonant matter effects due to  $\theta_{13}$  carrying the information on the hierarchy—are larger for large  $\sin^2 \theta_{23}$ .

Many future projects for long-baseline accelerator experiments use large volume detectors which are also able to observe atmospheric neutrinos. Therefore, it is an obvious idea to explore synergies between the data from the beam and atmospheric neutrinos [67]. Figure 6 (right panel) shows some examples, where information from beam experiments with relatively short baselines is combined with data from atmospheric neutrinos in a 440 kt water Cerenkov detector in order to resolve the mass hierarchy [68]. The beams considered there have baselines which are too short to address the mass hierarchy, and only the combination with atmospheric neutrinos allows to address this question. (Note that the combined data from the beta beam and SPL superbeam provides also some sensitivity to the hierarchy even without

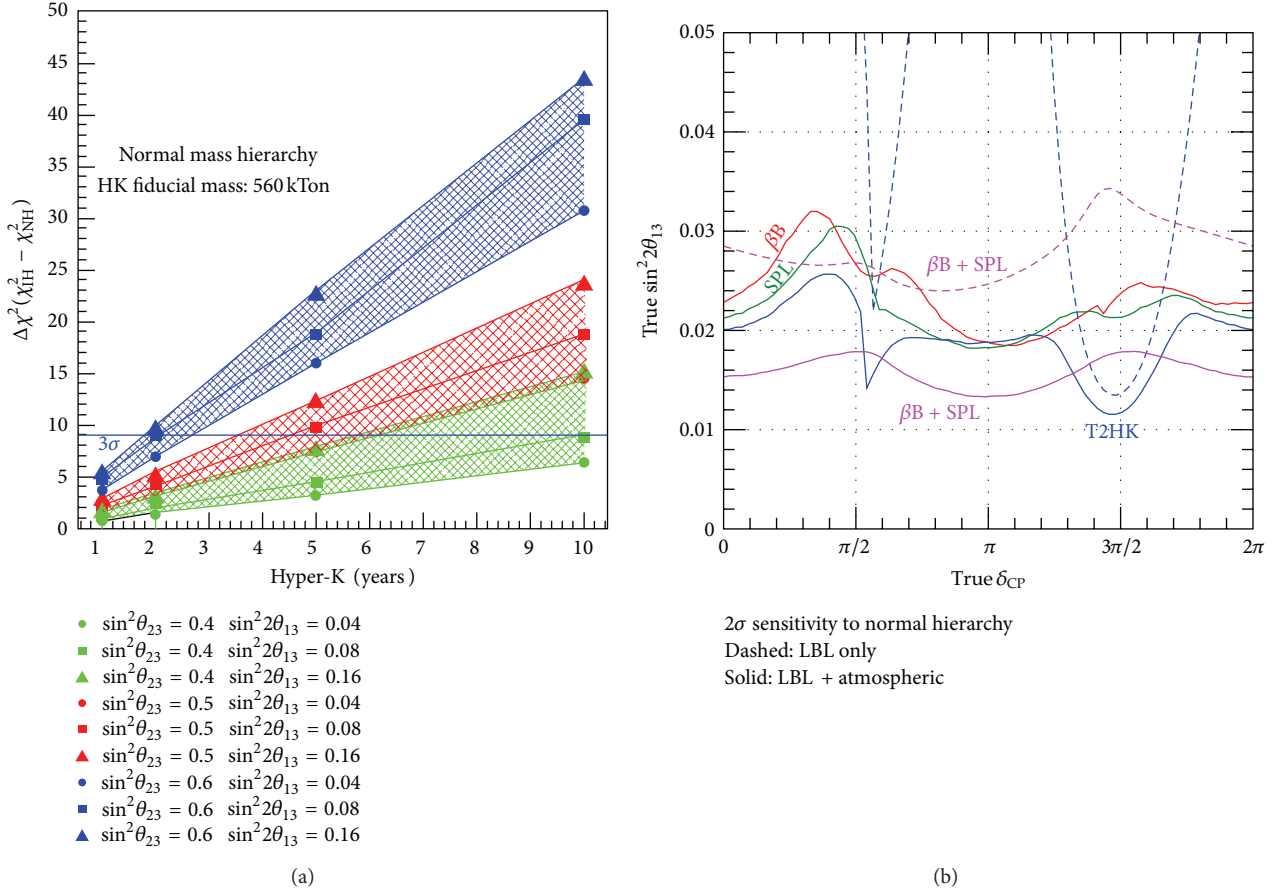


FIGURE 6: (a) Sensitivity to the neutrino mass hierarchy from Hyper Kamiokande atmospheric neutrino data.  $\theta_{23}$  and  $\theta_{13}$  are assumed to be known as indicated in the figure. Plot from [66]. (b) Sensitivity to the mass hierarchy at  $2\sigma$  from a combination of beams at relatively short baseline with 4.4 Mt yr atmospheric neutrino data from a water Cerenkov detector.  $\beta\text{B}$  and SPL refer to a beta-beam and a 4 MW superbeam from CERN to Frejus (130 km), respectively, whereas T2HK corresponds to a 4 MW beam from JPARC to the HyperKamiokande detector (295 km). Dashed curves are data from beams only, and solid curves are for beams + atmospheric neutrinos. Figure is based on the results of [68].

atmospheric data (dashed magenta curve). This is based on the combination of data from  $\nu_e \rightarrow \nu_\mu$  (beta beam) and  $\nu_\mu \rightarrow \nu_e$  (superbeam) oscillations, which allows to break the mass hierarchy degeneracy already at first order in the parameter  $A$  (see (5)), which works already at the distance of 130 km [69]; see also [70].) Both panels in Figure 6 are based on a water Cerenkov detector, but similar results can be achieved in large (100 kt scale) liquid argon detectors [57]. We mention also that atmospheric data from such big detectors (including also the sub-GeV samples) provide excellent sensitivity to the octant of  $\theta_{23}$  (see e.g., [67]) through the effects discussed already in the context of present data in Section 2.3.

**4.3. Atmospheric Neutrinos—Ice.** The IceCube neutrino telescope in Antarctica is able to collect a huge amount of atmospheric neutrino events. Due to the high energy threshold those data are not very sensitive to oscillations although they provide interesting constraints on nonstandard neutrino properties; see for example, [71]. With the so-called Deep-Core extension [72] a threshold of around 10 GeV has been achieved, and the first results on oscillations of atmospheric

neutrinos have been presented [73]; see [74] for a study on the neutrino mass hierarchy. With a further proposed extension of the IceCube detector called PINGU [75] the threshold could be even lowered to few GeV, opening the exciting possibility of a multimega ton scale detector exploring the matter resonance region. The most straight forward type of events will be muons without charge identification, and one has to rely on the huge statistic in order to identify the effect of the mass hierarchy. Below we discuss some results obtained recently in [76] focusing on the muon signal. Signatures from  $\nu_e$ - and  $\nu_\tau$ -induced events have also been studied in [76].

In order to identify the difference between normal and inverted mass hierarchy again a crucial issue will be the ability to reconstruct the neutrino energy and direction. In Figure 7 the difference between event numbers for NH and IH (weighted by the statistical error), binned in neutrino energy  $E_\nu$  and zenith angle  $\theta_z$ , is shown for two assumptions on the reconstruction abilities. In the left panel, with better resolutions, we can observe clearly the effects of the matter resonance. We note also that in different regions in the  $E_\nu - \cos\theta_z$  plane the difference between NH and IH changes

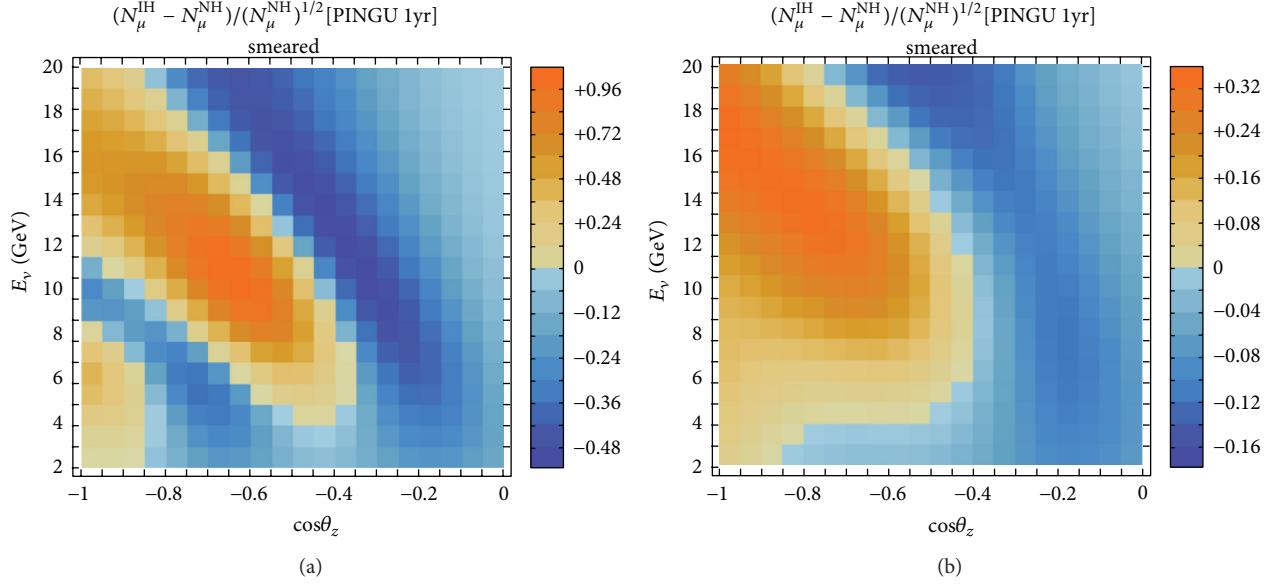


FIGURE 7: Statistical significance per bin of the difference between NH and IH for one year of PINGU data from  $\nu_\mu$ -induced events, binned in neutrino energy (bin width  $\Delta E_\nu = 1$  GeV) and cosine of the zenith angle (bin width  $\Delta \cos \theta_z = 0.05$ ). In the left (right) panel neutrino energy and angular reconstruction resolutions of 2 (4) GeV and  $11.25^\circ$  ( $22.5^\circ$ ) have been assumed. Figures from [76].

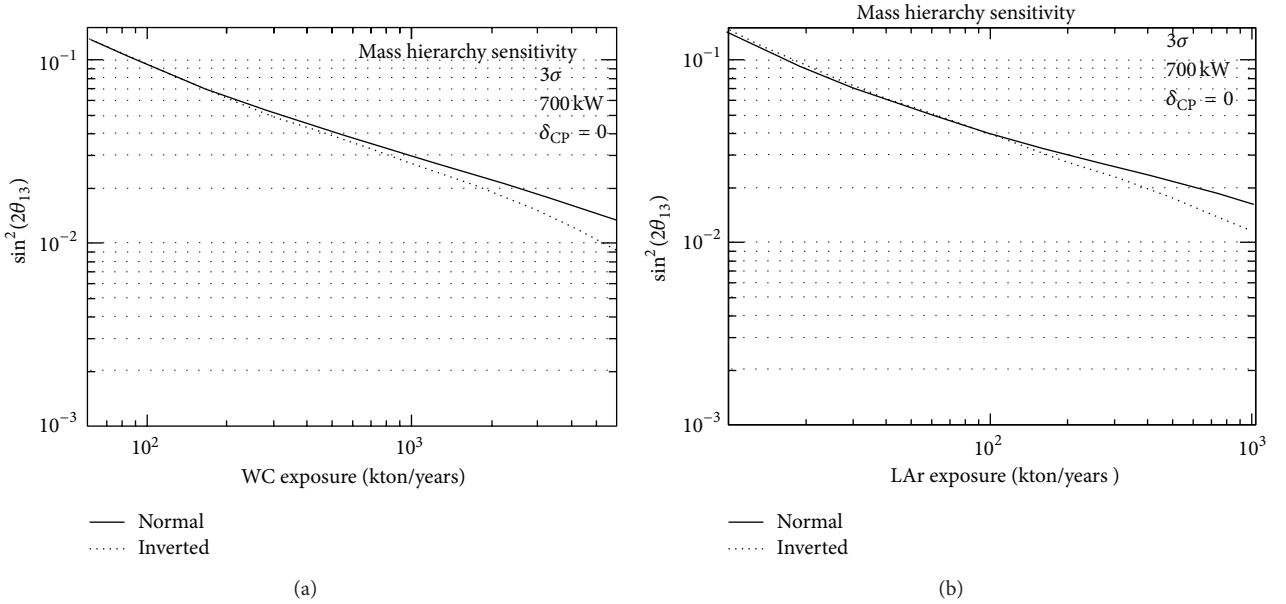


FIGURE 8: LBNE sensitivity to the mass hierarchy at  $3\sigma$  as a function of the exposure for WC (a) and LAr (b) detectors. The value of  $\delta$  is fixed at 0 but a similar behaviour is expected for other values of the phase. Figures taken from [103].

sign. This means that a worse resolution can easily wash out the effect. This is evident also from the right panel, where a worse resolution has been assumed, leading to reduced significance per bin. Therefore, aiming for good energy and angular reconstruction will be an important goal in the design of the PINGU project.

Figure 7 shows the quantity  $S_i \equiv (N_i^{\text{IH}} - N_i^{\text{NH}})/\sqrt{N_i^{\text{NH}}}$ , where  $N_i^{\text{NH}}$  ( $N_i^{\text{IH}}$ ) is the number of  $\mu$ -like events in the case

of NH (IH) in a given bin  $i$ . Hence,  $S_i$  corresponds to the statistical significance (in number of standard deviations) per bin. In the absence of systematical errors the total significance is given by  $\sqrt{\sum_i S_i^2}$ , and the configurations considered in Figure 7 would lead to sensitivities at the level of  $16\sigma$  (left panel) or  $7\sigma$  (right panel) [76]. Hence, considering only statistical errors, excellent sensitivity to the mass hierarchy is obtained already after one year of PINGU data. Those very

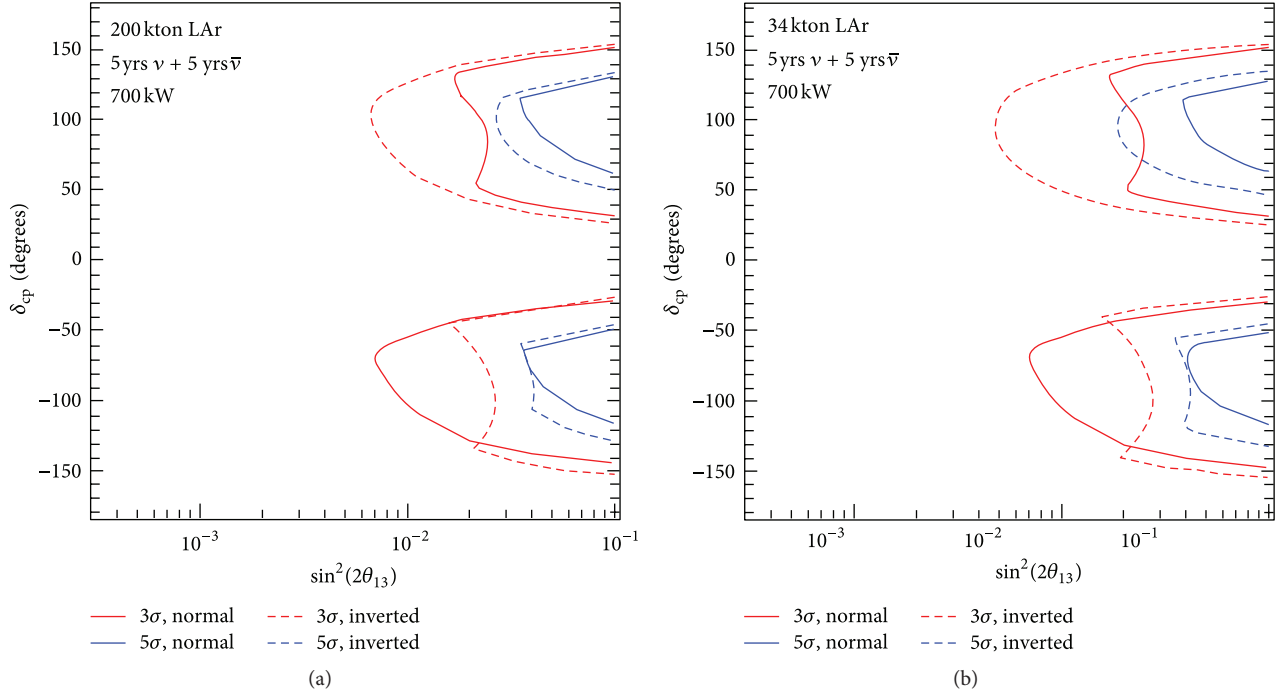


FIGURE 9: LBNE sensitivity to CPV at  $3\sigma$  (red curves) and  $5\sigma$  (blue curves) for 5 years of running in the neutrino channel plus 5 in the antineutrino one. A 200 kton WC (a) or a 34 kton LAr (b) are used in a 700 kW beam. Figure is taken from [103].

promising results are yet to be supported by detailed studies on the achievable energy and angular reconstruction as well as realistic investigations of systematical uncertainties.

**4.4. Mass Hierarchy from Reactors.** All the possibilities to identify the neutrino mass hierarchy discussed above are based on the matter effect in oscillations due to  $\theta_{13}$ . In [77] an alternative has been pointed out, based on oscillations of reactor neutrinos, where matter effects are negligible. The three-flavour survival probability of  $\bar{\nu}_e$  in vacuum is easily obtained as

$$\begin{aligned}
 P_{\bar{\nu}_e \rightarrow \bar{\nu}_e} &= 1 - \cos^4 \theta_{13} \sin^2 2\theta_{12} \sin^2 \left( \frac{\Delta m_{21}^2 L}{4E} \right) \\
 &\quad - \sin^2 2\theta_{13} \\
 &\quad \times \left[ \cos^2 \theta_{12} \sin^2 \left( \frac{\Delta m_{31}^2 L}{4E} \right) + \sin^2 \theta_{12} \sin^2 \left( \frac{\Delta m_{32}^2 L}{4E} \right) \right].
 \end{aligned} \tag{11}$$

The spectrum of reactor experiments ranges from neutrino energies of about 1.3 MeV to 12 MeV with a peak

around 4 MeV. Consider now a baseline  $L \approx 60$  km. Then we obtain for the arguments of the oscillating terms:

$$\begin{aligned}
 \frac{\Delta m_{21}^2 L}{4E} &\approx \frac{\pi}{2} \left( \frac{E}{4 \text{ MeV}} \right)^{-1}, \\
 \frac{|\Delta m_{31}^2| L}{4E} &\approx \frac{|\Delta m_{32}^2| L}{4E} \approx 50 \left( \frac{E}{4 \text{ MeV}} \right)^{-1}.
 \end{aligned} \tag{12}$$

Hence, considering the spectrum obtained in a reactor experiment at about 60 km, the first term in (11) gives a “slow” oscillation in  $1/E$ , with a large amplitude of  $\cos^4 \theta_{13} \sin^2 2\theta_{12} \approx 0.8$ . These are the oscillations due to the “solar” frequency as observed by the KamLAND experiment. For an experiment at 60 km the first minimum of the survival probability occurs close to  $E \sim 4$  MeV, at the peak of the expected number of events.

The terms in the second line of (11) lead to fast oscillations in  $1/E$  (see (12)) on top of the slow “solar” oscillation, with a small amplitude proportional to  $\sin^2 2\theta_{13} \approx 0.1$ . As evident from (11) there are actually two fast frequencies, one due to  $\Delta m_{31}^2$  and one due to  $\Delta m_{32}^2$ , which differ by  $\Delta m_{21}^2$  (about 3%). The sensitivity to the mass hierarchy appears as follows. First, note that depending on the hierarchy we have  $|\Delta m_{31}^2| > |\Delta m_{32}^2|$  for NH or  $|\Delta m_{31}^2| < |\Delta m_{32}^2|$  for IH. Second, the amplitudes of the two fast frequencies are different because of the nonmaximal value of  $\theta_{12}$ : the amplitude of the  $\Delta m_{31}^2$  frequency is  $\sin^2 2\theta_{13} \cos^2 \theta_{12} \approx 0.07$  while the one of the  $\Delta m_{32}^2$  frequency is  $\sin^2 2\theta_{13} \sin^2 \theta_{12} \approx 0.03$ . Hence, if an experiment can measure the fast frequencies and find out which one of



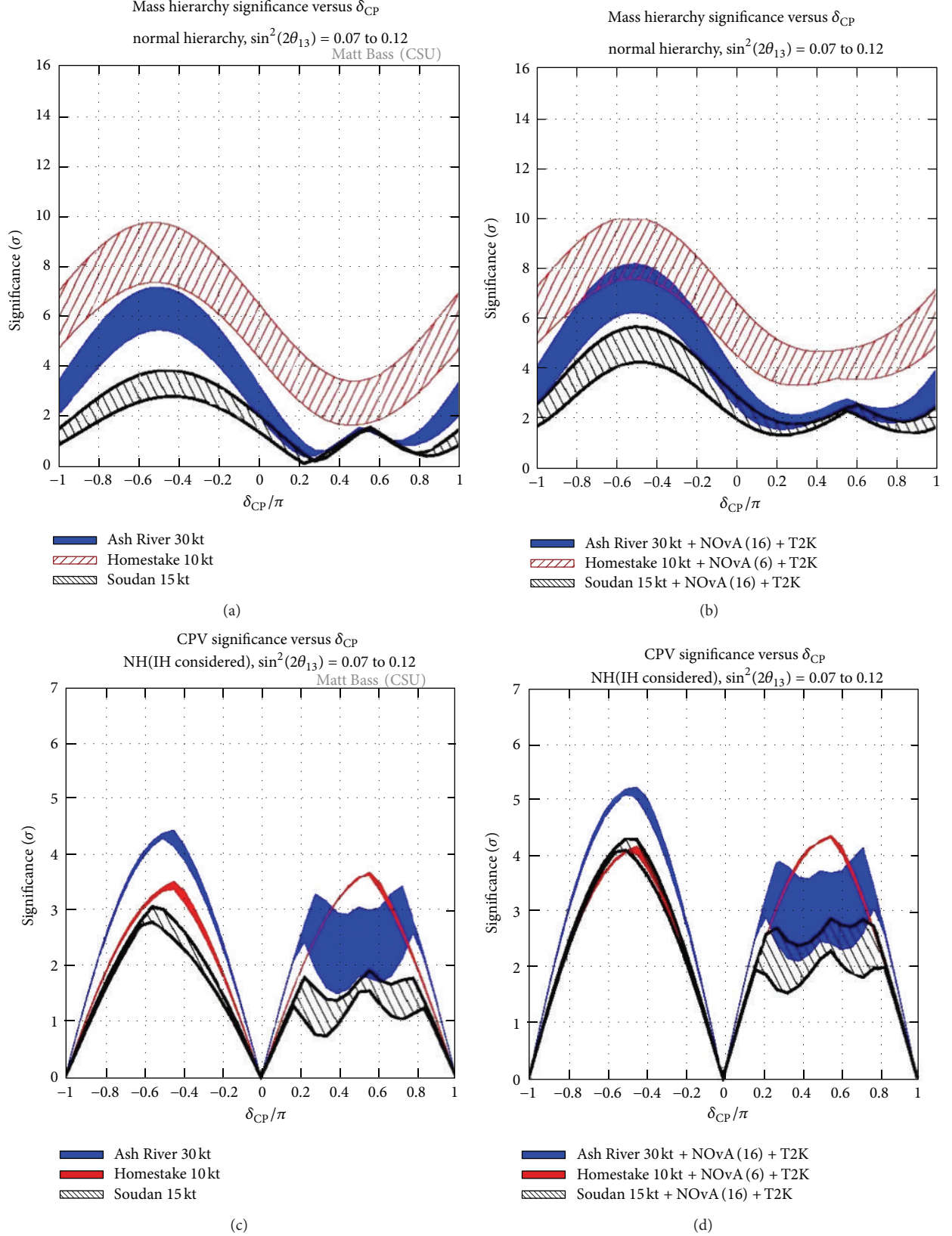


FIGURE 10: LBNE sensitivity to the mass hierarchy (upper plots) and CPV (lower plots) at  $3\sigma$  as a function of  $\delta$  for the three reconfiguration options, as described in the text. The sensitivities are reported for the experiment alone (left) and when combined with NOvA for  $3\nu + 3\bar{\nu}$  years and T2K. The Ash River and Soudan options use the NuMI beam line, and therefore additional  $5\nu + 5\bar{\nu}$  years for NOvA are included, assuming that this detector will be kept in operation in parallel to the LAr detector. Figure taken from [104].

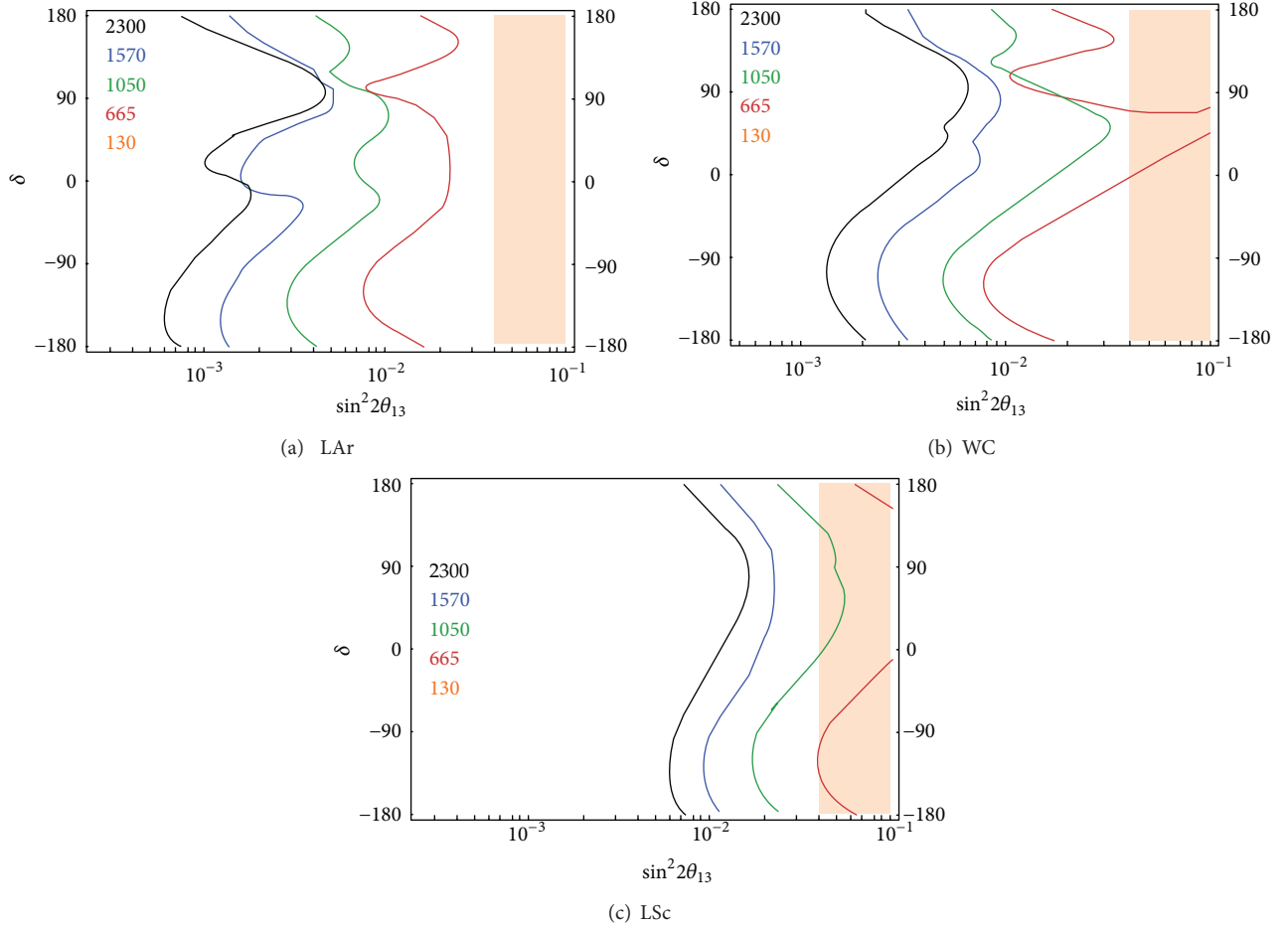


FIGURE 11: LAGUNA hierarchy discovery at  $3\sigma$  as a function of  $\sin^2 2\theta_{13}$  and  $\delta$ . The different lines correspond to different baselines, as indicated in the legend in km. The details of the beams used are reported in the text. The detectors are 100 kton LAr TPC, 50 kton LSc, and 440 WC detector. The shaded region reports the  $3\sigma$  allowed values from Daya Bay. Figure is taken from [107].

the two fast frequencies has the larger amplitude (the larger or the smaller frequency), the mass hierarchy is determined. The effect can be illustrated by performing a Fourier transform of the event spectrum, where the two frequencies appear as a high and low peaks in the transformed spectrum [78].

The experimental requirements are obvious from the above discussion: (i) a good energy resolution is required in order not to wash out the fast oscillations and (ii) because of the small amplitude of the fast oscillations one needs enough statistics to be able to establish their presence. Numerical studies have been performed in [78–80]. The results of [80] indicate that exposures of order few 100 kt GW yr and energy resolutions of order 3% are required, which makes this measurement challenging. (We recall that the KamLAND experiment has about 1 kt, the LENA proposal [65] is for 50 kt, and typical modern reactor neutrino experiments have an energy resolution of 5–6%.) The DayaBay collaboration has identified a suitable detector location at a distance of 60 km to several reactor cores with a total of 17.4 GW power (and another 17.4 GW in the planning stage) and is pursuing the possibility of a mass hierarchy measurement as the DayaBay-II project [81]. Let us also mention that such a big reactor

experiment at 60 km would provide ultimate precision on the determination of  $\theta_{12}$  and  $\Delta m_{21}^2$ ; see, for example, [82].

## 5. High-Precision Long-Baseline Facilities

As discussed above, the next generation of neutrino experiments will have some sensitivity to matter effects, and it may be possible to have the mass hierarchy determined by 2025. The search for CP violation is more challenging, and it is unlikely that its discovery can be achieved in the same time frame. Upgraded long baseline experiments with larger statistics and better control of systematics will be needed.

In order to understand how these experiments will be sensitive to CP violation and will achieve precise measurements of the oscillation parameters, let us consider the approximate formula for the oscillation probability  $P_{\nu_\mu \rightarrow \nu_e}$  given in (3). The first term in the probability is the “atmospheric term” which is dominant as  $\theta_{13}$  is large,  $\sin^2 2\theta_{13} \approx 0.09$ . This is the term which is most sensitive to matter effects and drives the ability of coming and next-generation experiments to establish the mass hierarchy. The second line is the “CP term” which contains the dependence on the

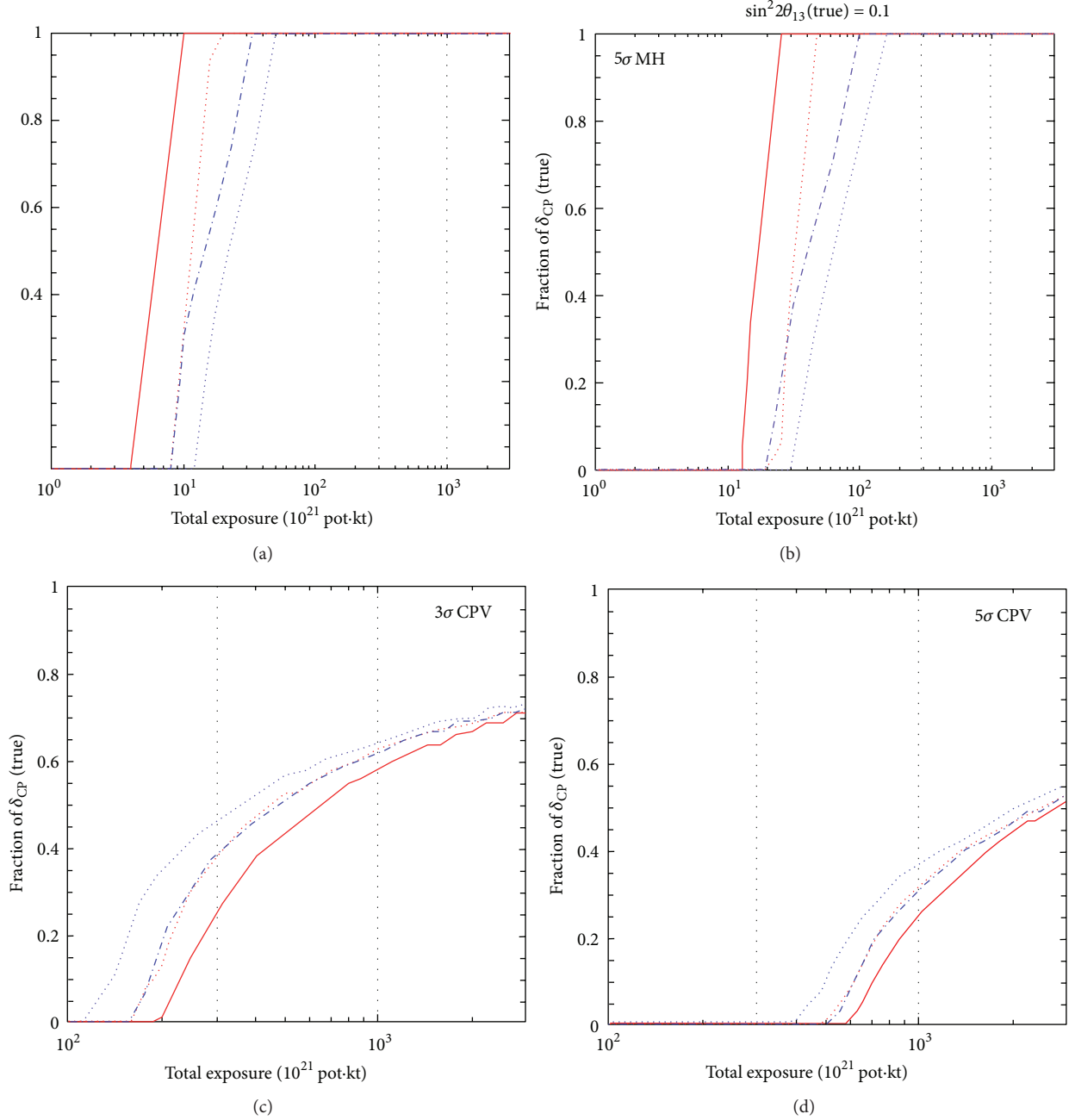


FIGURE 12: CP fraction for which a mass hierarchy (upper plots) and CP violation (lower plots) discovery at  $3\sigma$  (left) and  $5\sigma$  (right) is possible as a function of exposure for a staged LAGUNA setup. The different lines correspond to true normal (inverted) hierarchy for solid (dashed) lines and for a baseline of 2290 km (1540 km) for red (blue) lines. Figure is taken from [112] where more details about the simulations can be found.

CP violating phase  $\delta$ . As we see, this term becomes more important at lower energies, and for this reason access to the low energy part of the spectrum is critical to achieve good sensitivity to CP violation. It should also be noted that for large  $\theta_{13}$  the “CP term” is a small correction with respect to the dominant “atmospheric term,” and in fact the CP asymmetry, defined as  $(P_{\nu_\mu \rightarrow \nu_e} - P_{\bar{\nu}_\mu \rightarrow \bar{\nu}_e}) / (P_{\nu_\mu \rightarrow \nu_e} + P_{\bar{\nu}_\mu \rightarrow \bar{\nu}_e})$ , scales as  $\sin^{-1} \theta_{13}$  and is suppressed for large  $\theta_{13}$ . Therefore, despite the fact that large  $\theta_{13}$  implies large number of events at future LBL facilities, the discovery of CP violation remains

very challenging and requires precise measurements of the probabilities, with small statistical and systematic errors, (It has been shown that CP violation can also be searched for in short baseline experiments, such as (a Decay-At-rest Experiment for CP studies At the Laboratory for Underground Science) [83] DAE $\delta$ ALUS. This uses high-power proton accelerators to produce a  $\bar{\nu}_\mu$  beam with energies in the few tens of MeVs. The appearance oscillation  $P_{\bar{\nu}_\mu \rightarrow \bar{\nu}_e}$  will be detected via inverse beta decay by a large WC detector doped with gadolinium, to reduce the backgrounds, or scintillator

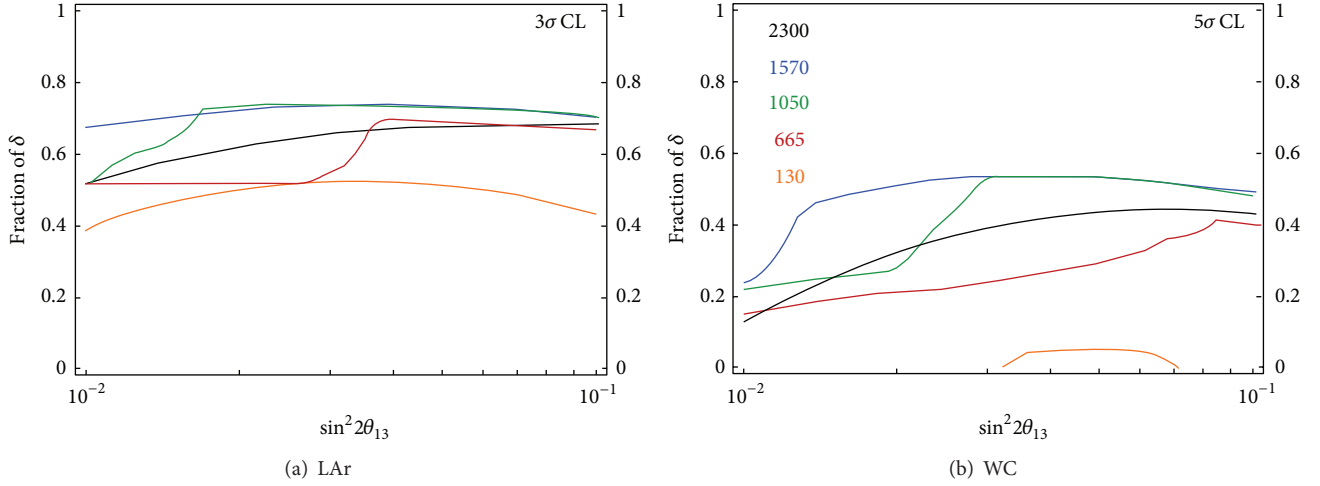


FIGURE 13: LAGUNA CP fraction for which a CP violation discovery at  $3\sigma$  (left) and  $5\sigma$  (right) is possible as a function of  $\sin^2 2\theta_{13}$  for the LAr (upper plots) and WC (lower plots) detector. Figure is taken from [107].

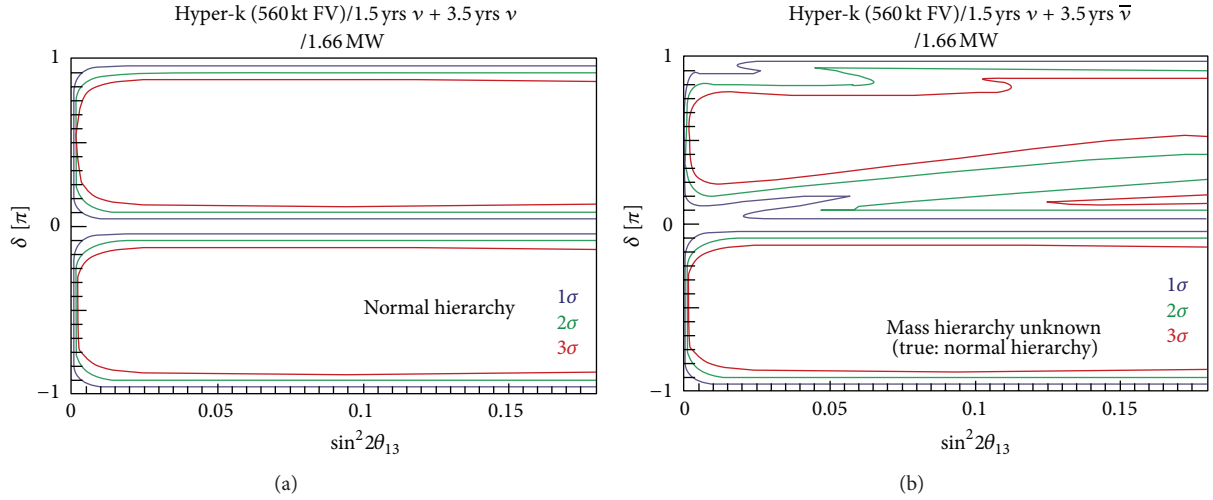


FIGURE 14: T2HK sensitivity to CP violation at 1, 2, and  $3\sigma$  as a function of  $\sin^2 2\theta_{13}$ . The mass hierarchy is assumed known (a) or not (b). Figure is taken from [66].

detectors. Further details are provided elsewhere in this volume).

Moreover, as it can be seen from the probability equation, CP-violating and matter effects are entangled, and the extraction of the parameters of interest, namely, the  $\text{sgn}(\Delta m_{31}^2)$ , the phase  $\delta$ , and  $\theta_{23}$ , is affected by the widely studied problem of degeneracies: different sets of parameters give the same probabilities in the neutrino and in the antineutrino channels at fixed  $L/E$  [20, 29, 47, 84, 85]. Therefore, even a very precise reconstruction of the probabilities does not allow to determine the true parameters, and the physics reach is severely affected. In vacuum three degeneracies can be identified. (i) The intrinsic degeneracy:  $\theta_{13}$ ,  $\delta$  have fake solutions which strongly depend on energy. For large  $\theta_{13}$  and in vacuum, the "fake" solutions are given by [84]

$$\theta'_{13} \simeq \theta_{13} + \cos \delta \sin 2\theta_{12} \frac{\Delta m_{21}^2 L}{4E} \cot \theta_{23} \cot \left( \frac{\Delta m_{21}^2 L}{4E} \right). \quad (13)$$

(ii) The sign degeneracy: in absence of matter effects, it is possible to change the sign of  $\Delta m_{31}^2$  and  $\delta$  to  $\pi - \delta$  without affecting the probabilities. In matter this degeneracy is broken. (iii) The octant of  $\theta_{23}$ : if the angle is not maximal as currently suggested by the data, see Section 1.

The problem of degeneracies has significant impact on the precision of the oscillation parameter measurements, and in particular on the ability to establish CP violation. A lot of effort has gone into devising strategies to weaken the impact of the degeneracies; see, for example, [47, 70, 86–102]. Long enough baselines ( $>800$ – $1000$  km) have strong matter effects and can be used to solve the sign degeneracy; information at several energies, for example, by using wideband beams, is important, with the one coming from the low-energy part of spectrum being critical for CP violation and the octant degeneracy. Other techniques have also been explored, for example, combining different channels which have different



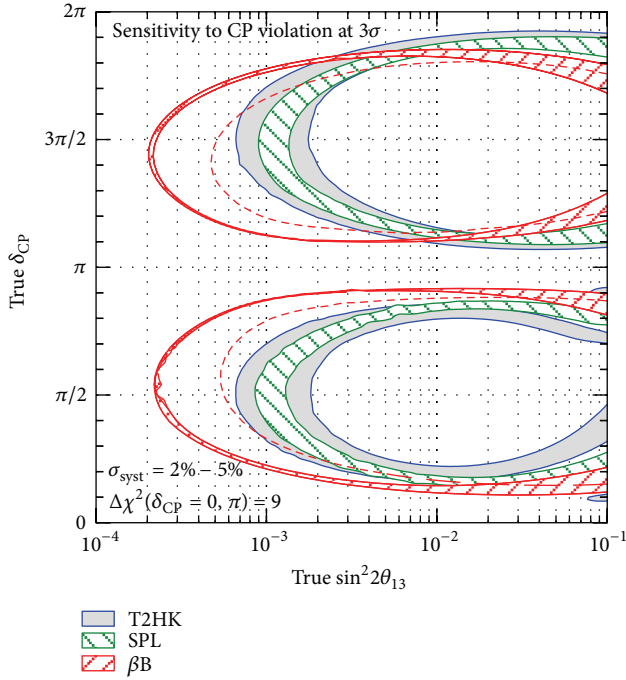


FIGURE 15: CP violation discovery at  $3\sigma$  as a function of  $\delta$  for a betabeam, SPL, and T2HK. The combination of SPL and a betabeam is also shown. The betabeam lines correspond to  $5.8(2.2) \times 10^{18}$  decays per year of  ${}^6\text{He}$  ( ${}^{18}\text{Ne}$ ). Details of the simulations can be found in [68]. The width of the bands reflects the change of the systematic errors from 2% to 5%. The dashed curves are obtained for a betabeam flux reduced by a factor of two.

dependence on the parameters, or different baselines and/or typical energies. Several of these studies have been performed focusing on small values of  $\theta_{13}$ . Thanks to the large value of  $\theta_{13}$ , some of the degeneracies become less important or more easily solved. For instance, determining the mass hierarchy will be easier than previously expected, and it is even possible that it will be achieved prior to the start of the next generation of long baseline experiments, as discussed in Section 4.

In this section we briefly review future LBL experiments which will provide improved sensitivity to the mass hierarchy and CP violation and the possibility to measure with various degree of precision the oscillation parameters. Several type of setup are under consideration, some of them being at the design study or proposal level and others more advanced: superbeams (LBNE, T2HK, LAGUNA-LBNO), betabeams, and neutrino factory (NF). In the following, we briefly review these three different types of facilities. We focus on their physics reach and we defer the readers to the relevant chapters in this volume for a detailed description of the experimental facilities.

**5.1. Future Superbeams.** Superbeams are based on currently used technology and require an upgrade in neutrino flux and detector size. The beam is constituted mainly by muon neutrinos which are produced by pion and kaon decays. The experiments search for the  $\nu_\mu \rightarrow \nu_\mu$  probability, sensitive to  $\Delta m_{31}^2$  and  $\theta_{23}$ , and, importantly, for the subdominant

oscillation  $\nu_\mu \rightarrow \nu_e$ . Detectors with excellent  $\nu_e$  reconstruction are needed, the technologies of choice being Water-Cherenkov, Liquid Argon (LAr), or scintillator (LSc) ones. A wide range of energies is currently under consideration, going from 200 MeV of SPL to several GeVs for CN2PY (CERN to Pyhäsalmi), with corresponding distances from 100 km to 2300 km. The detector can be located on-axis or off-axis: in the first case it sees a wide spectrum, while in the latter the beam is peaked at low energies and its high energy tail is suppressed. They typically have an excellent reach for the mass hierarchy, if  $L > 1000$  km or so, and very good sensitivity to CP violation. The main limiting factor is the intrinsic  $\nu_e$  contamination of the beam, at a level of 0.5%–1%. Another very important experimental issue is the background due to the misidentified  $\pi^0$  produced in neutral current (NC) interactions, as one of the  $\gamma$ s from the pion decay  $\pi^0 \rightarrow \gamma\gamma$  is missed. This background is particularly important at low energies for CP violation searches and impacts differently beams at different energies and with different detectors; for instance, LAr ones have an excellent NC rejection. For the antineutrino channel, a significant contribution to the signal and background can also come from the  $\nu_\mu$  and  $\nu_e$  components of the beam, in absence of detector magnetisation. Systematic errors are an important factor: for large  $\theta_{13}$ , as the “atmospheric term” dominates the appearance oscillation probability, those on the signal are more relevant than those on the backgrounds and need to be controlled at the few % level. Various superbeam options are under study or being proposed for the future.

**LBNE** [103]: in the US the Long-Baseline Neutrino Experiment (LBNE) is the most advanced proposal for a next generation long baseline option. According to the 2010 LBNE Interim Report [103], the beam is sourced at the Main Injector at Fermilab using a new neutrino beamline with 700 kW of power. Its main requirements include a broad beam which covers both first and second oscillation maxima located at 2.4 and 0.8 GeV, respectively, an increased flux at low energy in order to compensate for the lower detection cross the sections, a suppression at energies above 5 GeV in order to reduce the NC backgrounds which pile up at low energy, and the lowest level of  $\nu_e$  contamination possible. The detector is located at the DUSEL site, at a distance of 1300 km from Fermilab. Various options were contemplated in the 2010 LBNE Interim Report: two or three 100-kton fiducial mass Water Cherenkov detectors with 15% or 30% PMT coverage and with or without gadolinium loading, or multiple 17-kton fiducial mass LAr detectors or a combination of them. The location could be at 4850, 800, or 300 feet depth, depending on the emphasis put on nonaccelerator physics, such as proton decay, supernova, and other astrophysical neutrinos. The experiment was assumed to run for 5 years in neutrinos and 5 in antineutrinos. In this configuration, it could achieve the determination of the mass hierarchy in less than a year at  $3\sigma$  as shown in Figure 8. LBNE could also have very good sensitivity to CP violation with a 60% coverage at  $3\sigma$  in the allowed range of values of  $\sin^2 2\theta_{13}$ , for a 200 kton Water Cherenkov or 34 kton LAr detectors, see Figure 9.

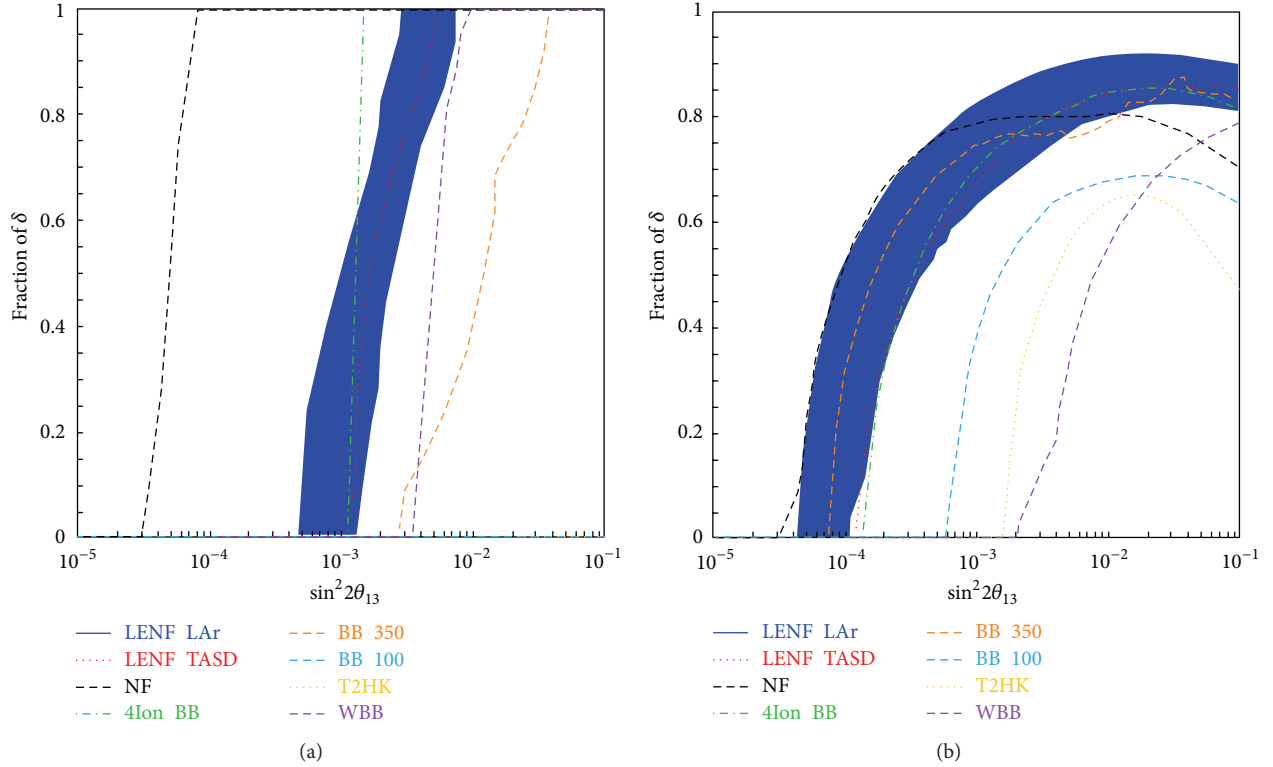


FIGURE 16: (a)  $3\sigma$  sensitivity to the mass hierarchy, in terms of the fraction of  $\delta$  values for which  $\delta = 0, \pi$  can be excluded, as a function of  $\sin^2 2\theta_{13}$  with a LENF with 20 kton TAsD, LENF with 100 kton LAr detector (the band corresponds to the varying detector performance), high energy neutrino factory, a wide band beam, 3 betabeam configurations and for T2HK. Figure is taken from [144] where further details of the simulations are reported. (b) Same as the left but for CP violation.

In 2011, the technology choice was made, favouring a LAr detector thanks to its excellent performance in energy resolution, efficiency, and background reduction for the range of energies of interest. In 2012, due to funding restrictions, the LBNE configuration was reconsidered, and a severe reduction of the detector size was necessary at a first stage, keeping open the possibility of an upgrade to a large/multiple detector at a later time. Three options were considered for the first step: (i) a beam from the the existing NuMI beamline in the low-energy configuration with a 30-kton LAr detector located at the surface 14 mrad off-axis at Ash River in Minnesota,  $L = 810$  km, (ii) using the beam above but with a 15-kton detector at the Soudan mine in Minnesota,  $L = 735$  km as MINOS, (iii) a new low-energy LBNE beamline aimed at a 10-kton LAr detector at Homestake (on-axis) in South Dakota,  $L = 1300$  km. A report by the Steering Committee [104] was prepared and the reach of each option is analysed in detail, see Figure 10. The report favoured option (iii). This configuration offers the best opportunities for a long-term programme with a 20–25 kton underground detector at Homestake and a Project X sourced beam. The recommendation was very well received and on 29 June 2012 DOE confirmed that CD1 will be reviewed towards the end of October 2012.

**LAGUNA-LBNO (CN2PY)** [105–107]: in Europe a next-generation superbeam experiment with a beam sourced at CERN is being considered in the LAGUNA and LAGUNA-LBNO FP7 Design Studies, funded by the

European Commission. The LAGUNA project, which is finished in 2011, considered seven possible locations for a European large underground laboratory which could host a megaton-scale detector for neutrino, astroparticle physics, and proton decay searches. The Design Study focussed on site investigations and on the development of the design of a facility for the neutrino underground observatory. Three detector technologies were considered: 100 kton liquid argon [108], 50 kton liquid scintillator [109, 110], and 440 kton Water Čerenkov [111] detectors. The study concluded that all locations would in principle allow to host the facility. Importantly, the chosen detector could also be the target for a superbeam from CERN. Depending on the site, the available distances, see Table 3, range from 130 km for Fréjus to 2300 km for Pyhäsalmi, the longest baseline considered at present for superbeams. The Design Study LAGUNA-LBNO, which started in October 2011, is further developing the study of the beam and the physics reach of the long baseline setup, with focus on the CERN to Pyhäsalmi option for the first phase and various options for a second stage.

A detailed study of the sensitivity to the mass hierarchy and CP violation has been performed in [107]. In the lowest energy configuration of the beam (the  $L = 130$  km baseline), the simulation assumed  $5.6 \times 10^{22}$  protons on target (PoT) per year, with an energy of 4.5 GeV, for 2 (8) years of running for neutrino (antineutrinos). In the multi-GeV regime, used for baselines with  $L > 130$  km, the CERN high-power PS2

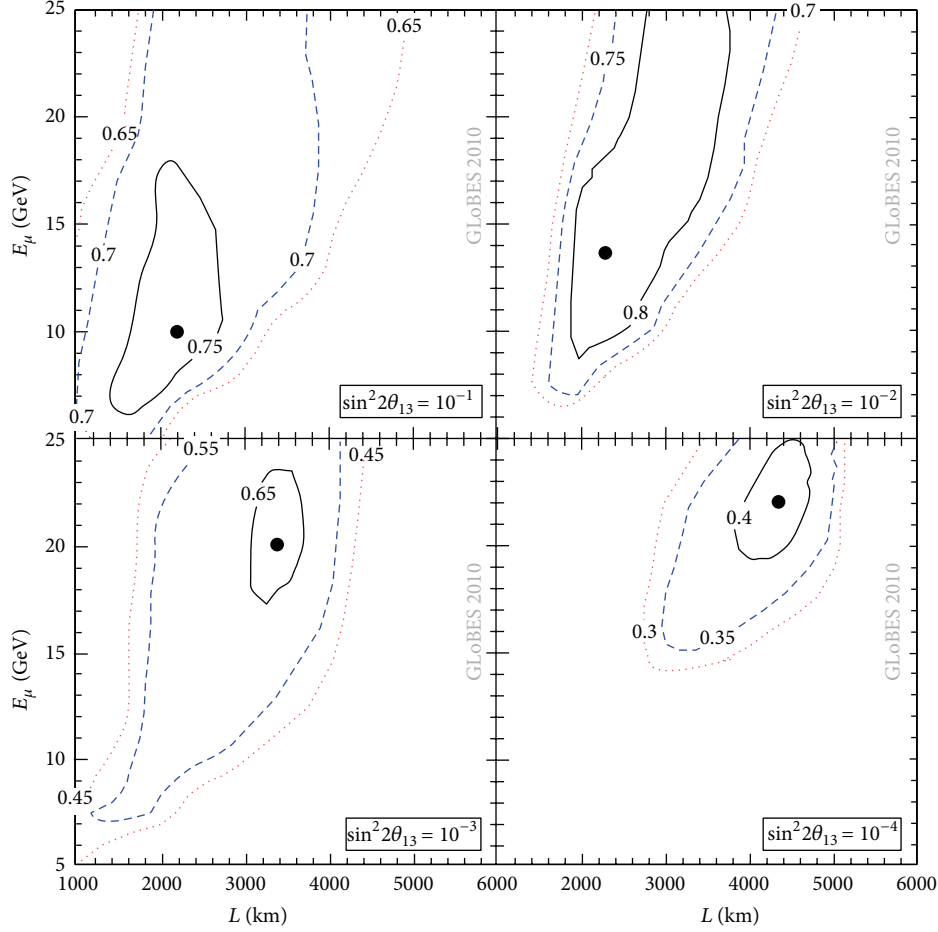


FIGURE 17: Fraction of the values of  $\delta$  for which there is sensitivity to CP violation at  $3\sigma$  as a function of  $L$  and muon energy. A single baseline Neutrino Factory is used with a 50 kton MIND detector. The optimal performance is marked by a dot. Figure is taken from [147].

TABLE 2: Summary of the “nominal” luminosities for the current generation of reactor and beam experiments. See [45] for details.

Setup	$t_v$ [yr]	$t_{\bar{v}}$ [yr]	$P_{Th}$ or $P_{Target}$	$L$ [km]	Detector technology	$m_{Det}$
Double Chooz	—	3	8.6 GW	1.05	Liquid scintillator	8.3 t
Daya Bay	—	3	17.4 GW	1.7	Liquid scintillator	80 t
RENO	—	3	16.4 GW	1.4	Liquid scintillator	15.4 t
T2K	5	—	0.75 MW	295	Water Cerenkov	22.5 kt
NOvA	3	3	0.7 MW	810	TASD	15 kt

configuration was considered with  $3 \times 10^{21}$  PoT per year with 50 GeV, corresponding to 2.4 MW with  $10^7$  useful second per year (or 1.6 MW assuming  $1.5 \times 10^7$  seconds per year). Given the large value of  $\theta_{13}$ , most of the configurations can determine the ordering of neutrino masses at high confidence level, as shown in Figure 11, with increased sensitivity for longer baselines. In view of this, the possibility of staging the detector, starting from a “pilot” detector of 10 to 20 kton mass, to be later upgraded to reach the baseline configuration of 100 kton, has been considered [112]. The study shows that the mass hierarchy can be reached in few years of data taking; see Figure 12.

These setups can also provide excellent sensitivity to CP violation both for the short baselines with a Water Cherenkov detector and the longer ones with a LAr detector. The LSc option could provide similar reach but only if the NC background could be controlled at a similar level. Current studies seem to indicate that NC could not be rejected at more than the 10%–20% level, severely affecting the sensitivity to CP violation for this type of detector. Typically, for the relevant range of values of  $\theta_{13}$ , CP violation can be established at  $3\sigma$  for  $\sim 70\%$  of the values of  $\delta$  phase and good reach is obtained even at the  $5\sigma$  level; see Figures 12 and 13. It should be noted that sufficiently long baselines, such as the 2300 km

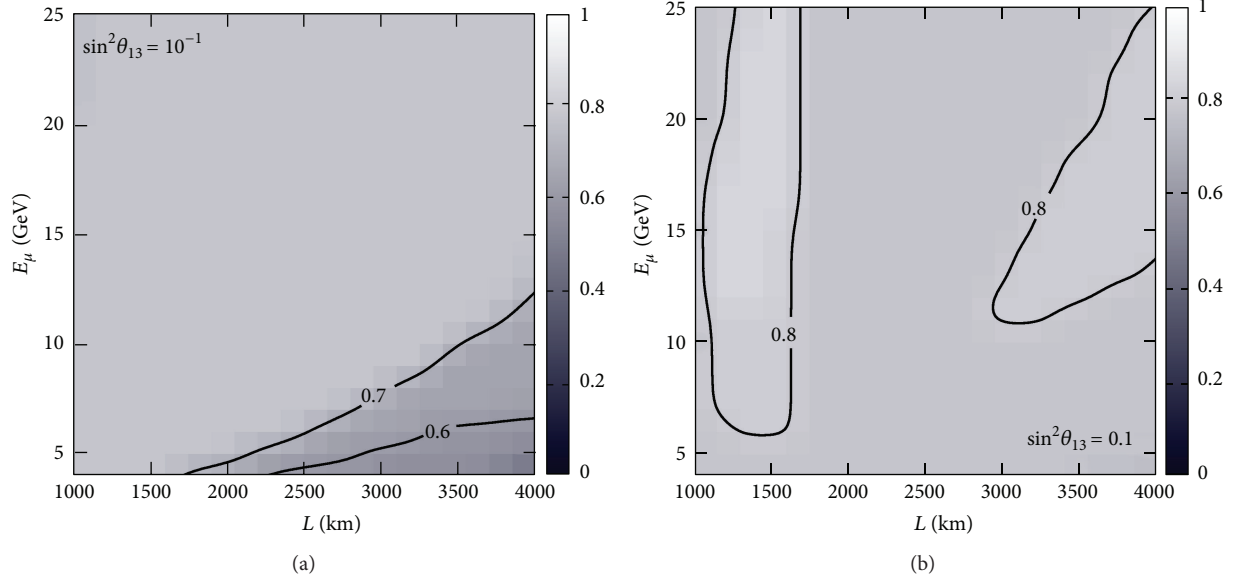


FIGURE 18: CP violation discovery at  $3\sigma$  fraction as a function of baseline,  $L$ , and stored-muon energy using the T ASD detector (a) and LAR one with optimistic performance (b). The lines indicate the fraction of values of  $\delta$  for which sensitivity can be achieved. Further details can be found in [148] from which the figures have been taken.

TABLE 3: The seven potential locations for an underground neutrino observatory under consideration in the LAGUNA Design Study: the distance from CERN and the energy of the first oscillation maximum, in the absence of matter effects, are given. From [106].

Location	Distance from CERN [km]	1st osc max [GeV]
Fréjus (France)	130	0.26
Canfranc (Spain)	630	1.27
Umbria (Italy)	665	1.34
Sierozsowice (Poland)	950	1.92
Boulby (UK)	1050	2.12
Slanic (Romania)	1570	3.18
Pyhäsalmi (Finland)	2300	4.65

one, and a broad spectrum with good energy resolution allow to have an excellent separation of the asymmetry due to matter effects (i.e., the mass hierarchy measurement) and the CP asymmetry and thus to break the parameter degeneracies discussed above. Therefore, the existence of matter and CP violation-induced effects will be tested explicitly, without overrelying on theoretical modelling and assumptions.

*J-PARC to Hyper-Kamiokande long baseline experiment (T2HK)* [66]: recently a letter of intent (LoI) has been published for a long baseline experiment which uses a 1.66 MW beam from the J-PARC accelerator to a 1 Mton Water Cherenkov detector located  $2.5^\circ$  off-axis at 295 km distance in the Kamiokande site. Its main goal is the discovery and/or measurement of CP violation in the leptonic sector. One of the advantages of this configuration is the excellent energy resolution provided by the WC detector at these energies, the large number of events, and, thanks to the off-axis location and the beam configuration, the low level of intrinsic background,  $<1\%$ . A running of 1.5 (3.5) years for neutrinos (antineutrinos) is assumed, with one year given by  $10^7$  seconds. Systematic errors play an important role

and, based on foreseen improvements with respect to T2K, a level of 5% is assumed for the neutrino flux uncertainty, the neutrino interaction cross-section, the near detector efficiency, and the far detector systematics. The baseline is too short to provide a good reach for the mass hierarchy, with some sensitivity only for favourable values of  $\delta$ . Additional information can be obtained from atmospheric neutrino events [67], as discussed in Section 4. The knowledge of the mass hierarchy plays an important role as it cannot be determined by the experiment itself but can induce significant degeneracies for large  $\theta_{13}$ . If the mass hierarchy is known, CP violation can be established at  $3\sigma$  for  $\sim 70\%$  of the values of  $\delta$  for  $\sin^2 2\theta_{13} > 0.03$ . In the opposite case, there is a loss of  $\sim 20\%$  of the coverage in  $\delta$  for  $\sin^2 2\theta_{13} = 0.1$ . A summary of the reach is reported in Figure 14.

*SPL* [68, 113]: another superbeam configuration is under consideration in Europe within the EUROnu Design study. This setup exploits a 4 MW beam to produce a very low energy superbeam aimed at a 440 kton MEMPHYS Water Cherenkov detector located 130 km away at Fréjus. The very high intensity of the beam and very large detector compensate



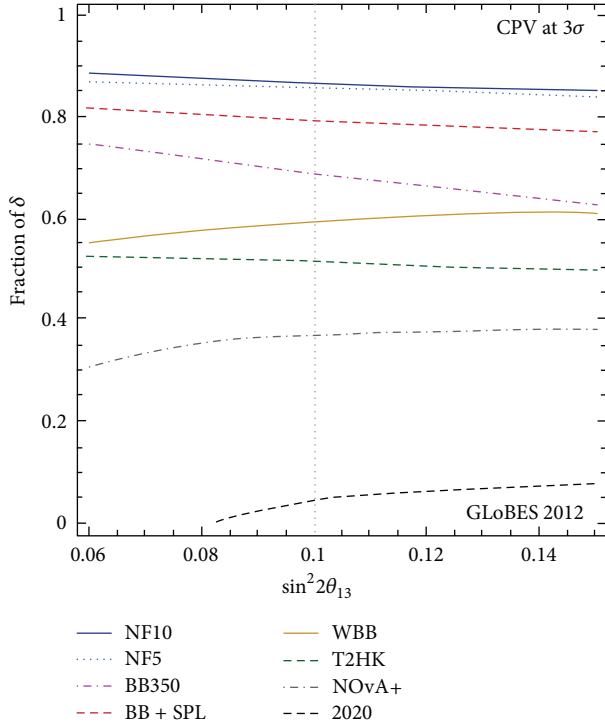


FIGURE 19:  $\delta$ -fraction for  $3\sigma$  CP violation sensitivity for an upgrade of NOvA with a 30 kton LAr detector (NOvA+), T2HK, a WBB with a baseline of 2300 km and a 100 kton LAr detector (WBB), a low energy betabeam combined with the SPL superbeam and aimed at WC detector at 130 km, a higher energy betabeam (BB350), a neutrino factory with 10 GeV (NF10) and 5 GeV (NF5) muons and a 100 kton MIND detector, as well as the expected reach by 2020 by combining NOvA, T2K, and reactor data. Figure is taken from [149].

for the low detection cross-section and excellent sensitivity to CP violation can be reached; see Figure 15. CP violation can be found at  $3\sigma$  for  $\sim 67\%$  of the values of  $\delta$  for  $\sin^2\theta_{13} = 0.1$  [68] (see also [113]). Due to the short distance, no matter effects arise and no sensitivity to the mass hierarchy can be achieved from long baseline neutrino oscillations. However, given the recently discovered large value of  $\theta_{13}$ , taking into account atmospheric neutrino events will allow to find the hierarchy for sufficient exposure; see Figure 6 [68].

**5.2. Betabeams.** Betabeams [114–116] have been proposed as an alternative type of setup which uses a very pure beam of electron neutrinos produced by beta-decays of highly accelerated ions. In this case, the main oscillation channel is the  $\nu_e \rightarrow \nu_\mu$ , one which provides sensitivity to the mass hierarchy and CP violation. The neutrino spectrum is very well known and depends on the  $Q$  value of the beta-decay and on the  $\gamma$  factor of the ions. In a given accelerator, for example, the Main Injector at Fermilab or the SPS at CERN, fully stripped ions can be accelerated to a maximum  $Z/A$  times the proton energy, with  $Z$  and  $A$  the number of protons and of nucleons, respectively. After the initial idea, subsequent studies were performed in the context of EURISOL and EUROnu Design Studies. The ions, which have suitable lifetimes and can be

copiously produced, are the combinations:  ${}^6\text{He}$ ,  ${}^{18}\text{Ne}$ , and  ${}^8\text{Li}$ ,  ${}^8\text{B}$ , for  $\nu_e$  and  $\bar{\nu}_e$  beams. The former has  $Q$  values of 3.5 MeV and 3.3 MeV, respectively, while  ${}^8\text{Li}$ ,  ${}^8\text{B}$  of 13.0 MeV and 13.9 MeV, respectively. The latter ions will yield higher neutrino energies for a given  $\gamma$ , but the flux will be lower for the same energy as it scales as  $\gamma^{-2}$ . All of these isotopes need to be produced artificially, and the production rate turns out to be a limiting factor for the physics reach of the facilities.  ${}^6\text{He}$ ,  ${}^{18}\text{Ne}$  pose less-significant challenges from the production point of view but do not allow to reach very high energies, while the other ions could provide higher energies without the need for high  $\gamma$ -factors, but, due to the challenges of production, it is still not clear what fluxes could be achievable.

The  $\gamma = 100$  option for a betabeam which uses  ${}^6\text{He}$ ,  ${}^{18}\text{Ne}$  has been studied in detail within the EURISOL Design Study. Given the very low energies, the most suitable baseline is the CERN to Fréjus one of 130 km. In principle, higher  $\gamma$  factors could be achieved if a significant upgrade of the present accelerators is envisaged [117]; see also [70, 118–125]. In this case, higher energies and consequently longer distances could be used which provide sensitivity not only to CP violation but also to matter effects. The ideal detector, given the low energies of the beam, is MEMPHYS, a one megaton Water-Cerenkov detector, which has excellent energy resolution and efficiency. Compared to superbeams, betabeams have an extremely pure beam, with no contamination from other flavours at the source. On the other hand, the absence of a  $\nu_\mu$  component implies that a betabeam cannot provide a precision measurement of  $\theta_{23}$ . Due to the short distance, no sensitivity to the mass hierarchy is achievable, as in the case of the SPL, unless atmospheric neutrinos are included [68]. Excellent reach for CP violation could be obtained, especially if the betabeam is combined with a superbeam from CERN to Fréjus. The two setups are sensitive to the T-conjugated channels, providing a clean measurement of the CP-violating phase  $\delta$ ; see Figure 15. Moreover the betabeam-superbeam combination offers also improved sensitivity to the mass hierarchy, even in the case of short baselines [69]; see Figure 6.

**5.3. Neutrino Factory.** In a Neutrino Factory [126–128] neutrinos are produced by highly accelerated muons which decay producing a highly collimated beam of muon and electron neutrinos. The spectrum is very well known and high energies can be achieved: the wide beam and high energies allow to reconstruct with precision the oscillatory pattern and typically achieve a superior performance with respect to the other options. Let us consider the decay of  $\mu^-$  ( $\mu^+$ ): it will generate an initial beam with two neutrino components,  $\nu_\mu$  and  $\bar{\nu}_e$  ( $\bar{\nu}_\mu$  and  $\nu_e$ ). These will oscillate inducing also  $\nu_e$  and  $\bar{\nu}_\mu$  ( $\bar{\nu}_e$  and  $\nu_\mu$ ). At the detector, for muon-like events, two different signals will be present: the *right-sign* muon events which derive from the observation of  $\nu_\mu$  coming from the disappearance channel,  $\nu_\mu \rightarrow \nu_\mu$ , and the *wrong-sign* muon events which are due to  $\bar{\nu}_e \rightarrow \bar{\nu}_\mu$  oscillations. As the appearance oscillation is sensitive to matter effects and CPV, it is necessary to distinguish the two signals. This is achieved by means of magnetized detectors which can distinguish  $\mu^+$  from  $\mu^-$  events. The mis-Id rate is typically very low at a

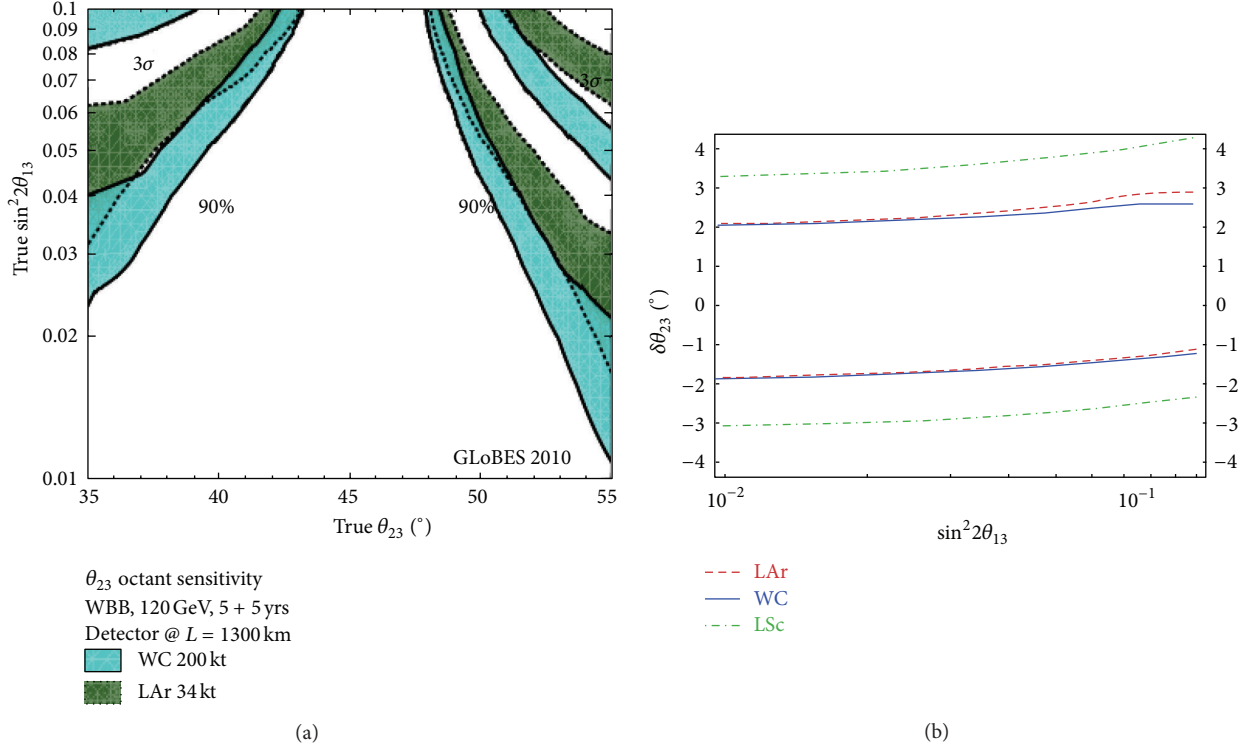


FIGURE 20: (a) LBNE sensitivity to resolve the  $\theta_{23}$  octant degeneracy. The standard configuration in 2010 has been used. The blue (green) band shows the results for 200 kt WC (34 kt LAr) and its width is obtained by varying  $\delta$ , ranging from 10% to 90% CP fraction. In the region above the bands, the  $\theta_{23}$  octant can be determined at 90% CL (lower bands) and  $3\sigma$  (upper bands). Taken from [103]. (b) Nonmaximal  $\theta_{23}$  discovery potential, with  $\delta\theta_{23} \equiv \theta_{23} - 45^\circ$ , as a function of  $\sin^2 2\theta_{13}$ , for the LBNO superbeam with 100 kton LAr, 440 kton WC and 50 kton LSc detectors. In the region enclosed by each couple of lines,  $\delta\theta_{23} = 0$  cannot be ruled out at a statistical significance of  $3\sigma$ . Results are shown for the detector placed at Pyhäsalmi and for a true normal hierarchy. Figure taken from [107].

level of  $10^{-4}$ – $10^{-3}$ , depending on the detector technology. The detector of choice [129] is an iron-magnetized detector (MIND) which provides excellent background rejection and very good energy resolution but low detection efficiency for neutrinos with energies in the few GeV range. This detector performs very well for high energies and is the default choice for muon energies above 8 GeV. For lower energies, detectors with lower- $Z$  would be preferred, such as a magnetized Totally-Active Scintillator Detector (TASD) or LAr. The latter detectors provide excellent efficiency for neutrinos with low energies, excellent energy resolution, and low backgrounds, but their magnetization is extremely challenging and not proven yet for the mass scales of interest. (In [130] the possibility to use nonmagnetized detectors for a neutrino factory has been put forward, which may become an option for large  $\theta_{13}$  and offers an interesting synergy with large-scale detectors for nonaccelerator physics. More detailed studies along these lines would be required, and this option is currently not considered within the context of neutrino factory study groups.)

The initial baseline configuration of the NF [129] used muons with an energy of 25 GeV and two different baselines, at approximately 4000 and 7500 km, with two MIND detectors, a 100 kton one at the shorter baseline and a 50 kton

one at the “magic” baseline [131]. This second baseline was designed to provide a very powerful determination of the mass hierarchy and a clean determination of  $\theta_{13}$ , thanks to the strong suppression of the “CP term” due to  $\sin \Delta A \sim 0$ , and to complement the shorter baseline in the search of CP violation, helping to resolve the degeneracies. Additional studies can be found, for example, in [84, 132–141]. This setup was optimised assuming small values of  $\theta_{13}$ , and several studies showed that it would outperform all other options for small  $\theta_{13}$ , thanks to its high number events, very low backgrounds, and small systematic errors [129, 140].

In the case of large  $\theta_{13}$ , a more conservative setup, named the Low-Energy Neutrino Factory (LENF), was proposed as a less-challenging option [142, 143] which used a single baseline of 1300 km, corresponding to the Fermilab to DUSEL distance, and, consequently, a lower muon energy, at  $\sim 4.5$  GeV [144]; see also [145, 146]. Given the low energy, a detector with good-energy resolution and low-energy threshold was needed in order to exploit the rich oscillatory pattern. The detector of choice was a Totally-Active Scintillator Detector (TASD) magnetized by means of a large magnetic cavern or a magnetized LAr TPC, which would be ideal due to the large size and the excellent detector performance, especially at low energy. This initial study showed that excellent reach could be

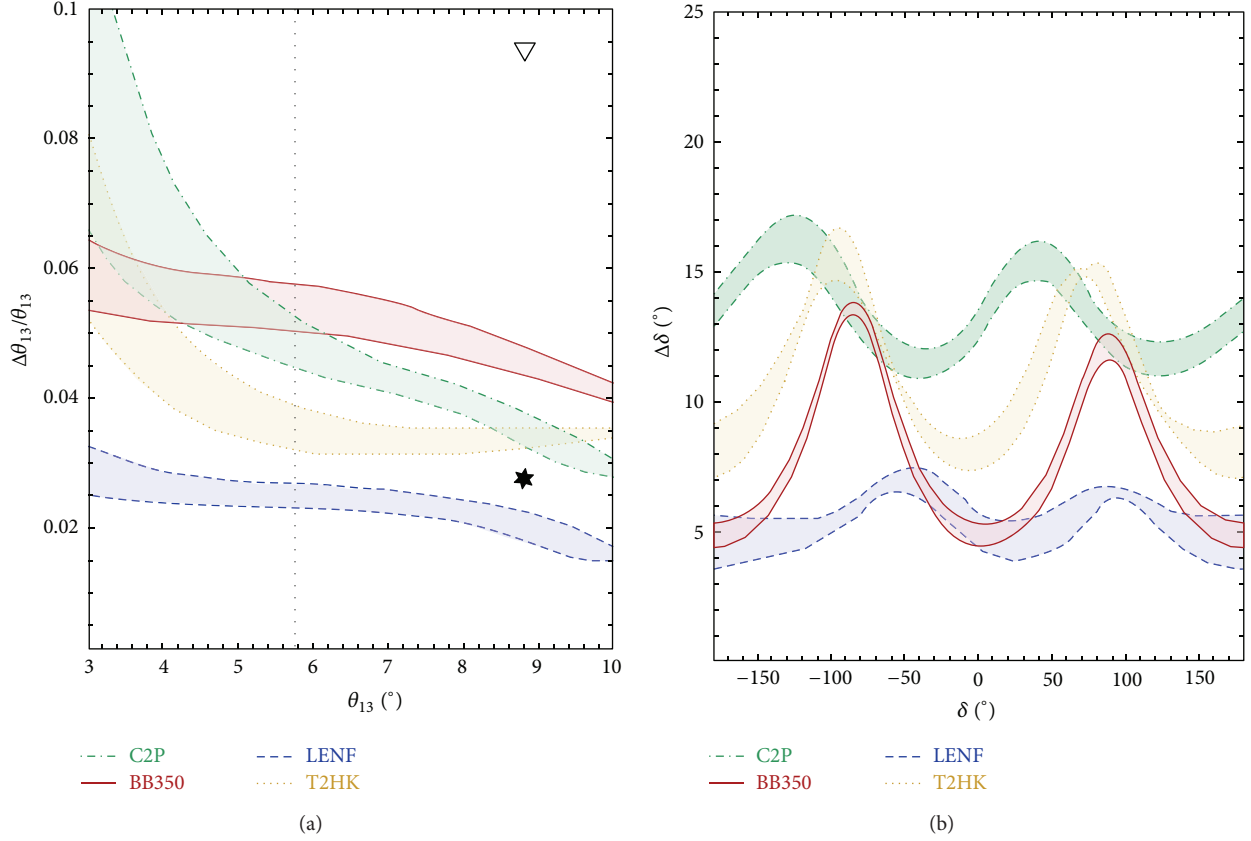


FIGURE 21:  $1\sigma$  precision on  $\theta_{13}$  (a) and  $\delta$  (b) for the CN2PY and T2HK superbeams, the  $\gamma = 350$  beta-beam, and the LBNF. On the left plot, the empty triangle represents the current precision for Daya Bay, and the star the ultimate attainable precision, assuming as true value the present Daya Bay best fit value. The width of the bands represent the dependence of the error on  $\theta_{13}$  on  $\delta$  and vice versa. For further details, see [46] from which the figure is reproduced.

achieved for the mass hierarchy and CP violation; see Figure 16. A subsequent study of the LBNF using a Magnetized Iron Neutrino Detector has also shown a promising performance [147], and its reach is reported in Figure 17. A similar study using a TASD and LAr detector [148] found a rather flat performance as a function of  $L$  and muon energy, for large  $\theta_{13}$ , as seen in Figure 18. Based on these analyses and in view of the discovery of large  $\theta_{13}$ , the International Design Study on a Neutrino Factory (IDS-NF) reviewed the baseline configuration in April 2012 and chose a LBNF with MIND detector with muon energy of 10 GeV and baseline of 2000 km.

A summary of the results for the LBNF and a comparison with other facilities are given in Figure 19 [149]. A table which summarises the setups described and their reach for CP violation is given in Table 4. A word of caution is necessary as the precise reach of each setup is affected by the assumption made on the beam, detector, and systematic errors. Nevertheless, thanks to the intense flux, pure beam, excellent background rejection, and long baselines, an NF has been shown to achieve the best physics reach in search for CP violation and the mass hierarchy.

Once CP violation is discovered, it will be important to measure the values of the phase and of  $\theta_{13}$  with high precision. In fact, in many models of leptonic flavour, these values are correlated with the deviations from maximality of

$\theta_{23}$  and/or with parameters in the quark sector. Examples of the precision achievable have been typically included in the analysis of the setups, but a comprehensive and detailed study is still at its beginnings. A first comparison between different experiments has been performed in [46]. The main results are reported in Figure 21 and indicate that for  $\theta_{13}$  reactor experiments, and in particular Daya Bay, will achieve the best precision, marginally improved by a LBNF. The precise measurement of the  $\delta$  phase depends significantly on the true value itself, with a significant loss of precision around  $\pi/2$  for experiments such as T2HK and beta beams. If instead matter effects are relevant, as it is the case for CN2PY and LBNF, the error on  $\delta$  tends to become more uniform in  $\delta$ , and the best performance is given by the LBNF which can typically achieve an error of around  $5^\circ$ .

**5.4. Precision Measurements.** With the discovery of large  $\theta_{13}$ , the focus of future long baseline experiments has shifted not only to the discovery of the mass hierarchy and CP violation as discussed above but also to the precise measurements of the oscillation parameters. Among these, determining if  $\theta_{23}$  is maximal or not is of great theoretical importance together with establishing its octant, if nonmaximal. The experiments discussed in the previous subsections, except beta beams, will have sensitivity to these parameters mainly

TABLE 4: Summary of the setups described in the text. From left to right, the columns list the names of the setups, the beam power for superbeams or  $\gamma$  factor for beta beams or muon energy for neutrino factories, the baseline, the detector choice, the running time in years for each polarity (the neutrino and antineutrinos runs are simultaneous for the neutrino factory), the systematic error on the signal and background, the fraction of the values of  $\delta$  for which CP-violation could be determined at  $3\sigma$  at  $\sin^2 2\theta_{13} = 0.1$ , and the reference from which the information has been collected. For LBNO with 10 kton and 30 kton LAr detectors, the values of the fraction of  $\delta$  are given separately for a true normal (NH) or inverted (IH) hierarchy. The number of seconds per year is  $1.7 \times 10^7$  for LBNO and  $1 \times 10^7$  for T2HK. BB + SPL considers the combination of the betabeam with  $1.1 \times 10^{18}$  ( $2.8 \times 10^{18}$ )  $^{18}\text{Ne}$  ( $^6\text{He}$ ) useful decays per year together with the SPL described above (with a 500 kton WC detector instead of a 440 kton one). The LENF uses  $1.4 \times 10^{21}$  useful muon decays per year per polarity, and NF10  $7 \times 10^{20}$ . The results quoted depend significantly on the assumptions made in the analysis and should be treated carefully.

Setup	MW	$L$	Detector	Years $\nu + \bar{\nu}$	Syst. errors (signal, backg.)	$3\sigma$ CPV reach	References
LBNE	0.7	1290 km	200 kton WC or 34 kton LAr	5 + 5	(1%, 5%)	~60%	[103]
LBNE12	0.7	1290 km	10 kton LAr	5 + 5	(1%, 5%)	27%	[104]
LBNO	4	130 km	440 kton WC	2 + 8	(5%, 5%)	~60%	[107]
	1.6	2290 km	10 kton LAr	5 + 5	(5%, 5%)	25% (NH)–38% (IH)	[112]
	1.6	2290 km	30 kton LAr	5 + 5	(5%, 5%)	58% (NH)–62% (IH)	[112]
	1.6	2290 km	100 kton LAr	5 + 5	(5%, 5%)	71%	[112]
T2HK	1.66	295	560 kton WC	1.5 + 3.5	~(5%, 5%)	75%	[66]
	1.66	295	560 kton WC	1.5 + 3.5	~(5%, 5%)	55% no mass hier.	[66]
SPL	4	130 km	440 kton WC	2 + 8	(2%, 2%)	73%	[68]
	4	130 km	440 kton WC	2 + 8	(5%, 5%)	53%	[68]
$\gamma$							
BB + SPL	100	130	500 kton WC	5 + 5	See [149]	80%	[149]
BB350	350	650	500 kton WC	5 + 5	See [149]	~70%	[149]
$E_\mu$							
LENF	4.5 GeV	1300 km	20 kton TASD 100 kton LAr	10	(2%, 2%)	85% 81%–90%	[144]
NF10	10 GeV	2000 km	100 kton MIND	10	(2%, 2%)	86%	[149]

via the disappearance channels  $\nu_\mu \rightarrow \nu_\mu$  and  $\bar{\nu}_\mu \rightarrow \bar{\nu}_\mu$ . Typically superbeams have a very good reach and a LENF can perform better especially if the low energy part of the spectrum can be reconstructed. It has been shown that the contamination from  $\nu_\tau$  events, coming from  $\nu_\mu \rightarrow \nu_\tau$  oscillations, can have a significant impact on the high energy neutrino factory [150, 151]. It is expected that a lower muon energy will reduce the number of  $\tau$  events but their impact in the 10 GeV LENF needs to be fully explored. In Figure 20 we report two examples of the capability of LBNE in the 2010 configuration and of the 4.5 GeV LENF for studying  $\theta_{23}$ .

## 6. Conclusions

Since the discovery of neutrino oscillations huge progress has been made and this phenomenon is now well established. Yet new important questions are open for the future, including what is the ordering of neutrino masses? Is there CP violation in the leptonic sector? What are the precise values of the neutrino mixing parameters? Are there new phenomena beyond the three-neutrino framework? With the recently discovered relatively large value of the mixing angle  $\theta_{13}$ , addressing those questions by upcoming oscillation experiments becomes a realistic possibility. In this paper, we have reviewed the phenomenology of oscillation experiments

by discussing some aspects of the determination of neutrino oscillation parameters by present global data, and we have tried to give an outlook for possible future developments. In the near term (the next 10 to 15 years), the interplay of complementary data sets will be important, such as long-baseline accelerator experiments, reactor experiments, and atmospheric neutrino experiments. We have discussed the potential to address questions like the nonmaximality and the octant of  $\theta_{23}$  and the determination of the neutrino mass hierarchy. In order to address CP violation, it seems from the current perspective that a more long-term program will be necessary. Future high-precision long-baseline neutrino experiments can provide crucial answers to the above questions by studying the subdominant  $\nu_\mu \rightarrow \nu_e$  transitions. A wide experimental program for the future is underway or at the discussion stage and includes superbeams, betabeams and neutrino factory. A table which summarises various setups and their reach for CP violation is given in Table 4.

## Acknowledgment

The authors acknowledge partial support from the European Union FP7 ITN INVISIBLES (Marie Curie Actions, PITN-GA-2011-289442).



## References

- [1] Y. Fukuda, T. Hayakawa, E. Ichihara et al., "Evidence for oscillation of atmospheric neutrinos," *Physical Review Letters*, vol. 81, no. 8, pp. 1562–1567, 1998.
- [2] Q. R. Ahmad, R. C. Allen, T. C. Andersen et al., "Direct evidence for neutrino flavor transformation from neutral current interactions in the sudbury neutrino observatory," *Physical Review Letters*, vol. 89, no. 1, Article ID 011301, 6 pages, 2002.
- [3] T. Araki, K. Eguchi, S. Enomoto et al., "Measurement of neutrino oscillation with KamLAND: evidence of spectral distortion," *Physical Review Letters*, vol. 94, no. 8, Article ID 081801, 2005.
- [4] P. Adamson, C. Andreopoulos, K. E. Arms et al., "Measurement of neutrino oscillations with the MINOS detectors in the NuMI beam," *Physical Review Letters*, vol. 101, no. 13, Article ID 131802, 5 pages, 2008.
- [5] K. Abe, N. Abgrall, Y. Ajima et al., "Indication of electron neutrino appearance from an accelerator-produced off-axis muon neutrino beam," *Physical Review Letters*, vol. 107, no. 4, Article ID 041801, 2011.
- [6] P. Adamson, MINOS Collaboration et al., "Improved search for muon-neutrino to electronneutrino oscillations in MINOS," *Physical Review Letters*, vol. 107, no. 18, Article ID 181802, 6 pages, 2011.
- [7] Y. Abe, C. Aberle, T. Akiri et al., "Indication for the disappearance of reactor electron antineutrinos in the Double Chooz experiment," *Physical Review Letters*, vol. 108, Article ID 131801, 7 pages, 2012.
- [8] F. An, J. Z. Bai, A. B. Balantekin et al., "Observation of electron-antineutrino disappearance at Daya Bay," *Physical Review Letters*, vol. 108, no. 17, Article ID 171803, 7 pages, 2012.
- [9] J. Ahn, S. Chebotaryov, J. H. Choi et al., "Observation of reactor electron antineutrino disappearance in the RENO experiment," *Physical Review Letters*, vol. 108, no. 19, Article ID 191802, 6 pages, 2012.
- [10] M. C. Gonzalez-Garcia, M. Maltoni, J. Salvado, and T. Schwetz, "Global fit to three neutrino mixing: critical look at present precision," *Journal of High Energy Physics*, vol. 2012, article 123, 2012.
- [11] D. Forero, M. Tortola, and J. Valle, "Global status of neutrino oscillation parameters after recent reactor measurements," *Physical Review D*, vol. 86, Article ID 073012, 8 pages, 2012.
- [12] G. Fogli, E. Lisi, A. Marrone et al., "Global analysis of neutrino masses, mixings and phases: entering the era of leptonic CP violation searches," *Physical Review D*, vol. 86, no. 1, Article ID 013012, 10 pages, 2012.
- [13] P. Machado, H. Minakata, H. Nunokawa, and R. Z. Funchal, "Combining accelerator and reactor measurements of  $\theta_{13}$  the first result," *Journal of High Energy Physics*, vol. 1205, article 023, 2012.
- [14] J. Bergstrom, "Bayesian evidence for non-zero  $\theta_{13}$  and CP-violation in neutrino oscillations," *Journal of High Energy Physics*, vol. 2012, article 163, 2012.
- [15] G. Mention, M. Fechner, Th. Lasserre et al., "The reactor antineutrino anomaly," *Physical Review D*, vol. 83, no. 7, Article ID 073006, 2011.
- [16] M. Apollonio, A. Baldini, C. Bemporad et al., "Search for neutrino oscillations on a long base-line at the CHOOZ nuclear power station," *The European Physical Journal*, vol. C27, Article ID 030101, p. 331, 2003.
- [17] J. Beringer, J. F. Arguin, R. M. Barnett et al., "Review of particle physics," *Physical Review D*, vol. 86, no. 1, Article ID 010001, 1528 pages, 2012.
- [18] H. Minakata, H. Sugiyama, O. Yasuda, K. Inoue, and F. Suekane, "Reactor measurement of  $\theta_{13}$  and its complementarity to long baseline experiments," *Physical Review D*, vol. 68, Article ID 033017, 21 pages, 2003.
- [19] P. Huber, M. Lindner, T. Schwetz, and W. Winter, "Reactor neutrino experiments compared to superbeams," *Nuclear Physics B*, vol. 665, pp. 487–519, 2003.
- [20] G. L. Fogli and E. Lisi, "Tests of three-flavor mixing in long-baseline neutrino oscillation experiments," *Physical Review D*, vol. 54, no. 5, pp. 3667–3670, 1996.
- [21] R. Nichols, "Results from MINOS," Talk at Neutrino 2012, Kyoto, Japan, June 2012.
- [22] K. B. M. Mahn and M. H. Shaevitz, "Comparisons and combinations of reactor and long-baseline neutrino oscillation measurements," *International Journal of Modern Physics A*, vol. 21, no. 18, pp. 3825–3843, 2006.
- [23] A. Cervera, A. Donini, M. B. Gavela, J. J. Gomez Cadenas, P. Hernández, and O. Mena, "Golden measurements at a neutrino factory," *Nuclear Physics*, vol. 579, no. 1, Article ID 000210, pp. 17–55, 2000.
- [24] M. Freund, "Analytic approximations for three neutrino oscillation parameters and probabilities in matter," *Physical Review*, vol. 64, no. 5, Article ID 053003, 12 pages, 2001.
- [25] E. K. Akhmedov, R. Johansson, M. Lindner et al., "Series expansions for three flavor neutrino oscillation probabilities in matter," *Journal of High Energy Physics*, vol. 0404, article 078, Article ID 040217, 2004.
- [26] L. Wolfenstein, "Neutrino oscillations in matter," *Physical Review D*, vol. 17, no. 9, pp. 2369–2374, 1978.
- [27] S. Mikheev and A. Y. Smirnov, "Resonance amplification of oscillations in matter and spectroscopy of solar neutrinos," *Soviet Journal of Nuclear Physics*, vol. 42, article 913, 1985.
- [28] D. Ayres and NOvA Collaboration, "NOvA: proposal to build a 30 kiloton off-axis detector to study  $\nu_\mu \rightarrow \nu_e$  oscillations in the NuMI beamline," In press, <http://arxiv.org/abs/hep-ex/0503053>.
- [29] V. Barger, D. Marfatia, and K. Whisnant, "Breaking eight-fold degeneracies in neutrino CP violation, mixing, and mass hierarchy," *Physical Review D*, vol. 65, Article ID 073023, 2002.
- [30] O. L. G. Peres and A. Y. Smirnov, "Atmospheric neutrinos: LMA oscillations,  $\text{Ue3}$  induced interference and CP-violation," *Nuclear Physics B*, vol. 680, no. 1–3, pp. 479–509, 2004.
- [31] S. T. Petcov, "Diffractive-like (or parametric-resonance-like?) enhancement of the Earth (day-night) effect for solar neutrinos crossing the Earth core," *Physics Letters B*, vol. 434, no. 3–4, pp. 321–332, 1998.
- [32] E. K. Akhmedov, "Parametric resonance of neutrino oscillations and passage of solar and atmospheric neutrinos through the earth," *Nuclear Physics B*, vol. 538, no. 1–2, pp. 25–51, 1999.
- [33] E. K. Akhmedov, A. Dighe, P. Lipari, and A. Y. Smirnov, "Atmospheric neutrinos at super-Kamiokande and parametric resonance in neutrino oscillations," *Nuclear Physics B*, vol. 542, no. 1–2, pp. 3–30, 1999.
- [34] M. Chizhov, M. Maris, and S. T. Petcov, "On the oscillation length resonance in the transitions of solar and atmospheric neutrinos crossing the earth core," In press, <http://arxiv.org/abs/hep-ph/9810501>.
- [35] M. V. Chizhov and S. T. Petcov, "New conditions for a total neutrino conversion in a medium," *Physical Review Letters*, vol. 83, no. 6, pp. 1096–1099, 1999.

- [36] E. K. Akhmedov, M. Maltoni, and A. Y. Smirnov, “1–3 leptonic mixing and the neutrino oscillograms of the Earth,” *Journal of High Energy Physics*, vol. 0705, article 077, Article ID 061228, 2007.
- [37] C. W. Kim and U. W. Lee, “Comment on the possible electron neutrino excess in the Super-Kamiokande atmospheric neutrino experiment,” *Physics Letters B*, vol. 444, no. 1-2, pp. 204–207, 1998.
- [38] O. Peres and A. Y. Smirnov, “Testing the solar neutrino conversion with atmospheric neutrinos,” *Physics Letters B*, vol. 456, article 204, Article ID 990231, 1999.
- [39] M. Gonzalez-Garcia, M. Maltoni, and A. Y. Smirnov, “Measuring the deviation of the 2-3 lepton mixing from maximal with atmospheric neutrinos,” *Physical Review D*, vol. 70, Article ID 093005, 2004.
- [40] E. K. Akhmedov, M. Maltoni, and A. Y. Smirnov, “Neutrino oscillograms of the Earth: effects of 1-2 mixing and CP-violation,” *Journal of High Energy Physics*, vol. 0806, article 072, 2008.
- [41] J. Bernab  , S. Palomares-Ruiz, and S. T. Petcov, “Atmospheric neutrino oscillations,  $\theta_{13}$  and neutrino mass hierarchy,” *Nuclear Physics B*, vol. 669, no. 1-2, pp. 255–276, 2003.
- [42] S. T. Petcov and T. Schwetz, “Determining the neutrino mass hierarchy with atmospheric neutrinos,” *Nuclear Physics B*, vol. 740, no. 1-2, pp. 1–22, 2006.
- [43] Y. Itow, “Results from running experiments,” Talk at Neutrino 2012, Kyoto, Japan, 2012.
- [44] M. Mezzetto and T. Schwetz, “ $\theta_{13}$  Phenomenology, present status and prospect,” *Journal of Physics G*, vol. 37, no. 10, Article ID 103001, 2010.
- [45] P. Huber, M. Lindner, T. Schwetz, and W. Winter, “First hint for CP violation in neutrino oscillations from upcoming superbeam and reactor experiments,” *Journal of High Energy Physics*, vol. 2009, no. 11, 2009.
- [46] P. Coloma, A. Donini, E. Fernandez-Martinez, and P. Hernandez, “Precision on leptonic mixing parameters at future neutrino oscillation experiments,” *Journal of High Energy Physics*, vol. 1206, article 073, 2012.
- [47] H. Minakata and H. Nunokawa, “Exploring neutrino mixing with low energy superbeams,” *Journal of High Energy Physics*, vol. 5, no. 10, 2001.
- [48] S. Prakash, S. K. Raut, and S. U. Sankar, “Getting the best out of T2K and NOvA,” *Physical Review D*, vol. 86, no. 3, Article ID 033012, 2012.
- [49] A. S. Dighe and A. Y. Smirnov, “Identifying the neutrino mass spectrum from a supernova neutrino burst,” *Physical Review D*, vol. 62, no. 3, Article ID 033007, pp. 1–24, 2000.
- [50] M. Kachelriess, R. Tomas, R. Buras et al., “Exploiting the neutronization burst of a galactic supernova,” *Physical Review D*, vol. 71, Article ID 063003, 2005.
- [51] P. D. Serpico, S. Chakraborty, T. Fischer et al., “Probing the neutrino mass hierarchy with the rise time of a supernova burst,” *Physical Review D*, vol. 85, Article ID 085031, 2012.
- [52] E. Borriello, S. Chakraborty, A. Mirizzi et al., “(Down-to-)Earth matter effect in supernova neutrinos,” *Physical Review D*, vol. 86, Article ID 083004, 2012.
- [53] S. Pascoli, S. T. Petcov, and T. Schwetz, “The absolute neutrino mass scale, neutrino mass spectrum, Majorana CP-violation and neutrinoless double-beta decay,” *Nuclear Physics B*, vol. 734, no. 1-2, pp. 24–49, 2006.
- [54] W. Rodjohann, “Neutrino-less double beta decay and particle physics,” *International Journal of Modern Physics E*, vol. 20, article 1833, 2011.
- [55] N. Mondal, “India-based neutrino observatory,” Talk at Lepton-Photon 2011, TIFR, Mumbai, India, 2011, <http://www.tifr.res.in/~lp11/>.
- [56] “India-Based Neutrino Observatory,” <http://www.ino.tifr.res.in/ino/>.
- [57] R. Gandhi, P. Ghoshal, S. Goswami, and S. U. Sankar, “Resolving the mass hierarchy with atmospheric neutrinos using a liquid argon detector,” *Physical Review D*, vol. 78, no. 7, Article ID 073001, 2008.
- [58] V. Barger, R. Gandhi, P. Ghoshal et al., “Neutrino mass hierarchy and octant determination with atmospheric neutrinos,” vol. 109, Article ID 091801, 2012.
- [59] T. T. de Fatis, “Prospects of measuring  $\sin^2 2\theta_{13}$  and the sign of  $\Delta m^2$  with a massive magnetized detector for atmospheric neutrinos,” *The European Physical Journal C*, vol. 24, no. 1, pp. 43–50, 2000.
- [60] M. Blennow and T. Schwetz, “Identifying the neutrino mass ordering with INO and NOvA,” *Journal of High Energy Physics*, vol. 2012, no. 8, article 058, 2012.
- [61] M. Blennow and T. Schwetz, “Erratum: Identifying the neutrino mass ordering with INO and NOvA (Journal of High Energy Physics (2012) 08 (058)),” *Journal of High Energy Physics*, vol. 2012, no. 11, article 098, 2012.
- [62] R. Gandhi, P. Ghoshal, S. Goswami, P. Mehta, S. U. Sankar, and S. Shalgar, “Mass hierarchy determination via future atmospheric neutrino detectors,” *Physical Review D*, vol. 76, no. 7, Article ID 073012, 20 pages, 2007.
- [63] A. Samanta, “A comparison of the ways of resolving mass hierarchy with atmospheric neutrinos,” *Physical Review D*, vol. 81, no. 3, Article ID 037302, 4 pages, 2010.
- [64] D. Indumathi and M. Murthy, “A question of hierarchy: matter effects with atmospheric neutrinos and anti-neutrinos,” *Physical Review D*, vol. 71, no. 1, Article ID 013001, 16 pages, 2005.
- [65] D. Autiero, J. Aysto, A. Badertscher et al., “Large underground, liquid based detectors for astro-particle physics in Europe: scientific case and prospects,” *Journal of Cosmology and Astroparticle Physics*, vol. 2007, article 011, 2007.
- [66] K. Abe, T. Abe, H. Aihara et al., “Letter of intent: the Hyper-Kamiokande experiment—detector design and physics potential,” In press, <http://arxiv.org/abs/1109.3262>.
- [67] P. Huber, M. Maltoni, and T. Schwetz, “Resolving parameter degeneracies in long-baseline experiments by atmospheric neutrino data,” *Physical Review D*, vol. 71, no. 5, Article ID 053006, 15 pages, 2005.
- [68] J.-E. Campagne, M. Maltoni, M. Mezzetto, and T. Schwetz, “Physics potential of the CERN-MEMPHYS neutrino oscillation project,” *Journal of High Energy Physics*, vol. 2007, article 003, 2007.
- [69] T. Schwetz, “Determination of the neutrino mass hierarchy in the regime of small matter effect,” *Journal of High Energy Physics*, vol. 2007, article 093, Article ID 070327, 2007.
- [70] A. Jansson, O. Mena, S. J. Parke, and N. Saoulidou, “Combining CPT-conjugate neutrino channels at Fermilab,” *Physical Review D*, vol. 78, no. 5, Article ID 053002, 11 pages, 2008.
- [71] M. C. Gonzalez-Garcia, F. Halzen, and M. Maltoni, “Physics reach of high-energy and high-statistics IceCube atmospheric neutrino data,” *Physical Review D*, vol. 71, no. 9, Article ID 093010, 13 pages, 2005.

- [72] R. Abbasi, Y. Abdou, M. Ackermann et al., “The design and performance of IceCube DeepCore,” *Astroparticle Physics*, vol. 35, no. 10, pp. 615–624, 2012.
- [73] The IceCube Collaboration, “Atmospheric neutrino oscillations with IceCube/DeepCore,” in *Proceedings of the International Conference on Neutrino Physics and Astrophysics (ICNPA '12)*, Kyoto, Japan, June 2012.
- [74] O. Mena, I. Mocioiu, and S. Razzaque, “Neutrino mass hierarchy extraction using atmospheric neutrinos in ice,” *Physical Review D*, vol. 78, no. 9, Article ID 093003, 10 pages, 2008.
- [75] D. J. Koskinen, “IceCube-DeepCore-PINGU: fundamental neutrino and dark matter physics at the South Pole,” *Modern Physics Letters A*, vol. 26, no. 39, pp. 2899–2915, 2011.
- [76] E. K. Akhmedov, S. Razzaque, and A. Y. Smirnov, “Mass hierarchy, 2-3 mixing and CP-phase with huge atmospheric neutrino detectors,” In press, <http://arxiv.org/abs/1205.7071>.
- [77] S. T. Petcov and M. Piai, “The LMA MSW solution of the solar neutrino problem, inverted neutrino mass hierarchy and reactor neutrino experiments,” *Physics Letters B*, vol. 533, no. 1-2, pp. 94–106, 2002.
- [78] J. G. Learned, S. T. Dye, S. Pakvasa, and R. C. Svoboda, “Determination of neutrino mass hierarchy and  $\theta_{13}$  with a remote detector of reactor antineutrinos,” *Physical Review D*, vol. 78, no. 7, Article ID 071302, 5 pages, 2008.
- [79] L. Zhan, Y. Wang, J. Cao, and L. Wen, “Experimental requirements to determine the neutrino mass hierarchy using reactor neutrinos,” *Physical Review D*, vol. 79, no. 7, Article ID 073007, 5 pages, 2009.
- [80] P. Ghoshal and S. Petcov, “Neutrino mass hierarchy determination using reactor antineutrinos,” *Journal of High Energy Physics*, vol. 2011, article 58, 2011.
- [81] J. Cao, “Observation of electron antineutrino disappearance at Daya Bay,” in *Proceedings of the Neutrino at the Turning Point (nu-TURN '12)*, Laboratori Nazionali del Gran Sasso, Assergi, Italy, May 2012.
- [82] S. T. Petcov and T. Schwetz, “Precision measurement of solar neutrino oscillation parameters by a long-baseline reactor neutrino experiment in Europe,” *Physics Letters B*, vol. 642, no. 5-6, pp. 487–494, 2006.
- [83] J. Alonso, F. T. Avignone, W. A. Barletta et al., “Expression of interest for a novel search for CP violation in the neutrino sector: DAEDALUS,” In press, <http://arxiv.org/abs/1006.0260>.
- [84] J. B. Castell, M. B. Gavela, J. J. Cadenas, P. Hernández, and O. Mena, “On the measurement of leptonic CP violation,” *Nuclear Physics B*, vol. 608, no. 1-2, pp. 301–318, 2001.
- [85] H. Minakata, H. Nunokawa, and S. J. Parke, “Parameter degeneracies in neutrino oscillation measurement of leptonic CP and  $T$  violation,” *Physical Review D*, vol. 66, no. 9, Article ID 093012, 15 pages, 2002.
- [86] V. D. Barger, S. Geer, R. Raja, and K. Whisnant, “Exploring neutrino oscillations with superbeams,” *Physical Review D*, vol. 63, no. 11, Article ID 113011, 24 pages, 2001.
- [87] T. Kajita, H. Minakata, and H. Nunokawa, “Method for determination of  $|U_{e3}|$  in neutrino oscillation appearance experiments,” *Physics Letters B*, vol. 528, no. 3-4, pp. 245–252, 2002.
- [88] H. Minakata, H. Nunokawa, and S. Parke, “Parameter degeneracies in neutrino oscillation measurement of leptonic CP and  $T$  violation,” *Physical Review D*, vol. 66, no. 9, Article ID 093012, 2002.
- [89] H. Minakata and H. Nunokawa, “How to measure CP violation in neutrino oscillation experiments?” *Physics Letters B*, vol. 413, no. 3-4, pp. 369–377, 1997.
- [90] V. Barger, D. Marfatia, and K. Whisnant, “Off-axis beams and detector clusters: resolving neutrino parameter degeneracies,” *Physical Review D*, vol. 66, no. 5, Article ID 053007, 2002.
- [91] O. M. Requejo, S. Palomares-Ruiz, and S. Pascoli, “Super-NOvA: a long-baseline neutrino experiment with two off-axis detectors,” *Physical Review D*, vol. 72, no. 5, Article ID 053002, 2005.
- [92] O. Mena, S. Palomares-Ruiz, and S. Pascoli, “Determining the neutrino mass hierarchy and CP-violation in NOvA with a second off-axis detector,” *Physical Review D*, vol. 73, no. 7, Article ID 073007, 2006.
- [93] J. Bernabeu, J. Burguet-Castell, C. Espinoza, and M. Lindroos, “Monochromatic neutrino beams,” *Journal of High Energy Physics*, no. 12, pp. 271–279, 2005.
- [94] M. Ishitsuka, T. Kajita, H. Minakata, and H. Nunokawa, “Resolving the neutrino mass hierarchy and CP degeneracy by two identical detectors with different baselines,” *Physical Review D*, vol. 72, no. 3, Article ID 033003, pp. 1–14, 2005.
- [95] K. Hagiwara, N. Okamura, and K. Senda, “Solving the neutrino parameter degeneracy by measuring the T2K off-axis beam in Korea,” *Physics Letters B*, vol. 637, no. 4-5, pp. 266–273, 2006.
- [96] P. Huber, M. Lindner, and W. Winter, “Synergies between the first-generation JHF-SK and NuMI superbeam experiments,” *Nuclear Physics B*, vol. 654, no. 1-2, pp. 3–29, 2003.
- [97] H. Minakata, H. Nunokawa, and S. Parke, “Complementarity of eastern and western hemisphere long-baseline neutrino oscillation experiments,” *Physical Review D*, vol. 68, no. 1, Article ID 013010, 2003.
- [98] V. Barger, D. Marfatia, and K. Whisnant, “How two neutrino superbeam experiments do better than one,” *Physics Letters B*, vol. 560, no. 1-2, pp. 75–86, 2003.
- [99] K. Whisnant, J. M. Yang, and B.-L. Young, “Measuring CP violation and mass ordering in joint long baseline experiments with superbeams,” *Physical Review D*, vol. 67, no. 1, Article ID 013004, 2003.
- [100] P. Huber, M. Lindner, M. Rolinec, T. Schwetz, and W. Winter, “Prospects of accelerator and reactor neutrino oscillation experiments for the coming ten years,” *Physical Review D*, vol. 70, no. 7, pp. 1–73014, 2004.
- [101] O. Mena, “Unveiling neutrino mixing and leptonic CP violation,” *Modern Physics Letters A*, vol. 20, no. 1, pp. 1–17, 2005.
- [102] O. Mena and S. Parke, “Untangling CP violation and the mass hierarchy in long baseline experiments,” *Physical Review D*, vol. 70, no. 9, Article ID 093011, 2004.
- [103] T. Akiri, D. Allspach, M. Andrews et al., “The 2010 Interim Report of the Long-Baseline Neutrino Experiment Collaboration Physics Working Groups,” In press, <http://arxiv.org/abs/1110.6249>.
- [104] LBNE Reconfiguration, *Steering Committee Interim Report*, June 2012, <https://indico.fnal.gov/getFile.py/access?resId=0&materialId=3&confId=5622>.
- [105] D. Angus, A. Ariga, D. Autiero et al., “The LAGUNA design study-towards giant liquid based underground detectors for neutrino physics and astrophysics and proton decay searches,” In press, <http://arxiv.org/abs/1001.0077>.
- [106] A. Rubbia, “A CERN-based high-intensity high-energy proton source for long baseline neutrino oscillation experiments with next-generation large underground detectors for proton decay searches and neutrino physics and astrophysics,” In press, <http://arxiv.org/abs/1003.1921>.



- [107] P. Coloma, T. Li, and S. Pascoli, "A comparative study of long-baseline superbeams within LAGUNA for large  $\theta_{13}$ ," In press, <http://arxiv.org/abs/1206.4038>.
- [108] A. Rubbia, "Underground neutrino detectors for particle and astroparticle Science: the Giant Liquid Argon Charge Imaging Experiment (GLACIER)," *Journal of Physics: Conference Series*, vol. 171, Article ID 012020, 2009.
- [109] T. M. Undagoitia, F. V. Feilitzsch, and M. G-Neff, "LENA: a multipurpose detector for low energy neutrino astronomy and proton decay," *Journal of Physics: Conference Series*, vol. 120, Article ID 052018, 2008.
- [110] M. Wurm, J. F. Beacom, L. B. Bezrukov et al., "The next-generation liquid-scintillator neutrino observatory LENA," In press, <http://arxiv.org/abs/1104.5620>.
- [111] A. de Bellefon, J. Bouchez, J. Busto et al., "MEMPHYS: a large scale water Cerenkov detector at Frejus," In press, <http://arxiv.org/abs/hepex/0607026>.
- [112] S. K. Agarwalla, T. Li, and A. Rubbia, "An incremental approach to unravel the neutrino mass hierarchy and CP violation with a long-baseline superbeam for large  $\theta_{13}$ ," *Journal of High Energy Physics*, vol. 2012, no. 5, Article ID 154, 2012.
- [113] J. Bernabeu, M. Blennow, P. Coloma et al., "EURONU WP6 2009 yearly report: update of the physics potential of NuFact, superbeams and betabeams," Tech. Rep. EURONU-WP6-10-19, 2009.
- [114] P. Zucchelli, "A novel concept for a  $\bar{\nu}_e/\nu_e$  neutrino factory: the beta-beam," *Physics Letters B*, vol. 532, no. 3-4, pp. 166–172, 2002.
- [115] M. Benedikt, A. Bechtold, and F. Borgnolutti, "Conceptual design report for a Beta-Beam facility," *European Physical Journal*, vol. A47, p. 24, 2011.
- [116] M. Mezzetto, "Physics reach of the beta beam," *Journal of Physics G*, vol. 29, no. 8, pp. 1771–1776, 2003.
- [117] J. Burguet-Castell, D. Casper, J. J. Gómez-Cadenas, P. Hernández, and F. Sánchez, "Neutrino oscillation physics with a higher- $\gamma\beta$ -beam," *Nuclear Physics B*, vol. 695, no. 1-2, pp. 217–240, 2004.
- [118] J. Burguet-Castell, D. Casper, E. Couce, and J. J. Gómez-Cadenas, "Optimal  $\beta$ -beam at the CERN-SPS," *Nuclear Physics B*, vol. 725, no. 1-2, pp. 306–326, 2005.
- [119] A. Donini, E. Fernandez-Martinez, P. Migliozi et al., "A beta beam complex based on the machine upgrades for the LHC," *European Physical Journal C*, vol. 48, no. 3, pp. 787–796, 2006.
- [120] A. Donini and E. Fernández-Martínez, "Alternating ions in a  $\beta$ -beam to solve degeneracies," *Physics Letters B*, vol. 641, no. 6, pp. 432–439, 2006.
- [121] A. Donini, E. Fernandez-Martinez, P. Migliozi et al., "Neutrino hierarchy from CP-blind observables with high density magnetized detectors," *European Physical Journal C*, vol. 53, no. 4, pp. 599–606, 2008.
- [122] D. Meloni, O. Mena, C. Orme, S. Palomares-Ruiz, and S. Pascoli, "An intermediate  $\gamma$  beta-beam neutrino experiment with long baseline," *Journal of High Energy Physics*, vol. 2008, no. 7, Article ID 115, 2008.
- [123] E. Fernandez-Martinez, "The  $\gamma=100$   $\beta$ -Beam revisited," *Nuclear Physics B*, vol. 833, no. 1-2, pp. 96–107, 2010.
- [124] C. Orme, "High-Beta Beams within the LAGUNA design study," In press, <http://arxiv.org/abs/1004.0939>.
- [125] P. Coloma, A. Donini, P. Migliozi, L. Scotto Lavina, and F. Terranova, "A minimal Beta Beam with high-Q ions to address CP violation in the leptonic sector," *European Physical Journal*, vol. C71, p. 1674, 2011.
- [126] S. Geer, "Neutrino beams from muon storage rings: characteristics and physics potential," *Physical Review D*, vol. 57, no. 11, pp. 6989–6997, 1998.
- [127] A. De Rújula, M. B. Gavela, and P. Hernández, "Neutrino oscillation physics with a neutrino factory," *Nuclear Physics B*, vol. 547, no. 1-2, pp. 21–38, 1999.
- [128] A. Bandyopadhyay, S. Choubey, R. Gandhi et al., "Physics at a future neutrino factory and super-beam facility," *Reports on Progress in Physics*, vol. 72, no. 10, Article ID 106201, 2009.
- [129] R. J. Abrams, S. K. Agarwalla, A. Alekou et al., "International design study for the neutrino factory, Interim Design Report," In press, <http://arxiv.org/abs/1112.2853>.
- [130] P. Huber and T. Schwetz, "A low energy neutrino factory with non-magnetic detectors," *Physics Letters B*, vol. 669, no. 5, pp. 294–300, 2008.
- [131] P. Huber and W. Winter, "Neutrino factories and the "magic" baseline," *Physical Review D*, vol. 68, no. 3, Article ID 037301, 2003.
- [132] V. Barger, S. Geer, and K. Whisnant, "Long baseline neutrino physics with a muon storage ring neutrino source," *Physical Review D*, vol. 61, no. 5, Article ID 053004, 2000.
- [133] A. Donini, M. B. Gavela, P. Hernández, and S. Rigolin, "Neutrino mixing and CP-violation," *Nuclear Physics B*, vol. 574, no. 1-2, pp. 23–42, 2000.
- [134] V. Barger, S. Geer, R. Raja, and K. Whisnant, "Neutrino oscillations at an entry-level neutrino factory and beyond," *Physical Review D*, vol. 62, no. 7, Article ID 073002, pp. 1–12, 2000.
- [135] V. Barger, S. Geer, R. Raja, and K. Whisnant, "Long-baseline study of the leading neutrino oscillation at a neutrino factory," *Physical Review D*, vol. 62, no. 1, Article ID 013004, pp. 1–14, 2000.
- [136] M. Freund, P. Huber, and M. Lindner, "Systematic exploration of the neutrino factory parameter space including errors and correlations," *Nuclear Physics B*, vol. 615, no. 1–3, pp. 331–357, 2001.
- [137] C. Albright, G. Anderson, and V. Barger, "Physics at a neutrino factory," In press, <http://arxiv.org/abs/hep-ex/0008064>.
- [138] M. Apollonio, A. Blondel, and A. Broncano, "Oscillation physics with a neutrino factory," In press, <http://arxiv.org/abs/hep-ph/0210192>.
- [139] P. Huber and W. Winter, "From parameter space constraints to the precision determination of the leptonic Dirac CP phase," *Journal of High Energy Physics*, no. 5, pp. 399–432, 2005.
- [140] P. Huber, M. Lindner, M. Rolinec, and W. Winter, "Optimization of a neutrino factory oscillation experiment," *Physical Review D*, vol. 74, no. 7, Article ID 073003, 2006.
- [141] A. Donini, P. Huber, S. Pascoli, W. Winter, and O. Yasuda, "Physics and performance evaluation group," in *Proceedings of the 9th International Workshop on Neutrino Factories, Superbeams, and Betabeams (NuFact '07)*, pp. 43–45, August 2007.
- [142] S. Geer, O. Mena, and S. Pascoli, "Low energy neutrino factory for large  $\theta_{13}$ ," *Physical Review D*, vol. 75, no. 9, Article ID 093001, 2007.
- [143] A. Bross, M. Ellis, S. Geer, O. Mena, and S. Pascoli, "Neutrino factory for both large and small  $\theta_{13}$ ," *Physical Review D*, vol. 77, no. 9, Article ID 093012, 2008.
- [144] E. Fernández Martínez, T. Li, S. Pascoli, and O. Mena, "Improvement of the low energy neutrino factory," *Physical Review D*, vol. 81, no. 7, Article ID 073010, 2010.
- [145] A. Bueno, M. Campanelli, S. Navas-Concha, and A. Rubbia, "On the energy and baseline optimization to study effects related



to the  $\delta$ -phase (CP-/T-violation) in neutrino oscillations at a neutrino factory,” *Nuclear Physics B*, vol. 631, no. 1-2, pp. 239–284, 2002.

- [146] P. Huber and W. Winter, “Neutrino factory superbeam,” *Physics Letters B*, vol. 655, no. 5-6, pp. 251–256, 2007.
- [147] S. K. Agarwalla, P. Huber, J. Tang, and W. Winter, “Optimization of the neutrino factory, revisited,” *Journal of High Energy Physics*, vol. 2011, no. 1, Article ID 120, 2011.
- [148] P. Ballett and S. Pascoli, “Understanding the performance of the low-energy neutrino factory: the dependence on baseline distance and stored-muon energy,” *Physical Review D*, vol. 86, no. 5, Article ID 053002, 2012.
- [149] P. Coloma, P. Huber, J. Kopp, and W. Winter, “Systematic uncertainties in long-baseline neutrino oscillations for large  $\theta_{13}$ ,” In press, <http://arxiv.org/abs/1209.5973>.
- [150] D. Indumathi and N. Sinha, “Effect of tau neutrino contribution to muon signals at neutrino factories,” *Physical Review D*, vol. 80, no. 11, Article ID 113012, 2009.
- [151] A. Donini, J. J. Gómez Cadenas, and D. Meloni, “The  $\tau$ -contamination of the golden muon sample at the Neutrino Factory,” *Journal of High Energy Physics*, vol. 2011, no. 2, Article ID 095, 2011.
- [152] P. Huber, “On the determination of anti-neutrino spectra from nuclear reactors,” *Physical Review D*, vol. C84, no. 2, Article ID 024617, 16 pages, 2011.

## Review Article

# Future Long-Baseline Neutrino Facilities and Detectors

**Milind Diwan,<sup>1</sup> Rob Edgecock,<sup>2</sup> Takuya Hasegawa,<sup>3</sup> Thomas Patzak,<sup>4</sup>  
Masato Shiozawa,<sup>5</sup> and Jim Strait<sup>6</sup>**

<sup>1</sup> *Physics Department, Brookhaven National Laboratory, Upton, NY 11973, USA*

<sup>2</sup> *University of Huddersfield and STFC Rutherford Appleton Laboratory, Didcot OX11 0QX, UK*

<sup>3</sup> *High Energy Accelerator Research Organization (KEK), Tsukuba, Ibaraki 305-0801, Japan*

<sup>4</sup> *AstroParticule et Cosmologie (APC), Université Paris Diderot, CNRS/IN2P3, CEA/Irfu, Observatoire de Paris, Sorbonne Paris Cité, 10 rue Alice Domon et Léonie Duquet, 75205 Paris Cedex 13, France*

<sup>5</sup> *Kamioka Observatory, Institute for Cosmic Ray Research, University of Tokyo, Kamioka, Gifu 506-1205, Japan*

<sup>6</sup> *Fermi Accelerator National Laboratory, Batavia, IL 60510, USA*

Correspondence should be addressed to Thomas Patzak; [patzak@apc.univ-paris7.fr](mailto:patzak@apc.univ-paris7.fr)

Received 25 June 2012; Revised 12 October 2012; Accepted 24 October 2012

Academic Editor: Koichiro Nishikawa

Copyright © 2013 Milind Diwan et al. This is an open access article distributed under the Creative Commons Attribution License, which permits unrestricted use, distribution, and reproduction in any medium, provided the original work is properly cited.

We review the ongoing effort in the US, Japan, and Europe of the scientific community to study the location and the detector performance of the next-generation long-baseline neutrino facility. For many decades, research on the properties of neutrinos and the use of neutrinos to study the fundamental building blocks of matter has unveiled new, unexpected laws of nature. Results of neutrino experiments have triggered a tremendous amount of development in theory: theories beyond the standard model or at least extensions of it and development of the standard solar model and modeling of supernova explosions as well as the development of theories to explain the matter-antimatter asymmetry in the universe. Neutrino physics is one of the most dynamic and exciting fields of research in fundamental particle physics and astrophysics. The next-generation neutrino detector will address two aspects: fundamental properties of the neutrino like mass hierarchy, mixing angles, and the CP phase, and low-energy neutrino astronomy with solar, atmospheric, and supernova neutrinos. Such a new detector naturally allows for major improvements in the search for nucleon decay. A next-generation neutrino observatory needs a huge, megaton scale detector which in turn has to be installed in a new, international underground laboratory, capable of hosting such a huge detector.

## 1. International Context and Motivation

For many decades, research on the properties of neutrinos and the use of neutrinos to study the fundamental building blocks of matter has unveiled new, unexpected laws of nature. In the basic version of the standard model of particle physics, neutrinos enter as massless, neutral, spin one-half particles. Left-handed neutrinos form an electroweak isospin doublet with their charged, massive partners, electrons, muons, and taus. The right-handed neutrinos form an electroweak isospin singlet. Today, we have strong experimental evidence that neutrinos have a nonvanishing mass and that they change flavor while propagating in space. This phenomenon is called neutrino oscillations. These experimental observations imply an extension of the standard model and point to a more

general formalism. Up to now, no other experimentally proven indication for physics beyond the standard model has been found with accelerator-based experiments at LEP, the Tevatron, and LHC. The search for neutrino oscillations has been triggered by astrophysics experiments with neutrinos, namely, the observation of neutrinos from the Sun and, later on, neutrinos generated in the interaction of cosmic rays with the Earth's atmosphere: atmospheric neutrinos. At the same time solar neutrino spectroscopy allows a much better understanding and theoretical description of our star. The detection of a handful of neutrinos from a supernova in 1987 by the Kamiokande and IMB experiments gave a fundamental input and verification of supernova models. Over the last few decades, the results of neutrino experiments have triggered a tremendous amount of development in

theory: theories beyond the standard model or at least extensions of it, development of the standard solar model and modeling of supernova explosions as well as the development of theories to explain the matter-antimatter asymmetry in the universe.

Today, the common way of describing neutrino oscillations is the following.

The neutrinos  $\nu_e$ ,  $\nu_\mu$ , and  $\nu_\tau$  are weak eigenstates while the mass eigenstates  $\nu_i$  are related to the weak eigenstates  $\nu_l$  via a neutrino mixing matrix:

$$|\nu_l\rangle = \sum_i U_{li}^* |\nu_i\rangle. \quad (1)$$

The coefficients  $U_{il}$  form a matrix, called MNSP (Maki, Nakagawa, Sakata, Pontecorvo):

$$\begin{pmatrix} \nu_e \\ \nu_\mu \\ \nu_\tau \end{pmatrix} = \begin{pmatrix} U_{e1} & U_{e2} & U_{e3} \\ U_{\mu1} & U_{\mu2} & U_{\mu3} \\ U_{\tau1} & U_{\tau2} & U_{\tau3} \end{pmatrix} \begin{pmatrix} \nu_1 \\ \nu_2 \\ \nu_3 \end{pmatrix}. \quad (2)$$

The MNSP matrix can be parametrized in three *mixing angles*,  $\theta_{12}$ ,  $\theta_{23}$ ,  $\theta_{13}$ , and a complex phase  $\delta$ , called the CP phase:

$$\begin{pmatrix} 1 & 0 & 0 \\ 0 & c_{23} & s_{23} \\ 0 & -s_{23} & c_{23} \end{pmatrix} \begin{pmatrix} c_{13} & 0 & s_{13}e^{-i\delta} \\ 0 & 1 & 0 \\ -s_{13}e^{i\delta} & 0 & c_{13} \end{pmatrix} \begin{pmatrix} c_{12} & s_{12} & 0 \\ -s_{12} & c_{12} & 0 \\ 0 & 0 & 1 \end{pmatrix}, \quad (3)$$

where  $s_{ij}$  and  $c_{ij}$  are, respectively,  $\sin \theta_{ij}$  and  $\cos \theta_{ij}$ , with  $i, j = (1, 2, 3)$ . Using this parameterization, we can calculate the probability for a neutrino with fixed flavor  $\nu_\alpha$  to oscillate to a different weak eigenstate,  $\nu_\beta$  after a time  $t$ . This probability that a neutrino  $\nu_\alpha$  after a time  $t$  changes flavor to  $\beta$  is expressed as

$$P_{\nu_\alpha \rightarrow \nu_\beta}(t) = \left| \langle \nu_\beta | \nu_\alpha(t) \rangle \right|^2, \quad (4)$$

where

$$|\nu_l(t)\rangle = \sum_i U_{li}^* e^{-i(E_i t/\hbar)} |\nu_i\rangle, \quad (5)$$

and the  $U_{\alpha i}^*$  are the coefficient of the MNSP matrix. It follows

$$P_{\nu_\alpha \rightarrow \nu_\beta}(t) = \left| \left\langle \sum_i U_{\alpha i}^* e^{-i(E_i t/\hbar)} U_{\beta i} \right\rangle \right|^2. \quad (6)$$

Developing the above equation leads to the probability expressed as

$$P_{\nu_\alpha \rightarrow \nu_\beta}(t) = \delta_{\alpha\beta} - 4 \sum_{k>j} U_{\alpha i}^* U_{\beta i} U_{\alpha j} U_{\beta j}^* \sin^2 \left( \frac{(E_k - E_j)t}{2\hbar} \right). \quad (7)$$

We can write  $t$  as  $L/c$  and rewrite the energy differences as

$$(E_k - E_j) \frac{t}{\hbar} = (E_k - E_j) \frac{L}{c\hbar} \sim \frac{c^4 L}{2\hbar c \cdot pc} (m_i^2 - m_k^2). \quad (8)$$

Using the notation  $\Delta m_{ki}^2 = (m_k^2 - m_i^2)c^4$  and the approximation of relativistic neutrinos ( $E \gg mc^2$ ), the previous equation becomes

$$P_{\nu_\alpha \rightarrow \nu_\beta} = \delta_{\alpha\beta} - 4 \sum_{k>j} U_{\alpha i}^* U_{\beta i} U_{\alpha j} U_{\beta j}^* \sin^2 \left( \frac{\Delta m_{ki}^2 L}{4E} \right). \quad (9)$$

This expression of the probability is exact for neutrino oscillations in vacuum.

It is important to remark that neutrino oscillation experiments have no access to the absolute neutrino mass. On the other hand, they are a powerful instrument to have information on the mass square differences:

$$\Delta m_{ij}^2 = m_j^2 - m_i^2. \quad (10)$$

It is evident that only two mass square differences are independent from each other:

$$(m_2^2 - m_1^2) + (m_3^2 - m_2^2) + (m_1^2 - m_3^2) = 0, \quad (11)$$

so, the measure of the  $\Delta m_{12}^2$  and the  $\Delta m_{23}^2$  is enough to constrain the system.

According to the sign of  $\Delta m_{32}^2$ , there are two possible mass hierarchies:

- (i)  $\Delta m_{23}^2 > 0$ : normal hierarchy (NH). In this situation, we have  $m_3 > m_2 > m_1$ . This case seems to be the more natural, as the lightest neutrinos would turn to be the  $\nu_e$ , as the electron is lighter than the  $\mu$  and  $\tau$ ;
- (ii)  $\Delta m_{23}^2 < 0$ : inverted hierarchy (IH). In this situation,  $m_3$  would be the lightest neutrino.

In this paper, we will use the definition of the observables from above to describe the physics case of the proposed new long-baseline experiments.

The above-mentioned examples make neutrinos physics one of the most dynamic and exciting fields of research in fundamental particle physics and astrophysics. The next-generation neutrino detector will address two aspects: fundamental properties of the neutrino like mass hierarchy, mixing angles and the CP phase, and low-energy neutrino astronomy with solar, atmospheric, and supernova neutrinos. Such a new detector naturally allows for major improvements in the search for nucleon decay. A next-generation neutrino observatory needs a huge, megaton scale detector which in turn has to be installed in a new, international underground laboratory, capable of hosting such a huge detector.

In the US, the strategy for a future long-baseline experiment has been under development over the last decade. The scientific goals of a future US-based long-baseline neutrino project have been discussed and reviewed extensively by the US National Research Council and the Particle Physics Advisory Panels. The National Research Council reports in 2003 and 2011 have endorsed a project with a large capability underground detector located at a distance of  $>1000$  km from Fermilab.

In Europe, a roadmap has been established in 2008 and updated in 2011 by ASPERA (ASTroParticle ERANet).

In the 2011 update one can read “*The goals of a megaton scale detector as addressed by the design studies LAGUNA range from low energy neutrino astrophysics (e.g., supernova, solar, geo and atmospheric neutrinos) to fundamental searches without accelerators (e.g., search for proton decay) and accelerator driven physics (e.g., observation of CP violation). Due to its high cost, the program can be developed only in a global context.*” The recent confirmation of a nonzero mixing angle  $\theta_{13}$  permits a series of very exciting measurements for neutrino mass hierarchy and CP violation using CERN beams. In Europe, there are three ongoing FP7 design studies: LAGUNA, Large Apparatus studying Grand Unification and Neutrino Astrophysics (Grant Agreement no. 212343, FP7-INFRA-2007-1), EUROnu (Grant Agreement no. 212372), and LAGUNA-LBNO, Large Apparatus studying Grand Unification and Neutrino Astrophysics and Long Baseline Neutrino Oscillations (Grant Agreement no. 284518, FP7-INFRA-2011-2.1.1.).

In Japan, projects exploring the lepton sector CP symmetry both with a 100 kt detector based on a liquid Argon time projection chamber and a 560 kt water Cherenkov detector (Hyper-Kamiokande) are being planned [1, 2]. In both scenarios, a high-intensity neutrino beam would be provided by J-PARC.

As shown above, there is a worldwide consensus among physicists on the scientific priorities and the next-generation neutrino detector and infrastructure. One can also see the very strong competition between different countries to host such observatory for the next 30 to 50 years.

## 2. The US Long-Baseline Neutrino Program

The US accelerator neutrino program at Fermilab consists of a diverse set of experiments with intense neutrinos beams. The Fermilab Main Injector with the NuMI neutrino beamline operates at 350 kW with a tunable neutrino beam covering from 0.5 GeV to 10 GeV, and the neutrino beamline from the 8 GeV Booster accelerator (BNB) operates with a low-energy neutrino beam covering from 0.2 GeV to 1 GeV. The current and near future program is listed as follows: the MINOS experiment is a 5 kt magnetized steel/scintillator detector operating in the NuMI beamline at a baseline of 735 km. The main goals of MINOS consist in the measurement of muon neutrino disappearance and the parameters that govern atmospheric neutrino oscillations [3]. The NOvA experiment is a totally active segmented liquid scintillation detector located off-axis (14 mrad) at a distance of 810 km from the NuMI target. The physics goal of NOvA is the measurement of muon to electron neutrino conversion [4] and the parameters that govern the electron appearance mode. The MINERVA experiment which will perform precision measurements of neutrino cross-sections is also located in the NuMI beamline on-site at Fermilab in an underground cavern [5]. The MiniBooNe experiment (Mineral Oil Cherenkov detector) [6] is in the low-energy neutrino beamline that uses protons from the Fermilab 8 GeV booster. The MicroBooNe experiment (liquid argon TPC) [7] will also be located in the booster neutrino beamline. The MiniBooNe and MicroBooNe experiments are

exploring the short baseline neutrino oscillation anomalies [8].

The strategy for a future long-baseline experiment in the US has been under development over the last decade [9–12]. The scientific goals of a future US-based long-baseline neutrino project have been discussed and reviewed extensively by the US National Research Council and the Particle Physics Advisory Panels. The National Research Council reports in 2003 and 2011 [13, 14] have endorsed a project with a large capability underground detector located at a distance of >1000 km from Fermilab. Furthermore, the NUSAG report in 2007 [15] and the P5 report in 2008 [16] considered the scientific benefits of a long-baseline experiment with a baseline of ~1300 km with a capable detector, either a water Cherenkov or a liquid argon TPC located deep in the former Homestake mine in Lead, SD, USA. As a consequence of these reports which constitute a consensus in the US particle physics community, the US Department of Energy funded the development of the long-baseline neutrino experiment (LBNE) with a goal of having a next-generation large detector located at a distance of 1300–1500 km in an intense broadband accelerator neutrino beam. With the recent discovery of the value of  $\theta_{13}$  [17], the LBNE program is scientifically highly motivated.

The long-baseline neutrino experiment (LBNE) is the next major planned neutrino program in the US. The experiment as currently envisioned comprises a new 700 kW beamline at Fermilab, whose spectrum is optimized for this physics and which is upgradable to handle more than 2 MW of beam power from the future high-intensity proton accelerator (named the Project-X upgrade [18]); a near detector complex to fully characterize the unoscillated beam and a large far detector at the Homestake mine in South Dakota, at a baseline of 1,300 km, to make precision measurements of neutrino oscillation phenomena and enable a broad program of nonaccelerator-based physics. The detector envisioned at the Homestake site is either a Water Cherenkov detector with a total fiducial mass of 200 kt or a liquid argon time projection chamber with a fiducial mass of 34 kt. The beam designed will be a horn-focused broadband beam with an energy spectrum from 0.5 GeV to 5 GeV and a mean energy near 2.5 GeV. The technical design for LBNE has been extensively documented in a draft Conceptual Design Report [19]. In the following sections, we will briefly review some of the technical details of the LBNE design.

### 2.1. Technical Design for LBNE

**2.1.1. Beam Design for LBNE.** The LBNE beam design is a conventional, horn-focused neutrino beamline. The components of the beamline will be designed to extract a proton beam from the Fermilab Main Injector (MI) and transport it to a target area where the collisions generate a beam of charged particles that decay in a decay pipe. The facility is designed for initial operation at proton-beam power of 700 kW, with the capability to support an upgrade to 2.3 MW. In the reference design, extraction of the proton beam occurs at MI-10, a new installation on the Main Injector accelerator. After extraction, this primary beam establishes a horizontally



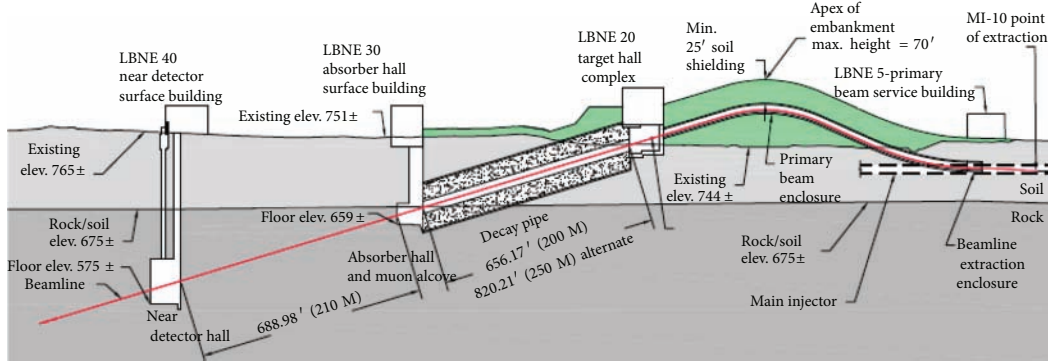


FIGURE 1: Schematic view of the LBNE beam design located at Fermilab.

straight heading west-northwest toward the far detector, but will be bent upward to an apex before being bent downward at the appropriate angle, 101 milliradians ( $5.79^\circ$ ) as shown in Figure 1. The primary beam will be above grade for about  $\sim 210$  meters; this design minimizes expensive underground construction and significantly enhances capability for groundwater radiological protection. The design requires, however, construction of an earthen embankment, or hill, whose dimensions are commensurate with the bending strength of the dipole magnets required for the beamline. The embankment will need to be approximately 335 m long and 20 m high above grade at its peak.

The target marks the transition from the intense, narrowly directed proton beam to the more diffuse, secondary beam of particles that in turn decay to produce the neutrino beam. After collection and focusing, the pions and kaons need a long, unobstructed volume in which to decay. This decay volume in the LBNE reference design is a pipe of circular cross-section with its diameter (4 meters) and length (200 meters) optimized such that decays of the pions and kaons result in neutrinos in the energy range useful for the experiment. The decay volume is followed immediately by the absorber, which removes the remaining beam hadrons.

The experience gained from the various neutrino projects at FNAL has been employed extensively in the LBNE beamline conceptual design. In particular, the NuMI beamline serves as the prototype design. Nevertheless, the LBNE beamline contains considerable innovation with regards to simplicity of construction and radiological protection.

The reference design for the primary beam and the neutrino beam is suitable for the initial beam power of  $\sim 700$  kW in all respects. Some aspects of the reference design are also appropriate for a beam power of  $\geq 2.3$  MW. These include the radiological shielding and the size of the underground enclosures as well as systems such as the beam absorber and the remote handling, which cannot be upgraded after exposure to a high-intensity beam. Some aspects of the reference design are planned for a beam power upgrade to 2.3 MW. The underground enclosures will have the appropriate steel and concrete shielding required for future beam upgrades.

**2.1.2. Event Rate.** The LBNE beamline is expected to initially use  $\sim 700$  kW of proton power from the Main injector at an energy of 120 GeV ( $4.9 \times 10^{13}$  protons per spill

every 1.33 sec). The spill length is approximately  $10 \mu\text{sec}$ . The beamline is designed to be able to run at a lower-energy proton beam of 60 GeV. Such flexibility can be used to reduce backgrounds from beam tails and change the beam spectrum for systematic studies in the future. A complete GEANT-based simulation of the beamline is used to evaluate the beam spectrum and expected numbers of events at a far detector at 1300 km. The expected muon neutrino charged current event rate superimposed on the  $\nu_\mu \rightarrow \nu_e$  oscillation probability is shown in Figure 2. The beam is designed to give maximum event rate across the 0.5 to 5 GeV energy region with the constraint that the maximum beam power from the FNAL injector is available at 120 GeV. It should be noted that for the appearance mode the maximum of the probability shifts from below 2 GeV (normal hierarchy for neutrinos) to above 3 GeV (normal hierarchy for antineutrinos); furthermore, the broadband beam allows separation of the degeneracies evident in the Figure, for example,  $\delta_{CP} = \pi/2, 0$  at  $\sim 1.8$  GeV and  $\delta_{CP} = -\pi/2, 0$  at  $\sim 4$  GeV. With this beam design, the total charged current muon neutrino event rate per year in a 34 kt liquid argon (200 kt water Cherenkov) detector will be 6000 events (35000 events) without oscillations with approximately 0.7% contamination of electron neutrinos and 4% contamination of muon antineutrinos. The total charged current muon antineutrino event rate per year in a 34 kt liquid argon (200 kt water Cherenkov) detector will be 2200 events (13000 events) without oscillations with approximately 1% contamination of electron neutrinos and antineutrinos and 30% contamination of muon neutrinos. For the above calculation, the Fermilab Main Injector is assumed to run  $2 \times 10^7$  sec per year.

**2.1.3. Water Cherenkov Detector Design for LBNE.** The LBNE water Cherenkov detector design consists of a very large excavated cavity in a very strong and stable rock formation at the 4850 ft level in the Homestake facility. The cylindrical cavity will be lined with a smooth liner and filled with extremely pure water. The reference design calls for a total water mass of 266 kt and a fiducial mass of 200 kt. PMTs will surround the fiducial volume on the top, bottom, and around the perimeter. The wall PMTs will be suspended by cables about half a meter from the inner surface of the liner. The top and floor PMTs will be mounted to the structural framework.

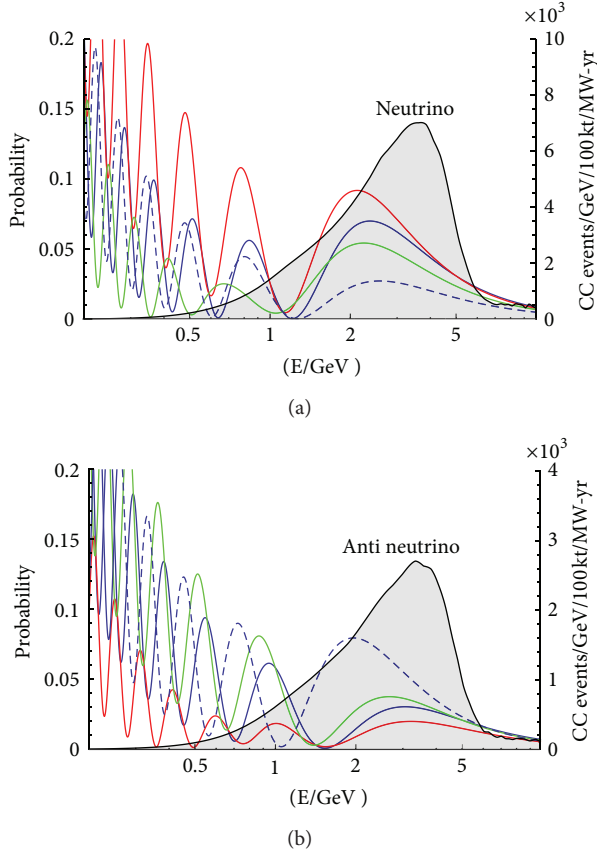


FIGURE 2: The muon charged current event rate in a 100 kt detector at 1300 km for neutrino (a) and antineutrino (b) running for the LBNE beam design with beam power of 700 kW and  $2 \times 10^7$  sec (1 year of running) of running time. The event rate as a function of energy is superimposed on the expected  $\nu_\mu \rightarrow \nu_e$  oscillation probability for  $\theta_{13} = 9^\circ$ . The various curves correspond to blue ( $\delta_{CP} = 0$ ), blue-dashed ( $\delta_{CP} = 0$  and inverted hierarchy), red ( $\delta_{CP} = \pi/2$ ), and green ( $\delta_{CP} = -\pi/2$ ).

Each PMT will be connected via cable to readout electronics on the balcony above the water detector. The baseline design includes a top veto region, which will consist of an array of horizontally oriented PMTs optically separated from the rest of the detector. The veto will be used to tag cosmic ray muons that enter the detector from above that form a background for astrophysical neutrino measurements.

Provisions will be made to fill the detector with purified water and to recycle this water through the purification system and cool it. There will be provision to periodically calibrate the detector and monitor its status and performance. Finally, there will be provisions to prevent radon contamination of the detector water.

The optimum shape of the detector from excavation considerations at the Homestake site in the Yates rock formation (an amphibolite formation with some rhyolite intrusions) is a vertical circular cylinder. There are two limitations on the maximum diameter: the light attenuation length in water ( $\sim 90$  meters) and the maximum rock excavation diameter that does not require extraordinary rock support. The studies

of both the Large Cavity Advisory Board (composed of world experts in underground construction) and Golder Associates concluded that an excavated cylindrical cavity with a diameter of 65 meters was completely feasible and cost efficient.

The major detector components are (1) the water containment system, (2) the photomultiplier mounting, housing and cable system, (3) the electronics readout and trigger system, (4) calibration procedures, (5) the water purification and cooling system, and (6) event reconstruction and data analysis. Table 1 summarizes the important detector parameters. Figure 3 shows a schematic 3-dimensional view of the detector design as located at the 4850 ft level of the Homestake facility.

**2.1.4. Liquid Argon Detector Design for LBNE.** The LBNE LArTPC consists of two massive cryostats in a single cavern, oriented end-to-end along the beam direction (roughly east to west), and located at the 4850 level (4850 L) of the Homestake underground facility. The fiducial mass of each, as defined for neutrino oscillation studies, is 17 kt and the active (instrumented) mass is 20 kt, resulting in a total active mass of 40 kt. Figure 4 shows the proposed layout of the far site, and Figure 5 shows the detector configuration.

In an LArTPC, a uniform electric field is created within the TPC volume between cathode planes and anode wire planes. Charged particles passing through the TPC release ionization electrons that drift to the anode wire planes. The bias voltage is set on the anode plane wires so that ionization electrons drift between the first several (induction) planes and are collected on the last (collection) plane. Readout electronics amplify and continuously digitize the induced waveforms on the sensing wires at several MHz and transmit these data to the data acquisition (DAQ) system for processing. The wire planes are oriented at different angles allowing a 3D reconstruction of the particle trajectories. In addition to these basic components, a photon-detection system provides a trigger for proton decay and galactic supernova neutrino interactions.

The principal parameters of the LBNE liquid argon far detector are given in Table 2.

The LBNE liquid argon detector design is an extension of the successful ICARUS design; nevertheless, it has several innovative elements: the cryostat construction uses commercial stainless steel membrane technology engineered and produced by industry. These vessels are widely deployed in liquefied natural gas (LNG) tanker ships and tanks and are typically manufactured in sizes much larger than that of the LAr-FD. This is an inherently clean technology with passive insulation. The time projection chamber (TPC) is the active detection element of the LAr-FD. The TPC is located inside the cryostat vessel and is completely submerged in LAr at 89 K. Its active volume is 14 m high, 22.4 m wide, and 45.6 m long in the beam direction. It has four rows of cathode plane assemblies (CPAs) planes interleaved with three rows of anode plane assemblies (APAs) planes that are oriented vertically, parallel to the beamline, with the electric field applied perpendicular to the planes. The maximum electron-drift distance between a cathode and an adjacent

TABLE 1: A summary of the important water Cherenkov detector design parameters.

Detector design parameter	Value
Fiducial volume	200 kt (200,000 m <sup>3</sup> )
Location	Homestake 4850 ft level
Shape	Right circular cylinder
Cylinder excavation dimensions	65.6 m diameter $\times$ 81.3 m height
Dome height	16 m
Vessel liner dimensions	65 m diameter $\times$ 80.3 m height
Water volume dimensions	65 m diameter $\times$ 79.5 m height
Total water volume	263,800 m <sup>3</sup>
Distance from Neat line to PMT equator	0.85 m
Dimensions of instrumented volume	63.3 m diameter $\times$ 76.6 m height
Instrumented volume	241,000 m <sup>3</sup>
Fiducial volume cut	2 m
Fiducial volume dimensions	59.3 m diameter $\times$ 72.6 m height
Number of PMTs	29,000
PMT diameter	12 in (304 mm)
Peak QE of PMTs (at 420 nm)	30%
PMT spectral response	300–650 nm
PMT transit time spread	2.7 ns
Light gain from light collectors	41%
Max water pressure on PMTs	7.9 bar
Number/type veto PMTs	200 $\times$ 12 in
Water fill rate	250 gal/min (0.95 m <sup>3</sup> /min)
Detector fill time	195 days
Water circulation rate	1200 gal/min (4.5 m <sup>3</sup> /min)
Water volume exchange time	~40 days
Water temperature	13°C
Electronics burst capability	>1 M events in 10 s
Electronics time resolution	<1 ns
Electronics dynamic range	1–1000 PE
Timing calibration	<1 ns
PMT pulse height calibration	<10%
Radon content	<1 mBq/m <sup>3</sup>

anode is 3.7 m. Both the cathode and anode plane assemblies are 2.5 m wide and 7 m high. Two 7 m modules (either APA or CPA) stack vertically to instrument the 14 m active depth. In each row, 18 such stacks are placed edge-to-edge along the beam direction, forming the 45.6 m active length of the detector. Each cryostat houses a total of 108 APAs and 144 CPAs. A “field cage” surrounds the top and ends of the detector to ensure uniformity of the electric field. The field cage is assembled from panels of FR-4 sheets with parallel copper strips connected to resistive divider networks.

Each APA has three wire planes that are connected to readout electronics: two induction planes and one collection plane (X). A fourth wire plane, grid plane (G), is held at a bias voltage but is not instrumented with readout electronics. The grid plane improves the signal-to-noise ratio on the U plane and provides electrostatic discharge protection for the readout electronics. A key innovative feature of the LBNE LAr detector is the use of cold electronics. Requirements for low noise and for extreme purity of the LAr motivate locating

the front-end electronics in the LAr (hence “cold electronics”) close to the anode wires, which reduces the signal capacitance (thereby minimizing noise). The use of CMOS electronics in this application is particularly attractive since the series noise of this process has a noise minimum at 89 K. The large number of readout channels required to instrument the LAr-FD TPCs motivates the use of CMOS ASICs. Signal zero-suppression and multiplexing will be implemented in the ASIC, minimizing the number of cables and feedthroughs in the ullage gas, and therefore reducing contamination from cable outgassing.

Both detector designs for LBNE, the water Cherenkov and liquid argon, were reviewed extensively for cost, schedule, and scientific performance. The fiducial masses of both detectors were chosen to achieve similar performance for neutrino oscillation physics, in particular the sensitivity to CP violation. The reviews concluded that both detectors could achieve the performance goals for neutrino physics; nevertheless, there were some advantages to the liquid argon

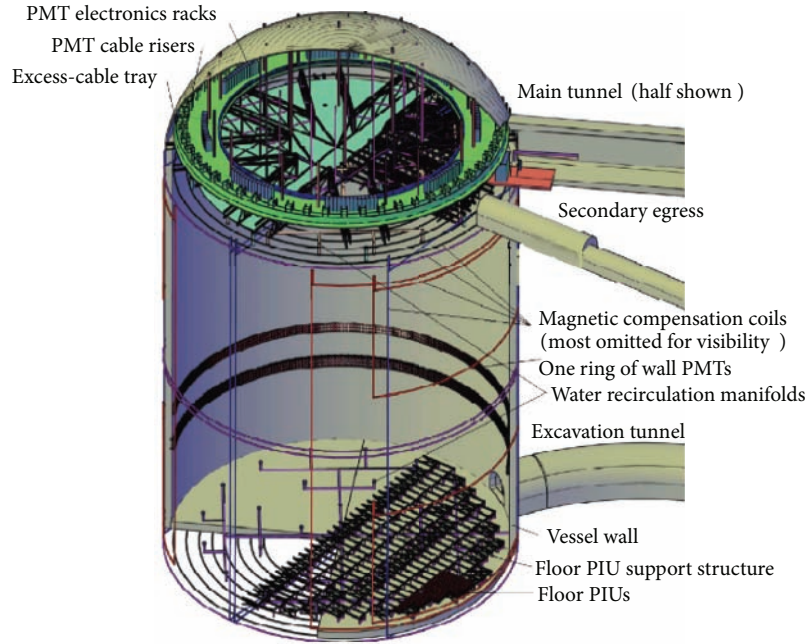


FIGURE 3: Schematic design of a 200 kt water Cherenkov detector in the Homestake underground facility.

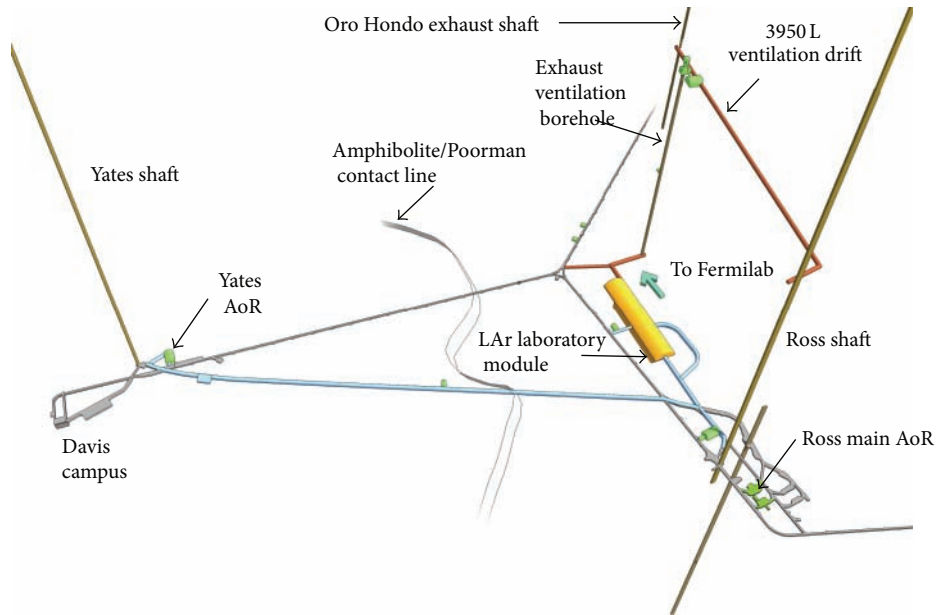


FIGURE 4: Location of LAr-FD at the 4850 L. Primary access to the upper level of the LAr-FD cavern is through a horizontal tunnel that connects to the Ross shaft. A second horizontal tunnel near the midpoint of the cavern provides secondary egress to the existing 4850 L tunnels. A decline tunnel to the lower level is used to remove waste rock during construction and serves as a secondary egress from the cryostat septum area during operations. Cavern supply air enters the cavern from the Ross shaft and exits through a new ventilation shaft that connects to the Oro Hondo.

detector due to its fine granularity. Liquid argon is also a complementary technology in terms of searching for proton decay and its sensitivity to low-energy electron neutrinos (instead of electron antineutrinos) from supernova. Furthermore, it was clearly cost-prohibitive to design and build both types of detectors; therefore, through an extensive process of

selection, the liquid argon option was selected as the reference design for LBNE.

In addition to the far detector, the LBNE design also includes near detectors to monitor the neutrino beam before it leaves the Fermilab site. The set of detector systems for the near detectors reference design consists of a



TABLE 2: LAr-FD principal parameters.

Parameter	Value
Active (fiducial) mass	40 (33) kt
Location	Homestake 4850 ft level
Number of detector modules (cryostats)	2
Shape	Rectangular
Drift cell configuration within module	3 wide $\times$ 2 high $\times$ 18 long drift cells
Drift cell dimensions	2 $\times$ 3.7 m wide (drift) $\times$ 7 m high $\times$ 2.5 m long
Detector module dimensions	22.4 m wide $\times$ 14 m high $\times$ 45.6 m long
Anode wire spacing	$\sim$ 5 mm
Wire planes (orientation from vertical)	Grid ( $0^\circ$ ), Induction 1 ( $45^\circ$ ), Induction 2 ( $-45^\circ$ ), and Collection ( $0^\circ$ )
Scintillation light detection	Yes
Photon yield	$>1$ pe /10 MeV
Drift electric field	500 V/cm
Maximum drift time	2.3 ms
Signal/noise for 1 MIP	$\sim$ 9

beamline-measurements system (BLM) and a neutrino-detection system (ND for “neutrino detectors”). The near detectors will be located at the near site (Fermilab), downstream of the beamline. The BLM will be located in the region of the Absorber Complex at the downstream end of the decay region to measure the muon fluxes from hadron decay. The neutrino detector will be placed in the near detector hall, 450 m downstream of the target, and underground. The reference-design neutrino measurements system technology is a liquid-argon-filled time projection chamber tracker (LArTPCT), matching the interaction material in the LAr-FD (described in Volume 4 of this CDR). The LArTPCT will consist of a  $1.8\text{ m} \times 6\text{ m} \times 1.8\text{ m} \times 4\text{ m}$  TPC and a  $2.7\text{ m}$  diameter  $\times$   $5\text{ m}$  long LAr cryostat inside of a large dipole magnet. This system is intended to measure the various neutrino fluxes and spectra and to measure the neutrino interaction channels important for predicting the signals and backgrounds at the far site.

**2.2. Scientific Sensitivity.** The LBNE project has a broad range of scientific objectives, listed below.

- (1) Measurements of the parameters that govern  $\nu_\mu \rightarrow \nu_e$  oscillations as discussed above. These include measurement of the CP violating phase  $\delta_{\text{CP}}$  and determination of the mass ordering (the sign of  $\Delta m_{32}^2$ ).
- (2) Precision measurements of  $\theta_{23}$  and  $-\Delta m_{32}^2$  in the  $\nu_\mu$ -disappearance channel.
- (3) Search for proton decay, yielding measurement of the partial lifetime of the proton ( $\tau/\text{BR}$ ) in one or more important candidate decay modes, for example,  $p \rightarrow e^+\pi^0$  or  $p \rightarrow K^+\nu$ , or significant improvement in limits on it.
- (4) Detection and measurement of the neutrino flux from a core-collapse supernova within our galaxy or a nearby galaxy, should one occur during the lifetime of the detector.
- (5) Other accelerator-based neutrino oscillation measurements.
- (6) Measurements of neutrino oscillation phenomena using atmospheric neutrinos.
- (7) Measurement of other astrophysical phenomena using medium-energy neutrinos.

The detector design was driven largely by objectives (1)–(4).

Observation of  $\nu_\mu \rightarrow \nu_e$  oscillations will allow us to determine the neutrino mass hierarchy and measure leptonic CP violation through the measurement of  $\delta_{\text{CP}}$ . In five years of neutrino (antineutrino) running, assuming  $\sin^2(2\theta_{13}) \sim 0.1$ ,  $\delta_{\text{CP}} = 0$ , and normal mass hierarchy, we expect 1160 (330) selected  $\nu_e$  or  $\bar{\nu}_e$  signal events with 300 (180) background events in a 34 kt liquid argon TPC detector with a 700 kW beam.

Figure 6 shows the fraction of possible  $\delta_{\text{CP}}$  values covered at the  $3\sigma$  level for determining  $\sin^2(2\theta_{13}) \neq 0$ , the mass hierarchy, and CP violation as a function of  $\sin^2(2\theta_{13})$  for a 34 kt detector in a 700 kW beam running for five years in neutrino mode and five years in antineutrino mode. At a value of  $\sin^2(2\theta_{13}) = 0.1$  (the measured value from Daya Bay), the mass hierarchy can be resolved at  $>3\sigma$  for 100% of  $\delta_{\text{CP}}$ . For CP violation, a  $3\sigma$  determination can be made for  $\sim 65\%$  of  $\delta_{\text{CP}}$  values.

In addition, a liquid argon detector of this size can achieve  $<1\%$  precision on measurements of  $\Delta m_{32}^2$  and  $\sin^2(2\theta_{23})$  through muon neutrino and antineutrino disappearance. There is also the potential to resolve the  $\theta_{23}$  octant degeneracy and improve model-independent bounds on nonstandard interactions.

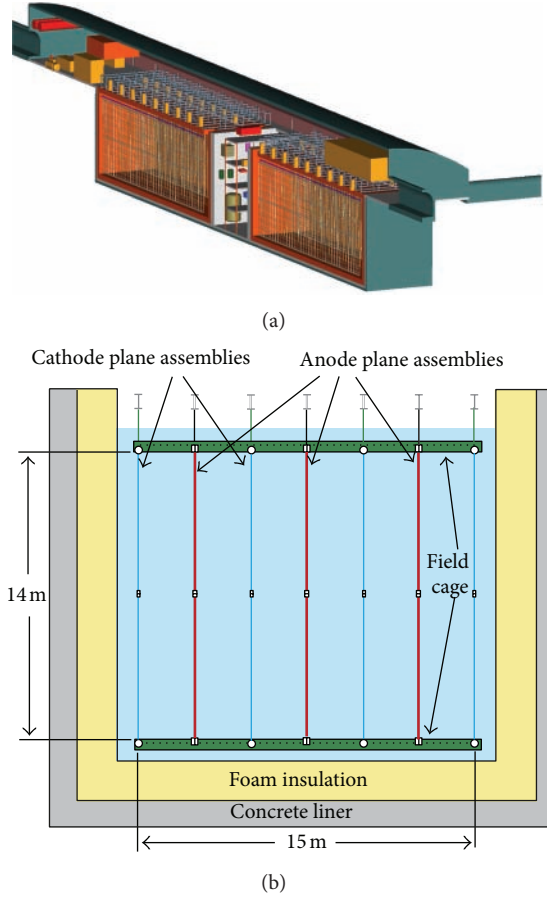


FIGURE 5: Detector configuration within the cavern. The TPC is located within a membrane cryostat, shown in orange. The interior dimensions of each cryostat are 24 m wide  $\times$  18 m high  $\times$  51 m long. The highbay is 150 m long and has a 32 m span. Cryogenic equipment is located in the septum area between the two cryostats. The right-hand side shows a cut view of the cryostat. The anode and cathode wire planes are hung from the ceiling of the cryostat. Each anode plane consists of  $u/v$  readout wires wrapped around a stainless steel frame and readout by electronics mounted on the planes.

The scientific capability for detection of nucleon decay and supernova using a large liquid argon TPC has been discussed elsewhere in this paper. We will not cover it in detail here. The 34 kt liquid argon TPC can achieve sensitivity to proton lifetimes of  $\sim 5 \times 10^{34}$  years after 10 yrs of running at 90% CL. If the detector energy threshold of  $\sim 10$  MeV can be achieved, then a galactic supernova burst at 10 kpc will produce over 3000 events. The threshold of the LArTPC depends on the data rate due to either the electronic noise or the background due to radioactivity in the detector either because of activity from the materials or because of spallation products due to cosmic ray muons. In case of a burst of supernova neutrino events, the photon system can be used to identify the burst rapidly, but each individual event is measured by the TPC. The LBNE cold electronics design keeps the electronic noise level at a low level so that a 10 MeV threshold can be easily achieved; however, the minimum depth requirement for spallation backgrounds is still under

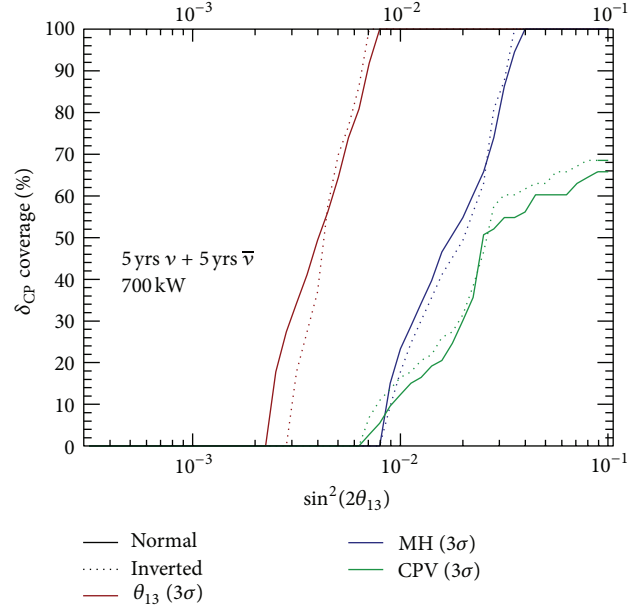


FIGURE 6:  $3\sigma$  discovery potential for determining  $\sin^2(2\theta_{13}) \neq 0$  (red), the mass hierarchy (blue), and CP violation (green) as a function of  $\sin^2(2\theta_{13})$  and the fraction of  $\delta_{CP}$  coverage. The sensitivities are shown for both normal (solid) and inverted (dashed) mass hierarchies for a 34 kt LAr detector given five years running in  $\nu$  mode + five years in  $\bar{\nu}$  mode in a 700 kW beam.

investigation. The liquid argon detector will also have unique and high-precision capability with respect to atmospheric neutrinos. The key detector requirement for nonaccelerator physics is the depth of the detector. The design depth of 4850 ft for the LBNE far detector has been evaluated to be sufficient for nonaccelerator physics [20].

**2.3. Phases or Alternatives for LBNE.** The cost of the LBNE project includes the design and constructions of the beam-line, the far and near detectors, and the surface and underground civil constructions needed for the beamline and to house the detectors and shield them from cosmic rays. A preliminary cost and schedule estimate for the entire project was assembled and reviewed in March 2012. The costs include the engineering and scientific manpower that is needed for the design and construction activities. It also includes appropriate contingencies and overheads. The total cost for the project as described above is approximately US \$1.5 B in FY2010 currency. The schedule for the project partly depends on the availability of funds; however a preliminary technical evaluation of the schedule suggests an experiment start in year  $\sim 2022$ .

The cost of the complete LBNE project is considered too high for the current budgetary climate in the US, and, therefore, the US, Department of Energy has asked for an approach to reach the scientific goals of LBNE in a phased manner. Furthermore, strategies and consultation are sought to enhance international participation in the project. In response to this request, various phasing strategies as well as alternatives have been examined. To address all of the

fundamental science goals listed above, a reconfigured LBNE would need a very long baseline ( $>1,000$  km from accelerator to detector) and a large detector deep underground. However, it is not possible to meet all of these requirements in a first phase of the experiment within the budget guideline of about half of the projected cost of the full project.

Therefore, options are being assessed that meet some of the requirements, and three viable options have been identified for a Phase I long-baseline experiment that have the potential to accomplish important science at realizable cost. There are listed below.

- (i) Using the existing NuMI beamline in the low-energy configuration with a 30 kt liquid argon time projection chamber (LAR-TPC) surface detector 14 mrad off-axis at Ash River in Minnesota, 810 km from Fermilab.
- (ii) Using the existing NuMI beamline in the low-energy configuration with a 15 kt LAR-TPC underground (at the 2340 ft level) detector on-axis at the Soudan mine in Minnesota near the MINOS detector, 735 km from Fermilab.
- (iii) Constructing a new low-energy LBNE beamline with a 10 kt LAR-TPC surface detector on-axis at Homestake in South Dakota, 1,300 km from Fermilab.

The scientific capabilities of the above options have been discussed in [21]. While each of these first-phase options is stronger than the others in some particular domain, the option to build a new beamline to Homestake with an initial 10 kt LAR-TPC detector on or near the surface is strongly favored. The neutrino beam physics reach of this first phase is comprehensive with good sensitivity to all important parameters.

This option is seen as a start of a long-term program that would achieve the full goals of LBNE in time and allow probing the standard model most incisively beyond its current state. Ultimately this option would exploit the full power provided by Project-X. At the present level of cost estimation, it appears that this preferred option may be 10% more expensive than the other two options, but cost evaluations are continuing. The major limitation of the preferred option is that the underground physics program including proton decay and supernova collapse cannot start until later phases of the project. Placing a 10 kt detector underground instead of the surface in the first phase would allow such a start and increase the cost by about \$135 M. Negotiations to obtain such funding from US domestic funding sources or international participants are in progress.

**2.4. High-Intensity Accelerator Upgrades in the US.** Project-X is a multimewatt proton facility being developed to support intensity frontier research in elementary particle physics, with possible applications to nuclear physics and nuclear energy research, at Fermilab. The centerpiece of this program is a superconducting  $H^-$  linac that will support programs in long-baseline neutrino experiments and the study of rare kaon and muon processes. Based on technology

shared with the International Linear Collider (ILC), Project-X will provide multi-MW beams at 60–120 GeV from the Main Injector, simultaneous with very-high-intensity beams at lower energies. Details of Project-X design can be obtained from [18].

In Table 3, we have made a list of beam conditions that could be possible from Project-X and further Project-X upgrade at 8 GeV. Figure 7 shows the beam power available from the Main Injector as a function of energy. With Project-X the beam power from the Main Injector can be maintained at or above 2 MW over the range 60–120 GeV. This is because the decrease in energy can be (mostly) compensated by increasing the repetition rate. This trend continues as the energy decreases, but at some point it is limited by the number of protons coming from the linac. The power achievable at 30 GeV would be  $\sim 1.3$  MW for the Project-X reference design. The Main Injector requires 270 kW of incident 8 GeV beam power at 8 GeV to produce  $\sim 2$  MW at 60 GeV. With additional upgrades to the 8 GeV pulsed linac, the 8 GeV power level could be increased to  $\sim 4$  MW. In such a scenario, the Fermilab accelerator complex could produce multi-MW power at both 60 GeV and 8 GeV simultaneously. The duty factor for any Main Injector operation would continue to remain small in the single turn extraction mode; however, the duty factor at 8 GeV will be  $\sim 5$ –10% unless a ring is deployed to compress the beam further. The large-intensity increase from these accelerator upgrades at FNAL would greatly improve the precision of long-baseline neutrino science. The event spectra and experimental approaches using possible beams from high-intensity protons are in [22]. The precision on the parameters  $\sin^2 2\theta_{13}$  and  $\delta_{CP}$  is shown in Figure 8 using the full simulation of the LBNE beam and the expected performance of a 34 kt liquid argon TPC detector [23]. The calculation of the sensitivity was performed using the GLOBES software tool which allows careful consideration of all parameter correlations and ambiguities. The long baseline and broadband beam for LBNE allows for determination of the parameters with no remaining ambiguities.

### 3. The Japanese Approach

Based on the indication of  $\nu_\mu \rightarrow \nu_e$  conversion phenomenon demonstrated by T2K [25] and subsequent confirmation by reactor experiments [26–28], a next-generation experiment aimed at the discovery of CP violation in the lepton sector would be recommended with high priority.

In Japan, two different approaches are considered for the study of lepton CP symmetry using the neutrino beam at J-PARC. One configuration is suitable for water Cherenkov technology, and the other is suitable for liquid argon TPC technology. Since water Cherenkov technology has an excellent performance for a sub-GeV low multiplicity final state environment, a relatively short baseline of 295 km with a low-energy narrowband neutrino beam is adopted to compare the difference between  $\nu_e$  and  $\bar{\nu}_e$  charged current events from appearance results at the first neutrino oscillation maximum. In the case of a Liquid argon TPC, since this technology has an excellent energy resolution for neutrino

TABLE 3: Beam conditions and power possible during the Project-X phase and further upgrades to the 8 GeV performance. An accumulator ring at 8 GeV could be used to improve the duty factor.

Accelerator stage	Energy	Current	Duty factor	Power available
Continuous wave linac	3 GeV	1 mA	Continuous wave	3000 kW
Pulsed linac	8 GeV	43 $\mu$ A	4.33 ms/0.1 sec	350 kW
8 GeV upgrade	8 GeV	500 $\mu$ A	6.67 ms/0.066 sec	4000 kW
Main injector	60 GeV	35 $\mu$ A	9.5 $\mu$ S/0.7 sec	2100 kW
Main injector	120 GeV	19 $\mu$ A	9.5 $\mu$ S/1.3 sec	2300 kW

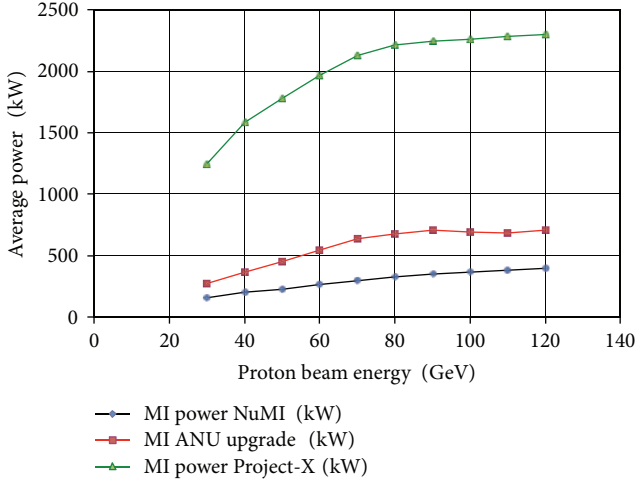


FIGURE 7: Proton beam power as a function of proton energy from the Fermilab Main Injector. Shown are current capabilities labeled as NuMI. The recently funded upgrades (labeled as ANU) will increase the power to 550 kW at 60 GeV or 700 kW at 120 GeV. Project-X as currently conceived will allow beam power of 2 MW at 60 GeV and 2.3 MW at 120 GeV.

energy measurement and an event reconstruction capability for a wide energy range, a relatively long baseline of 658 km with a wideband neutrino beam is adopted to precisely measure the  $\nu_e$  and  $\bar{\nu}_e$  appearance energy spectrum shape (peak position and height for 1st and 2nd neutrino oscillation maximum and minimum). Given the assumed location of each detector, namely, a 560 kt water Cherenkov detector (hyper-Kamiokande) at Kamioka, and a 100 kt liquid Argon TPC at Okinoshima, the required beam conditions for both approaches are satisfactorily provided by the single J-PARC neutrino beam simultaneously.

In this section we describe the Japanese approach, including the accelerator-based neutrino source in Japan, the Okinoshima Giant Liquid Argon Observatory, and the Hyper-Kamiokande project.

### 3.1. Accelerator-Based Neutrino Source in Japan

**3.1.1. J-PARC and the Main Ring Synchrotron.** J-PARC (Japan Proton Accelerator Research Complex) is a KEK-JAEA joint facility of a MW-class high-intensity proton accelerator research facility (Figure 9) [29]. It provides an unprecedented high flux of various secondary particles, such as neutrons,

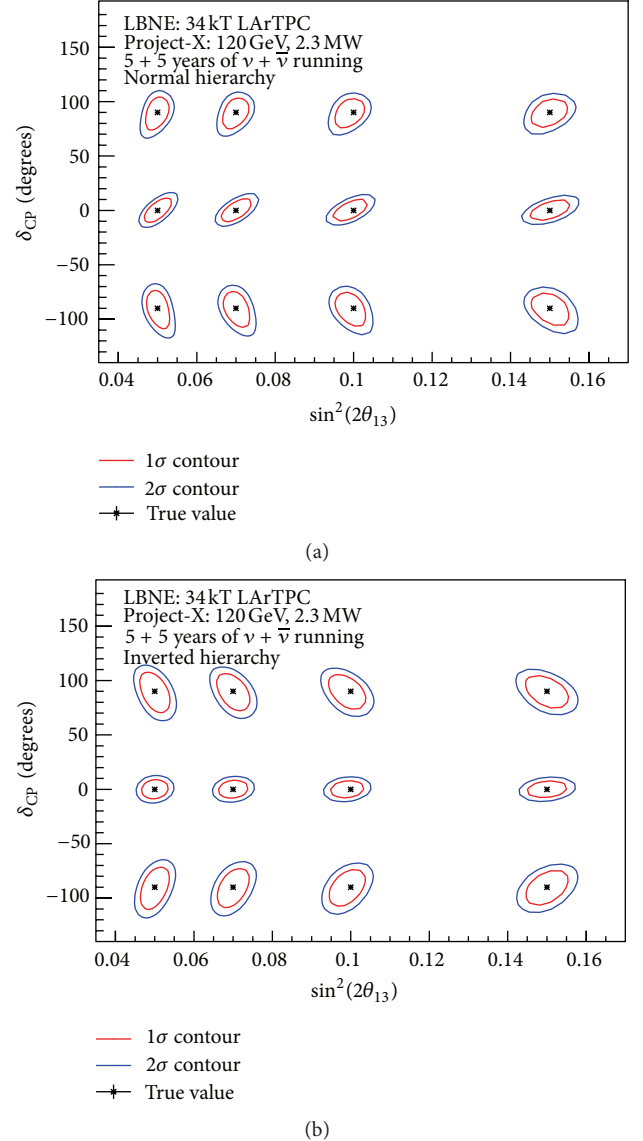


FIGURE 8: Precision on parameters  $\sin^2 2\theta_{13}$  and  $\delta_{CP}$  from the LBNE configuration using high-intensity beam from Project-X. The precision is shown as for various true parameters across the  $\delta_{CP}$  and  $\sin^2 2\theta_{13}$  space. This calculation was performed with the GLOBES sensitivity calculation tool [24] which marginalizes over all oscillation parameters, except for the ones being fit, including the mass hierarchy using known errors. The long-baseline LBNE setup allows separation of matter and CP effects with no remaining ambiguities because of the length of the baseline and the broadband beam.



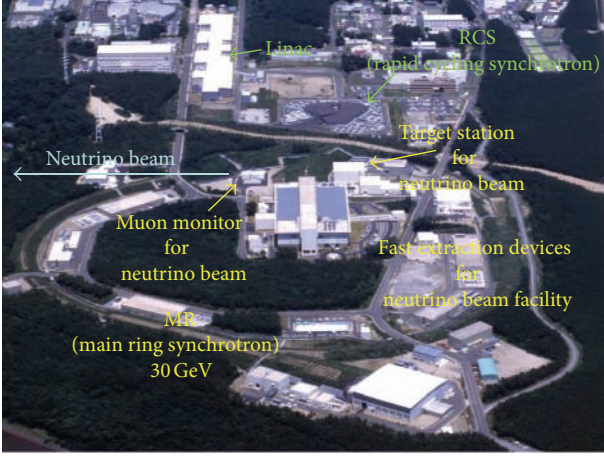


FIGURE 9: J-PARC accelerator and experimental facility.

muons, pions, kaons, and neutrinos, which are utilized for elementary particle physics and material and life science.

In the accelerator complex,  $H^-$  ions are accelerated to 181 MeV with a linac, fed into the rapid cycling synchrotron (RCS) with electrons stripped, and then accelerated to 3 GeV. At the final stage, the proton beam goes into main ring synchrotron and is accelerated to 30 GeV. For the neutrino experiment, accelerated protons are kicked inward to the neutrino beam facility in a single turn with fast extraction devices.

**3.1.2. The J-PARC Neutrino Beam Facility.** The proton beam from the main ring synchrotron (MR) travels the J-PARC neutrino beam facility and produces an intense beam of muon neutrinos pointing west. The J-PARC neutrino beam facility is composed of the following components (Figure 10) [29].

- (i) Preparation section: matches the beam optics to the arc section.
- (ii) Arc section: bends the beam  $\sim 90^\circ$  toward the west direction with a superconducting combined function magnet.
- (iii) Final focus section: matches the beam optics to the target both in position and in profile. The level of control at the mm level is necessary which corresponds to 1 mrad  $\nu$  direction difference. It is also important in order not to destroy the target.
- (iv) Graphite target and horn magnet: produce intense secondary  $\pi$ 's and focus them toward the west. There are 3 horns with 250 kA pulse operation.
- (v) Muon monitor: monitors the  $\mu$  direction (=  $\nu$  direction) pulse to pulse by measuring the centre of the muon profile.
- (vi) On-axis neutrino monitor: monitors the  $\nu$  direction and intensity.

This facility is designed to be tolerate around  $\sim 1$  MW beam power. This limitation is due to the temperature rise

and thermal shock for the components such as the Al horn, graphite target, and Ti vacuum window. Since this region is a high-radiation environment, a careful treatment of the radioactive water and air is required. Moreover, a maintenance scenario of radioactive components has to be carefully planned.

**3.1.3. J-PARC Neutrino Beam Intensity Upgrade Plan.** Till June 2012 the J-PARC neutrino beam delivered up to 0.19 MW to T2K (Tokai-to-Kamioka long-baseline neutrino experiment) [29]. With the goal of the improvement of the neutrino beam intensity, an MR power improvement scenario has been analyzed. The proposal by the J-PARC accelerator team is shown in Table 4.

The items to be modified are listed as follows.

- (i) For the linac, a 400 MeV operation is required to avoid severe space charge effects at RCS injection. The installation of necessary equipment is foreseen from the summer of 2013.
- (ii) The repetition cycle of the MR has to be improved from 2.56 seconds to 1.28 seconds. For this purpose, the RF and the magnet power supply improvements are necessary. The necessary R&D for these components has been started as of 2012.
- (iii) A system to localize the beam loss at the dedicated collimator system must be installed.

Assuming a successful R&D program on the higher repetition cycle and on the increase of the number of particles per bunch as well as sufficient resources the accelerator power will be upgraded to 0.75 MW within a time scale of five years.

**3.2. The Okinoshima Giant Liquid Argon Observatory.** The use of a giant liquid argon time projection chamber (TPC) with 100 kton size is an excellent opportunity to realize a broad range of scientific topics. It would be ideal for the next-generation accelerator-based neutrino research investigating the lepton sector CP symmetry and would extend the search for the proton decay via modes favored by the supersymmetric grand unified models (e.g.,  $p \rightarrow \nu K^+$ ) up to  $10^{35}$  years. Moreover, it would cover a wide range of neutrino physics stemming from astrophysical and terrestrial sources (e.g., solar and atmospheric neutrinos, neutrinos from stellar collapse and the neutrinos from dark matter annihilation). Specifications of the assumed detector are described in Table 5.

**3.2.1. Optimal Configuration for the Investigation of Lepton Sector CP Phase  $\delta_{CP}$  with a Liquid Argon TPC.** The effects of lepton sector CP phase  $\delta_{CP}$  appear either

- (1) in the energy spectrum shape of the appearance oscillated  $\nu_e$  charged current events (sensitive to all the nonvanishing  $\delta_{CP}$  values including  $180^\circ$ ) or
- (2) as a difference between  $\nu$  and  $\bar{\nu}$  behaviors (this is sensitive to the CP-odd term which vanishes for  $\delta_{CP} = 0$  or  $180^\circ$ ).

TABLE 4: MR power improvement scenario.

	Till June 2012	Next step	Target
Power (MW)	0.19	0.30	<b>0.75</b>
Energy (GeV)	30	30	<b>30</b>
Rep. cycle (sec.)	2.56	2.40	<b>1.28</b>
No. of bunches	8	8	<b>8</b>
Particles/bunch	$1.26 \times 10^{13}$	$1.9 \times 10^{13}$	<b><math>2.5 \times 10^{13}</math></b>
Particles/ring	$1.0 \times 10^{14}$	$1.5 \times 10^{14}$	<b><math>2.0 \times 10^{14}</math></b>
Linac (MeV)	181	400	<b>400</b>
RCS <sup>a</sup>	$h = 2$	$h = 2$	<b><math>h = 2</math></b>

<sup>a</sup>Harmonic member of RCS.

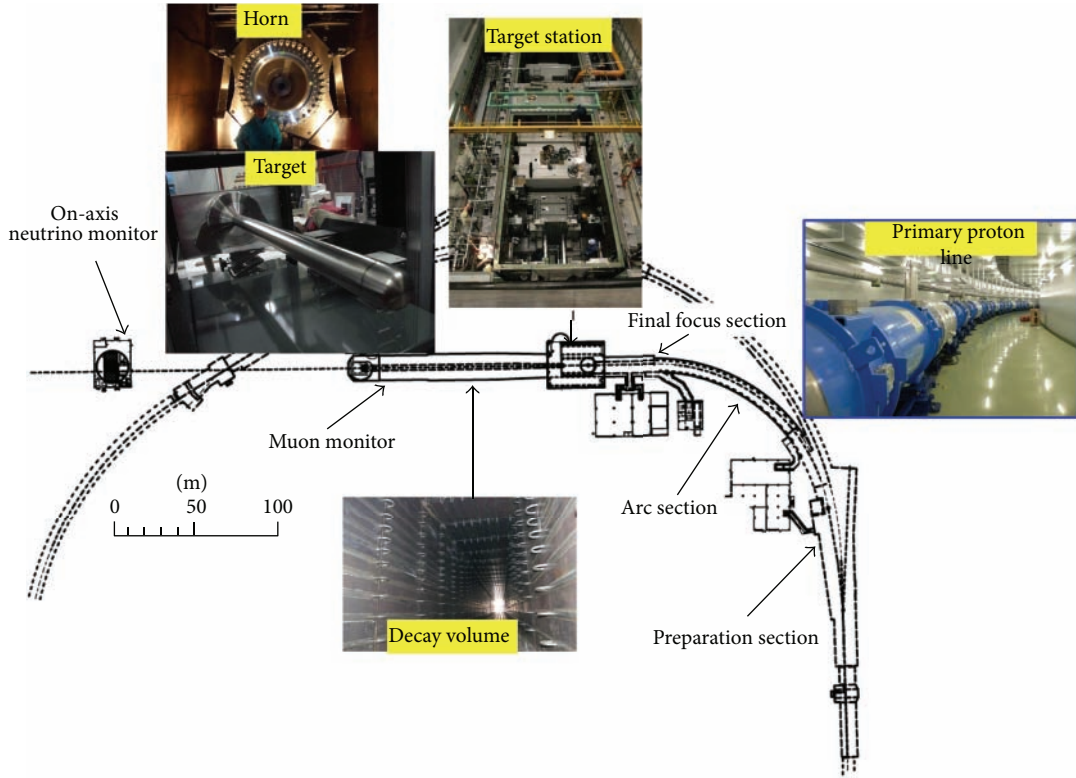


FIGURE 10: J-PARC neutrino beam facility.

It should be noted that if one precisely measures the  $\nu_e$  appearance energy spectrum shape (peak position and height for 1st and 2nd oscillation maximum and minimum) with high resolution, the CP effect could be investigated with neutrino running only. On the other hand, if one tries to extract CP information by comparing  $\nu$  and  $\bar{\nu}$  behaviour, it is necessary to run in antineutrino mode as well. Antineutrino beam conditions are known to be more difficult than those for neutrinos due to the lower beam flux, the leading charge effect in proton collisions on target, smaller antineutrino cross-sections at low energy, and so forth. Moreover, the systematic uncertainties for the neutrino mode experiment and antineutrino mode experiment are different and not much cancellation is foreseen.

An optimal experimental setup including parameters such as the length of the baseline, the angle with respect to the neutrino beam axis and the detector technology affects the

extraction of the CP phase [30]. Since the liquid argon TPC has an excellent energy resolution for the neutrino energy measurement and event reconstruction capability from sub-GeV to a few GeV and from single prong to high multiplicity configurations, it is suitable for spectrum measurement with wide energy coverage. To precisely measure the  $\nu_e$  and  $\bar{\nu}_e$  appearance energy, spectrum shape an on-axis wide band beam is necessary. In order to enable the measurement of the 2nd neutrino oscillation maximum, the energy of the 2nd neutrino oscillation maximum has to be set above about 400 MeV. As a consequence, the position of the 1st neutrino oscillation maximum, which also has to be measured, is also at a higher energy. As a consequence, events associated with  $\pi^0$ s originating from high-energy neutrino interactions will have to be dealt with as these mimic the signal  $\nu_e$  ( $\bar{\nu}_e$ ) charged current interaction. Therefore, a good discrimination between  $\pi^0$ s and electrons is indispensable for the required

TABLE 5: Specification of giant liquid argon time projection chamber.

Diameter for active argon (m)	70
Drift length (m)	20
Active mass (ton)	107753
Signal readout area (m <sup>2</sup> )	3848
Maximum drift time at 1 kV/cm (ms)	10
Charge readout views	3 mm pitch, two perpendicular strips
Scintillation light readout	1000 8" PMT

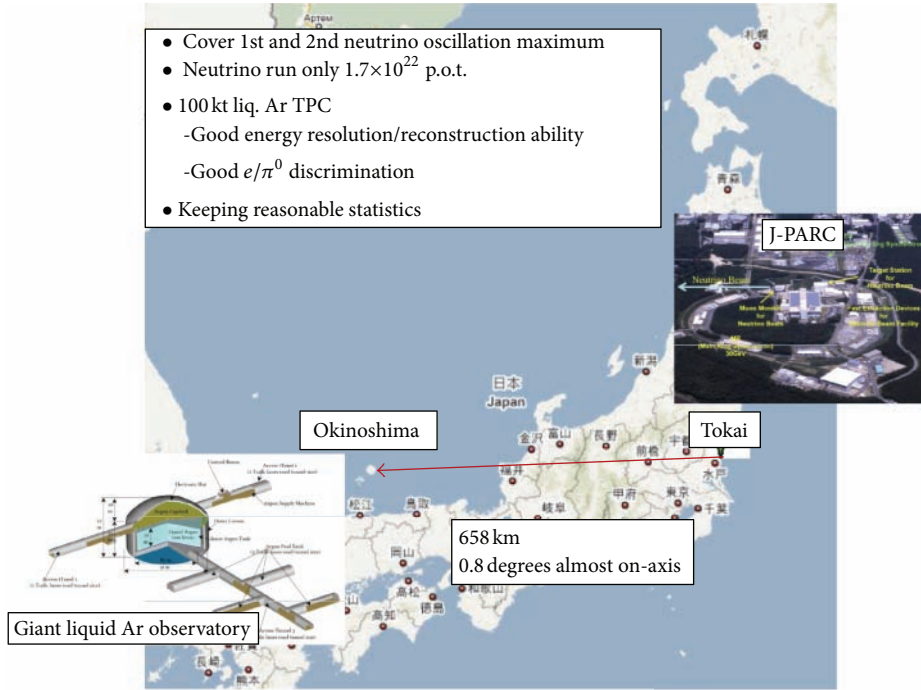


FIGURE 11: J-PARC to Okinoshima long-baseline neutrino experiment.

experimental configuration. Since the liquid argon TPC has an excellent discrimination capability between  $\pi^0$ s and electrons, a wideband on-axis beam for spectrum measurement is desirable.

In order to realize the project within a reasonable time scale, it makes sense to utilize the currently available facilities as much as possible. On the other hand, this may present boundary conditions for the project. In our case, J-PARC is a currently available and indispensable facility for our project. We have to consider the project taking into account its available intensity (750 kW) and energy (30 GeV). To obtain an experimental result within a reasonable time scale, it would be preferable if we could extract lepton CP symmetry information without relying on a time-consuming antineutrino beam setting. If the baseline of the experiment becomes longer, the neutrino energy has to increase in order to fit the neutrino spectrum within the neutrino oscillation maximum. Given the proton accelerator energy setting, which creates

a limitation on the available neutrino energy, there is a limitation on the baseline of the experiment, accordingly.

Thus, the optimal choice for the investigation of lepton sector CP symmetry using a liquid argon TPC is the measurement of the energy spectrum shape of the appearance oscillated  $\nu_e$  charged current events (with an emphasis on the 1st and 2nd oscillation maximum) using an on-axis neutrino beam. After this first phase measurement, an antineutrino beam (opposite horn polarity) experiment might be considered in a second stage in order to crosscheck the results obtained with the neutrino run.

The necessary conditions for the measurement are

- (1) a long baseline ( $>600$  km) to see the second oscillation maximum in a measurable energy region ( $>400$  MeV),
- (2) an on-axis beam for wide energy coverage, and

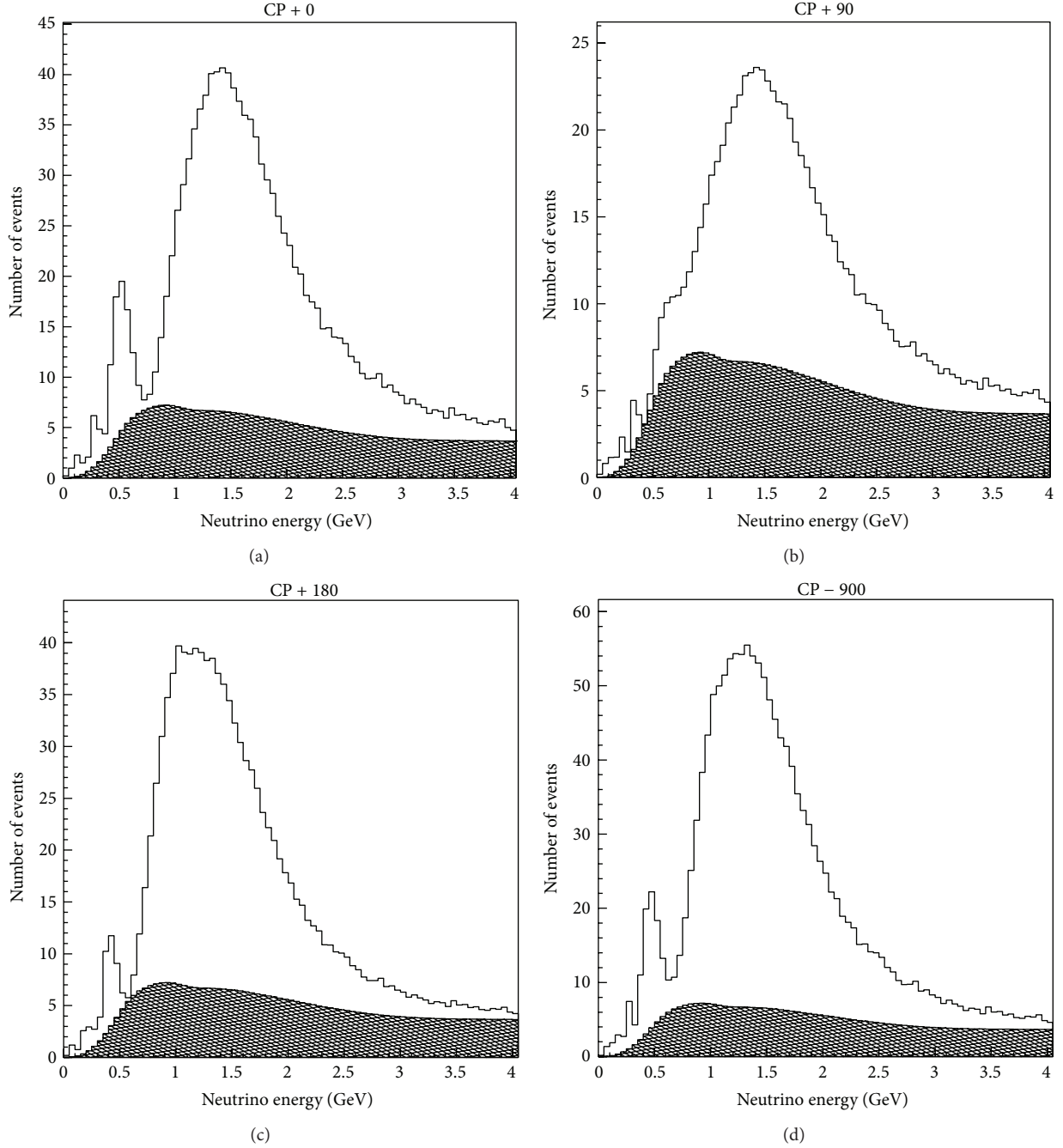


FIGURE 12: Energy spectra at  $\sin^2 2\theta_{13} = 0.03$  and normal mass hierarchy case, with  $\delta_{CP} = 0^\circ$  (a),  $90^\circ$  (b),  $180^\circ$  (c), and  $270^\circ$  (d) cases.

- (3) a giant detector to overcome the finite beam flux and long baseline.

**3.2.2. The J-PARC to Okinoshima Long-Baseline Neutrino Experiment with 100 kton Liquid Argon TPC.** With the same configuration as T2K ( $2.5^\circ$  off-axis angle), the center of the neutrino beam will traverse the earth and reach Okinoshima island (658 km baseline) with an off-axis angle  $0.76^\circ$  (almost on-axis). The scenario is depicted in Figure 11 [1].

The analysis presented here is based on the assumption of a neutrino run only with an exposure of  $1.7 \times 10^{22}$  protons on a pion production target. The detector is assumed to be a 100 kton liquid argon TPC. This type of detector should provide higher precision than other huge detectors to separate the two peaks in the energy spectrum. In addition, since the  $\pi^0$  background is expected to be highly suppressed due to the fine granularity of the readout, the main irreducible background will be the intrinsic  $\nu_e$  component of the beam.



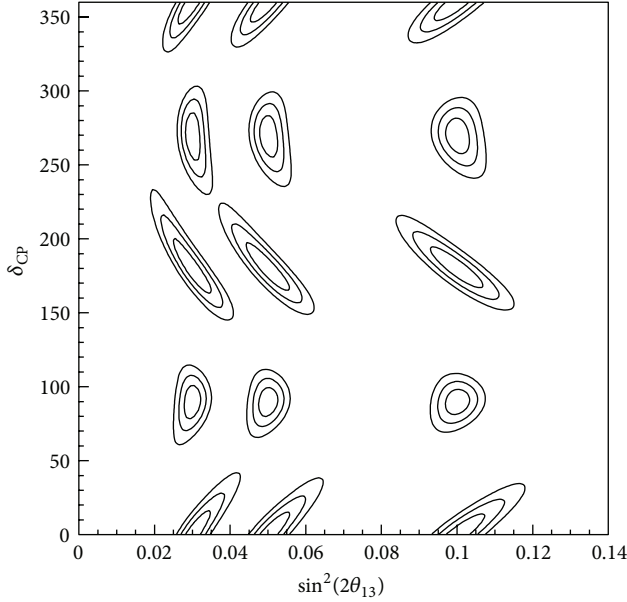


FIGURE 13: Allowed regions in the perfect resolution case. Twelve allowed regions are overlaid for twelve true values,  $\sin^2 2\theta_{13} = 0.1, 0.05, 0.02$ , and  $\delta_{CP} = 0^\circ, 90^\circ, 180^\circ, 270^\circ$ . The outermost boundary of the circles correspond to  $3\sigma$ .

Figure 12 shows the energy spectra of electron neutrinos for the cases of  $\delta_{CP}$  equal  $0^\circ, 90^\circ, 180^\circ$ , and  $270^\circ$  with normal mass hierarchy. The shaded region is common for all plots and shows the background from intrinsic beam  $\nu_e$ . Simulation includes smearing due to Fermi motion of nucleons in Argon nuclei. Here, a perfect resolution for the energy measurement of neutrinos is assumed. According to the simulation study, an energy measurement resolution of about 10% R.M.S. is expected. As shown, the value of  $\delta_{CP}$  affects the energy spectrum, especially in the first and the second oscillation peaks (heights and positions). Therefore, a comparison of the peaks can determine the value  $\delta_{CP}$ , while the value of  $\sin^2 2\theta_{13}$  changes the number of events predominantly.

Allowed regions in the perfect resolution case are shown in Figure 13. Twelve allowed regions are overlaid for twelve true values,  $\sin^2 2\theta_{13} = 0.1, 0.05, 0.02$ , and  $\delta_{CP} = 0^\circ, 90^\circ, 180^\circ, 270^\circ$ , respectively. The  $3\sigma$  sensitivity for the  $\delta_{CP}$  is 20–30° depending on the true  $\delta_{CP}$  value [1].

**3.2.3. Okinoshima Site Study.** The site study of the Okinoshima Giant Liquid Argon Observatory has been initiated taking into account geological, geographical, and infrastructure considerations [32].

The main island of Okinoshima, Dogo, is almost circular with a diameter of about 16 km and the center is a mountainous zone with an altitude of 500 m and more than one candidate location for the giant liquid argon observatory can be found. The distance from the main island of Japan (Honshu) is about 80 km. The population is about 16,000 and the economy mainly depends on the fishery and tourist business.

Though the islands were born of volcanic activity around 5 to 6 million years ago, there is stable bedrock, called Oki-Gneiss, which is the oldest rock in Japan (more than 3 billion years old) and which is suitable for the construction of a big cavern. Typical specific gravity and axial strength of Oki-Gneiss is  $27 \text{ kN/m}^3$  and 79 MPa, respectively.

The cross-sectional drawing of the potential location of the cavern is shown in Figure 14. Since a shallow depth ( $>600 \text{ m}$  water equivalent) is enough to suppress cosmogenic background for a liquid argon TPC [33], horizontal access from the outside is assumed. The earth covering between the top of the cavern and the mountain top is 252 m. Simulation study indicates that there are 1 to 2 muons/10 msec in the assumed 100 kt liquid Ar TPC configuration (10 msec corresponds to the signal electron drift time for an assumed 20 m drift distance.). Therefore, it is judged that the number of muons is small enough to operate the detector. If necessary, the bottom of the cavern could be lowered, for instance, by another 100 m.

A conceptual design of the cavern has been carried out and is also shown in Figure 14. In order to contain a cylindrical 100 kton liquid argon observatory with a base diameter of 80 m and a height of 20 m, the inner dimensions of the cylindrical cavern should provide a base diameter of 91 m, a height of 20 m, and a spherical cap of 20 m in height.

There would not be a difficulty in transportation since there are regular daily commercial connecting flights and ferry services between Honshu and the main harbor of Dogo (Saigou port) which is close to the location of the candidate site. Moreover, there is a sufficient traffic access route between Saigou port and the candidate site to carry heavy equipment needed for the civil engineering work, the large amount of liquid argon, and the detector components.

The Chugoku Electric Power Company provides electricity for Okinoshima. The existing total electricity capacity is 32 MW and may be enough for the construction and operation of the observatory.

The procurement of 100 kton of liquid argon, which should be done within about 5 years with minimum cost, is another important issue to be considered. One possible solution is to

- (1) purchase liquid Argon from several large-scale manufacturing plants which have large production capacities. The demand from the Giant Liquid Argon Observatory is estimated to be roughly 10 to 15% of their annual production capacity;
- (2) hire 4 tanker trucks dedicated for the liquid Argon ground transportation. The cost of trucks for 5 years is not the major part of the total cost for the project.

So far there is no show stopper to realize the Okinoshima Giant Liquid Argon Observatory.

**3.3. The Hyper-Kamiokande Project.** Hyper-Kamiokande (Hyper-K), being proposed by the Hyper-Kamiokande working group [2], is the third-generation underground water Cherenkov detector at Kamioka that serves as a far detector of a long-baseline neutrino oscillation experiment

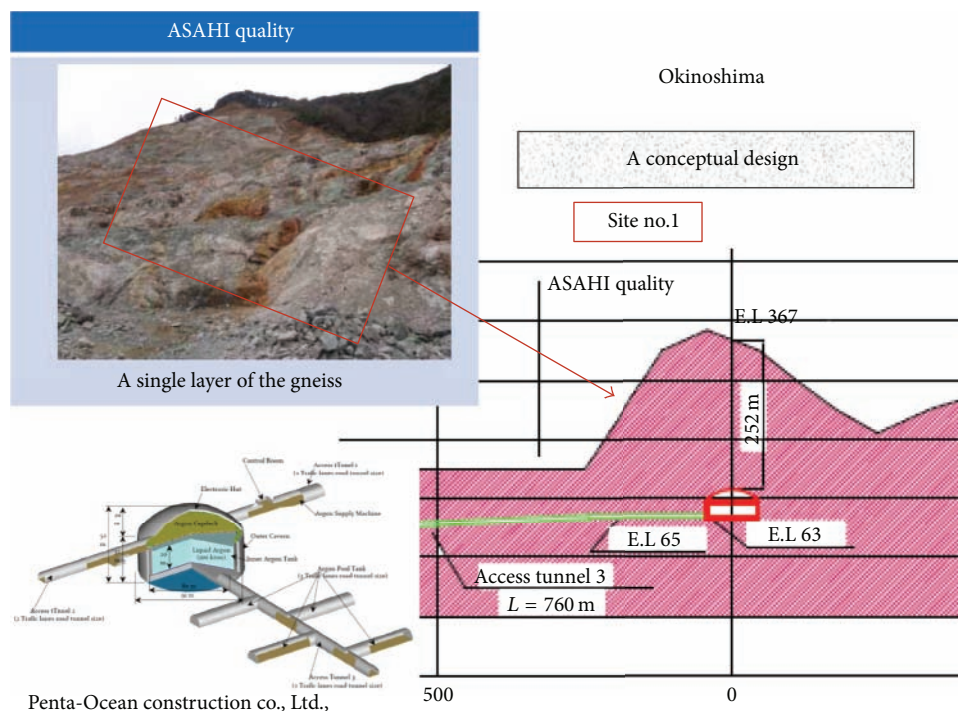


FIGURE 14: Potential cavern for Okinoshima Giant Liquid Argon Observatory.

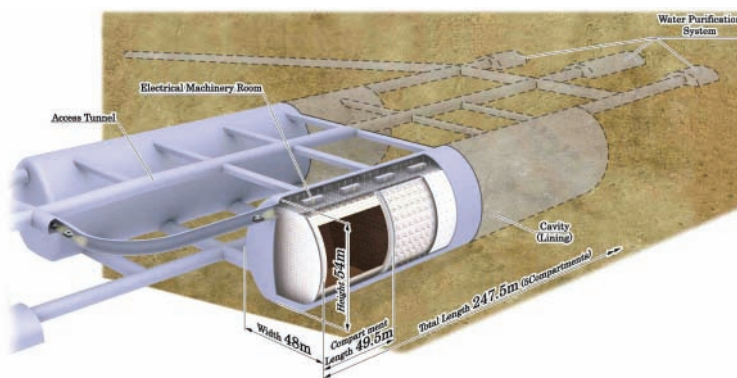


FIGURE 15: Schematic view of the Hyper-Kamiokande detector. The detector consists of two cylindrical water tanks lying side by side.

for the J-PARC neutrino beam and as a detector capable of observing proton decays, atmospheric neutrinos, and neutrinos from other astrophysical origins. The baseline design of the Hyper-K project is determined based on the established water Cherenkov detector technology in the successful Super-Kamiokande (Super-K) experiment. Its physics potential is estimated based on the detector performance proven by the Super-K detector.

The schematic view of the Hyper-K is shown in Figure 15. Table 6 summarizes the baseline design parameters of the Hyper-K detector. The detector consists of two cylindrical water tanks lying side by side. The water tank has dimensions of 54 (H)  $\times$  48 (W)  $\times$  250 (L) m<sup>3</sup>, containing  $0.5 \times 2 \sim 0.99$  million metric tonnes (mton) of ultra pure water in total. The fiducial volume of the two tanks is 0.56 mton and is 25 times larger than the fiducial volume of Super-K. The detector

will be optically separated into ten subdetectors by 50 m spacing segmentation walls and each subdetector is viewed by photomultiplier tubes (PMTs) to detect Cherenkov photons emitted by charged particles traversing the tank water. In the baseline design, 99,000 20 inch HAMAMATSU R3600 PMTs will be implemented on the detector walls to achieve 20% photocoverage, about half that of Super-K. The 2 m thick outer detector layers completely surround the inner detector volume and are instrumented with 8 inch PMTs.

The Hyper-K detector candidate site, located 8 km south of the Super-K, is in the Tochibora mine of the Kamioka Mining and Smelting Company, near Kamioka town in Gifu prefecture, Japan. The experiment site is accessible via a drive-in, 2.6 km long, horizontal mine tunnel. The detector will lie under the peak of Nijuugo-yama, having 648 meters of rock or 1,750 meters-water-equivalent (m.w.e.) overburden.

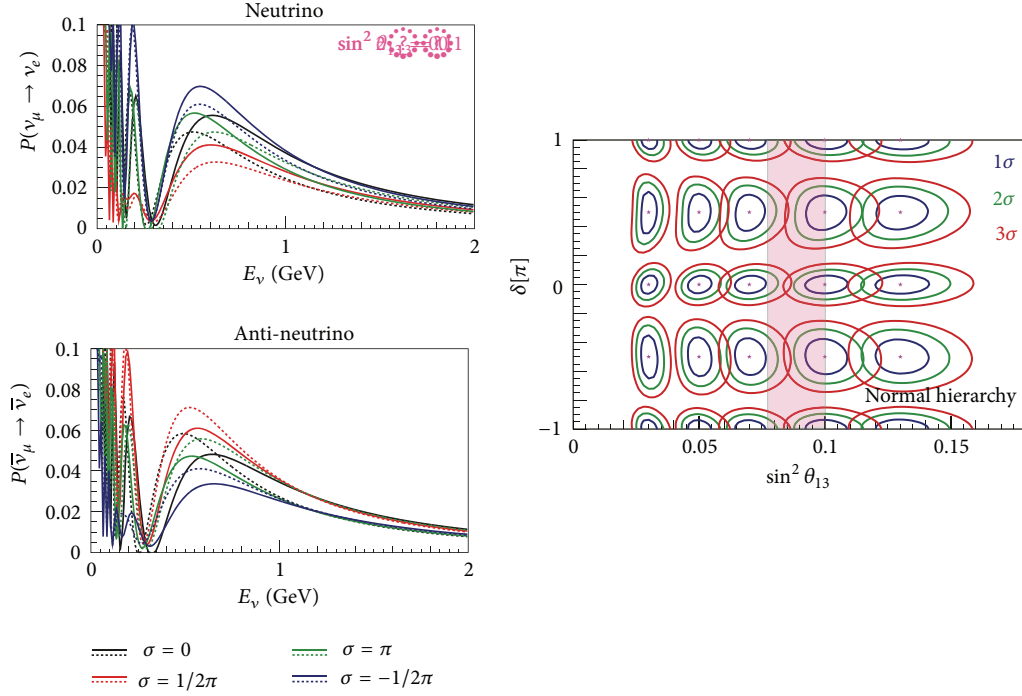


FIGURE 16: Transition probability of muon neutrino to electron neutrino at the distance of 295 km for neutrino (left top panel) and antineutrino (right top). Each color shows the appearance probability for each  $\delta_{CP}$  values. Solid and dashed lines represent normal and inverted mass hierarchy, respectively. The right panel shows expected contours for each true  $(\delta, \sin^2 2\theta_{13})$  parameter set by 7.5 MW-years JPARC-HK long-baseline neutrino oscillation experiment. Three colors show 1, 2, and 3  $\sigma$  significance. The pink band corresponds to the  $\theta_{13}$  value measured by the Daya Bay reactor experiment [31].

The cosmic ray muon rate at the candidate site is reduced to  $1.0 - 2.3 \times 10^{-6} \text{ s}^{-1} \text{ cm}^{-2}$  which enables us to perform nonaccelerator physics research programs. The off-axis angle for the J-PARC neutrino beam is  $2.5^\circ$  and the baseline is 295 km, both are same as those of the Super-K in the ongoing T2K experiment.

The expected detector performance of Hyper-K, assuming 20% photocoverage, is summarized in Table 7. The efficiency of  $\nu_e$  appearance signal for the J-PARC neutrino beam is as high as  $\sim 60\%$  while keeping excellent background rejection efficiency of 99.9% for  $\nu_\mu + \bar{\nu}_\mu$  CC and 95% for NC  $\pi^0$  interactions. We may improve the rejection efficiency in the future to optimize the leptonic CP violation search.

Hyper-K provides rich neutrino physics programs as summarized in Table 8. In particular, it will provide unprecedented discovery potential of leptonic CP violation by comparing  $\nu_\mu \rightarrow \nu_e$  and  $\bar{\nu}_\mu \rightarrow \bar{\nu}_e$  probabilities in J-PARC neutrino beam as shown in the left two panels of Figure 16. The right panel in Figure 16 shows an expected size of contours for each true  $(\delta, \sin^2 2\theta_{13})$  parameter set. By using 3.75 MW-years of J-PARC neutrino beam, where 1 year is equivalent to  $10^7$  seconds and the run time ratio of neutrino mode and antineutrino mode is assumed to be 1.5:3.5, Hyper-K will provide 3 $\sigma$  discovery reaching the leptonic CP violation for 69% of the  $\delta$  parameter space if the mass hierarchy is known. The accuracy of  $\delta$  determination is better than  $20^\circ$  at 1 $\sigma$  and does not depend much on true  $\theta_{13}$  value. If the beam time is increased to 7.5 MW-years,

the discovery coverage extends to 74% of the  $\delta$  parameter space. If the mass hierarchy is unknown, the sensitivity to the CP violation is somewhat reduced due to degeneracy. However, the mass hierarchy can be determined with more than 3 $\sigma$  significance for 43% (44%) of the  $\delta$  parameter space for normal (inverted) mass hierarchy if  $\sin^2 2\theta_{13} = 0.1$  as measured by the reactor neutrino oscillation experiments.

Natural, free, and atmospheric neutrinos also provide a good opportunity to study neutrino properties. In particular, thanks to the relatively large  $\sin^2 2\theta_{13}$  value of  $\sim 0.1$ , there is a good chance to determine the neutrino mass hierarchy by testing the  $\nu_e$  (or  $\bar{\nu}_e$ ) enhancements via MSW resonance effect by Earth's matter. As illustrated in Figure 17, the  $\nu_e$  flux enhancement happens in 5–10 GeV upward going neutrinos in the case that the mass ordering is normal. In the inverted hierarchy case, however,  $\bar{\nu}_e$  enhancement is expected to occur. The fundamental difference between  $\nu_e$  and  $\bar{\nu}_e$  interactions, for example, CC cross-sections and  $d\sigma/dy$  distributions where  $y$  is the Feynman  $y$ , allows statistical separation of  $\nu_e$  and  $\bar{\nu}_e$  interactions to examine the mass hierarchy. With a full 10-year period of data taking, the significance for the mass hierarchy determination is expected to reach 3 $\sigma$  or greater if  $\sin^2 2\theta_{13} \sim 0.1$ . Moreover, the octant of  $\sin^2 \theta_{23}$  can be determined to more than 90% CL if  $\sin^2 2\theta_{23} < 0.99$ .

The experimental search for nucleon decays by large detectors, which has been performed for more than three decades and gave stringent constraints on the grand

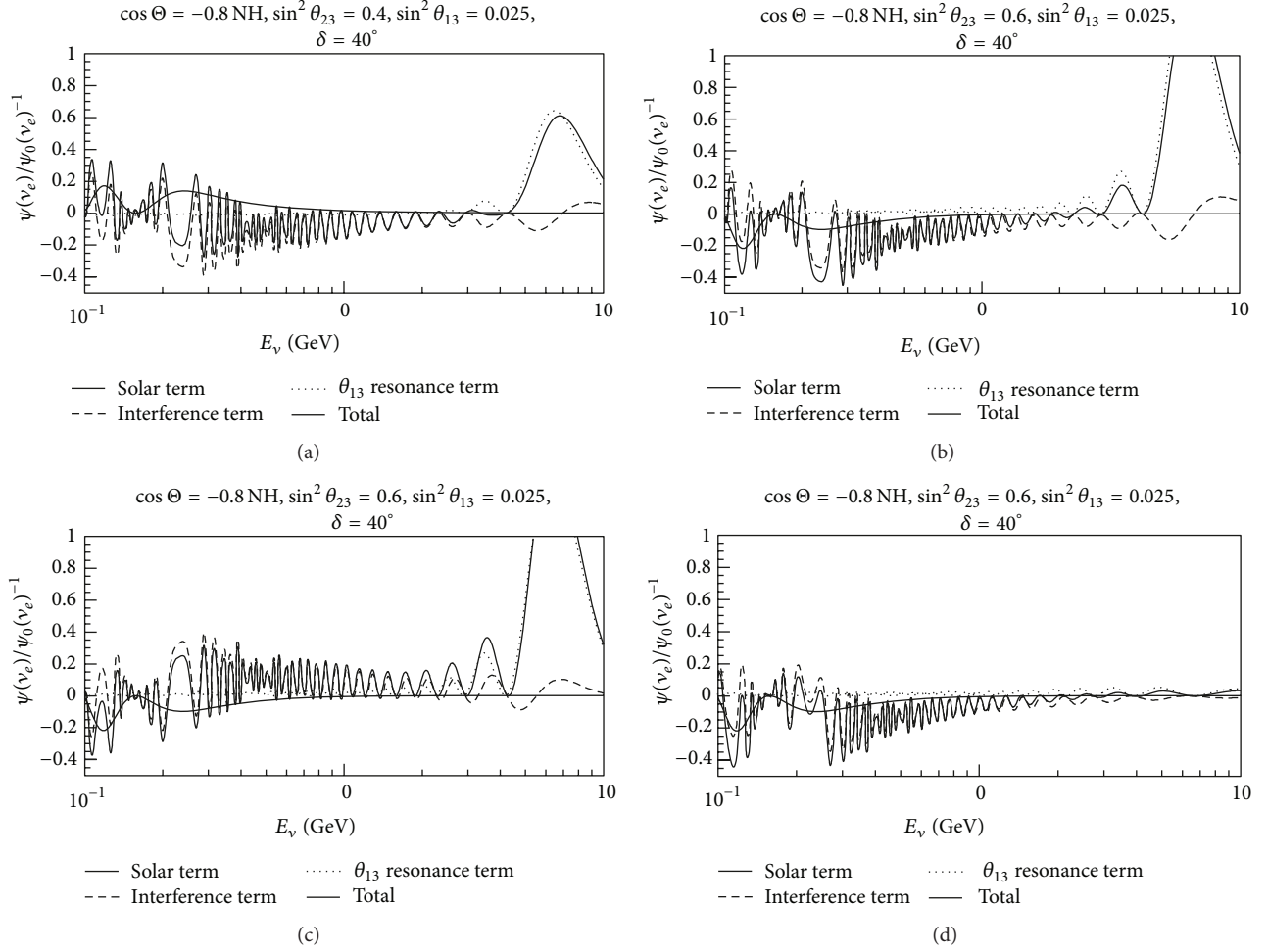


FIGURE 17: Oscillated  $\nu_e$  flux relative to the nonoscillated flux as a function of neutrino energy for the upward-going neutrinos with zenith angle  $\cos \Theta_\nu = -0.8$ .  $\bar{\nu}_e$  is not included in the plots. Thin solid lines, dashed lines, and dotted lines correspond to the solar term, the interference term, and the  $\theta_{13}$  resonance term, respectively. Thick solid lines are total fluxes. Parameters are set as  $(\sin^2 \theta_{12}, \sin^2 \theta_{13}, \sin^2 \theta_{23}, \delta, \Delta m_{21}^2, \Delta m_{32}^2) = (0.31, 0.025, 0.6, 40^\circ, 7.6 \times 10^{-5} \text{ eV}^2, +2.4 \times 10^{-3} \text{ eV}^2)$  unless otherwise noted. The mass hierarchy is normal in (a), (b), and (c); so  $\theta_{13}$  resonance (MSW) effect appears in 5–10 GeV neutrino energy region. For the inverted hierarchy case in (d), the MSW effect should appear in the  $\bar{\nu}_e$  flux, which is not shown in the plot. The  $\theta_{23}$  octant effect can be seen by comparing (a) ( $\sin^2 \theta_{23} = 0.4$ ) and (b) ( $\sin^2 \theta_{23} = 0.6$ ).  $\delta$  value is changed to  $220^\circ$  in (c) to be compared with  $40^\circ$  in (b).

unification picture of elementary particles, is also one of major goals of the Hyper-K project. Hyper-K extends the sensitivity to nucleon decays far beyond that of Super-K. The sensitivity to the partial lifetime of protons for the decay mode  $p \rightarrow e^+ + \pi^0$ , the mode considered to be most model-independent, is expected to be  $1.3 \times 10^{35}$  years at 90% CL and  $5.7 \times 10^{34}$  years at  $3\sigma$  CL with 10 years of Hyper-K data. This is the only realistic detector option known today able to reach this sensitivity. The 3% resolution of reconstructed proton mass by the water Cherenkov detector enhances its discovery potential for this decay mode. The sensitivity for the decay mode  $p \rightarrow \bar{\nu} + K^+$ , the mode favored if some supersymmetric model is correct, is also extended to  $2.5 \times 10^{34}$  years at 90% CL and  $1.0 \times 10^{34}$  years at  $3\sigma$  CL.

Hyper-K also serves as an astrophysical neutrino observatory and explores the inside of stars by using neutrinos

as a probe. Hyper-K will examine the possible flux variation of neutrinos from the Sun by detecting 200 solar neutrinos per day above 7 MeV total neutrino energy. If a Supernova explosion happens at the center of our galaxy, Hyper-K will accumulate 170,000–260,000 neutrinos in 10-second burst period. Even for a far Supernova at M31 (Andromeda galaxy), Hyper-K expects to collect 30–50 neutrinos. Hyper-K will provide precious data for Supernova and reveal the core collapse and explosion mechanism of massive stars. Moreover, neutrino arrival time distributions from Supernova will give constraints on the absolute neutrino mass with an expected sensitivity of  $0.5\text{--}1.3 \text{ eV}/c^2$  that does not depend on whether the neutrino is a Dirac or Majorana particle. For Supernova relic neutrinos, in which the history of heavy element synthesis in the universe is encoded, Hyper-K expects to observe 300 neutrinos above 20 MeV in 10 years of observation. This



TABLE 6: Detector parameters of the baseline design.

Detector type		Ring-imaging water Cherenkov detector
Candidate site	Address	Tochibora mine
		Kamioka town, Gifu, Japan
	Lat.	$36^{\circ}21'08.928''\text{N}$
	Long.	$137^{\circ}18'49.688''\text{E}$
	Alt.	508 m
	Overburden	648 m rock (1,750 m water equivalent)
	Cosmic ray muon flux	$1.0\sim 2.3 \times 10^{-6} \text{ sec}^{-1} \text{ cm}^{-2}$
	Off-axis angle for the J-PARC $\nu$	$2.5^{\circ}$ (same as Super-Kamiokande)
Detector geometry	Distance from the J-PARC	295 km (same as Super-Kamiokande)
	Total volume	0.99 megaton
	Inner volume (fiducial volume)	0.74 (0.56) megaton
Photomultiplier tubes	Outer volume	0.2 megaton
	Inner detector	99,000 20 inch $\phi$ PMTs
	Outer detector	20% photocoverage 25,000 8 inch $\phi$ PMTs
Water quality	Light attenuation length	$>100 \text{ m}$ at 400 nm
	Rn concentration	$<1 \text{ mBq/m}^3$

TABLE 7: Expected detector performance of Hyper-Kamiokande.

	Resolution or efficiency
Vertex resolution	
at 500 MeV/c	28 cm (electron)/23 cm (muon)
at 5 GeV/c	27 cm (electron)/32 cm (muon)
Particle ID	
at 500 MeV/c	$98.5 \pm 0.6\%$ (electron)/ $99.0 \pm 0.2\%$ (muon)
at 5 GeV/c	$99.8 \pm 0.2\%$ (electron)/ $100^{+0.0}_{-0.4}\%$ (muon)
Momentum resolution	
at 500 MeV/c	5.6% (electron)/3.6% (muon)
at 5 GeV/c	2.0% (electron)/1.6% (muon)
Electron tagging	
from 500 MeV/ $c\mu^+$ decays	98%
from 5 GeV/ $c\mu^+$ decays	58%
J-PARC $\nu_e$ signal efficiency	64% (nominal)/50% (tight)
J-PARC $\nu_\mu$ CC background rejection	$>99.9\%$
J-PARC $\nu\pi^0$ background rejection	95% (nominal)/97.6% (tight)
$p \rightarrow e^+ + \pi^0$ efficiency ( $w/\pi^0$ intranuclear scattering)	45%
Atmospheric $\nu$ background	1.6 events/Mton/year
$p \rightarrow \bar{\nu} + K^+$ efficiency by prompt $\gamma$ tagging method	7.1%
atmospheric $\nu$ background	1.6 events/Mton/year
$p \rightarrow \bar{\nu} + K^+, K^+ \rightarrow \pi^+ + \pi^0$ efficiency	6.7%
atmospheric $\nu$ background	6.7 events/Mton/year
Vertex resolution for 10 MeV electrons	90 cm
Angular resolution for 10 MeV electrons	$30^{\circ}$
Energy resolution for 10 MeV electrons	20%

TABLE 8: Physics targets and expected sensitivities of the hyper-Kamiokande experiment updated from [2].  $\sigma_{\text{SD}}$  is the WIMP-proton spin-dependent cross-section.

Physics target	Sensitivity	Conditions
Neutrino study w/J-PARC $\nu$		
(i) CP phase precision	$<20^\circ$	at $s^2 2\theta_{13} (\equiv \sin^2 2\theta_{13}) > 0.03$ and mass hierarchy (MH) is known
	74%	at $s^2 2\theta_{13} = 0.1$ , 7.5 MW·yrs MH known
	54%	at $s^2 2\theta_{13} = 0.1$ , 7.5 MW·yrs MH unknown
(ii) CPV $3\sigma$ discovery coverage	69%	at $s^2 2\theta_{13} = 0.1$ , 3.75 MW·yrs MH known
	42%	at $s^2 2\theta_{13} = 0.1$ , 3.75 MW·yrs MH unknown
Atmospheric neutrino study		
(i) MH determination	$>3\sigma$ CL	10-year observation at $0.4 < s^2 \theta_{23}$ and $0.04 < s^2 2\theta_{13}$
(ii) $\theta_{23}$ octant determination	$>90\%$ CL	at $s^2 2\theta_{23} < 0.99$ and $0.04 < s^2 2\theta_{13}$
Nucleon decay searches		
		10 years data
(i) $p \rightarrow e^+ + \pi^0$	$1.3 \times 10^{35}$ yrs (90% CL) $5.7 \times 10^{34}$ yrs (3 $\sigma$ CL)	
(ii) $p \rightarrow \bar{\nu} + K^+$	$2.5 \times 10^{34}$ yrs (90% CL) $1.0 \times 10^{34}$ yrs (3 $\sigma$ CL)	
Solar neutrinos		
(i) $^8\text{B } \nu$ from Sun	200 $\nu$ 's/day	7.0 MeV threshold (total energy)
(ii) $^8\text{B } \nu$ day/night accuracy	$<1\%$	5 years, only stat. error
Astrophysical objects		
(i) Supernova burst $\nu$	170,000–260,000 $\nu$ 's 30–50 $\nu$ 's	at Galactic center (10 kpc) at M31 (Andromeda galaxy)
(ii) Supernova relic $\nu$	300 $\nu$ 's/10 years	$>20$ MeV
(iii) WIMP annihilation at Sun	$\sigma_{\text{SD}} = 10^{-39} \text{ cm}^2$ $\sigma_{\text{SD}} = 10^{-40} \text{ cm}^2$	5-year observation at $M_{\text{WIMP}} = 10 \text{ GeV}$ $\chi\chi \rightarrow b\bar{b}$ dominant at $M_{\text{WIMP}} = 100 \text{ GeV}$ $\chi\chi \rightarrow W^+W^-$ dominant

large sample will enable us to explore the evolution of the universe. By doping Gadolinium salt in the detector water, the delayed gamma signal for the inverse beta decay of relic neutrinos— $\bar{\nu}_e + p \rightarrow e^+ + n$  and the reaction  $\text{Gd}(n, \gamma s)$ —enable us to much reduce the backgrounds and open up the signal energy window below 20 MeV. The expected signal in the 10–30 MeV energy region is 830 neutrinos in 10 years of Hyper-K. Another astrophysical target in Hyper-K is possible neutrinos emitted by weakly interacting massive particles (WIMPs) annihilating or decaying in the Sun, Earth, and galactic halo. Sensitivity to the WIMP-proton spin-dependent cross-section would reach  $10^{39} (10^{40}) \text{ cm}^2$  for a WIMP mass of 10 (100) GeV. Other astronomical neutrino searches such as solar flare neutrinos, GRB neutrinos,

and galactic diffuse neutrinos can be also performed in Hyper-K.

## 4. The European Approach

**4.1. EUROnu.** EUROnu is a design study within the European Commission Seventh Framework Program, Research Infrastructures. It is investigating the three possible options for a future, high-intensity neutrino oscillation facility in Europe. The aim is to undertake conceptual designs for the facilities, determine the performance of the corresponding baseline detectors, and compare the physics reach and cost of the facilities. The work is being undertaken by the EUROnu

consortium, consisting of 15 partners and a further 15 associate partners [34].

The three facilities being studied are as follows.

- (i) The CERN to Fréjus Super Beam, using the 4 MW version of the Superconducting Proton Linac (SPL) at CERN [35]. The baseline far detector is a 500 kT fiducial mass water Cherenkov detector, MEMPHYS [36].
- (ii) The Neutrino Factory, in which the neutrino beams are produced from the decay of muons in a storage ring. This work is being done in close collaboration with the International Design Study for a Neutrino Factory (IDS-NF) [37].
- (iii) The Beta Beam, in which the neutrino beams are produced from the decay of beta emitting ions, again stored in a storage ring.

The project started on September 1, 2008 and will finish on August 30, 2012, and thus, is very advanced at the time of writing. The work done on the accelerator facilities, the detectors, and in determining the physics performance will be described in the following subsections.

**4.1.1. The Super Beam.** A Super Beam creates neutrinos by impinging a high-power proton beam onto a target and focussing the pions produced towards a far detector using a magnetic horn. The neutrino beam comes from the pion decay (Figure 18). EUROnu is studying the CERN to Fréjus Super Beam, using the high-power superconducting proton Linac (HP-SPL) [35] as the proton driver, producing a 4 MW beam. The baseline is 130 km and the planned far detector is the 500 kT fiducial mass MEMPHYS water Cherenkov detector [36] in the Fréjus tunnel. The main activities consisted in designing and testing candidate targets and magnetic horns, integrating the targets and horns together, studying the required target station, designing the proton beam handling system beyond the SPL, and determining the characteristics of the resulting neutrino beam for physics simulations.

Given the difficulty in producing a single target and horn able to work in a 4 MW beam, the option taken in EUROnu is to use four of each instead. The beam will then be steered on to each target in turn, so that they all run at 12.5 rather than 50 Hz and receive 1 MW. For the targets and the horns, this results in a smaller extrapolation from technology already in use. An outline design for the 4 target and horn system is shown in Figure 18. The baseline design for the target is a pebble bed, consisting of 3 mm diameter spheres of titanium in a canister. These are cooled by flowing helium gas through vents in the canister. Modeling suggests that a sufficient flow rate can be achieved to cool the targets, even with a higher-power beam. Nevertheless, offline tests of the cooling system, using an inductive heating coil, are planned. A test target will also be subjected to a beam of the correct energy density using the HiRadMat [38] facility at CERN. The horn design is based on that of the MiniBooNE experiment [39] and will not have a reflector. The design has been modified to optimize the pion production. The horns will need to be pulsed at least 300 kA, resulting in significant heating

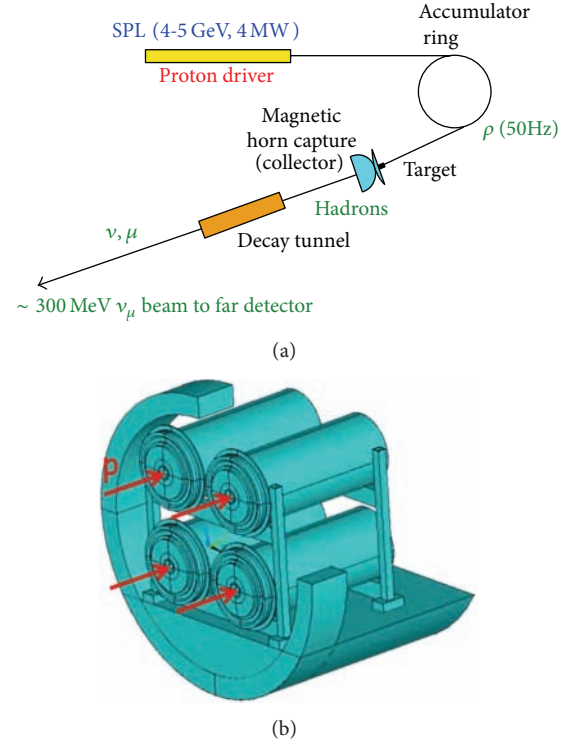


FIGURE 18: (a) Layout of the CERN to Fréjus Super Beam. (b) Conceptual engineering design of the 4 target and horn system for the Super Beam.

from both the current and beam loss, corresponding to a maximum of 12 kW on the surface closest to the target. Modeling suggests that this can be removed with sufficient water cooling. The thermal stresses in the target material are a maximum of 18 MPa and prototype tests will be required to determine the lifetime due to fatigue and radiation damage. A support system for the 4 horn system under this load has, however, been designed. Finally, a prototype pulsing circuit has been designed and will be built and tested. An initial design of the target station has also been made, based on radiation and activation studies. This incorporates the necessary shielding and remote handling for 4 MW and also has storage for the old targets and horns.

The final area studied is the beam delivery from the SPL to the target. As shown in Figure 18, this requires an accumulator ring to reduce the large number of bunches from the linac to a small number for delivery to the target. An initial design of this ring has been made. In addition, a design for the system to split the beam on to the 4 targets has been made and the engineering aspects of this are under study.

**4.1.2. The Neutrino Factory.** In a Neutrino Factory, the neutrinos are produced from the decay of muons in a storage ring. The muons are produced by impinging a 4 MW proton beam onto a heavy metal target and focussing the pions produced into a decay channel using a 20 T superconducting solenoid. In the original baseline, the muons from the pion decay are captured, bunched, phase rotated, and finally cooled in the muon front-end, before being accelerated using a

linac, two recirculating linear accelerators (RLAs) and a nonscaling fixed-field alternating gradient accelerator (ns-FFAG) to 0.9 GeV, 3.6 GeV, 12.6 GeV, and 25 GeV, respectively (see Figure 19). The muons are then injected into two storage rings, to produce beams of neutrinos and antineutrinos to two far detectors.

However, following the measurement of  $\theta_{13}$ , the required muon energy has been reduced to 10 GeV and only one decay ring will be used. The envisaged neutrino baseline is now around 2000 km.

The work in this project is being done in close collaboration with the International Design Study for a Neutrino Factory (IDS-NF) [37]. However, EUROnu is focussing on the section from the pion production target to the muon acceleration system. The baseline target is a liquid mercury jet. However, modeling done in EUROnu has shown that the heat load from the secondaries produced in the superconducting solenoids used to focus the pions is much too big, around 50 kW. The main problem is secondary neutrons. Although this can be fixed by adding more shielding, this would double the radius of the superconducting coils, making these significantly more difficult. A study of pion production has shown that similar production rates can be achieved with lower atomic number elements (see Figure 19), but these produce significantly fewer neutrons. As a result, targets with lower atomic number are under study. An interesting candidate is gallium, which has a low enough melting point that it could be used as a liquid.

A related issue is the transmission of secondaries into the muon front-end. As well as the required large flux of muons, there are also still many protons, pions, and electrons. If nothing is done about these, they will be lost throughout the front-end, resulting in levels of activation about 100 times above the canonical level for hands-on maintenance. The front-end is being redesigned in EUROnu to include a chicane, to remove the higher momentum unwanted particles, and an absorber, to remove those at lower momentum. The efficiency for transmission of useful muons is about 90%, while the unwanted particles are reduced to a manageable level. This scheme has recently been incorporated in the neutrino factory baseline.

For the cooling channel, an engineering demonstration of the cooling technique, ionization cooling, is being constructed at the STFC Rutherford Appleton Laboratory. This project, called MICE [40], is due to give a first demonstration of ionisation cooling during 2013. In addition, the RF cavities of the baseline cooling cell will be in a large magnetic field, resulting from the coils used to focus the beam to increase the cooling efficiency. Measurements done in the MuCool project [41] suggest this could limit the accelerating gradient before the cavities breakdown. Alternative cooling lattices have been studied in EUROnu that reduce the magnetic field at the cavities, while maintaining the same performance. One of these is under consideration to become the new baseline for the cooling channel.

The design of the acceleration system is well advanced, though full 6D tracking still needs to be done. Following the reduction to 10 GeV, two options now exist for this system. The first uses a linac and two RLAs, while the second replaces

the higher-energy RLA with a ns-FFAG. Both options are under study to determine which would be best based on performance and cost. As ns-FFAGs are an entirely novel type of accelerator, a proof-of-principle machine called EMMA [42] has been constructed at the STFC Daresbury Laboratory (see Figure 20). This has recently demonstrated that many of the novel features of the muon accelerator, in particular serpentine acceleration and multiple resonance crossings, work. The full EMMA experimental program has recently started and will study the remaining issues.

**4.1.3. The Beta Beam.** Production of (anti)neutrinos from beta decay of radioactive isotopes circulating in a race-track-shaped storage ring was proposed in 2002 [43]. Beta Beams produce pure  $\nu_e$  or  $\bar{\nu}_e$  beams, depending on whether the accelerated isotope is a  $\beta^+$  or a  $\beta^-$  emitter. The “Beta Beam facility” is based on CERN’s infrastructure and the fact that some existing accelerators can be reused will reduce the cost, though it will constrain the performance (see Figure 21).

One of the main issues studied by EUROnu is the production, acceleration, and storage of a sufficient flux of ions to meet the physics goals. The isotope pair that was first studied for neutrino production, in the EURISOL FP6 Design Study [44], is  $^6\text{He}$  and  $^{18}\text{Ne}$ , accelerated to  $\gamma = 100$  in the SPS and stored in the decay ring [44]. At the end of EURISOL, the flux of  $^{18}\text{Ne}$  that looked possible was a factor of 20 too small. This has been addressed in two ways in EUROnu. The first was to consider a production ring (12 m circumference) with an internal gas jet target [45] to make an alternative ion pair,  $^8\text{Li}$  and  $^8\text{B}$ . In this, a 25 MeV beam of  $^7\text{Li}$  and  $^6\text{B}$  is injected over a gas jet target of d and  $^3\text{He}$ , respectively. Significant studies of this have been undertaken, including the measurement of the double differential cross-sections for the reactions, studies of achievable gas flow rates in the ring and the construction of a prototype device for collection of the produced isotopes (see Figure 21). These have shown that the required target gas flow would be very challenging and that it would be very difficult to achieve the required rates.

As a result, research on a novel  $^{18}\text{Ne}$ -production method, using a molten salt loop (NaF) by the reaction  $^{19}\text{F}(p,2n)^{18}\text{Ne}$ , is currently being undertaken. Modeling suggests that this could achieve the required production rate with an upgrade of Linac 4 [46] at CERN from 4 to 6 mA. An experiment to demonstrate the method will take place at ISOLDE at CERN in June 2012. As a result of the work done so far, the  $^6\text{He}$  and  $^{18}\text{Ne}$  ion pair are currently the baseline for the Beta Beam.

Research and development of a 60 GHz pulsed ECR source to bunch the ions produced are continuing within EUROnu. A prototype device has been constructed and successful magnetic tests have been done. These will be followed by tests with the gyrotron and with beam. Compatibility and possible integration of Beta Beams in the upgrade program for the LHC is essential and is being actively studied. Requirements to have very short and intense bunches in the decay ring (due to signal/noise in the detector) favors beam instabilities for which solutions will be found by reoptimizing the bunch structure over the accelerator cycle.



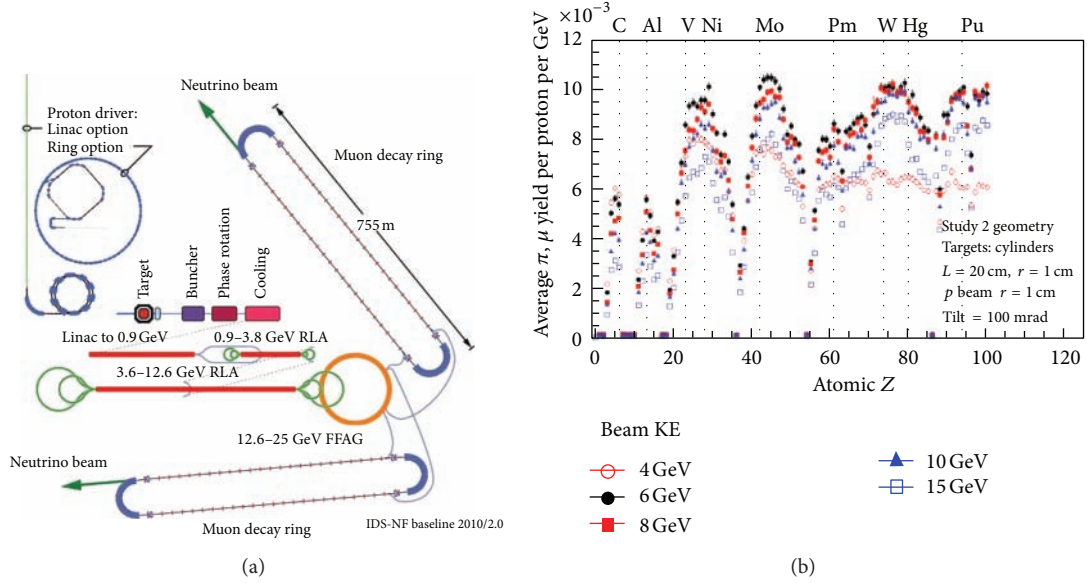


FIGURE 19: (a) Original baseline layout of the neutrino factory. (b) Pion production as a function of atomic number, assuming a cylindrical target 20 cm long and 2 cm in diameter.

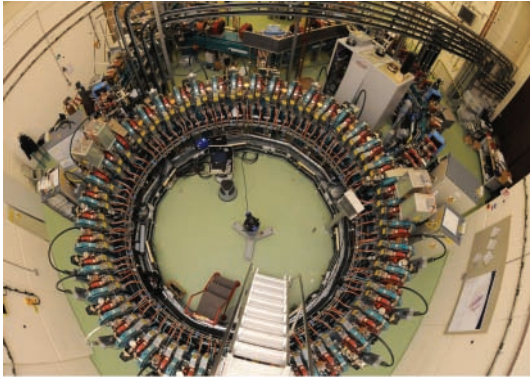
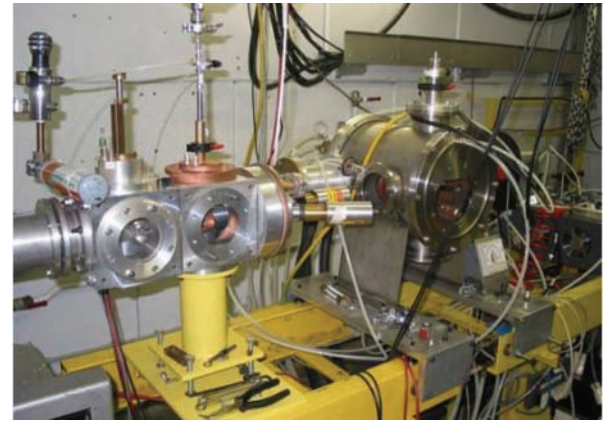
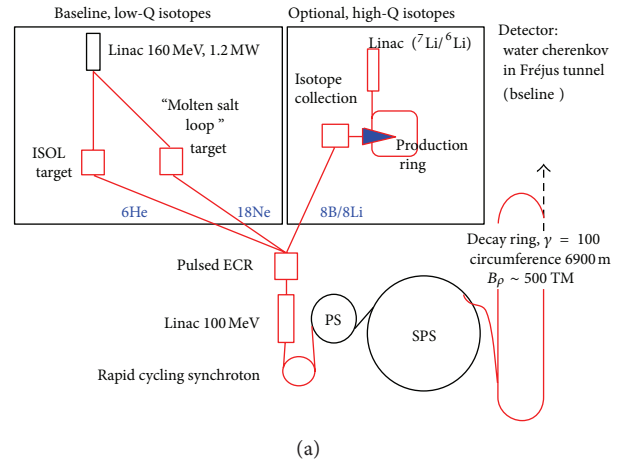


FIGURE 20: The EMMA proof-of-principle accelerator at the Daresbury Laboratory.



The baseline isotopes could use the MEMPHYS detector [36]. For the  $^8\text{Li}$  and  $^8\text{B}$  option, a detector some 700 km away would be needed.

**4.1.4. Detectors.** The focus of EUROnu is on the accelerator facilities. Nevertheless, to make a genuine comparison between physics performance and cost, it is also important to include the neutrino detectors in the study. Thus, the project includes the baseline detectors for each facility, with the aim of determining their performance in detecting neutrinos and the cost of construction.

The baseline for the Neutrino Factory is a magnetized iron neutrino detector (MIND). This is an iron-scintillator calorimeter, with alternating planes of 3 cm thick iron and 2 cm thick solid scintillator. One detector is now planned, of 100 kT mass at around 2000 km. This is based on the MINOS detector [47] and will have a transverse size of around 15 by

FIGURE 21: (a) Layout of the CERN Beta Beam. (b) The prototype ion collection device constructed for Beta Beam studies.

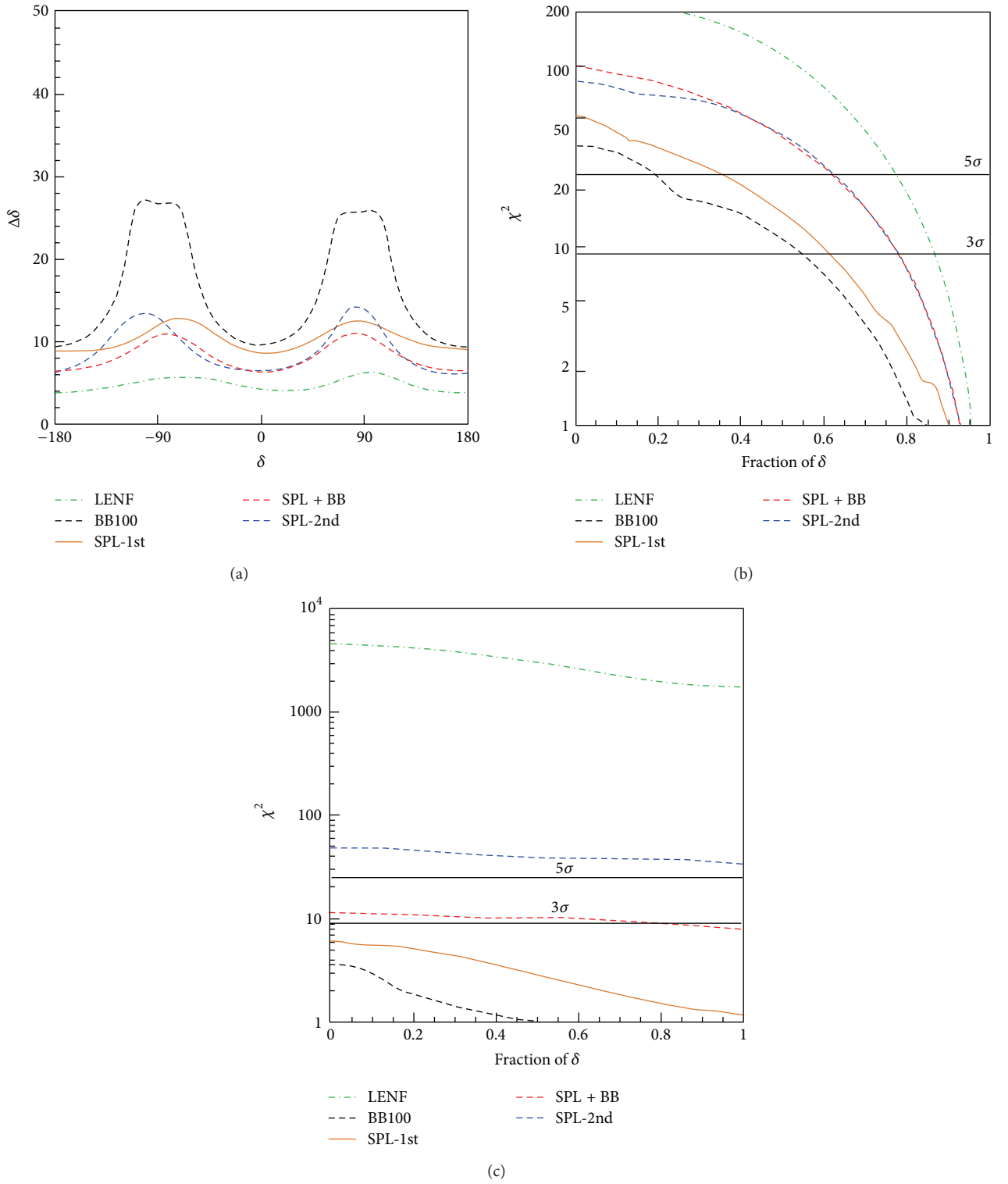


FIGURE 22: Summary of the physics performance of the facilities described in the text. (a) The  $1\sigma$  measurement errors for the CP angle  $\delta$  as a function of  $\delta$ . (b) The range of  $\delta$  for which a 3 and 5 $\sigma$  measurements of  $\delta$  can be made. (c) The range of  $\delta$  for which 3 and 5 $\sigma$  measurements of the neutrino mass hierarchy can be made.

15 m. The baseline for both the Super Beam and Beta Beam facilities is the MEMPHYS detector [36] in the Fréjus tunnel. This will be a 500 kT fiducial mass water Cherenkov detector. Note that using the same detector would make it possible to run the Super Beam and Beta Beam at the same time. Near detectors have also been designed for all three facilities.

**4.1.5. EUROnu Physics.** The physics group in EUROnu is determining the physics reach of each facility and combination of facilities using the parameters provided for the accelerators and detectors. They also assess and include the corresponding systematic errors in a uniform way and optimize performance based on information from other experiments. Following the recent indications of large  $\theta_{13}$ , they have now started a physics reach comparison between the EUROnu facilities and a number of others. Preliminary examples of this work are shown in Figure 22 [48]. The facilities being considered are the following.

- (i) LENF: the low-energy neutrino Factory, with a 10 GeV muon energy,  $1.4 \times 10^{21}$  decays per year and a single 100 kt mass MIND detector at a baseline of 2000 km.
- (ii) BB100: a  $\gamma = 100$  Beta Beam, with  $1.3/3.5 \times 10^{18}$  decays per year of Ne/He, a  $10^{-2}$  atmospheric background suppression, and a 500 kt water Cherenkov detector at Fréjus.
- (iii) SPL-1st: a 4 MW SPL Super Beam with 500 kt water Cherenkov detector at Fréjus, corresponding approximately to the first oscillation maximum.
- (iv) SPL-2nd: as above, but with the detector at Canfranc, corresponding to approximately the second oscillation maximum.
- (v) SPL+BB: the combination of BB100 and SPL-1st.

For the low-energy Neutrino Factory, the signal systematic error used is 2.4%, while it is 5% for the other facilities. The systematic error used for the background in all cases is 10% and 10-year running time is assumed.

**4.1.6. Costing and Safety.** The EUROnu comparative costing is based on the three facilities being located at CERN, to put the costing on the same basis. Similar assumptions are being made and common costs are being used wherever possible. It is being overseen by a costing panel. To complement this, the major safety aspects and technical risks of the facilities are being assessed. As only limited resources are available, the emphasis in costing is to achieve the best relative precision between the facilities. The same principle is being applied for the safety assessment. It will use existing experience, where that exists. The technical risks will be assessed by the facilities at the end of the design study.

**4.2. LAGUNA and LAGUNA-LBNO.** Neutrinos are messengers from astrophysical objects as well as from the early universe and can give us information on processes, which cannot be studied otherwise. Underground experiments, like

Super-Kamiokande (SK) [49], have made important discoveries. Next-generation very-large-volume underground experiments will answer fundamental questions on particle and astroparticle physics. The construction of a large-scale detector devoted to particle and astroparticle physics in Europe is one of the priorities of the ASPERA [50] roadmap (2008). These detectors will search for a possible finite lifetime for the proton with a sensitivity one order of magnitude better than the current limit. With a neutrino beam they will measure in a complementary way the mixing angle ( $\theta_{13}$ ) of neutrinos, the hierarchy of the mass eigenstates and unveil through neutrino oscillations the existence of CP violation in the leptonic sector, which in turn could provide an explanation of the matter-antimatter asymmetry in the Universe. Moreover, they will study astrophysical objects, in particular the Sun and Supernovae [51, 52]. The FP7 Design Studies LAGUNA (2008–2011) [53–55] and LAGUNA-LBNO (2011–2014) [56] support studies of European research infrastructures in deep underground cavities able to host a very large multipurpose next-generation neutrino observatory—GLACIER (liquid argon) [57], LENA (liquid scintillator) [58], and MEMPHYS (water Cherenkov) [36, 59].

The FP7 Design Study LAGUNA (2008–2011) was a Pan-European effort of 21 beneficiaries, composed of academic institutions from Denmark, Finland, France, Germany, Poland, Spain, Switzerland, and UK, as well as industrial partners specialized in civil and mechanical engineering and rock mechanics. The goal of the study was to assess the feasibility of this research infrastructure in Europe and the related costs.

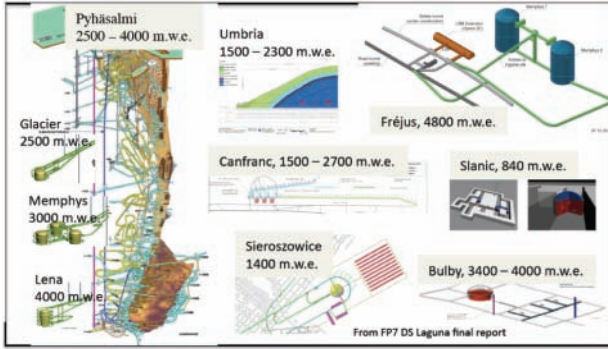
The LAGUNA consortium has evaluated possible extensions of the existing deep underground laboratories in Europe: Boulby (UK), Canfranc (Spain), and Modane (France) and considered the creation of new laboratories in the following sites: *Caso Umbria* Region (Italy), *Pyhäsalmi* (Finland), *Sieroszowice* (Poland), and *Slanic* (Romania). In Europe there are three different proposed detectors: GLACIER, LENA, and MEMPHYS. For all three detectors there are, in the LAGUNA context, specific studies concerning the construction feasibility, the required depth, the muon and reactor neutrino flux, and so forth. In Figure 23, the seven sites are shown, as well as an example of the construction studies developed by the different beneficiaries. The main conclusion of the LAGUNA study is that from a rock mechanical point of view all the proposed excavations are possible. Detailed cost estimations for the site construction and estimations for the detector constructions have been delivered. It turned out that the cavern construction itself is not the most important cost driver in such future project. In order to make a realistic overall cost estimation, the detector construction costs and the costs related to the operation of the infrastructure for at least 30 years or more have to be studied in more detail. Furthermore, the physics potential of each combination of site and detector has to be investigated in detail and in a common way. This led the collaboration to propose the second phase study: LAGUNA-LBNO, which was accepted within the European FP7 framework.

The LAGUNA collaboration decided to go ahead with a new study, LAGUNA-LBNO (2011–2014) to investigate two





(a)



(b)

FIGURE 23: (a) Map of the seven possible underground sites in Europe. (b) Exemplary layouts studied in LAGUNA DS for each site.

sites in detail: the shortest baseline from CERN, Fréjus at 130 km with no matter effect and therefore providing a clean measurement of CP violation and the longest baseline at Pyhäsalmi (2300 km) with matter effects and therefore able to determine the mass hierarchy. A third site, Umbria in Italy at 730 km from CERN, is investigated with lower priority. Umbria is a green field location in the existing CERN-CNGS beam.

LAGUNA-LBNO is a collaboration of about 300 physicists and engineers from 13 countries including 39 research institutions and industrial partners. Two non-European countries, Japan and Russia, are partners of the project. LAGUNA-LBNO will provide a realistic scheme for the tank construction and the costing of the detector itself. The costs involved with liquid procurement and long-term running of the new underground laboratory will be evaluated. New beam options based on the existing CERN accelerator complex are investigated and the physics potential of each detector option at the two locations will be studied.

At the Pyhäsalmi site, two options are studied: a 50 kt liquid scintillator detector (LENA) and the GLACIER detector with 20 kt and 50 kt liquid argon for a staged instrumentation. Both detectors are located at a depth of roughly 4000 m.w.e. For the Fréjus site, the MEMPHYS project in combination with a  $\beta$ -Beam ( $\beta\beta$ ) or a Superbeam (SB) from CERN is under investigation. In parallel, a hybrid option of one or two

MEMPHYS tanks together with the LENA experiment will be investigated [60].

#### 4.3. The Three Detectors: GLACIER, LENA, and MEMPHYS.

The GLACIER (Giant Liquid Argon Charge Imaging Experiment) detector is based on a new liquid argon detector concept, scalable to a single unit of mass 100 kt: it relies on a cryogenic storage tank developed by the petrochemical industry (LNG technology) and on a novel method of operation called the LAr LEM-TPC. LAr LEM-TPCs operate in double phase with charge extraction and amplification in the vapor phase. The concept has been very successfully demonstrated on small prototypes: ionization electrons, after drifting in the LAr volume, are extracted by a set of grids into the gas phase and driven into the holes of a double-stage Large Electron Multiplier (LEM), where charge amplification occurs.

Effective extrapolation to the required scale needs concrete R&D. A ton-scale LAr LEM-TPC detector has been successfully operated at CERN in B182 within the CERN RE18 experiment (ArDM). The detector has been moved to the Canfranc underground laboratory in Spain to search for direct WIMP signals. In order to prove the performance for neutrino physics, additional dedicated test beam campaigns are being considered, to test and optimize the readout methods and to assess the calorimetric performance of such detectors. A 1kt detector can be built assuming the GLACIER design with a 12 m diameter and 10 m vertical drift. The layout of the GLACIER tank and its implementation in the Pyhäsalmi mine is shown in Figure 24.

Thanks to the very good imaging capabilities of the GLACIER detector in combination with a neutrino beam from CERN the experiment has outstanding physics potential. The high resolution of the detector allows the precise measurement of the first and second oscillation maximum and therefore the precise determination of  $\theta_{13}$ , the CP violating phase  $\delta$ , and the mass hierarchy.

As stated above, the GLACIER experiment is scalable and therefore a staged approach is actively developed. The first phase is a 20 kt double phase LAr LEM-TPC (GLACIER) combined with a magnetized muon detector (MIND). The beam is based on a conventional neutrino beam line with a baseline of 2300 km towards Pyhäsalmi, Finland (CN2PY) with protons from an upgraded CERN SPS (700 kW). An Expression of Interest has been submitted to the CERN SPSC for this project [62].

The experiment allows the precise determination of oscillation parameters by measuring all transition probabilities ( $\nu_\mu \rightarrow \nu_\mu, \nu_\mu \rightarrow \nu_\tau, \nu_\mu \rightarrow \nu_e$ ) with neutrinos and antineutrinos. It can achieve a precise determination of the neutrino mass hierarchy ( $5\sigma$  CL) within a few years. In about 10 years, 60% of the CP violation parameter space will be covered at 90% CL. In Figure 25, we show in the left panel the 68% and 90% CL contours for  $\delta_{CP}$  and in the right panel the potential to determine the mass hierarchy.

Thanks to the deep underground location, this initial phase can reach a number of outstanding physics goals.



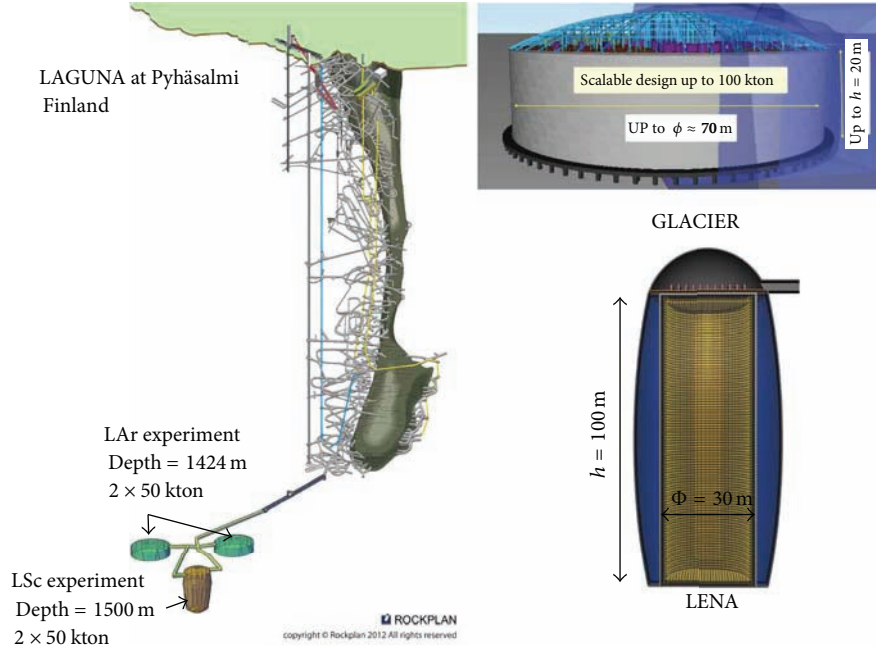


FIGURE 24: Schematic view of the Pyhäsalmi mine and the GLACIER and LENA detector with their access shafts.

The new underground neutrino observatory addresses the unification of elementary forces by searching for nucleon decay. The limit on the proton lifetime will be improved to  $\tau_p \geq 2 \times 10^{34}$  years in the channel  $p \rightarrow K\bar{\nu}$  at 90% CL. The first stage of GLACIER will contribute with major advances in the multimessenger neutrino astronomy with the detection of astrophysical and terrestrial neutrinos (solar, atmospheric neutrinos) and dark matter annihilation. GLACIER can detect neutrino bursts from galactic and extragalactic supernova which can unveil the mechanisms of the stellar collapse. For a supernova explosion at 10 kpc, 10,000 neutrino interactions will be recorded. Furthermore, 5600 atmospheric neutrino events per year will be measured.

In a second phase ( $\geq 2025$ ), the detector can be upgraded to reach the full size of 100 kt and the beam power will be increased with a HP-PS (2 MW) or a neutrino factory, for example, which allows 75% coverage of the CP violation parameter space at  $3\sigma$  CL [63].

The LENA (Low-Energy Neutrino Astronomy) detector design foresees the use of 50 kt of liquid scintillator (LSc) for neutrino detection. The LSc will be contained in a cylindrical concrete tank of 32 m diameter and 100 m height. Inside the detector tank, a scaffolding, optically separated from the tank walls will be installed as a framework for optical modules (OMs) facing the interior of the detector at a radius of 14 m. The PMT support structure is depicted in Figure 26(a).

The optical modules will contain 12'' PMTs equipped with Winston cones for light collection. They will be fully encapsulated for pressure resistance with an enclosed buffer of non-scintillating oil to impede  $\gamma$ -radiation from the PMT glass from reaching the scintillator. The setup of an OM is

shown in Figure 26(b). The design foresees the installation of 29600 OMs leading to an optical coverage of 30%.

The detector tank has to be placed in an underground cavern to provide shielding from cosmic radiation. The design foresees a volume around the detector tank to be filled with pure water acting as a Cherenkov veto for cosmic muons as well as a shielding for fast neutrons. The preferred locations are either in the Pyhäsalmi mine in central Finland, at a depth of 1400 m (4000 m.w.e.), or in the Laboratoire Souterrain de Modane adjacent to the Fréjus tunnel in the French-Italian Alps with a rock overburden corresponding to 4800 m.w.e. A detailed description of the LENA project can be found in [64].

The concept of neutrino spectroscopy has been successfully demonstrated by both KamLAND and Borexino. The low-energy threshold of LSc offers a wide range of physics based on neutrinos from terrestrial and astrophysical sources. The core research program will be the detection of neutrinos with energies reaching from sub-MeV to tens of MeV, but LENA can also contribute to several aspects of neutrino and particle physics associated to GeV energies.

The huge target mass of LENA gives the opportunity of a high statistics spectral measurement of the solar neutrino flux. Approx.  $10^4$  solar neutrino interactions per day allow for a measurement of the  $^7\text{Be}$  neutrino flux with an unprecedented accuracy. This offers the opportunity to search for temporal variations in the flux and thus to probe the effects of possible helioseismic g-modes [65]. A measurement of the up to now undetermined CNO neutrino flux would provide valuable information on the solar metallicity and fusion processes in the solar center. The high statistics spectral measurement of solar neutrinos will allow for a precise

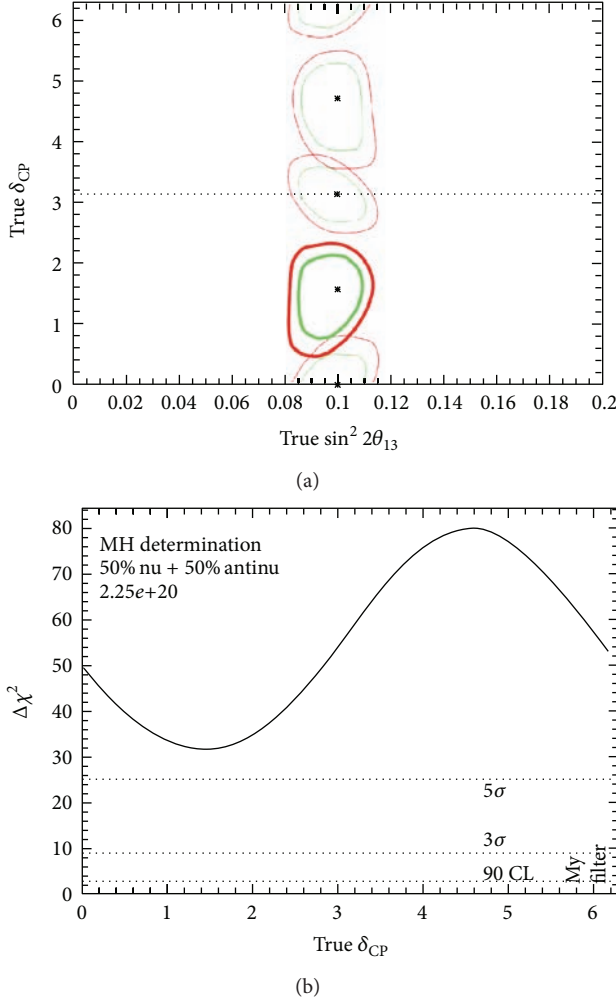


FIGURE 25: (a) The 68% and 90% CL contours in the  $\delta_{CP}$ - $\sin^2 2\theta_{13}$  plane. (b) Mass hierarchy determination at  $5\sigma$  [61].

determination of the  $\nu_e$  survival probability in the transition region between vacuum and matter dominated oscillations.

LENA offers excellent capabilities for the observation of a galactic core-collapse Supernova [64]. Different neutrino detection channels offer the opportunity to determine individual, time-dependent spectra for different neutrino types and thus allow for an energy and flavor resolved real-time analysis. For a standard Supernova in the center of our galaxy approx.  $10^4$  events are expected within a few seconds. These are predominately  $\bar{\nu}_e$  interactions; however, there will also be a large signal from  $\nu_\mu$  and  $\nu_\tau$  scattering on protons.

While the predicted rate of galactic Supernovae is about one to three per century, the isotropic neutrino background from Supernovae on cosmic scales is expected to provide a flux of approx.  $100 \nu/\text{cm}^2\text{s}$ . This so-called diffuse Supernova neutrino background (DSNB) has not yet been observed. Based on current models, LENA is almost certain to detect the  $\bar{\nu}_e$  component of the DSNB by looking in the energy window between 10 and 30 MeV formed by the reactor neutrino and atmospheric neutrino background. The expected event

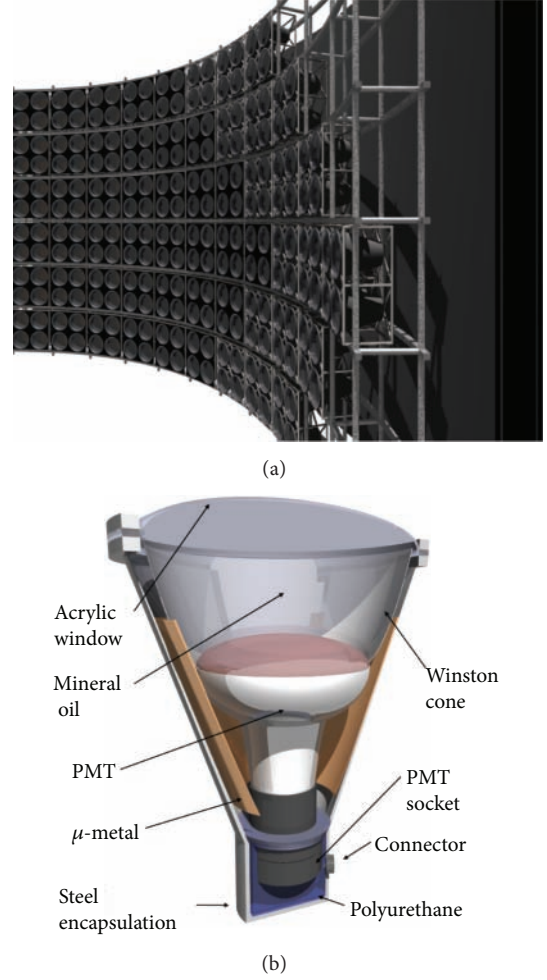


FIGURE 26: (a) The PMT support structure is optically shielded from the tank walls; (b) each optical module contains a fully enclosed PMT equipped with a Winston cone. Nonscintillating mineral oil is added to prevent gammas emerging from the PMTs from reaching the scintillator [64].

rate is of the order of 2 to 20 events per year, depending on the underlying Supernova model and Supernova rate [67].

The inverse beta decay offers an excellent detection channel for  $\bar{\nu}_e$  in LENA not only for Supernova physics. Because of the coincidence signal of the positron and the delayed neutron capture, this channel is virtually background-free. Due to the low detection threshold of 1.8 MeV, LENA will also be sensitive to geoneutrinos, expecting roughly 1000 events per year [68]. Geoneutrinos are produced in the decay of radioactive isotopes in the Earth's core, mantle, and crust. Measuring their spectra allows to determine the abundances of  $^{238}\text{U}$  and  $^{232}\text{Th}$  and their natural decay chains. The measurement of reactor  $\bar{\nu}_e$  offers the opportunity for precision measurement of  $\Delta m_{12}^2$  [69].

Furthermore, LENA allows for an indirect search for dark matter (DM) by observing neutrinos produced in the annihilation or decay of DM particles. LENA is especially sensitive in the region of 10 to 100 MeV which is not easily accessed by other experiments.

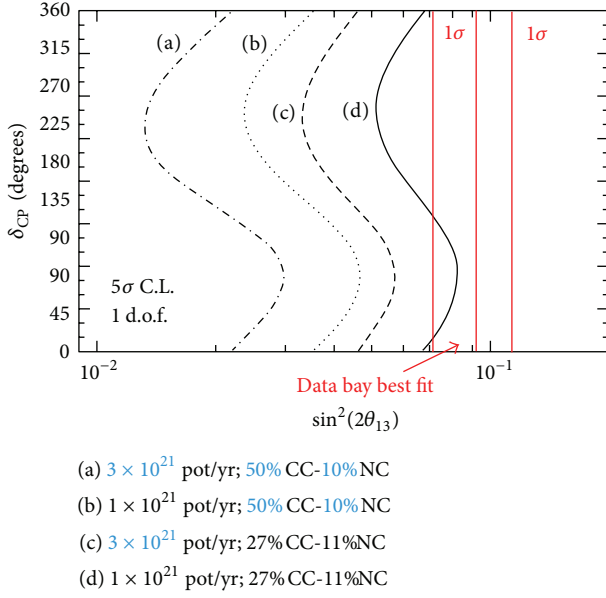


FIGURE 27: Sensitivity of LENA to the neutrino mass hierarchy for the 2288 km long-baseline CERN to Pyhäsalmi and for different detector and beam performances at 5σ CL. Detector performance parameters like the NC rejection efficiency are still under investigation [66].

Within LAGUNA-LBNO, the use of LENA as a target for a possible future neutrino beam is currently under investigation [71]. A realistic scenario is the use of a conventional  $\nu_\mu/\bar{\nu}_\mu$ -beam from CERN. Located in the Pyhäsalmi mine in central Finland, the LENA detector will be at a baseline distance to CERN of 2288 km. This corresponds to the first oscillation maximum of a  $\nu_\mu$  beam with an energy of 4.2 GeV. By searching for the appearance of  $\nu_e$  in the  $\nu_\mu$  beam, LENA can shed new light on the neutrino mass hierarchy and the neutrino mixing parameter  $\delta_{CP}$ . Figure 27 shows the sensitivity to the mass hierarchy. For the recently determined central value of  $\theta_{13}$ , LENA could determine the mass hierarchy at the 5σ CL level.

To reconstruct the complex vertices created by the interactions of GeV neutrinos, a reliable tracking and identification of all final state particles is needed. The possibility of particle tracking in unsegmented LSc detectors is currently investigated in a great effort, returning promising results on the neutrino energy reconstruction and NC background identification.

The NC/CC discrimination applied in this analysis relies on pulse shape analysis/tagging of muon decay electrons to suppress NC background events featuring charged pions and on a multivariate analysis (again relying mostly on pulse shape parameters) to distinguish  $\pi^0$  NC from  $\nu_e$  CC events. The combination 27% CC efficiency/11% residual NC (scenario “C” in Figure 27) corresponds to the most conservative scenario in which all CC  $\nu_e$  events also producing a charged pion are rejected. The more optimistic value of 50% CC efficiency assumes that they can be partly recovered.

When a high-energy charged particle passes through the LSc, it creates a superposition of spherical light waves,

forming a spherical backward running light front and a v-shaped forward light front resembling a Cherenkov cone, thus creating distinct arrival time patterns at the PMTs. Analyzing these patterns allows for a track reconstruction, as it has been shown for cosmic muons by KamLAND and Borexino. Recent studies investigate the capability of this method for  $\nu$  event reconstruction with increasing sophistication and accuracy. Figure 28 shows example tracks from the reconstruction of muons and electrons obtained by an algorithm capable of producing density profiles for the light emission inside the scintillator. Due to the broader and shorter profile of the emerging electromagnetic shower,  $e$  and  $\mu$  can be clearly distinguished.

Neutrino mixing parameters can also be determined in LENA using much shorter baselines. Based on high-intensity synchrotrons producing GeV protons,  $\bar{\nu}_\mu$  from the decay of stopped  $\pi^+$  can be used for an  $\bar{\nu}_\mu \leftrightarrow \bar{\nu}_e$  appearance experiment at baselines of the order of several km. As it has been demonstrated in the DAEδALUS proposal [72], a configuration using sources at three different baselines provides sensitivity to both  $\theta_{13}$  and  $\delta_{CP}$ , a measurement largely complementary to the long-baseline option. Furthermore, intense radioactive electron capture sources placed on top or inside the detector can be used to search for sterile neutrino oscillations at wavelengths of several meters by the observation of a spatial oscillation pattern inside the detector [73].

Last but not least, neutrino physics is not the only field where LENA can improve our current knowledge of elementary physics. Due to its high target mass and the excellent background discrimination, LENA is capable of increasing the limit of the proton lifetime to  $\tau_p \geq 4 \times 10^{34}$  years in the channel  $p \rightarrow K^+ \bar{\nu}$ , based on 10 years of measurement [74].

The LENA detector and its implementation in the Pyhäsalmi mine is shown in Figure 24.

The MEMPHYS (Megaton Mass Physics) project is discussed here with particular interest for deployment in an extended Modane Laboratory (LSM: Laboratoire Souterrain de Modane France), the distance from CERN being optimal for a low-energy neutrino beam [75]. Due to the short distance to CERN, this experiment has an excellent reach for leptonic CP violation search. The experiment is based on one of the most understood techniques for neutrino detection: Cherenkov light emission in water by charged particles resulting from neutrino interactions. At beam energies below 1 GeV, the water Cherenkov technique is well adapted to the physics scope of LAGUNA. Each tank of MEMPHYS is about 10 times Super-Kamiokande, and therefore only a mild extrapolation from an existing detector is necessary.

The project aims at a fiducial mass around half a megaton obtained with 2 cylindrical detector modules of 65 meters in diameter and 103 meters in height. A schematic view is shown in Figure 29. It takes into account the need to have a veto volume, 1.5 m thick, plus a minimal distance of about 2 meters between photodetectors and interaction vertices, leaving a sufficient space for ring development and to protect from  $\gamma$  from the PMTs natural radioactivity. The fiducial volume

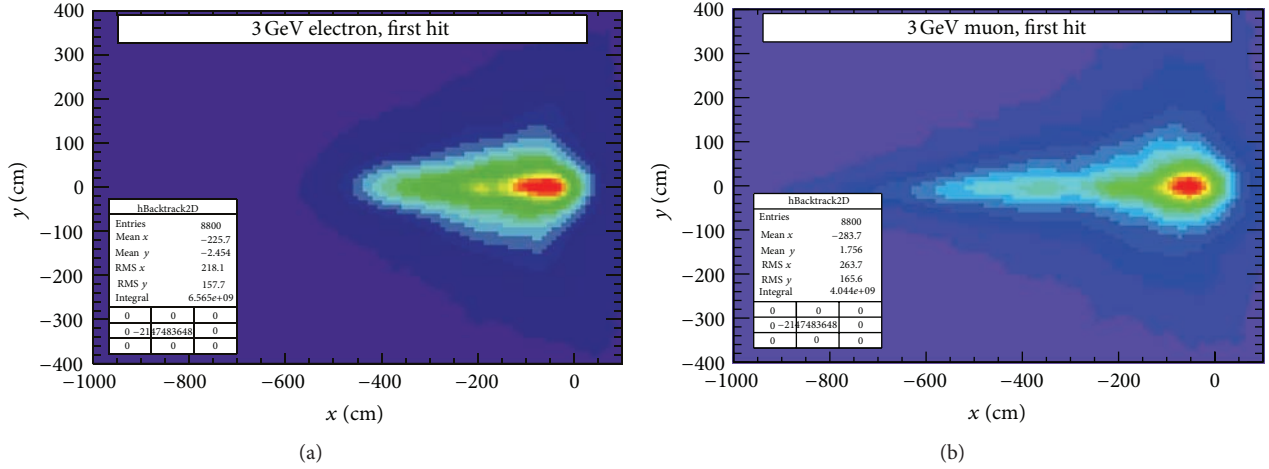


FIGURE 28: Visualization of the tracking for electron (a) and muon (b) events in LENA. The pictures show density profiles for the light emission inside the scintillator. Due to the broader and shorter profile of the emerging electromagnetic shower,  $e$  and  $\mu$  can be clearly distinguished [70].

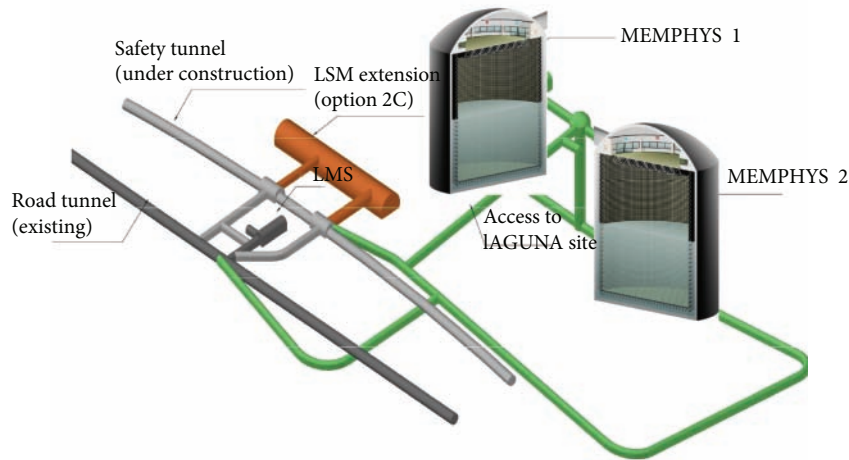


FIGURE 29: Possible layout for the future neutrino observatory at the Fréjus tunnel. The MEMPHYS detector is made of two independent tanks 60 m apart from each other. Each tank is 65 m in diameter and 103 m in height.

is 530 kilotons. The light sensors choice is to instrument the detector with photomultiplier tubes (PMTs) with a geometrical coverage of 30%. However, a number of technical aspects are under investigation. One of the challenges is the large number of photomultipliers required. The baseline design of MEMPHYS uses about 220,000  $8''$  PMTs.

For a MEMPHYS detector at the Fréjus site, situated at 130 km from CERN, the first peak of the neutrino oscillation probability occurs at a beam energy between 0.2 and 0.4 GeV. The sensitivity of the MEMPHYS experiment to CP violation is shown in Figure 30.

The deep underground position of the MEMPHYS neutrino observatory (4800 m.w.e.) allows a very rich nonaccelerator physics program. We summarize in Table 9 the results for nonaccelerator physics: the discovery potential of MEMPHYS for proton decay (90% CL in 10 years), the number of events for a supernova explosion at 10 kpc, the signal over background ratio for DSN neutrinos, and the rate

of solar, atmospheric, and reactor neutrinos in the detector per year. We assume an energy threshold of 5 MeV. The improvement of the new, optimized design (2 tanks 65 m  $\times$  10<sup>3</sup> m) for the detector is shown in the right column.

The coverage of large area with PMTs at a “low” cost implies a readout integrated electronics circuit (called ASIC) for groups of PMT (matrix of 4  $\times$  4). The development of such electronics is the aim of a dedicated French R&D program, called PMm<sup>2</sup> [76, 77]. The circuit under development allows to integrate for each group of PMTs: a high-speed discriminator on the signal photoelectron (ph.e), the digitization of the charge (on 12 bits ADC) to provide numerical signals, the digitization of time (on 12 bits TDC) to provide time information, a channel-to-channel gain adjustment, and a common high voltage. All the electronic and acquisition developed in the PMm<sup>2</sup> program is going to be fully tested with the MEMPHYS prototype installed at the APC laboratory. MEMPHYS is a test bench for any kind of light sensor



TABLE 9: Summary of nonaccelerator physics in MEMPHYS.

Topic	MEMPHYS (440 kt)	(~500 kt)
Proton decay:	In 10 years	In 10 years
$e^+ \pi^0$	$<1.0 \times 10^{35}$ [y] 90% CL	$\sim 1.2 \times 10^{35}$ [y] 90% CL
$\bar{\nu} K^+$	$<2 \times 10^{34}$ [y] 90% CL	$\sim 2.4 \times 10^{34}$ [y] 90% CL
SN $\nu$ (10 kpc):		
CC	$2.0 \times 10^5$ ( $\bar{\nu}_e$ )	$\sim 2.4 \times 10^5$ ( $\bar{\nu}_e$ )
ES	$1.0 \times 10^3$ (e)	$\sim 1.2 \times 10^3$ (e)
DSN $\nu$ (S/B 5 y)	(43–109)/47 (*)	(52–131)/57 (*)
Solar $\nu$		
$^8\text{B}$ ES	$1.1 \times 10^6$ per y	$\sim 1.3 \times 10^6$ per y
Atm. $\nu$ (per y)	$4.0 \times 10^4$	$\sim 4.8 \times 10^4$
Geo $\nu$	Needs 2 MeV thr.	Needs 2 MeV thr.
Reactor $\nu$ (per y)	$6.0 \times 10^4$ (*)	$\sim 7.2 \times 10^4$ (*)

The (\*) stands for the case where Gd salt is added to the water of one tank. The values on the right column are an extrapolation of the left ones.

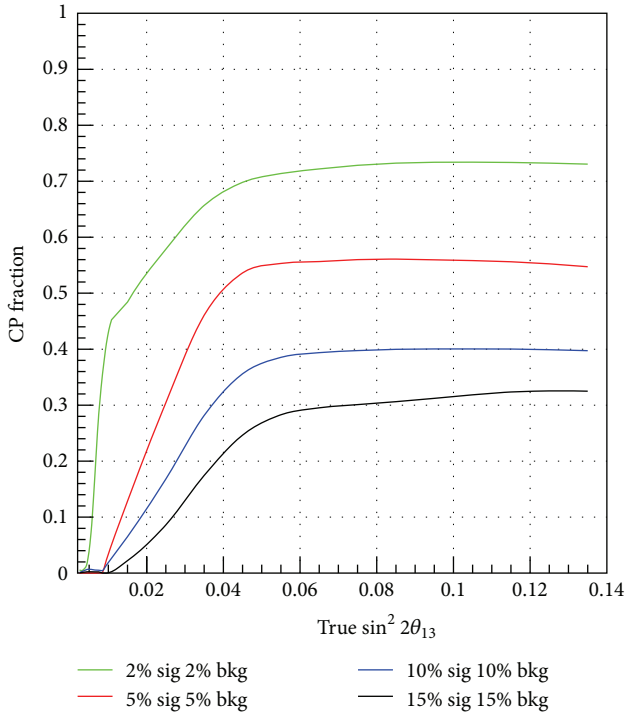


FIGURE 30: Sensitivity to leptonic CP violation of the MEMPHYS experiment at  $3\sigma$  for different assumptions on the systematic error for the signal (sig) and the background (bkg). The evaluation is based on the CERN to Fréjus Superbeam with 2 years running in neutrino mode and 8 years running in anti-neutrino mode.

or electronics solution for next-generation megaton size experiments. This prototype is realized with a PEHD (polyethylene) tank of  $2 \times 2 \times 2 \text{ m}^3$  filled with water and a hodoscope made by 4 scintillator planes (kindly donated by the OPERA [78] collaboration)—2 on the top and 2 on the bottom—for the trigger of the incoming cosmic muons. A schematic view of the Memphyno tank with the muon hodoscope (green) and the PMm2 matrix (read dots) is shown in Figure 31(a). In Figures 31(b) and 31(c), the PMT

matrix as well as the pressure resistant box for the electronics is shown.

The development on grouped electronics and photosensors is of very high interest for all the three detector options of the LAGUNA project. In particular the strong synergy with the LENA detector leads to a joint study within a collaborative effort between German and French groups [60].

In parallel to the development on photosensors and electronics, a large effort on the simulation of the detector performance is ongoing.

The neutrino event generator is based on GENIE [79] and the full simulation of the MEMPHYS detector is based on GEANT4 [80, 81]. The code has been developed starting from the Super-Kamiokande algorithm and adapted to the new geometry and PMT choice of MEMPHYS. A new event reconstruction algorithm for ring and vertex finding has been developed. Event reconstruction and analysis procedure have been essentially focalized on the reconstruction of the incoming neutrino energy and the identification of its flavor to perform appearance or disappearance analyses with the different types of beams. In order to properly take into account all the effects of the reconstruction, the detector performance has been conventionally described in terms of “migration matrices” representing the neutrino reconstructed energy versus the true one [82].

## 5. Conclusions

Neutrinos physics is one of the most dynamic and exciting fields of research in fundamental particle physics and astrophysics. The next-generation neutrino detector will address fundamental properties of the neutrino like mass hierarchy, the mixing angle  $\theta_{13}$ , and the CP phase. We will enter the era of precision measurement of all elements of the Pontecorvo-Maki-Nakagawa-Sakata (PMNS) matrix. A new deep underground neutrino observatory will allow neutrino astronomy with solar, atmospheric, and supernova neutrinos as well as the detection of geo-neutrinos in the case of the LENA detector. Such a new detector naturally allows for major improvements in the search for nucleon decay. A

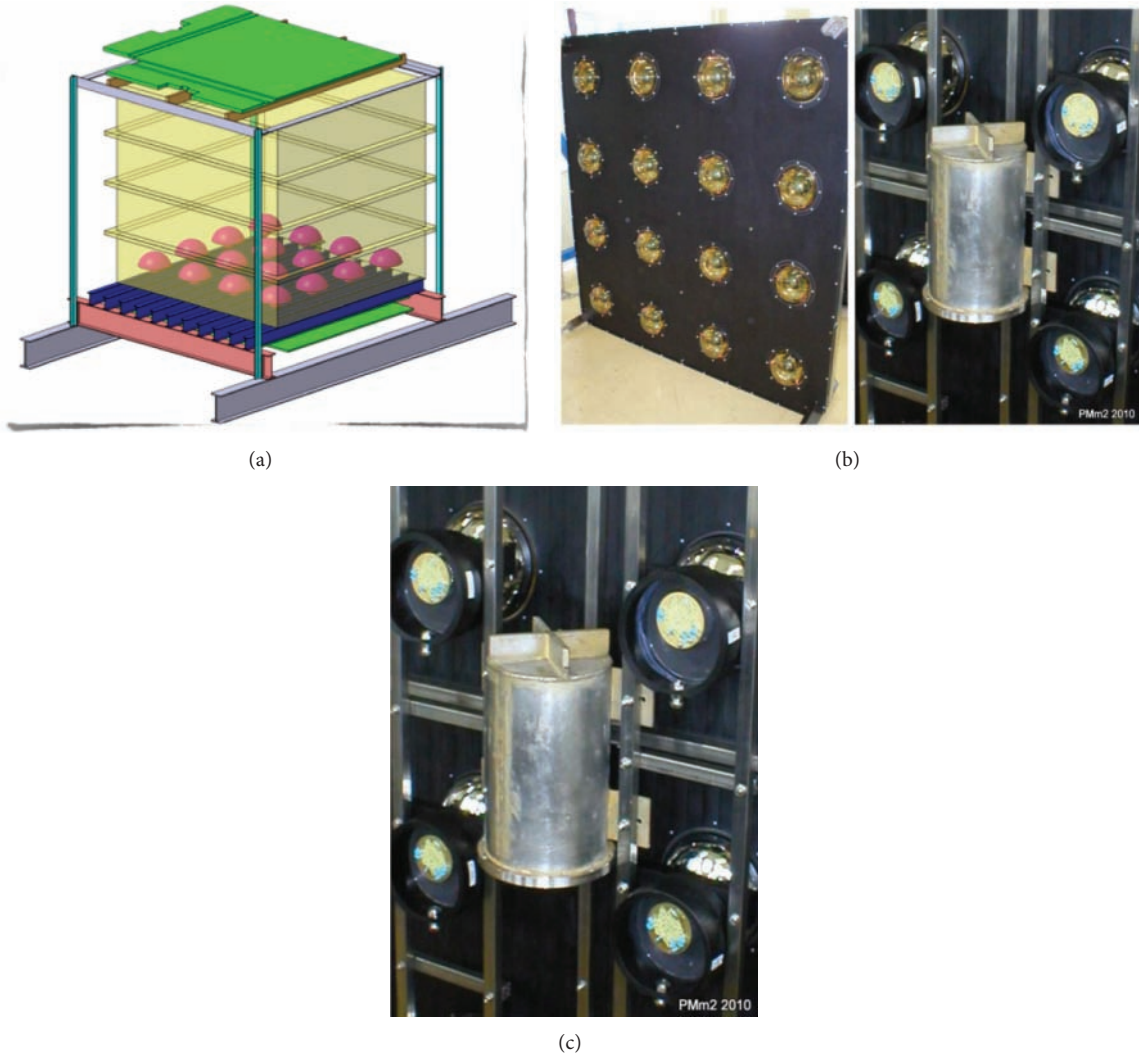


FIGURE 31: (a) Schematic view of the MEMPHYNO prototype. (b) Photograph of the PMm2 matrix of 16 8'' Hamamatsu PMTs. (c) Backside of the matrix showing the watertight box for the electronics.

next-generation neutrino observatory needs a huge, megaton scale detector which in turn has to be installed in a new, international underground laboratory, capable of hosting such a huge detector.

## Acknowledgments

The authors are grateful to the European Commission for the financial support of the project through the FP7 Design Studies LAGUNA (Project no. 212343), LAGUNA-LBNO (Project no. 284518), and EUROnu (Project no. 212372). The EC is not liable for any use that may be made of the information herein. They thank the French Centre National de Recherche Scientifique for the support of the project in form of the PICS. They are also grateful to the Japan Society for the Promotion of Science Grants-in-Aid for Scientific Research (Grant no. 23244058). This work was partially supported by the US Department of Energy.

## References

- [1] A. Badertscher, T. Hasegawa, T. Kobayashi et al., "A possible future long baseline neutrino and nucleon decay experiment with a 100 kton liquid argon TPC at Okinoshima using the J-PARC neutrino facility," <http://arxiv.org/abs/0804.2111>. In press.
- [2] K. Abe, T. Abe, H. Aihara et al., "Letter of intent: the hyperkamiokande experiment—detector design and physics potential," <http://arxiv.org/abs/1109.3262>. In press.
- [3] P. Adamson, C. Andreopoulos, R. Armstrong et al., "Measurement of the neutrino mass splitting and flavor mixing by MINOS," *Physical Review Letters*, vol. 106, Article ID 181801, 2011, <http://arxiv.org/abs/1103.0340>.
- [4] D. S. Ayres, G. R. Drake, M. C. Goodman et al., "The NOvA technical design report," Fermilab Design 2007-01, 2007.
- [5] K. S. McFarland and MINERvA Collaboration, "MINERvA: a dedicated neutrino scattering experiment at NuMI," *Nuclear Physics B*, vol. 159, pp. 107–112, 2006.
- [6] A. A. Aguilar-Arevalo, C. E. Anderson, and L. M. Bartoszek, "The MiniBooNE detector," *Nuclear Instruments and Methods in Physics Research Section A*, vol. 599, no. 1, pp. 28–46, 2009.

- [7] H. Chen, J. Farrell, F. Lanni et al., "Proposal for a new experiment using the booster and NuMI neutrino beamlines: Micro-BooNE," FERMILAB-PROPOSAL-0974, 2007.
- [8] K. N. Abazajian, M. A. Acero, S. K. Agarwalla et al., "Light sterile neutrinos: a white paper," <http://arxiv.org/abs/1204.5379>. In press.
- [9] W. J. Marciano, "Extra long baseline neutrino oscillations and CP violation," <http://arxiv.org/abs/hep-ph/0108181>. In press.
- [10] M. V. Diwan, D. Beavis, M.-C. Chen et al., "Very long baseline neutrino oscillation experiments for precise measurements of mixing parameters and CP violating effects," *Physical Review D*, vol. 68, Article ID 012002, 2003.
- [11] The US long-baseline study report, all associated documents, presentations, plots, studies, spectra, <http://www.phy.bnl.gov/~diwan/nwg/fnal-bnl>, Fermilab-0801-AD-E, BNL-77973-2007-IR, <http://arxiv.org/abs/0705.4396>.
- [12] M. V. Diwan, "The Case for a super neutrino beam," *Frascati Physics Series*, vol. 35, pp. 89–109, 2004, <http://arxiv.org/abs/quant-ph/0407047>.
- [13] National Research Council Report, *Neutrinos and Beyond, New Windows on Nature*, National Academy Press, 2003.
- [14] National Research Council, *An Assessment of the Science Proposed for the Deep Underground*, Science and Engineering Laboratory (DUSEL), National Research Council, National Academy Press, 2011.
- [15] Neutrino Scientific Assessment Group, *Recommendation to the Department of Energy and the National Science Foundation on the Future U.S. Program in Neutrino Oscillations*, Neutrino Scientific Assessment Group, 2007.
- [16] Report of the Particle Physics Projects Prioritization Panel, *U.S. Particle Physics: Scientific Opportunities. A Strategic Plan for the Next Ten Years*, 2008.
- [17] F. P. An, J. Z. Bai, H. R. Band et al., "Observation of electron-antineutrino disappearance at Daya Bay," *Physical Review Letters*, vol. 108, no. 17, Article ID 171803, 2012.
- [18] S. Nagaitsev, "Project X—a new multi-megawatt proton source at Fermilab," Tech. Rep. FERMILABCONF-11-092-AD, 2011.
- [19] The Conceptual Design Report for LBNE is available from Fermilab, <http://lbne.fnal.gov/reviews/CD1-review-top.shtml#DesignDocuments>.
- [20] A. Bernstein, M. Bishai, E. Blucher et al., "Report on the depth requirements for a massive detector at homestake," <http://arxiv.org/abs/0907.4183>. In press.
- [21] <http://www.fnal.gov/directorate/lbne/reconfiguration/>.
- [22] M. Bishai, M. V. Diwan, S. Kettell et al., "Neutrino oscillations in the precision era," <http://arxiv.org/abs/1203.4090>.
- [23] T. Akiri, D. Allspach, M. Andrews et al., "The 2010 interim report of the long-baseline neutrino experiment collaboration physics working groups," <http://arxiv.org/abs/1110.6249>.
- [24] P. Huber, J. Kopp, M. Lindner, and W. Winter, "GLoBES: general long baseline experiment simulator," PoS NUFAC 08, 145, 2008.
- [25] K. Abe, N. Abgrall, Y. Ajima et al., "Indication of electron neutrino appearance from an accelerator-produced off-axis muon neutrino beam," *Physical Review Letters*, vol. 107, Article ID 041801, 2011.
- [26] Y. Abe, C. Aberle, T. Akiri et al., "Indication of reactor  $\bar{\nu}_e$  disappearance in the double Chooz experiment," *Physical Review Letters*, vol. 108, no. 13, Article ID 131801, 7 pages, 2012.
- [27] F. P. An, J. Z. Bai, A. B. Balantekin et al., "Observation of electron-antineutrino disappearance at Daya Bay," *Physical Review Letters*, vol. 108, no. 17, Article ID 171803, 7 pages, 2012.
- [28] J. K. Ahn, S. Chebotaryov, J. H. Choi et al., "Observation of reactor electron antineutrinos disappearance in the RENO experiment," *Physical Review Letters*, vol. 108, no. 19, Article ID 191802, 6 pages, 2012.
- [29] K. Abeaw, N. Abgrallp, H. Aihara et al., "The T2K experiment," *Nuclear Instruments and Methods in Physics Research A*, vol. 659, no. 1, pp. 106–135, 2011.
- [30] T. Hasegawa, "Introductory remark on the first international workshop towards the giant liquid argon charge imaging experiment (GLA2010)," *Journal of Physics*, vol. 308, Article ID 012001, 2011.
- [31] D. Dwyer and Daya Bay collaboration, "Daya Bay results," in *Proceedings of the 25th International Conference on Neutrino Physics and Astrophysics*, Kyoto, Japan, June 2012.
- [32] M. Yoshioka, T. Hasegawa, O. Hirabayashi et al., "Okinoshima site study," *Journal of Physics*, vol. 308, no. 1, Article ID 012028, 2011.
- [33] A. Bueno, Z. Dai, Y. Ge et al., "Nucleon decay searches with large liquid Argon TPC detectors at shallow depths: atmospheric neutrinos and cosmogenic backgrounds," *Journal of High Energy Physics*, vol. 0704, article 041, 2007.
- [34] "EUROnu—A High Intensity Neutrino Oscillation Facility in Europe," FP7-INFRASTRUCTURES-2007-1, ref. 212372.
- [35] F. Gerigk et al., "Conceptual design of the SPL II: A high-power superconducting H-linac at CERN," CERN, 104 pages, 2006.
- [36] A. de Bellefon, J. Bouchez, J. Busto et al., "MEMPHYS: a large scale water Cherenkov detector at Frejus," <http://arxiv.org/abs/hepex/0607026>.
- [37] <https://www.ids-nf.org/wiki/FrontPage/Documentation/IDR>.
- [38] I. Efthymiopoulos, C. Hessler, H. Gaillard et al., "HiRadMat: a new irradiation facility for material testing at CERN," in *Proceedings of the 2nd International Particle Accelerator Conference*, p. TUPS058, San Sebastian, Spain, September 2011.
- [39] A. Pardons et al., "Horn Operational Experience in K2K, Mini-BooNE, NuMI and CNGS," in *Proceedings of the 10th International Workshop on Neutrino Factories, Superbeams and Betabeams*, p. 96, Valencia, Spain, June 2008.
- [40] M. Bogomilov et al., "The MICE Muon Beam on ISIS and the beam-line instrumentation of the muon ionization cooling experiment," <http://arxiv.org/abs/1203.4089>.
- [41] K. Yonehara, "Recent progress of RF Cavity Study at mucool test area," <http://arxiv.org/ftp/arxiv/papers/1201/1201.5903.pdf>.
- [42] R. Barlow et al., "EMMA: the worlds first non-scaling FFAG," *Nuclear Instruments and Methods in Physics Research A*, vol. 624, pp. 1–19, 2010.
- [43] P. Zucchelli, "A novel concept for a  $\bar{\nu}_e/\nu_e$  neutrino factory: the beta beam," *Physics Letters B*, vol. 532, pp. 166–172, 2002.
- [44] M. Benedikt et al., "Conceptual design report for a Beta-Beam facility," *The European Physical Journal A*, vol. 47, article 24, 2011.
- [45] C. Rubbia, A. Ferrari, Y. Kadi et al., "Beam cooling with ionisation losses," *Nuclear Instruments and Methods in Physics A*, vol. 568, pp. 475–487, 2006.
- [46] L. Arnaudon et al., "The LINAC4 Project at CERN," in *Proceedings of the 2nd International Particle Accelerator Conference*, San Sebastian, Spain, September 2011.
- [47] K. Habig, "MINOS neutrino oscillation results," *Journal für die Reine und Angewandte Mathematik*, vol. 668, pp. 149–190, 2012.
- [48] E. Fernandez-Martinez, P. Coloma, and P. Hernandez, "Physics comparison: future facilities in Europe and elsewhere," in *Proceedings of the 4th Annual EUROnu Meeting*, Paris, France, June 2012.
- [49] S. Fukuda, Y. Fukudaa, T. Hayakawa et al., "The super-kamiokande detector," *Nuclear Instruments and Methods in Physics Research Section A*, vol. 501, article 418, 2003.
- [50] "ASPERA," <http://www.aspera-eu.org>.
- [51] W. D. Arnett and J. L. Rosner, "Neutrino mass limits from SN1987a," *Physical Review Letters*, vol. 58, article 1906, 1987.



- [52] K. S. Hirata, T. Kajita, M. Koshiba et al., “Observation in the Kamiokande-II detector of the neutrino burst from supernova SN, 1987a,” *Physical Review D*, vol. 38, pp. 448–458, 1988.
- [53] Laguna FP7 design study, Grant Agreement 212343.
- [54] D. Autiero, J. Aysto, A. Badertscher et al., “Large underground, liquid based detectors for astro-particle physics in Europe: scientific case and proposals,” *Journal of Cosmology and Astroparticle Physics*, vol. 0711, Article ID 011, 2007.
- [55] T. Patzak et al., “LAGUNA: future megaton detectors in Europe,” *Journal of Physics*, vol. 309, Article ID 012022, 2011.
- [56] LAGUNA-LBNO FP7 design study, Grant agreement 284518.
- [57] A. Rubbia, “Underground neutrino detectors for particle and astroparticle science: the Giant Liquid Argon Charge Imaging Experiment (GLACIER),” *Journal of Physics*, vol. 171, Article ID 012020, 2009.
- [58] L. Oberauer, F. von Feilitzsch, and W. Potzel, “A large liquid scintillator detector for low-energy neutrino astronomy,” *Nuclear Physics*, vol. 138, pp. 108–111, 2005.
- [59] J. L. Borne, J. Busto, J.-E. Campagne et al., “The MEMPHYS project,” *Nuclear Instruments and Methods in Physics Research Section A*, vol. 639, pp. 287–289, 2011.
- [60] PICS (Projet international de cooperation scientifique) Grant Agreement 5226.
- [61] A. Rubbia, “Future liquid Argon detectors,” in *Proceedings of the 25th International Conference on Neutrino Physics and Astrophysics*, Kyoto, Japan, June 2012.
- [62] A. Stahl, C. Wiebusch, A. M. Guler et al. et al., “Expression of interest for a very long baseline neutrino oscillation experiment (LBNO),” Tech. Rep. CERN-SPSC-2012-021, SPSC-EOI-007, 2012.
- [63] A. Rubbia, “Underground neutrino detectors for particle and astroparticle Science: the Giant Liquid Argon Charge Imaging Experiment (GLACIER),” *Journal of Physics*, vol. 171, Article ID 012020, 2009.
- [64] M. Wurm, F. John Beacom, B. Leonid Bezrukov et al., “The next-generation liquid-scintillator neutrino observatory LENA,” *Astropart Physics*, vol. 35, pp. 685–732, 2012.
- [65] M. Wurm, B. Caccianiga, D. D’Angelo et al., “Search for modulations of the solar Be-7 ux in the next-generation neutrino observatory LENA,” *Physical Review D*, vol. 83, Article ID 032010, 2011.
- [66] C. Hagner, “LENA-Low Energy Neutrino Astronomy,” in *Proceedings of the Neutrino Town Meeting*, CERN, May 2012.
- [67] M. Wurm, F. von Feilitzsch, M. Göger-Neff et al., “Detection potential for the diffuse supernova neutrino background in the large liquid-scintillator detector LENA,” *Physical Review D*, vol. 75, Article ID 023007, 2007.
- [68] K. A. Hochmuth, F. V. Feilitzsch, B. D. Fields et al., “Probing the Earths interior with a large-volume liquid scintillator detector,” *Astroparticle Physics*, vol. 27, pp. 21–29, 2007.
- [69] S. T. Petcov and T. Schwetz, “Precision measurement of solar neutrino oscillation parameters by a long-baseline reactor neutrino experiment in Europe,” *Physics Letters B*, vol. 642, pp. 487–494, 2006.
- [70] Private communication from K. Loo, Department of Physics, University of Jyväskylä, Finland.
- [71] P. Coloma, T. Li, and S. Pascoli, “Long-baseline super-beam experiments in Europe within LAGUNA,” <http://arxiv.org/abs/1110.1402>.
- [72] J. Alonso, F. T. Avignone, W. A. Barletta et al., “Expression of interest for a novel search for CP violation in the neutrino sector: DAEdALUS,” <http://arxiv.org/abs/1006.0260>.
- [73] N. Yu. Novikov, T. Enqvist, A. N. Erykalov et al., “Neutrino oscillometry at the next generation neutrino observatory,” <http://arxiv.org/abs/1110.2983>.
- [74] T. Marrodán Undagoitia, von Feilitzsch, M. Goger-Neff et al., “Search for the proton decay  $P \rightarrow K^+ \text{ anti-}\nu$  in the large liquid scintillator low energy neutrino astronomy detector LENA,” *Physical Review D*, vol. 72, Article ID 075014, 2005.
- [75] J.-E. Campagne, M. Maltoni, M. Mezzetto et al., “Physics potential of the CERN-MEMPHYS neutrino oscillation project,” *Journal of High Energy Physics*, vol. 704, Article ID 003, 2007.
- [76] B. Genolini, P. Barrillon, S. Blin et al., “PMm\*\*2: large photo-multipliers and innovative electronics for the next-generation neutrino experiments,” *Nuclear Instruments and Methods in Physics A*, vol. 610, pp. 249–252, 2009.
- [77] J. E. Campagne, S. Conforti Di Lorenzo, S. Drouet et al., “PMm\*\*2: R&D on trigger less acquisition for the next generation neutrino experiments,” *JINST*, vol. 6, 2011.
- [78] OPERA Proposal, CERN/SPSC, 2000-028, SPSC/P318, LNGS P25/2000.
- [79] C. Andreopoulos, A. Bell, D. Bhattacharya et al., “The GENIE neutrino monte carlo generator,” *Nuclear Instruments and Methods A*, vol. 614, pp. 87–104, 2010.
- [80] S. Agostinelli, J. Allison, K. Amako et al., “GEANT4: a simulation toolkit,” *Nuclear Instruments and Methods A*, vol. 506, pp. 250–303, 2003.
- [81] J. Allison, K. Amako, Apostolakis, J et al., “GEANT4 developments and applications,” *IEEE Transactions on Nuclear Science*, vol. 53, pp. 270–278, 2006.
- [82] L. Agostino, M. Buizza-Avanzini, M. Dracos et al., “Study of the performance of a large scale water-Cherenkov detector (MEMPHYS),” <http://arxiv.org/abs/1206.6665>.



## Review Article

# The Era of Kilometer-Scale Neutrino Detectors

**Francis Halzen<sup>1</sup> and Uli Katz<sup>2</sup>**

<sup>1</sup> *Wisconsin IceCube Particle Astrophysics Center, University of Wisconsin-Madison, Madison, WI 53706, USA*

<sup>2</sup> *Erlangen Centre for Astroparticle Physics (ECAP), University of Erlangen-Nuremberg, 91058 Erlangen, Germany*

Correspondence should be addressed to Francis Halzen; [halzen@icecube.wisc.edu](mailto:halzen@icecube.wisc.edu)

Received 18 July 2012; Accepted 18 October 2012

Academic Editor: Jose Bernabeu

Copyright © 2013 F. Halzen and U. Katz. This is an open access article distributed under the Creative Commons Attribution License, which permits unrestricted use, distribution, and reproduction in any medium, provided the original work is properly cited.

Neutrino astronomy beyond the Sun was first imagined in the late 1950s; by the 1970s, it was realized that kilometer-scale neutrino detectors were required. The first such instrument, IceCube, transforms a cubic kilometer of deep and ultra-transparent Antarctic ice into a particle detector. KM3NeT, an instrument that aims to exploit several cubic kilometers of the deep Mediterranean sea as its detector medium, is in its final design stages. The scientific missions of these instruments include searching for sources of cosmic rays and for dark matter, observing Galactic supernova explosions, and studying the neutrinos themselves. Identifying the accelerators that produce Galactic and extragalactic cosmic rays has been a priority mission of several generations of high-energy gamma-ray and neutrino telescopes; success has been elusive so far. Detecting the gamma-ray and neutrino fluxes associated with cosmic rays reaches a new watershed with the completion of IceCube, the first neutrino detector with sensitivity to the anticipated fluxes. In this paper, we will first revisit the rationale for constructing kilometer-scale neutrino detectors. We will subsequently recall the methods for determining the arrival direction, energy and flavor of neutrinos, and will subsequently describe the architecture of the IceCube and KM3NeT detectors.

## 1. Introduction

Soon after the 1956 observation of the neutrino [1], the idea emerged that it represented the ideal astronomical messenger. Neutrinos travel from the edge of the Universe essentially without absorption and with no deflection by magnetic fields. Having essentially no mass and no electric charge, the neutrino is similar to the photon, except for one important attribute: its interactions with matter are extremely feeble. So, high-energy neutrinos may reach us unscathed from cosmic distances, from the inner neighborhood of black holes, and, hopefully, from the nuclear furnaces where cosmic rays are born. Their weak interactions also make cosmic neutrinos very difficult to detect. Immense particle detectors are required to collect cosmic neutrinos in statistically significant numbers [2]. By the 1970s, it was clear that a cubic-kilometer detector was needed to observe cosmic neutrinos produced in the interactions of cosmic rays with background microwave photons [3]. Newer estimates for observing potential cosmic accelerators such as Galactic supernova remnants and

gamma-ray bursts unfortunately point to the same exigent requirement [4–6]. Building a neutrino telescope has been a daunting technical challenge.

Given detector's required size, early efforts concentrated on transforming large volumes of natural water into Cherenkov detectors that catch the light produced when neutrinos interact with nuclei in or near the detector [7]. After a two-decade-long effort, building the Deep Underwater Muon and Neutrino Detector (DUMAND) in the sea off the main island of Hawaii unfortunately failed [8]. However, DUMAND paved the way for later efforts by pioneering many of the detector technologies in use today and by inspiring the deployment of a smaller instrument in Lake Baikal [9], as well as efforts to commission neutrino telescopes in the Mediterranean [10–12]. These have paved the way towards the construction of KM3NeT. The first telescope on the scale envisaged by the DUMAND collaboration was realized instead by transforming a large volume of the extremely transparent natural deep Antarctic ice into a particle detector, the Antarctic Muon and Neutrino Detector Array

(AMANDA). In operation since 2000, it represents a proof of concept for the kilometer-scale neutrino observatory, IceCube [13, 14].

Neutrino astronomy has already achieved spectacular successes: neutrino detectors have “seen” the Sun and detected a supernova in the Large Magellanic Cloud in 1987. Both observations were of tremendous importance; the former showed that neutrinos have a tiny mass, opening the first crack in the standard model of particle physics, and the latter confirmed the basic nuclear physics of the death of stars. Figure 1 illustrates the cosmic neutrino energy spectrum covering an enormous range, from microwave energies  $10^{-12}$  eV to  $10^{20}$  eV [15]. The figure is a mixture of observations and theoretical predictions. At low energy, the neutrino sky is dominated by neutrinos produced in the Big Bang. At MeV energy, neutrinos are produced by supernova explosions; the flux from the 1987 event is shown. The figure displays the measured atmospheric-neutrino flux up to energies of 100 TeV by the AMANDA experiment [16]. Atmospheric neutrinos are a key to our story, because they are the dominant background for extraterrestrial searches. The flux of atmospheric neutrinos falls dramatically with increasing energy; events above 100 TeV are rare, leaving a clear field of view for extraterrestrial sources.

The highest energy neutrinos in Figure 1 are the decay products of pions produced by the interactions of cosmic rays with microwave photons [17]. Above a threshold of  $\sim 4 \times 10^{19}$  eV, cosmic rays interact with the microwave background introducing an absorption feature in the cosmic-ray flux, the Greisen-Zatsepin-Kuzmin (GZK) cut-off. As a consequence, the mean free path of extragalactic cosmic rays propagating in the microwave background is limited to roughly 75 megaparsecs, and therefore, the secondary neutrinos are the only probe of the still-enigmatic sources at longer distances. What they will reveal is a matter of speculation. The calculation of the neutrino flux associated with the observed flux of extragalactic cosmic rays is straightforward and yields one event per year in a kilometer-scale detector. The flux, labeled GZK in Figure 1, shares the high-energy neutrino sky with neutrinos from gamma-ray bursts and active galactic nuclei [4–6].

## 2. The Cosmic-Ray Puzzle

Despite their discovery potential touching a wide range of scientific issues, the construction of ground-based gamma-ray telescopes and kilometer-scale neutrino detectors has been largely motivated by the possibility of opening a new window on the Universe in the TeV energy region and above. In this paper, we will revisit the prospects for detecting gamma rays and neutrinos associated with cosmic rays, thus revealing their sources at a time when we are commemorating the 100th anniversary of their discovery by Victor Hess in 1912. Unlike charges, cosmic rays, gamma rays, and neutrinos point back at their sources.

Cosmic accelerators produce particles with energies in excess of  $10^8$  TeV; we still do not know where or how [18–20]. The flux of cosmic rays observed at the Earth is shown

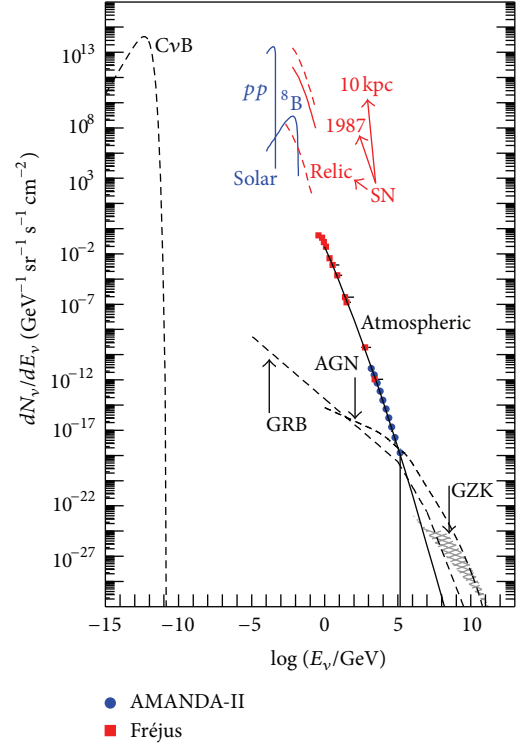


FIGURE 1: The cosmic-neutrino spectrum. Sources are the Big Bang (CvB), the Sun, supernovae (SN), atmospheric neutrinos, active galactic nuclei (AGN) galaxies, and GZK neutrinos. The data points are from detectors at the Fréjus underground laboratory [24] (red) and from AMANDA [16] (blue).

in Figure 2. The energy spectrum follows a sequence of three power laws. The first two are separated by a feature dubbed the “knee” at an energy (we will use energy units TeV, PeV, and EeV, increasing by factors of 1000 from GeV energy) of approximately 3 PeV. There is evidence that cosmic rays up to this energy are Galactic in origin. Any association with our Galaxy disappears in the vicinity of a second feature in the spectrum referred to as the “ankle”; see Figure 2. Above the ankle, the gyroradius of a proton in the Galactic magnetic field exceeds the size of the Galaxy, and we are witnessing the onset of an extragalactic component in the spectrum that extends to energies beyond 100 EeV. Direct support for this assumption now comes from three experiments [21–23] that have observed the telltale structure in the cosmic-ray spectrum resulting from the absorption of the particle flux by the microwave background, the so-called Greisen-Zatsepin-Kuzmin (GZK) cut-off. Neutrinos are produced in GZK interactions; it was already recognized in the 1970s that their observation requires kilometer-scale neutrino detectors. The origin of the cosmic-ray flux in the intermediate region covering PeV-to-EeV energies remains a mystery, although it is routinely assumed that it results from some high-energy extension of the reach of Galactic accelerators.

Acceleration of protons (or nuclei) to TeV energy and above requires massive bulk flows of relativistic charged

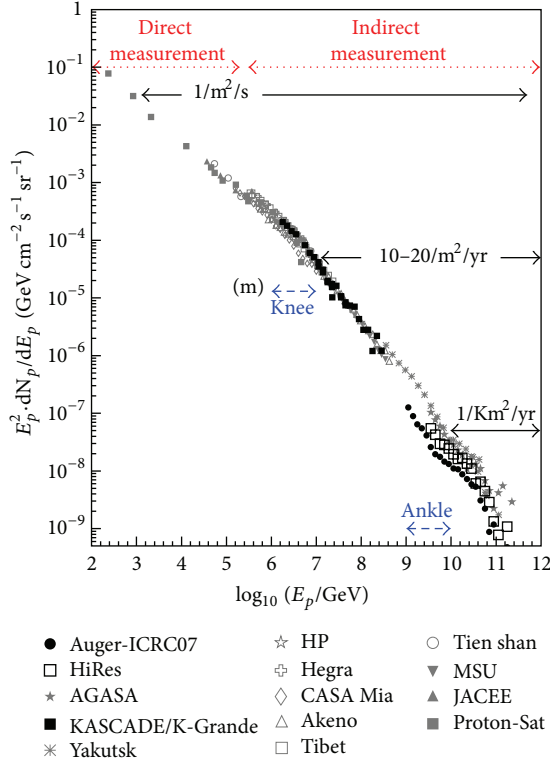


FIGURE 2: At the energies of interest here, the cosmic-ray spectrum follows a sequence of 3 power laws. The first 2 are separated by the “knee,” the 2nd and 3rd by the “ankle.” Cosmic rays beyond the ankle are a new population of particles produced in extragalactic sources.

particles. These are likely to originate from exceptional gravitational forces in the vicinity of black holes or neutron stars. The gravity of the collapsed objects powers large currents of charged particles that are the origin of high magnetic fields. These create the opportunity for particle acceleration by shocks. It is a fact that electrons are accelerated to high energy near black holes; astronomers detect them indirectly by their synchrotron radiation. Some must accelerate protons, because we observe them as cosmic rays.

The detailed blueprint for a cosmic-ray accelerator must meet two challenges: the highest energy particles in the beam must reach  $>10^3$  TeV ( $10^8$  TeV) for Galactic (extragalactic) sources and meet the total energy (luminosity) requirement to accommodate the observed cosmic-ray flux. Both represent severe constraints that have limited the imagination of theorists.

Supernova remnants were proposed as possible sources of Galactic cosmic rays as early as 1934 by Baade and Zwicky [25]; their proposal is still a matter of debate after more than 70 years [26]. Galactic cosmic rays reach energies of at least several PeV, the “knee” in the spectrum. Their interactions with Galactic hydrogen in the vicinity of the accelerator should generate gamma rays from the decay of secondary pions that reach energies of hundreds of TeV. Such sources should be identifiable by a relatively flat energy spectrum that extends to hundreds of TeV without attenuation, because

the cosmic rays themselves reach at least several PeV near the knee; they have been dubbed PeVatrons. The search to pinpoint them has so far been unsuccessful.

Although there is no incontrovertible evidence that supernovae accelerate cosmic rays, the idea is generally accepted because of energetics: three supernovae per century converting a reasonable fraction of a solar mass into particle acceleration can accommodate the steady flux of cosmic rays in the Galaxy. Originally, energetics also drove speculations on the origin of extragalactic cosmic rays.

By integrating the cosmic-ray spectrum in Figure 2 above the ankle, we find that the energy density of the Universe in extragalactic cosmic rays is  $\sim 3 \times 10^{-19}$  erg cm $^{-3}$  [27, 28]. The power required for a population of sources to generate this energy density over the Hubble time of  $10^{10}$  years is  $\sim 3 \times 10^{37}$  erg s $^{-1}$  per (Mpc) $^3$ . (In the astroparticle community, this flux is also known as  $5 \times 10^{44}$  TeV Mpc $^{-3}$  yr $^{-1}$ .) A gamma-ray burst (GRB) fireball converts a fraction of a solar mass into the acceleration of electrons, seen as synchrotron photons. The energy in extragalactic cosmic rays can be accommodated with the reasonable assumption that shocks in the expanding GRB fireball convert roughly equal energy into the acceleration of electrons and cosmic rays [29–31]. It so happens that  $\sim 2 \times 10^{52}$  erg per GRB will yield the observed energy density in cosmic rays after  $10^{10}$  years, given that the rate is of order 300 per Gpc $^3$  per year. Hundreds of bursts per year over Hubble time produce the observed cosmic-ray density, just like the three supernovae per century accommodate the steady flux in the Galaxy.

Problem solved? Not really: it turns out that the same result can be achieved assuming that active galactic nuclei (AGN) convert, on average,  $\sim 2 \times 10^{44}$  erg s $^{-1}$  each into particle acceleration. As is the case for GRB, this is an amount that matches their output in electromagnetic radiation. Whether GRB or AGN, the observation that these sources radiate similar energies in photons and cosmic rays is unlikely to be an accident. We will discuss the connection next; it will lead to a prediction of the neutrino flux.

### 3. Neutrinos (and Photons) Associated with Cosmic Rays

How many gamma rays and neutrinos are produced in association with the cosmic-ray beam? Generically, a cosmic-ray source should also be a beam dump. Cosmic rays accelerated in regions of high magnetic fields near black holes inevitably interact with radiation surrounding them, for example, UV photons in active galaxies or MeV photons in GRB fireballs. In these interactions, neutral and charged pion secondaries are produced by the processes

$$p + \gamma \longrightarrow \Delta^+ \longrightarrow \pi^0 + p, \quad p + \gamma \longrightarrow \Delta^+ \longrightarrow \pi^+ + n. \quad (1)$$

While secondary protons may remain trapped in the high magnetic fields, neutrons and the decay products of neutral and charged pions escape. The energy escaping the source is, therefore, distributed among cosmic rays, gamma rays, and

neutrinos produced by the decay of neutrons, neutral pions, and charged pions, respectively.

In the case of Galactic supernova shocks, discussed further on, cosmic rays mostly interact with the hydrogen in the Galactic disk, producing equal numbers of pions of all three charges in hadronic collisions  $p + p \rightarrow n[\pi^0 + \pi^+ + \pi^-] + X$ ;  $n$  is the pion multiplicity. These secondary fluxes should be boosted by the interaction of the cosmic rays with high-density molecular clouds that are ubiquitous in the star-forming regions where supernovae are more likely to explode. A similar mechanism may be relevant to extragalactic accelerators; here we will concentrate on the  $p\gamma$  mechanism, relevant, for instance, to GRB.

In a generic cosmic beam dump, accelerated cosmic rays, assumed to be protons for illustration, interact with a photon target. These may be photons radiated by the accretion disk in AGN and synchrotron photons that coexist with protons in the exploding fireball producing a GRB. Their interactions produce charged and neutral pions according to (1), with probabilities  $2/3$  and  $1/3$ , respectively. Subsequently, the pions decay into gamma rays and neutrinos that carry, on average,  $1/2$  and  $1/4$  of the energy of the parent pion. We here assume that the four leptons in the decay  $\pi^+ \rightarrow \nu_\mu + \mu^+ \rightarrow \nu_\mu + (e^+ + \bar{\nu}_e + \bar{\nu}_\mu)$  equally share the charged pion's energy. The energy of the pionic leptons relative to the proton is

$$x_\nu = \frac{E_\nu}{E_p} = \frac{1}{4} \langle x_{p \rightarrow \pi} \rangle \simeq \frac{1}{20}, \quad (2)$$

$$x_\gamma = \frac{E_\gamma}{E_p} = \frac{1}{2} \langle x_{p \rightarrow \pi} \rangle \simeq \frac{1}{10}. \quad (3)$$

Here,

$$\langle x_{p \rightarrow \pi} \rangle = \left\langle \frac{E_\pi}{E_p} \right\rangle \simeq 0.2 \quad (4)$$

is the average energy transferred from the proton to the pion. The secondary neutrino and photon fluxes are

$$\frac{dN_\nu}{dE} = 1 \frac{1}{3} \frac{1}{x_\nu} \frac{dN_p}{dE_p} \left( \frac{E}{x_\nu} \right), \quad (5)$$

$$\frac{dN_\gamma}{dE} = 2 \frac{2}{3} \frac{1}{x_\gamma} \frac{dN_p}{dE_p} \left( \frac{E}{x_\gamma} \right) = \frac{1}{8} \frac{dN_\nu}{dE}. \quad (6)$$

Here,  $N_\nu (= N_{\nu_\mu} = N_{\nu_e} = N_{\nu_\tau})$  represents the sum of the neutrino and antineutrino fluxes which are not distinguished by the experiments. Oscillations over cosmic baselines yield approximately equal fluxes for the 3 flavors.

It is important to realize that the high-energy protons may stay magnetically confined to the accelerator. This is difficult to avoid in the case of a GRB where they adiabatically lose their energy and trapped inside the fireball that expands under radiation pressure until it becomes transparent and produces the display observed by astronomers. Secondary neutrons (see (1)) do escape with high energies and decay

into protons that are the source of the observed extragalactic cosmic-ray flux:

$$\frac{dN_n}{dE} = 1 \frac{1}{3} \frac{1}{x_n} \frac{dN_p}{dE_p} \left( \frac{E}{x_n} \right), \quad (7)$$

with  $x_n = 1/2$ , the relative energy of the secondary neutron and the initial proton. For an accelerator blueprint where the accelerated protons escape with high energy, the energy in neutrinos is instead given by (5):

$$E^2 \frac{dN_\nu}{dE} = \frac{1}{3} x_\nu E_p^2 \frac{dN_p}{dE_p} (E_p) \quad (8)$$

resulting in a reduced neutrino flux compared to the neutron case. Identifying the observed cosmic-ray flux with the secondary neutron flux enhances the associated neutrino flux. For an accelerator with a generic  $E^{-2}$  shock spectrum where  $E_p^2 dN_p/dE_p$ , the energy of the particles, is constant, the neutron scenario leads to an increased neutrino flux by a factor  $3/x_n \simeq 6$ .

**3.1. Discussion.** The straightforward connection between the cosmic-ray, photon, and neutrino fluxes is subject to modification, both for particle-physics, and astrophysics reasons. From the particle-physic point of view, we assume that the initial proton interacts once and only once. If it interacts  $n_{\text{int}}$  times, a number that depends on the photon target density, (8), is generalized to

$$E_\nu^2 \frac{dN_\nu}{dE_\nu} = [1 - (1 - e^{-n_{\text{int}}})] \frac{1}{3} x_\nu E_p^2 \frac{dN_p}{dE_p} (E_p) f_{\text{GZK}} \quad (9)$$

$$\simeq n_{\text{int}} x_\nu E_p^2 \frac{dN_p}{dE_p} (E_p),$$

for  $n_{\text{int}}$  that is not too large. The additional factor  $f_{\text{GZK}} \simeq 3$  takes into account the fact that neutrinos, unlike protons, are not absorbed by the microwave background, and therefore, reach us from accelerators beyond a GZK proton absorption length of about 50 Mpc. The factor does vary with the specific redshift evolution of the sources considered. Waxman and Bahcall [29], Vietri [30], and Böttcher and Dermer [31] argued that for sources that are transparent to TeV gamma rays, the photon density is such that  $n_{\text{int}} < 1$  for protons, the heralded bound; indeed, the cross sections are such that the mean free path of photons by  $\gamma\gamma$  interactions at TeV energy is the same as for protons by  $p\gamma$  interactions at EeV. (For some reason, the factor  $1/3$  in (9) has been replaced by  $1/2$  in the original bound.) As was previously discussed, where secondary neutrons are the origin of the observed cosmic rays, the bound is increased. Sources with  $n_{\text{int}} > 1$  are referred to as obscured or hidden sources hidden in light, that is, Because IceCube has reached the upper limits of energy in cosmic neutrinos that are below either version of the bound, hidden sources do not exist, at least not the  $p\gamma$  version.

One can include photoproduction final states beyond the  $\Delta$ -resonance approximation that has been presented here [32].



There are also astrophysical issues obscuring the gamma-neutrino connection of (9), which only applies to the gamma-ray flux of pionic origin. Nonthermal sources produce gamma rays by synchrotron radiation, and their TeV fluxes can be routinely accommodated by scattering the photons on the electron beam to higher energy. Separating them from pionic photons has been somewhat elusive, and any application of (9) requires care.

The rationale for kilometer-scale neutrino detectors is that their sensitivity is sufficient to reveal generic cosmic-ray sources with an energy density in neutrinos comparable to their energy density in cosmic rays [27, 28] and pionic TeV gamma rays [33, 34].

#### 4. Sources of Galactic Cosmic Rays

The energy density of the cosmic rays in our Galaxy is  $\rho_E \sim 10^{-12} \text{ erg cm}^{-3}$ . Galactic cosmic rays are not forever; they diffuse within the microgauss fields and remain trapped for an average containment time of  $3 \times 10^6$  years. The power needed to maintain a steady energy density requires accelerators delivering  $10^{41} \text{ erg/s}$ . This happens to be 10% of the power produced by supernovae releasing  $10^{51} \text{ erg}$  every 30 years ( $10^{51} \text{ erg}$  correspond to 1% of the binding energy of a neutron star after 99% is initially lost to neutrinos). This coincidence is the basis for the idea that shocks produced by supernovae exploding into the interstellar medium are the accelerators of the Galactic cosmic rays.

Despite the rapid development of instruments with improved sensitivity, it has been impossible to conclusively pinpoint supernova remnants as the sources of cosmic rays by identifying accompanying gamma rays of pion origin. A generic supernova remnant releasing an energy of  $W \sim 10^{50} \text{ erg}$  into the acceleration of cosmic rays will inevitably generate TeV gamma rays by interacting with the hydrogen in the Galactic disk. The emissivity in pionic gamma rays  $Q_\gamma$  is simply proportional to the density of cosmic rays  $n_{\text{cr}}$  and to the target density  $n$  of hydrogen atoms. Here,  $n_{\text{cr}} \approx 4 \times 10^{-14} \text{ cm}^{-3}$  is obtained by integrating the proton spectrum for energies in excess of 1 TeV. For an  $E^{-2}$  spectrum,

$$Q_\gamma \approx c \left\langle \frac{E_\pi}{E_p} \right\rangle \lambda_{pp}^{-1} n_{\text{cr}} (> 1 \text{ TeV}) \approx 2c x_\gamma \sigma_{pp} n n_{\text{cr}}, \quad (10)$$

or

$$Q_\gamma (> 1 \text{ TeV}) \approx 10^{-29} \frac{\text{photons}}{\text{cm}^3 \text{ s}} \left( \frac{n}{1 \text{ cm}^{-3}} \right). \quad (11)$$

The proportionality factor in (10) is determined by particle physics;  $x_\gamma$  is the average energy of secondary photons relative to the cosmic-ray protons, and  $\lambda_{pp} = (n\sigma_{pp})^{-1}$  is the proton interaction length ( $\sigma_{pp} \approx 40 \text{ mb}$ ) in a density  $n$  of hydrogen atoms. The corresponding luminosity is

$$L_\gamma (> 1 \text{ TeV}) \approx Q_\gamma \frac{W}{\rho_E}, \quad (12)$$

where  $W/\rho_E$  is the volume occupied by the supernova remnant. We here made the approximation that the volume of the

young remnant is approximately given by  $W/\rho_E$  or that the density of particles in the remnant is not very different from the ambient energy density  $\rho_E \sim 10^{-12} \text{ erg cm}^{-3}$  of Galactic cosmic rays [4–6].

We thus predict [35, 36] a rate of TeV photons from a supernova at a nominal distance  $d$  of order 1 kpc of

$$\begin{aligned} \int_{E>1 \text{ TeV}} \frac{dN_\gamma}{dE_\gamma} dE_\gamma &= \frac{L_\gamma (> 1 \text{ TeV})}{4\pi d^2} \\ &\approx 10^{-12} - 10^{-11} \left( \frac{\text{photons}}{\text{cm}^2 \text{ s}} \right) \\ &\times \left( \frac{W}{10^{50} \text{ erg}} \right) \left( \frac{n}{1 \text{ cm}^{-3}} \right) \left( \frac{d}{1 \text{ kpc}} \right)^{-2}. \end{aligned} \quad (13)$$

As discussed in the introduction, the position of the knee in the cosmic-ray spectrum indicates that some sources accelerate cosmic rays to energies of several PeV. These PeVatrons, therefore, produce pionic gamma rays whose spectrum can extend to several hundred TeV without cutting off. For such sources, the  $\gamma$ -ray flux in the TeV energy range can be parametrized in terms of a spectral slope  $\alpha_\gamma$ , an energy  $E_{\text{cut},\gamma}$  where the accelerator cuts off and a normalization  $k_\gamma$

$$\frac{dN_\gamma(E_\gamma)}{dE_\gamma} = k_\gamma \left( \frac{E_\gamma}{\text{TeV}} \right)^{-\alpha_\gamma} \exp \left( -\sqrt{\frac{E_\gamma}{E_{\text{cut},\gamma}}} \right). \quad (14)$$

The estimate in (13) indicates that fluxes as large as  $dN_\gamma/dE_\gamma \sim 10^{-12} - 10^{-14} (\text{TeV}^{-1} \text{ cm}^{-2} \text{ s}^{-1})$  can be expected at energies of  $\mathcal{O}(10 \text{ TeV})$ .

We, therefore, concentrate on the search for PeVatrons, supernova remnants with the required energetics to produce cosmic rays, at least up to the “knee” in the spectrum. They may have been revealed by the highest energy all-sky survey in  $\sim 10 \text{ TeV}$  gamma rays from the Milagro detector [37]. A subset of sources, located within nearby star-forming regions in Cygnus and in the vicinity of Galactic latitude  $l = 40$  degrees, are identified; some cannot be readily associated with known supernova remnants or with nonthermal sources observed at other wavelengths. Subsequently, directional air Cherenkov telescopes were pointed at three of the sources, revealing them as PeVatron candidates with an approximate  $E^{-2}$  energy spectrum that extends to tens of TeV without evidence for a cut-off [38, 39], in contrast with the best studied supernova remnants RX J1713-3946 and RX J0852.0-4622 (Vela Junior).

Some Milagro sources may actually be molecular clouds illuminated by the cosmic-ray beam accelerated in young remnants located within  $\sim 100 \text{ pc}$ . One expects indeed that multi-PeV cosmic rays are accelerated only over a short time period when the shock velocity is high, that is, when the remnant transitions from free expansion to the beginning of the Sedov phase. The high-energy particles can produce photons and neutrinos over much longer periods when they diffuse through the interstellar medium to interact with nearby

molecular clouds [40]. An association of molecular clouds and supernova remnants is expected, of course, in star-forming regions. In this case, any confusion with synchrotron photons is unlikely.

Despite the rapid development of both ground-based and satellite-borne instruments with improved sensitivity, it has been impossible to conclusively pinpoint supernova remnants as the sources of cosmic-ray acceleration by identifying accompanying gamma rays of pion origin. In fact, recent data from Fermi LAT have challenged the hadronic interpretation of the GeV-TeV radiation from one of the best studied candidates, RX J1713-3946 [41]. In contrast, detecting the accompanying neutrinos would provide incontrovertible evidence for cosmic-ray acceleration. Particle physics dictates the relation between pionic gamma rays and neutrinos and basically predicts the production of a  $\nu_\mu + \bar{\nu}_\mu$  pair for every two gamma rays seen by Milagro. This calculation can be performed using the formalism discussed in the previous section with approximately the same outcome. Confirmation that some of the Milagro sources produced pionic gamma rays produced by a cosmic-ray beam is predicted to emerge after operating the complete IceCube detector for several years; see Figure 3.

The quantitative statistics can be summarized as follows. For average values of the parameters describing the flux, we find that the completed IceCube detector could confirm sources in the Milagro sky map as sites of cosmic-ray acceleration at the  $3\sigma$  level in less than one year and at the  $5\sigma$  level in three years [35]. We here assume that the source extends to 300 TeV or 10% of the energy of the cosmic rays near the knee in the spectrum. These results agree with previous estimates [42, 43]. There are intrinsic ambiguities in this estimate of an astrophysical nature that may reduce or extend the time required for a  $5\sigma$  observation [35]. Especially, the poorly known extended nature of some of the Milagro sources represents a challenge for IceCube observations that are optimized for point sources. In the absence of observation of TeV-energy supernova neutrinos by IceCube within a period of 10 years, the concept will be challenged.

## 5. Sources of the Extragalactic Cosmic Rays

Unlike the case for Galactic cosmic rays, there is no straightforward  $\gamma$ -ray path to the neutrino flux expected from extragalactic cosmic-ray accelerators. Neutrino fluxes from AGN are difficult to estimate. For GRB, the situation is qualitatively better, because neutrinos of PeV energy should be produced when protons and photons coexist in the GRB fireball [29]. As previously discussed, the model is credible because the observed cosmic-ray flux can be accommodated with the assumption that roughly equal energy is shared by electrons, observed as synchrotron photons and protons.

**5.1. GRB.** If GRB fireballs are the sources of extragalactic cosmic rays, the neutrino flux is directly related to the cosmic-ray flux. The relation follows from the fact that, for each

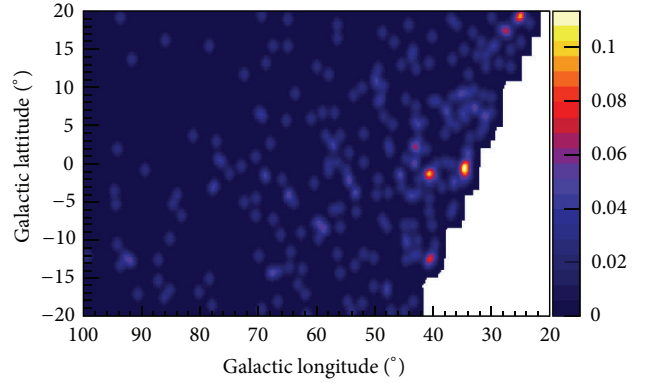


FIGURE 3: Simulated sky map of IceCube in Galactic coordinates after 5 years of operation of the completed detector. Two Milagro sources are visible with 4 events for MGRO J1852 + 01 and 3 events for MGRO J1908+06 with energy in excess of 40 TeV. These, as well as the background events, have been randomly distributed according to the resolution of the detector and the size of the sources.

secondary neutron decaying into a cosmic-ray proton, there are 3 neutrinos produced from the associated  $\pi^+$ :

$$E \frac{dN_\nu}{dE} = 3E_n \frac{dN_n}{dE_n}(E_n), \quad (15)$$

and, after oscillations, per neutrino flavor

$$E^2 \frac{dN_\nu}{dE} \simeq \left( \frac{x_\nu}{x_n} \right) E_n^2 \frac{dN_n}{dE_n}(E_n) f_{\text{GZK}}, \quad (16)$$

where the factor  $f_{\text{GZK}}$  is introduced for reasons explained in the context of (9).

An alternative approach is followed in routine IceCube GRB searches [44]: the proton content of the fireball is derived from the observed electromagnetic emission (the Band spectrum). The basic assumption is that a comparable amount of energy is dissipated in fireball protons and electrons, where the latter are observed as synchrotron radiation:

$$E^2 \frac{dN_\nu}{dE} = \left( \frac{\epsilon_p}{\epsilon_e} \right) \frac{1}{2} x_\nu \left[ E_\gamma^2 \frac{dN_\gamma}{dE_\gamma}(E_\gamma) \right]_{\text{syn}}, \quad (17)$$

where  $\epsilon_p$ ,  $\epsilon_e$  are the energy fractions in the fireball in protons and electrons [44].

The critical quantity normalizing the GRB neutrino flux is  $n_{\text{int}}$ ; its calculation is relatively straightforward. The phenomenology that successfully accommodates the astronomical observations is that of the creation of a hot fireball of electrons, photons, and protons that is initially opaque to radiation. The hot plasma, therefore, expands by radiation pressure, and particles are accelerated to a Lorentz factor  $\Gamma$  that grows until the plasma becomes optically thin and produces the GRB display. From this point on, the fireball coasts with a Lorentz factor that is constant and depends on its baryonic load. The baryonic component carries the bulk of the fireball's kinetic energy. The energetics and rapid

time structure of the burst can be successfully associated with successive shocks (shells), of width  $\Delta R$ , that develop in the expanding fireball. The rapid temporal variation of the gamma-ray burst,  $t_v$ , is of the order of milliseconds and can be interpreted as the collision of internal shocks with a varying baryonic load leading to differences in the bulk Lorentz factor. Electrons, accelerated by the first-order Fermi acceleration, radiate synchrotron gamma rays in the strong internal magnetic field and thus produce the spikes observed in the burst spectra.

The number of interactions is determined by the optical depth of the fireball shells to  $p\gamma$  interactions

$$n'_{\text{int}} = \frac{\Delta R'}{\lambda_{p\gamma}} = (\Gamma c t_v) (n'_\gamma \sigma_{p\gamma}). \quad (18)$$

The primes refer to the fireball rest frame; unprimed quantities are in the observer frame. The density of fireball photons depends on the total energy in the burst  $E_{\text{GRB}} \approx 2 \times 10^{52}$  erg, the characteristic photon energy of  $E_\gamma \approx 1$  MeV, and the volume  $V'$  of the shell:

$$n'_\gamma = \frac{E_{\text{GRB}}/E_\gamma}{V'}, \quad (19)$$

with

$$V' = 4\pi R'^2 \Delta R' = 4\pi (\Gamma^2 c t_v)^2 (\Gamma c t_v). \quad (20)$$

The only subtlety here is the  $\Gamma^2$  dependence of the shell radius  $R'$ ; for a simple derivation see Gaisser et al. [4], Learned and Mannheim [5], and Halzen and Hooper [6]. Finally, note that this calculation identifies the cosmic-ray flux with the fireball protons.

The back-of-the-envelope prediction for the GRB flux is given by (9) with  $n_{\text{int}} \approx 1$ , or

$$E^2 \frac{dN_\nu}{dE} \approx \frac{1}{3} x_\nu E_p^2 \frac{dN_p}{dE_p} (E_n) f_{\text{GZK}} \approx x_\nu E_p^2 \frac{dN_p}{dE_p} (E_n). \quad (21)$$

If one identifies the proton flux with neutrons escaping from the fireball, the calculation should be based on (16). This is almost certainly the correct procedure, as the protons lose their energy adiabatically with the expansion of the fireball. The neutrino flux is increased by a factor of approximately  $3/x_n \approx 6$ . This more straightforward approach has been pursued by Ahlers et al. [45].

For typical choices of the parameters,  $\Gamma \sim 300$  and  $t_v \sim 10^{-2}$  s, about 100 events per year are predicted in IceCube, a flux that is already challenged [45] by the limit on a diffuse flux of cosmic neutrinos obtained with one-half of IceCube in one year [46]. Facing this negative conclusion, Ahlers et al. [45] have investigated the dependence of the predicted neutrino flux on the cosmological evolution of the sources, as well as on the parameters describing the fireball, most notably  $E_{\text{GRB}}$ ,  $\Gamma$ , and  $t_v$ . Although these are constrained by the electromagnetic observations, and by the requirement that the fireball must accommodate the observed cosmic-ray spectrum, the predictions can be stretched to the point that it

will take 3 years of data with the now-completed instrument to conclusively rule out the GRB origin of the extragalactic cosmic rays; see Figure 4. Alternatively, detection of their neutrino emission may be imminent.

Is the GRB origin of sources of the highest energy cosmic rays challenged? Recall that calculation of the GRB neutrino flux is normalized to the observed total energy in extragalactic cosmic rays of  $\sim 3 \times 10^{49}$  erg cm $^{-2}$ , a value that is highly uncertain because it critically depends on the assumption that all cosmic rays above the ankle are extragalactic in origin. Also, the absolute normalization of the measured flux is uncertain. Although fits to the spectrum support this assumption [45], by artificially shifting the transition to higher energies above the knee, one can reduce the energy budget by as much as an order of magnitude. The lower value of  $0.5 \times 10^{44}$  TeV Mpc $^{-3}$  yr $^{-1}$  can be accommodated with a more modest fraction of  $\sim 2 \times 10^{51}$  erg (or  $\sim 1\%$  of a solar mass) going into particle acceleration in individual bursts. We will revisit this issue in the context of GZK neutrinos.

While this temporarily remedies the direct conflict with the present diffuse limit, IceCube has the alternative possibility to perform a direct search for neutrinos in spatial and time coincidence with GRB observed by the Swift and Fermi satellites; its sensitivity is superior by over one order of magnitude relative to a diffuse search. In this essentially background-free search, 14 events were expected when IceCube operated with 40 and 59 strings during 2 years of construction, even for the lowest value of the cosmic-ray energy budget of  $0.5 \times 10^{44}$  TeV Mpc $^{-3}$  yr $^{-1}$ . Two different and independent searches failed to observe this flux at the 90% confidence level [47]. IceCube has the potential to confirm or rule out GRB as the sources of the highest energy cosmic rays within 3 years of operation [45].

**5.2. Active Galaxies.** If, alternatively, AGN were the sources, we are in a situation where a plethora of models have produced a wide range of predictions for the neutrino fluxes; these range from unobservable to ruled out by IceCube data taken during construction. We, therefore, will follow the more straightforward path of deriving the neutrino flux from the TeV gamma-ray observations, as was done for supernova remnants. This approach is subject to the usual caveat that some, or all, of the photons may not be pionic in origin; in this sense, the estimate provides an upper limit. The proximity of the Fanaroff-Riley I (FRI) active galaxies Cen A and M 87 singles them out as potential accelerators [48, 49]. The Auger data provide suggestive evidence for a possible correlation between the arrival direction of 1–10 events and the direction of Cen A [48].

Interpreting the TeV gamma-ray observations is challenging because the high-energy emission of AGN is extremely variable, and it is difficult to compare multiwavelength data taken at different times. Our best guess is captured in Figure 5 where the TeV flux is shown along with observations of the multiwavelength emission of Cen A compiled by Lipari [50].

The TeV flux shown represents an envelope of observations.

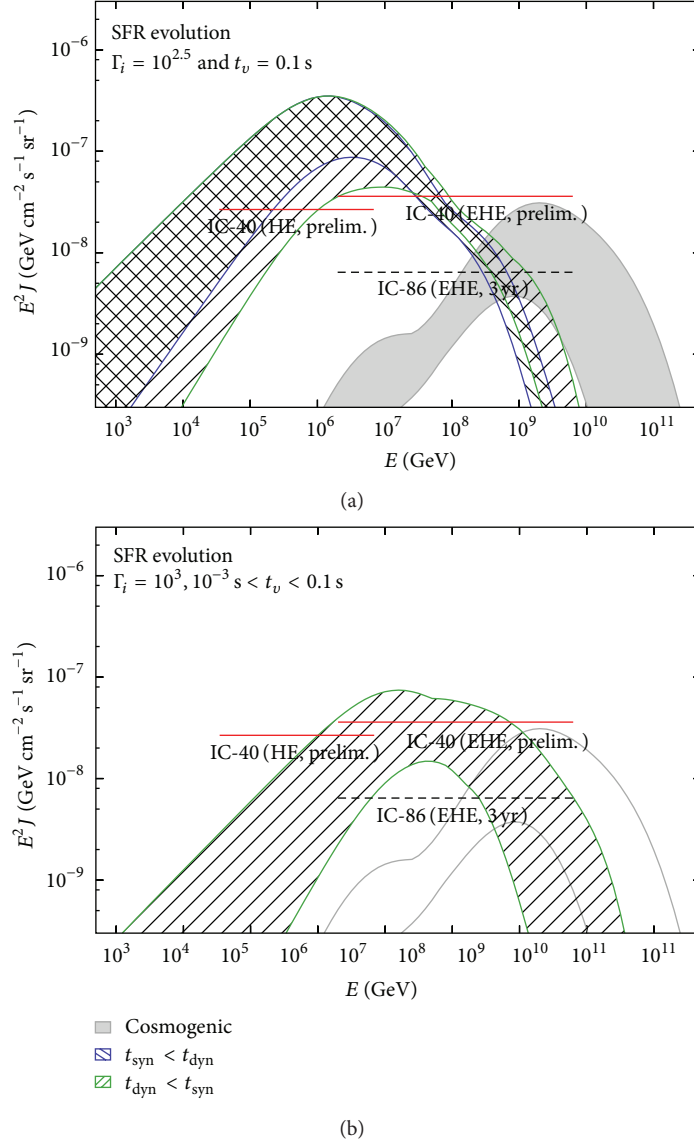


FIGURE 4: GRB neutrino spectra (the prompt spectrum emitted by the sources and neutrino spectrum generated in GZK interactions are shown separately), assuming the luminosity range  $0.1 < (\epsilon_B/\epsilon_e)L_{\gamma,52} < 10$  and star-forming redshift evolution of the sources. Here,  $\epsilon_{e,B}$  are the fractional energies in the fireball carried by the electrons and the magnetic field; the two are equal in the case of equipartition.  $L_{\gamma,52}$  is the photon energy in units of  $10^{52}$  erg. We show the prompt spectra separately for models where the fireball's dynamical time scale  $t_{\text{dyn}}$  is smaller (larger) than the synchrotron loss time scale  $t_{\text{syn}}$  (green right-hatched and blue cross-hatched, resp.). Here, the dynamical time scale is just the variability scale  $t_{\text{dyn}} = t_v$  and  $t'_{\text{dyn}} = t_v \Gamma$ . The IceCube limits [46] on the total neutrino flux from the analysis of high-energy and ultra-high-energy muon neutrinos with the 40-string subarray assume 1 : 1 : 1 flavor composition after oscillation. We also show the sensitivity of the full IceCube detector (IC-86) to muon neutrinos after 3 years of observation. The gray solid area shows the range of GZK neutrinos expected at the 99% C.L.

- (1) Archival observations of TeV emission of Cen A collected in the early 1970s with the Narrabri optical intensity interferometer of the University of Sydney [51–53]. The data show variability of the sources over periods of one year.
- (2) Observation by HEGRA [54–59] of M 87. We scaled the flux of M 87 at 16 Mpc to the distance to Cen A. After adjusting for the different thresholds of the HEGRA and Sydney experiments, we obtain

identical source luminosities for M 87 and Cen A of roughly  $7 \times 10^{40} \text{ erg s}^{-1}$ , assuming an  $E^{-2}$  gamma-ray spectrum.

- (3) And, most importantly, the time-averaged gamma-ray flux thus obtained is very close to the gamma-ray flux from Cen A recently observed at the  $3\sim 4\sigma$  level by the H.E.S.S. collaboration [60].

Given that we obtain identical intrinsic luminosities for Cen A and M 87, we venture the assumption that they may



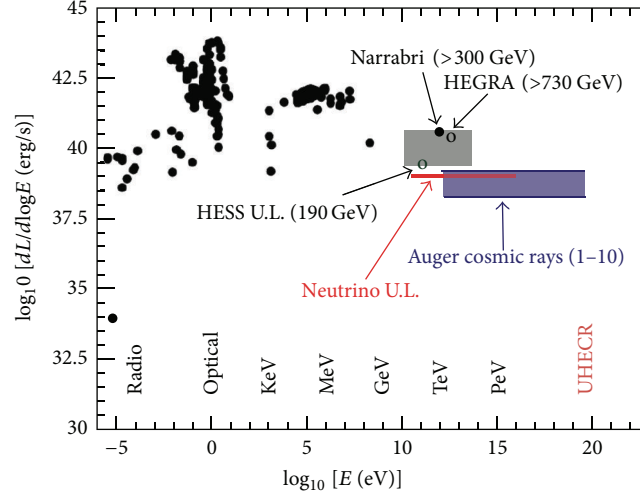


FIGURE 5: Spectral energy distribution of Cen A (black dots). Keeping in mind that the source is variable, we show our estimates for the flux of TeV gamma rays (upper gray shading) and cosmic rays assuming that between 1 and 10 events observed by Auger originated at Cen A (lower blue shading). We note that cosmic-ray and TeV gamma-ray fluxes estimated in this paper are at a level of the electromagnetic component shown from radio waves to GeV photons. Our estimate for the neutrino flux (labeled “neutrino upper limit”; see text) is shown as the red line.

be generic FRI, a fact that can be exploited to construct the diffuse neutrino flux from all FRI. The straightforward conversion of the TeV gamma-ray flux from a generic FRI to a neutrino flux yields

$$\frac{dN_\nu}{dE} \approx 5 \times 10^{-13} \left( \frac{E}{\text{TeV}} \right)^{-2} \text{TeV}^{-1} \text{cm}^{-2} \text{s}^{-1}. \quad (22)$$

The total diffuse flux from all such sources with a density of  $n \approx 8 \times 10^4 \text{ Gpc}^{-3}$  within a horizon of  $R \sim 3 \text{ Gpc}$  [61] is simply the sum of luminosities of the sources weighted by their distance, or

$$\frac{dN_\nu}{dE_{\text{diff}}} = \sum \frac{L_\nu}{4\pi d^2} = L_\nu n R = 4\pi d^2 n R \frac{dN_\nu}{dE}, \quad (23)$$

where  $dN_\nu/dE$  is given by the single-source flux. We performed the sum by assuming that the galaxies are uniformly distributed. This evaluates to

$$\frac{dN_\nu}{dE_{\text{diff}}} = 2 \times 10^{-12} \left( \frac{E}{\text{TeV}} \right)^{-2} \text{GeV}^{-1} \text{cm}^{-2} \text{s}^{-1} \text{sr}^{-1}. \quad (24)$$

The neutrino flux from a single source such as Cen A is clearly small: repeating the calculation for power-law spectra between 2.0 and 3.0, we obtain, in a generic neutrino detector of effective muon area  $1 \text{ km}^2$ , only 0.8 to 0.02 events per year. The diffuse flux yields a more comfortable event rate of between 0.5 and 19 neutrinos per year. Considering sources out to 3 Gpc, or a redshift of order 0.5 only, is probably conservative. Extending the sources beyond  $z \sim 1$ , and taking into account their possible evolution, may increase the flux by a factor 3 or so.

## 6. Neutrinos from GZK Interactions

Whatever the sources of extragalactic cosmic rays may be, a cosmogenic flux of neutrinos originates from the interactions

of cosmic rays with the cosmic microwave background (CMB). Produced within a GZK radius by a source located at a cosmological distance, a GZK neutrino points back to it with subdegree precision. The calculation of the GZK neutrino flux is relatively straightforward, and its magnitude is very much determined by their total energy density in the universe; as before, the crossover from the Galactic to the extragalactic component is the critical parameter. Recent calculations [62] are shown in Figure 6. It is also important to realize that, among the  $p\gamma$  final state products produced via the decay of pions, GZK neutrinos are accompanied by a flux of electrons, positrons, and  $\gamma$ -rays that quickly cascades to lower energies in the CMB and intergalactic magnetic fields. An electromagnetic cascade develops with a maximum in the GeV-TeV energy region. Here, the total energy in the electromagnetic cascade is constrained by recent Fermi-LAT measurements of the diffuse extragalactic  $\gamma$ -ray background [63].

The increased performance of IceCube at EeV energy has opened the possibility for IceCube to detect GZK neutrinos. We anticipate 2.3 events in 3 years of running the completed IceCube detector, assuming the best fit in Figure 6 and 4.8 events for the highest flux consistent with the Fermi constraint.

Throughout the discussion, we have assumed that the highest energy cosmic rays are protons. Experiments disagree on the composition of particles around  $10^{20} \text{ eV}$ . Little is known about the chemical composition just below to beyond the GZK cut-off, where the most significant contribution to cosmogenic neutrinos is expected. In any case, uncertainties in extrapolation of the proton-air interaction cross-section, elasticity, and multiplicity of secondaries from accelerator measurements to the high energies characteristic for air showers are large enough to undermine any definite conclusion on the chemical composition [64]. Therefore, the

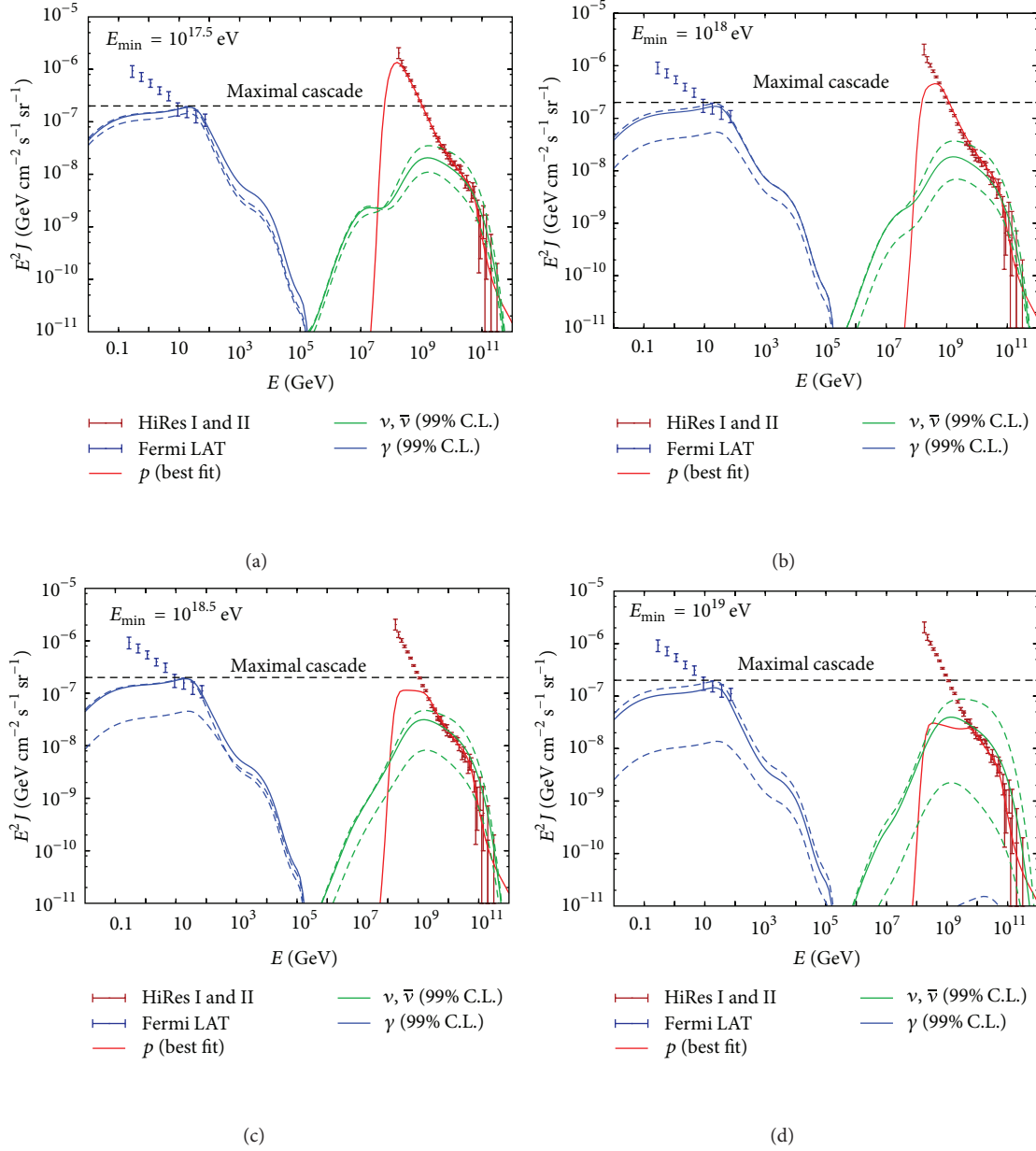


FIGURE 6: Comparison of proton, neutrino, and gamma-ray fluxes produced in interactions on the CMB by cosmic-ray protons fitted to HiRes data. We repeat the calculation for 4 values of the crossover energy marking the transition to the extragalactic cosmic-ray flux. We show the best fit values (solid lines) as well as neutrino and gamma-ray fluxes within the 99% C.L. with minimal and maximal energy density (dashed lines). The  $\gamma$ -ray fluxes are marginally consistent at the 99% C.L. with the highest energy measurements by Fermi-LAT. The contribution around 100 GeV is somewhat uncertain, due to uncertainties in the cosmic infrared background.

conflicting claims by these experiments most likely illustrate that the particle physics is not sufficiently known to derive a definite result. Dedicated experiments at the LHC may remedy this situation by constraining the shower simulations that are a central ingredient in determining the composition.

## 7. A Comment on the Science Reach of Neutrino “Telescopes”

We have emphasized the potential of IceCube to reveal the sources of the cosmic rays; this goal is clearly of primary

importance as it sets the scale of the detector. IceCube science includes other priorities.

- (1) As for conventional astronomy, neutrino astronomers observe the neutrino sky through the atmosphere. This is a curse and a blessing; the background of neutrinos produced by cosmic rays in interactions with atmospheric nuclei provides a beam essential for calibrating the instrument. It also presents us with an opportunity to do particle physics. Especially unique is the energy range of the background atmospheric neutrino beam covering the interval 1–10<sup>5</sup> TeV,

energies not within reach of accelerators. Cosmic beams of even higher energy may exist, but the atmospheric beam is guaranteed. IceCube is expected to collect a data set of order one million neutrinos over ten years with a scientific potential that is only limited by our imagination.

- (2) The passage of a large flux of MeV-energy neutrinos produced by a galactic supernova over a period of seconds will be detected as an excess of the background counting rate in all individual optical modules [65]. Although only a counting experiment, IceCube will measure the time profile of a neutrino burst near the center of the Galaxy with a statistics of about one million events, equivalent to the sensitivity of a 2-megaton detector.
- (3) IceCube will search for neutrinos from the annihilation of dark matter particles gravitationally trapped at the center of the Sun and the Earth [66]. In searching for generic weakly interacting massive dark matter particles (WIMPs) with spin-independent interactions with ordinary matter, IceCube is only competitive with direct detection experiments [67] if the WIMP mass is sufficiently large. For spin-dependent interactions, IceCube already has improved the best limits on spin-dependent WIMP cross-sections by two orders of magnitude [68, 69].

Construction of IceCube and other high-energy neutrino telescopes is mostly motivated by their potential to open a new window on the Universe using neutrinos as cosmic messengers; more about this will be in the rest of the talk. The IceCube experiment, nevertheless, appeared on the U.S. Roadmap to Particle Physics [70]. As the lightest of fermions and the most weakly interacting of particles, neutrinos occupy a fragile corner of the standard model, and one can realistically hope that they will reveal the first and the most dramatic signatures of new physics.

Besides its potential to detect dark matter, IceCube's opportunities for particle physics include the following [71].

- (1) The search for signatures of the unification of particle interactions, possibly including gravity at the TeV scale. In this case, neutrinos approaching TeV energies would interact gravitationally with large cross-sections, similar to those of quarks and leptons; this increase yields dramatic signatures in a neutrino telescope including, possibly, the production of black holes [72].
- (2) The search for modifications of neutrino oscillations that result from nonstandard neutrino interactions [73].
- (3) Searching for flavor changes or energy-dependent delays of neutrinos detected from cosmic distances as a signature for quantum decoherence.
- (4) The search for a breakdown of the equivalence principle as a result of nonuniversal interactions with the gravitational field of neutrinos with different flavor.

(5) Similarly, the search for a breakdown of Lorentz invariance resulting from different limiting velocities of neutrinos of different flavors. With energies of  $10^3$  TeV and masses of order  $10^{-2}$  eV or less, even the atmospheric neutrinos observed by IceCube reach Lorentz factors of  $10^{17}$  or larger.

- (6) The search for particle emission from cosmic strings or any other topological defects or heavy cosmological remnants created in the early Universe. It has been suggested that they may be the sources of the highest energy cosmic rays.
- (7) The search for magnetic monopoles, nuclearites, Q-balls, and the like.

The DeepCore upgrade of IceCube has significantly extended IceCube's scientific potential as an atmospheric neutrino detector. It will accumulate atmospheric neutrino data covering the first oscillation dip near 20 GeV with unprecedented statistics. Its instrumented volume is of order 10 Mton. With 6 additional strings instrumented with closely spaced (7 meters) high quantum efficiency photomultipliers buried deep inside IceCube, DeepCore uses the surrounding IceCube strings as a veto in order to observe the tracks of contained events; see Figure 7. It has been shown that the event statistics are sufficient to determine the mass hierarchy with at least 90% confidence level assuming the current best-fit values of the oscillation parameters [74]. A positive result does, however, require a sufficient understanding of the systematics of the measurement, and, more realistically, we should ask the question of how many additional strings, deployed within DeepCore, it takes to perform a definite determination. This is a work in progress, not only based on simulations, but also on DeepCore data that have already yielded evidence at the  $5\sigma$  level for atmospheric oscillations at 10–100 GeV, that is, at higher energy than any previous observation.

The physics behind the hierarchy measurement is the same as for long baseline experiments [75]; the key is to measure the Earth matter effects associated with the angle  $\theta_{13}$  which governs the transitions between  $\nu_e$  and  $\nu_{\mu,\tau}$ . The effective  $\theta_{13}$  mixing angle in matter in a two-flavor framework is given by

$$\sin^2 2\theta_{13}^m = \frac{\sin^2 2\theta_{13}}{\sin^2 2\theta_{13} + (\cos 2\theta_{13} \pm \sqrt{2}G_F N_e / \Delta_{13})^2}, \quad (25)$$

where the plus (minus) sign refers to (anti) neutrinos.  $N_e$  is the electron number density of the Earth,  $\sqrt{2}G_F N_e$  (eV) =  $7.6 \times 10^{-14} Y_e \rho$  (g/cm<sup>3</sup>), and  $Y_e$ ,  $\rho$  are the electron fraction and the density of the Earth's interior, respectively. The critical quantity is  $\Delta_{13} = (m_1^2 - m_3^2)/2E$ ; its sign determines the mass hierarchy. The resonance condition is satisfied for neutrino energies of order 15 GeV for the baselines of thousands of kilometers studied in atmospheric neutrino experiments. DeepCore extends the threshold of IceCube to this energy. Both the disappearance of muon neutrinos and the appearance of tau and electron neutrinos can be observed.

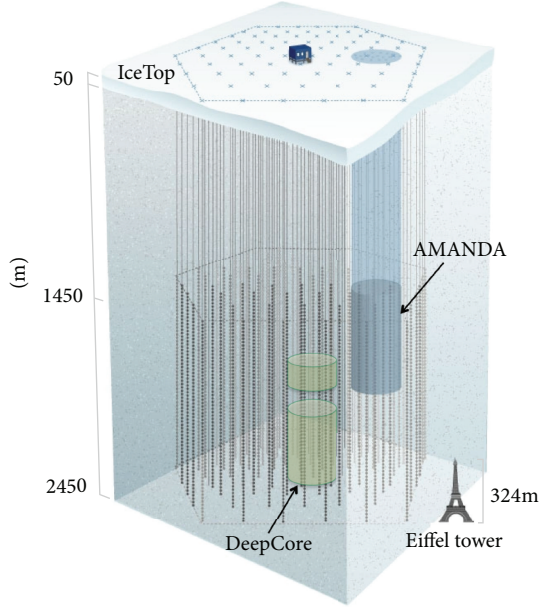


FIGURE 7: The IceCube detector, consisting of IceCube and IceTop and the low-energy sub-detector DeepCore. Also shown is the first-generation AMANDA detector.

In the presence of Earth matter effects, the neutrino (antineutrino) oscillation probability is enhanced if the hierarchy is normal (inverted). Long baseline detectors, unlike IceCube, measure the charge of the secondary muon, thus selecting the sign associated with each event in previous equation. The hierarchy is determined by simply looking in which channel, neutrino or antineutrino, the signal is enhanced by matter effects. With the large value of  $\sin^2 2\theta_{13}$ , recently observed by several experiments and sufficient statistics, the magnitude of the  $\Delta_{13}$  term can be measured even without charge discrimination. This is in principle possible with DeepCore [74] or a very modest extension (considering that the cost of an additional string deployed in ice is \$1.2 M, including logistic costs) but cannot be guaranteed until the systematics of the measurement has been fully understood in this newly explored energy range.

## 8. Neutrino Telescopes: Detection Methods

The detection of neutrinos of all flavors will be important in separating diffuse extraterrestrial neutrinos from atmospheric neutrinos. Generic cosmic accelerators produce neutrinos from the decay of pions with admixture  $\nu_e : \nu_\mu : \nu_\tau = 1 : 2 : 0$ . Over cosmic baselines, neutrino oscillations transform the ratio to 1 : 1 : 1, because approximately one-half of the  $\nu_\mu$  convert to  $\nu_\tau$ .

Neutrino telescopes exploit the relatively large neutrino cross-section and the long muon range above TeV energies to achieve a detection efficiency to reach the predicted point source and diffuse fluxes previously discussed. At the same time, detecting  $\nu_e$  and  $\nu_\tau$  neutrinos cannot be ignored; the case has been made in detail in [13]. The background from atmospheric neutrinos is much lower for  $\nu_e$  and  $\nu_\tau$  than for

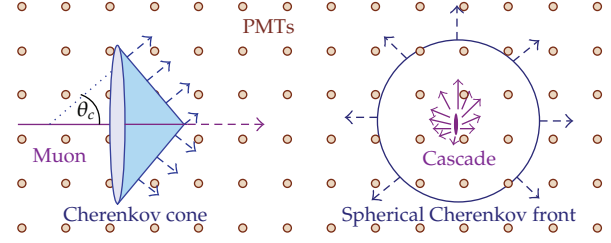


FIGURE 8: Contrasting Cherenkov light patterns produced by muons (left) and by showers initiated by electron and tau neutrinos (right) and by neutral current interactions. The patterns are routinely referred to as tracks and cascades (or showers). Cascades are produced by the radiation of particle showers of dimension of tens of meters, that is, an approximately point source of light with respect to the dimensions of the detector. At PeV energies,  $\tau$  leptons travel hundreds of meters before decaying, producing a third topology, with two cascades, one when the  $\tau$  interacts and the second when the  $\tau$  decays [76]. This is the “double bang” signature.

$\nu_\mu$ , energy determination is superior because the neutrino event is fully, or at least partially, contained in the detector. For a  $\nu_\mu$  one is limited to sampling the catastrophic energy loss of part of the secondary muon’s track. Finally, they can be detected from both hemispheres, and, as will be discussed further on,  $\nu_\tau$  neutrinos are not absorbed by the Earth, they just cascade to lower energy.

IceCube detects neutrinos by observing the Cherenkov radiation from the charged particles produced by neutrino interactions inside or in the vicinity of the detector. Charge current interactions produce a lepton that carries, on average, 50% of the neutrino energy for  $E \leq 10$  GeV to 80% at high energies; the remainder of the energy is released in the form of a hadronic shower. Both the secondary lepton and the hadronic shower produce Cherenkov radiation. In neutral current interactions, the neutrino transfers a fraction of its energy to a nuclear target, producing a hadronic shower. IceCube can differentiate neutrino flavors on the basis of their topology in the detector, as illustrated in Figure 8. There are two basic topologies: tracks from  $\nu_\mu$  and “cascades” from  $\nu_e$ ,  $\nu_\tau$  and the neutral current interactions from all flavors. On the scale of IceCube, cascades are approximately point sources of Cherenkov light. At PeV energies and above, an additional topology emerges, so-called double-bang events, when a  $\nu_\tau$  interacts producing a cascade and subsequently decays producing a second cascade. At PeV energies, a  $\tau$  lepton travels hundreds of meters before decaying; this determines the distance between the cascades.

Neutrino telescopes also measure neutrino energy. Muons range out, over kilometers at TeV energy to tens of kilometers at EeV energy, generating showers along their track by bremsstrahlung, pair production, and photonuclear interactions. The charged particles produced are the sources of additional Cherenkov radiation. Because the energy of the muon degrades along its track, also the energy of the secondary showers decreases, and the distance from the track over which the associated Cherenkov light can trigger a PMT is gradually reduced. The geometry of the light pool surrounding the muon track is, therefore, a kilometer-long cone



with a gradually decreasing radius. In its first kilometer, a high-energy muon typically loses energy in a couple of showers of one-tenth of its initial energy. So the initial radius of the cone is the radius of a shower with 10% of the muon energy. At lower energies of hundreds of GeV and less, the muon becomes minimum ionizing.

Because of the stochastic nature of the muon's energy loss, the relationship between observed (via Cherenkov light) energy loss and muon energy varies from muon to muon. The muon energy in the detector can be determined, and beyond that, one does not know how far the muon travelled (and how much energy it lost) before entering the detector; an unfolding process is required to determine the neutrino energy based on the observed muon energies. In contrast, for  $\nu_e$  and  $\nu_\tau$ , the detector is a total energy calorimeter and the determination of their energy superior.

The different topologies each have advantages and disadvantages. From  $\nu_\mu$  interactions, the long lever arm of muon tracks, up to tens of kilometers at very high energies, allows the muon direction (and the neutrino direction) to be determined accurately with an angular resolution on-line that is better than 0.5 degrees. Superior angular resolution can be reached for selected events. Sensitivity to point sources is, therefore, superior to other flavors. The disadvantages are a large background of atmospheric neutrinos at sub-PeV energies and from cosmic-ray muons at all energies and the indirect determination of the neutrino energy that has to be inferred from sampling the energy loss of the muon when it transits the detector.

Observation of  $\nu_e$  and  $\nu_\tau$  flavors represents significant observational advantages. They are detected for both Northern and Southern Hemispheres. (This is also true for  $\nu_\mu$  with energy in excess of 1 PeV, where the background from the steeply falling atmospheric spectrum becomes negligible.) At TeV energies and above, the background of atmospheric  $\nu_e$  is lower by an order of magnitude, and there are almost no atmospheric  $\nu_\tau$ . At higher energies, muons from  $\pi$  decay, the source of atmospheric  $\nu_e$ , no longer decay, and relatively rare K-decays become the dominant source of background  $\nu_e$ . Furthermore, because the neutrino events are totally, or at least partially contained inside the instrumented detector volume, the neutrino energy is determined by total absorption calorimetry. One can establish the cosmic origin of a single event by demonstrating that the energy cannot be reached by muons and neutrinos of atmospheric origin. Finally,  $\nu_\tau$  are not absorbed by the Earth [77]:  $\nu_\tau$  interacting in the Earth produce secondary  $\nu_\tau$  of lower energy, either directly in a neutral current interaction or via the decay of a secondary tau lepton produced in a charged current interaction. High-energy  $\nu_\tau$  will thus cascade down to energies of hundred of TeV where the Earth becomes transparent. In other words, they are detected with a reduced energy but are not absorbed.

Although cascades are nearly point-like, they are not isotropic but elliptic with the major axis aligned with the incident neutrino direction. This is reflected in the light pattern detected, especially in the detailed photon signals sampled by the optical sensors. While a fraction of cascade events can be reconstructed with degree accuracy [78], the precision is inferior to the one reached for  $\nu_\mu$  events.

At energies above about 1 PeV in ice, the LPM effect reduces the cross-sections for bremsstrahlung and pair production. At energies above about  $10^{17}$  eV, electromagnetic showers begin to elongate, reaching a length of about 80 meters at  $10^{20}$  eV [79]. At these energies, photonuclear interactions play a role, and even electromagnetic showers will have a hadronic component, including the production of secondary muons.

For an in-depth discussion of neutrino detection, energy measurement and flavor separation, and detailed references, see the IceCube Preliminary Design Document [2, 13].

To a first approximation, neutrinos are detected when they interact inside the instrumented volume. The path length  $L(\theta)$  traversed within the detector volume by a neutrino with zenith angle  $\theta$  is determined by the detector's geometry. Neutrinos are detected if they interact within the detector volume, that is, within the instrumented distance  $L$ . That probability is

$$P(E_\nu) = 1 - \exp\left[-\frac{L}{\lambda_\nu(E_\nu)}\right] \approx \frac{L}{\lambda_\nu(E_\nu)}, \quad (26)$$

where  $\lambda_\nu(E_\nu) = [\rho_{\text{ice}} N_A \sigma_{\nu N}(E_\nu)]^{-1}$  is the mean free path in ice for a neutrino of energy  $E_\nu$ . Here  $\rho_{\text{ice}} = 0.9 \text{ g cm}^{-3}$  is the density of the ice,  $N_A = 6.022 \times 10^{23}$  is Avogadro's number, and  $\sigma_{\nu N}(E_\nu)$  is the neutrino-nucleon cross-section. A neutrino flux  $dN/dE_\nu$  (neutrinos per GeV per  $\text{cm}^2$  per second) crossing a detector with energy threshold and cross-sectional area  $A(E_\nu)$  facing the incident beam will produce

$$N_{\text{ev}} = T \int_{E_\nu^{\text{th}}} A(E_\nu) P(E_\nu) \frac{dN}{dE_\nu} dE_\nu \quad (27)$$

events after a time  $T$ . The "effective" detector area  $A(E_\nu)$  is also a function of the zenith angle  $\theta$ . It is not strictly equal to the geometric cross-section of the instrumented volume facing the incoming neutrino, because even neutrinos interacting outside the instrumented volume may produce enough light inside the detector to be detected. In practice,  $A(E_\nu)$  is determined as a function of the incident neutrino direction and zenith angle by a full-detector simulation, including the trigger.

This formalism applies to contained events. For muon neutrinos, any neutrino producing a secondary muon that reaches the detector (and has sufficient energy to trigger it) will be detected. Because the muon travels kilometers at TeV energy and tens of kilometers at PeV energy, neutrinos can be detected outside the instrumented volume; the probability is obtained by substitution in (26):

$$L \longrightarrow \lambda_\mu, \quad (28)$$

therefore,

$$P = \frac{\lambda_\mu}{\lambda_\nu}. \quad (29)$$

Here,  $\lambda_\mu$  is the range of the muon determined by its energy losses. The complete expression for the flux of  $\nu_\mu$ -induced

muons at the detector is given by a convolution of the neutrino spectrum  $\phi (= dN/dE_\nu)$  with the probability  $P$  to produce a muon reaching the detector [4–6]:

$$\phi_\mu(E_\mu^{\min}, \theta) = \int_{E_\mu^{\min}} P(E_\nu, E_\mu^{\min}) \exp[-\sigma_{\text{tot}}(E_\nu) N_A X(\theta)] \phi(E_\nu, \theta) dE_\nu. \quad (30)$$

The additional exponential factor accounts for the absorption of neutrinos along the chord of the Earth of length  $X(\theta)$  at zenith angle  $\theta$ . Absorption becomes important for  $\sigma_\nu(E_\nu) \geq 10^{-33} \text{ cm}^2$  or  $E_\nu \geq 10^6 \text{ GeV}$ . For back-of-the-envelope calculations, the  $P$ -function can be approximated by

$$P \approx 1.3 \times 10^{-6} E^{2.2} \quad \text{for } E = 10^{-3} - 1 \text{ TeV} \\ \approx 1.3 \times 10^{-6} E^{0.8} \quad \text{for } E = 1 - 10^3 \text{ TeV}. \quad (31)$$

At EeV energy, the increase is reduced to only  $E^{0.4}$ . Clearly, high-energy neutrinos are more likely to be detected because of the increase with energy of both the cross-section and muon range.

Tau neutrinos can be observed provided that the tau lepton they produce reaches the instrumented volume within its lifetime. In (26),  $L$  is replaced by

$$L \longrightarrow \gamma c \tau = \frac{E}{m c \tau}, \quad (32)$$

where  $m$ ,  $\tau$  and  $E$  are the mass, lifetime, and energy of the tau, respectively. The tau's decay length  $\lambda_\tau = \gamma c \tau \approx 50 \text{ m} \times (E_\tau/10^6) \text{ GeV}$  grows linearly with energy and actually exceeds the range of the muon near 1 EeV. At yet higher energies, the tau eventually ranges out by catastrophic interactions, just like the muon, despite the reduction of the cross-sections by a factor  $(m_\mu/m_\tau)^2$ .

The taus trigger the detector, but the tracks and (or) showers they produce are difficult to be distinguished from those initiated by muon and electron neutrinos. To be clearly recognizable as  $\nu_\tau$ , both the initial neutrino interaction and the subsequent tau decay must be contained within the detector; for a cubic kilometer detector, this happens for neutrinos with energies from a few PeV to a few 10's of PeV. It may also be possible to identify  $\nu_\tau$  that only interact in the detector, or  $\nu_\tau$  that decay in the detector.

## 9. The First Kilometer-Scale Neutrino Detector: IceCube

The rationale for kilometer-scale neutrino detectors is that their sensitivity is sufficient to reveal generic cosmic-ray sources with an energy density in neutrinos comparable to their energy density in cosmic rays [27, 28] and pionic TeV gamma rays [33, 34]. While TeV gamma-ray astronomy has become a mature technique, the weak link in exploring the multiwavelength opportunities presented previously is the observation of neutrinos that requires detectors of kilometer

scale; this will be demonstrated de facto by the discussion of potential cosmic-ray sources as follows. A series of first-generation experiments [81, 82] have demonstrated that high-energy neutrinos with  $\sim 10 \text{ GeV}$  energy and above can be detected by observing Cherenkov radiation from secondary particles produced in neutrino interactions inside large volumes of highly transparent ice or water instrumented with a lattice of photomultiplier tubes. Construction of the first second-generation detector, IceCube, at the geographic South Pole was completed in December 2010 [83]; see Figure 7.

IceCube consists of 80 strings each instrumented with 60 10-inch photomultipliers spaced by 17 m over a total length of 1 kilometer. The deepest module is located at a depth of 2.450 km so that the instrument is shielded from the large background of cosmic rays at the surface by approximately 1.5 km of ice. Strings are arranged at apexes of equilateral triangles that are 125 m on a side. The instrumented detector volume is a cubic kilometer of dark, highly transparent, and sterile Antarctic ice. Radioactive background is dominated by the instrumentation deployed into this natural ice.

Each optical sensor consists of a glass sphere containing the photomultiplier and the electronics board that digitizes the signals locally using an on-board computer. The digitized signals are given a global time stamp with residuals accurate to less than 3 ns and are subsequently transmitted to the surface. Processors at the surface continuously collect these time-stamped signals from the optical modules; each functions independently. The digital messages are sent to a string processor and a global event trigger. They are subsequently sorted into the Cherenkov patterns emitted by secondary muon tracks, or electron and tau showers, that reveal the direction of the parent neutrino [84].

Based on data taken during construction with 40 of the 59 strings, the anticipated effective area of the completed IceCube detector is increased by a factor 2 to 3 over what had been expected [14]. The neutrino collecting area is expected to increase with improved calibration and development of optimized software tools for the 86-string detector, which has been operating stably in its final configuration since May 2011. Already reaching an angular resolution of better than 0.5 degree for high energies, reconstruction is also superior to what was anticipated.

A similar detector, that may eventually be more sensitive than IceCube, is planned for deployment in deep transparent Mediterranean water [85].

## 10. KM3NeT

Accelerators of cosmic rays produce neutrino fluxes limited in energy to roughly 5% of the maximal energy of the protons or nuclei (see (2)). For Galactic neutrino sources, even the as yet unidentified PeVatrons, we thus expect neutrino spectra with a cut-off (cf. (14)) in the range between a few and about 100 TeV. Detection of these neutrinos thus requires optimized sensitivities in the TeV range. In particular, the atmospheric muon background limits the field of view of neutrino telescopes to the downward hemisphere at these energies.

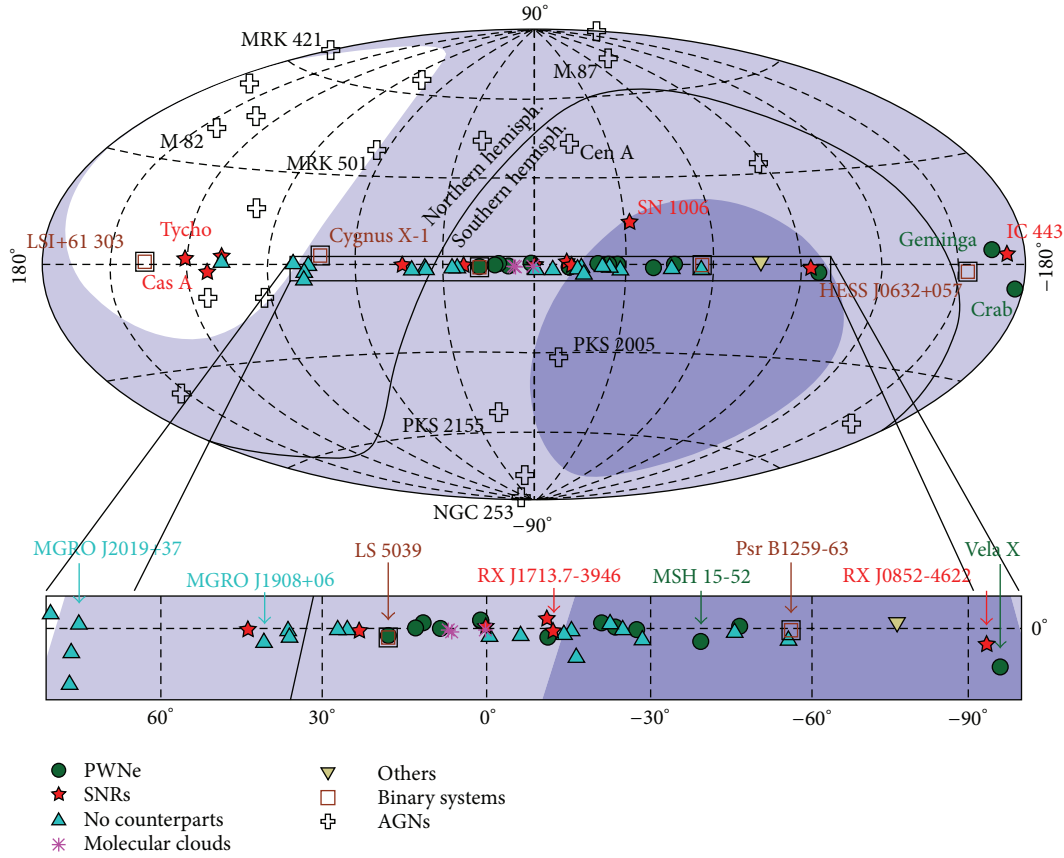


FIGURE 9: Field of view of IceCube (i.e., the Northern hemisphere) and of a Mediterranean-based neutrino telescope in Galactic coordinates.  $2\pi$  downward sensitivity is assumed. Shades of blue which indicate the fraction of time sources are visible for the Northern telescope (light blue:  $>25\%$  of the time; dark blue:  $>75\%$  of the time). Also indicated are sources of high-energy gamma rays, that is, candidates for neutrino emission. Figure courtesy of A. Kappes [80].

A second kilometer-scale neutrino telescope in the Northern hemisphere is, therefore, necessary to observe the Galactic center and the largest part of the Galactic plane—or, more generally speaking, to grant full sky coverage for neutrino astronomy. The sky coverage in Galactic coordinates of IceCube and a Mediterranean-based telescope is indicated in Figure 9.

Following up the pioneering work of DUMAND, several neutrino telescope projects have been initiated in the Mediterranean in the 1990s (see above). In 2008, the construction of the ANTARES detector near the French coast off Toulon has been completed. With an instrumented volume of a percent of a cubic kilometer, ANTARES [86, 87] has about the same effective area as AMANDA and is the currently most sensitive observatory for high-energy neutrinos in the Northern hemisphere. It has demonstrated the feasibility of neutrino detection in the deep sea and has provided a wealth of technical experience and design solutions for deep-sea components.

The next step will be the construction of a multi-cubic-kilometer neutrino telescope in the Mediterranean Sea, KM3NeT. Its technical design [88] has been elaborated in

EU-funded projects (FP6 Design Study and FP7 Preparatory Phase). Major progress has been made, in particular concerning the reliability and the cost effectiveness of the design. While the original goal was to reduce the price tag for one cubic kilometer of instrumented water to \$250 M, the plan is now to construct up to  $6 \text{ km}^3$  for this amount. A prime example for the many new technical developments is the digital optical module, which incorporates 31 3-inch photomultipliers instead of one large tube (see Figure 10). The advantages are a triplication of the photocathode area per optical module, a segmentation of the photocathode allowing for a clean identification of coincident Cherenkov photons, some directional sensitivity, and a reduction of the overall number of penetrators and connectors, which are expensive and failure prone. For all photomultiplier signals exceeding the noise level, time-over-threshold information will be digitized and time stamped by electronic modules housed inside the optical modules. Via optical fibres, this information is sent to shore, where the data stream will be filtered online for event candidates.

KM3NeT will consist of several 100 vertical structures (detection units) carrying more than 10 000 optical modules.



FIGURE 10: Prototype of a multi-photomultiplier optical module for KM3NeT. The module incorporates 31 3-inch photomultipliers, their high-voltage bases, and the electronic modules for signal digitization and communication to shore. Photograph by KM3NeT Collaboration.

The detection units are anchored to the sea bed with dead-weights and kept vertical by submerged buoys. The vertical distances between optical modules will be about 40 m, and the horizontal distances between detection units will be between 100 m and 180 m, depending on the outcome of ongoing optimization studies. The detector will be built in two or more large blocks, either next to each other at the same site or at different sites; candidate sites have been identified near Toulon/France (next to the ANTARES site), near Capo Passero (East of Sicily), and near Pylos (West of the Peloponnesus).

Due to the drag of deep-sea currents, the detection units will deform and deviate horizontally by up to several 10 m from their nominal vertical arrangement. Acoustic triangulation, tiltmeters, and compasses will be used to monitor the position and orientation of each optical module with a precision commensurate with a timing resolution of 1 ns.

Conservative estimates of the KM3NeT sensitivity to point sources with an  $E^{-2}$  flux (see Figure 11) indicate that this detector will be more sensitive than IceCube over a large declination range. The sensitivity is also high for neutrino fluxes with cut-offs; in particular, neutrinos from the supernova remnant RX J1713-3946 should be detectable with  $5\sigma$  within five years if the gamma emission from this object is of purely hadronic origin.

A first phase of KM3NeT construction is now imminent. About \$50 M of funding are available, and start of construction is expected for 2013. An option under discussion is to dedicate this first phase to a measurement of the neutrino mass hierarchy (see Section 7). A corresponding case study is in the works, and subject to its outcome, the installation of a dense array with intermodule distances much smaller than those indicated previously might be considered.

## 11. Conclusion: Stay Tuned

In summary, IceCube was designed for a statistically significant detection of cosmic neutrinos accompanying cosmic rays in 5 years. Here, we made the case that, based on multi-wavelength information from ground-based gamma-ray telescopes and cosmic-ray experiments, we are indeed closing

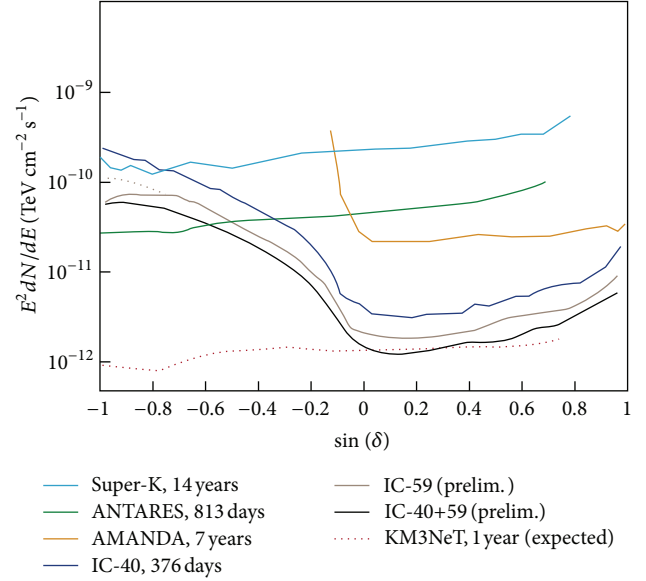


FIGURE 11: Sensitivities of running and future neutrino detectors to point source fluxes with  $E^{-2}$  spectrum as functions of the declination angle  $\delta$ . Figure from [82].

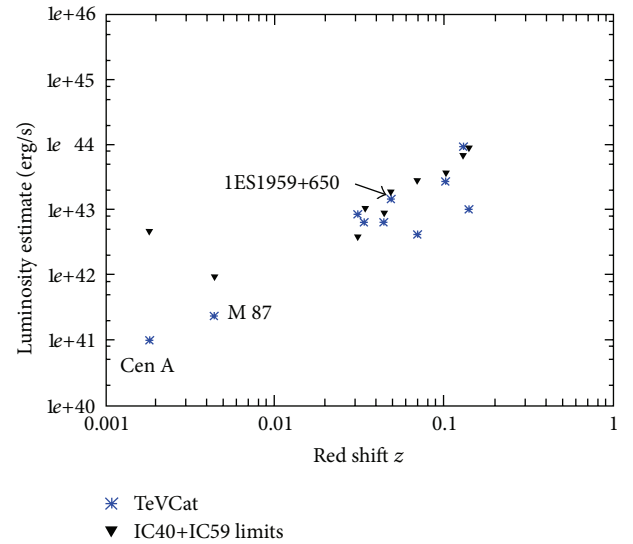


FIGURE 12: IceCube neutrino flux limits are compared with the TeV photon flux for nearby AGN. Figure courtesy of T. Gaisser [89].

in on supernova remnants, GRB (if they are the sources of cosmic rays), and GZK neutrinos. The discussion brought to the forefront the critical role of improved spectral gamma-ray data on candidate cosmic-ray accelerators. The synergy between CTA [101], IceCube, and KM3NeT as well as other next-generation neutrino detectors is likely to provide fertile ground for progress.

That, after decades of development, IceCube and KM3NeT create opportunities for discovery is illustrated by Figure 11. We recall (13) that sets the flux level of photons expected from supernova remnants if they are indeed the



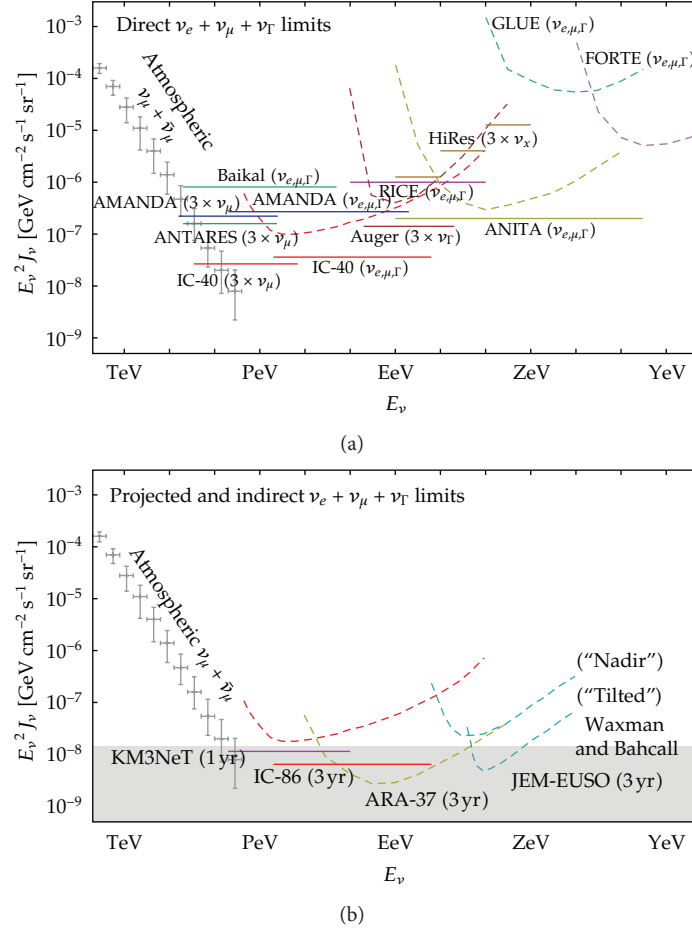


FIGURE 13: Limits on a diffuse neutrino flux from existing and, below, future experiments [16, 90–99]. Figure courtesy of M. Ahlers [100].

sources of the Galactic cosmic rays:  $10^{-12} \sim 10^{-11} \text{ TeV cm}^{-2} \text{ s}^{-1}$  for a source at 1 kpc. As discussed, the Milagro experiments do observe candidate cosmic accelerators at this flux level. As can be seen from Figure 11, with a neutrino flux reduced by a factor of two, IceCube already achieved the sensitivity for possible detection with data taken during the construction phase. Subject to details of the energy spectrum and the angular extension of the sources (which becomes a problem because IceCube's resolution has improved to less than 0.5 degrees), discovery should be possible after several years, as previously argued.

The same argument can be made for extragalactic sources as already discussed in detail for the scenario where GRBs are the sources of the highest energy cosmic rays. Alternatively, Figure 12 shows the present upper limits on the neutrino flux from nearby AGN as a function of their distance. Also shown is the TeV gamma-ray emission from the same sources; except for Cen A and M 87, the muon-neutrino limits have reached the level of the TeV photon flux. This is an interesting fact as previously emphasized, one expects approximate equipartition of the cosmic-ray, gamma-ray, and neutrino fluxes from a cosmic ray accelerator. One can sum the sources shown in the figure into a diffuse flux, and the result is, after dividing by  $4\pi$ ,  $3 \times 10^{-9} \text{ TeV cm}^{-2} \text{ s}^{-1} \text{ sr}^{-1}$ ,

or approximately  $\sim 10^{-8} \text{ TeV cm}^{-2} \text{ s}^{-1} \text{ sr}^{-1}$  for all neutrino flavors. This is known as the Waxman-Bahcall bound; the flux is basically equal to the flux observed in extragalactic cosmic rays.

In Figure 13, we show the limits from present experiments as well as the reach of IceCube and future experiments. The benchmark flux introduced previously rises above the atmospheric neutrino background for energies exceeding 100 TeV, and an energy range entered by the completed IceCube detector after one year of operation. In fact, candidate "cosmic" neutrino events have emerged from this analysis, although their origin has not been established. We are, in any case, moving into a critical time for neutrino astronomy.

## Acknowledgments

This research was supported in part by the US National Science Foundation under Grants nos. OPP-0236449 and PHY-0969061; by the US Department of Energy under Grant no. DE-FG02-95ER40896; by the University of Wisconsin Research Committee with funds granted by the Wisconsin Alumni Research Foundation and by the Alexander von Humboldt Foundation in Germany. The KM3NeT work has been supported by the EU through the KM3NeT Design

Study (Contract 011937) and the FP7 KM3NeT Preparatory Phase (Grant 212525).

## References

- [1] F. Reines and C. L. Cowan Jr., "The Neutrino," *Nature*, vol. 178, no. 4531, pp. 446–449, 1956.
- [2] F. Halzen and S. R. Klein, "Astronomy and astrophysics with neutrinos," *Physics Today*, vol. 61, no. 5, pp. 29–35, 2008.
- [3] A. Roberts, "The birth of high-energy neutrino astronomy: a personal history of the DUMAND project," *Reviews of Modern Physics*, vol. 64, no. 1, pp. 259–312, 1992.
- [4] T. K. Gaisser, F. Halzen, and T. Stanev, "Particle astrophysics with high energy neutrinos," *Physics Report*, vol. 258, no. 3, pp. 173–236, 1995, Erratum, *Physics Report*, vol. 271, pp. 355–356, 1995.
- [5] J. G. Learned and K. Mannheim, "High-energy neutrino astrophysics," *Annual Review of Nuclear and Particle Science*, vol. 50, no. 1, pp. 679–749, 2000.
- [6] F. Halzen and D. Hooper, "High-energy neutrino astronomy: the cosmic ray connection," *Reports on Progress in Physics*, vol. 65, no. 7, pp. 1025–1078, 2002.
- [7] M. A. Markov, "On high-energy neutrino physics," in *Proceedings of the Annual International Conference on High Energy Physics*, E. C. G. Sudarshan, J. H. Tinlot, and A. C. Melissinos, Eds., p. 578, University of Rochester, Rochester, NY, USA, 1960.
- [8] J. Babson, B. Barish, R. Becker-Szendy et al., "Cosmic-ray muons in the deep ocean," *Physical Review D*, vol. 42, no. 11, pp. 3613–3620, 1990.
- [9] V. Balkanov, I. Belolaptikov, N. Budnev et al., "The BAIKAL neutrino project: status report," *Nuclear Physics B*, vol. 118, pp. 363–370, 2003.
- [10] G. Aggouras, E. G. Anassontzis, A. E. Ball et al., "A measurement of the cosmic-ray muon flux with a module of the NESTOR neutrino telescope," *Astroparticle Physics*, vol. 23, no. 4, pp. 377–392, 2005.
- [11] J. A. Aguilar, A. Albert, F. Ameli et al., "First results of the Instrumentation Line for the deep-sea ANTARES neutrino telescope," *Astroparticle Physics*, vol. 26, no. 4-5, pp. 314–324, 2006.
- [12] E. Migneco, "Progress and latest results from Baikal, Nestor, NEMO and KM3NeT," *Journal of Physics: Conference Series*, vol. 136, no. 2, Article ID 022048, 2008.
- [13] IceCube collaboration, "IceCube preliminary design document," 2001, <http://www.icecube.wisc.edu/science/publications/pdd/pdd.pdf>.
- [14] J. Ahrens, J. N. Bahcall, X. Bai et al., "Sensitivity of the IceCube detector to astrophysical sources of high energy muon neutrinos," *Astroparticle Physics*, vol. 20, no. 5, pp. 507–532, 2004.
- [15] J. K. Becker, "High-energy neutrinos in the context of multi-messenger astrophysics," *Physics Reports*, vol. 458, no. 4-5, pp. 173–246, 2008.
- [16] A. Achterberg, M. Ackermann, J. Adams et al., "Multiyear search for a diffuse flux of muon neutrinos with AMANDA-II," *Physical Review D*, vol. 77, no. 8, Article ID 089904, 2008, Erratum, *Physical Review D*, vol. 77, Article ID 089904, 2007.
- [17] R. Engel, D. Seckel, and T. Stanev, "Neutrinos from propagation of ultrahigh energy protons," *Physical Review D*, vol. 64, no. 9, Article ID 093010, 2001.
- [18] P. Sommers and S. Westerhoff, "Cosmic ray astronomy," *New Journal of Physics*, vol. 11, Article ID 055004, 2009.
- [19] A. M. Hillas, "Cosmic rays: recent progress and some current questions," in *Proceedings of Cosmology, Galaxy Formation and Astroparticle Physics on the Pathway to the Square Kilometre Array*, H.-R. Klockner, S. Rawlings, M. Jarvis, and A. Taylor, Eds., p. 9, ASTRON, Oxford, UK, 2008.
- [20] V. Berezhinsky, "Astroparticle physics: puzzles and discoveries," *Journal of Physics: Conference Series*, vol. 120, Article ID 012001, 2008.
- [21] R. U. Abbasi, T. Abu-Zayyad, M. Allen et al., "First observation of the Greisen-Zatsepin-Kuzmin suppression," *Physical Review Letters*, vol. 100, no. 10, Article ID 101101, 2008.
- [22] J. Abraham, P. Abreu, M. Aglietta et al., "Observation of the suppression of the flux of cosmic rays above  $4 \times 10^{19}$  eV," *Physical Review Letters*, vol. 101, no. 6, Article ID 061101, 2008.
- [23] H. Tokuno, T. Abu-Zayyad, R. Aida et al., "The status of the telescope array experiment," *Journal of Physics: Conference Series*, vol. 293, no. 1, Article ID 012035, 2011.
- [24] W. Rhode, K. Daum, P. Bareyre et al., "Limits on the flux of very high energy neutrinos with the Fréjus detector," *Astroparticle Physics*, vol. 4, no. 3, pp. 217–225, 1996.
- [25] W. Baade and F. Zwicky, "Remarks on super-novae and cosmic rays," *Physical Review*, vol. 46, no. 1, pp. 76–77, 1934.
- [26] Y. Butt, "Beyond the myth of the supernova-remnant origin of cosmic rays," *Nature*, vol. 460, no. 7256, pp. 701–704, 2009.
- [27] T. K. Gaisser, "Neutrino Astronomy: physics goals, detector parameters," *OECD Megascience Forum, Taormina, Italy*, <http://arxiv.org/abs/astro-ph/9707283>.
- [28] M. Ahlers, L. A. Anchordoqui, H. Goldberg, F. Halzen, A. Ringwald, and T. J. Weiler, "Neutrinos as a diagnostic of cosmic ray galactic-extragalactic transition," *Physical Review D*, vol. 72, no. 2, Article ID 023001, pp. 1–8, 2005.
- [29] E. Waxman and J. Bahcall, "High energy neutrinos from cosmological gamma-ray burst fireballs," *Physical Review Letters*, vol. 78, no. 12, pp. 2292–2295, 1997.
- [30] M. Vietri, "Ultrahigh energy neutrinos from gamma ray bursts," *Physical Review Letters*, vol. 80, no. 17, pp. 3690–3693, 1998.
- [31] M. Böttcher and C. D. Dermer, "High-energy gamma rays from ultra-high-energy cosmic-ray protons in gamma-ray bursts," *Astrophysical Journal Letters*, vol. 499, no. 2, pp. L131–L134, 1998.
- [32] S. R. Kelner, F. A. Aharonian, and V. V. Bugayov, "Energy spectra of gamma rays, electrons, and neutrinos produced at proton-proton interactions in the very high energy regime," *Physical Review D*, vol. 74, no. 3, Article ID 034018, 2006, Erratum, *Physical Review D*, vol. 79, Article ID 034018, 1995.
- [33] J. Alvarez-Muñiz and F. Halzen, "Possible high-energy neutrinos from the cosmic accelerator RX J1713.7-3946," *Astrophysical Journal Letters*, vol. 576, no. 1 II, pp. L33–L36, 2002.
- [34] J. K. Becker, F. Halzen, A. O. Murchadha, and M. Olivo, "Neutrino emission from high-energy component gamma-ray bursts," *Astrophysical Journal Letters*, vol. 721, no. 2, pp. 1891–1899, 2010.
- [35] M. C. Gonzalez-Garcia, F. Halzen, and S. Mohapatra, "Identifying Galactic PeVatrons with neutrinos," *Astroparticle Physics*, vol. 31, no. 6, pp. 437–444, 2009.
- [36] M. Ahlers, P. Mertsch, and S. Sarkar, "Cosmic ray acceleration in supernova remnants and the FERMI/PAMELA data," *Physical Review D*, vol. 80, Article ID 123017, 14 pages, 2009.
- [37] A. A. Abdu, B. Allen, D. Berley et al., "Discovery of TeV gamma-ray emission from the cygnus region of the galaxy," *Astrophysical Journal Letters*, vol. 658, no. 1 II, pp. L33–L36, 2007.

- [38] A. Djannati-Atai, E. Ona-Wilhelmi, M. Renaud et al., “H.E.S.S. Galactic plane survey unveils a milagro hotspot,” in *Proceedings of the 30th International Cosmic Ray Conference*, vol. 2, p. 1316, Merida, Mexico, 2007.
- [39] J. Albert, E. Aliu, H. Anderhub et al., “Magic observations of the unidentified  $\gamma$ -ray source TeV J2032+4130,” *Astrophysical Journal Letters*, vol. 675, no. 1, part 2, pp. L25–L28, 2008.
- [40] S. Gabici and F. A. Aharonian, “Searching for galactic cosmic-ray pevatrons with multi-TeV gamma rays and neutrinos,” *Astrophysical Journal Letters*, vol. 665, no. 2, pp. L131–L134, 2007.
- [41] A. A. Abdo, M. Ackermann, M. Ajello et al., “Observations of the young supernova remnant RX J1713.7-3946 with the Fermi Large Area Telescope,” *Astrophysical Journal Letters*, vol. 734, no. 1, article 28, 2011.
- [42] F. Halzen, A. Kappes, and A. Ó. Murchadha, “Prospects for identifying the sources of the Galactic cosmic rays with IceCube,” *Physical Review D*, vol. 78, no. 6, Article ID 063004, 2008.
- [43] A. Kappes, F. Halzen, and A. O. Murchadha, “Prospects of identifying the sources of the Galactic cosmic rays with IceCube,” *Nuclear Instruments and Methods in Physics Research, Section A*, vol. 602, no. 1, pp. 117–119, 2009.
- [44] D. Guetta, D. Hooper, J. Alvarez-Muñiz, F. Halzen, and E. Reuveni, “Neutrinos from individual gamma-ray bursts in the BATSE catalog,” *Astroparticle Physics*, vol. 20, no. 4, pp. 429–455, 2004.
- [45] M. Ahlers, M. C. Gonzalez-Garcia, and F. Halzen, “GRBs on probation: testing the UHE CR paradigm with IceCube,” *Astroparticle Physics*, vol. 35, no. 2, pp. 87–94, 2011.
- [46] R. Abbasi, Y. Abdou, T. Abu-Zayyad et al., “Constraints on the extremely-high energy cosmic neutrino flux with the IceCube 2008-2009 data,” *Physical Review D*, vol. 83, no. 9, Article ID 092003, 2011.
- [47] R. Abbasi, Y. Abdou, T. Abu-Zayyad et al., “Limits on neutrino emission from gamma-ray bursts with the 40 string IceCube detector,” *Physical Review Letters*, vol. 106, no. 14, Article ID 141101, 2011.
- [48] J. Abraham, P. Abreu, M. Aglietta et al., “Correlation of the highest-energy cosmic rays with nearby extragalactic objects,” *Science*, vol. 318, no. 5852, pp. 938–943, 2007.
- [49] L. A. Anchordoqui, H. Goldberg, F. Halzen, and T. J. Weiler, “Neutrino bursts from Fanaroff-Riley I radio galaxies,” *Physics Letters, Section B*, vol. 600, no. 3-4, pp. 202–207, 2004.
- [50] P. Lipari, “Problems in high-energy astrophysics,” *Proceedings of NO-VE*, <http://arxiv.org/abs/0808.0417>.
- [51] J. E. Grindlay, H. F. Helmken, R. Handburg, J. Davis, and L. R. Allen, “Evidence for the detection of gamma rays from centaurus A at E, 1011 eV,” *The Astrophysical Journal Letters*, vol. 197, p. L9, 1975.
- [52] R. W. Clay, B. R. Dawson, and R. Meyhandan, “Evidence for the detection of gamma-rays up to 150 TeV from the active galaxy Centaurus A,” *Astroparticle Physics*, vol. 2, no. 4, pp. 347–352, 1994.
- [53] W. H. Allen, I. A. Bond, E. Budding et al., “Possible observation of 100 TeV gamma rays from the active galaxy Centaurus A,” *Astroparticle Physics*, vol. 1, no. 3, pp. 269–276, 1993.
- [54] M. Punch, C. W. Akeriof, M. F. Cawley et al., “Detection of TeV photons from the active galaxy Markarian 421,” *Nature*, vol. 358, no. 6386, pp. 477–482, 1992.
- [55] S. M. Bradbury, T. Deckers, D. Petry et al., “Detection of  $\gamma$ -rays above 1.5 TeV from Mkn 501,” *Astronomy and Astrophysics*, vol. 320, no. 2, pp. L5–L8, 1997.
- [56] F. Aharonian, A. Akhperjanian, M. Beilicke et al., “Variations of the TeV energy spectrum at different flux levels of Mkn 421 observed with the HEGRA system of Cherenkov telescopes,” *Astronomy and Astrophysics*, vol. 393, no. 1, pp. 89–99, 2002.
- [57] D. Petry, I. H. Bond, S. M. Bradbury et al., “The TeV spectrum of H1426+428,” *The Astrophysical Journal*, vol. 580, Article ID 020750, p. 104, 2002.
- [58] F. Aharonian, A. Akhperjanian, M. Beilicke et al., “Detection of TeV gamma-rays from the BL Lac 1ES 1959+650 in its low states and during a major outburst in 2002,” *Astrophys*, vol. 406, Article ID 030527, pp. L9–L13, 2003.
- [59] J. Holder, I. H. Bond, P. J. Boyle et al., “Detection of TeV gamma rays from the BL Lacertae object 1ES 1959+650 with the Whipple 10 meter telescope,” *Astrophysical Journal Letters*, vol. 583, no. 1 II, pp. L9–L12, 2003.
- [60] F. Aharonian, A. G. Akhperjanian, G. Anton et al., “Discovery of very high energy  $\gamma$ -ray emission from centaurus a with H.E.S.S.,” *Astrophysical Journal Letters*, vol. 695, no. 1, pp. L40–L44, 2009.
- [61] P. Padovani and C. M. Urry, “Fanaroff-riley I galaxies as the parent population of BL lacertae objects I. X-ray constraints,” *Astrophysical Journal Letters*, vol. 356, no. 1, pp. 75–82, 1990.
- [62] M. Ahlers, L. A. Anchordoqui, M. C. Gonzalez-Garcia, F. Halzen, and S. Sarkar, “GZK neutrinos after the Fermi-LAT diffuse photon flux measurement,” *Astroparticle Physics*, vol. 34, no. 2, pp. 106–115, 2010.
- [63] A. A. Abdo, M. Ackermann, M. Ajello et al., “Spectrum of the isotropic diffuse gamma-ray emission derived from first-year fermi large area telescope data,” *Physical Review Letters*, vol. 104, no. 10, Article ID 101101, 2010.
- [64] R. Ulrich, R. Engel, S. Müller, F. Schüssler, and M. Unger, “Proton-air cross section and extensive air showers,” *Nuclear Physics B*, vol. 196, no. C, pp. 335–340, 2009.
- [65] F. Halzen, J. E. Jacobsen, and E. Zas, “Ultratransparent Antarctic ice as a supernova detector,” *Physical Review D*, vol. 53, no. 12, pp. 7359–7361, 1996.
- [66] G. Bertone, D. Hooper, and J. Silk, “Particle dark matter: evidence, candidates and constraints,” *Physics Reports*, vol. 405, no. 5-6, pp. 279–390, 2005.
- [67] B. Sadoulet, “Particle dark matter in the universe: at the brink of discovery?” *Science*, vol. 315, no. 5808, pp. 61–63, 2007.
- [68] A. Rizzo, “Search for dark matter with AMANDA and IceCube detectors,” in *Proceedings of the 7th International Heidelberg Conference on Dark Matter in Astro- and Particle Physics (Dark '09)*, H. V. Klapdor-Kleingrothaus and I. V. Krivosheina, Eds., vol. 494, World Scientific, Christchurch, New Zealand.
- [69] C. DeClercq, “Dark matter searches with AMANDA and IceCube,” in *Proceedings of PANIC*, Eilat, Israel, 2008.
- [70] J. Bagger and B. Barish, <http://www.pha.jhu.edu/~bagger/talks/HEPAP.pdf>.
- [71] L. Anchordoqui and F. Halzen, “IceHEP high energy physics at the South Pole,” *Annals of Physics*, vol. 321, no. 11, pp. 2660–2716, 2006.
- [72] J. L. Feng, A. Rajaraman, and F. Takayama, “Probing gravitational interactions of elementary particles,” *International Journal of Modern Physics D*, vol. 13, no. 10, pp. 2355–2359, 2004.
- [73] S. Pakvasa and J. W. F. Valle, “Neutrino Properties before and after KamLAND,” *Proceedings of the National Academy of Sciences, India. Section A*, vol. 70, p. 189, 2003.
- [74] O. Mena, I. Mocioiu, and S. Razzaque, “Neutrino mass hierarchy extraction using atmospheric neutrinos in ice,” *Physical Review D*, vol. 78, no. 9, Article ID 093003, 2008.

- [75] V. Barger, M. Bishai, D. Bogert et al., "Report of the US long baseline neutrino experiment study," <http://arxiv.org/abs/0705.4396>.
- [76] J. G. Learned and S. Pakvasa, "Detecting  $\nu_\tau$  oscillations at PeV energies," *Astroparticle Physics*, vol. 3, no. 3, pp. 267–274, 1995.
- [77] F. Halzen and D. Saltzberg, "Tau neutrino appearance with a 1000 megaparsec baseline," *Physical Review Letters*, vol. 81, no. 20, pp. 4305–4308, 1998.
- [78] E. Middell, J. McCartin, and M. D. 'Agostino, "Improved reconstruction of cascade-like events," in *Proceedings of the 31st International Cosmic Ray Conference*, vol. 5, p. 708, Lodz, Poland, 2009.
- [79] S. R. Klein, "Cascades from  $\nu_e$  above  $10^{20}$  eV," *Radiation Physics and Chemistry*, vol. 75, p. 696, 2004.
- [80] A. Kappes, "Private Communication," <http://ecap.nat.uni-erlangen.de/members/kappes/homepage>.
- [81] C. Spiering, "High energy neutrino astronomy: status and perspectives," in *4th International Meeting on High Energy Gamma-Ray Astronomy*, F. A. Aharonian, W. Hofmann, and F. Rieger, Eds., pp. 18–29, July 2008.
- [82] U. F. Katz and C. Spiering, "High-energy neutrino astrophysics: status and perspectives," *Progress in Particle and Nuclear Physics*, vol. 67, no. 3, pp. 651–704, 2012.
- [83] F. Halzen and S. R. Klein, "IceCube: an instrument for neutrino astronomy," *Review of Scientific Instruments*, vol. 81, no. 8, Article ID 081101, 2010.
- [84] F. Halzen, "Astroparticle physics with high energy neutrinos: from AMANDA to IceCube," *European Physical Journal C*, vol. 46, no. 3, pp. 669–687, 2006.
- [85] <http://www.km3net.org/>.
- [86] <http://antares.in2p3.fr/>.
- [87] ANTARES Collaboration, "ANTARES: the rst undersea neutrino telescope," *Nuclear Instruments and Methods in Physics Research Section A*, vol. 656, pp. 11–38, 2011.
- [88] KM3NeT Collaboration et al., "KM3NeT technical design report," <http://www.km3net.org/TDR/TDRKM3NeT.pdf>.
- [89] T. Gaisser, "Review of TeV gamma-ray and neutrino data of relevance to UHECR," UHECR, at CERN in February 2012, to be published in the European Physical Journal Web of Conferences.
- [90] M. Ackermann, J. Adams, J. Ahrens et al., "Search for ultra-high-energy neutrinos with AMANDA-II," *The Astrophysical Journal*, vol. 675, p. 1014, 2008.
- [91] R. Abbasi, Y. Abdou, T. Abu-Zayyad et al., "First search for extremely high energy cosmogenic neutrinos with the IceCube Neutrino Observatory," *Physical Review D*, vol. 82, Article ID 072003, 11 pages, 2010.
- [92] V. Aynutdinova, V. Balkanova, I. Belolaptikov et al., "Search for a diffuse flux of high-energy extraterrestrial neutrinos with the NT200 neutrino telescope," *Astroparticle Physics*, vol. 25, no. 2, pp. 140–150, 2006.
- [93] K. Martens, "HiRes estimates and limits for neutrino fluxes at the highest energies," in *Proceedings of the 23rd Lepton-Photon Conference*, Daegu, Republic of Korea, 2007, <http://128.84.158.119/abs/0707.4417>.
- [94] I. Kravchenko, C. Cooley, S. Hussain et al., "RICE limits on the diffuse ultrahigh energy neutrino flux," *Physical Review D*, vol. 73, no. 8, Article ID 082002, 2006.
- [95] S. W. Barwick, J. J. Beatty, D. Z. Besson et al., "Constraints on cosmic neutrino fluxes from the antarctic impulsive transient antenna experiment," *Physical Review Letters*, vol. 96, no. 17, Article ID 171101, 2006.
- [96] N. G. Lehtinen, P. W. Gorham, A. R. Jacobson, and R. A. Roussel-Dupré, "FORTE satellite constraints on ultrahigh energy cosmic particle fluxes," *Physical Review D*, vol. 69, no. 1, Article ID 013008, 2004.
- [97] P. W. Gorham, C. L. Hebert, K. M. Liewer, C. J. Naudet, D. Saltzberg, and D. Williams, "Experimental limit on the cosmic diffuse ultrahigh energy neutrino flux," *Physical Review Letters*, vol. 93, no. 4, pp. 041101–1, 2004.
- [98] L. A. Anchordoqui, J. L. Feng, H. Goldberg, and A. D. Shapere, "Neutrino bounds on astrophysical sources and new physics," *Physical Review D*, vol. 66, no. 10, Article ID 103002, 2002.
- [99] R. Abbasi, Y. Abdou, T. Abu-Zayyad et al., "Measurement of the atmospheric neutrino energy spectrum from 100 GeV to 400 TeV with IceCube," *Physical Review D*, vol. 83, no. 1, Article ID 012001, 2011.
- [100] M. Ahlers, in *Gamma-Ray Burst Symposium*, Marbella, Spain, 2012, to be published in the European Astronomical Society Publication Series.
- [101] <http://www.cta-observatory.org/>.



## Review Article

# Neutrino Yukawa Textures within Type-I Seesaw

**Biswajit Adhikary<sup>1</sup> and Probir Roy<sup>2</sup>**

<sup>1</sup> *Department of Physics, Gurudas College, Narkeldanga, Kolkata 700054, India*

<sup>2</sup> *Theory Group, Saha Institute of Nuclear Physics, 1/AF Bidhan Nagar, Kolkata 700064, India*

Correspondence should be addressed to Biswajit Adhikary; [biswajitadhikary@gmail.com](mailto:biswajitadhikary@gmail.com)

Received 24 July 2012; Accepted 25 September 2012

Academic Editor: Gian Luigi Fogli

Copyright © 2013 B. Adhikary and P. Roy. This is an open access article distributed under the Creative Commons Attribution License, which permits unrestricted use, distribution, and reproduction in any medium, provided the original work is properly cited.

We review neutrino Yukawa textures with zeros within the framework of the type-I seesaw with three heavy right chiral neutrinos and in the basis where the latter and the charged leptons are mass diagonal. An assumed nonvanishing mass of every ultralight neutrino and the observed nondecoupling of any neutrino generation allow a maximum of four zeros in the Yukawa coupling matrix in family space. We show that the requirement of an exact  $\mu\tau$  symmetry, coupled with the observational constraints, reduces seventy-two allowed such textures to only four corresponding to just two different forms of the light neutrino mass matrix: one with an inverted and the other with a normal mass ordering. The masses and Majorana phases of ultralight neutrinos are predicted within definite ranges with laboratory and cosmological observational inputs. Within the same framework, we also study Yukawa textures with a fewer number of zeros, but with exact  $\mu\tau$  symmetry. We further formulate the detailed scheme of the explicit breaking of  $\mu\tau$  symmetry in terms of three small parameters for allowed four zero textures. The observed sizable mixing between the first and third generations of neutrinos is shown to follow for a suitable choice of these symmetry breaking parameters.

## 1. Introduction

The impressive experimental progress from neutrino oscillation studies [1–5] and the sharpening [6, 7] of the cosmological upper bound on the neutrino mass sum have underscored two fundamental but distinct puzzles. (1) Why are the observed neutrinos so ultralight, that is, with masses in the sub-eV range? (2) Why is the three neutrino mixing pattern of two large and one small (but measurable) angles so different from the sequentially small CKM mixing angles of quarks? There is a widespread feeling that the former is due to some kind of a seesaw mechanism [8–14] yielding ultralight Majorana neutrinos. It is our contention that the latter has to do with zeros in neutrino Yukawa textures plus a broken  $\mu\tau$  symmetry. Let us start with the simplest scheme of three weakly interacting flavored ultralight neutrinos discarding any possible light sterile ones mixing with them. We hold that there should be a fundamental principle behind a massless particle, as with gauge invariance and the photon. Since no such principle is identifiable with any single neutrino, we take each to have a nonzero mass. Though there are other types of

proposed seesaw mechanisms, such as type-II [11, 12], type-III [13], and inverse seesaw [14, 15], in a minimalist approach we stick to the original type-I with three heavy right chiral electroweak singlet neutrinos denoted by the column vector  $N_R$ .

We next turn to the issue of texture zeros. By a texture we mean a configuration of a Yukawa coupling matrix with some vanishing elements. Texture zeros have a long history in the quark sector where four zero Yukawa textures [18–20] have had distinguished success in fitting the known quark masses and CKM parameters. The problem is simpler there since the Dirac quark mass matrix of a given charge, which is the corresponding Yukawa coupling matrix times the Higgs VEV, contains all information about physical quark masses. In the case of seesaw induced ultralight Majorana neutrinos, the elements of the Dirac mass matrix  $M_D$  do not carry all information about physical neutrino masses. The latter are contained in the elements of the complex symmetric Majorana neutrino mass matrix  $M_\nu$ , which is related to  $M_D$  through the standard seesaw formula. There have been initial as well as continuing efforts [21–25] to assume the vanishing of certain elements in  $M_\nu$ . But, we

strongly feel that an occurrence of zeros must be linked to some fundamental symmetry [26–28] or suppression mechanism [29] inherent in the Lagrangian itself. It seems more natural then to postulate the occurrence of such zeros in some elements of the neutrino Yukawa coupling matrix (equivalently  $M_D$ ) which appears in the Lagrangian [16, 17, 30–36]. There are ways [37–39] to ensure the stability of such zeros under quantum corrections in type-I seesaw models.

An important point in the context of texture zeros is that of Weak Basis dependence. Both  $M_D$  and  $M_\nu$  change [40] under general (and different) unitary transformations of the left and right chiral fermion fields. In consequence, any Yukawa texture is basis dependent. It is further known that those fermions, which do not couple mutually in the Lagrangian, can be simultaneously put into a mass diagonal form by suitable basis transformations. Without loss of generality, we can therefore choose a Weak Basis in which the charged lepton fields  $l$  and the very heavy right chiral neutrino fields  $N_R$  are mass diagonal with real masses. The question arises as to how a flavor model, corresponding to a given set of texture zeros in such a basis, would be recognized in a different basis. It has been shown [40] that the vanishing of certain Weak Basis invariants would be a hallmark of those zeros. This is also related to the linkage of CP violation at low energies, probed in short or long baseline experiments, and at high energies, as relevant to leptogenesis. Though that linkage is a major motivation for postulating Yukawa texture zeros [30–32], it is outside the scope of the present paper.

In this paper we focus on the role of texture zeros, occurring in  $M_D$ , in understanding the observed pattern of neutrino masses and mixing angles. More generally, we show how they affect key aspects of low energy neutrino phenomenology. Four is shown to be the maximum number of such zeros allowed within our framework [30]. We classify all possible four zero textures, seventy two in total [30]. Then we introduce  $\mu\tau$  symmetry [16, 41–66] as an invariance under the interchange of flavors  $\mu$  (2) and  $\tau$  (3) in the neutrino sector which is motivated by an automatic prediction of vanishing (maximal) mixing between the first (second) and third generations of neutrinos. This symmetry reduces the preceding seventy two textures to four which lead to only two distinct forms of  $M_\nu$  whose phenomenological consequences are worked out [16, 17, 32]. Three zero textures with  $\mu\tau$  symmetry are also shown to have similar consequences, while textures with a lesser number of zeros have little predictivity [33]. We then discuss the general explicit breaking of  $\mu\tau$  symmetry in terms of three small parameters and show, within the lowest order of perturbation in those parameters, that the observed small mixing of first and third generations of neutrinos can be explained within our framework [33].

In Section 2 we set up our formalism. Section 3 contains the classification of all four zero textures and a discussion of  $\mu\tau$  symmetry. Section 4 addresses the consequent phenomenological implications. In Section 5 we discuss the realization of other  $\mu\tau$  symmetric texture zeros. Section 6 contains a general discussion of explicit  $\mu\tau$  symmetry breaking and how that fits observation. Finally, in Section 7 we summarize our conclusions.

## 2. Framework and Formalism

The relevant mass terms in our starting Lagrangian are

$$\begin{aligned} -\mathcal{L}^m &= \overline{\nu}_L^0 M_D N_R^0 + \frac{1}{2} \overline{N_R^0} M_R N_R^0 + \overline{l}_L^0 M_l l_R^0 + \text{h.c.} \\ &= \frac{1}{2} \begin{pmatrix} \overline{\nu}_L^0 & \overline{N_R^0} \end{pmatrix} \begin{pmatrix} 0 & M_D \\ M_D^T & M_R \end{pmatrix} \begin{pmatrix} \nu_R^0 \\ N_R^0 \end{pmatrix} + \overline{l}_L^0 M_l l_R^0 + \text{h.c.}, \end{aligned} \quad (1)$$

where we have used the general definition of a conjugate fermion field  $\psi^C = \gamma_0 C \psi^*$  ( $C$  being the charge conjugation matrix) and the identity

$$\overline{\psi}_L m \psi'_R = \overline{\psi'_R} m^T \psi_L^C. \quad (2)$$

Here  $M_R$ ,  $M_D$ , and  $M_l$ , respectively, denote the right chiral complex symmetric Majorana mass matrix, the neutrino Dirac mass, matrix and the charged lepton mass matrix in a three-dimensional family space. The superscripts “0” identifies the corresponding fields as flavor eigenstate ones. The complex symmetric  $6 \times 6$  neutrino mass matrix in the second line of (1) is denoted by  $\mathcal{M}$ , that is,

$$\mathcal{M} = \begin{pmatrix} 0 & M_D \\ M_D^T & M_R \end{pmatrix}. \quad (3)$$

The energy scale of  $M_R$  is taken to be very high ( $>10^9$  GeV), as compared with the electroweak scale  $v \simeq 246$  GeV.

The complete diagonalization of  $\mathcal{M}$  leads to

$$\mathcal{V}^\dagger \mathcal{M} \mathcal{V}^* = \text{diag}(d, D), \quad (4)$$

where  $\mathcal{V}$  is a  $6 \times 6$  unitary matrix

$$\mathcal{V} = \begin{pmatrix} K & G \\ S & T \end{pmatrix}, \quad (5)$$

with  $3 \times 3$  blocks  $K$ ,  $G$ ,  $S$ , and  $T$ . In (4)  $d$  and  $D$  are three dimensional diagonal mass matrices, each with ultralight and heavy real positive entries, respectively:

$$\begin{aligned} d &= \text{diag}(m_1, m_2, m_3), \quad m_{1,2,3} < 1 \text{ eV}, \\ D &= \text{diag}(M_1, M_2, M_3), \quad M_{1,2,3} > 10^9 \text{ GeV}. \end{aligned} \quad (6)$$

Charged current interactions can then be written in terms of the semiweak coupling strength  $g$  as well as the respective ultralight neutrino and heavy neutrino fields  $\nu_i$  and  $N_i$ :

$$\mathcal{L}^{cc} = -\frac{g}{\sqrt{2}} \left( \overline{l}_{iL} \gamma_\mu K_{ij} \nu_{jL} + \overline{l}_{iL} \gamma_\mu G_{ij} N_{jL} \right) W^\mu. \quad (7)$$

In an excellent approximation, the ultralight neutrino masses and mixing angles can now be obtained from

$$M_\nu \simeq -M_D M_R^{-1} M_D^T, \quad (8)$$

$$U^\dagger M_\nu U^* = d. \quad (9)$$

Equation (8) is the well-known seesaw formula. We also choose to define the matrix  $h_\nu = M_\nu M_\nu^\dagger$  and have

$$U^\dagger h_\nu U = d^2. \quad (10)$$

In (9),  $U$  is the Pontecorvo, Maki, Nakagawa, Sakata (PMNS) matrix admitting the standard parametrization:

$$U_{\text{PMNS}} = \begin{pmatrix} c_{12}c_{13} & s_{12}c_{13} & s_{13}e^{-i\delta_D} \\ -s_{12}c_{23} - c_{12}s_{23}s_{13}e^{i\delta_D} & c_{12}c_{23} - s_{12}s_{23}s_{13}e^{i\delta_D} & s_{23}c_{13} \\ s_{12}s_{23} - c_{12}c_{23}s_{13}e^{i\delta_D} & -c_{12}s_{23} - s_{12}c_{23}s_{13}e^{i\delta_D} & c_{23}c_{13} \end{pmatrix} \times \begin{pmatrix} e^{i\alpha_{M_1}/2} & 0 & 0 \\ 0 & e^{i\alpha_{M_2}/2} & 0 \\ 0 & 0 & 1 \end{pmatrix}, \quad (11)$$

with  $c_{ij} = \cos \theta_{ij}$ ,  $s_{ij} = \sin \theta_{ij}$ , and  $\delta_D(\alpha_{M_1}, \alpha_{M_2})$  being the yet unknown Dirac (Majorana) phase(s). We note for the sake of completeness that the unitary transformation between the column of mass eigenstate of left chiral neutrino fields  $\nu_L$  and the corresponding flavor eigenstate  $\nu_L^0$  is

$$\nu_L^0 = U \nu_L. \quad (12)$$

The additional approximate relations to keep in mind are those between  $U$  and the submatrices  $K$ ,  $G$  of  $\mathcal{V}$  and  $M_D$  of  $\mathcal{M}$ :

$$K_{ij} = U_{ij} + O\left(\frac{v^2}{M_R^2}\right), \quad (13)$$

$$M_k G_{jk} = (M_D)_{jk} + O\left(\frac{v^3}{M_R^2}\right), \quad k \text{ not summed.}$$

Needless to add, we always neglect terms of order  $v^2/M_R^2$ .

As mentioned earlier, without loss of generality, we can choose the Weak Basis in which  $M_l$  and  $M_R$  are

$$M_l = \text{diag}(m_e, m_\mu, m_\tau), \quad (14)$$

$$M_R = \text{diag}(M_1, M_2, M_3),$$

with real positive entries. All CP-violating phases, stemming from  $\mathcal{M}$ , are contained in the Dirac mass matrix  $M_D$  in this Weak Basis. As a consequence of (6) and (8), (9)  $M_D$  can be written in the Casas-Ibarra form [67]:

$$M_D = iU\sqrt{d}R\sqrt{M_R}, \quad (15)$$

where  $R$  is a complex orthogonal matrix:  $R^T R = R R^T = I$ . An important comment on  $M_D$ , following from (8), is that, our condition of no massless neutrino, that is  $\det M_\nu \neq 0$ , implies that  $\det M_D \neq 0$ . This means that textures of  $M_D$  with one vanishing row or column or with a quartet of zeros (i.e., zeros in  $ij$ ,  $lk$ ,  $ik$ , and  $lj$  elements with  $i \neq l$  and  $k \neq j$  and  $l = 1, 2$ , or  $3$ ) are inadmissible since they make  $\det M_D$  vanish. Furthermore, in our Weak Basis, for any nonzero entry in  $M_D$  with all other elements in its row or column

being zero,  $M_\nu$  from (8) develops a block diagonal form that is incompatible with the observed simultaneous mixing of three neutrinos. The same logic holds for any block diagonal texture of  $M_D$ . Indeed, if any row in a texture of  $M_D$  is orthogonal, element by element, to both the others, one neutrino family decouples and therefore makes such a texture inadmissible. These arguments have been shown [30] to be sufficient to rule out all textures in  $M_D$  with more than four zeros. Four is then the maximum permitted number of zeros in a neutrino Yukawa texture.

### 3. Classification of Four Zero Textures and the Role of $\mu\tau$ Symmetry

In this section we provide the classification of all possible four zero neutrino Yukawa textures and forms of the surviving textures, since these details were not given in [30, 68]. There are  ${}^9C_4 = 126$  possible four zero neutrino Yukawa textures which can be classified into four classes [68]. In making this classification, we rule out the orthogonality between any two rows or columns by some artificial cancellation; orthogonality is to be ensured in terms of a vanishing product, element by element. We can now enumerate four cases.

- (i)  $\det M_D \neq 0$  and one family of neutrinos decouples: 9 textures. For each texture of  $M_D$  here, one row is orthogonal to the other rows. It follows that, in the neutrino mass matrix  $M_\nu$  in our chosen basis with a diagonal  $M_R$ , one neutrino family always decouples. So, though all neutrinos are massive here, these textures are to be discarded.
- (ii)  $\det M_D = 0$  and one family of neutrinos decouples: 18 textures. Here each texture has a vanishing row and there are six such textures for every such row. Such a row generates a vanishing mass eigenvalue and the corresponding family decouples. Hence this class is also excluded.
- (iii)  $\det M_D = 0$  and no family decouples: 27 textures [68]. Each of 18 textures in this class has a vanishing column and each of the remaining 9 has a quartet of zeros, leading to a vanishing  $\det M_\nu$ . So, this class is rejected.
- (iv)  $\det M_D \neq 0$  and no family decouples: 72 textures. These remaining textures are allowed by the criteria we have set up.

The retained textures are subdivided into two categories A and B. We wish to elaborate on this categorization [30]. Let us consistently use the complex parameters  $a_k$ ,  $b_k$ , and  $c_k$  for elements in  $M_D$  belonging to the  $k$ th column and the first, second, and third rows, respectively. The two categories then are as follows.

**Category A.** Here every texture has two mutually orthogonal rows ( $i, j$  say, with  $i \neq j$ ) and the corresponding derived  $M_\nu$  has  $(M_\nu)_{ij} = 0$ . Thus there are 54 such textures divided into three sub-categories, each containing 18 textures: (A1) those with orthogonal rows 1 and 2 which generate

TABLE 1: Four zero Yukawa textures of  $M_D$  in Category A with subcategories A1, A2, and A3.

Category A1 (orthogonality between rows 1 and 2)			
$\begin{pmatrix} 0 & a_2 & 0 \\ b_1 & 0 & b_3 \\ 0 & c_2 & c_3 \end{pmatrix}$	$\begin{pmatrix} 0 & a_2 & 0 \\ b_1 & 0 & b_3 \\ c_1 & c_2 & 0 \end{pmatrix}$	$\begin{pmatrix} 0 & 0 & a_3 \\ b_1 & b_2 & 0 \\ 0 & c_2 & c_3 \end{pmatrix}$	$\begin{pmatrix} 0 & 0 & a_3 \\ b_1 & b_2 & 0 \\ c_1 & 0 & c_3 \end{pmatrix}$
$\begin{pmatrix} 0 & a_2 & 0 \\ 0 & 0 & b_3 \\ c_1 & c_2 & c_3 \end{pmatrix}$	$\begin{pmatrix} 0 & a_2 & 0 \\ 0 & 0 & b_3 \\ c_1 & c_2 & c_3 \end{pmatrix}$	$\begin{pmatrix} 0 & 0 & a_3 \\ b_1 & 0 & 0 \\ c_1 & c_2 & c_3 \end{pmatrix}$	$\begin{pmatrix} 0 & 0 & a_3 \\ 0 & b_2 & 0 \\ c_1 & c_2 & c_3 \end{pmatrix}$
$\begin{pmatrix} a_1 & 0 & a_3 \\ 0 & b_2 & 0 \\ 0 & c_2 & c_3 \end{pmatrix}$	$\begin{pmatrix} a_1 & 0 & a_3 \\ 0 & b_2 & 0 \\ c_1 & c_2 & 0 \end{pmatrix}$	$\begin{pmatrix} a_1 & a_2 & 0 \\ 0 & 0 & b_3 \\ 0 & c_2 & c_3 \end{pmatrix}$	$\begin{pmatrix} a_1 & a_2 & 0 \\ 0 & 0 & b_3 \\ c_1 & 0 & c_3 \end{pmatrix}$
$\begin{pmatrix} a_1 & 0 & 0 \\ 0 & b_2 & b_3 \\ c_1 & 0 & c_3 \end{pmatrix}$	$\begin{pmatrix} a_1 & 0 & 0 \\ 0 & b_2 & b_3 \\ c_1 & c_2 & 0 \end{pmatrix}$	$\begin{pmatrix} a_1 & 0 & 0 \\ 0 & b_2 & b_3 \\ c_1 & 0 & c_3 \end{pmatrix}$	$\begin{pmatrix} a_1 & 0 & 0 \\ 0 & b_2 & b_3 \\ c_1 & c_2 & 0 \end{pmatrix}$
Category A2 (orthogonality between rows 2 and 3)			
$\begin{pmatrix} 0 & a_2 & a_3 \\ 0 & b_2 & 0 \\ c_1 & 0 & c_3 \end{pmatrix}$	$\begin{pmatrix} a_1 & a_2 & 0 \\ 0 & b_2 & 0 \\ c_1 & 0 & c_3 \end{pmatrix}$	$\begin{pmatrix} 0 & a_2 & a_3 \\ 0 & 0 & b_2 \\ c_1 & c_2 & 0 \end{pmatrix}$	$\begin{pmatrix} a_1 & 0 & a_3 \\ 0 & 0 & b_3 \\ c_1 & c_2 & 0 \end{pmatrix}$
$\begin{pmatrix} a_1 & a_2 & a_3 \\ 0 & b_2 & 0 \\ 0 & 0 & c_3 \end{pmatrix}$	$\begin{pmatrix} a_1 & a_2 & a_1 \\ 0 & b_2 & 0 \\ c_1 & 0 & 0 \end{pmatrix}$	$\begin{pmatrix} a_1 & a_2 & a_3 \\ 0 & 0 & b_2 \\ c_1 & 0 & 0 \end{pmatrix}$	$\begin{pmatrix} a_1 & a_2 & a_3 \\ 0 & 0 & b_3 \\ c_1 & 0 & 0 \end{pmatrix}$
$\begin{pmatrix} 0 & a_2 & a_3 \\ b_1 & 0 & b_3 \\ 0 & c_2 & 0 \end{pmatrix}$	$\begin{pmatrix} a_1 & a_2 & 0 \\ b_1 & 0 & b_3 \\ 0 & c_2 & 0 \end{pmatrix}$	$\begin{pmatrix} 0 & a_2 & a_3 \\ b_1 & b_2 & 0 \\ 0 & 0 & c_3 \end{pmatrix}$	$\begin{pmatrix} a_1 & 0 & a_3 \\ b_1 & b_2 & 0 \\ 0 & 0 & c_3 \end{pmatrix}$
Category A3 (orthogonality between rows 1 and 3)			
$\begin{pmatrix} 0 & a_2 & 0 \\ 0 & b_2 & b_3 \\ c_1 & 0 & c_3 \end{pmatrix}$	$\begin{pmatrix} 0 & a_2 & 0 \\ 0 & b_2 & b_3 \\ c_1 & 0 & c_3 \end{pmatrix}$	$\begin{pmatrix} 0 & 0 & a_3 \\ 0 & b_2 & b_3 \\ c_1 & c_2 & 0 \end{pmatrix}$	$\begin{pmatrix} 0 & 0 & a_3 \\ b_1 & 0 & b_3 \\ c_1 & c_2 & 0 \end{pmatrix}$
$\begin{pmatrix} 0 & a_2 & 0 \\ b_1 & b_2 & b_3 \\ 0 & 0 & c_3 \end{pmatrix}$	$\begin{pmatrix} 0 & a_2 & 0 \\ b_1 & b_2 & b_3 \\ c_1 & 0 & 0 \end{pmatrix}$	$\begin{pmatrix} 0 & 0 & a_3 \\ b_1 & b_2 & b_3 \\ 0 & c_2 & 0 \end{pmatrix}$	$\begin{pmatrix} 0 & 0 & a_3 \\ b_1 & b_2 & b_3 \\ c_1 & 0 & 0 \end{pmatrix}$
$\begin{pmatrix} a_1 & 0 & a_3 \\ 0 & b_2 & b_3 \\ 0 & c_2 & 0 \end{pmatrix}$	$\begin{pmatrix} a_1 & 0 & a_3 \\ b_1 & b_2 & 0 \\ 0 & c_2 & 0 \end{pmatrix}$	$\begin{pmatrix} a_1 & a_2 & 0 \\ 0 & b_2 & b_3 \\ 0 & 0 & c_3 \end{pmatrix}$	$\begin{pmatrix} a_1 & a_2 & 0 \\ b_1 & 0 & b_3 \\ 0 & 0 & c_3 \end{pmatrix}$

$(M_\nu)_{12} = (M_\nu)_{21} = 0$ ; (A2) those with orthogonal rows 2 and 3 which generate  $(M_\nu)_{23} = (M_\nu)_{32} = 0$ ; (A3) those with orthogonal rows 1 and 3 which generate  $(M_\nu)_{13} = (M_\nu)_{31} = 0$ . The explicit form of each of the 54 textures in Category A within the three sub-categories is shown in Table 1.

*Category B.* There are 18 textures in this category. Each has two orthogonal columns, while no pair of rows is orthogonal. Invariably, then, it turns out that one row ( $i$ , say) has two zeroes and the other two rows (say  $k, l \neq i$ ) have one zero each. It is now a consequence of (8) that, in the derived neutrino mass-matrix  $M_\nu$ , we have the relation

$$\det \text{cofactor} [(M_\nu)_{kl}] = 0. \quad (16)$$

Once again, one can make three subcategories with six entries each. B1 has two zeros in the first row and one zero in each of the other two rows. B2 has two zeros in the second row and one zero in each of the other two rows. B3 has two zeros in the third row and one zero in each of the other two rows. All 18 textures of Category B are shown in Table 2 within the three subcategories.

We now raise the question of  $\mu\tau$  symmetry which we had explained in the Introduction. This symmetry is evidently invalid for the charged lepton mass terms. However, for elements in the Dirac mass matrix  $M_D$  of neutrinos, it immediately implies the relations

$$\begin{aligned} (M_D)_{12} &= (M_D)_{13}, & (M_D)_{21} &= (M_D)_{31}, \\ (M_D)_{23} &= (M_D)_{32}, & (M_D)_{22} &= (M_D)_{33}. \end{aligned} \quad (17)$$

Moreover, for the masses of the very heavy right-chiral neutrinos, we have

$$(M_R)_{22} = (M_R)_{33}, \quad (18)$$

a result which is transparent as  $M_2 = M_3$  in our chosen basis. On account of (8) and (17) as well as (18), one is immediately led to the following relations among elements of the complex symmetric ultralight neutrino Majorana mass matrix  $M_\nu$ :

$$(M_\nu)_{12} = (M_\nu)_{13}, \quad (M_\nu)_{22} = (M_\nu)_{33}. \quad (19)$$

We take these as statements of a custodial  $\mu\tau$  symmetry in the ultralight neutrino sector. One can now invert (9) and



TABLE 2: Four zero Yukawa textures of  $M_D$  in Category B with subcategories B1, B2, and B3.

Category B1					
First row with two zeros, a pair of orthogonal columns, non-orthogonal rows					
$\begin{pmatrix} 0 & a_2 & 0 \\ 0 & b_1 & b_3 \\ c_1 & c_2 & 0 \end{pmatrix}$	$\begin{pmatrix} 0 & a_2 & 0 \\ b_1 & b_2 & 0 \\ 0 & c_2 & c_3 \end{pmatrix}$	$\begin{pmatrix} 0 & 0 & a_3 \\ 0 & b_2 & b_3 \\ c_1 & 0 & c_3 \end{pmatrix}$	$\begin{pmatrix} 0 & 0 & a_3 \\ b_1 & 0 & b_3 \\ 0 & c_2 & c_3 \end{pmatrix}$	$\begin{pmatrix} a_1 & 0 & 0 \\ b_1 & 0 & b_3 \\ c_1 & c_2 & 0 \end{pmatrix}$	$\begin{pmatrix} a_1 & 0 & 0 \\ b_1 & b_2 & 0 \\ c_1 & 0 & c_3 \end{pmatrix}$
Category B2					
Second row with two zeros, a pair of orthogonal columns, non-orthogonal rows					
$\begin{pmatrix} 0 & a_2 & a_3 \\ 0 & b_2 & 0 \\ c_1 & c_2 & 0 \end{pmatrix}$	$\begin{pmatrix} a_1 & a_2 & 0 \\ 0 & b_2 & 0 \\ 0 & c_2 & c_3 \end{pmatrix}$	$\begin{pmatrix} 0 & a_2 & a_3 \\ 0 & 0 & b_2 \\ c_1 & 0 & c_3 \end{pmatrix}$	$\begin{pmatrix} a_1 & 0 & a_3 \\ 0 & 0 & b_3 \\ 0 & c_2 & c_3 \end{pmatrix}$	$\begin{pmatrix} a_1 & 0 & a_3 \\ b_1 & 0 & 0 \\ c_1 & c_2 & 0 \end{pmatrix}$	$\begin{pmatrix} a_1 & a_2 & 0 \\ b_1 & 0 & 0 \\ c_1 & 0 & c_3 \end{pmatrix}$
Category B3					
Third row with two zeros, a pair of orthogonal columns, non-orthogonal rows					
$\begin{pmatrix} a_1 & a_2 & 0 \\ 0 & b_2 & b_3 \\ 0 & c_2 & 0 \end{pmatrix}$	$\begin{pmatrix} 0 & a_2 & a_3 \\ b_1 & b_2 & 0 \\ 0 & c_2 & 0 \end{pmatrix}$	$\begin{pmatrix} a_1 & 0 & a_3 \\ 0 & b_2 & b_3 \\ 0 & 0 & c_3 \end{pmatrix}$	$\begin{pmatrix} 0 & a_2 & a_3 \\ b_1 & 0 & b_3 \\ 0 & 0 & c_3 \end{pmatrix}$	$\begin{pmatrix} a_1 & 0 & a_3 \\ b_1 & b_2 & 0 \\ c_1 & 0 & 0 \end{pmatrix}$	$\begin{pmatrix} a_1 & a_2 & 0 \\ b_1 & 0 & b_3 \\ c_1 & 0 & 0 \end{pmatrix}$

explore the consequences of (19) in the parametrization of (11). An immediate consequence is the fixing of the two mixing angles pertaining to the third flavor:  $\theta_{23} = \pi/4$ ,  $\theta_{13} = 0$ . Since the measured former angle is compatible with  $45^\circ$  within errors and the latter has been found to be small ( $\approx 9^\circ$ ), the occurrence of at least a broken  $\mu\tau$  symmetry in nature is a reasonable supposition that we adhere to. An interesting footnote to this discussion is the issue of tribimaximal mixing [69, 70] which subsumes  $\mu\tau$  symmetry but posits the additional relation

$$(M_\nu)_{11} + (M_\nu)_{13} = (M_\nu)_{22} + (M_\nu)_{23}, \quad (20)$$

leading to a fixation of the remaining mixing angle  $\theta_{12} = \sin^{-1}(1/\sqrt{3}) \approx 35.26^\circ$ . However, we will not make use of (20).

An immediate consequence of the imposition of  $\mu\tau$  symmetry, via (17), is the drastic reduction of the seventy two allowed four zero textures of  $M_D$  to only four [16]. This is seen just by inspection. The allowed  $\mu\tau$  symmetric textures are the following, each involving only three complex parameters.

*Category A.* One has

$$M_{DA1} = \begin{pmatrix} a_1 & a_2 & a_2 \\ 0 & 0 & b_1 \\ 0 & b_1 & 0 \end{pmatrix}, \quad M_{DA2} = \begin{pmatrix} a_1 & a_2 & a_2 \\ 0 & b_1 & 0 \\ 0 & 0 & b_1 \end{pmatrix}. \quad (21)$$

*Category B.* One has

$$M_{DB1} = \begin{pmatrix} a_1 & 0 & 0 \\ b_1 & 0 & b_2 \\ b_1 & b_2 & 0 \end{pmatrix}, \quad M_{DB2} = \begin{pmatrix} a_1 & 0 & 0 \\ b_1 & b_2 & 0 \\ b_1 & 0 & b_2 \end{pmatrix}. \quad (22)$$

It may be noted that, in either category, any texture can be obtained from the other by the interchange of rows 2 and 3 or columns 2 and 3. Because of  $\mu\tau$  symmetry, this means that the physical content of the two textures in each category is the same. Indeed, by use of (8), we obtain the same  $M_\nu$  for either

of them. Thus we have just two allowed ultralight neutrino Majorana mass matrices

$$M_{\nu A} = - \begin{pmatrix} \frac{a_1^2}{M_1} + \frac{2a_2^2}{M_2} & \frac{a_2 b_1}{M_2} & \frac{a_2 b_1}{M_2} \\ \frac{a_2 b_1}{M_2} & \frac{b_1^2}{M_2} & 0 \\ \frac{a_2 b_1}{M_2} & 0 & \frac{b_1^2}{M_2} \end{pmatrix}, \quad (23)$$

$$M_{\nu B} = - \begin{pmatrix} \frac{a_1^2}{M_1} & \frac{a_1 b_1}{M_1} & \frac{a_1 b_1}{M_1} \\ \frac{a_1 b_1}{M_1} & \frac{b_1^2}{M_1} + \frac{b_2^2}{M_2} & \frac{b_1^2}{M_1} \\ \frac{a_1 b_1}{M_1} & \frac{b_1^2}{M_1} & \frac{b_1^2}{M_1} + \frac{b_2^2}{M_2} \end{pmatrix}, \quad (24)$$

for Categories A and B, respectively.

#### 4. Phenomenology with $\mu\tau$ Symmetric Four Zero Yukawa Textures

Given  $\mu\tau$  symmetry, one automatically obtains that  $\theta_{23} = \pi/4$  and  $\theta_{13} = 0$ . The current  $3\sigma$  limits on these are  $36.86^\circ < \theta_{23} < 55.55^\circ$  and  $7.49^\circ < \theta_{13} < 10.46^\circ$  [1]. We shall later consider a small breaking of  $\mu\tau$  symmetry. But, for the moment, let us assume the latter to be the exact. The other mass and mixing parameters in the ultralight neutrino sector are kept free. Their experimentally allowed  $3\sigma$  ranges to be used to constrain the nonzero elements of  $M_{\nu A}$  and  $M_{\nu B}$  in Table 3. We define  $\Delta_{ij}^2 = m_i^2 - m_j^2$ , where  $i, j$  ( $= 1, 2, 3$ ) refer to the mass eigenstate neutrinos. It will now be convenient to reparametrize the elements of  $M_{\nu A}$  and  $M_{\nu B}$  in (23) and (24), respectively, in the way given in Table 3. Here  $k_1, k_2, l_1$ , and  $l_2$  are real and positive quantities while  $\alpha, \alpha', \beta$ , and  $\beta'$  are phases. However, the phases  $\alpha'$  and  $\beta'$  can be absorbed in

TABLE 3: Reparametrized quantities and relevant functions in Category A and Category B.

Category A	Category B
$M_{\nu A}$	$M_{\nu B}$
$m_A = \frac{-b_1^2}{M_2}$	$m_B = \frac{-b_2^2}{M_2}$
$k_1 e^{i(\alpha+\alpha')} = \frac{a_1}{b_1} \sqrt{\frac{M_2}{M_1}}$	$l_1 e^{i\beta'} = \frac{a_1}{b_2} \sqrt{\frac{M_2}{M_1}}$
$k_2 e^{i\alpha'} = \frac{a_2}{b_1}$	$l_2 e^{i\beta} = \frac{b_1}{b_2} \sqrt{\frac{M_2}{M_1}}$
$\alpha = \arg \frac{a_1}{a_2}$	$\beta = \arg \frac{b_1}{b_2}$
$X_1^A = 2\sqrt{2}k_2[(1+2k_2^2)^2 + k_1^4 + 2k_1^2(1+2k_2^2)\cos 2\alpha]^{1/2}$	$X_1^B = 2\sqrt{2}l_1l_2[(l_1^2+2l_2^2)^2 + 1 + 2(l_1^2+2l_2^2)\cos 2\beta]^{1/2}$
$X_2^A = 1 - k_1^4 - 4k_2^4 - 4k_1^2k_2^2\cos 2\alpha$	$X_2^B = 1 + 4l_2^2\cos 2\beta + 4l_1^4 - l_1^4$
$X_3^A = 1 - 4k_2^4 - k_1^4 - 4k_1^2k_2^2\cos 2\alpha - 4k_2^2$	$X_3^B = 1 - (l_1^2+2l_2^2)^2 - 4l_2^2\cos 2\beta$
$X_4^A = k_1^4 + 4k_2^4 + 4k_1^2k_2^2\cos 2\alpha$	$X_4^B = l_1^4$

TABLE 4: Input experimental values [1].

Quantity	Experimental $3\sigma$ range
$\Delta_{21}^2$	$7.12 \times 10^{-5} \text{ eV}^2 < \Delta_{21}^2 < 8.20 \times 10^{-5} \text{ eV}^2$
$\Delta_{32}^2 < 0$	$-2.76 \times 10^{-3} \text{ eV}^2 < \Delta_{32}^2 < -2.22 \times 10^{-3} \text{ eV}^2$
$\Delta_{32}^2 > 0$	$2.18 \times 10^{-3} \text{ eV}^2 < \Delta_{32}^2 < 2.70 \times 10^{-3} \text{ eV}^2$
$\theta_{12}$	$31.30^\circ < \theta_{12} < 37.46^\circ$

the definition of the first family neutrino field  $\nu_e$  for  $M_{\nu A}$  and  $M_{\nu B}$  respectively and therefore are not physical. Moreover, the overall phase in  $m_{A,B}$  can also be absorbed by a further redefinition of all flavor eigenstate neutrino fields. So we can treat  $m_{A,B}$  as real for further discussions. In addition, we have defined in Table 3 sets of derived real quantities  $X_{1-4}^{A,B}$  which will be related to various observables.

With the reparametrization given in Table 3,  $M_{\nu A}$  and  $M_{\nu B}$  assume the simple forms

$$M_{\nu A} = m_A \begin{pmatrix} k_1^2 e^{2i\alpha} + 2k_2^2 & k_2 & k_2 \\ k_2 & 1 & 0 \\ k_2 & 0 & 1 \end{pmatrix},$$

$$M_{\nu B} = m_B \begin{pmatrix} l_1^2 & l_1 l_2 e^{i\beta} & l_1 l_2 e^{i\beta} \\ l_1 l_2 e^{i\beta} & l_2^2 e^{2i\beta} + 1 & l_2^2 e^{2i\beta} \\ l_1 l_2 e^{i\beta} & l_2^2 e^{2i\beta} & l_2^2 e^{2i\beta} + 1 \end{pmatrix}. \quad (25)$$

These lead us, through the diagonalization of the matrix  $h_\nu$  of (10), to the relations

$$\Delta_{21}^2 = m^2 X, \quad \Delta_{32}^2 = \frac{m^2}{2} (X_3 - X), \quad \tan 2\theta_{12} = \frac{X_1}{X_2}, \quad (26)$$

where  $m = m_{A,B}$  for Categories A, B and

$$X = \sqrt{X_1^2 + X_2^2}. \quad (27)$$

One can further make use of (9) to calculate [17] the ultralight masses  $m_{1,2,3}$  in terms  $\Delta_{21}^2$  and also the Majorana phases  $\alpha_{M_1}, \alpha_{M_2}$ , compare (11), in terms of  $m_1, m_2$ , and  $m_3$ . The former are given by

$$m_{1,2} = \left| \Delta_{21}^2 \left( \frac{2 - X_3 \mp X}{2X} \right) \right|^{1/2}, \quad m_3 = \left| \frac{\Delta_{21}^2}{X} \right|^{1/2} \quad (28)$$

and the latter by

$$\cos(\alpha_{M_1} - \arg \cdot Z) = \frac{|Z|^2 m_3^2 + m_1^2 \sin^4 \theta_{12} - m_2^2 \cos^4 \theta_{12}}{2m_1 m_3 \sin^2 \theta_{12} |Z|},$$

$$\cos(\alpha_{M_2} - \arg \cdot Z) = \frac{|Z|^2 m_3^2 + m_2^2 \cos^4 \theta_{12} - m_1^2 \sin^4 \theta_{12}}{2m_2 m_3 \cos^2 \theta_{12} |Z|}. \quad (29)$$

Here  $Z = [(\mathcal{M}_\nu)_{22} + (\mathcal{M}_\nu)_{23}][(\mathcal{M}_\nu)_{22} - (\mathcal{M}_\nu)_{23}]^{-1}$ . The last quantity of physical interest that we calculate in this section is the effective mass  $m_{\beta\beta} = |(\mathcal{M}_\nu)_{11}|$  appearing in the transition amplitude for the yet unobserved neutrinoless nuclear double beta decay. That is given by

$$m_{\beta\beta} = |\Delta_{21}^2 X_4 X^{-1}|^{1/2}, \quad (30)$$

with  $X_4$  as given in Table 3.

Feeding the experimental  $3\sigma$  ranges from Table 4, we find that only the inverted mass ordering  $\Delta_{32}^2 < 0$  is allowed in Category A while only the normal mass ordering  $\Delta_{32}^2 > 0$  is permitted for Category B. Moreover, in the corresponding

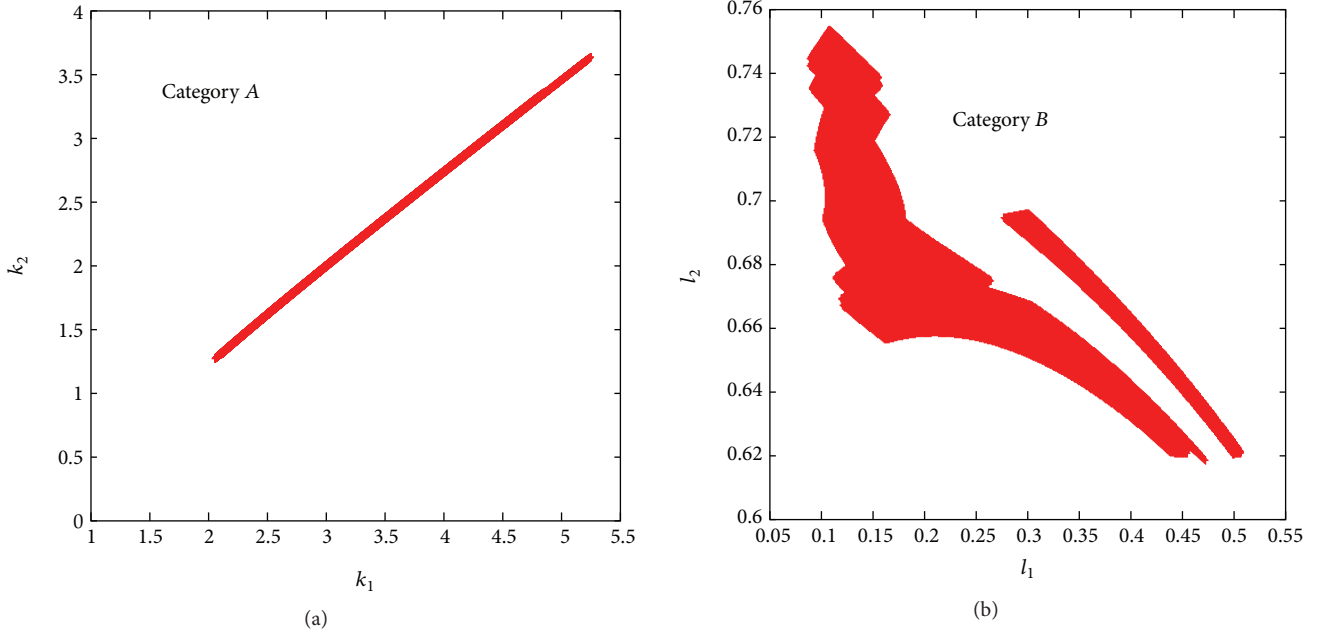


FIGURE 1: Variation of  $k_1$  and  $k_2$  in Category A and of  $l_1$  and  $l_2$  in Category B with  $\mu\tau$  symmetry over the  $3\sigma$  allowed ranges of  $\Delta_{21}^2$ ,  $|\Delta_{32}^2|$ , and  $\theta_{12}$  [16].

$k_1 - k_2/l_1 - l_2$  parameter plane [16], very constrained domains are allowed, as shown in Figure 1. The phases  $\alpha$ ,  $\beta$  are also severely restricted in magnitude, specifically  $89.0^\circ \leq |\alpha| < 90^\circ$  and  $87.0^\circ \leq |\beta| < 90^\circ$ . These allow just a very limited region in the  $X_3 - X$  plane, leading to  $3\sigma$  lower and upper bounds on the neutrino mass sum  $m_1 + m_2 + m_3$ , namely,  $[0.156, 0.5] \text{ eV}/[0.074, 0.132] \text{ eV}$  for an inverted/normal mass ordering [17]. It may be recalled that there is already a lower bound of  $0.05 \text{ eV}$  on the said sum from atmospheric neutrino data. Furthermore the general consensus [7] on the least model-dependent cosmological upper bound on it is  $0.5 \text{ eV}$ .

Turning to the individual neutrino masses  $m_1/\text{eV}$ ,  $m_2/\text{eV}$ , and  $m_3/\text{eV}$ , respectively, we obtain by use of (28) the respective  $3\sigma$  intervals  $[0.0452, 0.1682]$ ,  $[0.0457, 0.1684]$ ,  $[0.077, 0.1632]$  for Category A and  $[0.0110, 0.0335]$ ,  $[0.0144, 0.0345]$ , and  $[0.0485, 0.0638]$  for Category B. However, there are correlated constraints among these masses. These are shown in the left-most panel of Figure 2. Given these allowed intervals and correlated constraints, it is not possible right now to distinguish between the hierarchical and quasi-degenerate possibilities. But a future reduction of these ranges and domains could pin this down. We next come to the Majorana phases  $\alpha_{M_1}$ ,  $\alpha_{M_2}$ . One can ab initio restrict them to the interval  $-\pi$  to  $\pi$  and utilize (29) as well as the expressions for  $Z$ ,  $m_1$ ,  $m_2$ ,  $m_3$  and  $\tan 2\theta_{12}$  in terms of the basic parameters  $(k_1, k_2, \alpha)/(l_1, l_2$  and  $\beta)$ , depending on the category. The further application of the phenomenologically acceptable ranges of these parameters, as given above, leads to the allowed  $3\sigma$  intervals  $-98.0^\circ \leq \alpha_{M_1} \leq 20.0^\circ$ ,  $9.2^\circ \leq \alpha_{M_2} \leq 36.4^\circ$  for Category A and  $-88.6^\circ \leq \alpha_{M_1} \leq 7.97^\circ$ ,  $90.7^\circ \leq \alpha_{M_2} \leq 128.8^\circ$  for Category B. Allowed values of  $\alpha_{M_1}$  and  $\alpha_{M_2}$  are shown in the middle panel of Figure 2.

Another quantity to be considered in this section is the double  $\beta$ -decay effective mass  $m_{\beta\beta}$ , compare (30). The currently accepted upper bound [71] on it is  $m_{\beta\beta} < 0.35 \text{ eV}$ . In comparison, our allowed values  $m_{\beta\beta}$  versus the neutrino mass sum  $\sum_i m_i$  are shown in the rightmost panels of Figure 2. More absolutely, we can say that  $0.038 \leq m_{\beta\beta}/\text{eV} \leq 0.161$  for Category A and  $0.003 \leq m_{\beta\beta}/\text{eV} \leq 0.0186$  for Category B. The region near the upper bound in Category A may be accessible in forthcoming experiments.

An interesting question pertains to the consequences of the effect of  $\mu\tau$  symmetry on couplings between the heavy right chiral and the ultralight left chiral neutrinos. The corresponding neutral gauge boson induced interactions are down by factor  $O(v^2/M_R^2)$ . On the other hand, the Higgs boson induced interactions affect leptogenesis modes and have been discussed in detail in [32]. Since leptogenesis is outside the scope of the present paper, we do not go into those discussions here.

## 5. Realization of Other Texture Zeros with $\mu\tau$ Symmetry

Though four is the maximum number of allowed neutrino Yukawa texture zeros, we examine other textures with a lesser number of zeros for completeness [33]. Let us work in the same Weak Basis of real diagonal  $M_l$  and  $M_R$ . We wish to study only those textures that are compatible with  $\mu\tau$  symmetry which we believe to be approximately valid in the real world. The  $\mu\tau$  symmetric forms of  $M_D$  and  $M_R$  now are

$$M_D = \begin{pmatrix} a & b & b \\ c & d & e \\ c & e & d \end{pmatrix}, \quad M_R = \text{diag}(M_1, M_2, M_2), \quad (31)$$

with  $a, b, c, d$ , and  $e$  as complex numbers.

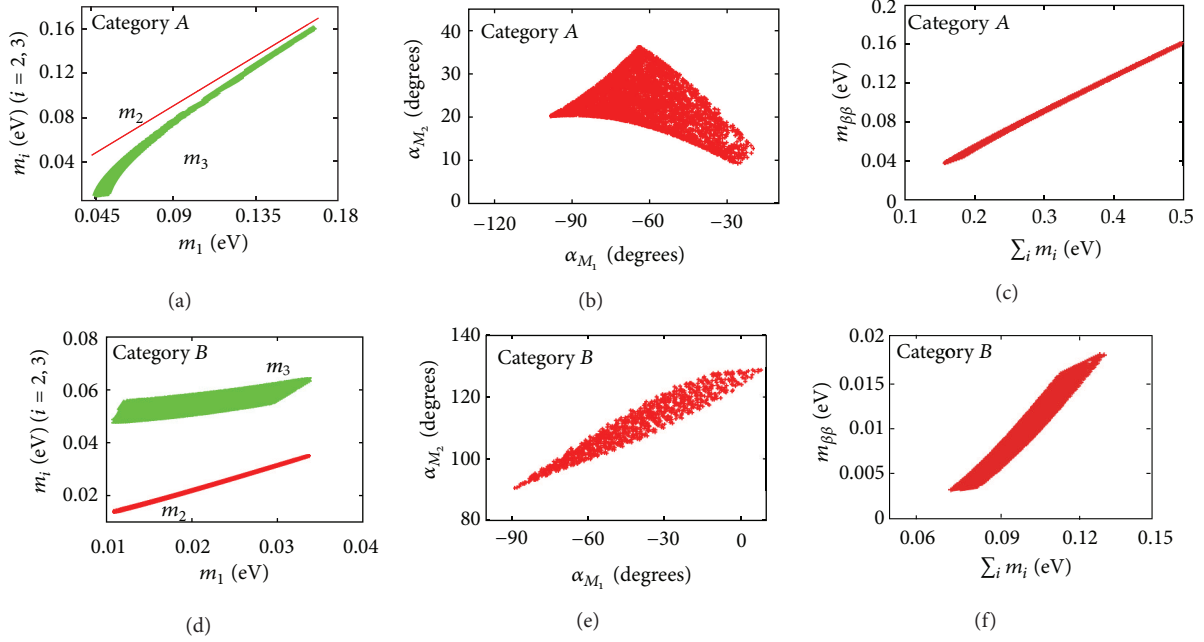


FIGURE 2: Allowed  $m_{2,3}$  versus  $m_1$  (left),  $\alpha_{M_2}$  versus  $\alpha_{M_1}$  (middle), and  $m_{\beta\beta}$  versus  $\Sigma m_i$  (right) for Category A (top) and Category B (bottom) [17].

**5.1. Three Zero Textures.** We first identify possible three zero textures which are compatible with (31). Apart from  $a$ , the other four complex parameters in  $M_D$  come in pairs. So, for any texture with an odd number of zeros,  $a$  must vanish. For three zero textures the remaining two zeros can be arranged in  ${}^4C_1 = 4$  ways. So, the four allowed three zero  $\mu\tau$  symmetric textures of  $M_D$  are

$$\begin{pmatrix} 0 & b & b \\ c & 0 & e \\ c & e & 0 \end{pmatrix}, \quad \begin{pmatrix} 0 & b & b \\ c & d & 0 \\ c & 0 & d \end{pmatrix}, \quad (32)$$

$$\begin{pmatrix} 0 & 0 & 0 \\ c & d & e \\ c & e & d \end{pmatrix}, \quad \begin{pmatrix} 0 & b & b \\ 0 & d & e \\ 0 & e & d \end{pmatrix}.$$

The last two textures have one vanishing row and one vanishing column, respectively. These can be discarded with our requirement of no massless neutrino, that is,  $\det M_\nu \neq 0$ , leaving only the first two textures as acceptable. In general, there can be  ${}^9C_3 = 84$  three zero textures. The conditions of (1)  $\mu\tau$  symmetry, (2) the non-zero value of  $\det M_\nu$ , and (3) the nondecoupling of any neutrino generation reduce this number to only two.

The first two textures of (32) have only three complex parameters each and we can just use  $b$ ,  $c$ , and  $d$  for both allowed textures of  $M_D$ :

$$\begin{pmatrix} 0 & b & b \\ c & 0 & d \\ c & d & 0 \end{pmatrix}, \quad \begin{pmatrix} 0 & b & b \\ c & d & 0 \\ c & 0 & d \end{pmatrix}. \quad (33)$$

Using the seesaw formula, we obtain an identical form of  $M_\nu$  for both textures in (33), namely,

$$M_\nu = - \begin{pmatrix} \frac{2b^2}{M_2} & \frac{bd}{M_2} & \frac{bd}{M_2} \\ \frac{bd}{M_2} & \frac{c^2}{M_1} + \frac{d^2}{M_2} & \frac{c^2}{M_1} \\ \frac{bd}{M_2} & \frac{c^2}{M_1} & \frac{c^2}{M_1} + \frac{d^2}{M_2} \end{pmatrix}. \quad (34)$$

Equation (34) can be written in the following form under a further reparametrization:

$$M_\nu = m_0 \begin{pmatrix} 2k_1^2 e^{i2\alpha_1} & k_1 e^{i\alpha_1} & k_1 e^{i\alpha_1} \\ k_1 e^{i\alpha_1} & k_2^2 e^{i\alpha_2} + 1 & k_2^2 e^{i\alpha_2} \\ k_1 e^{i\alpha_1} & k_2^2 e^{i\alpha_2} & k_2^2 e^{i\alpha_2} + 1 \end{pmatrix}, \quad (35)$$

with  $m_0 = -d^2/M_2$ ,  $k_1 e^{i\alpha_1} = b/d$ , and  $k_2 e^{i\alpha_2} = c/d\sqrt{M_2/M_1}$ . From  $M_\nu$ , we can remove the phase  $\alpha_1$  and any phase  $\theta_m$  in  $m_0$  by rotating  $M_\nu$  with the diagonal phase matrix  $\text{diag}(e^{-i\alpha_1}, 1, 1)e^{-i\theta_m/2}$ . Thus,  $M_\nu$  has three real parameters, namely,  $m_0$ ,  $k_1$  and  $k_2$ , and only one phase  $\alpha_2$ . The interesting point to be noted is that the number of independent parameters in  $M_\nu$  for  $\mu\tau$  symmetric three zero Yukawa textures is the same as that for  $\mu\tau$  symmetric four zero textures. We then have the same phenomenological



expressions as in (26)–(30), but now with changed definitions of  $X_{1,2,3,4}$ , namely,

$$\begin{aligned} X_1 &= 2\sqrt{2}k_1 \sqrt{(1+2k_1^2)^2 + 4k_2^4 + 4k_2^2(1+2k_1^2)\cos 2\alpha_2}, \\ X_2 &= 4k_2^4 + 1 + 4k_2^2 \cos 2\alpha_2 - 4k_1^4, \\ X_3 &= 1 - 4k_1^4 - 4k_1^2 - 4k_2^4 - 4k_2^2 \cos 2\alpha_2, \\ X_4 &= 4k_1^2. \end{aligned} \quad (36)$$

**5.2. Two Zero Textures.** Again, looking at the  $\mu\tau$  symmetric form of  $M_D$  in (31), we can conclude that, for any even zero textures,  $a \neq 0$ . Two zeros can be fitted to each of the remaining four pairs of parameters in four ways. The four possible two zero textures of  $M_D$  are

$$\begin{aligned} \begin{pmatrix} a & b & b \\ c & 0 & d \\ c & 0 & d \end{pmatrix}, \quad \begin{pmatrix} a & b & b \\ c & d & 0 \\ c & 0 & d \end{pmatrix}, \\ \begin{pmatrix} a & 0 & 0 \\ c & b & d \\ c & d & b \end{pmatrix}, \quad \begin{pmatrix} a & b & b \\ 0 & c & d \\ 0 & d & c \end{pmatrix}, \end{aligned} \quad (37)$$

and are all allowed. So, the number of allowed  $\mu\tau$  symmetric two zero textures is the same as that of similar four zero textures. We need only the four parameters  $a, b, c$  and  $d$  to write down all four textures. The latter lead to three allowed forms of  $M_\nu$ ; the first two such textures yield one form and the remaining two lead to two forms of  $M_\nu$ . These are respectively given by

$$M_\nu = - \begin{pmatrix} \frac{a^2}{M_1} + \frac{2b^2}{M_2} & \frac{ac}{M_1} + \frac{bd}{M_2} & \frac{ac}{M_1} + \frac{bd}{M_2} \\ \frac{ac}{M_1} + \frac{bd}{M_2} & \frac{c^2}{M_1} + \frac{d^2}{M_2} & \frac{c^2}{M_1} \\ \frac{ac}{M_1} + \frac{bd}{M_2} & \frac{c^2}{M_1} & \frac{c^2}{M_1} + \frac{d^2}{M_2} \end{pmatrix}, \quad (38)$$

$$M_\nu = - \begin{pmatrix} \frac{a^2}{M_1} & \frac{ac}{M_1} & \frac{ac}{M_1} \\ \frac{ac}{M_1} & \frac{c^2}{M_1} + \frac{d^2}{M_2} + \frac{b^2}{M_2} & \frac{c^2}{M_1} + \frac{2bd}{M_2} \\ \frac{ac}{M_1} & \frac{c^2}{M_1} + \frac{2bd}{M_2} & \frac{c^2}{M_1} + \frac{d^2}{M_2} + \frac{b^2}{M_2} \end{pmatrix}, \quad (39)$$

$$M_\nu = - \begin{pmatrix} \frac{a^2}{M_1} + \frac{2b^2}{M_2} & \frac{bc}{M_2} + \frac{bd}{M_2} & \frac{bc}{M_2} + \frac{bd}{M_2} \\ \frac{bc}{M_2} + \frac{bd}{M_2} & \frac{c^2}{M_2} + \frac{d^2}{M_2} & \frac{2cd}{M_2} \\ \frac{bc}{M_2} + \frac{bd}{M_2} & \frac{2cd}{M_2} & \frac{c^2}{M_2} + \frac{d^2}{M_2} \end{pmatrix}. \quad (40)$$

Compared to four and three zero Yukawa textures, there are more independent parameters here. Apart from the overall mass scale, there will be three moduli and two irremovable phases. It is easier to fit the neutrino data with such a larger number of parameters and we do not discuss it any further.

**5.3. One Zero.** One zero textures represent the most trivial case among the  $\mu\tau$  symmetric neutrino Yukawa texture zeros. This is since, as an odd zero texture, it must have  $a = 0$  in (31). The single allowed texture of  $M_D$  is

$$\begin{pmatrix} 0 & b & b \\ c & d & e \\ c & e & d \end{pmatrix}, \quad (41)$$

and yields the following form of  $M_\nu$ :

$$M_\nu = - \begin{pmatrix} \frac{2b^2}{M_2} & \frac{be}{M_2} + \frac{bd}{M_2} & \frac{be}{M_2} + \frac{bd}{M_2} \\ \frac{be}{M_2} + \frac{bd}{M_2} & \frac{c^2}{M_1} + \frac{d^2}{M_2} + \frac{e^2}{M_2} & \frac{c^2}{M_1} + \frac{2ed}{M_2} \\ \frac{be}{M_2} + \frac{bd}{M_2} & \frac{c^2}{M_1} + \frac{2ed}{M_2} & \frac{c^2}{M_1} + \frac{d^2}{M_2} + \frac{e^2}{M_2} \end{pmatrix}. \quad (42)$$

Like the two zero textures, this allowed one zero texture to have six parameters: one overall real mass scale, three moduli, and two phases. These can easily fit the extant neutrino data.

## 6. The Breaking of $\mu\tau$ Symmetry

As mentioned in previous sections, the results  $\theta_{13} = 0$  and  $\theta_{23} = \pi/4$  are consequences of the custodial  $\mu\tau$  symmetry in  $M_\nu$ . But present neutrino data from T2K, DOUBLE CHOOZ, RENO, and DAYA BAY experiments rule out  $\theta_{13} = 0$  by  $5\sigma$ . So, the breaking of  $\mu\tau$  symmetry is an inevitable need in order to generate a nonzero value of  $\theta_{13}$ . In addition, a departure from  $\theta_{23} = \pi/4$  would arise from the same breaking. Another interesting consequence of a nonzero  $\theta_{13}$  would be the observability of a CKM-type of CP violation in the lepton sector. Our previous expressions for  $\Delta_{21}^2$ ,  $\Delta_{32}^2$  and  $\tan 2\theta_{12}$  will be modified if  $\mu\tau$  symmetry is broken.

This symmetry can be broken explicitly or spontaneously or dynamically as with the Renormalization Group evolution of Lagrangian parameters. Spontaneous breakdown generally requires the presence of extra scalars and needs a model with them. We do not go into a discussion of such models here. On the other hand, RG effects on neutrino masses can be incorporated with the methodology presented in [72, 73] in terms of the  $\tau$  lepton mass arising through the running of the Yukawa coupling strength from the GUT scale  $\Lambda$  to the weak scale  $\lambda$ . The effect is characterized by the parameter  $\Delta_\tau$  which has the 1-loop expression

$$\Delta_\tau \simeq \frac{m_\tau^2}{8\pi^2 v^2} (\tan^2 \beta + 1) \ln \left( \frac{\Lambda}{\lambda} \right), \quad (43)$$

where  $\tan \beta$  is the ratio of the VEVs of the up-type and down-type neutral Higgs fields in the MSSM and  $v^2$  is twice the sum

of their squares. Even for a large  $\tan \beta$ , ( $\tan \beta \simeq 60$ )  $\Delta_\tau$  is  $O(10^{-3})$  and cannot generate a  $\theta_{13}$  of the order of  $9^\circ$ .

We therefore turn to an explicit breaking of  $\mu\tau$  symmetry in  $M_D$ . That can be realized in the following way.

*Category A.* One has

$$M_{DA1} = \begin{pmatrix} a_1 & a_2 & a_2(1 - \epsilon_1 e^{i\theta}) \\ 0 & 0 & b_1(1 - \epsilon_2 e^{i\phi}) \\ 0 & b_1 & 0 \end{pmatrix}, \quad (44)$$

$$M_{DA2} = \begin{pmatrix} a_1 & a_2 & a_2(1 - \epsilon_1 e^{i\theta}) \\ 0 & b_1(1 - \epsilon_2 e^{i\phi}) & 0 \\ 0 & 0 & b_1 \end{pmatrix}.$$

*Category B.* One has

$$M_{DB1} = \begin{pmatrix} a_1 & 0 & 0 \\ b_1(1 - \epsilon_1 e^{i\theta}) & 0 & b_2(1 - \epsilon_2 e^{i\phi}) \\ b_1 & b_2 & 0 \end{pmatrix}, \quad (45)$$

$$M_{DB2} = \begin{pmatrix} a_1 & 0 & 0 \\ b_1(1 - \epsilon_1 e^{i\theta}) & b_2(1 - \epsilon_2 e^{i\phi}) & 0 \\ b_1 & 0 & b_2 \end{pmatrix}.$$

Furthermore,

$$M_R = \begin{pmatrix} M_1 & 0 & 0 \\ 0 & M_2 & 0 \\ 0 & 0 & M_2(1 - \epsilon_3) \end{pmatrix}, \quad (46)$$

where  $\epsilon_1 e^{i\theta}$ ,  $\epsilon_2 e^{i\phi}$  are complex  $\mu\tau$  symmetry breaking parameters ( $\epsilon_{1,2}$  real) and  $\epsilon_3$  is a real  $\mu\tau$  symmetry breaking parameter in  $M_R$ . For these modified  $M_D$  and  $M_R$ , we have the following  $M_\nu$ 's.

*Category A.* One has

$$M_{\nu A1} = m_A \left[ \begin{pmatrix} k_1^2 e^{2i\alpha} + 2k_2^2 & k_2 & k_2 \\ k_2 & 1 & 0 \\ k_2 & 0 & 1 \end{pmatrix} - \epsilon_1 e^{i\theta} \begin{pmatrix} 2k_2^2 & k_2 & 0 \\ k_2 & 0 & 0 \\ 0 & 0 & 0 \end{pmatrix} - \epsilon_2 e^{i\phi} \begin{pmatrix} 0 & k_2 & 0 \\ k_2 & 2 & 0 \\ 0 & 0 & 0 \end{pmatrix} - \epsilon_3 \begin{pmatrix} -k_2^2 & -k_2 & 0 \\ -k_2 & -1 & 0 \\ 0 & 0 & 0 \end{pmatrix} \right],$$

$$M_{\nu A2} = m_A \left[ \begin{pmatrix} k_1^2 e^{2i\alpha} + 2k_2^2 & k_2 & k_2 \\ k_2 & 1 & 0 \\ k_2 & 0 & 1 \end{pmatrix} - \epsilon_1 e^{i\theta} \begin{pmatrix} 2k_2^2 & 0 & k_2 \\ 0 & 0 & 0 \\ k_2 & 0 & 0 \end{pmatrix} - \epsilon_2 e^{i\phi} \begin{pmatrix} 0 & k_2 & 0 \\ k_2 & 2 & 0 \\ 0 & 0 & 0 \end{pmatrix} - \epsilon_3 \begin{pmatrix} -k_2^2 & 0 & -k_2 \\ 0 & 0 & 0 \\ -k_2 & 0 & -1 \end{pmatrix} \right]. \quad (47)$$

*Category B.* One has

$$M_{\nu B1} = m_B \left[ \begin{pmatrix} l_1^2 & l_1 l_2 e^{i\beta} & l_1 l_2 e^{i\beta} \\ l_1 l_2 e^{i\beta} & l_2^2 e^{2i\beta} + 1 & l_2^2 e^{2i\beta} \\ l_1 l_2 e^{i\beta} & l_2^2 e^{2i\beta} & l_2^2 e^{2i\beta} + 1 \end{pmatrix} - \epsilon_1 e^{i\theta} \begin{pmatrix} 0 & l_1 l_2 e^{i\beta} & 0 \\ l_1 l_2 e^{i\beta} & 2l_2^2 e^{2i\beta} & l_2^2 e^{2i\beta} \\ 0 & l_2^2 e^{2i\beta} & 0 \end{pmatrix} - \epsilon_2 e^{i\phi} \begin{pmatrix} 0 & 0 & 0 \\ 0 & 2 & 0 \\ 0 & 0 & 0 \end{pmatrix} - \epsilon_3 \begin{pmatrix} 0 & 0 & 0 \\ 0 & -1 & 0 \\ 0 & 0 & 0 \end{pmatrix} \right],$$

$$M_{\nu B2} = m_B \left[ \begin{pmatrix} l_1^2 & l_1 l_2 e^{i\beta} & l_1 l_2 e^{i\beta} \\ l_1 l_2 e^{i\beta} & l_2^2 e^{2i\beta} + 1 & l_2^2 e^{2i\beta} \\ l_1 l_2 e^{i\beta} & l_2^2 e^{2i\beta} & l_2^2 e^{2i\beta} + 1 \end{pmatrix} - \epsilon_1 e^{i\theta} \begin{pmatrix} 0 & l_1 l_2 e^{i\beta} & 0 \\ l_1 l_2 e^{i\beta} & 2l_2^2 e^{2i\beta} & l_2^2 e^{2i\beta} \\ 0 & l_2^2 e^{2i\beta} & 0 \end{pmatrix} - \epsilon_2 e^{i\phi} \begin{pmatrix} 0 & 0 & 0 \\ 0 & 2 & 0 \\ 0 & 0 & 0 \end{pmatrix} - \epsilon_3 \begin{pmatrix} 0 & 0 & 0 \\ 0 & 0 & 0 \\ 0 & 0 & -1 \end{pmatrix} \right]. \quad (48)$$

The detailed diagonalization and expressions for mass differences and mixing angles are given in the appendix.

A nonzero  $\theta_{13}$  arises after  $\mu\tau$  symmetry breaking. The value  $\theta_{13} \simeq 9^\circ$  is possible for  $3\sigma$  variations of  $(\Delta_{21}^2)^{\epsilon_{1,2,3}}$ ,  $(\Delta_{32}^2)^{\epsilon_{1,2,3}}$ ,  $\theta_{12}^{\epsilon_{1,2,3}}$ ,  $\theta_{23}^{\epsilon_{1,2,3}}$ , compare the appendix. An appropriate choice of symmetry breaking parameters, that is,  $\epsilon_{1,2,3} \simeq 0.1$ , and slightly shifted parameter spaces for  $k_1, k_2, \alpha$  in Category A and  $l_1, l_2, \beta$  in Category B are needed. A nonzero CP violating effect can be effected through the Jarlskog invariant  $J_{CP}$ :

$$J_{CP} = \text{Im} \frac{H_{12} H_{23} H_{31}}{(\Delta_{21}^2)^{\epsilon_{1,2,3}} (\Delta_{32}^2)^{\epsilon_{1,2,3}} (\Delta_{31}^2)^{\epsilon_{1,2,3}}}, \quad (49)$$

where elements of  $H$  and mass squared differences  $(\Delta_{21}^2)^{\epsilon_{1,2,3}}$ ,  $(\Delta_{32}^2)^{\epsilon_{1,2,3}}$  are given in the appendix. Note that  $(\Delta_{31}^2)^{\epsilon_{1,2,3}} = (\Delta_{21}^2)^{\epsilon_{1,2,3}} + (\Delta_{32}^2)^{\epsilon_{1,2,3}}$ . A detailed treatment of explicitly broken  $\mu\tau$  symmetric four zero and three zero textures is given in [33].

TABLE 5: Expressions for  $P, Q, R, S, x_{1-6}, y_{1-6}$  and  $z_{1-6}$  for Categories A1, A2, B1 and B2 from (47) and (48).

Quantity	Category A1	Category A2	Category B1	Category B2
$P$	$k_1^2 e^{2i\alpha} + 2k_2^2$	$k_1^2 e^{2i\alpha} + 2k_2^2$	$l_1^2$	$l_1^2$
$Q$	$k_2$	$k_2$	$l_1 l_2 e^{i\beta}$	$l_1 l_2 e^{i\beta}$
$R$	1	1	$l_2^2 e^{2i\beta} + 1$	$l_2^2 e^{2i\beta} + 1$
$S$	0	0	$l_2^2 e^{2i\beta}$	$l_2^2 e^{2i\beta}$
$x_1$	$2k_2^2$	$2k_2^2$	0	0
$x_2$	$k_2$	0	$l_1 l_2 e^{i\beta}$	$l_1 l_2 e^{i\beta}$
$x_3$	0	$k_2$	0	0
$x_4$	0	0	$2l_2^2 e^{2i\beta}$	$2l_2^2 e^{2i\beta}$
$x_5$	0	0	$l_2^2 e^{2i\beta}$	$l_2^2 e^{2i\beta}$
$x_6$	0	0	0	0
$y_1$	0	0	0	0
$y_2$	$k_2$	$k_2$	0	0
$y_3$	0	0	0	0
$y_4$	2	2	2	2
$y_5$	0	0	0	0
$y_6$	0	0	0	0
$z_1$	$-k_2^2$	$-k_2^2$	0	0
$z_2$	$-k_2$	0	0	0
$z_3$	0	$-k_2$	0	0
$z_4$	-1	0	-1	0
$z_5$	0	0	0	0
$z_6$	0	-1	0	-1

## 7. Concluding Summary

We have reviewed neutrino Yukawa textures with zeros within the type-I seesaw with three heavy right chiral neutrinos and in the basis where the latter and the charged leptons are mass diagonal. The conditions of a nonvanishing mass of every ultralight neutrino and of the non-decoupling of any neutrino generation allow a maximum of four zeros in the neutrino Yukawa coupling matrix  $Y_\nu$ . There are seventy two such textures. We show that the requirement of an exact  $\mu\tau$  symmetry, coupled with observational constraints, reduces the *seventy two* allowed textures in such a  $Y_\nu$  to *only four* corresponding to *just two* different forms of the light neutrino mass matrix  $M_{\nu A}/M_{\nu B}$ , resulting in an inverted/normal mass ordering. Apart from an overall mass scale,  $M_\nu$  for every category has two real parameters and an irremovable phase. These parameters  $k_1, k_2$ , and  $|\alpha|$  for Category A and  $l_1, l_2$ , and  $|\beta|$  for Category B get highly restricted, given the  $3\sigma$  ranges of measured neutrino mass squared differences and mixing angles. Neutrino masses and Majorana phases are predicted within definite ranges with  $3\sigma$  laboratory and cosmological inputs. The predicted respective masses  $m_1/\text{eV}$ ,  $m_2/\text{eV}$ , and  $m_3/\text{eV}$  are  $[0.0452, 0.1682]$ ,  $[0.0457, 0.1684]$ ,  $[0.077, 0.1632]$  for Category A and  $[0.0110, 0.0335]$ ,  $[0.0144, 0.0345]$ , and  $[0.0485, 0.0638]$  for Category B. The corresponding intervals of the Majorana phases are  $-98.0^\circ \leq \alpha_{M_1} \leq 20.0^\circ$ ,  $9.2^\circ \leq \alpha_{M_2} \leq 36.4^\circ$  for Category A and  $-88.6^\circ \leq \alpha_{M_1} \leq 7.97^\circ$ ,  $90.7^\circ \leq \alpha_{M_2} \leq 128.8^\circ$  for Category B. In addition, we predict the range of the mass scale associated with  $0\nu\beta\beta$  decay, most of which

is well below the reach of planned experiments. We have also studied Yukawa textures with a fewer number of zeros, but with exact  $\mu\tau$  symmetry. Finally, we have formulated the detailed scheme of three-parameter explicit breaking of  $\mu\tau$  symmetry for allowed four zero textures. A value of  $\theta_{13} \simeq 9^\circ$  can be arranged for a suitable choice of small values of these symmetry breaking parameters.

## Appendix

### Expressions for Measurable Quantities

We can write the general form of a broken  $\mu\tau$  symmetric  $M_\nu$  in the following way [33]:

$$M_\nu = m \left[ \begin{pmatrix} P & Q & Q \\ Q & R & S \\ Q & S & R \end{pmatrix} - \epsilon_1 e^{i\theta} \begin{pmatrix} x_1 & x_2 & x_3 \\ x_2 & x_4 & x_5 \\ x_3 & x_5 & x_6 \end{pmatrix} - \epsilon_2 e^{i\phi} \begin{pmatrix} y_1 & y_2 & y_3 \\ y_2 & y_4 & y_5 \\ y_3 & y_5 & y_6 \end{pmatrix} - \epsilon_3 \begin{pmatrix} z_1 & z_2 & z_3 \\ z_2 & z_4 & z_5 \\ z_3 & z_5 & z_6 \end{pmatrix} \right]. \quad (\text{A.1})$$

The explicit expressions of  $P, Q, R, S, x_{1-6}, y_{1-6}$  and  $z_{1-6}$  for four forms of neutrino mass matrices after  $\mu\tau$  symmetry breaking are given in Table 5.

We can now have

$$\begin{aligned}
 H &= M_\nu M_\nu^\dagger \\
 &= m^2 \left[ \begin{pmatrix} |P|^2 + 2|Q|^2 & PQ^* + Q(R^* + S^*) & PQ^* + Q(R^* + S^*) \\ P^*Q + Q^*(R + S) & |Q|^2 + |R|^2 + |S|^2 & |Q|^2 + RS^* + R^*S \\ P^*Q + Q^*(R + S) & |Q|^2 + R^*S + RS^* & |Q|^2 + |R|^2 + |S|^2 \end{pmatrix} \right. \\
 &\quad \left. - \epsilon_1 \begin{pmatrix} u_1 & u_2^* & u_3^* \\ u_2 & u_4 & u_5^* \\ u_3 & u_5 & u_6 \end{pmatrix} - \epsilon_2 \begin{pmatrix} v_1 & v_2^* & v_3^* \\ v_2 & v_4 & v_5^* \\ v_3 & v_5 & v_6 \end{pmatrix} - \epsilon_3 \begin{pmatrix} w_1 & w_2^* & w_3^* \\ w_2 & w_4 & w_5^* \\ w_3 & w_5 & w_6 \end{pmatrix} \right]. \quad (A.2)
 \end{aligned}$$

Here

$$\begin{aligned}
 u_1 &= [P^* x_1 + Q^* (x_2 + x_3)] e^{i\theta} + [Px_1^* + Q(x_2^* + x_3^*)] e^{-i\theta}, \\
 u_2 &= [P^* x_2 + Q^* (x_4 + x_5)] e^{i\theta} + [Qx_1^* + Rx_2^* + Sx_3^*] e^{-i\theta}, \\
 u_3 &= [P^* x_3 + Q^* (x_5 + x_6)] e^{i\theta} + [Qx_1^* + Sx_2^* + Rx_3^*] e^{-i\theta}, \\
 u_4 &= [Q^* x_2 + R^* x_4 + S^* x_5] e^{i\theta} + [Qx_2^* + Rx_4^* + Sx_5^*] e^{-i\theta}, \\
 u_5 &= [Q^* x_3 + R^* x_5 + S^* x_6] e^{i\theta} + [Qx_2^* + Sx_4^* + Rx_5^*] e^{-i\theta}, \\
 u_6 &= [Q^* x_3 + S^* x_5 + R^* x_6] e^{i\theta} + [Qx_3^* + Sx_5^* + Rx_6^*] e^{-i\theta}. \quad (A.3)
 \end{aligned}$$

Note that  $v_i$  and  $w_i$  have similar functional forms as  $u_i$ . If we write  $u_i$  in the following way

$$u_i = f_i(x_1, x_2, \dots, x_6, \theta), \quad (A.4)$$

then  $v_i$  and  $w_i$  will be

$$\begin{aligned}
 v_i &= f_i(y_1, y_2, \dots, y_6, \phi), \\
 w_i &= f_i(z_1, z_2, \dots, z_6, 0). \quad (A.5)
 \end{aligned}$$

The diagonalization of  $H$  yields  $\text{diag} \cdot (m_1^2, m_2^2, m_3^2)$  and also expressions for five relevant measurable quantities. The latter are:  $\Delta_{21}^2$ ,  $\Delta_{32}^2$ ,  $\theta_{12}$ ,  $\theta_{23}$  and  $\theta_{13}$ . We will associate

superscripts  $\epsilon_{1,2,3}$  with all of these five quantities to distinguish them from their unperturbed expressions. The relevant functions for these physical quantities are given below

$$\begin{aligned}
 U_1 &= \frac{1}{2} \left[ -2c_{12}^2 u_1 + \sqrt{2}c_{12}s_{12} \{ (u_2 + u_3) e^{-i\psi} + (u_2^* + u_3^*) e^{i\psi} \} \right. \\
 &\quad \left. - s_{12}^2 (u_4 + u_6 + u_5 + u_5^*) \right], \\
 U_2 &= \frac{1}{2} \left[ -\sqrt{2}c_{12}^2 (u_2 + u_3) e^{-i\psi} + \sqrt{2}s_{12}^2 (u_2^* + u_3^*) e^{i\psi} \right. \\
 &\quad \left. + c_{12}s_{12} (u_4 + u_6 - 2u_1 + u_5 + u_5^*) \right], \\
 U_3 &= \frac{1}{2} \left[ \sqrt{2}c_{12} (u_2 - u_3) e^{-i\psi} + s_{12} (u_6 - u_4 + u_5 - u_5^*) \right], \\
 U_4 &= \frac{1}{2} \left[ -2s_{12}^2 u_1 - \sqrt{2}c_{12}s_{12} \{ (u_2 + u_3) e^{-i\psi} + (u_2^* + u_3^*) e^{i\psi} \} \right. \\
 &\quad \left. - c_{12}^2 (u_4 + u_6 + u_5 + u_5^*) \right], \\
 U_5 &= \frac{1}{2} \left[ \sqrt{2}s_{12} (u_2 - u_3) e^{-i\psi} - c_{12} (u_6 - u_4 + u_5 - u_5^*) \right], \\
 U_6 &= \frac{1}{2} [u_5 + u_5^* - u_4 - u_6], \quad (A.6)
 \end{aligned}$$

where  $\psi = \arg[P^*Q + Q^*(R + S)]$ ,  $c_{12} = \cos \theta_{12}$ ,  $s_{12} = \sin \theta_{12}$ ,  $\theta_{12}$  being the unperturbed mixing angle in (26). There are also  $V_i$  and  $W_i$ ,  $i = 1-6$  which have similar functional forms as  $U_i$ . If we write  $U_i$  as

$$U_i = F_i(u_1, u_2, \dots, u_6), \quad (A.7)$$

then  $V_i$  and  $W_i$  will be

$$\begin{aligned}
 V_i &= F_i(v_1, v_2, \dots, v_6), \\
 W_i &= F_i(w_1, w_2, \dots, w_6). \quad (A.8)
 \end{aligned}$$

The final results with three  $\mu\tau$  symmetry breaking parameters are

$$\begin{aligned}
 (\Delta_{21}^2)^{\epsilon_{1,2,3}} &= \Delta_{21}^2 + m^2 \{ (U_4 - U_1) \epsilon_1 + (V_4 - V_1) \epsilon_2 + (W_4 - W_1) \epsilon_3 \}, \\
 (\Delta_{32}^2)^{\epsilon_{1,2,3}} &= \Delta_{32}^2 + m^2 \{ (U_6 - U_4) \epsilon_1 + (V_6 - V_4) \epsilon_2 + (W_6 - W_4) \epsilon_3 \},
 \end{aligned}$$



$$\begin{aligned}
(\sin \theta_{12})^{\epsilon_{1,2,3}} &= \left| s_{12} + c_{12} m^2 \left\{ \frac{U_2^* \epsilon_1 + V_2^* \epsilon_2 + W_2^* \epsilon_3}{\Delta_{21}^2} \right\} \right|, \\
(\sin \theta_{23})^{\epsilon_{1,2,3}} &= \left| \frac{1}{\sqrt{2}} + \frac{s_{12} m^2}{\sqrt{2}} \left\{ \frac{U_3^* \epsilon_1 + V_3^* \epsilon_2 + W_3^* \epsilon_3}{\Delta_{21}^2 + \Delta_{32}^2} \right\} \right. \\
&\quad \left. - \frac{c_{12} m^2}{\sqrt{2}} \left\{ \frac{U_5^* \epsilon_1 + V_5^* \epsilon_2 + W_5^* \epsilon_3}{\Delta_{32}^2} \right\} \right|, \\
(\sin \theta_{13})^{\epsilon_{1,2,3}} &= \left| c_{12} m^2 \left\{ \frac{U_3^* \epsilon_1 + V_3^* \epsilon_2 + W_3^* \epsilon_3}{\Delta_{21}^2 + \Delta_{32}^2} \right\} \right. \\
&\quad \left. + s_{12} m^2 \left\{ \frac{U_5^* \epsilon_1 + V_5^* \epsilon_2 + W_5^* \epsilon_3}{\Delta_{32}^2} \right\} \right|.
\end{aligned}
\tag{A.9}$$

## Acknowledgments

The authors would like to thank Prof. Ambar Ghosal for his long collaboration in almost all works discussed in this review. P. Roy acknowledges partial support from a DAE Raja Ramanna Fellowship.

## References

- [1] D. V. Forero, M. Tortola, and J. W. F. Valle, “Global status of neutrino oscillation parameters after Neutrino-2012,” *Physical Review D*, vol. 86, Article ID 073012, 2012.
- [2] Y. Abe, C. Aberle, T. Akiri et al., “Indication for the disappearance of reactor electron antineutrinos in the Double Chooz experiment,” *Physical Review Letters*, vol. 108, Article ID 131801, 2012.
- [3] K. Abe, N. Abgrall, Y. Ajima et al., “Indication of electron neutrino appearance from an accelerator-produced off-axis muon neutrino beam,” *Physical Review Letters*, vol. 107, Article ID 041801, 2011.
- [4] F. P. An, J. Z. Bai, and A. B. Balantekin, “Observation of electron-antineutrino disappearance at Daya Bay,” *Physical Review Letters*, vol. 108, Article ID 171803, 2012.
- [5] J. K. Ahn, J. Z. Bai, and A. B. Balantekin, “Observation of reactor electron antineutrino disappearance in the RENO experiment,” *Physical Review Letters*, vol. 108, Article ID 191802, 2012.
- [6] S. A. Thomas, F. B. Abdalla, and O. Lahav, “Upper bound of 0.28 eV on neutrino masses from the largest photometric redshift survey,” *Physical Review Letters*, vol. 105, no. 3, Article ID 031301, 2010.
- [7] S. Parke, “Unravelling the neutrino mysteries: present and future,” <http://www.ino.tifr.res.in/nufact2010/proceedings.php/>.
- [8] T. Yanagida, “Horizontal symmetry and masses of neutrinos,” in *Proceedings of the Workshop on Unified Theories*, vol. 95, C 7902131, 1979.
- [9] M. Gell-Mann, P. Ramond, and R. Slansky, “Complex spinors and unified theories,” in *Proceedings of the Stony Brook Workshop*, vol. 315, C 790927, 1979.
- [10] R. N. Mohapatra and G. Senjanovic, “Neutrino mass and spontaneous parity violation,” *Physical Review Letters*, vol. 44, p. 912, 1980.
- [11] J. Schechter and J. W. F. Valle, “Neutrino masses in  $SU(2) \otimes U(1)$  theories,” *Physical Review D*, vol. 22, no. 9, pp. 2227–2235, 1980.
- [12] E. Ma and U. Sarkar, “Neutrino masses and leptogenesis with heavy Higgs triplets,” *Physical Review Letters*, vol. 80, no. 26, pp. 5716–5719, 1998.
- [13] R. Foot, H. Lew, X. G. He, and G. C. Joshi, “See-saw neutrino masses induced by a triplet of leptons,” *Zeitschrift für Physik C*, vol. 44, no. 3, pp. 441–444, 1989.
- [14] R. N. Mohapatra and J. W. F. Valle, “Neutrino mass and baryon-number nonconservation in superstring models,” *Physical Review D*, vol. 34, no. 5, pp. 1642–1645, 1986.
- [15] M. C. Gonzalez-Garcia and J. W. F. Valle, “Fast decaying neutrinos and observable flavour violation in a new class of majoron models,” *Physics Letters B*, vol. 216, no. 3-4, pp. 360–366, 1989.
- [16] B. Adhikary, A. Ghosal, and P. Roy, “ $\mu\tau$  symmetry, tribimaximal mixing and four zero neutrino Yukawa textures,” *Journal of High Energy Physics*, vol. 2009, no. 10, article 040, 2009.
- [17] B. Adhikary, A. Ghosal, and P. Roy, “Neutrino masses, cosmological bound and four zero Yukawa textures,” *Modern Physics Letters A*, vol. 26, p. 2427, 2011.
- [18] H. Fritzsch and Z. Z. Xing, “Four-zero texture of Hermitian quark mass matrices and current experimental tests,” *Physics Letters Section B*, vol. 555, no. 1-2, pp. 63–70, 2003.
- [19] H. Fritzsch and Z.-Z. Xing, “Mass and flavor mixing schemes of quarks and leptons,” *Progress in Particle and Nuclear Physics*, vol. 45, no. 1, 2000.
- [20] K. S. Babu and J. Kubo, “Dihedral families of quarks, leptons and Higgses,” *Physical Review D*, vol. 71, Article ID 056006, 2005.
- [21] Z. Z. Xing, “Texture zeros and majorana phases of the neutrino mass matrix,” *Physics Letters Section B*, vol. 530, no. 1-4, pp. 159–166, 2002.
- [22] P. H. Frampton, S. L. Glashow, and D. Marfatia, “Zeroes of the neutrino mass matrix,” *Physics Letters Section B*, vol. 536, no. 1-2, pp. 79–82, 2002.
- [23] Z. Z. Xing, “A full determination of the neutrino mass spectrum from two-zero textures of the neutrino mass matrix,” *Physics Letters Section B*, vol. 539, no. 1-2, pp. 85–90, 2002.
- [24] S. Dev, S. Kumar, S. Verma, and S. Gupta, “Phenomenology of two-texture zero neutrino mass matrices,” *Physical Review D*, vol. 76, no. 1, Article ID 013002, 2007.
- [25] A. Merle and W. Rodejohann, “The elements of the neutrino mass matrix: allowed ranges and implications of texture zeros,” *Physical Review D*, vol. 73, Article ID 073012, 2006.
- [26] W. Grimus, A. S. Joshipura, L. Lavoura, and M. Tanimoto, “Symmetry realization of texture zeros,” *European Physical Journal C*, vol. 36, no. 2, pp. 227–232, 2004.
- [27] S. Kaneko, H. Sawanaka, T. Shingai, M. Tanimoto, and K. Yoshioka, “New approach to texture-zeros with  $S(3)$  symmetry—flavor symmetry and vacuum aligned mass textures,” <http://arxiv.org/abs/hep-ph/0703250>.
- [28] S. Dev, S. Gupta, and R. R. Gautam, “Zero textures of the neutrino mass matrix from cyclic family symmetry,” *Physics Letters Section B*, vol. 701, no. 5, pp. 605–608, 2011.
- [29] C. D. Froggatt and H. B. Nielsen, “Hierarchy of quark masses, cabibbo angles and CP violation,” *Nuclear Physics Section B*, vol. 147, no. 3-4, pp. 277–298, 1979.
- [30] G. C. Branco, D. Emmanuel-Costa, M. N. Rebelo, and P. Roy, “Four-zero neutrino Yukawa textures in the minimal seesaw framework,” *Physical Review D*, vol. 77, no. 5, Article ID 053011, 2008.
- [31] S. Choubey, W. Rodejohann, and P. Roy, “Phenomenological consequences of four zero neutrino Yukawa textures,” *Nuclear Physics B*, vol. 808, no. 1-2, pp. 272–291, 2009.

- [32] B. Adhikary, A. Ghosal, and P. Roy, “Baryon asymmetry from leptogenesis with four zero neutrino Yukawa textures,” *Journal of Cosmology and Astroparticle Physics*, vol. 2011, no. 1, article 025, 2011.
- [33] B. Adhikary, A. Ghosal, and P. Roy, “ $\theta_{13}$ ,  $\mu\tau$  symmetry breaking and neutrino Yukawa textures,” <http://arxiv.org/abs/arXiv:1210.5328>.
- [34] P. Roy, “The magic of four zero neutrino Yukawa textures,” <http://arxiv.org/abs/1004.0065>.
- [35] S. Goswami, S. Khan, and W. Rodejohann, “Minimal textures in seesaw mass matrices and their low and high energy phenomenology,” *Physics Letters Section B*, vol. 680, no. 3, pp. 255–262, 2009.
- [36] A. Dighe and N. Sahu, “Texture zeroes and discrete flavor symmetries in light and heavy Majorana neutrino mass matrices: a bottom-up approach,” <http://arxiv.org/abs/0812.0695>.
- [37] C. Hagedorn, J. Kersten, and M. Lindner, “Stability of texture zeros under radiative corrections in see-saw models,” *Physics Letters Section B*, vol. 597, no. 1, pp. 63–72, 2004.
- [38] S. Antusch, J. Kersten, M. Lindner, M. Ratz, and M. A. Schmidt, “Running neutrino mass parameters in see-saw scenarios,” *Journal of High Energy Physics*, vol. 2005, no. 3, article 024, 2005.
- [39] J.-W. Mei, “Running neutrino masses, leptonic mixing angles and CP-violating phases: from  $M_z$  to  $\Lambda_{\text{GUT}}$ ,” *Physical Review D*, vol. 71, Article ID 073012, 2005.
- [40] G. C. Branco, M. N. Rebelo, and J. I. Silva-Marcos, “Leptogenesis, Yukawa textures and weak-basis invariants,” *Physics Letters Section B*, vol. 633, no. 2-3, pp. 345–354, 2006.
- [41] T. Fukuyama and H. Nishiura, “Mass matrix of Majorana neutrinos,” <http://arxiv.org/abs/hep-ph/9702253>.
- [42] J. C. Gomez-Izquierdo and A. Perez-Lorenzana, “Softly broken  $\mu \leftrightarrow \tau$  symmetry in the minimal see-saw model,” *Physical Review D*, vol. 77, Article ID 113015, 2008.
- [43] T. Baba, “What does  $\mu\text{-}\tau$  symmetry imply about leptonic CP violation?” *International Journal of Modern Physics E*, vol. 16, no. 5, pp. 1373–1381, 2007.
- [44] N. Nimai Singh, H. Zeen Devi, and M. Patgiri, “Normal versus inverted hierarchical models within  $\mu\text{-}\tau$  symmetry,” <http://arxiv.org/abs/0707.2713v3>.
- [45] A. S. Joshipura and B. P. Kodrani, “Complex CKM matrix, spontaneous CP violation and generalized  $\mu\text{-}\tau$  symmetry,” *Physics Letters Section B*, vol. 670, no. 4-5, pp. 369–373, 2009.
- [46] B. Adhikary, “Soft breaking of  $L_\mu\text{-}L_\tau$  symmetry: light neutrino spectrum and leptogenesis,” *Physical Review D*, vol. 74, Article ID 033002, 2006.
- [47] T. Baba and M. Yasue, “Correlation between leptonic CP violation and  $\mu\text{-}\tau$  symmetry breaking,” *Physical Review D*, vol. 75, Article ID 055001, 2007.
- [48] W. Grimus, “Realizations of  $\mu\text{-}\tau$  interchange symmetry,” <http://arxiv.org/abs/hep-ph/0610158>.
- [49] Z. Z. Xing, H. Zhang, and S. Zhou, “Nearly tri-bimaximal neutrino mixing and CP violation from  $\mu\text{-}\tau$  symmetry breaking,” *Physics Letters Section B*, vol. 641, no. 2, pp. 189–197, 2006.
- [50] N. Haba and W. Rodejohann, “A supersymmetric contribution to the neutrino mass matrix and breaking of  $\mu\text{-}\tau$  symmetry,” *Physical Review D*, vol. 74, Article ID 017701, 2006.
- [51] R. N. Mohapatra, S. Nasri, and H. B. Yu, “Grand unification of  $\mu\text{-}\tau$  symmetry,” *Physics Letters Section B*, vol. 636, p. 114, 2006.
- [52] Y. H. Ahn, S. K. Kang, C. S. Kim, and J. Lee, “Phased breaking of  $\mu\text{-}\tau$  symmetry and leptogenesis,” *Physical Review D*, vol. 73, Article ID 093005, 2006.
- [53] K. Fuki and M. Yasue, “What does  $\mu\text{-}\tau$  symmetry imply in neutrino mixings?” *Physical Review D*, vol. 73, Article ID 055014, 2006.
- [54] S. Nasri, “Implications of  $\mu \leftrightarrow \tau$  symmetry on neutrinos and leptogenesis,” *International Journal of Modern Physics A*, vol. 20, no. 27, pp. 6258–6267, 2005.
- [55] I. Aizawa and M. Yasue, “A new type of complex neutrino mass texture and  $\mu\text{-}\tau$  symmetry,” *Physical Review D*, vol. 73, Article ID 015002, 2006.
- [56] R. N. Mohapatra and W. Rodejohann, “Broken  $\mu\text{-}\tau$  symmetry and leptonic CP violation,” *Physical Review D*, vol. 72, Article ID 053001, 2005.
- [57] I. Aizawa, M. Ishiguro, M. Yasue, and T. Kitabayashi, “ $\mu\tau$  permutation symmetry and neutrino mixing for a two-loop radiative mechanism,” *Journal of the Korean Physical Society*, vol. 46, no. 3, pp. 597–600, 2005.
- [58] T. Kitabayashi and M. Yasue, “ $\mu\text{-}\tau$  symmetry and maximal CP violation,” *Physics Letters Section B*, vol. 621, p. 133, 2005.
- [59] R. N. Mohapatra, S. Nasri, and H. B. Yu, “Leptogenesis,  $\mu\text{-}\tau$  Symmetry and  $\theta_{13}$ ,” *Physics Letters Section B*, vol. 615, p. 231, 2005.
- [60] R. N. Mohapatra and S. Nasri, “Leptogenesis and  $\mu\text{-}\tau$  symmetry,” *Physical Review D*, vol. 71, Article ID 033001, 2005.
- [61] R. N. Mohapatra, “ $\theta_{13}$  as a probe of  $\mu \leftrightarrow \tau$  symmetry for leptons,” *Journal of High Energy Physics*, vol. 2004, no. 10, article 027, 2004.
- [62] I. Aizawa, M. Ishiguro, T. Kitabayashi, and M. Yasue, “Bilarge neutrino mixing and  $\mu\text{-}\tau$  permutation symmetry for two-loop radiative mechanism,” *Physical Review D*, vol. 70, Article ID 015011, 2004.
- [63] I. de Medeiros Varzielas and G. G. Ross, “ $SU(3)$  family symmetry and neutrino bi-tri-maximal mixing,” *Nuclear Physics B*, vol. 733, no. 1-2, pp. 31–47, 2006.
- [64] P. F. Harrison and W. G. Scott, “ $\mu\text{-}\tau$  reflection symmetry in lepton mixing and neutrino oscillations,” *Physics Letters Section B*, vol. 547, p. 219, 2002.
- [65] T. Kitabayashi and M. Yasue, “ $S_{2L}$  permutation symmetry for left-handed mu and tau families and neutrino oscillations in an  $SU(3)_L \times U(1)_N$  gauge model,” *Physical Review D*, vol. 67, Article ID 015006, 2003.
- [66] A. Ghosal, “A neutrino mass model with reflection symmetry,” *Modern Physics Letters A*, vol. 19, no. 34, pp. 2579–2586, 2004.
- [67] J. A. Casas and A. Ibarra, “Oscillating neutrinos and  $\mu \rightarrow e, \gamma$ ,” *Nuclear Physics B*, vol. 618, p. 171, 2001.
- [68] B. Adhikary, M. Chakraborty, and A. Ghosal, “Scaling ansatz, four zero Yukawa textures and large  $\theta_{13}$ ,” *Physical Review D*, vol. 86, Article ID 013015, 2012.
- [69] P. F. Harrison, D. H. Perkins, and W. G. Scott, “Tri-bimaximal mixing and the neutrino oscillation data,” *Physics Letters Section B*, vol. 530, p. 167, 2002.
- [70] P. F. Harrison and W. G. Scott, “Status of Tri/Bi-maximal neutrino mixing,” <http://arxiv.org/abs/hep-ph/0402006>.
- [71] J. J. Gómez-Cadenas, J. Martín-Albo, M. Sorel et al., “Sense and sensitivity of double beta decay experiments,” *Journal of Cosmology and Astroparticle Physics*, vol. 2011, no. 6, article 007, 2011.
- [72] A. Dighe, S. Goswami, and P. Roy, “Radiatively broken symmetries of nonhierarchical neutrinos,” *Physical Review D*, vol. 76, Article ID 096005, 2007.
- [73] A. Dighe, S. Goswami, and P. Roy, “Quark-lepton complementarity with quasidegenerate Majorana neutrinos,” *Physical Review D*, vol. 73, no. 7, Article ID 071301, 2006.

## Review Article

# Current Direct Neutrino Mass Experiments

G. Drexlin,<sup>1</sup> V. Hannen,<sup>2</sup> S. Mertens,<sup>1</sup> and C. Weinheimer<sup>2</sup>

<sup>1</sup> Institut für Experimentelle Kernphysik, Karlsruher Institut für Technologie, 76021 Karlsruhe, Germany

<sup>2</sup> Institut für Kernphysik, Westfälische Wilhelms-Universität Münster, 48149 Münster, Germany

Correspondence should be addressed to G. Drexlin; [guido.drexlin@kit.edu](mailto:guido.drexlin@kit.edu)

Received 12 July 2012; Accepted 9 October 2012

Academic Editor: Arthur B. McDonald

Copyright © 2013 G. Drexlin et al. This is an open access article distributed under the Creative Commons Attribution License, which permits unrestricted use, distribution, and reproduction in any medium, provided the original work is properly cited.

In this contribution, we review the status and perspectives of direct neutrino mass experiments, which investigate the kinematics of  $\beta$ -decays of specific isotopes ( $^3\text{H}$ ,  $^{187}\text{Re}$ ,  $^{163}\text{Ho}$ ) to derive model-independent information on the averaged electron (anti)neutrino mass. After discussing the kinematics of  $\beta$ -decay and the determination of the neutrino mass, we give a brief overview of past neutrino mass measurements (SN1987a-ToF studies, Mainz and Troitsk experiments for  $^3\text{H}$ , cryobolometers for  $^{187}\text{Re}$ ). We then describe the Karlsruhe Tritium Neutrino (KATRIN) experiment currently under construction at Karlsruhe Institute of Technology, which will use the MAC-E-Filter principle to push the sensitivity down to a value of 200 meV (90% C.L.). To do so, many technological challenges have to be solved related to source intensity and stability, as well as precision energy analysis and low background rate close to the kinematic endpoint of tritium  $\beta$ -decay at 18.6 keV. We then review new approaches such as the MARE, ECHO, and Project8 experiments, which offer the promise to perform an independent measurement of the neutrino mass in the sub-eV region. Altogether, the novel methods developed in direct neutrino mass experiments will provide vital information on the absolute mass scale of neutrinos.

## 1. Introduction

The various experiments with atmospheric, solar, accelerator, and reactor neutrinos [1–5] provide compelling evidence that neutrino flavor states are nontrivial superpositions of neutrino mass eigenstates and that neutrinos oscillate from one flavor state into another during flight. By these neutrino oscillation experiments, we can determine the neutrino mixing angles and the differences between the squares of neutrino masses. In the case of the so-called *solar or reactor mass splitting*  $\Delta m_{12}^2$ , we not only know the modulus of this difference but also its sign. Clearly these findings prove that neutrinos have nonzero masses, but neutrino oscillation experiments being a kind of *interference experiment* cannot determine absolute masses. We may parameterize our missing knowledge by a free parameter  $m_{\min}$ , the mass of the smallest neutrino mass eigenstate (see Figure 1).

We should note that throughout this paper, we will not distinguish between the mass of a neutrino and the mass of an antineutrino, which should be the same if the CPT theorem holds. Therefore, we will use the term neutrino when we

speak of neutrinos and of antineutrinos. But we will explain for each measurement whether the result is obtained for neutrinos or antineutrinos.

The absolute value of the neutrino masses is very important for astrophysics and cosmology because of the role of neutrinos in structure formation due to the huge abundance of *relic neutrinos* left over in the universe from the big bang ( $336/\text{cm}^3$ ) [6]. In addition, the key role of neutrino masses in understanding, which of the possible extensions or new theories beyond the Standard Model of particle physics is the right one [7, 8], makes the quest for the absolute value of the neutrino mass among of the most urgent questions of nuclear and particle physics.

Three different approaches can lead to the absolute neutrino mass scale as follows.

(i) *Cosmology.* Today's visible structure of the universe has been formed out of fluctuations of the very early universe. Due to the large abundance of relic neutrinos and their low masses they acted as hot dark matter: neutrinos have smeared out fluctuations at small scales. How small or large

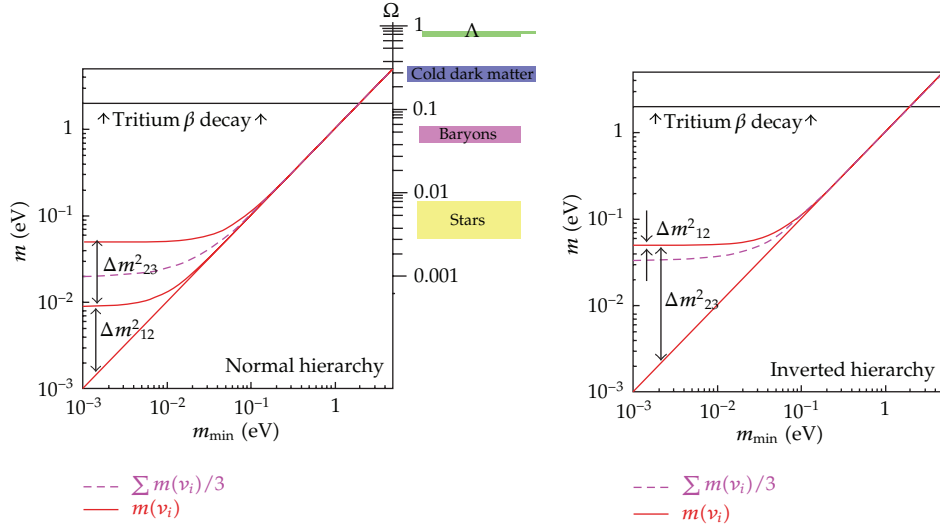


FIGURE 1: Neutrino mass eigenvalues  $m(\nu_i)$  (solid lines) and one-third of the cosmologically relevant sum of the three neutrino mass eigenvalues  $\sum m(\nu_i)/3$  (dashed line) as a function of the smallest neutrino mass eigenvalue  $m_{\min}$  for normal hierarchy  $m(\nu_3) > m(\nu_2) > m(\nu_1) = m_{\min}$  (left) and inverted hierarchy  $m(\nu_2) > m(\nu_1) > m(\nu_3) = m_{\min}$  (right). The upper limit from the tritium  $\beta$ -decay experiments at Mainz and Troitsk on  $m(\nu_e)$  (solid line), which holds in the degenerate neutrino mass region for each  $m(\nu_i)$ , and for  $\sum m(\nu_i)/3$  (dashed line) is also marked. We plot here the third of the sum of the neutrino mass eigenstates because it coincides with the mass  $m(\nu_i)$  of the individual neutrino mass states in the case of quasi-degenerate neutrino masses (for  $m(\nu_i) > 0.1$  eV). The temperature of the cosmic microwave background photons together with the different decoupling times of the relic photons and the relic neutrinos after the big bang yields a relic neutrino density of  $336/\text{cm}^3$  [6]. Using this number, the hot dark matter contribution  $\Omega_\nu$  of neutrinos to the matter/energy density of the universe relates directly to the average neutrino mass  $\sum m(\nu_i)/3$ . This hot dark matter component  $\Omega_\nu$  is indicated by the right scale of the normal hierarchy plot and compared to all other known matter/energy contributions in the universe (middle). Thus, the laboratory neutrino mass limit from tritium  $\beta$ -decay  $m(\nu_e) < 2$  eV corresponds to a maximum allowed neutrino matter contribution in the universe of  $\Omega_\nu < 0.12$ .

these scales are is described by the free streaming length of the neutrinos which depends on their mass. By determining the early fluctuations imprinted on the cosmic microwave background with the WMAP satellite [9] and mapping out today's structure of the universe by large galaxy surveys like SDSS [10] conclusions on the sum of the neutrino masses  $\sum m(\nu_i)$  can be drawn. Up to now, only upper limits on the sum of the neutrino masses have been obtained around  $\sum m(\nu_i) < 0.5$  eV [11], which are to some extent model and analysis dependent [6].

(ii) *Neutrinoless Double  $\beta$ -Decay ( $0\nu\beta\beta$ )*. A neutrinoless double  $\beta$ -decay (two  $\beta$ -decays in the same nucleus at the same time with emission of two  $\beta$ -electrons (positrons) while the antineutrino (neutrino) emitted at one vertex is absorbed at the other vertex as a neutrino (antineutrino)) is forbidden in the Standard Model of particle physics. It could exist, if the neutrino is its own antiparticle ("Majorana-neutrino" in contrast to "Dirac-neutrino") [12]. Furthermore, a finite neutrino mass is the most natural explanation to produce in the chirality-selective interaction a neutrino with a small component of opposite handedness on which this neutrino exchange subsists. Then the decay rate will scale with the absolute square of the so-called effective Majorana neutrino mass, which takes into account the neutrino mixing matrix  $U$

$$\Gamma_{0\nu\beta\beta} \propto \left| \sum U_{ei}^2 m(\nu_i) \right|^2 := m_{ee}^2. \quad (1)$$

Here  $m_{ee}$  represents the sum of the neutrino masses  $m(\nu_i)$  contribution coherently to the  $0\nu\beta\beta$ -decay. Hence this coherent sum carries their relative phases (the usual CP-violating phase of a unitary  $3 \times 3$  mixing matrix plus two so-called Majorana-phases). A significant additional uncertainty which enters the relation of  $m_{ee}$  and the decay rate is the nuclear matrix element of the neutrinoless double  $\beta$ -decay [12]. There is one claim for evidence at  $m_{ee} \approx 0.3$  eV by part of the Heidelberg-Moscow collaboration [13], which is being challenged by limits from different experiments in the same range, for example, very recently by the EXO-200 experiment [14].

(iii) *Direct Neutrino Mass Determination*. The direct neutrino mass determination is based purely on kinematics without further assumptions. Essentially, the neutrino mass is determined by using the relativistic energy-momentum relationship  $E^2 = p^2 + m^2$ . Therefore it is sensitive to the neutrino mass squared  $m^2(\nu)$ . In principle there are two methods: time-of-flight measurements and precision investigations of weak decays. The former requires very long baselines and therefore very strong sources, which only cataclysmic astrophysical events like a core-collapse supernova could provide. The supernova explosion SN1987a in the Large Magellanic Cloud gave limits of 5.7 eV (95% C.L.) [16] or of 5.8 eV (95% C.L.) [17] on the neutrino mass depending somewhat on the underlying supernova model. Unfortunately nearby



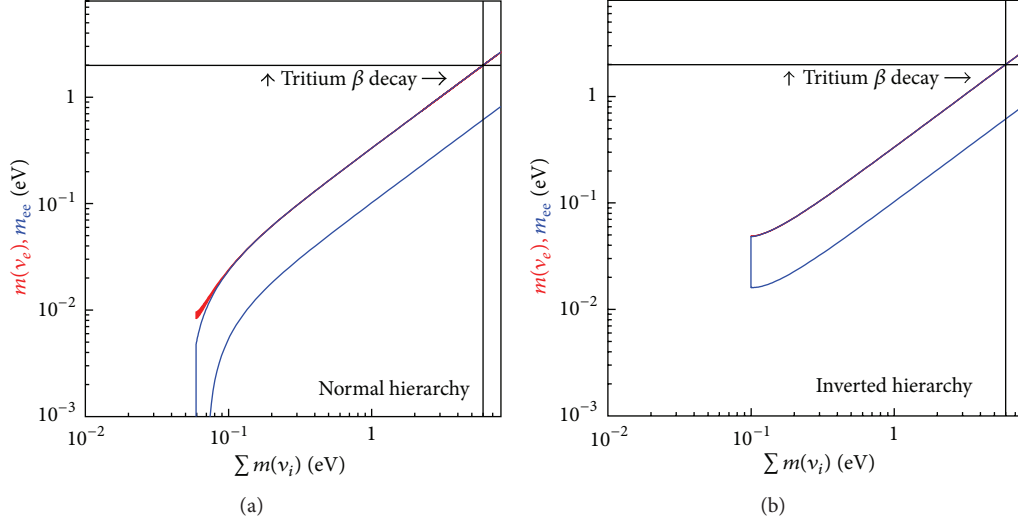


FIGURE 2: Observables of neutrinoless double  $\beta$ -decay  $m_{ee}$  (open blue band) and of direct neutrino mass determination by single  $\beta$ -decay  $m(\nu_e)$  (red) versus the cosmologically relevant sum of neutrino mass eigenvalues  $\sum m(\nu_i)$  for the case of normal hierarchy (a) and of inverted hierarchy (b). The width of the bands/areas is caused by the experimental uncertainties ( $2\sigma$ ) of the neutrino mixing angles [15] and in the case of  $m_{ee}$  also by the completely unknown Majorana- and CP-phases. Uncertainties of the nuclear matrix elements, which enter the determination of  $m_{ee}$  from the measured values of half-lives or of half-live limits of neutrinoless double  $\beta$ -decay, are not considered.

supernova explosions are too rare and seem to be not well enough understood to allow to compete with the laboratory direct neutrino mass experiments.

Therefore, aiming for this sensitivity, the investigation of the kinematics of weak decays and more explicitly the investigation of the endpoint region of a  $\beta$ -decay spectrum (or an electron capture) is still the most sensitive model-independent and direct method to determine the neutrino mass. Here the neutrino is not observed but the charged decay products are precisely measured. Using energy and momentum conservation, the neutrino mass can be obtained. In the case of the investigation of a  $\beta$ -spectrum usually the “average electron neutrino mass”  $m(\nu_e)$  is determined (see (20) in the next subsection)

$$m(\nu_e)^2 := \sum |U_{ei}^2| m(\nu_i)^2. \quad (2)$$

In contrast to  $m_{ee}$  in neutrinoless double  $\beta$ -decay (see (1)), this sum averages over all neutrino mass states  $m(\nu_i)$  contributing to the electron neutrino and no phases of the neutrino mixing matrix  $U$  enter. The decay into the different neutrino mass eigenstates  $\nu_i$  add incoherently, which we will discuss in more detail for the neutrino mixture to sterile neutrinos in Section 2.1.

Figure 2 demonstrates that the different methods are complementary to each other and compares them.

This paper is structured as follows. In Section 2, the neutrino mass determination from the kinematics of  $\beta$ -decay is described. Section 3 presents the analysis of the spectrum of neutrinos from supernova SN1987a and the recent  $\beta$ -decay experiments in search for the neutrino mass scale. In Section 4, an overview of the present KATRIN experiment is given. New approaches to directly determine the neutrino mass are presented in Section 5. This paper ends with a conclusion in Section 6. For a more detailed and complete

overview on this subject, we would like to refer to the reviews [18–23].

## 2. $\beta$ -Decay and $\nu$ -Mass

According to Fermi’s Golden Rule, the decay rate for a  $\beta$ -decay is given by the square of the transition matrix element  $M$  summed and integrated over all possible discrete and continuous final states  $f$  (we use the convention  $\hbar = 1 = c$  for simplicity).

$$\Gamma = 2\pi \sum_f |M^2| df. \quad (3)$$

Let us first calculate the density of the final states. The number of different final states  $dn$  of outgoing particles inside a normalization volume  $V$  into the solid angle  $d\Omega$  with momenta between  $p$  and  $p+dp$ , or, respectively, with energies in the corresponding interval around the total energy  $E_{\text{tot}}$ , is

$$\begin{aligned} dn &= \frac{V \cdot p^2 \cdot dp \cdot d\Omega}{h^3} \\ &= \frac{V \cdot p^2 \cdot dp \cdot d\Omega}{(2\pi)^3} \\ &= \frac{V \cdot p \cdot E_{\text{tot}} \cdot dE_{\text{tot}} \cdot d\Omega}{(2\pi)^3}. \end{aligned} \quad (4)$$

This gives a state density per energy interval and solid angle of

$$\frac{dn}{dE_{\text{tot}} d\Omega} = \frac{V \cdot p \cdot E_{\text{tot}}}{(2\pi)^3}. \quad (5)$$

Since the mass of the nucleus is much larger than the energies of the two emitted leptons, we can use for the next steps the following simplification: the nucleus takes nearly no energy but balances all momenta (we will consider the recoil energy of the nucleus later.). Therefore we need to count the state density of the electron and the neutrino only

$$\begin{aligned} \rho(E_e, E_\nu, d\Omega_e, d\Omega_\nu) &= \frac{dn_e}{dE_e d\Omega_e} \cdot \frac{dn_\nu}{dE_\nu d\Omega_\nu} \\ &= \frac{V^2 \cdot p_e \cdot E_e \cdot p_\nu \cdot E_\nu}{(2\pi)^6} \\ &= \frac{V^2 \cdot \sqrt{E_e^2 - m_e^2} \cdot E_e \cdot \sqrt{E_\nu^2 - m^2(\nu_e)} \cdot E_\nu}{(2\pi)^6}. \end{aligned} \quad (6)$$

The transition matrix element  $M$  can be divided into a leptonic part,  $M_{\text{lep}}$ , and a nuclear one,  $M_{\text{nuc}}$ . Usually the coupling is written separately and expressed in terms of Fermi's coupling constant  $G_F$  and the Cabibbo angle  $\Theta_C$

$$M = G_F \cdot \cos \Theta_C \cdot M_{\text{lep}} \cdot M_{\text{nuc}}. \quad (7)$$

**2.1. Allowed and Superaligned Transitions.** We first discuss the case of allowed or superallowed decays like that of tritium. Here, none of the leptons has to carry away angular momentum. Hence, the leptonic part  $|M_{\text{lep}}^2|$  essentially results in the probability of the two leptons to be found at the nucleus, which is  $1/V$  for the neutrino and  $1/V \cdot F(E, Z')$  for the electron, yielding

$$|M_{\text{lep}}^2| = \frac{1}{V^2} \cdot F(E, Z'). \quad (8)$$

The Fermi function  $F(E, Z')$  takes into account the final electromagnetic interaction of the emitted  $\beta$ -electron with the daughter nucleus of nuclear charge ( $Z'$ ). The Fermi function is approximately given by [19]

$$F(E, Z') = \frac{2\pi\eta}{1 - \exp(-2\pi\eta)} \quad (9)$$

with the Sommerfeld parameter  $\eta = \alpha Z' / \beta$ .

For an allowed or superallowed transition the nuclear matrix element  $M_{\text{nuc}}$  is independent of the kinetic energy of the electron. The coupling of the lepton spins to the nuclear spin is usually contracted into the nuclear matrix element. This nuclear matrix element of an allowed or superallowed transition can be divided into a vector current or Fermi part ( $\Delta I_{\text{nuc}} = 0$ ) and into an axial current or Gamov-Teller part ( $\Delta I_{\text{nuc}} = 0, \pm 1$  but no  $I_{\text{nuc}} = 0 \rightarrow I_{\text{nuc}} = 0$ ). In the former case, the spins of electron and neutrino couple to  $S = 0$ , in the latter case to  $S = 1$ . What remains is an angular correlation of the two outgoing leptons. Since charge current weak interactions like  $\beta$ -decay maximally violate parity they prefer—depending on velocity—negative helicities for particles and positive helicities for antiparticles.

Thus the momenta or directions of the leptons are correlated with respect to their spins and therefore to each other. This results are an  $(\beta, \nu)$  angular correlation factor

$$1 + a \cdot (\vec{\beta} \vec{\beta}_\nu) \quad (10)$$

with the electron velocity  $\beta = v/c$  and the neutrino velocity  $\beta_\nu = v_\nu/c$ . The angular correlation coefficient  $a$  amounts to  $a = 1$  for pure Fermi transitions and to  $a = -1/3$  for pure Gamov-Teller transitions within the Standard Model [24].

The phase space density (6) is distributed over a surface in the two-particle phase space which is defined by a  $\delta$ -function conserving the decay energy. With this prescription, we can integrate (3) over the continuum states and get the partial decay rate into a single channel; for instance, the ground state of the daughter system with probability  $P_0$

$$\begin{aligned} \Gamma_0 = P_0 \cdot \int_{E_e, E_\nu, \Omega_e, \Omega_\nu} &\frac{G_F^2 \cdot \cos^2 \Theta_C \cdot |M_{\text{nuc}}^2|}{(2\pi)^5} \cdot F(E, Z') \\ &\cdot \sqrt{E_e^2 - m_e^2} \cdot E_e \cdot \sqrt{E_\nu^2 - m^2(\nu_e)} \\ &\cdot E_\nu \cdot (1 + a \cdot (\vec{\beta} \vec{\beta}_\nu)) \\ &\cdot \delta(Q + m_e - E_e - E_\nu - E_{\text{rec}}) dE_e dE_\nu d\Omega_e d\Omega_\nu. \end{aligned} \quad (11)$$

In direct neutrino mass measurements usually the formulas are given in terms of the kinetic energy of the electron  $E$

$$E := E_e - m_e. \quad (12)$$

The maximal kinetic energy of the electron for the case of zero neutrino mass zero is called endpoint energy  $E_0$  which is defined by a vanishing neutrino energy  $E_\nu$

$$E_0 := \max(E) = \max(E_e - m_e). \quad (13)$$

A correct integration over the unobserved neutrino variables in (11) has to respect the  $(\beta, \nu)$  angular correlation factor (10), which also has to be considered in calculating the exact recoil energy of the nucleus  $E_{\text{rec}}$ . If we consider that the  $\beta$ -electrons of interest have a certain minimal kinetic energy  $E_{\text{min}}$  then we can calculate the range of recoil energies of the daughter nucleus of mass  $m_{\text{daughter}}$ : the recoil energy  $E_{\text{rec}}$  is bound upwards by the case, in which the outgoing electron takes the maximum kinetic energy  $E_0$  and downwards by the case, in which the electron of kinetic energy  $E_{\text{min}}$  is emitted opposite to the direction of the neutrino, which has in this case a momentum  $p_\nu = E_\nu = E_0 - E_{\text{min}}$  (neglecting for a moment the nonzero value of the neutrino mass)

$$\begin{aligned} \frac{(p_e - p_\nu)^2}{2m_{\text{daughter}}} &= \frac{\left(\sqrt{E_{\text{min}}^2 + 2E_{\text{min}}m_e} - (E_0 - E_{\text{min}})\right)^2}{2m_{\text{daughter}}} \\ &\leq E_{\text{rec}} \leq E_{\text{rec, max}} \\ &= \frac{p_{\text{max}}^2}{2m_{\text{daughter}}} = \frac{E_0^2 + 2E_0m_e}{2m_{\text{daughter}}}. \end{aligned} \quad (14)$$

Due to the largeness of  $m_{\text{daughter}}$  even for sizeable electron energy ranges below the endpoint  $E_0$ , according to (14) the recoil energy  $E_{\text{rec}}$  does not change much (numbers are given for the example of tritium in the next section). Therefore, for the region of interest below the endpoint  $E_0$ , we can apply a constant recoil energy correction  $E_{\text{rec}} = \text{const.}$  and (13) becomes (We should note here that we cannot use (15) to derive the endpoint energy  $E_0$  from a measured nuclear  $Q$ -value with the precision required for the direct measurement of the neutrino mass due to the uncertainty of  $Q$ , which is  $\mathcal{O}(1)$  eV at best. Therefore  $E_0$  has to be fitted from the  $\beta$ -spectrum together with the neutrino mass squared. For the case of tritium there is currently a large experimental effort to improve significantly the precision on the  $Q$ -value of tritium  $\beta$ -decay by ultrahigh precision ion cyclotron resonance mass spectroscopy in a multi-Penning trap setup measuring the  ${}^3\text{He}$ - ${}^3\text{H}$  mass difference [25] with the final goal to use the measured  $Q$ -value in the neutrino mass fit.)

$$E_0 = Q - E_{\text{rec}}. \quad (15)$$

Further integration over the angles yields through (10) an averaged nuclear matrix element, as mentioned above. Besides integrating over the  $(\beta, \nu)$ -continuum, we have to sum over all other final states. For a  $\beta$ -decaying atom or molecule it is a double sum: one summation runs over all neutrino mass eigenstates  $m(\nu_i)$  with probabilities  $|U_{\text{ei}}^2|$  which are kinematically accessible ( $m(\nu_i) \leq E_0$ ). The second summation has to be done over all of the electronic final states of the daughter system with probabilities  $P_j$  and excitation energies  $V_j$ . These comprise excitations of the electron shell but also—in the case of  $\beta$ -decaying molecules—rotational and vibrational excitations. These excitations are caused by the sudden change of the nuclear charge from  $Z$  to  $Z' = Z + 1$  which requests a rearrangement of the electronic orbitals of the daughter atom or molecule and the interatomic distances in case of a molecule. They give rise to shifted endpoint energies. Introducing the definition

$$\varepsilon := (E_0 - E), \quad (16)$$

the total neutrino energy now amounts for this excitation to  $E_{\nu,j} = \varepsilon - V_j$ . The  $\beta$ -electrons are leaving the nucleus on a time scale much shorter than the typical Bohr velocities of the shell electrons of the mother isotope. Therefore, the excitation probabilities of electronic states—and of vibrational-rotational excitations in the case of molecules—can be calculated in the so-called sudden approximation from the overlap of the primary electron wave function  $\Psi_0$  with the wave functions of the daughter ion  $\Psi_{f,j}$

$$P_j = \left| \langle \Psi_0 | \Psi_{f,j} \rangle \right|^2. \quad (17)$$

Rather than in the total decay rate, we are interested in its energy spectrum  $\dot{N}(E) := dT/dE$ , which we can read directly from (11) without performing the second integration over the

$\beta$ -energy. Using  $\varepsilon = E_0 - E$  and summing up over the final states it reads

$$\begin{aligned} \dot{N}(E) = & \frac{G_F^2 \cdot \cos^2 \Theta_C}{2\pi^3} \cdot |M_{\text{nucl}}^2| \\ & \cdot F(E, Z') \cdot (E + m_e) \\ & \cdot \sqrt{(E + m_e)^2 - m_e^2} \\ & \cdot \sum_{i,j} |U_{\text{ei}}^2| \cdot P_j \cdot (\varepsilon - V_j) \\ & \cdot \sqrt{(\varepsilon - V_j)^2 - m^2(\nu_i)} \\ & \cdot \Theta(\varepsilon - V_j - m(\nu_i)). \end{aligned} \quad (18)$$

The  $\Theta$ -function confines the spectral components to the physical sector  $\varepsilon - V_j - m(\nu_i) > 0$ . This causes a technical difficulty in fitting mass values smaller than the sensitivity limit of the data, as statistical fluctuations of the measured spectrum might occur which can no longer be fitted within the allowed physical parameter space. Therefore, one has to define a reasonable mathematical continuation of the spectrum into the region which leads to  $\chi^2$ -parabolas around  $m^2(\nu_i) \approx 0$  (see, e.g., [26]).

Assuming unitarity of the kinematic accessible neutrino mass states ( $\sum_i |U_{\text{ei}}^2| = 1$ ), we can expand the second line of (18) for  $(\varepsilon - V_j)^2 \gg m^2(\nu_i)$

$$\dot{N}(E) \propto \sum_{i,j} |U_{\text{ei}}^2| \cdot P_j \cdot (\varepsilon - V_j) \quad (19)$$

$$\begin{aligned} & \cdot \sqrt{(\varepsilon - V_j)^2 - m^2(\nu_i)} \\ & \approx \sum_j P_j \cdot \left( (\varepsilon - V_j)^2 - \frac{1}{2} \sum_i |U_{\text{ei}}^2| m^2(\nu_i) \right) \\ & =: \sum_j P_j \cdot \left( (\varepsilon - V_j)^2 - \frac{1}{2} m^2(\nu_e) \right). \end{aligned} \quad (20)$$

This average over the squared masses of the neutrino mass states  $m^2(\nu_i)$  in (20) defines what we called the *electron neutrino mass*  $m(\nu_e)$  in (2). This simplification always applies, if we cannot resolve the different neutrino mass states.

Figure 3 shows the  $\beta$ -spectrum at the endpoint according to (18). The influence of the neutrino mass on the  $\beta$ -spectrum shows only at the upper end below  $E_0$ , where the neutrino is not fully relativistic and can exhibit its massive character. The relative influence decreases in proportion to  $m^2(\nu_e)/\varepsilon^2$  (see Figure 3), which leads far below the endpoint—according to (20)—to a small constant offset proportional to  $-m^2(\nu_e)$ .

Concerning the various neutrino mass states, we can also assume that there is one heavy neutrino mass state  $m(\nu_h)$  (this heavy state might comprise more than one heavy state, which are experimentally not distinguishable) and one light one  $m(\nu_l)$  (again this could be the sum of more than one

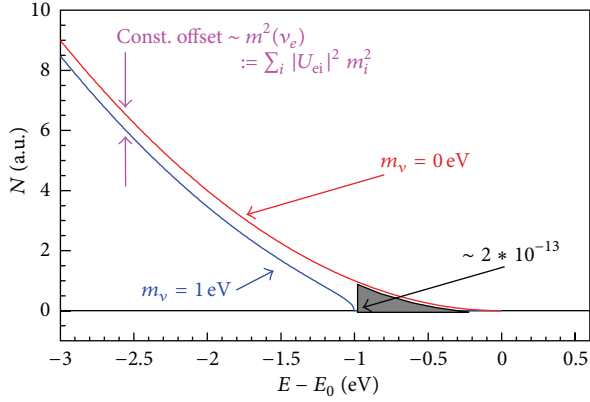


FIGURE 3: Expanded  $\beta$ -spectrum of an allowed or superallowed  $\beta$ -decay around its endpoint  $E_0$  for  $m(\nu_e) = 0$  (red line) and for an arbitrarily chosen neutrino mass of 1 eV (blue line). In the case of tritium (see Section 2.2), the gray-shaded area corresponds to a fraction of  $2 \cdot 10^{-13}$  of all tritium  $\beta$ -decays.

light neutrino). Such a situation could arise, if 3 light active neutrinos and one heavy sterile neutrino are mixed. With  $\sum_{i,l} |U_{ei}^2| =: \cos^2\theta$  and  $\sum_{i,h} |U_{ei}^2| = 1 - \sum_{i,l} |U_{ei}^2| = \sin^2\theta$ , we can rewrite the last line of (18) for this case into

$$\dot{N}(E) \propto \sum_{i,j} |U_{ei}^2| \cdot P_j \cdot (\epsilon - V_j) \cdot \sqrt{(\epsilon - V_j)^2 - m^2(\nu_i)} \quad (21)$$

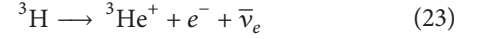
$$\approx \sum_j P_j \cdot \left( \sin^2\theta \cdot (\epsilon - V_j) \sqrt{(\epsilon - V_j)^2 - m^2(\nu_h)} + \cos^2\theta \cdot (\epsilon - V_j) \sqrt{(\epsilon - V_j)^2 - m^2(\nu_l)} \right). \quad (22)$$

Figure 3 defines the requirements of a direct neutrino mass experiment which investigates a  $\beta$ -spectrum: the task is to resolve the tiny change of the spectral shape due to the neutrino mass in the region just below the endpoint  $E_0$ , where the count rate is going to vanish. Therefore a high sensitivity experiment requires high energy resolution, large  $\beta$ -decay source strength and acceptance, and low background rate.

Now we should firstly discuss, what is the best  $\beta$ -emitter for such a task. Figure 4 shows the total count rate of a superallowed  $\beta$ -emitter as function of the endpoint energy. Of course, the total count rate rises strongly with  $E_0$ , while the relative fraction in the last 10 eV below  $E_0$  decreases. Interestingly, the total count rate in the last 10 eV below  $E_0$ , which we can take as a measure of our energy region of interest for determining the neutrino mass, is increases with regard to  $E_0$ . This increase is caused by the larger phase space for the  $\beta$ -electron. From Figure 4 one might argue that the endpoint energy does not play a significant role in selecting the right  $\beta$ -isotope, but we have to consider the fact that we need a certain energy resolution  $\Delta E$  to determine the neutrino mass. Experimentally it makes a huge difference,

whether we have to achieve a certain  $\Delta E$  at a low energy  $E_0$  or at a higher one. Secondly, the  $\beta$ -electrons of no interest with regard to the neutrino mass could cause experimental problems (e.g., as background or pileup) and again this argument favors a low  $E_0$ .

**2.2. Tritium  $\beta$ -Decay.** The heaviest of the hydrogen isotopes tritium undergoes  $\beta$ -decay



with a half-life of 12.3 y. Tritium and Helium-3 are mirror nuclei of the same isospin doublet; therefore, the decay is superallowed. Thus the nuclear matrix element for tritium is close to that of the  $\beta$ -decay of the free neutron and amounts to [18]

$$|M_{\text{nucl}}^2(\text{tritium})| = 5.55. \quad (24)$$

With an endpoint energy of 18.6 keV, it has one of the lowest endpoints of all  $\beta$  emitters together with a reasonable long half-life. Its superallowed shape of the  $\beta$ -spectrum and its simple electronic structure allow the tritium  $\beta$ -spectrum to be measured with small systematic uncertainties.

The recoil correction for tritium is not an issue. Up to now all tritium  $\beta$ -decay experiments used molecular tritium, which give a maximal recoil energy to the daughter molecular ion of  $E_{\text{rec,max}} = 1.72$  eV. Even for the most sensitive tritium  $\beta$ -decay experiment, the upcoming KATRIN experiment (see Section 4.1), the maximum variation of  $E_{\text{rec}}$  over the energy interval of investigation (the last 30 eV below the endpoint) amounts to  $\Delta E_{\text{rec}} = 3.5$  meV only. It was checked [27] that this variation can be neglected and the recoil energy can be replaced by a constant value of  $E_{\text{rec}} = 1.72$  eV, yielding a fixed endpoint according to (15).

Furthermore, one may apply radiative corrections to the spectrum [28, 29]. However, they are quite small and would influence the result on  $m^2(\nu_e)$  even for the KATRIN experiment only by a few percent of its present systematic uncertainty. One may also raise the point of whether possible contributions from right-handed currents might lead to measurable spectral anomalies [30, 31]. It has been checked that the present limits on the corresponding right-handed boson mass [24] rule out a sizeable contribution within present experimental uncertainties. Even the forthcoming KATRIN experiment will hardly be sensitive to this problem [32, 33].

Concerning the calculation of the electronic final states according to (17), we have to consider molecular tritium since all tritium  $\beta$ -decay experiments so far have been using molecular tritium sources, containing the molecule  $\text{T}_2$ . The wave functions of the tritium molecule are much more complicated, since in addition to two identical electrons they comprise also the description of rotational and vibrational states, which may be excited during the  $\beta$ -decay as well. Figure 5 shows a recent numerical calculation of the final states of the  $\text{T}_2$  molecule. The transition to the electronic ground state of the  $({}^3\text{HeT})^+$  daughter ion as well as the transition to higher excited electronic states are not sharp in energy,



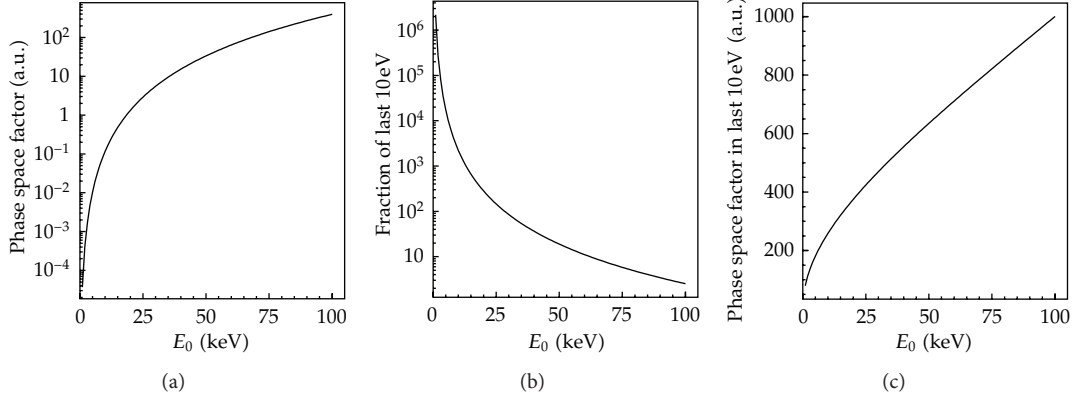


FIGURE 4: Dependence on endpoint energy  $E_0$  of total count rate (a), relative fraction in the last 10 eV below the endpoint (b), and total count rate in the last 10 eV of a  $\beta$ -emitter (c). These numbers have been calculated for a superallowed  $\beta$ -decay using (18) for  $m(\nu_e) = 0$  and neglecting possible final states as well as the Fermi function  $F$ .

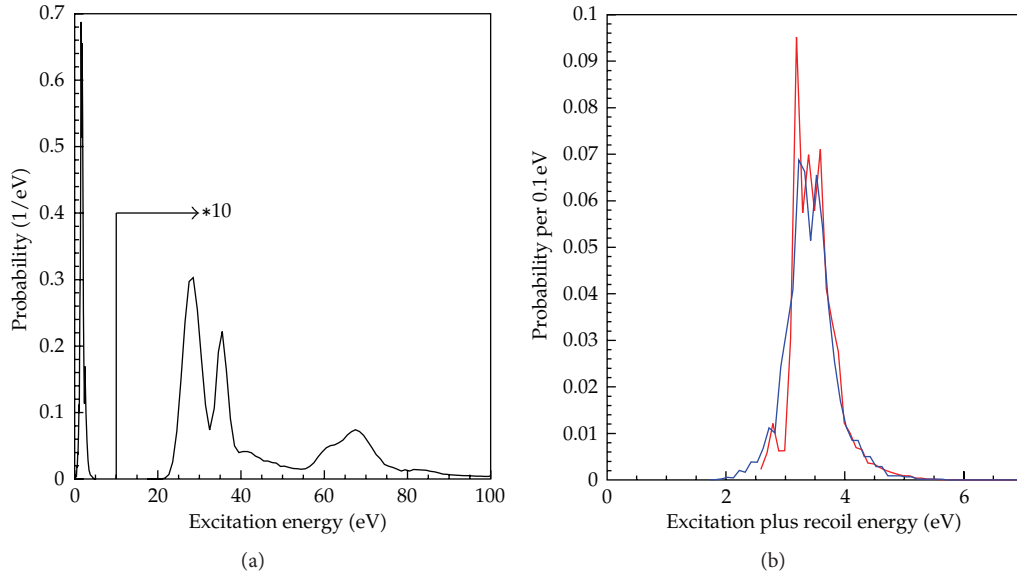


FIGURE 5: Excitation spectrum of the daughter  $(^3\text{HeT})^+$  in  $\beta$ -decay of molecular tritium (a) and rotational-vibrational excitations of the  $(^3\text{HeT})^+$  molecular ion only (right, red solid curve). In comparison, the rotational-vibrational excitations of the  $(^3\text{HeH})^+$  molecular ion from HT  $\beta$ -decay are shown ((b), blue line) [34]. Please note, that the abscissa of the right plot reads excitation energy plus maximum recoil energy according to (14).

but broadened due to rotational-vibrational excitations. More recent calculations agree with these results [35, 36].

The first group of excited electronic states starts at around  $V_j = 25$  eV [34]. Therefore excited states play almost no role for the energy interval considered for the upcoming KATRIN experiment: only the decay to the ground state of the  $(^3\text{HeT})^+$  daughter molecule, which is populated with about 57% probability, has to be taken into account. Due to the nuclear recoil, however, a large number of rotational-vibrational states with a mean excitation energy of 1.7 eV and a standard deviation of 0.4 eV are populated. These values hold for a pure  $\text{T}_2$  source without contamination by other hydrogen isotopes. But a contamination of the  $\text{T}_2$  molecules by DT or HT molecules does not matter in first order: the

shift of the mean rotational-vibrational excitation of HT with respect to  $\text{T}_2$  is compensated by a corresponding change of the nuclear recoil energy of HT with respect to the 1.5 times heavier  $\text{T}_2$  molecule [34] (see Figure 5(b)).

Summarizing the properties of tritium for direct neutrino mass measurements: it is the standard isotope for this kind of study due to its low endpoint of 18.6 keV, its rather short half-life of 12.3 y, its superallowed shape of the  $\beta$ -spectrum, and its simple electronic structure. Tritium  $\beta$ -decay experiments using a tritium source and a separated electron spectrometer have been performed in search for the neutrino mass for more than 60 years. But when the electron spectrometer is identical to the  $\beta$ -source, the situation is different and a  $\beta$ -isotope with an even lower endpoint energy  $E_0$  is preferred, even if it does not have an allowed decay.

**2.3. Forbidden Transitions Like  $^{187}\text{Re}$ .** The isotope  $^{187}\text{Re}$  exhibits the lowest endpoint energy with  $E_0 = 2.47 \text{ keV}$  of all known  $\beta$ -emitters decaying to the ground-state of the daughter nucleus (there is even a decay of the  $^{115}\text{In}$  into an excited nuclear  $(3/2^+)$ -state of the daughter nucleus  $^{115}\text{Sn}$  with a much lower  $Q$ -value of  $(155 \pm 24) \text{ eV}$  [37, 38]. But there are two reasons, why such a decay cannot be used for a direct neutrino mass measurement: this partial decay has an ultra-long half-life of  $(4.1 \pm 0.6) \cdot 10^{20} \text{ y}$  [37] and the signature of the neutrino mass is hidden in the  $\beta$ -spectrum of the decay into the ground state of  $^{115}\text{Sn}$ ). The ground state of the mother isotope  $^{187}\text{Re}$  has spin and parity  $J^\pi = 5/2^+$ . The  $\beta$ -decay goes to the ground state of the daughter  $^{187}\text{Os}$  with spin and parity  $J^\pi = 1/2^-$ . Therefore, the decay is a first unique forbidden transition. The lepton pair, electron and antineutrino, has to carry away two units of angular momentum and has to change parity. The two leptons will couple to spin  $S = 1$  in this case, one unit of orbital momentum has to be carried away by either the electron or the antineutrino. Therefore the half life of  $t_{1/2}(^{187}\text{Re}) = 4.3 \cdot 10^{10} \text{ y}$  is huge and about as long as the age of the universe. The advantage of the 7 times lower endpoint energy  $E_0 = 2.47 \text{ keV}$  of  $^{187}\text{Re}$  with respect to tritium does not compensate the fact that one needs a large number of  $^{187}\text{Re}$  atoms to obtain enough count rate near the endpoint to measure the neutrino mass. Therefore, a classical *source*  $\neq$  *spectrometer* arrangement like for the tritium experiments is not feasible for  $^{187}\text{Re}$ , because the  $\beta$ -electrons will undergo too many inelastic scattering processes within the  $^{187}\text{Re}$  source. Secondly, the isotope  $^{187}\text{Re}$  has a complicated electron shell and the electronic final states might not be calculable precisely enough.

Therefore, the  $\beta$ -decay of  $^{187}\text{Re}$  can only be exploited if the  $\beta$ -spectrometer measures the entire released energy, except that of the neutrino but including the energy loss by inelastic scattering processes and electronic excitations. This situation can be realized by using a cryogenic bolometer as the  $\beta$ -spectrometer, which at the same time contains the  $\beta$ -emitter  $^{187}\text{Re}$  [23] (see Section 3.4).

We discuss now the consequences for the  $\beta$ -spectrum. Since either the electron or the antineutrino has to be emitted with orbital angular momentum  $l = 1$  we cannot, expand the plain wave of this lepton to zeroth order anymore as we did in (8), but we have to go to first order

$$\exp(-pR) \approx 1 - pR. \quad (25)$$

In contrast to an allowed decay, the matrix element will become dependent on energy. According to (25), an additional factor proportional to  $p_e = \sqrt{(E + m_e)^2 - m_e^2} = \sqrt{(E_0 + m_e - \varepsilon)^2 - m_e^2}$  or to  $p_\nu = \sqrt{\varepsilon^2 - m^2(\nu_i)}$  will occur, depending on whether the electron or the antineutrino carries away the unit of orbital angular momentum. In the decay rate the square of these momenta will appear. For both cases, a Fermi function  $F_1$  or  $F_0$  needs to be considered which

describes the Coulomb interaction of the outgoing electron in a  $l = 1$  or  $l = 0$  state with the remaining osmium ion [39]

$$\begin{aligned} \dot{N}(E) = & \frac{G_F^2 \cdot \cos^2 \Theta_C}{2\pi^3} \\ & \cdot |M_{\text{nuc}}^2| \cdot (E_0 + m_e - \varepsilon) \\ & \cdot \sqrt{(E_0 + m_e - \varepsilon)^2 - m_e^2} \\ & \cdot \sum_i |U_{ei}^2| \cdot \frac{R_{\text{nuc}}^2}{3} \\ & \times (F_1(E, Z') \cdot ((E_0 + m_e - \varepsilon)^2 - m_e^2) \\ & + F_0(E, Z') \cdot (\varepsilon^2 - m^2(\nu_i))) \\ & \cdot \varepsilon \cdot \sqrt{\varepsilon^2 - m^2(\nu_i)} \cdot \Theta(\varepsilon - m(\nu_i)), \end{aligned} \quad (26)$$

where  $R_{\text{nuc}}$  is the nuclear radius. The first term of (26) proportional to  $p^2$  is by 4 orders of magnitude larger than the second term proportional to  $p_\nu^2$  [39]. The nuclear matrix element  $M_{\text{nuc}}$  is more complex than that of an allowed  $\beta$ -decay.

In contrast to the case of tritium, we do not account in (26) for excited electronic final states, since we assume that all losses by electromagnetic excitations will be added to the energy of the  $\beta$ -electron as well as to the recoil energy in the *source = detector* arrangement by the signal integration of the cryobolometer. Thus the  $\beta$ -spectrum looks simpler (we will discuss later that some excited states may live longer than the signal integration time of the cryobolometer and that the corresponding excitation energy may not be measured, which would cause systematic uncertainties). But this is only true up to first order. In second order, the electronic final states with excitation energy  $V_j$  and probability  $P_j$  have to be considered since the modification of the phase space of the outgoing electron and the squared matrix element ( $\propto (F_1 p_e^3 (E + m_e) p_\nu E_\nu + F_0 p_e (E + m_e) p_\nu^3 E_\nu)$ ) have to be taken into account.

We will discuss the influence of electronic final states for the case of cryobolometers in some detail: when an electronic final state takes the excitation energy  $V_j$ , in the calculation for an allowed decay (see (18)), we had just shifted the effective endpoint energy by this amount ( $E_0 \rightarrow E'_0 = E_0 - V_j$ ) and multiplied this fraction of the  $\beta$ -spectrum with its probability  $P_j$ . Thus the whole  $\beta$ -spectrum including the phase space of the outgoing leptons was calculated correctly up to possible electron energies  $E'_0$ . When we measure with a cryobolometer the sum energy  $E$  in the case of an electronic excitation  $V_j$ , the true kinetic energy of the electron amounts only to  $E' = E - V_j$ . The residual energy release  $V_j$  detected in the cryobolometer stems from the deexcitation of the electronic excitation. Therefore the  $\beta$ -decay probability, or the corresponding phase space factor and the squared matrix

element have to be calculated for the true electron kinetic energy  $E'$  and the reduced endpoint energy  $E'_0$  as

$$E' = E - V_j, \quad E'_0 = E_0 - V_j. \quad (27)$$

We can expand the relevant parameters for the phase space and squared matrix element calculation to first order assuming  $V_j \ll p$  and  $V_j \ll E_e$

$$\begin{aligned} E'_e &= E' + m_e = E - V_j + m_e \\ &= (E + m_e) \cdot \left(1 - \frac{V_j}{E + m_e}\right) = E_e \cdot \left(1 - \frac{V_j}{E_e}\right), \end{aligned} \quad (28)$$

$$\begin{aligned} p'_e &= \sqrt{E'^2_e - m_e^2} = \sqrt{(E' + m_e)^2 - m_e^2} \\ &= \sqrt{E'^2 + 2m_e E'} = \sqrt{(E - V_j)^2 + 2m_e (E - V_j)} \\ &\approx \sqrt{E^2 + 2m_e E - 2(E + m_e)V_j} \end{aligned} \quad (29)$$

$$\begin{aligned} &= \sqrt{p_e^2 \left(1 - \frac{2E_e V_j}{p_e^2}\right)} \approx p_e \left(1 - \frac{E_e V_j}{p_e^2}\right), \\ E'_v &= E'_0 - E' = (E_0 - V_j) - (E - V_j) \\ &= E_0 - E = E_\nu, \end{aligned} \quad (30)$$

$$p'_v = \sqrt{E'^2_v - m^2(v_e)} = \sqrt{E_v^2 - m^2(v_e)} = p_v. \quad (31)$$

Equation (26) then becomes

$$\begin{aligned} \dot{N}(E) &= \frac{G_F^2 \cdot \cos^2 \Theta_C}{2\pi^3} \cdot |M_{\text{nucl}}^2| \\ &\cdot \sum_{i,j} (E_0 + m_e - \varepsilon) \cdot |U_{ei}^2| \cdot P_j \cdot \frac{R_{\text{nucl}}^2}{3} \\ &\cdot \left( F_1(E, Z') \cdot ((E_0 + m_e - \varepsilon)^2 - m_e^2)^{3/2} \right. \\ &\cdot \left( 1 - 3 \frac{E_e V_j}{p_e^2} \right) + F_0(E, Z') \\ &\cdot ((E_0 + m_e - \varepsilon)^2 - m_e^2)^{1/2} \\ &\cdot \left( 1 - \frac{E_e V_j}{p_e^2} \right) \cdot (\varepsilon^2 - m^2(v_i)) \Bigg) \\ &\cdot \varepsilon \cdot \sqrt{\varepsilon^2 - m^2(v_i)} \cdot \Theta(\varepsilon - m(v_i)). \end{aligned} \quad (32)$$

For a typical electronic excitation  $V_j \approx 20$  eV and a typical kinetic energy of the electron  $E \approx 2$  keV the correction factor  $(1 - 3E_e V_j / p_e^2) = 0.985$  in (32) might have enough influence on the shape of the  $\beta$ -spectrum that it needs to be considered in future high precision cryobolometer experiments.

Secondly for a  $^{187}\text{Re}$  atom within a crystalline environment the so-called *beta-environmental fine structure* (BEFS) has to be taken into account (see Section 3.5), which leads to a modulation of the  $\beta$ -spectrum. Similarly to the extended X-ray absorption fine structure (EXAFS) this fine structure is caused by an interference of the outgoing wave of the  $\beta$ -electron with waves scattered on the neighboring atoms.

### 3. Past Direct Neutrino Mass Experiments

**3.1. Neutrino Mass Limit from Supernova SN1987a.** On February 23, 1987, neutrinos from the supernova SN1987a in the Large Magellanic Cloud (LMC) have been observed by the three neutrino detectors Kamiokande II [40], IMB [41], and at Baksan [42] (see Figure 6). This core-collapse supernova emitted a total energy of about  $3 \cdot 10^{53}$  erg =  $3 \cdot 10^{46}$  J, 99% of this energy was released by neutrinos [43]. These neutrinos traveled over a distance of about  $L = 50$  kpc (165,000 lyr). Although core collapse supernovae emit neutrinos and antineutrinos of all flavors at different phases of the collapse only electron antineutrinos from SN1987a have been detected via the famous inverse  $\beta$ -decay reaction on the proton  $\bar{\nu}_e + p \rightarrow n + e^+$ . Other neutrino reactions were suppressed by too high thresholds or too low cross-sections.

To calculate the time-of-flight, we first express the velocity  $\beta$  of a relativistic particle by its mass  $m$  and total energy  $E$  as

$$\begin{aligned} m^2 &= E^2 - p^2 = E^2 (1 - \beta^2) \\ &= E^2 (1 + \beta)(1 - \beta) \approx 2E^2 (1 - \beta) \\ \Rightarrow \beta &= 1 - \frac{m^2}{2E^2}. \end{aligned} \quad (33)$$

The delay of the arrival of a supernova neutrino at earth with regard to a particle at speed of light can be expressed as function of the neutrino mass  $m_\nu$  and its total energy  $E_\nu$  as

$$\begin{aligned} \Delta t &= \frac{L}{\beta_\nu} - \frac{L}{c} = \frac{L}{1 - (m_\nu^2 / 2E_\nu^2)} - L \\ &\approx L \cdot \left( 1 + \frac{m_\nu^2}{2E_\nu^2} \right) - L = L \cdot \frac{m_\nu^2}{2E_\nu^2}. \end{aligned} \quad (34)$$

Therefore we would expect the neutrino energy to follow hyperbolas for each neutrino mass state  $v_i$  as function of the square root of the neutrino arrival time. Of course this only holds, if the neutrino emission is sharp in time with respect to the spread of arrival times on earth. The energy versus time spectra of the three experiments which detected neutrinos from supernova SN1987a do not exhibit a dependence following equation (34) (see Figure 6). Therefore only upper limits of 5.7 eV (95% C.L.) [16] or of 5.8 eV (95% C.L.) [17] on the neutrino mass can be deduced which depend somewhat on the underlying supernova model.

Nowadays more and larger neutrino detectors are online and capable to measure neutrinos from a galactic or nearby core-collapse supernova. They are interconnected by the SuperNova Early Warning System SNEWS [44]. No core-collapse supernova from our galaxy or from a satellite galaxy

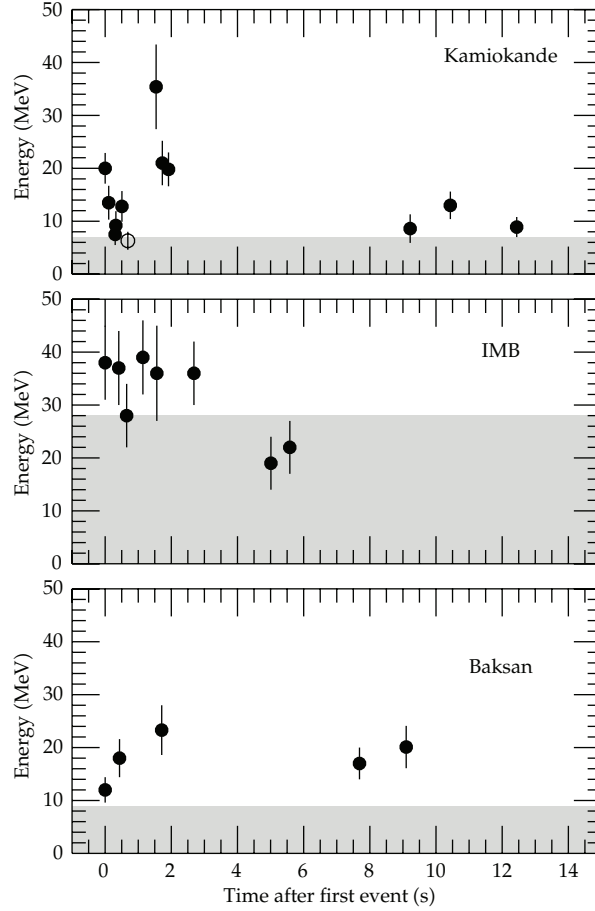


FIGURE 6: SN1987A neutrino observations at the neutrino detectors Kamiokande II [40], IMB [41], and at Baksan [42]. The energies refer to the secondary positrons from the reaction  $\bar{\nu}_e + p \rightarrow n + e^+$ . In the shaded area, the trigger efficiency is less than 30%. The clocks of the various experiments had unknown relative offsets. Therefore, for each detector spectrum, the time was calibrated such, that the first event was recorded at  $t = 0$ . In Kamiokande II, the event marked as an open circle is attributed to background (reprinted with permission from [43], Copyright 1999, Annual Reviews).

like the LMC has been observed since then. The expected rate for galactic core-collapse supernovae is 2-3 per century. Even if a new supernova will yield many more neutrino events than supernova SN1987a it would be difficult getting a much more precise limit on the neutrino mass. The limiting factors are the time and energy spectra of the neutrino emission of a core-collapse supernova, which are not known well enough. One possibility to bypass this problem exists for core-collapse supernovae, if the core-collapse supernova forms a black-hole. Then the neutrino emission will stop abruptly [45] and this stamp on the latest neutrino start time could be used in the analysis. A possible limit of the present neutrino detectors would be in the eV range. Whether new detectors with larger masses and possibly lower energy thresholds would allow a higher sensitivity on the neutrino mass still needs to be studied.

**3.2. Laboratory Direct Neutrino Mass Limits.** The majority of the published direct laboratory results on  $m(\nu_e)$  originate from the investigation of  $\beta$ -decays, which are sensitive to the average of the antineutrino mass states contributing to

the electron antineutrino. The mass of the neutrino could in principle be accessed by the investigation of  $\beta^+$  decays, but measuring electron capture decays is much more sensitive [46]. By the investigation of the electron capture of  $^{163}\text{Ho}$  two groups obtained upper limits on the average mass of the electron neutrino of  $m(\nu_e) < 225$  eV at 95% C.L. [47] and of  $m(\nu_e) < 490$  eV at 68% C.L. [48]. These experiments will be discussed in some detail in Section 5.3.

An exotic way of a direct neutrino mass measurement was using bound-state  $\beta^-$ -decay, where the outgoing  $\beta$ -electron is captured into a bound electronic state: totally ionized  $^{163}\text{Dy}^{66+}$  ions were circulating in a storage ring and undergoing bound-state  $\beta^-$ -decay although neutral  $^{163}\text{Dy}$  atoms are stable. The measurement of this bound state  $\beta^-$ -decay resulted in a limit on the neutrino mass of 410 eV at 68% C.L. [49].

Except  $^{187}\text{Re}$   $\beta$ -decay, on which the investigations have been started only within the last decade, all direct neutrino mass experiments using  $\beta^-$ -decays were done with the isotope tritium. In the long history of these tritium  $\beta$ -decay experiments, about a dozen results have been reported



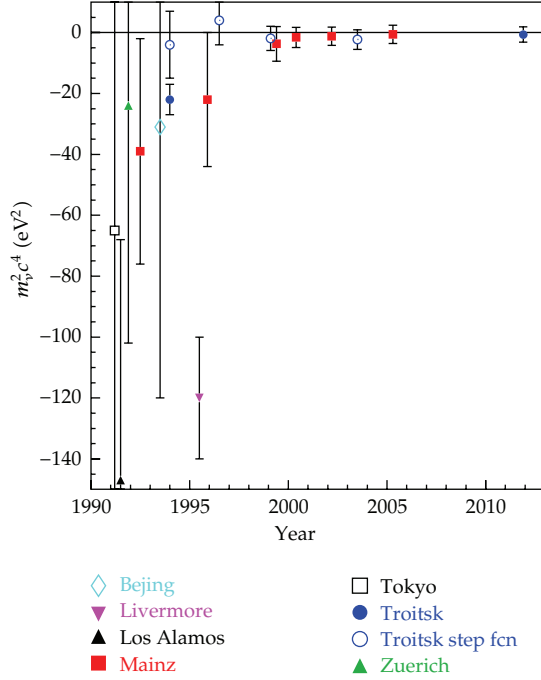


FIGURE 7: Results of previous tritium  $\beta$ -decay experiments on the observable  $m^2(\nu_e)$ . The experiments at Los Alamos, Zürich, Tokyo, Beijing, and Livermore [58–62] used magnetic spectrometers; the tritium experiments at Mainz and Troitsk [63–67] applied electrostatic spectrometers of the MAC-E-Filter type.

starting with the experiment of Curran in the late forties yielding  $m^2(\nu_e) < 1 \text{ keV}$  [50].

In the beginning of the eighties a group from the Institute of Theoretical and Experimental Physics (ITEP) at Moscow [51, 52] claimed the discovery of a nonzero neutrino mass of around 30 eV. The ITEP group used as  $\beta$ -source a thin film of tritiated valine combined with a new type of magnetic spectrometer, the *Tretyakov spectrometer* (a Tretyakov spectrometer uses a toroidal magnet field with a  $1/r$  dependent strength like it is used for magnetic horns of neutrino beam facilities at accelerators to focus the secondary pions behind the proton target). The first tests of the ITEP claim came from the experiments at the University of Zürich [53] and the Los Alamos National Laboratory (LANL) [54]. Both experiments applied similar Tretyakov-type spectrometers, but more advanced tritium sources with respect to the ITEP group. The Zürich experiment used a solid source of tritium implanted into carbon and later a self-assembling film of tritiated hydrocarbon chains. The LANL group was the first to develop a gaseous molecular tritium source avoiding solid state corrections. Both experiments disproved the ITEP result. The reason for the *mass signal* at ITEP was twofold: the energy loss correction was probably overestimated, and a  $^3\text{He-T}$  mass difference measurement [55] confirming the endpoint energy of the ITEP result, turned out only later to be significantly wrong [56, 57].

Also in the nineties tritium  $\beta$ -decay experiments yielded controversially discussed results: Figure 7 shows the final results of the experiments at LANL and Zürich together

with the results from other more recent measurements with magnetic spectrometers at University of Tokyo, Lawrence Livermore National Laboratory, and Beijing. The sensitivity on the neutrino mass had improved a lot but the values for the observable  $m^2(\nu_e)$  populated the nonphysical negative  $m^2(\nu_e)$  region. In 1991 and 1994 two new experiments started data taking at Mainz and at Troitsk, which used a new type of electrostatic spectrometer, so-called MAC-E-Filters, which were superior in energy resolution and luminosity with respect to the previous magnetic spectrometers. However, even their early data were confirming the large negative  $m^2(\nu_e)$  values of the LANL and Livermore experiments when being analyzed over the last 500 eV of the  $\beta$ -spectrum below the endpoint  $E_0$ . But the large negative values of  $m^2(\nu_e)$  disappeared when analyzing only small intervals below the endpoint  $E_0$ . This effect, which could only be investigated by the high luminosity MAC-E-Filters, pointed towards an underestimated or missing energy loss process, seemingly to be present in all experiments. The only common feature of the various experiments seemed to be the calculations of the electronic excitation energies and excitation probabilities of the daughter ions. Different theory groups checked these calculations in detail. The expansion was calculated to one order further and new interesting insight into this problem was obtained, but no significant changes were found [34, 36].

Then the Mainz group found the origin of the missing energy loss process for its experiment. The Mainz experiment used as tritium source a film of molecular tritium quench-condensed onto aluminum or graphite substrates. Although the film was prepared as a homogenous thin film with flat surface, detailed studies showed [68] that the film was not stable: it underwent a temperature-activated roughening transition into an inhomogeneous film by forming microcrystals. Thus, unexpected large inelastic scattering probabilities were obtained, which were not taken into account in previous analyses. This extra energy losses were only significant when analyzing larger energy intervals below the endpoint.

The Troitsk experiment on the other hand used a windowless gaseous molecular tritium source, similar to the LANL apparatus. Here, the influence of large-angle scattering of electrons magnetically trapped in the tritium source was not considered in the first analysis. After correcting for this effect the negative values for  $m^2(\nu_e)$  disappeared.

The fact that more experimental results of the early nineties populate the region of negative  $m^2(\nu_e)$  values (see Figure 7) can be understood by the following consideration [18]. For  $\varepsilon \gg m(\nu_e)$ , (19) can be expanded into

$$\frac{dN}{dE} \propto \varepsilon^2 - \frac{m^2(\nu_e)}{2}. \quad (35)$$

On the other hand the convolution of a  $\beta$ -spectrum (18) at  $m^2(\nu_e) = 0$  with a Gaussian of width  $\sigma$  leads to

$$\frac{dN}{dE} \propto \varepsilon^2 + \sigma^2. \quad (36)$$

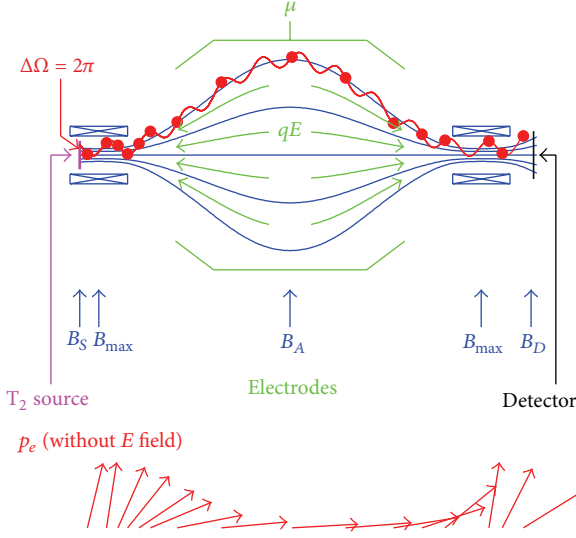


FIGURE 8: Principle of the MAC-E-Filter. Top: experimental setup, bottom: momentum transformation due to adiabatic invariance of the orbital magnetic momentum  $\mu$  in the inhomogeneous magnetic field.

Therefore, in the presence of a missed experimental broadening with Gaussian width  $\sigma$  one expects a shift of the result on  $m^2(\nu_e)$  of

$$\Delta m^2(\nu_e) \approx -2 \cdot \sigma^2, \quad (37)$$

which gives rise to a negative value of  $m^2(\nu_e)$  [18].

**3.2.1. MAC-E-Filter.** The significant improvement in the neutrino mass sensitivity by the Troitsk and the Mainz experiments are due to MAC-E-Filters (Magnetic Adiabatic Collimation with an Electrostatic Filter). This new type of spectrometer—based on early work by Kruit and Read [69]—was developed for the application to the tritium  $\beta$ -decay at Mainz and Troitsk independently [70, 71]. The MAC-E-Filter combines high luminosity at low background and a high energy resolution, which are essential features to measure the neutrino mass from the endpoint region of a  $\beta$ -decay spectrum.

The main features of the MAC-E-Filter are illustrated in Figure 8: two superconducting solenoids are producing a magnetic guiding field. The  $\beta$ -electrons, starting from the tritium source in the left solenoid into the forward hemisphere, are guided magnetically on a cyclotron motion along the magnetic field lines into the spectrometer yielding an accepted solid angle of nearly  $2\pi$ . On the way of an electron into the center of the spectrometer the magnetic field  $B$  decreases smoothly by several orders of magnitude keeping the magnetic orbital moment of the electron  $\mu$  invariant (equation given in nonrelativistic approximation)

$$\mu = \frac{E_{\perp}}{B} = \text{const.} \quad (38)$$

Therefore nearly all cyclotron energy  $E_{\perp}$  is transformed into longitudinal motion (see Figure 8 bottom) giving rise to a

broad beam of electrons flying almost parallel to the magnetic field lines. This is just the opposite of the so-called *magnetic mirror* or *magnetic bottle* effect.

This parallel beam of electrons is energetically analyzed by applying an electrostatic barrier created by a system of one or more cylindrical electrodes. The relative sharpness of this energy high-pass filter is only given by the ratio of the minimum magnetic field  $B_{\min}$  reached at the electrostatic barrier in the so-called analyzing plane and the maximum magnetic field between  $\beta$ -electron source and spectrometer  $B_{\max}$

$$\frac{\Delta E}{E} = \frac{B_{\min}}{B_{\max}}. \quad (39)$$

It is beneficial to place the electron source in a magnetic field  $B_S$  somewhat lower than the maximum magnetic field  $B_{\max}$ . Thus the *magnetic mirror* effect based on the adiabatic invariant (38) hinders electrons with large starting angles at the source and long paths inside the source to enter the MAC-E-Filter. Only electrons are able to pass the pinch field  $B_{\max}$  which exhibit starting angles  $\theta_S$  at  $B_S$  of

$$\sin^2(\theta_S) \leq \frac{B_S}{B_{\max}}. \quad (40)$$

In principle, the pinch magnet could also be installed between the MAC-E-Filter and the detector, which counts the electrons transmitted by the MAC-E-Filter, as long as the electron transport is always adiabatically. Such an arrangement has been realized at the KATRIN experiment.

The exact shape of the transmission function can be calculated analytically. For an isotropically emitting monoenergetic source of particles with kinetic energy  $E$  and charge  $q$  it reads as function of the retarding potential  $U$  as

$$T(E, U) = \begin{cases} 0 & \text{for } E \leq qU, \\ 1 - \sqrt{1 - \frac{E - qU}{E} \cdot \frac{B_S}{B_{\min}}} & \text{for } qU < E < qU + \Delta E, \\ 1 - \sqrt{1 - \frac{B_S}{B_{\max}}} & \text{for } E \geq qU + \Delta E. \end{cases} \quad (41)$$

Figure 9 shows the transmission function of a MAC-E-Filter at the example of the KATRIN experiment at its default settings (see Section 4.4).

The  $\beta$ -electrons are spiralling around the guiding magnetic field lines in zeroth approximation. Additionally, in non-homogeneous electrical and magnetic fields they feel a small drift  $u$ , which reads in first order [70]:

$$\vec{u} = \left( \frac{\vec{E} \times \vec{B}}{B^2} - \frac{(E_{\perp} + 2E_{\parallel})}{e \cdot B^3} (\vec{B} \times \nabla_{\perp} \vec{B}) \right). \quad (42)$$

The clear advantages of the MAC-E-Filter of large angular acceptance and high energy resolution come together with the danger to store charged particles in Penning, magnetic

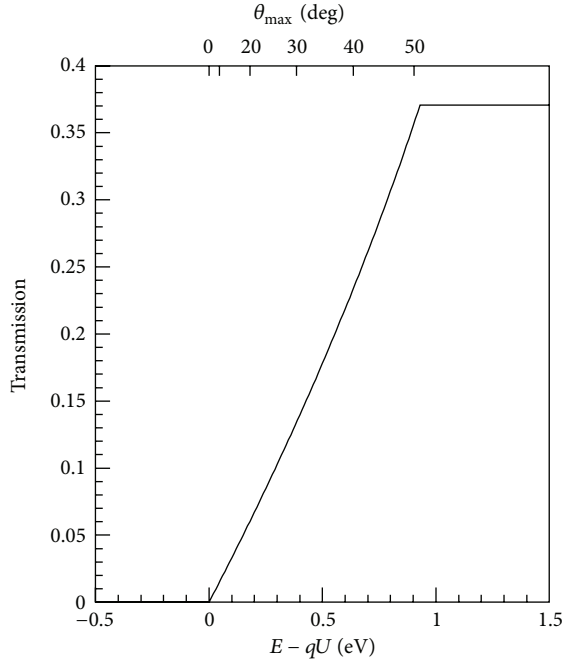


FIGURE 9: Transmission function of the KATRIN experiment as a function of the surplus energy  $E - qU$  according to (41). The KATRIN default design settings [72] were used as follows:  $B_{\min} = 3 \cdot 10^{-4}$  T,  $B_{\max} = 6$  T,  $B_s = 3.6$  T. The upper horizontal axis illustrates the dependence of the maximum starting angle  $\theta_{s,\max}$ , which is transmitted at a given surplus energy. Clearly, electrons with larger starting angles  $\theta_s \leq \theta_{s,\max}$  reach the transmission condition later, since they still have a significant amount of cyclotron energy in the analyzing plane at  $B_{\min}$ .

mirror and combined traps [73]. This problem and countermeasures will be discussed later at the example of the KATRIN experiment (see Sections 4.4 and 4.5).

A very interesting application is using the MAC-E-Filter in time-of-flight mode. This mode has the advantage to be nonintegrating but requests to measure to or restrict the start time of the electron under investigation. The analysis can be done on cutting on the time-of-flight [74] or fully making use of the individual measured time-of-flights [75].

The two tritium  $\beta$ -decay experiments at Mainz and at Troitsk used similar MAC-E-Filters with an energy resolution of 4.8 eV (3.5 eV) at Mainz (Troitsk). The spectrometers differed slightly in size: the diameter and length of the Mainz (Troitsk) spectrometer are 1 m (1.5 m) and 4 m (7 m). The major differences between the two setups are the tritium sources: The Mainz Neutrino Mass Experiment used a novel condensed solid tritium source, whereas the experiment at Troitsk applied a windowless gaseous molecular tritium source similar to the ones of the experiments at Los Alamos and at Livermore before.

**3.2.2. The Mainz Neutrino Mass Experiment.** The tritium source was a thin film of molecular tritium, which was quench-condensed on a cold graphite substrate. By laser ellipsometry the film thickness was determined. Typically

film thicknesses of 20 to 40 monolayers were applied before and of 150 monolayers after the upgrade of the experiment in 1995–1997. The retarding potential of the MAC-E-Filter was created by a complex system of cylindrical electrodes. The upgrade of the Mainz setup in 1995–1997 ( $\rightarrow$  Mainz phase II, see Figure 10) includes the installation of a new tilted pair of superconducting solenoids between the tritium source and the spectrometer and the use of a new cryostat to keep the temperature of the tritium film below 2 K. The first measure eliminated source-correlated background and allowed the source strength to be increased significantly. From this upgrade on, the Mainz experiment ran with a similar signal and similar background rate as the Troitsk experiment. The second measure avoided the roughening transition of the homogeneously condensed tritium films with time [68], which before had given rise to negative values of  $m^2(\nu_e)$  when the data analysis used large intervals of the  $\beta$ -spectrum below the endpoint  $E_0$  [26]. The upgrade was completed by the application of HF pulses on one of the electrodes in between measurements every 20 s, and a full automation of the apparatus and remote control. The former improvement lowered and stabilized the background, the latter one allowed long-term measurements.

Figure 11 shows the endpoint region of the Mainz phase II data (from 1998, 1999, and 2001) in comparison with the former Mainz 1994 data. An improvement of the signal-to-background ratio by a factor 10 by the upgrade as well as a significant enhancement of the statistical quality of the data by long-term measurements are clearly visible. The main systematic uncertainties of the Mainz experiment are the inelastic scattering of  $\beta$ -electrons within the tritium film, the excitation of neighbour molecules due to sudden change of the nuclear charge during  $\beta$ -decay, and the self-charging of the tritium film as a consequence of its radioactivity. As a result of detailed investigations in Mainz [64, 76–78]—mostly by dedicated experiments—the systematic corrections became much better understood and their uncertainties were reduced significantly. The high-statistics Mainz phase II data from 1998–2001 allowed the first determination of the probability of the neighbour excitation to occur in  $(5.0 \pm 1.6 \pm 2.2)\%$  of all  $\beta$ -decays [64] in good agreement with the theoretical expectation [79].

The analysis of the last 70 eV below the endpoint of the phase II data resulted in [64]

$$m^2(\nu_e) = (-0.6 \pm 2.2 \pm 2.1) \text{ eV}^2, \quad (43)$$

which—using the Feldman-Cousin method [80]—corresponds to an upper limit of

$$m(\nu_e) < 2.3 \text{ eV} \quad (95\% \text{ C.L.}). \quad (44)$$

An analysis of the Mainz phase II data with respect to setting a limit on the contribution of a light sterile neutrino is underway [81].

**3.3. The Troitsk Neutrino Mass Experiment.** The windowless gaseous tritium source of the Troitsk experiment [66] is essentially a tube of 5 cm diameter filled with  $T_2$  resulting

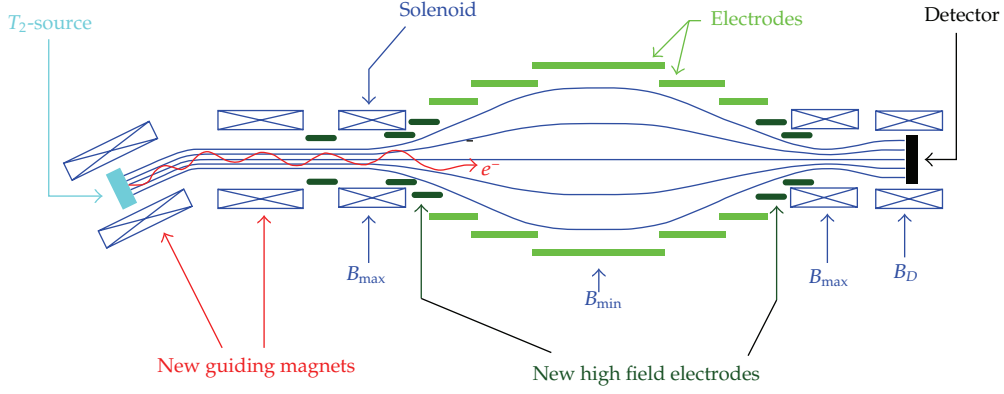


FIGURE 10: The upgraded Mainz setup shown schematically. The outer diameter amounts to 1 m, the distance from source to detector is 6 m.

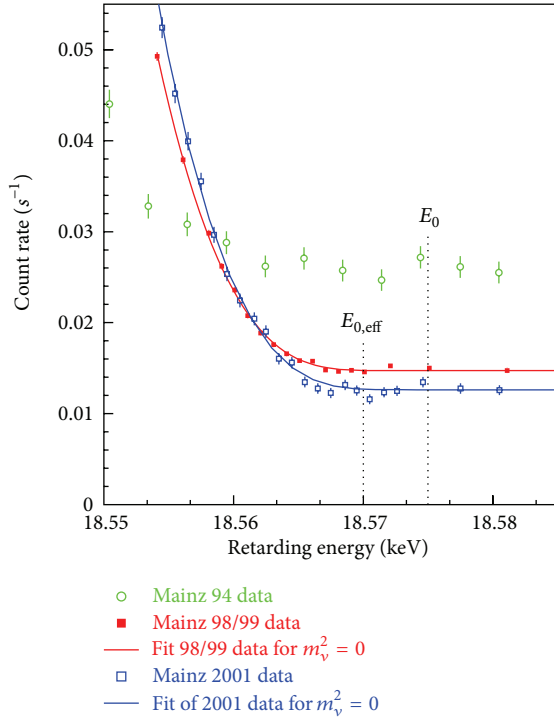


FIGURE 11: Averaged count rate of the Mainz 1998/1999 data (filled red squares) with fit for  $m(\nu_e) = 0$  (red line) and of the 2001 data (open blue squares) with fit for  $m(\nu_e) = 0$  (blue line) in comparison with previous Mainz data from 1994 (open green circles) as a function of the retarding energy near the endpoint  $E_0$  and effective endpoint  $E_{0,\text{eff}}$  (taking into account the width of the response function of the setup and the mean rotation-vibration excitation energy of the electronic ground state of the  $(^3\text{HeT})^+$  daughter molecule).

in a column density of  $10^{17}$  molecules/cm<sup>2</sup>. The source is connected to the ultrahigh vacuum of the MAC-E-Filter type spectrometer by a series of differential pumping stations (see Figure 12).

From their first measurement in 1994 the Troitsk group had reported for more than a decade the observation of a

small, but significant anomaly in its experimental spectra starting a few eV below the  $\beta$ -endpoint  $E_0$ . This anomaly appeared as a sharp step of the count rate [65]. Because of the integrating property of the MAC-E-Filter, this step should correspond to a narrow line in the primary spectrum with a relative intensity of about  $10^{-10}$  of the total decay rate. In 1998, the Troitsk group claimed that the position of this line was oscillating with a frequency of 0.5 years between 5 eV and 15 eV below  $E_0$  [66]. By 2000 the anomaly no longer followed the 0.5 year periodicity, but still existed in most data sets. The reason for such an anomaly with these features was not clear but gave rise to many speculations. In presence of this problem, the Troitsk experiment corrected for this anomaly by fitting an additional line to the  $\beta$ -spectrum run-by-run.

In 2011 the Troitsk group repeated the analysis of their data [67]. Special care was taken for calculating the time-dependent column density of the windowless tritium source and applying these values to the analysis. Secondly the data were very carefully selected with regard to data quality and stability of the experiment. Thus a time and intensity varying anomaly was not any more needed to describe the Troitsk  $\beta$ -spectra. Combining all the selected Troitsk data from 1994 to 2004 gave [67]

$$m^2(\nu_e) = (-0.67 \pm 1.89 \pm 1.68) \text{ eV}^2 \quad (45)$$

from which using the Feldman-Cousin method [80] an upper limit can be deduced

$$m(\nu_e) < 2.05 \text{ eV} \quad (95\% \text{ C.L.}). \quad (46)$$

**3.4. Cryobolometers.** Due to the complicated electronic structure of  $^{187}\text{Re}$  and its  $\beta$ -decay (compare to Section 2) the advantage of the 7 times lower endpoint energy  $E_0$  of  $^{187}\text{Re}$  with respect to tritium can only be exploited if the  $\beta$ -spectrometer measures the entire released energy, except that of the neutrino. This situation requires a  $\beta$ -spectrometer, which at the same time contains the  $\beta$ -electron emitting  $^{187}\text{Re}$ . The advantage of this approach is that many systematic uncertainties—like the electronic final state spectrum, energy losses by inelastic scattering, and so forth—drop out in first order, since all released energy except that of the neutrino



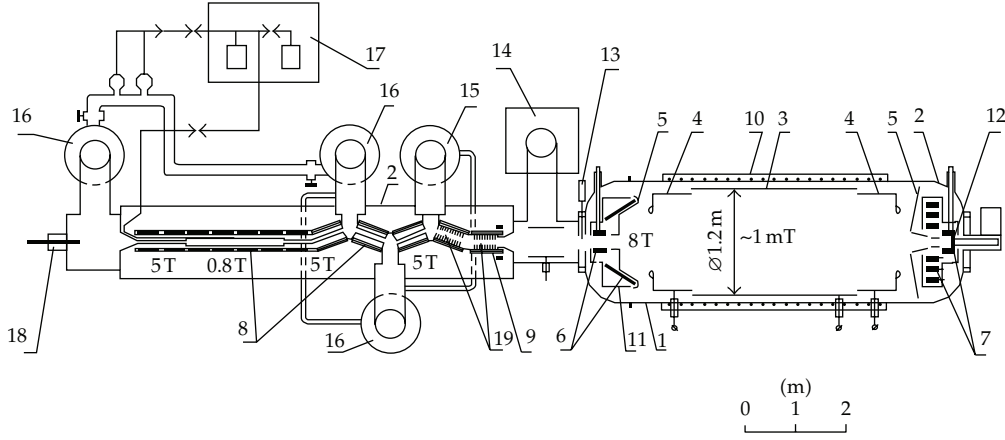


FIGURE 12: The Troitsk Neutrino Mass Experiment: vacuum vessel of MAC-E-Filter (1) and of windowless gaseous tritium source (2), retarding electrodes (3, 4), ground electrode (5), superconducting solenoids (6–9), warm solenoid (10),  $\text{LN}_2$  shield (11), Si(Li) detector (12), emergency valve (13), magnetodischarge pump (14), mercury diffusion pumps (15–16) tritium purification system (17), electron gun (18), and argon trap (19). (Reprinted with permission from [67], Copyright (2011) by the American Physical Society).

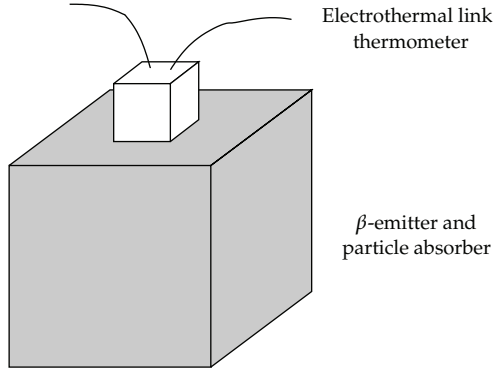


FIGURE 13: Principle scheme of a cryobolometer for direct neutrino mass measurements consisting of a  $\beta$ -emitting crystal, which serves at the same time as the particle and energy absorber. The electric read-out wires of the thermometer link the whole bolometer to a thermal bath.

is measured in the same way and summed up automatically (we assume that all deexcitation processes are faster than the integration time of a detector signal).

To reach the required energy resolution such a *source = detector* arrangement can be ideally realized by a cryobolometer (see Figure 13) [23]. The energy release  $\Delta W$  by the  $\beta$ -decay results in a temperature rise  $\Delta T$  of the crystal. This temperature increase can be measured by the thermometer, if  $\Delta T$  is large enough. The temperature rise  $\Delta T$  depends on the energy release  $\Delta W$  and on the heat capacity  $C$

$$\Delta T = \frac{\Delta W}{C}. \quad (47)$$

In order to obtain a large temperature increase  $\Delta T$  in the presence of a very small energy release  $\Delta W$  (it should be noted, that the sensitivity on the neutrino mass requires a very low endpoint energy  $E_0$ ), the heat capacity  $C$  has to be

extremely small. The first measure is using tiny cryobolometers of typical masses of  $\mathcal{O}(1)$  mg. Secondly, the temperature of the cryobolometer has to be as low as possible. The Debye model states that the phonon part of the heat capacitance of a crystal consisting of  $N$  atoms scales with the third power on temperature in units of the Debye temperature  $\Theta_D$

$$C = \frac{12\pi^4}{5} \cdot N \cdot k_B \cdot \left( \frac{T}{\Theta_D} \right)^3. \quad (48)$$

There is a second reason why the crystals should be small: The cryobolometer is not an integral spectrometer like the MAC-E-Filter but measures always the entire spectrum. Therefore pileup of two random events may pollute the endpoint region of a  $\beta$ -decay on which the neutrino mass is imprinted. The pileup rate of a detector of random rate  $\dot{N}_{\text{tot}}$  requiring a minimal time interval to distinguish two events of  $\delta t$  amounts to  $\dot{N}_{\text{tot}}^2 \delta t$ . With a half-life  $4.3 \cdot 10^{10}$  y and a natural abundance of 62.6% the specific activity of pure rhenium amounts to about  $1 \text{ Bq mg}^{-1}$ . The rise time  $\delta t$  typically scales with the mass of the cryobolometers. Rise times of cryobolometers with temperature read-out of  $\mathcal{O}(1)$  mg mass are typically in the  $\mathcal{O}(100) \mu\text{s}$  range (new cryobolometer approaches like Metallic Magnetic Calorimeters (MMC) as discussed in Section 5.4 could be much faster). Therefore cryobolometer detectors with mg masses are required to suppress pileup by 4 or more orders of magnitude. This has to be compared to the fraction of the  $\beta$ -spectrum which contains the information on the neutrino mass. Even for the lowest known endpoint energy of  $^{187}\text{Re}$  with  $E_0 = 2.47 \text{ keV}$ , the relative fraction of  $^{187}\text{Re}$   $\beta$ -decay events in the last eV below  $E_0$  is of order  $10^{-11}$  only (compare to Figure 3). Therefore arrays of many bolometers are required to reach a high sensitivity on the neutrino mass.

Another technical challenge is the energy resolution of the cryobolometers. Although cryogenic bolometers with an energy resolution of a few eV have been produced with other

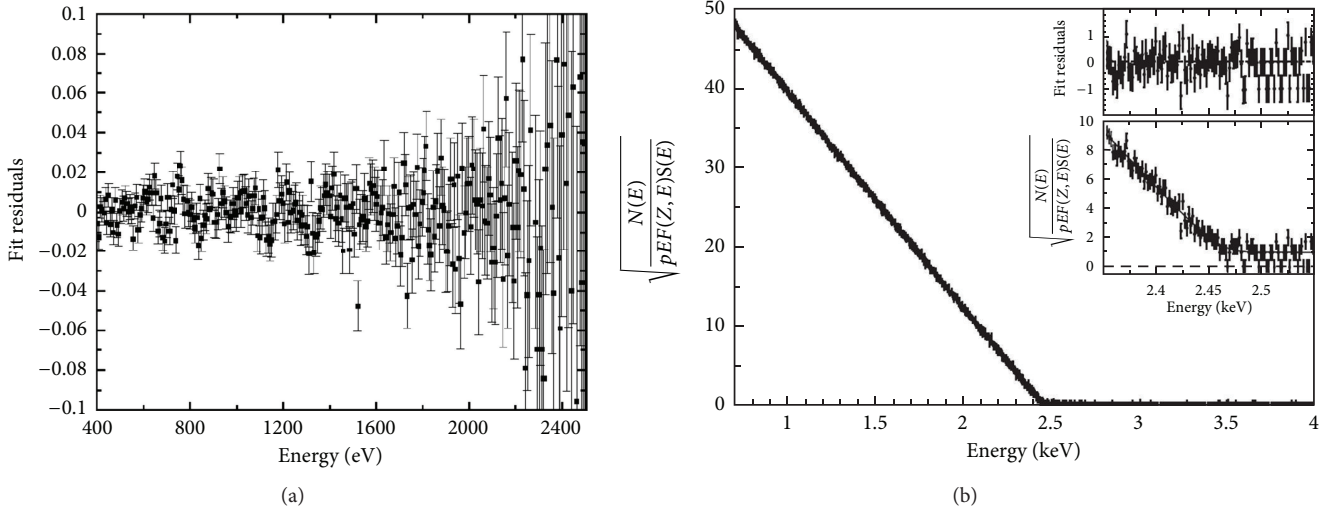


FIGURE 14: (a): The residuals of the theoretically expected  $^{187}\text{Re}$   $\beta$ -spectrum that has been fitted to the data collected by the MANU experiment exhibit effects of a  $\beta$ -environmental fine structure (BEFS) modulation most clearly visible at low electron energies (Reprinted with permission from [82], Copyright (2000) by the American Physical Society). (b): Kurie plot of the experimental  $^{187}\text{Re}$   $\beta$ -spectrum obtained by the MiBeta collaboration (reprinted with permission from [83], Copyright (2006) by the American Physical Society).

absorbers, this resolution has not yet been achieved with rhenium.

**3.5.  $^{187}\text{Re}$   $\beta$ -Decay Experiments.** Two groups have started the field of  $^{187}\text{Re}$   $\beta$ -decay experiments at Milan (MiBeta) and Genoa (MANU): The MANU experiment used a single metallic rhenium crystal of about 1.6 mg as absorber read out by a neutron transmutation doped (NTD) germanium thermistor [82]. Sensor and absorber were connected using epoxy glue and were suspended by aluminum wires used for readout of the device. These lines also provided the thermal link to a heat bath cooled down to temperatures below 100 mK using a  $^3\text{He}$ - $^4\text{He}$  dilution refrigerator. At a detector threshold of 350 eV, an event rate of about 1.1 counts per second was observed with this absorber. The rise time of this early detector was of the order of 1 ms with a decay time of the signals of several tens of ms. This clearly limits the amount of activity allowed per absorber crystal, in order to avoid pileup problems. The energy resolution of the detector was determined to be 96 eV FWHM. While the main objective of the initial measurement was a determination of the endpoint energy and the half life of  $^{187}\text{Re}$   $\beta$ -decay, an interesting side effect was the first observation of the so-called  $\beta$ -environmental fine structure (BEFS) in pure rhenium [82]. This fine structure is caused by an interference of the outgoing direct wave of the beta-electron with incoming waves reflected by the neighboring atoms and leads to a modulation of the shape of the  $\beta$ -spectrum that is most pronounced at low electron energies. (see Figure 14(a)). This effect is of concern to future calorimetric neutrino mass experiments, as it produces difficulties to calculate distortions of the  $^{187}\text{Re}$   $\beta$ -spectrum which will become important for experiments aiming at a sensitivities in the sub-eV region [83]. The effect was later also observed in the MiBeta experiment [84], albeit with a different characteristic due to the use of a different

absorber material. In the subsequent analysis the data taken by MANU set an upper limit on the neutrino mass of  $m(\nu_e) < 26 \text{ eV}/c^2$  at 95% CL [85].

The second pioneering  $^{187}\text{Re}$   $\beta$ -decay experiment was set up by the MiBeta collaboration who were working with  $\text{AgReO}_4$  absorbers with a mass of about 0.25–0.30 mg each, read out by silicon implanted thermistors. The group was the first to work with an array of detectors to circumvent the problem of the low maximum activity allowed for the individual crystals. Their setup contained 10 detectors with an average energy resolution of 28.5 eV FWHM [84]. The rise times of the detector signals were of the order 0.5 ms. Figure 14(b) shows a Kurie plot of the accumulated spectrum obtained during one year of data taking. The analysis of the spectrum near the endpoint resulted in an upper limit on the electron neutrino mass of  $m(\nu_e) < 15 \text{ eV}$  at 90% CL.

#### 4. The KATRIN Experiment

The Karlsruhe Tritium Neutrino (KATRIN) experiment is a next-generation direct neutrino mass experiment which is currently under construction by a large international collaboration with groups from Lawrence Berkeley National Laboratory (LBNL), Bonn University, Fulda University of Applied Sciences, Max-Planck-Institute for Nuclear Physics Heidelberg (MPIK), Karlsruhe Institute of Technology (KIT), Mainz University, Massachusetts Institute of Technology (MIT), Münster University, University of North Carolina at Chapel Hill, Academy of Sciences of the Czech Republic, University of Santa Barbara, University of Washington (UW) Seattle, Swansea University and Institute for Nuclear Research (INR) Troitsk, with associated groups from Aarhus University, University College London (UCL), and Federal University of Paraná. The experiment is housed at Tritium Laboratory Karlsruhe (TLK) at KIT's Campus North site. KATRIN has

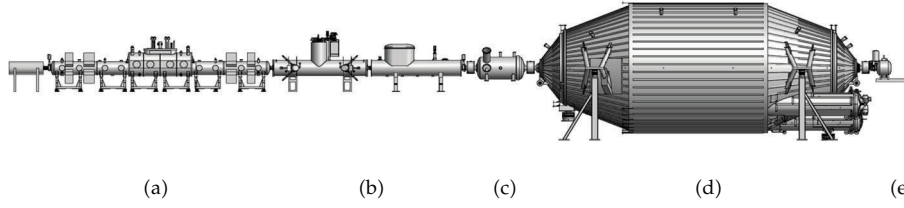


FIGURE 15: Schematic view of the complete 70 m long KATRIN setup. (a) Windowless Gaseous Tritium Source (WGTS). (b) Transport section consisting of a differential (DPS2-F) and a cryogenic (CPS) pumping section. (c) Prespectrometer: prefilter of  $\beta$ -spectrum. (d) Main spectrometer: energy analysis of  $\beta$ -electrons. (e) Detector: position-sensitive detection of transmitted electrons [72].

been designed to substantially increase the sensitivity of the Mainz and Troitsk forerunners, while employing the same general spectroscopic principles. It will push the MAC-E-filter technology and tritium process technology, as well as many other methods, to their technological limits to press forward into the sub-eV sensitivity regime of the averaged electron (anti)neutrino mass  $m(\nu_e)$ .

**4.1. Introduction.** KATRIN has been designed to improve the  $m(\nu_e)$  sensitivity by a factor of 10 from the present value of 2 eV to 200 meV at 90% C.L. This increase in sensitivity by one order of magnitude will allow covering almost the entire region of quasi-degenerate neutrino masses (nuclear and particle physics motivation) and to directly probe the neutrino hot dark matter fraction in the universe down to a contribution  $\Omega_{\text{HDM}} \approx 0.01$  of the total matter-energy budget of the universe (cosmological motivation) [86]. As the experimental observable in  $\beta$ -decay is the *square* of the averaged electron (anti)neutrino mass  $m^2(\nu_e)$ , this requires an improvement of the experimental precision in  $\beta$ -spectroscopy by two orders of magnitude as compared to Mainz and Troitsk. This in turn requires significant, major improvements to key experimental parameters such as source activity, energy resolution, and background rate. In addition, it requires a much better control of systematic effects (by one order of magnitude). The systematic effects mainly arise from parameters related to the tritium source such as fluctuations of the source temperature or the injection pressure or source composition (such as different hydrogen isotopologues or ions), but other systematics such as fluctuations of the retarding potential have to be limited to very small values as well.

Extensive design work by the KATRIN Collaboration reported in [72] has revealed that the key statistical parameters to reach a neutrino mass sensitivity of 200 meV are an increase of the source strength by a factor of 100 and of the measurement time by a factor of 10. The required energy resolution  $\Delta E$  is less critical, as the information on the neutrino mass is derived from an energy interval which typically extends to about 30 eV below the endpoint, so that an improvement by about a factor of four to a value of  $\Delta E = 0.93$  eV at KATRIN is sufficient. On the other hand, the background rate close to the endpoint has to be limited to a very low value of  $<10^{-2}$  cps (counts per second) to achieve the design sensitivity. This is identical to the background value obtained at the Mainz and Troitsk experiments, so that novel

background reduction mechanisms have to be developed for the much larger KATRIN spectrometer section.

The 70 m long KATRIN setup has been designed along these general criteria (see Figure 15). The experimental configuration can be grouped into the following major components: (a) the Windowless Gaseous Tritium Source (WGTS), where  $10^{11}$  electrons are produced per second by the  $\beta$ -decay of molecular high-purity tritium gas at a temperature of 30 K, (b) an electron transport and tritium elimination section, comprising an active differential pumping (DPS) followed by a passive cryo-pumping section (CPS), where the tritium flow is reduced by more than 14 orders of magnitude (c) the electrostatic prespectrometer of MAC-E-Filter type, which offers the option to prefilter the low-energy part of the tritium  $\beta$ -decay spectrum, (d) the large electrostatic main spectrometer of MAC-E-Filter type which represents the precision energy filter for electrons and which is, with its dimensions of 10 m diameter and 24 m length, the largest UHV recipient in the world (not shown here are its inner electrode system and its outer air coil system) and (e) a segmented Si-PIN diode array to count the transmitted electrons. The experiment is completed by a rear section which allows to control and monitor key source-related parameters as well as the monitor spectrometer for redundant monitoring of the retarding potential. Finally, there are extensive infrastructure facilities.

The unique properties of the gaseous molecular tritium source (high activity and stability) and of the large main spectrometer (ppm precision of the retarding high voltage) allow KATRIN to extend its physics reach from its main goal of measuring the neutrino mass in the sub-eV range to look for contributions by possible sterile neutrinos from the sub-eV up to the multi-keV range. The sensitivity of KATRIN for (sub-)eV sterile neutrinos, as suggested by [87–90] is expected to be very high [91–93]. Interestingly, a high precision search of Warm Dark Matter in form of keV sterile neutrinos looks very attractive, as a heavy sterile neutrino would manifest itself as a tiny kink and subsequent spectral distortion deep in the  $\beta$ -spectrum further away from the endpoint. Finally, KATRIN will allow performing stringent tests of other physics issues beyond the Standard Model such as large extra dimensions [94], right handed currents [33] and Lorentz violation [95].

**4.2. KASSIOPEIA: A Full Monte Carlo Simulation Software for KATRIN.** The main principles of the MAC-E filter and its

application in the KATRIN experiment can be understood analytically via the adiabatic approximation. However, in order to understand the behavior of electrons not only in perfect vacuum and beyond the assumption of adiabatic motion, a precise and fast computational tool is required. Over the past years the KATRIN Collaboration has developed the universal code package KASSIOPEIA [96], which is based on the ground-laying work described in [97, 98]. The software package includes various particle generators for signal electrons as well as background processes.

KASSIOPEIA comprises a number of modules for the creation of particles, the calculation of their subsequent trajectories in electromagnetic fields, and the detection of particles in Si-based detectors. To do so, KASSIOPEIA provides a detailed WGTS model, a number of electric and magnetic field calculation methods and different methods for the calculation of particle trajectories. The particle detection module includes backscattering of electrons on the detector surface and a comprehensive number of physical phenomena of low-energy electrons in silicon [99].

At KATRIN very large dimensions of the order of tens of meters (main spectrometer) concur with very small dimensions of the order of  $\mu\text{m}$  (e.g., wire electrode). This fact constitutes the biggest challenge for the electromagnetic field calculation, that cannot be handled adequately by commercial programs. A fast and precise field calculation is achieved by a variety of field calculation methods, ranging from very fast axisymmetric field calculations [97, 98], to fully three-dimensional field calculation methods [100] based on the boundary element methods which is most suitable for large dimensional differences.

The particle trajectory calculations are based on explicit Runge-Kutta methods described in [101–103] and include physical processes like synchrotron radiation and elastic, electronic excitation and ionization collisions of electrons with molecular hydrogen [104–106].

The detailed tritium source model allows to simulate the actual neutrino mass measurement with high precision. The source model includes, among other things, the final state distribution of tritium [35, 36], the Doppler broadening, and scattering in the source [107, 108].

KASSIOPEIA was successfully used to study background processes [109] and transmission properties of the spectrometer [110], to optimize the electromagnetic design of the spectrometer section and to study systematic effects related to the source section of KATRIN [108].

**4.3. Source and Transport Section.** The tritium source-related parts of KATRIN comprise the Windowless Gaseous Tritium Source (WGTS), the Differential (DPS) and Cryogenic (CPS) Pumping Sections, as well as the Calibration and Monitoring System (CMS) at the rear end. The main tasks of these elements are to (a) control and monitor the tritium column density in the source tube to a precision of better than  $10^{-3}$  and (b) reduce the tritium partial pressure from the source inlet to the entrance into the spectrometers by more than 14 orders of magnitude, while at the same time transporting the  $\beta$ -decay electrons adiabatically towards the spectrometers.

The extensive tritium infrastructure required for the continuous operation of the KATRIN tritium source is provided by Tritium Laboratory Karlsruhe (TLK), which has developed key technologies for experiments involving large amounts of tritium since the early 1990s. As of today, TLK has an amount 24 g of tritium on-site and holds a license for up to 40 g. Tritium process technology at TLK is based on closed tritium cycles with their central elements of tritium storage, isotope recovery and separation, and tritium retention, among others. The yearly throughput of 10 kg of high purity tritium in the KATRIN source will be equivalent to the ITER operation in the late 2020s [111]. The KATRIN tritium cycle is subdivided into two closed loops, with an Inner Loop being optimized for a highly stabilized injection pressure into the WGTS, and an Outer Loop designed to maintain a high tritium purity by withdrawing a small tritium fraction ( $<1\%$ ) for clean-up and isotope separation (the amount withdrawn is reinjected to the Inner Loop after purification).

**4.3.1. Gas Dynamics of the WGTS.** The geometry of the tritium source of KATRIN is defined by a cylindrical stainless steel beam tube of 90 mm diameter and 10 m length, which is housed inside the WGTS cryostat. At the center of the beam tube, high purity molecular tritium gas is injected via capillaries with an inlet pressure of about  $10^{-3}$  mbar. At both ends of the beam tube the injected flow is pumped out by large turbomolecular pumps (TMP). The isotopic composition of the injected hydrogen isotopologues ( $\text{T}_2$ , D,  $\text{H}_2$ , HT, DT, HD), with  $\text{T}_2$  dominating by a large factor, is constantly being monitored by Laser Raman spectroscopy. In this windowless geometry the systematic effects for electrons close to the 18.6 keV end point of tritium  $\beta$ -decay are minimized, allowing to adiabatically transport electrons out of the source by a homogeneous magnetic field of  $B = 3.6$  T. This field is provided by a system of three large superconducting solenoids surrounding the beam tube. The operating temperature of the beam tube is in the 27–30 K temperature range to minimize the tritium throughput through the beam tube as well as the contribution of thermal Doppler broadening of electron energies due to the molecular motion. Finally, this temperature regime also mitigates systematic effects due to clustering and condensation of hydrogen isotopologues.

Over the past years, a detailed 2D/3D model of the gas dynamical characteristics of the tritium source has been developed, which is much more detailed than the initial 1D model described in [72], where perfect temperature homogeneity and isotropy of the source was assumed. The new gas dynamical model of the source has been used to derive precise values for the integral WGTS column density and its radial variation and the pressure distribution along the beam tube [112]. The stability of the column density, which is of the order of  $5 \cdot 10^{17} \text{ T}_2\text{-molecules/cm}^2$ , plays a central role in the sensitivity of KATRIN, as it impacts not only the statistical accuracy of the measurement, but also defines the energy losses of the  $\beta$ -decay electrons inside the source due to inelastic scattering [113]. An important aspect in the detailed modelling of the source characteristics is the fact that the gas rarefaction parameter along the tube varies



from the strong hydrodynamic regime at the injection point to free molecular flow at the beginning of the differential pumping chambers. Accordingly, a significant part of the beam tube exhibits values in the intermediate regime, where the phenomenological intermediate conductance formula of Knudsen is applied [114].

**4.3.2. The WGTS Cryostat and Associated Control and Monitoring Systems.** Initial estimates in [72] have revealed that a stabilisation of the column density on the 0.1% level is required to obtain a neutrino mass sensitivity of 200 meV. This translates into a stabilisation of the inlet pressure and the beam tube temperature on the same level, which certainly is a major technological challenge, given the macroscopic WGTS beam tube dimensions. A stable gas feed into the WGTS is achieved by injecting high-purity tritium gas from a pressure controlled buffer vessel over a 5 m long tritium capillary with constant conductance, while pumping out the gas at both ends of the beam tube with large TMPs. To fulfil the requirements on temperature stability, a novel beam tube cooling system based on a 2-phase boiling fluid has been designed and tested successfully (a two phase system, when used as a cooling method, has the well-known distinct advantage that it can absorb heat without changing its temperature). The choice of neon as cooling fluid has the advantage that it coexists in two phases at temperatures around 30 K for moderate pressures in the range from 1–3 bar.

In combination with the requirements of adiabatic electron transport and safe tritium throughput in a closed loop system, the required stability of the tritium column density on the  $10^{-3}$  level has resulted in a technical design of a complex cryostat (see Figure 16) with a length of 16.1 m and a weight of 27 tons [115] and a cryogenic system comprising 13 fluid circuits where 6 cryogenic fluids are processed. The cryostat also houses an extensive array of more than 500 sensors (magnetic field, pressure, gas flow, liquid levels, voltage taps) as part of a dedicated measurement and control system. The precision temperature readings of the sensor array will later on be used as input to model minute fluctuations of the actual source characteristics over typical time scales of about 1 min.

In order to test the advanced cryogenic technologies required for the cooling of the beam tube, a large-scale test unit, the WGTS demonstrator, was built. This 10 m long (1:1 scale) unit makes use of many original components which will be used later on in the final WGTS cryostat. In 2011 extensive measurements with the WGTS demonstrator were performed at TLK targeted at a proof-of-principle and optimization of the beam tube cooling system. To obtain a precise measurement of the beam tube temperature, an array of 24 metallic resistance temperature sensors (Pt500) were distributed along the beam tube. The sensors feature a sub-mK resolution and, via calibration with sensors measuring the saturation pressure of neon [116], an uncertainty for the absolute temperature of 4 mK only. During the measurements, a peak to peak variation of  $\Delta T = 3$  mK over a time period of 4 h at  $T = 30$  K was obtained, which is one order of magnitude better than required [107, 116]. This result offers the potential to substantially reduce the systematic errors

from the tritium source during the long-term measurements. At present, the WGTS demonstrator is being reassembled to the final WGTS cryostat. These extensive works will be completed by the end of 2014.

A dedicated Laser Raman (LARA) system, based on inelastic Raman scattering [117] of photons from gas molecules, is connected to the inner tritium loop and allows for inline and near time monitoring of the gas composition. The different tritiated gas species ( $T_2$ , DT, HT) have to be distinguished not only because of their different properties in the gas dynamical calculations, but also due to their slightly different endpoint energies as well as rotational and vibrational final states. Test measurements with a Raman cell suitable for operation with tritium [118, 119] show that a precision of  $\Delta_{\text{prec}}(e_{T_2})/e_{T_2} = 0.1\%$  for  $T_2$  monitoring can be achieved in measurement intervals of <250 s under KATRIN operating conditions [120, 121]. With an optimized setup, the acquisition time recently has been reduced to 60 s only.

**4.3.3. Calibration and Monitoring System Upstream of the WGTS.** To monitor the stability of the tritium activity and of the column density of the windowless gaseous tritium source, the rear side of the WGTS is connected to a calibration and monitoring system. An angular-selective electron gun is used to measure the energy loss function of the electrons due to inelastic scattering in the WGTS and to monitor the integral column density at different source radii. This novel UV-laser-based e-gun is based on the photoelectric effect producing monoenergetic electrons with stable intensity and with a well-defined starting angle  $\theta$  with respect to the magnetic  $\vec{B}$ -field [122–125]. Secondly this electron source will be used to determine the transmission function of the main spectrometer and the response function of the whole setup with high precision.

The calibration and monitoring system has another very important task related to the source operation. The  $\beta$ -electrons will be guided from the source to the spectrometer and mapped onto the detector within a magnetic flux tube of  $191 \text{ T cm}^2$ . The guiding by superconducting solenoids implies a tight transverse confinement by the Lorentz force to all charged particles. This includes the  $10^{11}$  daughter ions per second, which emerge from  $\beta$ -decay in the source tube, as well as the  $10^{12}$  electron-ion pairs per second produced therein by the  $\beta$ -electron-flux through ionization of  $T_2$  molecules. The strong magnetic field of 3.6 T within the source is confining this plasma strictly in the transverse direction so that charged particles cannot diffuse to the conducting wall of the source tube where they would get neutralized [126]. The charges within the windowless gaseous tritium source will thus be neutralized by a gold-plated crystalline rear wall which is part of the calibration and monitoring system, and on which all magnetic field lines from the windowless gaseous tritium source end. Accordingly, the high longitudinal conductance of the plasma will define and also stabilise the electric potential within the tritium source.

Finally, the source activity will be monitored by  $\beta$ -induced X-ray spectroscopy (BIXS), where the potential-defining rear wall acts as an X-ray converter. An encapsulated

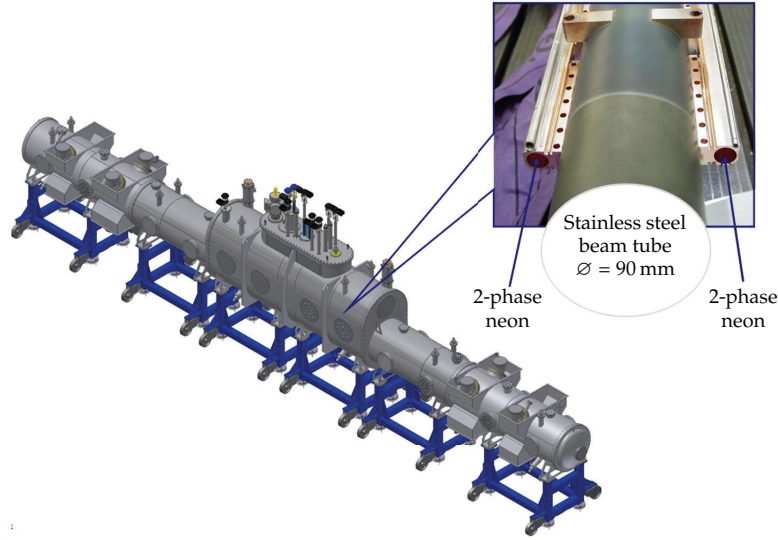


FIGURE 16: Schematic view of the 16 m long WGTS cryostat. The inlet shows the beam tube with the two phase liquid neon cooling system.

X-ray detector positioned behind the rear wall will monitor the source activity by recording the X-ray intensity, while the fluorescence lines from the surrounding structures would allow an inline calibration of the setup.

**4.3.4. Tritium Retention Techniques.** Since the spectrometer section must be essentially tritium-free for background reasons (see next chapter), the tritium flow along the beam line must be reduced from its initial value at the injection point of 1.8 mbar·l/s to a level of  $10^{-14}$  mbar·l/s at the entry to the spectrometers. This unprecedented large suppression factor will be achieved by a combination of differential and cryogenic pumping [127–130]. While reducing the tritium flux by 14 orders of magnitude, these sections also have to maintain adiabatic guidance of  $\beta$ -decay electrons from the WGTS to the spectrometers over a distance of more than 15 m.

**4.3.5. Differential Pumping Section (DPS2-F).** Differential pumping by large TMPs is the first tritium retention technique in use at the KATRIN beam line, with the initial stages being performed inside the WGTS cryostat by pump ports at the rear (DPS1-R) and front (DPS1-F) section. Thus, the DPS2-F cryostat is the second pumping unit in the forward direction. Its scientific objectives are the following: (a) active pumping of tritium molecules with TMPs, (b) reduction of the tritium flow by a factor larger than  $10^4$ , (c) maintaining a stable tritium circulation in the Outer Loop, and (d) diagnostics of the composition and suppression of ion species from the WGTS.

The DPS2-F has been designed as a single large cryostat of 6.96 m length (see Figure 17). It was the first KATRIN source-related component on site at KIT and was successfully commissioned in 2010/11 [131]. The unit features a beam line with an  $\Omega$ -shaped chicane to avoid the *molecular beaming* effect, in which case gas particles would not be pumped out

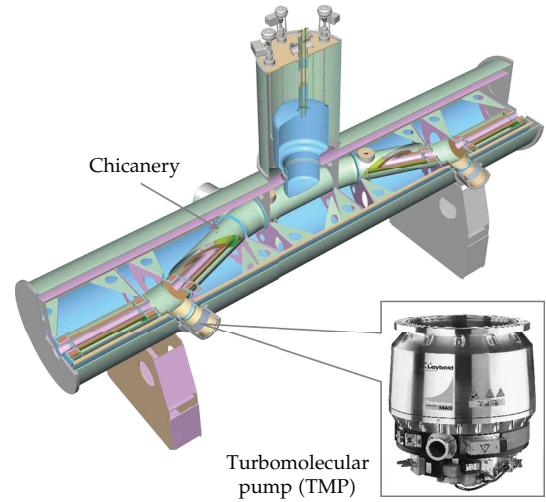


FIGURE 17: Schematic view of the 6.96 m long DPS2-F cryostat. The beam tube guiding the  $\beta$ -decay electrons features a chicane to avoid the molecular beaming effect. At the four pump ports large TMPs are installed for differential pumping. The beam tube instrumentation includes FT-ICR units and through-shaped electrodes for ion diagnostics and suppression.

due to the alignment between gas particle momenta and beam tube axis. The cascaded differential pumping system consists of four large TMPs mounted on pump ducts, which minimize the effect of thermal radiation from the TMPs operated at room temperature to the beam tube kept at 77 K, while also limiting TMP rotor heating due to induced eddy-currents [132]. During the commissioning measurements a retention factor for tritium (based on measurements for other hydrogen-like and noble gas species) of  $\approx 2.5 \times 10^4$  was obtained, demonstrating the excellent tritium retention characteristics of differential pumping already at room temperature [127].

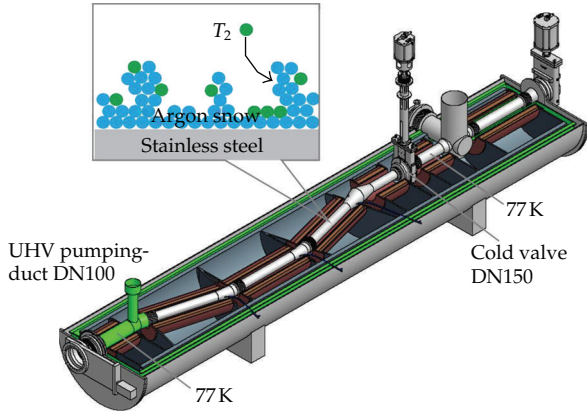


FIGURE 18: Schematic view of the seven beam tube elements of the CPS. The inner surface of the cryopump elements is covered with argon snow to capture the remaining tritium molecules.

The DPS2-F beam tube instrumentation is used for diagnostics and suppression of ions which result from ionization processes of primary  $\beta$ -decay-electrons with the neutral gas molecules of the source. As ions are guided by the field lines (and thus are not being pumped out) they remain trapped between a ring electrode at the end of the DPS2-F, where they are reflected electrostatically, and the WGTS, where they are reflected back by the gas pressure. The number density and composition of ions will be measured on a near-time basis by two Fourier Transform-Ion Cyclotron Resonance (FT-ICR) devices [133], which discriminate Penning-trapped ions by detecting differences in Ion Cyclotron frequencies in the 5.6 T  $B$ -field at the center of the DPS2-F solenoids. The ions stored between the WGTS and the end of the DPS2-F are eliminated by a system of three electrostatic dipoles by an induced  $\vec{E} \times \vec{B}$ -drift, irrespective of their mass, charge sign, or motion with respect to the electric field, within a time period of 20 ms or less, which is much shorter than the allowed upper time limit of 10 s for ion storage.

The magnetic flux tube of  $191 \text{ T cm}^2$  of  $\beta$ -decay electrons which is used for the neutrino mass analysis is guided through the beam tube chicane with a minimum margin of 10 mm from the walls of the inner vacuum system. The system of 15 superconducting solenoids is cooled by liquid helium supplied from an external Linde TCF 50 refrigerator, with a measured DPS2-F cryogenic stand-alone time of about eight hours [134]. Unfortunately, due to a malfunction of one of the protective diodes of the magnet system during the commissioning measurements, further tests with the DPS2-F had to be stopped in mid-2011. At present different options to ensure a future fail-safe operation of the differential pumping system during long-term tritium running are being studied.

**4.3.6. Cryogenic Pumping Section (CPS).** The Cryogenic Pumping Section (CPS) is the final tritium retention unit in the KATRIN beam line, featuring a large-area cryosorption pump based on a thin layer of argon snow frosted onto gold-plated steel as adsorbent (see Figure 18) [135]). It is designed for a tritium flow reduction factor of  $\geq 3 \times 10^7$ .

The 6.73 m long CPS cryostat features an even more complex beam tube design than DPS2-F with a beam tube segmented into 7 sections, as shown in Figure 18. To prevent residual tritium absorption onto the walls, the inner surfaces of the beam tube elements are gold-plated. The beam tubes of the cryopump section are tilted by an angle of  $15^\circ$  with respect to each other and are covered by a thin argon frost layer to enlarge the inner surface for sorption. The CPS design allows the insertion of a Condensed  $^{83\text{m}}\text{Kr}$  Source (CKrS) [136] for calibration purposes, as well as a small Si-diode for source intensity monitoring. The CPS is currently being manufactured by an industrial partner in Genoa (Italy) and will be shipped to KIT at the end of 2013. After commissioning and initial bake-out, the CPS will regularly cycle through several modes of operation. In a first step the beam tube elements will be cooled to their respective operational temperature, which is followed by the preparation of an argon frost layer. This requires a temperature in the range of 6 K to favour the growth of small to medium sized crystallites. After argon frost preparation, the cryopump temperature will be lowered again to 3 K. After a data collection cycle of about 60 days, the CPS has to be regenerated to remove the adsorbed tritium activity of about 2 Ci by purging 100 K gaseous helium through the cryopumping segments.

By combining differential pumping by TMPs in the DPS with cryosorption on a large-area argon frost pump in the CPS, the number of migrating HT-molecules to the pre- and main spectrometer is kept at a minimum. When including all relevant tritium retention techniques, that is, not only DPS and CPS, but also tritium interactions with the spectrometer walls and tritium pumping by the large nonevaporable getter (NEG) strips in the spectrometers, a tritium partial pressure in the main spectrometer of about  $10^{-22}$  mbar can be expected [131]. This ultralow level should result in a tritium-related background rate of only  $10^{-4}$  cps, which is two orders of magnitude below the design specification. It is only by this huge tritium reduction factor that the KATRIN experiment can combine an ultra-luminous windowless gaseous tritium source of  $10^{11}$   $\beta$ -decay electrons with a high-resolution electrostatic spectrometer operated with an extremely low background level of 0.01 cps [137].

**4.4. Spectrometer and Detector Section.** In the following the non-tritium-related parts of KATRIN will be described. First the tandem spectrometer system performing the energy analysis of the  $\beta$ -electrons is addressed and then the detector and data acquisition system are described.

**4.4.1. Overview: Prefiltering and Precision Scanning.** The spectrometer section consists of two electrostatic retarding filters of the MAC-E-Filter type: the prespectrometer and the main spectrometer. The prespectrometer offers the option to act as a prefilter, reflecting all electrons with energies up to 300 eV below the endpoint, while transmitting the interesting part of the spectrum undisturbed. All electrons transmitted through this first stage are guided to the main spectrometer for precise energy analysis close to the endpoint. A third spectrometer, the monitor spectrometer, is used to monitor precisely the high voltage of the main spectrometer.



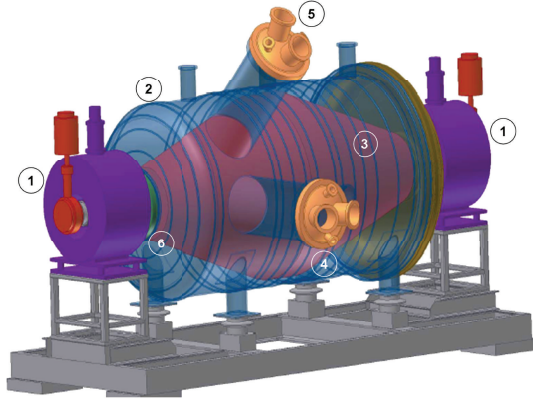


FIGURE 19: Schematic view of prespectrometer. (1) superconducting solenoids, (2) prespectrometer vessel, (3) inner electrode system, (4) 90° pump port, (5) 45° pump port, (6) insulator.

**4.4.2. Prespectrometer.** The prespectrometer has a length of 3.4 m and a diameter of 1.7 m. At both ends a superconducting magnet is installed providing a magnetic field of 4.5 T at the center of the magnet and 15.6 mT in the center of the spectrometer. As a novel electromagnetic design feature, if compared to the Mainz and Troitsk set-ups, the tank itself is set on high voltage. An inner electrode system consisting of two conical full electrodes and a central cylindrical wire electrode can be set to a different potential as the vessel. Figure 19 shows a schematic view of the prespectrometer.

One of the prespectrometer's major tasks has been to serve as a prototype for advanced technologies and experimental methods later applied to the much larger main spectrometer. Many basic concepts, such as the design of the ultra high vacuum (UHV) system and high voltage stabilization were successfully tested at the prespectrometer. Especially important was the detailed investigation of background processes in MAC-E-filters. Two new classes of background were identified and studied at the prespectrometer: background due to small Penning traps and radon induced background [138]. The knowledge gained during the extensive measurement period at the prespectrometer has proven to be extremely valuable for the design and operation of the main spectrometer.

**4.4.3. Main Spectrometer.** The exceedingly large dimensions of the main spectrometer are essential to operate it as an extremely precise high-energy filter with an energy resolution of  $\Delta E = 0.93 \text{ eV}$  (0%–100% transmission). This sharp resolution requires that the stability of the retarding high voltage is in the ppm range. The scanning voltage is varied in steps of  $\Delta U = 0.5\text{--}1 \text{ V}$  around a narrow region close to the endpoint at  $qU = E_0 = 18.6 \text{ keV}$ . The highest electrostatic potential is located in the central plane of the spectrometer, perpendicular to the beam axis, the so-called “analyzing plane.”

To achieve a very high energy resolution, the cyclotron motion of the electrons, being isotropically created in the



FIGURE 20: Photograph of the spectrometer transport during the final careful maneuvering through the nearby village of Leopoldshafen in November 2006. Due to its size, it could not be transported to Karlsruhe on motorways, but had to travel nearly 9000 km through the Danube River, the Black Sea, the Mediterranean Sea, the Atlantic Ocean, the North Sea, and the River Rhine [139].

WGTS, needs to be almost fully transformed into longitudinal motion parallel to the magnetic field lines, since only the latter is analyzed by the retarding potential (see Section 3.2). To obtain adequate parallelization, the magnetic field drops by four orders of magnitude from the entrance to the center of the main spectrometer. Since the magnetic flux  $\Phi$  is conserved, the cross-section of the flux tube in the center plane has to be four orders of magnitude larger than at the entrance. This scaling explains the huge size of the main spectrometer (length  $L = 23.8 \text{ m}$ , diameter  $d = 9.8 \text{ m}$ , surface area  $A = 650 \text{ m}^2$ , and volume  $V = 1450 \text{ m}^3$ ) (see Figure 20).

To compensate for the distorting earth magnetic field and to fine-tune the magnetic field inside the main spectrometer, the vessel is surrounded by a large external air coil system (see Figure 21). It consists of 10 horizontal current loops and 16 vertical ones to compensate the earth magnetic field (EMCS). Additionally, a system of 15 Helmholtz-like coils with individually adjustable currents allows for precise adjusting of the gradients and the overall strength of the magnetic field (LFCS). Two arrays of magnetic field sensors, one at fixed positions, and the other a mobile one attached to robots [140], allow to measure and monitor precisely the magnetic field.

The main background source of the Mainz experiment was secondary electrons from the electrodes at high potential. These electrons are created by cosmic muons or by environmental radioactivity. The shielding effect of the magnetic field will prohibit most of these electrons to enter the magnetic flux tube and thus to reach the detector. However, measurements at Mainz [141] and Troitsk yielded a transmission rate of  $10^{-5}\text{--}10^{-7}$  through the magnetic shielding of a MAC-E-filter. A large shielding factor is important considering the large surface of  $650 \text{ m}^2$  of the KATRIN main spectrometer. To suppress this kind of background, a new idea of additional background suppression has been developed and successfully tested at the Mainz spectrometer [142, 143] and optimized at the prespectrometer. This technique will also be applied





FIGURE 21: Photograph of air coil system surrounds the main spectrometer vessel. Its purpose is to compensate the earth magnetic field and to fine-tune the magnetic field inside the main spectrometer.

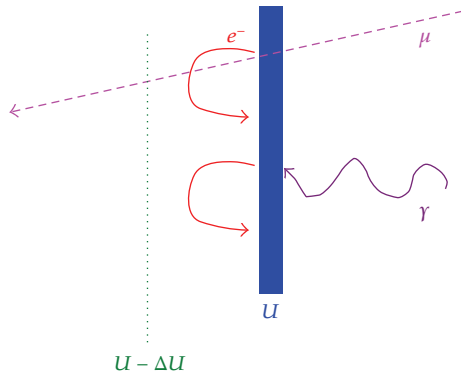
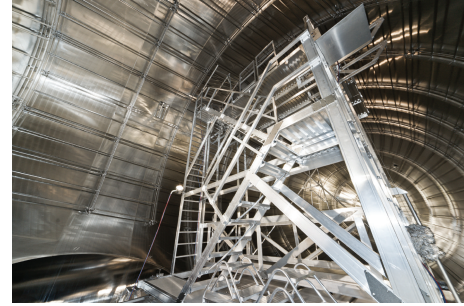


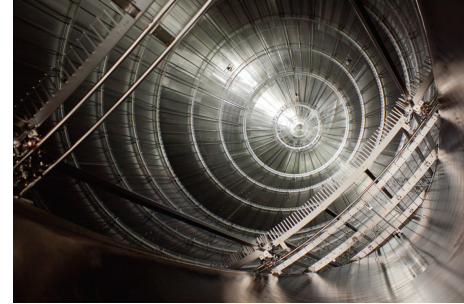
FIGURE 22: Principle of electrical screening of a surface at high voltage  $U$  by a nearly massless wire electrode at a slightly more negative voltage  $U - \Delta U$ . Secondary electrons, which are emitted from the surface at potential  $U$ —for example, by the interaction of cosmic muons or  $\gamma$  radiation by environmental radioactivity—will be reflected by the wire potential back to the wall, if the kinetic energy of the secondary electrons is not sufficient to pass the electrical potential barrier  $U - \Delta U$ . If the wire electrode has a sufficiently small cross-section, the probability that unscreened secondary electrons emitted from the wires is small.

to the KATRIN main spectrometer: The vessel walls at high potential will be covered by a system of nearly massless wire electrodes, which are put to a slightly more negative potential (see Figure 22). Secondary electrons ejected by cosmic rays or environmental radioactivity from the vessel wall will thus be repelled and prohibited from entering the magnetic flux tube. To achieve a high suppression factor of 10, as demonstrated in the Mainz experiment, the KATRIN main spectrometer has been instrumented by a two-layer wire electrode system [144–146] (see Figure 23).

This system consists of 248 modules of a typical size of  $2 \times 1.5 \text{ m}^2$ . The wires of the inner (outer) layer have a diameter of  $200 \mu\text{m}$  ( $300 \mu\text{m}$ ) and a distance of 22 cm (15 cm) from the surface of the spectrometer vessel. Essentially the inner (outer) wire layer will be on a potential of  $-200 \text{ V}$  ( $-100 \text{ V}$ ) with respect to the main spectrometer vessel. The total number of wires amounts to 23440. Stringent demands are required for this electrode system: The two wire layers in the central part have to be mounted with a precision of



(a)



(b)

FIGURE 23: Photographs of the oil- and dust-free scaffold to install the wire electrode system in the main spectrometer (a) and view into the main spectrometer before the last two wire electrode modules at one of the pump ports were installed to finish the wire electrode installation (b). Photographs: Michael Zacher.

$200 \mu\text{m}$  to avoid distortions of the electrical potential. The wires have to withstand baking at  $350^\circ\text{C}$ . The outgassing of the wire electrode system has to be extremely low to allow a final residual gas pressure of  $10^{-11} \text{ mbar}$ . The mounting of the wire electrode system within the huge KATRIN main spectrometer under clean-room conditions was a big challenge on its own (see Figure 23). The installation of the wire electrode system was successfully completed in January 2012.

In addition to the background reduction, the wire electrode serves three other purposes: fine-shaping of the electric retarding potential is achieved by applying slightly different voltages on the different axial rings of the wire modules to guarantee full adiabatic motion of the electrons. Reducing fluctuations of the electric retarding potential is done by decoupling the low-noise high-precision retarding voltage of the inner-most wire layer from the high-voltage of the vessel, on which electrical devices such as TMPs are mounted. The multilayer system acts as a Faraday cage. Finally, by splitting the wire module arrangement into an eastern and a western half an electric dipole voltage can be applied to eject low-energy stored particles by an induced  $\vec{E} \times \vec{B}$  drift (see, (42)).

**4.4.4. High Voltage and Monitoring Layout.** The energy analysis of  $\beta$ -decay electrons based on the MAC-E filter principle [70, 71] relies primarily on the stability of the electrostatic filter potential [147, 148]. The latter has been identified as one

of the five main contributions to the KATRIN uncertainty budget [72]. Its contribution to the systematic error of the energy filter potential has to be restricted to  $\Delta m^2 < 0.0075 \text{ eV}^2$  in order to meet the desired level of sensitivity.

We showed earlier in (37) that any unknown fluctuation of the retarding voltage  $U$  with variance  $\sigma_U^2$  leads to a shift of the squared neutrino rest mass  $\Delta m^2(\nu_e) \approx -2 \cdot q^2 \sigma_U^2$  (the electron charge  $q$  takes care of the conversion from voltage to energy). This relation and the systematic error limit given above have been taken into account in order to define the stability requirements for the KATRIN high voltage monitoring system, which is  $\sigma_U < 60 \text{ mV}$  [72]. At the tritium endpoint energy  $E_0 = qU = -18.6 \text{ keV}$ , this corresponds to a relative voltage stability of  $\Delta U/U < 3.3 \cdot 10^{-6}$ , which has to be maintained for the whole KATRIN measurement time.

Therefore KATRIN will apply two redundant monitoring methods, one being based on two high voltage dividers with highest possible precision, that is,  $10^{-6}$  relative precision and long-term stability for up to 35 kV [149], and the other one being based on a monitoring beam-line which observes a monoenergetic electron source [72]. To do so in both cases, the low-noise retarding high voltage applied to the inner layer of the central wire electrode modules is distributed to the precision high voltage dividers and to the monitor spectrometer.

The monitor spectrometer consists of the refurbished and upgraded MAC-E filter spectrometer of the Mainz experiment (see Section 3.2) and observes an implanted  $^{83}\text{Rb}/^{83\text{m}}\text{Kr}$  source [150, 151]. For the calibration source  $^{83}\text{Rb}$  is produced either at the ISOLDE facility at CERN or at the cyclotrons at Nuclear Research Institute (Rez) in the Czech Republic or at Bonn University in Germany [152, 153]. The  $^{83\text{m}}\text{Kr}$  decay provides monoenergetic conversion electrons of the K shell with an energy close to the tritium endpoint at  $E_{K-32} = 17.8 \text{ keV}$  [154]. While applying the MAC-E filter principle as well as the main spectrometer retarding potential, the  $^{83\text{m}}\text{Kr}$  source has to be elevated by about 800 eV in order to monitor the K conversion electrons. This method relies on atomic and nuclear physics standards and provides monitoring with a stability at the 50 meV level as required by the systematic uncertainty limit.

Based on a self-compensating principle [155], two precision high voltage dividers have been developed in cooperation with PTB Braunschweig. These HV dividers rank among the most stable ones in the world. For voltages of up to 35 kV, they provide a long-term stability of  $<10^{-6}$  per month as well as negligible temperature and voltage dependencies [149]. The two dividers have served recently to calibrate the ISOLDE facility at CERN [156]. The permanent voltage monitoring with the precision voltage divider and frequent  $^{83\text{m}}\text{Kr}$  calibration measurements at the monitor spectrometer will provide reliable and stable calibration and monitoring for the retarding potential of the main spectrometer over long periods of time.

**4.4.5. Focal Plane Detector.** The focal plane detector is a semiconductor-based silicon PIN diode [157]. Its main goal is to

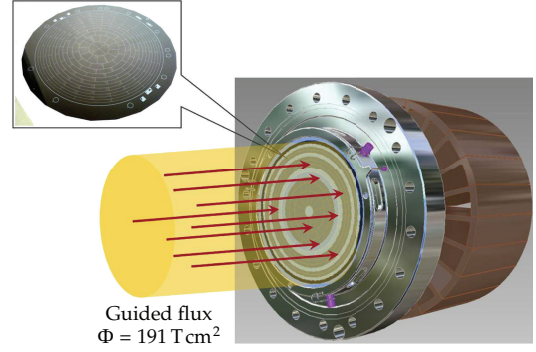


FIGURE 24: Schematic view of the detector. The electrons are guided along magnetic field lines to the sensitive area of the detector, which has a diameter of 10 cm. The inset shows a photograph of the detector, in which the 148 pixels are visible.

detect transmitted electrons with a detection efficiency of  $>90\%$ .

The detector is subdivided into 148 pixels to achieve good spatial resolution (see Figure 24). This is important, as electrons passing the analyzing plane at different radii will experience slightly different retarding potentials, due to the radial inhomogeneity of the electric potential. To account for this effect the detector consists of 12 concentric rings subdivided azimuthally into 12 pixels each. The innermost part is composed of 4 quarter circle pixels. This pixel arrangement allows for a precise mapping of inhomogeneities of the retarding potential as well as of the magnetic field. Each detector pixel measures an independent tritium  $\beta$ -spectrum which has to be corrected for the actual retarding potential and magnetic field value at the analyzing plane.

The signal of each detector pixel is connected by pogo-pins to a charge-sensitive pre-amplifier. The amplified signals are digitized by FADC- and FPGA-boards [158] developed for the Pierre Auger Observatory. The Data Acquisition System is based on the software package ORCA (Object-oriented Real-time Control and Acquisition), which was originally developed at the University of Washington as a general purpose, highly modular, object-oriented, acquisition and control system. Since 2008 further development continues at the University of North Carolina at Chapel Hill [159].

The detector is cooled by  $\text{LN}_2$ . To suppress external background, it is surrounded by low radioactivity lead shield. Additionally an active muon veto system consisting of a cylindrical plastic scintillator read out by wavelength shifting fibers is installed. There is an option to use postacceleration to increase the kinetic energy of the  $\beta$ -electrons to about 30 keV or above before they hit the detector. This could help in discriminating signal from fluorescence background. Additionally, the impact angle of the electrons relative to the detector surface would be increased, which decreases the probability of backscattering from the detector surface [99].

The detector is situated in a superconducting magnet providing a magnetic field of  $B_{\text{det}} = 3\text{--}6 \text{ T}$ . The detector magnet is adjacent to the so-called pinch magnet which

provides the maximal magnetic field of  $B_{\max} = 6 \text{ T}$  of the entire KATRIN setup. All electrons that started in the source with an angle larger than  $51^\circ$  will be reflected by the pinch magnet before they reach the detector (see (40)). This is advantageous, as electrons emitted under a large angle perform a lot of cyclotron motion, which in turn increases their total path length and therefore their scattering probability and also their synchrotron losses. To exclude those electrons, the magnetic field of the source is smaller than the maximal field.

**4.5. Signal and Sensitivity.** By counting  $\beta$ -electrons at different retarding potentials, KATRIN measures the integral  $\beta$ -spectrum (18)

$$\begin{aligned} N(qU, E_0, m^2(v_e)) \\ = N_{\text{tot}} t_U \int_0^{E_0} \dot{N}(E, E_0, m^2(v_e)) R(E, qU) dE, \end{aligned} \quad (49)$$

which is a convolution of the response function  $R(E, qU)$ , incorporating the energy loss in the WGTS and the spectrometer transmission function, with the differential energy spectrum  $\dot{N}(E, E_0, m^2(v_e))$ , describing the number of decays per second, nucleus and energy bin. In contrast to (18), here we have explicitly stated the dependence of  $\dot{N}$  on the endpoint energy  $E_0$  and on the squared neutrino mass  $m^2(v_e)$ . The parameters  $N_{\text{tot}}$  and  $t_U$  denote the total number of tritium nuclei and the measurement time at a certain retarding potential, respectively. Assuming a constant background rate  $\dot{N}_b$  the fit function to the measured spectrum is given by

$$\begin{aligned} N_{\text{th}}(qU, R_s, R_b, E_0, m^2(v_e)) \\ = R_s \cdot N(qU, E_0, m^2(v_e)) + R_b \cdot \dot{N}_b \cdot t_U, \end{aligned} \quad (50)$$

where  $R_s$  and  $R_b$  are the relative fraction of signal and background. In the fit  $R_s$ ,  $R_b$ ,  $E_0$ , and  $m^2(v_e)$  are free parameters.

**4.5.1. Sources of Systematic Errors.** Sources of systematic uncertainties arise from

- (i) unconsidered corrections to the  $\beta$ -spectrum  $\dot{N}(E, E_0, m^2(v_e))$ ,
- (ii) unaccounted variations of experimental parameters, for example retarding potential  $U$  and number of decays  $N_{\text{tot}}$ ,
- (iii) an imprecise knowledge of the response function  $R(E, qU)$ ,
- (iv) and a non-constant background  $\dot{N}_b$  in time and energy.

Most of the systematic effects are related to the tritium source. They include energy losses of  $\beta$ -electrons, primarily due to inelastic scattering in the source, fluctuations of the column density, potential charging effects due to remaining ions, and the accuracy of the quantum-chemical calculations of the final state distribution of molecular tritium (see

Section 4.3). The main systematic effect related to the spectrometer section is the high voltage stability (see Section 4.4).

New physics effects such as right handed currents [33], sterile neutrinos [91–93, 160], extra dimensions [94], and so forth, also affect the shape of the tritium spectrum (see (21)). However, the influence of these phenomena typically becomes important only further away from the endpoint. Another new physics contribution that might affect the spectrum also close to the endpoint is violation of Lorentz invariance [95].

**4.5.2. Background Sources.** Only a small fraction of  $10^{-13}$  of the  $10^{11}$  tritium decays per second in the WGTS will produce  $\beta$ -electrons in the interesting energy region close to the endpoint (1 eV below the endpoint). This leads to a generic rather low count rate of only  $10^{-2}$  cps in this energy region. To achieve a sensitivity of 200 meV (90% C.L.), the background must be of the same order of magnitude, or smaller. Of major concern in this context are backgrounds which are not constant in time or energy.

The background originates mainly from the spectrometer section and partly from the detector. With a detector energy resolution of the order of 1 keV, all nonsignal electrons detected in the region-of-interest (i.e., from approximately 15 keV to 20 keV) will contribute to the background level. Possible detector background sources are electrons produced by cosmic muons (and subsequent neutrons and gammas), high energetic gammas of environmental radioactivity (mainly from the thorium and uranium decay chains in the surrounding area) and decays of radionuclei in the detector material.

To reduce the backgrounds, the materials used in the construction of the detector system were radioassayed very thoroughly. In addition, the detector is surrounded by a muon veto system. Finally, there is the option to use postacceleration to increase the energy of signal electrons up to 30 keV, which would allow for better signal-background discrimination. The total expected detector background is about  $10^{-3}$  cps, which has been verified in the on-going commissioning measurements of the focal plane detector system.

The spectrometer-related background is especially challenging since all low-energy electrons created in the spectrometer are accelerated to the retarding potential before hitting the detector. Consequently, they cannot be distinguished from signal electrons. In Section 4.4, we have already discussed that secondary electrons produced at the spectrometer walls are prevented from entering the sensitive magnetic flux tube by the dominant inherent magnetic shielding of the MAC-E filter, and by subdominant electrostatic shielding of the wire electrode system. However, secondary electrons can also be generated inside the sensitive flux tube as a result of ionisation processes of residual gas. Of particular concern are electrons that are stored, either in Penning traps, or by the inherent magnetic bottle property of the MAC-E-configuration. These processes have been studied in the pre-spectrometer set-up in an extended measurement program.

In [137, 138], it was shown that small Penning traps of the size of  $V < 100 \text{ cm}^3$  can lead to background rates easily exceeding  $10^3$  cps. Electrons being stored in Penning



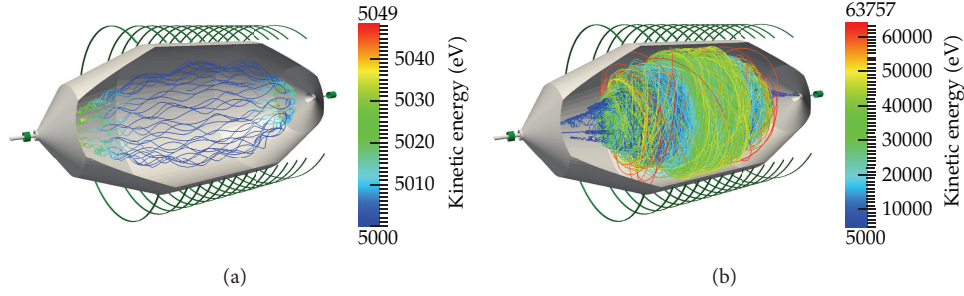


FIGURE 25: (a) shows the stable storage condition without external RF field, where the electron trajectory is a superposition of a fast cyclotron motion, axial oscillation, and much slower magnetron drift. (b) shows an electron trajectory in presence of an RF field with a frequency which is tuned to the cyclotron frequency of the electron in the central part of the spectrometer. The stored electron is stochastically heated up every time it passes the resonance region. After less than 5 ms its cyclotron radius is so large that the electron hits the wall and is absorbed there.

traps produce background via messenger particles, such as positive ions or photons, which can leave the trap and subsequently can create secondaries in the sensitive volume. This background has been tackled by a very precise and careful electromagnetic design [161, 162] that avoids the creation of Penning traps *ab initio*.

The simultaneous operation of two electrostatic retarding spectrometers (prespectrometer and main spectrometer) next to each other in the beam line, and with ground potential between them, would create a large Penning trap for electrons [163]. Signal electrons that experience no energy loss on their way through the spectrometers are not affected. However, all electrons that are created between the spectrometers with less kinetic energy than the prespectrometer retarding energy remain trapped. A stored electron will fill the trap in an avalanche effect by continually ionizing residual gas molecules. Simulations have shown that a primary stored electron together with all its secondaries may create up to  $10^8$  positive ions, which are not trapped and can freely propagate into the main spectrometer. There, they can ionize residual hydrogen molecules thereby producing further electrons that can reach the detector and contribute to the background level.

A possible countermeasure would be the installation of a wire scanner between the spectrometers which regularly wipes through the trap, thereby removing the stored electrons and suppressing the background production [163, 164]. Another most promising option would be to operate the prespectrometer at reduced filter energy [99, 110], even down to zero potential. This mode would avoid the creation of the Penning trap. Test measurements and simulations have proven the effectiveness of both approaches.

Another major background source results from magnetically stored electrons [165, 166]. At the main spectrometer, this will cause all electrons with (transversal) energies larger than 1 eV (i.e., larger than the width of the transmission function) to be stored. Owing to the excellent UHV conditions in the KATRIN main spectrometer ( $p = 10^{-11}$  mbar) the storage times of electrons in the multi-keV-range can reach several hours. During its cooling time, a stored electron produces several hundred secondary electrons, which eventually leave the spectrometer and hit the detector. The main source of primary electrons originate from  $^{219}\text{Rn}$ ,  $^{220}\text{Rn}$  [165] and tritium

decays inside the spectrometer volume. This background source features large time fluctuations and thereby a strong non-Poissonian characteristic. This fact has a large impact on the neutrino mass sensitivity [166].

As a counter measure liquid nitrogen cooled baffles will passively shield the spectrometer volume from  $^{219}\text{Rn}$ , which is mainly emanating from the large NEG pumps [165]. The tritium decay rate inside the main spectrometer volume can be reduced by the option to use the prespectrometer as an additional tritium pump. Finally, a number of active background reduction techniques, which are targeted at removing the stored electrons, have been successfully investigated experimentally and via extensive MC simulations. A method based on stochastic heating with an RF field by the well known technique of Electron Cyclotron Resonance (ECR) [167] and a method based on nulling the magnetic field by magnetic pulsing [164] seem most promising. Figure 25 shows the strong background-reducing effect of a very short RF-pulse fed into the main spectrometer on magnetically stored electrons as calculated by KASSIOPEIA (even for very moderate RF-amplitudes). These short RF-pulses would empty all stored particles with negligible duty-cycle.

**4.5.3. Neutrino Mass Sensitivity of KATRIN.** For the reference setup of the KATRIN experiment, the quadratic sum of all known systematic uncertainties is expected to be  $\sigma_{\text{sys,tot}} \leq 0.017 \text{ eV}^2$ . After three “full beam” years of measurement time the statistical error is about as small as the systematic error. This yields a total error of  $\sigma_{\text{tot}} = 0.025 \text{ eV}^2$ . Figure 26 shows the discovery potential of KATRIN as a function of beam time for different neutrino masses. Accordingly, a neutrino mass of  $m_\nu = 350 \text{ meV}$  would be seen with  $5\sigma$  significance. The figure also shows the 90% C.L. upper limit as a function of measurement time in case that no neutrino mass signal is seen. In this case, an upper limit of  $m_\nu \leq 200 \text{ meV}$  can be stated at 90% C.L after three full beam years of measurements.

**4.6. Status and Outlook.** The commissioning of the KATRIN beam line elements is progressing well. On one side, the multifaceted technical hurdles are challenging, causing the commissioning of the overall setup to take longer than originally planned. On the other side, the excellent results



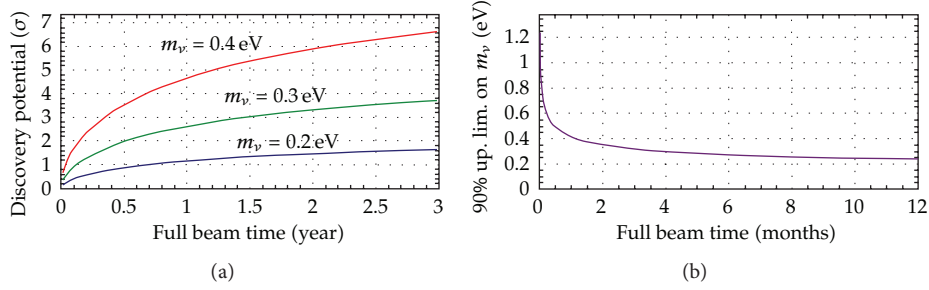


FIGURE 26: (a) Discovery potential of KATRIN as function of time for different neutrino masses. (b) Upper limit on neutrino mass at 90% C.L. as a function of time.

of the large-scale test units have opened the possibility to substantially reduce the systematic effects during the long-term measurements with the final configuration, thus improving the neutrino mass sensitivity of the experiment.

Beginning at the source-related components, an important breakthrough was the verification of the novel beam tube cooling system. In a dedicated setup, consisting largely of original components, the WGTS demonstrator, a temperature stabilization of the 10 m long beam tube of  $\Delta T/T$  of  $\approx 10^{-4}$  was achieved by using two-phase neon fluid as cooling agent. This is one order of magnitude better than specified. Together with the achieved pressure stabilisation of the inner loop mock-up of  $\Delta p/p$  of  $\approx 10^{-4}$ , this opens up the possibility of reduced systematic errors from column density fluctuations (this is one of the largest overall systematic errors). At present the WGTS demonstrator is being reassembled to the final WGTS cryostat. The final WGTS assembly at KIT is expected to be completed by the end of 2014. Further progress has been made with regard to tritium analytics (LARA setup), as well as the design of the rear section which will include extensive control and monitoring units.

Major progress has also been achieved in the field of large-scale tritium retention. After the successful commissioning of the DPS2-F cryostat, first tritium retention measurements with a beam tube at room temperature have yielded experimental flow suppression factors which are in very good agreement with corresponding MC simulations. Due to the malfunction of a protective diode of the superconducting magnet system of DPS2-F, a new magnet safety concept for all s.c. solenoids has been designed. This concept is currently being implemented for WGTS and CPS, as well as a fail-safe differential pumping section. The manufacture of the cryopump CPS is well under way with assembly works expected to be finished by the end of 2013.

In the spectrometer section, the extensive measurement program with the prespectrometer facility has given important insights into background reduction techniques, precision electromagnetic layout, vacuum technologies, and high voltage stability. At present the prespectrometer is ready for beam line integration.

The main spectrometer together with its external air coil system and its inner electrode system, which was completed at the beginning of 2012, is currently being prepared for test measurements. These measurements will be focused first on

extensive background studies, with the objective to remove any remaining small-scale Penning traps, to quantify the contribution of cosmic muon induced background and to study its signature by making use of external muon detectors. An important aspect of the background studies will be the identification of background due to stored electrons following nuclear decays, and the optimisation of active and passive background reduction techniques to limit the spectrometer background to a level of  $< 10^{-2}$  cps. Another important task will be to map the transmission properties of the spectrometer with an angular-selective electron gun. In all these investigations the recently commissioned focal plane detector system with its excellent properties will be of vital importance. Finally, the extensive software developments for simulation and analysis tools are in an advanced state and the software packages are continually being refined and extended.

After integration of all source-related and spectrometer-related components, the first runs in the final KATRIN configuration are expected in the second half of 2015.

## 5. New Approaches

While spectrometer experiments based on the MAC-E filter principle [70] currently provide the highest sensitivities in direct neutrino mass experiments, there are alternative approaches that aim for comparable performance and better scalability in the study of weak decays.

A very recent development is promoted by the Project 8 team (see Section 5.1) where tritium technology from the KATRIN experiment is used in conjunction with microwave antennas to detect coherent cyclotron radiation emitted by individual decay electrons in a magnetic field. The aim is to extract a  $\beta$ -decay spectrum without the need for a large electrostatic spectrometer.

Most of the work on alternative experimental methods is, however, focused on using microcalorimeters to study rhenium  $\beta$ -decays (see Section 5.2) or holmium electron capture decays (see Sections 5.3 and 5.4). The main advantage of using microcalorimeters lies in the *source = detector* principle that allows to measure the complete decay energy (excluding the energy carried away by the emitted neutrino) as opposed to only measuring the kinetic energy of the decay electrons. On the other hand the comparably slow signals produced by calorimetric detectors bring the challenge of

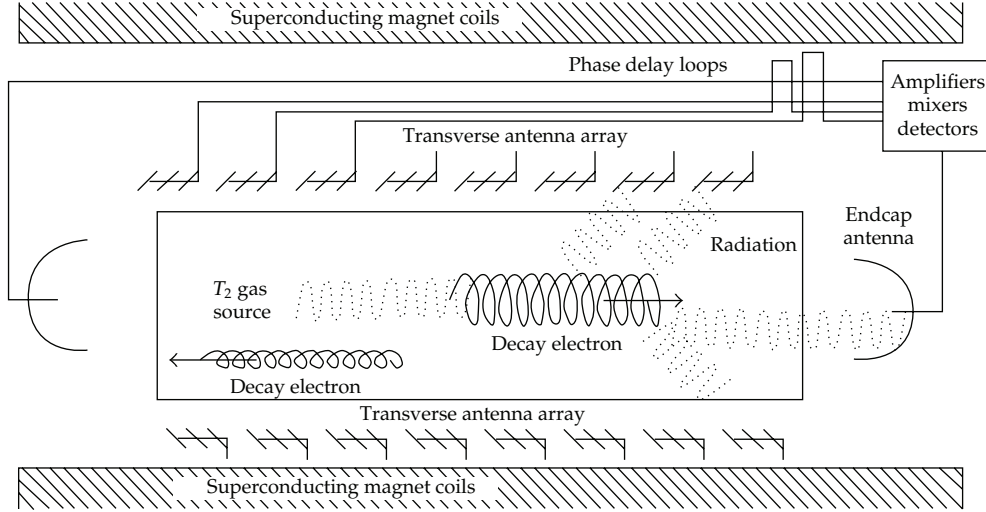


FIGURE 27: Schematic view of the experimental layout to measure coherent cyclotron radiation from tritium decay electrons (reprinted with permission from [170], Copyright (2009) by the American Physical Society).

using large arrays of small detectors to avoid pileup in the individual calorimeter crystals.

Another approach has been proposed by Jerkins and coworkers [168] who suggest to perform a full kinematic reconstruction of the decays of trapped tritium atoms. This idea, however, seems to be hampered by conceptual difficulties [169].

**5.1. Project 8.** Project 8 is a new effort to measure the neutrino mass lead by groups from MIT, University of California, Santa Barbara and University of Washington. The idea is to use technology from KATRIN's gaseous tritium source combined with a sensitive array of microwave antennae to extract energy spectra of tritium decay electrons from the coherent cyclotron radiation emitted by individual electrons in a magnetic field (see Figure 27). In such a setup, electrons will follow a circular or spiral path with a cyclotron frequency  $\omega$  of

$$\omega = \frac{\omega_0}{\gamma} = \frac{qB}{m + E}, \quad (51)$$

where  $E$  is the kinetic energy of the electron,  $B$  is the magnetic field of the source,  $q$  is the electron charge,  $m$  is the electron mass,  $\omega_0$  is the unshifted cyclotron frequency, and  $\gamma$  is the Lorentz factor. The total power emitted by each electron depends on its relative velocity  $\beta$  and the pitch angle  $\theta$  between the direction of movement and the magnetic field vector

$$P(\beta, \theta) = \frac{1}{4\pi\epsilon_0} \frac{2q^2\omega_0^2}{3c} \frac{\beta^2 \sin^2(\theta)}{1 - \beta^2}. \quad (52)$$

With a suitable set of source parameters, the power of the cyclotron radiation emitted will be large enough to be detected, but not large enough to rapidly change the electron's momentum and will therefore allow to reconstruct its kinetic energy. The energy resolution  $\Delta E$  of the method depends on

the relative uncertainty with which the cyclotron frequency can be determined, which in turn depends on the observation time for an individual decay electron.

Monreal and Formaggio [170] discuss a reference design with a 1 T magnetic field strength. In this design  $f_0 = \omega_0/2\pi \approx 27$  GHz for decay electrons near the endpoint energy  $E_0 = 18575$  eV. For a resolution of  $\Delta E = 1$  eV we therefore require a relative uncertainty  $\Delta f/f = \Delta E/m = 2 \cdot 10^{-6}$  and, via the Nyquist theorem, a minimum observation time of  $t_{\min} = 2/\Delta f \approx 38 \mu s$ . This observation time determines the necessary mean free path of decay electrons in the source before they undergo inelastic scattering from  $T_2$  molecules and therefore places constraints on the density of the source. In the reference design the required free path length is given by  $t_{\min}\beta c \approx 3000$  m corresponding to a maximum  $T_2$  density of  $\rho_{\max} = (t_{\min}\beta c\sigma_i)^{-1} \approx 1.1 \cdot 10^{12}/\text{cm}^3$  with a total cross-section  $\sigma_i \approx 3 \cdot 10^{-18} \text{ cm}^2$  for inelastic scattering of electrons near the endpoint energy from molecular tritium.

Given the long pathlength required for the electrons to achieve the necessary observation time, it becomes clear that the decay electrons need to be trapped within an instrumented volume to realize the actual experiment. This can be achieved using the magnetic mirror effect, where the  $B$ -field of the source volume is increased by some amount at both ends of the apparatus. The ratio between the field strength in the source volume to that at the edges then determines the minimum pitch angle  $\theta_{\min}$  of the stored electrons. Only storing electrons with pitch angles above  $\theta_{\min}$  has the added benefit that they are also emitting higher signal powers via the dependence of equation 53 on  $\theta$ . For stored electrons the emitted signal powers are in the  $10^{-15}$  W region while the authors of [170] estimate the thermal noise contribution of suitable amplifiers for the signal detection to be of the order  $10^{-17}$  W. Incoherent noise from non-endpoint and/or low-pitch beta electrons is expected to contribute about  $10^{-24}$  W/Bq in the signal region which would allow a tritium activity of the source of the order  $10^8$ – $10^9$  Bq. Of

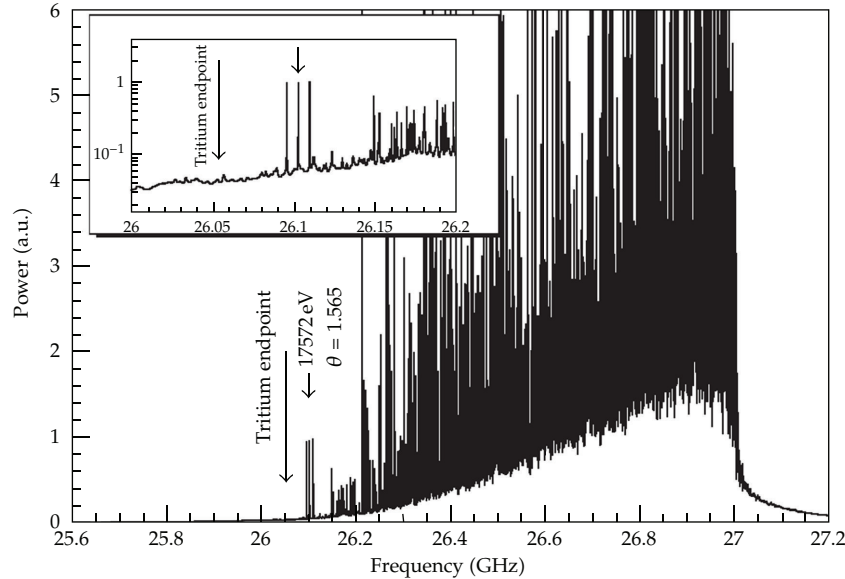


FIGURE 28: Simulated frequency spectrum of  $10^5$  tritium decays observed within a  $30 \mu\text{s}$  interval in a 10 m long source with a field of 1 T. The inset shows the triplet of lines produced by a high energy electron (reprinted with permission from [170], Copyright (2009) by the American Physical Society).

course these estimates also depend on how efficient an actual antenna configuration could collect the signal power emitted by the electrons.

The correct reconstruction of electron energies from the detected cyclotron radiation is complicated by the Doppler shift the signals experience due to the motion of the electrons parallel to the magnetic field lines. Two different antenna configurations are proposed to remedy this problem. In the first case, two antennae are placed on axis at both ends of the source volume (see endcap antennae on Figure 27). While one of the antennae will detect a blue-shifted signal due to the parallel velocity component of the electron towards it, the other will detect the red-shifted version of the same signal. Combining these signals, the unshifted electron energy can then be reconstructed.

The second configuration discussed consists of arrays of evenly spaced microwave antennae oriented transverse to the magnetic field. Passing electrons will induce signals that sweep from blue shift to red shift in the individual antennae. When these signals are summed up with an appropriate choice of delay lines, the unshifted cyclotron frequency should sum coherently, while the contributions from Doppler shifts sum incoherently and should thus be suppressed. The resulting output will then appear at the unshifted frequency  $\omega$  with an amplitude modulated due to the periodically varying response function of the antennae along the array. This modulation gives rise to two sideband peaks in the signal that can help to discriminate a real high energy electron signal from background signals caused for example by sidebands from lower energy signals.

A simulation performed by Monreal and Formaggio [170] for  $10^5$  tritium decays observed within a  $30 \mu\text{s}$  interval is shown in Figure 28. As discussed above, signals of high energy electrons show up as triplets of lines in the lower

part of the frequency spectrum. Because this region is also populated by sideband signals from lower energy electrons, the coincident detection of at least two of the three lines is required to confidently identify an endpoint electron. Extending this requirement to all three lines for the positive identification of a high energy electron, a total source strength of ca.  $10^9$  Bq can be allowed to keep background from accidental coincidences on an acceptable level.

The proposed technique presents very different systematic errors than those present in MAC-E filter experiments like KATRIN. Advantages are the ability to correct for fluctuations of the source density, as the complete spectrum is monitored by the experiment. The absence of an electrostatic spectrometer should enable a more scalable experiment as the energy resolution is not limited by the size of a MAC-E filter, but by the observation time for individual electrons and ultimately by the irreducible energy spread due to the excitation of rotational and vibrational final states of the daughter molecule emerging from the tritium decay. On the other hand, care has to be taken to eliminate the effects of Doppler shifts that alter the frequency picked up by the microwave antennae. Inhomogeneities in the  $B$ -field are a source of line broadening, while drifts of the magnetic field will shift the overall spectrum. Electron- $T_2$  scattering and signal pileup will limit the allowed source density and therefore influence the achievable signal rate in the important endpoint region of the spectrum.

To verify the ability to detect the cyclotron emission of individual electrons and to investigate the achievable resolution, a test experiment [171] is currently being set up at the University of Washington. In the setup, a small magnetic bottle within a 1 T superconduction magnet is used to capture 17.8 keV conversion electrons from a  $^{83\text{m}}\text{Kr}$  source. Different

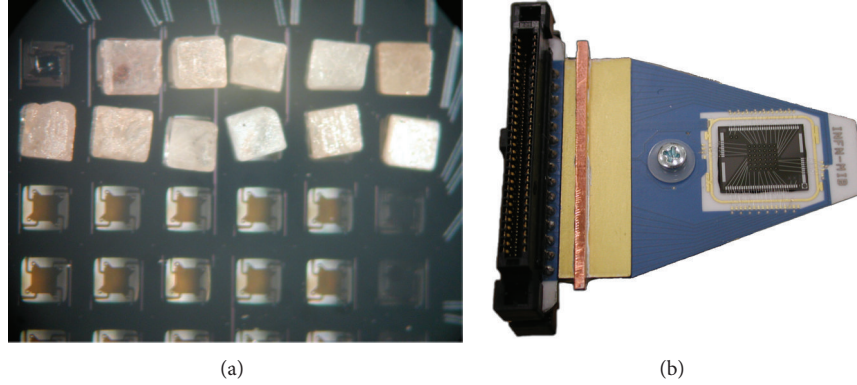


FIGURE 29: (a)  $\text{AgReO}_4$  crystals glued to a  $6 \times 6$  pixel XRS thermistor array. (b) View of the  $6 \times 6$  array with readout lines (images courtesy of Nucciotti [177]).

antenna designs will be tested in an attempt to observe the cyclotron emission from these electrons.

**5.2. MARE.** The “Microcalorimeter Arrays for a Rhenium Experiment” (MARE) collaboration is working to further the development of sensitive microcalorimeters to investigate  $^{187}\text{Re}$   $\beta$ -decay. The current activities in the MARE collaboration are organized in two phases [172]: in MARE-1 several groups are working on alternative microcalorimeter concepts which will be tested by setting up neutrino mass experiments with sensitivities in the order of a few eV. Besides the selection of the most sensitive detector technology, this phase will also be used to investigate the use of the EC decay of  $^{163}\text{Ho}$  as an alternative to the study of rhenium  $\beta$ -decay to determine the neutrino mass [173] (see also Section 5.3). The consideration of  $^{163}\text{Ho}$  was triggered by persisting difficulties with superconducting metallic rhenium absorbers coupled to the sensors [174]. Thermalization of the energy deposited in  $\beta$ -decays seems to be hindered by the excitation of long lived states in the rhenium absorber. The nature of these states can presently only be speculated upon [175]. After selecting the most successful technique, a full scale experiment with sub-eV sensitivity to the neutrino mass will then be set up in MARE phase 2.

The technical developments generally aim at two main goals: first to improve the energy resolution of the detectors and secondly to shorten the response time of the signals in order to reduce pileup problems. The various groups in the MARE collaboration work on different techniques to achieve these goals.

Groups from University Milano-Bicocca, NASA/GSFC, and Wisconsin are working together to develop arrays of silicon implanted thermistors coupled to  $\text{AgReO}_4$  absorbers [176] (see Figure 29). The experiment that is currently being set up can accommodate up to eight  $36$  pixel arrays with  $0.5\text{ mg}$   $\text{AgReO}_4$  absorbers of  $0.27\text{ Bq}$  activity each. The absorber crystals used are cut in a regular shape of  $600 \times 600 \times 250\text{ }\mu\text{m}^3$  from large single crystals and are glued to the thermistors with an intermediate layer of thin pure silicon spacers. For readout of the thermistors a cold buffer stage using JFETs at  $120\text{ K}$  is installed as close as possible

to the sensors, followed by a main amplifier stage at room temperature. With this system, it is possible to achieve an energy and time resolutions of  $25\text{ eV}$  and  $250\text{ }\mu\text{s}$ , respectively [174]. After a first test run with 10  $\text{AgReO}_4$  crystals on one array and two Sn absorbers on a second array to investigate the environmental background near the rhenium endpoint, a  $^{187}\text{Re}$   $\beta$ -decay measurement with 72 channels should start and provide a sensitivity of  $4.5\text{ eV}$  at 90% C.L. within three years running time [174]. With all 8 arrays instrumented a sensitivity of  $3.3\text{ eV}$  at 90% C.L. would be reached with  $7 \cdot 10^9$  rhenium decays.

Besides their work on thermistors with  $\text{AgReO}_4$  absorbers, the group from Milano-Bicocca is also investigating the use of Microwave Kinetic Inductance Detectors (MKIDs) for measurements of  $^{163}\text{Ho}$  EC decays. These devices are superconducting resonators in the  $1\text{--}10\text{ GHz}$  region that exploit the temperature dependence of superconducting films. An advantage with these sensors is the easy readout of a few thousand detectors using frequency multiplexing techniques [178].

The University of Genoa is working together with groups from University of Miami and University Lisbon/ITN on the development of Transition Edge Sensors (TES) coupled to metallic rhenium absorber crystals [179]. TES sensors exploit the sharp rise of resistance with temperature of a superconductor operated at the phase transition from normal to superconducting behaviour. This allows for a very sensitive detector compared to conventional semiconductor thermistors, but has the drawback of being less stable in operation and having a lower saturation energy. The sensors are based on a Ir-Au bi-layer configured in a double S-shape. The normal resistance of the circuit is  $2\text{ }\Omega$  and by adjusting the layer thickness, the transition temperature is brought to ca.  $80\text{ mK}$ . The superconducting layer is deposited on a silicon substrate onto which, on the other side, a superconducting rhenium absorber of  $200\text{--}300\text{ mg}$  is glued (see Figure 30). Two Al-Si wires are used for readout of the TES and for connection to a heat bath cooled by a dilution refrigerator. With this design an energy resolution of  $11\text{ eV FWHM}$  and a rise time of  $160\text{ }\mu\text{s}$  have been achieved [179]. Their planned phase I experiment will accommodate 300 TES detectors with



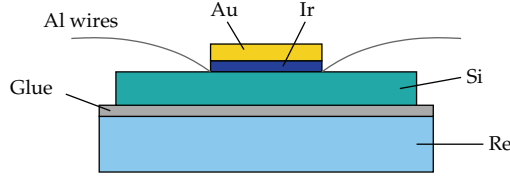


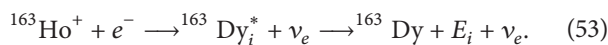
FIGURE 30: Schematic drawing of the Ir-Au/Re TES microcalorimeter developed at Genoa.

about 0.25 Bq activity per element, which would allow a sensitivity on the neutrino mass of 2 eV with three years worth of data taking. As an alternative to rhenium the group at Genoa is also working on the development of TES sensors with  $^{163}\text{Ho}$  loaded absorbers.

At the University of Heidelberg, work is ongoing on the development of so-called Metallic Magnetic Calorimeters (MMC) [180]. In contrast to TES sensors or thermistors that exploit the change of resistivity of the sensors with temperature, these detectors are measuring the change in magnetization of a paramagnetic material. Promising results have been obtained with gold absorbers, where resolutions down to 2 eV FWHM and signal rise times of about 90 ns have been achieved for soft X-rays around 6 keV energy [181]. The resolution with rhenium absorbers, however, was found to be 44 eV FWHM at signal rise times below 10  $\mu\text{s}$ . The use of MMC detectors with holmium implanted absorbers produced more encouraging results and led to the formation of the ECHO collaboration to further investigate this technique (see Section 5.4).

All these activities should finally lead to a selection of the most suitable technique for a rhenium or holmium based large-scale neutrino mass experiment with sub-eV sensitivity. According to [172], a staged approach, where a total of five  $10^4$  detector arrays is deployed one per year, would, after 10 years running time, enable a statistical sensitivity better than 0.25 eV. One has to keep in mind however that effects like the beta-environmental fine structure (see Section 3.5) are difficult to estimate and have to be investigated in parallel to the technical developments within the next years.

**5.3. Electron Capture on  $^{163}\text{Ho}$ .** A promising alternative to  $\beta$ -decay measurements is the study of electron capture (EC) decays of  $^{163}\text{Ho}$  to measure the neutrino mass. The decay process considered is



The deexcitation spectrum of the intermediate state  $^{163}\text{Dy}_i^*$  is given by a series of lines at energies  $E_i$  which correspond to the dissipated binding energy of the electron hole in the final atom. The  $Q$ -value of the reaction is given by the mass difference of mother and daughter nucleus in the ground

state. Like the electron energy spectrum in  $\beta$ -decay this spectrum depends on the square of the neutrino mass [182]

$$\begin{aligned} \dot{N}(E_C) = \frac{d\lambda_{EC}}{dE_C} = \frac{G_F^2 \cos^2 \theta_C}{4\pi^2} (Q - E_C) \sqrt{(Q - E_C)^2 - m_{\nu_e}^2} \\ \cdot \sum_i n_i C_i \beta_i^2 B_i \frac{\Gamma_i}{2\pi} \frac{1}{(E_C - E_i)^2 + \Gamma_i^2/4}. \end{aligned} \quad (54)$$

The measured calorimetric energy  $E_C$  when the source is embedded in a microcalorimeter contains the complete deexcitation energy of the daughter atom that is dispersed in the form of electrons and X-rays. The atomic levels involved are described by Breit-Wigner resonances with finite widths  $\Gamma_i$ . Additionally,  $n_i$  is the fraction of occupancy of the  $i$ th atomic shell,  $C_i$  is the nuclear shape factor,  $\beta_i$  is the squared Coulomb amplitude of the electron radial wave function at the origin of the electron radial wave function and  $B_i$  is an atomic correction for electron exchange and overlap. The use of  $^{163}\text{Ho}$  is favored due to its very low  $Q$ -Value in the range of 2.3 keV to 2.8 keV [182]. Due to the low  $Q$ -value and selection rules only electrons from the  $M_1$ ,  $M_2$ ,  $N_1$ ,  $N_2$ ,  $O_1$ ,  $O_2$ , and  $P_1$  shells can be captured and the spectrum is expected to have the shape shown in Figure 31(a), with the influence of the neutrino mass most pronounced near the endpoint as shown in Figure 31(b). The count rate in the endpoint region strongly drops with increasing distance between the closest atomic level and the  $Q$ -value of the reaction. At the same time the amount of activity that can be allowed in a single calorimetric detector has to be limited in order to reduce the unresolvable pileup of signals which otherwise distorts the measured spectrum. In order to gather the required statistics to reach sub-eV sensitivity with this method it is therefore necessary to operate large numbers of small detectors in parallel.

In contrast to the calorimetric method described above, the first measurements applying  $^{163}\text{Ho}$  EC decay to constrain the neutrino mass actually made use either of X-rays emitted after the decay [183] or of inner Bremsstrahlung photons created in the process of radiative electron capture [46]. Studying X-rays emitted after the EC decay allows one to determine the ratios of capture rates from the  $M$  and  $N$  shells as well as the absolute  $M$  capture rates, from which the neutrino mass can be reconstructed. Applying this method, Yasumi et al. obtained an upper limit on the electron neutrino mass of  $m(\nu_e) < 490$  eV at 68% C.L. [48]. On the other hand, Springer et al. made use of the inner Bremsstrahlung method to obtain an upper limit of  $m(\nu_e) < 225$  eV at 95% C.L. [47].

First measurements of the calorimetric  $^{163}\text{Ho}$  EC spectrum [184–186] have not yet achieved sufficient sensitivity to improve on the above mentioned limits due to limitations in energy resolution and statistics of the measurements. A very recent measurement of the calorimetric deexcitation spectrum using Metallic Magnetic Calorimeters (see Section 5.4) reached a high energy resolution of 12 eV FWHM [175], but was hampered by a background of EC decays from  $^{144}\text{Pm}$  that contaminated the detector during the  $^{163}\text{Ho}$  implantation process.

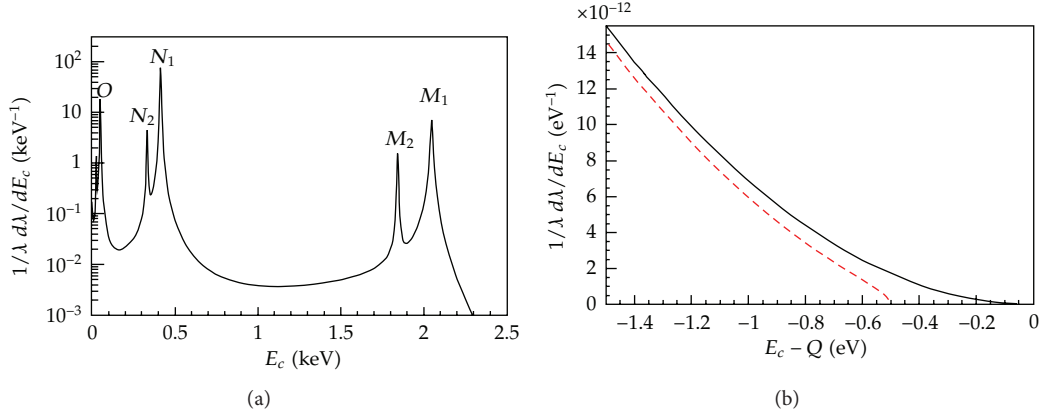


FIGURE 31: Deexcitation spectrum of  $^{163}\text{Ho}$  for  $Q = 2.5$  keV (a). (b) shows a zoom into the endpoint region of the spectrum with the effect of a 0.5 eV neutrino mass indicated by the red dashed line (reprinted from [182], Copyright 2011, with permission from Elsevier).

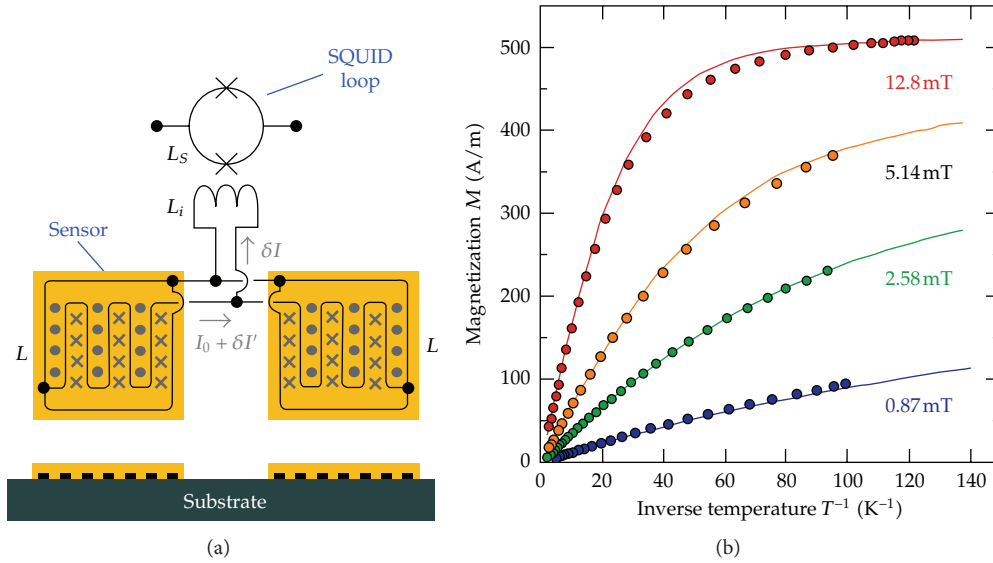


FIGURE 32: (a) Schematic view of a microstructured MMC type detector. (b) Dependence of the sensor magnetization on the inverse sensor temperature (figures courtesy of Gastaldo [188]).

**5.4. ECHO.** Groups from Heidelberg University and MPIK, the Saha institute, ISOLDE/CERN, and the Petersburg Nuclear Physics institute are working on the development of the Electron Capture  $^{163}\text{Ho}$  experiment ECHO [175], that is based on micro-structured MMC detectors [187]. In these detectors, the temperature change following an energy absorption is measured by the change of magnetization of a paramagnetic sensor material (Au:Er) sitting in an external magnetic field.

The MMC detectors developed by the Heidelberg group consist of pairs of superconducting meander shaped Nb pickup coils covered with planar Au:Er sensors (see Figure 32(a)). To produce a magnetic field in the sensor material, a persistent current is injected into the superconducting loop formed by the two meanders. A temperature rise in one of the sensors leads to a decrease in magnetization of the material (see Figure 32(b)) and consequently to a small

current  $\delta I$  through the input coil of a SQUID circuit connected for readout in parallel to the meander coils. The sensors, which are operated at temperatures below 100 mK, are coupled via thermalization leads to the heat-sink areas on the chip that act as a thermal bath. Absorber materials containing radioisotopes can be coupled to the Au:Er sensor areas. Energy deposited in the absorber due to a radioactive decay is thermalized and causes a temperature pulse in the sensor.

For Holmium EC decay measurements the relatively short half-life of the isotope of about 4570 years makes it possible to work with  $^{163}\text{Ho}$  implanted gold absorbers that are deposited onto the Au:Er sensors. In a measurement with a prototype detector [175], this technique enabled an energy resolution of 12 eV (FWHM) and fast rise times of the signals of about 90 ns. Figure 33 shows the calorimetric spectrum obtained in that measurement from which a  $Q$ -value of  $(2.80 \pm 0.08)$  keV has been extracted. This is not

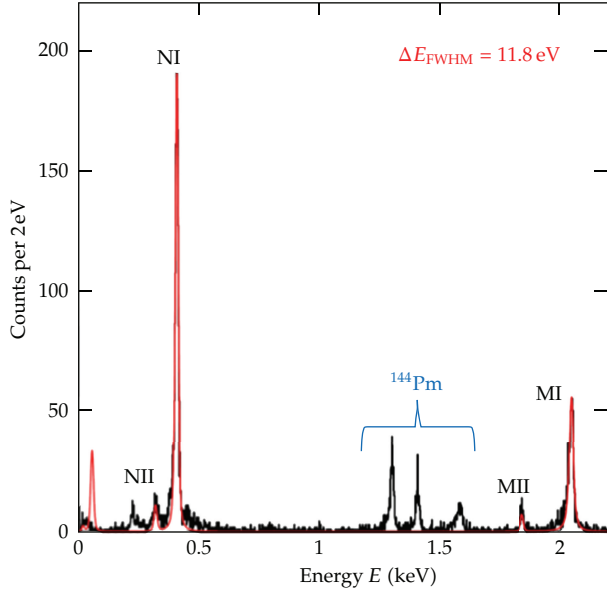


FIGURE 33: Calorimetric energy spectrum for electron capture decays of  $^{163}\text{Ho}$ . The peaks around 1.5 keV originate from  $^{144}\text{Pm}$  decays.  $^{144}\text{Pm}$  was present as an admixture in the implantation beam (figure courtesy of Gastaldo [188]).

compatible with the recommended value from atomic mass measurements of  $Q = (2.555 \pm 0.016) \text{ keV}$  [189], but agrees with other calorimetric measurements [186]. The reasons for this discrepancy are suspected to be uncertainties in the theoretical parameters required to extract the  $Q$ -value (namely the square of the electron wavefunction at the nucleus and exchange and overlap corrections as well as the width of the peaks  $\Gamma_i$ ). Clearly more investigations are needed to resolve this discrepancy, as the  $Q$ -value is crucial for the interpretation of future neutrino mass experiments based on Holmium EC decay.

Besides the single pixel performance, where work is ongoing to further improve the energy resolution into the  $\Delta E < 3 \text{ eV}$  range, the use of MMC detectors in a neutrino mass experiment requires parallel operation and readout of a large number of detector pixels in order to gather the necessary statistics. The ECHO team proposes to read out arrays of MMC detector pixels using frequency domain multiplexing techniques in the microwave region. For this purpose the SQUIDS of the individual detector pixels are coupled to superconducting resonators, each operating at a characteristic frequency between 4 and 8 GHz and connected to a single readout line.

In order to set up a competitive neutrino mass experiment based on the EC decay of  $^{163}\text{Ho}$ , efforts are made to improve on the experimental and theoretical aspects of the method. Precision mass measurements using high resolution Penning traps [25] should enable a determination of the  $Q$ -value of the decay with eV accuracy. Alternative methods are tested to produce a high purity  $^{163}\text{Ho}$  source, as EC decays of  $^{144}\text{Pm}$ , that was implanted together with the Holmium ions, contributed the largest background to the present

measurement. An improved description of the atomic physics aspects of the decay will be worked on to obtain a more accurate shape of the  $^{163}\text{Ho}$  calorimetric spectrum. The aim of these efforts of the ECHO collaboration is to set up a first neutrino mass experiment with sufficiently large detector arrays ( $\leq 1000$  sensors) to reach a sensitivity on the electron neutrino mass in the few eV range. If this is successful, a large-scale experiment with up to  $10^5$  detectors can then be deployed to reach sub-eV sensitivity.

## 6. Conclusion

Direct neutrino mass measurements only rely on kinematic variables in  $\beta$ -decay (as well as energy-momentum conservation) to deduce the average electron neutrino mass  $m^2(\nu_e)$  in a model-independent way. The experimental observable  $m^2(\nu_e)$  in  $\beta$ -decay (or EC) is formed by the incoherent sum of the neutrino mass eigenstates  $m(\nu_i)$ , resulting in a tiny spectral modification in a narrow region close to  $E_0$ , where the emitted neutrino is still nonrelativistic. Experimental challenges in  $\beta$ -spectroscopy are thus related to obtaining excellent statistics close to the  $\beta$ -decay endpoint, favoring  $\beta$ -emitters with a very short half-life such as tritium and a low endpoint energy such as  $^{187}\text{Re}$ , tritium and the EC isotope  $^{163}\text{Ho}$ , as well as to maintaining a very small background rate at  $E_0$ . The latter is a nontrivial issue, given that direct neutrino mass experiments are performed at the surface of the earth, where they are exposed to the full flux of cosmic rays. Finally, an excellent energy resolution with precisely known characteristics as well as an excellent control of systematic effects is mandatory. These requirements have resulted in the development of two generic experimental techniques.

On the one side, there is the calorimetric approach, where the  $\beta$ -emitter is embedded into or identical to the detector, usually operated as a microcalorimeter (absorber materials include  $\text{AgReO}_4$  crystals or  $^{163}\text{Ho}$  implanted gold absorbers). This method allows to measure the entire decay energy; however, the entire  $\beta$ -spectrum has to be recorded. This calls for the operation of large arrays of microcalorimeters to circumvent potential pulse pileup effects due to the rather slow signal read-out of bolometers. The main focus in this field is thus targeted at developing new read-out schemes to improve the energy resolution (down to a few eV) while at the same time improving signal read-out times (down to a few  $\mu\text{s}$ ).

Over the past years, substantial progress has been made by several groups (MARE, ECHO) with regard to improved read-out methods, which now include silicon implanted thermistors, transition edge sensors (TES) and microwave kinetic inductance detectors (MKID). These methods are complemented by metallic magnetic calorimeters (MMC), which measure the change in magnetization. The field is characterized by a rapid progress in this area, so that the most important decision with regard to a future microcalorimeter array with sub-eV sensitivity will be to select the most suitable read-out technique for high-precision spectroscopy of the  $\beta$ -decay of  $^{187}\text{Re}$  or the EC-process of  $^{163}\text{Ho}$ . The big advantage

here is the possibility to follow a staged approach by continuously enlarging and upgrading the microcalorimeter array in operation.

On the other side, there is the spectrometer approach, where the  $\beta$ -emitter and the energy analysis of  $\beta$ -decay electrons close to the endpoint by a spectrometer are separated. This approach has been refined by a long list of tritium  $\beta$ -experiments. Over the past two decades the Mainz and Troitsk experiments have pioneered the so-called MAC-E-filter technique, where  $\beta$ -decay electrons from a gaseous or quench-condensed source are adiabatically guided to an electrostatic retarding spectrometer for energy analysis in an integral mode. This technique allows to combine a source of high intensity with a spectrometer of high energy resolution to perform superior  $\beta$ -spectroscopy. This technique has improved the neutrino mass sensitivity to the present value of 2 eV.

The successor to the Mainz and Troitsk experiments is the large-scale KATRIN project, which is currently being assembled by an international collaboration at KIT. The experiment will combine a gaseous molecular tritium source of highest intensity and stability with a very large electrostatic retarding spectrometer of unprecedented energy resolution to improve the experimental sensitivity by one order of magnitude to 200 meV (90% C.L.). This sensitivity is the benchmark for the entire field and will allow investigating almost the entire parameter space of quasi-degenerated neutrino masses.

Over the past years, extensive R&D work and test measurements by KATRIN groups have resulted in substantial improvements of the performance of key components (e.g., with regard to source stability and HV stability). Moreover, a variety of novel background reduction techniques in the electrostatic spectrometers have been implemented successfully, offering the potential of measurements almost free of background. An important tool in doing so has been the KASSIOPEIA code, which allows field calculations and particle tracking with unprecedented precision and speed. The long-term scanning of the tritium spectrum will prospectively start at the end of 2015 with first KATRIN sub-eV results shortly thereafter. At present the experiment is investigating its physics reach in the search for sterile neutrinos from the sub-eV up to the multi-keV mass regime, as well as for other physics beyond the Standard Model.

A novel ansatz in  $\beta$ -spectroscopy is finally pursued by the Project 8 collaboration through developing methods to detect the coherent cyclotron radiation emitted by individual  $\beta$ -decay electrons from a gaseous tritium source by a sensitive array of microwave antennae. The project is also developing other methods to detect this radiation and thus still in the early stages of R&D work.

The challenges in further improving the precision in  $\beta$ -spectroscopy to ultimately push the neutrino mass sensitivity to the lowest possible value are formidable indeed, but major advances have already been made in diverse areas such as tritium process control, cryo-technology, ultra high vacuum methods, precision high voltage, precision electron spectroscopy as well as bolometer read-out technology, and detector and electronics technology in general. Over the

next 5–10 years, we can thus expect high-quality and high-precision neutrino mass results from the large-scale KATRIN experiment, as well as from other promising techniques, which are exploited in the framework of the MARE, ECHO, and Project 8 collaborations.

In conclusion, we would like to emphasize that it is only by comparing high-precision results from direct neutrino mass measurements with searches for neutrinoless double  $\beta$ -decay and cosmological studies that we can obtain the complete picture of neutrino masses to fully assess the unique role of neutrinos in particle physics and in cosmology.

## Acknowledgments

This work has been supported in part by the Bundesministerium für Bildung und Forschung (BMBF) under Contract nos. 05A11PM2 and 05A08VK2, the Deutsche Forschungsgemeinschaft (DFG) via Transregio 27 “Neutrinos and beyond,” and Open Access Publishing Fund of KIT. S. Mertens would like to thank Karlsruhe House of Young Scientists (KHYS) for support. The authors would like to express their gratitude and thanks to their colleagues in the ECHO, KATRIN, MARE, Mainz, Troitsk, and Project 8 Collaborations, who have given us generous support and information when preparing this paper. Their special thanks go to Ernst Otten, Markus Steidl, and Thomas Thümmel. Finally, the authors would like to dedicate this paper to two of their colleagues, who died within the last two years and to whom they are very much indebted: our colleague Academician Vladimir M. Lobashev of the INR Troitsk, who has pioneered many techniques described in this paper as head of the Troitsk experiment, and who has contributed significantly to the progress in this field and others, and our colleague Jochen Bonn from Mainz, the kind and genius motor in the laboratory of the Mainz experiment and one of the most imaginative and smartest colleagues in designing and constructing the KATRIN experiment.

## References

- [1] T. Kajita, “Atmospheric neutrinos,” *Advances in High Energy Physics*, vol. 2012, Article ID 504715, 24 pages, 2012.
- [2] V. Antonelli, L. Miramonti, C. Peña Garay, and A. Serenelli, “Solar neutrinos,” *Advances in High Energy Physics*. In press.
- [3] J. M. Conrad, C. M. Ignarra, G. Karagiorgi, M. H. Shaevitz, and J. Spitz, “Sterile neutrino fits to short baseline neutrino oscillation measurements,” *Advances in High Energy Physics*. In press.
- [4] J. J. Hartnell, T. Kobayashi, and G. Feldman, “Long baseline neutrino oscillation experiments,” *Advances in High Energy Physics*. In press.
- [5] T. Lasserre, Y. Wang, and S. B. Kim, “Reactor neutrinos,” *Comptes Rendus Physique*, vol. 6, pp. 749–757, 2005.
- [6] J. Lesgourgues and S. Pastor, “Neutrino mass from cosmology,” *Advances in High Energy Physics*, vol. 2012, Article ID 608515, 34 pages, 2012.
- [7] S. Petcov, “The nature of massive neutrinos,” *Advances in High Energy Physics*. In press.
- [8] R. N. Mohapatra, “Origin of neutrino masses and mixings,” *Nuclear Physics*, vol. 91, no. 1–3, pp. 313–320, 2001.



- [9] E. Komatsu, K. M. Smith, J. Dunkley et al., “Seven-Year Wilkinson Microwave Anisotropy Probe (WMAP) observations: cosmological interpretation,” *Astrophysical Journal Supplement*, vol. 192, article 18, 2011.
- [10] H. Aihara, C. Allende Prieto, D. An et al., “The eighth data release of the Sloan Digital Sky Survey: first data from SDSS-III,” *Astrophysical Journal, Supplement Series*, vol. 193, no. 2, article 29, 2011, Erratum in *Astrophysical Journal, Supplement Series*, vol. 195, article 26, 2011.
- [11] K. N. Abazajian, E. Calabrese, A. Cooray et al., “Cosmological and astrophysical neutrino mass measurements,” *Astroparticle Physics*, vol. 35, no. 4, pp. 177–184, 2011.
- [12] A. Giuliani and A. Poves, “Neutrinoless double-beta decay,” *Advances in High Energy Physics*, vol. 2012, Article ID 857016, 38 pages, 2012.
- [13] H. V. Klapdor-Kleingrothaus and I. V. Krivosheina, “The evidence for the observation of  $0\nu\beta\beta$  decay: the identification of  $0\nu\beta\beta$  events from the full spectra,” *Modern Physics Letters A*, vol. 21, no. 20, pp. 1547–1566, 2006.
- [14] M. Auger, D. J. Auty, P. S. Barbeau et al., “Search for neutrinoless double-beta decay in  $^{136}\text{Xe}$  with EXO-200,” *Physical Review Letters*, vol. 109, no. 3, Article ID 032505, 6 pages, 2012.
- [15] G. L. Fogli, E. Lisi, A. Marrone et al., “Global analysis of neutrino masses, mixings and phases: entering the era of leptonic CP violation searches,” *Physical Review D*, vol. 86, no. 1, Article ID 013012, 10 pages, 2012.
- [16] T. J. Loredo and D. Q. Lamb, “Bayesian analysis of neutrinos observed from supernova SN 1987A,” *Physical Review D*, vol. 65, no. 6, Article ID 063002, 2002.
- [17] G. Pagliaroli, F. Rossi-Torres, and F. Vissani, “Neutrino mass bound in the standard scenario for supernova electronic antineutrino emission,” *Astroparticle Physics*, vol. 33, no. 5–6, pp. 287–291, 2010.
- [18] R. G. H. Robertson and D. A. Knapp, “Direct measurement of neutrino mass,” *Annual Review of Nuclear and Particle Science*, vol. 38, p. 185, 1988.
- [19] E. Holzschuh, “Measurement of the neutrino mass from tritium  $\beta$ -decay,” *Reports on Progress in Physics*, vol. 55, no. 7, pp. 1035–1091, 1992.
- [20] J. F. Wilkerson and R. G. H. Robertson, “Direct measurement of neutrino mass,” in *Current Aspects of Neutrino Physics*, D. O. Caldwell, Ed., p. 39, Springer, Berlin, Germany, 2001.
- [21] C. Weinheimer, “Laboratory limits on neutrino masses,” in *Massive Neutrinos*, G. Altarelli and K. Winter, Eds., Springer Tracts in Modern Physics, p. 25, Springer, 2003.
- [22] E. W. Otten and C. Weinheimer, “Neutrino mass limit from tritium  $\beta$  decay,” *Reports on Progress in Physics*, vol. 71, no. 8, Article ID 086201, 2008.
- [23] A. Giuliani, “Neutrino physics with low-temperature detectors,” *Journal of Low Temperature Physics*, vol. 167, pp. 991–1003, 2012.
- [24] N. Severijns, M. Beck, and O. Naviliat-Cuncic, “Tests of the standard electroweak model in nuclear beta decay,” *Reviews of Modern Physics*, vol. 78, no. 3, pp. 991–1040, 2006.
- [25] K. Blaum, Y. N. Novikov, and G. Werth, “Penning traps as a versatile tool for precise experiments in fundamental physics,” *Contemporary Physics*, vol. 51, no. 2, pp. 149–175, 2010.
- [26] Ch. Weinheimer, M. Przyrembel, H. Backe et al., “Improved limit on the electron-antineutrino rest mass from tritium  $\beta$ -decay,” *Physics Letters B*, vol. 300, no. 3, pp. 210–216, 1993.
- [27] S. S. Masood, S. Nasri, J. Schechter, M. A. Tórtola, J. W. F. Valle, and C. Weinheimer, “Exact relativistic  $\beta$  decay endpoint spectrum,” *Physical Review C*, vol. 76, no. 4, Article ID 045501, 2007.
- [28] W. W. Repko and C.-E. Wu, “Radiative corrections to the end point of the tritium decay spectrum,” *Physical Review C*, vol. 28, no. 6, pp. 2433–2436, 1983.
- [29] S. Gardner, V. Bernard, and U.-G. Meißner, “Radiative tritium  $\beta$ -decay and the neutrino mass,” *Physics Letters B*, vol. 598, no. 3–4, pp. 188–196, 2004.
- [30] G. J. Stephenson and T. Goldman, “A possible solution to the tritium endpoint problem,” *Physics Letters B*, vol. 440, no. 1–2, pp. 89–93, 1998.
- [31] A. Y. Ignatiev and B. H. J. McKellar, “Possible new interactions of neutrino and the KATRIN experiment,” *Physics Letters B*, vol. 633, no. 1, pp. 89–92, 2006.
- [32] R. Dvornický, F. Šimkovic, and A. Faessler, “Beyond the standard model interactions in  $\beta$ -decay of tritium,” *Progress in Particle and Nuclear Physics*, vol. 64, no. 2, pp. 303–305, 2010.
- [33] J. Bonn, K. Eitel, F. Glück, D. Sevilla-Sanchez, N. Titov, and K. Blaum, “The KATRIN sensitivity to the neutrino mass and to right-handed currents in beta decay,” *Physics Letters B*, vol. 703, no. 3, pp. 310–312, 2011.
- [34] A. Saenz, S. Jonsell, and P. Froelich, “Improved molecular final-state distribution of  $\text{HeT}^+$  for the  $\beta$ -decay process of  $\text{T}_2$ ,” *Physical Review Letters*, vol. 84, no. 2, pp. 242–245, 2000.
- [35] N. Doss, J. Tennyson, A. Saenz, and S. Jonsell, “Molecular effects in investigations of tritium molecule  $\beta$  decay endpoint experiments,” *Physical Review C*, vol. 73, no. 2, pp. 1–10, 2006.
- [36] N. Doss and J. Tennyson, “Excitations to the electronic continuum of  $^3\text{HeT}^+$  in investigations of  $\text{T}_2\beta$ -decay experiments,” *Journal of Physics B*, vol. 41, no. 12, Article ID 125701, 2008.
- [37] B. J. Mount, M. Redshaw, and E. G. Myers, “Q value of  $^{115}\text{In} \rightarrow ^{115}\text{Sn}(3/2^+)$ : the lowest known energy  $\beta$  decay,” *Physical Review Letters*, vol. 103, Article ID 122502, 2009.
- [38] J. S. E. Wieslander, J. Suhonen, T. Eronen et al., “Known Q value of any nuclear decay: the rare  $\beta^-$  decay of  $^{115}\text{In}(9/2^+) \rightarrow ^{115}\text{Sn}(3/2^+)$ ,” *Physical Review Letters*, vol. 103, Article ID 122501, 2009.
- [39] R. Dvornický, K. Muto, F. Šimkovic, and A. Faessler, “Absolute mass of neutrinos and the first unique forbidden  $\beta$  decay of  $^{187}\text{Re}$ ,” *Physical Review C*, vol. 83, no. 4, Article ID 045502, 2011.
- [40] K. S. Hirata, T. Kajita, M. Koshiba et al., “Observation in the Kamiokande-II detector of the neutrino burst from supernova SN1987A,” *Physical Review D*, vol. 38, no. 2, pp. 448–458, 1988.
- [41] C. B. Bratton, D. Casper, A. Ciocio et al., “Angular distribution of events from SN1987A,” *Physical Review D*, vol. 37, no. 12, pp. 3361–3363, 1988.
- [42] E. N. Alekseev, L. N. Alekseeva, V. I. Volchenko et al., “Possible detection of a neutrino signal on 23 February 1987 at the Baksan underground scintillation telescope of the Institute of Nuclear Research,” *Journal of Experimental and Theoretical Physics Letters*, vol. 45, pp. 589–592, 1987.
- [43] G. G. Raffelt, “Particle physics from stars,” *Annual Review of Nuclear and Particle Science*, vol. 49, no. 1, pp. 163–216, 1999.
- [44] “Webpage of the SuperNova Early Warning System,” <http://snews.bnl.gov>.
- [45] J. F. Beacom, R. N. Boyd, and A. Mezzacappa, “Technique for direct eV-scale measurements of the Mu and Tau neutrino masses using supernova neutrinos,” *Physical Review Letters*, vol. 85, no. 17, pp. 3568–3571, 2000.
- [46] A. De Rújula, “A new way to measure neutrino masses,” *Nuclear Physics B*, vol. 188, no. 3, pp. 414–458, 1981.

- [47] P. T. Springer, C. L. Bennett, and P. A. Baisden, "Measurement of the neutrino mass using the inner bremsstrahlung emitted in the electron-capture decay of  $^{163}\text{Ho}$ ," *Physical Review A*, vol. 35, no. 2, pp. 679–689, 1987.
- [48] S. Yasumi, H. Maezawa, K. Shima et al., "The mass of the electron neutrino from electron capture in  $^{163}\text{Ho}$ ," *Physics Letters B*, vol. 334, no. 1-2, pp. 229–233, 1994.
- [49] M. Jung, F. Bosch, K. Beckert et al., "First observation of bound-state  $\beta$ -decay," *Physical Review Letters*, vol. 69, no. 15, pp. 2164–2167, 1992.
- [50] S. C. Curran, J. Angus, A. L. Cockcroft et al., "Investigation of soft radiations—II. The beta spectrum of tritium," *Philosophical Magazine Series*, vol. 40, pp. 53–60, 1949.
- [51] V. A. Lubimov et al., "An estimate of the  $\nu_e$  mass from the  $\beta$ -spectrum of tritium in the valine molecule," *Physics Letters B*, vol. 94, p. 266, 1980.
- [52] S. Boris, A. Golutvin, L. Laptin et al., "Neutrino mass from the beta spectrum in the decay of tritium," *Physical Review Letters*, vol. 58, no. 20, pp. 2019–2022, 1987.
- [53] M. Fritschi, E. Holzschuh, W. Kündig, J. W. Petersen, R. E. Pixley, and H. Stüssi, "An upper limit for the mass of  $\bar{\nu}_e$  from tritium  $\beta$ -decay," *Physics Letters B*, vol. 173, no. 4, pp. 485–489, 1986.
- [54] J. F. Wilkerson, T. J. Bowles, J. C. Browne et al., "Limit on anti- $\nu_e$  mass from free-molecular-tritium beta decay," *Physical Review Letters*, vol. 58, pp. 2023–2026, 1987.
- [55] E. T. Lippmaa, R. I. Pikver, E. R. Suurmaa et al., "Mass difference of the  $T - 3\text{He}$  doublet and the problem of the rest mass of the electron antineutrino," *Soviet Physics Doklady*, vol. 30, p. 393, 1985.
- [56] R. S. Van Dyck Jr., D. L. Farnham, and P. B. Schwinberg, "Tritium-helium-3 mass difference using the penning trap mass spectroscopy," *Physical Review Letters*, vol. 70, no. 19, pp. 2888–2891, 1993.
- [57] Sz. Nagy, T. Fritioff, M. Björkhage, I. Bergström, and R. Schuch, "On the Q-value of the tritium  $\beta$ -decay," *Europhysics Letters*, vol. 74, no. 3, pp. 404–410, 2006.
- [58] R. G. H. Robertson, T. J. Bowles, G. J. Stephenson et al., "Limit on anti- $\nu_e$  mass from the observation of the  $\beta$  decay of molecular tritium," *Physical Review Letters*, vol. 67, pp. 957–960, 1991.
- [59] E. Holzschuh, M. Fritschi, and W. Kündig, "Measurement of the electron neutrino mass from tritium  $\beta$ -decay," *Physics Letters B*, vol. 287, no. 4, pp. 381–388, 1992.
- [60] H. Kawakami, S. Kato, T. Ohshima et al., "New upper bound on the electron anti-neutrino mass," *Physics Letters B*, vol. 256, no. 1, pp. 105–111, 1991.
- [61] C. R. Ching, T.-H. Ho, D.-Q. Liang et al., "A possible explanation of the negative values of  $m_{\nu_e}^2$  obtained from the  $\beta$  spectrum shape analyses," *International Journal of Modern Physics A*, vol. 10, pp. 2841–2850, 1995.
- [62] W. Stoeffl and D. J. Decman, "Anomalous structure in the  $\beta$  decay of gaseous molecular tritium," *Physical Review Letters*, vol. 75, no. 18, pp. 3237–3240, 1995.
- [63] Ch. Weinheimer, B. Degenddag, A. Bleile et al., "High precision measurement of the tritium  $\beta$  spectrum near its endpoint and upper limit on the neutrino mass," *Physics Letters B*, vol. 460, no. 1-2, pp. 219–226, 1999.
- [64] C. Kraus, B. Bornschein, L. Bornschein et al., "Final results from phase II of the Mainz neutrino mass search in tritium  $\beta$  decay," *European Physical Journal C*, vol. 40, pp. 447–468, 2005.
- [65] A. I. Belesev, A. I. Bleuie, E. V. Geraskin et al., "Results of the Troitsk experiment on the search for the electron antineutrino rest mass in tritium beta-decay," *Physics Letters B*, vol. 350, no. 2, pp. 263–272, 1995.
- [66] V. M. Lobashev, V. N. Aseev, A. I. Belesev et al., "Direct search for mass of neutrino and anomaly in the tritium beta-spectrum," *Physics Letters B*, vol. 460, no. 1-2, pp. 227–235, 1999.
- [67] V. N. Aseev, A. I. Belesev, A. I. Berlev et al., "Upper limit on the electron antineutrino mass from the Troitsk experiment," *Physical Review D*, vol. 84, no. 11, Article ID 112003, 2011.
- [68] L. Fleischmann, J. Bonn, B. Bornschein et al., "On dewetting dynamics of solid films of hydrogen isotopes and its influence on tritium  $\beta$  spectroscopy," *European Physical Journal B*, vol. 16, no. 3, pp. 521–529, 2000.
- [69] P. Kruit and F. H. Read, "Magnetic field paralleliser for  $2\pi$  electron-spectrometer and electron-image magnifier," *Journal of Physics E*, vol. 16, no. 4, Article ID 016, pp. 313–324, 1983.
- [70] A. Picard, H. Backe, H. Barth et al., "A solenoid retarding spectrometer with high resolution and transmission for keV electrons," *Nuclear Instruments and Methods in Physics Research B*, vol. 63, no. 3, pp. 345–358, 1992.
- [71] V. M. Lobashev, "The search for the neutrino mass by direct method in the tritium beta-decay and perspectives of study it in the project KATRIN," *Nuclear Physics A*, vol. 719, no. 1-4, pp. C153–C160, 2003.
- [72] J. Angrik, T. Armbrust, A. Beglarian et al., "KATRIN design report 2004," Tech. Rep., Forschungszentrum, Karlsruhe, Germany, 2005.
- [73] B. Müller, T. Thümmel, J. Bonn et al., "Particle storage in MAC-E-filters," *Nuclear Physics B*, vol. 118, p. 481, 2003.
- [74] J. Bonn, L. Bornschein, B. Degen, E. W. Otten, and Ch. Weinheimer, "A high resolution electrostatic time-of-flight spectrometer with adiabatic magnetic collimation," *Nuclear Instruments and Methods in Physics Research A*, vol. 421, no. 1-2, pp. 256–265, 1999.
- [75] N. Steinbrink, *Simulation of electron neutrino mass measurements by time-of-flight with KATRIN [Ph.D. thesis]*, University of Münster, 2012.
- [76] V. N. Aseev, A. I. Belesev, A. I. Berlev et al., "Energy loss of 18 keV electrons in gaseous  $\text{T}_2$  and quench condensed  $\text{D}_2$  films," *European Physical Journal D*, vol. 10, no. 1, pp. 39–52, 2000.
- [77] H. Barth, L. Bornschein, B. Degen et al., "Status and perspectives of the Mainz neutrino mass experiment," *Progress in Particle and Nuclear Physics*, vol. 40, no. 1, pp. 353–376, 1998.
- [78] B. Bornschein, J. Bonn, L. Bornschein, E. W. Otten, and Ch. Weinheimer, "Self-charging of quench condensed tritium films," *Journal of Low Temperature Physics*, vol. 131, no. 1-2, pp. 69–88, 2003.
- [79] W. Kolos, B. Jeziorski, J. Rychlewski, K. Szalewicz, H. J. Monkhorst, and O. Fackler, "Molecular effects in tritium decay. IV. Effect of crystal excitations on neutrino mass determination," *Physical Review A*, vol. 37, no. 7, pp. 2297–2303, 1988.
- [80] G. J. Feldman and R. D. Cousins, "Unified approach to the classical statistical analysis of small signals," *Physical Review D*, vol. 57, no. 7, pp. 3873–3889, 1998.
- [81] C. Kraus, A. Singer, K. Valerius et al., "Limit on sterile neutrino contribution from the Mainz Neutrino Mass Experiment," <http://arxiv.org/abs/1210.4194>.
- [82] M. Galeazzi, F. Fontanelli, F. Gatti, and S. Vitale, "End-point energy and half-life of the  $^{187}\text{Re}$   $\beta$  decay," *Physical Review C*, vol. 63, no. 1, pp. 143021–143027, 2001.

- [83] C. Arnaboldi, G. Benedek, C. Brofferio et al., "Measurement of the p to s wave branching ratio of  $^{187}\text{Re}$   $\beta$  decay from beta environmental fine structure," *Physical Review Letters*, vol. 96, no. 4, Article ID 042503, 2006.
- [84] M. Sisti, C. Arnaboldi, C. Brofferio et al., "New limits from the Milano neutrino mass experiment with thermal microcalorimeters," *Nuclear Instruments and Methods in Physics Research A*, vol. 520, no. 1–3, pp. 125–131, 2004.
- [85] F. Gatti, "Microcalorimeter measurements," *Nuclear Physics B*, vol. 91, no. 1–3, pp. 293–296, 2001.
- [86] G. Drexlin, "KATRIN—direct measurement of a sub-eV neutrino mass," *Nuclear Physics B*, vol. 145, no. 1–3, pp. 263–267, 2005.
- [87] G. Mention, M. Fechner, Th. Lasserre et al., "Reactor antineutrino anomaly," *Physical Review D*, vol. 83, no. 7, Article ID 073006, 2011.
- [88] P. Anselmann, W. Hampel, G. Heusser et al., "GALLEX solar neutrino observations: complete results for GALLEX II," *Physics Letters B*, vol. 357, no. 1–2, pp. 237–247, 1995.
- [89] J. N. Abdurashitov, V. N. Gavrin, S. V. Girin et al., "Measurement of the response of a Ga solar neutrino experiment to neutrinos from a  $^{37}\text{Ar}$  source," *Physical Review C*, vol. 73, no. 4, Article ID 045805, 2006.
- [90] A. A. Aguilar-Arevalo, A. O. Bazarko, S. J. Brice et al., "Search for electron neutrino appearance at the  $\Delta m^2 \approx 1 \text{ eV}^2$  scale," *Physical Review Letters*, vol. 98, no. 23, Article ID 231801, 2007.
- [91] A. Seiersen-Riis and S. Hannestad, "Detecting sterile neutrinos with KATRIN like experiments," *Journal of Cosmology and Astroparticle Physics*, vol. 2011, no. 2, Article ID 011, 2011.
- [92] J. A. Formaggio and J. Barrett, "Resolving the reactor neutrino anomaly with the KATRIN neutrino experiment," *Physics Letters B*, vol. 706, no. 1, pp. 68–71, 2011.
- [93] A. Esmaili and O. L. G. Peres, "KATRIN sensitivity to sterile neutrino mass in the shadow of lightest neutrino mass," *Physical Review D*, vol. 85, no. 11, Article ID 117301, 2012.
- [94] V. S. Bastro-Gonzalez, A. Esmaili, and O. L. G. Peres, "Kinematical test of large extra dimension in beta decay experiments," *Physics Letters B*, vol. 718, no. 3, pp. 1020–1023, 2013.
- [95] J. M. Carmona and J. L. Cortés, "Testing Lorentz invariance violations in the tritium beta-decay anomaly," *Physics Letters B*, vol. 494, no. 1–2, pp. 75–80, 2000.
- [96] D. Furse et al., "KASSIOPEIA—the simulation package for the KATRIN experiment," to be published.
- [97] F. Glück, "Axisymmetric electric field calculation with zonal harmonic expansion," *Progress in Electromagnetics Research B*, vol. 32, pp. 319–350, 2011.
- [98] F. Glück, "Axisymmetric magnetic field calculation with zonal harmonic expansion," *Progress in Electromagnetics Research B*, vol. 32, pp. 351–388, 2011.
- [99] P. Renschler, *KESS—a new Monte Carlo simulation code for low-energy electron interactions in silicon detectors [Ph.D. thesis]*, KIT, 2011.
- [100] J. A. Formaggio, P. Lazić, T. J. Corona, H. Štefančič, H. Abraham, and F. Glück, "Solving for micro- and macro-scale electrostatic configurations using the Robin Hood algorithm," *Progress in Electromagnetics Research B*, vol. 39, pp. 1–37, 2012.
- [101] J. H. Verner, "Explicit Runge-Kutta methods with estimates of the local truncation error," *SIAM Journal on Numerical Analysis*, vol. 15, no. 4, pp. 772–790, 1978.
- [102] P. J. Prince and J. R. Dormand, "High order embedded Runge-Kutta formulae," *Journal of Computational and Applied Mathematics*, vol. 7, no. 1, pp. 67–75, 1981.
- [103] Ch. Tsitouras and S. N. Papakostas, "Cheap error estimation for Runge-Kutta methods," *Journal on Scientific Computing*, vol. 20, no. 6, pp. 2067–2088, 1999.
- [104] W. Hwang, Y.-K. Kim, and M. E. Rudd, "New model for electron-impact ionization cross sections of molecules," *Journal of Chemical Physics*, vol. 104, no. 8, pp. 2956–2966, 1996.
- [105] S. Trajmar, D. F. Register, and A. Chutjian, "Electron scattering by molecules II. Experimental methods and data," *Physics Reports*, vol. 97, no. 5, pp. 219–356, 1983.
- [106] H. Tawara, Y. Itikawa, H. Nishimura et al., "Cross sections and related data for electron collisions with hydrogen molecules and molecular ions," *Journal of Physical and Chemical Reference Data*, vol. 19, pp. 617–636, 1990.
- [107] M. Babutzka, M. Bahr, J. Bonn et al., "Monitoring of the properties of the KATRIN Windowless gaseous tritium source," <http://arxiv.org/abs/1205.5421v1>.
- [108] W. Käfer, *Sensitivity studies for the KATRIN experiment [Ph.D. thesis]*, KIT, 2012.
- [109] N. Wandkowsky et al., "Simulation of background from trapped electrons following radon  $\alpha$ -decays in the KATRIN pre-spectrometer," to be published.
- [110] M. Prall, P. Renschler, F. Glück et al., "The KATRIN pre-spectrometer at reduced filter energy," *New Journal of Physics*, vol. 14, Article ID 073054, 2012.
- [111] B. Bornschein, "Between fusion and cosmology—the future of the tritium laboratory karlsruhe," *Fusion Science and Technology*, vol. 60, no. 3, pp. 1088–1091, 2011.
- [112] F. Glück, "Tritium gas flow in the KATRIN source tube," to be published.
- [113] V. N. Aseev, A. I. Belev, A. I. Berlev et al., "Energy loss of 18 keV electrons in gaseous  $\text{T}_2$  and quench condensed  $\text{D}_2$  films," *European Physical Journal D*, vol. 10, no. 1, pp. 39–52, 2000.
- [114] S. Dushman, *Scientific Foundations of Vacuum Technique*, John Wiley & Sons, New York, NY, USA, 1962.
- [115] S. Grohmann, J. Bonn, B. Bornschein et al., "Cryogenic design of the KATRIN source cryostat," in *Proceedings of the Transactions of the Cryogenic Engineering Conference (CEC '07)*, vol. 985, pp. 1277–1284, Chattanooga, TN, USA, July 2008.
- [116] S. Grohmann, T. Bode, H. Schön, and M. Süßer, "Precise temperature measurement at 30 K in the KATRIN source cryostat," *Cryogenics*, vol. 51, no. 8, pp. 438–445, 2011.
- [117] D. A. Long, *The Raman Effect: A Unified Treatment of the Theory of Raman Scattering by Molecules*, Wiley, Chichester, UK, 2002.
- [118] R. J. Lewis, H. H. Telle, B. Bornschein, O. Kazachenko, N. Kernert, and M. Sturm, "Dynamic Raman spectroscopy of hydrogen isotopomer mixtures in-line at TILO," *Laser Physics Letters*, vol. 5, no. 7, pp. 522–531, 2008.
- [119] M. Sturm, M. Schlösser, R. J. Lewis, B. Bornschein, G. Drexlin, and H. H. Telle, "Monitoring of all hydrogen isotopologues at tritium laboratory Karlsruhe using Raman spectroscopy," *Laser Physics*, vol. 20, no. 2, pp. 493–507, 2010.
- [120] M. Schlösser, S. Fischer, M. Sturm, B. Bornschein, R. J. Lewis, and H. H. Telle, "Design implications for laser raman measurement systems for tritium sample-analysis, accountancy or process-control applications," *Fusion Science and Technology*, vol. 60, no. 3, pp. 976–981, 2011.
- [121] S. Fischer, M. Sturm, M. Schlösser et al., "Monitoring of tritium purity during long-term circulation in the KATRIN test experiment LOOPINO using laser raman spectroscopy," *Fusion Science and Technology*, vol. 60, no. 3, pp. 925–930, 2011.



- [122] M. Beck et al., "An angular selective electron source for the KATRIN experiment," to be published.
- [123] K. Valerius, M. Beck, H. Arlinghaus et al., "A UV LED-based fast-pulsed photoelectron source for time-of-flight studies," *New Journal of Physics*, vol. 11, Article ID 063018, 2009.
- [124] K. Hugenberg, "An angular resolved pulsed UV LED photoelectron source for KATRIN," *Progress in Particle and Nuclear Physics*, vol. 64, no. 2, pp. 288–290, 2010.
- [125] K. Valerius, H. Hein, H. Baumeister et al., "Prototype of an angular-selective photoelectron calibration source for the KATRIN experiment," *Journal of Instrumentation*, vol. 6, no. 1, Article ID P01002, 2011.
- [126] A. R. Nastoyashchii, N. A. Titov, I. N. Morozov, F. Glück, and E. W. Otten, "Effects of plasma phenomena on neutrino mass measurements process using a gaseous tritium  $\beta$ -source," *Fusion Science and Technology*, vol. 48, pp. 743–746, 2005.
- [127] S. Lukic, B. Bornschein, L. Bornschein et al., "Measurement of the gas-flow reduction factor of the KATRIN DPS2-F differential pumping section," *Vacuum*, vol. 86, no. 8, pp. 1126–1133, 2012.
- [128] X. Luo, Ch. Day, V. Hauera et al., "Monte Carlo simulation of gas flow through the KATRIN DPS2-F differential pumping system," *Vacuum*, vol. 80, no. 8, pp. 864–869, 2006.
- [129] W. Gil, J. Bonn, B. Bornschein et al., "The cryogenic pumping section of the KATRIN experiment," *IEEE Transactions on Applied Superconductivity*, vol. 20, no. 3, pp. 316–319, 2010.
- [130] X. Luo and Ch. Day, "Test particle Monte Carlo study of the cryogenic pumping system of the Karlsruhe tritium neutrino experiment," *Journal of Vacuum Science and Technology A*, vol. 26, no. 5, pp. 1319–1325, 2008.
- [131] A. Kosmider, *Tritium retention techniques in the KATRIN transport section and commissioning of its DPS2-F cryostat* [Ph.D. thesis], KIT, 2012.
- [132] J. Wolf, B. Bornschein, G. Drexlin et al., "Investigation of turbomolecular pumps in strong magnetic fields," *Vacuum*, vol. 86, no. 4, pp. 361–369, 2011.
- [133] M. Ubieto-Díaz, D. Rodríguez, S. Lukic, Sz. Nagy, S. Stahl, and K. Blaum, "A broad-band FT-ICR Penning trap system for KATRIN," *International Journal of Mass Spectrometry*, vol. 288, no. 1–3, pp. 1–5, 2009.
- [134] W. Gil, J. Bonn, O. Dormicchi et al., "Status of the magnets of the two tritium pumping sections for KATRIN," *IEEE Transactions on Applied Superconductivity*, vol. 22, no. 3, Article ID 6072243, 2012.
- [135] O. Kazachenko, B. Bornschein, L. Bornschein, F. Eichelhardt, N. Kernert, and H. Neumann, "TRAP—a cryo-pump for pumping tritium on pre-condensed argon," *Nuclear Instruments and Methods in Physics Research A*, vol. 587, no. 1, pp. 136–144, 2008.
- [136] B. Ostrick, *Eine kondensierte  $^{83m}\text{Kr}$ -Kalibrationsquelle für das KATRIN-Experiment* [Ph.D. thesis], University of Münster, 2009.
- [137] S. Mertens, *Study of background processes in the electrostatic spectrometers of the KATRIN experiment* [Ph.D. thesis], KIT, 2012.
- [138] F. Fränkle, *Background investigations of the KATRIN pre-spectrometer* [Ph.D. thesis], KIT, 2010.
- [139] KATRIN Webpage, <http://www.katrin.kit.edu/>.
- [140] A. Osipowicz, W. Seller, J. Letnev et al., "A mobile magnetic sensor unit for the KATRIN main spectrometer," *Journal of Instrumentation*, vol. 7, no. 6, Article ID T06002, 2012.
- [141] J.-P. Schall, *Untersuchungen zu Untergrundprozessen am Mainzer Neutrinomassenexperiment* [Ph.D. thesis], Mainz University, 2001.
- [142] B. Müller, *Umbau des Mainzer Neutrinomassenexperiments und Untergrunduntersuchungen im Hinblick auf KATRIN* [Ph.D. thesis], Mainz University, 2002.
- [143] B. Flatt, *Voruntersuchungen zu den Spektrometern des KATRIN-Experiments* [Ph.D. thesis], Mainz University, 2005.
- [144] K. Valerius, "Electromagnetic design and inner electrode for the KATRIN main spectrometer," *Progress in Particle and Nuclear Physics*, vol. 57, no. 1, pp. 58–60, 2006.
- [145] K. Valerius, "The wire electrode system for the KATRIN main spectrometer," *Progress in Particle and Nuclear Physics*, vol. 64, no. 2, pp. 291–293, 2010.
- [146] M. Prall et al., "The wire electrode system for the KATRIN main spectrometer," to be published.
- [147] E. W. Otten, J. Bonn, and Ch. Weinheimer, "The Q-value of tritium  $\beta$ -decay and the neutrino mass," *International Journal of Mass Spectrometry*, vol. 251, no. 2–3, pp. 173–178, 2006.
- [148] J. Kašpar, M. Ryšavý, A. Špalek, and O. Dragoun, "Effect of energy scale imperfections on results of neutrino mass measurements from  $\beta$ -decay," *Nuclear Instruments and Methods in Physics Research A*, vol. 527, no. 3, pp. 423–431, 2004.
- [149] Th. Thümmeler, R. Marx, and Ch. Weinheimer, "Precision high voltage divider for the KATRIN experiment," *New Journal of Physics*, vol. 11, Article ID 103007, 2009.
- [150] D. Vénos, M. Zbořil, J. Kašpar et al., "The development of a super-stable datum point for monitoring the energy scale of electron spectrometers in the energy range up to 20 keV," *Measurement Techniques*, vol. 53, no. 3, pp. 305–312, 2010.
- [151] M. Zbořil, *Solid electron sources for the energy scale monitoring in the KATRIN experiment* [Ph.D. thesis], University of Münster, 2011.
- [152] D. Vénos, A. Špalek, O. Lebeda, and M. Fiser, "Kr-83m radioactive source based on Rb-83 trapped in cation-exchange paper or in zeolite," *Applied Radiation and Isotopes*, vol. 63, p. 323, 2005.
- [153] M. Rasulbaev, K. Maier, R. Vianden, T. Thümmeler, B. Ostrick, and Ch. Weinheimer, "Production of  $^{83}\text{Rb}$  for the KATRIN experiment," *Applied Radiation and Isotopes*, vol. 66, no. 12, pp. 1838–1843, 2008.
- [154] D. Vénos, O. Dragoun, A. Špalek, and M. Vobecký, "Precise energy of the weak 32-keV gamma transition observed in  $^{83m}\text{Kr}$  decay," *Nuclear Instruments and Methods in Physics Research A*, vol. 560, no. 2, pp. 352–359, 2006.
- [155] R. Marx, "New concept of PTBs standard divider for direct voltages of up to 100 kV," *IEEE Transactions on Instrumentation and Measurement*, vol. 50, no. 2, pp. 426–429, 2001.
- [156] A. Krieger, C. Geppert, R. Catherall et al., "Calibration of the ISOLDE acceleration voltage using a high-precision voltage divider and applying collinear fast beam laser spectroscopy," *Nuclear Instruments and Methods in Physics Research A*, vol. 632, no. 1, pp. 23–31, 2011.
- [157] B. A. Vandevender, L. I. Bodine, A. W. Myers et al., "Performance of a TiN-coated monolithic silicon pin-diode array under mechanical stress," *Nuclear Instruments and Methods in Physics Research A*, vol. 673, pp. 46–50, 2012.
- [158] J. Abraham, P. Abreu, M. Aglietta et al., "The fluorescence detector of the Pierre Auger Observatory," *Nuclear Instruments and Methods in Physics Research A*, vol. 620, no. 2–3, pp. 227–251, 2010.
- [159] M. Howe and J. Wilkerson, ORCA webpage at UNC.



- [160] H. J. de Vega, O. Moreno, E. Moya de Guerra et al., “Search of keV sterile neutrino warm dark matter in the rhenium and tritium beta decays,” *Nuclear Physics B*, vol. 866, no. 2, p. 177, 2013.
- [161] M. Zacher, *Design of the high-field region of the KATRIN spectrometers and a pulsed angularselective UV laser photoelectron source for investigating their transmission functions [Ph.D. thesis]*, University of Münster, 2012.
- [162] S. Mertens, “Electromagnetic design of the spectrometer section of the KATRIN experiment,” *Progress in Particle and Nuclear Physics*, vol. 64, no. 2, pp. 294–296, 2010.
- [163] M. Beck, K. Valerius, J. Bonn et al., “Effect of a sweeping conductive wire on electrons stored in a Penning-like trap between the KATRIN spectrometers,” *European Physical Journal A*, vol. 44, p. 499, 2010.
- [164] B. Hillen, *Untersuchung von Methoden zur Unterdrückung des Spektrometeruntergrunds beim KATRIN Experiment [Ph.D. thesis]*, University of Münster, 2011.
- [165] F. M. Fränkle, L. Bornschein, G. Drexlin et al., “Radon induced background processes in the KATRIN pre-spectrometer,” *Astroparticle Physics*, vol. 35, pp. 128–134, 2011.
- [166] S. Mertens, G. Drexlin, F. M. Fränkle et al., “Background due to stored electrons following nuclear decays in the KATRIN spectrometers and its impact on the neutrino mass sensitivity,” *Astroparticle Physics*, vol. 41, pp. 52–62, 2013.
- [167] S. Mertens, A. Beglarian, L. Bornschein et al., “Stochastic heating by ECR as a novel means of background reduction in the KATRIN spectrometers,” *Journal of Instrumentation*, vol. 7, Article ID P08025, 2012.
- [168] M. Jerkins, J. R. Klein, J. H. Majors et al., “Using cold atoms to measure neutrino mass,” *New Journal of Physics*, vol. 12, Article ID 043022, 2010.
- [169] E. W. Otten, “Comment on “Using cold atoms to measure neutrino mass”,” *New Journal of Physics*, vol. 13, Article ID 078001, 2011.
- [170] B. Monreal and J. Formaggio, “Relativistic cyclotron radiation detection of tritium decay electrons as a new technique for measuring the neutrino mass,” *Physical Review D*, vol. 80, Article ID 051301, 2009.
- [171] J. Formaggio, “Project 8: using radio-frequency techniques to measure neutrino mass,” <http://arxiv.org/abs/1101.6077>.
- [172] A. Nucciotti, “The MARE project,” *Journal of Low Temperature Physics*, vol. 151, pp. 597–602, 2008.
- [173] M. Galeazzi, F. Gatti, M. Lusignoli et al., “The electron capture decay of  $^{163}\text{Ho}$  to measure the electron neutrino mass with sub-eV accuracy,” <http://arxiv.org/abs/1202.4763>.
- [174] E. Ferri, “MARE-1 in Milan: status and perspectives,” *Journal of Low Temperature Physics*, vol. 167, p. 1035, 2012.
- [175] P. C.-O. Ranitzsch, J.-P. Porst, S. Kempf et al., “Development of metallic magnetic calorimeters for high precision measurements of calorimetric  $^{187}\text{Re}$  and  $^{163}\text{Ho}$  spectra,” *Journal of Low Temperature Physics*, vol. 167, pp. 1004–1014, 2012.
- [176] S. Kraft-Bermuth, C. Arnaboldi, E. Ferri et al., “Development and characterization of microcalorimeters for a next generation  $^{187}\text{Re}$  beta-decay experiment,” *Journal of Low Temperature Physics*, vol. 151, pp. 619–622, 2008.
- [177] A. Nucciotti for the MARE collaboration, “The MARE experiment and its capabilities to measure the mass of light (active) and heavy (sterile) neutrinos, presentation at the Workshop CIAS Meudon, 2011.
- [178] M. Faverzani, P. Day, A. Nucciotti, and E. Ferri, “Developments of microresonators detectors for neutrino physics in milan,” *Journal of Low Temperature Physics*, vol. 167, p. 1041, 2012.
- [179] R. Vaccarone, F. Strata, F. Gatti et al., “The design of a frequency multiplexed Ir-Au TES array,” *Journal of Low Temperature Physics*, vol. 151, no. 3–4, pp. 921–926, 2008.
- [180] L. Gastaldo, J. P. Porst, F. Von Seggern et al., “Low temperature magnetic calorimeters for neutrino mass direct measurement,” in *Proceedings of the 13th International Workshop on Low Temperature Detectors (LTD-13 '09)*, vol. 1185, pp. 607–611, Stanford, Calif, USA, July 2009.
- [181] C. Pies, S. Schäfer, S. Heuser et al., “MaXs: microcalorimeter arrays for high-resolution x-ray spectroscopy at GSI/FAIR,” *Journal of Low Temperature Physics*, vol. 167, no. 3–4, pp. 269–279, 2012.
- [182] M. Lusignoli and M. Vignati, “Relic antineutrino capture on  $^{163}\text{Ho}$  decaying nuclei,” *Physics Letters B*, vol. 697, no. 1, pp. 11–14, 2011.
- [183] C. L. Bennett, A. L. Hallin, R. A. Naumann et al., “The X-ray spectrum following  $^{163}\text{Ho}$  M electron capture,” *Physics Letters B*, vol. 107, no. 1–2, pp. 19–22, 1981.
- [184] H. L. Ravn, “The N/M electron-capture ratio of the neutrino-mass probe  $^{163}\text{Ho}$ , in massive neutrinos in astrophysics and in particle physics,” in *Proceedings of the Fourth Moriond Workshop*, pp. 287–294, La Plagne-Savoie, France, 1984.
- [185] F. X. Hartmann and R. A. Naumann, “High temperature gas proportional detector techniques and application to the neutrino mass limit using  $^{163}\text{Ho}$ ,” *Nuclear Instruments and Methods in Physics Research A*, vol. 313, no. 1–2, pp. 237–260, 1992.
- [186] F. Gatti, P. Meunier, C. Salvo, and S. Vitale, “Calorimetric measurement of the  $^{163}\text{Ho}$  spectrum by means of a cryogenic detector,” *Physics Letters B*, vol. 398, no. 3–4, pp. 415–419, 1997.
- [187] A. Burck, S. Kempf, S. Schäfer et al., “Microstructured magnetic calorimeter with Meander-shaped pickup coil,” *Journal of Low Temperature Physics*, vol. 151, no. 1–2, pp. 337–344, 2008.
- [188] L. Gastaldo et al., “ $^{163}\text{Ho}$  electron capture decay: high precision measurement of the calorimetric spectrum,” in *Proceedings of the Spring Meeting of the DPG in Karlsruhe*, 2011.
- [189] G. Audi, A. H. Wapstra, and C. Thibault, “The Ame2003 atomic mass evaluation—(II). Tables, graphs and references,” *Nuclear Physics A*, vol. 729, no. 1, pp. 337–676, 2003.

## Review Article

# Geoneutrinos

**Ondřej Šrámek,<sup>1</sup> William F. McDonough,<sup>1</sup> and John G. Learned<sup>2</sup>**

<sup>1</sup> *Department of Geology, University of Maryland, College Park, MD 20742, USA*

<sup>2</sup> *Department of Physics and Astronomy, University of Hawaii, Honolulu, HI 96822, USA*

Correspondence should be addressed to Ondřej Šrámek, [sramek@umd.edu](mailto:sramek@umd.edu)

Received 9 July 2012; Accepted 20 October 2012

Academic Editor: Arthur B. McDonald

Copyright © 2012 Ondřej Šrámek et al. This is an open access article distributed under the Creative Commons Attribution License, which permits unrestricted use, distribution, and reproduction in any medium, provided the original work is properly cited.

Neutrino geophysics is an emerging interdisciplinary field with the potential to map the abundances and distribution of radiogenic heat sources in the continental crust and deep Earth. To date, data from two different experiments quantify the amount of Th and U in the Earth and begin to put constraints on radiogenic power in the Earth available for driving mantle convection and plate tectonics. New improved detectors are under construction or in planning stages. Critical testing of compositional models of the Earth requires integrating geoneutrino and geological observations. Such tests will lead to significant constraints on the absolute and relative abundances of U and Th in the continents. High radioactivity in continental crust puts limits on land-based observatories' capacity to resolve mantle models with current detection methods. Multiple-site measurement in oceanic areas away from continental crust and nuclear reactors offers the best potential to extract mantle information. Geophysics would benefit from directional detection and the detectability of electron antineutrinos from potassium decay.

## 1. Introduction

In the simplest view, the Earth formed hot and has been cooling since [1]. The initial hot state 4.5 billion years ago was a result of gravitational energy of accretion and global differentiation largely released as heat. As a first-order estimate, the gravitational energy  $GM^2/R$  released by accumulating the Earth of mass  $M$  and radius  $R$  from spatially dispersed building blocks is enough to increase the temperature by tens of thousands of Kelvin [2] if entirely converted to heat. Further heat is released upon differentiation and gravitational segregation of the metallic core from the overlying silicate shell and possibly also provided by short-lived radioactivity. Compared to melting temperatures of silicates and metal that make up the Earth ( $\lesssim 2000$  K), these observations suggest an early period of large-scale melting.

In 1862, William Thomson, future Lord Kelvin, communicated his now famous estimate of Earth's age [3]. Assuming conductive cooling of an initially molten Earth, and

**Table 1:** Terminology used in the paper.

BSE	Bulk silicate Earth
CC	Continental crust
CL	Confidence level
CMB	Core-mantle boundary
DM	Depleted mantle
HPE	Heat producing elements
LLSVPs	Large low shear-wave velocity provinces
MORB	Mid-ocean ridge basalt
TNU	Terrestrial neutrino unit
ULVZs	Ultra-low velocity zones

using best existing estimates of rock melting temperature, subsurface temperature gradient, and thermal conductivity, he arrived at age of 98 My, allowing for a span between 20 and 400 My. Kelvin later downgraded his estimate to 20–40 My [4]. (More on the interesting subject of Earth’s age determination in [5, 6].) We now understand the reasons why Kelvin’s calculation underestimated the age of the Earth by two orders of magnitude: an internal source of heat is provided by long-lived radioactivity [7] and, more importantly, thermal diffusion is not the primary process of controlling heat loss from the Earth’s interior [8].

Constraining Earth’s thermal history is a major task of geophysics. It requires knowledge of the present-day thermal state, the energy sources available for the planet, and the processes that operate over time. Uncertainties remain, even if great progress has been made, especially in the last several decades since the acceptance of the plate tectonics paradigm in the 1970s [9]. The progress was made possible thanks to advances in geophysical observations, chemical analyses of rock samples, laboratory experiments on Earth constituents, and understanding of Earth’s internal dynamics based on theoretical arguments and numerical modeling. Current understanding of Earth’s thermal evolution appreciates the dominant role of advective transport of heat by large-scale convection in large part of Earth’s interior. Knowledge of present-day thermal state is limited by uncertainties in abundances of heat-producing elements (HPEs; Table 1 explains abbreviations used in this paper), long-lived radioactive isotopes of U, Th, and K. Distribution of the HPEs within the Earth volume must be known as well.

Geoscience is a broadly interdisciplinary field and now embraces particle physics experiments. The first detection of weakly interacting neutrinos—in fact, nuclear reactor-generated antineutrinos—by Reines and Cowan’s research team was confirmed in 1956 [10]. Counting electron antineutrinos generated in  $\beta$ -decays of HPEs in Earth’s interior can provide direct information about the deep-seated radioactivity, not obtainable by any other means. Measurement of Earth’s internal radioactivity by terrestrial neutrino detection was first proposed by Eder [11], and the idea was further developed by Marx and coworkers [12–14]. Krauss et al. [15] presented a comprehensive overview of antineutrino geophysics, including emission predictions based on a geological model and discussion of possible detection mechanisms. Raghavan et al. [16] and Rothschild et al. [17] were the first to examine the potential of KamLAND and Borexino detectors for geoneutrino measurement. Experimental efforts resulted in the first geoneutrino detections by KamLAND [18, 19] and Borexino [20], which begin to answer relevant geophysical questions. New geoneutrino detectors are being developed: SNO+ [21] is scheduled to go online in 2013, and several other experiments with geoneutrino detection capabilities have been proposed.

Neutrino physics gains momentum in the geophysical community. Kobayashi and Fukao's 1991 paper [22] marks the first geoneutrino publication in a specialized geophysical journal. Meetings with specific focus on neutrino geophysics took place at University of Hawaii in 2005 [23] and 2007 [24], at SNOLAB in 2008 [25], in Gran Sasso in 2010 [26], and in Deadwood, South Dakota in 2011 [27]. A special session on geoneutrinos was convened at American Geophysical Union 2006 Joint Assembly [28]. Proceedings from the 2005 meeting were collectively published in Volume 99 of *Earth, Moon, and Planets* (Neutrino Geophysics, Proceedings of Neutrino Sciences 2005, <http://link.springer.com/journal/11038/99/1/>) and reprinted in a book format [29]. Geoneutrino physics is a subject of Master's [30] and Ph.D. [31] theses, as well as outreach and popular articles aimed at broader scientific community [32–35].

In this paper we focus on the use of neutrinos for geology. Other aspects of neutrino research are covered by other papers throughout this comprehensive issue. Recent review articles on geoneutrinos include Enomoto et al. [36], Fiorentini et al. [37], Dye [38], and Dye [39]. Parts of this paper closely follow the presentation of Dye [39]. The structure of this paper is as follows. We first present the “state of the Earth” in Section 2 and discuss the geophysical motivation for geoneutrino studies. We then review the relevant details of geoneutrino production (Section 3) and oscillation (Section 4), introduce calculation of geoneutrino flux (Section 5), discuss geoneutrino detection (Section 6) and detectors (Section 7), show predictions of geoneutrino flux (Section 8), review geoneutrino observations (Section 9), and discuss future prospects (Section 10).

## 2. Geophysical Questions Driving Geoneutrino Research

Seismic observation combined with gravity data and geochemical inputs inform us about the architecture of the Earth. The first-order internal structure has been known, at least qualitatively, since the 1930s by which time the main domains of the differentiated Earth were identified: the inner core, the outer core, the mantle, and the crust, as shown in Figure 1. The mantle and the crust constitute the silicate Earth, the core is mostly metallic iron.

The rate at which the Earth loses heat is a balance between the secular cooling of the Earth and the radiogenic heat production, which is the only significant heat source. Understanding the relative contributions is important for understanding the Earth's dynamics and evolution over time. The most recent assessment of the present-day energy budget is provided by Mareschal et al. [40]. Detailed discussion of Earth's thermal history can be found in reviews by Jaupart et al. [41], Korenaga [42], and Lay et al. [43].

The Earth's heat loss can be estimated from heat flow measurements supplemented with geophysical modeling in oceanic areas [41, 44–47]. In the latest analysis of surface heat flux, J. H. Davies and D. R. Davies [47] used ~38000 heat flow measurements and geological data. Heat flow on young sea floor is described by half-space cooling model [48] to account for hydrothermal circulation near oceanic spreading centers, which provides advective heat transport mechanism in addition to measurable conducted heat. J. H. Davies and D. R. Davies [47] arrive at total heat loss of  $47 \pm 2$  TW, where 16 TW is lost from the continents and 31 TW from oceans. The analysis of Jaupart et al. [41] reports  $46 \pm 3$  TW, with 14 TW lost over continental regions. The recent proposition of much lower oceanic heat loss [49] seems untenable [50, 51]. While the heat loss estimates are robust, it has been suggested that present-day heat loss is below the long-term average due to recent slowdown in oceanic spreading rates [52].



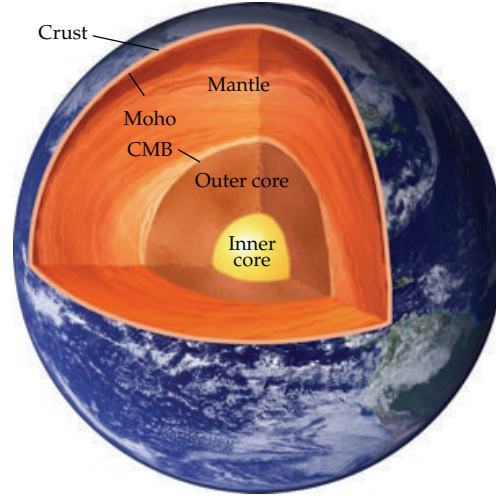


**Figure 1:** Schematic of Earth's internal structure. Adapted from <http://tinyurl.com/lblgeonu>.

A significant part of heat flux over continents comes from radiogenic heat produced in the continental crust (CC) of average thickness  $\sim 40$  km. The high abundances of HPEs are a consequence of CC formation that involves repeated melting, a fractionation process which concentrates the so-called incompatible elements (including U, Th, and K) in the melt phase. Generally the crustal concentrations of HPEs are the highest near the surface and decrease downwards by a factor of ten to its base [53]. As we discuss later, this has implications for geoneutrino studies where the signal at continental measurement sites is dominated by locally produced crustal geoneutrinos. The radiogenic heat production in the CC is estimated from crustal compositional models and heat flux analysis and adds to  $\sim 8$  TW of power [40]. The crustal heat source does not fuel convection in the Earth's mantle and can be subtracted from the total heat loss ( $\sim 47$  TW) to obtain a mantle heat flow of  $\sim 39$  TW.

Heat supplied by the core to the mantle across the core-mantle boundary (CMB) provides basal heating for mantle convection. In addition to secular cooling of the core, the CMB heat flux includes contributions from the latent heat of crystallization and from the gravitational energy release as the solid inner core grows (the possibility of core radiogenic heating will be discussed shortly) [43]. Estimates of CMB heat flow are largely based on scaling analyses of compositionally driven convection in the molten outer core and are tightly linked to age and evolution of the inner core and the operation of the geodynamo. The uncertainty on the CMB heat flow, with values estimated in the range of 5–15 TW, is large [40, 43, 54].

Rock samples available for direct chemical analysis only come from shallow depths of 100 to 200 km at most. Composition of the uppermost mantle can be inferred from analyses of basalts erupted at midoceanic ridges (i.e., MORBs). Estimation of HPE abundances and distribution in the remainder of Earth interior has to be deduced indirectly. Main points to consider are (i) with how much HPEs did the Earth accrete, (ii) what was the fate of these elements during core formation, a global differentiation (and chemical fractionation) process, and (iii) how did the distribution of HPEs evolve after core formation was completed until present day, especially in the silicate part of the Earth.

**Table 2:** Abundance estimates of U, Th, and K in BSE and DM. Uncertainties are included where available.

U (ppb)	Th (ppb)	K (ppm)	Th/U	K/U	Power (TW)	Reference
Bulk silicate Earth (BSE)						
<i>Collisional erosion model</i>						
10	38	120	3.8	12000	9.6	O'Neill and Palme [62]
<i>Based on enstatite chondrites</i>						
13.5	41.7	385	3.1	28500	15	Javoy [63]
12.1	49.2	146	3.5	12000	11	Javoy et al. [64] <sup>†</sup>
<i>Based on terrestrial rocks and C1 carbonaceous chondrite ratios of RLE abundances</i>						
20.8	79.0	264	3.8	12700	20	Hart and Zindler [58]
20.3 ± 20%	79.5 ± 15%	240 ± 20%	3.9	11800	20 ± 4	McDonough and Sun [55]
21.8 ± 15%	83.4 ± 15%	260 ± 15%	3.8	11900	21 ± 3	Palme and O'Neill [59]
17.3 ± 3.0	62.6 ± 10.7	190 ± 40	3.6	11000	16 ± 3	Lyubetskaya and Korenaga [61]
20 ± 4	80 ± 12	280 ± 60	4.0	13800	20 ± 4	Arevalo et al. [60]
<i>Based on energetics of mantle convection ("conventional" scaling)</i>						
31	124	310	4.0	10000	30	Turcotte and Schubert [65]
Depleted mantle (DM)—MORB source						
3.2 ± 0.5	7.9 ± 1.1	50	2.5	15600	2.8 ± 0.4*	Workman and Hart [66]
4.7 ± 30%	13.7 ± 30%	60 ± 28%	2.9	12800	4.1 ± 1.2*	Salters and Stracke [67]
8 ± 20%	22 ± 20%	152 ± 20%	2.8	19000	7.5 ± 1.5*	Arevalo and McDonough [68]

<sup>†</sup>Model of Javoy et al. [64] is constructed following Javoy's recipe as described in [69]. \*Calculation of radiogenic power for DM estimates assumes that the entire mantle has DM composition.

The first issue is usually addressed by relating the Earth composition in some way to chemical abundances measured in primitive meteorites. One approach consists of using the available rock samples from the crust and shallow mantle to infer the original composition of the primitive (or primordial) mantle prior to crust formation. An additional constraint imposes that the ratios of so-called refractory lithophile elements (RLE) match those of C1 carbonaceous chondrites, the most primitive chondrites whose composition best matches the solar photosphere. The lithophile elements (according to Goldschmidt's classification) are those excluded from the metallic core because during differentiation these elements partition effectively into the silicates and not the sulfides nor metals. The term refractory signifies a high temperature of condensation from the solar nebula. The actual model RLE abundances are ~2.75 times larger relative to the C1 chondrites [55]. Both U and Th are RLEs. Potassium is also lithophile but moderately volatile during accretion, which makes the K abundance estimate particularly difficult. Indeed, the K/U abundance ratio of the Earth is estimated to be some eight times less than that in C1 chondritic meteorites [56]. The affinity of U, Th, and K for silicate phase argues for no radiogenic heat production in the core [57]. HPE abundances in the bulk silicate Earth (BSE, i.e., mantle + crust combined) for several estimates from this class of models are shown in Table 2. The typical radiogenic heat production from these models is ~20 TW in the BSE [55, 58–60], even though a somewhat lower power (~17 TW) was recently proposed [61]. We call this class of estimates "geochemical" BSE models.

An alternative meteorite-based approach toward estimation of bulk Earth composition appreciates the isotopic similarity of enstatite chondrites with terrestrial samples and uses the chondritic abundances at face value [63, 64]. Javoy et al. [64] argue for a BSE composition that produces a mere ~11 TW of radiogenic power (Table 2). We call these

models “cosmochemical” estimates. Other models exist that yield similarly low abundance of the heat producing elements. O’Neill and Palme [62] recently proposed a model whereby the early developed Earth crust, enriched in highly incompatible elements (e.g., U, Th, and K) was stripped off by collisional erosion, which resulted in marked depletions of these elements from the bulk silicate Earth. Consequently, the O’Neill and Palme model has a bulk silicate Earth that contains as little as 10 ppb U, 38 ppb Th and 120 ppm K. In terms of absolute concentration, this is comparable to the Javoy et al. model.

Geodynamical modeling of mantle dynamics provides a different type of constraints on the radiogenic power. Mantle radioactivity is an important energy source that contributes to the power that drives the solid-state convection in the mantle. Tremendous progress has been made over the last fifty years in theoretical understanding as well as numerical modeling of thermal convection in planetary interiors [70, 71]. An important class of Earth’s thermal evolution models consider the simple energy balance, where the net heat loss out of the mantle has to reflect a combination of mantle cooling and heat production. The dynamical link between the mantle internal temperature and the heat loss comes from the relation between the vigor of convection and the heat flux. This is known as the Nusselt number-Rayleigh number (Nu-Ra) scaling, which refers to the characteristic dimensionless quantities in convective heat transfer problems. In these so-called parameterized thermal evolution models, the mantle temperature and heat loss can be traced back in time starting from present-day initial conditions. In principle, a smaller power of radiogenic heat sources requires a larger temperature increase (backward in time) in order to account for a given heat flux. Classical parameterized models call for a significant fraction, ~60–80 percent, of present-day mantle heat loss to come from radiogenic heating (this is often referred to as a requirement on the mantle Urey ratio being 0.6–0.8) in order to avoid unrealistically high mantle temperature in Earth’s history, in conflict with early rock record [65, 70, 72]. This translates to  $\gtrsim 23$  TW of mantle radiogenic power or  $\gtrsim 30$  TW in BSE as required by a “geodynamical” model (Table 2) and is at odds with the geochemical BSE estimates.

It must be pointed out that our high Urey number geodynamical BSE estimate is based on a simple Nu-Ra scaling of the “conventional” parameterized convection models. Another way to avoid the Archean thermal catastrophe is to assume a different scaling law with a weaker coupling between the heat loss and mantle temperature (first suggested by Christensen [73]). A specific mechanism for the modification of the scaling law in early Earth has been proposed [74] (see also [75]). Other solutions invoke the specifics of the Earth-like convection which are not accounted for in the simple scaling [41, 76–80]. These alternative thermal evolution models are motivated by the geochemical constraint on HPE abundances (i.e., low mantle Urey ratio, ~0.3). Overall there is a large variance in Urey number predictions from geodynamical models of different degrees of sophistication. We use the conventional scaling as a high estimate for the HPE abundances in the Earth.

The discussion of BSE composition shows that there are three competing estimates—cosmochemical (poor in HPE), geochemical (intermediate), and geodynamical (rich). Figure 2 shows the temporal evolution of available radiogenic power throughout Earth’s history as predicted by the three models. The breakdown of the heating contributed by the four radionuclides is also shown, and somewhat differs between the cosmochemical [64] and geochemical [60] estimates because of differences in Th/U and K/U ratios. At present, about 80% of radiogenic powers is supplied in roughly equal measure by  $^{238}\text{U}$  and  $^{232}\text{Th}$ , the remaining 20% being provided by  $^{40}\text{K}$ ; present-day  $^{235}\text{U}$  contribution is below 2% of total power. Heating by  $^{40}\text{K}$  and  $^{235}\text{U}$ , however, dominated in the planet’s early history.

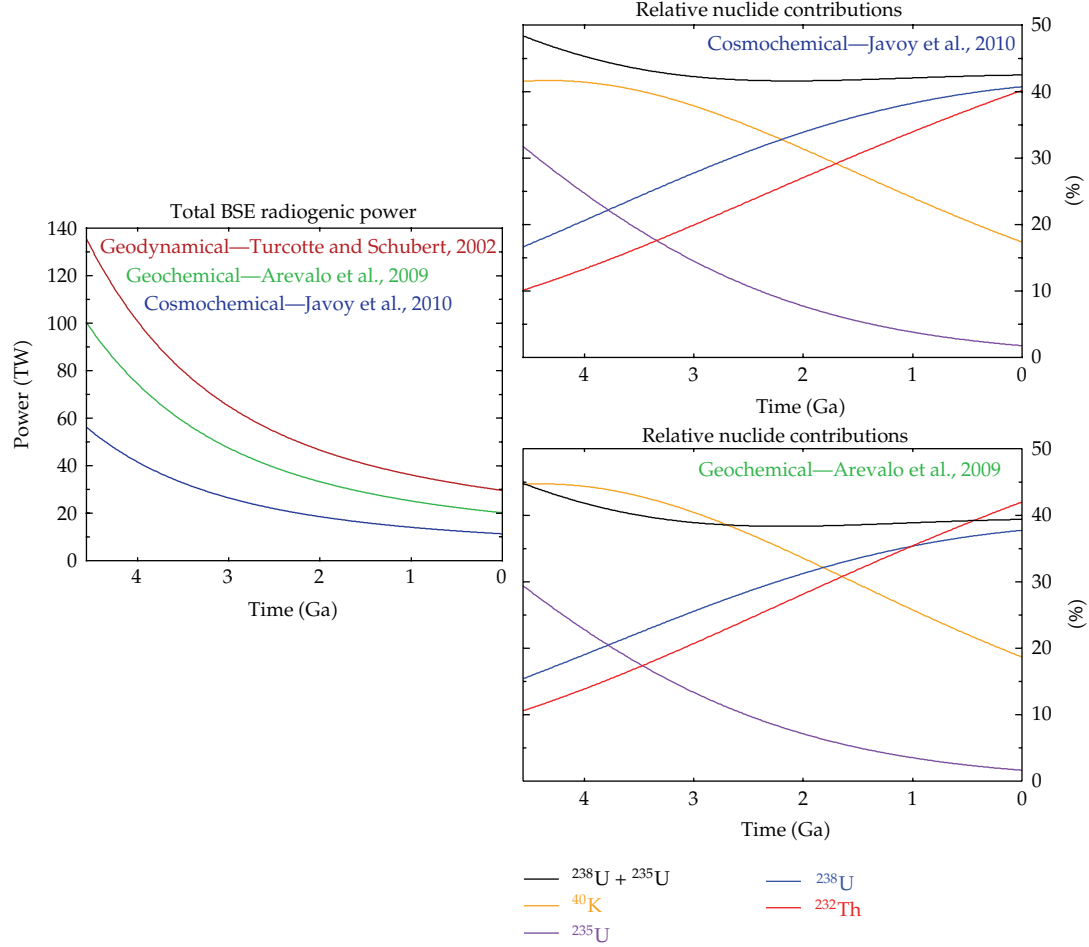


**Figure 2:** (left) Total radiogenic power over Earth's history as predicted by cosmochemical, geochemical, and geodynamical BSE estimates. (right) Relative contributions of each radionuclide for cosmochemical (top) and geochemical (bottom) estimates.

Further uncertainty pertains to the spatial distribution of HPEs in the mantle and the architecture of the mantle in general. Analyses of MORBs reveal the composition of their source region in the shallow mantle. When compared to BSE abundances, one concludes that neither the geochemical nor geodynamical mantle can consist entirely of MORB source material. Mass balances require the existence of a mantle volume enriched in HPEs, and some other elements as well. This has been a long-standing issue in geophysics [81]. Early models argued for mantle layering at  $\sim 660$  km depth, which separated the shallow depleted mantle (DM) from the deep layer of primordial composition with supposedly no mixing between these two reservoirs. This picture was overturned when seismologists began to image slabs subducting into the deep mantle [82, 83]. Current ideas still embrace the possibility of a mantle reservoir enriched in incompatible elements, but place it much deeper. One suggestion employs the anomalous, possibly partially molten “ultra-low velocity zones” (ULVZ) in the “D” layer of the deepest mantle [84, 85]. Another consideration are the two “large low shear-wave velocity provinces” (LLSVPs) in deep mantle below the Pacific and below Africa



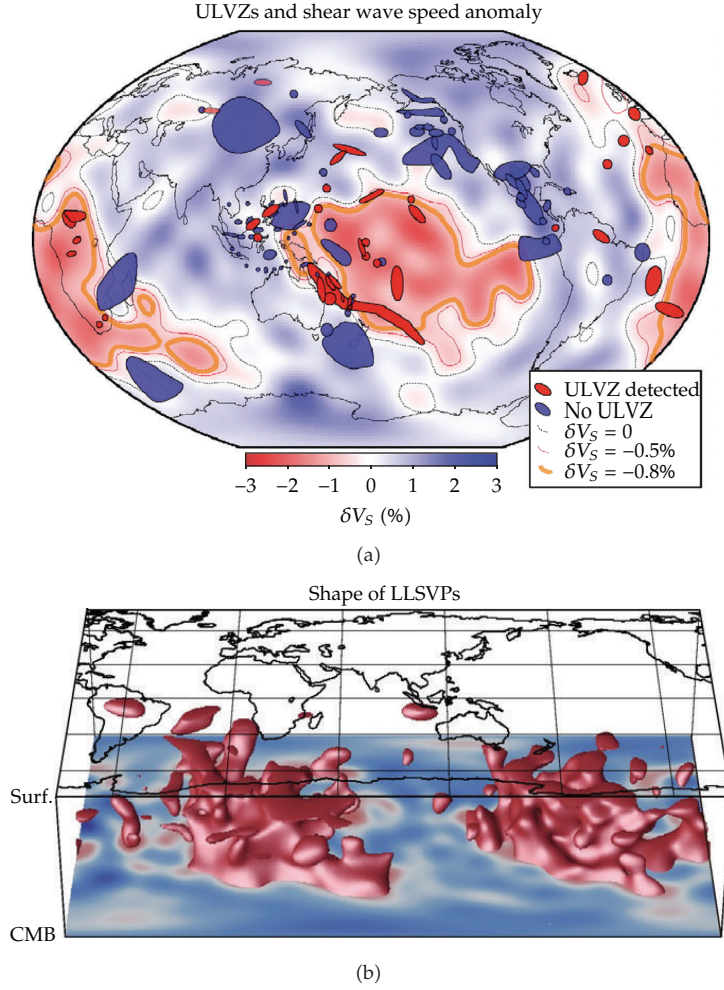


**Figure 3:** (a) Locations where ULVZ was detected superimposed on color map of shear wave speed anomaly ( $\delta V_S$ ) at CMB. (b) Isocontour of  $\delta V_S$  showing the 3D structure of LLSVPs below Africa and the Pacific. Based on seismic model S20RTS [93, 94]. Reprinted from [86, 95] with permission from Elsevier.

[85, 86]. In addition to lower-than-average shear wave seismic speeds, the LLSVPs seem to be bounded by sharp velocity gradients [87] and show anticorrelation between shear and bulk sound speeds [88], observations which support a compositional component to the seismic speed anomaly. Figure 3 shows the location of seismically detected ULVZ as well as the shape of the LLSVPs. It was proposed that such a deep-mantle geochemical reservoir may have formed very early in Earth's history [89–92].

The cosmochemical BSE estimate, unlike the geochemical and geodynamical models, is consistent with a uniform composition of the whole mantle and may even show HPE depletion in the lower mantle [64]. The bulk composition of the silicate Earth remains a hotly debated issue and an area of current active research [96–102]. Accurate new information on mantle composition provided by geoneutrino studies is needed. Figure 4 shows a breakdown of the present-day energy budget, which uses the geochemical BSE abundances and includes uncertainties. The mantle cooling rate required to balance the budget was calculated from the

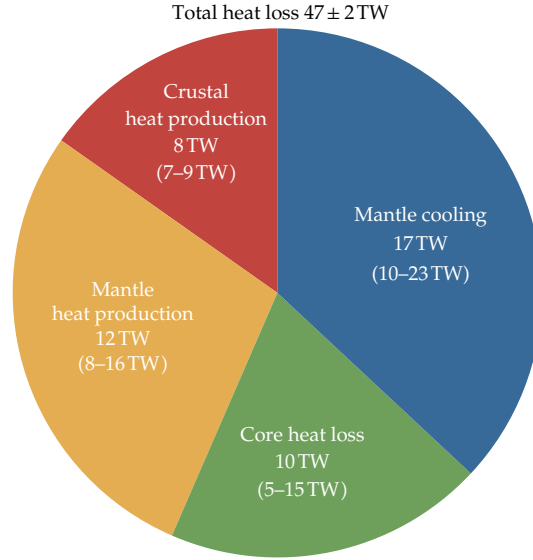


**Figure 4:** Present-day thermal budget of the Earth, which assumes a geochemical BSE composition ( $\sim 20$  TW of radiogenic power). Adapted from [40, 43]. See also [104].

remaining terms in the energy balance. The calculated cooling rate, equivalent of  $17 \pm 7$  TW, is higher than a long-term cooling rate estimated by petrological studies of MORB-like rocks,  $\sim 50 \text{ K Gy}^{-1}$  or  $\sim 7$  TW [103]. This discrepancy would become even more pronounced with a cosmochemical model for the BSE.

In addition to the aforementioned conventional models, some unorthodox propositions regarding the Earth's composition have been put forward. Even though geochemical arguments strongly disfavor HPEs in the Earth's core, these are discussed in detail in [57], some studies argue for the presence of K [105–107] and even U and Th [108]. In the 1970s it was discovered at the uranium mine at Oklo in Gabon, Africa that a natural fast breeder nuclear georeactor had operated there at around 1.8 Ga [109]. Some argue for a present-day operation of such a georeactor at depth in the core-mantle boundary region [110] or in the center of the Earth [111]. This would affect the terrestrial antineutrino production as well and Earth's radioactivity budget, and can be, in essence, resolved by geoneutrino studies.

In summary, these are the fundamental questions geophysics asks, which can be addressed by terrestrial antineutrino detection:

- (i) How much U, Th, and K are there in the Earth? (Or equivalently, what is the planetary U abundance and Th/U and K/U ratios?)
- (ii) Is the mantle chemically uniform, layered, or more complicated? (Presence of a mantle reservoir enriched in HPEs?)
- (iii) Is there radioactivity in the core?
- (iv) Is there an operating nuclear georeactor?

As we discuss in detail later, while some of these questions can, in principle, be—and have been—addressed using existing detection methods by accurate measurement at specific locations, answering others will require development of new detection mechanisms. In particular, this applies to antineutrinos from potassium decay, which are not detectable

with the currently used inverse  $\beta$ -decay mechanism. Current analyses of U + Th geoneutrino flux also have insufficient sensitivity to Th/U ratio.

### 3. Geoneutrino Production

Electron antineutrinos ( $\bar{\nu}_e$ ) are generated upon transmutation of neutron-rich nuclei by  $\beta$ -decay, accompanied by emission of an electron ( $e^-$ ) and release of decay energy ( $Q_\beta$ ),

$${}^A_ZX \longrightarrow {}^A_{Z+1}X' + e^- + \bar{\nu}_e + Q_\beta, \quad (3.1)$$

where  $A$  is the mass (nucleon) number, and  $Z$  is the atomic (proton) number. Part of the decay energy  $Q_\beta = Q_\nu + Q_h$  is carried away by antineutrinos ( $Q_\nu$ ), the remainder is available for heating ( $Q_h$ ). Geologically important isotopes of U, Th, and K that heat the Earth's interior decay into stable nuclei according to [36, 37, 39]:

$$\begin{aligned} {}^{238}_{92}\text{U} &\longrightarrow {}^{206}_{82}\text{Pb} + 8\alpha + 6e^- + 6\bar{\nu}_e + 51.698 \text{ MeV}, \\ {}^{235}_{92}\text{U} &\longrightarrow {}^{207}_{82}\text{Pb} + 7\alpha + 4e^- + 4\bar{\nu}_e + 46.402 \text{ MeV}, \\ {}^{232}_{90}\text{Th} &\longrightarrow {}^{208}_{82}\text{Pb} + 6\alpha + 4e^- + 4\bar{\nu}_e + 42.652 \text{ MeV}, \\ {}^{40}_{19}\text{K} &\xrightarrow{89.3\%} {}^{40}_{20}\text{Ca} + e^- + \bar{\nu}_e + 1.311 \text{ MeV}, \\ {}^{40}_{19}\text{K} + e^- &\xrightarrow{10.7\%} {}^{40}_{18}\text{Ar} + \nu_e + 1.505 \text{ MeV}. \end{aligned} \quad (3.2)$$

Decay of  ${}^{40}\text{K}$  branches into  $\beta$ -decay and electron capture. The complete decay networks can be found in Fiorentini et al. [37]. The decay networks of  ${}^{238}\text{U}$  and  ${}^{232}\text{Th}$  contain nine and five  $\beta$ -decaying nuclei, respectively. Decay energies are taken from Dye [39], who used inputs from the standard table of atomic masses [112]. The antineutrino energy spectra are needed in order to assess detection possibilities and to determine available energy for heating. Spectrum for each decay chain comes from all  $\beta$ -transitions within that chain, and depends on branching ratios, decay constants, fractional intensities, and energy spectra of the individual transitions [37, 39]. The individual energy spectra are calculated using the Fermi theory of  $\beta$ -decay. The calculations are laid out in Fiorentini et al. [37], and the inputs are available in the table of isotopes [113] (data available online at <http://isotopes.lbl.gov/education/isotopes.htm>). Fiorentini et al. [114] propose that theoretically calculated decay spectra should be compared to directly measured spectra.

The antineutrino energy spectra for the three decay chains and  ${}^{40}\text{K}$   $\beta$ -decay in (3.2) are shown in Figure 5(a). For each decay, the average energy of the spectrum multiplied by the number of antineutrinos  $n_\nu$  emitted per chain yields the energy carried away by antineutrinos. The remainder  $Q_h$  of the decay energy heats the Earth per decay of a parent

**Table 3:** Atomic parameters ( $X$ ,  $\mu$ ,  $\lambda$ ,  $\tau_{1/2}$ , and  $n_\nu$ ), total and heating energies per decay ( $Q$ ,  $Q_h$ ), specific heating rates ( $h$ ), and antineutrino luminosities ( $l$ ) per unit mass of radionuclide. Adapted from Dye [39].

		$^{238}\text{U}$	$^{235}\text{U}$	$^{232}\text{Th}$	$^{40}\text{K}$
Natural isotopic fraction	$X$	0.9927	0.007204	1.000000	0.000117
Atomic mass	$\mu$ (g mol $^{-1}$ )	238.051	235.044	232.038	39.9640
Decay constant	$\lambda$ (10 $^{-18}$ s $^{-1}$ )	4.916	31.210	1.563	17.200
Half life	$\tau_{1/2}$ (Gy)	4.468	0.7038	14.05	1.277
Decay energy	$Q$ (pJ)	8.282	7.434	6.833	0.213
Energy for heating	$Q_h$ (pJ)	7.648	7.108	6.475	0.110
Specific heat generation	$h$ ( $\mu\text{W kg}^{-1}$ )	95.13	568.47	26.28	28.47 $^\dagger$
$\bar{\nu}_e$ 's per chain	$n_\nu$	6	4	4	0.893 $^\dagger$
Specific $\bar{\nu}_e$ luminosity	$l$ (kg $^{-1}$ $\mu\text{s}^{-1}$ )	74.6	319.9	16.2	231.2

$^\dagger$ Noninteger  $\bar{\nu}_e$ 's per chain value for  $^{40}\text{K}$  reflects branching into  $\beta$  decay and electron capture.  $^\ddagger$ Heat generation from  $^{40}\text{K}$  includes energy heat released in electron capture.

**Table 4:** Specific heat generation  $h_{el}$  and antineutrino luminosity  $l_{el}$ , per unit mass of element. From Dye.

	U	Th	K
$h_{el}$ ( $\mu\text{W kg}^{-1}$ )	98.5	26.3	0.00333
$l_{el}$ (kg $^{-1}$ $\mu\text{s}^{-1}$ )	76.4	16.2	0.0271

nuclide. Specific heating rates  $h$  and specific antineutrino luminosities  $l$ , per unit mass of each parent nuclide, can be calculated from

$$h = \frac{\lambda N_A Q_h}{\mu}, \quad (3.3)$$

$$l = \frac{\lambda N_A n_\nu}{\mu}, \quad (3.4)$$

where  $\lambda$  is decay constant,  $\mu$  is molar mass, and  $N_A$  is Avogadro's number. Heating rates  $h_{el}$  and luminosities  $l_{el}$  per unit mass of element are sums of isotopic values weighted by isotopic abundances  $X$ ,

$$l_{el} = \sum_{\text{nuclides}} Xl, \quad (3.5)$$

and similarly for  $h_{el}$ . The atomic parameters, decay energies per decay, and specific heating rates and antineutrino luminosities per unit mass of radionuclide, as reported by [39], are listed in Table 3. The heating rates and luminosities per unit mass of element are shown in Table 4. When the total decay powers and heating powers (per unit mass of rock) are evaluated for various BSE compositions (Table 2), it follows that  $\sim 80\%$  of decay energy heats the planet's interior while the remaining  $\sim 20\%$  is carried away by geoneutrinos [39]. This result is roughly independent of the choice of BSE model since the Th/U and K/U ratios are similar between all BSE estimates.



#### 4. Geoneutrino Oscillation

Neutrino oscillations (albeit  $\nu$ - $\bar{\nu}$  oscillation) were first hypothesized by Pontecorvo in 1957 [115] and have now been observed as neutrino flavor oscillation for solar, atmospheric, reactor, and accelerator-produced neutrinos. (Neutral current—neutrino in and neutrino out, no charged lepton—interactions are also possible for all neutrino flavors, but in practice here, are negligible in rate for a given visible energy.) Of the three flavors, only the terrestrial electron antineutrino is detectable by the neutron inverse  $\beta$ -decay mechanism, which reduces the observable geoneutrino signal. Most recently the evidence [116] for a nonzero value of the last mixing angle of three-flavor oscillation was confirmed [117, 118]. The three-flavor survival probability of electron antineutrino of energy  $E_\nu$  after flying a distance  $L$  is [39]

$$P_{ee}^{3\nu}(E_\nu, L) = 1 - \left\{ \cos^4\theta_{13} \sin^2 2\theta_{12} \sin^2 \Delta_{21} + \sin^2 2\theta_{13} \left[ \cos^2 2\theta_{12} \sin^2 \Delta_{31} + \sin^2 2\theta_{12} \sin^2 \Delta_{32} \right] \right\}, \quad (4.1)$$

where  $\theta_{12}$  and  $\theta_{13}$  are mixing angles,

$$\Delta_{ij}(E_\nu, L) = \frac{1.27 \left| \delta m_{ji}^2 \right| [\text{eV}^2] L [\text{m}]}{E_\nu [\text{MeV}]}, \quad (4.2)$$

and  $\delta m_{ji}^2 = m_j^2 - m_i^2$  is the neutrino mass-squared difference (by definition  $\delta_{31}^2 = \delta_{32}^2 + \delta_{21}^2$ ). Given the small value of  $\delta_{21}^2$  relative to  $\delta_{31}^2 \approx \delta_{32}^2$  [119] ( $\sim 3\%$ ), the survival probability (4.1) can be approximated by

$$P_{ee}(E_\nu, L) = 1 - \left[ \cos^4\theta_{13} \sin^2 2\theta_{12} \sin^2 \Delta_{21} + \frac{1}{2} \sin^2 2\theta_{13} \right]. \quad (4.3)$$

The oscillation length for antineutrinos with energies within the detectable range (1.8–3.3 MeV) is 60–110 km. Given the Earth's radius of  $\approx 6400$  km, the average survival probability,

$$\langle P_{ee} \rangle = 1 - \frac{1}{2} \left[ \cos^4\theta_{13} \sin^2 2\theta_{12} + \sin^2 2\theta_{13} \right] = 0.544_{-0.013}^{+0.017}, \quad (4.4)$$

can be used to oscillate the terrestrial antineutrino flux, which only introduces minimal error. According to analysis by Dye [39], the use of average survival probability underestimates the geoneutrino flux at the detector location. This effect comes from radionuclides distributed within the first oscillation length around the detector and is more pronounced at higher antineutrino energies. In oceanic regions with a thin and less enriched oceanic crust, the underestimation does not exceed 1%. It can reach few percent over continents. There are also interesting effects due to “matter effects” and the order of the neutrino masses, but they are negligible for our concerns herein.

## 5. Geoneutrino Flux

The fully oscillated geoneutrino flux spectrum from each radionuclide at observation location  $\vec{r}$  is calculated from [36]

$$\frac{d\phi(E_\nu, \vec{r})}{dE_\nu} = \frac{Xl}{n_\nu} \frac{dn(E_\nu)}{dE_\nu} \int_{\Omega} d^3\vec{r}' \frac{A(\vec{r}') \rho(\vec{r}') P_{ee}(E_\nu, |\vec{r} - \vec{r}'|)}{4\pi |\vec{r} - \vec{r}'|^2}, \quad (5.1)$$

where  $dn(E_\nu)/dE_\nu$  is the intensity energy spectrum, and  $\Omega$  is the volumetric domain with rock of density  $\rho$  that contains HPEs with elemental abundance  $A$  (mass of element per unit mass of rock). For an emission domain of uniform composition and using the average survival probability, (5.1) simplifies to yield the flux from a given radionuclide:

$$\phi(\vec{r}) = XlA \langle P_{ee} \rangle \int_{\Omega} d^3\vec{r}' \frac{\rho(\vec{r}')}{4\pi |\vec{r} - \vec{r}'|^2}. \quad (5.2)$$

The integral in (5.2) has been traditionally defined as the geological response factor  $G$  [15],

$$G \equiv \int_{\Omega} d^3\vec{r}' \frac{\rho(\vec{r}')}{4\pi |\vec{r} - \vec{r}'|^2}. \quad (5.3)$$

For a uniform density spherical shell geoneutrino emission domain bounded by radii  $r_1$  and  $r_2$ , both are smaller than the observation point radius  $a$  ( $\sim$ Earth's radius), the integral can be evaluated exactly [15, 37] (note that this is a different situation than that in calculating the force of gravity from a shell, as this is a scalar addition not vector, and there is no cancellation of opposing transverse components),

$$\begin{aligned} G_{\text{unif. shell}} &= \frac{\rho}{4\pi} \int_{r_1}^{r_2} dr' \int_0^\pi d\vartheta' \int_0^{2\pi} d\varphi' \frac{r'^2 \sin \vartheta'}{a^2 + r'^2 - 2ar' \cos \vartheta'} \\ &= \frac{\rho a}{4} \left[ 2 \frac{r_2 - r_1}{a} - \left( 1 - \frac{r_2^2}{a^2} \right) \ln \left( \frac{a + r_2}{a - r_2} \right) + \left( 1 - \frac{r_1^2}{a^2} \right) \ln \left( \frac{a + r_1}{a - r_1} \right) \right]. \end{aligned} \quad (5.4)$$

## 6. Geoneutrino Detection

The same detection mechanism that Reines and Cowan [120, 121] used in their pioneering experiment is employed in present-day geoneutrino-counting detectors. It uses the neutron inverse  $\beta$ -decay process, where an electron antineutrino scatters on a free proton to produce a neutron and a positron,

$$\bar{\nu}_e + p \rightarrow e^+ + n. \quad (6.1)$$

A subsequent prompt annihilation of the positron with an electron and delayed capture of neutron on a proton provide light flashes in a scintillating liquid, coincident in time

and in space, which offers a powerful method for identification of antineutrino events and elimination of single-flash background (Figure 6). Reaction (6.1) works for antineutrinos with energies  $E_\nu$  above the kinematic threshold, the difference between rest mass energies of neutron plus positron and proton,  $\Delta + m_e = 1.804 \text{ MeV}$ , where  $\Delta = M_n - M_p$ .

The positron carries most of the energy, its starting kinetic energy being  $T_e \approx E_\nu - 1.8 \text{ MeV}$ . The prompt signal of the positron annihilation with an electron in the medium,

$$e^+ + e^- \rightarrow \gamma + \gamma, \quad (6.2)$$

comes within few nanoseconds of the antineutrino interaction in currently used organic scintillating liquids. The energy of the light flash  $E_{\text{vis1}}$  scales with the incident antineutrino energy,  $E_{\text{vis1}} \approx T_e + 2m_e = E_\nu - 0.8 \text{ MeV}$ . The neutron receives most of the antineutrino momentum. It slows down and in 20–200  $\mu\text{s}$  combines with a proton in the medium to form a deuteron,

$$n + p \rightarrow d + \gamma. \quad (6.3)$$

The release of deuteron binding energy of 2.2 MeV causes a second light flash in the scintillating medium.

Above the threshold energy ( $\approx 1.8 \text{ MeV}$ ) of reaction (6.1), the cross-section scales with the square of the positron energy  $E_e = E_\nu - \Delta$  [123]. Written in terms of antineutrino energy,

$$\sigma(E_\nu) = 9.52(E_\nu - \Delta)^2 \sqrt{1 - \frac{m_e^2}{(E_\nu - \Delta)^2}} \times 10^{-44} \text{ cm}^2, \quad (6.4)$$

where  $E_\nu$ ,  $\Delta$ , and  $m_e$  are in MeV. The cross-section is plotted in Figure 5(b). For each decay chain, the product of antineutrino intensity energy spectrum with the cross-section yields the interaction energy spectrum (Figure 5(c)). Out of the nine  $\beta$ -decaying nuclei in the  $^{238}\text{U}$  decay network, only three nuclides ( $^{234}\text{Pa}$ ,  $^{214}\text{Bi}$ , and  $^{210}\text{Tl}$ ) emit antineutrinos with energy exceeding the detection threshold 1.8 MeV. One transition of  $^{234}\text{Pa}$  together with two transitions of  $^{214}\text{Bi}$  accounts for 99.8% of signal from  $^{238}\text{U}$  decay chain [114]. In  $^{232}\text{Th}$  decay chain, only two nuclides ( $^{228}\text{Ac}$ ,  $^{212}\text{Bi}$ ) emit detectable antineutrinos, and 99.8% of the signal comes from one transition of  $^{212}\text{Bi}$  and the first of two transitions of  $^{228}\text{Ac}$  [114]. Antineutrinos from  $^{40}\text{K}$  of maximum energy 1.311 MeV, as well as  $^{235}\text{U}$  antineutrinos, are below the threshold of inverse beta decay. This is inconvenient for geophysics as information on terrestrial K is desirable.

The cross-section of inverse  $\beta$ -decay reaction (6.4) is extremely small. In their 1950's experiment, Cowan and Reines used a cubic meter-sized detector placed some 10 m from Savannah River power. With the high reactor antineutrino flux they achieved an event rate of up to  $\sim 3$  events per hour [10]. A typical detectable geoneutrino flux from the entire Earth is of the order of  $10^6 \text{ cm}^{-2}\text{s}^{-1}$ . It requires an order of  $10^{32}$  free protons to reach reasonable interaction rates (tens of events per year). This translates into a required detector mass of  $\gtrsim 1$  kiloton.

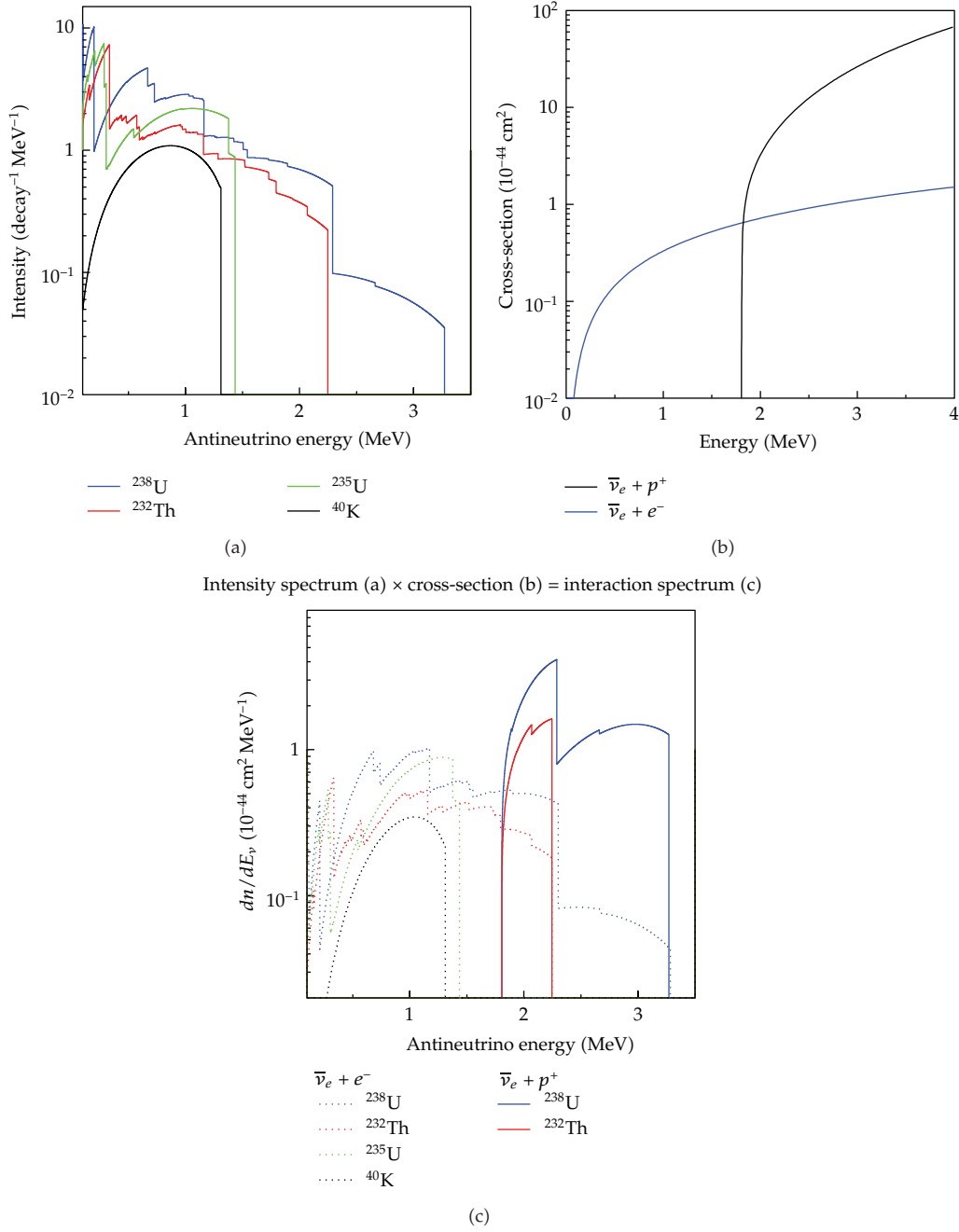


**Figure 5:** (a) Antineutrino intensity energy spectra. The area below each curve equals the number of antineutrinos  $n_\nu$  emitted per decay. (b) Total cross-sections for scattering of antineutrinos on protons and electrons. (c) Antineutrino interaction energy spectra per decay of parent nuclide. Solid lines in (b) and (c) show antineutrino scattering on protons; dashed lines show scattering on electrons. Adapted from [39], reproduced/modified by permission of American Geophysical Union.



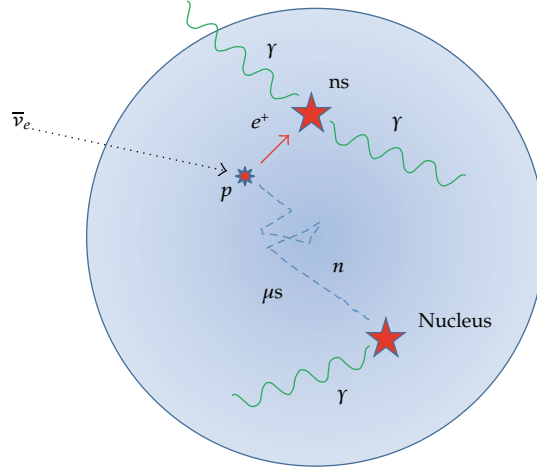


**Figure 6:** Schematic of antineutrino detection by scattering on protons. Prompt signal comes from positron annihilation, delayed signal occurs when neutron captures a proton.

Similarly to (5.1) for antineutrino flux spectrum, the event spectrum of detection at efficiency  $\varepsilon$  is

$$\frac{dN(E_\nu, \vec{r})}{dE_\nu} = \frac{\varepsilon X l}{n_\nu} \frac{dn(E_\nu)}{dE_\nu} \sigma(E_\nu) \int_{\Omega} d^3 \vec{r}' \frac{A(\vec{r}') \rho(\vec{r}') P_{ee}(E_\nu, |\vec{r} - \vec{r}'|)}{4\pi |\vec{r} - \vec{r}'|^2}, \quad (6.5)$$

where  $\sigma(E_\nu) dn(E_\nu)/dE_\nu$  is the interaction spectrum. For emission from a uniform composition domain and with the average survival probability, (6.5) simplifies to

$$N(\vec{r}) = \frac{\varepsilon X l A \langle P_{ee} \rangle G}{C}, \quad (6.6)$$

where a conversion factor  $C$  was introduced such that

$$\frac{1}{C} = \frac{1}{n_\nu} \int dE_\nu \frac{dn(E_\nu)}{dE_\nu} \sigma(E_\nu). \quad (6.7)$$

It relates the antineutrino event rate  $N$  (number of events detected per unit time) to the antineutrino flux  $\phi$  (number or  $\bar{\nu}_e$  per unit area and unit time) at the detector. Comparing (5.2) and (6.6), we arrive at

$$N = \frac{\varepsilon \phi}{C}. \quad (6.8)$$

It is convenient to introduce the signal rate  $R$  (number of interactions per unit time) counted in “terrestrial neutrino unit” (TNU), defined as one interaction over a year-long fully efficient exposure of  $10^{32}$  free protons [124]. Unlike the event rate  $N$  which depends on detector size

and efficiency of detection  $\epsilon$ , the signal rate  $R$  only depends on the detection mechanism. It follows that

$$R = \frac{\phi}{C} = \frac{XlA\langle P_{ee}\rangle G}{C}. \quad (6.9)$$

The signal-rate-to-flux conversion factors are [36, 37, 39]

$$\begin{aligned} C_U &= 7.6 \times 10^4 \text{ cm}^{-2} \text{ s}^{-1} \text{ TNU}^{-1}, \\ C_{\text{Th}} &= 2.5 \times 10^5 \text{ cm}^{-2} \text{ s}^{-1} \text{ TNU}^{-1}. \end{aligned} \quad (6.10)$$

Radiogenic heat generated in a uniform composition domain of mass  $M$  is

$$H = XhAM. \quad (6.11)$$

Equations (6.9) and (6.11) provide a proportionality relation between signal rate  $R$  or flux  $\phi$  and heat production  $H$ ,

$$\begin{aligned} R &= \frac{\langle P_{ee} \rangle}{C} \frac{G}{M} \frac{l}{h} H, \\ \phi &= \langle P_{ee} \rangle \frac{G}{M} \frac{l}{h} H, \end{aligned} \quad (6.12)$$

coming from each radionuclide. For a given Th to U abundance ratio,  $\kappa \equiv A_{\text{Th}}/A_U$ , we get the following heating, flux, and signal rate ratios:

$$\begin{aligned} \frac{H_{\text{Th}}}{H_U} &= \frac{X_{\text{Th}}h_{\text{Th}}}{X_Uh_U} \kappa = 0.278 \kappa, \\ \frac{\phi_{\text{Th}}}{\phi_U} &= \frac{X_{\text{Th}}l_{\text{Th}}}{X_Ul_U} \kappa = 0.219 \kappa, \\ \frac{R_{\text{Th}}}{R_U} &= \frac{C_U}{C_{\text{Th}}} \frac{\phi_{\text{Th}}}{\phi_U} \kappa = 0.066 \kappa. \end{aligned} \quad (6.13)$$

For a whole Earth Th/U ratio of 4.0 [60], these relations imply that while radiogenic heating and the geoneutrino flux are contributed roughly equally by  $^{232}\text{Th}$  and  $^{238}\text{U}$  (53% and 47%, resp., come from from Th and U), only 21% of detected signal is comes from Th. Table 5 lists the masses  $M$  and geological response factors  $G$  for Earth reservoirs.

Background signal adds to the geologically interesting signal in the geoneutrino energy range. Background signal consists of nuclear reactor antineutrinos, fast neutrons generated by cosmic ray muon interactions, long-lived neutron-rich radionuclides ( $^8\text{He}$  and  $^9\text{Li}$ ),  $^{13}\text{C}(\alpha, n)^{16}\text{O}$  reaction, and accidental  $\gamma$ -ray background. It is important to realize that inverse  $\beta$ -decay provides strong rejection to single-hit backgrounds such as those from solar neutrinos. Requiring two hits close in spaces and time, with the second (delayed hit being of

**Table 5:** Masses of Earth reservoirs  $M$  and geological response factors  $G$  (5.3) based on PREM [125], where each reservoir is a spherical shell of uniform thickness. More precise crustal mass calculated using a seismically determined crustal structure (model CRUST2.0 [126]) is also included.

	$M$ ( $10^{24}$ kg)	$G$ ( $10^{10}$ kg m $^{-2}$ )
Crust	0.0312 (C2: 0.0277)	0.0218
Mantle	4.00	1.18
Outer core	1.84	0.386
Inner core	0.0984	0.0194
Earth	5.97	1.60

**Table 6:** Geographical location, size, and depth of geoneutrino detectors. Size in number of free protons, depth in meter water equivalent. Adapted from [38].

Detector	Location	Lat. °N	Lon. °E	Free $p$ $10^{32}$	Depth m.w.e.
<i>Operating or under construction</i>					
KamLAND	Kamioka, Japan	36.43	137.31	0.6	2700
Borexino	LNGS, Gran Sasso, Italy	42.45	13.57	0.1	3700
SNO+	SNOLAB, Sudbury, Ontario, Canada	46.47	-81.20	0.6	6000
<i>Proposed</i>					
LENA	CUPP, Pyhäsalmi, Finland	63.66	26.05	36.7	4000
Homestake	DUSEL, Lead, South Dakota, USA	44.35	-103.75	0.5	4500
Baksan	BNO, Caucasus, Russia	43.29	42.70	4.0	4800
Daya Bay II	Daya Bay, China			8–42	
Hanohano	Pacific	19.72	-156.32	7.3	4500

known energy, is a very powerful tool for rejecting most backgrounds. Complete discussion and estimates of the background are presented in Dye [39].

Another possible mechanism for geoneutrino detection involves antineutrino scattering on electrons [127], which would broaden the energy range of detectable geoneutrinos below the 1.8 MeV energy threshold of inverse  $\beta$ -decay including signal from  $^{40}\text{K}$  decay. The interaction cross-sections and antineutrino energy spectra are shown in Figure 5. While the lack of a coincidence tag makes the detection challenging, the recoiling electrons offer the possibility to determine the direction of the incoming antineutrino [39]. The electron events can be recorded in a device such as the miniTimeCube [128] near a reactor as a demonstration. Further development is needed before this method can be employed for geoneutrino detection.

## 7. Detectors

Instruments capable of geoneutrino detection contain a large volume of liquid scintillator (LS), monitored by inward facing photomultiplier tubes (PMTs), and are operated underground in order to reduce the cosmic-ray-induced atmospheric muon flux. They are used to investigate neutrino oscillations, nucleon decay, issues in astrophysics and geophysics, and to monitor nuclear reactors. Table 6 lists selected parameters of operating and proposed geoneutrino detectors.

KamLAND (Kamioka liquid-scintillator antineutrino detector, website at <http://www.awa.tohoku.ac.jp/KamLAND/>), is a 1 kiloton LS detector located 1 km underground beneath Mt. Ikenoyama summit in the old Kamioka zinc mine, Japan. The LS is composed of 80% of dodecane (diluter), 20% of pseudocumene (energy transferor), and  $1.36 \text{ g liter}^{-1}$  of diphenyloxazole (PPO, scintillating molecule). The fiducial volume is monitored by  $\sim 1900$  PMTs, which cover 34% of the surface area. Number of free protons is  $\sim 6 \times 10^{23}$ , and detection efficiency is 80.7% and 75.1% for signals from U and Th, respectively [19, 31].

Borexino (website at <http://borex.lngs.infn.it/>) is a 278-ton LS detector at Laboratori Nazionali del Gran Sasso (LNGS) located midway a 10 km long highway tunnel below the Central Apennine Mountains in Italy. The scintillating liquid is pseudocumene doped with  $1.5 \text{ g liter}^{-1}$  of PPO. Scintillations are monitored by  $\sim 2200$  PMTs covering 30% of surface area [20, 129].

SNO+ (website at <http://snoplus.phy.queensu.ca/>) is a follow-up experiment to SNO (Sudbury Neutrino Observatory) at SNOLAB near Sudbury, Ontario, Canada. Located 2 km underground in a nickel mine, it will be refilled with linear alkylbenzene (LAB) LS. It is expected to become operational in 2013.

Several other geoneutrino-detecting experiments have been proposed: LENA (website at [http://www.e15.ph.tum.de/research\\_and\\_projects/lena/](http://www.e15.ph.tum.de/research_and_projects/lena/)), a 50-kiloton detector at the Center for Underground Particle Physics (CUPP) located at the Pyhäsalmi mine near Pyhäjärvi, Finland [130]; Homestake at the Deep Underground Science and Engineering Laboratory (DUSEL) in Lead, South Dakota, USA [131]; Baksan at the Baksan Neutrino Observatory (BNO) in Russia [132]; Hanohano (online information at <http://www.phys.hawaii.edu/~jgl/hanohano.html>), a 10–50 kiloton ocean-faring transportable detector based in Hawaii [133, 134]; a 10–50 kiloton detector of the Daya Bay II experiment [135].

## 8. Earth's Reference Model and Flux Prediction

The development of reference models for terrestrial antineutrino emission and evaluation of geoneutrino flux predictions is critical for two main reasons. First, these predictions guide the design of geoneutrino detectors. Second, they are necessary for interpretation of the antineutrino data. Since the first attempts in the 1960s [11, 12] and a presentation of systematic approach to geoneutrino predictions by Krauss et al. [15], the emission models have been refined, following advances in both geological sciences and neutrino physics [16–18, 22, 30, 31, 36–39, 69, 124, 136–139].

The geological inputs for calculation of geoneutrino emission are the rock density  $\rho(\vec{r})$  and chemical abundances  $A(\vec{r})$  of U, Th, and K throughout the Earth's interior. The predicted geoneutrino flux is then calculated from (5.1) and (5.2), respectively, assuming the neutrino physics inputs are known.

### 8.1. Crustal Flux

The proportionality of antineutrino flux to inverse square source distance means that a significant portion of the signal originates near the observation point. Furthermore, the continental crust is highly enriched in geoneutrino producing HPEs, as was discussed in Section 2. Figure 7, showing cumulative flux within a given distance from a detector,



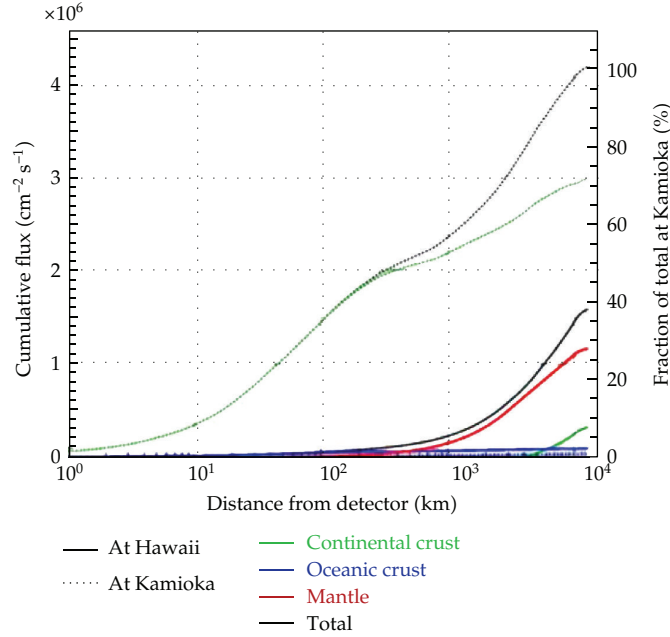


**Figure 7:** Cumulative geoneutrino flux within a given distance from a detector, for observation at Kamioka (continental site) and Hawaii (oceanic site). Reprinted from [36] with permission from Elsevier.

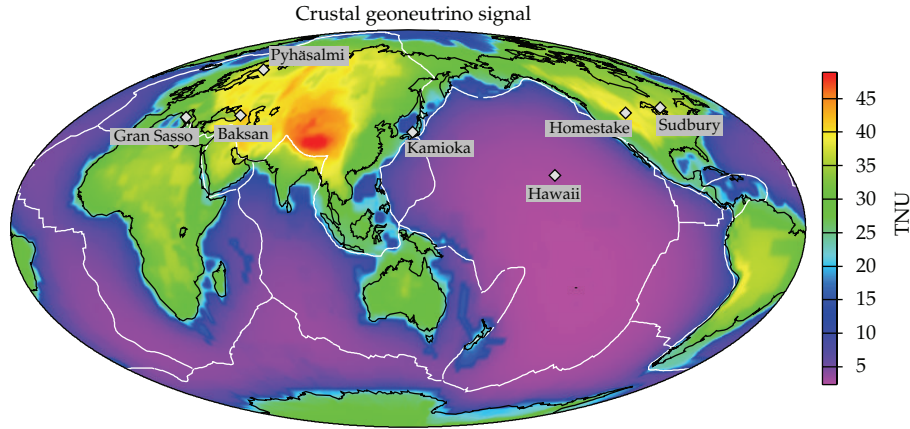
illustrates the point. Both operating geoneutrino detectors, KamLAND and Borexino, as well as SNO+ and all but one of the proposed future experiments are located in continental areas. At Kamioka, for example,  $\sim 50\%$  of the signal originates within 500 km distance from the detector, almost exclusively in the continental crust [36]. Any attempts to extract mantle information from geoneutrino data require construction of accurate crustal geological models [31, 36, 37, 39, 124, 136, 137]. This involves constructing a global crustal model and local refinements in the vicinity (few hundred kms) of the detector. Effects of local geology were carefully evaluated for both KamLAND [36, 37, 136] and Borexino [140].

Current global crustal models use CRUST2.0 model of the crustal structure [126], supplemented with estimates of crustal composition coming from petrological studies. CRUST2.0 describes a  $2^\circ \times 2^\circ$  tiled, vertically layered crustal geometry; includes rock densities in each of the five rock layers (upper and lower sediments, and upper, middle, and lower crust) in each tile. Chemical abundance estimates are given by Rudnick and Gao [53] for continental crust, White and Klein [141] for oceanic crust, and Plank [142] for oceanic sediments. A new, more detailed reference model for the crust and uppermost mantle is being developed [143].

In Figure 8, we show a global map of predicted crustal geoneutrino signal from [68]. The spatial pattern of the geoneutrino signal correlates with crustal thickness and continental distribution. HPE abundances used in the calculation are listed in Table 7. A- and B-type tiles of CRUST2.0 are considered oceanic, all other tile types are continental. This model outputs  $7.8 \pm 0.9$  TW of radiogenic power from continental crust and  $0.22 \pm 0.03$  TW from oceanic crust (Table 7).

**Table 7:** HPE abundances used in calculation of the global crustal flux in Figure 8 and calculated abundances for the bulk crust and bulk mantle.

	U (ppm)	Th (ppm)	K (%)	Reference	
Input for crust calculation					
Upper cont. crust + sed.	2.7 ± 21%	10.5 ± 10%	2.32 ± 10%	[53]	
Middle cont. crust	1.3 ± 31%	6.5 ± 8%	1.91 ± 14%	[53]	
Lower cont. crust	0.2 ± 80%	1.2 ± 80%	0.51 ± 30%	[53]	
Oceanic sediments	1.73 ± 9%	8.10 ± 7%	1.83 ± 7%	[142]	
Oceanic crust	0.07 ± 30%	0.21 ± 30%	0.072 ± 30%	[141]	
				Th/U	Power TW
Bulk crust, calculated					
Bulk continental crust	1.47 ± 0.25	6.33 ± 0.50	1.63 ± 0.12	4.3	7.8 ± 0.9
Bulk oceanic crust	0.15 ± 0.02	0.58 ± 0.07	0.16 ± 0.02	3.9	0.22 ± 0.03
Bulk crust	1.17 ± 0.19	5.02 ± 0.38	1.30 ± 0.09	4.3	8.1 ± 0.9
	U (ppb)	Th (ppb)	K (ppm)	Th/U	Power TW
Bulk mantle, calculated					
Cosmochemical mantle	4.1	8.4	57	2.0	3.3
Geochemical mantle	12	46	192	3.8	12
Geodynamical mantle	23	90	310	3.9	22

**Figure 8:** Global map of crustal geoneutrino signal (U + Th) in TNU. Prediction is based on CRUST2.0 crustal structure and HPE abundances listed in Table 7. Continental outlines (black), plate boundaries (white), and locations of geoneutrino detectors are plotted. Mollweide equal-area projection was used. See [69].

## 8.2. Mantle Flux

Density in the Earth increases with depth. In addition to the density increase due to compressibility, pressure induces solid-solid mineral phase transitions which modify the density. For the sake of geoneutrino prediction, lateral density variations caused by temperature anomalies ( $\delta\rho \lesssim 1\%$ ) can be neglected, and only depth-dependent density used,  $\rho(\vec{r}) = \rho(r)$ . The Preliminary Reference Earth Model (PREM) [125] has been a

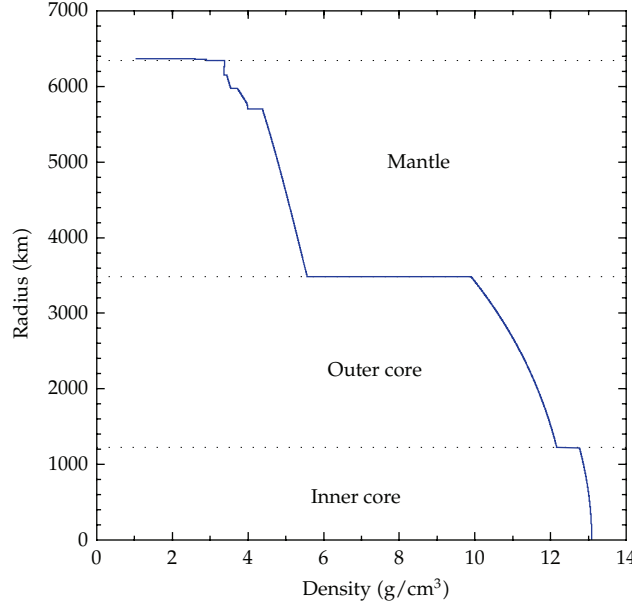


**Figure 9:** Depth dependence of density as given by PREM [125].

**Table 8:** Mantle geoneutrino signal in TNU predicted under the assumption of uniform distribution of U and Th.

Uniform mantle	$R_U$ (TNU)	$R_{Th}$ (TNU)	$R_{U+Th}$ (TNU)
Cosmochemical mantle	2.6	0.35	2.9
Geochemical mantle	7.5	1.9	9.4
Geodynamical mantle	14	3.7	18

standard in geophysics. PREM provides a parameterization of density as a piecewise third-order (at most) polynomial in radius (Figure 9). The density increases from  $\sim 3400 \text{ kg m}^{-3}$  to  $\sim 5600 \text{ kg m}^{-3}$  across the mantle.

The average radionuclide abundances in the mantle are calculated from the elemental mass balance as follows:

$$A_{BSE} M_{BSE} = A_{crust} M_{crust} + A_{mantle} M_{mantle}, \quad (8.1)$$

using BSE abundance from Table 2, crustal abundance from Table 7, and the reservoir masses from Table 5. The mantle abundances, based on three different BSE estimates—cosmochemical [64], geochemical [60], and geodynamical [65]—are reported in Table 7. The predicted geoneutrino signal coming from a mantle of uniform composition can be easily evaluated from (6.9). The predictions, listed in Table 8, should be compared to the crustal prediction at continental sites ( $\gtrsim 30$  TNU, Figure 8) to appreciate the difficulty of extracting information about the mantle from continent-based geoneutrino detection. See [39, 69] for complete treatment including model uncertainties.

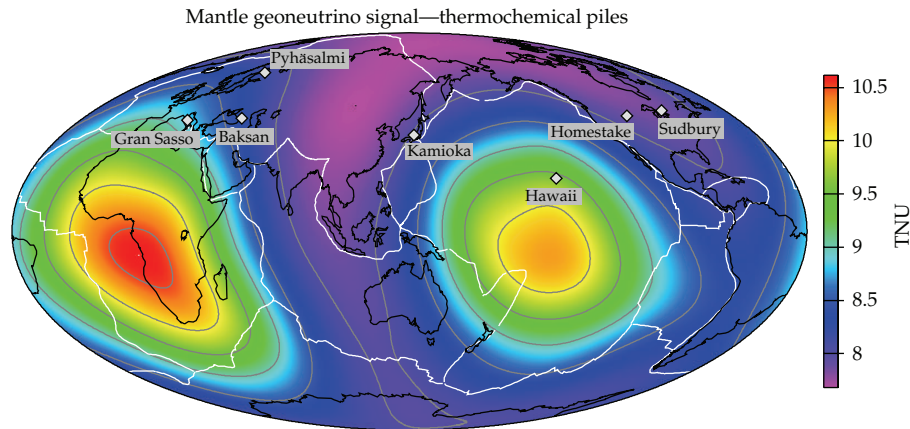


**Figure 10:** Lateral variation of mantle geoneutrino signal predicted for a “thermochemical piles” model. Uses BSE and DM compositional estimates of [60, 68]. See [69].

As we discussed in Section 2, geochemical and geodynamical abundance estimates, combined with compositions inferred for shallow mantle, are not consistent with uniform composition of the whole mantle. The usual fix calls for the existence of a mantle reservoir enriched in incompatible elements. Geophysical observations now disfavor the traditional mantle layering at 660 km depth. An enriched reservoir, however, may exist in the lowermost mantle within few hundred kms of the CMB. The effect of such segregation of HPEs at depth is a decrease in mantle geoneutrino signal [38]. For an enriched layer of uniform thickness atop the CMB, the effect is moderate, with a mantle signal reduction by 25% at most [69]. It has also been suggested that LLSVPs below Africa and Pacific (Figure 3) may be compositionally distinct from the ambient mantle. Consequences of such antipodal deep mantle piles for mantle geoneutrino detection were investigated in [69, 139]. Figure 10 shows the lateral variation of mantle geoneutrino flux predicted for a “thermochemical piles” model, where the piles are enriched in HPEs. The enrichment follows from the compositional estimates used for BSE and DM. One particular model from [69] is shown here, which uses a geochemical BSE [60] and the relatively “warm” DM composition of [68], and results in the piles enriched by factors of 6.3 and 12 relative to the ambient mantle for U and Th, respectively. Some model combinations result in higher enrichments, and therefore a more pronounced variation of the geoneutrino signal. However, strong enrichment in radiogenic heat production has dynamical consequences on the stability and longevity of such piles and may work against the geochemical requirement of primordial nature of the enriched reservoir. This is an area of active research in geodynamics [86, 144, 145].

Figure 11 follows from Figures 8 and 10 and shows the fraction of the total signal (from crust + mantle, assuming no radioactivity in the core) that is coming from the mantle. It clearly shows the benefit of geoneutrino detection at an oceanic site in the Pacific ocean away from nuclear reactors, where the proportion of the signal from a mantle with geochemical BSE abundances can be as high as 80%. Pacific ocean basin as also the location of a mantle flux maximum is predicted from the thermochemical piles model. It is proposed that geoneutrino detection at two Pacific sites, one being at the predicted peak of mantle flux and the other away from it, may be exploited to test the chemical piles hypothesis [69].



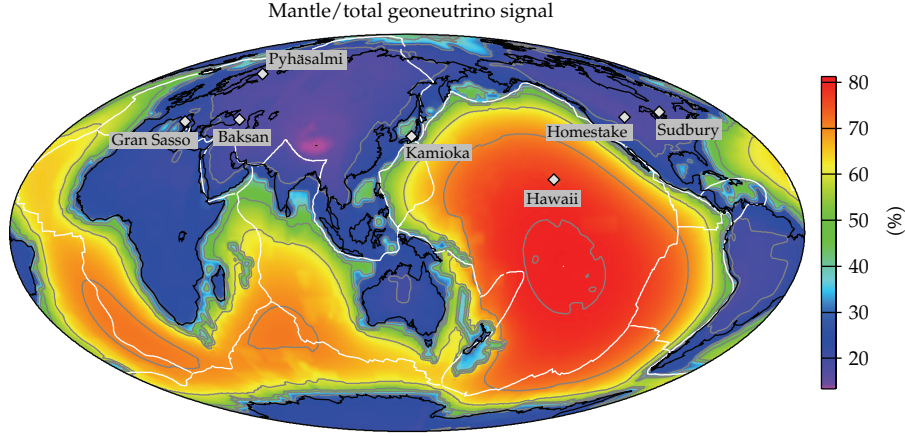


**Figure 11:** Ratio of mantle to total (mantle + crust) geoneutrino signal as predicted from crustal and mantle models shown in Figures 8 and 10. See [69].

## 9. Geoneutrino Observations

Geoneutrinos have been now observed at  $\sim 4\sigma$  confidence level (CL) by both operating detectors: KamLAND and Borexino. Extracting geophysical information from geoneutrino measurements is not straightforward. The geoneutrino event rate prediction is obtained with an integration of the energy spectrum of antineutrino contributions coming from U and Th distributed in the Earth volume, weighted by the inverse square distance, subject to oscillations, and modulated by interaction cross-section ([146] and (6.5)).

### 9.1. KamLAND Measurement

The first detection of geoneutrinos was reported by KamLAND group in 2005 [18]. It is based on detector live-time of  $749.1 \pm 0.5$  days,  $(3.46 \pm 0.17) \times 10^{31}$  of target protons, that is, an exposure of  $(7.09 \pm 0.35) \times 10^{31}$  target proton years. The detector efficiency is estimated at  $0.687 \pm 0.007$ . Their maximum-likelihood analysis, constrained to Th/U ratio of 3.9, gives  $28^{+16}_{-15}$  geoneutrino events. The corresponding flux is  $6.4^{+3.6}_{-3.4} \text{ cm}^{-2} \mu\text{s}^{-1}$ . The 99% CL upper limit is 71 geoneutrino events or flux of  $16.2 \text{ cm}^{-2} \mu\text{s}^{-1}$ , which translates into a radiogenic power of 60 TW from  $^{238}\text{U} + ^{232}\text{Th}$  (i.e., heat production that would exceed the Earth's heat loss).

Continued KamLAND measurement benefited from instrumentation improvements and decreased in nuclear reactor flux (shutdown of Kashiwazaki-Kariwa nuclear power plant following a 2007 earthquake). New results reported in 2011 [19] extend the previous data set. Data are based on exposure of  $(3.49 \pm 0.07) \times 10^{32}$  target proton years, or a live-time of 2135 days (5.8 years) and  $(5.98 \pm 0.12) \times 10^{31}$  target protons in the fiducial volume. Of the 841 candidate  $\bar{\nu}_e$  events within the geoneutrino energy limits,  $729 \pm 32$  is the predicted background, and  $111^{+45}_{-43}$  were considered geoneutrino events. Maximum-likelihood analysis of the data, unconstrained with respect to Th/U ratio, gives 65 and 33 geoneutrino events from  $^{238}\text{U}$  and  $^{232}\text{Th}$ , respectively. This translates to Th/U ratio of 7.6 (6.13); however, Th/U remains unconstrained at  $1\sigma$  level. Constraining Th/U to 3.9 yields a total number of  $106^{+29}_{-28}$  geoneutrino events, or a geoneutrino signal rate of  $38 \pm 10$  TNU and heat production of  $20^{+8.8}_{-8.6}$  TW from  $^{238}\text{U} + ^{232}\text{Th}$ . Null hypothesis of no geoneutrinos is rejected at 99.997%

CL. KamLAND results also provide a 90% CL upper limit of 5.2 TW on the power of a hypothetical nuclear georeactor in the Earth's core. Assessment of KamLAND data by Dye [39] argues for a mantle signal rate of  $12 \pm 11$  TNU at Kamioka.

## 9.2. Borexino Measurement

Borexino collaboration reported geoneutrino detection in 2010 [20]. Of the 15 candidate event in the geoneutrino energy window,  $5.3 \pm 0.3$  constitute background. An unconstrained maximum-likelihood analysis yields  $9.9^{+4.4}_{-3.4}$  geoneutrino events. Assuming  $\text{Th}/\text{K} = 3.9$ , this translates to a signal rate of  $65^{+27}_{-22}$  TNU. A geoneutrino null hypothesis rejected at 99.997 CL. Borexino data give a 95% CL upper limit of 3 TW on the power of a nuclear georeactor in the core. This is a better constraint compared to one from KamLAND, a benefit of much lower man-made reactor  $\bar{\nu}_e$  signal at Gran Sasso. According to Dye [39], Borexino registers a mantle geoneutrino signal at a rate of  $40^{+27}_{-23}$  TNU at Gran Sasso.

## 9.3. Combined KamLAND + Borexino Analysis

A combined analysis of the KamLAND and Borexino data was performed by Fogli et al. [147] and most recently by Fiorentini et al. [146] with a focus on constraining the mantle component of the geoneutrino signal. In [146], the null hypothesis of no geoneutrino flux is rejected at  $4.2\sigma$ . After subtraction of crustal signal, based on a crustal reference model that includes local refinements, the mantle rate emerges at  $2.4\sigma$  (98.4% CL) assuming that the mantle signal is identical at the two sites. The preferred value of  $\text{Th}/\text{U}$  ratio  $\sim 8$  is not statistically significant, since any  $\text{Th}/\text{U}$  value is permissible at  $1\sigma$  level. When  $\text{Th}/\text{U}$  is constrained to reflect variation between various BSE abundance estimates,  $1.7 \leq \text{Th}/\text{U} \leq 3.9$ , the analysis results in a mantle signal rate of  $23 \pm 10$  TNU from  $^{238}\text{U} + ^{232}\text{Th}$  [146]. Figure 12 shows the results in relation to various models of BSE composition.

# 10. Discussion and Prospects

Geologists already know that there is a lot of radioactivity in the continental crust (8 TW) and they know it quite well ( $\pm 1$  TW). They are asking about the mantle: is it "cosmochemical" (so that it produces  $3 \pm 2$  TW of radiogenic power), "geochemical" ( $12 \pm 4$  TW), or "geodynamical" ( $25 \pm 3$  TW)? Nondirectional geoneutrino detection at the existing and future continental sites cannot resolve mantle models, even with the improved precision of future detectors [39]. Oceanic deployment of a geoneutrino detector away from continental crust and nuclear power plants has been repeatedly suggested as a way to optimize the sensitivity to mantle signal [17, 19, 36, 38, 40]. It is proposed that an oceanic site detection in the Pacific can resolve the mantle models [39, 69].

## 10.1. $^{40}\text{K}$ Geoneutrinos?

Potassium accounts for some 20% of radiogenic power within the Earth. Antineutrinos from potassium are produced entirely below the energy threshold of antineutrino quasielastic scattering on free protons, thus currently undetectable. Dye [39] discusses possibilities of  $^{40}\text{K}$

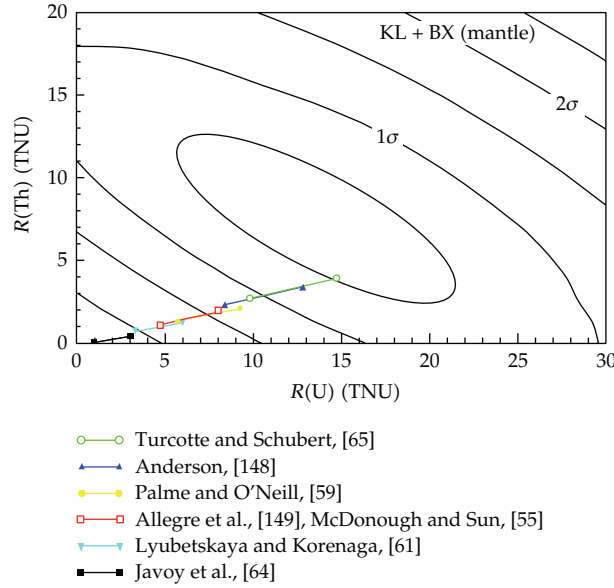


**Figure 12:** Experimental constraints on mantle flux from combined analysis of KamLAND and Borexino data (black contour lines), compared to predictions from various BSE abundance estimates [55, 59, 61, 64, 65, 148, 149]. Adapted from [146].

antineutrino detections, which include scattering on other nuclear targets ( $^3\text{He}$  or  $^{106}\text{Cd}$ ) and elastic scattering on atomic electrons. Both methods require further development.

### 10.2. Directionality?

The angular distribution of geoneutrinos was investigated in [38, 150–152] and most recently in [40]. Differences in angular distribution of geoneutrinos arriving from the crust and the mantle could be used to separate the signals if the directional information was available. Directional measurement away from continents might resolve a deep-seated mantle reservoir [40]. Directional detection was achieved in a statistical sense in the CHOOZ experiment, which uses a loaded liquid scintillator, by observing the weak correlation between the incident and the prompt-to-delayed-signal direction in inverse  $\beta$ -decay [153]. In principle, it is possible to exploit this correlation also for unloaded scintillators, such as those used in geoneutrino studies, however, obtaining statistically significant result requires thousands of events, well above the yield of geoneutrino detectors [154]. As we have noted earlier, electron (charged current) events below the inverse beta threshold will preserve neutrino directionality rather well. So, despite the more difficult extraction of these signatures from background (no delayed neutron tag) these events offer interesting potential for resolving source directions and ultimately geoneutrino Earth tomography.

## 11. Conclusion

We have reviewed the short history of geoneutrinos, the budding study of electron antineutrinos from inside the Earth as a unique telltale of the source of internal Earth heating.

While the notion of using the neutrinos from the uranium and thorium decay chains has been around for decades, notably stimulated by the landmark paper of Krauss et al. in 1984 [15], it is only in the last decade that the tiny geoneutrino interaction rate has begun to be revealed by the hundreds of tons KamLAND and Borexino experiments. The signals are feeble and we have barely reached five standard deviation detection, yet we are now less than a factor of two off from our predictions about the absolute source of Earth heating. In other words, there is no surprising new source of electron antineutrinos in the energy range of 1.8 to 3.6 MeV. And it is no surprise that a geoneutrino signal does exist, inescapably since we know the U/Th content of at least the top few hundred kilometers of the Earth and we now know neutrino properties fairly well.

At present, since both KamLAND and Borexino are located near continental plate margins, the neutrino flux is dominated by sources in the local ( $<500$  km) crust. Unfortunately the count of neutrinos from the mantle, which is where we want to know the U/Th content, is so far only a minute fraction of the total. We have reviewed some extreme models as arise from differing approaches in geoscience, and we find that we cannot yet distinguish between models, though the cosmochemical model [64] and the extremes of the collisional erosion model [62] seem to be disfavored at the  $2.5\sigma$  level.

Progress is on the horizon with the launch of the SNO+ experiment in Canada. There are proposals for several very large experiments, the fifty-kiloton LENA to be located in a mine in Finland, the deep ocean Hanohano in the deep Pacific, and a twenty-kiloton scale (not surely determined yet) Daya Bay II detector in China. All of these are at least five years out.

Beyond simple counting of neutrinos from a given location, there is much to be done. First of all, moving detectors to various deep ocean locations can begin to explore the lateral inhomogeneity of the U/Th distribution. There is much opportunity for discovery here, should the hot spots or peculiar areas such as the mid-Pacific Rise be associated with concentrations of U/Th. Moreover, though largely dismissed by geologists, there have been multiple suggestions of natural deep reactors either in the core (deemed by most experts as extremely unlikely) to accumulations near the CMB (not as difficult to imagine, but also deemed unlikely). Such discoveries would of course be revolutionary in geology and planetary studies; long shots, but huge payoff. In any event, simply finding evidence for the curious upwelling regions as due to increased U/Th content would be a great discovery and fundamental to geodynamics as we have discussed herein.

Large electron antineutrino detectors have multiple uses, and happily these are not exclusive. For example, a geoneutrino detector would ineluctably record a signal from a galactic supernova over a few seconds. Other types of extremely infrequent astrophysical phenomena (such as a burst of neutrinos associated with a GRB event), may also be recorded, without interference with geoneutrino mapping. Also depending upon placement, such detectors would inevitably contribute to worldwide monitoring of reactors and for clandestine nuclear weapons testing. Some elementary particle studies can also be carried out, particularly with respect to the mass hierarchy and neutrino mixing angles. As well, there are possible experiments to be carried out with higher energy neutrinos, including those in the GeV energy range from a distant particle accelerator. The point, for this paper, is that there is a large physics and astrophysics community which is interested in collaborating in the geoneutrino venture, providing scientific stimulus, dissertation topics, and possibly cooperative funding opportunities. It is reasonable to expect large geoneutrino detectors to provide a cornucopia of scientific data.



On the experimental side, there is much to be improved upon over present-day instruments. Large and cost-effective detectors, particularly mobile (deep ocean) instruments are sought. New technology in doping of water for cost-effective light emission in huge volumes (needed as one gets to the 100-kiloton scale), new flat panel twenty-first-century light detectors, and advances in electronics (high-speed waveform digitizing, along with low-power and inexpensive channel costs), are under development. Some novel methods of inverse beta event imaging are being developed (miniTimeCube [128]). And there is ongoing work studying how to improve neutrino direction resolution, inverse beta tagging (time delay in positron annihilation), and seeking a means to (cost effectively) detect neutrinos from  $^{40}\text{K}$  decays. A study by a team from the University of Hawaii and the National Geospatial Agency has determined that remote nuclear reactor monitoring is indeed possible and have christened their techniques as NUDAR (NeUtrino Direction And Ranging) [155]. For point source recording, the neutrinos from a reactor carry not only direction but also range information due to the neutrino oscillation distorted spectrum. This group has shown that neutrino oscillations provide surprising ability to determine range given as few as hundreds of counts attributable to a given point source (unlike radar, NUDAR needs no active pinging of the target, but waits for a signal from the target). The relevance of this work to geoneutrinos is still being investigated, but one immediately sees the potential, even though oscillation signatures are smeared out due to distributed sources. This opens the door in the future, however, to real Earth tomography.

We expect the study of electron antineutrinos from the Earth to blossom into a rich cross disciplinary field, cutting across traditional boundaries and for which we predict a bright and exciting future.

## Acknowledgments

This paper benefited from reviews by two anonymous reviewers. The authors gratefully acknowledge support for this research from NSF EAR 0855791 CSEDI Collaborative Research: Neutrino Geophysics: Collaboration between Geology and Particle Physics.

## References

- [1] W. Hopkins, "Preliminary observations on the refrigeration of the globe," *Philosophical Transactions of the Royal Society of London*, vol. 129, pp. 381–385, 1839.
- [2] D. J. Stevenson, "Earth formation and evolution," in *Evolution of the Earth*, D. J. Stevenson, Ed., vol. 9 of *Treatise on Geophysics*, chapter 9.01, p. 111, Elsevier Scientific Publishing Company, New York, NY, USA, 2007, Editor-in-chief G. Schubert.
- [3] W. Thomson, "On the secular cooling of the Earth," *Philosophical Magazine Series 4*, vol. 25, no. 165, pp. 1–14, 1863.
- [4] L. Kelvin, "The age of the earth as an abode fitted for life," *Annual Report of the Smithsonian Institution*, 1897.
- [5] J. D. Burchfield, *Lord Kelvin and the Age of the Earth*, Science History Publications, New York, NY, USA, 1975.
- [6] G. B. Dalrymple, *The Age of the Earth*, Stanford University Press, Stanford, Calif, USA, 1991.
- [7] E. Rutherford, *Radio-Activity*, Cambridge Physical Series, University Press, Cambridge, UK, 2nd edition, 1905.
- [8] G. F. Davies, "Thermal evolution of the mantle," in *Evolution of the Earth*, D. J. Stevenson, Ed., vol. 9 of *Treatise on Geophysics*, chapter 9.08, pp. 197–216, Elsevier Scientific Publishing Company, New York, NY, USA, 2007, Editor-in-chief G. Schubert.

- [9] N. H. Sleep, "Plate tectonics through time," in *Evolution of the Earth*, D. J. Stevenson, Ed., vol. 9 of *Treatise on Geophysics*, chapter 9.06, pp. 145–169, Elsevier Scientific Publishing Company, New York, NY, USA, 2007, Editor-in-chief G. Schubert.
- [10] C. L. Cowan, F. Reines, F. B. Harrison, H. W. Kruse, and A. D. McGuire, "Detection of the free neutrino: a confirmation," *Science*, vol. 124, no. 3212, pp. 103–104, 1956.
- [11] G. Eder, "Terrestrial neutrinos," *Nuclear Physics*, vol. 78, no. 3, pp. 657–662, 1966.
- [12] G. Marx, "Geophysics by neutrinos," *Czechoslovak Journal of Physics B*, vol. 19, no. 12, pp. 1471–1479, 1969.
- [13] G. Marx and I. Lux, "Hunting for soft antineutrinos," *Acta Physica Academiae Scientiarum Hungaricae*, vol. 28, no. 1–3, pp. 63–70, 1970.
- [14] C. Avilez, G. Marx, and B. Fuentes, "Earth as a source of antineutrinos," *Physical Review D*, vol. 23, no. 5, pp. 1116–1117, 1981.
- [15] L. M. Krauss, S. L. Glashow, and D. N. Schramm, "Antineutrino astronomy and geophysics," *Nature*, vol. 310, no. 5974, pp. 191–198, 1984.
- [16] R. S. Raghavan, S. Schoenert, S. Enomoto, J. Shirai, F. Suekane, and A. Suzuki, "Measuring the global radioactivity in the earth by multidetector antineutrino spectroscopy," *Physical Review Letters*, vol. 80, no. 3, pp. 635–638, 1998.
- [17] C. G. Rothschild, M. C. Chen, and F. P. Calaprice, "Antineutrino geophysics with liquid scintillator detectors," *Geophysical Research Letters*, vol. 25, no. 7, pp. 1083–1086, 1998.
- [18] T. Araki, S. Enomoto, K. Furuno et al., "Experimental investigation of geologically produced antineutrinos with KamLAND," *Nature*, vol. 436, no. 7050, pp. 499–503, 2005.
- [19] A. Gando, Y. Gando, K. Ichimura et al., "Partial radiogenic heat model for Earth revealed by geoneutrino measurements," *Nature Geoscience*, vol. 4, no. 9, pp. 647–651, 2011.
- [20] G. Bellini, J. Benziger, S. Bonetti et al., "Observation of geo-neutrinos," *Physics Letters B*, vol. 687, no. 4–5, pp. 4299–5304, 2010.
- [21] M. C. Chen, "Geo-neutrinos in SNO+," *Earth, Moon and Planets*, vol. 99, no. 1–4, pp. 221–228, 2006.
- [22] M. Kobayashi and Y. Fukao, "The Earth as an antineutrino star," *Geophysical Research Letters*, vol. 18, no. 4, pp. 633–636, 1991.
- [23] Neutrino Sciences 2005, Neutrino Geophysics, Honolulu, Hawaii, USA, December 2005, <http://www.phys.hawaii.edu/~sdye/hnsc.html>.
- [24] Neutrino Sciences 2007, Deep Ocean Anti-Neutrino Observatory Workshop, Honolulu, Hawaii, USA, March 2007, <http://www.phys.hawaii.edu/~sdye/hano.html>.
- [25] Neutrino Geoscience 2008 at SNOLAB, Sudbury, Ontario, Canada, September 2008, <http://geonu.snolab.ca>.
- [26] Neutrino Geoscience 2010 at Gran Sasso National Laboratory—Italy, October, 2010, <http://geoscience.lngs.infn.it/>.
- [27] Neutrino Geoscience Workshop, Deadwood, South Dakota, June 2011, <http://www.dsu.edu/research/CETUP/2011.html>.
- [28] Geoneutrinos: A new tool for the study of the solid Earth I, Session U41F at AGU 2006 Joint Assembly, Baltimore, Md, USA, May 25, 2006.
- [29] S. T. Dye, Ed., *Neutrino Geophysics: Proceedings of Neutrino Sciences 2005*, Springer, Dordrecht, The Netherlands, 2007.
- [30] C. Lan, *SNO+ and geoneutrino physics [M.S. thesis]*, Queen's University, Kingston, Ontario, Canada, 2007.
- [31] S. Enomoto, *Neutrino geophysics and observation of geo-neutrinos at KamLAND [Ph.D. thesis]*, Tohoku University, 2005.
- [32] W. F. McDonough, "Geophysics: mapping the Earth's engine," *Science*, vol. 317, no. 5842, pp. 1177–1178, 2007.
- [33] S. T. Dye, W. F. McDonough, and J. Mahoney, "Geoneutrino measurements and models investigate deep Earth," *Eos*, vol. 89, no. 44, pp. 433–434, 2008.
- [34] W. F. McDonough, J. G. Learned, and S. T. Dye, "The many uses of electron antineutrinos," *Physics Today*, vol. 65, no. 3, pp. 46–51, 2012.
- [35] A. Ananthaswamy, "Messengers from the underworld," *New Scientist*, vol. 214, no. 2862, pp. 32–35, 2012.
- [36] S. Enomoto, E. Ohtani, K. Inoue, and A. Suzuki, "Neutrino geophysics with KamLAND and future prospects," *Earth and Planetary Science Letters*, vol. 258, no. 1–2, pp. 147–159, 2007.
- [37] G. Fiorentini, M. Lissia, and F. Mantovani, "Geo-neutrinos and earth's interior," *Physics Reports*, vol. 453, no. 5–6, pp. 117–172, 2007.

- [38] S. T. Dye, "Geo-neutrinos and silicate earth enrichment of U and Th," *Earth and Planetary Science Letters*, vol. 297, no. 1-2, pp. 1-9, 2010.
- [39] S. T. Dye, "Geoneutrinos and the radioactive power of the Earth," *Reviews of Geophysics*, vol. 50, no. 3, Article ID RG3007, 2012.
- [40] J.-C. Mareschal, C. Jaupart, C. Phaneuf, and C. Perry, "Geoneutrinos and the energy budget of the Earth," *Journal of Geodynamics*, vol. 54, pp. 43-54, 2012.
- [41] C. Jaupart, S. Labrosse, and J. C. Mareschal, "Temperatures, heat and energy in the mantle of the Earth," in *Mantle Dynamics*, D. Bercovici, Ed., vol. 7 of *Treatise on Geophysics*, chapter 7.06, pp. 253-303, Elsevier Scientific Publishing Company, New York, NY, USA, 2007, editor-in-chief G. Schubert.
- [42] J. Korenaga, "Urey ratio and the structure and evolution of Earth's mantle," *Reviews of Geophysics*, vol. 46, no. 2, Article ID RG2007, 2008.
- [43] T. Lay, J. Hernlund, and B. A. Buffett, "Core-mantle boundary heat flow," *Nature Geoscience*, vol. 1, no. 1, pp. 25-32, 2008.
- [44] J. G. Sclater, C. Jaupart, and D. Galson, "The heat flow through oceanic and continental crust and the heat loss of the earth," *Reviews of Geophysics and Space Physics*, vol. 18, no. 1, pp. 269-311, 1980.
- [45] G. F. Davies, "Review of oceanic and global heat flow estimates," *Reviews of Geophysics*, vol. 18, no. 3, pp. 718-722, 1980.
- [46] H. N. Pollack, S. J. Hurter, and J. R. Johnson, "Heat flow from the Earth's interior: analysis of the global data set," *Reviews of Geophysics*, vol. 31, no. 3, pp. 267-280, 1993.
- [47] J. H. Davies and D. R. Davies, "Earth's surface heat flux," *Solid Earth*, vol. 1, no. 1, pp. 5-24, 2010.
- [48] C. A. Stein and S. Stein, "A model for the global variation in oceanic depth and heat flow with lithospheric age," *Nature*, vol. 359, no. 6391, pp. 123-129, 1992.
- [49] A. M. Hofmeister and R. E. Criss, "Earth's heat flux revised and linked to chemistry," *Tectonophysics*, vol. 395, no. 3-4, pp. 159-177, 2005.
- [50] R. Von Herzen, E. E. Davis, A. T. Fisher, C. A. Stein, and H. N. Pollack, "Comments on 'Earth's heat flux revised and linked to chemistry' by A.M. Hofmeister and R.E. Criss," *Tectonophysics*, vol. 409, no. 1-4, pp. 193-198, 2005.
- [51] M. Wei and D. Sandwell, "Estimates of heat flow from Cenozoic seafloor using global depth and age data," *Tectonophysics*, vol. 417, no. 3-4, pp. 325-335, 2006.
- [52] T. W. Becker, C. P. Conrad, B. Buffett, and R. D. M. Müller, "Past and present sea floor age distributions and the temporal evolution of plate tectonic heat transport," *Earth and Planetary Science Letters*, vol. 278, no. 3-4, pp. 233-242, 2009.
- [53] R. L. Rudnick and S. Gao, "Composition of the continental crust," in *The Crust*, R. L. Rudnick, Ed., vol. 3 of *Treatise on Geochemistry*, chapter 3.01, pp. 10-6408, Elsevier Scientific Publishing Company, Oxford, UK, 2003, Editors-in-chief H. D. Holland and K. K. Turekian.
- [54] F. Nimmo, "Energetics of the core," in *Core Dynamics*, P. Olson, Ed., vol. 8 of *Treatise on Geophysics*, chapter 8.02, pp. 31-65, Elsevier Scientific Publishing Company, New York, NY, USA, 2007.
- [55] W. F. McDonough and S. Sun, "The composition of the Earth," *Chemical Geology*, vol. 120, no. 3-4, pp. 223-253, 1995.
- [56] G. J. Wasserburg, G. J. F. Macdonald, F. Hoyle, and W. A. Fowler, "Relative contributions of uranium, thorium, and potassium to heat production in the earth," *Science*, vol. 143, no. 3605, pp. 465-467, 1964.
- [57] W. F. McDonough, "Compositional model for the Earth's core," in *The Mantle and Core*, *Treatise on Geochemistry*, R. W. Carlson, Ed., vol. 2, chapter 2.15, pp. 547-568, Elsevier Scientific Publishing Company, Oxford, UK, 2003, Editors-in-chief H. D. Holland and K. K. Turekian.
- [58] S. R. Hart and A. Zindler, "In search of a bulk-Earth composition," *Chemical Geology*, vol. 57, no. 34, pp. 247-267, 1986.
- [59] H. Palme and H. S. C. O'Neill, "Cosmochemical estimates of mantle composition," in *Treatise on Geochemistry*, R. W. Carlson, Ed., vol. 2, chapter 2.01, pp. 1380-1308, Elsevier Scientific Publishing Company, Oxford, UK, 2003, Editors-in-chief H. D. Holland and K. K. Turekian.
- [60] R. Arevalo Jr., W. F. McDonough, and M. Luong, "The K/U ratio of the silicate Earth: insights into mantle composition, structure and thermal evolution," *Earth and Planetary Science Letters*, vol. 278, no. 3-4, pp. 361-369, 2009.
- [61] T. Lyubetskaya and J. Korenaga, "Chemical composition of Earth's primitive mantle and its variance: 1. Method and results," *Journal of Geophysical Research B*, vol. 112, no. 3, Article ID B03211, 2007.
- [62] H. S. C. O'Neill and H. Palme, "Collisional erosion and the non-chondritic composition of the terrestrial planets," *Philosophical Transactions of the Royal Society A*, vol. 366, no. 1883, pp. 4205-4238, 2008.

- [63] M. Javoy, "Chemical Earth models," *Comptes Rendus de l'Académie des Sciences*, vol. 329, no. 8, pp. 537–555, 1999.
- [64] M. Javoy, E. Kaminski, F. Guyot et al., "The chemical composition of the Earth: enstatite chondrite models," *Earth and Planetary Science Letters*, vol. 293, no. 3–4, pp. 259–268, 2010.
- [65] D. L. Turcotte, G. Schubert, and Geodynamics, *Applications of Continuum Physics to Geological Problems*, Cambridge University Press, 2nd edition, 2002.
- [66] R. K. Workman and S. R. Hart, "Major and trace element composition of the depleted MORB mantle (DMM)," *Earth and Planetary Science Letters*, vol. 231, no. 1–2, pp. 53–72, 2005.
- [67] V. J. M. Salters and A. Stracke, "Composition of the depleted mantle," *Geochemistry, Geophysics, Geosystems*, vol. 5, no. 5, Article ID Q05B07, 27 pages, 2004.
- [68] R. Arevalo Jr. and W. F. McDonough, "Chemical variations and regional diversity observed in MORB," *Chemical Geology*, vol. 271, no. 1–2, pp. 70–85, 2010.
- [69] O. Šrámek, W. F. McDonough, E. S. Kite, V. Lekić, S. T. Dye, and S. Zhong, "Geophysical and geochemical constraints on geoneutrino fluxes from Earth's mantle," *Earth and Planetary Science Letters*.
- [70] G. Schubert, D. L. Turcotte, and P. Olson, *Mantle Convection in Earth and Planets*, Cambridge University Press, Cambridge, UK, 2001.
- [71] D. Bercovici, "Mantle dynamics past, present and future: an introduction and overview," in *Mantle Dynamics, Treatise on Geo-physics*, D. Bercovici, Ed., vol. 7, chapter 7.01, p. 130, Elsevier Scientific Publishing Company, New York, NY, USA, 2007, Editor-in-chief G. Schubert.
- [72] G. F. Davies, *Dynamic Earth: Plates, Plumes and Mantle Convection*, Cambridge University Press, 1999.
- [73] U. Christensen, "Thermal evolution models for the Earth," *Journal of Geophysical Research*, vol. 90, no. 4, pp. 2995–3007, 1985.
- [74] J. Korenaga, "Archean geodynamics and the thermal evolution of earth," in *Archean Geodynamics and Environments*, K. Benn, J. C. Mareschal, and K. Condie, Eds., vol. 164 of *AGU Geophysical Monograph*, p. 732, American Geophysical Union, 2006.
- [75] G. F. Davies, "Effect of plate bending on the Urey ratio and the thermal evolution of the mantle," *Earth and Planetary Science Letters*, vol. 287, no. 3–4, pp. 513–518, 2009.
- [76] S. Labrosse and C. Jaupart, "Thermal evolution of the Earth: secular changes and fluctuations of plate characteristics," *Earth and Planetary Science Letters*, vol. 260, no. 3–4, pp. 465–481, 2007.
- [77] P. G. Silver and M. D. Behn, "Intermittent plate tectonics," *Science*, vol. 319, no. 5859, pp. 85–88, 2008.
- [78] A. Lenardic, C. M. Cooper, and L. Moresi, "A note on continents and the Earth's Urey ratio," *Physics of the Earth and Planetary Interiors*, vol. 188, no. 1–2, pp. 127–130, 2011.
- [79] J. W. Crowley, M. Gérard, and R. J. O'Connell, "On the relative influence of heat and water transport on planetary dynamics," *Earth and Planetary Science Letters*, vol. 310, no. 34, pp. 380–388, 2011.
- [80] T. Nakagawa and P. J. Tackley, "Influence of magmatism on mantle cooling, surface heat flow and Urey ratio," *Earth and Planetary Science Letters*, vol. 329–330, pp. 1–10, 2012.
- [81] A. W. Hofmann, "Mantle geochemistry: the message from oceanic volcanism," *Nature*, vol. 385, no. 6613, pp. 219–229, 1997.
- [82] R. D. van der Hilst, S. Widiyantoro, and E. R. Engdahl, "Evidence for deep mantle circulation from global tomography," *Nature*, vol. 386, no. 6625, pp. 578–584, 1997.
- [83] Y. Fukao, S. Widiyantoro, and M. Obayashi, "Stagnant slabs in the upper and lower mantle transition region," *Reviews of Geophysics*, vol. 39, no. 3, pp. 291–323, 2001.
- [84] T. Lay, Q. Williams, and E. J. Garnero, "The core-mantle boundary layer and deep Earth dynamics," *Nature*, vol. 392, no. 6675, pp. 461–468, 1998.
- [85] E. J. Garnero and A. K. McNamara, "Structure and dynamics of Earth's lower mantle," *Science*, vol. 320, no. 5876, pp. 626–628, 2008.
- [86] A. K. McNamara, E. J. Garnero, and S. Rost, "Tracking deep mantle reservoirs with ultra-low velocity zones," *Earth and Planetary Science Letters*, vol. 299, no. 1–2, pp. 1–9, 2010.
- [87] L. Wen, P. Silver, D. James, and R. Kuehnel, "Seismic evidence for a thermo-chemical boundary at the base of the Earth's mantle," *Earth and Planetary Science Letters*, vol. 189, no. 3–4, pp. 141–153, 2001.
- [88] W.-J. Su and A. M. Dziewonski, "Simultaneous inversion for 3-D variations in shear and bulk velocity in the mantle," *Physics of the Earth and Planetary Interiors*, vol. 100, no. 1–4, pp. 135–156, 1997.



- [89] M. J. Walter and R. G. Tronnes, "Early Earth differentiation," *Earth and Planetary Science Letters*, vol. 225, no. 3-4, pp. 253–269, 2004.
- [90] C.-T. A. Lee, Q. Z. Yin, A. Lenardic, A. Agranier, C. J. O'Neill, and N. Thiagarajan, "Trace-element composition of Fe-rich residual liquids formed by fractional crystallization: implications for the Hadean magma ocean," *Geochimica et Cosmochimica Acta*, vol. 71, no. 14, pp. 3601–3615, 2007.
- [91] V. C. Bennett, A. D. Brandon, and A. P. Nutman, "Coupled  $^{142}\text{Nd}$ - $^{143}\text{Nd}$  isotopic evidence for Hadean mantle dynamics," *Science*, vol. 318, no. 5858, pp. 1907–1910, 2007.
- [92] S. Labrosse, J. W. Hernlund, and N. Coltice, "A crystallizing dense magma ocean at the base of the Earth's mantle," *Nature*, vol. 450, no. 7171, pp. 866–869, 2007.
- [93] J. Ritsema, H. J. van Heijst, and J. H. Woodhouse, "Complex shear wave velocity structure imaged beneath Africa and Iceland," *Science*, vol. 286, no. 5446, pp. 1925–1928, 1999.
- [94] J. Ritsema, H. J. van Heijst, and J. H. Woodhouse, "Global transition zone tomography," *Journal Of Geophysical Research*, vol. 109, Article ID B02302, 14 pages, 2004.
- [95] A. L. Bull, A. K. McNamara, and J. Ritsema, "Synthetic tomography of plume clusters and thermochemical piles," *Earth and Planetary Science Letters*, vol. 278, no. 3-4, pp. 152–162, 2009.
- [96] M. G. Jackson and R. W. Carlson, "An ancient recipe for ood-basalt genesis," *Nature*, vol. 476, pp. 316–319, 2011.
- [97] M. Willbold, T. Elliott, and S. Moorbath, "The tungsten isotopic composition of the Earth's mantle before the terminal bombardment," *Nature*, vol. 477, no. 7363, pp. 195–198, 2011.
- [98] P. H. Warren, "Stable-isotopic anomalies and the accretionary assemblage of the Earth and Mars: A subordinate role for carbonaceous chondrites," *Earth and Planetary Science Letters*, vol. 311, no. 1-2, pp. 93–100, 2011.
- [99] C. Fitoussi and B. Bourdon, "Silicon isotope evidence against an enstatite chondrite Earth," *Science*, vol. 335, no. 6075, pp. 1477–1480, 2012.
- [100] I. H. Campbell and H. St. C. O'Neill, "Evidence against a chondritic Earth," *Nature*, vol. 483, no. 7391, pp. 553–558, 2012.
- [101] J. Zhang, N. Dauphas, A. M. Davis, I. Leya, and A. Fedkin, "The proto-Earth as a significant source of lunar material," *Nature Geoscience*, vol. 5, no. 4, pp. 251–255, 2012.
- [102] M. Murakami, Y. Ohishi, N. Hirao, and K. Hirose, "A perovskitic lower mantle inferred from high-pressure, high-temperature sound velocity data," *Nature*, vol. 485, no. 7396, pp. 90–94, 2012.
- [103] D. Abbott, L. Burgess, J. Longhi, and W. H. F. Smith, "An empirical thermal history of the Earth's upper mantle," *Journal of Geophysical Research*, vol. 99, no. 7, pp. 13835–13850, 1994.
- [104] W. F. McDonough and R. Arevalo Jr., "Uncertainties in the composition of Earth, its core and silicate sphere," *Journal of Physics: Conference Series*, vol. 136, no. 2, Article ID 022006, 2008.
- [105] C. K. Gessmann and B. J. Wood, "Potassium in the Earth's core?" *Earth and Planetary Science Letters*, vol. 200, no. 1-2, pp. 63–78, 2002.
- [106] V. R. Murthy, W. van Westrenen, and Y. Fei, "Experimental evidence that potassium is a substantial radioactive heat source in planetary cores," *Nature*, vol. 423, no. 6936, pp. 163–165, 2003.
- [107] V. R. Murthy, "Radioactivity of the Earth and the case for potassium in the Earth's core," *Earth, Moon, Planets*, vol. 99, no. 1, pp. 23–32, 2006.
- [108] J. M. Herndon, "Substructure of the inner core of the Earth," *Proceedings of the National Academy of Sciences*, vol. 93, no. 2, pp. 646–648, 1996.
- [109] J. R. Lancelot, A. Vitrac, and C. J. Allegre, "The Oklo natural reactor: age and evolution studies by U—Pb and Rb—Sr systematics," *Earth and Planetary Science Letters*, vol. 25, no. 2, pp. 189–196, 1975.
- [110] R. J. D. Meijer and W. van Westrenen, "The feasibility and implications of nuclear georeactors in Earth's core-mantle boundary region," *South African Journal of Science*, vol. 104, no. 3-4, pp. 111–118, 2008.
- [111] J. M. Herndon, "Nuclear georeactor origin of oceanic basalt  $^3\text{He}/^4\text{He}$ , evidence, and implications," *Proceedings of the National Academy of Sciences*, vol. 100, no. 6, pp. 3047–3050, 2003.
- [112] G. Audi and A. Wapstra, "The update to the atomic mass evaluation," *Nuclear Physics A*, vol. 595, no. 4, pp. 409–480, 1995.
- [113] R. B. Firestone and V. S. Shirley, *Table of Isotopes*, John Wiley & Sons, New York, NY, USA, 8th edition, 1996.
- [114] G. Fiorentini, A. Ianni, G. Korga et al., "Nuclear physics for geo-neutrino studies," *Physical Review C*, vol. 81, no. 3, Article ID 034602, 9 pages, 2010.

- [115] B. Pontecorvo, "Mesonium and antimesonium," *Soviet Journal of Experimental and Theoretical Physics*, vol. 6, no. 2, pp. 429–431, 1958.
- [116] G. L. Fogli, E. Lisi, A. Marrone, A. Palazzo, and A. M. Rotunno, "Evidence of  $\theta_{13} > 0$  from global neutrino data analysis," *Physical Review D*, vol. 84, no. 5, Article ID 053007, 7 pages, 2011.
- [117] The Daya Bay Collaboration, "Observation of electron-antineutrino disappearance at Daya Bay," *Physical Review Letters*, vol. 108, no. 17, Article ID 171803, 2012.
- [118] RENO Collaboration, "Observation of reactor electron antineutrinos disappearance in the RENO experiment," *Physical Review Letters*, vol. 108, no. 19, Article ID 191802, 2012.
- [119] K. Nakamura and P. D. Group, "Review of particle physics," *Journal of Physics G*, vol. 37, no. 7, Article ID 075021, 2010.
- [120] C. L. Cowan, F. Reines, F. B. Harrison, E. C. Anderson, and F. N. Hayes, "Large liquid scintillation detectors," *Physical Review*, vol. 90, no. 3, pp. 493–494, 1953.
- [121] F. Reines and C. L. Cowan, "A proposed experiment to detect the free neutrino," *Physical Review*, vol. 90, no. 3, pp. 492–493, 1953.
- [122] J. Learned, S. Dye, and S. Pakvasa, "Neutrino geophysics conference introduction," *Earth, Moon, Planets*, vol. 99, no. 1, pp. 1–15, 2006.
- [123] P. Vogel and J. F. Beacom, "Angular distribution of neutron inverse beta decay,  $\bar{\nu}_e + p \rightarrow e^+ + n$ ," *Physical Review D*, vol. 60, no. 5, Article ID 053003, 1999.
- [124] F. Mantovani, L. Carmignani, G. Fiorentini, and M. Lissia, "Antineutrinos from Earth: a reference model and its uncertainties," *Physical Review D*, vol. 69, no. 1, Article ID 013001, 2004.
- [125] A. M. Dziewonski and D. L. Anderson, "Preliminary reference Earth model," *Physics of the Earth and Planetary Interiors*, vol. 25, no. 4, pp. 297–356, 1981.
- [126] C. Bassin, G. Laske, and G. Masters, "The current limits of resolution for surface wave tomography in North America," *Eos, Transactions, American Geophysical Union*, vol. 81, no. 48, p. F897, 2000, <http://igppweb.ucsd.edu/~gabi/crust2.html>.
- [127] F. Reines, H. S. Gurr, and H. W. Sobel, "Detection of  $\bar{\nu}_e - e$  scattering," *Physical Review Letters*, vol. 37, no. 6, pp. 315–318, 1976.
- [128] J. G. Learned, "The mini-Time-Cube—A portable directional anti-neutrino detector," presentation at Advances in Neutrino Technology 2011, Philadelphia, Pa, USA, 2011.
- [129] G. Alimonti, C. Arpesella, H. Back et al., "The Borexino detector at the Laboratori Nazionali del Gran Sasso," *Nuclear Instruments and Methods in Physics*, vol. 600, no. 3, pp. 568–593, 2009.
- [130] M. Wurm, J. F. Beacom, L. B. Bezrukov et al., "The next-generation liquid-scintillator neutrino observatory LENA," *Astroparticle Physics*, vol. 35, no. 11, pp. 685–732, 2012.
- [131] N. Tolich, Y.-D. Chan, C. A. Currat et al., "A geoneutrino experiment at Homestake," *Earth, Moon, Planets*, vol. 99, no. 1, pp. 229–240, 2006.
- [132] I. R. Barabanov, G. Y. Novikova, V. V. Sinev, and E. A. Yanovich, "Research of the natural neutrino uxes by use of large volume scintillation detector at Baksan," <http://arxiv.org/abs/0908.1466>.
- [133] S. Dye, E. Guillian, J. G. Learned et al., "Earth radioactivity measurements with a deep ocean anti-neutrino observatory," *Earth, Moon, Planets*, vol. 99, no. 1–4, pp. 241–252, 2006.
- [134] J. G. Learned, S. T. Dye, and S. Pakvasa, "Hanohano: a deep ocean anti-neutrino detector for unique neutrino physics and geophysics studies," in *Proceedings of the 12th International Workshop on Neutrino Telescopes*, Venice, Italy, March 2007.
- [135] Y. Wang, "Daya Bay experiment and its future," presentation at XIV International Workshop on Neutrino Telescopes, Venice, Italy, March 2011, <http://neutrino.pd.infn.it/Neutel2011/>.
- [136] G. Fiorentini, M. Lissia, F. Mantovani, and R. Vannucci, "How much uranium is in the Earth? Predictions for geoneutrinos at KamLAND," *Physical Review D*, vol. 72, no. 3, Article ID 033017, 2005.
- [137] G. Fiorentini, M. Lissia, F. Mantovani, and R. Vannucci, "Geo-neutrinos: a new probe of Earth's interior," *Earth and Planetary Science Letters*, vol. 238, no. 1–2, pp. 235–247, 2005.
- [138] K. A. Hochmuth, F. V. Feilitzsch, B. D. Fields et al., "Probing the Earth's interior with a large volume liquid scintillator detector," *Astroparticle Physics*, vol. 27, no. 1, pp. 21–29, 2007.
- [139] E. S. Kite and V. Lekic, "Feasibility of mantle radiogenic power determination with geoneutrinos," unpublished.
- [140] M. Coltorti, R. Borasoa, F. Mantovani et al., "U and Th content in the Central Apennines continental crust: a contribution to the determination of the geo-neutrinos ux at LNGS," *Geochimica et Cosmochimica Acta*, vol. 75, no. 9, pp. 2271–2294, 2011.

- [141] W. M. White and E. M. Klein, "The oceanic crust," in *The Crust*, R. L. Rudnick, Ed., vol. 3 of *Treatise on Geochemistry*, chapter 14, Elsevier Scientific Publishing Company, Oxford, UK, 2nd edition, 2013, editors-in-chief H. D. Holland and K. K. Turekian.
- [142] T. Plank, "The oceanic crust," in *The Crust*, R. L. Rudnick, Ed., vol. 3 of *Treatise on Geochemistry*, Elsevier Scientific Publishing Company, Oxford, UK, 2nd edition, 2013, editors-in-chief H. D. Holland and K. K. Turekian.
- [143] Y. Huang, V. Chubakov, F. Mantovani, W. F. McDonough, and R. L. Rudnick, "A reference Earth model for the heat producing elements and associated geoneutrino flux," submitted to *Geochemistry, Geophysics, Geosystems*.
- [144] F. Deschamps, E. Kaminski, and P. J. Tackley, "A deep mantle origin for the primitive signature of ocean island basalt," *Nature Geoscience*, vol. 4, no. 12, pp. 879–882, 2011.
- [145] P. J. Tackley, "Dynamics and evolution of the deep mantle resulting from thermal, chemical, phase and melting effects," *Earth-Science Reviews*, vol. 110, no. 1–4, pp. 1–25, 2012.
- [146] G. Fiorentini, G. L. Fogli, E. Lisi, F. Mantovani, and A. M. Rotunno, "Mantle geoneutrinos in KamLAND and Borexino," *Physical Review D*, vol. 86, no. 3, Article ID 033004, 2012.
- [147] G. L. Fogli, E. Lisi, A. Palazzo, and A. M. Rotunno, "Combined analysis of KamLAND and Borexino neutrino signals from Th and U decays in the Earth's interior," *Physical Review D*, vol. 82, no. 9, Article ID 093006, 2010.
- [148] D. L. Anderson, *The New Theory of the Earth*, Cambridge University Press, 2007.
- [149] C. J. Allègre, J. P. Poirier, E. Humler, and A. W. Hofmann, "The chemical composition of the Earth," *Earth and Planetary Science Letters*, vol. 134, no. 3–4, pp. 515–526, 1995.
- [150] B. Fields and K. Hochmuth, "Imaging the Earth's interior: the angular distribution of terrestrial neutrinos," *Earth, Moon, Planets*, vol. 99, no. 1, pp. 155–181, 2006.
- [151] A. Suzuki, "Physics in next geoneutrino detectors," *Earth, Moon, Planets*, vol. 99, no. 1, pp. 359–368, 2006.
- [152] K. A. Hochmuth, "The angular distribution of geoneutrinos," *Progress in Particle and Nuclear Physics*, vol. 57, no. 1, pp. 293–295, 2006.
- [153] M. Apollonio, A. Baldini, C. Bemporad et al., "Determination of neutrino incoming direction in the CHOOZ experiment and its application to supernova explosion location by scintillator detectors," *Physical Review D*, vol. 61, no. 1, Article ID 012001, 1999.
- [154] M. Batygov, "On the possibility of directional analysis for geo-neutrinos," *Earth, Moon, Planets*, vol. 99, no. 1, pp. 183–192, 2006.
- [155] G. R. Jocher, D. A. Bondy, B. M. Dobbs et al., "Theoretical antineutrino detection, direction and ranging at long distances," *Physics Reports*. In press.

## *Review Article*

# **Search for GeV-Scale Sterile Neutrinos Responsible for Active Neutrino Oscillations and Baryon Asymmetry of the Universe**

**S. N. Gninenko,<sup>1</sup> D. S. Gorbunov,<sup>1,2</sup> and M. E. Shaposhnikov<sup>3</sup>**

<sup>1</sup> *Institute for Nuclear Research of Russian Academy of Sciences, 117312 Moscow, Russia*

<sup>2</sup> *Moscow Institute of Physics and Technology, 141700 Dolgoprudny, Russia*

<sup>3</sup> *Institut de Théorie des Phénomènes Physiques, (École Polytechnique Fédérale de Lausanne), 1015 Lausanne, Switzerland*

Correspondence should be addressed to D. S. Gorbunov, [gorby@ms2.inr.ac.ru](mailto:gorby@ms2.inr.ac.ru)

Received 27 July 2012; Accepted 25 September 2012

Academic Editor: Gian Luigi Fogli

Copyright © 2012 S. N. Gninenko et al. This is an open access article distributed under the Creative Commons Attribution License, which permits unrestricted use, distribution, and reproduction in any medium, provided the original work is properly cited.

Standard Model fails to explain neutrino oscillations, dark matter, and baryon asymmetry of the Universe. All these problems can be solved with three sterile neutrinos added to SM. Quite remarkably, if sterile neutrino masses are well below the electroweak scale, this modification—Neutrino Minimal Standard Model ( $\nu$ MSM)—can be tested experimentally. We discuss a new experiment on search for decays of GeV-scale sterile neutrinos, which are responsible for the matter-antimatter asymmetry generation and for the active neutrino masses. If lighter than 2 GeV, these particles can be produced in decays of charm mesons generated by high energy protons in a target, and subsequently decay into SM particles. To fully explore this sector of  $\nu$ MSM, the new experiment requires data obtained with at least  $10^{20}$  incident protons on target (achievable at CERN SPS in future) and a big volume detector constructed from a large amount of identical single modules, with a total sterile neutrino decay length of few kilometers. The preliminary feasibility study for the proposed experiment shows that it has sensitivity which may either lead to the discovery of new particles below the Fermi scale—right-handed partners of neutrinos—or rule out seesaw sterile neutrinos with masses below 2 GeV.

## **1. Introduction**

The discovery of neutrino oscillations provides an undisputed signal that the Standard Model (SM) of elementary particles is not complete. However, what kind of new physics it brings to us remains still unclear: we do not know yet the properties of new particles which are believed to be behind this phenomenon. An attractive possibility is the extension of the SM by three right-handed neutrinos, making the leptonic sector similar to the quark one, see Figure 1.



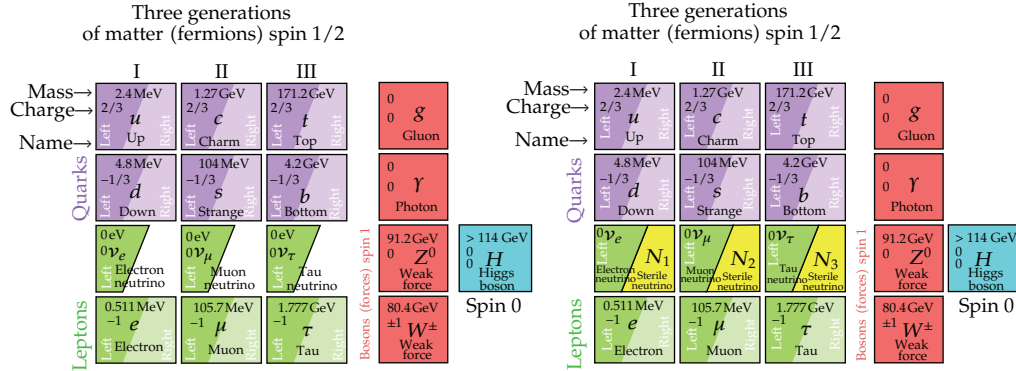


**Figure 1:** Particle content of the SM and its minimal extension in neutrino sector. In the SM (left) the right-handed partners of neutrinos are absent. In the  $\nu$ MSM (right) all fermions have both left and right-handed components.

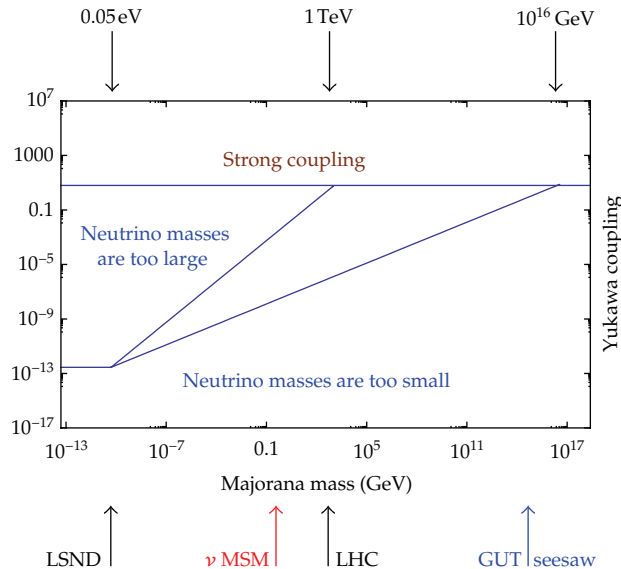


**Figure 2:** The admitted values of the Yukawa couplings of sterile neutrinos as a function of their seesaw Majorana masses.

The masses  $M$  and Yukawa couplings  $Y$  of new leptons remain largely unknown. Basically,  $M$  can have any value between zero (corresponding to Dirac neutrinos) and  $10^{16}$  GeV, whereas  $Y$  can vary from  $10^{-13}$  (Dirac neutrino case) to  $\sim \pi$  (the onset of the strong coupling). The admitted region is sketched in Figure 2.

Independently on their mass, the new Majorana leptons can explain oscillations of active neutrinos. So, an extra input is needed to fix their mass range. It can be provided by the LHC experiments.

Suppose that the resonance found at the LHC by Atlas and CMS in the region 125-126 GeV is indeed the Higgs boson of the Standard Model. This number is remarkably close to the lower limit on the Higgs mass coming from the requirement of the absolute stability of

the electroweak vacuum and from Higgs inflation, and to prediction of the Higgs mass from asymptotic safety of the Standard Model (see detailed discussion in [1] and in a proposal submitted to European High Energy Strategy Group by Bezrukov et al. [2]). The existence of the Higgs boson with this particular mass tells that the Standard Model vacuum is stable or metastable with the life-time exceeding that of the Universe. The SM in this case is a valid effective field theory up to the Planck scale, and no new physics is required *above* the Fermi scale from this point of view. Suppose also that the LHC finds no new particle and no deviations from the Standard Model. In this case the “naturalness paradigm”, leading the theoretical research over the last few decades will be much less attractive, as the proposals for new physics stabilizing the electroweak scale by existence of new particles in the TeV region and based on low energy supersymmetry, technicolor or large extra dimensions would require severe fine-tunings.

The solution of the hierarchy problem does not require in fact the presence of new particles or new physics above the Fermi scale. Moreover, *the absence* of new particles between the electroweak and Planck scales, supplemented by extra symmetries (such as the scale invariance) may itself be used as an instrument towards a solution of the problem of stability of the Higgs mass against radiative corrections (for detailed arguments see [3–5]).

Even regardless the hierarchy problem, it is clear that the Standard Model of elementary particles is not complete. It is in conflict with several observations. These are nonzero neutrino masses and oscillations discussed above, the excess of matter over antimatter in the Universe, and the presence of nonbaryonic dark matter. Any model of physics beyond the SM (BSM) should be able to deal with the experimental troubles of the SM.

Guided by the arguments steaming from alternative solutions to the hierarchy problem it is natural to ask whether the observational problems of the SM can be solved by new physics *below* the Fermi scale. And the answer is *affirmative*: an economic way to handle in a unified way the problems of neutrino masses, dark matter, and baryon asymmetry of the Universe is to add to the SM three Majorana singlet fermions with masses roughly *of the order of masses of known quarks and leptons*. This theory is called the  $\nu$ MSM, for “Neutrino Minimal Standard Model” (for a review see [6]). The lightest of the three new leptons is expected to have a mass from 1 keV to 50 keV and plays the role of the dark matter particle (see detailed discussion in [6] and in a proposal submitted to European High Energy Strategy Group by Boyarsky et al. [7]). Two other neutral fermions are responsible for giving masses to ordinary neutrinos via the seesaw mechanism at the *electroweak scale* and to creation of the baryon asymmetry of the Universe. The masses of these particles and their couplings to ordinary leptons are constrained by particle physics experiments and cosmology. Two leptons should be almost degenerate, forming thus nearly Dirac fermion (this is coming from the requirement of successful baryogenesis). For comparison, we show in Figure 3 the summary of different possibilities for the masses of Majorana leptons.

A lot of experimental efforts were devoted to the direct search of Majorana neutral leptons in the past [8–16]. No new particles were found, but several constraints on their mixing angles with ordinary leptons were derived. The interest to these searches declined considerably at nineties, most probably due to the theoretical prejudice that the masses of Majorana leptons should be associated with the *Grand Unified scale*  $\sim 10^{16}$  GeV [17–20], making their direct search impossible. As a result, no dedicated searches of relatively light neutral leptons were performed in the last decade, with an exception of several experiments [13–15] related to the so-called Karmen anomaly [21]. Today, the reason for the negative result became clear: in the domain of parameters accessible to most of these experiments the neutral leptons

	$N$ mass	$\nu$ masses	eV $\nu$ anoma- lies	BAU	DM	$M_H$ stability	Direct search	experi- ment
GUT seesaw	10–16 10 GeV	Yes	No	Yes	No	No	No	—
EWSB	2–3 10 GeV	Yes	No	Yes	No	Yes	Yes	LHC
$\nu$ MSM	keV–GeV	Yes	No	Yes	Yes	Yes	Yes	a’la CHARM
$\nu$ scale	eV	Yes	Yes	No	No	Yes	Yes	a’la LSND

**Figure 3:** This table shows whether a given choice of the mass of sterile neutrinos can explain neutrino masses and oscillations, accommodate eV neutrino anomalies, lead to baryogenesis, provide a dark matter candidate, ensure the stability of the Higgs mass against radiative corrections, and is directly searched at some experiments.

interact too strongly to produce the baryon asymmetry of the Universe, not satisfying one of the Sakharov conditions for baryogenesis.

The recent theory developments provide a guideline for the required experimental sensitivity [22], which was absent at the time when the early experiments were made. The aim of the present work is to discuss the experimental signatures of the existence of these particles and estimate the parameters of the experiment of beam-target type required to fully explore the model parameter space if sterile neutrinos are lighter than  $D$ -mesons (see a proposal submitted to European High Energy Strategy Group by Gorbunov and Shaposhnikov [23]).

The paper is organized as follows. In Section 2 we give the essential features of the model and discuss the constraints on new particles. Section 3 is devoted to general description of experiments on searches for sterile neutrinos of masses in GeV range. In Section 4 we present an estimate of sensitivity required to test the model and suggest the experimental setup to accomplish the ultimate task. Section 5 contains conclusions.

## 2. The Model and Constraints on Properties of New Particles

The  $\nu$ MSM is described by the most general renormalizable Lagrangian of all the SM particles and 3 singlet fermions. For the purpose of the present discussion we take away from it the lightest singlet fermion  $N_1$  (the “dark matter sterile neutrino”), which is coupled extremely weakly to the ordinary leptons. In addition, we take  $N_2$  and  $N_3$  degenerate in mass,  $M_2 = M_3 = M$ . The approximate equality of the masses of  $N_{2,3}$  comes from requirement of resonance production of the baryon asymmetry of the Universe. Then a convenient parameterization of the mass term and the interaction of  $N$ ’s with the leptons of SM is given in terms of three parameters  $(M, \epsilon, \eta)$ :

$$L_{\text{singlet}} = \left( \frac{M \sum m_i}{2v^2} \right)^{1/2} \left[ \frac{1}{\sqrt{\epsilon} e^{i\eta}} \bar{L}_2 N_2 + \sqrt{\epsilon} e^{i\eta} \bar{L}_3 N_3 \right] \widetilde{H} - M \bar{N}_2^c N_3 + \text{h.c.}, \quad (2.1)$$

where  $L_2$  and  $L_3$  are the combinations of the left-handed doublets  $L_e, L_\mu$ , and  $L_\tau$ ,

$$L_2 = \sum_\alpha x_\alpha L_\alpha, \quad L_3 = \sum_\alpha y_\alpha L_\alpha, \quad (2.2)$$

with  $\sum_\alpha |x_\alpha|^2 = \sum_\alpha |y_\alpha|^2 = 1$ . In (2.1)  $v = 246 \text{ GeV}$  is the vacuum expectation value of the Higgs field  $H$ ,  $\widetilde{H}_i = \epsilon_{ij} H_j^*$ , and  $m_i$  are the active neutrino masses. Note that one of them is negligibly small in comparison with others in the  $\nu\text{MSM}$  [6], so that  $\sum m_i = \kappa m_{\text{atm}}$  with  $m_{\text{atm}} \equiv \sqrt{|\Delta m_{\text{atm}}^2|} \simeq 0.05 \text{ eV}$  being the atmospheric neutrino mass difference,  $\kappa = 1(2)$  for normal (inverted) hierarchy of neutrino masses. Mixing parameters  $x_\alpha$  and  $y_\alpha$  can be expressed through the parameters of the active neutrino mixing matrix (explicit relations can be found in [24]). The parameter  $\epsilon$  (by definition,  $\epsilon < 1$ ) and the CP-breaking phase  $\eta$  cannot be determined by neutrino oscillation experiments.

If the value of mass parameter  $M$  is fixed, smaller  $\epsilon$  yields stronger interactions of singlet fermions to the SM leptons. This leads to equilibration of these particles in the early Universe above the electroweak temperatures, and, therefore, to erasing of the baryon asymmetry. In other words, the *mixing angle*  $U^2$  between neutral leptons and active neutrinos must be small, explaining why these new particles have not been seen previously. For small  $\epsilon$ ,

$$U^2 = \frac{\sum m_i}{4M\epsilon}. \quad (2.3)$$

The region, where baryogenesis is possible in  $(U^2, M)$  plane is shown in Figure 4. We also plot there the exclusion regions coming from different experiments such as CHARM [10], NuTeV [13], and CERN PS191 experiment [11, 12] (see also discussion of different experiments in [25, 26]). Only CERN PS191 significantly entered into the cosmologically interesting part of the parameter space of the  $\nu\text{MSM}$  for sterile neutrinos lighter than kaon. In Figure 5 we present the expected lifetime of the singlet fermions in an experimentally interesting region  $M < 1.8 \text{ GeV}$ .

As we see, the mass of these particles is limited from below by current experiments and cosmological considerations by  $\sim 100 \text{ MeV}$ , while no known solid upper bound, better than the electroweak scale, can be applied. At the same time, various considerations indicate that their mass may be in  $\mathcal{O}(1) \text{ GeV}$  region [24].

### 3. General Considerations for the Experiment

The most efficient mechanism of sterile neutrino production is associated with weak decays of heavy mesons and baryons, see left panel of Figure 6 for examples of relevant two- and three-body decays. Therefore, from experimental point of view, the distinct mass ranges are associated with the masses of mesons in which sterile neutrinos can be created: below  $500 \text{ MeV}$  ( $K$ -meson), between  $500 \text{ MeV}$  and  $2 \text{ GeV}$  ( $D$ -mesons), between  $2$  and  $5 \text{ GeV}$  ( $B$ -mesons), and above  $5 \text{ GeV}$ . We will concentrate here on the masses below the charm threshold, the higher values will be discussed shortly in Section 5.

The mechanism works as follows. Heavy mesons (and baryons) can be produced by energetic protons scattering off the target material. As a reference machine we take CERN



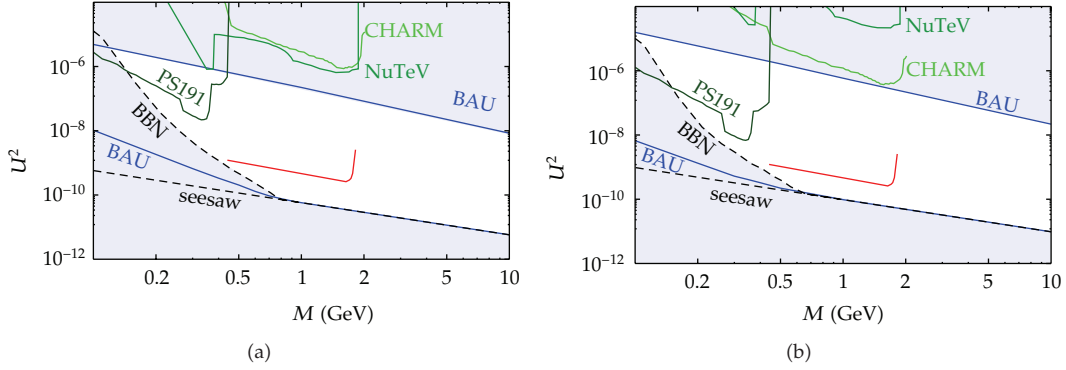


**Figure 4:** The allowed region of parameters of sterile neutrinos, responsible for neutrino oscillations (region above the dotted “seesaw” line) and for baryo/leptogenesis (region between two black solid lines). Sterile neutrinos with the parameters in the shaded region to the left of the “BBN” line would spoil predictions of primordial nucleosynthesis. Accelerator experiments, searching for heavy neutral leptons exclude regions above green lines. (a) restrictions for normal hierarchy (b) inverted hierarchy. Adopted from [27]. The region above the red curve can be probed with a single section of the detector of length  $l_{||} \sim 100$  m, height 5 m and width  $l_{\perp} \sim 5$  m, placed at a distance of about hundred meters, see the text for details.

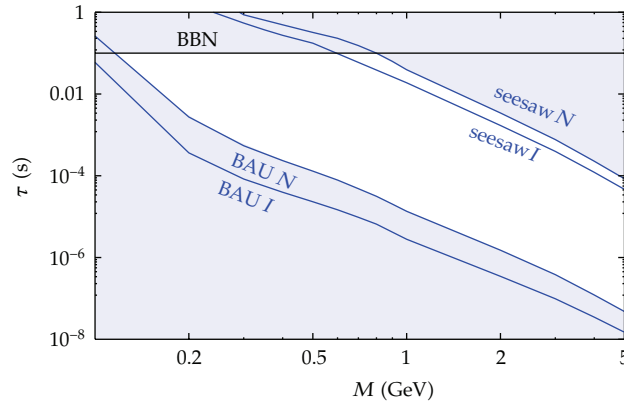


**Figure 5:** Constraints on the sterile neutrino lifetime  $\tau_N$  coming from the baryon asymmetry of the Universe (blue solid lines: “BAU N” refers to the normal hierarchy, “BAU I” refers to the inverted hierarchy), from the seesaw mechanism (blue solid lines: “Seesaw N” refers to normal hierarchy, “Seesaw I” refers to the inverted hierarchy) and big bang nucleosynthesis (black line: “BBN”). The allowed region of parameter space is in white. Limits from direct searches presented in Figure 4 are not outlined.

SPS with beam energy of 400 GeV. Here the relevant heavy hadrons contain charm as the heaviest quark:  $D$ ,  $D_s$ ,  $\Lambda_c$ ,  $D^*$ , ... With typical weak lifetime (in the rest frame) of about  $10^{-10}$  s these mesons mostly decay before further interaction in the target, no matter how thick it is. Sterile-active neutrino mixing gives rise to sterile neutrino production in weak decays of the heavy mesons (note that searches for those heavy hadron decays is one of the possible strategy of exploring the  $\nu$ MSM parameter space in full, which at the present level of experimental technique seems unrealistic, see discussion in Section 5). For charmed mesons typical branching ratios expected for the  $\nu$ MSM parameter space are at the level of [22]

$$\text{Br}(D \rightarrow N) \sim 10^{-8} - 10^{-12}, \quad (3.1)$$

(referring to upper and lower limits in Figure 4, resp.).

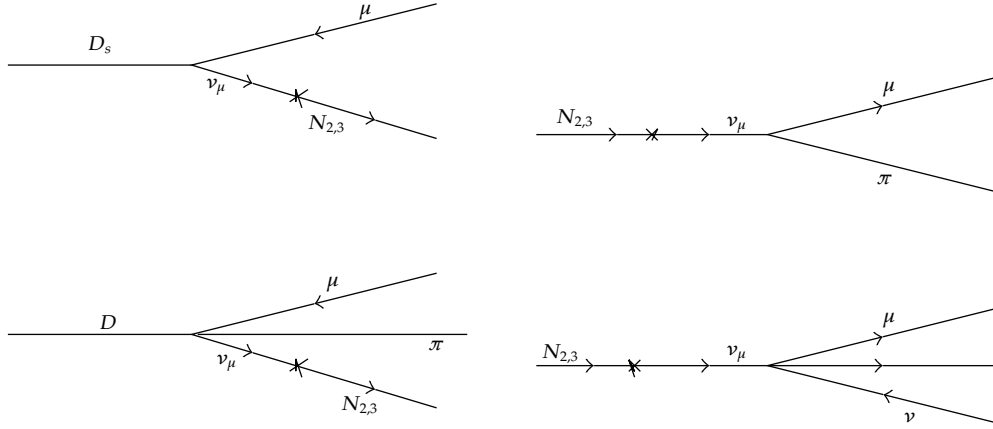


**Figure 6:** Left panel: Feynman diagrams of meson decays to heavy sterile neutrinos. Right panel: Feynman diagrams of sterile neutrino decays.

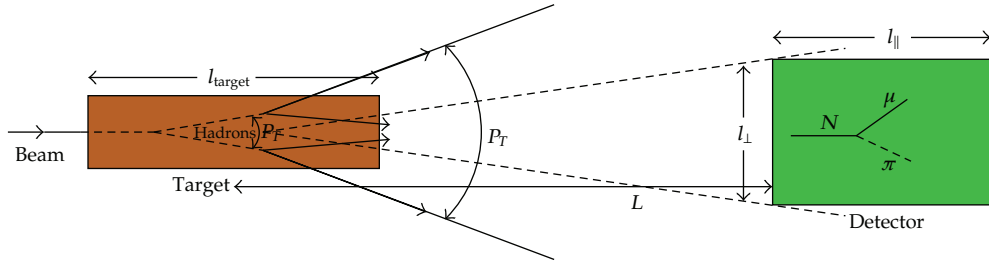


**Figure 7:** Sketch of typical beam-target experiment on searches for sterile neutrino decays.

These sterile neutrinos further weakly decay to the SM particles due to mixing with active neutrinos. In the  $\nu$ MSM mixing angles are small, see Figure 4, hence the sterile neutrinos live much longer (see Figure 5) as compared to that of the weakly decaying SM particles of similar masses. Before the decay (and with account of  $\gamma$ -factor) relativistic sterile neutrinos would cover quite a large distance significantly exceeding ten kilometers. Hence, sterile neutrino decays into SM particles due to mixing with active neutrino can be searched for in the near detector, see Figure 7. Two examples of the interesting decay modes are presented in right panel of Figure 6. More examples and typical patterns of sterile neutrino decay branching ratios expected within the  $\nu$ MSM can be found in [22].

Let us first make rough estimates of length-scale of the detector needed to *fully explore* the  $\nu$ MSM parameter space for sterile neutrino masses in the interesting range  $M_N \sim 0.5$ – $2$  GeV, where sterile neutrinos are dominantly produced in charmed hadron decays. Let  $P_T$  and  $P_L$  be average transverse and longitudinal momenta of produced sterile neutrinos. We start with detector of a special geometry designed to *cover entirely* the solid angle  $\sim \pi P_T^2 / P_L^2$  around the beam axis. Then all the sterile neutrinos travel through the fiducial volume of the detector which has a conical form. For 400 GeV proton beam operating at SPS the charm

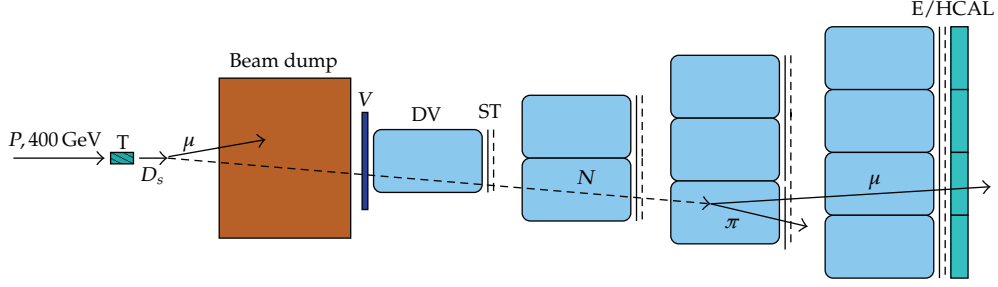


**Figure 8:** Schematic illustration of a proton beam dump experiment on search for  $D_s \rightarrow \mu N, N \rightarrow \mu\pi$  decay chain: charm mesons  $D_s$  generated by the proton beam in the target (T) produce a flux of high energy  $N$ 's through the  $U_{\mu N}$  mixing in the decay  $D_s \rightarrow \mu\nu_\mu$ , which penetrate the downstream shielding and decay into  $\mu\pi$  pair in a neutrino decay volume (DV). The same setup can be used to search for the process  $N \rightarrow \mu\nu$ . See text.

production cross section  $\sigma_c$  was measured by LEBC/EHS collaboration revealing  $\sigma_c \approx 30 \mu\text{b}$  [28]. Thus for  $N_{\text{pot}} = 10^{20}$  protons incident on the target per year one expects

$$\frac{\sigma_c}{\sigma_p} N_{\text{pot}} \sim 0.75 \times 10^{17} \quad (3.2)$$

charmed hadrons ( $\sigma_p \approx 40 \text{ mb}$  [29] is the total proton cross section at SPS energy). With charm branching ratio to sterile neutrino given above (3.1) one expects about

$$N_N \sim 0.75 \times (10^5 - 10^9) \quad (3.3)$$

sterile neutrinos crossing the detector each year of operating.

Then, for reference sterile neutrino mass of 1 GeV one estimates the decay length of  $10^2 - 10^5 \text{ km}$  (see Figure 5) and hence

$$N_N^{\text{dec}} \sim 1 - 10^7 \quad (3.4)$$

decay events per year for 1 km-length detector. Note, that with  $P_T/P_L \sim 1 \text{ GeV} / 40 \text{ GeV}$  [28] and heavy neutrino following the parent meson travel direction, the detector at a distance of 1 km has to cover the area of about  $25 \text{ m} \times 25 \text{ m}$  to accomplish the task.

Considering a more realistic setup, where detector is placed on the Earth surface and its height is of about 5 m (cf. the size of CHARM detector [10]) one concludes that the detector has to be about 5 times longer to achieve the same sensitivity to the sterile neutrinos as in the previous conical configuration.

To register all the expected sterile neutrino decays it seems appropriate to install many detectors of a reasonable  $5 \text{ m} \times 5 \text{ m} \times 100 \text{ m}$  size rather than one large detector. These small detectors may operate separately by independent groups of experimentalists but together cover the same volume as the large detector, see Figure 8.

#### 4. Preliminary Study for the Feasibility of the Proposed Experiment

The searches for Majorana leptons were undertaken in the past at PS191, BEBC, CHARM, and NuTeV and led to a negative result, not surprising in view of the cosmological constraints on the properties of sterile neutrinos, that were derived later on. The decays of the  $\nu_{\text{MSM}}$  sterile neutrinos are very rare events, and their observation presents a challenge for the detector design and performance. The sensitivity of the search has  $|U_{\mu N}|^4$  dependence on the mixing strength, and in order to increase it substantially as compared to the previous searches, one has to use,

- (i) higher intensity of the proton beam and larger amounts of pot's,
- (ii) shorter distance to the proton target,
- (iii) larger  $N$  decay fiducial volume,
- (iv) longer time of data accumulation,
- (v) better efficiency of events detection and reconstruction, background rejection, and so forth.

To compromise the cost of the detector and its performance, we focus mainly on discussions of the experimental setup to search for the  $N$  decays in a detector volume filled with a (diluted) gas, not in vacuum. The setup with vacuum requirements would provide possibly better sensitivity, but is more complicated and costly.

The main components of the experimental setup to search for the  $N$  decays of sterile neutrino are schematically illustrated in Figure 8. The full detector is composed of single identical modules. Each module consists of a decay volume tank (DV) with diameter of about 5–7 meters and length of 20–30 meters. To minimize cost and amount of passive material, the decay tank could be, for example, a rubber balloon filled with helium. Each DV is followed by a high precision tracker, which could be a layers of straw tube (ST), see, for example, [30]. The entire detector is assembled from  $\approx 50$ –100 such modules and is followed by a calorimeter (E/HCAL) which has the electromagnetic and hadronic parts. The detector is protected against charged secondaries from neutrino interactions in the dump by a Veto (V).

The design of a single module is similar to that one used in the PS191, or CHARM experiments, that searched for decays  $N \rightarrow \nu e^+ e^-, \mu\pi, \mu e\nu, \dots$  of heavy neutrinos in the  $N$  mass range from 10 MeV to 1.8 GeV originated from decays  $\pi, K$ , and charmed  $D$  mesons decays [10–12]. The later experiment, specifically designed to search for neutrino decays in a high-energy neutrino beam, was performed by using 400 GeV protons from the CERN Super Proton Synchrotron (SPS) with the total number of  $2.4 \times 10^{18}$  protons on (Cu) target (pot). The CHARM decay detector, located at the distance of 480 m from the target, consists of decay volume of  $3 \times 3 \times 35 \text{ m}^3$ , three chambers modules located inside the volume to detect charged tracks and followed by a calorimeter. The decay volume was essentially an empty region to substantially reduced the number of ordinary neutrino interactions. The signature of the heavy neutrino decay  $\nu_h \rightarrow \nu e^+ e^-$  were events originating in the decay region at a small angle with respect to the neutrino beam axis with one or two separate electromagnetic showers in the calorimeter [10]. No such events were observed and limits were established on the  $\nu_{e,\mu} - \nu_h$  mixing strength as a function of the  $\nu_h$  mass.



#### 4.1. Production and Decay of Sterile Neutrinos

If the decays  $D_s, D \rightarrow \mu N$  exist, one expects a flux of high energy  $N$ 's from the SPS target, since neutral mesons  $D_s$  and  $D$  are abundantly produced in the forward direction by high energy protons in the target. If  $N$  is a relatively long-lived particle, this flux would penetrate the downstream shielding without significant attenuation and would be observed in the proposed detector via the  $N \rightarrow \mu\pi, \mu e\nu$  decay into a high energy  $\mu\pi$  or  $\mu e$  pair, as schematically illustrated in Figure 7. The experimental signature of the sterile neutrino decays is an observation of either  $\mu\pi$  or  $\mu e$  pairs originated from a common vertex located in empty space. This signature is clean and the signal events are expected to be selected in the detector with a small background. The occurrence of  $N \rightarrow \mu\pi, \mu e\nu$  decays would appear as an excess of  $\mu\pi$  or  $\mu e$  pairs in the detector above those expected from standard neutrino interactions. Up to a  $N$  mass of  $\lesssim 2$  GeV, the mass difference between the  $D_s$  and the  $\mu$ ,  $N$ 's can originate both from the  $\nu_\mu$  produced directly in the  $D_s$  decay and from the  $\nu_\mu$  produced indirectly in the subsequent decay of  $\tau$  produced in  $D_s$  decays. For a  $N$  mass below than  $\lesssim 1.8$  GeV  $\nu_\mu$ 's produced in  $\tau$  decay can contribute. However these indirect  $N$ 's have a lower acceptance resulting in a smaller probability to observe the  $N$  decays in the detector. Therefore we focus mainly on directly produced  $N$ 's.

As discussed previously, the mixing between the sterile neutrino and the muon neutrino results in the decay  $D_s \rightarrow \mu N$ , as illustrated in Figure 8. The  $D_s$  meson, which is normally decays into a  $\mu$  and  $\nu_\mu$ , might instead decay to a  $\mu$  and a heavy neutrino  $N$ . For the mass interval  $m_{\nu_h} \lesssim 2$  GeV the chirality-flip is mostly due to sterile neutrino mass which results in

$$\Gamma(D_s \rightarrow \mu N) \approx \Gamma(D_s \rightarrow \mu \nu_\mu) |U_{\mu N}|^2 \left( \frac{m_N}{m_\mu} \right)^2. \quad (4.1)$$

In the SM,  $D_s$  meson decays leptonically via annihilation of the  $c$  and  $\bar{s}$  quarks through a virtual  $W^+$ . The decay rate of this process is given by

$$\Gamma(D_s \rightarrow l \nu) = \frac{G_F^2}{8\pi} f_{D_s}^2 m_l^2 M_{D_s} \left( 1 - \frac{m_l^2}{M_{D_s}^2} \right)^2 |V_{cs}|^2, \quad (4.2)$$

where the  $M_{D_s}$  is the  $D_s$  meson mass,  $m_l$  is the mass of the charged lepton,  $f_{D_s}^2$  is the decay constant,  $G_F$  is the Fermi constant, and  $V_{cs}$  is a Cabibbo-Kobayashi-Maskawa matrix element which value equals 0.97334 [31]. The decay rate (4.2) is suppressed by the lepton mass squared, since the very leptonic decay is due to chirality-flip. As follows from (4.1), in neutrino scattering experiments the  $N$  decay signal rate is proportional to  $\propto |U_{\mu N}|^4$  (the mixing  $|U_{\mu h}|^2$  appears twice, through the heavy neutrino production, and through the its decays in the detector) and, thus is more suppressed. The branching ratio of a particular decay mode, for example,  $N \rightarrow \mu\pi$  (or  $N \rightarrow \mu e\nu$ ) is given by

$$\text{Br}(N \rightarrow \mu\pi) = \frac{\Gamma(\mu\pi)}{\Gamma_{\text{tot}}} = F(M_N, |U_{\mu N}|^2), \quad (4.3)$$

where the function  $F(M_N, |U_{\mu N}|^2)$  is calculated in [22], and the total rate  $\Gamma_{\text{tot}}$  is dominated by the  $N \rightarrow 3\nu$  decay channel.

To make quantitative estimates, we performed simplified simulations of the  $N$  production in the inclusive reaction

$$p + Be \longrightarrow D_s + X, \quad D_s \longrightarrow \mu + N \rightarrow \mu\pi, \mu e\nu \quad (4.4)$$

with the emission of a GeV-scale sterile neutrino  $N$  subsequently decaying semileptonically or leptonically in the detector, as illustrated in Figures 7 and 8. In the simulations it is assumed, that the  $N$  is a long-lived particle and the flux of  $N$ 's penetrates the downstream shielding without significant attenuation. The decay  $N \rightarrow \mu\pi, \mu e\nu$  cannot be distinguished from the antineutrino decay  $\bar{N} \rightarrow \mu\pi$  or  $\bar{N} \rightarrow \mu e\nu$  and the obtained result therefore refers to the sum of all these decay modes.

The flux of sterile neutrinos from decays of  $D_s$ 's and  $D$ 's produced in the target by primary protons can be expressed as follows:

$$\Phi(N) \propto N_{\text{pot}} \int \frac{d^3\sigma(p + N \rightarrow D_s(D) + X)}{d^3p_{D_s(D)}} \text{Br}(D_s(D) \rightarrow \mu N) f d^3p_{D_s(D)}, \quad (4.5)$$

where  $N_{\text{pot}}$  is the number of pot,  $\sigma(p + N \rightarrow D_s(D) + X)$  is the  $D_s(D)$  meson production cross-section,  $\text{Br}(D_s(D) \rightarrow \mu N)$  is the  $D_s(D) \rightarrow \mu N$  decay mode branching fraction [31], and  $f$  is the decay phase space factor, respectively.

To perform quantitative we used simulations of the process shown in Figure 7 by taking into account the relative normalization of the yield of charmed meson species  $D_s$  and  $D$  from the original publications. The invariant cross-section of a charm meson production can be expressed as [31]

$$E \frac{d^3\sigma}{d^3p} = \frac{d^3\sigma}{p_T dp_T dy d\phi} = \frac{d^2\sigma}{2\pi p_T dp_T dy}, \quad (4.6)$$

where  $p_T$  is the transverse momentum of the particle,  $y$  is its rapidity, and in the last equality integration over the full  $2\pi$  azimuthal angle  $\phi$  is performed. For the production cross-sections of  $D_s$  and  $D$  charm mesons we used the Bourquin-Gaillard (B-G) formula from [32]:

$$E \frac{d^3\sigma(p + N \rightarrow D_s(D) + X)}{d^3p} = A \left( \frac{2}{E_T + 2} \right)^{12.3} \exp\left(-\frac{5.13}{Y^{0.38}}\right) f(p_T), \quad (4.7)$$

where

$$f(p_T) = \begin{cases} \exp(-p_T), & p_T < 1 \text{ GeV}, \\ \exp\left(-1 - \frac{23(p_T - 1)}{\sqrt{s}}\right), & p_T > 1 \text{ GeV} \end{cases} \quad (4.8)$$

with  $Y = y_{\text{max}} - y$ , being the rapidity,  $s$  is the Mandelstam variable in  $\text{GeV}^2$ , and  $E_T(p_T)$  is the transverse energy (momentum) in  $\text{GeV}$ . The coefficient  $A$  in (4.7) is a normalization factor

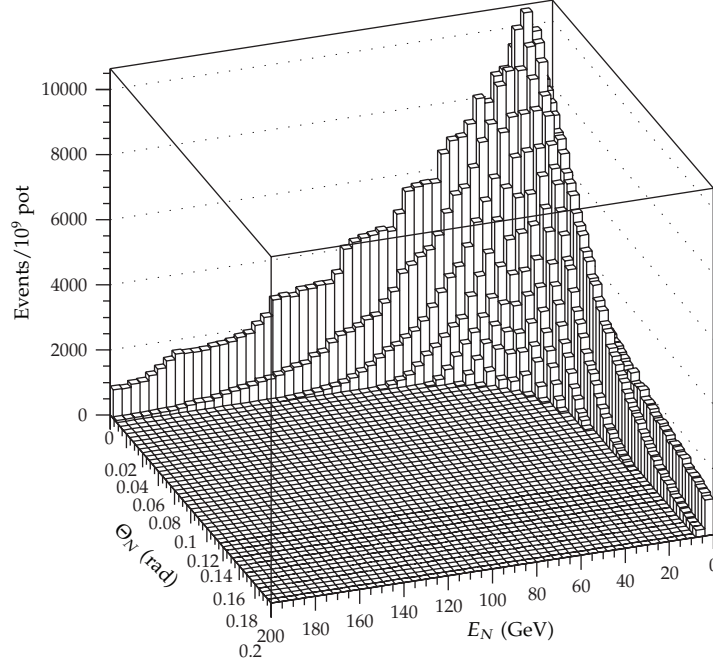


**Figure 9:** Two dimensional distribution of flux for 1 GeV sterile neutrino as a function of  $\Theta_N$ , the angle between the proton beam axis and momentum of  $N$ , and its energy calculated for 400 GeV proton incident on Be target. The  $N$ 's are produced through the decay  $D_s \rightarrow \mu N$  assuming mixing strength  $|U_{\mu N}|^2 = 1$ .

that was tuned to obtain the cross sections of the charm production in pp collisions at 400 GeV. The spectra of  $\nu_\tau$ 's produced in the Be target by primary protons could be calculated by using the approach reported in [33] (see also [34]). However, the Bourquin-Gaillard (B-G) approach gives the parametric form of (4.6) for the production of many different hadrons, including charm, which is in good agreement with data over the full phase-space in high-energy hadronic collisions and with a precision which is satisfactory at the level of our accuracy. The total  $D_s$  and  $D$  production cross sections in  $p$ -Be collisions were calculated from its linear extrapolation to the target atomic number. The contribution of protons not interacting in the Be target and interacting in the SPS beam dump was not taken into account.

The calculated fluxes and energy distributions of  $D_s$ ,  $D$  produced in the Be target were used to predict the flux of  $N$ 's, as a function of its mass. An example of 2D-flux distribution calculated for 1 GeV sterile neutrino as a function of  $\Theta_N$ , the angle between the proton beam axis and momentum of  $N$ , and the  $N$  energy for 400 GeV proton incident on target is shown in Figure 9. In these calculation the  $N$ 's are produced through the decay  $D_s \rightarrow \mu N$  assuming mixing strength  $|U_{\mu N}|^2 = 1$ . One can see, that for detector located at the distance  $\approx 100$  m from the target its fiducial area for efficient  $N$  detection should be of the order  $S \approx \pi L^2 \Theta^2 \approx 300 \text{ m}^2$ .

#### 4.2. Background

There are several expected sources of background in the experiment, which come from

- (i) neutrino interactions in helium,
- (ii) neutrino interactions in surrounding materials,

- (iii) cosmics,
- (iv) accidentals,
- (v) punch-through energetic neutral particles, such as  $K_L^0$  or  $n$ .

Because of the high number of pot's and many possible sources of background the detail study for the feasibility of the proposed search would require the simulation of a very large number of events resulting in a prohibitively large amount of computer time. Consequently, only small fraction of the required statistics for  $\nu_\mu CC(NC)$  inelastic reactions and other background components, for example, such as coherent and quasielastic reactions, and so forth. . . , were considered for preliminary estimate and combined with numerical calculations.

The estimate shows that the dominant background is expected from the primary  $\nu_\mu$  interactions in passive material, which correspond roughly to  $\approx 10^6 \nu_\mu CC / 10^{20}$  pot events per 1 ton of matter. The largest contribution to background is expected from neutrino interactions yielding a single  $\mu\pi$  pair with little hadronic activity in the final state. Neutrino interactions that occur in the surrounding material, for example, upstream of the DV fiducial volume or in material of the decay tanks, also may produce an isolated  $\mu\pi$  pairs if the accompanying particles are not detected. These background events from surrounding material could be rejected with an effective method developed in [15], by introducing the collinearity variable  $1 - \cos \Theta$ , where  $\Theta$  is the angle between, for example, the  $\mu\pi$  pair momentum direction and the neutrino beam axis. The main idea is that if the  $\mu\pi$  pair originates from the decay chain  $D_s \rightarrow \mu N, N \rightarrow \mu\pi$ , at high energies the  $\mu\pi$  pair momentum extrapolated back should point to the  $D_s$  production target. An example of the distribution of the variable  $1 - \cos \Theta$  obtained in the NOMAD experiment, searching for the decay  $N \rightarrow e^+ e^- \nu$ , is shown in Figure 5 of [15]. One can see that potentially one could measure the  $\mu\pi$  pair momentum direction with precision  $1 - \cos \Theta \approx 10^{-5}$ . By using this variable, two independent techniques could be used for the background estimation in the signal region. The first is obviously based on the MC. The second method relies on the data themselves. By extrapolating the observed events to the signal region with the shape of the fully simulated MC events a background estimate can be obtained from the data. Using this technique would result in an additional rejection of background events.

### 4.3. Sensitivity Estimate

For a given flux  $d\Phi(M_N, E_N, N_{\text{pot}})/dE_N$  of  $N$ 's the expected number of  $N \rightarrow \mu\pi, \mu e \nu$  decays occurring within the fiducial length  $L$  of the detector located at a distance  $L'$  from the neutrino target is given by

$$N_{N \rightarrow \mu\pi, \mu e \nu} = \text{Br}(D_s \rightarrow \mu N) \text{Br}(N \rightarrow \mu\pi) \int \frac{d\Phi}{dE_N} \cdot \exp\left(-\frac{L' M_N}{P_N \tau_N}\right) \left[1 - \exp\left(-\frac{L M_N}{P_N \tau_N}\right)\right] \zeta S dE_N, \quad (4.9)$$

where  $E_N, P_N$ , and  $\tau_N$  are the  $N$  energy, momentum, and the lifetime at rest, respectively, and  $\zeta (\approx 50\%)$  is the  $\mu\pi$  ( $\mu e$ ) pairs reconstruction efficiency. The acceptance  $S$  was calculated by tracing  $N$ 's produced in the Be-target to the detector taking the relevant momentum and angular distributions into account. In this estimate the average momentum is  $\langle p_N \rangle \approx 45 \text{ GeV}$  and  $S \approx 50\%$ .



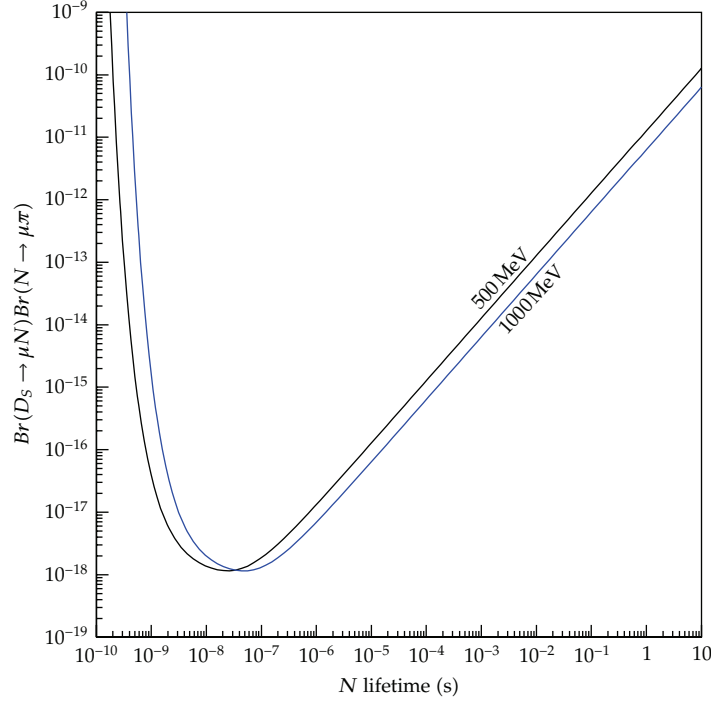


**Figure 10:** The expected 90% C.L. upper limits on the branching ratio  $\text{Br}(D_s \rightarrow \mu N)\text{Br}(N \rightarrow \mu\pi)$  versus  $\tau_N$  estimated for the proposed experiment in the background free case. The numbers near the curves indicate the corresponding values of sterile neutrino masses.

In the case of no signal observation, the background free experiment would result in stringent constraints on existence of the sub-GeV sector of the  $\nu\text{MSM}$ . An example of the exclusion region calculated in the  $(\text{Br}(D_s \rightarrow \mu N)\text{Br}(N \rightarrow \mu\pi) \approx \tau_N)$  plane for  $\approx 10^{20}$  pot and the detector assembled from  $\approx 10^2$  modules, assuming  $N_{N \rightarrow \mu\pi, \mu e \nu} < 2.3$  at 90% CL, is shown in Figure 10. For the mass range  $0.5 \lesssim m_N \lesssim 2 \text{ GeV}$  these limits correspond to the bounds on the mixing strength which are in the range  $10^{-6} \lesssim |U_{\mu N}|^2 \lesssim 10^{-10}$  and exclude seesaw sterile neutrinos with masses below 2 GeV.

Note, that the uncertainty for the  $D_s$  production at low  $p_T$  does not significantly affect the sensitivity estimate. For example, the variation of the  $D_s$  yield in (4.9) by 30% results in the corresponding variation of the limits on mixing strength  $U_{\mu N}$  of order 5%. This is because the sensitivity of the search is proportional to the  $|U_{\mu N}|^4$ . Indeed, in (4.9) the branching fraction of (4.2) and the decay rate  $\Gamma(N \rightarrow \mu\pi, \mu e \nu)$  of (4.1) both are proportional to  $|U_{\mu N}|^2$ .

## 5. Conclusions

The energy scale of new physics is not known. If it exists at energies above the Fermi scale (examples include supersymmetry, large or warped extra dimensions, and models with dynamical electroweak symmetry breaking), the search for new particles can be carried out in direct experiments, such as ATLAS and CMS at LHC. In addition, new hypothetical heavy particles inevitably appear as virtual states, leading to different rare processes, absent in the SM. These effects can be found at experiments such as LHCb and are competitive with the

direct searches. If no new physics is found at the LHC, this may indicate the absence of new physics all the way between the Fermi and Planck scales.

Quite paradoxically, the largely unexplored up to now domain of energies where the new physics can be hidden is related to physics *below* the Fermi scale. If the new particles are light and weakly interacting (as in the  $\nu$ MSM, discussed here) then the search for rare processes is superior to high energy experiments. It provides a unique possibility for discovery of new physics, not accessible by any of the LHC experiments.

The present proposal deals with the searches of new relatively light Majorana leptons which “give” the masses to ordinary neutrinos and produce baryon asymmetry of the Universe. We discussed here the parameters of the beam-target experiment which can explore completely the mass range below 2 GeV. Due to the weak coupling of these particles to other fermions these experiments are very challenging and require construction of a kilometer scale detector. However, an experiment at much smaller scales, with 100 meters detectors, would be able to explore the dominant fraction of the parameter space.

Below we describe shortly the prospect for other experiments and higher range of sterile neutrino masses.

We start with remark that signal statistics in beam-target experiment proposed in this paper is determined by the *fourth power of sterile-active neutrino mixing*,  $U^2 \times U^2$ , since both sterile neutrino production in meson decays and rate of subsequent neutrino decay within a detector are proportional to  $U^2$ . Experiments on searches of meson decays to sterile neutrinos requires (potentially) less statistics of mesons, since the signal statistics are proportional only to the *second power* of sterile-active neutrino mixing  $U^2$ .

With expected for  $\nu$ MSM branching ratios (3.1) the relevant experiment has to collect not less than  $10^{12}$  hadrons in order to fully explore the entire part of parameter space at  $M_N < 2$  GeV. This statistics is far above what has been obtained at previous  $c$ - and  $b$ -factories (CLEO(- $c$ ), BaBar, Belle) or at proposed future  $c$ - $\tau$  (Novosibirsk) and  $B$ -factories (Tsukuba, Frascati), where total number of  $D$ -meson is planned at the level of  $10^9$ , see, for example, [35]. Only at LHC the  $D$ -meson production rate is enough to perform this search, however, limits from data taking rate, QCD-background, vertex resolution, particle misidentification etc, prevent measurement of  $D$ -meson branching ratios at the required level (3.1).

As we have already mentioned, there are no solid-motivated upper limits on sterile neutrino mass of subelectroweak scale. Sterile neutrinos can be heavier than  $D$ -meson, and then charmed hadrons are out of use. If sterile neutrinos are lighter than 5 GeV, they can be produced in beauty hadron decays. This mass range is favorable [27] for a particular mechanism of dark matter production (resonant oscillations in the primordial plasma with lepton asymmetry) in the early Universe. There are other options for dark matter production, which are insensitive to the 1 GeV scale sterile neutrinos, see, for example, [36, 37]. Typical branching ratios of  $B$ -mesons to sterile neutrino expected within  $\nu$ MSM are [22] by one-two orders of magnitude smaller, than those of  $D$ -mesons, as both upper and lower bounds on mixing  $U^2$  decrease with increase of sterile neutrino masses, see Figure 4. Proposed upgrade of LHCb [38] will be able of entering the interesting region of  $\nu$ MSM parameter space by searching for  $b$ -meson decays into sterile neutrinos, but cannot cover the entire region. One can further discuss an idea of using LHC-beam (4 TeV, 7 TeV, higher) for a beam-target experiment of the kind proposed in this paper, in order to fully explore the  $\nu$ MSM parameter space, if sterile neutrino mass belongs to the interval 2–5 GeV.

The preliminary analysis shows that the quoted sensitivity could be obtained with a proton beam and a detector optimized for several its properties. Namely, (i) the primary beam intensity and the total number of pot's, (ii) the fiducial decay volume of the detector,

(iii) the composition of the material of decay tank and surrounding material and (iv) the efficiency and precision of the tracking system, (v) the E/HCAL granularity, energy resolution, and particle identification, and (vi) different sources of background are of importance.

As far as the cost concerned, each module may be relatively cheap, empty-space with simple tracker system either inside or behind the decay volume, and the calorimeter at the far end. Its design may repeat the design of the experiment on precision neutrino measurements and searches for sterile neutrino decays at FNAL [30]. The detector of the 100 length has a sensitivity to  $U^2 \times U^2$  worth by a factor only 50. Thus even one (the first) section will be able to deepen considerably into the parameter range interesting for cosmology, see Figure 4.

## Acknowledgments

The work was supported in part by the Grant of the President of the Russian Federation NS-5590.2012.2, by the SCOPES program (D.G. and M.S.), and by the RFBR Grant 11-02-01528a (DG).

## References

- [1] F. Bezrukov, M. Kalmykov, B. Kniehl, and M. Shaposhnikov, "Higgs boson mass and new physics," In press. <http://arxiv.org/abs/1205.2893>.
- [2] F. Bezrukov, M. Kalmykov, B. Kniehl, and M. Shaposhnikov, " $t - \bar{t}$  factory and Planck physics," Proposal submitted to European Strategy Group, 2012.
- [3] M. Shaposhnikov, "Is there a new physics between electroweak and Planck scales?" In press. <http://arxiv.org/abs/0708.3550>.
- [4] M. Shaposhnikov and D. Zenhäusern, "Scale invariance, unimodular gravity and dark energy," *Physics Letters B*, vol. 671, no. 1, pp. 187–192, 2009.
- [5] M. Shaposhnikov and D. Zenhäusern, "Quantum scale invariance, cosmological constant and hierarchy problem," *Physics Letters B*, vol. 671, no. 1, pp. 162–166, 2009.
- [6] A. Boyarsky, O. Ruchayskiy, and M. Shaposhnikov, "The role of sterile neutrinos in cosmology and astrophysics," *Annual Review of Nuclear and Particle Science*, vol. 59, p. 191, 2009.
- [7] A. Boyarsky, O. Ruchayskiy, and M. Shaposhnikov, "Search for keV-scale sterile neutrinos responsible for dark matter in the universe," Proposal submitted to European Strategy Group, 2012.
- [8] T. Yamazaki, T. Ishikawa, Y. Akiba et al., "Search for heavy neutrinos in kaon decay," in *Proceedings of the High Energy Physics*, vol. 1, Leipzig, Germany, 1984.
- [9] A. M. Cooper-Sarkara, S. J. Haywooda, M. A. Parkera et al., "Search for heavy neutrino decays in the BEBC beam dump experiment," *Physics Letters B*, vol. 160, no. 1–3, pp. 207–211, 1985.
- [10] J. V. Allaby, U. Amaldi, G. Barbiellini, C. Berger, F. Bergsma et al., "A search for decays of heavy neutrinos in the mass range 0.5–2.8 GeV," *Physics Letters B*, vol. 166, no. 4, pp. 473–478, 1986.
- [11] G. Bernardi, G. Carugno, J. Chauveau et al., "Search for neutrino decay," *Physics Letters B*, vol. 166, no. 4, pp. 479–483, 1986.
- [12] G. Bernardi, G. Carugno, J. Chauveau et al., "Further limits on heavy neutrino couplings," *Physics Letters B*, vol. 203, no. 3, pp. 332–334, 1988.
- [13] A. Vaitaitis, R. B. Drucker, J. Formaggio et al., "Search for neutral heavy leptons in a high-energy neutrino beam," *Physical Review Letters*, vol. 83, no. 24, pp. 4943–4946, 1999.
- [14] M. Daum, M. Janousch, P.-R. Kettle et al., "KARMEN time anomaly: search for a neutral particle of mass 33.9 MeV in pion decay," *Physical Review Letters*, vol. 85, no. 9, pp. 1815–1818, 2000.
- [15] P. Astier, D. Autiero, A. Baldisseri et al., "Search for heavy neutrinos mixing with tau neutrinos," *Physics Letters B*, vol. 506, no. 1–2, pp. 27–38, 2001.
- [16] P. Achard, O. Adriani, M. Aguilar-Benitez et al., "Search for heavy neutral and charged leptons in  $e^+e^-$  annihilation at LEP," *Physics Letters B*, vol. 517, no. 1–2, pp. 75–85, 2001.
- [17] P. Minkowski, " $\mu \rightarrow e\gamma$  at a rate of one out of  $10^9$  muon decays?" *Physics Letters B*, vol. 67, no. 4, pp. 421–428, 1977.
- [18] T. Yanagida, "Horizontal symmetry and masses of neutrinos," *Progress of Theoretical Physics*, vol. 64, no. 3, p. 1103, 1980.

- [19] M. Gell-Mann, P. Ramond, and R. Slansky, "Complex spinors and unified theories," in *Supergravity*, Amsterdam, The Netherlands, 1980.
- [20] R. N. Mohapatra and G. Senjanovic, "Neutrino mass and spontaneous parity nonconservation," *Physical Review Letters*, vol. 44, no. 14, pp. 912–915, 1980.
- [21] B. Armbruster, I. Blair, B. A. Bodmann et al., "Anomaly in the time distribution of neutrinos from a pulsed beam stop source," *Physics Letters B*, vol. 348, no. 1-2, pp. 19–28, 1995.
- [22] D. Gorbunov and M. Shaposhnikov, "How to find neutral leptons of the  $\nu$ MSM?" *Journal of High Energy Physics*, vol. 2007, 2007.
- [23] D. Gorbunov and M. Shaposhnikov, "Search for GeV-scale sterile neutrinos responsible for active neutrino masses and baryon asymmetry of the Universe," Proposal submitted to European Strategy Group, 2012.
- [24] M. Shaposhnikov, "The  $\nu$ MSM, leptonic asymmetries, and properties of singlet fermions," *Journal of High Energy Physics*, vol. 2008, 2008.
- [25] A. Atre, T. Han, S. Pascoli, and B. Zhang, "The search for heavy Majorana neutrinos," *Journal of High Energy Physics*, vol. 2009, 2009.
- [26] O. Ruchayskiy and A. Ivashko, "Experimental bounds on sterile neutrino mixing angles," *Journal of High Energy Physics*, vol. 2012, article 100, 2012.
- [27] L. Canetti, M. Drewes, and M. Shaposhnikov, "Sterile neutrinos as the origin of dark and baryonic matter," In press. <http://arxiv.org/abs/1204.3902>.
- [28] M. Aguilar-Benitez, W. W. M. Allison, J. L. Bailly et al., "D-Meson production from 400 GeV/c pp interactions," *Physics Letters B*, vol. 189, no. 4, pp. 476–482, 1987.
- [29] K. Nakamura, "Review of particle physics," *Journal of Physics G*, vol. 37, no. 7, Article ID 075021, 2010.
- [30] S. R. Mishra, R. Petti, and C. Rosenfeld, "A high resolution neutrino experiment in a magnetic field for project-X at fermilab," *High Energy Physics*. In press. <http://arxiv.org/abs/0812.4527>.
- [31] J. Beringer, J.-F. Arguin, R. M. Barnett et al., "Review of particle physics," *Physical Review D*, vol. 86, no. 1, 2012.
- [32] M. Bourquin and J.-M. Gaillard, "A simple phenomenological description of hadron production," *Nuclear Physics B*, vol. 114, no. 2, pp. 334–364, 1976.
- [33] M. C. Gonzalez-Garcia and J. J. Gomez-Cadenas, "Prompt  $\nu_\tau$  fluxes in present and future  $\tau$  neutrino experiments," *Physical Review D*, vol. 55, no. 3, pp. 1297–1306, 1997.
- [34] B. Van de Vyver, "Prompt  $V_T$  background in wide band  $V_\mu$  beams," *Nuclear Instruments and Methods in Physics Research A*, vol. 385, no. 1, pp. 91–99, 1997.
- [35] B. Meadows, M. Blanke, A. Stocchi et al., "The impact of SuperB on flavour physics," In press. <http://arxiv.org/abs/1109.5028>.
- [36] M. Shaposhnikov and I. Tkachev, "The  $\nu$ MSM, inflation, and dark matter," *Physics Letters B*, vol. 639, no. 5, pp. 414–417, 2006.
- [37] F. Bezrukov and D. Gorbunov, "Light inflaton hunter's guide," *Journal of High Energy Physics*, vol. 2010, 2010.
- [38] R. Aaij, C. Abellán Beteta, B. Adeva et al., "Letter of Intent for the LHCb Upgrade," Tech. Rep. CERN-LHCC-2011-001, CERN, Geneva, Switzerland, 2011.



## Review Article

# Leptogenesis in the Universe

**Chee Sheng Fong,<sup>1</sup> Enrico Nardi,<sup>1</sup> and Antonio Riotto<sup>2</sup>**

<sup>1</sup> INFN Laboratori Nazionali di Frascati, Via Enrico Fermi 40, 00044 Frascati, Italy

<sup>2</sup> Department of Theoretical Physics, University of Geneva and Center for Astroparticle Physics (CAP), 24 quai E. Ansermet, 1211 Geneva 4, Switzerland

Correspondence should be addressed to Enrico Nardi, enrico.nardi@lnf.infn.it

Received 25 June 2012; Accepted 30 October 2012

Academic Editor: Gian Luigi Fogli

Copyright © 2012 Chee Sheng Fong et al. This is an open access article distributed under the Creative Commons Attribution License, which permits unrestricted use, distribution, and reproduction in any medium, provided the original work is properly cited.

Leptogenesis is a class of scenarios in which the cosmic baryon asymmetry originates from an initial lepton asymmetry generated in the decays of heavy sterile neutrinos in the early Universe. We explain why leptogenesis is an appealing mechanism for baryogenesis. We review its motivations and the basic ingredients and describe subclasses of effects, like those of lepton flavours, spectator processes, scatterings, finite temperature corrections, the role of the heavier sterile neutrinos, and quantum corrections. We then address leptogenesis in supersymmetric scenarios, as well as some other popular variations of the basic leptogenesis framework.

## 1. The Baryon Asymmetry of the Universe

### 1.1. Observations

Up to date no traces of cosmological antimatter have been observed. The presence of a small amount of antiprotons and positrons in cosmic rays can be consistently explained by their secondary origin in cosmic particles collisions or in highly energetic astrophysical processes, but no antinuclei, even as light as antideuterium or as tightly bounded as anti- $\alpha$  particles, have ever been detected.

The absence of annihilation radiation  $p\bar{p} \rightarrow \dots\pi^0 \rightarrow \dots 2\gamma$  excludes significant matter-antimatter admixtures in objects up to the size of galactic clusters  $\sim 20$  Mpc [1]. Observational limits on anomalous contributions to the cosmic diffuse  $\gamma$ -ray background and the absence of distortions in the cosmic microwave background (CMB) imply that little antimatter is to be found within  $\sim 1$  Gpc and that within our horizon an equal amount of matter and antimatter can be excluded [2]. Of course, at larger superhorizon scales the vanishing of the average asymmetry cannot be ruled out, and this would indeed be the

case if the fundamental Lagrangian is C and CP symmetric and charge invariance is broken spontaneously [3].

Quantitatively, the value of baryon asymmetry of the Universe is inferred from observations in two independent ways. The first way is by confronting the abundances of the light elements,  $D$ ,  $^3\text{He}$ ,  $^4\text{He}$ , and  $^7\text{Li}$ , with the predictions of Big Bang nucleosynthesis (BBN) [4–9]. The crucial time for primordial nucleosynthesis is when the thermal bath temperature falls below  $T \lesssim 1 \text{ MeV}$ . With the assumption of only three light neutrinos, these predictions depend on a single parameter, that is, the difference between the number of baryons and antibaryons normalized to the number of photons:

$$\eta \equiv \left. \frac{n_B - n_{\bar{B}}}{n_\gamma} \right|_0, \quad (1.1)$$

where the subscript 0 means “at present time.” By using only the abundance of deuterium, that is particularly sensitive to  $\eta$ , [4] quotes:

$$10^{10} \eta = 5.7 \pm 0.6 \quad (95\% \text{ c.l.}). \quad (1.2)$$

In this same range there is also an acceptable agreement among the various abundances, once theoretical uncertainties as well as statistical and systematic errors are accounted for [6].

The second way is from measurements of the CMB anisotropies (for pedagogical reviews, see [10, 11]). The crucial time for CMB is that of recombination, when the temperature dropped down to  $T \lesssim 1 \text{ eV}$  and neutral hydrogen can be formed. CMB observations measure the relative baryon contribution to the energy density of the Universe multiplied by the square of the (reduced) Hubble constant  $h \equiv H_0 / (100 \text{ km sec}^{-1} \text{ Mpc}^{-1})$ :

$$\Omega_B h^2 \equiv h^2 \frac{\rho_B}{\rho_{\text{crit}}}, \quad (1.3)$$

that is related to  $\eta$  through  $10^{10} \eta = 274 \Omega_B h^2$ . The physical effect of the baryons at the onset of matter domination, which occurs quite close to the recombination epoch, is to provide extra gravity which enhances the compression into potential wells. The consequence is enhancement of the compressional phases which translates into enhancement of the odd peaks in the spectrum. Thus, a measurement of the odd/even peak disparity constrains the baryon energy density. A fit to the most recent observations (WMAP7 data only, assuming a  $\Lambda\text{CDM}$  model with a scale-free power spectrum for the primordial density fluctuations) gives at 68% c.l. [12]

$$10^2 \Omega_B h^2 = 2.258^{+0.057}_{-0.056}. \quad (1.4)$$

There is a third way to express the baryon asymmetry of the Universe, that is, by normalizing the baryon asymmetry to the entropy density  $s = g_*(2\pi^2/45)T^3$ , where  $g_*$  is the number of degrees of freedom in the plasma and  $T$  is the temperature:

$$Y_{\Delta B} \equiv \left. \frac{n_B - n_{\bar{B}}}{s} \right|_0. \quad (1.5)$$

The relation with the previous definitions is given by the conversion factor  $s_0/n_{\gamma 0} = 7.04$ .  $Y_{\Delta B}$  is a convenient quantity in theoretical studies of the generation of the baryon asymmetry from very early times, because it is conserved throughout the thermal evolution of the Universe. In terms of  $Y_{\Delta B}$  the BBN results (1.2) and the CMB measurement (1.4) (at 95% c.l.) read

$$Y_{\Delta B}^{\text{BBN}} = (8.10 \pm 0.85) \times 10^{-11}, \quad Y_{\Delta B}^{\text{CMB}} = (8.79 \pm 0.44) \times 10^{-11}. \quad (1.6)$$

The impressive consistency between the determinations of the baryon density of the Universe from BBN and CMB that, besides being completely independent, also refer to epochs with a six orders of magnitude difference in temperature, provides a striking confirmation of the hot Big Bang cosmology.

## 1.2. Theory

From the theoretical point of view, the question is where the Universe baryon asymmetry comes from. The inflationary cosmological model excludes the possibility of a fine tuned initial condition, and since we do not know any other way to construct a consistent cosmology without inflation, this is a strong veto.

The alternative possibility is that the Universe baryon asymmetry is generated dynamically, a scenario that is known as *baryogenesis*. This requires that baryon number ( $B$ ) is not conserved. More precisely, as Sakharov pointed out [13], the ingredients required for baryogenesis are three.

- (1)  $B$  violation is required to evolve from an initial state with  $Y_{\Delta B} = 0$  to a state with  $Y_{\Delta B} \neq 0$ .
- (2)  $C$  and  $CP$  violation: if either  $C$  or  $CP$  was conserved, then processes involving baryons would proceed at the same rate as the  $C$ - or  $CP$ -conjugate processes involving antibaryons, with the overall effect that no baryon asymmetry is generated.
- (3) Out of equilibrium dynamics: equilibrium distribution functions  $n_{\text{eq}}$  are determined solely by the particle energy  $E$ , chemical potential  $\mu$ , and by its mass which, because of the CPT theorem, is the same for particles and antiparticles. When charges (such as  $B$ ) are not conserved, the corresponding chemical potentials vanish, and thus  $n_B = \int (d^3p / (2\pi^3)) n_{\text{eq}} = n_{\bar{B}}$ .

Although these ingredients are all present in the Standard Model (SM), so far all attempts to reproduce quantitatively the observed baryon asymmetry have failed.

- (1) In the SM  $B$  is violated via the triangle anomaly. Although at zero temperature  $B$  violating processes are too suppressed to have any observable effect [14], at high temperatures they occur with unsuppressed rates [15]. The first condition is then quantitatively realized in the early Universe.
- (2) SM weak interactions violate  $C$  maximally. However, the amount of  $CP$  violation from the Kobayashi-Maskawa complex phase [16], as quantified by means of the Jarlskog invariant [17], is only of order  $10^{-20}$ , and this renders impossible generating  $Y_{\Delta B} \sim 10^{-10}$  [18–20].

- (3) Departures from thermal equilibrium occur in the SM at the electroweak phase transition (EWPT) [21, 22]. However, the experimental lower bound on the Higgs mass implies that this transition is not sufficiently first order as required for successful baryogenesis [23].

This shows that baryogenesis requires new physics that extends the SM in at least two ways. It must introduce new sources of CP violation and it must either provide a departure from thermal equilibrium in addition to the EWPT or modify the EWPT itself. In the past thirty years or so, several new physics mechanisms for baryogenesis have been put forth. Some among the most studied are *GUT baryogenesis* [24–33], *electroweak baryogenesis* [21, 34, 35], the *affleck-Dine mechanism* [36, 37], and *spontaneous Baryogenesis* [38, 39]. However, soon after the discovery of neutrino masses, because of its connections with the seesaw model [40–44] and its deep interrelations with neutrino physics in general, the mechanism of baryogenesis via *Leptogenesis* acquired a continuously increasing popularity. Leptogenesis was first proposed by Fukugita and Yanagida in [45]. Its simplest and theoretically best motivated realization is precisely within the seesaw mechanism. To implement the seesaw, new Majorana  $SU(2)_L$  singlet neutrinos with a large mass scale  $M$  are added to the SM particle spectrum. The complex Yukawa couplings of these new particles provide new sources of CP violation, departure from thermal equilibrium can occur if their lifetime is not much shorter than the age of the Universe when  $T \sim M$ , and their Majorana masses imply that lepton number is not conserved. A lepton asymmetry can then be generated dynamically, and SM sphalerons will partially convert it into a baryon asymmetry [46]. A particularly interesting possibility is “thermal leptogenesis” where the heavy Majorana neutrinos are produced by scatterings in the thermal bath starting from a vanishing initial abundance, so that their number density can be calculated solely in terms of the seesaw parameters and of the reheat temperature of the Universe.

This paper is organized as follows. In Section 2 the basis of leptogenesis is reviewed in the simple scenario of the one-flavour regime, while the role of flavour effects is described in Section 3. Theoretical improvements of the basic pictures, like spectator effects, scatterings and CP violation in scatterings, thermal corrections, the possible role of the heavier singlet neutrinos, and quantum effects, are reviewed in Section 4. Leptogenesis in the supersymmetric seesaw is reviewed in Section 5, while in Section 6 we mention possible leptogenesis realizations that go beyond the type-I seesaw. Finally, in Section 7 we draw the conclusions.

## 2. $N_1$ Leptogenesis in the Single Flavour Regime

The aim of this section is to give a pedagogical introduction to leptogenesis [45] and establish the notations. We will consider the classic example of leptogenesis from the lightest right-handed (RH) neutrino  $N_1$  (the so-called  $N_1$  leptogenesis) in the type-I seesaw model [40, 41, 43, 44] in the single flavour regime. First in Section 2.1 we introduce the type-I seesaw Lagrangian and the relevant parameters. In Section 2.2, we will review the CP violation in RH neutrino decays induced at 1-loop level. Then in Section 2.3, we will write down the classical Boltzmann equations taking into account only decays and inverse decays of  $N_1$  and give a simple but rather accurate analytical estimate of the solution. In Section 2.4 we will relate the lepton asymmetry generated to the baryon asymmetry of the Universe. Finally in Section 2.5, we will discuss the lower bound on  $N_1$  mass and the upper bound on light neutrino mass scale from successful leptogenesis.



### 2.1. Type-I Seesaw, Neutrino Masses, and Leptogenesis

With  $m$  ( $m \geq 2$ ) (neutrino oscillation data and leptogenesis both require  $m \geq 2$ .) singlet RH neutrinos  $N_{R_i}$  ( $i = 1, m$ ), we can add the following Standard Model (SM) gauge invariant terms to the SM Lagrangian:

$$\mathcal{L}_I = \mathcal{L}_{\text{SM}} + i\overline{N_{R_i}}\not{\partial}N_{R_i} - \left( \frac{1}{2}M_i\overline{N_{R_i}^c}N_{R_i} + \epsilon_{ab}Y_{ai}\overline{N_{R_i}}\ell_\alpha^a H^b + \text{h.c.} \right), \quad (2.1)$$

where  $M_i$  are the Majorana masses of the RH neutrinos,  $\ell_\alpha = (\nu_{\alpha L}, \alpha_L^-)$  with  $\alpha = e, \mu, \tau$  and  $H = (H^+, H^0)$  are, respectively, the left-handed (LH) lepton and Higgs  $\text{SU}(2)_L$  doublets and  $\epsilon_{ab} = -\epsilon_{ba}$  with  $\epsilon_{12} = 1$ . Without loss of generality, we have chosen the basis where the Majorana mass term is diagonal. The physical mass eigenstates of the RH neutrinos are the Majorana neutrinos  $N_i = N_{R_i} + N_{R_i}^c$ . Since  $N_i$  are gauge singlets, the scale of  $M_i$  is naturally much larger than the electroweak (EW) scale  $M_i \gg \langle \Phi \rangle \equiv v = 174 \text{ GeV}$ . Hence after EW symmetry breaking, the light neutrino mass matrix is given by the famous seesaw relation [40, 41, 43, 44]:

$$m_\nu \simeq -v^2 Y \frac{1}{M} Y^T. \quad (2.2)$$

Assuming  $Y \sim \mathcal{O}(1)$  and  $m_\nu \simeq \sqrt{\Delta m_{\text{atm}}^2} \simeq 0.05 \text{ eV}$ , we have  $M \sim 10^{15} \text{ GeV}$  not far below the GUT scale.

Besides giving a natural explanation of the light neutrino masses, there is another bonus: the *three* Sakharov's conditions [13] for leptogenesis are implicit in (2.1) with the *lepton number violation* provided by  $M_i$ , the *CP violation* from the complexity of  $Y_{i\alpha}$ , and the *departure from thermal equilibrium condition* given by an additional requirement that  $N_i$  decay rate  $\Gamma_{N_i}$  is not very fast compared to the Hubble expansion rate of the Universe  $H(T)$  at temperature  $T = M_i$  with

$$\Gamma_{N_i} = \frac{(Y^\dagger Y)_{ii} M_i}{8\pi}, \quad H(T) = \frac{2}{3} \sqrt{\frac{g_* \pi^3}{5}} \frac{T^2}{M_{\text{Pl}}}, \quad (2.3)$$

where  $M_{\text{Pl}} = 1.22 \times 10^{19} \text{ GeV}$  is the Planck mass,  $g_*$  ( $=106.75$  for the SM excluding RH neutrinos) is the total number of relativistic degrees of freedom contributing to the energy density of the Universe.

To quantify the departure from thermal equilibrium, we define the *decay parameter* as follows:

$$K_i \equiv \frac{\Gamma_{N_i}}{H(M_i)} = \frac{\tilde{m}_i}{m_*}, \quad (2.4)$$

where  $\tilde{m}_i$  is the *effective neutrino mass* defined as [47]

$$\tilde{m}_i \equiv \frac{(Y^\dagger Y)_{ii} v^2}{M_i}, \quad (2.5)$$

with  $m_* \equiv (16\pi^2 v^2 / 3M_{\text{pl}}) \sqrt{g_* \pi / 5} \simeq 1 \times 10^{-3} \text{ eV}$ . The regimes where  $K_i \ll 1$ ,  $K_i \approx 1$  and  $K_i \gg 1$  are, respectively, known as weak, intermediate, and strong washout regimes.

## 2.2. CP Asymmetry

The CP asymmetry in the decays of RH neutrinos  $N_i$  can be defined as

$$\epsilon_{i\alpha} = \frac{\gamma(N_i \rightarrow \ell_\alpha H) - \gamma(N_i \rightarrow \bar{\ell}_\alpha H^*)}{\sum_\alpha \gamma(N_i \rightarrow \ell_\alpha H) + \gamma(N_i \rightarrow \bar{\ell}_\alpha H^*)} \equiv \frac{\Delta\gamma_{N_i}^\alpha}{\gamma_{N_i}}, \quad (2.6)$$

where  $\gamma(i \rightarrow f)$  is the thermally averaged decay rate defined as (here the Pauli-blocking and Bose-enhancement statistical factors have been ignored and we also assume Maxwell-Boltzmann distribution for the particle  $i$ , that is,  $f_i = e^{-E_i/T}$ ; see [48, 49] for detailed studies of their effects)

$$\gamma(i \rightarrow f) \equiv \int \frac{d^3 p_i}{(2\pi)^3 2E_i} \frac{d^3 p_f}{(2\pi)^3 2E_f} (2\pi)^4 \delta^{(4)}(p_i - p_f) |\mathcal{A}(i \rightarrow f)|^2 e^{-E_i/T}, \quad (2.7)$$

where  $\mathcal{A}(i \rightarrow f)$  is the decay amplitude. Ignoring all thermal effects [48, 49], (2.6) simplifies to

$$\epsilon_{i\alpha} = \frac{|\mathcal{A}_0(N_i \rightarrow \ell_\alpha H)|^2 - |\mathcal{A}_0(N_i \rightarrow \bar{\ell}_\alpha H^*)|^2}{\sum_\alpha |\mathcal{A}_0(N_i \rightarrow \ell_\alpha H)|^2 + |\mathcal{A}_0(N_i \rightarrow \bar{\ell}_\alpha H^*)|^2}, \quad (2.8)$$

where  $\mathcal{A}_0(i \rightarrow f)$  denotes the decay amplitude at zero temperature. Equation (2.8) vanishes at tree level but is induced at 1-loop level through the interference between tree and 1-loop diagrams shown in Figure 1. There are two types of contributions from the 1-loop diagrams: the self-energy or wave diagram (middle) [50] and the vertex diagram (right) [45]. At leading order, we obtain the CP asymmetry [51]:

$$\begin{aligned} \epsilon_{i\alpha} = & \frac{1}{8\pi} \frac{1}{(Y^\dagger Y)_{ii}} \sum_{j \neq i} \text{Im} \left[ (Y^\dagger Y)_{ji} Y_{ai} Y_{aj}^* \right] g \left( \frac{M_j^2}{M_i^2} \right) \\ & + \frac{1}{8\pi} \frac{1}{(Y^\dagger Y)_{ii}} \sum_{j \neq i} \text{Im} \left[ (Y^\dagger Y)_{ij} Y_{ai} Y_{aj}^* \right] \frac{M_i^2}{M_i^2 - M_j^2}, \end{aligned} \quad (2.9)$$

where the loop function is

$$g(x) = \sqrt{x} \left[ \frac{1}{1-x} + 1 - (1+x) \ln \left( \frac{1+x}{x} \right) \right]. \quad (2.10)$$

The first term in (2.9) comes from  $L$ -violating wave and vertex diagrams, while the second term is from the  $L$ -conserving wave diagram. The terms of the form  $(M_i^2 - M_j^2)^{-1}$  in (2.9)

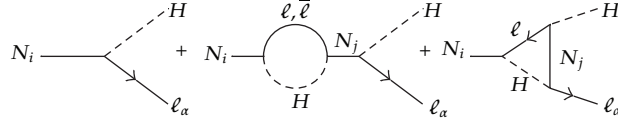


**Figure 1:** The CP asymmetry in type-I seesaw leptogenesis results from the interference between tree and 1-loop wave and vertex diagrams. For the 1-loop wave diagram, there is an additional contribution from  $L$ -conserving diagram to the CP asymmetry which vanishes when summing over lepton flavours.

are from the wave diagram contributions which can resonantly enhance the CP asymmetry if  $M_i \approx M_j$  (resonant leptogenesis scenario, see Section 6.1). Notice that the resonant term becomes singular in the degenerate limit  $M_i = M_j$ . This singularity can be regulated by using, e.g., an effective field-theoretical approach based on resummation [52]. Let us also note that at least two RH neutrinos are needed otherwise the CP asymmetry vanishes because the Yukawa couplings combination becomes real.

In the one flavour regime, we sum over the flavour index  $\alpha$  in (2.9) and obtain

$$\epsilon_i \equiv \sum_{\alpha} \epsilon_{i\alpha} = \frac{1}{8\pi} \frac{1}{(Y^\dagger Y)_{ii}} \sum_{j \neq i} \text{Im} \left[ (Y^\dagger Y)_{ji}^2 \right] g \left( \frac{M_j^2}{M_i^2} \right), \quad (2.11)$$

where the second term in (2.9) vanishes because the combination of the Yukawa couplings is real.

### 2.3. Classical Boltzmann Equations

We work in the one-flavour regime and consider only the decays and inverse decays of  $N_1$ . If leptogenesis occurs at  $T \gtrsim 10^{12}$  GeV, then the charged lepton Yukawa interactions are out of equilibrium, and this defines the one-flavour regime. The assumption that only the dynamics of  $N_1$  is relevant can be realized if, for example, the reheating temperature after inflation is  $T_{\text{RH}} \ll M_{2,3}$  such that  $N_{2,3}$  are not produced. In order to scale out the effect of the expansion of the Universe, we will introduce the *abundances*, that is, the ratios of the particle densities  $n_i = \int d^3p f_i$  to the entropy density  $s = (2\pi^2/45)g_*T^3$ :

$$Y_i \equiv \frac{n_i}{s}. \quad (2.12)$$

The evolution of the  $N_1$  density and the lepton asymmetry  $Y_{\Delta L} = 2Y_{\Delta \ell} \equiv 2(Y_\ell - Y_{\bar{\ell}})$  (the factor of 2 comes from the  $\text{SU}(2)_L$  degrees of freedoms) can be described by the following classical Boltzmann equations (BE) [53]:

$$\frac{dY_{N_1}}{dz} = -D_1(Y_{N_1} - Y_{N_1}^{\text{eq}}), \quad (2.13)$$

$$\frac{dY_{\Delta L}}{dz} = \epsilon_1 D_1(Y_{N_1} - Y_{N_1}^{\text{eq}}) - W_1 Y_{\Delta L}, \quad (2.14)$$

where  $z \equiv M_1/T$  and the decay and washout terms are, respectively, given by

$$D_1(z) = \frac{Y_{N_1} z}{sH(M_1)} = K_1 z \frac{\mathcal{K}_1(z)}{\mathcal{K}_2(z)}, \quad W_1(z) = \frac{1}{2} D_1(z) \frac{Y_{N_1}^{\text{eq}}(z)}{Y_\ell^{\text{eq}}}, \quad (2.15)$$

with  $\mathcal{K}_n$  the  $n$ th order modified Bessel function of second kind.  $Y_{N_1}^{\text{eq}}$  and  $Y_\ell^{\text{eq}}$  read (to write down a simple analytic expression for the equilibrium density of  $N_1$ , we assume Maxwell-Boltzmann distribution. However, following [54], the normalization factor  $Y_\ell^{\text{eq}}$  is obtained from a Fermi-Dirac distribution)

$$Y_N^{\text{eq}}(z) = \frac{45}{2\pi^4 g_*} z^2 \mathcal{K}_2(z), \quad Y_\ell^{\text{eq}} = \frac{15}{4\pi^2 g_*}. \quad (2.16)$$

From (2.13) and (2.14), the solution for  $Y_{\Delta L}$  can be written down as follows:

$$Y_{\Delta L}(z) = Y_{\Delta L}(z_i) e^{-\int_{z_i}^z dz' W_1(z')} - \int_{z_i}^z dz' \epsilon_1(z') \frac{dY_{N_1}}{dz'} e^{-\int_{z'}^z dz'' W_1(z'')}, \quad (2.17)$$

where  $z_i$  is some initial temperature when  $N_1$  leptogenesis begins, and we have assumed that any preexisting lepton asymmetry vanishes  $Y_{\Delta L}^0(z_i) = 0$ . Notice that ignoring thermal effects, the CP asymmetry is independent of the temperature  $\epsilon_1(z) = \epsilon_1$  (c.f. (2.11)).

### 2.3.1. Weak Washout Regime

In the weak washout regime ( $K_1 \ll 1$ ), the initial condition on the  $N_1$  density  $Y_{N_1}(z_i)$  is important. If we assume thermal initial abundance of  $N_1$ , that is,  $Y_{N_1}(z_i) = Y_{N_1}^{\text{eq}}(0)$ , we can ignore the washout when  $N_1$  starts decaying at  $z \gg 1$  and we have

$$Y_{\Delta L}^t(\infty) \simeq -\epsilon_1 \int_0^\infty dz' \frac{dY_{N_1}^{\text{eq}}}{dz'} = \epsilon_1 Y_{N_1}^{\text{eq}}(0). \quad (2.18)$$

On the other hand, if we have zero initial  $N_1$  abundance, that is,  $Y_{N_1}(z_i) = 0$ , we have to consider the opposite sign contributions to lepton asymmetry from the inverse decays when  $N_1$  is being populated ( $Y_{N_1} < Y_{N_1}^{\text{eq}}$ ) and from the period when  $N_1$  starts decaying ( $Y_{N_1} > Y_{N_1}^{\text{eq}}$ ). Taking this into account the term which survives the partial cancellations is given by [55] (this differs from the efficiency in [55] by the factor  $12/\pi^2$ , which is due to the different normalization  $Y_\ell^{\text{eq}}$  (2.16))

$$Y_{\Delta L}^0(\infty) \simeq \frac{27}{16} \epsilon_1 K_1^2 Y_{N_1}^{\text{eq}}(0). \quad (2.19)$$

### 2.3.2. Strong Washout Regime

In the strong washout regime ( $K_1 \gg 1$ ) any lepton asymmetry generated during the  $N_1$  creation phase is efficiently washed out. Here we adopt the *strong washout balance*



*approximation* [56] which states that in the strong washout regime, the lepton asymmetry at each instant takes the value that enforces a balance between the production and the destruction rates of the asymmetry. Equating the decay and washout terms in (2.14), we have

$$Y_{\Delta L}(z) \approx -\frac{1}{W(z)} \epsilon_1 \frac{dY_{N_1}}{dz} \simeq -\frac{1}{W(z)} \epsilon_1 \frac{dY_{N_1}^{\text{eq}}}{dz} = \frac{2}{zK_1} \epsilon_1 Y_{\ell}^{\text{eq}}, \quad (2.20)$$

where in the second approximation, we assume  $Y_{N_1} \simeq Y_{N_1}^{\text{eq}}$ . The approximation no longer holds when  $Y_{\Delta L}$  freezes, and this happens when the washout decouples at  $z_f$ , that is,  $W(z_f) < 1$ . Hence, the final lepton asymmetry is given by (compare this to a more precise analytical approximation in [55])

$$Y_{\Delta L}(\infty) = \frac{2}{z_f K_1} \epsilon_1 Y_{\ell}^{\text{eq}} = \frac{\pi^2}{6z_f K_1} \epsilon_1 Y_{N_1}^{\text{eq}}(0). \quad (2.21)$$

The freeze out temperature  $z_f$  depends mildly on  $K_1$ . For  $K_1 = 10$ –100 we have, for example,  $z_f = 7$ –10. We also see that independently of initial conditions, in the strong regime  $Y_{\Delta L}(\infty)$  goes as  $K_1^{-1}$ .

## 2.4. Baryon Asymmetry from EW Sphaleron

The final lepton asymmetry  $Y_{\Delta L}(\infty)$  can be conveniently parametrized as follows:

$$Y_{\Delta L}(\infty) = \epsilon_1 \eta_1 Y_{N_1}^{\text{eq}}(0), \quad (2.22)$$

where  $\eta_1$  is known as the *efficiency factor*. In the weak washout regime ( $K_1 \ll 1$ ) from (2.18) we have  $\eta_1 = 1$  ( $= (27/16)K_1^2 < 1$ ) for thermal (zero) initial  $N_1$  abundance. In the strong washout regime ( $K_1 \gg 1$ ), from (2.21), we have  $\eta_1 = (\pi^2/6z_f K_1) < 1$ .

If leptogenesis ends before EW sphaleron processes become active ( $T \gtrsim 10^{12}$  GeV), the  $B - L$  asymmetry  $Y_{\Delta B-L}$  is simply given by

$$Y_{\Delta B-L} = -Y_{\Delta L}. \quad (2.23)$$

At the later stage, the  $B - L$  asymmetry is partially transferred to a  $B$  asymmetry by the EW sphaleron processes through the relation [57]

$$Y_{\Delta B}(\infty) = \frac{28}{79} Y_{\Delta B-L}(\infty), \quad (2.24)$$

that holds if sphalerons decouple before EWPT. This relation will change if the EW sphaleron processes decouple after the EWPT [57, 58] or if threshold effects for heavy particles like the top quark and Higgs are taken into account [58, 59].

### 2.5. Davidson-Ibarra Bound

Assuming a hierarchical spectrum of the RH neutrinos ( $M_1 \ll M_2, M_3$ ), and that the dominant lepton asymmetry is from the  $N_1$  decays, from (2.11) the CP asymmetry from  $N_1$  decays can be written as

$$\epsilon_1 = -\frac{3}{16\pi} \frac{1}{(Y^\dagger Y)_{11}} \sum_{j \neq 1} \text{Im} \left[ \left( Y^\dagger Y \right)_{j1}^2 \right] \frac{M_1}{M_j}. \quad (2.25)$$

Assuming three generations of RH neutrinos ( $n = 3$ ) and using the Casas-Ibarra parametrization [60] for the Yukawa couplings

$$Y_{ai} = \frac{1}{v} \left( \sqrt{D_{m_N}} R \sqrt{D_{m_\nu}} U_{\nu}^\dagger \right)_{ai}, \quad (2.26)$$

where  $D_{m_N} = \text{diag}(M_1, M_2, M_3)$ ,  $D_{m_\nu} = \text{diag}(m_{\nu_1}, m_{\nu_2}, m_{\nu_3})$  and  $R$  any complex orthogonal matrix satisfying  $R^T R = R R^T = 1$ , (2.25) becomes

$$\epsilon_1 = -\frac{3}{16\pi} \frac{M_1}{v^2} \frac{\sum_i m_{\nu_i} \text{Im}(R_{1i}^2)}{\sum_i m_{\nu_i} |R_{1i}|^2}. \quad (2.27)$$

Using the orthogonality condition  $\sum_i R_{1i}^2 = 1$ , we then obtain the Davidson-Ibarra (DI) bound [61]

$$|\epsilon_1| \leq \epsilon^{\text{DI}} = \frac{3}{16\pi} \frac{M_1}{v^2} (m_{\nu_3} - m_{\nu_1}) = \frac{3}{16\pi} \frac{M_1}{v^2} \frac{\Delta m_{\text{atm}}^2}{m_{\nu_1} + m_{\nu_3}}, \quad (2.28)$$

where  $m_{\nu_3}$  ( $m_{\nu_1}$ ) is the heaviest (lightest) light neutrino mass. Applying the DI bound on (2.22)–(2.24), and requiring that  $Y_{\Delta B}(\infty) \geq Y_B^{\text{CMB}} \simeq 10^{-10}$ , we obtain

$$M_1 \left( \frac{0.1 \text{ eV}}{m_{\nu_1} + m_{\nu_3}} \right) \eta_1^{\text{max}}(M_1) \gtrsim 10^9 \text{ GeV}, \quad (2.29)$$

where the  $\eta_1^{\text{max}}(M_1)$  is the efficiency factor maximized with respect to  $K_1$  (2.4) for a particular value of  $M_1$ . This allows us to make a plot of region which satisfies (2.29) on the  $(M_1, m_{\nu_1})$  plane and hence obtain bounds on  $M_1$  and  $m_{\nu_1}$ . Many careful numerical studies have been carried out, and it was found that successful leptogenesis with a hierarchical spectrum of the RH neutrinos requires  $M_1 \gtrsim 10^9 \text{ GeV}$  [61–63] and  $m_{\nu_1} \lesssim 0.1 \text{ eV}$  [55, 64–66]. This bound implies that the RH neutrinos must be produced at temperatures  $T \gtrsim 10^9 \text{ GeV}$  which in turn implies the reheating temperature after inflation has to be  $T_{\text{RH}} \gtrsim 10^9 \text{ GeV}$  in order to have sufficient RH neutrinos in the thermal bath. To conclude this section, let us note that the DI bound (2.28) holds if and only if all the following conditions apply.

- (1)  $N_1$  dominates the contribution to leptogenesis.
- (2) The mass spectrum of RH neutrinos is hierarchical  $M_1 \ll M_2, M_3$ .
- (3) Leptogenesis occurs in the unflavoured regime  $T \gtrsim 10^{12} \text{ GeV}$ .

As we will see in the following sections, violation of one or more of the previous conditions allows us to lower somewhat the scale of leptogenesis.

### 3. Lepton Flavour Effects

#### 3.1. When Are Lepton Flavour Effects Relevant?

The first leptogenesis calculations were performed in the single lepton flavour regime. In short, this amounts to assuming that the leptons and antileptons which couple to the lightest RH neutrino  $N_1$  maintain their coherence as flavour superpositions throughout the leptogenesis era, that is  $\ell_1 = \sum_\alpha c_{\alpha 1} \ell_\alpha$  and  $\bar{\ell}'_1 = \sum_\alpha c'_{\alpha 1} \bar{\ell}_\alpha$ . Note that at the tree level the coefficients  $c$  and  $c^*$  are simply the Yukawa couplings:  $c_{\alpha 1} = Y_{\alpha 1}$  and  $c'_{\alpha 1} = Y_{\alpha 1}^*$ . However it should be kept in mind that since CP is violated by loops, beyond the tree level approximation the antilepton state  $\bar{\ell}'_1$  is not the CP conjugate of the  $\ell_1$ , that is,  $c'_{\alpha 1} \neq c_{\alpha 1}$ .

The single flavour regime is realized only at very high temperatures ( $T \gtrsim 10^{12}$  GeV) when both  $\ell_1$  and  $\bar{\ell}'_1$  remain coherent flavour superpositions and thus are the correct states to describe the dynamics of leptogenesis. However, at lower temperatures scatterings induced by the charged lepton Yukawa couplings occur at a sufficiently fast pace to distinguish the different lepton flavours,  $\ell_1$  and  $\bar{\ell}'_1$  decohere in their flavour components, and the dynamics of leptogenesis must then be described in terms of the flavour eigenstates  $\ell_\alpha$ . Of course, there is great interest to extend the validity of quantitative leptogenesis studies also at lower scale  $T \lesssim 10^{12}$  GeV, and this requires accounting for flavour effects. The role of lepton flavour in leptogenesis was first discussed in [67]; however the authors did not highlight in what the results were significantly different from the single flavour approximation. Therefore, until the importance of flavour effects was fully clarified in [68–70], they had been included in leptogenesis studies only in a few cases [71–75]. Nowadays lepton flavour effects have been investigated in full detail [76–89] and are a mandatory ingredient of any reliable analysis of leptogenesis.

The specific temperature when leptogenesis becomes sensitive to lepton flavour dynamics can be estimated by requiring that the rates of processes  $\Gamma_\alpha$  ( $\alpha = e, \mu, \tau$ ) that are induced by the charged lepton Yukawa couplings  $h_\alpha$  become faster than the Universe expansion rate  $H(T)$ . An approximate relation gives [90, 91]

$$\Gamma_\alpha(T) \simeq 10^{-2} h_\alpha^2 T, \quad (3.1)$$

which implies that (in supersymmetric case, since  $h_\alpha = m_\alpha / (v_u \cos \beta)$ , we have  $T \lesssim T_\alpha (1 + \tan^2 \beta)$ )

$$\Gamma_\alpha(T) > H(T) \quad \text{when } T \lesssim T_\alpha, \quad (3.2)$$

where  $T_e \simeq 4 \times 10^4$  GeV,  $T_\mu \simeq 2 \times 10^9$  GeV, and  $T_\tau \simeq 5 \times 10^{11}$  GeV. Notice that to fully distinguish the three flavours it is sufficient that the  $\tau$  and  $\mu$  Yukawa reactions attain thermal equilibrium. It has been pointed out that besides being faster than the expansion of the Universe, the charged lepton Yukawa interactions should also be faster than the  $N_1$  interactions [69, 83, 84]. In general whenever  $\Gamma_\tau(M_1) > H(M_1)$  we also have  $\Gamma_\tau(M_1) > \Gamma_{N_1}(M_1)$ . However, there

exists parameter space where  $\Gamma_\tau(M_1) > H(M_1)$  but  $\Gamma_\tau(M_1) < \Gamma_{N_1}(M_1)$ . This scenario was studied in [83].

### 3.2. The Effects on CP Asymmetry and Washout

The CP violation in  $N_i$  decays can manifest itself in two ways [69]

- (i) The leptons and antileptons are produced at different rates:

$$\gamma_i \neq \bar{\gamma}_i, \quad (3.3)$$

where  $\gamma_i \equiv \gamma(N_i \rightarrow \ell_i H)$  and  $\bar{\gamma}_i \equiv \gamma(N_i \rightarrow \bar{\ell}'_i H^*)$ .

- (ii) The leptons and antileptons produced are not CP conjugate states:

$$\text{CP}(\bar{\ell}'_i) = \ell'_i \neq \ell_i, \quad (3.4)$$

that is, due to loops effects they are slightly misaligned in flavour space.

We can rewrite the CP asymmetry for  $N_i$  decays from (2.6) as follows:

$$\epsilon_{i\alpha} = \frac{P_{i\alpha}\gamma_i - \bar{P}_{i\alpha}\bar{\gamma}_i}{\gamma_i + \bar{\gamma}_i} = \frac{P_{i\alpha} + \bar{P}_{i\alpha}}{2} \epsilon_i + \frac{P_{i\alpha} - \bar{P}_{i\alpha}}{2} \simeq P_{i\alpha}^0 \epsilon_i + \frac{\Delta P_{i\alpha}}{2}, \quad (3.5)$$

where terms of order  $\mathcal{O}(\epsilon_i \Delta P_{i\alpha})$  and higher have been neglected.  $P_{i\alpha}$  is the projector from state  $\ell_i$  into flavour state  $\ell_\alpha$  and  $\Delta P_{i\alpha} = P_{i\alpha} - \bar{P}_{i\alpha}$ . At tree level, clearly,  $P_{i\alpha} = \bar{P}_{i\alpha} \equiv P_{i\alpha}^0$  where the tree level flavour projector is given by

$$P_{i\alpha}^0 = \frac{Y_{ai} Y_{ai}^*}{(Y^\dagger Y)_{ii}}. \quad (3.6)$$

From (3.5), we can identify the two types of CP violation, the first term being of type (i) equation (3.3) while the second being of type (ii) equation (3.4). Since  $\sum_\alpha P_{i\alpha} = \sum_\alpha \bar{P}_{i\alpha} = 1$ , when summing over flavour indices  $\alpha$ , the second term vanishes  $\sum_\alpha \Delta P_{i\alpha} = 0$ . Note that the lepton-flavour-violating but  $L$ -conserving terms in the second line of (2.9) are part of type (ii). In fact, they come from  $d = 6$   $L$ -conserving operators which have nothing to do with the unique  $d = 5$   $L$ -violating operator (the Weinberg operator [92]) responsible for neutrino masses. However, in some cases they can still dominate the CP asymmetries but, as we will see in Section 3.4, lepton flavour equilibration effects [93] then impose important constraints on their overall effects. Note also that due to flavour misalignment, the CP asymmetry in a particular flavour direction  $\epsilon_{i\alpha}$  can be much larger and even of opposite sign from the total CP asymmetry  $\epsilon_i$ . In fact the relevance of CP violation of type (ii) in the flavour regimes is what allows to evade the DI bound (2.28). As regards the washout of the lepton asymmetry of flavour  $\alpha$ , it is proportional to

$$W_{i\alpha} \propto P_{i\alpha}\gamma_i + \bar{P}_{i\alpha}\bar{\gamma}_i \simeq P_{i\alpha}^0 W_i, \quad (3.7)$$



which results in a reduction of washout by a factor of  $P_{i\alpha}^0 \leq 1$  compared to unflavoured case. As we will see next, the new CP-violating sources from flavour effects and the reduction in the washout could result in great enhancement of the final lepton asymmetry, and, as was first pointed out in [69], leptogenesis with a vanishing total CP asymmetry  $\epsilon_i = 0$  also becomes possible.

### 3.3. Classical Flavoured Boltzmann Equations

Here again we only consider leptogenesis from the decays and inverse decays of  $N_1$ . In this approximation, the BE for  $Y_{N_1}$  is still given by (2.13) while the BE for  $Y_{\Delta L_\alpha}$  the lepton asymmetry in the flavour  $\alpha$  is given by (to study the transition between different flavour regimes (from one to two or from two to three flavours), a density matrix formalism has to be used [68, 84, 94]).

$$\frac{dY_{\Delta L_\alpha}}{dz} = \epsilon_{1\alpha} D_1 \left( Y_{N_1} - Y_{N_1}^{\text{eq}} \right) - P_{1\alpha}^0 W_1 Y_{\Delta L_\alpha}. \quad (3.8)$$

Notice that as long as  $L$  violation from sphalerons is neglected (see Section 4) the BEs for  $Y_{\Delta L_\alpha}$  are independent of each other, and hence the solutions for the weak and strong washout regimes are given, respectively, by (2.19) and (2.21), after replacing  $\epsilon_1 \rightarrow \epsilon_{1\alpha}$  and  $K_1 \rightarrow K_{1\alpha} \equiv P_{1\alpha}^0 K_1$ .

As an example let us assume that leptogenesis occurs around  $T \sim 10^{10}$  GeV, that is, in the two-flavour regime. Due to the fast  $\tau$  Yukawa interactions  $\ell_1(\ell'_1)$  gets projected onto  $\ell_\tau(\ell'_\tau)$  and a coherent mixture of  $e + \mu$  eigenstate  $\ell_{e+\mu}(\ell'_{e+\mu})$ . For illustrative purpose, here we consider a scenario in which lepton flavour effects are most prominent. We take both  $K_{1\tau}, K_{1e+\mu} \gg 1$ , so that both  $Y_{\Delta L_\tau}$  and  $Y_{\Delta L_{e+\mu}}$  are in the strong regime. From (2.21) we can write down the solution:

$$\begin{aligned} Y_{\Delta L}(\infty) &= Y_{\Delta L_\tau}(\infty) + Y_{\Delta L_{e+\mu}}(\infty) \\ &= \frac{\pi^2}{6z_f K_1} Y_{N_1}^{\text{eq}}(0) \left( \frac{\epsilon_{1\tau}}{P_{1\tau}^0} + \frac{\epsilon_{1e+\mu}}{P_{1e+\mu}^0} \right) \\ &\simeq \frac{\pi^2}{3z_f K_1} \epsilon_1 Y_{N_1}^{\text{eq}}(0) + \frac{\pi^2}{12z_f K_1} Y_{N_1}^{\text{eq}}(0) \left( \frac{\Delta P_{1\tau}}{P_{1\tau}^0} + \frac{\Delta P_{1e+\mu}}{P_{1e+\mu}^0} \right), \end{aligned} \quad (3.9)$$

where in the last line we have used (3.5). If  $P_{1\tau}^0 \simeq P_{1e+\mu}^0$ , then since  $\Delta P_{1\tau} + \Delta P_{1e+\mu} = 0$ , the second term approximately cancels, and (3.9) reduces to

$$Y_{\Delta L}(\infty) \simeq \frac{\pi^2}{3z_f K_1} \epsilon_1 Y_{N_1}^{\text{eq}}(0). \quad (3.10)$$

We see that the final asymmetry is enhanced by a factor of 2 compared to the unflavoured case. If there exists some hierarchy between the flavour projectors, then the second term in (3.9) plays an important role and can further enhance the asymmetry. For example, we can

have  $P_{1\tau}^0 > P_{1e+\mu}^0$  while  $\Delta P_{1\tau} \ll \Delta P_{1e+\mu}$ . In this case, the second term can dominate over the first term. Finally from (3.9) we also notice that leptogenesis with  $\epsilon_1 = 0$ , the so-called *purely flavoured leptogenesis* (PFL) (this can also refer to the case where the total CP asymmetry is negligible  $\epsilon_1 \approx 0$ ), can indeed proceed [69, 95–98]. In this scenario some symmetry has to be imposed to realize the condition  $\epsilon_1 = 0$ , as, for example, an approximate global lepton number  $U(1)_L$ . In the limit of exact  $U(1)_L$  the active neutrinos will be exactly massless. Instead of the seesaw mechanism, the small neutrino masses are explained by  $U(1)_L$  which is slightly broken by a small parameter  $\mu$  (the “inverse seesaw”) [99] which is technically natural since the Lagrangian exhibits an enhanced symmetry when  $\mu \rightarrow 0$  [100]. In the next section, we will discuss another aspect of flavour effects which are in particular crucial for PFL.

### 3.4. Lepton Flavour Equilibration

Another important effect is lepton flavour equilibration (LFE) [93]. LFE processes violate lepton flavour but conserve total lepton number, for example,  $\ell_\alpha H \rightarrow \ell_\beta H$ , and can proceed, for example, via off-shell exchange of  $N_{2,3}$ . In thermal equilibrium, LFE processes can quickly equilibrate the asymmetries generated in different flavours. In practice this would be equivalent to a situation where all the flavour projector equations (3.6) are equal, in which case the flavoured BE equation (3.8) can be summed up into a single BE:

$$\frac{dY_{\Delta L}}{dz} = \epsilon_1 D_1 (Y_{N_1} - Y_{N_1}^{\text{eq}}) - P_{1\alpha}^0 W_1 Y_{\Delta L}, \quad (3.11)$$

where  $P_{1\alpha}^0 = 1/2$  ( $1/3$ ) in the two- (three-) flavour regime. In this case the BE is just like the unflavoured case but with a reduced washout which, in the strong washout regime, would result in enhancement of a factor of 2 (3) in the two- (three-) flavour regime (c.f. (3.10)). Clearly, LFE can make PFL with  $\epsilon_1 = 0$  impotent [56, 93]. Since LFE  $N_{2,3}$  processes scale as  $T^3$  while the Universe expansion scales as  $T^2$ , in spite of the fact that PFL evades the DI bound, they eventually prevent the possibility of lowering too much the leptogenesis scale. A generic study in PFL scenario taking into account LFE effects concluded that successful leptogenesis still requires  $M_1 \gtrsim 10^8$  GeV [97]. A more accurate study in the same direction recently carried out in [98] showed that in fact the leptogenesis scale can be lowered down to  $M_1 \sim 10^6$  GeV.

## 4. Beyond the Basic Boltzmann Equations

Within factors of a few, the amount of baryon asymmetry that is generated via leptogenesis in  $N_1$  decays is determined essentially by the size of the (flavoured) CP asymmetries and by the rates of the (flavoured) washout reactions. However, to obtain more precise results (say, within an  $\mathcal{O}(1)$  uncertainty) several additional effects must be taken into account, and the formalism must be extended well beyond the basic BE discussed in the previous sections. In the following we review some of the most important sources of corrections, namely, spectator processes (Section 4.1), scatterings with top quarks and gauge bosons (Section 4.2), thermal effects (Section 4.3), contributions from heavier RH neutrinos (Section 4.4), and we also discuss the role of quantum corrections evaluated in the quantum BE approach (Section 4.5). Throughout this paper we use integrated BE; that is, we assume kinetic equilibrium for all particle species, and thus we use particles densities instead than particles distribution

functions. Corrections arising from using nonintegrated BE have been studied for example in [101–104], and are generally subleading.

#### 4.1. Spectator Processes

Reactions that without involving violation of  $B - L$  can still affect the final amount of baryon asymmetry are classified as “*spectator processes*” [105, 106]. The basic way through which they act is that of redistributing the asymmetry generated in the lepton doublets among the other particle species. Since the density asymmetries of the lepton doublets are what weights the rates of the washout processes, it can be expected that spectator processes would render the washouts less effective and increase the efficiency of leptogenesis. However, in most cases this is not true: proper inclusion of spectator processes implies accounting for all the particle asymmetries and in particular also for the density asymmetry of the Higgs  $Y_{\Delta H}$  [106]. This was omitted in Section 2 but in fact has to be added to the density asymmetry of the leptons  $Y_{\Delta \ell}$  in weighting, for example, washouts from inverse decays. Equation (2.14) would then become

$$\frac{dY_{\Delta L}}{dz} = \epsilon_1 D_1 (Y_{N_1} - Y_{N_1}^{\text{eq}}) - 2 (Y_{\Delta \ell} + Y_{\Delta H}) W_1, \quad (4.1)$$

where the factor of two in front of the washout term counts the leptons and Higgs gauge multiplicity. Clearly, in some regimes in which  $Y_{\Delta \ell}$  and  $Y_{\Delta H}$  are not sufficiently diluted by interacting with other particles, this can have the effect of enhancing the washout rates and suppressing the efficiency.

In the study of spectator processes it is fundamental to specify the range of temperature in which leptogenesis occurs. This is because at each specific temperature  $T$ , particle reactions must be treated in a different way depending on if their characteristic time scale  $\tau$  (given by inverse of their thermally averaged rates) is [89, 107]

- (1) much shorter than the age of the Universe:  $\tau \ll t_U(T)$ ;
- (2) much larger than the age of the Universe:  $\tau \gg t_U(T)$ ;
- (3) comparable with the Universe age:  $\tau \sim t_U(T)$ .

Spectator processes belong to the first type of reactions which occur very frequently during one expansion time. Their effects can be accounted for by imposing on the thermodynamic system the chemical equilibrium condition appropriate for each specific reaction, that is,  $\sum_I \mu_I = \sum_F \mu_F$ , where  $\mu_I$  denotes the chemical potential of an initial state particle and  $\mu_F$  that of a final state particle (the relation between chemical potentials and particle density asymmetries is given in (5.3)). The numerical values of the parameters that are responsible for these reactions only determine the precise temperature  $T$  when chemical equilibrium is attained but, apart from this, have no other relevance and do not appear explicitly in the formulation of the problem. Reactions of type (2) cannot have any effect on the system, since they basically do not occur. All physical processes are blind to the corresponding parameters, that can be set to zero in the effective Lagrangian. In most cases this results in exact global symmetries corresponding to conserved charges, and these conservation laws impose constraints on the particle chemical potentials. Reactions of type (3) in general violate some symmetry and thus spoil the corresponding conservation conditions, but are not fast enough to enforce chemical equilibrium. These are the only

reactions that need to be studied by means of BE, and for which the precise value of the parameters that control their rates is of utmost importance.

A simple case to illustrate how to include spectator processes is the one-flavour regime at particularly high temperatures (say,  $T \gtrsim 10^{13}$  GeV). The Universe expansion is fast implying that except for processes induced by the large Yukawa coupling of the top and for gauge interactions, all other  $B - L$ -conserving reactions fall in class (ii). Then there are several conserved quantities as, for example, the total number density asymmetries of the RH leptons as well as those of all the quarks except the top. Since electroweak sphalerons are also out of equilibrium,  $B$  is conserved too (and vanishing, if we assume that there is no preexisting asymmetry).  $B = 0$  then translates in the condition:

$$2Y_{\Delta Q_3} + Y_{\Delta t} = 0, \quad (4.2)$$

where  $Y_{\Delta Q_3}$  is the density asymmetries of one degree of freedom of the top  $SU(2)_L$  doublet and color triplet which, being gauge interactions in equilibrium, is the same for all the six gauge components and  $Y_{\Delta t}$  is the density asymmetry of the  $SU(2)_L$  singlet top. Hypercharge is always conserved, yielding

$$Y_{\Delta Q_3} + 2Y_{\Delta t} - Y_{\Delta \ell} + Y_{\Delta H} = 0. \quad (4.3)$$

Finally, in terms of density asymmetries chemical equilibrium for the top-Yukawa-related reactions  $\mu_{Q_3} + \mu_H = \mu_t$  translates into

$$Y_{\Delta Q_3} + \frac{1}{2}Y_{\Delta H} = Y_{\Delta t}. \quad (4.4)$$

We have three conditions for four density asymmetries, which allows to express the Higgs density asymmetry in terms of the density asymmetry of the leptons as  $Y_{\Delta H} = (2/3)Y_{\Delta \ell}$ . Moreover, given that only the LH lepton degrees of freedom are populated, we have  $Y_{\Delta L} = 2Y_{\Delta \ell}$  so that the coefficient weighting  $W_1$  in (4.1) becomes  $2(Y_{\Delta \ell} + Y_{\Delta H}) = (5/3)Y_{\Delta L}$  and the washout is accordingly stronger.

With decreasing temperatures, more reactions attain chemical equilibrium, and accounting for spectator processes becomes accordingly more complicated. When the temperature drops below  $T \sim 10^{12}$  GeV, EW sphalerons are in equilibrium, and baryon number is no more conserved. Then the condition (4.2) is no more satisfied, and, more importantly, the BE equation (4.1) is no more valid since sphalerons violate also lepton number within equilibrium rates. However, sphalerons conserve  $B - L$ , which is then violated only by slow reactions of type (3), and we should then write down a BE for this quantity. Better said, since at  $T \lesssim 10^{12}$  GeV all the third generation Yukawa reactions, including the ones of the  $\tau$ -lepton, are in equilibrium, the dynamical regime is that of two flavours in which the relevant quasiconserved charges are  $\Delta_\tau = B/3 - L_\tau$  and  $\Delta_{e\mu} = B/3 - L_{e\mu}$ . The fact that only two charges are relevant is because there is always a direction in  $e-\mu$  space which remains decoupled from  $N_1$ . The corresponding third charge  $\Delta'_{e\mu}$  is then exactly conserved, its value



can be set to zero, and the corresponding BE dropped. In this regime, the BE corresponding to (4.1) becomes

$$-\frac{dY_{\Delta_\alpha}}{dz} = \epsilon_\alpha D_1 (Y_{N_1} - Y_{N_1}^{\text{eq}}) - 2 (Y_{\Delta_{\ell_\alpha}} + Y_{\Delta_H}) W_1 \quad (\alpha = \tau, e\mu). \quad (4.5)$$

To rewrite these equations in a solvable closed form,  $Y_{\Delta_{\ell_\tau}}$ ,  $Y_{\Delta_{\ell_{e\mu}}}$ , and  $Y_{\Delta_H}$  must be expressed in terms of the two charge densities  $Y_{\Delta_\tau}$  and  $Y_{\Delta_{e\mu}}$ . This can be done by imposing the hypercharge conservation condition (4.3) and the chemical equilibrium conditions that, in addition to (4.4), are appropriate for the temperature regime we are considering. They are [106] (1) QCD sphaleron equilibrium; (2) EW sphaleron equilibrium; (3)  $b$ -quark and  $\tau$ -lepton Yukawa equilibrium. The “rotation” from the particle density asymmetries  $Y_{\Delta_{\ell_\alpha}}$  and  $Y_{\Delta_H}$  to the charge densities  $Y_{\Delta_\alpha}$  can be expressed in terms of the  $A$  matrix introduced in [67]  $Y_{\Delta_{\ell_\alpha}} = A_{\alpha\beta}^\ell Y_{\Delta_\beta}$  ( $\alpha, \beta = \tau, e\mu$ ) and  $C$ -vector  $Y_{\Delta_H} = C_\alpha^H Y_{\Delta_\alpha}$  introduced in [69]. For the present case, with the ordering  $(e\mu, \tau)$  they are [69]

$$A^\ell = \frac{1}{460} \begin{pmatrix} 196 & -24 \\ -9 & 156 \end{pmatrix}, \quad C^H = \frac{1}{230} (41, 56). \quad (4.6)$$

It is important to stress that in each temperature regime there are always enough constraints (conservation laws and chemical equilibrium conditions) to allow to express all the relevant particle density asymmetries in terms of the quasiconserved charges  $Y_{\Delta_\alpha}$ . This is because each time a conservation law has to be dropped (like  $B$  conservation above), it gets replaced by a chemical equilibrium condition (like EW sphalerons equilibrium), and each time the chemical potential of a new particle species becomes relevant, it is precisely because a new reaction involving that particle attains chemical equilibrium, enforcing the corresponding condition. As regards the quantitative corrections ascribable to spectator processes, several numerical studies have confirmed that they generally remain below order one. Thus, differently from flavour effects, for order of magnitude estimates they can be neglected.

## 4.2. Scatterings and CP Violation in Scatterings

Scattering processes are relevant for the production of the  $N_1$  population, because decay and inverse decay rates are suppressed by a time dilation factor  $\propto M_1/T$ . The  $N_1 = \bar{N}_1$  particles can be produced by scatterings with the top quark in  $s$ -channel  $H$ -exchange  $qt^c \rightarrow N\ell_\alpha$  and  $\bar{q}\bar{t}^c \rightarrow N\bar{\ell}_\alpha$ , by  $t$ -channel  $H$ -exchange in  $q\bar{\ell}_\alpha \rightarrow N\bar{t}^c$ ,  $\bar{q}\ell_\alpha \rightarrow Nt^c$  and by  $u$ -channel  $H$ -exchange in  $\ell_\alpha\bar{t}^c \rightarrow Nq$ ,  $t^c\bar{\ell}_\alpha \rightarrow N\bar{q}$ ; see the diagrams (a) in Figure 2. Several scattering channels with gauge bosons also contribute to the production of  $N_1$ ; the corresponding diagrams are (b) and (c) in the same figure.

When the effects of scatterings in populating the  $N_1$  degree of freedom are included, for consistency CP violation in scatterings must also be included. In doing so some care has to be put in treating properly also all the processes of higher order in the couplings ( $h_i^2\lambda^4$ ,  $g^2\lambda^4$ , where  $g$  is a gauge coupling) with an on-shell intermediate state  $N_1$  subtracted out. This can be done by following the procedure adopted in [108], and we refer to that paper for details.

In the first approximation, the CP asymmetry in scattering processes is the same as in decays and inverse decays [70, 109]. This result was first found in [75, 110, 111] for

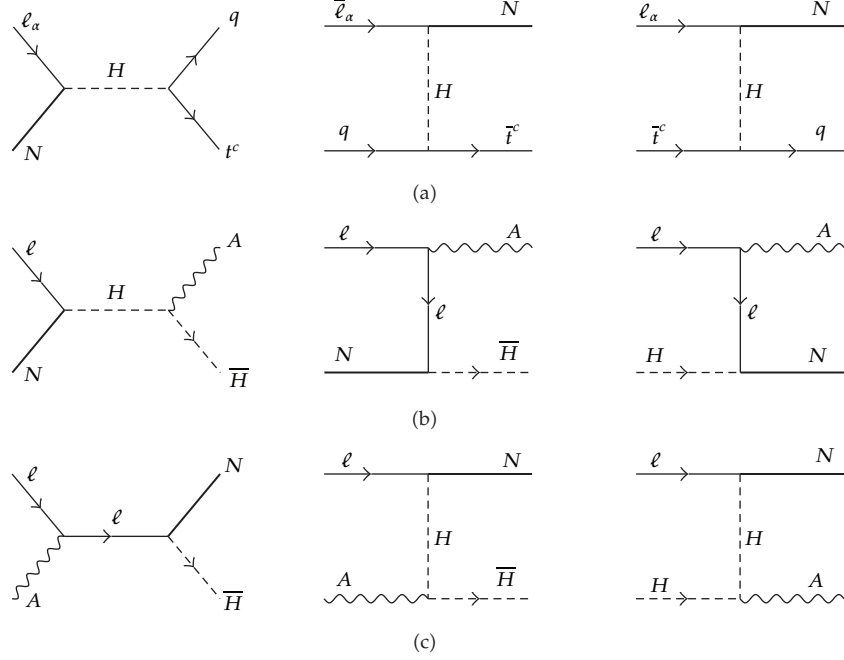


**Figure 2:** Diagrams for various  $2 \leftrightarrow 2$  scattering processes: (a) scatterings with the top quarks; (b) and (c) scatterings with the gauge bosons ( $A = B, W_i$  with  $i = 1, 2, 3$ ).

the case of resonant leptogenesis and was later derived in [70] for the case of hierarchical  $N_j$ . A full calculation of the CP asymmetry in scatterings involving the top quark was carried out in [108], and the validity of approximating it with the CP asymmetry in decays was analyzed, finding that the approximation is generally good for sufficiently strong RH neutrino hierarchies, for example,  $M_2/M_1 \gg 10$ . Corrections up to several tens of percent can appear around temperatures of order  $T \sim M_2/10$  and can be numerically relevant in case of milder hierarchies.

Regarding the scattering processes with gauge bosons such as  $N\ell_\alpha \rightarrow A\bar{H}NH \rightarrow A\bar{\ell}_\alpha$  or  $NA \rightarrow \ell_\alpha H$ , their effects in leptogenesis were estimated in [108] under the assumption that it can also be factorized in terms of the decay CP asymmetry. However, with respect to scatterings involving the top quark, there is a significant difference that now box diagrams in which the gauge boson is attached to a lepton or Higgs in the loop of the vertex-type diagrams are also present, leading to more complicated expressions that were explicitly calculated in [112]. There it was shown that the presence of box diagrams implies that for scatterings with gauge bosons the CP asymmetry is different from the decay CP asymmetry even for hierarchical RH neutrinos. Still, this difference remains within a factor of two [112] so that related effects are in any case not very large. In general, it turns out that CP asymmetry in scatterings is more relevant at high temperatures ( $T > M_1$ ) when the scattering rates are larger than the decay rate. Hence, it can be of some relevance to the final value of the baryon asymmetry when some of the lepton flavours are weakly washed out, and some memory of the asymmetries generated at high temperature is preserved in the final result.

### 4.3. Thermal Corrections

At the high temperatures at which leptogenesis occurs, the light particles involved in the leptogenesis processes are in equilibrium with the hot plasma. Thermal effects give corrections to several ingredients in the analysis: (i) coupling constants, (ii) particle propagators (leptons, quarks, gauge bosons, and the Higgs), and (iii) CP-violating asymmetries, which we briefly discuss later. A detailed study of thermal corrections can be found in [49].

#### 4.3.1. Coupling Constants

Renormalization of gauge and Yukawa couplings in a thermal plasma is studied in [113]. In practice, it is a good approximation to use the zero-temperature renormalization group equations for the couplings, with a renormalization scale  $\Lambda \sim 2\pi T$  [49]. The value  $\Lambda > T$  is related to the fact that the average energy of the colliding particles in the plasma is larger than the temperature.

The renormalization effects for the neutrino couplings are also well known [114, 115]. In the nonsupersymmetric case, to a good approximation these effects can be described by a simple rescaling of the low energy neutrino mass matrix  $m(\mu) = r \cdot m$ , where  $1.2 \lesssim r \lesssim 1.3$  for  $10^8 \text{ GeV} \lesssim \mu \lesssim 10^{16} \text{ GeV}$  [49], and therefore can be accounted for by increasing the values of the neutrino mass parameters (e.g.,  $\tilde{m}$ ) as measured at low energy by  $\approx 20\%–30\%$  (depending on the leptogenesis scale). In the supersymmetric case one expects a milder enhancement, but uncertainties related with the precise value of the top-Yukawa coupling can be rather large (see Figure 3 in [49]).

#### 4.3.2. Decays and Scatterings

In the thermal plasma, any particle with sizable couplings to the background acquires a thermal mass which is proportional to the plasma temperature. Consequently, decay and scattering rates get modified. Particle thermal masses have been thoroughly studied in both the SM and the supersymmetric SM [91, 116–120]. The singlet neutrinos have no gauge interactions, their Yukawa couplings are generally small, and, during the relevant era, their bare masses are of the order of the temperature or larger. Consequently, to a good approximation, corrections to their masses can be neglected. We thus need to account for the thermal masses of the leptons and Higgs doublets and, when scatterings are included, also of the third generation quarks and of the gauge bosons (and of their superpartners in the supersymmetric case). For a qualitative discussion, it is enough to keep in mind that, within the leptogenesis temperature range, we have  $m_H(T) \gtrsim m_{q,t}(T) \gg m_\ell(T)$ . The most important effects are related to four classes of leptogenesis processes.

- (i) *Decays and inverse decays*: since thermal corrections to the Higgs mass are particularly large ( $m_H(T) \approx 0.4 T$ ), decays and inverse decays become kinematically forbidden in the temperature range in which  $m_H(T) - m_\ell(T) < M_{N_1} < m_H(T) + m_\ell(T)$ . For lower temperatures, the usual processes  $N_1 \leftrightarrow \ell H$  can occur. For higher temperatures, the Higgs is heavy enough that it can decay:  $H \leftrightarrow \ell N_1$ . A rough estimate of the kinematically forbidden region yields  $2 \lesssim T/M_1 \lesssim 5$ . The important point is that these corrections are effective only at  $T > M_1$ . In the parameter

region  $\tilde{m} > 10^{-3}$  eV, that is favoured by the measurements of the neutrino mass-squared differences, the  $N_1$  number density and its  $L$ -violating reactions attain thermal equilibrium at  $T \approx M_1$  and erase quite efficiently any memory of the specific conditions at higher temperatures. Consequently, in the strong washout regime, these corrections have practically no effect on the final value of the baryon asymmetry.

- (ii)  $\Delta L = 1$  scatterings with top quark: a comparison between the corrected and uncorrected rates of the top-quark scattering  $\gamma_{H_s}^{\text{top}} \equiv \gamma(q_3 \bar{t} \leftrightarrow \ell N_1)$  with the Higgs exchanged in the  $s$ -channel and of the sum of the  $t$ - and  $u$ -channel scatterings  $\gamma_{H_{t+u}}^{\text{top}} \equiv \gamma(q_3 N_1 \leftrightarrow \ell t) + \gamma(\bar{t} N_1 \leftrightarrow \ell \bar{q}_3)$  shows that the only corrections appearing at low temperatures, and thus more relevant, are for  $\gamma_{H_{t+u}}^{\text{top}}$  (see Figure 7.1 in [109]). They reduce the scattering rates and suppress the related washouts. This peculiar situation arises from the fact that in the zero temperature limit there is a large enhancement  $\sim \ln(M_{N_1}/m_H)$  from the quasimassless Higgs exchanged in the  $t$ - and  $u$ -channels, which disappears when the Higgs thermal mass  $m_H(T) \sim T \sim M_{N_1}$  is included.
- (iii)  $\Delta L = 1$  scatterings with the gauge bosons: here the inclusion of thermal masses is required to avoid IR divergences that would arise when massless  $\ell$  (and  $H$ ) states are exchanged in the  $t$ - and  $u$ -channels. A naive use of some cutoff for the phase space integrals to control the IR divergences can yield incorrect estimates of the gauge bosons scattering rates [49] and would be particularly problematic at low temperatures, where gauge bosons scatterings dominate over top-quark scatterings.

#### 4.3.3. CP Asymmetries

CP asymmetries arise from the interference of tree level and one-loop amplitudes when the couplings involved have complex phases and the loop diagrams have an absorptive part. This last requirement is satisfied whenever the loop diagram can be cut in such a way that the particles in the cut lines can be produced on shell. For the CP asymmetry in decay (at zero temperature) this is guaranteed by the fact that the Higgs and the lepton final states coincide with the states circulating in the loops. However, in the hot plasma in which  $N_1$  decays occur, the Higgs and the lepton doublets are in thermal equilibrium and their interactions with the background introduce in the CP asymmetries a dependence on the temperature  $\epsilon \rightarrow \epsilon(T)$  that arises from various effects

- (i) Absorption and reemission of the loop particles by the medium require the use of finite temperature propagators.
- (ii) Stimulation of decays into bosons and blocking of decays into fermions in the dense background require proper modification of the final states density distributions.
- (iii) Thermal motion of the decaying  $N$ 's with respect to the background breaks the Lorentz symmetry and affects the evaluation of the CP asymmetries.
- (iv) Thermal masses should be included in the finite temperature resummed propagators, and they also modify the fermion and boson dispersion relations. Their inclusion yields the most significant modifications to the zero temperature results for the CP asymmetries.



The first three effects were investigated in [48] while the effects of thermal masses were included in [49]. In principle, at finite temperature, there are additional effects related to new cuts that involve the heavy  $N_{2,3}$  neutrino lines. These new cuts appear because the heavy particles in the loops may absorb energy from the plasma and go onshell. However, for hierarchical spectrum,  $M_{2,3} \gg M_1$ , the related effects are Boltzmann suppressed by  $\exp(-M_{2,3}/T)$  that at  $T \sim M_1$  is a tiny factor. For a nonhierarchical spectrum, the effect of these new cuts can however be sizable. A detailed study can be found in [121].

#### 4.3.4. Propagators and Statistical Distributions

Particle propagators at finite temperature are computed in the real-time formalism of thermal field theory [122, 123]. In this formalism, ghost fields dual to each of the physical fields have to be introduced, and consequently the thermal propagators have  $2 \times 2$  matrix structures. For the one-loop computations of the absorptive parts of the Feynman diagrams, the relevant propagator components are just those of the physical lepton and Higgs fields. The usual zero temperature propagators  $-iS_\ell^0(p, m_\ell) = (\not{p} - m_\ell + i0^+)^{-1}$  and  $-iD_H^0(p, m_H) = (p^2 - m_H^2 + i0^+)^{-1}$  acquire an additive term that is proportional to the particle density distribution  $n_{\ell,H} = [\exp(E_{\ell,H}/T) \pm 1]^{-1}$ :

$$\begin{aligned}\delta S_\ell(T) &= -2\pi n_\ell (\not{p} - m_\ell) \delta(p^2 - m_\ell^2), \\ \delta D_H(T) &= +2\pi n_H \delta(p^2 - m_H^2).\end{aligned}\tag{4.7}$$

For the fermionic thermal propagators, there are other higher order corrections (see [49]). Unlike the case of bosons, the interactions of the fermions with the thermal bath lead to two different types of excitations with different dispersion relations, that are generally referred to as “particles” and “holes” [49]. The contributions of these two fermionic modes were studied in [124–126] where it was argued that in the strong washout regime they could give nonnegligible effects [126]. The leading effects in (i) are proportional to the factor  $-n_\ell + n_H - 2n_\ell n_H$  that vanishes when the final states thermal masses are neglected, because the Bose-Einstein and Fermi-Dirac statistical distributions depend on the same argument,  $E_\ell = E_H = M_1/2$ . As a consequence, the thermal corrections to the fermion and boson propagators ( $n_\ell$  and  $n_H$ ) and the product of the two thermal corrections ( $n_\ell n_H$ ) cancel each other. This was interpreted as a complete compensation between stimulated emission and Pauli blocking. As regards the effects in (ii), they lead to overall factors that cancel between numerator and denominator in the expression for the CP asymmetry. (A similar cancellation holds also in the supersymmetric case. However, because of the presence of the superpartners  $\tilde{\ell}, \tilde{H}$  both as final states and in the loops, the cancellation is more subtle and it involves a compensation between the two types of corrections (i) and (ii). We refer to [48] for details.) More recently, on the basis of a first principle derivation of the CP asymmetry within a quantum BE approach (see Section 4.5) it has been claimed that the statistical factor induced by thermal loops is instead  $-n_\ell + n_H$ , which does not vanish even in the massless approximation. This would result in a further enhancement in the CP asymmetry from the thermal effects [127].

#### 4.3.5. Particle Motion

Given that the decaying particle  $N_1$  is moving with respect to the background (with velocity  $\vec{\beta}$ ) the fermionic decay products are preferentially emitted in the direction antiparallel to the plasma velocity (for which the thermal distribution is less occupied), while the bosonic ones are emitted preferentially in the forward direction (for which stimulated emission is more effective). Particle motion then induces an angular dependence in the decay distribution at order  $\mathcal{O}(\beta)$ . In the total decay rate the  $\mathcal{O}(\beta)$  anisotropy effect is integrated out, and only  $\mathcal{O}(\beta^2)$  effects remain [48]. Therefore, while accounting for thermal motion does modify the zero temperature results, these corrections are numerically small [48, 49] and generally negligible.

#### 4.3.6. Thermal Masses

When the finite values of the light particle thermal masses are taken into account, the arguments of the Bose-Einstein and Fermi-Dirac statistical distributions are different. It is a good approximation [49] to use for the particle energies  $E_{\ell,H} = M_1/2 \mp (m_H^2 - m_\ell^2)/2M_1$ . Since now  $E_\ell \neq E_H$ , the prefactor  $-n_\ell + n_H - 2n_\ell n_H$  that multiplies the thermal corrections does not vanish anymore, and sizable corrections become possible. The most relevant effect is that the CP asymmetry vanishes when, as the temperature increases, the sum of the light particles thermal masses approaches  $M_1$  [49]. This is not surprising, since the particles in the final state coincide with the particles in the loop, and therefore when the decay becomes kinematically forbidden, also the particles in the loop cannot go on the mass shell. When the temperature is large enough that  $m_H(T) > m_\ell(T) + M_1$ , the Higgs can decay, and then there is a new source of lepton number asymmetry associated with  $H \rightarrow \ell N_1$ . The CP asymmetry in Higgs decays  $\epsilon_H$  can be up to one order of magnitude larger than the CP asymmetry in  $N_1$  decays [49]. While this could represent a dramatic enhancement of the CP asymmetry,  $\epsilon_H$  is nonvanishing only at temperatures  $T \gtrsim T_H \sim 5M_1$ , when the kinematic condition for its decays is satisfied. Therefore, in the strong washout regime, no trace of this effect survives. On the other hand, rather large couplings are required in order that Higgs decays can occur before the phase space closes: the decay rate can attain thermal equilibrium only when  $\tilde{m} \gtrsim (T_H/M_1)^2 m_* \gg m_*$ , and therefore, in the weak washout regime ( $\tilde{m} \lesssim m_*$ ), these decays always remain strongly out of equilibrium. This means that only a small fraction of the Higgs particles have actually time to decay, and the lepton asymmetry generated in this way is accordingly suppressed.

In summary, while the corrections to the CP asymmetries can be significant at  $T \gtrsim M_1$  (and quite large at  $T \gg M_1$  for Higgs decays), in the low temperature regime, where the precise value of  $\epsilon$  plays a fundamental role in determining the final value of the baryon asymmetry, there are almost no effects, and the zero temperature results still give a reliable approximation.

### 4.4. Decays of the Heavier Right-Handed Neutrinos

In leptogenesis studies, the effects of  $N_{2,3}$  are often neglected, which in many cases is not a good approximation. This is obvious, for example, when  $N_1$  dynamics is irrelevant for leptogenesis:  $\epsilon_1 \ll 10^{-6}$  cannot provide enough CP asymmetry to account for baryogenesis, and  $\tilde{m}_1 \ll m_*$  implies that  $N_1$  washout effects are negligible. It is then clear that any asymmetry generated in  $N_{2,3}$  decays can survive and becomes crucial for the success of

leptogenesis. Another case in which it is intuitively clear that  $N_{2,3}$  effects can be important is when the RH neutrino spectrum is compact, which means that  $M_{2,3}$  have values within a factor of a few from  $M_1$ . Then  $N_1$  and  $N_{2,3}$  contributions to leptogenesis can be equally important and must be summed up. A model with compact RH neutrino spectrum in which  $N_{2,3}$  dynamics is of crucial importance was recently discussed in [128].

It is less obvious that  $N_{2,3}$  effects can also be important for a hierarchical RH spectrum and when  $N_1$  is strongly coupled. This can happen because decoherence effects related to  $N_1$ -interactions can project the asymmetry generated in  $N_{2,3}$  decays onto a flavour direction that remains protected against  $N_1$  washouts [67, 129–131]. Let us illustrate this with an example. Let us assume that a sizable asymmetry is generated in  $N_2$  decays, while  $N_1$  leptogenesis is inefficient and fails, that is:

$$\tilde{m}_2 \not\gg m_*, \quad \tilde{m}_1 \gg m_*. \quad (4.8)$$

Assuming also a strong hierarchy and that leptogenesis occurs thermally guarantees that [131]

$$n_{N_1}(T \sim M_2) \approx 0, \quad n_{N_2}(T \sim M_1) \approx 0. \quad (4.9)$$

Thus, the dynamics of  $N_2$  and  $N_1$  are decoupled: there are neither  $N_1$ -related washout effects during  $N_2$  leptogenesis nor  $N_2$ -related washout effects during  $N_1$  leptogenesis. The  $N_2$  decays into a combination of lepton doublets that we denote by  $\ell_2$ :

$$|\ell_2\rangle = \left(Y^\dagger Y\right)_{22}^{-1/2} \sum_\alpha Y_{a2} |\ell_\alpha\rangle. \quad (4.10)$$

The second condition in (4.8) implies that already at  $T \gtrsim M_1$  the  $N_1$ -Yukawa interactions are sufficiently fast to quickly destroy the coherence of  $\ell_2$ . Then a statistical mixture of  $\ell_1$  and of the state orthogonal to  $\ell_1$  builds up, and it can be described by a suitable diagonal density matrix. Let us consider the simple case where both  $N_2$  and  $N_1$  decay at  $T \gtrsim 10^{12}$  GeV, so that flavour effects are irrelevant. A convenient choice for an orthogonal basis for the lepton doublets is  $(\ell_1, \ell_0, \ell'_0)$  where, without loss of generality,  $\ell'_0$  satisfies  $\langle \ell'_0 | \ell_2 \rangle = 0$ . Then the asymmetry  $\Delta Y_{\ell_2}$  produced in  $N_2$  decays decomposes into two components:

$$\Delta Y_{\ell_0} = c^2 \Delta Y_{\ell_2}, \quad \Delta Y_{\ell_1} = s^2 \Delta Y_{\ell_2}, \quad (4.11)$$

where  $c^2 \equiv |\langle \ell_0 | \ell_2 \rangle|^2$  and  $s^2 = 1 - c^2$ . The crucial point here is that we expect, in general,  $c^2 \neq 0$  and, since  $\langle \ell_0 | \ell_1 \rangle = 0$ ,  $\Delta Y_{\ell_0}$  is protected against  $N_1$  washout. Consequently, a finite part of the asymmetry  $\Delta Y_{\ell_2}$  from  $N_2$  decays survives through  $N_1$  leptogenesis. A more detailed analysis [131] finds that  $\Delta Y_{\ell_1}$  is not entirely washed out, resulting in the final lepton asymmetry  $Y_{\Delta L} = (3/2) \Delta Y_{\ell_0} = (3/2) c^2 \Delta Y_{\ell_2}$ .

For  $10^9 \text{ GeV} \lesssim M_1 \lesssim 10^{12} \text{ GeV}$ , flavour issues modify the quantitative details, but the qualitative picture, and in particular the survival of a finite part of  $\Delta Y_{\ell_2}$ , still holds. In contrast, for  $M_1 \lesssim 10^9 \text{ GeV}$ , the full flavour basis  $(\ell_e, \ell_\mu, \ell_\tau)$  is resolved, and thus there are no directions in flavour space where an asymmetry is protected, so that  $Y_{\ell_2}$  can be erased entirely.

A dedicated study in which the various flavour regimes for  $N_{1,2,3}$  decays are considered can be found in [132].

In conclusion  $N_{2,3}$  leptogenesis cannot be ignored, unless one of the following conditions holds.

- (1) The reheat temperature is below  $M_2$ .
- (2) The asymmetries and/or the washout factors vanish,  $\epsilon_{N_2}\eta_2 \approx 0$  and  $\epsilon_{N_3}\eta_3 \approx 0$ .
- (3)  $N_1$ -related washout is still significant at  $T \lesssim 10^9$  GeV.

#### 4.5. Quantum Boltzmann Equations

So far we have analyzed the leptogenesis dynamics by adopting the classical BE of motion. An interesting question which has attracted some attention recently [85, 94, 121, 127, 133–139] is under which circumstances the classical BE can be safely applied to get reliable results and, conversely, when a more rigorous quantum approach is needed. Quantum BEs are obtained starting from the nonequilibrium quantum field theory based on the closed time-path (CTP) formulation [140]. Both, CP violation from wave function and vertex corrections are incorporated. Unitarity issues are resolved, and an accurate account of all quantum-statistical effects on the asymmetry is made. Moreover, the formulation in terms of Green functions bears the potential of incorporating corrections from thermal field theory within the CTP formalism.

In the CTP formalism, particle number densities are replaced by Green's functions obeying a set of equations which, under some assumptions, can be reduced to a set of kinetic equations describing the evolution of the lepton asymmetry and the RH neutrinos. These kinetic equations are nonMarkovian and present memory effects. In other words, differently from the classical approach where every scattering in the plasma is independent of the previous one, the particle abundances at a given time depend upon the history of the system. The more familiar energy-conserving delta functions are replaced by retarded time integrals of time-dependent kernels, and cosine functions whose arguments are the energy involved in the various processes. Therefore, the nonMarkovian kinetic equations include the contribution of coherent processes throughout the history of the kernels and the relaxation times are expected to be typically longer than the one dictated by the classical approach.

If the time range of the kernels is shorter than the relaxation time of the particles abundances, the solutions to the quantum and the classical BE differ only by terms of the order of the ratio of the timescale of the kernel to the relaxation timescale of the distribution. In thermal leptogenesis this is typically the case. However, there are situations where this does not happen. For instance, in the case of resonant leptogenesis, two RH (s)neutrinos  $N_1$  and  $N_2$  are almost degenerate in mass, and the CP asymmetry from the decay of the first RH neutrino  $N_1$  is resonantly enhanced if the mass difference  $\Delta M = (M_2 - M_1)$  is of the order of the decay rate of the second RH neutrino  $\Gamma_{N_2}$ . The typical timescale to build up coherently the CP asymmetry is of the order of  $1/\Delta M$ , which can be larger than the timescale  $\sim 1/\Gamma_{N_1}$  for the change of the abundance of the  $N_1$ 's.

Since we need the time evolution of the particle asymmetries with definite initial conditions and not simply the transition amplitude of particle reactions, the ordinary equilibrium quantum field theory at finite temperature is not the appropriate tool. The most appropriate extension of the field theory to deal with nonequilibrium phenomena amounts to generalizing the time contour of integration to a closed time path. More precisely, the time



integration contour is deformed to run from  $t_0$  to  $+\infty$  and back to  $t_0$ . The CTP formalism is a powerful Green's function formulation for describing nonequilibrium phenomena in field theory. It allows to describe phase-transition phenomena and to obtain a self-consistent set of quantum BE. The formalism yields various quantum averages of operators evaluated in the instate without specifying the out-state. On the contrary, the ordinary quantum field theory yields quantum averages of the operators evaluated with an instate at one end and an outstate at the other.

For example, because of the time-contour deformation, the partition function in the in-in formalism for a complex scalar field is defined to be

$$\begin{aligned} Z[J, J^\dagger] &= \text{Tr} \left[ \mathcal{T} \left( \exp \left[ i \int_C \left( J(x) \phi(x) + J^\dagger(x) \phi^\dagger(x) \right) d^4x \right] \right) \rho \right] \\ &= \text{Tr} \left[ \mathcal{T}_+ \left( \exp \left[ i \int \left( J_+(x) \phi_+(x) + J_+^\dagger(x) \phi_+^\dagger(x) \right) d^4x \right] \right) \right. \\ &\quad \left. \times \mathcal{T}_- \left( \exp \left[ -i \int \left( J_-(x) \phi_-(x) + J_-^\dagger(x) \phi_-^\dagger(x) \right) d^4x \right] \right) \rho \right], \end{aligned} \quad (4.12)$$

where  $C$  in the integral denotes that the time integration contour runs from  $t_0$  to plus infinity and then back to  $t_0$  again. The symbol  $\rho$  represents the initial density matrix, and the fields are in the Heisenberg picture and defined on this closed time contour (plus and minus subscripts refer to the positive and negative directional branches of the time path, resp.). The time-ordering operator along the path is the standard one ( $\mathcal{T}_+$ ) on the positive branch, and the antitime-ordering ( $\mathcal{T}_-$ ) on the negative branch. As with the Euclidean-time formulation, scalar (fermionic) fields  $\phi$  are still periodic (antiperiodic) in time, but with  $\phi(t, \vec{x}) = \phi(t - i\beta, \vec{x})$ ,  $\beta = 1/T$ . The temperature  $T$  appears due to boundary condition, and time is now explicitly present in the integration contour.

We must now identify field variables with arguments on the positive or negative directional branches of the time path. This doubling of field variables leads to six different real-time propagators on the contour. These six propagators are not independent, but using all of them simplifies the notation. For a generic charged scalar field  $\phi$  they are defined as

$$\begin{aligned} G_\phi^>(x, y) &= -G_\phi^{+-}(x, y) = -i \langle \phi(x) \phi^\dagger(y) \rangle, \\ G_\phi^<(x, y) &= -G_\phi^{+ -}(x, y) = -i \langle \phi^\dagger(y) \phi(x) \rangle, \\ G_\phi^t(x, y) &= G_\phi^{++}(x, y) = \theta(x, y) G_\phi^>(x, y) + \theta(y, x) G_\phi^<(x, y), \\ G_\phi^{\bar{t}}(x, y) &= G_\phi^{--}(x, y) = \theta(y, x) G_\phi^>(x, y) + \theta(x, y) G_\phi^<(x, y), \\ G_\phi^r(x, y) &= G_\phi^t - G_\phi^< = G_\phi^> - G_\phi^{\bar{t}}, \quad G_\phi^a(x, y) = G_\phi^t - G_\phi^> = G_\phi^< - G_\phi^{\bar{t}}, \end{aligned} \quad (4.13)$$

where the last two Green's functions are the retarded and advanced Green's functions, respectively, and  $\theta(x, y) \equiv \theta(t_x - t_y)$  is the step function.

For a generic fermion field  $\psi$  the six different propagators are analogously defined as

$$\begin{aligned}
G_{\psi}^>(x, y) &= -G_{\psi}^{+}(x, y) = -i\langle\psi(x)\bar{\psi}(y)\rangle, \\
G_{\psi}^<(x, y) &= -G_{\psi}^{+-}(x, y) = +i\langle\bar{\psi}(y)\psi(x)\rangle, \\
G_{\psi}^t(x, y) &= G_{\psi}^{++}(x, y) = \theta(x, y)G_{\psi}^>(x, y) + \theta(y, x)G_{\psi}^<(x, y), \\
G_{\psi}^{\bar{t}}(x, y) &= G_{\psi}^{--}(x, y) = \theta(y, x)G_{\psi}^>(x, y) + \theta(x, y)G_{\psi}^<(x, y), \\
G_{\psi}^r(x, y) &= G_{\psi}^t - G_{\psi}^< = G_{\psi}^> - G_{\psi}^{\bar{t}}, \quad G_{\psi}^a(x, y) = G_{\psi}^t - G_{\psi}^> = G_{\psi}^< - G_{\psi}^{\bar{t}}.
\end{aligned} \tag{4.14}$$

From the definitions of the Green's functions, one can see that the hermiticity properties

$$\left(i\gamma^0 G_{\psi}(x, y)\right)^{\dagger} = i\gamma^0 G_{\psi}(y, x), \quad (iG_{\phi}(x, y))^{\dagger} = iG_{\phi}(y, x) \tag{4.15}$$

are satisfied. For interacting systems, whether in equilibrium or not, one must define and calculate self-energy functions. Again, there are six of them:  $\Sigma^t$ ,  $\Sigma^{\bar{t}}$ ,  $\Sigma^<$ ,  $\Sigma^>$ ,  $\Sigma^r$ , and  $\Sigma^a$ . The same relationships exist among them as for the Green's functions in (4.13) and (4.14), such as

$$\Sigma^r = \Sigma^t - \Sigma^< = \Sigma^> - \Sigma^{\bar{t}}, \quad \Sigma^a = \Sigma^t - \Sigma^> = \Sigma^< - \Sigma^{\bar{t}}. \tag{4.16}$$

The self-energies are incorporated into the Green's functions through the use of Dyson's equations. A useful notation may be introduced which expresses four of the six Green's functions as the elements of two-by-two matrices:

$$\tilde{G} = \begin{pmatrix} G^t & \pm G^< \\ G^> & -G^{\bar{t}} \end{pmatrix}, \quad \tilde{\Sigma} = \begin{pmatrix} \Sigma^t & \pm \Sigma^< \\ \Sigma^> & -\Sigma^{\bar{t}} \end{pmatrix}, \tag{4.17}$$

where the upper signs refer to the bosonic case and the lower signs to the fermionic case. For systems either in equilibrium or in nonequilibrium, Dyson's equation is most easily expressed by using the matrix notation:

$$\tilde{G}(x, y) = \tilde{G}^0(x, y) + \int d^4 z_1 \int d^4 z_2 \tilde{G}^0(x, z_1) \tilde{\Sigma}(z_1, z_2) \tilde{G}(z_2, y), \tag{4.18}$$

where the superscript "0" on the Green's functions means to use those for noninteracting system. It is useful to notice that Dyson's equation can be written in an alternative form, instead of (4.18), with  $\tilde{G}^0$  on the right in the interaction terms:

$$\tilde{G}(x, y) = \tilde{G}^0(x, y) + \int d^4 z_3 \int d^4 z_4 \tilde{G}(x, z_3) \tilde{\Sigma}(z_3, z_4) \tilde{G}^0(z_4, y). \tag{4.19}$$

Equations (4.18) and (4.19) are the starting points to derive the quantum BE describing the time evolution of the CP-violating particle density asymmetries.

To proceed, one has to choose a form for the propagators. For a generic fermion  $\psi$  (and similarly for scalars) one may adopt the real-time propagator in the form  $G_\psi^t(\mathbf{k}, t_x - t_y)$  in terms of the spectral function  $\rho_\psi(\mathbf{k}, k_0)$

$$G_\psi^t(\mathbf{k}, t_x - t_y) = \int_{-\infty}^{+\infty} \frac{dk^0}{2\pi} e^{-ik^0(t_x - t_y)} \rho_\psi(\mathbf{k}, k^0) \times \left\{ \left[ 1 - f_\psi(k^0) \right] \theta(t_x - t_y) - f_\psi(k^0) \theta(t_y - t_x) \right\}, \quad (4.20)$$

where  $f_\psi(k^0)$  represents the fermion distribution function. Again, particles must be substituted by quasiparticles, dressed propagators are to be adopted, and self-energy corrections to the propagator modify the dispersion relations by introducing a finite width  $\Gamma_\psi(k)$ . For a fermion with chiral mass  $m_\psi$ , one may safely choose

$$\rho_\psi(\mathbf{k}, k^0) = i(\not{k} + m_\psi) \left[ \frac{1}{(k^0 + i\epsilon + i\Gamma_\psi)^2 - \omega_\psi^2(k)} - \frac{1}{(k^0 - i\epsilon - i\Gamma_\psi)^2 - \omega_\psi^2(k)} \right], \quad (4.21)$$

where  $\omega_\psi^2(k) = \mathbf{k}^2 + M_\psi^2(T)$  and  $M_\psi(T)$  is the effective thermal mass of the fermion in the plasma (not a chiral mass). Performing the integration over  $k^0$  and picking up the poles of the spectral function (which is valid for quasiparticles in equilibrium or very close to equilibrium), one gets

$$\begin{aligned} G_\psi^>(\mathbf{k}, t_x - t_y) &= -\frac{i}{2\omega_\psi} \left\{ (\not{k} + m_\psi) [1 - f_\psi(\omega_\psi - i\Gamma_\psi)] e^{-i(\omega_\psi - i\Gamma_\psi)(t_x - t_y)} \right. \\ &\quad \left. + \gamma^0 (\not{k} - m_\psi) \gamma^0 \bar{f}_\psi(\omega_\psi + i\Gamma_\psi) e^{i(\omega_\psi + i\Gamma_\psi)(t_x - t_y)} \right\}, \\ G_\psi^<(\mathbf{k}, t_y - t_x) &= \frac{i}{2\omega_\psi} \left\{ (\not{k} + m_\psi) f_\psi(\omega_\psi + i\Gamma_\psi) e^{-i(\omega_\psi + i\Gamma_\psi)(t_x - t_y)} \right. \\ &\quad \left. + \gamma^0 (\not{k} - m_\psi) \gamma^0 [1 - \bar{f}_\psi(\omega_\psi - i\Gamma_\psi)] e^{i(\omega_\psi - i\Gamma_\psi)(t_x - t_y)} \right\}, \end{aligned} \quad (4.22)$$

where  $k^0 = \omega_\psi$  and  $f_\psi, \bar{f}_\psi$  denote the distribution function of the fermion particles and antiparticles, respectively. The expressions (4.22) are valid for  $t_x - t_y > 0$ .

The above definitions hold for the lepton doublets (after inserting the chiral LH projector  $P_L$ ), as well as for the Majorana RH neutrinos, for which one has to assume identical particle and antiparticle distribution functions and insert the inverse of the charge conjugation matrix  $C$  in the dispersion relation.

To elucidate further the impact of the CTP approach and to see under which conditions one can obtain the classical BE from the quantum ones, one may consider the dynamics of the

lightest RH neutrino  $N_1$ . To find its quantum BE we start from (4.18) for the Green's function  $G_{N_1}^<$  of the RH neutrino  $N_1$  :

$$\begin{aligned} (i\vec{\partial}_x - M_1)G_{N_1}^<(x, y) &= - \int d^4z \left[ -\Sigma_{N_1}^t(x, z)G_{N_1}^<(z, y) + \Sigma_{N_1}^<(x, z)G_{N_1}^t(z, y) \right] \\ &= \int d^3z \int_0^t dt_z \left[ \Sigma_{N_1}^>(x, z)G_{N_1}^<(z, y) - \Sigma_{N_1}^<(x, z)G_{N_1}^>(z, y) \right]. \end{aligned} \quad (4.23)$$

Adopting the corresponding form for the RH neutrino propagator and the center-of-mass coordinates

$$X \equiv (t, \vec{X}) \equiv \frac{1}{2}(x + y), \quad (\tau, \vec{r}) \equiv x - y, \quad (4.24)$$

one ends up with the following equation:

$$\begin{aligned} \frac{\partial f_{N_1}(\mathbf{k}, t)}{\partial t} &= -2 \int_0^t dt_z \int \frac{d^3\mathbf{p}}{(2\pi)^3} \frac{1}{2\omega_\ell(\mathbf{p})} \frac{1}{2\omega_H(\mathbf{k} - \mathbf{p})} \frac{1}{\omega_{N_1}(\mathbf{k})} |\mathcal{M}(N_1 \rightarrow \ell H)|^2 \\ &\quad \times [f_{N_1}(\mathbf{k}, t)(1 - f_\ell(\mathbf{p}, t))(1 + f_H(\mathbf{k} - \mathbf{p}, t)) \\ &\quad - f_\ell(\mathbf{p}, t)f_H(\mathbf{k} - \mathbf{p}, t)(1 - f_{N_1}(\mathbf{k}, t))] \\ &\quad \times \cos[(\omega_{N_1}(\mathbf{k}) - \omega_\ell(\mathbf{p}) - \omega_H(\mathbf{k} - \mathbf{p}))(t - t_z)] \\ &\simeq -2 \int_0^t dt_z \int \frac{d^3\mathbf{p}}{(2\pi)^3} \frac{1}{2\omega_\ell(\mathbf{p})} \frac{1}{2\omega_H(\mathbf{k} - \mathbf{p})} \frac{1}{\omega_{N_1}(\mathbf{k})} |\mathcal{M}(N_1 \rightarrow \ell H)|^2 \\ &\quad \times (f_{N_1}(\mathbf{k}, t) - f_\ell^{\text{eq}}(\mathbf{p})f_H^{\text{eq}}(\mathbf{k} - \mathbf{p})) \\ &\quad \times \cos[(\omega_{N_1}(\mathbf{k}) - \omega_\ell(\mathbf{p}) - \omega_H(\mathbf{k} - \mathbf{p}))(t - t_z)]. \end{aligned} \quad (4.25)$$

This equations holds under the assumption that the relaxation timescale for the distribution functions is longer than the timescale of the nonlocal kernels so that they can be extracted out of the time integral. This allows to think of the distributions as functions of the center-of-mass time only. We have set to zero the damping rates of the particles in (4.22) and retained only those cosines giving rise to energy delta functions that can be satisfied. Under these assumptions, the distribution function may be taken out of the time integral, leading—at large times—to the so-called Markovian description. The kinetic equation (4.25) has an obvious interpretation in terms of gain minus loss processes, but the retarded time integral and the cosine function replace the familiar energy-conserving delta functions. In the second passage, we have also made the usual assumption that all distribution functions are smaller than unity and that those of the Higgs and lepton doublets are in equilibrium and much smaller than unity,  $f_\ell f_H \simeq f_\ell^{\text{eq}} f_H^{\text{eq}}$ . Elastic scatterings are typically fast enough to keep kinetic



equilibrium. For any distribution function we may write  $f = (n/n^{\text{eq}})f^{\text{eq}}$ , where  $n$  denotes the total number density. Therefore, (4.25) can be rewritten as

$$\begin{aligned}
\frac{\partial n_{N_1}}{\partial t} &= -\langle \Gamma_{N_1}(t) \rangle n_{N_1} + \langle \tilde{\Gamma}_{N_1}(t) \rangle n_{N_1}^{\text{eq}}, \\
\langle \Gamma_{N_1}(t) \rangle &= \int_0^t dt_z \int \frac{d^3 \mathbf{k}}{(2\pi)^3} \frac{f_{N_1}^{\text{eq}}}{n_{N_1}^{\text{eq}}} \Gamma_{N_1}(t), \\
\Gamma_{N_1}(t) &= 2 \int \frac{d^3 \mathbf{p}}{(2\pi)^3} \frac{|\mathcal{M}(N_1 \rightarrow \ell H)|^2}{2\omega_\ell 2\omega_H \omega_{N_1}} \cos[(\omega_{N_1} - \omega_\ell - \omega_H)(t - t_z)], \\
\langle \tilde{\Gamma}_{N_1}(t) \rangle &= \int_0^t dt_z \int \frac{d^3 \mathbf{k}}{(2\pi)^3} \frac{f_{N_1}^{\text{eq}}}{n_{N_1}^{\text{eq}}} \tilde{\Gamma}_{N_1}(t), \\
\tilde{\Gamma}_{N_1}(t) &= 2 \int \frac{d^3 \mathbf{p}}{(2\pi)^3} \frac{f_\ell^{\text{eq}} f_H^{\text{eq}}}{f_{N_1}^{\text{eq}}} \frac{|\mathcal{M}(N_1 \rightarrow \ell H)|^2}{2\omega_\ell 2\omega_H \omega_{N_1}} \cos[(\omega_{N_1} - \omega_\ell - \omega_H)(t - t_z)],
\end{aligned} \tag{4.26}$$

where  $\langle \Gamma_{N_1}(t) \rangle$  is the time-dependent thermal average of the Lorentz-dilated decay width. Integrating over large times,  $t \rightarrow \infty$ , thereby replacing the cosines by energy-conserving delta functions:

$$\int_0^\infty dt_z \cos[(\omega_{N_1} - \omega_\ell - \omega_H)(t - t_z)] = \pi \delta(\omega_{N_1} - \omega_\ell - \omega_H), \tag{4.27}$$

we find that the two averaged rates  $\langle \Gamma_{N_1} \rangle$  and  $\langle \tilde{\Gamma}_{N_1} \rangle$  coincide and we recover the usual classical BE for the RH distribution function

$$\begin{aligned}
\frac{\partial n_{N_1}}{\partial t} &= -\langle \Gamma_{N_1} \rangle (n_{N_1} - n_{N_1}^{\text{eq}}), \\
\langle \Gamma_{N_1} \rangle &= \int \frac{d^3 \mathbf{k}}{(2\pi)^3} \frac{f_{N_1}^{\text{eq}}}{n_{N_1}^{\text{eq}}} \int \frac{d^3 \mathbf{p}}{(2\pi)^3} \frac{|\mathcal{M}(N_1 \rightarrow \ell H)|^2}{2\omega_\ell 2\omega_H \omega_{N_1}} (2\pi) \delta(\omega_{N_1} - \omega_\ell - \omega_H).
\end{aligned} \tag{4.28}$$

Taking the time interval to infinity, namely, implementing Fermi's golden rule, results in neglecting memory effects, which in turn results only in on-shell processes contributing to the rate equation. The main difference between the classical and the quantum BE can be traced to memory effects and to the fact that the time evolution of the distribution function is nonMarkovian. The memory of the past time evolution translates into off-shell processes.

Similarly, one can show that the equation obeyed by the asymmetry reads

$$\begin{aligned}
\frac{\partial n_{\Delta L_\alpha}(X)}{\partial t} &= - \int d^3 z \int_0^t dt_z \text{Tr} \left[ \Sigma_{\ell_\alpha}^>(X, z) G_{\ell_\alpha}^<(z, X) - G_{\ell_\alpha}^>(X, z) \Sigma_{\ell_\alpha}^<(z, X) \right. \\
&\quad \left. + G_{\ell_\alpha}^<(X, z) \Sigma_{\ell_\alpha}^>(z, X) - \Sigma_{\ell_\alpha}^<(X, z) G_{\ell_\alpha}^>(z, X) \right].
\end{aligned} \tag{4.29}$$

Proceeding as for the RH neutrino equation one finds (including the moment only for the 1-loop wave contribution to the CP asymmetry  $\epsilon_w^\alpha$ )

$$\begin{aligned}
\frac{\partial n_{\Delta L_\alpha}}{\partial t} &= \epsilon_w^\alpha(t) \langle \Gamma_{N_1} \rangle (n_{N_1} - n_{N_1}^{\text{eq}}), \\
\epsilon_w^\alpha(t) &= -\frac{4}{\langle \Gamma_{N_1} \rangle} \sum_{\beta=1}^3 \text{Im} \left( \Upsilon_{1\alpha} \Upsilon_{1\beta} \Upsilon_{\beta 2}^\dagger \Upsilon_{\alpha 2}^\dagger \right) \\
&\quad \times \int_0^t dt_z \int_0^{t_z} dt_2 \int_0^{t_2} dt_1 e^{-\Gamma_{N_2}(t_z-t_2)} e^{-(\Gamma_{\ell_\beta} + \Gamma_H)(t_2-t_1)} \int \frac{d^3 \mathbf{k}}{(2\pi)^3} \frac{f_{N_1}^{\text{eq}}}{n_{N_1}^{\text{eq}}} \\
&\quad \times \int \frac{d^3 \mathbf{p}}{(2\pi)^3} \frac{1 - f_{\ell_\beta}^{\text{eq}}(\mathbf{p}) + f_H^{\text{eq}}(\mathbf{k} - \mathbf{p})}{2\omega_{\ell_\beta}(\mathbf{p}) 2\omega_H(\mathbf{k} - \mathbf{p}) \omega_{N_1}(\mathbf{k})} \int \frac{d^3 \mathbf{q}}{(2\pi)^3} \frac{1 - f_{\ell_\alpha}^{\text{eq}}(\mathbf{q}) + f_H^{\text{eq}}(\mathbf{k} - \mathbf{q})}{2\bar{\omega}_{\ell_\alpha}(\mathbf{q}) 2\bar{\omega}_H(\mathbf{k} - \mathbf{q}) \omega_{N_2}(\mathbf{k})} \\
&\quad \times \sin \left( \omega_{N_1}(t - t_1) + (\omega_{\ell_\beta} + \omega_H)(t_1 - t_2) + \omega_{N_2}(t_2 - t_z) + (\bar{\omega}_{\ell_\alpha} + \bar{\omega}_H)(t_z - t) \right) \\
&\quad \times \text{Tr}(M_1 P_L \not{p} M_2 \not{q}),
\end{aligned} \tag{4.30}$$

where, to avoid double counting, we have not inserted the decay rates in the propagators of the initial and final states and, for simplicity, we have assumed that the damping rates of the lepton doublets and the Higgs field are constant in time. This should be a good approximation as the damping rates are to be computed for momenta of order of the mass of the RH neutrinos. As expected from first principles, we find that the CP asymmetry is a function of time and its value at a given instant depends upon the previous history of the system.

Performing the time integrals and retaining only those pieces which eventually give rise to energy-conserving delta functions in the Markovian limit, we obtain

$$\begin{aligned}
\epsilon_w^\alpha(t) &= -\frac{4}{\langle \Gamma_{N_1} \rangle} \sum_{\beta=1}^3 \text{Im} \left( \Upsilon_{1\alpha} \Upsilon_{1\beta} \Upsilon_{\beta 2}^\dagger \Upsilon_{\alpha 2}^\dagger \right) \\
&\quad \times \int_0^t dt_z \frac{\cos[(\omega_{N_1} - \bar{\omega}_{\ell_\alpha} - \bar{\omega}_H)(t - t_z)]}{\left( \Gamma_{N_2}^2 + (\omega_{N_2} - \omega_{N_1})^2 \right) \left( (\Gamma_{\ell_\beta} + \Gamma_H)^2 + (\omega_{N_1} - \omega_{\ell_\beta} - \omega_H)^2 \right)} \\
&\quad \times \int \frac{d^3 \mathbf{k}}{(2\pi)^3} \frac{f_{N_1}^{\text{eq}}}{n_{N_1}^{\text{eq}}} (\Gamma_{\ell_\beta} + \Gamma_H) \\
&\quad \times \left( 2(\omega_{N_2} - \omega_{N_1}) \sin^2 \left[ \frac{(\omega_{N_2} - \omega_{N_1}) t_z}{2} \right] - \Gamma_{N_2} \sin[(\omega_{N_2} - \omega_{N_1}) t_z] \right) \\
&\quad \times \int \frac{d^3 \mathbf{p}}{(2\pi)^3} \frac{1 - f_{\ell_\beta}^{\text{eq}}(\mathbf{p}) + f_H^{\text{eq}}(\mathbf{k} - \mathbf{p})}{2\omega_{\ell_\beta}(\mathbf{p}) 2\omega_H(\mathbf{k} - \mathbf{p}) \omega_{N_1}(\mathbf{k})} \\
&\quad \times \int \frac{d^3 \mathbf{q}}{(2\pi)^3} \frac{1 - f_{\ell_\alpha}^{\text{eq}}(\mathbf{q}) + f_H^{\text{eq}}(\mathbf{k} - \mathbf{q})}{2\bar{\omega}_{\ell_\alpha}(\mathbf{q}) 2\bar{\omega}_H(\mathbf{k} - \mathbf{q}) \omega_{N_2}(\mathbf{k})} \text{Tr}(M_1 P_L \not{p} M_2 \not{q}).
\end{aligned} \tag{4.31}$$

From this expression it is already manifest that the typical timescale for the building up of the coherent CP asymmetry depends crucially on the difference in energy of the two RH neutrinos.

If we now let the upper limit of the time integral take large values, we neglect the memory effects; the CP asymmetry picks contribution only from the on-shell processes. Taking the damping rates of the lepton doublets equal for all the flavours and the RH neutrinos nearly at rest with respect to the thermal bath, the CP asymmetry reads (now summing over all flavour indices)

$$\epsilon_w(t) \simeq - \frac{\text{Im}(YY^\dagger)_{12}^2}{(YY^\dagger)_{11}(YY^\dagger)_{22}} \frac{M_1}{M_2} \Gamma_{N_2} \frac{1}{(\Delta M)^2 + \Gamma_{N_2}^2} \times \left( 2\Delta M \sin^2 \left[ \frac{\Delta M t}{2} \right] - \Gamma_{N_2} \sin[\Delta M t] \right), \quad (4.32)$$

where  $\Delta M = (M_2 - M_1)$ . The CP asymmetry (4.32) is resonantly enhanced when  $\Delta M \simeq \Gamma_{N_2}$ , and at the resonance point it is given by

$$\epsilon_w(t) \simeq - \frac{1}{2} \frac{\text{Im}(YY^\dagger)_{12}^2}{(YY^\dagger)_{11}(YY^\dagger)_{22}} (1 - \sin[\Delta M t] - \cos[\Delta M t]). \quad (4.33)$$

The timescale for the building up of the CP asymmetry is  $\sim 1/\Delta M$ . The CP asymmetry grows starting from a vanishing value, and, for  $t \gg (\Delta M)^{-1}$ , it averages to the constant standard value. This is true if the timescale for the other processes relevant for leptogenesis is larger than  $\sim 1/\Delta M$ . In other words, one may define an “average” CP asymmetry

$$\langle \epsilon_w \rangle = \frac{1}{\tau_p} \int_{t-\tau_p}^t dt' \epsilon_{N_1}^W(t'), \quad (4.34)$$

where  $\tau_p$  represents the typical timescale of the other processes relevant for leptogenesis, for example, the  $\Delta L = 1$  scatterings. If  $\tau_p \gg 1/\Delta M \sim \Gamma_{N_2}^{-1}$ , the oscillating functions in (4.33) are averaged to zero and the average CP asymmetry is given by the value used in the literature. However, the expression (4.32) should be used when  $\tau_p \lesssim 1/\Delta M \sim \Gamma_{N_2}^{-1}$ .

The fact that the CP asymmetry is a function of time is particularly relevant in the case in which the asymmetry is generated by the decays of two heavy states which are nearly degenerate in mass and oscillate into one another with a timescale, given by the inverse of the mass difference and has been studied in [86, 141]. From (4.32) it is manifest that the CP asymmetry itself oscillates with the very same timescale and such a dependence may or may not be neglected depending upon the rates of the other processes in the plasma. If  $\Gamma_{N_1} \gtrsim \Gamma_{N_2}$ , the time dependence of the CP asymmetry may not be neglected. The expression (4.32) can also be used, once it is divided by a factor 2 (because in the wave diagram also the charged states of Higgs and lepton doublets may propagate) and the limit  $M_2 \gg M_1$  is taken, for the CP asymmetry contribution from the vertex diagram:

$$\epsilon_v(t) \simeq - \frac{\text{Im}(YY^\dagger)_{12}^2}{16\pi(YY^\dagger)_{11}} \frac{M_1}{M_2} \left( 2 \sin^2 \left[ \frac{M_2 t}{2} \right] - \frac{\Gamma_{N_2}}{M_2} \sin[M_2 t] \right). \quad (4.35)$$

In this case, the timescale for this CP asymmetry is  $\sim M_2$  and much larger than any other timescale in the dynamics. Therefore, one can safely average over many oscillations, getting the expression present in the literature.

What has been discussed here provides only one example for which a quantum Boltzmann approach is needed. In general, the lesson is that quantum BEs are relevant when the typical timescale in a quantum physical process, such as the timescale for the unflavour-to-flavour transition or the timescale to build up coherently the CP asymmetry (of the order of  $1/\Delta M$ ), is larger than the timescale for the change of the abundances.

## 5. Supersymmetric Leptogenesis

### 5.1. What's New?

Supersymmetric leptogenesis constitutes a theoretically appealing generalization of leptogenesis for the following reason: while the SM equipped with the seesaw provides the simplest way to realize leptogenesis, such a framework is plagued by an unpleasant fine-tuning problem. For a nondegenerate spectrum of heavy Majorana neutrinos, successful leptogenesis requires generically a scale for the singlet neutrino masses that is much larger than the EW scale [61] but at the quantum level the gap between these two scales becomes unstable. Low-energy supersymmetry (SUSY) can naturally stabilize the required hierarchy, and this provides a sound motivation for studying leptogenesis in the framework of the supersymmetrized version of the seesaw mechanism. Supersymmetric leptogenesis, however, introduces a certain conflict between the gravitino bound on the reheat temperature and the thermal production of the heavy singlets neutrinos [142–145]. In this section, we will not be concerned with the gravitino problem, nor with its possible ways out but focus on the new features SUSY brings in for leptogenesis.

The supersymmetric type-I seesaw model is described by the superpotential of the minimal supersymmetric SM (MSSM) with the additional terms:

$$W = \frac{1}{2} M_{pq} N_p^c N_q^c + \lambda_{\alpha p} N_p^c \ell_\alpha H_u, \quad (5.1)$$

where  $p, q = 1, 2, \dots$  label the heavy singlet states in order of increasing mass and  $\alpha = e, \mu, \tau$  labels the lepton flavour. In (5.1)  $\ell$ ,  $H_u$ , and  $N^c$  are, respectively, the chiral superfields for the lepton and the up-type Higgs  $SU(2)_L$  doublets and for the heavy  $SU(2)_L$  singlet neutrinos defined according to usual conventions in terms of their LH Weyl spinor components (e.g., the  $N^c$  supermultiplet has scalar component  $\widetilde{N}^*$  and fermion component  $N_L^c$ ). Finally the  $SU(2)_L$  index contraction is defined as  $\ell_\alpha H_u = \epsilon_{\rho\sigma} \ell_\alpha^\rho H_u^\sigma$  with  $\epsilon_{12} = +1$ .

Originally, the issue of MSSM leptogenesis was approached in conjunction with SM leptogenesis [49, 51] as well as in dedicated studies [146, 147]. However in this first analysis, several features that are specific of SUSY in the high temperature regime relevant for leptogenesis, in which soft SUSY breaking parameters can be effectively set to zero, had been overlooked. In that case, in spite of the large amount of new reactions, the differences between SM and MSSM leptogenesis can be resumed by means of simple counting of a few numerical factors [109, 130, 148], like, for example, the number of relativistic degrees of freedom in the thermal bath, the number of loop diagrams contributing to the CP asymmetries, and the



multiplicities of the final states in the decays of the heavy neutrinos and sneutrinos, and one can estimate [109]

$$\frac{Y_{\Delta B}(\infty)^{\text{MSSM}}}{Y_{\Delta B}(\infty)^{\text{SM}}} \approx \begin{cases} \sqrt{2} & (\text{strong washout}), \\ 2\sqrt{2} & (\text{weak washout}). \end{cases} \quad (5.2)$$

Recently it was pointed out in [89] that in fact MSSM leptogenesis is rich in new and nontrivial features, and genuinely different from the simpler realization within the SM. The two important effects are as follows.

- (a) If the SUSY breaking scale does not exceed by much 1 TeV, above  $T \sim 5 \times 10^7$  GeV the particle and superparticle density asymmetries do not equilibrate [149], and it is mandatory to account in the BE for the differences in the number density asymmetries of the boson and fermion degrees of freedom. This can be given in terms of a nonvanishing gaugino chemical potential.
- (b) When soft SUSY breaking parameters are neglected, additional anomalous global symmetries that involve both  $SU(2)_L$  and  $SU(3)_C$  fermion representations emerge [150]. As a consequence, the EW and QCD sphaleron equilibrium conditions are modified with respect to the SM, and this yields a different pattern of sphaleron-induced lepton-flavour mixing [67, 69, 70]. In addition, a new anomaly-free exactly conserved  $\mathcal{R}$ -symmetry provides an additional constraint that is not present in the SM, and a careful counting reveals that *four* independent quantities, rather than the *three* of the SM case, are required to give a complete description of the various particle asymmetries in the thermal bath, with the additional quantity corresponding to the number density asymmetry of the heavy scalar neutrinos.

Although the modifications above are interesting from the theoretical point of view, a quantitative comparison with the results obtained when the new effects are ignored shows that the corrections remain below  $\mathcal{O}(1)$  [89]. (This modification would be important for certain supersymmetric leptogenesis scenarios which contain new sources of CP violation e.g. soft leptogenesis (see Section 6.2).) Finally, it should be pointed out that in the supersymmetric case, the temperature in which the lepton flavour effects (see Section 3) come into play is enhanced by a factor of  $(1 + \tan^2 \beta)$  since the charged Yukawa couplings are given by  $h_\alpha = m_\alpha / (v_u \cos \beta)$ .

The purpose of the following sections is twofold. We describe the chemical equilibrium conditions and conservation laws for MSSM in conjunction to SM. In Section 5.2 we list the constraints that hold independently of assuming a regime in which particle and sparticle chemical potentials equilibrate (superequilibration (SE) regime) or do not equilibrate (nonsuperequilibration (NSE) regime). In Section 5.3 we list the constraints that hold only in the SE regime and in Section 5.4 the ones that hold in NSE regime. The question of NSE is irrelevant in the SM since there are no superparticles. Hence the parts relevant for the SM are Sections 5.2 and 5.3, with the chemical potential of the gaugino set to zero, the chemical potential of the down-type higgsino replaced by the minus of the up-type higgsino (see (5.11) and (5.12)), and all the quantities related to superparticles replaced by the ones for particles.

## 5.2. General Constraints

We first list in items (1), (2), and (3) the conditions that hold in the whole temperature range  $M_W = T \lesssim 10^{14}$  GeV. Conversely, some of the Yukawa coupling conditions given in items (4) and (5) will have to be dropped as the temperature is increased and the corresponding reactions go out of equilibrium. First we will relate the number density asymmetry of a particle  $\Delta n \equiv n - \bar{n}$  for which a chemical potential can be defined to its chemical potential. For both bosons ( $b$ ) and fermions ( $f$ ) this relation acquires a particularly simple form in the relativistic limit  $m_{b,f} \ll T$ , and at first order in the chemical potential  $\mu_{b,f}/T \ll 1$ :

$$\Delta n_b = \frac{g_b}{3} T^2 \mu_b, \quad \Delta n_f = \frac{g_f}{6} T^2 \mu_f. \quad (5.3)$$

For simplicity of notations, in the following we denote the chemical potentials with the same notation that labels the corresponding field:  $\phi \equiv \mu_\phi$ .

- (1) At scales much higher than  $M_W$ , gauge fields have vanishing chemical potential  $W = B = g = 0$  [57]. This also implies that all the particles belonging to the same  $SU(2)_L$  or  $SU(3)_C$  multiplets have the same chemical potential. For example  $\phi(I_3 = +1/2) = \phi(I_3 = -1/2)$  for a field  $\phi$  that is a doublet of weak isospin  $\bar{I}$ , and similarly for color.
- (2) Denoting by  $\widetilde{W}_R, \widetilde{B}_R$ , and  $\widetilde{g}_R$  the RH winos, binos, and gluinos chemical potentials and by  $\ell, Q$  ( $\tilde{\ell}, \tilde{Q}$ ) the chemical potentials of the (s)lepton and (s)quarks LH doublets, the following reactions:  $\tilde{Q} + \widetilde{g}_R \rightarrow Q$ ,  $\tilde{Q} + \widetilde{W}_R \rightarrow Q$ ,  $\tilde{\ell} + \widetilde{W}_R \rightarrow \ell$ ,  $\tilde{\ell} + \widetilde{B}_R \rightarrow \ell$ , imply that all gauginos have the same chemical potential:  $-\widetilde{g} = Q - \tilde{Q} = -\widetilde{W} = \ell - \tilde{\ell} = -\widetilde{B}$ , where  $\widetilde{W}, \widetilde{B}$ , and  $\widetilde{g}$  denote the chemical potentials of LH gauginos. It follows that the chemical potentials of the SM particles are related to those of their respective superpartners as

$$\begin{aligned} \tilde{Q}, \tilde{\ell} &= Q, \ell + \widetilde{g}, \\ H_{u,d} &= \widetilde{H}_{u,d} + \widetilde{g}, \\ \tilde{u}, \tilde{d}, \tilde{e} &= u, d, e - \widetilde{g}. \end{aligned} \quad (5.4)$$

The last relation, in which  $u, d, e \equiv u_R, d_R, e_R$  denote the RH  $SU(2)_L$  singlets, follows, for example, from  $\tilde{u}_L^c = u_L^c + \widetilde{g}$  for the corresponding LH fields, together with  $u_L^c = -u_R$ , and from the analogous relation for the  $SU(2)_L$  singlet squarks.

- (3) Before EW symmetry breaking hypercharge is an exactly conserved quantity, and we can assume a vanishing total hypercharge for the Universe:

$$\sum_i (Y_{\Delta Q_i} + 2Y_{\Delta u_i} - Y_{\Delta d_i}) - \sum_\alpha (Y_{\Delta \ell_\alpha} + Y_{\Delta e_\alpha}) + Y_{\Delta \widetilde{H}_u} - Y_{\Delta \widetilde{H}_d} = 0. \quad (5.5)$$

- (4) When the reactions mediated by the lepton Yukawa couplings are faster than the Universe expansion rate (see Section 3.1 for the temperature regime when

lepton Yukawa interactions are in thermal equilibrium), the following chemical equilibrium conditions are enforced:

$$\ell_\alpha - e_\alpha + \widetilde{H}_d + \widetilde{g} = 0, \quad (\alpha = e, \mu, \tau). \quad (5.6)$$

If the temperature is not too low lepton flavour equilibration (see Section 3.4) induced by off-diagonal slepton soft masses will not occur. We assume that this is the case, and thus we take the three  $\ell_\alpha$  to be independent quantities.

- (5) Reactions mediated by the quark Yukawa couplings enforce the following six chemical equilibrium conditions:

$$Q_i - u_i + \widetilde{H}_u + \widetilde{g} = 0, \quad (u_i = u, c, t), \quad (5.7)$$

$$Q_i - d_i + \widetilde{H}_d + \widetilde{g} = 0, \quad (d_i = d, s, b). \quad (5.8)$$

The upquark Yukawa coupling maintains chemical equilibrium between the LH and RH up-type quarks up to  $T \sim 2 \cdot 10^6$  GeV. Note that when the Yukawa reactions of at least two families of quarks are in equilibrium, the mass basis is fixed for all the quarks and squarks. Intergeneration mixing then implies that family-changing charged-current transitions are also in equilibrium:  $b_L \rightarrow c_L$  and  $t_L \rightarrow s_L$  imply  $Q_2 = Q_3$ ;  $s_L \rightarrow u_L$  and  $c_L \rightarrow d_L$  imply  $Q_1 = Q_2$ . Thus, up to temperatures  $T \lesssim 10^{11}$  GeV, that are of the order of the equilibration temperature for the charm Yukawa coupling, the three quark doublets have the same chemical potential:

$$Q \equiv Q_3 = Q_2 = Q_1. \quad (5.9)$$

At higher temperatures, when only the third family is in equilibrium, we have instead  $Q \equiv Q_3 = Q_2 \neq Q_1$ . Above  $T \sim 10^{13}$  when (for moderate values of  $\tan \beta$ ) also  $b$ -quark (as well as the  $\tau$ -lepton)  $SU(2)_L$  singlets decouple from their Yukawa reactions, all intergeneration mixing becomes negligible and  $Q_3 \neq Q_2 \neq Q_1$ .

### 5.3. Superequilibration Regime

At relatively low temperatures, additional conditions from reactions in chemical equilibrium hold. Since the constraints below apply only in the SE regime, we number them including this label.

$6_{SE}$  : Equilibration of the particle-sparticle chemical potentials  $\mu_\phi = \mu_{\widetilde{\phi}}$  [149] is ensured when reactions like  $\widetilde{\ell}\widetilde{\ell} \rightarrow \ell\ell$  are faster than the Universe expansion rate. These reactions are induced by gaugino interactions, but since they require a gaugino chirality flip, they turn out to be proportional to its mass  $m_{\widetilde{g}}$  and can be neglected in the limit  $m_{\widetilde{g}} \rightarrow 0$ .

Furthermore, since the  $\mu$  parameter of the  $H_u H_d$  superpotential term is expected to be of the order of the soft gaugino masses, it is reasonable to consider in the same temperature range also the effect of the higgsino mixing term, which implies that

the sum of the up- and downhiggsino chemical potentials vanishes. The rates of the corresponding reactions, given approximately by  $\Gamma_{\tilde{g}} \sim m_{\tilde{g}}^2/T$  and  $\Gamma_{\mu} \sim \mu^2/T$ , are faster than the Universe expansion rate up to temperatures

$$T \lesssim 5 \cdot 10^7 \left( \frac{m_{\tilde{g}}, \mu}{500 \text{ GeV}} \right)^{2/3} \text{ GeV}. \quad (5.10)$$

The corresponding chemical equilibrium relations enforce the conditions:

$$\tilde{g} = 0, \quad (5.11)$$

$$\widetilde{H}_u + \widetilde{H}_d = 0. \quad (5.12)$$

$7_{\text{SE}}$  : Up to temperatures given by (5.10) the MSSM has the same global anomalies than the SM, that are the EW  $\text{SU}(2)_L$ - $\text{U}(1)_{B+L}$  mixed anomaly and the QCD chiral anomaly. They generate the effective operators  $O_{\text{EW}} = \Pi_{\alpha}(QQQ\ell_{\alpha})$  [151] and  $O_{\text{QCD}} = \Pi_i(QQu_{Li}^c d_{Li}^c)$  [151–153]. Above the EW phase transition reactions induced by these operators are in thermal equilibrium, and the corresponding conditions read

$$9Q + \sum_{\alpha} \ell_{\alpha} = 0, \quad (5.13)$$

$$6Q - \sum_i (u_i + d_i) = 0, \quad (5.14)$$

where we have used the same chemical potential for the three quark doublets (5.9), which is always appropriate in the SE regime below the limit (5.10).

Equations (5.6), (5.7)–(5.9), together with the SE conditions (5.11)–(5.12), the two anomaly conditions (5.13)–(5.14), and the hypercharge neutrality condition equation (5.5), give  $11 + 2 + 2 + 1 = 16$  constraints for the 18 chemical potentials. Note however that there is one redundant constraint, that we take to be the QCD sphaleron condition, since by summing up (5.7) and (5.8) and taking into account (5.9), (5.11), and (5.12), we obtain precisely (5.14). Therefore, like in the SM, we have three independent chemical potentials. We can define three linear combinations of the chemical potentials corresponding to the  $\text{SU}(2)_L$  anomaly free flavour charges  $\Delta_{\alpha} \equiv B/3 - L_{\alpha}$  that being anomaly-free and perturbatively conserved by the low energy MSSM Lagrangian evolve *slowly* because the corresponding symmetries are violated only by the heavy Majorana neutrino dynamics. Their evolution needs to be computed by means of three independent BEs. In terms of the abundances (2.12) the density of the  $\Delta_{\alpha}$  charges normalized to the entropy density can be written as

$$Y_{\Delta_{\alpha}} = 3 \left[ \frac{1}{3} \sum_i (2Y_{\Delta Q_i} + Y_{\Delta u_i} + Y_{\Delta d_i}) - (2Y_{\Delta \ell_{\alpha}} + Y_{\Delta e_{\alpha}}) - \frac{2}{3} Y_{\Delta \tilde{g}} \right]. \quad (5.15)$$

The expression above is completely general and holds in all temperature regimes, including the NSE regime (see Section 5.4).



The density asymmetries of the doublet leptons and higgsinos, that weight the washout terms in the BE, can now be expressed in terms of the anomaly-free charges by means of the  $A$  matrix and  $C$  vectors introduced, respectively, in [67, 69] that are defined as:

$$Y_{\Delta\ell_\alpha} = A_{\alpha\beta}^\ell Y_{\Delta\beta}, \quad Y_{\Delta\widetilde{H}_{u,d}} = C_\alpha^{\widetilde{H}_{u,d}} Y_{\Delta\alpha}. \quad (5.16)$$

Here and in the following we will give results for the  $A$  and  $C$  matrices for the fermion states. We recall that in the SE regime the density asymmetry of a scalar boson that is in chemical equilibrium with its fermionic partner is given simply by  $Y_{\Delta b} = 2Y_{\Delta f}$  with the factor of 2 from statistics.

### 5.3.1. First Generation Yukawa Reactions out of Equilibrium (SE Regime)

As an example let us now consider the temperatures  $T \gtrsim 4 \cdot 10^6 (1 + \tan^2 \beta) \text{ GeV}$ , when the  $d$ -quark Yukawa coupling can be set to zero (in order to remain within the SE regime we assume  $\tan \beta \sim 1$ ). In this case the equilibrium dynamics is symmetric under the exchange  $u \leftrightarrow d$  (both chemical potentials enter only the QCD sphaleron condition equation (5.14) with equal weights) and so must be any physical solution of the set of constraints. Thus, the first condition in (5.8) can be replaced by the condition  $d = u$ , and again three independent quantities suffice to determine all the particle density asymmetries. The corresponding result is

$$A^\ell = \frac{1}{3 \times 2148} \begin{pmatrix} -906 & 120 & 120 \\ 75 & -688 & 28 \\ 75 & 28 & -688 \end{pmatrix}, \quad C^{\widetilde{H}_u} = -C^{\widetilde{H}_d} = \frac{-1}{2148} (37, 52, 52). \quad (5.17)$$

Note that since in this regime the chemical potentials for the scalar and fermion degrees of freedom of each chiral multiplet equilibrate, the analogous results for  $Y_{\Delta\ell_\alpha} + Y_{\Delta\widetilde{\ell}_\alpha}$  can be obtained by simply multiplying the  $A$  matrix in (5.17) by a factor of 3. This gives the same  $A$  matrix obtained in the nonsupersymmetric case in the same regime (see, e.g., (4.12) in [69]). The  $C$  matrix (multiplied by the same factor of 3) differs from the nonsupersymmetric result by a factor 1/2. This is because after substituting  $\widetilde{H}_d = -\widetilde{H}_u$  (see (5.12)) all the chemical potential conditions are formally the same than in the SM with  $\widetilde{H}_u$  identified with the chemical potential of the scalar Higgs, but since  $C$  expresses the result for number densities, in the SM, a factor of 2 from boson statistics appears for the SM Higgs. This agrees with the analysis in [58] and is a general result that holds for SUSY within the SE regime.

## 5.4. Nonsuperequilibration Regime

At temperatures above the limit given in (5.10) the Universe expansion is fast enough that reactions induced by  $m_{\widetilde{g}}$  and  $\mu$  do not occur. Setting to zero in the high temperature effective theory these two parameters has the following consequences

- (i) Condition equation (5.11) has to be dropped, and gauginos acquire a nonvanishing chemical potential  $\widetilde{g} \neq 0$  (corresponding to the difference between the number of LH and RH helicity states). The chemical potentials of the members of the same

matter supermultiplets are no more equal (nonsuperequilibration) but related as in (5.4).

- (ii) Condition (5.12) also has to be dropped, and the chemical potentials of the up- and down-type Higgs and higgsinos do not necessarily sum up to zero.
- (iii) The MSSM gains two new global symmetries:  $m_{\tilde{g}} \rightarrow 0$  yields a global  $R$ -symmetry, while  $\mu \rightarrow 0$  corresponds to a global symmetry of the Peccei-Quinn (PQ) type.

#### 5.4.1. Anomalous and Nonanomalous Symmetries

Two linear combinations  $R_2$  and  $R_3$  of  $R$  and PQ, having, respectively, only  $SU(2)_L$  and  $SU(3)_C$  mixed anomalies, have been identified in [150]:

$$R_2 = R - 2PQ, \quad R_3 = R - 3PQ. \quad (5.18)$$

The authors of [150] have also constructed the effective multifermions operators generated by the mixed anomalies:

$$\tilde{O}_{EW} = \Pi_{\alpha}(QQQ\ell_{\alpha})\widetilde{H}_u\widetilde{H}_d\widetilde{W}^4, \quad (5.19)$$

$$\tilde{O}_{QCD} = \Pi_i(QQu^c d^c)_i \tilde{g}^6. \quad (5.20)$$

Given that three global symmetries  $B$ ,  $L$ , and  $R_2$  have mixed  $SU(2)_L$  anomalies (but are free of  $SU(3)_C$  anomalies) we can construct two anomaly-free combinations, the first one being  $B - L$  which is only violated perturbatively by  $N^c \ell H_u$  and the second anomaly free combination which is also an exact symmetry of the MSSM+seesaw in the NSE regime [89]:

$$\mathcal{R} = \frac{5}{3}B - L + R_2, \quad (5.21)$$

and is exactly conserved. In the  $SU(3)_C$  sector, besides the chiral anomaly we now have also  $R_3$  mixed anomalies. Thus also in this case anomaly-free combinations can be constructed, and in particular we can define one combination for each quark superfield. Assigning to the LH supermultiplets chiral charge  $\chi = -1$  these combinations have the form [89]:

$$\chi_{q_L} + \kappa_{q_L} R_3, \quad (5.22)$$

where, for example,  $\kappa_{u_L^c} = \kappa_{d_L^c} = 1/3$  and  $\kappa_{Q_L} = 2/3$ . Note that since  $R_3$  is perturbatively conserved by the complete MSSM+seesaw Lagrangian, when the Yukawa coupling of one quark is set to zero, the corresponding charge (5.22) will be exactly conserved.

#### 5.4.2. Constraints in the Nonsuperequilibration Regime

In the NSE regime, the conditions listed in items 6<sub>SE</sub> and 7<sub>SE</sub> of the previous section have to be dropped, but new conditions arise.

6<sub>NSE</sub>: The conservation law for the  $\mathcal{R}$  charge yields the following global neutrality condition:

$$\begin{aligned}\mathcal{R}_{\text{tot}} &= \sum_f \Delta n_f \mathcal{R}_f + \sum_b \Delta n_b \mathcal{R}_b + \Delta n_{\widetilde{N}_1} \mathcal{R}_{\widetilde{N}_1} \\ &= \frac{T^2}{6} \left( \sum_i (2Q_i - 5u_i + 4d_i) + 2 \sum_\alpha (\ell_\alpha + e_\alpha) + 5\widetilde{H}_d - \widetilde{H}_u + 31\widetilde{g} \right) - \Delta n_{\widetilde{N}_1} = 0.\end{aligned}\quad (5.23)$$

The last terms in both lines of (5.23) correspond to the contribution to  $\mathcal{R}$ -neutrality from the lightest sneutrino asymmetry  $\Delta n_{\widetilde{N}_1} = n_{\widetilde{N}_1} - n_{\widetilde{N}_1^*}$  with charge  $\mathcal{R}_{\widetilde{N}_1} = -\mathcal{R}_{\widetilde{N}_1^*} = -1$ . Note that since in general  $\widetilde{N}_1$  is not in chemical equilibrium, no chemical potential can be associated to it, and hence this constraint needs to be formulated in terms of its number density asymmetry that has to be evaluated by solving a BE for  $Y_{\Delta_{\widetilde{N}}} \equiv Y_{\widetilde{N}_1} - Y_{\widetilde{N}_1^*}$  (see Section 5.5).

7<sub>NSE</sub>: The operators in (5.19) induce transitions that in the NSE regime are in chemical equilibrium. This enforces the generalized EW and QCD sphaleron equilibrium conditions [150]:

$$\begin{aligned}3 \sum_i Q_i + \sum_\alpha \ell_\alpha + \widetilde{H}_u + \widetilde{H}_d + 4\widetilde{g} &= 0, \\ 2 \sum_i Q_i - \sum_i (u_i + d_i) + 6\widetilde{g} &= 0,\end{aligned}\quad (5.24)$$

that replace (5.13) and (5.14).

8<sub>NSE</sub>: The chiral- $R_3$  charges in (5.22) are anomaly-free, but clearly they are not conserved by the quark Yukawa interactions. However, when a quark supermultiplet decouples from its Yukawa interactions, an exact conservation law arises. (Note that  $h_{u,d} \rightarrow 0$  implies  $u$  and  $d$  decoupling, but  $Q_1$  decoupling is ensured only if also  $h_{c,s} \rightarrow 0$ .) The conservation laws corresponding to these symmetries read

$$\frac{T^2}{6} [3q_R + 6(q_R - \widetilde{g})] + \frac{1}{3} R_{3\text{tot}} = 0, \quad (5.25)$$

$$\frac{T^2}{6} [3Q_L + 6(Q_L + \widetilde{g})] - \frac{2}{3} R_{3\text{tot}} = 0 \quad (5.26)$$

and hold for  $q_R = u_i, d_i$  and  $Q_L = Q_i$  in the regimes when the appropriate Yukawa reactions are negligible. Note the factor of 2 for the  $Q_L$  chiral charge in front of

the first square bracket in (5.26) that is due to  $SU(2)_L$  gauge multiplicity. In terms of chemical potentials and  $\Delta n_{\widetilde{N}_1}$ , the total  $R_3$  charge in (5.25) and (5.26) reads

$$R_{3\text{tot}} = \frac{T^2}{6} \left( 82\tilde{g} - 3 \sum_i (2Q_i + 11u_i - 4d_i) + \sum_\alpha (16\ell_\alpha + 13e_\alpha) + 16\widetilde{H}_d - 14\widetilde{H}_u \right) + \Delta n_{\widetilde{N}_1} R_{3\widetilde{N}_1}, \quad (5.27)$$

where  $R_{3\widetilde{N}_1} = -1$ . As regards the leptons, since they do not couple to the QCD anomaly, by setting  $h_e \rightarrow 0$ , a symmetry under chiral supermultiplet rotations is directly gained for the RH leptons implying  $\Delta n_e + \Delta \tilde{n}_e = 0$  and giving the condition:

$$e - \frac{2}{3}\tilde{g} = 0. \quad (5.28)$$

No analogous condition arises for the lepton doublets relevant for leptogenesis, since by assumption they remain coupled via Yukawa couplings to the heavy  $N$ 's.

In the NSE regime there are different flavour mixing matrices for the scalar and fermion components of the leptons and Higgs supermultiplets. To express more concisely all the results, it is convenient to introduce a new  $C$  vector to describe the gaugino number density asymmetry per degree of freedom in terms of the relevant charges:

$$Y_{\Delta\tilde{g}} = C_a^{\tilde{g}} Y_{\Delta_a}, \quad \text{with} \quad \Delta_a = (\Delta_\alpha, \Delta_{\widetilde{N}}). \quad (5.29)$$

#### 5.4.3. First Generation Yukawa Reactions out of Equilibrium (NSE Regime)

As an example, in the temperature range between  $10^8$  and  $10^{11}$  GeV, and for moderate values of  $\tan\beta$ , all the first generation Yukawa couplings can be set to zero. Using for  $u, d$  conditions equation (5.25) and for  $e$  condition equation (5.28) as implied by  $h_{u,d}, h_e \rightarrow 0$  we obtain

$$\begin{aligned} A^\ell &= \frac{1}{9 \times 162332} \begin{pmatrix} -198117 & 33987 & 33987 & -8253 \\ 26634 & -147571 & 14761 & -8055 \\ 26634 & 14761 & -147571 & -8055 \end{pmatrix}, \\ C^{\tilde{g}} &= \frac{-11}{162332} (163, 165, 165, -255), \\ C^{\widetilde{H}_u} &= \frac{-1}{162332} (3918, 4713, 4713, 95), \\ C^{\widetilde{H}_d} &= \frac{1}{3 \times 162332} (5413, 9712, 9712, -252), \end{aligned} \quad (5.30)$$

where the rows correspond to  $(Y_{\Delta_e}, Y_{\Delta_\mu}, Y_{\Delta_\tau}, Y_{\Delta_{\widetilde{N}}})$ . For completeness, in (5.30) we have also given the results for  $C^{\widetilde{H}_d}$  even if only the up-type Higgs density asymmetry is relevant for the



leptogenesis processes. Note that neglecting the contribution of  $\Delta n_{\tilde{N}_1}$  to the global charges  $\mathcal{R}_{\text{tot}}$  in (5.23) and  $R_{3\text{tot}}$  in (5.27) corresponds precisely to setting to zero the fourth column in all the previous matrices. Then, analogously with the SE and SM cases, within this “3-column approximation” all particle density asymmetries can be expressed just in terms of the three  $Y_{\Delta_a}$  charge densities.

### 5.5. Supersymmetric Boltzmann Equations

In order to illustrate how the new effects described above modify the structure of the BE, here we write down a simpler expressions in which only decays and inverse decays are included: (the complete set of BE including decays, inverse decays, and scatterings with top-quark is given in the Appendix of [89].)

$$sHz \frac{dY_{N_1}}{dz} = - \left( \frac{Y_{N_1}}{Y_{N_1}^{\text{eq}}} - 1 \right) \gamma_{N_1}, \quad (5.31)$$

$$sHz \frac{dY_{\tilde{N}_+}}{dz} = - \left( \frac{Y_{\tilde{N}_+}}{Y_{\tilde{N}_1}^{\text{eq}}} - 2 \right) \gamma_{\tilde{N}_1}, \quad (5.32)$$

$$sHz \frac{dY_{\Delta_{\tilde{N}}}}{dz} = - \frac{Y_{\Delta_{\tilde{N}}}}{Y_{\tilde{N}_1}^{\text{eq}}} \gamma_{\tilde{N}_1} - \frac{3}{2} \gamma_{\tilde{N}_1} \sum_a C_a^{\tilde{g}} \frac{Y_{\Delta_a}}{Y_{\ell}^{\text{eq}}} + \dots, \quad (5.33)$$

$$\begin{aligned} sHz \frac{dY_{\Delta_a}}{dz} = & -\epsilon_a \left[ \left( \frac{Y_{N_1}}{Y_{N_1}^{\text{eq}}} - 1 \right) \gamma_{N_1} + \left( \frac{Y_{\tilde{N}_+}}{Y_{\tilde{N}_1}^{\text{eq}}} - 2 \right) \gamma_{\tilde{N}_1} \right] \\ & + P_{1a}^0 \left( \gamma_{N_1} + \frac{1}{2} \gamma_{\tilde{N}_1} \right) \sum_a \left( A_{aa}^{\ell} + C_a^{\tilde{H}_u} + C_a^{\tilde{g}} \right) \frac{Y_{\Delta_a}}{Y_{\ell}^{\text{eq}}}, \end{aligned} \quad (5.34)$$

where  $\gamma_{\tilde{N}_1}$  is the corresponding thermally averaged decay rate for RH sneutrino  $\tilde{N}_1$ . In (5.32) we have introduced the overall sneutrino abundance  $Y_{\tilde{N}_+} = Y_{\tilde{N}_1} + Y_{\tilde{N}_1^*}$ , while  $Y_{\Delta_{\tilde{N}}} \equiv Y_{\tilde{N}_1} - Y_{\tilde{N}_1^*}$  in (5.33) is the sneutrino density asymmetry that was already introduced in Section 5.4. In the washout terms we have normalized the charge densities  $Y_{\Delta_a} = (Y_{\Delta_a}, Y_{\Delta_{\tilde{N}}})$  to the equilibrium density of a fermion with one degree of freedom  $Y_{\ell}^{\text{eq}}$ . In (5.31) and (5.34) we have also neglected for simplicity all finite temperature effects. Taking these effects into account would imply, for example, that the CP asymmetry for  $\tilde{N}$  decays into fermions is different from the one for decays into scalars [49], while we describe both CP asymmetries with  $\epsilon_a$ . A few remarks regarding (5.33) are in order. In the SE regime  $\tilde{g} = 0$ , and thus it would seem that the sneutrino density asymmetry  $Y_{\Delta_{\tilde{N}}}$  vanishes. However, this only happens for decays and inverse decays, and it is no more true when additional terms related to scattering processes, that are represented in the equation by the dots, are also included (see [147] and the Appendix of [89]). Therefore, also in the SE regime  $Y_{\tilde{N}_1}$  and  $Y_{\tilde{N}_1^*}$  in general differ. However, in this case recasting their equations in terms of two equations for  $Y_{\tilde{N}_+}$  and  $Y_{\Delta_{\tilde{N}}}$  is just a convenient parametrization. On the contrary, in the NSE regime this is mandatory, because the sneutrinos carry a globally conserved  $\mathcal{R}$ -charge and  $Y_{\Delta_{\tilde{N}}}$  is required to formulate properly the corresponding conservation law. As we have seen, this eventually results in  $Y_{\Delta_{\tilde{N}}}$

contributing to the expressions of the lepton flavour density asymmetries in terms of slowly varying quantities.

In [89] a complete numerical analysis was carried out, and it was shown that numerical corrections with respect to the case when NSE effects are neglected remain at the  $\mathcal{O}(1)$  level. This is because only spectator processes get affected, while the overall amount of CP violation driving leptogenesis remains the same than in previous treatments.

## 6. Beyond Type-I Seesaw and Beyond the Seesaw

There exist many variants of leptogenesis models beyond the standard type-I seesaw. In this section, we try to classify them into appropriate groups. Unavoidably there would be some overlap; that is, a hybrid model of leptogenesis which can belong to more than one group, for example, soft leptogenesis (Section 6.2) from resonantly enhanced CP asymmetry could rightly fall under resonant leptogenesis (Section 6.1). However we try our best to categorize them according to the main features of the model, and, when appropriate, they will be quoted in more than one place. Clearly, the number of beyond type-I seesaw leptogenesis models is quite large. We have not attempted in any way to be exhaustive, and we apologize in advance for the unavoidable several omissions.

### 6.1. Resonant Leptogenesis

A resonant enhancement of the CP asymmetry in  $N_1$  decay occurs when the mass difference between  $N_1$  and  $N_2$  is of the order of the decay widths. Such a scenario has been termed “resonant leptogenesis,” and has benefited from many studies in different formalisms (see [154] for a comparison of the different calculations) [50, 52, 75, 85–87, 110, 111, 155–168] (see [169] for a recent review). The resonant effect is related to the self-energy contribution to the CP asymmetry. Consider, for simplicity, the case where only  $N_2$  is quasidegenerate with  $N_1$ . Then, the self-energy contribution involving the intermediate  $N_2$  to the total CP asymmetry (we neglect important flavour effects [75]) is given by

$$\epsilon_1(\text{self-energy}) = -\frac{M_1}{M_2} \frac{\Gamma_{N_2}}{M_2} \frac{M_2^2(M_2^2 - M_1^2)}{(M_2^2 - M_1^2)^2 + M_1^2 \Gamma_{N_2}^2} \frac{\text{Im}[(\lambda^\dagger \lambda)_{12}^2]}{(\lambda^\dagger \lambda)_{11}(\lambda^\dagger \lambda)_{22}}. \quad (6.1)$$

The resonance condition reads

$$|M_2 - M_1| = \frac{\Gamma_{N_2}}{2}. \quad (6.2)$$

In this case

$$|\epsilon_1(\text{resonance})| \simeq \frac{1}{2} \frac{|\text{Im}[(\lambda^\dagger \lambda)_{12}^2]|}{(\lambda^\dagger \lambda)_{11}(\lambda^\dagger \lambda)_{22}}. \quad (6.3)$$

Thus, in the resonant case, the asymmetry is suppressed by neither the smallness of the light neutrino masses, nor the smallness of their mass splitting, nor small ratios between the

singlet neutrino masses. Actually, the CP asymmetry could be of order one (more accurately,  $|\epsilon_1| \leq 1/2$ ).

With resonant leptogenesis, the BEs are different. The densities of  $N_1$  and  $N_2$  are followed, since both contribute to the asymmetry, and the relevant timescales are different. For instance, the typical timescale to build up coherently the CP asymmetry is unusually long, of order  $1/\Delta M$ . In particular, it can be larger than the timescale for the change of the abundance of the sterile neutrinos. This situation implies that for resonant leptogenesis quantum effects in the BE can be significant [85, 86, 141, 170] (see Section 4.5).

The fact that the asymmetry could be large, independently of the singlet neutrino masses, opens up the possibility of low scale resonant leptogenesis. Models along these lines have been constructed in [75, 156, 161, 171]. It is a theoretical challenge to construct models where a mass splitting as small as the decay width is naturally achieved. For attempts that utilize approximate flavour symmetries see, for example, [157, 158, 160, 164, 166, 172], while studies of this issue in the framework of minimal flavour violation can be found in [87, 162, 163]. The possibility of observing resonant CP violation due to heavy RH neutrinos at the LHC was studied in [173, 174].

## 6.2. Soft Leptogenesis

The modifications to standard type-I leptogenesis due to SUSY have been discussed in Section 5. The important parameters are the Yukawa couplings and the singlet neutrino parameters, which appear in the superpotential equation (5.1). SUSY must, however, be broken. In the framework of the MSSM extended to include singlet neutrinos (MSSM+N), there are, in addition to the soft SUSY breaking terms of the MSSM, terms that involve the singlet sneutrinos  $\widetilde{N}_i$ , in particular bilinear ( $B$ ) and trilinear ( $A$ ) scalar couplings. These terms provide additional sources of lepton number violation and of CP violation. Scenarios where these terms play a dominant role in leptogenesis have been termed “soft leptogenesis” [102, 107, 175–196] (see also [54] for a recent review).

Soft leptogenesis can take place even with a single RH neutrino because the presence of the  $B$  term implies that  $\widetilde{N}$  and  $\widetilde{N}^\dagger$  states mix to form two mass eigenstates with mass splitting proportional to  $B$  itself. Furthermore when  $B \sim \Gamma_{\widetilde{N}}$ , the CP asymmetry is resonantly enhanced realizing the resonant leptogenesis scenario (see Section 6.1). In the following we will consider a single generation MSSM+N. The relevant soft SUSY terms involving  $\widetilde{N}$ , the  $SU(2)_L$  gauginos  $\widetilde{\lambda}_2^{\pm,0}$ , the  $U(1)_Y$  gauginos  $\widetilde{\lambda}_1$ , and the three sleptons  $\widetilde{\ell}_\alpha$  in the basis in which charged lepton Yukawa couplings are diagonal are given by

$$\begin{aligned} -\mathcal{L}_{\text{soft}} = & \widetilde{M}^2 \widetilde{N}^* \widetilde{N} + \left( AY_\alpha \epsilon_{ab} \widetilde{N} \widetilde{\ell}_\alpha^a H_u^b + \frac{1}{2} BM \widetilde{N} \widetilde{N} + \text{h.c.} \right) \\ & + \frac{1}{2} \left( m_2 \widetilde{\lambda}_2^{\pm,0} P_L \widetilde{\lambda}_2^{\pm,0} + m_1 \widetilde{\lambda}_1 P_L \widetilde{\lambda}_1 + \text{h.c.} \right), \end{aligned} \quad (6.4)$$

where for simplicity, proportionality of the bilinear and trilinear soft breaking terms to the corresponding SUSY invariant couplings has been assumed:  $B_M = BM$  and  $A_\alpha = AY_\alpha$ . The Lagrangian derived from (5.1) and (6.4) is characterized by only three independent physical phases:  $\phi_A \equiv \arg(AB^*)$ ,  $\phi_{g_2} \equiv (1/2) \arg(Bm_2^*)$  and  $\phi_{g_Y} \equiv (1/2) \arg(Bm_1^*)$ , which can be assigned to  $A$  and to the gaugino coupling operators  $g_2, g_Y$ , respectively. As mentioned

earlier, a crucial role in soft leptogenesis is played by the  $\widetilde{N} - \widetilde{N}^\dagger$  mixing to form the mass eigenstates

$$\begin{aligned}\widetilde{N}_+ &= \frac{1}{\sqrt{2}} \left( e^{i\Phi/2} \widetilde{N} + e^{-i\Phi/2} \widetilde{N}^* \right), \\ \widetilde{N}_- &= -\frac{i}{\sqrt{2}} \left( e^{i\Phi/2} \widetilde{N} - e^{-i\Phi/2} \widetilde{N}^* \right),\end{aligned}\tag{6.5}$$

where  $\Phi \equiv \arg(BM)$  and the corresponding mass eigenvalues are  $M_\pm^2 = M^2 + \widetilde{M}^2 \pm |BM|$ . Without loss of generality, we can set  $\Phi = 0$ , which is equivalent to assigning the phases only to  $A$  and  $Y_\alpha$ .

It has been pointed out that the CP asymmetries for the decays of  $\widetilde{N}_\pm$  into scalars and fermions have opposite sign and cancel each other at the leading order [176, 177, 192], resulting in a strongly suppressed total CP asymmetry  $\sim \mathcal{O}(m_{\text{soft}}^3/M^3)$  where  $m_{\text{soft}}$  is the scale of soft SUSY breaking terms. There are two possibilities that can rescue leptogenesis. Firstly, thermal effects which break SUSY can spoil this cancellation [176, 177, 192]. Secondly, nonsuperequilibration effects (see Section 5.4) which imply that lepton and slepton asymmetries differ can also spoil this cancellation [107]. The CP asymmetries for the decays of  $\widetilde{N}_\pm$  into scalars and fermions are, respectively, given by

$$\begin{aligned}e_\alpha^s(T) &= \bar{e}_\alpha \Delta^s(T), \\ e_\alpha^f(T) &= -\bar{e}_\alpha \Delta^f(T),\end{aligned}\tag{6.6}$$

where  $\bar{e}_\alpha$  is the temperature independent term of  $\sim \mathcal{O}(m_{\text{soft}}/M)$  which contains contributions from the self-energy correction, vertex correction, and the interference between the two. In the limit  $T \rightarrow 0$ , we have  $\Delta^s(T), \Delta^f(T) \rightarrow 1/2$ , and thus the inclusion of thermal effects and/or nonsuperequilibration is mandatory to avoid the cancellation between the asymmetries into scalars and fermions.

We can make a rough estimate of the scale relevant for soft leptogenesis by requiring  $|\bar{e}| \sim m_{\text{soft}}/M \gtrsim 10^{-6}$  which gives  $M \lesssim 10^9 \text{ GeV}$  for  $m_{\text{soft}} \sim 1 \text{ TeV}$ . Hence soft leptogenesis always happens in the temperature regime where lepton flavour effects are relevant [190]. In general, the CP asymmetry from self-energy contribution requires  $B \ll m_{\text{soft}}$  to be resonantly enhanced. However it was shown in [195] that flavour effects can greatly enhance the efficiency, and eventually  $B \sim m_{\text{soft}}$  is allowed. The nice feature of soft leptogenesis is that the tension with the gravitino problem gets generically relaxed and, in the lower temperature window, is completely avoided.

### 6.3. Dirac Leptogenesis

The extension of the SM with singlet neutrinos allows for two different ways for generating tiny neutrino masses. The first one is the seesaw mechanism which has at least three attractive features



- (i) No extra symmetries (and, in particular, no global symmetries) have to be imposed.
- (ii) The extreme lightness of neutrino masses is linked to the existence of a high scale of new physics, which is well motivated for various other reasons (e.g., gauge unification).
- (iii) Lepton number is violated, which opens the way to leptogenesis.

The second way is to impose lepton number and give to the neutrinos Dirac masses. A priori, one might think that all three attractive features of the seesaw mechanism are lost. Indeed, one must usually impose additional symmetries. But one can still construct natural models where the tiny Yukawa couplings that are necessary for small Dirac masses are related to a small breaking of a symmetry. What is perhaps most surprising is the fact that leptogenesis could proceed successfully even if neutrinos are Dirac particles, and lepton number is not (perturbatively) broken [197, 198]. Such scenarios have been termed “Dirac leptogenesis” [198–207].

An implementation of the idea is the following. A CP-violating decay of a heavy particle can result in a nonzero lepton number for LH particles and an equal and opposite nonzero lepton number for RH particles, so that the total lepton number is zero. For the charged fermions of the SM, the Yukawa interactions are fast enough that they quickly equilibrate the LH and the RH particles, and the lepton number stored in each chirality goes to zero. This is not true, however, for Dirac neutrinos. The size of their Yukawa couplings is  $\lambda \lesssim 10^{-11}$ , which means that equilibrium between the lepton numbers stored in LH and RH neutrinos will not be reached until the temperature falls well below the electroweak breaking scale. To see this, note that the rate of the Yukawa interactions, given by  $\Gamma_\lambda \sim \lambda^2 T$ , becomes significant when it equals the expansion rate of the Universe,  $H \sim T^2/m_{\text{pl}}$ . Thus, the temperature of equilibration between LH and RH neutrinos is  $T \sim \lambda^2 m_{\text{pl}} \sim (\lambda/10^{-11})^2 \text{ MeV}$ , that is, well below the temperature when sphalerons, after having converted part of the LH lepton asymmetry into a net baryon asymmetry, are switched off.

A specific example of a supersymmetric model where Dirac neutrinos arise naturally is presented in [199]. The Majorana masses of the  $N$ -superfields are forbidden by  $U(1)_L$ . The neutrino Yukawa couplings are forbidden by a  $U(1)_N$  symmetry where, among all the MSSM+N fields, only the  $N$  superfields are charged. The symmetry is spontaneously broken by the vacuum expectation value of a scalar field  $\chi$  that can naturally be at the weak scale,  $\langle \chi \rangle \sim v_u$ . This breaking is communicated to the MSSM+N via extra, vector-like lepton doublet fields,  $\phi + \bar{\phi}$ , that have masses  $M_\phi$  much larger than  $v_u$ . Consequently, the neutrino Yukawa couplings are suppressed by the small ratio  $\langle \chi \rangle / M_\phi$ . The CP violation arises in the decays of the vector-like leptons, whereby  $\Gamma(\phi \rightarrow NH_u^c) \neq \Gamma(\bar{\phi} \rightarrow N^c H_u)$  and  $\Gamma(\phi \rightarrow L\chi) \neq \Gamma(\bar{\phi} \rightarrow L^c \chi^c)$ . The resulting asymmetries in  $N$  and in  $L$  are equal in magnitude and opposite in sign. Finally note that the main phenomenological implication of Dirac leptogenesis is the absence of any signal in neutrinoless double beta decays.

#### 6.4. Triplet Scalar (Type-II) Leptogenesis

One can generate seesaw masses for the light neutrinos by tree-level exchange of  $SU(2)_L$ -triplet scalars  $T$  [44, 208–211]. The relevant new terms in the Lagrangian are

$$\mathcal{L}_T = -M_T^2 |T|^2 + \frac{1}{2} \left( [\lambda_L]_{\alpha\beta} \ell_\alpha \ell_\beta T + M_T \lambda_\phi \phi \phi T^* + \text{h.c.} \right). \quad (6.7)$$

Here,  $M_T$  is a real mass parameter,  $\lambda_L$  is a symmetric  $3 \times 3$  matrix of dimensionless, complex Yukawa couplings, and  $\lambda_\phi$  is a dimensionless complex coupling. Since this mechanism necessarily involves lepton number violation and allows for new CP-violating phases, it is interesting to examine it in the light of leptogenesis [81, 180, 185, 212–233]. One obvious problem in this scenario is that, unlike singlet fermions, the triplet scalars have gauge interactions that keep them close to thermal equilibrium at temperatures  $T \lesssim 10^{15}$  GeV. It turns out, however, that successful leptogenesis is possible even at a much lower temperature. This subsection is based in large part on [220] where further details and, in particular, an explicit presentation of the relevant BE can be found.

The CP asymmetry that is induced by the triplet scalar decays is defined as follows:

$$\epsilon_T \equiv 2 \frac{\Gamma(\bar{T} \rightarrow \ell \ell) - \Gamma(T \rightarrow \bar{\ell} \bar{\ell})}{\Gamma_T + \Gamma_{\bar{T}}}, \quad (6.8)$$

where the overall factor of 2 comes because the triplet scalar decay produces two (anti)leptons.

To calculate  $\epsilon_T$ , one should use the Lagrangian in (6.7). While a single triplet is enough to produce three light massive neutrinos, there is a problem in leptogenesis if indeed this is the only source of neutrinos masses. The asymmetry is generated only at higher loops and is unacceptably small. It is still possible to produce the required lepton asymmetry from a single triplet scalar decays if there are additional sources for neutrino masses, such as type I, type III, or type II contributions from additional triplet scalars. Define  $m_{\text{II}}$  ( $m_{\text{I}}$ ) as the part of the light neutrino mass matrix that comes (does not come) from the contributions of the triplet scalar responsible for  $\epsilon_T$ :

$$m = m_{\text{II}} + m_{\text{I}}. \quad (6.9)$$

Then, assuming that the particles exchanged to produce  $m_{\text{I}}$  are all heavier than  $T$ , we obtain the CP asymmetry

$$\epsilon_T = \frac{1}{4\pi} \frac{M_T}{v_u^2} \sqrt{B_L B_H} \frac{\text{Im}[\text{Tr}(m_{\text{II}}^\dagger m_{\text{I}})]}{\text{Tr}(m_{\text{II}}^\dagger m_{\text{II}})}, \quad (6.10)$$

where  $B_L(B_H)$  is the tree-level branching ratio to leptons (Higgs doublets). If these are the only decay modes, that is,  $B_L + B_H = 1$ , then  $B_L/B_H = \text{Tr}(\lambda_L \lambda_L^\dagger)/(\lambda_H \lambda_H^\dagger)$ , and there is an upper bound on the asymmetry

$$|\epsilon_T| \leq \frac{1}{4\pi} \frac{M_T}{v_u^2} \sqrt{B_L B_H \sum_i m_{\nu_i}^2}. \quad (6.11)$$

Note that, unlike the singlet fermion case,  $|\epsilon_T|$  increases with larger  $m_{\nu_i}$ .

As concerns the efficiency factor, it can be close to maximal,  $\eta \sim 1$ , in spite of the fact that the gauge interactions tend to maintain the triplet abundance very close to thermal

equilibrium. There are two necessary conditions that have to be fulfilled by the decay rates  $T \rightarrow \bar{\ell}\bar{\ell}$  and  $T \rightarrow \phi\phi$  in order that this will happen [220]

- (1) One of the two decay rates is faster than the  $T\bar{T}$  annihilation rate.
- (2) The other decay mode is slower than the expansion rate of the Universe.

The first condition guarantees that gauge scatterings are ineffective: the triplets decay before annihilating. The second condition guarantees that the fast decays do not wash out strongly the lepton asymmetry: lepton number is violated only by the simultaneous presence of  $T \rightarrow \bar{\ell}\bar{\ell}$  and  $T \rightarrow \phi\phi$ .

Combining a calculation of  $\eta$  with the upper bound on the CP asymmetry (6.11), successful leptogenesis implies a lower bound on the triplet mass  $M_T$  varying between  $10^9$  GeV and  $10^{12}$  GeV, depending on the relative weight of  $m_{\text{II}}$  and  $m_{\text{I}}$  in the light neutrino mass.

Interestingly, in the supersymmetric framework, “soft leptogenesis” (see Section 6.2) can be successful even with the minimal set of extra fields—a single  $T + \bar{T}$ —that generates both neutrino masses and the lepton asymmetry [180, 185].

### 6.5. Triplet Fermion (Type-III) Leptogenesis

One can generate neutrino masses by the tree-level exchange of  $\text{SU}(2)_L$ -triplet fermions  $T_i^a$  [234–236] ( $i$  denotes a heavy mass eigenstate while  $a$  is an  $\text{SU}(2)_L$  index) with the Lagrangian

$$\mathcal{L}_{T^a} = [\lambda_T]_{ak} \tau_{\rho\sigma}^a \ell_\alpha^\rho \phi^\sigma T_k^a - \frac{1}{2} M_i T_i^a T_i^a + \text{h.c.} \quad (6.12)$$

Here  $\tau^a$  are the Pauli matrices,  $M_i$  are real mass parameters, and  $\lambda_T$  is a  $3 \times 3$  matrix of complex Yukawa couplings.

This mechanism necessarily involves lepton number violation and allows for new CP-violating phases so we should examine it as a possible source of leptogenesis [228, 237–243]. This subsection is based in large part on [238] where further details and the relevant BE can be found.

As concerns neutrino masses, all the qualitative features are very similar to the singlet fermion case. As concerns leptogenesis there are, however, qualitative and quantitative differences. With regard to the CP asymmetry from the lightest triplet fermion decay, the relative sign between the vertex and self-energy loop contributions is opposite to that of the singlet fermion case. Consequently, in the limit of strong hierarchy in the heavy fermion masses, the asymmetry in triplet decays is three times smaller than in the decays of the singlets. On the other hand, since the triplet has three components, the ratio between the final baryon asymmetry and  $\epsilon\eta$  is three times bigger. The decay rate of the heavy fermion is the same in both cases. This, however, means that the thermally averaged decay rate is three times bigger for the triplet, as is the on-shell part of the  $\Delta L = 2$  scattering rate.

A significant qualitative difference arises from the fact that the triplet has gauge interactions. The effect on the washout factor  $\eta$  is particularly significant for  $\tilde{m} \ll 10^{-3}$  eV, the so-called weak washout regime (note that this name is inappropriate for triplet fermions). The gauge interactions still drive the triplet abundance close to thermal equilibrium. A relic

fraction of the triplet fermions survives. The decays of these relic triplets produce a baryon asymmetry, with

$$\eta \approx M_1/10^{13} \text{ GeV} \quad (\text{for } \tilde{m} \ll 10^{-3} \text{ eV}). \quad (6.13)$$

The strong dependence on  $M_1$  results from the fact that the expansion rate of the Universe is slower at lower temperatures. On the other hand, for  $\tilde{m} \gg 10^{-3} \text{ eV}$ , the Yukawa interactions keep the heavy fermion abundance close to thermal equilibrium, so the difference in  $\eta$  between the singlet and triplet case is only  $\mathcal{O}(1)$ . Ignoring flavour effects, and assuming strong hierarchy between the heavy fermions, [216] obtained the lower bound

$$M_1 \gtrsim 1.5 \times 10^{10} \text{ GeV}. \quad (6.14)$$

When the triplet fermion scenario is incorporated in a supersymmetric framework, and the soft breaking terms do not play a significant role, the modifications to the previous analysis are by factors of  $\mathcal{O}(1)$ .

## 7. Conclusions

During the last few decades, a large set of experiments involving solar, atmospheric, reactor, and accelerator neutrinos have converged to establish that the neutrinos are massive. The seesaw mechanism extends the Standard Model in a way that allows neutrino masses, and it provides a nice explanation of the suppression of the neutrino masses with respect to the electroweak breaking scale. Furthermore, without any addition or modification, it can also account for the observed baryon asymmetry of the Universe. The possibility of giving an explanation of two apparently unrelated experimental facts—neutrino masses and the baryon asymmetry—within a single framework that is a natural extension of the Standard Model, together with the remarkable “coincidence” that the same neutrino mass scale suggested by neutrino oscillation data is also optimal for leptogenesis, makes the idea that baryogenesis occurs through leptogenesis a very attractive one.

Leptogenesis can be quantitatively successful without any fine tuning of the seesaw parameters. Yet, in the nonsupersymmetric seesaw framework, a fine-tuning problem arises due to the large corrections to the mass-squared parameter of the Higgs potential that are proportional to the heavy Majorana neutrino masses. Supersymmetry can cure this problem, avoiding the necessity of fine tuning; however, it brings in the gravitino problem [144] that requires a low reheat temperature after inflation, in conflict with generic leptogenesis models. Thus, constructing a fully satisfactory theoretical framework that implements leptogenesis within the seesaw framework is not a straightforward task.

From the experimental side, the obvious question to ask is if it is possible to test whether the baryon asymmetry has been really produced through leptogenesis. Unfortunately it seems impossible that any direct test can be performed. To establish leptogenesis experimentally, we need to produce the heavy Majorana neutrinos and measure the CP asymmetry in their decays. However, in the most natural seesaw scenarios, these states are simply too heavy to be produced, while if they are light, then their Yukawa couplings must be very tiny, again preventing any chance of direct measurements.



Lacking the possibility of a direct proof, experiments can still provide circumstantial evidence in support of leptogenesis by establishing that (some of) the Sakharov conditions for leptogenesis are realized in nature. Planned neutrinoless double beta decay ( $0\nu\beta\beta$ ) experiments (GERDA [244], MAJORANA [245], and CUORE [246]) aim at a sensitivity to the effective  $0\nu\beta\beta$  neutrino mass in the few  $\times 10$  meV range. If they succeed in establishing the Majorana nature of the light neutrinos, this will strengthen our confidence that the seesaw mechanism is at the origin of the neutrino masses and, most importantly, will establish that the first Sakharov condition for the dynamical generation of a lepton asymmetry ( $L$  violation) is realized. Proposed SuperBeam facilities [247, 248] and second generation off-axis SuperBeam experiments (T2HK [249] and NO $\nu$ A [250]) can discover CP violation in the leptonic sector. These experiments can only probe the Dirac phase of the neutrino mixing matrix. They cannot probe the Majorana low energy or the high energy phases, but the important point is that they can establish that the second Sakharov condition for the dynamical generation of a lepton asymmetry is satisfied. As regards the third condition, that is, that the heavy neutrino decays occurred out of thermal equilibrium, it might seem the most difficult one to test experimentally. In reality the opposite is true, and in fact we already know that an absolute neutrino mass scale of the order of the solar or atmospheric mass differences is perfectly compatible with sufficiently out of equilibrium heavy neutrinos decays.

Given that we do not know how to prove that leptogenesis is the correct theory, we might ask if there is any chance to falsify it. Indeed, future neutrino experiments could weaken the case for leptogenesis, or even falsify it, mainly by establishing that the seesaw mechanism is not responsible for the observed neutrino masses. By itself, failure in revealing signals of  $0\nu\beta\beta$  decays will not disprove leptogenesis. Indeed, with normal neutrino mass hierarchy one expects that the rates of lepton-number-violating processes are below experimental sensitivity. However, if neutrinos masses are quasidegenerate or inversely hierarchical, and future measurements of the oscillation parameters will not fluctuate too much away from the present best fit values, the most sensitive  $0\nu\beta\beta$  decay experiments scheduled for the near future should be able to detect a signal [251]. If instead the limit on  $|m_{\beta\beta}|$  is pushed below  $\sim 10$  meV (a quite challenging task), this would suggest that either the mass hierarchy is normal or neutrinos are not Majorana particles. The latter possibility would disprove the seesaw model and standard leptogenesis. Thus, determining the order of the neutrino mass spectrum is extremely important to shed light on the connection between  $0\nu\beta\beta$  decay experiments and leptogenesis. In summary, if it is established that the neutrino mass hierarchy is inverted and at the same time no signal of  $0\nu\beta\beta$  decays is detected at a level  $|m_{ee}| \lesssim 10$  meV, one could conclude that the seesaw is not at the origin of the neutrino masses and that (standard) leptogenesis is not the correct explanation of the baryon asymmetry. As concerns CP violation, a failure in detecting leptonic CP violation will not weaken the case for leptogenesis in a significant way. Instead, it would mean that the Dirac CP phase is small enough to render  $L$ -conserving CP-violating effects unobservable.

Finally, the CERN LHC has the capability of providing information that is relevant to leptogenesis, since it can play a fundamental role in establishing that the origin of the neutrino masses is not due to the seesaw mechanism, thus leaving no strong motivation for leptogenesis. This may happen in several different ways. For example (assuming that the related new physics is discovered), the LHC will be able to test if the detailed phenomenology of any of the following models is compatible with an explanation of the observed pattern of neutrino masses and mixing angles: supersymmetric  $R$ -parity violating couplings and/or  $L$ -violating bilinear terms [252, 253]; leptoquarks [254, 255]; triplet Higgs [256, 257]; new scalar particles of the type predicted in the Zee-Babu [258, 259] types of models [260–262]. It is

conceivable that such discoveries can eventually exclude the seesaw mechanism and rule out leptogenesis.

## References

- [1] G. Steigman, "Observational tests of antimatter cosmologies," *Annual Review of Astronomy and Astrophysics*, vol. 14, pp. 339–372, 1976.
- [2] A. G. Cohen, A. De Rújula, and S. L. Glashow, "A matter-antimatter universe?" *Astrophysical Journal Letters*, vol. 495, no. 2, pp. 539–549, 1998.
- [3] A. D. Dolgov, "Non-GUT baryogenesis," *Physics Report*, vol. 222, no. 6, pp. 309–386, 1992.
- [4] F. Iocco, G. Mangano, G. Miele, O. Pisanti, and P. D. Serpico, "Primordial nucleosynthesis: from precision cosmology to fundamental physics," *Physics Reports*, vol. 472, no. 1–6, pp. 1–76, 2009.
- [5] G. Steigman, "Primordial nucleosynthesis in the precision cosmology era," *Annual Review of Nuclear and Particle Science*, vol. 57, pp. 463–491, 2007.
- [6] K. Nakamura et al., "Review of particle physics," *Journal of Physics G*, vol. 37, no. 7, Article ID 075021, 2010.
- [7] G. Steigman, "Primordial nucleosynthesis: successes and challenges," *International Journal of Modern Physics E*, vol. 15, no. 1, pp. 1–36, 2006.
- [8] R. H. Cyburt, B. D. Fields, K. A. Olive, and E. Skillman, "New BBN limits on physics beyond the standard model from 4He," *Astroparticle Physics*, vol. 23, no. 3, pp. 313–323, 2005.
- [9] K. A. Olive, G. Steigman, and T. P. Walker, "Primordial nucleosynthesis: theory and observations," *Physics Report*, vol. 333–334, no. 4–6, pp. 389–407, 2000.
- [10] W. Hu and S. Dodelson, "Cosmic microwave background anisotropies," *Annual Review of Astronomy and Astrophysics*, vol. 40, pp. 171–216, 2002.
- [11] S. Dodelson, *Modern Cosmology*, Academic Press, Amsterdam, Netherlands, 2003.
- [12] D. Larson, J. Dunkley, G. Hinshaw et al., "Seven-year wilkinson microwave anisotropy probe (WMAP) observations: power spectra and WMAP-derived parameters," *Astrophysical Journal, Supplement Series*, vol. 192, no. 2, article 16, 2011.
- [13] A. D. Sakharov, "Violation of CP invariance, C asymmetry, and baryon asymmetry of the universe," *Zhurnal Eksperimental'noi i Teoreticheskoi Fiziki*, vol. 5, pp. 32–35, 1967.
- [14] G. Hooft, "Symmetry breaking through Bell-Jackiw anomalies," *Physical Review Letters*, vol. 37, no. 1, pp. 8–11, 1976.
- [15] V. A. Kuzmin, V. A. Rubakov, and M. E. Shaposhnikov, "On anomalous electroweak baryon-number non-conservation in the early universe," *Physics Letters B*, vol. 155, no. 1-2, pp. 36–42, 1985.
- [16] M. Kobayashi and T. Maskawa, "CP violation in the renormalizable theory of weak interaction," *Progress of Theoretical Physics*, vol. 49, pp. 652–657, 1973.
- [17] C. Jarlskog, "Commutator of the quark mass matrices in the standard electroweak model and a measure of maximal CP nonconservation," *Physical Review Letters*, vol. 55, no. 10, pp. 1039–1042, 1985.
- [18] M. B. Gavela, M. Lozano, J. Orloff, and O. Pène, "Standard model CP-violation and baryon asymmetry (I). Zero temperature," *Nuclear Physics B*, vol. 430, no. 2, pp. 345–381, 1994.
- [19] M. B. Gavela, P. Hernandez, J. Orloff, O. Pène, and C. Quimbay, "Standard model CP-violation and baryon asymmetry (II). Finite temperature," *Nuclear Physics B*, vol. 430, no. 2, pp. 382–426, 1994.
- [20] P. Huet and E. Sather, "Electroweak baryogenesis and standard model CP violation," *Physical Review D*, vol. 51, no. 2, pp. 379–394, 1995.
- [21] V. A. Rubakov and M. E. Shaposhnikov, "Electroweak baryon number non-conservation in the early Universe and in high-energy collisions," *Uspekhi Fizicheskikh Nauk*, vol. 166, no. 5, pp. 534–537, 1996.
- [22] M. Trodden, "Electroweak baryogenesis," *Reviews of Modern Physics*, vol. 71, no. 5, pp. 1463–1500, 1999.
- [23] K. Kajantie, M. Laine, K. Rummukainen, and M. Shaposhnikov, "The electroweak phase transition: a non-perturbative analysis," *Nuclear Physics B*, vol. 466, no. 1-2, pp. 189–258, 1996.
- [24] A. Y. Ignatiev, N. V. Krasnikov, V. A. Kuzmin, and A. N. Tavkhelidze, "Universal CP-noninvariant superweak interaction and bayron asymmetry of the universe," *Physics Letters B*, vol. 76, no. 4, pp. 436–438, 1978.

- [25] M. Yoshimura, "Unified gauge theories and the baryon number of the universe," *Physical Review Letters*, vol. 41, no. 5, pp. 281–284, 1978.
- [26] D. Toussaint, S. B. Treiman, F. Wilczek, and A. Zee, "Matter-antimatter accounting, thermodynamics, and black-hole radiation," *Physical Review D*, vol. 19, no. 4, pp. 1036–1045, 1979.
- [27] S. Dimopoulos and L. Susskind, "Baryon number of the universe," *Physical Review D*, vol. 18, no. 12, pp. 4500–4509, 1978.
- [28] J. R. Ellis, M. K. Gaillard, and D. V. Nanopoulos, "Baryon number generation in grand unified theories," *Physics Letters B*, vol. 80, no. 4-5, pp. 360–364, 1979.
- [29] S. Weinberg, "Cosmological production of baryons," *Physical Review Letters*, vol. 42, no. 13, pp. 850–853, 1979.
- [30] M. Yoshimura, "Origin of cosmological baryon asymmetry," *Physics Letters B*, vol. 88, no. 3-4, pp. 294–298, 1979.
- [31] S. M. Barr, G. Segrè, and H. A. Weldon, "Magnitude of the cosmological baryon asymmetry," *The Physical Review D*, vol. 20, no. 10, pp. 2494–2498, 1979.
- [32] D. V. Nanopoulos and S. Weinberg, "Mechanisms for cosmological baryon production," *Physical Review D*, vol. 20, no. 10, pp. 2484–2493, 1979.
- [33] A. Yildiz and P. H. Cox, "Net baryon number and CP nonconservation with unified fields," *Physical Review D*, vol. 21, no. 4, pp. 906–909, 1980.
- [34] A. Riotto and M. Trodden, "Recent progress in baryogenesis," *Annual Review of Nuclear and Particle Science*, vol. 49, no. 1, pp. 35–75, 1999.
- [35] J. M. Cline, "Baryogenesis," <http://arxiv.org/abs/hep-ph/0609145>.
- [36] I. Affleck and M. Dine, "A new mechanism for baryogenesis," *Nuclear Physics B*, vol. 249, no. 2, pp. 361–380, 1985.
- [37] M. Dine, L. Randall, and S. D. Thomas, "Baryogenesis from flat directions of the supersymmetric standard model," *Nuclear Physics B*, vol. 458, no. 1-2, pp. 291–326, 1996.
- [38] A. G. Cohen and D. B. Kaplan, "Thermodynamic generation of the baryon asymmetry," *Physics Letters B*, vol. 199, no. 2, pp. 251–258, 1987.
- [39] A. G. Cohen and D. B. Kaplan, "Spontaneous baryogenesis," *Nuclear Physics B*, vol. 308, no. 4, pp. 913–928, 1988.
- [40] P. Minkowski, " $\mu \rightarrow e\gamma$  at a rate of one out of 109 muon decays?" *Physics Letters B*, vol. 67, no. 4, pp. 421–428, 1977.
- [41] T. Yanagida, "Horizontal gauge symmetry and masses of neutrinos," in *Proceedings of the Workshop on the Baryon Number of the Universe and Unified Theories*, Tsukuba, Japan, February 1979.
- [42] S. L. Glashow, "Quarks and leptons," in *Cargèse Lectures*, p. 687, Plenum, NY, USA, 1980.
- [43] M. Gell-Mann, P. Ramond, and R. Slansky, "Complex spinors and unified theories," in *Supergravity*, P. van Nieuwenhuizen and D. Z. Freedman, Eds., North Holland, 1979.
- [44] R. N. Mohapatra and G. Senjanović, "Neutrino masses and mixings in gauge models with spontaneous parity violation," *Physical Review D*, vol. 23, no. 1, pp. 165–180, 1981.
- [45] M. Fukugita and T. Yanagida, "Baryogenesis without grand unification," *Physics Letters B*, vol. 174, no. 1, pp. 45–47, 1986.
- [46] S. Y. Khlebnikov and M. E. Shaposhnikov, "The statistical theory of anomalous fermion number non-conservation," *Nuclear Physics B*, vol. 308, no. 4, pp. 885–912, 1988.
- [47] M. Plümacher, "Baryogenesis and lepton number violation," *Zeitschrift für Physik C-Particles and Fields*, vol. 74, no. 3, pp. 549–559, 1997.
- [48] L. Covi, N. Rius, E. Roulet, and F. Vissani, "Finite temperature effects on CP-violating asymmetries," *Physical Review D*, vol. 57, no. 1, pp. 93–99, 1998.
- [49] G. F. Giudice, A. Notari, M. Raidal, A. Riotto, and A. Strumia, "Towards a complete theory of thermal leptogenesis in the SM and MSSM," *Nuclear Physics B*, vol. 685, no. 1–3, pp. 89–149, 2004.
- [50] M. Flanz, E. A. Paschos, and U. Sarkar, "Baryogenesis from a lepton asymmetric universe," *Physics Letters B*, vol. 345, no. 3, pp. 248–252, 1995.
- [51] L. Covi, E. Roulet, and F. Vissani, "CP violating decays in leptogenesis scenarios," *Physics Letters B*, vol. 384, no. 1–4, pp. 169–174, 1996.
- [52] A. Pilaftsis, "CP violation and baryogenesis due to heavy Majorana neutrinos," *Physical Review D*, vol. 56, no. 9, pp. 5431–5451, 1997.
- [53] E. W. Kolb and S. Wolfram, "Baryon number generation in the early universe," *Nuclear Physics*, vol. 172, pp. 224–284, 1980.
- [54] C. S. Fong, M. C. Gonzalez-Garcia, and E. Nardi, "Leptogenesis from soft supersymmetry breaking (Soft Leptogenesis)," *International Journal of Modern Physics A*, vol. 26, pp. 3491–3604, 2011.

- [55] W. Buchmüller, P. Di Bari, and M. Plümacher, “Leptogenesis for pedestrians,” *Annals of Physics*, vol. 315, no. 2, pp. 305–351, 2005.
- [56] C. S. Fong and J. Racker, “On fast CP violating interactions in leptogenesis,” *Journal of Cosmology and Astroparticle Physics*, vol. 2010, no. 07, article 001, 2010.
- [57] J. A. Harvey and M. S. Turner, “Cosmological baryon and lepton number in the presence of electroweak fermion-number violation,” *Physical Review D*, vol. 42, no. 10, pp. 3344–3349, 1990.
- [58] T. Inui, T. Ichihara, Y. Mimura, and N. Sakai, “Cosmological baryon asymmetry in supersymmetric standard models and heavy particle effects,” *Physics Letters B*, vol. 325, no. 3–4, pp. 392–400, 1994.
- [59] D. J. H. Chung, B. Garbrecht, and S. Tulin, “The effect of the sparticle mass spectrum on the conversion of B-L to B,” *Journal of Cosmology and Astroparticle Physics*, vol. 0903, p. 008, 2009.
- [60] J. A. Casas and A. Ibarra, “Oscillating neutrinos and  $\mu \rightarrow e, \gamma$ ,” *Nuclear Physics B*, vol. 618, no. 1–2, pp. 171–204, 2001.
- [61] S. Davidson and A. Ibarra, “A lower bound on the right-handed neutrino mass from leptogenesis,” *Physics Letters B*, vol. 535, no. 1–4, pp. 25–32, 2002.
- [62] W. Buchmüller, P. Di Bari, and M. Plumacher, “Cosmic microwave background, matter-antimatter asymmetry and neutrino masses,” *Nuclear Physics B*, vol. 643, no. 1–3, pp. 367–390, 2002.
- [63] J. R. Ellis and M. Raidal, “Leptogenesis and the violation of lepton number and CP at low energies,” *Nuclear Physics B*, vol. 643, no. 1–3, pp. 229–246, 2002.
- [64] W. Buchmüller, P. Di Bari, and M. Plumacher, “A bound on neutrino masses from baryogenesis,” *Physics Letters B*, vol. 547, no. 3–4, pp. 128–132, 2002.
- [65] W. Buchmüller, P. Di Bari, and M. Plumacher, “The neutrino mass window for baryogenesis,” *Nuclear Physics B*, vol. 665, pp. 445–468, 2003.
- [66] E. Nardi, “Leptogenesis and neutrino masses,” *Nuclear Physics B—Proceedings Supplements*, vol. 217, pp. 27–32, 2011.
- [67] R. Barbieri, P. Creminelli, A. Strumia, and N. Tetradis, “Baryogenesis through leptogenesis,” *Nuclear Physics B*, vol. 575, no. 1–2, pp. 61–77, 2000.
- [68] A. Abada, S. Davidson, F. X. Josse-Michaux, M. Losada, and A. Riotto, “Flavour issues in leptogenesis,” *Journal of Cosmology and Astroparticle Physics*, vol. 0604, p. 004, 2006.
- [69] E. Nardi, Y. Nir, E. Roulet, and J. Racker, “The importance of flavor in leptogenesis,” *Journal of High Energy Physics*, vol. 0601, p. 164, 2006.
- [70] A. Abada, S. Davidson, A. Ibarra, F.-X. Josse-Michaux, M. Losada, and A. Riotto, “Flavour matters in leptogenesis,” *Journal of High Energy Physics*, vol. 0609, p. 010, 2006.
- [71] T. Endoh, T. Morozumi, and Z. Xiong, “Primordial lepton family asymmetries in seesaw model,” *Progress of Theoretical Physics*, vol. 111, no. 1, pp. 123–149, 2004.
- [72] A. Abada, H. Aissaoui, and M. Losada, “A model for leptogenesis at the TeV scale,” *Nuclear Physics B*, vol. 728, no. 1–3, pp. 55–66, 2005.
- [73] O. Vives, “Flavoured leptogenesis: a successful thermal leptogenesis with  $N_1$  mass below  $10^8$  GeV,” *Journal of Physics: Conference Series*, vol. 171, Article ID 012076, 2009.
- [74] T. Fujihara, S. Kaneko, S. Kang, D. Kimura, T. Morozumi, and M. Tanimoto, “Cosmological family asymmetry and CP violation,” *Physical Review D*, vol. 72, no. 1, Article ID 016006, 12 pages, 2005.
- [75] A. Pilaftsis and T. E. J. Underwood, “Electroweak-scale resonant leptogenesis,” *Physical Review D*, vol. 72, no. 11, Article ID 113001, 27 pages, 2005.
- [76] G. C. Branco, R. González Felipe, and F. R. Joaquim, “A new bridge between leptonic CP violation and leptogenesis,” *Physics Letters B*, vol. 645, no. 5–6, pp. 432–436, 2007.
- [77] S. Pascoli, S. T. Petcov, and A. Riotto, “Connecting low energy leptonic CP violation to leptogenesis,” *Physical Review D*, vol. 75, no. 8, Article ID 083511, 2007.
- [78] S. Pascoli, S. T. Petcov, and A. Riotto, “Leptogenesis and low energy CP-violation in neutrino physics,” *Nuclear Physics B*, vol. 774, no. 1–3, pp. 1–52, 2007.
- [79] S. Antusch, S. F. King, and A. Riotto, “Flavour-dependent leptogenesis with sequential dominance,” *Journal of Cosmology and Astroparticle Physics*, vol. 0611, p. 011, 2006.
- [80] S. Antusch and A. M. Teixeira, “Towards constraints on the SUSY seesaw from flavour-dependent leptogenesis,” *Journal of Cosmology and Astroparticle Physics*, vol. 0702, p. 024, 2007.
- [81] S. Antusch, “Flavour-dependent type II leptogenesis,” *Physical Review D*, vol. 76, Article ID 023512, 2007.
- [82] S. Blanchet and P. Di Bari, “Flavour effects on leptogenesis predictions,” *Journal of Cosmology and Astroparticle Physics*, vol. 0703, p. 018, 2007.
- [83] S. Blanchet, P. Di Bari, and G. G. Raffelt, “Quantum Zeno effect and the impact of flavor in leptogenesis,” *Journal of Cosmology and Astroparticle Physics*, vol. 0703, p. 012, 2007.



- [84] A. De Simone and A. Riotto, "On the impact of flavour oscillations in leptogenesis," *Journal of Cosmology and Astroparticle Physics*, vol. 0702, p. 005, 2007.
- [85] A. De Simone and A. Riotto, "Quantum boltzmann equations and leptogenesis," *Journal of Cosmology and Astroparticle Physics*, vol. 0708, p. 002, 2007.
- [86] A. De Simone and A. Riotto, "On Resonant Leptogenesis," *Journal of Cosmology and Astroparticle Physics*, vol. 0708, p. 013, 2007.
- [87] V. Cirigliano, A. De Simone, G. Isidori, I. Masina, and A. Riotto, "Quantum resonant leptogenesis and minimal lepton flavour violation," *Journal of Cosmology and Astroparticle Physics*, vol. 0801, 004 pages, 2008.
- [88] V. Cirigliano, C. Lee, M. J. Ramsey-Musolf, and S. Tulin, "Flavored quantum Boltzmann equations," *Physical Review D*, vol. 81, no. 10, Article ID 103503, 2010.
- [89] C. S. Fong, M. C. Gonzalez-Garcia, E. Nardi, and J. Racker, "Supersymmetric leptogenesis," *Journal of Cosmology and Astroparticle Physics*, vol. 1012, p. 013, 2010.
- [90] B. A. Campbell, S. Davidson, J. Ellis, and K. A. Olive, "On the baryon, lepton-flavour and right-handed electron asymmetries of the universe," *Physics Letters B*, vol. 297, no. 1-2, pp. 118–124, 1992.
- [91] J. M. Cline, K. Kainulainen, and K. A. Olive, "Protecting the primordial baryon asymmetry from erasure by sphalerons," *Physical Review D*, vol. 49, no. 12, pp. 6394–6409, 1994.
- [92] S. Weinberg, "Baryon- and lepton-nonconserving processes," *Physical Review Letters*, vol. 43, no. 21, pp. 1566–1570, 1979.
- [93] D. A. Sierra, M. Losada, and E. Nardi, "Lepton flavor equilibration and leptogenesis," *Journal of Cosmology and Astroparticle Physics*, vol. 0912, p. 015, 2009.
- [94] M. Beneke, B. Garbrecht, C. Fidler, M. Herranen, and P. Schwaller, "Flavoured leptogenesis in the CTP formalism," *Nuclear Physics B*, vol. 843, no. 1, pp. 177–212, 2011.
- [95] D. Aristizabal Sierra, L. A. Munoz, and E. Nardi, "Purely Flavored Leptogenesis," *Physical Review D*, vol. 80, Article ID 016007, 2009.
- [96] M. C. Gonzalez-Garcia, J. Racker, and N. Rius, "Leptogenesis without violation of B-L," *Journal of High Energy Physics*, vol. 0911, article 079, 2009.
- [97] S. Antusch, S. Blanchet, M. Blennow, and E. Fernandez-Martinez, "Non-unitary leptonic mixing and leptogenesis," *Journal of High Energy Physics*, vol. 2010, no. 1, 2010.
- [98] J. Racker, M. Pena, and N. Rius, "Leptogenesis with small violation of B-L," *Journal of Cosmology and Astroparticle Physics*, vol. 1207, article 030, 2012.
- [99] R. N. Mohapatra and J. W. F. Valle, "Neutrino mass and baryon-number nonconservation in superstring models," *Physical Review D*, vol. 34, no. 5, pp. 1642–1645, 1986.
- [100] G. Hooft, "Naturalness, chiral symmetry, and spontaneous chiral symmetry breaking," *NATO Advanced Science Institute B*, vol. 59, article 135, 23 pages, 1980.
- [101] A. Basbøll and S. Hannestad, "Decay of heavy Majorana neutrinos studied using the full Boltzmann equation, including its implications for leptogenesis," *Journal of Cosmology and Astroparticle Physics*, vol. 0701, p. 003, 2007.
- [102] J. Garayoa, S. Pastor, T. Pinto, N. Rius, and O. Vives, "On the full Boltzmann equations for leptogenesis," *Journal of Cosmology and Astroparticle Physics*, vol. 0909, p. 035, 2009.
- [103] F. Hahn-Woernle, M. Plümacher, and Y. Y. Y. Wong, "Full boltzmann equations for leptogenesis including scattering," *Journal of Cosmology and Astroparticle Physics*, vol. 0908, p. 028, 2009.
- [104] F. Hahn-Woernle, "Wash-out in  $N_2$ -dominated leptogenesis," *Journal of Cosmology and Astroparticle Physics*, vol. 1008, p. 029, 2010.
- [105] W. Buchmuller and M. Plumacher, "Spectator processes and baryogenesis," *Physics Letters B*, vol. 511, pp. 74–76, 2001.
- [106] E. Nardi, Y. Nir, J. Racker, and E. Roulet, "On Higgs and sphaleron effects during the leptogenesis era," *Journal of High Energy Physics*, no. 1, pp. 1743–1760, 2006.
- [107] C. S. Fong, M. C. Gonzalez-Garcia, and E. Nardi, "Early universe effective theories: the soft leptogenesis and R-genesis cases," *Journal of Cosmology and Astroparticle Physics*, vol. 1102, p. 032, 2011.
- [108] E. Nardi, J. Racker, and E. Roulet, "CP violation in scatterings, three body processes and the Boltzmann equations for leptogenesis," *Journal of High Energy Physics*, vol. 2007, no. 9, article 090, 2007.
- [109] S. Davidson, E. Nardi, and Y. Nir, "Leptogenesis," *Physics Reports*, vol. 466, no. 4-5, pp. 105–177, 2008.
- [110] A. Pilaftsis and T. E. J. Underwood, "Resonant leptogenesis," *Nuclear Physics B*, vol. 692, no. 3, pp. 303–345, 2004.



- [111] A. Anisimov, A. Broncano, and M. Plümacher, “The C P-asymmetry in resonant leptogenesis,” *Nuclear Physics B*, vol. 737, no. 1-2, pp. 176–189, 2006.
- [112] C. S. Fong, M. C. Gonzalez-Garcia, and J. Racker, “CP violation from scatterings with gauge bosons in leptogenesis,” *Physics Letters B*, vol. 697, no. 5, pp. 463–470, 2011.
- [113] K. Kajantie, M. Laine, K. Rummukainen, and M. Shaposhnikov, “Generic rules for high temperature dimensional reduction and their application to the Standard Model,” *Nuclear Physics B*, vol. 458, no. 1-2, pp. 90–136, 1996.
- [114] J. A. Casas, J. R. Espinosa, A. Ibarra, and I. Navarro, “General RG equations for physical neutrino parameters and their phenomenological implications,” *Nuclear Physics B*, vol. 573, no. 3, pp. 652–684, 2000.
- [115] S. Antusch, J. Kersten, M. Lindner, and M. Ratz, “Running neutrino masses, mixings and CP phases: analytical results and phenomenological consequences,” *Nuclear Physics B*, vol. 674, no. 1-2, pp. 401–433, 2003.
- [116] D. Comelli and J. R. Espinosa, “Bosonic thermal masses in supersymmetry,” *Physical Review D*, vol. 55, no. 10, pp. 6253–6263, 1997.
- [117] P. Elmfors, K. Enqvist, and I. Vilja, “Thermalization of the Higgs field at the electroweak phase transition,” *Nuclear Physics B*, vol. 412, no. 1-2, pp. 459–476, 1994.
- [118] H. A. Weldon, “Dynamical holes in the quark-gluon plasma,” *Physical Review D*, vol. 40, no. 7, pp. 2410–2420, 1989.
- [119] H. A. Weldon, “Effective fermion masses of order  $gT$  in high-temperature gauge theories with exact chiral invariance,” *Physical Review D*, vol. 26, no. 10, pp. 2789–2796, 1982.
- [120] V. V. Klimov, “Spectrum of elementary Fermi excitations in quark gluon plasma,” *Soviet Journal of Nuclear Physics*, vol. 33, pp. 934–935, 1981 (Russian).
- [121] B. Garbrecht, “Leptogenesis: the other cuts,” *Nuclear Physics B*, vol. 847, no. 2, pp. 350–366, 2011.
- [122] M. Le Bellac, *Thermal Field Theory*, Cambridge University Press, 1996.
- [123] N. P. Landsman and C. G. van Weert, “Real- and imaginary-time field theory at finite temperature and density,” *Physics Reports*, vol. 145, no. 3-4, pp. 141–249, 1987.
- [124] C. P. Kießig, M. Plümacher, and M. H. Thoma, “Decay of a Yukawa fermion at finite temperature and applications to leptogenesis,” *Physical Review D*, vol. 82, no. 3, Article ID 036007, 2010.
- [125] C. Kiessig and M. Plumacher, “Hard-thermal-loop corrections in leptogenesis I: CP-asymmetries,” vol. 2012, no. 07, article 014, 2012.
- [126] C. Kiessig and M. Plumacher, “Hard-thermal-loop corrections in leptogenesis II: solving the boltzmann equations,” *Journal of Cosmology and Astroparticle Physics*, vol. 2012, no. 09, article 012, 2012.
- [127] M. Garny, A. Hohenegger, and A. Kartavtsev, “Medium corrections to the CP-violating parameter in leptogenesis,” *Physical Review D*, vol. 81, no. 8, Article ID 085028, 2010.
- [128] F. Buccella, D. Falcone, C. S. Fong, E. Nardi, and G. Ricciardi, “Squeezing out predictions with leptogenesis from  $SO(10)$ ,” vol. 86, no. 3, Article ID 035012, 15 pages, 2012.
- [129] H. B. Nielsen and Y. Takanishi, “Baryogenesis via lepton number violation in anti-GUT model,” *Physics Letters B*, vol. 507, no. 1–4, pp. 241–251, 2001.
- [130] A. Strumia, “Baryogenesis via leptogenesis,” <http://arxiv.org/abs/hep-ph/0608347>.
- [131] G. Engelhard, Y. Grossman, E. Nardi, and Y. Nir, “Importance of the heavier singlet neutrinos in leptogenesis,” *Physical Review Letters*, vol. 99, no. 8, Article ID 081802, 2007.
- [132] S. Blanchet, P. Di Bari, D. A. Jones, and L. Marzola, “Leptogenesis with heavy neutrino avours: from density matrix to Boltzmann equations,” <http://arxiv.org/abs/1112.4528>.
- [133] W. Buchmüller and S. Fredenhagen, “Quantum mechanics of baryogenesis,” *Physics Letters B*, vol. 483, pp. 217–224, 2000.
- [134] M. Garny, A. Hohenegger, A. Kartavtsev, and M. Lindner, “Systematic approach to leptogenesis in nonequilibrium QFT: vertex contribution to the CP-violating parameter,” *Physical Review D*, vol. 80, no. 12, Article ID 125027, 2009.
- [135] M. Garny, A. Hohenegger, A. Kartavtsev, and M. Lindner, “Systematic approach to leptogenesis in nonequilibrium QFT: self-energy contribution to the CP-violating parameter,” *Physical Review D*, vol. 81, no. 8, Article ID 085027, 2010.
- [136] A. Anisimov, W. Buchmüller, M. Drewes, and S. Mendizabal, “Leptogenesis from quantum interference in a thermal bath,” *Physical Review Letters*, vol. 104, no. 12, Article ID 121102, 2010.
- [137] M. Beneke, B. Garbrecht, M. Herranen, and P. Schwaller, “Finite number density corrections to leptogenesis,” *Nuclear Physics B*, vol. 838, no. 1-2, pp. 1–27, 2010.

- [138] M. Garny, A. Hohenegger, and A. Kartavtsev, "Medium corrections to the  $CP$ -violating parameter in leptogenesis," *Physical Review D*, vol. 81, no. 8, Article ID 085028, 2010.
- [139] A. Anisimov, W. Buchmüller, M. Drewes, and S. Mendizabal, "Quantum leptogenesis I," *Annals of Physics*, vol. 326, no. 8, pp. 1998–2038, 2011.
- [140] K. C. Chou, Z. B. Su, B. L. Hao, and L. Yu, "Equilibrium and nonequilibrium formalisms made unified," *Physics Reports*, vol. 118, no. 1-2, pp. 1–131, 1985.
- [141] B. Garbrecht and M. Herranen, "Effective theory of resonant leptogenesis in the closed-time-path approach," *Nuclear Physics B*, vol. 861, no. 1, pp. 17–52, 2012.
- [142] H. Pagels and J. R. Primack, "Supersymmetry, cosmology, and new physics at teraelectronvolt energies," *Physical Review Letters*, vol. 48, no. 4, pp. 223–226, 1982.
- [143] S. Weinberg, "Cosmological constraints on the scale of supersymmetry breaking," *Physical Review Letters*, vol. 48, no. 19, pp. 1303–1306, 1982.
- [144] M. Y. Khlopov and A. D. Linde, "Is it easy to save the gravitino?" *Physics Letters B*, vol. 138, no. 4, pp. 265–268, 1984.
- [145] J. Ellis, J. E. Kim, and D. V. Nanopoulos, "Cosmological gravitino regeneration and decay," *Physics Letters B*, vol. 145, no. 3-4, pp. 181–186, 1984.
- [146] B. A. Campbell, S. Davidson, and K. A. Olive, "Inflation, neutrino baryogenesis, and (s)neutrino-induced baryogenesis," *Nuclear Physics B*, vol. 399, no. 1, pp. 111–136, 1993.
- [147] M. Plümacher, "Baryon asymmetry, neutrino mixing and supersymmetric  $SO(10)$  unification," *Nuclear Physics B*, vol. 530, no. 1-2, pp. 207–246, 1998.
- [148] P. Di Bari, "Leptogenesis, neutrino mixing data and the absolute neutrino mass scale," <http://arxiv.org/abs/hep-ph/0406115>.
- [149] D. J. H. Chung, B. Garbrecht, M. J. Ramsey-Musolf, and S. Tulin, "Supergauge interactions and electroweak baryogenesis," *Journal of High Energy Physics*, vol. 12, p. 067, 2009.
- [150] L. E. Ibáñez and F. Quevedo, "Supersymmetry protects the primordial baryon asymmetry," *Physics Letters B*, vol. 283, no. 3-4, pp. 261–269, 1992.
- [151] L. Bento, "Sphaleron relaxation temperatures," *Journal of Cosmology and Astroparticle Physics*, vol. 0311, article 002, 2003.
- [152] R. N. Mohapatra and X. Zhang, "QCD sphalerons at high temperature and baryogenesis at the electroweak scale," *Physical Review D*, vol. 45, no. 8, pp. 2699–2705, 1992.
- [153] G. D. Moore, "Computing the strong sphaleron rate," *Physics Letters B*, vol. 412, no. 3-4, pp. 359–370, 1997.
- [154] R. Rangarajan and H. Mishra, "Leptogenesis with heavy Majorana neutrinos reexamined," *Physical Review D*, vol. 61, no. 4, Article ID 043509, 7 pages, 2000.
- [155] L. Covi and E. Roulet, "Baryogenesis from mixed particle decays," *Physics Letters B*, vol. 399, no. 1-2, pp. 113–118, 1997.
- [156] T. Hambye, J. March-Russell, and S. M. West, "TeV scale resonant leptogenesis from supersymmetry breaking," *Journal of High Energy Physics*, vol. 0407, p. 070, 2004.
- [157] A. Pilaftsis, "Resonant  $\tau$  leptogenesis with observable lepton number violation," *Physical Review Letters*, vol. 95, no. 8, Article ID 081602, 4 pages, 2005.
- [158] C. H. Albright and S. M. Barr, "Resonant leptogenesis in a predictive  $SO(10)$  grand unified model," *Physical Review D*, vol. 70, no. 3, Article ID 033013, 2004.
- [159] C. H. Albright, "Bounds on the neutrino mixing angles for an  $SO(10)$  model with lopsided mass matrices," *Physical Review D*, vol. 72, Article ID 013001, 2005.
- [160] Z. Z. Xing and S. Zhou, "Tri-bimaximal neutrino mixing and flavor-dependent resonant leptogenesis," *Physics Letters B*, vol. 653, no. 2–4, pp. 278–287, 2007.
- [161] S. M. West, "Neutrino masses and TeV scale resonant leptogenesis from supersymmetry breaking," *Modern Physics Letters A*, vol. 21, no. 21, pp. 1629–1646, 2006.
- [162] V. Cirigliano, G. Isidori, and V. Porretti, "CP violation and leptogenesis in models with minimal lepton flavour violation," *Nuclear Physics B*, vol. 763, no. 1-2, pp. 228–246, 2007.
- [163] G. C. Branco, A. J. Buras, S. Jager, S. Uhlig, and A. Weiler, "Another look at minimal lepton flavour violation,  $l(i)$  to  $l(j)$  gamma, leptogenesis, and the ratio  $M(\nu)/\Lambda_{LFV}$ ," *Journal of High Energy Physics*, vol. 0709, p. 004, 2007.
- [164] K. S. Babu, A. G. Bachri, and Z. Tavartkiladze, "Predictive model of inverted neutrino mass hierarchy and resonant leptogenesis," *International Journal of Modern Physics A*, vol. 23, no. 11, pp. 1679–1696, 2008.
- [165] A. Pilaftsis, "Electroweak resonant leptogenesis in the singlet Majoron model," *Physical Review D*, vol. 78, no. 1, Article ID 013008, 2008.

- [166] F. F. Deppisch and A. Pilaftsis, "Lepton flavor violation and  $\theta_{13}$  in minimal resonant leptogenesis," *Physical Review D*, vol. 83, no. 7, Article ID 076007, 2011.
- [167] S. Iso, N. Okada, and Y. Orikasa, "Resonant leptogenesis in the minimal B-L extended standard model at TeV," *Physical Review D*, vol. 83, no. 9, Article ID 093011, 2011.
- [168] P. H. Gu, "Resonant leptogenesis and a verifiable seesaw model from large extra dimensions," *Physical Review D*, vol. 81, no. 7, Article ID 073002, 2010.
- [169] A. Pilaftsis, "The little review on leptogenesis," *Journal of Physics*, vol. 171, Article ID 012017, 2009.
- [170] M. Garny, A. Kartavtsev, and A. Hohenegger, "Leptogenesis from first principles in the resonant regime," <http://arxiv.org/abs/1112.6428>.
- [171] S. M. West, "Naturally degenerate right handed neutrinos," *Physical Review D*, vol. 71, no. 1, Article ID 013004, 8 pages, 2005.
- [172] G. C. Branco, R. González Felipe, F. R. Joaquim, and B. M. Nobre, "Enlarging the window for radiative leptogenesis," *Physics Letters B*, vol. 633, no. 2-3, pp. 336–344, 2006.
- [173] S. Bray, J. S. Lee, and A. Pilaftsis, "Resonant CP violation due to heavy neutrinos at the LHC," *Nuclear Physics B*, vol. 786, no. 1-2, pp. 95–118, 2007.
- [174] S. Blanchet, Z. Chacko, S. S. Granor, and R. N. Mohapatra, "Probing resonant leptogenesis at the LHC," *Physical Review D*, vol. 82, no. 7, Article ID 076008, 2010.
- [175] L. Boubekur, "Leptogenesis at low scale," <http://arxiv.org/abs/hep-ph/0208003>.
- [176] Y. Grossman, T. Kashti, Y. Nir, and E. Roulet, "Leptogenesis from supersymmetry breaking," *Physical Review Letters*, vol. 91, Article ID 251801, 2003.
- [177] G. D'Ambrosio, G. F. Giudice, and M. Raidal, "Soft leptogenesis," *Physics Letters B*, vol. 575, no. 1-2, pp. 75–84, 2003.
- [178] E. J. Chun, "Late leptogenesis from radiative soft terms," *Physical Review D*, vol. 69, no. 11, Article ID 117303, 2004.
- [179] L. Boubekur, T. Hambye, and G. Senjanović, "Low-scale leptogenesis and soft supersymmetry breaking," *Physical Review Letters*, vol. 93, no. 11, Article ID 111601, 4 pages, 2004.
- [180] G. D'Ambrosio, T. Hambye, A. Hektor, M. Raidal, and A. Rossi, "Leptogenesis in the minimal supersymmetric triplet seesaw model," *Physics Letters B*, vol. 604, no. 3-4, pp. 199–206, 2004.
- [181] M. C. Chen and K. T. Mahanthappa, "Lepton flavor violating decays and soft leptogenesis in a supersymmetric SO(10) model," *Physical Review D*, vol. 70, no. 11, Article ID 113013, 2004.
- [182] T. Kashti, "Phenomenological consequences of soft leptogenesis," *Physical Review D*, vol. 71, Article ID 013008, 2005.
- [183] Y. Grossman, R. Kitano, and H. Murayama, "Natural soft leptogenesis," *Journal of High Energy Physics*, vol. 06, 058 pages, 2005.
- [184] J. R. Ellis and S. K. Kang, "Sneutrino leptogenesis at the electroweak scale," <http://arxiv.org/abs/hep-ph/0505162>.
- [185] E. J. Chun and S. Scopel, "Soft leptogenesis in Higgs triplet model," *Physics Letters B*, vol. 636, no. 5, pp. 278–285, 2006.
- [186] A. D. Medina and C. E. M. Wagner, "Soft leptogenesis in warped extra dimensions," *Journal of High Energy Physics*, vol. 2006, no. 12, article 037, 2006.
- [187] J. Garayoa, M. C. Gonzalez-Garcia, and N. Rius, "Soft leptogenesis in the inverse seesaw model," *Journal of High Energy Physics*, vol. 2007, no. 2, article 021, 2007.
- [188] E. J. Chun and L. Velasco-Sevilla, "SO(10) unified models and soft leptogenesis," *Journal of High Energy Physics*, vol. 8, p. 075, 2007.
- [189] O. Bahat-Treidel and Z. Surujon, "The Ir(relevance) of initial conditions in soft leptogenesis," *Journal of High Energy Physics*, vol. 11, p. 046, 2008.
- [190] C. S. Fong and M. C. Gonzalez-Garcia, "Flavoured soft leptogenesis," *Journal of High Energy Physics*, vol. 0806, p. 076, 2008.
- [191] C. S. Fong and M. C. Gonzalez-Garcia, "On quantum effects in soft leptogenesis," *Journal of Cosmology and Astroparticle Physics*, vol. 2008, no. 8, article 008, 2008.
- [192] C. S. Fong and M. C. Gonzalez-Garcia, "On gaugino contributions to soft leptogenesis," *Journal of High Energy Physics*, vol. 0903, p. 073, 2009.
- [193] K. S. Babu, Y. Meng, and Z. Tavartkiladze, "New ways to leptogenesis with gauged B-L symmetry," *Physics Letters B*, vol. 681, no. 1, pp. 37–43, 2009.
- [194] Y. Kajiyama, S. Khalil, and M. Raidal, "Electron EDM and soft leptogenesis in supersymmetric B-L extension of the Standard Model," *Nuclear Physics B*, vol. 820, no. 1-2, pp. 75–88, 2009.
- [195] C. S. Fong, M. C. Gonzalez-Garcia, E. Nardi, and J. Racker, "Flavoured soft leptogenesis and natural values of the B term," *Journal of High Energy Physics*, vol. 1007, p. 001, 2010.

- [196] K. Hamaguchi and N. Yokozaki, "Soft leptogenesis and gravitino dark matter in gauge mediation," *Physics Letters B*, vol. 694, no. 4-5, pp. 398–401, 2011.
- [197] E. K. Akhmedov, V. A. Rubakov, and A. Y. Smirnov, "Baryogenesis via neutrino oscillations," *Physical Review Letters*, vol. 81, no. 7, pp. 1359–1362, 1998.
- [198] K. Dick, M. Lindner, M. Ratz, and D. Wright, "Leptogenesis with dirac neutrinos," *Physical Review Letters*, vol. 84, no. 18, pp. 4039–4042, 2000.
- [199] H. Murayama and A. Pierce, "Realistic dirac leptogenesis," *Physical Review Letters*, vol. 89, no. 27, Article ID 271601, p. 4, 2002.
- [200] M. Boz and N. K. Pak, "Dirac leptogenesis and anomalous  $U(1)$ ," *European Physical Journal C*, vol. 37, no. 4, pp. 507–510, 2004.
- [201] S. Abel and V. Page, "Affleck-dine (Pseudo)-dirac neutrinogenesis," *Journal of High Energy Physics*, vol. 0605, p. 024, 2006.
- [202] D. G. Cerdeño, A. Dedes, and T. E. J. Underwood, "The minimal phantom sector of the standard model: higgs phenomenology and Dirac leptogenesis," *Journal of High Energy Physics*, vol. 0609, p. 067, 2006.
- [203] B. Thomas and M. Toharia, "Phenomenology of Dirac neutrinogenesis in split supersymmetry," *Physical Review D*, vol. 73, no. 6, Article ID 063512, 21 pages, 2006.
- [204] B. Thomas and M. Toharia, "Lepton flavor violation and supersymmetric Dirac leptogenesis," *Physical Review D*, vol. 75, no. 1, Article ID 013013, 2007.
- [205] E. J. Chun and P. Roy, "Dirac leptogenesis in extended nMSSM," *Journal of High Energy Physics*, vol. 0806, p. 089, 2008.
- [206] A. Bechinger and G. Seidl, "Resonant dirac leptogenesis on throats," *Physical Review D*, vol. 81, no. 6, Article ID 065015, 2010.
- [207] M.-C. Chen, J. Huang, and W. Shepherd, "Dirac leptogenesis with a non-anomalous  $U(1)'$  family symmetry," *Journal of High Energy Physics*, vol. 1211, article 059, 2012.
- [208] M. Maggand and C. Wetterich, "Neutrino mass problem and gauge hierarchy," *Physics Letters B*, vol. 94, no. 1, pp. 61–64, 1980.
- [209] J. Schechter and J. W. F. Valle, "Neutrino masses in  $SU(2) \times U(1)$  theories," *Physical Review D*, vol. 22, no. 9, pp. 2227–2235, 1980.
- [210] C. Wetterich, "Neutrino masses and the scale of B-L violation," *Nuclear Physics B*, vol. 187, no. 2, pp. 343–375, 1981.
- [211] G. Lazarides, Q. Shafi, and C. Wetterich, "Proton lifetime and fermion masses in an  $SO(10)$  model," *Nuclear Physics B*, vol. 181, no. 2, pp. 287–300, 1981.
- [212] E. Ma and U. Sarkar, "Neutrino masses and leptogenesis with heavy Higgs triplets," *Physical Review Letters*, vol. 80, no. 26, pp. 5716–5719, 1998.
- [213] E. J. Chun and S. K. Kang, "Baryogenesis and degenerate neutrinos," *Physical Review D*, vol. 63, no. 9, Article ID 097902, 2001.
- [214] T. Hambye, E. Ma, and U. Sarkar, "Supersymmetric triplet Higgs model of neutrino masses and leptogenesis," *Nuclear Physics B*, vol. 602, no. 1-2, pp. 23–38, 2001.
- [215] A. S. Joshipura, E. A. Paschos, and W. Rodejohann, "Leptogenesis in left-right symmetric theories," *Nuclear Physics B*, vol. 611, no. 1–3, pp. 227–238, 2001.
- [216] T. Hambye and G. Senjanović, "Consequences of triplet seesaw for leptogenesis," *Physics Letters B*, vol. 582, no. 1-2, pp. 73–81, 2004.
- [217] W.-l. Guo, "Neutrino mixing and leptogenesis in type II seesaw mechanism," *Physical Review D*, vol. 70, no. 5, Article ID 053009, 7 pages, 2004.
- [218] S. Antusch and S. F. King, "Type II leptogenesis and the neutrino mass scale," *Physics Letters B*, vol. 597, no. 2, pp. 199–207, 2004.
- [219] S. Antusch and S. F. King, "Leptogenesis in unified theories with type II see-saw," *Journal of High Energy Physics*, vol. 0601, p. 117, 2006.
- [220] T. Hambye, M. Raidal, and A. Strumia, "Efficiency and maximal  $CP$ -asymmetry of scalar triplet leptogenesis," *Physics Letters B*, vol. 632, no. 5-6, pp. 667–674, 2006.
- [221] E. J. Chun and S. Scopel, "Analysis of leptogenesis in a supersymmetric triplet seesaw model," *Physical Review D*, vol. 75, no. 2, Article ID 023508, 2007.



- [222] P.-H. Gu, H. Zhang, and S. Zhou, "A minimal type II seesaw model," *Physical Review D*, vol. 74, no. 7, Article ID 076002, 5 pages, 2006.
- [223] N. Sahu and U. Sarkar, "Predictive model for dark matter, dark energy, neutrino masses, and leptogenesis at the TeV scale," *Physical Review D*, vol. 76, no. 4, Article ID 045014, 2007.
- [224] J. McDonald, N. Sahu, and U. Sarkar, "Type-II seesaw at collider, lepton asymmetry and singlet scalar dark matter," *Journal of Cosmology and Astroparticle Physics*, vol. 0804, p. 037, 2008.
- [225] W. Chao, S. Luo, and Z. Z. Xing, "Neutrino mixing and leptogenesis in type-II seesaw scenarios with left-right symmetry," *Physics Letters B*, vol. 659, no. 1-2, pp. 281–289, 2008.
- [226] T. H  llgren, T. Konstandin, and T. Ohlsson, "Triplet leptogenesis in left-right symmetric seesaw models," *Journal of Cosmology and Astroparticle Physics*, vol. 0801, p. 014, 2008.
- [227] M. Frigerio, P. Hosteins, S. Lavignac, and A. Romanino, "A new, direct link between the baryon asymmetry and neutrino masses," *Nuclear Physics B*, vol. 806, no. 1-2, pp. 84–102, 2009.
- [228] A. Strumia, "Sommerfeld corrections to type-II and type-III leptogenesis," *Nuclear Physics B*, vol. 809, no. 1-2, pp. 308–317, 2009.
- [229] P. H. Gu, M. Hirsch, U. Sarkar, and J. W. F. Valle, "Neutrino masses, leptogenesis, and dark matter in a hybrid seesaw model," *Physical Review D*, vol. 79, no. 3, Article ID 033010, 2009.
- [230] L. Calibbi, M. Frigerio, S. Lavignac, and A. Romanino, "Flavour violation in supersymmetric SO(10) unification with a type II seesaw mechanism," *Journal of High Energy Physics*, vol. 0912, p. 057, 2009.
- [231] C. S. Chen and C. M. Lin, "Type II seesaw Higgs triplet as the inflaton for chaotic inflation and leptogenesis," *Physics Letters B*, vol. 695, no. 1–4, pp. 9–12, 2011.
- [232] D. Aristizabal Sierra, F. Bazzocchi, and I. de Medeiros Varzielas, "Leptogenesis in avor models with type I and II seesaws," *Nuclear Physics B*, vol. 858, pp. 196–213, 2012.
- [233] C. Arina and N. Sahu, "Asymmetric inelastic inert doublet dark matter from triplet scalar leptogenesis," *Nuclear Physics B*, vol. 854, pp. 666–699, 2012.
- [234] R. Foot, H. Lew, X. G. He, and G. C. Joshi, "Seesaw neutrino masses," *Zeitschrift fur Physik C*, vol. 44, p. 441, 1989.
- [235] E. Ma, "Pathways to naturally small neutrino masses," *Physical Review Letters*, vol. 81, no. 6, pp. 1171–1174, 1998.
- [236] E. Ma and D. P. Roy, "Heavy triplet leptons and new gauge boson," *Nuclear Physics B*, vol. 644, no. 1-2, pp. 290–302, 2002.
- [237] B. Brahmachari, E. Ma, and U. Sarkar, "Supersymmetric model of neutrino mass and leptogenesis with string-scale unification," *Physics Letters B*, vol. 520, no. 1-2, pp. 152–158, 2001.
- [238] T. Hambye, Y. Lin, A. Notari, M. Papucci, and A. Strumia, "Constraints on neutrino masses from leptogenesis models," *Nuclear Physics B*, vol. 695, no. 1-2, pp. 169–191, 2004.
- [239] S. Blanchet and P. Fileviez P  rez, "Baryogenesis via leptogenesis in adjoint SU(5)," *Journal of Cosmology and Astroparticle Physics*, vol. 0808, p. 037, 2008.
- [240] S. Blanchet and P. F. P  rez, "On the role of low-energy CP violation in leptogenesis," *Modern Physics Letters A*, vol. 24, no. 18, pp. 1399–1409, 2009.
- [241] S. Patra, A. Sarkar, and U. Sarkar, "Spontaneous left-right symmetry breaking in supersymmetric models with only Higgs doublets," *Physical Review D*, vol. 82, no. 1, Article ID 015010, 2010.
- [242] D. A. Sierra, J. F. Kamenik, and M. Nemev  sek, "Implications of flavor dynamics for fermion triplet leptogenesis," *Journal of High Energy Physics*, vol. 1010, p. 036, 2010.
- [243] K. Kannike and D. V. Zhuridov, "New solution for neutrino masses and leptogenesis in adjoint SU(5)," *Journal of High Energy Physics*, vol. 1107, p. 102, 2011.
- [244] I. Abt et al., "GERDA collaboration, proposal to the LNGS," <http://www.mpi-hd.mpg.de/ge76/home.html>.
- [245] C. E. Aalseth, D. Anderson, R. Arthur et al., "The Majorana neutrinoless double-beta decay experiment," *Physics of Atomic Nuclei*, vol. 67, no. 11, pp. 2002–2010, 2004.
- [246] R. Ardito et al., "CUORE: a cryogenic underground observatory for rare events," <http://arxiv.org/abs/hepex/0501010>.
- [247] B. Autin, A. Blondel, K. . Bongardt et al., "Conceptual design of the SPL, a high-power superconducting H<sup>+</sup> linac at CERN," CERN 2000-012, 2000.



- [248] M. Mezzetto, "Physics potential of the SPL super beam," *Journal of Physics G*, vol. 29, no. 8, pp. 1781–1784, 2003.
- [249] Y. Itow, T. Kajita, K. Kaneyuki et al., "The JHF-Kamioka neutrino project," <http://arxiv.org/abs/hep-ex/0106019>.
- [250] D. S. Ayres et al., "NOvA proposal to build a 30-kiloton o-axis detector to study neutrino oscillations in the Fermilab NuMI beamline," <http://arxiv.org/abs/hep-ex/0503053>.
- [251] A. Strumia and F. Vissani, "Neutrino masses and mixings and...," <http://arxiv.org/abs/hep-ph/0606054>.
- [252] F. de Campos, O. J. P. Éboli, M. B. Magro et al., "Probing bilinear R-parity violating supergravity at the LHC," *Journal of High Energy Physics*, vol. 0805, p. 048, 2008.
- [253] B. C. Allanach, M. A. Bernhardt, H. K. Dreiner, S. Grab, C. H. Kom, and P. Richardson, "R-Parity violating minimal supergravity at the LHC," in *Proceedings of the 15th International Conference on Supersymmetry and the Unification of Fundamental Interactions (SUSY '07)*, pp. 334–337, Karlsruhe, Germany, 2007, <http://arxiv.org/abs/0710.2034>.
- [254] U. Mahanta, "Neutrino masses and mixing angles from leptoquark interactions," *Physical Review D*, vol. 62, no. 7, Article ID 073009, 4 pages, 2000.
- [255] D. Aristizabal Sierra, M. Hirsch, and S. G. Kovalenko, "Leptoquarks: neutrino masses and related accelerator signals," *Physical Review D*, vol. 77, no. 5, Article ID 055011, 2008.
- [256] J. Garayoa and T. Schwetz, "Neutrino mass hierarchy and Majorana  $CP$  phases within the Higgs triplet model at the LHC," *Journal of High Energy Physics*, vol. 0803, p. 009, 2008.
- [257] M. Kadastik, M. Raidal, and L. Rebane, "Direct determination of neutrino mass parameters at future colliders," *Physical Review D*, vol. 77, no. 11, Article ID 115023, 2008.
- [258] A. Zee, "Quantum numbers of Majorana neutrino masses," *Nuclear Physics B*, vol. 264, pp. 99–110, 1986.
- [259] K. S. Babu, "Model of "calculable" Majorana neutrino masses," *Physics Letters B*, vol. 203, no. 1-2, pp. 132–136, 1988.
- [260] D. A. Sierra and M. Hirsch, "Experimental tests for the Babu-Zee two-loop model of Majorana neutrino masses," *Journal of High Energy Physics*, vol. 2006, no. 12, article 052, 2006.
- [261] C. S. Chen, C. Q. Geng, J. N. Ng, and J. M. S. Wu, "Testing radiative neutrino mass generation at the LHC," *Journal of High Energy Physics*, vol. 0708, p. 022, 2007.
- [262] M. Nebot, J. F. Oliver, D. Palao, and A. Santamaria, "Prospects for the Zee-Babu model at the CERN LHC and low energy experiments," *Physical Review D*, vol. 77, no. 9, Article ID 093013, 2008.

## Review Article

# Neutrinos and Big Bang Nucleosynthesis

**Gary Steigman**

*Center for Cosmology and Astro-Particle Physics, Department of Physics, Department of Astronomy, The Ohio State University, 191 W. Woodruff Avenue, Columbus, OH 43210, USA*

Correspondence should be addressed to Gary Steigman, [steigman.1@asc.ohio-state.edu](mailto:steigman.1@asc.ohio-state.edu)

Received 6 July 2012; Accepted 8 October 2012

Academic Editor: Arthur B. McDonald

Copyright © 2012 Gary Steigman. This is an open access article distributed under the Creative Commons Attribution License, which permits unrestricted use, distribution, and reproduction in any medium, provided the original work is properly cited.

According to the standard models of particle physics and cosmology, there should be a background of cosmic neutrinos in the present Universe, similar to the cosmic microwave photon background. The weakness of the weak interactions renders this neutrino background undetectable with current technology. The cosmic neutrino background can, however, be probed indirectly through its cosmological effects on big bang nucleosynthesis (BBN) and the cosmic microwave background (CMB) radiation. In this BBN review, focused on neutrinos and more generally on dark radiation, the BBN constraints on the number of “equivalent neutrinos” (dark radiation), on the baryon asymmetry (baryon density), and on a possible lepton asymmetry (neutrino degeneracy) are reviewed and updated. The BBN constraints on dark radiation and on the baryon density following from considerations of the primordial abundances of deuterium and helium-4 are in excellent agreement with the complementary results from the CMB, providing a suggestive, but currently inconclusive, hint of the presence of dark radiation, and they constrain any lepton asymmetry. For all the cases considered here there is a “lithium problem”: the BBN-predicted lithium abundance exceeds the observationally inferred primordial value by a factor of  $\sim 3$ .

## 1. Introduction

According to the standard models of particle physics and cosmology, neutrinos (known and hypothesized) are produced, thermalized and contribute to the total energy density in the early, hot, dense Universe, regulating the early Universe expansion rate. Indeed, at the time of big bang nucleosynthesis (BBN), the contributions to the energy density from baryons, dark matter, and dark energy are all subdominant to those from the thermal populations of photons, electrons ( $e^\pm$  pairs), and neutrinos. Since the abundances of the elements formed during the first few minutes of the evolution of the Universe depend on the competition between the universal expansion rate and the nuclear and weak interaction rates, the very good agreement between the BBN predictions and observations (see, e.g., [1–4] for reviews

and further references) depends crucially on the early Universe thermalization of neutrinos and places restrictions on the presence of too many (or too few) of them or of too much “dark radiation.” At present, BBN and the cosmic microwave background (CMB) radiation provide the only probes of the cosmic neutrino background. In addition to their contribution to the total energy density, electron neutrinos and antineutrinos play a special role in regulating the production of  $^4\text{He}$ , the second most abundance element in the Universe. An excess of electron neutrinos over electron antineutrinos (lepton asymmetry; neutrino degeneracy) or vice versa will change the neutron-to-proton ratio during BBN, modifying, mainly, the BBN-predicted primordial helium abundance.

BBN provides a window on the early evolution of the Universe and a probe of particle physics (neutrino physics and more) beyond the standard model (SM). The primordial abundances of the elements produced in observationally accessible abundances by BBN (primarily D,  $^3\text{He}$ ,  $^4\text{He}$ ,  $^7\text{Li}$ ) depend on three fundamental parameters related to cosmology and particle physics: the baryon abundance (related to the Universal baryon asymmetry), the expansion rate of the Universe at BBN (a probe of dark radiation and the cosmic neutrino background), and any neutrino degeneracy (lepton asymmetry).

### 1.1. Baryon Density Parameter

The most obvious of these parameters is related to the abundance of the reactants, the baryons (nucleons). Although the very early Universe may have begun symmetric between matter and antimatter ( $n_B = n_{\bar{B}}$ ), long before BBN some yet to be determined mechanism involving the interplay between particle physics (violation of the conservation of baryon number, violation of C and CP symmetries) and cosmology (out of equilibrium evolution) led to a small but crucial local asymmetry between the amount of matter and antimatter in the Universe. After nucleon-antinucleon annihilation, the excess (nucleons, by definition) survives ( $n_B - n_{\bar{B}} \rightarrow n_B \equiv n_N$ ) and the number of nucleons in a comoving volume is preserved up to the present epoch (and far into the future as well). Since the nuclear reaction rates depend on the nucleon density, which decreases as the Universe expands, it is convenient to normalize the nucleon density to the photon density. After  $e^\pm$  annihilation, the ratio of the nucleon number density to the photon number density is unchanged as the Universe expands and cools. Since the number of nucleons in a comoving volume is conserved and, since entropy conservation guarantees that after  $e^\pm$  annihilation, the number of photons in a comoving volume is also conserved, after  $e^\pm$  annihilation the ratio of the nucleon number density to the photon number density is unchanged as the Universe expands and cools. BBN depends on the baryon density parameter  $\eta_{10}$ , defined by

$$\eta_{10} \equiv 10^{10} \eta_B \equiv 10^{10} \left( \frac{n_B}{n_\gamma} \right). \quad (1.1)$$

The present value ( $t = t_0$ , when the photon (CMB) temperature is  $T_0 = 2.725 \text{ K}$ ) of the baryon density is often measured by comparing the nucleon mass density to the critical mass density ( $\Omega_B \equiv (\rho_B/\rho_{\text{crit}})_0$ ) and the critical mass density depends on the present value of the Hubble parameter, the Hubble constant ( $H_0 \equiv 100 h \text{ km s}^{-1} \text{ Mpc}^{-1}$ ) [5],

$$\Omega_B h^2 = \frac{\eta_{10}}{273.9}. \quad (1.2)$$

Predicting the baryon asymmetry of the Universe is one of the key challenges confronting the search for new physics beyond the standard model. BBN constraints on  $\eta_B$  can help to identify potentially successful models of new physics.

## 1.2. Expansion Rate Parameter

The scale factor,  $a = a(t)$ , describes the evolution of the expansion of the Universe. During the early evolution of the Universe the expansion rate, as measured by the Hubble parameter,  $H \equiv (1/a)da/dt$ , is determined by the total energy density which, during those epochs, is dominated by the contributions from massless or extremely relativistic particles, “radiation” (R):

$$H^2 = \frac{8\pi G\rho}{3}, \quad (1.3)$$

where  $G$  is Newton’s gravitational constant and  $\rho = \rho_R$ . New physics may lead to  $\rho_R \rightarrow \rho'_R$  (dark radiation) or to a modification of the cosmology (general relativity)  $G \rightarrow G'$ , replacing the SM expansion rate with  $H \rightarrow H' \equiv SH$ . The expansion rate factor,  $S$ , quantifies any departure from the standard models of particle physics and/or cosmology.

Prior to the start of BBN and prior to  $e^\pm$  annihilation (e.g.,  $m_e \lesssim T \ll m_\mu$ ) the only relativistic SM particles present are the photons (with  $g_\gamma = 2$  degrees of freedom or helicities), the  $e^\pm$  pairs ( $g_e = 4$ ), and the  $N_\nu = 3$ , left-handed neutrinos and their right-handed antineutrinos ( $g_\nu = 2N_\nu$ ), so that  $\rho_R = \rho_\gamma + \rho_e + \rho_\nu$ . The evolution of the Universe can be scaled out by comparing the total energy density to the energy density in the CMB photons. Prior to  $e^\pm$  annihilation,  $T_\gamma = T_e = T_\nu$ , so that accounting for the different contributions to  $\rho_R$  from relativistic fermions and bosons,

$$\frac{\rho_R}{\rho_\gamma} = 1 + \frac{\rho_e}{\rho_\gamma} + N_\nu \left( \frac{\rho_\nu}{\rho_\gamma} \right) = 1 + \frac{7}{8} \left[ \left( \frac{4}{2} \right) + \left( \frac{3 \times 2}{2} \right) \right] = \frac{43}{8}, \quad (1.4)$$

for  $N_\nu = 3$ . The contribution from possible dark radiation (e.g., sterile neutrinos) may be expressed in terms of an equivalent number of SM neutrinos,  $\Delta N_\nu$  [6]. At BBN, which begins prior to  $e^\pm$  annihilation,  $N_\nu = 3 + \Delta N_\nu$ . In this case

$$\rho'_R \equiv \rho_R + \Delta N_\nu \rho_\nu, \quad (1.5)$$

or

$$\frac{\rho'_R}{\rho_\gamma} = \frac{43}{8} + \frac{7}{8} \Delta N_\nu = \frac{43}{8} \left( 1 + \frac{7\Delta N_\nu}{43} \right). \quad (1.6)$$

Allowing for dark radiation, the expansion rate factor,  $S$ , is directly related to  $\Delta N_\nu$ ,

$$S \equiv \frac{H'}{H} = \left( \frac{\rho'_R}{\rho_R} \right)^{1/2} = \left( 1 + \frac{7\Delta N_\nu}{43} \right)^{1/2}. \quad (1.7)$$

It should be kept in mind that new physics ( $S_{\text{BBN}} \neq 1$ ) may manifest itself as  $G_{\text{BBN}} \neq G_0$  instead of  $\Delta N_\nu \neq 0$ . In this case, comparing  $G_{\text{BBN}}$  when  $T \gtrsim m_e$  to its present value,

$$\frac{G_{\text{BBN}}}{G_0} = S_{\text{BBN}}^2 = 1 + 0.163\Delta N_\nu. \quad (1.8)$$

After  $e^\pm$  annihilation the only relativistic SM particles present are the photons and the neutrinos. The SM neutrinos decouple prior to  $e^\pm$  annihilation, when  $T \sim 2\text{-}3\text{ MeV}$ , so that when the  $e^\pm$  pairs annihilate, the photons are heated relative to the neutrinos. On the assumption that the neutrinos are fully decoupled at  $e^\pm$  annihilation,  $T_\nu/T_\gamma = (4/11)^{1/3}$  and, for the SM ( $\Delta N_\nu = 0$ ),

$$\frac{\rho_R}{\rho_\gamma} = 1 + \left(\frac{\rho_\nu}{\rho_\gamma}\right) = 1 + \frac{21}{8} \left(\frac{T_\nu}{T_\gamma}\right)^{4/3} = 1 + \frac{21}{8} \left(\frac{4}{11}\right)^{4/3} = 1.681. \quad (1.9)$$

However, in the presence of dark radiation or “equivalent neutrinos” (decoupled, with  $T = T_\nu \neq T_\gamma$ ),

$$S^2 = \frac{\rho'_R}{\rho_R} = 1 + \left(\frac{1}{1.681}\right) \frac{7}{8} \left(\frac{4}{11}\right)^{4/3} \Delta N_\nu = 1 + 0.135\Delta N_\nu. \quad (1.10)$$

Since the SM neutrinos are not fully decoupled at  $e^\pm$  annihilation, they do share some of the energy (entropy) when the  $e^\pm$  pairs annihilate [7]. This has the effect of increasing the relative contribution of the neutrinos to the total radiation density so that, after  $e^\pm$  annihilation,  $N_\nu = 3 + \Delta N_\nu \rightarrow N_{\text{eff}} = 3.046 + \Delta N_\nu$ . As a result, later in the evolution of the Universe (e.g., at recombination),  $\rho_R/\rho_\gamma \rightarrow 1.692$  and  $\rho'_R/\rho_\gamma \rightarrow 1.692 + 0.227\Delta N_\nu$ , so that for  $T \ll m_e$ ,

$$S^2 = \frac{\rho'_R}{\rho_R} = 1 + \left(\frac{1}{1.692}\right) \frac{7}{8} \left(\frac{4}{11}\right)^{4/3} \Delta N_\nu = 1 + 0.134\Delta N_\nu. \quad (1.11)$$

Of course, this post-BBN relation between the expansion rate ( $S$ ) and the equivalent number of neutrinos ( $\Delta N_\nu$ ) is only relevant for those epochs when the Universe is radiation-dominated.

BBN codes track the evolution of  $S$  from  $T \gtrsim m_e$ , prior to  $e^\pm$  annihilation, to  $T \ll m_e$ , well after  $e^\pm$  annihilation has ended. Since it is important for BBN to follow the evolution of the neutron to proton ratio beginning when  $T \gtrsim \text{few MeV}$ , prior to  $e^\pm$  annihilation,

$$S_{\text{BBN}} \equiv \left(1 + \frac{7\Delta N_\nu}{43}\right)^{1/2} = (1 + 0.163\Delta N_\nu)^{1/2}. \quad (1.12)$$

A BBN constraint on  $S$  is equivalent to one on  $\Delta N_\nu$  (or, on the ratio of  $G_{\text{BBN}}$  to its present value,  $G_0$ ) and, later in the evolution of the Universe,  $N_{\text{eff}} = 3.046 + \Delta N_\nu$ . A BBN determination that  $\Delta N_\nu$  differs from zero at a significant level of confidence can provide evidence for new physics (dark radiation) such as the existence of one, or more, sterile neutrinos (thermally populated) or a modification of the equations describing the expansion rate of the early Universe ( $S_{\text{BBN}} \neq 1$ ).



### 1.3. Neutrino Degeneracy Parameter

Since the charge neutrality of the Universe ensures that any electron excess is tied to the proton excess (the baryon asymmetry), a non zero lepton asymmetry much larger than the baryon asymmetry ( $\eta_B \lesssim 10^{-9}$ ) must be hidden in the neutrino sector. An excess of neutrinos over antineutrinos (or, vice-versa) requires a non zero neutrino chemical potential,  $\mu_\nu$ . The dimensionless degeneracy parameter is the ratio of the neutrino chemical potential to the neutrino temperature,  $\xi_\nu \equiv \mu_\nu/T_\nu$ ;  $\xi_\nu$  is preserved as the Universe expands and cools. In analogy with the parameterization of the baryon asymmetry by  $\eta_B \equiv (n_B - n_{\bar{B}})/n_\gamma \rightarrow n_B/n_\gamma$ , a lepton (neutrino) asymmetry may be parameterized by

$$\eta_L = \eta_\nu = \sum_\alpha \frac{(n_\nu - n_{\bar{\nu}})_\alpha}{n_\gamma} = \frac{\pi^3}{12\zeta(3)} \sum_\alpha \left[ \left( \frac{\xi_\alpha}{\pi} \right) + \left( \frac{\xi_\alpha}{\pi} \right)^3 \right], \quad (1.13)$$

where the sum is over the three SM neutrino flavors ( $\alpha = e, \mu, \tau$ ). Generally, mixing among the SM neutrinos ensures that the three chemical potentials are equilibrated [7, 8]. In the following it is assumed that  $\xi \equiv \xi_e = \xi_\mu = \xi_\tau$ . In this case,

$$\eta_L = \eta_\nu = \frac{\pi^3}{4\zeta(3)} \left( \frac{\xi}{\pi} \right) \left[ 1 + \left( \frac{\xi}{\pi} \right)^2 \right]. \quad (1.14)$$

An asymmetry between electron neutrinos and electron antineutrinos has a direct effect on BBN through the charged current weak interactions which regulate the neutron-to-proton ratio ( $p + e^- \leftrightarrow n + \nu_e$ ,  $n + e^+ \leftrightarrow p + \bar{\nu}_e$ ,  $n \leftrightarrow p + e^- + \bar{\nu}_e$ ) (see, e.g., [9–15] and further references therein). Since the relic abundance of  $^4\text{He}$  depends directly on the neutron-to-proton ratio when BBN begins (and during BBN), it provides a sensitive probe of any lepton asymmetry. The abundances of the other light nuclides produced during BBN are less sensitive to  $\xi$ .

A subdominant effect (usually) of a nonnegligible neutrino degeneracy ( $\eta_L \gg \eta_B$ ) is to enhance the contribution of the neutrinos to the early Universe energy density. This is equivalent to a contribution to  $\Delta N_\nu$ , where, for  $\xi_e = \xi_\mu = \xi_\tau \equiv \xi$ ,

$$\Delta N_\nu(\xi) = \frac{90}{7} \left( \frac{\xi}{\pi} \right)^2 \left[ 1 + \frac{1}{2} \left( \frac{\xi}{\pi} \right)^2 \right]. \quad (1.15)$$

Note that, for  $|\xi| \lesssim 0.1$ ,  $\Delta N_\nu(\xi) \lesssim 0.013$ , which is likely small compared with anticipated uncertainties in  $\Delta N_\nu$  inferred from BBN or the CMB.

At present and, likely for the foreseeable future, BBN provides the only window to a universal lepton asymmetry.

## 2. The BBN-Predicted Abundances

For BBN within the context of the standard models of particle physics and cosmology (SBBN), along with some well-defined extensions of them, only the light elements D,  $^3\text{He}$ ,  $^4\text{He}$ , and  $^7\text{Li}$  are produced in observationally interesting abundances. The BBN-predicted relic abundances

of these light nuclides depend on the three fundamental parameters introduced in Section 1 [1, 2, 11, 13–16]. Over limited, but interesting, ranges of these parameters, the results for the abundances of these nuclides extracted from numerical BBN codes are well fit (within the quoted errors) by [1, 2, 14, 15]

$$y_{\text{DP}} \equiv 10^5 \left( \frac{\text{D}}{\text{H}} \right)_P = 2.60(1 \pm 0.06) \left( \frac{6}{\eta_{\text{D}}} \right)^{1.6} = 45.7(1 \pm 0.06) \eta_{\text{D}}^{-1.6}, \quad (2.1)$$

$$Y_{\text{P}} = 0.2477 \pm 0.0006 + 0.0016(\eta_{\text{He}} - 6) = 0.2381 \pm 0.0006 + 0.0016\eta_{\text{He}}, \quad (2.2)$$

$$y_{\text{LiP}} \equiv 10^{10} \left( \frac{\text{Li}}{\text{H}} \right)_P = 4.82(1 \pm 0.10) \left( \frac{\eta_{\text{Li}}}{6} \right)^2, \quad A(\text{Li}) \equiv 12 + \log \left( \frac{\text{Li}}{\text{H}} \right)_P, \quad (2.3)$$

where

$$\eta_{\text{D}} = \eta_{10} - 6(S - 1) + \frac{5\xi}{4}, \quad (2.4)$$

$$\eta_{\text{He}} = \eta_{10} + 100(S - 1) - \frac{575\xi}{4}, \quad (2.5)$$

$$\eta_{\text{Li}} = \eta_{10} - 3(S - 1) - \frac{7\xi}{4}. \quad (2.6)$$

The relation of  $\eta_{\text{He}}$  to  $\xi$  in (2.5) is the one that appears in Kneller and Steigman [14]. An inadvertent typo in Steigman [1] was propagated in Simha and Steigman [2]. The very small difference this typo generated, 575 versus 574, has no effect on the quantitative results presented in those papers. In the above equations,  $(\text{D}/\text{H})_P$  and  $(\text{Li}/\text{H})_P$  are the ratios by number of deuterium and of lithium ( ${}^7\text{Li}$ ) to hydrogen, respectively, and  $Y_{\text{P}}$  is the  ${}^4\text{He}$  mass fraction.

There are some small but interesting changes in the numerical values in (2.1)–(2.3) from earlier versions of these relations [1, 2, 14, 15]; equations (2.4)–(2.6) are unchanged. In a recent paper, Nollett and Holder [4] called attention to the tension between the experimental and theoretical determinations of the  $d(p, \gamma){}^3\text{He}$  cross section, important for predicting the BBN deuterium abundance. Nollett and Holder argue for preferring the theoretical calculation over the experimental result which, they suggest, may be affected by a normalization error. Adoption of the theoretical calculation results in a  $\sim 6\%$  reduction in the BBN-predicted D abundance. I have preferred to “split the difference,” reducing the previously predicted abundance by 3% but, doubling the error uncertainty (the error in the BBN-predicted value of D/H for a fixed value of  $\eta_{\text{D}}$ ) from 3% to 6%, resulting in the numerical values shown in (2.1).

Given the role of the neutron-to-proton ratio at BBN on the predicted relic abundance of  ${}^4\text{He}$ ,  $Y_{\text{P}}$  depends, albeit weakly, on the value of the neutron lifetime (mean life). Quite recently, the Particle Data Group [17], in response to discrepant experimental data, decided to change its recommended value for the neutron lifetime from  $\tau_n = 885.7 \pm 0.8\text{ s}$  to  $\tau_n = 881.5 \pm 1.5\text{ s}$ . This change results in a small but noticeable reduction in the predicted value of  $Y_{\text{P}}$  by 0.0008 and a very small increase in the associated uncertainty in the predicted value of  $Y_{\text{P}}$ ,  $0.0005 \rightarrow 0.0006$ . Also incorporated into (2.2) is the Mangano et al. [7] correction

to the helium abundance resulting from the incomplete decoupling of the neutrinos at  $e^\pm$  annihilation.

The intense interest in recent years in the “lithium problem(s)” has led to an extensive reevaluation of the relevant nuclear reaction rates [18–20], leading to an increase in the BBN-predicted abundance by  $\sim 12\%$  from the result presented in Steigman 2007 [1], further exacerbating the lithium problem to be discussed below. This is reflected in (2.3). The  $d(p, \gamma)^3\text{He}$  rate which plays a role in the primordial deuterium abundance also impacts the BBN-predicted lithium abundance [4] (K. Nollett, Private Communication). This is taken into account in our error estimate.

It should be emphasized that these fits are *not* analytic approximations to the results from a numerical BBN code. Rather, they are fits to the results from such a code which are primarily *simple*, involving a minimal number of numerical values, chosen to only one or two significant figures. For limited but interesting ranges of the parameters ( $5.5 \lesssim \eta_{10} \lesssim 6.5$ ,  $0.85 \lesssim S \lesssim 1.15$  ( $-1.7 \lesssim \Delta N_\nu \lesssim 2.0$ ),  $-0.1 \lesssim \xi \lesssim 0.1$ ) these fits agree with the numerical results from this and other codes within the quoted uncertainties.

It is worth noting that the BBN-predicted abundances of D and  $^7\text{Li}$  are mainly sensitive to the baryon abundance while that of  $^4\text{He}$  is more sensitive to nonstandard physics ( $\Delta N_\nu$  and/or  $\xi$ ). However, both D and  $^7\text{Li}$  are weakly dependent on  $\Delta N_\nu$  and/or  $\xi$ , and  $^4\text{He}$  is weakly dependent on  $\eta_B$ .

### 3. The Observationally Inferred Primordial Abundances

Any conclusions about new physics (e.g.,  $\Delta N_\nu \neq 0?$ ,  $\xi \neq 0?$ ) based on BBN depend on the adopted primordial abundances. The relic abundances of D and  $^4\text{He}$  are key to the conclusions reviewed and updated here. It may have been noticed that  $^3\text{He}$  failed to be included in the discussion in the previous section. The reason is that  $^3\text{He}$  is only observed in the interstellar medium of our galaxy, which consists of gas that has been processed through many generations of stars. The large and uncertain corrections for post-BBN stellar processing make it difficult to infer the primordial abundance of  $^3\text{He}$  using the current data (see, e.g., [21] for discussion and further references). In addition, the observationally inferred abundances of lithium in the oldest, most metal-poor stars in the Galaxy are systematically lower, by factors of  $\sim 3$ -4, than the BBN-predicted values (the lithium problem or one of several lithium problems). Whether this discrepancy results from poorly understood corrections for stellar structure and/or evolution or is a hint of new physics remains unclear at present. In the confrontation of the BBN predictions with the observational data only D and  $^4\text{He}$  will be used to constrain various combinations of  $\eta_{10}$ ,  $\Delta N_\nu$ ,  $\xi$ , and the results will be used to *predict* the primordial lithium abundance which will then be compared to the observations. For a much more detailed, albeit not entirely up to date, discussion of the observational data and, in particular, the problems (real and potential) associated with them, see my recent reviews [1, 3].

#### 3.1. Primordial Deuterium

In the post-BBN Universe, as gas is cycled through successive generations of stars, deuterium is destroyed, not produced [22]. The post-BBN evolution of deuterium is simple and monotonic (decreasing abundance). As a result, observations of deuterium at high redshifts ( $z$ ) and/or of gas at low metallicity ( $Z$ ), where very little of the primordial gas has been

cycled through stars, should provide a view of very nearly primordial deuterium. While interesting on their own, observations of deuterium in the chemically evolved Galaxy or the solar system are of relatively little use in constraining the relic deuterium abundance. Observations of D at high- $z$  and low- $Z$  are provided by the QSO absorption-line systems (QSOALS) [24–28]. Since deuterium is observed by absorption of background QSO light in the wings of the much larger hydrogen absorption, exquisite velocity information about the absorbing gas is crucial to a meaningful determination of the D/H ratio. This and other contributors to potential systematic errors have limited the number of “robust” D abundance determinations from high- $z$ , low- $Z$ , QSOALS. In Figure 1 are shown 12 high- $z$ , low- $Z$  D/H determinations as a function of the absorbing redshift (a), of the metallicity (b), and of the HI column density (c). The open symbols reflect a subjective judgment of abundance determinations which may be more uncertain than indicated by their error bars (perhaps all the data should be plotted with open symbols).

For all 12 D abundance determinations, the weighted mean abundance is  $\langle \log y_D \rangle = 0.42$ . However, it is clear (by eye) that there is an excessively large dispersion among the individual abundance determinations (e.g., the reduced  $\chi^2$  for 11 degrees of freedom is  $\chi^2/\text{dof} = 4$ ). It is also clear from the three panels in Figure 1 that the spread in abundances does not correlate with either redshift, metallicity, or HI column density. The absence of any correlations suggests that it is unlikely that the spread in the observed deuterium abundances results from post-BBN evolution. Lacking a well-motivated understanding of the cause(s) of the observed dispersion, various statistical approaches have been adopted for estimating the uncertainty when identifying the weighted mean abundance from the observations with the primordial deuterium abundance. Consistent with these more sophisticated approaches, if the quoted errors for each of the data points are simply doubled (lowering the reduced  $\chi^2/\text{dof}$  from 4 to 1), it leads to the following estimate of the relic abundance:

$$\log y_{\text{DP}} = 0.42 \pm 0.02 \quad \left( y_{\text{DP}} \equiv 10^5 \left( \frac{\text{D}}{\text{H}} \right)_P = 2.63 \pm 0.12 \right). \quad (3.1)$$

This result is consistent with that quoted in Pettini and Cooke [28], who used a slightly different set of D/H observations. Adopting this estimate for the primordial D abundance, (2.1) results in

$$\eta_D = 5.96 \pm 0.28. \quad (3.2)$$

For their new, most precise individual deuterium abundance determination, Pettini and Cooke [28] find  $y_D = 2.53 \pm 0.05$  which, if identified with the primordial deuterium abundance, corresponds to  $\eta_D = 6.10 \pm 0.24$ .

### 3.2. Primordial Helium

As was the case for deuterium, the post-BBN evolution of helium ( $^4\text{He}$ ) is simple and monotonic. As gas is cycled through stars, hydrogen is burned to helium (and beyond), and the helium abundance increases with time and with metallicity. The strategy, therefore, is to concentrate on determining the helium abundance in the most nearly primordial regions of low metallicity which, as with deuterium, lie outside of the Galaxy. In H II regions, regions of hot, ionized gas, recombinations of hydrogen and helium result in observable emission lines

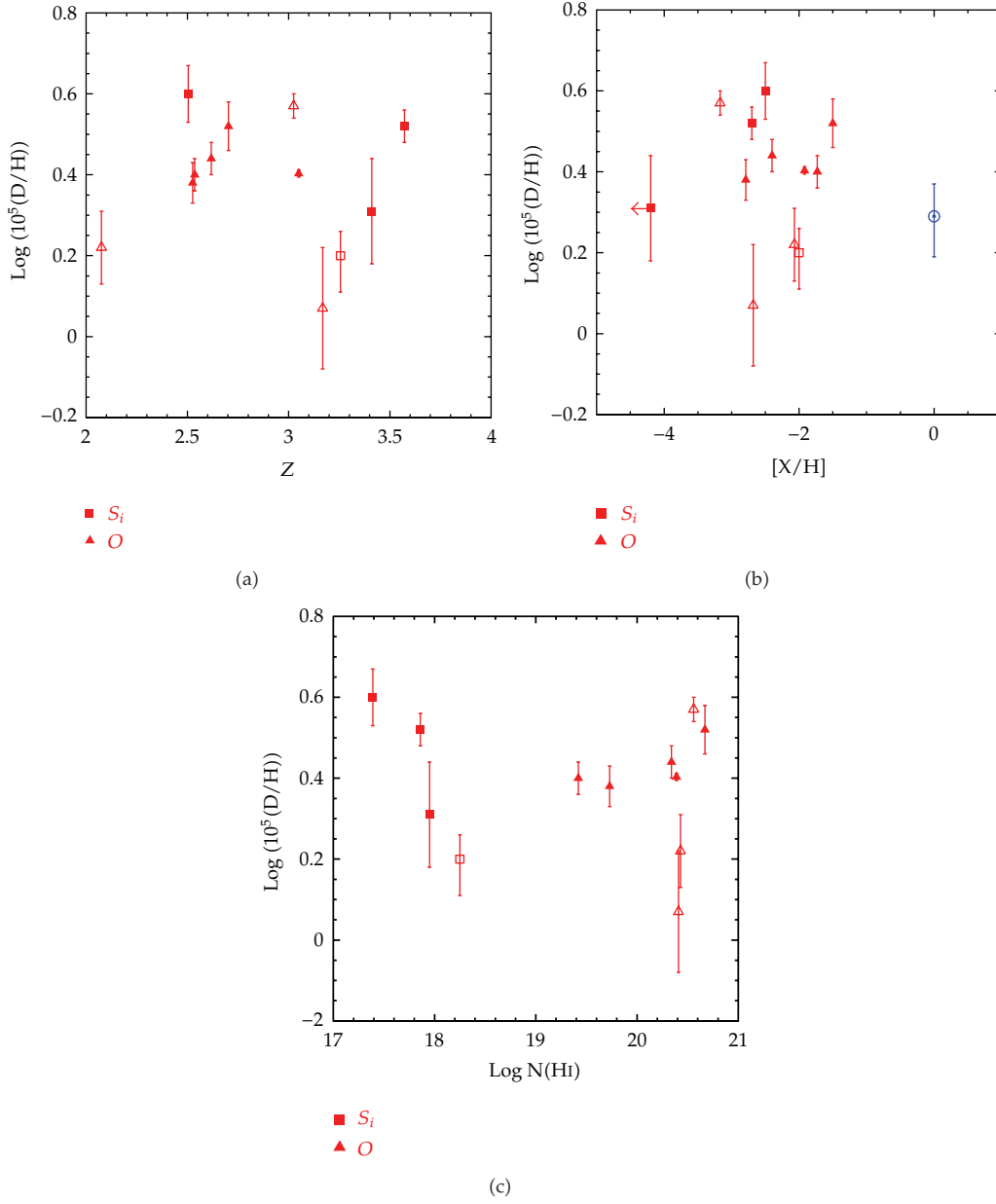


**Figure 1:** The log of the deuterium abundances ( $y_D \equiv 10^5(D/H)$ ), and their  $1\sigma$  uncertainties, inferred from 12 low- $Z$ , high- $z$  QSOALS. In (a)  $y_D$  is shown as a function of the redshift. In (b)  $y_D$  is shown as a function of the metallicity (squares for silicon and triangles for oxygen). In (c)  $y_D$  is shown as a function of the neutral hydrogen column density. The filled symbols reflect a subjective determination of the more robust determinations of  $D/H$  compared to the open symbols. The blue solar symbol in (b) is the solar system (presolar nebula) D abundance [23].



which can be used, along with models of the H II regions and a knowledge of the associated atomic physics, to infer the helium abundance. The current inventory of helium abundance determinations from relatively low metallicity, extragalactic H II regions approaches  $\sim 100$  (Izotov and Thuan 2010 (IT) [29]). These data for the inferred helium mass fraction ( $Y$ ) as a function of the corresponding oxygen abundance ( $O/H$  by number) are shown in Figure 2. The sheer size of this data set leads to relatively small, formal statistical errors, magnifying the importance of taking proper account of the many possible sources of systematic errors. While some have employed *a posteriori* selected subsets of the IT data for more detailed analyses, the sources and magnitudes of systematic errors have rarely been addressed. As a result, the uncertainty in the inferred primordial helium mass fraction is currently dominated by systematic errors (both the known unknowns and the unknown unknowns). As a result, estimating the size of the true uncertainty in the observational determination of  $Y_P$  is largely guesswork. From a linear fit to their  $Y-O/H$  data, IT find the intercept, providing an estimate of the primordial helium abundance,

$$Y_P = 0.2565 \pm 0.0010 \text{ (stat)} \pm 0.0050 \text{ (syst)}. \quad (3.3)$$

In the analysis presented here the statistical and systematic errors are, arbitrarily, combined *linearly*, leading to the estimate of the primordial abundance adopted here,

$$Y_P = 0.2565 \pm 0.0060. \quad (3.4)$$

This estimate of the relic  ${}^4\text{He}$  abundance is consistent with other, recent estimates based on analyses involving limited subsets of the IT data. In some of those other analyses, a linear  $Y$  versus  $O/H$  fit is forced on data which is consistent with no correlation between  $Y$  and  $O/H$ . Not surprisingly, the result of such analyses is a slope which is consistent with zero at less than  $1\sigma$ . However, the large uncertainty in the slope inferred from such fits leads to an estimate of the intercept ( $Y_P$ ) with excessively large errors, which have nothing to do with either the statistical or systematic errors. The errors simply reflect the uncertainty in the slope for uncorrelated data. Even worse, since these fits are consistent with an unphysical, negative  $Y-O/H$  slope at  $\lesssim 1\sigma$ , they lead to an unphysical upper bound to  $Y_P$ .

In combination with (2.2), the relic abundance adopted here results in

$$\eta_{\text{He}} = 11.50 \pm 3.77. \quad (3.5)$$

### 3.3. Primordial Lithium

Compared to the post-BBN evolution of  $D$  and  ${}^4\text{He}$ , the evolution of lithium is more complicated and uncertain, similar to that of  ${}^3\text{He}$ . As gas is cycled through stars, most of the prestellar lithium is destroyed. However, some lithium may avoid nuclear burning if it remains in the cooler, surface regions of the coolest, lowest mass stars. Observations suggest that some stars (the “super-lithium rich” red giants), during some part of their evolution, are net producers of lithium, although it is not entirely clear if such stellar produced lithium is returned to the interstellar gas before being destroyed. Finally, it is well known that collisions in the interstellar medium between cosmic rays, mainly protons and alpha particles, and interstellar gas nuclei, primarily CNO nuclei, break up those nuclei producing lithium

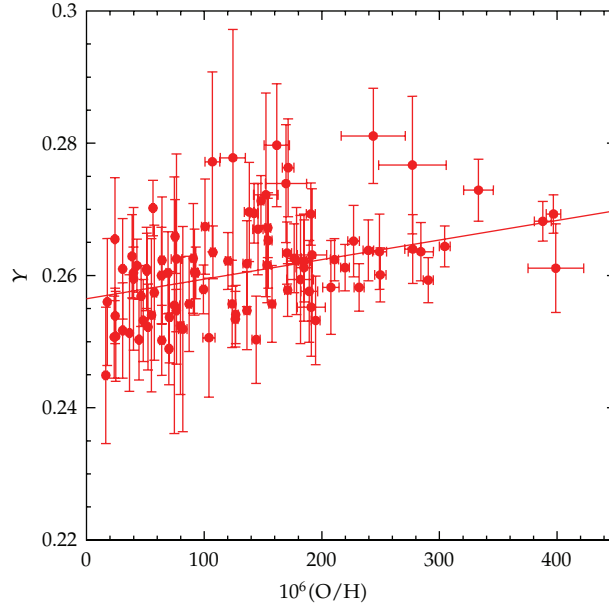


**Figure 2:** Helium abundance (mass fractions,  $Y$ ) determinations from the sample of extragalactic HII regions studied by Izotov and Thuan (2010) [29] as a function of the corresponding oxygen abundances ( $O/H$  by number). The solid line is the Izotov and Thuan best fit to a linear  $Y$  versus  $O/H$  correlation.

( ${}^7\text{Li}$ , along with  ${}^6\text{Li}$ , and isotopes of Be and B). The net effect of post-BBN production, destruction, and survival is difficult to model precisely. However, there is observational evidence supporting a lithium abundance which increases along with the heavy element abundance (metallicity), suggesting an overall increase of the lithium abundance with time.

As we are interested in samples of the most nearly primordial material, the best (only) targets for determining the relic lithium abundance are the oldest, most metal poor stars in the Galaxy. If the metallicity is sufficiently small, so that the material in these stars has suffered very little processing, observations should find a “lithium plateau.” That is, for such metal poor stars the lithium abundance should be uncorrelated with metallicity, revealing the primordial lithium abundance. Since the observationally inferred lithium abundance (relative to hydrogen) is so small (by number,  $\text{Li}/\text{H} \sim 10^{-10}$ – $10^{-9}$ ), it is common to measure it on a logarithmic scale by the quantity  $A(\text{Li}) \equiv 12 + \log(\text{Li}/\text{H})$ . The metallicity is usually quantified by comparing, also on a logarithmic scale, the iron abundance ( $\text{Fe}/\text{H}$ ) to that in the Sun:  $[\text{Fe}/\text{H}] \equiv \log(\text{Fe}/\text{H}) - \log(\text{Fe}/\text{H})_{\odot}$ . Observations of stars with  $-2.5 \lesssim [\text{Fe}/\text{H}] \lesssim -1.0$  (those with  $\sim 0.3\%$  to  $\sim 1\%$  of the metallicity of the Sun) do appear to lie on a plateau, the “Spite plateau” [30], at a level of  $A(\text{Li}) \approx 2.2 \pm 0.1$ . Recently, Nissen and Schuster [31] have suggested that stars with  $-1.5 \lesssim [\text{Fe}/\text{H}] \lesssim -0.7$  were formed with a lithium abundance close to primordial, which they estimate as  $A(\text{Li}) = 2.58 \pm 0.04$  (stat)  $\pm 0.10$  (syst), much closer to the BBN-predicted abundances discussed below. They attribute the lower observed abundances to lithium depletion in the stellar atmospheres. As will be seen below, all of the BBN predictions are close to  $A(\text{Li}) \approx 2.7$  or a factor of  $\sim 3$  higher than that suggested by the observations [32–34]. This is one of the lithium problems. However, as recent observations of even more metal poor stars ( $-3.5 \lesssim [\text{Fe}/\text{H}] \lesssim -2.5$ ) have accumulated, the lithium plateau appears to be transforming into a “lithium cliff” with, for some stars, lower lithium

abundances ( $A(\text{Li}) \approx 2.1 \pm 0.1$ ) correlating with lower metallicities [32–35]. This trend is puzzling and not understood at present, another lithium problem. Since this second lithium problem is currently unresolved, it is not clear if the lower abundances are to be interpreted as suggesting an even lower value for the primordial lithium abundance, further exacerbating the original lithium problem or, if they are telling us something about the evolution of the oldest, most metal poor stars in the Galaxy which will require us to reevaluate both lithium problems, along with the observationally inferred value of the primordial lithium abundance.

For these reasons (the lithium problems), lithium does not provide a useful probe of BBN at present. For a recent review of the current lithium data and possible resolution of the lithium problem(s), see Fields 2011 [36] and the recent overview of Spite et al. 2012 [37]. In the following, BBN, possibly in combination with the CMB, will constrain the key parameters using the observationally inferred primordial D and  $^4\text{He}$  abundances, and those parameter combinations will be used to predict the BBN abundance of lithium (reinforcing the problem of the low observed abundances).

#### 4. BBN Constraints on the Fundamental Parameters

The BBN-predicted primordial abundances depend on all three parameters:  $\eta_{10}, \Delta N_\nu, \xi$ . Because of the uncertainty of if, or how, to use lithium ( $^7\text{Li}$ ), here we limit ourselves to employing only the D and  $^4\text{He}$  abundances. Then, without recourse to additional, non-BBN data, only two of these parameters can be constrained at a time. Here, we will consider constraints on the baryon density ( $\eta_{10}$ ) from BBN (using D as our primary baryometer) and on the parameter pairs  $\{\eta_{10}, \Delta N_\nu\}$  and  $\{\eta_{10}, \xi\}$  (using D and  $^4\text{He}$  in combination) and, we will comment on the result of using complementary data on  $\eta_{10}$  or  $\Delta N_\nu$  from the CMB in order to constrain all three parameters simultaneously.

##### 4.1. BBN Constraint on the Standard Model Baryon Density ( $\Delta N_\nu = 0 = \xi$ )

Before entertaining the possibility of new physics (dark radiation and/or lepton asymmetry), the D abundance may be used to provide a standard model BBN (SBBN) constraint on the baryon density; the SBBN-predicted D abundance is much more sensitive to the baryon density than is the helium abundance. Assuming that  $\Delta N_\nu = 0 = \xi$ ,  $\eta_D = \eta_{10} = 5.96 \pm 0.28$  ( $\Omega_B h^2 = 0.0218 \pm 0.0010$ ), in excellent agreement with the value found from the CMB (e.g., from WMAP [38]).

This SBBN-inferred value of the baryon density may be used to predict the primordial abundances of the other light nuclides,  $^3\text{He}$ ,  $^4\text{He}$ , and  $^7\text{Li}$ . There is good agreement between the SBBN-predicted value of the  $^3\text{He}$  abundance and an upper bound to it inferred from observations stellar-processed gas in the Galaxy [21]. For SBBN the relic  $^4\text{He}$  mass fraction is predicted to be  $Y_P = 0.2476 \pm 0.0007$ , a value smaller than the observationally inferred abundance adopted here but within  $\sim 1.5 \sigma$  of it (see Section 3.2). The problem for SBBN is lithium. For the above value of the baryon density and for  $\Delta N_\nu = 0 = \xi$ , the predicted primordial lithium abundance is  $A(\text{Li}) = 2.68 \pm 0.06$ . This is higher, by a factor of  $\sim 3$ -4, than the values inferred from observations of the most metal poor (most nearly primordial) stars in the Galaxy. This is (one of) the lithium problem(s).

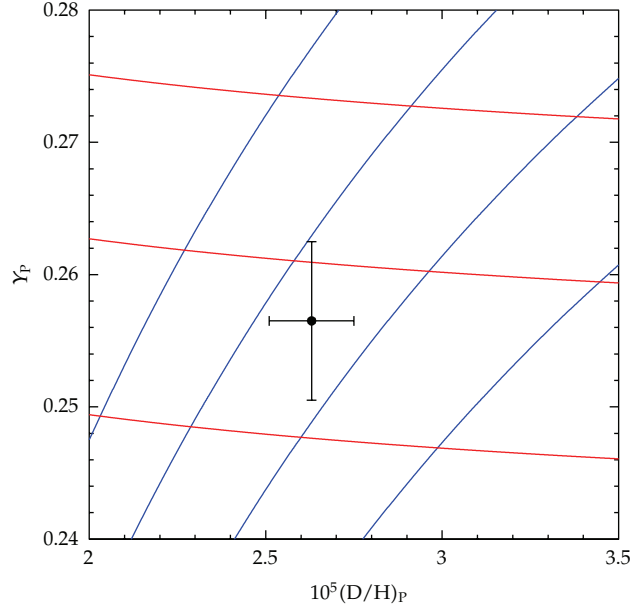


**Figure 3:** Contours of constant values of  $\Delta N_\nu$  (red) and  $\eta_{10}$  (blue) in the  $Y_P$ - $y_{DP}$  plane. From bottom to top the red curves correspond to  $\Delta N_\nu = 0, 1, 2$ . From left to right the blue curves correspond to  $\eta_{10} = 7.0, 6.5, 6.0, 5.5$ . Also shown (filled circle and error bars) are the adopted primordial abundances of D and  $^4\text{He}$  and their  $1\sigma$  uncertainties.

#### 4.2. BBN Constraints on the Baryon Density ( $\eta_{10}$ ) and Dark Radiation ( $\Delta N_\nu$ )

If it is assumed that there is no lepton asymmetry,  $\xi = 0$ , (2.4) and (2.5) may be solved for  $\eta_{10}$  and  $S$  ( $\Delta N_\nu$ ) in terms of  $\eta_D$  and  $\eta_{\text{He}}$ :

$$\begin{aligned} 106(S - 1) &= \eta_{\text{He}} - \eta_D = 5.54 \pm 3.78, \\ 106\eta_{10} &= 100\eta_D + 6\eta_{\text{He}} = 665 \pm 36. \end{aligned} \quad (4.1)$$

In Figure 3 are shown contours of constant values of  $\eta_{10}$  and  $\Delta N_\nu$  in the  $Y_P$ - $y_{DP}$  plane, along with the observationally inferred values of  $y_{DP}$  and  $Y_P$  and their  $1\sigma$  error bars. Measurements of  $y_{DP}$  and  $Y_P$  constrain  $\eta_{10}$  and  $\Delta N_\nu$ . From BBN, using D and  $^4\text{He}$ , it is found that  $\eta_{10} = 6.27 \pm 0.34$  ( $\Omega_B h^2 = 0.0229 \pm 0.0012$ ) and  $\Delta N_\nu = 0.66^{+0.47}_{-0.45}$  ( $N_{\text{eff}} = 3.71^{+0.47}_{-0.45}$ ). Figure 4 shows the 68% and 95% confidence contours corresponding to these results. While  $\Delta N_\nu \approx 1$  (a sterile neutrino?) is somewhat favored, this result is also consistent with no dark radiation ( $\Delta N_\nu = 0$ ) within 95% confidence. However, as may be seen from Figure 4, the presence of two sterile neutrinos, thermalized by mixing with the standard model neutrinos, is disfavored at  $\gtrsim 95\%$  confidence.

The observationally inferred values of  $\eta_D$  and  $\eta_{\text{He}}$  may be used to predict the primordial abundance of lithium synthesized during BBN:

$$106\eta_{\text{Li}} = 103\eta_D + 3\eta_{\text{He}} = 648 \pm 31. \quad (4.2)$$

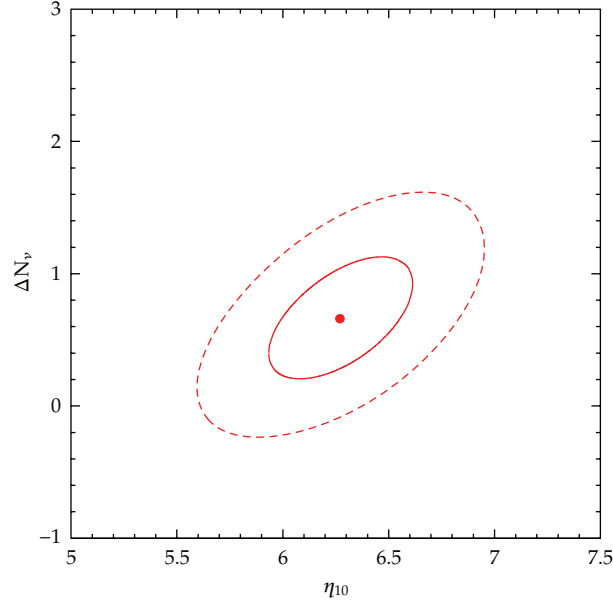


**Figure 4:** The BBN-inferred 68% (solid) and 95% (dashed) contours in the  $\Delta N_\nu$ - $\eta_{10}$  plane derived from D and  ${}^4\text{He}$  assuming that  $\xi = 0$ .

This leads to the prediction that  $A(\text{Li}) = 2.70 \pm 0.06$ , far in excess of the lithium abundances inferred from the observations of the most metal-poor stars in the Galaxy, reinforcing the SBBN result of a lithium problem (see Section 4.1).

#### 4.3. BBN Constraints on the Baryon Density ( $\eta_{10}$ ) and Lepton Asymmetry ( $\xi$ )

If it is assumed that there is no dark radiation ( $\Delta N_\nu = 0$ ), the observationally inferred abundances of D and  ${}^4\text{He}$  may be used to constrain the baryon density and any lepton asymmetry:

$$\begin{aligned} 145\xi &= \eta_D - \eta_{\text{He}} = -5.54 \pm 3.78, \\ 116\eta_{10} &= 115\eta_D + \eta_{\text{He}} = 697 \pm 32. \end{aligned} \tag{4.3}$$

In Figure 5 are shown contours of constant values of  $\eta_{10}$  and  $\xi$  in the  $Y_P$ - $y_{\text{DP}}$  plane, along with the adopted values of  $y_{\text{DP}}$  and  $Y_P$  and their  $1\sigma$  error bars. Measurements of  $y_{\text{DP}}$  and  $Y_P$  constrain  $\eta_{10}$  and  $\xi$ . From BBN using the adopted primordial D and  ${}^4\text{He}$  abundances it is found in this case that  $\eta_{10} = 6.01 \pm 0.28$  ( $\Omega_B h^2 = 0.0219 \pm 0.0010$ ) and  $\xi = -0.038 \pm 0.026$ . The latter result is consistent with  $\xi = 0$  at  $\sim 1.5\sigma$ . At  $2\sigma$ , this result provides an upper bound to the *magnitude* of the neutrino degeneracy parameter ( $|\xi| \lesssim 0.090$ ) which can be used to constrain the contribution to  $\Delta N_\nu$  resulting from the presence of the “extra” energy density associated with an excess of neutrinos over antineutrinos or vice versa:  $\Delta N_\nu(\xi) \lesssim 0.011$  at  $\sim 2\sigma$ . Figure 6 shows the 68% and 95% confidence contours corresponding to these results. This result is consistent with no lepton asymmetry to better than 95% confidence.



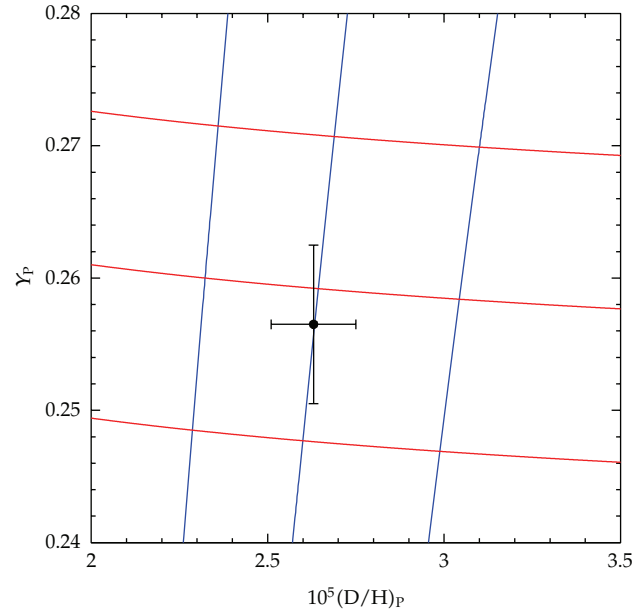


**Figure 5:** Contours of constant values of  $\xi$  (red) and  $\eta_{10}$  (blue) in the  $Y_P$ - $y_{DP}$  plane. From bottom to top the red curves correspond to  $\Delta N_\nu = 0, -0.05, -0.10$ . From left to right the blue curves correspond to  $\eta_{10} = 6.5, 6.0, 5.5$ . Also shown (filled circle and error bars) are the adopted primordial abundances of D and  ${}^4\text{He}$  and their  $1\sigma$  uncertainties.

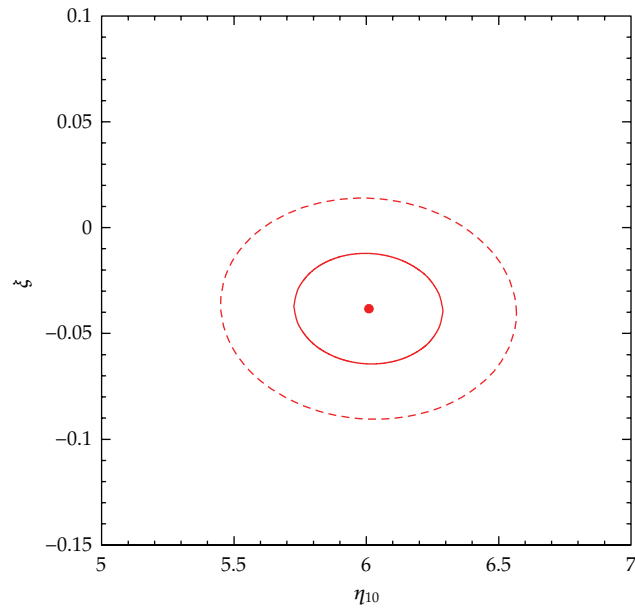


**Figure 6:** The BBN-inferred 68% (solid) and 95% (dashed) contours in the  $\xi$ - $\eta_{10}$  plane derived from D and  ${}^4\text{He}$  assuming that  $\Delta N_\nu = 0$ .

As before (see Section 4.2) the observationally inferred values of  $\eta_D$  and  $\eta_{\text{He}}$  may be used to predict the BBN lithium abundance

$$145\eta_{\text{Li}} = 142\eta_D + 3\eta_{\text{He}} = 881 \pm 41. \quad (4.4)$$

This leads to the prediction that  $A(\text{Li}) = 2.69 \pm 0.06$ , in almost exact agreement with the corresponding prediction in the presence of dark radiation (assuming that  $\xi = 0$ ), reinforcing, once again, the lithium problem.

## 5. Discussion

The simplest (least interesting?) assumption is that of no new physics, the standard model with no dark radiation (e.g., no sterile neutrinos) or a significant lepton asymmetry ( $\eta_B \ll \eta_L \ll 1$ ). In this case the SBBN-predicted baryon abundance (see Section 4.1),  $\Omega_B h^2 = 0.0218 \pm 0.0010$ , is in excellent agreement with the more precise value found from the CMB,  $\Omega_B h^2 = 0.0226 \pm 0.0004$  [38]. For this value of the baryon density (and  $\Delta N_\nu = \xi = 0$ ) the SBBN-predicted abundance of  $^3\text{He}$  is consistent with the primordial value inferred from Galactic observations, and the relic abundance of  $^4\text{He}$  agrees with the observationally inferred value adopted here, within  $\sim 1.5\sigma$ . As is by now well established, the predicted relic lithium abundance exceeds the values of the lithium abundance inferred from observations of the most metal-poor stars in the Galaxy by factor of  $\sim 3$ -4.

Setting aside for the moment the possibility of a large neutrino degeneracy ( $\eta_\nu \gg \eta_B$ ) but allowing for the presence of dark radiation ( $\Delta N_\nu \neq 0$ ), BBN along with the adopted primordial abundances of D and  $^4\text{He}$  may be used to constrain  $\Delta N_\nu$  and  $\Omega_B h^2$ . In this case (see Section 4.2) it is found that  $\Delta N_\nu = 0.66^{+0.47}_{-0.45}$  ( $N_{\text{eff}} = 3.71^{+0.47}_{-0.45}$ ) and  $\Omega_B h^2 = 0.0229 \pm 0.0012$ , in excellent agreement with the values of these parameters inferred from various CMB observations [38–41]. When derived from the CMB, the errors on  $N_{\text{eff}} = 3.046 + \Delta N_\nu$  are larger (typically by a factor of  $\sim 1.5$ –2) and those on  $\Omega_B h^2$  smaller (typically by a factor of  $\sim 3$ ) than the corresponding BBN uncertainties. This is likely to change when the PLANCK collaboration analyzes its CMB data. The PLANCK constraint on  $\Delta N_\nu$  is expected to be more precise compared to the BBN value by a factor of  $\sim 2.5$ , while that on the baryon density parameter should be more precise than the BBN value by an order of magnitude [42, 43]. The BBN-predicted relic lithium abundance when  $\Delta N_\nu \neq 0$  is hardly changed from the SBBN case, reinforcing the lithium problem. As may be seen from Figure 4, while the result for  $\Delta N_\nu$  ( $N_{\text{eff}}$ ) is closer to  $\Delta N_\nu = 1$  than to  $\Delta N_\nu = 0$ , offering some support for the existence of one sterile neutrino, it is consistent with  $\Delta N_\nu = 0$  at  $\sim 1.5\sigma$ . In contrast, the existence of two sterile neutrinos is disfavored by the BBN data at  $\gtrsim 95\%$  confidence.

In Figure 7 the BBN constraints on  $\Delta N_\nu$  and  $\Omega_B h^2$  are compared with those from recent CMB analyses. Here, too, it appears that current data have a preference for one sterile neutrino while being slightly inconsistent with two sterile neutrinos (e.g., BBN and SPT in Figure 7) or with no dark radiation (e.g., WMAP7 and ACT in Figure 7).

Unlike the CMB, BBN has the potential to probe a nonzero (albeit relatively large) lepton asymmetry (neutrino degeneracy). Current data, driven by the adopted  $^4\text{He}$  abundance, are consistent with a small, negative value for the neutrino degeneracy parameter,  $\xi = -0.038 \pm 0.026$  which, however, is only  $\sim 1.5\sigma$  from zero. A more precise result will only come when (if) there is a reduction in the error of the observationally inferred value of  $Y_P$ , whose uncertainty is dominated by systematics.

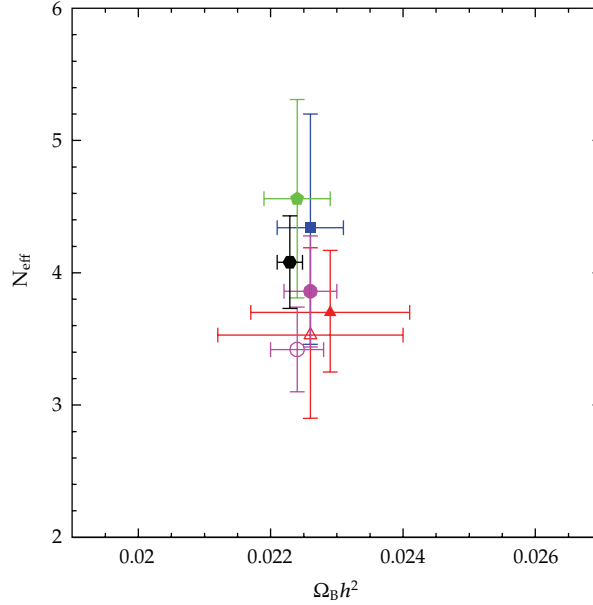


**Figure 7:** Comparing the BBN predictions of  $N_{\text{eff}}$  and  $\Omega_B h^2$  with those from various CMB determinations: BBN D +  $^4\text{He}$  (red-filled triangle), BBN D + WMAP7 [38]  $\Omega_B h^2$  (red open triangle), WMAP7 [38] (blue filled square), ACT [39] (green-filled pentagon), SPT [40] (purple filled circle), SPT + Clusters [40] (purple open circle), and WMAP7 + ACBAR + ACT + SPT [41] (black-filled hexagon).

### 5.1. Sensitivity of $\Delta N_\nu$ and $\xi$ to Primordial Helium and Its Uncertainty

The BBN-predicted helium abundance is sensitive to the early Universe expansion rate ( $S$  or, dark radiation  $\Delta N_\nu$ ) and to a lepton asymmetry ( $\xi$ ) and very insensitive to the baryon density ( $\eta_B$ ). The results which have been presented here for  $\Delta N_\nu$  and  $\xi$  are mainly driven by the adopted value for the primordial helium abundance and its uncertainty. But the observationally inferred helium abundance,  $Y_P$ , is a quantity which has changed dramatically over time as more and better data have been acquired and more careful analyses of the data have been performed. In Figure 8(a) is shown a chronology, over the past  $\sim 20$  years, of the published observational determinations of the primordial helium mass fraction, revealing a nearly monotonic increase of  $Y_P$  with time. In Figure 8(b) the chronology of the corresponding BBN-predicted values of  $\Delta N_\nu$  is shown, mirroring the increase in  $Y_P$ . Notice that only very recently, within the past few years, do the data begin to favor  $\Delta N_\nu > 0$ . This is largely the result of new (revised) atomic physics data [55, 56] required to derive the H II region helium abundances from the observational data, an unanticipated systematic effect. A similar trend may be seen in the chronology of the BBN-predicted values of the lepton asymmetry.

### 5.2. Constraints on $\Delta N_\nu$ from BBN D and the CMB-Inferred Baryon Density

The extreme sensitivity of the BBN-inferred estimates of  $\Delta N_\nu$  to the adopted helium abundance (and its large errors) is responsible for the relatively large error in the BBN-inferred value of  $\Delta N_\nu$ . An alternate approach avoiding  $^4\text{He}$  has been suggested by Nollett and Holder [4] (see, also, Pettini and Cooke [28]).

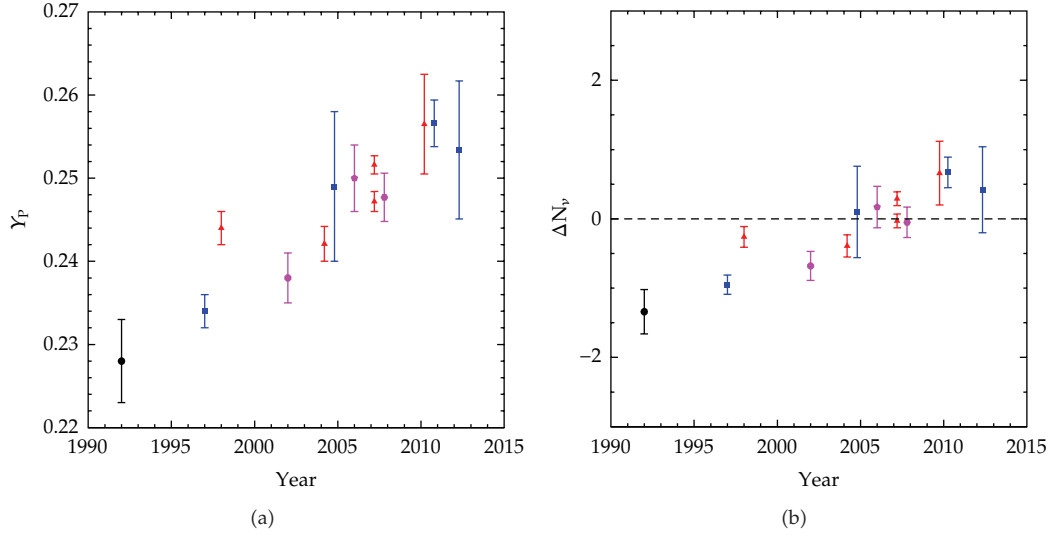


**Figure 8:** (a) shows a history of the primordial helium mass fraction ( $Y_p$ ) determinations as a function of time. The same symbols/colors correspond to determinations from collaborations involving many of the same participants and/or the same observational data (blue circle [44], blue squares [45–48], red triangles [49–51], purple circles [52, 53], and purple pentagon [54]). (b) shows the corresponding chronology of  $\Delta N_\nu$ , determined from BBN using the current best estimate of the primordial deuterium abundance. The dashed line shows the SM result,  $\Delta N_\nu = 0$ .

In the best of all worlds the BBN-inferred parameter values should be compared with those inferred, independently, from the CMB, complemented when necessary to break degeneracies among the parameters by other astrophysical data from, for example, large-scale structure, supernovae, and the Hubble constant. In the presence of possible new physics, this would enable a probe of the constancy (or not) of these parameters in the early Universe epochs from BBN until recombination. However, if it is *assumed* that  $\Delta N_\nu$  and  $\eta_{10}$  are unchanged from BBN to recombination, the information provided by BBN using the helium abundance may be replaced with that from the CMB-determined baryon density:  $\eta_{10}(\text{CMB}) = 6.190 \pm 0.115$  [38]. Using this value in combination with deuterium,  $\eta_D = \eta_{10} - 6(S - 1) = 5.96 \pm 0.28$  (for  $\xi = 0$ ), leads to a smaller estimate of  $\Delta N_\nu$  but with a larger uncertainty resulting from the much weaker dependence of  $\eta_D$  on  $\Delta N_\nu$ :  $\Delta N_\nu = 0.48^{+0.66}_{-0.63}$  ( $N_{\text{eff}} = 3.53^{+0.66}_{-0.63}$ ). The 68% and 95% contours for these results are shown in Figure 9. For the single, most precise deuterium abundance was found by Pettini and Cooke [28],  $\eta_D = 6.10 \pm 0.24$ . If this abundance is identified with the primordial deuterium abundance,  $\Delta N_\nu = 0.18 \pm 0.55$  ( $N_{\text{eff}} = 3.22 \pm 0.55$ ). While this provides some support, once again, for the presence of one sterile neutrino, the absence of dark radiation ( $\Delta N_\nu = 0$ ) is consistent with these results at the  $\sim 68\%$  confidence level. For these values of  $\eta_D$  and  $\eta_{10}$  the BBN-predicted helium abundance is  $Y_p = 0.2541 \pm 0.0081$ , very close to (well within the errors of) the observationally inferred value adopted here. Once again, the BBN-predicted lithium abundance is a problem:  $A(\text{Li}) = 2.69 \pm 0.05$ .

This approach, replacing  $^4\text{He}$  with the CMB determined baryon density parameter, could also be used to constrain a lepton asymmetry. The corresponding constraint on the neutrino degeneracy,  $\xi = -0.18 \pm 0.24$ , while entirely consistent with  $\xi = 0$ , has an uninterestingly large uncertainty resulting from the very weak dependence of  $\eta_D$  on  $\xi$ .

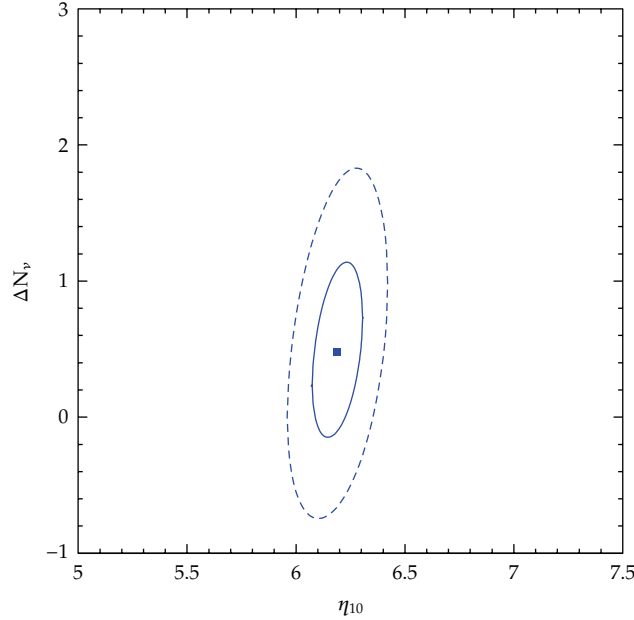


**Figure 9:** The 68% (solid) and 95% (dashed) contours in the  $\Delta N_\nu$ - $\eta_{10}$  plane derived from BBN deuterium and the CMB constraint on the baryon density [38].

### 5.3. Supplementing BBN with the CMB to Constrain $\xi \neq 0$ and $\Delta N_\nu \neq 0$

The BBN-predicted primordial light element abundances depend on all three of the key parameters  $\{\eta_{10}, \Delta N_\nu, \xi\}$ . However, the uncertainty in the observationally inferred relic abundance of  ${}^3\text{He}$ , along with the lithium problem(s), leaves only two, relatively well-constrained primordial abundances, those for D and  ${}^4\text{He}$ . From BBN alone and these abundances, all three parameters cannot be determined independently but one of them can be eliminated resulting in a relation (degeneracy) between the remaining two. For example,  $\eta_{\text{D}}$  and  $\eta_{\text{He}}$  may be used to eliminate  $\eta_{10}$ , leading to  $\xi = \xi(\Delta N_\nu; y_{\text{DP}}, Y_{\text{P}})$ , where

$$145\xi = 106(S - 1) + \eta_{\text{D}} - \eta_{\text{He}}. \quad (5.1)$$

This constraint on  $\xi$  versus  $\Delta N_\nu$  is shown by the red band in Figure 10. Without an independent constraint on  $\Delta N_\nu$ , the degeneracy between  $\xi$  and  $\Delta N_\nu$  seen in Figure 10 cannot be broken. The CMB provides such a constraint. If BBN, using the observationally inferred D and  ${}^4\text{He}$  abundances, is now supplemented with an independent constraint on  $\Delta N_\nu$  from the CMB, then a combined constraint, allowing for both dark radiation and lepton asymmetry, may be found. Using the CMB results from WMAP7 [38], ACT [39], and the SPT [40, 41], along with complementary constraints from large scale structure, the Hubble constant, supernovae, and galaxy clusters, Joudaki [57] finds  $N_{\text{eff}} = 3.87 \pm 0.42$ , corresponding to  $S = 1.065 \pm 0.032$ . Using this result in (5.1) leads to  $\xi = 0.009 \pm 0.035$ , entirely consistent with  $\xi = 0$ . The  $2\sigma$  upper bound to  $|\xi|$  is 0.079, corresponding to an upper bound to  $\Delta N_\nu(\xi) = 0.008$ . Once again, the BBN-predicted lithium abundance is high,  $A(\text{Li}) = 2.70 \pm 0.06$ , reinforcing the lithium problem.



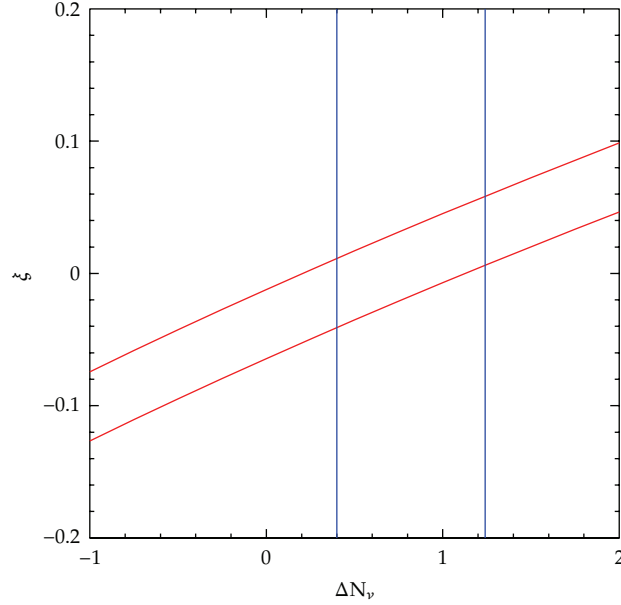


**Figure 10:** The  $\pm 1\sigma$  band (red) in the  $\xi$ - $\Delta N_\nu$  plane from BBN using the D and  $^4\text{He}$  constraints. The blue band is the  $\pm 1\sigma$  range for  $\Delta N_\nu$  from Joudaki [57].

A similar approach may be used to eliminate  $\Delta N_\nu$  instead of  $\eta_{10}$  to find  $\xi = \xi(\eta_{10}; y_{\text{DP}}, Y_{\text{P}})$  and to use the CMB for a constraint on  $\eta_{10}$ . But this approach, which is also consistent with  $\xi = 0$ , leads to a less precise constraint:  $\xi = -0.012 \pm 0.052$ .

## 6. Summary and Anticipation of Future Results

The BBN results presented here provide modest support for the presence of dark radiation ( $\Delta N_\nu \gtrsim 0$  at  $\sim 1.5\sigma$ ), to go along with the more robust evidence for dark matter and dark energy. The current observational data (D and  $^4\text{He}$ ), while allowing for the presence of a sterile neutrino ( $\Delta N_\nu = 1$  at  $\lesssim 1\sigma$ ), disfavors the presence of two sterile neutrinos ( $\Delta N_\nu = 2$  at  $\sim 2.8\sigma$ ). If, instead, it is *assumed* that  $\Delta N_\nu = 0$ , a small, but non zero lepton asymmetry is favored, also at the  $\sim 1.5\sigma$  confidence level. In contrast, if both  $\Delta N_\nu$  and  $\xi$  are allowed to vary freely and if BBN (D and  $^4\text{He}$ ) is supplemented by a CMB constraint on  $\Delta N_\nu$ , a vanishing lepton asymmetry ( $\xi = 0.009 \pm 0.035$ ) is favored.

Currently, as may be seen from Figure 7, there is very good agreement between the BBN and CMB constraints on the baryon density and dark radiation (the CMB is insensitive to a small or modest lepton asymmetry). For many years BBN provided the best constraints on the baryon density ( $\eta_{10}$  or  $\Omega_B h^2$ ) and on dark radiation ( $\Delta N_\nu$  or  $S$ ), as well as the only constraint on lepton asymmetry. With WMAP7 [38] and other CMB datasets [39–41] the best constraints on the baryon density now are from the CMB, which allow for a factor of  $\sim 2$ -3 more precise determination of  $\eta_{10}$ . However, in the present, pre-PLANCK era, BBN still provides the best dark radiation constraint, albeit with an uncertainty smaller than that from the CMB by only a factor of  $\sim 1.5$ -2. It is expected that with the publication of the PLANCK data the dark radiation torch will pass to the CMB. Depending on what PLANCK finds, it may be possible to establish the presence of dark radiation (a sterile neutrino?) at the  $\sim 5\sigma$

level *if*, for example, PLANCK should find  $\Delta N_\nu = 1 \pm 0.2$ . If, however, PLANCK should find (the best or worst of all worlds?)  $\Delta N_\nu = 0.5 \pm 0.2$ , the presence dark radiation will be favored but that of a sterile neutrino will be somewhat disfavored. It is perhaps worth recalling that the contribution of a light, thermalized scalar corresponds to  $\Delta N_\nu = 4/7 = 0.57$ .

For all the possibilities considered here ( $\Delta N_\nu = \xi = 0$ ;  $\xi = 0$ ,  $\Delta N_\nu \neq 0$ ;  $\Delta N_\nu = 0$ ,  $\xi \neq 0$ ;  $\Delta N_\nu \neq 0$ ,  $\xi \neq 0$ ), the BBN-predicted lithium abundance hardly changed at all ( $2.68 \pm 0.06 \leq A(\text{Li}) \leq 2.70 \pm 0.06$ ). This insensitivity is easy to understand since the BBN-predicted lithium and deuterium abundances are strongly correlated:

$$\eta_{\text{Li}} = \eta_{\text{D}} + 3[(S - 1) - \xi]. \quad (6.1)$$

Because the values of  $3(S - 1)$  and  $3\xi$  are almost always small compared to  $\eta_{\text{D}}$ , the corrections to a perfect lithium-deuterium correlation are generally at only the few percent level. A solution to the lithium problem is not to be found with dark radiation or a lepton asymmetry.

### 6.1. Anticipating the Future

The future for the key parameters related to the baryon abundance ( $\eta_{\text{B}}$ ) and the presence, or not, of dark radiation ( $\Delta N_\nu$ ) lies with the CMB and the anticipated results from the PLANCK mission. While it is impossible to predict the central values PLANCK will find for  $\eta_{\text{B}}$  or  $\Delta N_\nu$ , it is possible to forecast the precision to be expected from the PLANCK data and analyses [42, 43]. Such forecasts suggest that the uncertainty in the baryon abundance determination will be of order  $\sigma(\eta_{10}) \approx 0.03$ , nearly an order of magnitude better than the current BBN precision. The same forecasts suggest that  $\Delta N_\nu$  will be constrained to  $\sigma(\Delta N_\nu) \approx 0.2$ , or better. This would result in an improvement over the current BBN precision by a factor of  $\sim 2.5$ .

If it is *assumed* that the PLANCK values of the key parameters are identical to those at BBN, ignoring their possible evolution from the epoch of BBN until recombination, then these values may be used in combination with BBN to predict the relic abundances. This is in contrast with the current approach of using BBN in concert with the observationally inferred relic abundances to predict the values of the key parameters. For example, for deuterium, it is anticipated that PLANCK will constrain  $\eta_{\text{D}}$  with a precision of  $\sigma(\eta_{\text{D}}) \approx 0.1$  or, to  $\lesssim 2\%$  for  $\eta_{\text{D}} \approx 6$ . The largest uncertainty in the BBN-predicted deuterium abundance at present and in this anticipated future arises from uncertain nuclear reaction rates [4]. It can be hoped that this uncertainty may be reduced by new laboratory data, reducing the error in the BBN-predicted value of  $y_{\text{DP}}$  by perhaps a factor of  $\sim 2$ . This would lead to a reduction in the error in the inferred value of  $\eta_{\text{D}}$  by nearly a factor of two,  $\sigma(\eta_{\text{D}}) \approx 0.3 \rightarrow 0.15$ .

For helium, PLANCK may constrain  $\eta_{\text{He}}$  to  $\sigma(\eta_{\text{He}}) \approx 1.6$  which, while still large, is a factor  $\sim 2.3$  smaller than the current BBN uncertainties. This suggests that using the CMB determined values of  $\eta_{10}$  and  $\Delta N_\nu$ , the BBN-predicted primordial helium mass fraction will be known to  $\sigma(Y_{\text{P}}) \lesssim 0.003$ , a precision anticipated to also be attainable in an independent determination of  $Y_{\text{P}}$  from the CMB [42, 43].

For lithium, PLANCK may constrain  $\eta_{\text{Li}}$  to  $\sigma(\eta_{\text{Li}}) \approx 0.06$  or to better than  $\sim 1\%$  for  $\eta_{\text{Li}} \approx 6$ . However, as for deuterium, the precision of the BBN-predicted primordial lithium abundance is limited by the nuclear physics uncertainties ( $\sim 10\%$ ). Nonetheless, it will be very interesting to see if the PLANCK data support or, possibly eliminate, the lithium problem(s).

Although the CMB is insensitive to a lepton asymmetry, as may be seen from (5.1), a combination of BBN and CMB constraints on  $\Delta N_\nu$ ,  $y_{\text{DP}}$ , and  $Y_{\text{P}}$  can constrain a neutrino degeneracy, provided that the lepton asymmetry is very large compared to the baryon asymmetry. For example, for the anticipated CMB constraints on  $\sigma(\Delta N_\nu) \approx 0.2$  and on the primordial helium abundance,  $\sigma(Y_{\text{P}}) \approx 0.003$ , along with a BBN constraint on  $y_{\text{DP}}$ ,  $\sigma_\xi \approx 0.018$  or,  $\sigma_{\eta_{\text{L}}} \approx (\pi^2/4\zeta(3))\sigma_\xi \approx 0.036 \approx 6 \times 10^7 \eta_{\text{B}}$ .

## 6.2. Summary

This paper finds itself on the cusp of potentially great changes. Current BBN and CMB data provide strong support for the presence of (at least) three SM neutrinos, thermally populated during the early evolution of the Universe. This provides indirect support for the so far invisible, relic neutrino background. The new CMB and large-scale structure data have the potential to constrain the baryon asymmetry and the presence, or not, of dark radiation to new levels of precision, testing BBN and the current estimates of the relic abundances of the light elements. It will be of great interest to compare and contrast the current BBN results with those from the new data and to see what we may learn about new physics, including neutrino physics, beyond the standard models of particle physics and cosmology.

## Acknowledgments

The author pleased to acknowledge informative conversations and e-mail exchanges with R. Cyburt, M. Fumagalli, L. Knox, A. Melchiorri, K. Nollett, M. Pettini and, J. X. Prochaska. The author's research is supported at OSU by the DOE Grant DE-FG02-91ER40690.

## References

- [1] G. Steigman, "Primordial nucleosynthesis in the precision cosmology era," *Annual Review of Nuclear and Particle Science*, vol. 57, pp. 463–491, 2007.
- [2] V. Simha and G. Steigman, "Constraining the early-Universe baryon density and expansion rate," *Journal of Cosmology and Astroparticle Physics*, vol. 2008, no. 6, 2008.
- [3] G. Steigman, "Primordial nucleosynthesis: the predicted and observed abundances and their consequences," in *Proceedings of the 11th Symposium on Nuclei in the Cosmos (NIC '11)*, N. Christlieb, Ed., PoS, Trieste, Italy, 2010.
- [4] K. M. Nollett and G. P. Holder, "An analysis of constraints on relativistic species from primordial nucleosynthesis and the cosmic microwave background," *Physical Review D*. In press.
- [5] G. Steigman, "The cosmological evolution of the average mass per baryon," *Journal of Cosmology and Astroparticle Physics*, vol. 2006, no. 10, article 016, 2006.
- [6] G. Steigman, D. N. Schramm, and J. E. Gunn, "Cosmological limits to the number of massive leptons," *Physics Letters B*, vol. 66, no. 2, pp. 202–204, 1977.
- [7] G. Mangano, G. Miele, S. Pastor, T. Pinto, O. Pisanti, and P. D. Serpico, "Relic neutrino decoupling including flavour oscillations," *Nuclear Physics B*, vol. 729, no. 1-2, pp. 221–234, 2005.
- [8] S. Pastor, T. Pinto, and G. G. Raffelt, "Relic density of neutrinos with primordial asymmetries," *Physical Review Letters*, vol. 102, no. 24, Article ID 241302, 2009.
- [9] G. Beaudet and P. Goret, "Leptonic numbers and the neutron to proton ratio in the hot big bang model," *Astronomy & Astrophysics*, vol. 49, p. 415, 1976.
- [10] G. Beaudet and A. Yahil, "More on big-bang nucleosynthesis with nonzero lepton numbers," *Astrophysical Journal*, vol. 218, pp. 253–262, 1977.
- [11] A. M. Boesgaard and G. Steigman, "Big bang nucleosynthesis—theories and observations," *The Annual Review of Astronomy and Astrophysics*, vol. 23, p. 319, 1985.

- [12] H. S. Kang and G. Steigman, "Cosmological constraints on neutrino degeneracy," *Nuclear Physics B*, vol. 372, no. 1-2, pp. 494–520, 1992.
- [13] V. Barger, J. P. Kneller, P. Langacker, D. Marfatia, and G. Steigman, "Hiding relativistic degrees of freedom in the early universe," *Physics Letters B*, vol. 569, no. 3-4, pp. 123–128, 2003.
- [14] J. P. Kneller and G. Steigman, "BBN for pedestrians," *New Journal of Physics*, vol. 6, no. 117, pp. 1–22, 2004.
- [15] V. Simha and G. Steigman, "Constraining the universal lepton asymmetry," *Journal of Cosmology and Astroparticle Physics*, vol. 2008, no. 8, article 011, 2008.
- [16] V. Barger, J. P. Kneller, H. S. Lee, D. Marfatia, and G. Steigman, "Effective number of neutrinos and baryon asymmetry from BBN and WMAP," *Physics Letters B*, vol. 566, no. 1-2, pp. 8–18, 2003.
- [17] K. Nakamura, K. Hagiwara, K. Hikasa et al., "2011 review of particle physics," *Journal of Physics G*, vol. 37, Article ID 075021, 2010, (and 2011 partial update for the 2012 edition).
- [18] R. H. Cyburt, B. D. Fields, and K. A. Olive, "Primordial nucleosynthesis in light of WMAP," *Physics Letters B*, vol. 567, no. 3-4, pp. 227–234, 2003.
- [19] R. H. Cyburt, "Primordial nucleosynthesis for the new cosmology: determining uncertainties and examining concordance," *Physical Review D*, vol. 70, no. 2, Article ID 023505, 2004.
- [20] R. H. Cyburt, B. D. Fields, and K. A. Olive, "An update on the big bang nucleosynthesis prediction for  ${}^7\text{Li}$ : the problem worsens," *Journal of Cosmology and Astroparticle Physics*, vol. 2008, no. 11, article 012, 2008.
- [21] T. M. Bania, R. T. Rood, and D. S. Balser, "The cosmological density of baryons from observations of  ${}^3\text{He}^+$  in the Milky Way," *Nature*, vol. 415, no. 6867, pp. 54–57, 2002.
- [22] R. I. Epstein, J. M. Lattimer, and D. N. Schramm, "The origin of deuterium," *Nature*, vol. 263, no. 5574, pp. 198–202, 1976.
- [23] J. Geiss and G. Gloeckler, "Abundances of deuterium and helium-3 in the protosolar cloud," *Space Science Reviews*, vol. 84, no. 1-2, pp. 239–250, 1998.
- [24] D. Kirkman, D. Tytler, N. Suzuki, J. M. O'Meara, and D. Lubin, "The cosmological baryon density from the deuterium-to-hydrogen ratio in QSO absorption systems: D/H toward Q1243+3047," *Astrophysical Journal*, vol. 149, no. 1, pp. 1–28, 2003.
- [25] J. M. O'Meara, S. Burles, J. X. Prochaska, G. E. Prochter, R. A. Bernstein, and K. M. Burgess, "The deuterium-to-hydrogen abundance ratio toward the QSO SDSS J155810.16–003120.01," *Astrophysical Journal*, vol. 649, no. 2, pp. L61–L65, 2006.
- [26] M. Pettini, B. J. Zych, M. T. Murphy, A. Lewis, and C. C. Steidel, "Deuterium abundance in the most metal-poor damped Lyman alpha system: converging on  $\Omega_{\text{b}} h^2$ ," *Monthly Notices of the Royal Astronomical Society*, vol. 391, no. 4, pp. 1499–1510, 2008.
- [27] M. Fumagalli, J. M. O'Meara, and J. X. Prochaska, "Detection of pristine gas two billion years after the big bang," *Science*, vol. 334, no. 6060, pp. 1245–1249, 2011.
- [28] M. Pettini and R. Cooke, "A new, precise measurement of the primordial abundance of deuterium," *Monthly Notices of the Royal Astronomical Society (MNRAS)*, vol. 425, no. 4, pp. 2477–2486, 2012.
- [29] Y. I. Izotov and T. X. Thuan, "The primordial abundance of  ${}^4\text{He}$ : evidence for non-standard big bang nucleosynthesis," *Astrophysical Journal Letters*, vol. 710, no. 1, pp. L67–L71, 2010.
- [30] F. Spite and M. Spite, "Abundance of lithium in unevolved halo stars and old disk stars—interpretation and consequences," *Astronomy & Astrophysics*, vol. 115, pp. 357–366, 1982.
- [31] P. E. Nissen and W. J. Schuster, "Two distinct halo populations in the solar neighborhood: IV. Lithium abundances," *Astronomy and Astrophysics*, vol. 543, article A28, 2012.
- [32] M. Asplund, D. L. Lambert, P. E. Nissen, F. Primas, and V. V. Smith, "Lithium isotopic abundances in metal-poor halo stars," *Astrophysical Journal*, vol. 644, no. 1, pp. 229–259, 2006.
- [33] W. Aoki, P. Barklem, T. C. Beers, N. Christlieb, and S. Inoue, "Lithium abundances in extremely metal-poor turn off stars," *Astrophysical Journal*, vol. 698, pp. 1803–1812, 2009.
- [34] K. Lind, F. Primas, C. Charbonnel, F. Grundahl, and M. Asplund, "Signatures of intrinsic Li depletion and Li-Na anti-correlation in the metal-poor globular cluster NGC 6397," *Astronomy and Astrophysics*, vol. 503, no. 2, pp. 545–557, 2009.
- [35] P. Bonifacio, L. Sbordone, E. Caffau et al., "Chemical abundances of distant extremely metal-poor unevolved stars," *Astronomy and Astrophysics*, vol. 542, article A87, 2012.
- [36] B. D. Fields, "The primordial lithium problem," *Annual Review of Nuclear and Particle Science*, vol. 61, pp. 47–68, 2011.
- [37] M. Spite, F. Spite, and P. Bonifacio, "The cosmic Lithium problem," *Memorie della Società Astronomica Italiana*, vol. 22, pp. 9–18, 2012.

- [38] E. Komatsu, K. M. Smith, J. Dunkley et al., "Seven-year wilkinson microwave anisotropy probe (WMAP) observations: cosmological interpretation," *Astrophysical Journal*, vol. 192, no. 2, article 18, 2011.
- [39] J. Dunkley, R. Hlozek, J. Sievers et al., "The atacama cosmology telescope: cosmological parameters from the 2008 power spectrum," *Astrophysical Journal*, vol. 739, no. 1, article 52, 2011.
- [40] R. Keisler, C. L. Reichardt, K. A. Aird et al., "A measurement of the damping tail of the cosmic microwave background power spectrum with the South Pole Telescope," *Astrophysical Journal*, vol. 743, no. 1, article 28, 2011.
- [41] M. Archidiacono, E. Calabrese, and A. Melchiorri, "Case for dark radiation," *Physical Review D*, vol. 84, no. 12, Article ID 123008, 2011.
- [42] J. Hamann, J. Lesgourgues, and G. Mangano, "Using big bang nucleosynthesis in cosmological parameter extraction from the cosmic microwave background: a forecast for PLANCK," *Journal of Cosmology and Astroparticle Physics*, vol. 2008, no. 3, article 004, 2008.
- [43] S. Galli, M. Martinelli, A. Melchiorri, L. Pagano, B. D. Sherwin, and D. N. Spergel, "Constraining fundamental physics with future CMB experiments," *Physical Review D*, vol. 82, no. 12, Article ID 123504, 2010.
- [44] B. E. J. Pagel, E. A. Simonson, R. J. Terlevich, and M. G. Edmunds, "The primordial helium abundance from observations of extragalactic HII regions," *Monthly Notices of the Royal Astronomical Society*, vol. 255, pp. 325–345, 1992.
- [45] K. A. Olive, G. Steigman, and E. D. Skillman, "The primordial abundance of  $^4\text{He}$ : an update," *Astrophysical Journal Letters*, vol. 483, no. 2, pp. 788–797, 1997.
- [46] K. A. Olive and E. D. Skillman, "A realistic determination of the error on the primordial helium abundance: steps toward nonparametric nebular helium abundances," *Astrophysical Journal*, vol. 617, no. 1, pp. 29–49, 2004.
- [47] E. Aver, K. A. Olive, and E. D. Skillman, "A new approach to systematic uncertainties and self-consistency in helium abundance determinations," *Journal of Cosmology and Astroparticle Physics*, vol. 2010, no. 5, article 003, 2010.
- [48] E. Aver, K. A. Olive, and E. D. Skillman, "An MCMC determination of the primordial helium abundance," *Journal of Cosmology and Astroparticle Physics*, vol. 2012, no. 4, article 004, 2012.
- [49] Y. I. Izotov and T. X. Thuan, "The primordial abundance of  $^4\text{He}$  revisited," *Astrophysical Journal Letters*, vol. 500, no. 1, pp. 188–216, 1998.
- [50] Y. I. Izotov and T. X. Thuan, "Systematic effects and a new determination of the primordial abundance of  $^4\text{He}$  and  $dY/dZ$  from observations of blue compact galaxies," *Astrophysical Journal*, vol. 602, no. 1, pp. 200–230, 2004.
- [51] Y. I. Izotov, T. X. Thuan, and G. Stasińska, "The primordial abundance of  $^4\text{He}$ : a self-consistent empirical analysis of systematic effects in a large sample of low-metallicity H II regions," *Astrophysical Journal*, vol. 662, no. 1 I, pp. 15–38, 2007.
- [52] A. Peimbert, M. Peimbert, and V. Luridiana, "Temperature bias and the primordial helium abundance determination," *Astrophysical Journal Letters*, vol. 565, no. 2, pp. 668–680, 2002.
- [53] M. Peimbert, V. Luridiana, and A. Peimbert, "Revised primordial helium abundance based on new atomic data," *Astrophysical Journal Letters*, vol. 666, no. 2 I, pp. 636–646, 2007.
- [54] M. Fukugita and M. Kawasaki, "Primordial helium abundance: a reanalysis of the Izotov-Thuan spectroscopic sample," *Astrophysical Journal*, vol. 646, no. 2, pp. 691–695, 2006.
- [55] R. L. Porter, G. J. Ferland, and K. B. Macadam, "He I emission in the Orion Nebula and implications for primordial helium abundance," *Astrophysical Journal*, vol. 657, no. 1 I, pp. 327–337, 2007.
- [56] R. L. Porter, G. J. Ferland, K. B. MacAdam, and P. J. Storey, "Uncertainties in theoretical He I emissivities: H II regions, primordial abundance and cosmological recombination," *Monthly Notices of the Royal Astronomical Society*, vol. 393, no. 1, pp. L36–L40, 2009.
- [57] S. Joudaki, "Constraints on neutrino mass and light degrees of freedom in extended cosmological parameter spaces," <http://arxiv.org/abs/1202.0005>.



## *Review Article*

# **Recent Developments in Neutrino/Antineutrino-Nucleus Interactions**

**Jorge G. Morfín,<sup>1</sup> Juan Nieves,<sup>2</sup> and Jan T. Sobczyk<sup>1</sup>**

<sup>1</sup> *Fermi National Accelerator Laboratory, Batavia, IL 60510, USA*

<sup>2</sup> *Instituto de Física Corpuscular (IFIC), Centro Mixto Universidad de Valencia-CSIC,  
Institutos de Investigacion de Paterna, E-46071 Valencia, Spain*

Correspondence should be addressed to Jorge G. Morfín, morfín@fnal.gov

Received 20 July 2012; Accepted 6 September 2012

Academic Editor: Gian Luigi Fogli

Copyright © 2012 Jorge G. Morfín et al. This is an open access article distributed under the Creative Commons Attribution License, which permits unrestricted use, distribution, and reproduction in any medium, provided the original work is properly cited.

Recent experimental results and developments in the theoretical treatment of neutrino-nucleus interactions in the energy range of 1–10 GeV are discussed. Difficulties in extracting neutrino-nucleon cross sections from neutrino-nucleus scattering data are explained and significance of understanding nuclear effects for neutrino oscillation experiments is stressed. Detailed discussions of the status of two-body current contribution in the kinematic region dominated by quasielastic scattering and specific features of partonic nuclear effects in weak DIS scattering are presented.

## **1. Introduction**

Recent interest in neutrino interactions in the few GeV energy region comes from neutrino oscillation experiments and their need to reduce systematic errors. Neutrino fluxes used in contemporary long and short baseline experiments (K2K, T2K, MINOS, NOvA, MiniBooNE) are peaked in the 1–5 GeV energy domain and during the last ~10 years there has been considerable theoretical and experimental activity in the investigation of neutrino cross sections in this domain with reference [1] being a good summary of the lower-energy situation. Several new cross section measurements have been performed by neutrino oscillation collaborations and there are two dedicated cross section experiments (SciBooNE and MINERvA) which have been launched at Fermilab.

Even with this degree of activity, the precision with which the basic neutrino-nucleon cross sections are known is still not better than 20–30%. There are two main reasons for this: the poor knowledge of neutrino fluxes and the fact that all the recent cross section measurements have been performed on nuclear targets. It is important to recall that what

current neutrino experiments are measuring are events that are a convolution of energy-dependent neutrino flux  $\otimes$  energy-dependent cross section  $\otimes$  energy-dependent nuclear effects. The experiments have, for example, then measured an effective neutrino-carbon cross section and to extract a neutrino-nucleon cross section from these measurements requires separation of nuclear physics effects that can be done with only limited precision. For many oscillation experiments, using the same nuclear targets for their near and far detectors is a good start. However, even with the same nuclear target in both the near and far detectors, there is no automatic cancellation of effects between detectors. This is attributable to the different effective neutrino energy distributions, due to oscillations, entering the near and far detectors. With different energy spectra, the convolution of flux  $\otimes$  cross section  $\otimes$  nuclear effects is different near and far and there is no automatic cancellation. For a thorough comparison of measured neutrino-nucleon cross sections with theoretical models, these convoluted effects have to be understood.

Some of the new cross section measurements raised doubts in the areas which seemed to be well understood. The list of new *puzzles* is quite long and seems to be expanding. What is the value of the quasielastic axial mass? How large is the two-body current contribution that can mimic genuine quasielastic interactions? How large is CC (charged current) coherent pion production at a few GeV neutrino energies? What is behind the large discrepancy between MiniBooNE pion production measurements and theoretical model predictions? It can be seen as a paradox that the more than 30-year old ANL and BNL low statistics deuterium pion production data, with its minimal nuclear corrections, is still used as the best source of information about the nucleon- $\Delta$  transition matrix element.

Analysis of neutrino scattering data is certainly more complicated than the analysis of electron scattering data. In the electron case, one knows exactly the initial electron energy and so also the values of energy—and momentum—transfer. It is then possible to explicitly study separate interesting kinematical regions like QE (quasielastic) peak or the  $\Delta$  peak. Neutrino scattering data is always flux (often wide band!) integrated. Interacting neutrino energy must be evaluated based on kinematics of particles in the final state, taking into account detector acceptance and measurement accuracy.

For neutrino-nucleon interactions one can distinguish: charged current quasielastic (CCQE), neutral current elastic (NCEI), resonance production (RES), and more inelastic reactions up to the deep-inelastic (a rather misleading “DIS” term is often used to describe all the interactions which are neither CCQE/NCEI nor RES) domain. Quite different theoretical tools are used to model each of them. The simplest neutrino hadronic reaction is the charge current quasielastic (CCQE) interaction:  $\nu_\ell + n \rightarrow \ell^- + p$  with two particles: charged lepton and proton in the final state. One would like to extend this definition to the neutrino-nucleus interaction occurring on bound neutrons. The obvious question arises: what is the experimental signature of CCQE on a nuclear target? The ejected proton is not necessarily seen in a detector because quite often its momentum is below the acceptance threshold. However, events with a single reconstructed charged lepton track can result from a variety of initial interactions, for example, from a two-body current interaction or from real pion production and its subsequent absorption. Similar problems arise in other type of interactions. It is becoming clear that interpretation of neutrino-nucleus interaction must rely on a careful data/Monte Carlo (MC) comparison done with reliable MC neutrino event generators. This is why we decided to include in the paper some information about development of MC event generators.

From the experimental point of view it is natural to speak about events with no pions in the final state, with only one pion, and so forth. In fact, in several recent

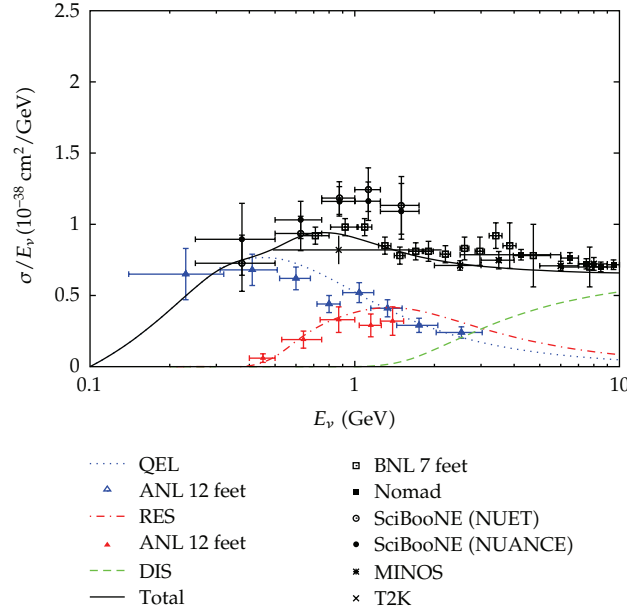


**Figure 1:** Breakdown of the inclusive CC muon neutrino cross section on free isoscalar target to QE, RES, and DIS contributions, as viewed by NuWro MC event generator.

experimental measurements that investigated quantities defined in this way, the dependence on assumptions of Monte Carlo event generators were minimal. To compare with the experimental data given in this format one must add contributions from various dynamical mechanisms and also to model FSI effects. Several ingredients of the theoretical models are verified simultaneously. It is clear that in order to validate a model one needs many samples of precise neutrino-nucleus scattering measurements on a variety of nuclear targets with various neutrino fluxes.

Our paper is organized as follows, we review recent inclusive measurements in the lower  $E_\nu$  region and then concentrate on exclusive states in increasing  $W$ , the mass of the hadronic system. Due to the limited length of this paper, we do have to limit our coverage to only the most recent developments.

## 2. Neutrino-Charged Current and Neutral Current Inclusive Reactions

### 2.1. Recent Measurements

There are four recent CC inclusive neutrino and antineutrino cross section measurements in the  $E_\nu \leq 10$  GeV energy region [2–5], see Figure 1. We notice a mild tension between SciBooNE and T2K measurements. In the following sections QE, RES, and DIS contributions will be discussed separately.

### 2.2. Theory: General Formulae—Outgoing Lepton Differential Cross Sections

In this paper, we will discuss the neutrino CC or NC (neutral current) inclusive reaction:

$$\nu_\ell(k) + A_Z \longrightarrow \ell(k') + X. \quad (2.1)$$

The generalization of the expressions to antineutrino-induced reactions is straightforward. In the equation above, the outgoing lepton could be either a negatively charged lepton,  $\ell^-$ , of flavor  $\ell$  or a neutrino  $\nu_\ell$ , for CC or NC processes, respectively.

The double differential cross section, with respect to the outgoing lepton kinematical variables, for the process of (2.1) is given in the Laboratory (LAB) frame by

$$\frac{d^2\sigma_{\nu_\ell\ell}}{d\Omega(\vec{k}')dE'_\ell} = \frac{|\vec{k}'|}{|\vec{k}|} \frac{G_F^2}{4\pi^2\eta} L_{\mu\sigma}^{(\nu)} W^{\mu\sigma}, \quad (2.2)$$

with  $\vec{k}$  and  $\vec{k}'$  the LAB lepton momenta,  $E'_\ell = (\vec{k}'^2 + m_\ell^2)^{1/2}$  and  $m_\ell$  the energy and the mass of the outgoing lepton,  $G_F = 1.1664 \times 10^{-11} \text{ MeV}^{-2}$  the Fermi constant, and  $L$  and  $W$  the leptonic and hadronic tensors, respectively. Besides,  $\eta$  takes the values 1 or 4 for CC or NC processes, respectively. The leptonic tensor is given by (in this convention,  $\epsilon_{0123} = +1$  and the metric is  $g^{\mu\nu} = (+, -, -, -)$ ):

$$L_{\mu\sigma}^{(\nu)} = L_{\mu\sigma}^s + iL_{\mu\sigma}^a = k'_\mu k_\sigma + k'_\sigma k_\mu - g_{\mu\sigma} k \cdot k' + i\epsilon_{\mu\sigma\alpha\beta} k'^\alpha k^\beta. \quad (2.3)$$

The hadronic tensor includes a collection of nonleptonic vertices and corresponds to the charged or neutral electroweak transitions of the target nucleon or nucleus,  $i$ , to all possible final states. It is thus given by

$$W^{\mu\sigma} = \frac{1}{2M_i} \sum_f (2\pi)^3 \delta^4(P'_f - P - q) \langle f | j_{\text{CC+NC}}^\mu(0) | i \rangle \langle f | j_{\text{CC+NC}}^\sigma(0) | i \rangle^*, \quad (2.4)$$

with  $P^\mu$  the four momentum of the initial target,  $M_i^2 = P^2$  the target mass square,  $P'_f$  the total four momentum of the hadronic state  $f$ , and  $q = k - k'$  the four momentum transferred to the hadronic system. The bar over the sum denotes the average over initial spins.

The hadronic tensor is completely determined by six independent, Lorentz scalar and real, structure functions  $W_i(q^2, q \cdot P)$ ,

$$\begin{aligned} \frac{W^{\mu\nu}}{2M_i} = & -g^{\mu\nu}W_1 + \frac{P^\mu P^\nu}{M_i^2}W_2 + i\frac{\epsilon^{\mu\nu\gamma\delta}P_\gamma q_\delta}{2M_i^2}W_3 + \frac{q^\mu q^\nu}{M_i^2}W_4 \\ & + \frac{P^\mu q^\nu + P^\nu q^\mu}{2M_i^2}W_5 + i\frac{P^\mu q^\nu - P^\nu q^\mu}{2M_i^2}W_6. \end{aligned} \quad (2.5)$$

Taking  $\vec{q}$  in the  $z$  direction and  $P^\mu = (M_i, \vec{0})$ , it is straightforward to find the six structure functions in terms of the  $W^{00}, W^{xx} = W^{yy}, W^{zz}, W^{xy}$ , and  $W^{0z}$  components of the hadronic tensor. After contracting with the leptonic tensor, one obtains that for massless leptons only three of them are relevant, namely,

$$\frac{d^2\sigma_{\nu_\ell\ell}}{dx dy} = \frac{G_F^2 M E_\nu}{\eta \pi} \left\{ \left( 1 - y - \frac{Mxy}{2E_\nu} \right) F_2^\nu + xy^2 F_1^\nu + y \left( 1 - \frac{y}{2} \right) x F_3^\nu \right\}, \quad (2.6)$$

with  $E_\nu$  the incoming neutrino energy,  $M$  the nucleon mass,  $x = -q^2/2Mq^0$ ,  $y = q^0/E_\nu$ , while the nuclear structure functions  $F_{1,2,3}^\nu$  are given by,  $F_1^\nu = 2MM_iW_1$ ,  $F_2^\nu = 2(q \cdot P)W_2$  and  $F_3^\nu/M = -2(q \cdot P)W_3/M_i$ . The cross section for the CC antineutrino-induced nuclear reaction is easily obtained by (i) changing the sign of the parity-violating term, proportional to  $F_3$ , in the differential cross section (this is because  $L_{\mu\sigma}^{(\bar{\nu})} = L_{\sigma\mu}^{(\nu)}$ ), (2.6), and (ii) using  $j_{CC-}^\mu = j_{CC+}^{\mu\dagger}$  in the definition/computation of the hadron tensor in (2.4)). In the case of antineutrino NC-driven processes, it is only needed to flip the sign of the term proportional to  $F_3$  in the differential cross section, since the hadron NC is not affected.

The hadronic tensor is determined by the  $W$  or  $Z$  gauge boson self energy,  $\Pi_{W,Z}^{\mu\rho}(q)$ , in the nuclear medium. To evaluate this latter object requires a theoretical scheme, where the relevant degrees of freedom and nuclear effects could be taken into account.

In the next two sections we will discuss CCQE and pion production reactions. The general formalism described above will be used in the section devoted to DIS.

### 3. Charged Current Quasielastic

As discussed in the Introduction, we define CCQE as either the reaction on a free nucleon or on a quasi-free nucleon inside a nucleus yielding a muon and nucleon. In the case of neutrino nucleus scattering we also use the term CCQE-like reaction defined as one in which there are no pions in the final state. It then includes events with real pion production followed by absorption. Such a definition may seem awkward but as will be seen, it is close to what was experimentally measured by the MiniBooNE collaboration.

A theoretical description of the free nucleon target CCQE reaction is based on the conserved vector current (CVC) and the partially conserved axial current (PCAC) hypotheses. The only unknown quantity is the nucleon axial form-factor  $G_A(Q^2)$  for which one typically assumes a dipole form  $G_A(0)(1 + Q^2/M_A^2)^{-2}$  with one free parameter, the axial mass  $M_A$ . The nondipole axial form factor was investigated, for example, in [6].

In the past, several measurements of  $M_A$  were performed on a deuterium target for which most of nuclear physics complications are minimal and it seemed that the results converged to a value of the order of 1.03 GeV [7]. There is an additional argument in favor of a similar value of  $M_A$  coming from the weak pion-production at low  $Q^2$ . PCAC-based evaluation gives an axial mass value of  $1.077 \pm 0.039$  GeV [8]. On the other hand, all of the more recent high statistics measurements of  $M_A$ , with the exception of the NOMAD higher-energy experiment, reported larger values: K2 K (oxygen,  $Q^2 > 0.2 \text{ GeV}^2$ )  $\rightarrow 1.2 \pm 0.12$  [9]; K2 K (carbon,  $Q^2 > 0.2 \text{ GeV}^2$ )  $\rightarrow 1.14 \pm 0.11$  [10]; MINOS (iron,  $Q^2 > 0 \text{ GeV}^2$ )  $\rightarrow 1.19 \pm 0.17$ ; MINOS (iron,  $Q^2 > 0.3 \text{ GeV}^2$ )  $\rightarrow 1.26 \pm 0.17$  [11]; MiniBooNE (carbon,  $Q^2 > 0 \text{ GeV}^2$ )  $\rightarrow 1.35 \pm 0.17$  [12]; MiniBooNE (carbon,  $Q^2 > 0.25 \text{ GeV}^2$ )  $\rightarrow 1.27 \pm 0.14$  (for completeness: NOMAD (carbon,  $Q^2 > 0 \text{ GeV}^2$ )  $\rightarrow 1.07 \pm 0.07$  [13]).

The difference between MiniBooNE and NOMAD measurements could come from different definitions of the CCQE signal. In the case of MiniBooNE a sample of 2 subevents (Cherenkov light from muon and from decay electron) is analyzed and ejected protons are not detected. In the case of NOMAD 1-track (muon) and 2-tracks (muon and proton) samples of events are analyzed simultaneously. With a suitable chosen value of the formation zone parameter  $\tau_0$  values of  $M_A$  extracted separately from both data samples are approximately the same, see [13, Table 9]. We note that the procedures in which the formation zone concept is applied to nucleons that already exist may seem little controversial. We would like to mention also the CCQE data not yet published in peer review journals. MINOS tried to



evaluate better the pion production background [14]. A function of  $Q^2$  which corrects Monte Carlo (NEUGEN) RES predictions was proposed. The shape of the curve is similar to MiniBooNE's DATA/MC correction function (see below) but in the case of MiniBooNE for  $Q^2 > 0.1 \text{ GeV}^2$  the correction factor is  $>1$ . The new MINOS best fit value of  $M_A$  is  $1.16 \text{ GeV}$  and the error was reduced by a factor of 3 with respect to [11]. SciBooNE showed partial results of the CCQE analysis [15]. Results are given in terms of fits for CCQE cross-section DATA/MC multiplicative factors  $a_j$  ( $j$  label true neutrino energy bins) and a scaling factor  $F_N$ . The obtained best fit values in the neutrino energy region  $E_\nu \in (0.6, 1.6) \text{ GeV}$  are between 1.00 and 1.09 which with  $F_N = 1.02$  and the value of the axial mass used in the NEUT Monte Carlo generator ( $1.2 \text{ GeV}$ ) should translate to the axial mass value  $M_A \sim 1.25\text{--}1.3 \text{ GeV}$ . In the SciBooNE analysis there are some instabilities in the wider region of  $E_\nu$  [16, Figure 11.2]. A use of the universal background scaling factor  $a_{bcg}$  for three different event samples is perhaps not sufficient (its best fit value is as large as  $1.37 \text{ GeV}$ ).

An important antineutrino CCQE measurement was reported by MiniBooNE [17]. The DATA/MC average cross-section ratio was reported to be  $1.21 \pm 0.12$  which is a surprising result because in the NUANCE carbon CCQE computations the  $M_A$  value was set to be  $1.35 \text{ GeV}$ . In the experimental analysis, it was important to evaluate correctly neutrino contamination in the antineutrino flux. Three independent measurements indicate that the  $\nu_\mu$  flux in the antineutrino beam should be scaled down by a factor of  $\sim 0.8$  with an obvious important impact on the final results.

The most recent MINERvA preliminary results for CCQE antineutrino reaction are still subject to large flux normalization uncertainties but they seem to be consistent with  $M_A = 0.99 \text{ GeV}$  [18].

### 3.1. MiniBooNE Data

In recent discussions of the CCQE, MiniBooNE measurement plays a special role. For the first time the data was presented in the form of double differential cross section in muon scattering angle and kinetic energy. Such data is the actual observable for the MiniBooNE experiment and more complete than a distribution of events in  $Q^2$  which is calculated assuming an obviously incorrect nuclear model (the nucleon is assumed to be at rest). The signal events form a subset of events with no pions in the final state. MiniBooNE subtracted as a background, events with real pion production and subsequent absorption and also a contribution from pionless  $\Delta$  decays implemented in the NUANCE MC [19] as constant fractions of  $\Delta^{++}$  and  $\Delta^+$  decays, following the approach of [20]. The background estimate, based on MC predictions, was later corrected by a  $Q^2$  dependent function, which accounts for a data/MC discrepancy in the sample of events containing one  $\pi^+$  in the final state. The shape of the correction function is not well understood [21] but it has an important impact on the extracted value of  $M_A$ . The function quantifies a lack of understanding of processes like pion absorption and can have a significant effect on the understanding of both samples of events.

MiniBooNE also provided data for the CCQE signal plus background together as the measurement of the cross section of the process in which there are no pions in the final state, the observable which is maximally independent of MC assumptions.

### 3.2. Theoretical Approaches to CCQE Generalities

Several approaches have been followed/derived to compute the relevant gauge boson absorption modes (self-energy) to describe the CCQE process. For moderate and intermediate neutrino energies, in the few GeV region, the most relevant ones are the absorption

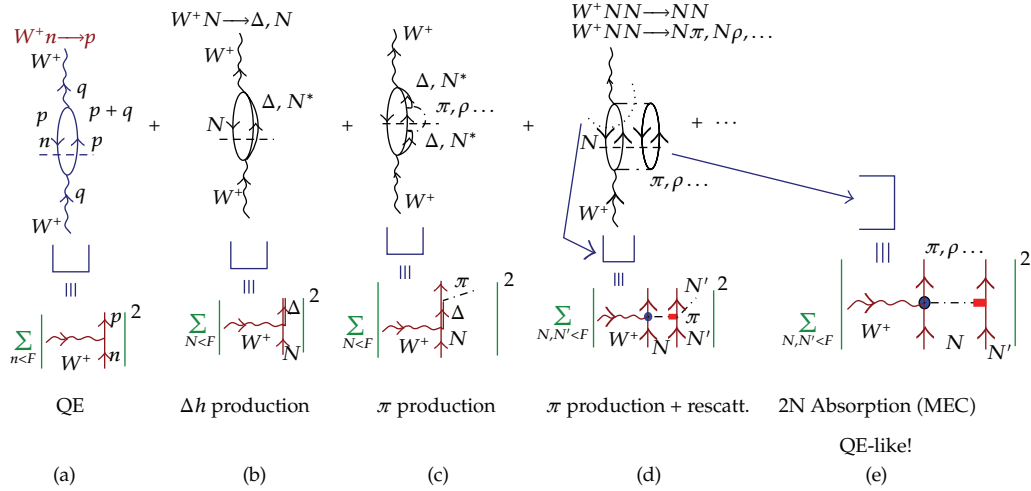


**Figure 2:** Diagrammatic representation of some diagrams contributing to the  $W^+$ -self energy.

by one nucleon, or a pair of nucleons or even three nucleon mechanisms, real and virtual meson ( $\pi, \rho, \dots$ ) production, excitation of  $\Delta$  or higher resonance degrees of freedom, and so forth (e.g., some absorption modes are depicted in Figure 2 for the case of neutrino CC processes). A review of theoretical model results can be found in [22]. Almost all approaches, used at intermediate neutrino energies, deal with hadron, instead of quarks and gluons, degrees of freedom. In addition they consider several nuclear effects such as RPA or short range correlations (SRC). The free space couplings between hadrons and/or the weak  $W$  and  $Z$  bosons are parametrized in terms of form factors, which are fitted to the available data on electroweak scattering off free nucleons. In the few GeV energy region, theoretical models rely on the impulse approximation (IA) and neutrino-nucleus CCQE interactions are viewed as a two-step process: primary interaction and final state interactions (FSI), propagation of resulting hadrons through the nucleus. The validity of the IA is usually related to typical values of the momentum transfer  $q$ . Experience from the electron scattering tells us that for  $q > 300\text{--}500\text{ MeV}/c$  IA-based models are able to reproduce the data well. Thus, the expectations is that for a few GeV neutrino interactions IA is an acceptable approach and if necessary simpler nuclear model computations can be supplemented with RPA corrections for lower momentum transfers (see below). In the neutrino nucleus cross section measurements a goal is to learn about neutrino free nucleon target scattering parameters (an obvious exception is coherent pion production). *Effective* parameters like sometimes discussed quasielastic axial mass  $M_A^{\text{eff}}$  are of little use as their values can depend on the neutrino flux, target, and perhaps also on the detection technique/acceptance.

The definition of neutrino-nucleus CCQE scattering can be made more rigorous in the language of many body field theory. CCQE process originates from a first step mechanism where the gauge boson is being absorbed by just one nucleon. This corresponds to the first of the selfenergy diagrams depicted in Figure 2 (contribution (a)). This contribution, that from now on we will call *genuine* QE, has been computed within different theoretical models and used to predict the corresponding outgoing lepton differential cross section.

The simplest model, commonly used in Monte Carlo event generators, is the relativistic Fermi gas (RFG) model proposed by Smith and Moniz more than 35 years ago [23, 24] corresponding to only one many body Feynman diagram. The model combines

the bare nucleon physics with a model to account for Fermi motion and nucleon binding within the specific nucleus. The model can be made more realistic in many ways (when the axial mass and electromagnetic form factors are kept unchanged, the inclusion of more sophisticated nuclear effects makes the cross section generally smaller with respect to the RFG (relativistic Fermi gas) model) to achieve better agreement with a broad range of electron scattering data. For example, the inclusion of a realistic joint distribution of target nucleon momenta and binding energies based on short range correlation effects leads to the spectral function (SF) approach. Spectral functions for nuclei, ranging from carbon ( $A = 12$ ) to iron ( $A = 56$ ) have been modeled using the local density approximation (LDA) [25], in which the experimental information obtained from nucleon knock-out measurements is combined with the results of theoretical calculations in nuclear matter at different densities, and they have been extensively validated with electron scattering data. Calculations by Benhar and Meloni [26] and Ankowski and Sobczyk [27] show that the SF effects moderately modify the muon neutrino differential cross sections, and they lead to reductions of the order of 15% in the total cross sections. This is corroborated by the results obtained within the semiphenomenological model (density dependent mean-field potential in which the nucleons are bound) [28] employed within the GiBUU model to account for these effects.

Inclusion of nucleon-nucleon long-range correlations leads to RPA (random phase approximation) which improves predictions at lower momentum transfers (and also low  $Q^2$ ). RPA corrections have been discussed by many authors in the past and recently included in computations of three groups (IFIC, Lyon, and Aligarh (the Aligarh group uses a similar approach to that derived in [29, 30], but with some simplifications that though well suited to study the related process of muon capture in nuclei, might not be totally appropriate for the case of larger energies and momenta being transferred to the nucleus (see the discussion in [29, 30])) in [29–34], respectively. When the electroweak interactions take place in nuclei, the strengths of electroweak couplings may change from their free nucleon values due to the presence of strongly interacting nucleons. Indeed, since the nuclear experiments on  $\beta$  decay in the early 1970s [35, 36], the quenching of axial current is a well-established phenomenon. The RPA resummation accounts for the medium polarization effects in the  $1p1h$  contribution (Figure 2(a)) to the  $W$  and  $Z$  selfenergy by substituting it by a collective response as shown diagrammatically in Figure 3(a). Evaluating these effects, requires an in-medium baryon-baryon effective force, which in both sets (IFIC and Lyon) of calculations was successfully used/tested in previous works on inclusive nuclear electron scattering. RPA effects are important as can be appreciated in Figure 3(b). In this plot, we show results from both IFIC and Lyon models, presented in [37, 38], respectively, for the CC quasielastic  $\nu_\mu$ - $^{12}\text{C}$  double differential cross sections convoluted with the MiniBooNE flux [39]. There, we also see that predictions of both groups for these genuine QE contribution, with and without RPA effects, turn out to be in a quite good agreement. Finally, it is important to stress also that RPA corrections strongly decrease as the neutrino energy increases, while its effects should account for a low  $Q^2$  deficit of CCQE events reported by several experimental groups (see Figures 3(c) and 3(d)). Continuum RPA (CRPA) computations for neutrino scattering were performed by the Ghent group [40].

### 3.2.1. Other Theoretical Developments

In [41–43] the bound-state wave functions are described as self-consistent Dirac-Hartree solutions, derived within a relativistic mean field approach by using a Lagrangian containing  $\sigma$  and  $\omega$  mesons [44]. This scheme also accounts for some SF effects. Moreover, these models

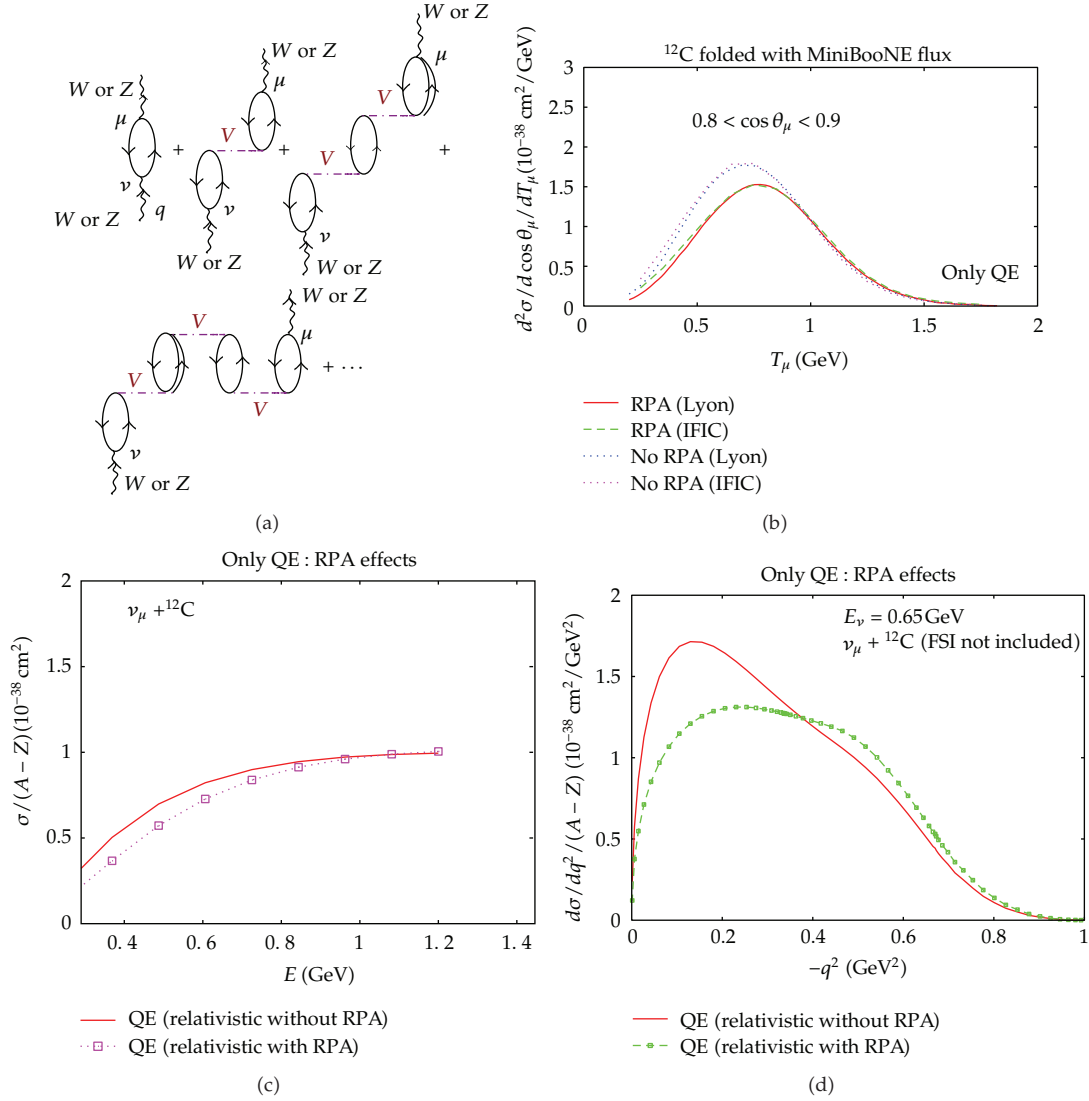


**Figure 3:** (a) Set of irreducible diagrams responsible for the polarization (RPA) effects in the 1p1h contribution to the  $W$  or  $Z$  self energies. (b) MiniBooNE flux-averaged CC quasielastic  $\nu_\mu$ - $^{12}\text{C}$  double differential cross section per neutron for  $0.8 < \cos \theta_\mu < 0.9$  as a function of the muon kinetic energy. (c, d) Different theoretical predictions for muon neutrino CCQE total cross section off  $^{12}\text{C}$ , as a function of the neutrino energy (c) and  $q^2$  (d), obtained from the relativistic model of [29, 30]. In all cases  $M_A \sim 1.05 \text{ GeV}$ .

also incorporate the FSI between the ejected nucleon and the residual nucleus. The final nucleon is described either, as a scattering solution of the Dirac equation [42, 43] in the presence of the same relativistic nuclear mean field potential applied to the initial nucleon, or adopting a relativistic multiple-scattering Glauber approach [41].

The relativistic Green's function model [45] would be also appropriate to account for FSI effects between the ejected nucleon and the residual nucleus for the inclusive scattering, where only the outgoing lepton is detected. There, final-state channels are included, and the flux lost in each channel is recovered in the other channels just by the imaginary part of an empirical optical potential and the total flux is thus conserved.

Another interesting approach starts with a phenomenological model for the neutrino interactions with nuclei that is based on the superscaling behavior of electron scattering data. Analysis of inclusive  $(e, e')$  data have demonstrated that for momentum transfers  $q > \sim 500 \text{ MeV}/c$  at energy transfers below the QE peak superscaling is fulfilled rather well [46, 47]. The general procedure consists on dividing the experimental  $(e, e')$  cross section by an appropriate single-nucleon cross section to obtain the experimental scaling function, which is then plotted as a function of a certain scaling variable for several kinematics and for several nuclei. If the results do not depend on the momentum transfer  $q$ , then scaling of the first kind occurs, if there is no dependence on the nuclear species, one has scaling of the second kind. The simultaneous occurrence of scaling of both kinds is called superscaling. The superscaling property is exact in the RFG models, and it has been tested in more realistic models of the  $(e, e')$  reaction. The superscaling approach (SuSA) is based on the assumed universality of the scaling function for electromagnetic and weak interactions [48]. The scaling function thus determined from  $(e, e')$  data is then directly taken over to neutrino interactions [48, 49]. There are no RPA correlations or SF corrections explicitly taken into account, but they may be contained in the scaling function. Nevertheless, such approach is far from being microscopic. Moreover, it is difficult to estimate its theoretical uncertainties, as for example to what extent the quenching of the axial current, that is due to RPA corrections, is accounted for by means of scaling functions determined in  $(e, e')$  experiments, which are driven by the vector current.

### 3.2.2. Theoretical Models versus MiniBooNE 2D Data

The MiniBooNE data [12] have been quite surprising. Firstly, the absolute values of the cross section are too large as compared to the consensus of theoretical models [22, 50]. Actually, the cross section per nucleon on  $^{12}\text{C}$  is clearly larger than for free nucleons. Secondly, their fit to the shape (excluding normalization) of the  $Q^2$  distribution done within the RFG model leads to the axial mass,  $M_A = 1.35 \pm 0.17 \text{ GeV}$ , much larger than the previous world average ( $\approx 1.03 \text{ GeV}$ ) [8, 13]. Similar results have been later obtained analyzing MiniBooNE data with more sophisticated treatments of the nuclear effects that work well in the study of electron scattering. For instance, [51, 52] using the impulse approximation with state of the art spectral functions for the nucleons fail to reproduce data with standard values of  $M_A$ . Large axial mass values have also been obtained in [53] where the 2D differential cross section was analyzed for the first time using RFG model and spectral function. Similar results were obtained in [54], where the data have been analyzed in a relativistic distorted-wave impulse approximation supplemented with a RFG model.

### 3.3. Multinucleon Mechanisms

A plausible solution to the large axial mass puzzle was firstly pointed out by Martini et al. [32, 33] (the papers of Martini et al. are based on the older investigation by Marteau [55]). The relevant features of the model were known already at the end of 1990s and at that time the goal was to understand better SuperKamiokande atmospheric neutrino oscillation signal), and later corroborated by the IFIC group [37, 56]. In the MiniBooNE measurement of [12], QE is related to processes in which only a muon is detected in the final state. As was already discussed above, besides genuine QE events, this definition includes multinucleon processes (Figure 2(e) (note that the intermediate pion in this term is virtual and it is part



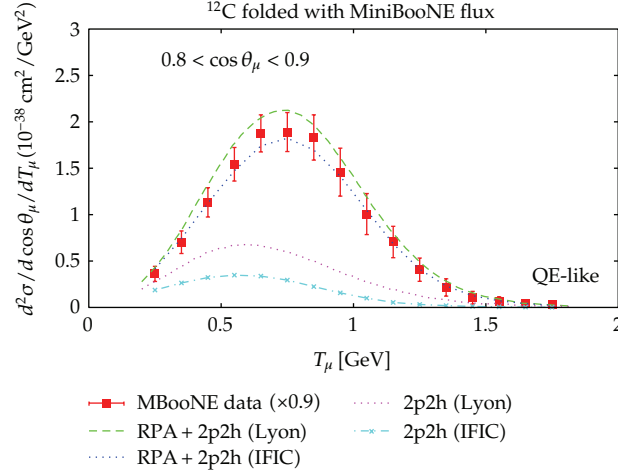


**Figure 4:** MiniBooNE flux-averaged CC quasielastic  $\nu_\mu$ - $^{12}\text{C}$  double differential cross section per neutron for  $0.8 < \cos\theta_\mu < 0.9$ , as a function of the muon kinetic energy. Experimental data from [12] are multiplied by 0.9. In all the cases  $M_A \sim 1.05 \text{ GeV}$ .

of the  $\Delta N \rightarrow NN$  interaction inside of the nucleus. Indeed, one should consider a full interaction model for the in medium baryon-baryon interaction), where the gauge boson is being absorbed by two or more nucleons, and others like real pion production followed by absorption (Figures 2(c) and 2(d)). The MiniBooNE analysis of the data attempts to correct (through a Monte Carlo estimate) for some of these latter effects, such as real pion production that escapes detection through reabsorption in the nucleus leading to multinucleon emission. But, it seems clear that to describe the data of [12], it is necessary to consider, at least, the sum of the selfenergy diagrams depicted in Figures 2(a) and 2(e). Those correspond to the genuine QE (absorption by just one nucleon), and the multinucleon contributions, respectively. These two mechanisms contribute to the CCQE-like cross section (also for simplicity, we will often refer to the multinucleon mechanism contributions, though they include effects beyond gauge boson absorption by a nucleon pair, as 2p2h (two-particle hole) effects).

The inclusion of the 2p2h contributions enables [37, 38] the double differential cross section  $d^2\sigma/dE_\mu d\cos\theta_\mu$  and the integrated flux unfolded cross section (we should warn the reader here, because of the multinucleon mechanism effects, the algorithm used to reconstruct the neutrino energy is not adequate when dealing with quasielastic-like events, a distortion of the total flux unfolded cross section shape could be produced. We will address this point in Section 3.5) measured by MiniBooNE, to be described with values of  $M_A$  (nucleon axial mass) around  $1.03 \pm 0.02 \text{ GeV}$  [8, 13]. This is reassuring from the theoretical point of view and more satisfactory than the situation envisaged by some other works that described the MiniBooNE data in terms of a larger value of  $M_A$  of around 1.3–1.4 GeV, as mentioned above.

### 3.3.1. Similarities and Differences between Multinucleon Ejection Models

As shown in Figures 3(a) and 3(b), the IFIC group predictions [37, 56] for QE cross sections agree quite well with those obtained in [32, 33, 38] (Lyon group). However, both above presented approaches considerably differ (about a factor of two) in their estimation of the size of the multinucleon effects, as can be appreciated in Figure 4. IFIC predictions, when

the 2p2h contribution is included, favor a global normalization scale of about 0.9 (see [37]). This is consistent with the MiniBooNE estimate of a total normalization error as 10.7%. The IFIC evaluation in [37, 56], of multinucleon emission contributions to the cross section is fully microscopical and it contains terms, which were either not considered or only approximately taken into account in [32, 33, 38]. Indeed, the results of these latter works rely on some computation of the 2p2h mechanisms for the  $(e, e')$  inclusive reaction [57], which results are simply used for neutrino-induced processes without modification. Thus, it is clear that these latter calculations do not contain any information on axial or axial-vector contributions (the evaluation of the nuclear response induced by these 2p2h mechanisms carried out in [32] is approximated, as acknowledge there. Only, the contributions in [32] that can be cast as a  $\Delta$ -selfenergy diagram should be quite similar to those derived in [56] by the IFIC group, since in both cases the results of [20] for the  $\Delta$ -selfenergy are used). For antineutrinos the IFIC model predicts, contrary to the results of the Lyon group, also a sizeable effect of 2p2h excitations.

Another microscopic approach to 2p2h excitations was proposed by Amaro et al. These authors have used the empirical  $(e, e')$  SuSA scaling function to describe the CCQE MinibooNE data, including some 2p2h contributions due to MEC (meson exchange currents) [58, 59]. The approach, used in these latter works, to evaluate the 2p2h effects, though fully relativistic, does not contain the axial contributions. The authors of [58, 59] also find an increase of the inclusive cross section for neutrinos; at forward muon angles the calculations come close to the data, but the MEC contributions die out fast with increasing angle so that the cross section is significantly underestimated at backward angles. As a consequence, the energy-separated (flux unfolded) cross section obtained for the MiniBooNE experiment, while being higher than that obtained from SuSA alone still, underestimates the experimental result even when 2p2h contributions are added. Recently, a strong difference between neutrino and antineutrino cross sections has been obtained within this model, with the 2p2h effects being significantly larger for antineutrinos than for neutrinos [59].

Two other effective models to account for MEC/2p2h effects have been proposed by Bodek et al. [60] (transverse enhancement model (TEM)) and Lalakulich et al. [61]. The TEM can easily be implemented in MC event generators [62]. It assumes that it is sufficient to describe properly an enhancement of the transverse electron QE response function keeping all other ingredients as in the free nucleon target case. Thus, some effective proton and neutron magnetic form factors are fitted to electron-nucleus data and later they are used, together with the free nucleon axial current, to study CCQE processes. It is to say, the TEM assumes that there are no nuclear medium effects (RPA, 2p2h mechanisms, etc...) affecting those nuclear response functions induced by the nucleon axial-vector current. Despite of a certain phenomenological success to describe the MiniBooNE data [60, 62], such assumption seems quite unjustified.

In the model of [61], the multinucleon mechanism contributions are parametrized as phase space multiplied by a constant which is fitted to the difference of the energy-separated MiniBooNE data and the calculated QE cross section. RPA effects are not taken into account in [61]. Since these tend to lower the cross section in particular at forward muon angles, the model of [61] underestimates the contributions of 2p2h effects there. Indeed, the authors of this reference find that the shape and over-all size of the 2p2h contribution turns out to be rather independent of the muon angle. This is in sharp contrast with the microscopical results obtained within the IFIC [37, 56] and SuSa models [59], that find the 2p2h contribution becomes significantly less important as the muon scattering angle increases.

### 3.3.2. Perspectives to Measure the MEC/2p2h Contribution

The unambiguous experimental measurement of the MEC contribution to the CC inclusive cross section can be made by detecting hadrons in the final state. All the microscopic models provide up to now only the MEC/2p2h contribution to the muon inclusive 2D differential cross section:  $d^2\sigma_{\nu\ell}/d\Omega(\hat{k}')dE'_\ell$ . Such models cannot describe detailed exclusive cross sections (looking into the nucleon side), as explicit FSI effects, that modify the outgoing nucleon spectra, have not been addressed yet in these microscopical models. It is reasonable to assume that at the level of the primary reaction mechanism, they produce only slight changes in  $d^2\sigma_{\nu\ell}/d\Omega(\hat{k}')dE'_\ell$ , leaving almost unchanged the integrated cross sections [26, 27].

A model to describe hadrons in the final state was proposed in [62]. It was implemented in the NuWro MC event generators and its predictions were used in the analysis of recent MINERvA antineutrino CCQE data.

In the papers [61, 62] various observables are discussed which can be used to detect MEC contribution. One option is to look at proton pairs in the final state. Another possibility is to investigate the distribution of visible energy which allows to include contributions from protons below reconstruction threshold. The basic intuition from the electron scattering is that MEC events populate the region between QE and  $\Delta$  peaks. Typically, to have an MEC event more energy must be transferred to the hadronic system than for a CCQE one. However, it should be stressed that the precision with which FSI effects are currently handled in MC codes can make such a measurement difficult. During the last few years FSI studies were focused on pions only [63] aiming at understanding recent pion production data on nuclear targets [64]. Nucleons in the final state were never studied with a similar precision so there is less data to benchmark nucleon FSI effects.

### 3.4. Monte Carlo Event Generators

Monte Carlo codes (GENIE, NuWro, Neut, Nuance, etc.) describe CCQE events using a simple RFG model, with FSI effects implemented by means of a semiclassical intranuclear cascade. NuWro offers also a possibility to run simulations with spectral function and an effective momentum-dependent nuclear potential. It is also by now the only MC generator with implementation of MEC dynamics. Since the primary interaction and the final state effects are effectively decoupled, FSI do not change the total and outgoing lepton differential cross sections.

### 3.5. Neutrino Energy Reconstruction

Neutrino oscillation probabilities depend on the neutrino energy, unknown for broad fluxes and often estimated from the measured angle and energy of the outgoing charged lepton  $\ell$  only. This is the situation of the experiments with Cherenkov detectors where protons in the final state are usually below the Cherenkov threshold. Then, it is common to define a reconstructed neutrino energy  $E_{\text{rec}}$  (neglecting binding energy and the difference of proton and neutron masses) as follows:

$$E_{\text{rec}} = \frac{ME_\ell - m_\ell^2/2}{M - E_\ell + |\vec{p}_\ell| \cos \theta_\ell}, \quad (3.1)$$

which would correspond to the energy of a neutrino that emits a lepton, of energy  $E_\ell$  and three-momentum  $\vec{p}_\ell$ , with a gauge boson  $W$  being absorbed by a free nucleon of mass  $M$  *at rest* in a CCQE event. Each event contributing to the flux averaged double-differential cross section  $d\sigma/dE_\ell d\cos\theta_\ell$  defines unambiguously a value of  $E_{\text{rec}}$ . The actual (“true”) energy,  $E$ , of the neutrino that has produced the event will not be exactly  $E_{\text{rec}}$ . Actually, for each  $E_{\text{rec}}$ , there exists a distribution of true neutrino energies that give rise to events whose muon kinematics would lead to the given value of  $E_{\text{rec}}$ . In the case of genuine QE events, this distribution is sufficiently peaked (the Fermi motion broadens the peak and binding energy shifts it a little) around the true neutrino energy to make the algorithm in (3.1) accurate enough to study the neutrino oscillation phenomenon [65] or to extract neutrino flux unfolded CCQE cross sections from data (assuming that the neutrino flux spectrum is known) [66, 67]. The effect of this assumption on the much more demanding measurement of CP-violation effects is currently being evaluated.

However, and due to presence of multinucleon events, there is a long tail in the distribution of true energies associated to each  $E_{\text{rec}}$  that makes the use of (3.1) unreliable. The effects of the inclusion of multinucleon processes on the energy reconstruction have been noticed in [62] and investigated in [66], within the Lyon 2p2h model and also estimated in [68], using the simplified model of [61] for the multinucleon mechanisms. This issue has been more recently also addressed in the context of the IFIC 2p2h model in [67], finding results in a qualitative agreement with those of [66, 68].

In [67] it is also studied in detail the  $^{12}\text{C}$  unfolded cross section published in [12]. It is shown there that the unfolding procedure is model dependent. Moreover, it is also shown that the MiniBooNE published CCQE cross section as a function of neutrino energy differs from the real one. This is because the MiniBooNE analysis assumes that all the events are QE. The authors of [67] finally conclude that the MiniBooNE unfolded cross section exhibits an excess (deficit) of low (high) energy neutrinos, which is mostly an artifact of the unfolding process that ignores multinucleon mechanisms.

### 3.6. NC Elastic

MiniBooNE has also measured flux integrated NC elastic reaction cross section [69]. Using these data, the best fit value of the axial mass was found to be  $M_A = 1.39 \pm 0.11 \text{ GeV}$ . The measurement was possible because the MiniBooNE Cherenkov detector can observe also scintillation light from low momentum nucleons. An attempt was done to measure the nucleon strange quark component using the proton enriched sample of events with a result consistent with zero:  $\Delta s = 0.08 \pm 0.26$ .

#### 3.6.1. Theoretical Considerations

The MiniBooNE NCEI data were analyzed in [70]. The fit was done to the  $Q^2$  distribution of events with the best fit value of  $M_A$  equal to  $1.28 \pm 0.05 \text{ GeV}$ . Moreover the authors of [71] concluded that axial mass as large as  $1.6 \text{ GeV}$  is still too small to reproduce the MiniBooNE NCEI data. Critical discussion of this statement can be found in [72].

## 4. The Resonance Region

In the RES region the degrees of freedom are hadronic resonances, with the most important being the  $\Delta(1232)$ . Typical final states are those with a single pion. During the last five

years several new pion production measurements have been performed. In all of them the targets were nuclei (most often carbon) and interpretation of the data in terms of the neutrino-nucleon cross section needed to account for nuclear effects, impossible to do in a model independent manner. Because of that it has become a standard that the published data include nuclear effects with most uncertain FSI. Perhaps not surprisingly, in several papers old deuterium ANL and BNL pion production data were reanalyzed aiming to better understand the pion production reaction on free nucleons. Theoretical models became more sophisticated and the major improvement was a development of well justified mechanisms for the nonresonant contribution in the  $\Delta$  region. Some papers addressed the problem of higher resonances, a topic which will be investigated experimentally with future MINERvA results. On the other hand, there has been a lot of activity in the area of the coherent pion production and this subject will be discussed separately.

## 4.1. Experimental Results

### 4.1.1. $NC\pi^0$

Neutral current  $\pi^0$  production ( $NC\pi^0$ ) is a background to  $\nu_e$  appearance oscillation signal. One is interested in a  $\pi^0$  leaving the nucleus and recent experimental data are given in this format with all the FSI effects included. Signal events originate mostly from:  $NC1\pi^0$  primary interaction with a  $\pi^0$  not being affected by FSI and  $NC1\pi^+$  primary interaction with the  $\pi^+$  being transformed into  $\pi^0$  in a charge exchange FSI reaction. An additional difficulty in interpreting the  $NC\pi^0$  production comes from a coherent (COH) contribution. In the case of MiniBooNE flux neutrino-carbon reactions ( $\langle E_\nu \rangle \sim 1$  GeV) it is estimated to account for  $\sim 20\%$  of signal events [73].

Four recent measurements of  $NC\pi^0$  production (K2K [74], MiniBooNE neutrinos, MiniBooNE antineutrinos [75], SciBooNE [76]) are complementary. They use three different fluxes: (K2K, Fermilab Booster neutrinos, and antineutrinos) and three targets:  $H_2O$  (K2K),  $CH_2$  (MiniBooNE), and  $C_8H_8$  (SciBooNE). MiniBooNE presented the results in the form of absolutely normalized cross section while K2K and SciBooNE reported only the ratios  $\sigma(NC1\pi^0)/\sigma(CC)$ . There is an important difference in what was actually measured: K2K and MiniBooNE present their results as measurements of final states with only one  $\pi^0$  and no other mesons. SciBooNE defines the signal as states with *at least* one  $\pi^0$  in the final state so that a contamination from  $1\pi^0 1\pi^\pm$ ,  $2\pi^0$ , and  $> 2\pi$  (with  $> 1\pi^0$ ) final states is included and its fraction can be estimated to be 17% [64]. Final results are presented as flux averaged distributions of events as a function of the  $\pi^0$  momentum, and in the case of MiniBooNE and SciBooNE also as a function of the  $\pi^0$  production angle.

### 4.1.2. $CC\pi^+$

MiniBooNE measured  $CC1\pi^+$  production cross sections, where the signal is defined as exactly one  $\pi^+$  in the final state with no other mesons [77]. A variety of flux integrated differential cross sections, often double differential were reported in  $Q^2$  and final state particles momenta. Also absolute  $\pi^+$  production cross sections as a function of neutrino energy are provided in [77]. The cross section results are much larger than NUANCE MC predictions and the difference is on average 23%. In Figure 5(a) GiBUU and NuWro predictions for  $CC\pi^+$  are compared to the MiniBooNE data.



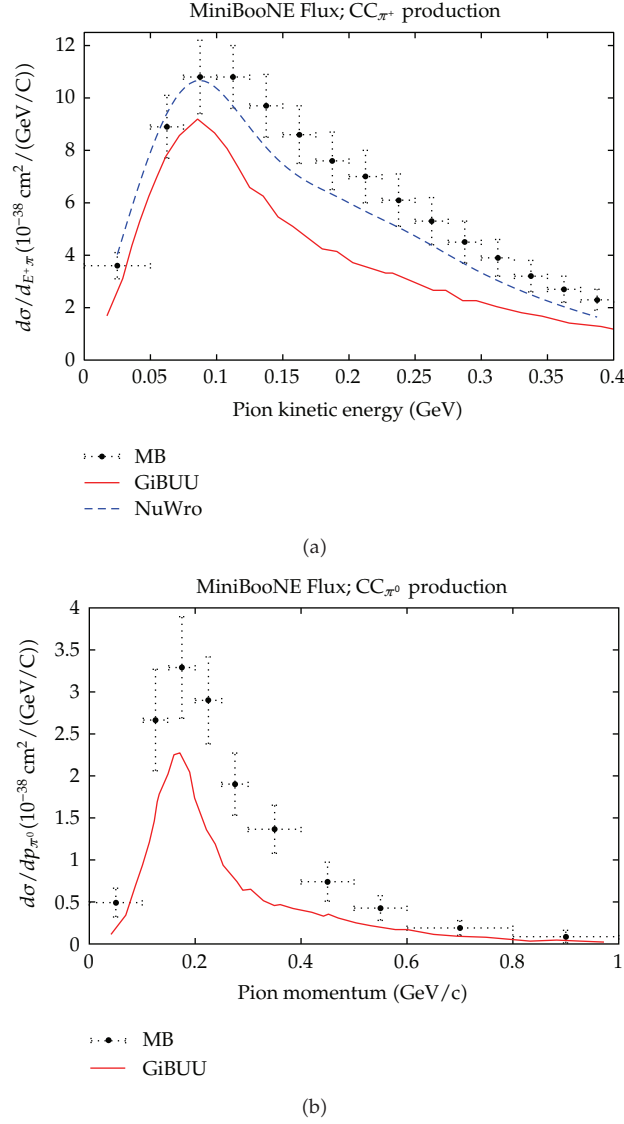


**Figure 5:** (a) Differential cross section for  $\text{CC}1\pi^+$  production in the final state (all the FSI effects are included). MiniBooNE measurement [77] is compared to GiBUU [78] and NuWro computations. (b) The same for  $\text{CC}\pi^0$  production, but only GiBUU results are shown.

#### 4.1.3. $\text{CC}\pi^0$

MiniBooNE measured also  $\text{CC}1\pi^0$  production cross sections. As before, the signal is defined as exactly one  $\pi^0$  in the final state [79]. Various differential distributions are available. There is a dramatic discrepancy between the measured  $\text{CC}1\pi^0$  production cross section as a function of neutrino energy and NUANCE MC predictions in the region of lower energies. On average the data is larger by  $56 \pm 20\%$ , but for  $E_\nu < 1 \text{ GeV}$  the disagreement is as large as a factor of 2. In Figure 5(b) GiBUU predictions for  $\text{CC}\pi^+$  are compared to the MiniBooNE data.

#### 4.1.4. Ratio $\sigma(CC1\pi^+)/\sigma(CCQE)$

Another useful MiniBooNE measurement was the ratio  $\sigma(CC1\pi^+)/\sigma(CCQE)$  [80]. The ratio of  $CC1\pi^+$ -like (one pion in the final state) to CCQE-like cross sections on  $\text{CH}_2$  as a function of neutrino energy was measured with an accuracy of  $\sim 10\%$  in bins with highest statistics. This measurement puts constraints on the theoretical models which include QE,  $\Delta$  excitation, and MEC/2p2h dynamics. But still, in order to compare with theoretical model predictions to these data, FSI effects must be included. In order to make such a comparison easier, MiniBooNE provided also FSI-corrected data representing the ratio of  $CC1\pi^+/CCQE$  cross sections at the primary interaction. The corrected results are biased by MC assumptions and in particular they neglect most of the MEC/2p2h contributions which is contained in the QE-like sample of events. Finally, MiniBooNE rescaled their results in order to get data points for an isoscalar target and enable comparison to old ANL and also more recent K2K data [81]. K2K measured ratio of cross sections on bound nucleons inside the nucleus corrected for FSI effects.  $CC1\pi^+$  events were not identified on an event-by-event basis.

#### 4.1.5. Phenomenological Considerations

Due to nuclear effects a comparison to the new data is possible only for MC event generators, sophisticated computation tools like GiBUU and also a few theoretical groups which are able to evaluate FSI effects.

Most of the interesting work was done within GiBUU. It turned out to be very difficult reproduce the MiniBooNE  $CC1\pi^+$  and  $CC1\pi^0$  results: the measured cross section is much larger than theoretical computations. In the case of  $CC1\pi^+$  production the discrepancy is as large as 100%. It was also noted that the reported shape of the distribution of  $\pi^+$  kinetic energies is different from theoretical calculations and does not show a strong decrease at  $T_{\pi^+} > 120$  MeV located in the region of maximal probability for pion absorption.

The authors of [78] mention three possible reasons for the data/GiBUU predictions discrepancy: (i) the fact that  $\Delta$  excitation axial form factor was chosen to agree with the ANL data only, neglecting the larger cross section BNL measurements; (ii) hypothetical 2p2h- $1\pi$  pion production contribution analogous to 2p2h discussed in the Section 3.3; (iii) flux underestimation in the MiniBooNE experiment. For the last point, the argument gets support from the better data/theory agreement found for the ratio, as discussed below.

In the case of  $NC\pi^0$  production, a systematical comparison was done with NuWro MC predictions with an updated FSI model for pions [64]. The overall agreement is satisfactory. Shapes of the distributions of final state  $\pi^0$ 's are affected by an interplay between pion FSI such as absorption and *formation time* effects, understood here as an effect of a finite  $\Delta$  lifetime. It is argued that  $NC\pi^0$  production data can be very useful for benchmarking neutrino MC event generators.

Because of the apparent data/MC normalization discrepancy for the  $CC\pi^+$  production, the interesting data is that for the ratio  $\sigma(CC1\pi^+\text{-like})/\sigma(CCQE\text{-like})$ . This observable is free from the overall flux normalization uncertainty. However, it is not a direct observable quantity because in the experimental analysis it is necessary to reconstruct the neutrino energy and the procedures applied for the denominator and numerator are different. Three theoretical predictions for the ratio were published. The Giessen group compared to the MiniBooNE ratio data using the model described in [82] with the FSI effects modeled by the GiBUU code [83]. There is a significant discrepancy between the model and the data

points: the calculated ratio is smaller. For the K2K data, the GiBUU model computations are consistent with the experimental results.

The  $\sigma(\text{CC}1\pi^+)/\sigma(\text{CCQE})$  ratio was also analyzed in [84]. In this analysis many nuclear effects were included: the in medium  $\Delta$  self-energy (both real and imaginary parts), FSI effects within the cascade model of [85], RPA corrections for the CCQE. ... Computations did not include contributions from the nonresonant background and from higher resonances. The contribution from the coherent pion production evaluated with the model of [86] (about 5% of the  $\pi^+$  signal, a surprisingly large fraction) was also included in computations. The model predictions agree with MiniBooNE measurement for  $E_\nu < 1\text{ GeV}$  and are below MiniBooNE data for larger neutrino energies.

Finally, NuWro MC results for the ratio given in [87] are slightly below the data points for larger neutrino energies.

## 4.2. Theoretical Analyses

It has been known since ANL and BNL pion production measurements that although being a dominant mechanism,  $\Delta$  excitation alone cannot reproduce the data and that nonresonant background terms must be included in the theoretical models. There were many attempts in the past to develop suitable models but usually they were not very well justified from the theoretical point of view.

### 4.2.1. Nonresonant Background

A general scheme to analyze weak pion production in the  $\Delta$  region based on the chiral symmetry was proposed a few years ago in [88]. The model is supposed to work well in the kinematical region  $W < 1.3\text{--}1.4\text{ GeV}$  that is, in the  $\Delta$  region. The background contribution is particularly important at the pion production threshold, for values of  $W$  near  $M + m_\pi$ . Vector form factors are taken from the electroproduction data and fits to helicity amplitudes [89]. Although particularly important for the channels  $\nu_\ell n \rightarrow \ell^- p \pi^0$  and  $\nu_\ell n \rightarrow \ell^- n \pi^+$  the background terms contribute also to the channel  $\nu_\ell p \rightarrow \ell^- p \pi^+$  changing the fitted values of the nucleon- $\Delta$  transition matrix elements. A comparison to existing NC pion production data was done as well and a good agreement was also found. An interesting question raised by the authors of [88] is that of unitarity. Their approach does not satisfy requirements of the Watson theorem and this can have some consequences for example, worse agreement with the antineutrino pion production data.

The model of the nonresonant background was used by the Giessen group which made several qualitative comparisons to both the ANL and BNL pion production data in the region  $W < 1.4\text{ GeV}$  neglecting deuterium effects [90]. In the case of neutron channels the model predictions are much below the BNL data points and this is because the axial form factor parameters were optimized to the ANL data only. This choice goes back to the paper [89] where the authors came to the conclusion that the ANL and BNL data for the  $\Delta^{++}$  excitation are not compatible.

### 4.2.2. Reanalysis of Old Bubble Chamber Data

The issue of nucleon- $\Delta$  transition matrix element was discussed also in other papers. The questions are what is the value of the  $C_5^A(0)$ ? How relevant are deuterium nuclear effects in dealing with ANL and BNL data? How much tension is there between both data samples?

In [88] a fit was done to the ANL data in the  $\Delta^{++}$  channel only with the results:  $C_5^A(0) = 0.867 \pm 0.075$  and  $M_{A\Delta} = 0.985 \pm 0.082$  GeV. The obtained value of  $C_5^A(0)$  was very different from what follows from off-diagonal Goldberger-Treiman relations ( $C_5^A(0) \approx 1.15$ ).

The authors of [87] made a fit to both ANL and BNL data including in the  $\chi^2$ , terms with the overall flux normalization uncertainties, separate for ANL and BNL. In the fit the deuterium nuclear effects were included as correction factors to the  $Q^2$  distributions of events, using the results of [91]. The main conclusion was that ANL and BNL data are in fact consistent. This statement was verified in a rigorous way using parameter goodness of fit method [92]. In the dipole parameterization of the  $C_5^A(Q^2)$  form factor the best fit values were found to be  $C_5^A(0) = 1.14 \pm 0.08$  and  $M_A = 0.95 \pm 0.04$ . Only  $\Delta^{++}$  channel was analyzed and like in [75] non-resonant background contributions was not included.

So far the most complete analysis of both ANL and BNL data was performed in [93]: a nonresonant background was included and also deuterium effects were taken into account in the systematic way. The authors made several fits with various assumptions and in the fit IV they obtained  $C_A^5(0) = 1.00 \pm 0.11$ .

#### 4.2.3. Other Theoretical Approaches

In [94] the dynamical pion cloud effects are imposed on bare quark  $N - \Delta$  transition matrix elements. The model is able to reproduce both ANL and BNL weak pion production data.

The authors of [95] focus on the consistent use of the  $\Delta$  propagator. They show that the computations relying on the standard Rarita-Schwinger propagator could lead to an underestimation of the weak pion production cross section.

### 4.3. Coherent Pion Production

In coherent pion production (COH) the target nucleus remains in the ground state. There are four possible channels, for CC and NC reactions, neutrinos, and antineutrinos. A clear experimental signal for the COH reaction for high energies was observed and the aim of recent measurements was to fill a gap in the knowledge of a region around  $\sim 1$  GeV COH cross-sections. At larger neutrino energies a recent measurement was done by MINOS which reported a NC reaction cross section at  $\langle E_\nu \rangle = 4.9$  GeV to be consistent with the predictions of the Berger-Sehgal model (see below).

#### 4.3.1. Experimental Results

In the case of the NC reaction, MiniBooNE [73] and SciBooNE [96] searched for the COH component. SciBooNE [96] evaluated the ratio of the COH  $\text{NC}\pi^0$  production to the total CC cross section as  $(1.16 \pm 0.24)\%$ .

For the NC reaction MiniBooNE evaluated the COH component (plus possible hydrogen diffractive contribution about which little is known) in the  $\text{NC}\pi^0$  production as 19.5% (at  $\langle E_\nu \rangle \sim 1$  GeV) and then the overall flux averaged overall  $\text{NC}1\pi^0$  cross section as  $(4.76 \pm 0.05 \pm 0.76) \cdot 10^{-40} \text{ cm}^2/\text{nucleon}$ . Unfortunately, it is difficult to translate both measurements into the absolutely normalized value of the NC COH cross section because of strong dependence on the NUANCE MC generator used in the data analysis. In NUANCE, RES, COH, and BGR (nonresonance background)  $\text{NC}\pi^0$  reactions are defined according to primary interaction and COH pions are also subject to FSI. In the MiniBooNE analysis the fit

is done for the composition of the sample of  $\text{NC}\pi^0$  events in terms of three components, and the COH fraction is defined as  $x_{\text{COH}}/(x_{\text{COH}} + x_{\text{RES}})$ .

In the case of the CC reaction, K2K [97] and SciBooNE [98] reported no evidence for the COH component. For the K2K analysis, the 90% confidence limit upper bound for the COH cross sections on carbon was estimated to be 0.6% of the inclusive CC cross section. The SciBooNE upper limits (also for the carbon target) are 0.67% at  $\langle E_\nu \rangle \sim 1.1$  GeV, and 1.36% at  $\langle E_\nu \rangle \sim 2.2$  GeV. SciBooNE reported also the measurement of the ratio of CC COH  $\pi^+$  to NC COH  $\pi^0$  production and estimated it as  $0.14^{+0.30}_{-0.28}$ . This is a surprisingly low value, which disagrees with results from the theoretical models which at SciBooNE energies typically predict values somehow smaller 2. For massless charged leptons isospin symmetry implies the value of 2 for this ratio and the finite mass corrections make the predicted ratio smaller.

#### 4.3.2. Theoretical Developments

Higher neutrino energy ( $\langle E_\nu \rangle \geq 2$  GeV) COH production data (including recent NOMAD measurement) were successfully explained with a PCAC based model [99]. Adler's theorem relates  $\sigma_{\text{COH}}(\nu + X \rightarrow \nu + X + \pi^0)$  at  $Q^2 \rightarrow 0$  to  $\sigma(\pi^0 + X \rightarrow \pi^0 + X)$ . Subsequently, the model for the CC reaction, has been upgraded [100] to include lepton mass effects important for low  $E_\nu$  studies. The new model predicts the  $\sigma_{\text{COH}}(\pi^+)/\sigma_{\text{COH}}(\pi^0)$  ratio at  $E_\nu = 1$  GeV to be 1.45 rather than 2. Another important improvement was to use a better model for  $d\sigma(\pi + {}^{12}\text{C} \rightarrow \pi + {}^{12}\text{C})/dt$  in the region of pion kinematical energy  $100 \text{ MeV} < T_\pi < 900 \text{ MeV}$ . As a result, the predicted COH cross section from the model became reduced by a factor of 2-3 [101]. The PCAC-based approach was also discussed in [102] and critically rederived in [103].

At lower energies the microscopic  $\Delta$  dominance models for the COH reaction [104–108] are believed to be more reliable. Within microscopic models there are still various approaches, for example, due to differences in the treatment of the nonresonant background. The absolute normalization of the predicted cross section depends on the adopted value of the  $N \rightarrow \Delta$  form factor  $C_5^A(0)$  because  $\sigma_{\text{COH}} \sim (C_5^A(0))^2$ .

#### 4.4. MC Generators

Almost all MC events generators rely on the old Rein-Sehgal resonance model for pion resonance production [109]. The model is based on the quark resonance model and includes contributions from 18 resonances covering the region  $W < 2$  GeV. The model is easily implementable in MC generators and it has only one set of vector and axial form factors. In the original model, the charged lepton is assumed to be massless and prescriptions to cope with this problem were proposed in [100, 110]. It was also realized that the RS model can be improved in the  $\Delta$  region by modifying both vector and axial form factors using either old deuterium or new MiniBooNE pion production data [21, 111, 112].

As for coherent pion production, all the MCs use the Rein-Sehgal COH model [99]. The analysis of MC event generators and theoretical models done in [22] show that in the 1-2 GeV energy region, the Rein Sehgal COH model predictions disagree significantly with all the recent theoretical computations and experimental results.

A crucial element of MC is the FSI model. These are typically semiclassical intra-nuclear cascade models. The topic of FSI goes far beyond the scope of this paper and we only note that the progress in understanding the experimental data requires more reliable FSI models. The existing models should be systematically benchmarked with electro- and photoproduction data as it was done in the case of GIBUU.



### 4.5. Duality

Bridging the region between RES and DIS (where with a good approximation interactions occur on quarks) dynamics is a practical problem which must be resolved in all MC event generators. In MC event generators “DIS” is defined as “anything but QE and RES,” what is usually expressed as a condition on the invariant hadronic mass of the type  $W > 1.6 \text{ GeV}$  or  $W > 2 \text{ GeV}$  or so. Notice however that such a definition of “DIS” contains a contribution from the kinematical region  $Q^2 < 1 \text{ GeV}^2$  which is beyond the applicability of the genuine DIS formalism. RES/DIS transition region is not only a matter of an arbitrary choice but is closely connected with the hypothesis of quark-hadron duality.

Investigation of structure functions introduced in the formalism of the inclusive electron-nucleon scattering led Bloom and Gilman to the observation that the average over resonances is approximately equal to the leading twist contribution measured in the completely different DIS region. One can distinguish two aspects of duality: (i) resonant structure functions oscillate around a DIS scaling curve; (ii) the resonant structure functions for varying values of  $Q^2$  slide along the DIS curve evaluated at fixed  $Q_{\text{DIS}}^2$ .

In order to quantify the degree in which the duality is satisfied one defines the ratio of integrals over structure functions from RES and DIS:

$$\mathcal{R}(Q^2, Q_{\text{DIS}}^2) = \frac{\int_{\xi_{\min}}^{\xi_{\max}} d\xi F_j(\xi, Q^2)}{\int_{\xi_{\min}}^{\xi_{\max}} d\xi F_j(\xi, Q_{\text{DIS}}^2)}. \quad (4.1)$$

The integrals are in the Nachtmann variable  $\xi(x, Q^2) = 2x/(1 + \sqrt{1 + 4x^2 M^2/Q^2})$  and the integration region is defined as  $W_{\min} < W < W_{\max}$ . Typically  $W_{\min} = M + m_\pi$  and  $W_{\max} = 1.6, \dots, 2.0 \text{ GeV}$ . In the case of DIS, the value of  $Q_{\text{DIS}}^2$  is much larger and as a consequence the integral over  $\xi$  runs over a quite different region in  $W$ .

Neutrino-nucleon scattering duality studies are theoretical in their nature because the precise data in the resonance region are still missing. The duality was studied in three papers: [94, 113, 114]. For neutrino interactions the duality can be satisfied only for the isospin average target. This is because the RES structure functions for proton are much larger than for neutron and in the case of DIS structure functions the situation is opposite.

Theoretical studies were done with a model which contains resonances from the first and second resonance region but not the background contribution and with the Rein-Sehgal model which is commonly used in MC event generators. If the resonance region is confined to  $W < 1.6 \text{ GeV}$  the duality as defined in (4.1) is satisfied at the 75–80% level. If the resonance region is extended to  $W < 2 \text{ GeV}$  the value of the integral in (4.1) is only about 50%. These results are to some extent model dependent but a general tendency is that for larger  $W$ , DIS structure functions are much larger than the resonance contribution, as clearly seen from Figure 3 in [113] and Figure 7 in [114]. As shown in [114] there is also a 5% uncertainty coming from an arbitrary choice of  $Q_{\text{DIS}}^2$ .

Two component duality hypothesis states that resonance contribution is dual to the valence quarks and the nonresonant background to the sea. Investigation done within the Rein Sehgal model with  $W < 2 \text{ GeV}$  revealed no signature of two component duality. Quark-hadron duality was also investigated in the case of neutrino nucleus interactions [115].

As a practical procedure for addressing this region, Bodek and Yang [116] have introduced and refined a model that is used by many contemporary neutrino event generators such as NEUGEN and its successor GENIE to bridge the kinematic region between

the Delta and full DIS. The model has been developed for both neutrino- and electron-nucleon inelastic scattering cross sections using leading order parton distribution functions and introducing a new scaling variable they call  $\xi_w$ .

Nonperturbative effects that are prevalent in the kinematic region bridging the resonance and DIS regimes are described using the  $\xi_w$  scaling variable, in combination with multiplicative  $K$  factors at low  $Q^2$ . The model is successful in describing inelastic charged lepton-nucleon scattering, including resonance production, from high-to-low  $Q^2$ . In particular, the model describes existing inelastic neutrino-nucleon scattering measurements.

Their proposed scaling variable,  $\xi_w$  is derived using energy momentum conservation and assumptions about the initial/final quark mass and  $P_T$ . Parameters are built into the derivation of  $\xi_w$  to account (on average) for the higher order QCD terms and dynamic higher twist that is covered by an enhanced target mass term.

At the juncture with the DIS region, the Bodek-Yang model incorporates the GRV98 [117] LO parton distribution functions replacing the variable  $x$  with  $\xi_w$ . They introduce “ $K$ -factors”, different for sea and valence quarks, to multiply the PDFs so that they are correct at the low  $Q^2$  photo-production limit. A possible criticism of the model is the requirement of using the rather dated GRV98 parton distribution functions in the DIS region so the bridge to the lower  $W$  kinematic region is seamless.

## 5. $\nu$ -A Deep-Inelastic Scattering: Introduction

Although deep-inelastic scattering (DIS) is normally considered to be a topic for much higher energy neutrinos, wide-band beams such as the Fermilab NuMI and the planned LBNE beams do have real contributions from DIS that are particularly important in feed down to the background that must be carefully considered. In addition, there are  $x$ -dependent nuclear effects that should be taken into account when comparing results from detectors with different nuclei and even when comparing results from “identical” near and far detectors when the neutrino spectra entering the near and far detectors are different.

For this paper, the definition of deep-inelastic scattering (DIS) is the kinematic-based definition with  $W \geq 2.0 \text{ GeV}$  and  $Q^2 \geq 1.0 \text{ GeV}^2$ . This is mostly out of the resonance production region and allows a fit to parton distribution functions. As said in Introduction, this is unfortunately not the definition used by several modern Monte Carlo generators that do not differentiate between simply “inelastic” interactions and deep-inelastic interactions calling everything beyond the Delta simply DIS. This is an unfortunate confusing use of nomenclature by the generators.

In general, deep-inelastic scattering offers an opportunity to probe the partonic structure of the nucleon both in its free state and when the nucleon is bound in a nucleus. Description of the partonic structure can include *parton distribution functions* (PDFs) giving the longitudinal, transverse, and spin distributions of quarks within the nucleon as well as, for example, the hadron formation zone giving the time/length it takes for a struck quark to fully hadronize into a strong-interacting hadron.

Neutrino scattering can play an important role in extraction of these fundamental parton distribution functions (PDFs) since only neutrinos via the weak interaction can resolve the flavor of the nucleon’s constituents:  $\nu$  interacts with  $d, s, \bar{u}$  and  $\bar{c}$  while the  $\bar{\nu}$  interacts with  $u, c, \bar{d}$  and  $\bar{s}$ . The weak current’s unique ability to “taste” only particular quark flavors significantly enhances the study of parton distribution functions. High-statistics measurement of the nucleon’s partonic structure, using neutrinos, could complement studies with electromagnetic probes.

In the pursuit of precision measurements of neutrino oscillation parameters, large data samples and dedicated effort to minimize systematic errors could allow neutrino experiments to independently isolate all *SIX* of the weak structure functions  $F_1^{\nu N}(x, Q^2)$ ,  $F_1^{\bar{\nu} N}(x, Q^2)$ ,  $F_2^{\nu N}(x, Q^2)$ ,  $F_2^{\bar{\nu} N}(x, Q^2)$ ,  $xF_3^{\nu N}(x, Q^2)$ , and  $xF_3^{\bar{\nu} N}(x, Q^2)$  for the first time. Then, by taking differences and sums of these structure functions, specific parton distribution functions in a given  $(x, Q^2)$  bin can in turn be better isolated. Extracting this full set of structure functions will rely on the  $y$ -variation of the structure function coefficients in the expression for the cross-section. In the helicity representation, for example:

$$\begin{aligned} \frac{d^2\sigma^\nu}{dx dQ^2} = \frac{G_F^2}{2\pi x} \left[ \frac{1}{2} \left( F_2^\nu(x, Q^2) + xF_3^\nu(x, Q^2) \right) \right. \\ \left. + \frac{(1-y)^2}{2} \left( F_2^\nu(x, Q^2) - xF_3^\nu(x, Q^2) \right) - 2y^2 F_L^\nu(x, Q^2) \right], \end{aligned} \quad (5.1)$$

where  $F_L$  is the longitudinal structure function representing the absorption of longitudinally polarized Intermediate Vector Boson.

By analyzing the data as a function of  $(1-y)^2$  in a given  $(x, Q^2)$  bin for both  $\nu$  and  $\bar{\nu}$ , all six structure functions could be extracted.

Somewhat less demanding in statistics and control of systematics, the “average” structure functions  $F_2(x, Q^2)$  and  $xF_3(x, Q^2)$  can be determined from fits to combinations of the neutrino and antineutrino differential cross sections and several assumptions. The sum of the  $\nu$  and  $\bar{\nu}$  differential cross sections, yielding  $F_2$  then can be expressed as follows:

$$\frac{d^2\sigma^\nu}{dx dy} + \frac{d^2\sigma^{\bar{\nu}}}{dx dy} = \frac{G_F^2 ME}{\pi} \left[ 2 \left( 1 - y - \frac{Mxy}{2E} + \frac{y^2}{2} \frac{1 + 4M^2 x^2 / Q^2}{1 + R_L} \right) F_2 + y \left( 1 - \frac{y}{2} \right) \Delta x F_3 \right], \quad (5.2)$$

where  $R_L$  is equal to  $\sigma_L/\sigma_T$  and now  $F_2$  is the *average* of  $F_2^\nu$  and  $F_2^{\bar{\nu}}$  and the last term is proportional to the difference in  $xF_3$  for neutrino and antineutrino probes,  $\Delta x F_3 = xF_3^\nu - xF_3^{\bar{\nu}}$ . In terms of the strange and charm parton distribution function  $s$  and  $c$ , at leading order, assuming symmetric  $s$  and  $c$  seas, this is  $4x(s - c)$ .

The cross sections are also corrected for the excess of neutrons over protons in the target (e.g., the Fe correction is 5.67%) so that the presented structure functions are for an isoscalar target. A significant step in the determination of  $F_2(x, Q^2)$  in this manner that affects the low- $x$  values is the assumed  $\Delta x F_3$  and  $R_L(x, Q^2)$ . Recent analyses use, for example, a NLO QCD model as input (TRVFS [118, 119]) and assumes an input value of  $R_L(x, Q^2)$  that comes from a fit to the world’s charged-lepton measurements [120]. This could be an additional problem since, as will be suggested,  $R_L(x, Q^2)$  can be different for neutrino as opposed to charged-lepton scattering.

The structure function  $xF_3$  can be determined in a similar manner by taking the difference in  $\nu$  and  $\bar{\nu}$  differential cross sections.

### 5.1. The Physics of Deep-Inelastic Scattering

There have been very few recent developments in the theory of deep-inelastic scattering. The theory has been well established for years. The most recent developments in neutrino DIS scattering involve the experimental determination of parton distribution functions of nucleons within a nucleus, so-called *nuclear* parton distribution functions (nPDF). The more contemporary study of  $\nu$  nucleus deep-inelastic scattering using high-statistics experimental results with careful attention to multiple systematic errors began with the CDHSW, CCFR/NuTeV  $\nu$  Fe, the NOMAD  $\nu$  C, and the CHORUS  $\nu$  Pb experiments. Whereas NuTeV [121] and CHORUS [122] Collaborations have published their full data sets, NOMAD [123] has not yet done so. This short summary of DIS physics will concentrate on nuclear/nucleon parton distribution functions.

#### 5.1.1. Low-and-High $Q^2$ Structure Functions: Longitudinal and Transverse

Since the current and future neutrino beams designed for neutrino oscillation experiments will be concentrating on lower energy neutrinos (1–5 GeV), many of the interactions will be at the lower- $Q$  edge of DIS or even in the “soft” DIS region, namely,  $W \geq 2.0$  GeV however, with  $Q^2 \leq 1.0$  GeV<sup>2</sup>. Understanding the physics of this kinematic region is therefore important.

Since both the vector and axial-vector part of the transverse structure function  $F_T$  go to 0 at  $Q^2 = 0$  (similar to  $\ell^\pm$  charged-lepton vector current scattering), the low- $Q^2$  region  $\nu$  and  $\bar{\nu}$  cross sections are dominated by the longitudinal structure function  $F_L$ . The longitudinal structure function is composed of a vector and axial-vector component  $F_L^{\text{VC}}$  and  $F_L^{\text{AC}}$  and the low- $Q^2$  behavior of these components is not the same as in the transverse case. The conservation of the vector current (CVC) suggests that  $F_L^{\text{VC}}$  behaves as the vector current in charged-lepton scattering and vanishes at low  $Q^2$ . However, the axial-vector current is not conserved and is related to the pion field via PCAC, so there is a surviving low  $Q^2$  contribution from this component [124] and  $F_L^{\text{AC}}$  dominates the low  $Q^2$  behavior. Consequently, the ratio  $R = F_L/F_T$  is divergent for neutrino interactions. This is substantially different from the scattering of charged leptons for which  $R$  is vanishing as  $Q^2$  and using measurement of  $R$  from charged lepton scattering to determine  $F_2$  for neutrino scattering is obviously wrong for lower  $Q$ . In addition, this non-vanishing and dominant longitudinal structure function could be important for the interpretation of low- $Q^2$  nuclear effects with neutrinos to be described shortly.

#### 5.1.2. Low-and-High $Q^2$ Structure Functions: $1/Q^2$ Corrections

Using a notation similar to that of [125], the total structure function can be expressed in a phenomenological form:

$$F_i(x, Q^2) = F_i^{\text{LT}}(x, Q^2) \left( 1 + \frac{C_4(x)}{Q^2} \right), \quad (5.3)$$

where  $i = 1, 2, 3$  refers to the type of the structure function. Using  $i = 2$  as an example, then  $F_2^{\text{LT}}$  is the leading twist component that has already included target mass corrections (TMC) and  $C_4$  is the coefficient of the twist-4 term, the first higher-twist term proportional to  $(1/Q^2)$ . There are, of course, further higher-twist terms  $H_i^{(T=6)}(x)/Q^4 + \dots$  proportional to ever increasing powers of  $1/Q^2$  however, for most phenomenological fits, the dominant leading twist plus twist-4 term are sufficient to describe the data. The target mass corrections are kinematic in origin and involve terms suppressed by powers of  $M^2/Q^2$  while the higher

twist terms are dynamical in origin and are suppressed as mentioned by powers of  $1/Q^2$ . These higher-twist terms are associated with multiquark or quark and gluon fields and it is difficult to evaluate their magnitude and shape from first principles. As with the kinematic target mass corrections, these must be taken into account in analyses of data at low  $Q^2$  and especially at large  $x$ . At higher  $Q^2$  the contribution of the HT terms is negligible and there are various global fits [126, 127] to the structure functions (among various scattering input) to determine the parton distribution functions (PDFs) that do not include any HT terms.

The analysis of nuclear PDFs to be described shortly uses data from a TeVatron neutrino experiment at very high neutrino energies and thus is one of the analyses that does not need to be concerned with higher-twist corrections. However, the current neutrino-oscillation oriented beam-lines are not high-energy and the analyses of this data may indeed need to consider both target mass corrections and higher-twist. If indeed inclusion of higher-twist in these analyses becomes necessary, the authors of [125] stress the importance of explicitly including *both* the target mass corrections *and* the higher twist corrections, even though they have very different physical origin and can have very different  $x$  dependence. It is important to note, as mentioned, that there are both *nucleon* and *nuclear* PDFs depending on the target. The relation between them, called nuclear correction factors, are currently being studied for both  $\nu$ - $A$  and  $\ell^\pm$ - $A$ . There are early indications that the nuclear correction factors for these two processes may not be the same.

## 6. Recent DIS Measurements: Neutrino Iron Scattering Results

The difficulty, of course, is that modern neutrino oscillation experiments demand high statistics which means that the neutrinos need massive nuclear targets to acquire these statistics. This, in turn, complicates the extraction of free nucleon PDFs and demands nuclear correction factors that scale the results on a massive target to the corresponding result on a nucleon target. The results of the latest study of QCD using neutrino scattering comes from the NuTeV experiment [121]. The NuTeV experiment was a direct followup of the CCFR experiment using nearly the same detector as CCFR but with a different neutrino beam. The NuTeV experiment accumulated over 3 million  $\nu$  and  $\bar{\nu}$  events in the energy range of 20 to 400 GeV off a mainly Fe target. A comparison of the NuTeV results with those of CCFR and the predictions of the major PDF-fitting collaborations (CTEQ and MRST [126, 127]) is shown in Figure 6.

The main points are that the NuTeV  $F_2$  agrees with CCFR for values of  $x_{Bj} \leq 0.4$  but is systematically higher for larger values of  $x_{Bj}$  culminating at  $x_{Bj} = 0.65$  where the NuTeV result is 20% higher than the CCFR result. NuTeV agrees with charged lepton data for  $x_{Bj} \leq 0.5$  but there is increasing disagreement for higher values. Although NuTeV  $F_2$  and  $xF_3$  agree with theory for medium  $x$ , they find a different  $Q^2$  behavior at small  $x$  and are systematically higher than theory at high  $x$ . These results can be summarized in four main questions to ask subsequent neutrino experiments.

- (i) At high  $x$ , what is the behavior of the valence quarks as  $x \rightarrow 1.0$ ?
- (ii) At all  $x$  and  $Q^2$ , what is yet to be learned if we can measure all six  $\nu$  and  $\bar{\nu}$  structure functions to yield maximal information on the parton distribution functions?
- (iii) At all  $x$ , how do nuclear effects with incoming neutrinos differ from nuclear effects with incoming charged leptons?



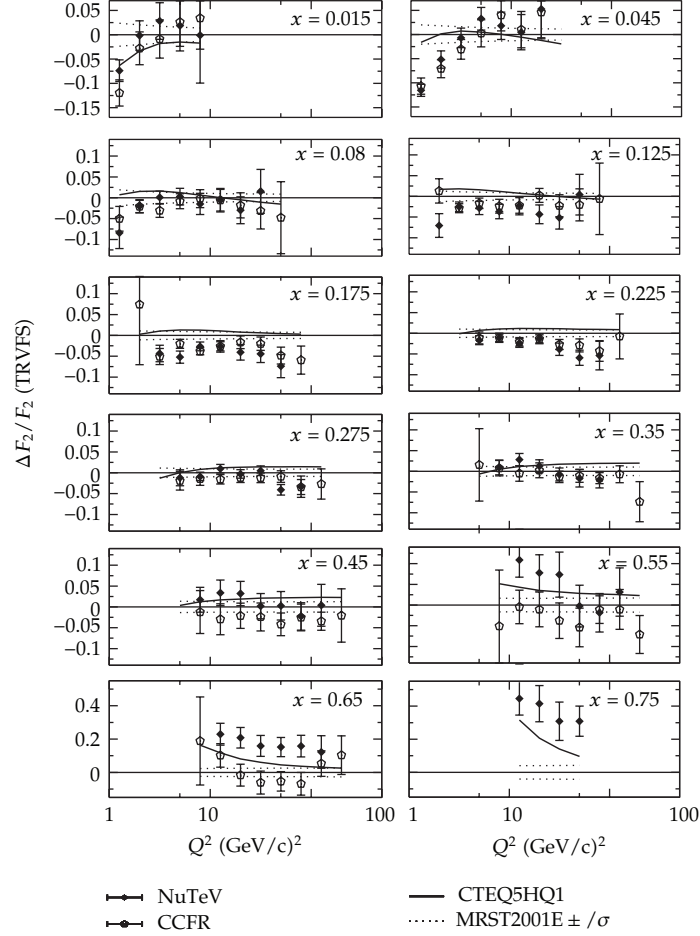


**Figure 6:** A comparison of the measurements of the  $F_2$  structure function by NuTeV and CCFR and the predictions from the global PDF fits of the MRST and CTEQ collaboration [128] that does not use the NuTeV data points as input to their fit. The model predictions have already been corrected for target mass and, most significantly, nuclear effects *assuming these corrections are the same for charge-lepton and neutrino interactions*.

This last item highlights an overriding question when trying to get a global view of structure functions from both neutrino and charged-lepton scattering data. How do we compare data off nuclear targets with data off nucleons and, the associated question, how do we scale nuclear target data to the comparable nucleon data. In most PDF analyses, the nuclear correction factors were taken from  $\ell^\pm$ -nucleus scattering and used for both charged-lepton and neutrino scattering. Recent studies by a CTEQ-Grenoble-Karlsruhe collaboration (called nCTEQ) [129] have shown that there may indeed be a difference between the charged-lepton and neutrino correction factors.

The data from the high-statistics  $\nu$ -DIS experiment, NuTeV summarized above, was used to perform a dedicated PDF fit to neutrino-iron data [130]. The methodology for this fit is parallel to that of the previous global analysis [131] *but* with the difference that only Fe data has been used and no nuclear corrections have been applied to the analyzed data; hence, the resulting PDFs are for a proton in an iron nucleus-nuclear parton distribution functions

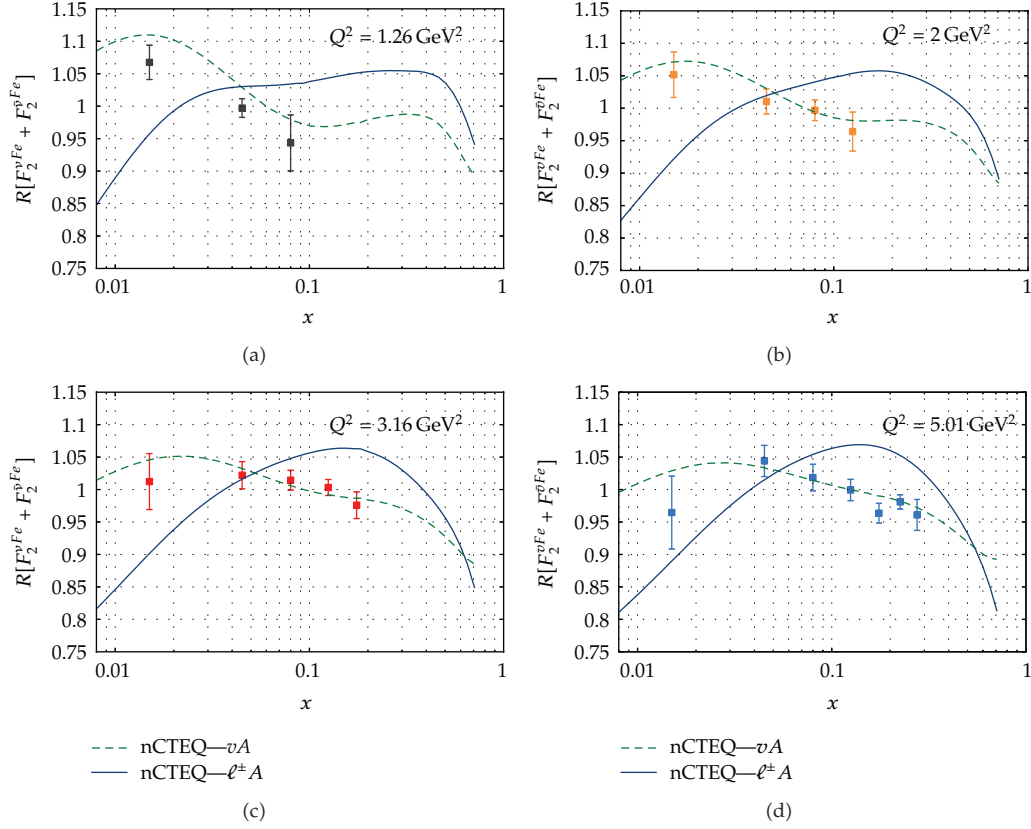


**Figure 7:** Nuclear correction factor  $R$  for the average  $F_2$  structure function in charged current  $\nu\text{Fe}$  scattering at  $Q^2 = 1.2, 2.0, 3.2$ , and  $5.0 \text{ GeV}^2$  compared to the measured NuTeV points. The green dashed curve shows the result of the nCTEQ analysis of  $\nu A$  (CHORUS, CCFR, and NuTeV) differential cross sections plotted in terms of the average  $F_2^{\text{Fe}}$  divided by the results obtained with the reference fit (free proton) PDFs. For comparison, the nCTEQ fit to the charged-lepton data is shown by the solid blue curve.

(for more details of the fitting techniques and resulting comparisons with charged-lepton scattering see Part II of [132]).

By comparing these iron PDFs with the free-proton PDFs (appropriately scaled) a neutrino-specific heavy target nuclear correction factor  $R$  can be obtained which should be applied to relate these two quantities. It is also of course possible to combine these fitted nPDFs to form the individual values of the average of  $F_2(\nu A)$  and  $F_2(\bar{\nu} A)$  for a given  $x, Q^2$  to compare directly with the NuTeV published values of this quantity. This was recently done and the nCTEQ preliminary results [133] for low- $Q^2$  are shown in Figure 7. Although the neutrino fit has general features in common with the charged-lepton parameterization, the magnitude of the effects and the  $x$ -region where they apply are quite different. The present results are noticeably flatter than the charged-lepton curves, especially at low- and moderate- $x$  where the differences are significant. The comparison between the nCTEQ fit, that passes through the NuTeV measured points, and the charged-lepton fit is very different in the lowest- $x$ , lowest- $Q^2$  region and gradually approaches the charged-lepton fit with increasing  $Q^2$ . However, the slope of the fit approaching the shadowing region from higher  $x$  where the NuTeV measured points and the nCTEQ fit are consistently below the charged-lepton  $A$

fit, make it difficult to reach the degree of shadowing evidenced in charged-lepton nucleus scattering at even higher  $Q^2$ .

The general trend is that the antishadowing region is shifted to smaller  $x$  values, and any turn-over at low  $x$  is minimal given the PDF uncertainties. More specifically, there is no indication of “shadowing” in the NuTeV neutrino results at low- $Q^2$ . In general, these plots suggest that the size of the nuclear corrections extracted from the NuTeV data are smaller than those obtained from charged lepton scattering.

### 6.1. Comparison of the $\ell^\pm A$ and $\nu A$ Nuclear Correction Factors

For the nCTEQ analysis, the contrast between the charged-lepton ( $\ell^\pm A$ ) case and the neutrino ( $\nu A$ ) case is striking. While the nCTEQ fit to charged-lepton and Drell-Yan data generally align with the other charged-lepton determinations, the neutrino results clearly yield different behavior as a function of  $x$ , particularly in the shadowing/antishadowing region. In the  $\bar{\nu}$  case, these differences are smaller but persist in the low- $x$  shadowing region. The nCTEQ collaboration emphasize that both the charged-lepton and neutrino results come directly from global fits to the data, there is no model involved. They further suggest that this difference between the results in charged-lepton and neutrino DIS is reflective of the long-standing “tension” between the light-target charged-lepton data and the heavy-target neutrino data in the historical global PDF fits [134, 135]. Their latest results suggest that the tension is not only between charged-lepton *light-target* data and neutrino heavy-target data, but also between neutrino and charged-lepton *heavy-target* data. In other words a difference between charged-lepton ( $\ell^\pm A$ ) and the neutrino ( $\nu A$ ) when comparing the same  $A$ .

Concentrating on this interesting difference found by the nCTEQ group, if the nuclear corrections for the  $\ell^\pm A$  and  $\nu A$  processes are indeed different there are several far-reaching consequences. Considering this, the nCTEQ group has performed a unified global analysis [129] of the  $\ell^\pm A$ , DY, and  $\nu A$  data (accounting for appropriate systematic and statistical errors) to determine if it is possible to obtain a “compromise” solution including both  $\ell^\pm A$  and  $\nu A$  data. Using a hypothesis-testing criterion based on the  $\chi^2$  distribution that can be applied to both the total  $\chi^2$  as well as to the  $\chi^2$  of individual data sets, they found it was *not possible* to accommodate the data from  $\nu A$  and  $\ell^\pm A$  DIS by an acceptable combined fit.

That is, when investigating the results in detail, the tension between the  $\ell^\pm \text{Fe}$  and  $\nu \text{Fe}$  data sets permits *no possible compromise fit* which adequately describes the neutrino DIS data along with the charged-lepton data and, consequently,  $\ell^\pm \text{Fe}$  and  $\nu \text{Fe}$  based on the NuTeV results, have different nuclear correction factors.

A compromise solution between  $\nu A$  and  $\ell^\pm A$  data can be found *only* if the full correlated systematic errors of the  $\nu A$  data are not used and the statistical and all systematic errors are combined in quadrature thereby neglecting the information contained in the correlation matrix. In other words the larger errors resulting from combining statistical and all systematic errors in quadrature reduces the discriminatory power of the fit such that the difference between  $\nu A$  and  $\ell^\pm A$  data are no longer evident. This conclusion underscores the fundamental difference [129] of the nCTEQ analysis with other contemporary analyses.

On the other hand, a difference between  $\nu A$  and  $\ell^\pm A$  is not completely unexpected, particularly in the shadowing region, and has previously been discussed in the literature [136, 137]. The charged-lepton processes occur (dominantly) via  $\gamma$ -exchange, while the neutrino-nucleon processes occur via  $W^\pm$ -exchange. The different nuclear corrections could simply be a consequence of the differing propagation of the hadronic fluctuations of the intermediate bosons (photon,  $W$ ) through dense nuclear matter. Furthermore, since the

structure functions in neutrino DIS and charged lepton DIS are distinct observables with different parton model expressions, it is clear that the nuclear correction factors will not be exactly the same. What is, however, unexpected is the degree to which the  $R$  factors differ between the structure functions  $F_2^{\nu\text{Fe}}$  and  $F_2^{\ell\text{Fe}}$ . In particular the lack of evidence for shadowing in neutrino scattering at low  $Q^2$  down to  $x \sim 0.02$  is quite surprising.

Should subsequent experimental results confirm the rather substantial difference between charged-lepton and neutrino scattering in the shadowing region at low- $Q^2$  it is interesting to speculate on the possible cause of the difference. A recent study of EMC, BCDMS and NMC data by a Hampton University, Jefferson Laboratory collaboration [138] suggests that anti-shadowing in charged-lepton nucleus scattering may be dominated by the longitudinal structure function  $F_L$ . As a by-product of this study, their figures hint that shadowing in the data of EMC, BCDMS, and NMC  $\mu A$  scattering was being led by the transverse cross section with the longitudinal component crossing over into the shadowing region at lower  $x$  compared to the transverse.

As summarized earlier, in the low- $Q^2$  region, the neutrino cross section is dominated by the longitudinal structure function  $F_L$  via axial-current interactions since  $F_T$  vanishes as  $Q^2 \rightarrow 0$  similar to the behavior of charged lepton scattering. If the results of the NuTeV analysis are verified, one contribution to the different behavior of shadowing at low- $Q^2$  demonstrated by  $\nu A$  and  $\ell A$ , in addition to the different hadronic fluctuations in the two interactions, could be due to the different mix of longitudinal and transverse contributions to the cross section of the two processes in this kinematic region.

Another hypothesis of what is causing the difference between neutrino and charged-lepton shadowing results comes from Guzey et al. [139] who speculates that at low  $x$ , low- $Q^2$  the value of  $y$  is close to unity and the neutrino interactions primarily probe the down and strange quarks. This is very different than the situation with charged-lepton scattering where the contribution from down and strange quarks are suppressed by a factor of  $1/4$  compared to the up and charm. Therefore, the discrepancy between the observed nuclear shadowing in lepton-nucleus total cross section at small  $x$  and shadowing in total neutrino-nucleus cross section could be caused by the absence of nuclear shadowing in the nuclear strange quark distributions as extracted from the neutrino-nucleus data or even the poor knowledge of the strange-quark distribution in the free-nucleon that affects the neutrino-nucleus ratio more than the charged-lepton ratio.

## Acknowledgments

This research was supported by DGI and FEDER funds, under Contracts FIS2011-28853-C02-02 and the Spanish Consolider-Ingenio 2010 Programme CPAN (CSD2007-00042), by Generalitat Valenciana under Contract PROMETEO/2009/0090, and by the EU HadronPhysics2 project, Grant agreement no. 227431. J. T. Sobczyk (on leave from Wrocław University and partially supported by Grants NN202 368439 and DWM/57/T2K/2007) thanks T. Golan for making Figure 1. Fermilab is operated by Fermi Research Alliance, LLC under Contract no. De-AC02-07CH11359 with the United States Department of Energy.

## References

- [1] H. Gallagher, G. Garvey, and G. P. Zeller, "Neutrino-nucleus interactions," *Annual Review of Nuclear and Particle Science*, vol. 61, pp. 355–378, 2011.
- [2] Q. Wu, S. R. Mishra, A. Godley et al., "A precise measurement of the muonneutrino–nucleon inclusive charged current cross section off an isoscalar target in the energy range  $2.5 < E_\nu < 40$  by NOMAD," *Physics Letters B*, vol. 660, no. 1-2, pp. 19–25, 2008.

- [3] P. Adamson, C. Andreopoulos, K. E. Arms et al., "Neutrino and antineutrino inclusive charged-current cross section measurements with the MINOS near detector," *Physical Review D*, vol. 81, no. 7, Article ID 072002, 16 pages, 2010.
- [4] Y. Nakajima, J. L. Alcaraz-Aunión, S. J. Brice et al., "Measurement of inclusive charged current interactions on carbon in a few-GeV neutrino beam," *Physical Review D*, vol. 83, no. 1, Article ID 012005, 21 pages, 2011.
- [5] M. Ravonel Salzgeber, "Measurement of the flux averaged Inclusive Charged Current cross section," in *A Poster Presented at International Conference on Neutrino Physics and Astrophysics (NEUTRINO '12)*, Kyoto, Japan, June 2012.
- [6] B. Bhattacharya, R. J. Hill, and G. Paz, "Model independent determination of the axial mass parameter in quasielastic neutrino-nucleon scattering," *Physical Review D*, vol. 84, no. 7, Article ID 073006, 10 pages, 2011.
- [7] A. Bodek, S. Avvakumov, R. Bradford, and H. S. Budd, "Extraction of the axial nucleon form-factor from neutrino experiments on deuterium," *The European Physical Journal C*, vol. 63, p. 355, 2009.
- [8] V. Bernard, L. Elouadrhiri, and U. G. Meissner, "Axial structure of the nucleon: topical review," *Journal of Physics G*, vol. 28, no. 1, p. R1, 2002.
- [9] R. Gran, E. J. Jeon et al., "Measurement of the quasielastic axial vector mass in neutrino interactions on oxygen," *Physical Review D*, vol. 74, no. 6, Article ID 052002, 15 pages, 2006.
- [10] X. Espinal and F. Sanchez, "Measurement of the axial vector mass in neutrino-carbon interactions at K2K," *AIP Conference Proceedings*, vol. 967, no. 1, p. 117, 2007.
- [11] M. Dorman, "Preliminary results for CCQE scattering with the MINOS near detector," in *AIP Conference Proceedings*, vol. 1189, pp. 133–138, 2009.
- [12] A. A. Aguilar-Arevalo, C. E. Anderson, A. O. Bazarko et al., "First measurement of the muon neutrino charged current quasielastic double differential cross section," *Physical Review D*, vol. 81, no. 9, Article ID 092005, 22 pages, 2010.
- [13] V. Lyubushkin, B. Popov, J. J. Kim et al., "Study of quasi-elastic muon neutrino and antineutrino scattering in the NOMAD experiment," *The European Physical Journal C*, vol. 63, no. 3, pp. 355–381, 2009.
- [14] N. Mayer and N. Graf, "Improvements to MINOS CCQE analysis," in *AIP Conference Proceedings*, vol. 1405, pp. 41–46, 2011.
- [15] Y. Nakajima, "Measurement of CC and CCQE interactions at SciBooNE," in *AIP Conference Proceedings*, vol. 1405, pp. 47–52, 2011.
- [16] L. Alcaraz Aunión, "Measurement of the absolute  $\nu_\mu$ -CCQE cross section at the Sci-BooNE experiment," PhD Thesis supervised by F. Sánchez, Barcelona, July 2010, <http://lss.fnal.gov/archive/thesis/fermilab-thesis-2010-45.pdf>.
- [17] J. Grange, "New results from MiniBooNE charged-current quasi-elastic anti-neutrino data," in *AIP Conference Proceedings*, vol. 1405, p. 83, 2011.
- [18] J. G. Morfin, "Inclusive neutrino cross section measurements at MINERvA," in *A Poster Presented at International Conference International Conference on Neutrino Physics and Astrophysics (NEUTRINO '12)*, AIP Conference Proceedings, pp. 243–248, Kyoto, Japan, June 2012.
- [19] D. Casper, "The Nuance neutrino physics simulation, and the future," *Nuclear Physics B (Proceedings Supplement)*, vol. 112, no. 1–3, pp. 161–170, 2002.
- [20] E. Oset and L. L. Salcedo, " $\Delta$  self-energy in nuclear matter," *Nuclear Physics A*, vol. 468, no. 3–4, pp. 631–652, 1987.
- [21] J. A. Nowak, "Four momentum transfer discrepancy in the charged current  $\pi^+$  production in the MiniBooNE: data vs. theory," in *Proceedings of the 6th International Workshop on Neutrino-Nucleus Interactions in the Few-GeV Region (NUIINT '09)*, vol. 1189 of *AIP Conference Proceedings*, pp. 243–248, 2009.
- [22] S. Boyd, S. Dytman, E. Hernandez, J. Sobczyk, and R. Tacik, "Comparison of models of neutrino-nucleus interactions," in *AIP Conference Proceedings*, vol. 1189, pp. 60–73, 2009.
- [23] R. A. Smith and E. J. Moniz, "Neutrino reactions on nuclear targets," *Nuclear Physics B*, vol. 43, pp. 605–622, 1972.
- [24] R. A. Smith and E. J. Moniz, "Erratum: neutrino reactions on nuclear targets," *Nuclear Physics B*, vol. 101, p. 547, 19.
- [25] O. Benhar, A. Fabrocini, S. Fantoni, and I. Sick, "Spectral function of finite nuclei and scattering of GeV electrons," *Nuclear Physics A*, vol. 579, no. 3–4, pp. 493–517, 1994.
- [26] O. Benhar and D. Meloni, "Total neutrino and antineutrino nuclear cross sections around 1 GeV," *Nuclear Physics A*, vol. 789, no. 1–4, pp. 379–402, 2007.



- [27] A. M. Ankowski and J. T. Sobczyk, "Construction of spectral functions for medium-mass nuclei," *Physical Review C*, vol. 77, no. 4, Article ID 044311, 14 pages, 2008.
- [28] T. Leitner, O. Buss, L. Alvarez-Ruso, and U. Mosel, "Electron- and neutrino-nucleus scattering from the quasielastic to the resonance region," *Physical Review C*, vol. 79, no. 3, Article ID 034601, 26 pages, 2009.
- [29] J. Nieves, J. E. Amaro, and M. Valverde, "Inclusive quasi-elastic neutrino reactions," *Physical Review C*, vol. 70, Article ID 055503, 2004.
- [30] J. Nieves, J. E. Amaro, and M. Valverde, "Erratum: inclusive quasi-elastic neutrino reactions," *Physical Review C*, vol. 72, Article ID 019902, 2005.
- [31] J. Nieves, M. Valverde, and M. J. Vicente Vacas, "Inclusive nucleon emission induced by quasielastic neutrino-nucleus interactions," *Physical Review C*, vol. 73, no. 2, Article ID 025504, 18 pages, 2006.
- [32] M. Martini, M. Ericson, G. Chanfray, and J. Marteau, "A unified approach for nucleon knock-out, coherent and incoherent pion production in neutrino interactions with nuclei," *Physical Review C*, vol. 80, no. 6, Article ID 065501, 16 pages, 2009.
- [33] M. Martini, M. Ericson, G. Chanfray, and J. Marteau, "Neutrino and antineutrino quasielastic interactions with nuclei," *Physical Review C*, vol. 81, no. 4, Article ID 045502, 5 pages, 2010.
- [34] M. Sajjad Athar, S. Chauhan, and S. K. Singh, "Theoretical study of lepton events in the atmospheric neutrino experiments at SuperK," *The European Physical Journal A*, vol. 43, no. 2, pp. 209–227, 2010.
- [35] D. H. Wilkinson, "Renormalization of the axial-vector coupling constant in nuclear  $\beta$ -decay (II)," *Nuclear Physics A*, vol. 209, no. 3, pp. 470–484, 1973.
- [36] D. H. Wilkinson, "Renormalization of the axial-vector coupling constant in nuclear  $\beta$ -decay (III)," *Nuclear Physics A*, vol. 225, no. 3, pp. 365–381, 1974.
- [37] J. Nieves, I. Ruiz Simo, and M. J. Vicente Vacas, "The nucleon axial mass and the MiniBooNE Quasielastic Neutrino-Nucleus Scattering problem," *Physics Letters B*, vol. 707, p. 72, 2012.
- [38] M. Martini, M. Ericson, and G. Chanfray, "Neutrino quasielastic interaction and nuclear dynamics," *Physical Review C*, vol. 84, Article ID 055502, 2011.
- [39] A. A. Aguilar-Arevalo et al., "The Neutrino Flux prediction at MiniBooNE," *Physical Review D*, vol. 79, no. 7, Article ID 072002, 38 pages, 2009.
- [40] N. Jachowicz, C. Praet, and J. Ryckebusch, "Modeling neutrino-nucleus interactions in the few-GeV regime," *Acta Physica Polonica B*, vol. 40, no. 9, pp. 2559–2564, 2009.
- [41] N. Jachowicz, P. Vancraeyveld, P. Lava, C. Praet, and J. Ryckebusch, "Strangeness content of the nucleon in quasielastic neutrino-nucleus reactions of the nucleon in quasielastic neutrino-nucleus reactions," *Physical Review C*, vol. 76, no. 5, Article ID 055501, 11 pages, 2007.
- [42] C. Maieron, M. C. Martinez, J. A. Caballero, and J. M. Udias, "Nuclear model effects in charged current neutrino nucleus quasielastic scattering," *Physical Review C*, vol. 68, Article ID 048501, 2003.
- [43] J. E. Amaro, M. B. Barbaro, J. A. Caballero, T. W. Donnelly, and J. M. Udias, "Relativistic analyses of quasielastic neutrino cross sections at MiniBooNE kinematics," *Physical Review D*, vol. 84, no. 3, Article ID 033004, 8 pages, 2011.
- [44] B. Serot and J. Walecka, "The relativistic many-body problem," *Advances in Nuclear Physics*, vol. 16, p. 1, 1986.
- [45] A. Meucci, C. Giusti, and F. D. Pacati, "Relativistic descriptions of final-state interactions in neutral-current neutrino-nucleus scattering at MiniBooNE kinematics," *Physical Review D*, vol. 84, Article ID 113003, 2011.
- [46] T. W. Donnelly and I. Sick, "Superscaling of inclusive electron scattering from nuclei," *Physical Review Letters*, vol. 82, no. 16, pp. 3212–3215, 1999.
- [47] T. W. Donnelly and I. Sick, "Superscaling in inclusive electron-nucleus scattering," *Physical Review C*, vol. 60, Article ID 065502, 1999.
- [48] J. E. Amaro, M. B. Barbaro, J. A. Caballero, T. W. Donnelly, A. Molinari, and I. Sick, "Using electron scattering superscaling to predict charge-changing neutrino cross sections in nuclei," *Physical Review C*, vol. 71, no. 1, Article ID 015501, 17 pages, 2005.
- [49] J. E. Amaro, M. B. Barbaro, J. A. Caballero, and T. W. Donnelly, "Superscaling and neutral current quasielastic neutrino-nucleus scattering beyond the relativistic fermi gas model," *Physical Review C*, vol. 73, no. 6, Article ID 035503, 8 pages, 2006.
- [50] L. Alvarez-Ruso, "Neutrino interactions: challenges in the current theoretical picture," *Nuclear Physics B (Proceedings Supplement)*, vol. 229–232, pp. 167–173, 2012.
- [51] O. Benhar and D. Meloni, "Impact of nuclear effects on the determination of the nucleon axial mass," *Physical Review D*, vol. 80, no. 7, Article ID 073003, 6 pages, 2009.

- [52] O. Benhar, P. Coletti, and D. Meloni, "Electroweak nuclear response in quasi-elastic regime," *Physical Review Letters*, vol. 105, no. 13, Article ID 132301, 4 pages, 2010.
- [53] C. Juszczak, J. T. Sobczyk, and J. Żmuda, "Extraction of the axial mass parameter from MiniBooNE neutrino quasielastic double differential cross-section data," *Physical Review C*, vol. 82, no. 4, Article ID 045502, 6 pages, 2010.
- [54] A. V. Butkevich, "Analysis of flux-integrated cross sections for quasi-elastic neutrino charged-current scattering off  $^{12}\text{C}$  at MiniBooNE energies," *Physical Review C*, vol. 82, Article ID 055501, 2010.
- [55] J. Marteau, "Effects of the nuclear correlations on the neutrino-oxygen interactions," *The European Physical Journal A*, vol. 5, no. 2, pp. 183–190, 1999.
- [56] J. Nieves, I. Ruiz Simo, and M. J. Vicente Vacas, "Inclusive charged—current neutrino—nucleus reactions," *Physical Review C*, vol. 83, Article ID 045501, 2011.
- [57] W. M. Alberico, M. Ericson, and A. Molinari, "The role of two particle-two hole excitations in the spin-isospin nuclear response," *Annals of Physics*, vol. 154, no. 2, pp. 356–395, 1984.
- [58] J. E. Amaro, M. B. Barbaro, J. A. Caballero, T. W. Donnelly, and C. F. Williamson, "Meson-exchange currents and quasielastic neutrino cross sections in the Super Scaling Approximation model," *Physics Letters B*, vol. 696, p. 151, 2011.
- [59] J. E. Amaro, M. B. Barbaro, J. A. Caballero, and T. W. Donnelly, "Meson-exchange currents and quasielastic antineutrino cross sections in the SuperScaling Approximation," *Physical Review Letters*, vol. 108, Article ID 152501, 2012.
- [60] A. Bodek, H. S. Budd, and M. E. Christie, "Neutrino quasielastic scattering on nuclear targets parametrizing transverse enhancement (meson exchange currents)," *The European Physical Journal C*, vol. 71, no. 9, p. 1726, 2011.
- [61] O. Lalakulich, K. Gallmeister, and U. Mosel, "Many-body interactions of neutrinos with nuclei—observables," *Physical Review C*, vol. 86, Article ID 014614, 2012.
- [62] J. T. Sobczyk, "Multinucleon ejection model for Meson Exchange Current neutrino interactions," *Physical Review C*, vol. 86, Article ID 015504, 2012.
- [63] P. de Perio, "NEUT pion FSI," in *Proceedings of the 7th International Workshop on Neutrino-Nucleus Interactions in the Few GeV Region (NuInt '11)*, vol. 1405 of *AIP Conference Proceedings*, p. 223, Dehradun, India, March 2011.
- [64] T. Golan, C. Juszczak, and J. T. Sobczyk, "Final state interactions effects in neutrino-nucleus interactions," *Physical Review C*, vol. 86, Article ID 015505, 2012.
- [65] D. Meloni and M. Martini, "Revisiting the T2K data using different models for the neutrino-nucleus cross sections," *Physics Letters B*, vol. 716, p. 186, 2012.
- [66] M. Martini, M. Ericson, and G. Chanfray, "Neutrino energy reconstruction problems and neutrino oscillations," *Physical Review D*, vol. 85, Article ID 09312, 2012.
- [67] J. Nieves, F. Sanchez, I. Ruiz Simo, and M. J. Vicente Vacas, "Neutrino energy reconstruction and the shape of the CCQE-like total cross section," *Physical Review D*, vol. 85, Article ID 113008, 2012.
- [68] U. Mosel and O. Lalakulich, "Neutrino-long-baseline experiments and nuclear physics," in *Proceedings of 50th International Winter Meeting on Nuclear Physics (PoS BORMIO '12)*, Bormio, Italy, January 2012, 034.
- [69] A. A. Aguilar-Arevalo, C. E. Anderson, A. O. Bazarko et al., "Measurement of the neutrino neutral-current elastic Differential cross section," *Physical Review D*, vol. 82, no. 9, Article ID 092005, 16 pages, 2010.
- [70] A. V. Butkevich and D. Perevalov, "Neutrino neutral-current elastic scattering on  $^{12}\text{C}$ ," *Physical Review C*, vol. 84, no. 1, Article ID 015501, 9 pages, 2011.
- [71] O. Benhar and G. Veneziano, "Nuclear effects in neutral current quasi-elastic neutrino interactions," *Physics Letters B*, vol. 702, p. 326, 2011.
- [72] A. M. Ankowski, "Consistent analysis of neutral- and charged-current neutrino scattering off carbon," *Physical Review C*, vol. 86, no. 2, Article ID 024616, 13 pages, 2012.
- [73] A. A. Aguilar-Arevalo, C. E. Anderson, A. O. Bazarko et al., "First observation of coherent  $\pi^0$  production in neutrino-nucleus interactions with  $E_\nu < 2 \text{ GeV}$ ," *Physics Letters B*, vol. 664, no. 1-2, pp. 41–46, 2008.
- [74] S. Nakayama, S. Nakayama, C. Mauger et al., "Measurement of the single  $\pi^0$  production in neutral current neutrino interactions with water by a 1.3 GeV wide band muon neutrino beam," *Physics Letters B*, vol. 619, no. 3-4, pp. 255–262, 2005.
- [75] A. A. Aguilar-Arevalo, C. E. Anderson, A. O. Bazarko et al., "Measurement of  $\nu_\mu$  and  $\bar{\nu}_\mu$  induced neutral current single  $\pi^0$  production cross sections on mineral oil at  $E_\nu \sim O(1\text{GeV})$ ," *Physical Review D*, vol. 81, Article ID 013005, 2010.

- [76] Y. Kurimoto, J. L. Alcaraz-Aunión, S. J. Brice et al., "Measurement of inclusive neutral current neutral pion production on carbon in a Few-GeV neutrino beam," *Physical Review D*, vol. 81, Article ID 033004, 2009.
- [77] A. A. Aguilar-Arevalo, C. E. Anderson, A. O. Bazarko et al., "Measurement of neutrino-induced charged-current charged pion production cross sections on mineral oil at  $E_\nu 1 \text{ GeV}$ ," *Physical Review D*, vol. 83, Article ID 052007, 2011.
- [78] O. Lalakulich, K. Gallmeister, T. Leitner, and U. Mosel, "Pion production in the MiniBooNE," in *Proceedings of the 7th International Workshop on Neutrino-Nucleus Interactions in the Few GeV Region (NuInt '11)*, vol. 1405 of *AIP Conference Proceedings*, Dehradun, India, March 2011.
- [79] A. A. Aguilar-Arevalo, C. E. Anderson, A. O. Bazarko et al., "Measurement of  $\nu_\mu$ -induced charged-current neutral pion production cross sections on mineral oil at  $E_\nu \in 0.5 - 2.0 \text{ GeV}$ ," *Physical Review D*, vol. 83, no. 5, Article ID 052009, 2011.
- [80] A. A. Aguilar-Arevalo et al., "Measurement of the  $\nu_\mu \text{ CC}\pi^+/\text{QE}$  cross section ratio on mineral oil in a 0.8 GeV neutrino beam," *Physical Review Letters*, vol. 103, Article ID 081801, 2009.
- [81] A. Rodriguez, L. Whitehead, J. L. Alcaraz Aunión et al., "Measurement of single charged pion production in the charged-current interactions of neutrinos in a 1.3 GeV wide band beam," *Physical Review D*, vol. 78, no. 3, Article ID 032003, 2008.
- [82] T. Leitner, O. Buss, L. Alvarez-Ruso, and U. Mosel, "Electron- and neutrino-nucleus scattering from the quasielastic to the resonance region," *Physical Review C*, vol. 79, no. 3, Article ID 034601, 26 pages, 2009.
- [83] T. Leitner, O. Buss, U. Mosel, and L. Alvarez-Ruso, "Neutrino-induced pion production at energies relevant for the MiniBooNE and K2K experiments," *Physical Review C*, vol. 79, no. 3, Article ID 038501, 2009.
- [84] M. Sajjad Athar, S. Chauhan, and S. K. Singh, "CC $1\pi^+$  to CCQE cross sections ratio at accelerator energies," *Journal of Physics G*, vol. 37, no. 1, Article ID 015005, 2010.
- [85] M. J. Vicente Vacas, M. Kh. Khankhasaev, and S. G. Mashnik, "Inclusive pion double-charge-exchange above .5 GeV," <http://arxiv.org/abs/nucl-th/9412023>.
- [86] S. K. Singh, M. Sajjad Athar, and S. Ahmad, "Nuclear effects in neutrino induced coherent pion production at K2K and MiniBooNE," *Physical Review Letters*, vol. 96, no. 24, Article ID 241801, 4 pages, 2006.
- [87] K. M. Graczyk, D. Kielczewska, P. Przewłocki, and J. T. Sobczyk, " $C_5^A$  axial form factor from bubble chamber experiments," *Physical Review D*, vol. 80, no. 9, Article ID 093001, 14 pages, 2009.
- [88] E. Hernandez, J. Nieves, and M. Valverde, "Weak pion production off the nucleon," *Physical Review D*, vol. 76, no. 3, Article ID 033005, 22 pages, 2007.
- [89] O. Lalakulich and E. A. Paschos, "Resonance production by neutrinos:  $J = 3/2$  resonances," *Physical Review D*, vol. 71, no. 7, Article ID 074003, 10 pages, 2005.
- [90] O. Lalakulich, T. Leitner, O. Buss, and U. Mosel, "One pion production in neutrino reactions: including non-resonant background," *Physical Review D*, vol. 82, no. 9, Article ID 093001, 18 pages, 2010.
- [91] L. Alvarez-Ruso, S. K. Singh, and M. J. Vicente Vacas, "Neutrino  $d \rightarrow \mu^- \Delta^{++} n$  reaction and axial vector  $N\Delta$  coupling," *Physical Review C*, vol. 59, Article ID 3386, 1999.
- [92] M. Maltoni and T. Schwetz, "Testing the statistical compatibility of independent data sets," *Physical Review D*, vol. 68, no. 3, Article ID 033020, 9 pages, 2003.
- [93] E. Hernandez, J. Nieves, M. Valverde, and M. J. Vicente Vacas, " $N-\Delta(1232)$  axial form factors from weak pion production," *Physical Review D*, vol. 81, no. 8, Article ID 085046, 5 pages, 2010.
- [94] T. Sato, D. Uno, and T. S. H. Lee, "Dynamical model of weak pion production reactions," *Physical Review C*, vol. 67, no. 6, Article ID 065201, 13 pages, 2003.
- [95] C. Barbero, G. Lopez Castro, and A. Mariano, "Single pion production in CC  $\nu_\mu N$  scattering within a consistent effective Born approximation," *Physics Letters B*, vol. 664, pp. 70–77, 2008.
- [96] Y. Kurimoto, J. L. Alcaraz Aunión, S. J. Brice et al., "Improved measurement of neutral current coherent  $\pi^0$  production on carbon in a Few-GeV neutrino beam," *Physical Review D*, vol. 81, Article ID 111102, 2010.
- [97] M. Hasegawa, E. Aliu, S. Andringa et al., "Search for coherent charged pion production in neutrino-carbon interactions," *Physical Review Letters*, vol. 95, no. 25, Article ID 252301, 5 pages, 2005.
- [98] K. Hiraide, J. L. Alcaraz Aunión, S. J. Brice et al., "Search for charged current coherent pion production on carbon in a Few-GeV neutrino beam," *Physical Review D*, vol. 78, no. 11, Article ID 112004, 19 pages, 2008.

- [99] D. Rein and L. M. Sehgal, "Coherent  $\pi^0$  production in neutrino reactions," *Nuclear Physics B*, vol. 223, article 29, 1983.
- [100] Ch. Berger and L. M. Sehgal, "Lepton mass effects in single pion production by neutrinos," *Physical Review D*, vol. 76, no. 11, Article ID 113004, 8 pages, 2007.
- [101] Ch. Berger and L. M. Sehgal, "Partially conserved axial vector current and coherent pion production by low energy neutrinos," *Physical Review D*, vol. 79, no. 5, Article ID 053003, 6 pages, 2009.
- [102] E. A. Paschos and D. Schalla, "Coherent pion production by neutrinos," *Physical Review D*, vol. 80, Article ID 033005, 2009.
- [103] E. Hernandez, J. Nieves, and M. J. Vicente-Vacas, "Neutrino induced coherent pion production off nuclei and the partial conservation of the axial current," *Physical Review D*, vol. 80, no. 1, Article ID 013003, 15 pages, 2009.
- [104] S. X. Nakamura, T. Sato, T.-S. H. Lee, B. Szczerbinska, and K. Kubodera, "Dynamical model of coherent pion production in neutrino-nucleus scattering," *Physical Review C*, vol. 81, no. 3, Article ID 035502, 22 pages, 2010.
- [105] J. E. Amaro, E. Hernandez, J. Nieves, and M. Valverde, "Theoretical study of neutrino-induced coherent pion production off nuclei at T2K and MiniBooNE energies," *Physical Review D*, vol. 79, Article ID 013002, 18 pages, 2009.
- [106] E. Hernandez, J. Nieves, and M. Valverde, "Coherent pion production off nuclei at T2K and MiniBooNE energies revisited," *Physical Review D*, vol. 82, no. 7, Article ID 077303, 4 pages, 2010.
- [107] L. Alvarez-Ruso, L. S. Geng, S. Hirenzaki, and M. J. Vicente Vacas, "Charged current neutrino induced coherent pion production," *Physical Review C*, vol. 75, no. 5, Article ID 055501, 8 pages, 2007.
- [108] L. Alvarez-Ruso, L. S. Geng, S. Hirenzaki, and M. J. Vicente Vacas, "Erratum: charged current neutrino induced coherent pion production," *Physical Review C*, vol. 80, Article ID 019906, 2009.
- [109] D. Rein and L. M. Sehgal, "Neutrino excitation of baryon resonances and single pion production," *Annals of Physics*, vol. 133, pp. 79–153, 1981.
- [110] K. M. Graczyk and J. T. Sobczyk, "Lepton mass effects in weak charged current single pion production," *Physical Review D*, vol. 77, no. 5, Article ID 053003, 7 pages, 2008.
- [111] K. M. Graczyk and J. T. Sobczyk, "Form factors in the quark resonance model," *Physical Review D*, vol. 77, no. 5, Article ID 053001, 12 pages, 2008.
- [112] K. M. Graczyk and J. T. Sobczyk, "Erratum: form factors in the quark resonance model," *Physical Review D*, vol. 79, Article ID 079903, 2009.
- [113] O. Lalakulich, W. Melnitchouk, and E. A. Paschos, "Quark-hadron duality in neutrino scattering," *Physical Review C*, vol. 75, no. 1, Article ID 015202, 10 pages, 2007.
- [114] K. M. Graczyk, C. Juszczak, and J. T. Sobczyk, "Quark-hadron duality in the Rein-Sehgal model," *Nuclear Physics A*, vol. 781, no. 1-2, pp. 227–246, 2007.
- [115] O. Lalakulich, N. Jachowicz, Ch. Praet, and J. Ryckebusch, "Quark-hadron duality in lepton scattering off nuclei," *Physical Review C*, vol. 79, no. 1, Article ID 015206, 12 pages, 2009.
- [116] A. Bodek and U.-K. Yang, "NUFACT09 update to the Bodek-Yang unified model for electron- and neutrino- nucleon scattering cross sections," in *Proceedings of the 11th International Workshop on Neutrino Factories, Superbeams and Beta Beams-NuFact*, vol. 1222 of *AIP Conference Proceedings*, pp. 233–237, March 2010.
- [117] M. Gluck, E. Reya, and A. Vogt, "Dynamical parton distributions revisited," *The European Physical Journal C*, vol. 5, no. 3, pp. 461–470, 1998.
- [118] R. Thorne and R. Roberts, "Practical procedure for evolving heavy flavor structure functions," *Physics Letters B*, vol. 421, p. 303, 1998.
- [119] A. D. Martin, R. G. Roberts, W. J. Stirling, R. S. Thorne et al., "Estimating the effect of NNLO contributions on global parton analyses," *The European Physical Journal C*, vol. 18, no. 1, pp. 117–126, 2000.
- [120] L. W. Whitlow, S. Rock, A. Bodek et al., "A precise extraction of  $R = \sigma_L/\sigma_T$  from a global analysis of the SLAC deep inelastic e-p and e-d scattering cross sections," *Physics Letters B*, vol. 250, no. 1-2, pp. 193–198, 1990.
- [121] M. Tzanov, D. Naples, S. Boyd et al., "Precise measurement of neutrino and anti-neutrino differential cross sections," *Physical Review D*, vol. 74, no. 1, Article ID 012008, 16 pages, 2006.
- [122] G. Onengut, R. Van Dantzig, M. De Jong et al., "Measurement of nucleon structure functions in neutrino scattering," *Physics Letters B*, vol. 632, pp. 65–75, 2006.
- [123] J. Altegoer, M. Anfreville, C. Angelini et al., "The NOMAD experiment at the CERN SPS," *Nuclear Instruments and Methods in Physics Research Section A*, vol. 404, no. 1, pp. 96–128, 1998.

- [124] R. Petti, "Cross-section measurements in the NOMAD experiment," *Nuclear Physics B (Proceedings Supplement)*, vol. 159, pp. 56–62, 2006.
- [125] A. Accardi, M. E. Christy, C. E. Keppel et al., "New parton distributions from large- $x$  and low- $Q^2$  data," *Physical Review D*, vol. 81, no. 3, Article ID 034016, 2010.
- [126] J. Pumplin, D. R. Stump, J. Huston, H. L. Lai, P. M. Nadolsky, and W. K. Tung, "New generation of parton distributions with uncertainties from global QCD analysis," *JHEP*, vol. 0207, p. 012, 2002.
- [127] W. J. Stirling, A. D. Martin, R. G. Roberts, and R. S. Thorne, "MRST parton distributions," in *AIP Conference Proceedings*, vol. 747, p. 16, 2005.
- [128] M. Tzanov, "NuTeV structure function measurement," in *Proceedings of the 13th International Workshop on Deep Inelastic Scattering*, vol. 792 of *AIP Conference Proceedings*, pp. 241–244, 2005.
- [129] K. Kovarik, I. Schienbein, F. I. Olness et al., "Nuclear corrections in neutrino-nucleus DIS and their compatibility with global nPDF analyses," *Physical Review Letters*, vol. 106, no. 12, Article ID 122301, 4 pages, 2011.
- [130] I. Schienbein, J. Y. Yu, C. Keppel, J. G. Morfin, F. Olness, and J. F. Owens, "Nuclear PDFs from neutrino deep inelastic scattering," *Physical Review D*, vol. 77, Article ID 054013, 2008.
- [131] J. F. Owens, J. Huston, J. Pumplin et al., "Nuclear corrections and parton distribution functions: lessons learned from global fitting," in *AIP Conference Proceedings*, vol. 967, pp. 259–263, 2007.
- [132] B. Z. Kopeliovich, J. G. Morfin, and I. Schmidt, "Nuclear shadowing in electro-weak interactions," *Progress in Particle and Nuclear Physics*, vol. 68, pp. 314–372, 2013.
- [133] <http://www.praktika.physik.uni-bonn.de/conferences/dis-2012?set.language=en>.
- [134] J. Botts, J. G. Morfin, J. F. Owens, J. Qiu, W.-K. Tunga, H. Weerts et al., "CTEQ parton distributions and flavor dependence of sea quarks," *Physics Letters B*, vol. 304, no. 1-2, pp. 159–166, 1993.
- [135] H. L. Lai, J. Botts, J. Huston et al., "Global QCD analysis and the CTEQ parton distributions," *Physical Review D*, vol. 51, no. 9, pp. 4763–4782, 1995.
- [136] S. J. Brodsky, I. Schmidt, and J. J. Yang, "Nuclear antishadowing in neutrino deep inelastic scattering," *Physical Review D*, vol. 70, Article ID 116003, 2004.
- [137] J.-W. Qiu and I. Vitev, "Nuclear shadowing in neutrino nucleus deeply inelastic scattering," *Physics Letters B*, vol. 587, pp. 52–61, 2004.
- [138] V. Guzey, L. Zhu, C. Keppel et al., "Impact of nuclear dependence of  $R = \sigma_L/\sigma_T$  on antishadowing in nuclear structure functions," *Physical Review C*, vol. 86, no. 4, Article ID 045201, 9 pages, 2012.
- [139] V. Guzey et al., "Nuclear shadowing in charged-lepton-nucleus and neutrino-nucleus scattering," Work in Progress.



## Research Article

# Charged-Current Neutrino-Nucleus Scattering off the Even Molybdenum Isotopes

**E. Ydrefors and J. Suhonen**

*Department of Physics, University of Jyväskylä, P.O. Box 35 (YFL), 40114 Jyväskylä, Finland*

Correspondence should be addressed to E. Ydrefors, [emanuel.ydrefors@jyu.fi](mailto:emanuel.ydrefors@jyu.fi)

Received 5 July 2012; Revised 19 October 2012; Accepted 6 November 2012

Academic Editor: Gian Luigi Fogli

Copyright © 2012 E. Ydrefors and J. Suhonen. This is an open access article distributed under the Creative Commons Attribution License, which permits unrestricted use, distribution, and reproduction in any medium, provided the original work is properly cited.

Neutrinos from supernovae constitute important probes of both the currently unknown supernova mechanisms and of neutrino properties. Reliable information about the nuclear responses to supernova neutrinos is therefore crucial. In this work, we compute the cross sections for the charged-current neutrino-nucleus scattering off the even-even molybdenum isotopes. The nuclear responses to supernova neutrinos are subsequently calculated by folding the cross sections with a Fermi-Dirac distribution.

## 1. Introduction

Studies of neutrino-nucleus interactions with neutrinos of low and intermediate incoming energies (i.e., neutrino energies in the range up to a few hundred MeV) are of great importance for the disentanglement of various unresolved questions in astrophysics, particle physics, and nuclear physics [1, 2]. Supernovae (type II) constitute the inevitable deaths of very massive stars initiated by the collapse of their iron cores. For the details of supernova physics, see for example, [3–5]. In a supernova event, about 99% of the explosion energy is emitted as neutrinos of all flavors. A future detection of neutrinos from a coming supernova would therefore provide a wealth of valuable information both on the currently unknown supernova mechanisms and the associated nucleosynthesis of heavy elements. A high-statistics observation of the neutrino signal from the next nearby supernova could in addition provide important information on unknown neutrino properties (see e.g., [6]). It has for example, been shown by simulations [7] that the signal produced by supernova neutrinos in a large-scale detector such as the IceCube [8] probably could be used to disentangle the important question of normal-or-inverted neutrino-mass hierarchy. As has been proposed by Volpe [9, 10], charged-current neutrino-nucleus scattering with neutrinos from low-energy

neutrino beams could in the future be exploited for spectroscopy of the virtual states involved in neutrinoless double-beta decay (see e.g., [11]) and consequently constrain theoretical predictions for the associated nuclear matrix elements.

Neutrinos from astrophysical sources can be detected by Earth-bound detectors by using charged-current and/or neutral-current interactions in nuclei [12]. For a recent review on experimental methods for detection of supernova neutrinos, see [13]. One planned possibility for measurements of astrophysical neutrinos (solar and supernova neutrinos) is the MOON (Mo Observatory Of Neutrinos) experiment [14].

In this paper, we perform theoretical calculations of the cross sections for the charged-current neutrino-nucleus scattering off the stable even-even molybdenum isotopes for neutrino energies, which are relevant for supernova neutrinos. We also present results for the averaged cross sections obtained by folding the cross sections with a Fermi-Dirac distribution. The calculations are based on the general theory for the treatment of semileptonic processes in nuclei, which was first introduced by O'Connell et al. [15]. This theory is discussed comprehensively in [16]. In the present calculations, the initial and final nuclear states are constructed by using the proton-neutron quasiparticle random-phase approximation (pnQRPA, see e.g., [17]).

The nuclear-structure dependence of the  $\nu$ -nucleus cross sections is contained in the reduced nuclear matrix elements of various one-body operators, which depend on the momentum transfer. With an increasing number of nuclear final states, the calculations of these matrix elements are obviously increasingly time consuming. Therefore, in [18] we introduced a fast method for the calculation of the involved matrix elements, which is based on the barycentric Lagrange interpolation [19]. This method is adopted in this work and it is shown that the obtained results are in very good agreement with exact calculations.

This paper is organized as follows. In Section 2 we outline the theoretical framework for calculations of charged-current neutrino-nucleus cross sections. First the pnQRPA is introduced. We then briefly summarize the formalism for computations of charged-current neutrino-nucleus scattering off nuclei. Then, in Section 3 we present our results. Finally, in Section 4 we draw the conclusions.

## 2. Theory

### 2.1. pnQRPA

In this work, the proton-neutron quasiparticle random-phase approximation (pnQRPA) is adopted to construct the nuclear final and initial states. In this section, we therefore briefly summarize the formalism of the pnQRPA. For a more detailed treatment, the reader is referred to [17, 20].

The nuclear Hamiltonian for a general two-body residual interaction  $V$  can be expressed in the form

$$H = \sum_a \varepsilon_a c_a^\dagger c_a + \frac{1}{4} \sum_{\alpha\beta\gamma\delta} \bar{v}_{\alpha\beta\gamma\delta} c_\alpha^\dagger c_\beta^\dagger c_\delta c_\gamma, \quad (2.1)$$

where the index  $a$  contains the single-particle quantum numbers  $n_a$ ,  $l_a$ , and  $j_a$  and  $\alpha$  holds in addition the magnetic quantum number  $m_\alpha$ . Here  $c_\alpha^\dagger$  is the particle creation operator and  $c_\alpha$  denotes the corresponding particle annihilation operator. In (2.1)  $\varepsilon_a$  are single-particle

energies and the antisymmetric two-body matrix elements are defined as  $\bar{v}_{\alpha\beta\gamma\delta} = \langle \alpha\beta | V | \gamma\delta \rangle - \langle \alpha\beta | V | \delta\gamma \rangle$ .

The pairing correlations in this work are taken into account by adopting the BCS (Bardeen-Cooper-Schrieffer) theory. The starting point in the BCS approach is the variational ansatz for the BCS vacuum

$$|\text{BCS}\rangle = \prod_{\alpha>0} (u_{\alpha} - v_{\alpha} c_{\alpha}^{\dagger} \tilde{c}_{\alpha}^{\dagger}) |\text{HF}\rangle, \quad (2.2)$$

where  $|\text{HF}\rangle$  is the Hartree-Fock vacuum and  $\tilde{c}_{\alpha}$  denotes the time-reversed particle annihilation operator, which is defined as  $\tilde{c}_{\alpha} = (-1)^{j_{\alpha}+m_{\alpha}} c_{-\alpha}$  where  $-\alpha = (a, -m_{\alpha})$ . The variational parameters  $u_{\alpha}$  and  $v_{\alpha}$  in (2.2) are obtained by solving the BCS equations [17].

The quasiparticles subsequently are defined via the Bogoliubov-Valatin transformation

$$\begin{aligned} a_{\alpha}^{\dagger} &= u_{\alpha} c_{\alpha}^{\dagger} + v_{\alpha} \tilde{c}_{\alpha}, \\ \tilde{a}_{\alpha} &= u_{\alpha} \tilde{c}_{\alpha} - v_{\alpha} c_{\alpha}^{\dagger}. \end{aligned} \quad (2.3)$$

By using this transformation the nuclear Hamiltonian (2.1) can be cast into the form

$$H = H_{11} + H_{02} + H_{20} + H_{13} + H_{31} + H_{04} + H_{40}, \quad (2.4)$$

where the term  $H_{ij}$  is proportional to a normal ordered product of  $i$  quasiparticle creation operators and  $j$  quasiparticle annihilation operators.

In practice, the parameters of the BCS calculation are adjusted to reproduce the experimental pairing gaps for the reference even-even nucleus under consideration. In this work, the empirical pairing gaps have been deduced from the three-point formulae (see e.g., [17])

$$\begin{aligned} \Delta_p &= \frac{1}{4} (-1)^{Z+1} [S_p(A+1, Z+1) - 2S_p(A, Z) + S_p(A-1, Z-1)], \\ \Delta_n &= \frac{1}{4} (-1)^{A-Z+1} [S_n(A+1, Z) - 2S_n(A, Z) + S_n(A-1, Z)], \end{aligned} \quad (2.5)$$

where  $S_p(A, Z)$  ( $S_n(A, Z)$ ) is the proton (neutron) separation energy for the nucleus  $(A, Z)$  having mass number  $A$  and proton number  $Z$ .

In the pnQRPA, the states of the odd-odd nucleus subsequently are constructed by coupling two-quasiparticle operators to good angular momentum  $J_{\omega}$  and parity  $\pi_{\omega}$ . The state vector corresponding to the excitation  $\omega = (J_{\omega}, \pi_{\omega}, k_{\omega})$  then is defined by

$$|\omega\rangle = Q_{\omega}^{\dagger} |\text{pnQRPA}\rangle, \quad (2.6)$$

where  $|\text{pnQRPA}\rangle$  denotes the pnQRPA vacuum and the additional quantum number  $k_\omega$  enumerates the states with the same angular momentum and parity. Here the pnQRPA creation operator  $Q_\omega^\dagger$  is given by

$$Q_\omega^\dagger = \sum_{pn} \left( X_{pn}^\omega [a_p^\dagger a_n^\dagger]_{J_\omega M_\omega} + Y_{pn}^\omega [\tilde{a}_p \tilde{a}_n]_{J_\omega M_\omega} \right), \quad (2.7)$$

where the sum runs over all possible proton-neutron configurations in the adopted valence space. The pnQRPA equations can then be written in the matrix form [17]

$$\begin{pmatrix} \mathbf{A} & \mathbf{B} \\ -\mathbf{B}^* & -\mathbf{A}^* \end{pmatrix} \begin{pmatrix} \mathbf{X}^\omega \\ \mathbf{Y}^\omega \end{pmatrix} = E_\omega \begin{pmatrix} \mathbf{X}^\omega \\ \mathbf{Y}^\omega \end{pmatrix}, \quad (2.8)$$

where  $E_\omega$  denotes the pnQRPA energy of the phonon  $\omega$ . In (2.8)  $\mathbf{A}$  is the well-known pnQTDA matrix and the matrix  $\mathbf{B}$  contains the induced ground-state correlations. Matrices  $\mathbf{A}$  and  $\mathbf{B}$  contain both a particle-particle and a particle-hole channel of the proton-neutron two-body interaction. As is customary [11] also in this work the particle-particle and particle-hole channels are scaled by phenomenological constants  $g_{pp}$  and  $g_{ph}$ , respectively. This is done for each multipole  $J^\pi$  separately. For more details on the scaling of the pnQRPA Hamiltonian, see [20, 21]. In the present computations, these parameters are tuned for the  $1^+$  multipole only by using experimental observables such as beta-decay rates, the energy of the giant Gamow-Teller resonance, and experimental energies of the low-lying states in the odd-odd nucleus under consideration.

## 2.2. Charged-Current Neutrino-Nucleus Scattering

In this work, we consider charged-current neutrino and antineutrino scatterings off a nucleus  $(A, Z)$  with mass number  $A$  and proton number  $Z$ , that is, neutrino-induced reactions of either the form

$$\nu_l + (A, Z) \longrightarrow (A, Z + 1) + l^-, \quad (2.9)$$

or

$$\bar{\nu}_l + (A, Z) \longrightarrow (A, Z - 1) + l^+, \quad (2.10)$$

for the lepton flavors  $l = e, \mu, \tau$ . The Feynman diagram for the  $\nu$ -nucleus scattering that proceed, via an exchange of a  $W^+$  boson is shown in Figure 1. In the figure  $k_\mu, (k'_\mu)$  represents the four-momentum of the incoming (outgoing), lepton and  $p_\mu$  and  $p'_\mu$  are the four-momenta of the initial and final nuclei. The antineutrino reaction (2.10), which is mediated by a  $W^-$  boson, can be obtained via charge-conjugation operation on Figure 1 and therefore is not displayed here.

In this work, we employ conventions that are similar to the ones used in [22]. We consequently define the covariant and contravariant four-vectors as  $a_\mu = (a_0, -\mathbf{a})$  and  $a^\mu = g^{\mu\nu} a_\nu = (a_0, \mathbf{a})$ , respectively, with the metric  $g^{\mu\nu} = g_{\mu\nu} = \text{diag}(1, -1, -1, -1)$ . We thus write

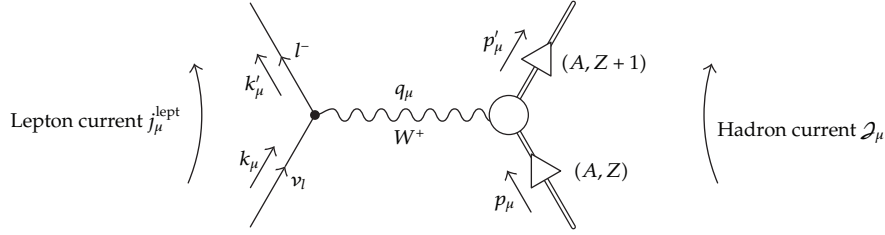


**Figure 1:** Charged-current neutrino scattering off a nucleus  $(A, Z)$  via the exchange of a  $W^+$  boson. The transferred four momentum is  $q_\mu = k'_\mu - k_\mu = p_\mu - p'_\mu$ .

$k_\mu = (E_k, -\mathbf{k})$  and  $k'_\mu = (E_{k'}, -\mathbf{k}')$ , where  $E_k$  and  $E_{k'}$  are the energies and  $\mathbf{k}$  and  $\mathbf{k}'$  denote the three-momenta of the incoming and outgoing leptons. The four-momenta of the initial and final nuclear states take similarly the forms  $p_\mu = (E_p, -\mathbf{p})$  and  $p'_\mu = (E_{p'}, -\mathbf{p}')$ , respectively.

For low-energy neutrinos, such as the supernova neutrinos that are considered in this work, the transferred four momentum is small compared to the mass of the gauge boson ( $W^+$  and  $W^-$  resp.), that is,  $Q^2 = -q_\mu q^\mu \ll M_W^2$ . The process in Figure 1 can consequently be treated in lowest order in the coupling constant  $G$ . The effective Hamiltonian density can then be written for the neutrino-induced reaction (2.9) in the current-current form

$$H_{\text{eff}}^\nu(\mathbf{r}) = \frac{G}{\sqrt{2}} j_\mu^{(-),\text{lept}}(\mathbf{r}) \mathcal{J}^{(+),\mu}(\mathbf{r}), \quad \mathbf{r} = (x, y, z), \quad (2.11)$$

where  $j_\mu^{(-),\text{lept}}(\mathbf{r})$  represents the charged-current lepton current and  $\mathcal{J}^{(+),\mu}(\mathbf{r})$  is the hadron current. For charge-changing interactions, the coupling constant  $G$  is given by  $G = G_F \cos \theta_C$  where  $G_F = 1.1644 \times 10^{-5}$ , GeV denotes the Fermi constant, and  $\theta_C \approx 13^\circ$  is the Cabibbo angle. For the antineutrino scattering, the effective Hamiltonian density similarly is given by

$$H_{\text{eff}}^{\bar{\nu}}(\mathbf{r}) = \frac{G}{\sqrt{2}} j_\mu^{(+),\text{lept}}(\mathbf{r}) \mathcal{J}^{(-),\mu}(\mathbf{r}), \quad (2.12)$$

where  $j_\mu^{(+),\text{lept}}(\mathbf{r}) = (j_\mu^{(-),\text{lept}}(\mathbf{r}))^\dagger$  and  $\mathcal{J}^{(-),\mu}(\mathbf{r}) = (\mathcal{J}^{(+),\mu}(\mathbf{r}))^\dagger$ . The nuclear matrix elements for both the considered processes then take the form

$$\begin{aligned} \langle f | H_{\text{eff}}^{\nu/\bar{\nu}} | i \rangle &= \frac{G}{\sqrt{2}} \int d^3\mathbf{r} \langle f | j_\mu^{\text{lept}}(\mathbf{r}) | f_{\nu_l} \rangle \langle f | \mathcal{J}^\mu(\mathbf{r}) | i \rangle \\ &= \frac{G}{\sqrt{2}} \int d^3\mathbf{r} e^{-i\mathbf{q}\cdot\mathbf{r}} l_\mu \langle f | \mathcal{J}^\mu(\mathbf{r}) | i \rangle \\ &= \frac{G}{\sqrt{2}} \int d^3\mathbf{r} e^{-i\mathbf{q}\cdot\mathbf{r}} [l_0 \langle f | \mathcal{J}_0 | i \rangle - \mathbf{l} \cdot \langle f | \boldsymbol{\mathcal{J}}(\mathbf{r}) | i \rangle], \end{aligned} \quad (2.13)$$

where  $f_l = l^-$  ( $l^+$ ) and  $f_{\nu_l} = \nu_l$  ( $\bar{\nu}_l$ ) for neutrino (antineutrino) scattering. We have here defined  $\mathcal{J}^\mu(\mathbf{r}) = (\mathcal{J}_0(\mathbf{r}), \mathbf{J}(\mathbf{r})) = \mathcal{J}^{(\pm),\mu}(\mathbf{r})$ , and  $j_\mu^{\text{lept}}(\mathbf{r}) = j^{(\pm),\mu}(\mathbf{r})$ . This should be understood such that the appropriate hadron and lepton currents for the process under consideration are



combined according to (2.11) and (2.12), respectively. In (2.13) we have moreover introduced the lepton matrix element

$$l_\mu = e^{iq \cdot r} \langle f_l | j_\mu^{\text{lept}}(\mathbf{r}) | f_v \rangle. \quad (2.14)$$

Here the hadron currents  $\mathcal{J}^{(\pm),\mu}(\mathbf{r})$  can be decomposed into vector (V) and axial-vector (A) pieces according to

$$\mathcal{J}^{(\pm),\mu}(\mathbf{r}) = \mathcal{J}^{(\pm),V,\mu}(\mathbf{r}) - \mathcal{J}^{(\pm),A,\mu}(\mathbf{r}). \quad (2.15)$$

At the origin ( $\mathbf{r} = 0$ ), the single-nucleon matrix elements of the currents  $\mathcal{J}^{(+),V,\mu}$  and  $\mathcal{J}^{(+),A,\mu}$  are given by

$$\begin{aligned} {}_p \langle \mathbf{p}' \sigma' | J^{(+),V,\mu}(0) | \mathbf{p} \sigma \rangle_n &= \frac{\bar{u}(\mathbf{p}', \sigma')}{V} \left[ F_1^{\text{CC}}(Q^2) \gamma^\mu - i \frac{F_2^{\text{CC}}(Q^2)}{2m_N} \sigma^{\mu\nu} q_\nu \right] u(\mathbf{p}, \sigma), \\ {}_p \langle \mathbf{p}' \sigma' | J^{(+),A,\mu}(0) | \mathbf{p} \sigma \rangle_n &= \frac{\bar{u}(\mathbf{p}', \sigma')}{V} \left[ F_A^{\text{CC}}(Q^2) \gamma_5 \gamma^\mu - F_P^{\text{CC}}(Q^2) \gamma_5 q^\mu \right] u(\mathbf{p}, \sigma), \end{aligned} \quad (2.16)$$

where  $|\mathbf{p} \sigma\rangle_{p(n)}$  denotes the state vector of a proton (neutron) having the three momentum  $\mathbf{p}$  and spin projection  $\sigma$  and  $m_N$  is the nucleon mass. The corresponding one-nucleon matrix elements for the nuclear current  $\mathcal{J}^{(-),\mu}(\mathbf{r})$  are related to the ones of  $\mathcal{J}^{(+),\mu}(\mathbf{r})$  through the charge symmetries [23]

$$\begin{aligned} {}_n \langle \mathbf{p}' \sigma' | J^{(-),V,\mu}(0) | \mathbf{p} \sigma \rangle_p &= {}_p \langle \mathbf{p}' \sigma' | J^{(+),V,\mu}(0) | \mathbf{p} \sigma \rangle_n, \\ {}_n \langle \mathbf{p}' \sigma' | J^{(-),A,\mu}(0) | \mathbf{p} \sigma \rangle_p &= {}_p \langle \mathbf{p}' \sigma' | J^{(+),A,\mu}(0) | \mathbf{p} \sigma \rangle_n. \end{aligned} \quad (2.17)$$

By the conservation of the vector current (CVC), the vector form factors  $F_{1,2}^{\text{CC}}(Q^2)$  in (2.16) can be written in terms of the proton and neutron electromagnetic form factors  $F_{1,2}^{\text{EM},p}(Q^2)$  and  $F_{1,2}^{\text{EM},n}(Q^2)$  as (see e.g., [23])

$$F_{1,2}^{\text{CC}}(Q^2) = F_{1,2}^{\text{EM},p}(Q^2) - F_{1,2}^{\text{EM},n}(Q^2). \quad (2.18)$$

In the present work, we use the electromagnetic form factors of [22]. The axial-vector form factor  $F_A^{\text{CC}}(Q^2)$  in (2.16) is assumed to be of dipole form with the quenched static value  $F_A^{\text{CC}}(0) = -1.0$ . Moreover, the pseudoscalar form factor  $F_P^{\text{CC}}(Q^2)$  in (2.16) is obtained from the Goldberger-Treiman relation (see e.g., [16])

$$F_P^{\text{CC}}(Q^2) \approx \frac{2m_N}{m_\pi^2 + Q^2} F_A^{\text{CC}}(Q^2), \quad (2.19)$$

where  $m_\pi = 139.57 \text{ MeV}$  [5] represents the mass of the charged pion.

We assume in this work that the final and initial nuclear states have well-defined angular momenta  $J_f$  and  $J_i$  and parities  $\pi_f$  and  $\pi_i$ , respectively. The double-differential cross section for the charged-current neutrino-nucleus scattering with transition from an initial nuclear state  $i$  to a final nuclear state  $f$  can then be written in the form (see e.g., [24])

$$\left( \frac{d^2\sigma_{i \rightarrow f}}{d\Omega dE_{\text{exc}}} \right)_{\nu/\bar{\nu}} = \frac{G^2 F(\pm Z_f, E_{\mathbf{k}'}) |\mathbf{k}'| E_{\mathbf{k}'}}{\pi(2J_i + 1)} \left( \sum_J \sigma_{\text{CL}}^J + \sum_{J \geq 1} \sigma_{\text{T}}^J \right), \quad (2.20)$$

where

$$\begin{aligned} \sigma_{\text{CL}}^J &= (1 + a \cos \theta) |(J_f \| \mathcal{M}_J(q) \| J_i)|^2 \\ &+ (1 + a \cos \theta - 2b \sin^2 \theta) |(J_f \| \mathcal{L}_J(q) \| J_i)|^2 \\ &+ \frac{E_{\text{exc}}}{q} ((1 + a \cos \theta) + c) 2 \text{Re} [(J_f \| \mathcal{L}_J(q) \| J_i) (J_f \| \mathcal{M}_J(q) \| J_i)^*], \end{aligned} \quad (2.21)$$

$$\begin{aligned} \sigma_{\text{T}}^J &= (1 - a \cos \theta + b \sin^2 \theta) \left[ |(J_f \| \mathcal{T}_J^{\text{mag}}(q) \| J_i)|^2 + |(J_f \| \mathcal{T}_J^{\text{el}}(q) \| J_i)|^2 \right] \\ &\mp \frac{(E_{\mathbf{k}} + E_{\mathbf{k}'})}{q} [((1 - a \cos \theta) - c) 2 \text{Re} [(J_f \| \mathcal{T}_J^{\text{mag}}(q) \| J_i) (J_f \| \mathcal{T}_J^{\text{el}}(q) \| J_i)^*]. \end{aligned} \quad (2.22)$$

Here the excitation energy  $E_{\text{exc}}$  of the final nuclear state is defined with respect to the initial nuclear state, that is,  $E_{\text{exc}} = E_{\mathbf{p}'} - E_{\mathbf{p}}$ . In the above expressions, we have introduced

$$\begin{aligned} a &= \sqrt{1 - \frac{m_f^2}{E_{\mathbf{k}'}^2}}, \\ b &= \frac{a^2 E_{\mathbf{k}} E_{\mathbf{k}'}}{q^2}, \\ c &= \frac{m_f^2}{q E_{\mathbf{k}'}} \end{aligned} \quad (2.23)$$

where the magnitude of the three-momentum transfer  $q$  is given by

$$q = |\mathbf{q}| = \sqrt{a^2 E_{\mathbf{k}'}^2 + E_{\mathbf{k}}^2 - a \cos \theta (2E_{\mathbf{k}} E_{\mathbf{k}'})} \quad (2.24)$$

and  $m_f$  denotes the rest mass of the outgoing lepton. In (2.20), the function  $F(\pm Z_f, E_{\mathbf{k}'})$ , where  $Z_f$  is the proton number of the final nucleus, takes into account the distortion of the outgoing lepton wave function due to the interaction with the (final) nucleus and the  $+$  ( $-$ ) sign is used in the case of neutrinos (antineutrinos). Furthermore, in (2.22) the minus sign is used for neutrinos and the plus sign for antineutrinos.

For the treatment of final-state interactions, we use the method introduced by Engel in [25]. Consequently, we define the effective momentum of the outgoing lepton within the nucleus as

$$k_{\text{eff}} = \sqrt{E_{\text{eff}} - m_l^2}, \quad (2.25)$$

where the effective energy is given by

$$E_{\text{eff}} = E_{k'} - V_C(0). \quad (2.26)$$

Here  $V_C(0)$  is the value at the origin of the Coulomb potential produced by the final nucleus. In this work, we approximate the Coulomb field with that of a uniformly charged sphere and therefore  $V_C(0) = -\alpha Z(3/2R)$  where  $Z = Z_f$  for leptons and  $Z = -Z_f$  for antileptons and  $R$  denotes the nuclear radius. In the region where  $k_{\text{eff}}$  is small, that is,  $k_{\text{eff}}R \ll 1$ , one can, just as in beta-decay calculations, adopt a Fermi function of the form [26]

$$F(Z, E_{k'}) = 2(1 + \gamma_0)(2|\mathbf{k}'|R)^{-2(1-\gamma_0)} e^{\pi\nu} \frac{|\Gamma(\gamma_0 + i\nu)|^2}{\Gamma(2\gamma_0 + 1)^2}, \quad (2.27)$$

where

$$\gamma_0 = \sqrt{1 - Z^2\alpha}, \quad \nu = \frac{Z\alpha E_{k'}}{|\mathbf{k}'|}. \quad (2.28)$$

For larger values of the energy  $E_{k'}$  of the final lepton, we employ in the present work the so-called modified effective momentum approximation (EMA) introduced in [25]. In this approximation, the absolute value of the three momentum and the energy of the outgoing lepton are replaced by the effective values given by (2.25) and (2.26), respectively. The effective energy and momentum are also used in the calculation of the three-momentum transfer  $q$  defined by (2.24).

Guided by [10, 25], we adopt in the present calculations for the neutrino interaction (2.9) the Coulomb treatment which, gives the smallest cross section. For the antineutrino reaction (2.10), the final-state interactions decrease the cross section. Therefore, we choose in this case the Coulomb treatment (Fermi function or modified EMA), which gives the largest cross section.

### 3. Results and Discussion

In this section, we adopt the formalism presented in Section 2 to compute the cross sections for the charged-current neutrino and antineutrino scatterings off the even-even molybdenum isotopes.

The initial and final nuclear states are first constructed by using the pnQRPA (proton-neutron quasiparticle random-phase approximation) discussed in Section 2.1. In the calculations, the single-particle energies were generated by using the Coulomb-corrected

**Table 1:** Cross sections for the charged-current neutrino-nucleus scattering off the even molybdenum nuclei in units of  $10^{-42} \text{ cm}^2$ . Exponents are shown in parenthesis. In the last column, we also show for comparison the results for  $^{100}\text{Mo}$  calculated in [10].

$E_k/\text{MeV}$	$^{92}\text{Mo}$	$^{94}\text{Mo}$	$^{96}\text{Mo}$	$^{98}\text{Mo}$	$^{100}\text{Mo}$	$^{100}\text{Mo}$ [10]
5.0	—	3.16 (−2)	4.00 (−1)	1.02 (0)	2.83 (0)	—
10.0	9.43 (−2)	1.97 (0)	4.45 (0)	7.51 (0)	1.38 (1)	0.68 (1)
15.0	8.96 (0)	1.89 (1)	2.98 (1)	4.21 (1)	5.91 (1)	4.60 (1)
20.0	4.75 (1)	8.13 (1)	1.19 (2)	1.59 (2)	2.13 (2)	2.09 (2)
25.0	1.54 (2)	2.28 (2)	3.04 (2)	3.78 (2)	4.84 (2)	5.01 (2)
30.0	3.27 (2)	4.48 (2)	5.70 (2)	6.73 (2)	8.57 (2)	9.04 (2)
40.0	8.20 (2)	1.04 (3)	1.25 (3)	1.39 (3)	1.75 (3)	1.96 (3)
50.0	1.58 (3)	1.94 (3)	2.25 (3)	2.43 (3)	3.02 (3)	3.02 (3)
60.0	2.61 (3)	3.07 (3)	3.47 (3)	3.73 (3)	4.48 (3)	4.67 (3)
70.0	3.78 (3)	4.33 (3)	4.82 (3)	5.15 (3)	6.04 (3)	6.80 (3)
80.0	4.99 (3)	5.63 (4)	6.21 (4)	6.60 (3)	7.63 (3)	9.36 (3)

**Table 2:** Cross sections for the charged-current antineutrino scattering off the even molybdenum nuclei in units of  $10^{-42} \text{ cm}^2$ . Exponents are shown in parenthesis.

$E_k/\text{MeV}$	$^{92}\text{Mo}$	$^{94}\text{Mo}$	$^{96}\text{Mo}$	$^{98}\text{Mo}$	$^{100}\text{Mo}$
5.0	2.57 (−1)	4.95 (−2)	1.30 (−2)	—	—
10.0	1.41 (0)	6.30 (−1)	3.33 (−1)	6.12 (−2)	9.88 (−3)
15.0	3.82 (0)	2.14 (0)	1.32 (0)	4.08 (−1)	1.33 (−1)
20.0	8.21 (0)	5.14 (0)	3.51 (0)	1.53 (0)	6.91 (−1)
25.0	1.56 (1)	1.05 (1)	7.73 (0)	4.18 (0)	2.22 (0)
30.0	2.68 (1)	1.92 (1)	1.49 (1)	9.22 (0)	5.43 (0)
40.0	6.52 (1)	4.97 (1)	4.14 (1)	2.97 (1)	2.01 (1)
50.0	1.33 (2)	1.05 (2)	9.04 (1)	6.94 (1)	5.10 (1)
60.0	2.44 (2)	1.97 (2)	1.75 (2)	1.39 (2)	1.07 (2)
70.0	4.00 (2)	3.34 (2)	3.02 (2)	2.50 (2)	2.00 (2)
80.0	5.95 (2)	5.09 (2)	4.67 (2)	3.99 (2)	3.33 (2)

Woods-Saxon potential with the parameters of [27]. For the  $^{100}\text{Mo}$  nucleus, some of the single-particle energies close to the respective Fermi surfaces were then adjusted according to [28].

We employ the formalism discussed in Section 2.2 to calculate the double-differential cross sections (2.20) for all the final nuclear states  $f$  separately. The total cross section  $\sigma(E_k)$  as a function of the energy of the impinging neutrino  $E_k$  then is computed by integrating over the scattering angle  $\theta$  and adding up all the individual contributions coming from the final states. For the calculations of the involved nuclear matrix elements, we use the efficient method introduced in [18]. For more details, we refer to [29, 30].

In Table 1, we show our calculated cross sections  $\sigma(E_k)$  for the charged-current neutrino-nucleus scattering off the even molybdenum isotopes as functions of the energy  $E_k$  of the incoming neutrino. In the table, the cross sections are tabulated for a large set of neutrino energies which, are relevant for supernova neutrinos, that is,  $E_k \leq 80 \text{ MeV}$ . The results for the antineutrino-induced reactions are similarly shown in Table 2. As is seen in the tables, both the neutrino and antineutrino cross sections increase strongly with increasing neutrino energy. We can also conclude that the neutrino cross sections increase significantly with increasing neutron number  $N$ . For low energies of the incoming neutrino, the  $\nu$  cross

sections are dominated by Gamow-Teller-like transitions mediated by the operator  $j_0(qr)\sigma\tau_+$  and Fermi-like ones, which proceed via the operator  $j_0(qr)\tau_+$ . At zero momentum transfer ( $q = 0$ ), these operators reduce to the usual Gamow-Teller ( $\sigma\tau_+$ ) and Fermi ( $\tau_+$ ) operators. It is well known that the Gamow-Teller operator obeys the Ikeda sum rule [31]

$$S_{1^+}(\beta^-) - S_{1^+}(\beta^+) = 3(N - Z), \quad (3.1)$$

where  $S_{1^+}(\beta^-)$  ( $S_{1^+}(\beta^+)$ ) is the total Gamow-Teller strength for the  $\beta^-$  ( $\beta^+$ ) channel. The nuclei in this work have large neutron excess and hence the  $\beta^+$  branch is small and therefore  $S_{1^+}(\beta^-) \approx 3(N - Z)$ . Similarly, for the transitions to  $0^+$  final states one has that  $S_{0^+}(\beta^-) \approx N - Z$ . Furthermore, the energy threshold,  $Q_{EC}$ , is decreasing from 7.870 MeV ( $^{92}\text{Mo}$ ) to 0.168 MeV ( $^{100}\text{Mo}$ ). This explains the increase of the neutrino cross sections with increasing neutron number at low neutrino energies. Contrary to this, the antineutrino cross sections decrease with increasing  $N$ . This is explained by the fact that the  $Q_{\beta^-}$  values are increasing significantly with increasing neutron number.

In the last column of Table 1, we compare our results for  $^{100}\text{Mo}$  with those of [10]. It is seen in the table that our results agree well with the ones published in the aforementioned reference. Our computed neutrino cross sections for  $^{100}\text{Mo}$  are also in qualitative agreement with the results displayed in Figure 1 of [14].

As already mentioned above, we use in the present calculations the method of barycentric Lagrange interpolation for the computations of the required nuclear matrix elements. Therefore, in Figure 2 we compare the cross sections computed with this method with exact calculations in the case of the neutrino scattering off  $^{100}\text{Mo}$ . The results for the antineutrino reaction are similarly shown in Figure 3. It is seen in the figures that the results computed by the approximate method (based on numerical interpolation) are accurate to 4-5 significant digits. Consequently, the numerical errors are very small compared to the errors coming from, for example, uncertainties in the nuclear wave functions. The results for the other isotopes are similar and are thus not shown here.

From the experimental point-of-view, an interesting quantity is the flux-averaged cross section  $\langle\sigma\rangle$ , which is obtained by folding the cross sections  $\sigma(E_k)$  with an appropriate energy profile of the incoming neutrinos. In this work, we adopt a two-parameter Fermi-Dirac distribution

$$n_{\text{FD}}(E_k) = \frac{1}{T_\nu^3 F_2(\alpha_\nu)} \frac{E_k^2}{\exp(E_k/T_\nu - \alpha_\nu) + 1}, \quad (3.2)$$

where  $T_\nu$  denotes the effective neutrino temperature and  $\alpha_\nu$  is the so-called pinching parameter. Here the constant  $F_2(\alpha_\nu)$  normalizes the total flux to unity.

Because of interactions with the matter, the neutrinos undergo flavor conversions when they propagate through the star (see e.g., [32]). Consequently, the energy profiles of the neutrinos (or antineutrinos) which arrive at the Earth-bound detector are different from the initial ones. For simplicity, we assume in this work that the oscillations occur in the outer layers of the star. Furthermore, we neglect collective neutrino-neutrino interactions.



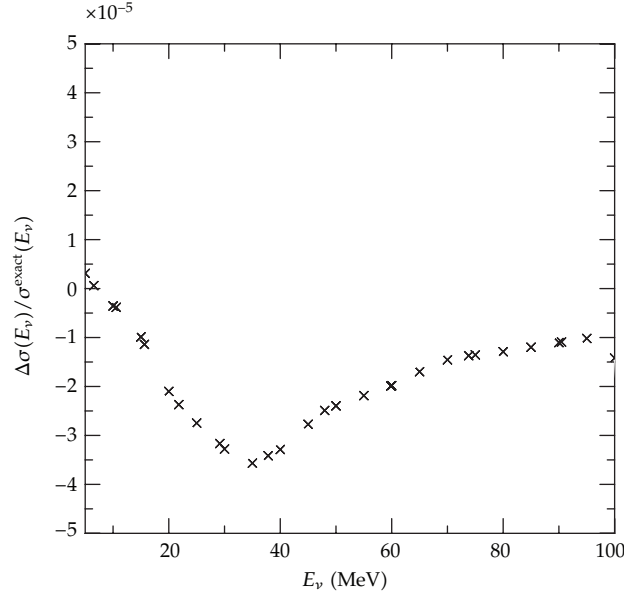


**Figure 2:** Numerical errors in the cross section for the charged-current neutrino-nucleus scattering off  $^{100}\text{Mo}$  due to the use of barycentric Lagrange interpolation. The errors are shown for various energies  $E_\nu$  of the incoming neutrino. In the figure,  $\Delta\sigma(E_\nu) = \sigma^{\text{approx}}(E_\nu) - \sigma^{\text{exact}}(E_\nu)$ .

The neutrino profiles for the neutrinos, which reach the detector can then be written in the forms [32]

$$F_{\nu_e} = \begin{cases} \sin^2\theta_{13}F_{\nu_e}^0 + \cos^2\theta_{13}F_{\nu_x}^0 & \text{Normal hierarchy,} \\ \sin^2\theta_{12}F_{\nu_e}^0 + \cos^2\theta_{12}F_{\nu_x}^0 & \text{Inverted hierarchy,} \end{cases} \quad (3.3)$$

$$F_{\bar{\nu}_e} = \begin{cases} \cos^2\theta_{12}F_{\bar{\nu}_e}^0 + \sin^2\theta_{12}F_{\bar{\nu}_x}^0 & \text{Normal hierarchy,} \\ \sin^2\theta_{13}F_{\bar{\nu}_e}^0 + \cos^2\theta_{13}F_{\bar{\nu}_x}^0 & \text{Inverted hierarchy,} \end{cases} \quad (3.4)$$

for neutrinos and antineutrinos, respectively. Here  $F_{\nu_e}^0$  ( $F_{\nu_x}^0$ ) is the energy profile of electron neutrinos (non-electron neutrinos) and correspondingly for the antineutrinos. We also point out that due to the large rest masses of the muon and tau (and their antiparticles), only supernova  $\nu_e$  and  $\bar{\nu}_e$  can be detected by charged-current neutrino-nucleus scattering.

In Table 3 are shown the computed averaged cross sections for the supernova  $\nu$  and  $\bar{\nu}$  induced scatterings off  $^{100}\text{Mo}$ . In the table,  $\nu_e$  ( $\bar{\nu}_e$ ) represents nonoscillating electron neutrinos (electron antineutrinos). We moreover denote with  $\nu_{\text{ex}}^{\text{NH}}$  ( $\bar{\nu}_{\text{ex}}^{\text{NH}}$ ) and  $\nu_{\text{ex}}^{\text{IH}}$  ( $\bar{\nu}_{\text{ex}}^{\text{IH}}$ ) the oscillating electron neutrinos (electron antineutrinos) for the normal and inverted hierarchies, respectively. According to (3.3) (see (3.4)), these neutrinos have energy profiles that are altered with respect to the initial ones by the flavor conversions  $\nu_x \rightarrow \nu_e$ . Here results are shown for the two sets of neutrino parameters shown in Table 4. Averaged cross sections for other energy profiles of the incoming neutrinos (antineutrinos) can be easily computed by using the original cross sections tabulated in Table 1 (Table 2). We conclude from Table 3 that the flavor transformations significantly increase the averaged cross sections both for neutrinos and antineutrinos. The antineutrino cross sections are also much smaller

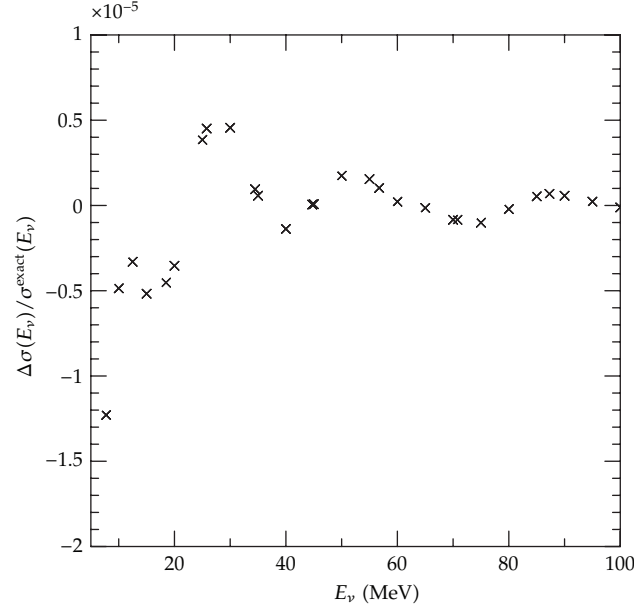


**Figure 3:** Same as Figure 2 for the charged-current antineutrino scattering off  $^{100}\text{Mo}$ .

**Table 3:** Averaged cross sections for the charged-current neutrino and antineutrino scatterings off  $^{100}\text{Mo}$  in units of  $10^{-41} \text{ cm}^2$  calculated for the two sets of neutrino parameters (I and II) displayed in Table 4. In the table, we also show for comparison the results computed in [33].

	$\nu_e$	$\nu_{\text{ex}}^{\text{NH}}$	$\nu_{\text{ex}}^{\text{IH}}$	$\bar{\nu}_e$	$\bar{\nu}_{\text{ex}}^{\text{NH}}$	$\bar{\nu}_{\text{ex}}^{\text{IH}}$
pnQRPA (I)	5.80	24.1	18.7	0.048	0.093	0.189
pnQRPA (II)	6.79	77.9	56.7	0.177	0.492	1.182
Ejiri et al. [33]	5.84	76.5				

than the corresponding ones for neutrinos. This is explained by the large neutron excess for  $^{100}\text{Mo}$  ( $N - Z = 16$ ) since then the antineutrino-induced reactions are suppressed because of Pauli blocking. In the table, we also compare our results with the ones of [33] for the parameter set II of Table 4. The numbers computed in the aforementioned reference have here been transformed to take into account the oscillation effect (3.3) with the updated value of  $\sin^2\theta_{13} = 0.025$  [34] adopted in the present calculations. The discrepancy between the two calculations for  $\nu_e$  is about 16% and for the flavor converted neutrinos in the normal hierarchy the results are almost exactly the same. Here it should be noted that in the aforementioned reference the measured  $0^-$ ,  $1^+$ , and  $2^-$  strength distributions of [35] were adopted instead of those calculated by the use of the pnQRPA. We therefore conclude that the results are in very good agreement with each other despite the rather different methods used in the calculations.

The proposed MOON detector can be realized by either using enriched  $^{100}\text{Mo}$  or natural molybdenum [33, 36]. Consequently, accurate estimates of the nuclear responses for all the stable molybdenum isotopes are important. Therefore, we show in Table 5 our calculated averaged cross sections for all the stable even-even ( $A = 92, 94, 96, 98, 100$ ) Mo nuclei. It is seen in the table that the values of the neutrino cross sections are increasing significantly with increasing neutron number, while for the antineutrino reaction (2.10) the trend is opposite. We also conclude again that the cross sections for the neutrino scattering are

**Table 4:** Average neutrino energies and values of the parameter  $\alpha$  for the two sets of neutrino parameters adopted in the present calculations. In the table,  $x$  denotes the nonelectron flavors, that is,  $x = \mu, \tau$ .

Parameter set	$(\langle E_{\nu_e} \rangle, \alpha_{\nu_e})$	$(\langle E_{\bar{\nu}_e} \rangle, \alpha_{\bar{\nu}_e})$	$(\langle E_{\nu_x} \rangle, \alpha_{\nu_x})$	$(\langle E_{\bar{\nu}_x} \rangle, \alpha_{\bar{\nu}_x})$
I	(11.5, 3.0)	(13.6, 3.0)	(16.3, 0.0)	(16.3, 0.0)
II	(11.0, 0.0)	(16.0, 0.0)	(25.0, 0.0)	(25.0, 0.0)

**Table 5:** Averaged cross sections for the charged-current neutrino-nucleus scattering from the even Mo isotopes in units of  $10^{-41} \text{ cm}^2$  computed with the neutrino parameters corresponding to set I of Table 4.

Nucleus	$\nu_e$	$\nu_{\text{ex}}^{\text{NH}}$	$\nu_{\text{ex}}^{\text{IH}}$	$\bar{\nu}_e$	$\bar{\nu}_{\text{ex}}^{\text{NH}}$	$\bar{\nu}_{\text{ex}}^{\text{IH}}$
$^{92}\text{Mo}$	1.30	8.74	6.54	0.457	0.606	0.934
$^{94}\text{Mo}$	2.19	12.2	9.18	0.283	0.396	0.645
$^{96}\text{Mo}$	3.16	15.6	11.9	0.196	0.290	0.495
$^{98}\text{Mo}$	4.20	18.6	14.8	0.094	0.160	0.304
$^{100}\text{Mo}$	6.41	25.7	20.0	0.048	0.093	0.189

notably larger than the ones for the antineutrino channel. Computations of the cross sections of the charged-current neutrino-nucleus scattering off the odd isotopes,  $^{95}\text{Mo}$  and  $^{97}\text{Mo}$ , are still in progress and the results will be published elsewhere.

## 4. Conclusions

In this work, we have computed the cross sections for the charged-current neutrino and antineutrino scatterings off the stable molybdenum isotopes for neutrino energies, which are relevant for supernova neutrinos. In the calculations, the initial and final nuclear states have been constructed by using the pnQRPA. We have tabulated the cross sections for an extensive set of neutrino energies. The nuclear responses for the aforementioned nuclei have subsequently been calculated by using a two-parameter Fermi-Dirac distribution. However, averaged cross sections for other energy profiles of the incoming neutrino (or antineutrino) can be easily computed by using the cross sections given in this paper.

Our results for the neutrino-nucleus scattering off  $^{100}\text{Mo}$  agree well with previously published results. We have found for the studied chain of nuclei that the neutrino-scattering cross sections increase significantly with the neutron number  $N$ . Contrary to this, the cross sections for the antineutrino scattering decrease notably with increasing neutron number.

## Acknowledgments

This work was supported by the Academy of Finland under the Finnish Center Of Excellence Program 2012–2017 (Nuclear and Accelerator Based Program at JYFL). Dr. E. Ydrefors would like to thank Professor H. Ejiri for fruitful discussions.

## References

- [1] C. Volpe, "Neutrino-nucleus interactions: open questions and future projects," *Nuclear Physics B. Proceedings Supplements*, vol. 143, pp. 43–50, 2005.
- [2] C. Volpe, "What about a beta-beam facility for low-energy neutrinos?" *Journal of Physics G*, vol. 30, no. 7, p. L1, 2004.

- [3] H.-T. Janka, K. Langanke, A. Marek, G. Martínez-Pinedo, and B. Müller, "Theory of core-collapse supernovae," *Physics Reports*, vol. 442, no. 1-6, pp. 38–74, 2007.
- [4] H. T. Janka, "Explosion mechanisms of core-collapse supernovae," *Annual Review of Nuclear and Particle Science*, vol. 62, pp. 407–451, 2012, <http://arxiv.org/abs/1206.2503>.
- [5] C. Giunti and C. W. Kim, *Fundamentals of Neutrino Physics and Astrophysics*, Oxford University Press, New York, NY, USA, 2007.
- [6] G. G. Raffelt, "Physics opportunities with supernova neutrinos," *Progress in Particle and Nuclear Physics*, vol. 64, no. 2, pp. 393–399, 2010.
- [7] P. D. Serpico, S. Chakraborty, T. Fischer, L. Hudepohl, H.-T. Janka, and A. Mirizzi, "Probing the neutrino mass hierarchy with the rise time of a supernova burst," *Physical Review D*, vol. 85, Article ID 085031, 13 pages, 2012.
- [8] South Pole Neutrino Observatory, <http://icecube.wisc.edu/>.
- [9] C. Volpe, "Neutrino-nucleus interactions as a probe to constrain double-beta decay predictions," *Journal of Physics G*, vol. 31, no. 8, p. 903, 2005.
- [10] R. Lazauskas and C. Volpe, "Neutrino beams as a probe of the nuclear isospin and spin-isospin excitations," *Nuclear Physics A*, vol. 792, no. 3-4, pp. 219–228, 2007.
- [11] J. Suhonen and O. Civitarese, "Weak-interaction and nuclear-structure aspects of nuclear double beta decay," *Physics Report*, vol. 300, no. 3-4, pp. 123–214, 1998.
- [12] H. Ejiri, "Nuclear spin isospin responses for low-energy neutrinos," *Physics Reports*, vol. 338, no. 3, pp. 265–351, 2000.
- [13] K. Scholberg, "Supernova neutrino detection," *Annual Review of Nuclear and Particle Science*, vol. 62, pp. 81–103, 2012.
- [14] H. Ejiri, P. Doe, S. R. Elliott et al., "MOON for neutrino-less double beta decays," *European Physical Journal: Special Topics*, vol. 162, no. 1, pp. 239–250, 2008.
- [15] J. S. O'Connell, T. W. Donnelly, and J. D. Walecka, "Semileptonic weak interactions with  $C^{12}$ ," *Physical Review C*, vol. 6, no. 3, pp. 719–733, 1972.
- [16] J. D. Walecka, *Theoretical Nuclear and Subnuclear Physics*, Imperial College Press, London, UK, 2004.
- [17] J. Suhonen, *From Nucleons to Nucleus: Concepts of Microscopic Nuclear Theory*, Theoretical and Mathematical Physics, Springer, Berlin, Germany, 2007.
- [18] E. Ydrefors, K. G. Balasi, T. S. Kosmas, and J. Suhonen, "The response of  $^{95,97}\text{Mo}$  to supernova neutrinos," *Nuclear Physics A*, vol. 866, no. 1, pp. 67–78, 2011.
- [19] J.-P. Berrut and L. N. Trefethen, "Barycentric lagrange interpolation," *SIAM Review*, vol. 46, no. 3, pp. 501–517, 2004.
- [20] J. Suhonen, T. Taigel, and A. Faessler, "pnQRPA calculation of the  $\beta^+/\text{EC}$  quenching for several neutron-deficient nuclei in mass regions  $A = 94\text{--}110$  and  $A = 146\text{--}156$  {black star}," *Nuclear Physics, Section A*, vol. 486, no. 1, pp. 91–117, 1988.
- [21] J. Suhonen, "Calculation of allowed and first-forbidden beta-decay transitions of odd-odd nuclei," *Nuclear Physics A*, vol. 563, no. 2, pp. 205–224, 1993.
- [22] E. Ydrefors, K. G. Balasi, J. Suhonen, and T. S. Kosmas, "Nuclear responses to supernova neutrinos for the stable molybdenum isotopes," in *Neutrinos: Properties, Reactions, Sources and Detection*, J. P. Greene, Ed., p. 151, Nova Science, 2011.
- [23] W. M. Alberico, S. M. Bilenky, and C. Maieron, "Strangeness in the nucleon: neutrino-nucleon and polarized electron-nucleon scattering," *Physics Reports*, vol. 358, no. 4, pp. 227–308, 2002.
- [24] E. Kolbe, K. Langanke, G. Martínez-Pinedo, and P. Vogel, "Neutrino-nucleus reactions and nuclear structure," *Journal of Physics G*, vol. 29, no. 11, pp. 2569–2596, 2003.
- [25] J. Engel, "Approximate treatment of lepton distortion in charged-current neutrino scattering from nuclei," *Physical Review C*, vol. 57, pp. 2004–2009, 1998.
- [26] H. Behrens and W. Bühring, *Electron Radial Wave Functions and Nuclear Beta Decay*, Clarendon, Oxford, UK, 1982.
- [27] A. Bohr and B. R. Mottelson, *Nuclear Structure*, vol. 1, Benjamin, New York, NY, USA, 1969.
- [28] J. Suhonen, "Opening of the  $Z = 40$  subshell gap and the double-beta decay of  $^{100}\text{Mo}$ ," *Nuclear Physics A*, vol. 700, no. 1-2, pp. 649–665, 2002.
- [29] E. Ydrefors, K. G. Balasi, T. S. Kosmas, and J. Suhonen, "The response of  $^{95,97}\text{Mo}$  to supernova neutrinos," *Nuclear Physics A*, vol. 866, no. 1, pp. 67–78, 2011.
- [30] E. Ydrefors, K. G. Balasi, T. S. Kosmas, and J. Suhonen, "Erratum: the response of  $^{95,97}\text{Mo}$  to supernova neutrinos," *Nuclear Physics A*, vol. 878, pp. 1–2, 2012.
- [31] K. Ikeda, "Collective excitation of unlike pair states in heavier nuclei," *Progress of Theoretical Physics*, vol. 31, no. 3, pp. 434–451, 1964.

- [32] A. S. Dighe and A. Y. Smirnov, "Identifying the neutrino mass spectrum from a supernova neutrino burst," *Physical Review D*, vol. 62, no. 3, Article ID 033007, pp. 1–24, 2000.
- [33] H. Ejiri, J. Engel, and N. Kudomi, "Supernova-neutrino studies with  $^{100}\text{Mo}$ ," *Physics Letters, Section B*, vol. 530, no. 1–4, pp. 27–32, 2002.
- [34] D. V. Forero, M. Toero, and J. W. F. Valle, "Global status of neutrino oscillation parameters after Neutrino-2012," *Physical Review D*, vol. 86, Article ID 073012, 8 pages, 2012.
- [35] H. Akimune, H. Ejiri, M. Fujiwara et al., "GT strengths studied by ( $^3\text{He}$ , t) reactions and nuclear matrix elements for double beta decays," *Physics Letters, Section B*, vol. 394, no. 1-2, pp. 23–28, 1997.
- [36] H. Ejiri, Private Communication, 2012.



## Review Article

# Neutrino Mass from Cosmology

**Julien Lesgourgues<sup>1, 2, 3</sup> and Sergio Pastor<sup>4</sup>**

<sup>1</sup> *Theory Division, CERN, 1211 Geneva 23, Switzerland*

<sup>2</sup> *Institut de Théorie des Phénomènes Physiques, EPFL, 1015 Lausanne, Switzerland*

<sup>3</sup> *LAPTH, CNRS-Université de Savoie, BP 110, 74941 Annecy-le-Vieux Cedex, France*

<sup>4</sup> *Instituto de Física Corpuscular, CSIC-Universitat de València, Apartado de Correos 22085, 46071 Valencia, Spain*

Correspondence should be addressed to Sergio Pastor, [pastor@ific.uv.es](mailto:pastor@ific.uv.es)

Received 2 July 2012; Accepted 1 October 2012

Academic Editor: Jose Bernabeu

Copyright © 2012 J. Lesgourgues and S. Pastor. This is an open access article distributed under the Creative Commons Attribution License, which permits unrestricted use, distribution, and reproduction in any medium, provided the original work is properly cited.

Neutrinos can play an important role in the evolution of the universe, modifying some of the cosmological observables. In this contribution we summarize the main aspects of cosmological relic neutrinos, and we describe how the precision of present cosmological data can be used to learn about neutrino properties, in particular their mass, providing complementary information to beta decay and neutrinoless double-beta decay experiments. We show how the analysis of current cosmological observations, such as the anisotropies of the cosmic microwave background or the distribution of large-scale structure, provides an upper bound on the sum of neutrino masses of order 1 eV or less, with very good perspectives from future cosmological measurements which are expected to be sensitive to neutrino masses well into the sub-eV range.

## 1. Introduction

The subject of this contribution is the role of neutrinos in cosmology, one of the best examples of the very close ties that have developed between nuclear physics, particle physics, astrophysics, and cosmology. Here we focus on the most interesting aspects related to the case of massive (and light) relic neutrinos, but many others that were left out can be found in [1, 2].

We begin with a description of the properties and evolution of the background of relic neutrinos that fills the universe. Then we review the possible effects of neutrino oscillations on cosmology. The topic of neutrinos and Big Bang Nucleosynthesis is reviewed in a different contribution to this special issue [3]. The largest part of this contribution is devoted to the impact of massive neutrinos on cosmological observables that can be used to extract bounds

on neutrino masses from present data. Finally we discuss the sensitivities on neutrino masses from future cosmological experiments.

Note that massive neutrinos could also play a role in the generation of the baryon asymmetry of the universe from a previously created lepton asymmetry. In these leptogenesis scenarios, one can also obtain quite restrictive bounds on light neutrino masses, which are, however, strongly model dependent. We do not discuss this subject here, it is covered in other contribution to this special issue [4].

For further details, the reader is referred to recent reviews on neutrino cosmology such as [5–7] and in particular [8]. A more general review on the connection between particle physics and cosmology can be found in [9].

## 2. The Cosmic Neutrino Background

The existence of a relic sea of neutrinos is a generic feature of the standard hot big bang model, in number only slightly below that of relic photons that constitute the cosmic microwave background (CMB). This cosmic neutrino background (CNB) has not been detected yet, but its presence is indirectly established by the accurate agreement between the calculated and observed primordial abundances of light elements, as well as from the analysis of the power spectrum of CMB anisotropies and other cosmological observables. In this section we will summarize the evolution and main properties of the CNB.

### 2.1. Relic Neutrino Production and Decoupling

Produced at large temperatures by frequent weak interactions, cosmic neutrinos of any flavour ( $\nu_{e,\mu,\tau}$ ) were kept in equilibrium until these processes became ineffective in the course of the expansion of the early universe. While coupled to the rest of the primeval plasma (relativistic particles such as electrons, positrons, and photons), neutrinos had a momentum spectrum with an equilibrium Fermi-Dirac form with temperature  $T$ ,

$$f_{\text{eq}}(p, T) = \left[ \exp\left(\frac{p - \mu_\nu}{T}\right) + 1 \right]^{-1}, \quad (2.1)$$

which is just one example of the general case of particles in equilibrium (fermions or bosons, relativistic or nonrelativistic), as shown for example, in [10]. In the previous equation we have included a neutrino chemical potential  $\mu_\nu$  that would exist in the presence of a neutrino-antineutrino asymmetry, but we will see later in Section 4.1 that even if it exists its contribution cannot be very relevant.

As the universe cools, the weak interaction rate  $\Gamma_\nu$  falls below the expansion rate and one says that neutrinos decouple from the rest of the plasma. An estimate of the decoupling temperature  $T_{\text{dec}}$  can be found by equating the thermally averaged value of the weak interaction rate

$$\Gamma_\nu = \langle \sigma_\nu n_\nu \rangle, \quad (2.2)$$

where  $\sigma_\nu \propto G_F^2$  is the cross section of the electron-neutrino processes with  $G_F$  the Fermi constant and  $n_\nu$  is the neutrino number density, with the expansion rate given by the Hubble parameter  $H$

$$H^2 = \frac{8\pi\rho}{3M_P^2}. \quad (2.3)$$

Here  $\rho \propto T^4$  is the total energy density, dominated by relativistic particles, and  $M_P = 1/G^{1/2}$  is the Planck mass. If we approximate the numerical factors to unity, with  $\Gamma_\nu \approx G_F^2 T^5$  and  $H \approx T^2/M_P$ , we obtain the rough estimate  $T_{\text{dec}} \approx 1 \text{ MeV}$ . More accurate calculations give slightly higher values of  $T_{\text{dec}}$  which are flavour dependent because electron neutrinos and antineutrinos are in closer contact with electrons and positrons, as shown for example, in [1].

Although neutrino decoupling is not described by a unique  $T_{\text{dec}}$ , it can be approximated as an instantaneous process. The standard picture of *instantaneous neutrino decoupling* is very simple (see e.g., [10] or [11]) and reasonably accurate. In this approximation, the spectrum in (2.1) is preserved after decoupling, because both neutrino momenta and temperature redshift identically with the expansion of the universe. In other words, the number density of noninteracting neutrinos remains constant in a comoving volume since the decoupling epoch. We will see later that active neutrinos cannot possess masses much larger than 1 eV, so they were ultrarelativistic at decoupling. This is the reason why the momentum distribution in (2.1) does not depend on the neutrino masses, even after decoupling, that is, there is no neutrino energy in the exponential of  $f_{\text{eq}}(p)$ .

When calculating quantities related to relic neutrinos, one must consider the various possible degrees of freedom per flavour. If neutrinos are massless or Majorana particles, there are two degrees of freedom for each flavour, one for neutrinos (one negative helicity state) and one for antineutrinos (one positive helicity state). Instead, for Dirac neutrinos there are in principle twice more degrees of freedom, corresponding to the two helicity states. However, the extra degrees of freedom should be included in the computation only if they are populated and brought into equilibrium before the time of neutrino decoupling. In practice, the Dirac neutrinos with the “wrong-helicity” states do not interact with the plasma at temperatures of the MeV order and have a vanishingly small density with respect to the usual left-handed neutrinos (unless neutrinos have masses close to the keV range, as explained in section 6.4 of [1], but such a large mass is excluded for active neutrinos). Thus the relic density of active neutrinos does not depend on their nature, either Dirac or Majorana particles.

Shortly after neutrino decoupling the temperature drops below the electron mass, favouring  $e^\pm$  annihilations that heat the photons. If one assumes that this entropy transfer did not affect the neutrinos because they were already completely decoupled, it is easy to calculate the change in the photon temperature before any  $e^\pm$  annihilation and after the electron-positron pairs disappear by assuming entropy conservation of the electromagnetic plasma. The result is

$$\frac{T_\gamma^{\text{after}}}{T_\gamma^{\text{before}}} = \left(\frac{11}{4}\right)^{1/3} \simeq 1.40102, \quad (2.4)$$

which is also the ratio between the temperatures of relic photons and neutrinos  $T_\gamma/T_\nu = (11/4)^{1/3}$ . The evolution of this ratio during the process of  $e^\pm$  annihilations is shown in the

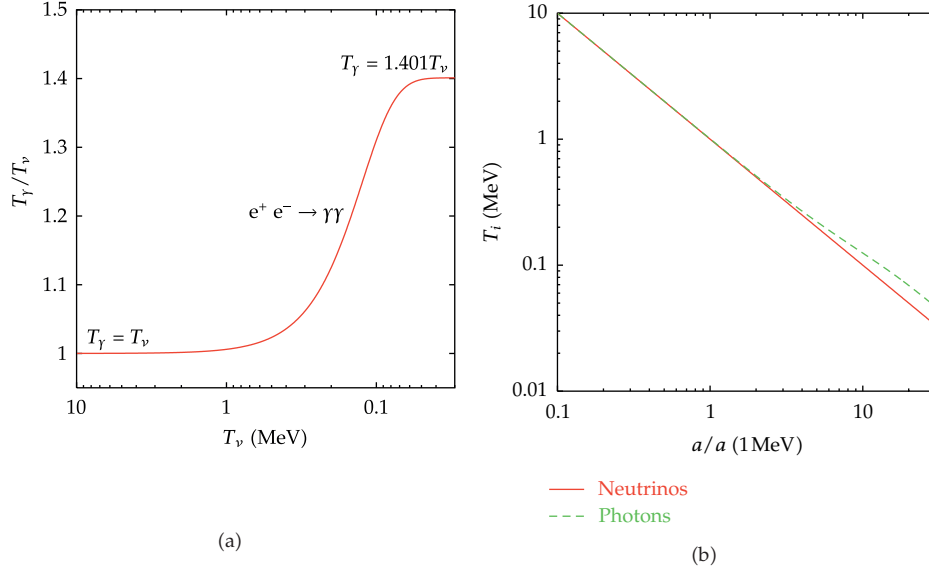


**Figure 1:** Photon and neutrino temperatures during the process of  $e^\pm$  annihilations: evolution of their ratio (a) and their decrease with the expansion of the universe (b).

left panel of Figure 1(a), while one can see in Figure 1(b) how in this epoch the photon temperature decreases with the expansion less than the inverse of the scale factor  $a$ . Instead the temperature of the decoupled neutrinos always falls as  $1/a$ .

It turns out that the standard picture of neutrino decoupling described above is slightly modified: the processes of neutrino decoupling and  $e^\pm$  annihilations are sufficiently close in time so that some relic interactions between  $e^\pm$  and neutrinos exist. These relic processes are more efficient for larger neutrino energies, leading to nonthermal distortions in the neutrino spectra at the percent level and a slightly smaller increase of the comoving photon temperature, as noted in a series of works listed in [1, 2]. A proper calculation of the process of noninstantaneous neutrino decoupling demands solving the momentum-dependent Boltzmann equations for the neutrino spectra, a set of integrodifferential kinetic equations that are difficult to solve numerically. This problem was considered in [12] including the effect of flavour neutrino oscillations on the neutrino decoupling process. One finds an increase in the neutrino energy densities with respect to the instantaneous decoupling approximation (0.73% and 0.52% for  $\nu_e$ 's and  $\nu_{\mu,\tau}$ 's, resp.) and a value of the comoving photon temperature after  $e^\pm$  annihilations which is a factor 1.3978 larger, instead of 1.40102. These changes modify the contribution of relativistic relic neutrinos to the total energy density which is taken into account using  $N_{\text{eff}} \simeq 3.046$ , as defined later in (3.1). In practice, the distortions calculated in [12] only have small consequences on the evolution of cosmological perturbations, and for many purposes they can be safely neglected.

Any quantity related to relic neutrinos can be calculated after decoupling with the spectrum in (2.1) and  $T_\nu$ . For instance, the number density per flavour is fixed by the temperature,

$$n_\nu = \frac{3}{11} n_\gamma = \frac{6\zeta(3)}{11\pi^2} T_\gamma^3, \quad (2.5)$$

which leads to a present value of 113 neutrinos and antineutrinos of each flavour per  $\text{cm}^3$ . Instead, the energy density for massive neutrinos should in principle be calculated numerically, with two well-defined analytical limits,

$$\begin{aligned}\rho_\nu(m_\nu \ll T_\nu) &= \frac{7\pi^2}{120} \left(\frac{4}{11}\right)^{4/3} T_\nu^4, \\ \rho_\nu(m_\nu \gg T_\nu) &= m_\nu n_\nu.\end{aligned}\tag{2.6}$$

## 2.2. Background Evolution

Let us discuss the evolution of the CNB after decoupling in the expanding universe, which is described by the Friedmann-Robertson-Walker metric [11]

$$ds^2 = dt^2 - a(t)^2 \delta_{ij} dx^i dx^j,\tag{2.7}$$

where we assumed negligible spatial curvature. Here  $a(t)$  is the scale factor usually normalized to unity now ( $a(t_0) = 1$ ) and related to the redshift  $z$  as  $a = 1/(1+z)$ . General relativity tells us the relation between the metric and the matter and energy in the universe via the Einstein equations, whose time-time component is the Friedmann equation

$$\left(\frac{\dot{a}}{a}\right)^2 = H^2 = \frac{8\pi G}{3} \rho = H_0^2 \frac{\rho}{\rho_c^0}\tag{2.8}$$

that gives the Hubble rate in terms of the total energy density  $\rho$ . At any time, the critical density  $\rho_c$  is defined as  $\rho_c = 3H^2/8\pi G$ , and the current value  $H_0$  of the Hubble parameter gives the critical density today

$$\rho_c^0 = 1.8788 \times 10^{-29} h^2 \text{ g cm}^{-3},\tag{2.9}$$

where  $h \equiv H_0/(100 \text{ km s}^{-1} \text{ Mpc}^{-1})$ . The different contributions to the total energy density are

$$\rho = \rho_\gamma + \rho_{\text{cdm}} + \rho_b + \rho_\nu + \rho_\Lambda,\tag{2.10}$$

and the evolution of each component is given by the energy conservation law in an expanding universe  $\dot{\rho} = -3H(\rho + p)$ , where  $p$  is the pressure. Thus the homogeneous density of photons  $\rho_\gamma$  scales like  $a^{-4}$ , that of nonrelativistic matter ( $\rho_{\text{cdm}}$  for cold dark matter and  $\rho_b$  for baryons) like  $a^{-3}$ , and the cosmological constant density  $\rho_\Lambda$  is of course time-independent. Instead, the energy density of neutrinos contributes to the radiation density at early times, but they behave as matter after the nonrelativistic transition.

The evolution of all densities is depicted in Figure 2, starting at MeV temperatures until now. The various density fractions  $\Omega_i \equiv \rho_i/\rho_c$  are shown in this figure, where it is easy to see which of the universe components is dominant, fixing its expansion rate: first radiation in the form of photons and neutrinos (radiation domination or RD), then matter which can be CDM, baryons, and massive neutrinos at late times (matter domination or MD), and finally the cosmological constant density takes over at low redshift (typically  $z < 0.5$ ).



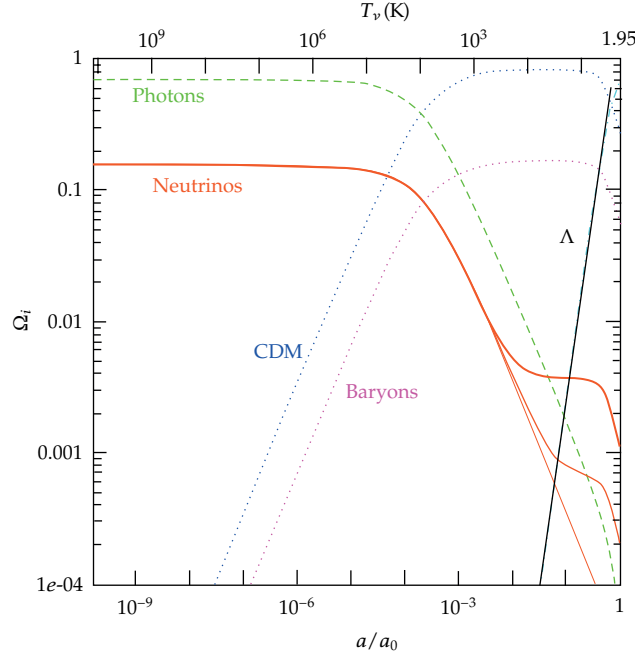


**Figure 2:** Evolution of the background energy densities in terms of the fractions  $\Omega_i$ , from the time when  $T_\nu = 1$  MeV until now, for each component of a flat universe with  $h = 0.7$  and current density fractions  $\Omega_\Lambda = 0.70$ ,  $\Omega_b = 0.05$ , and  $\Omega_{\text{cdm}} = 1 - \Omega_\Lambda - \Omega_b - \Omega_\nu$ . The three neutrino masses are  $m_1 = 0$ ,  $m_2 = 0.009$  eV, and  $m_3 = 0.05$  eV.

Massive neutrinos are the only particles that present the transition from radiation to matter, when their density is clearly enhanced (upper solid lines in Figure 2). Obviously the contribution of massive neutrinos to the energy density in the nonrelativistic limit is a function of the mass (or the sum of all masses for which  $m_i \gg T_\nu$ ), and the present value  $\Omega_\nu$  could be of order unity for eV masses (see Section 5).

Shortly after neutrino decoupling, the CNB plays an interesting role in Big Bang Nucleosynthesis (BBN), the period of the universe when the primordial abundances of light elements are created. This subject is described in the contribution [3] (for a recent review, see [13]). Here we just summarize the two main effects of relic neutrinos at BBN. The first one is that they contribute to the relativistic energy density of the universe (if  $m_\nu \ll T_\nu$ ), thus fixing the expansion rate. This is why BBN gave the first allowed range of the number of neutrino species before accelerators (see the next section). On the other hand, BBN is the last cosmological epoch sensitive to neutrino flavour, because electron neutrinos and antineutrinos play a direct role in the weak processes. We will see some examples of BBN bounds on neutrinos (effective number or oscillations) in the following sections.

### 3. Extra Radiation and the Effective Number of Neutrinos

Together with photons, in the standard case neutrinos fix the expansion rate during the cosmological era when the universe is dominated by radiation. Their contribution to the total

radiation content can be parametrized in terms of the effective number of neutrinos  $N_{\text{eff}}$ , through the relation

$$\rho_r = \rho_\gamma + \rho_\nu = \left[ 1 + \frac{7}{8} \left( \frac{4}{11} \right)^{4/3} N_{\text{eff}} \right] \rho_\gamma, \quad (3.1)$$

where we have normalized  $\rho_r$  to the photon energy density because its value today is known from the measurement of the CMB temperature. This equation is valid when neutrino decoupling is complete and holds as long as all neutrinos are relativistic.

We know that the number of light neutrinos sensitive to weak interactions (flavour or active neutrinos) equals three from the analysis of the invisible Z-boson width at LEP,  $N_\nu = 2.9840 \pm 0.0082$  [14], and we saw in a previous section from the analysis of neutrino decoupling that they contribute as  $N_{\text{eff}} \simeq 3.046$ . Any departure of  $N_{\text{eff}}$  from this last value would be due to nonstandard neutrino features or to the contribution of other relativistic relics. For instance, the energy density of a hypothetical scalar particle  $\phi$  in equilibrium with the same temperature as neutrinos would be  $\rho_\phi = (\pi/30)T_\nu^4$ , leading to a departure of  $N_{\text{eff}}$  from the standard value of 4/7. A detailed discussion of cosmological scenarios where  $N_{\text{eff}}$  is not fixed to three can be found in [1, 2, 15].

The expansion rate during BBN fixes the produced abundances of light elements and in particular that of  $^4\text{He}$ . Thus the value of  $N_{\text{eff}}$  can be constrained at the BBN epoch from the comparison of theoretical predictions and experimental data on the primordial abundances of light elements [3, 13]. In addition, a value of  $N_{\text{eff}}$  different from the standard one would modify the transition epoch from a radiation dominated to a matter dominated universe, which has some consequences on some cosmological observables such as the power spectrum of CMB anisotropies, leading to independent bounds on the radiation content. These are two complementary ways of constraining  $N_{\text{eff}}$  at very different epochs.

A recent analysis of the BBN constraints on  $N_{\text{eff}}$  can be found in [16] (see the references therein for a list of recent works). The authors have discussed a new and more conservative approach to derive BBN constraints on  $N_{\text{eff}}$ , motivated by growing concerns on the reliability of astrophysical determinations of primordial  $^4\text{He}$ . According to [16], the extra radiation at the BBN epoch is limited to  $\Delta N_{\text{eff}} \leq 1$  at 95% C.L. On the other hand, recent analyses of late cosmological observables seem to favor  $N_{\text{eff}} > 3$ , with best-fit values of order 4.3–4.4, although with large errorbars as shown for instance in [17]. The considered data include CMB temperature anisotropies and polarization, combined with other data such as measurements of the present value of the Hubble parameter ( $H_0$ ), the power spectrum of Luminous Red Galaxies (LRG), or distance measurements from the baryon acoustic oscillations (BAO) in the distribution of galaxies. The allowed regions at 95% C.L. from [17] are  $2.8 < N_{\text{eff}} < 5.9$  (WMAP + BAO +  $H_0$ ) and  $2.7 < N_{\text{eff}} < 6.2$  (WMAP + LRG +  $H_0$ ). Other recent analyses of  $N_{\text{eff}}$  bounds from cosmological data can be found in [18–20]. These ranges are in reasonable agreement with the standard prediction of  $N_{\text{eff}} \simeq 3.046$ , although they show a marginal preference for extra relativistic degrees of freedom whose robustness is still unclear. Moreover, they show that there exists an allowed region of  $N_{\text{eff}}$  values that is common at early (BBN) and more recent epochs, although with large error bars. The upcoming CMB measurements by the PLANCK satellite will soon pin down the radiation content of the universe, clarifying whether one really needs new physics leading to relativistic degrees of freedom beyond the contribution of flavour neutrinos.

## 4. Neutrino Oscillations in the Early Universe

Nowadays there exist compelling evidences for flavour neutrino oscillations from a variety of experimental data on solar, atmospheric, reactor, and accelerator neutrinos. These are very important results, because the existence of flavour change implies that neutrinos mix and have nonzero masses, which in turn requires particle physics beyond the standard model. Thus it is interesting to check whether neutrino oscillations can modify any of the cosmological observables. More on neutrino oscillations and their implications can be found in other contributions to this special issue or any of the existing reviews such as [21–23], to which we refer the reader for more details.

It turns out that in the standard cosmological picture all flavour neutrinos were produced with the same energy spectrum, as we saw in Section 2.1, so we do not expect any effect from the oscillations among these three states. This is true up to the small spectral distortion caused by the heating of neutrinos from  $e^+e^-$  annihilations [12], as described before. In this section we will briefly consider two cases where neutrino oscillations could have cosmological consequences: flavour oscillations with nonzero relic neutrino asymmetries and active-sterile neutrino oscillations.

### 4.1. Active-Active Neutrino Oscillations: Relic Neutrino Asymmetries

A nonzero relic neutrino asymmetry exists when the number densities of neutrinos and antineutrinos of a given flavour are different and can be parameterized by the ratio  $\eta_{\nu_\alpha} = (n_{\nu_\alpha} - n_{\bar{\nu}_\alpha})/n_\gamma$ . Such a putative asymmetry, that could have been produced by some mechanism well before the thermal decoupling epoch, is expected to be of the same order of the cosmological baryon number  $\eta_B$ , that is, a few times  $10^{-10}$ , from the equilibration of lepton and baryon numbers by sphalerons in the very early universe. In such a case, cosmological neutrino asymmetries would be too small to have any observable consequence. However, values for these parameters which are orders of magnitude larger than  $\eta_B$  are not excluded by observations. Actually, large  $\eta_{\nu_\alpha}$  are predicted in theoretical models where the generation of lepton asymmetry took place after the electroweak phase transition or the electroweak washing out of preexisting asymmetries is not effective.

Neutrino asymmetries can be quantified assuming that a given flavour is characterized by a Fermi-Dirac distribution as in (2.1) with a nonzero chemical potential  $\mu_\nu$ , or equivalently with the dimensionless degeneracy parameter  $\xi_\nu \equiv \mu_\nu/T$  (for antineutrinos,  $\xi_{\bar{\nu}} = -\xi_\nu$ ). In such a case, sometimes one says that the relic neutrinos are degenerate (but not in the sense of equal masses). Degenerate electron neutrinos have a direct effect on BBN: any change in the  $\nu_e/\bar{\nu}_e$  spectra modifies the primordial neutron-to-proton ratio, which in this case is  $n/p \propto \exp(-\xi_{\nu_e})$ . Therefore, a positive  $\xi_{\nu_e}$  decreases the primordial  ${}^4\text{He}$  mass fraction, while a negative  $\xi_{\nu_e}$  increases it [24], leading to an allowed range

$$-0.01 < \xi_{\nu_e} < 0.07, \quad (4.1)$$

compatible with  $\xi_{\nu_e} = 0$  and very restrictive for negative values. In addition a nonzero relic neutrino asymmetry always enhances the contribution of the CNB to the relativistic energy

density, because for any  $\xi_\nu$  one has a departure from the standard value of the effective number of neutrinos  $N_{\text{eff}}$  given, if the neutrino spectra follow an equilibrium form, by

$$\Delta N_{\text{eff}} = \frac{15}{7} \left[ 2 \left( \frac{\xi_\nu}{\pi} \right)^2 + \left( \frac{\xi_\nu}{\pi} \right)^4 \right]. \quad (4.2)$$

We have seen that this increased radiation modifies the outcome of BBN and that bounds on  $N_{\text{eff}}$  can be obtained. In addition, another consequence of the extra radiation density is that it postpones the epoch of matter-radiation equality, producing observable effects on the spectrum of CMB anisotropies and the distribution of cosmic large-scale structures (LSS). Both independent bounds on the radiation content can be translated into flavour-independent limits on  $\xi_\nu$ .

Altogether these cosmological limits on the neutrino chemical potentials or relic neutrino asymmetries are not very restrictive, because at least for BBN their effect in the  $\nu_\mu$  or  $\nu_\tau$  sector can be compensated by a positive  $\xi_{\nu_e}$ . For example, an analysis of the combined effect of a nonzero neutrino asymmetry on BBN and CMB/LSS yields the allowed regions [25]

$$-0.01 < \xi_{\nu_e} < 0.22, \quad \left| \xi_{\nu_{\mu,\tau}} \right| < 2.6, \quad (4.3)$$

in agreement with similar but more updated bounds as cited in [8]. These limits allow for a very significant radiation contribution of degenerate neutrinos, leading many authors to discuss the implications of a large neutrino asymmetry in different physical situations (see e.g., [1]).

It is obvious that the limits in (4.3) would be modified if neutrino flavour oscillations were effective before BBN, changing the initial distribution of flavour asymmetries. Actually, it was shown in [26–28] that this is the case for the neutrino mixing parameters in the region favoured by present data. This result is obtained only after the proper inclusion of the refractive terms produced by the background neutrinos, which synchronize the oscillations of neutrinos with different momenta (which would evolve independently without them). If flavour equilibrium is reached before BBN and the momentum distributions of neutrinos keep a Fermi-Dirac form as in (2.1), the restrictive limits on  $\xi_{\nu_e}$  in (4.1) apply to all flavours. The bounds on the common value of the neutrino degeneracy parameter  $\xi_\nu \equiv \mu_\nu/T$  would be  $-0.05 < \xi_\nu < 0.07$  at  $2\sigma$  [29].

More recent analyses [30, 31] have shown that this conclusion does not always hold. For the present measured values of neutrino mixing parameters, the degree of flavour equilibration depends on the value of the mixing angle  $\theta_{13}$ , which fixes the onset of flavour oscillations involving  $\nu_e$ 's. This in turn determines whether neutrinos interact enough with electrons and positrons to transfer the excess of energy density due to the initial  $\eta_{\nu_\alpha}$  to the electromagnetic plasma.

In [31] the BBN bounds on the total neutrino asymmetry (cosmological lepton number) were found for a range of initial flavour neutrino asymmetries. An example of this analysis is shown in Figure 3, taken from [32]. From this plot one can easily see the effect of flavour oscillations on the BBN constraints on the total neutrino asymmetry. With no neutrino mixing the value of  $\eta_{\nu_e}$  is severely constrained by  $^4\text{He}$  data, while the asymmetry for other neutrino flavours could be much larger. On the other hand, flavour oscillations imply

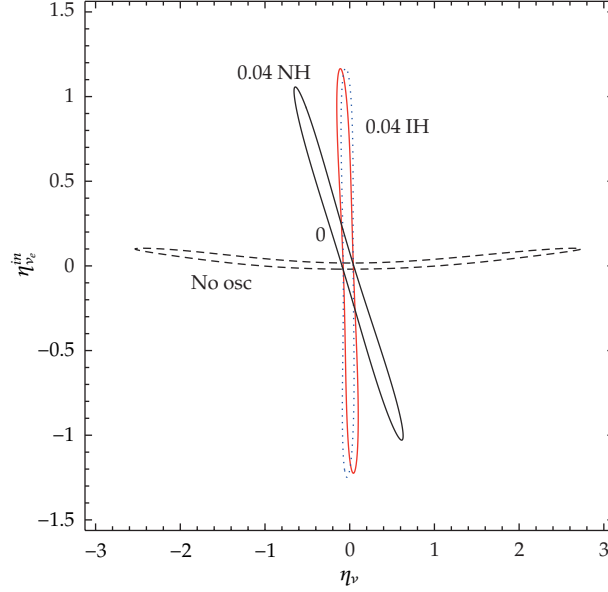


**Figure 3:** BBN contours at 95% C.L. in the  $\eta_\nu$ - $\eta_{\nu_e}^{\text{in}}$  plane for several values of  $\sin^2\theta_{13}$ : 0 (solid line), 0.04 and normal mass hierarchy (NH) (almost vertical solid line), 0.04 and inverted mass hierarchy (IH) (dotted line) [32].

that an initially large  $\eta_{\nu_e}^{\text{in}}$  can be compensated by an asymmetry in the other flavours with opposite sign. The most restrictive BBN bound on  $\eta_{\nu_e}$  applies then to the total asymmetry, an effect that can be seen graphically in Figure 3 as a *rotation* of the allowed region from a quasi-horizontal one for zero mixing to an almost vertical region for  $\sin^2\theta_{13} = 0.04$ , in particular for the inverted mass hierarchy. In all cases depicted in Figure 3 the allowed values of the asymmetries are fixed by both deuterium and  $^4\text{He}$ , the latter imposing that the value of  $\eta_{\nu_e}$  at BBN must be very close to zero. Finally, in [33] it has been shown that  $^4\text{He}$  data still fix the bounds on  $\eta_\nu$  when CMB results and other cosmological parameters such as neutrino masses are included in the analysis, and only for future CMB data the bounds on the asymmetry could be improved. At the same time the contribution of neutrino asymmetries to an enhancement of radiation is limited to  $N_{\text{eff}} \lesssim 3.1$ -3.2 for values of  $\theta_{13}$  in the region allowed by oscillation data.

#### 4.2. Active-Sterile Neutrino Oscillations

In addition to the flavour or active neutrinos (three species as we saw from accelerator data), there could also exist extra massive neutrino states that are sterile, that is, singlets of the Standard Model gauge group and thus insensitive to weak interactions. Most of the current data on neutrino oscillations can be perfectly explained with only the three active species, but there exist a few experimental results, sometimes called anomalies, that cannot be explained in this framework. If neutrino oscillations are responsible for all the experimental data, a solution might require additional, sterile, neutrino species. These kinds of particles are predicted by many theoretical models beyond the SM, being neutral leptons insensitive to weak interactions whose only interaction is gravitational. Their masses are usually heavy,



while lighter sterile neutrinos are rarer but possible. Here we will briefly summarize these anomalies observed in neutrino experiments, whereas an updated review of this subject is given in [34].

The long-standing evidence (more than  $3\sigma$ ) for  $\bar{\nu}_\mu \rightarrow \bar{\nu}_e$  oscillations comes from the LSND experiment. Its results pointed out a  $\Delta m^2 \sim 1 \text{ eV}^2$ , much larger than those required from a three-neutrino analysis, as shown later in (5.3). At the same time, the KARMEN experiment, very similar but not identical to LSND, provided no support for such evidence, while a recent data release of the MiniBooNE experiment, designed to check the LSND results with larger distance  $L$  and energy  $E$  but similar ratio  $L/E$ , is still consistent with the LSND signal. In addition, an unexplained excess of electron-like events is observed in MiniBooNE at low energies. The simultaneous interpretation of LSND (antineutrino) and MiniBooNE (neutrino and antineutrino) results in terms of sterile neutrino oscillations requires CP-violation or some other exotic scenarios, as reviewed in [34].

A new anomaly supporting oscillations with sterile neutrinos appeared from a reevaluation of reactor antineutrino fluxes, which found a 3% increase relative to previous flux calculations. As a result, data from reactor neutrino experiments at very short distances can be interpreted as an apparent deficit of  $\bar{\nu}_e$ . This is known as the reactor antineutrino anomaly and is again compatible with sterile neutrinos having a  $\Delta m^2 > 1 \text{ eV}^2$ . Finally, an independent experimental evidence for  $\nu_e$  disappearance at very short baselines exists from the Gallium radioactive source experiments GALLEX and SAGE.

The existence of all these experimental hints for sterile neutrinos and a mass scale at the eV is intriguing, but so far a fully consistent picture has not emerged. Many analyses have been performed trying to explain all experimental data with 1 or 2 additional sterile neutrinos, known as the  $3 + 1$  or  $3 + 2$  schemes, with the corresponding additional mixing parameters. It seems that none of these schemes does describe well all data, as explained in detail in [34], but for the topics of this paper the potential existence of oscillations into sterile neutrinos would lead to important cosmological consequences, such as extra radiation from fully or partly thermalized sterile neutrinos or a larger Hot or Warm Dark Matter component. The required values of neutrino masses in these  $3 + 1$  or  $3 + 2$  scenarios are, as we will see in Section 7, in tension with the current cosmological bounds.

In any case, it is interesting to consider the main effects of additional sterile neutrino species in cosmology. Because sterile neutrinos are insensitive to weak interactions, they do not follow the behaviour of active neutrinos and are not expected to be present in the early universe at MeV temperatures. Even if they could interact through other kinds of interactions, significantly weaker than the standard weak ones, as predicted by extended particle physics models, they would have a thermal spectrum at very high temperatures, but their density would have been strongly diluted by many subsequent particle-antiparticle annihilations. Therefore, barring the nonthermal production from additional physics beyond the SM, the main way of obtaining a significant abundance of sterile neutrinos is through their mixing with the active ones.

In principle, the cosmological evolution of the active-sterile neutrino system should be found solving the corresponding Boltzmann kinetic equations for the density matrices. There exists a vast literature on this subject, where different analyses considered several approximations. For a list of references, see for instance [1, 2]. Although in general one should consider, at least, a  $4 \times 4$  mixing of three active neutrinos and one sterile species (with 4 masses, 6 mixing angles, and 3 CP-violating phases), let us first assume an admixture of one sterile state to electron neutrinos. In the early universe one expects that neutrino oscillations could be effective when the vacuum oscillation term becomes larger than the

main matter potential term from charged leptons at a temperature  $T_c$ . The evolution of the active-sterile neutrino system depends on the sign of  $\Delta m^2$ . For negative values there could be resonant oscillations (or resonant production, RP). Instead, for  $\Delta m^2 > 0$  one has the so-called nonresonant production of sterile neutrinos (NRP). Comparing the value of  $T_c$  with the decoupling temperature of active neutrinos  $T_{\nu D} \sim 2 \text{ MeV}$ , one obtains that for values:

$$\Delta m^2 \lesssim 1.3 \times 10^{-7} \text{ eV}^2 \quad (4.4)$$

active-sterile oscillations are effective after neutrino decoupling. In such a case, the total comoving number density of active and sterile neutrinos will be constant because active neutrinos are no longer interacting with the rest of the primeval plasma. Correspondingly, distortions in the momentum spectra of neutrinos are expected which directly affect the production of  ${}^4\text{He}$  at BBN when the active neutrinos are of the electron flavour (see e.g., [35], also for the case of nonzero initial  $\nu_s$  abundance). Instead, for much larger values of  $\Delta m^2$  oscillations are effective before neutrino decoupling, when weak interactions are frequent. In this case the actual growth of the sterile neutrino population depends on the interplay between oscillations and interactions, while the energy spectrum of the active ones will be kept in equilibrium. Their combined contribution to radiation can be as large as  $N_{\text{eff}} = 2$ , depending on the specific value of the mixing angle and on the sign of  $\Delta m^2$ . This “thermalization” of the sterile neutrinos is a well-known phenomenon that is very difficult to avoid unless the cosmological scenario is drastically modified.

In the NRP case, it was shown in [36] that the production probability of sterile neutrinos is

$$\Gamma_s = \langle \sin^2 2\theta_m \sin^2(\omega_{\text{osc}} t) \Gamma_a \rangle, \quad (4.5)$$

where  $\theta_m$  is the mixing angle in matter and  $\omega_{\text{osc}}$  the frequency of oscillations in the medium. Here  $\Gamma_a$  is the production rate of active neutrinos in the plasma, and the averaging is made over the thermal background. If the oscillation frequency is very high one can substitute  $\sin^2(\omega_{\text{osc}} t) \simeq 1/2$ , and if  $\theta_m$  is small one obtains

$$\Gamma_s \approx \theta_m^2 \Gamma_a \quad (4.6)$$

for a small number density of  $\nu_s$  and active neutrinos close to equilibrium. Therefore, a thermal or close to thermal population of sterile neutrinos is expected provided that such a production rate of  $\nu_s$  is larger than the expansion rate of the universe, a condition that holds unless either  $\Delta m^2$  or  $\theta$  is very small.

For RP of sterile neutrinos at temperatures below  $T_c$  the resonance propagates from small to large values of the neutrino comoving momentum, covering the whole momentum distribution while the active neutrinos are repopulated by interactions. The thermalization of  $\nu_s$  is thus significantly enhanced, even for quite small values of the mixing angle.

In order to illustrate this discussion with an actual calculation of the active-sterile system with the kinetic equations in the two-flavour approximation, among the many published analyses we have chosen a recent one [37]. Their results for the final extra contribution of sterile neutrinos to radiation, in the case of zero initial lepton asymmetry, are shown as isocontours of  $\Delta N_{\text{eff}}$  in Figure 4 as a function of the mixing parameters  $\delta m_s^2 \equiv \Delta m^2$

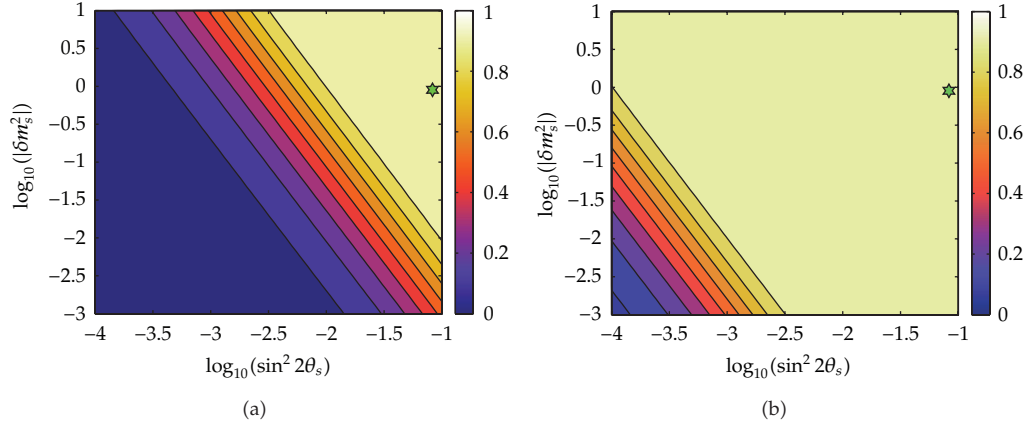


**Figure 4:** Isocontours of the final value of  $\Delta N_{\text{eff}}$  in the  $\sin^2 2\theta_s$ - $\delta m_s^2$  plane for vanishing lepton asymmetry and  $\delta m_s^2 > 0$  (a) and  $\delta m_s^2 < 0$  (b). The star denotes the best-fit mixing parameters as in the 3 + 1 global fit in [41]:  $(\delta m_s^2, \sin^2 2\theta_s) = (0.9 \text{ eV}^2, 0.089)$ . Adapted from [37].

(in  $\text{eV}^2$  units) and  $\sin^2 2\theta_s \equiv \sin^2 2\theta$ . In the NRP case (Figure 4(a)) one can clearly see that the same final  $N_{\text{eff}}$  corresponds to constant values of  $\sin^4 2\theta \Delta m^2$ . For RP  $\nu_s$ 's are more efficiently brought into equilibrium, even for quite small values of the mixing angle. All calculations described so far correspond to the two-neutrino limit of one active and one sterile states, but a proper calculation should also include the unavoidable presence of mixing among the active neutrinos. A full four-flavour calculation has not been performed, but a few analyses did solve simplified kinetic equations taking into account active neutrino mixing, such as [38–40].

We note that for the active-sterile parameters needed to solve the oscillation anomalies described at the beginning of this section, the thermalization of sterile neutrinos is achieved, that is,  $N_{\text{eff}} = 4$ . An example of the best-fit values of a particular calculation in the 3 + 1 neutrino model is indicated in the plot. Therefore, it seems that such an extra radiation is guaranteed in these situations unless oscillations are suppressed, as in the case of a nonzero initial lepton asymmetry  $\eta_\nu$ , much larger than  $\eta_B$  [42, 43].

## 5. Massive Neutrinos as Dark Matter

Nowadays the existence of Dark Matter (DM), the dominant nonbaryonic component of the matter density in the universe, is well established. A priori, massive neutrinos are excellent DM candidates, in particular because we are certain that they exist, in contrast with other candidate particles. Together with CMB photons, relic neutrinos can be found anywhere in the universe with a number density given by the present value of (2.5) of 339 neutrinos and antineutrinos per  $\text{cm}^3$ , and their energy density in units of the critical value of the energy density (see (2.9)) is

$$\Omega_\nu = \frac{\rho_\nu}{\rho_c^0} = \frac{\sum_i m_i}{93.14 h^2 \text{ eV}}. \quad (5.1)$$

Here  $\sum_i m_i$  includes all masses of the neutrino states which are nonrelativistic today. It is also useful to define the neutrino density fraction  $f_\nu$  with respect to the total matter density

$$f_\nu \equiv \frac{\rho_\nu}{(\rho_{\text{cdm}} + \rho_b + \rho_\nu)} = \frac{\Omega_\nu}{\Omega_m}. \quad (5.2)$$

In order to check whether relic neutrinos can have a contribution of order unity to the present values of  $\Omega_\nu$  or  $f_\nu$ , we should consider which neutrino masses are allowed by noncosmological data. Oscillation experiments measure the differences of squared neutrino masses  $\Delta m_{21}^2 = m_2^2 - m_1^2$  and  $\Delta m_{31}^2 = m_3^2 - m_1^2$ , the relevant ones for solar, and atmospheric neutrinos, respectively. As a reference, we take the following  $3\sigma$  ranges of mixing parameters from [44] (see also [45, 46]):

$$\begin{aligned} \Delta m_{21}^2 (10^{-5} \text{ eV}^2) &= 7.62_{-0.50}^{+0.58} \\ \Delta m_{31}^2 (10^{-3} \text{ eV}^2) &= 2.55_{-0.24}^{+0.19} (-2.43_{-0.22}^{+0.21}) \\ s_{12}^2 &= 0.32 \pm 0.05 \\ s_{23}^2 &\in [0.36, 0.68] ([0.37, 0.67]) \\ s_{13}^2 &= 0.0246_{-0.0076}^{+0.0084} (0.025 \pm 0.008). \end{aligned} \quad (5.3)$$

Here  $s_{ij}^2 = \sin^2 \theta_{ij}$ , where  $\theta_{ij}$  ( $ij = 12, 23$  or  $13$ ) are the three mixing angles. Unfortunately oscillation experiments are insensitive to the absolute scale of neutrino masses, because the knowledge of  $\Delta m_{21}^2 > 0$  and  $|\Delta m_{31}^2|$  leads to the two possible schemes shown in figure 1 of [8], but leaves one neutrino mass unconstrained. These two schemes are known as normal (NH) and inverted (IH) mass hierarchies, characterized by the sign of  $\Delta m_{31}^2$ , positive and negative, respectively. In the above equation the values in parentheses correspond to the IH, otherwise the mixing parameters present the same allowed regions for both hierarchies. For small values of the lightest neutrino mass  $m_0$ , that is,  $m_1$  ( $m_3$ ) for NH (IH), the mass states follow a hierarchical scenario, while for masses much larger than the differences all neutrinos share in practice the same mass and then we say that they are degenerate. In general, the relation between the individual masses and the total neutrino mass can be found numerically, as shown in Figure 5.

There are two types of laboratory experiments searching for the absolute scale of neutrino masses, a crucial piece of information for constructing models of neutrino masses and mixings. The neutrinoless double beta decay ( $Z, A \rightarrow (Z+2, A) + 2e^-$  (in short  $0\nu 2\beta$ ) is a rare nuclear processes where lepton number is violated and whose observation would mean that neutrinos are Majorana particles. If the  $0\nu 2\beta$  process is mediated by a light neutrino, the results from neutrinoless double beta decay experiments are converted into an upper bound or a measurement of the effective mass  $m_{\beta\beta}$

$$m_{\beta\beta} = \left| c_{12}^2 c_{13}^2 m_1 + s_{12}^2 c_{13}^2 m_2 e^{i\phi_2} + s_{13}^2 m_3 e^{i\phi_3} \right|, \quad (5.4)$$

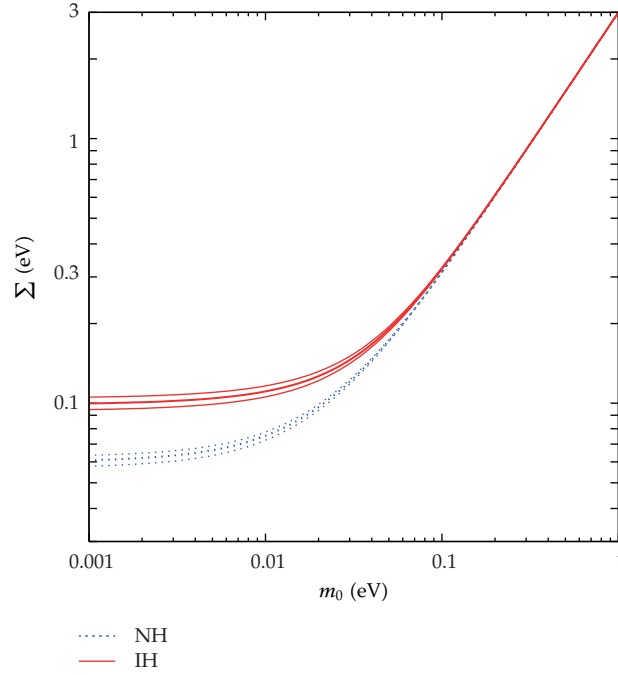


**Figure 5:** Allowed values of the total neutrino mass as a function of the lightest state within the  $3\sigma$  regions of the mixing parameters in (5.3). Blue dotted (red solid) lines correspond to normal (inverted) hierarchy for neutrino masses, where  $m_0 = m_1$  ( $m_0 = m_3$ ).

where  $\phi_{1,2}$  are the two Majorana phases that appear in lepton-number-violating processes. An important issue for  $0\nu 2\beta$  results is related to the uncertainties on the corresponding nuclear matrix elements. For more details and the current experimental results, see [47].

Beta decay experiments, which involve only the kinematics of electrons, are in principle the best strategy for measuring directly the neutrino mass [48]. The current limits from tritium beta decay apply only to the range of degenerate neutrino masses, so that  $m_\beta \simeq m_0$ , where

$$m_\beta = \left( c_{12}^2 c_{13}^2 m_1^2 + s_{12}^2 c_{13}^2 m_2^2 + s_{13}^2 m_3^2 \right)^{1/2} \quad (5.5)$$

is the relevant parameter for beta decay experiments. The bound at 95% CL is  $m_0 < 2.05\text{--}2.3$  eV from the Troitsk and Mainz experiments, respectively. This value is expected to be improved by the KATRIN project to reach a discovery potential for  $0.3\text{--}0.35$  eV masses (or a sensitivity of  $0.2$  eV at 90% CL). Taking into account this upper bound and the minimal values of the total neutrino mass in the normal (inverted) hierarchy, the sum of neutrino masses is restricted to the approximate range

$$0.06(0.1) \text{ eV} \lesssim \sum_i m_i \lesssim 6 \text{ eV}. \quad (5.6)$$



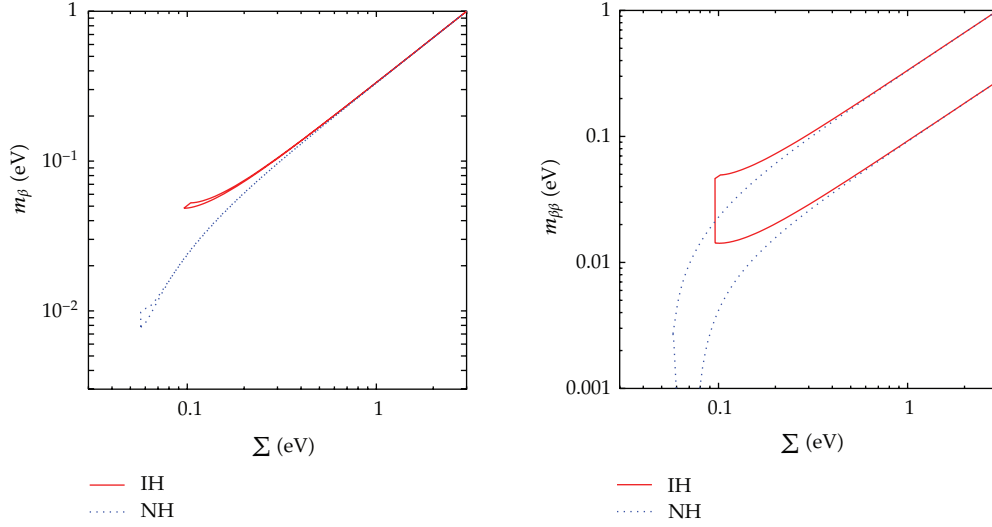


**Figure 6:** Allowed regions by oscillation data at the  $3\sigma$  level (5.3) of the three main observables sensitive to the absolute scale of neutrino masses. We show the regions in the planes  $m_\beta$ - $\Sigma$  and  $m_{\beta\beta}$ - $\Sigma$ , see the text for the corresponding definitions. Blue dotted (red solid) regions correspond to normal (inverted) hierarchy.

As we discuss in the next sections, cosmology is at first order sensitive to the total neutrino mass  $\Sigma \equiv \sum_i m_i$  if all states have the same number density, providing information on  $m_0$  but blind to neutrino mixing angles or possible CP violating phases. Thus cosmological results are complementary to terrestrial experiments. The interested reader can find the allowed regions in the parameter space defined by any pair of parameters  $(\Sigma, m_{\beta\beta}, m_\beta)$  in [21, 49, 50]. The two cases involving  $\Sigma$  are shown in Figure 6.

Now we can find the possible present values of  $\Omega_\nu$  in agreement the approximate bounds of (5.6). Note that even if the three neutrinos are nondegenerate in mass, (5.1) can be safely applied, because we know from neutrino oscillation data that at least two of the neutrino states are nonrelativistic today, because both  $(\Delta m_{31}^2)^{1/2} \simeq 0.05 \text{ eV}$  and  $(\Delta m_{21}^2)^{1/2} \simeq 0.009 \text{ eV}$  are larger than the temperature  $T_\nu \simeq 1.96 \text{ K} \simeq 1.7 \times 10^{-4} \text{ eV}$ . If the third neutrino state is very light and still relativistic, its relative contribution to  $\Omega_\nu$  is negligible and (5.1) remains an excellent approximation of the total density. One finds that  $\Omega_\nu$  is restricted to the approximate range

$$0.0013(0.0022) \lesssim \Omega_\nu \lesssim 0.13, \quad (5.7)$$

where we already included that  $h \approx 0.7$ . This applies only to the standard case of three light active neutrinos, while in general a cosmological upper bound on  $\Omega_\nu$  has been used since the 1970s to constrain the possible values of neutrino masses. For instance, if we demand that neutrinos should not be heavy enough to overclose the universe ( $\Omega_\nu < 1$ ), we obtain an upper bound  $\Sigma \lesssim 45 \text{ eV}$  (again fixing  $h = 0.7$ ). Moreover, because from present analyses

of cosmological data we know that the approximate contribution of matter is  $\Omega_m \simeq 0.3$ , the neutrino masses should obey the stronger bound  $\Sigma \lesssim 15 \text{ eV}$ . We see that with this simple argument one obtains a bound which is roughly only a factor 2 worse than the bound from tritium beta decay but of course with the caveats that apply to any cosmological analysis. In the three-neutrino case, these bounds should be understood in terms of  $m_0 = \Sigma/3$ .

Dark matter particles with a large velocity dispersion such as that of neutrinos are called hot dark matter (HDM). The role of neutrinos as HDM particles has been widely discussed since the 1970s, and the reader can find a historical review in [51]. It was realized in the mid 1980s that HDM affects the evolution of cosmological perturbations in a particular way: it erases the density contrasts on wavelengths smaller than a mass-dependent free-streaming scale. In a universe dominated by HDM, this suppression is in contradiction with various observations. For instance, large objects such as superclusters of galaxies form first, while smaller structures like clusters and galaxies form via a fragmentation process. This top-down scenario is at odds with the fact that galaxies seem older than clusters.

Given the failure of HDM-dominated scenarios, the attention then turned to cold dark matter (CDM) candidates, that is, particles which were nonrelativistic at the epoch when the universe became matter dominated, which provided a better agreement with observations. Still in the mid 1990s it appeared that a small mixture of HDM in a universe dominated by CDM fitted better the observational data on density fluctuations at small scales than a pure CDM model. However, within the presently favoured  $\Lambda$ CDM model dominated at late times by a cosmological constant (or some form of dark energy) there is no need for a significant contribution of HDM. Instead, one can use the available cosmological data to find how large the neutrino contribution can be, as we will see later.

Before concluding this section, we would like to mention the case of a sterile neutrino with a mass of the order of a few keV's and a very small mixing with the flavour neutrinos. Such "heavy" neutrinos could be produced by active-sterile oscillations but not fully thermalized, so that they could play the role of dark matter and replace the usual CDM component. But due to their large thermal velocity (slightly smaller than that of active neutrinos), they would behave as Warm Dark Matter and erase small-scale cosmological structures. Their mass can be bounded from below using Lyman- $\alpha$  forest data from quasar spectra and from above using X-ray observations. The viability of this scenario is currently under careful examination (see e.g., [52]).

## 6. Effects of Neutrino Masses on Cosmology

In this section we will briefly describe the main cosmological observables and the effects that neutrino masses cause on them. A more detailed discussion of the effects of massive neutrinos on the evolution of cosmological perturbations can be found in Sections 4.5 and 4.6 of [8].

### 6.1. Brief Description of Cosmological Observables

Although there exist many different types of cosmological measurements, here we will restrict the discussion to those that are at present the more important for obtaining an upper bound or eventually a measurement of neutrino masses.

First of all, we have the CMB temperature anisotropy power spectrum, defined as the angular two-point correlation function of CMB maps  $\delta T/\bar{T}(\hat{n})$  ( $\hat{n}$  being a direction in the sky). This function is usually expanded in Legendre multipoles

$$\left\langle \frac{\delta T}{\bar{T}}(\hat{n}) \frac{\delta T}{\bar{T}}(\hat{n}') \right\rangle = \sum_{l=0}^{\infty} \frac{(2l+1)}{4\pi} C_l P_l(\hat{n} \cdot \hat{n}'), \quad (6.1)$$

where  $P_l(x)$  are the Legendre polynomials. For Gaussian fluctuations, all the information is encoded in the multipoles  $C_l$  which probe correlations on angular scales  $\theta = \pi/l$ . We have seen that each neutrino state can only have a mass of the order of 1 eV, so that the transition of relic neutrinos to the nonrelativistic regime is expected to take place after the time of recombination between electrons and nucleons, that is, after photon decoupling. Because the shape of the CMB spectrum is related mainly to the physical evolution *before* recombination, it will only be marginally affected by the neutrino mass, except through a modified background evolution and some secondary anisotropy corrections. There exists interesting complementary information to the temperature power spectrum if the CMB polarization is measured, and currently we have some less precise data on the temperature  $\times$  E-polarization (TE) correlation function and the E-polarization self-correlation spectrum (EE).

The current Large Scale Structure (LSS) of the universe is probed by the matter power spectrum, observed with various techniques described in the next section (directly or indirectly, today or in the near past at redshift  $z$ ). It is defined as the two-point correlation function of nonrelativistic matter fluctuations in Fourier space

$$P(k, z) = \left\langle |\delta_m(k, z)|^2 \right\rangle, \quad (6.2)$$

where  $\delta_m = \delta\rho_m/\bar{\rho}_m$ . Usually  $P(k)$  refers to the matter power spectrum evaluated today (at  $z = 0$ ). In the case of several fluids (e.g., CDM, baryons, and nonrelativistic neutrinos), the total matter perturbation can be expanded as

$$\delta_m = \frac{\sum_i \bar{\rho}_i \delta_i}{\sum_i \bar{\rho}_i}. \quad (6.3)$$

Because the energy density is related to the mass density of nonrelativistic matter through  $E = mc^2$ ,  $\delta_m$  represents indifferently the energy or mass power spectrum. The shape of the matter power spectrum is affected in a scale-dependent way by the free-streaming caused by small neutrino masses of  $\mathcal{O}(\text{eV})$ , and thus it is the key observable for constraining  $m_\nu$  with cosmological methods.

## 6.2. Neutrino Free Streaming

After thermal decoupling, relic neutrinos constitute a collisionless fluid, where the individual particles free stream with a characteristic velocity that, in average, is the thermal velocity  $v_{\text{th}}$ . It is possible to define a horizon as the typical distance on which particles travel between time  $t_i$  and  $t$ . When the universe was dominated by radiation or matter  $t \gg t_i$ , this horizon is,

as usual, asymptotically equal to  $v_{\text{th}}/H$ , up to a numerical factor of order one. Similar to the definition of the Jeans length (see section 4.4 in [8]), we can define the neutrino free-streaming wavenumber and length as

$$k_{\text{FS}}(t) = \left( \frac{4\pi G \bar{\rho}(t) a^2(t)}{v_{\text{th}}^2(t)} \right)^{1/2}, \quad (6.4)$$

$$\lambda_{\text{FS}}(t) = 2\pi \frac{a(t)}{k_{\text{FS}}(t)} = 2\pi \sqrt{\frac{2}{3}} \frac{v_{\text{th}}(t)}{H(t)}.$$

As long as neutrinos are relativistic, they travel at the speed of light and their free-streaming length is simply equal to the Hubble radius. When they become nonrelativistic, their thermal velocity decays like

$$v_{\text{th}} \equiv \frac{\langle p \rangle}{m} \simeq \frac{3.15 T_\nu}{m} = \frac{3.15 T_\nu^0}{m} \left( \frac{a_0}{a} \right) \simeq 158(1+z) \left( \frac{1 \text{ eV}}{m} \right) \text{ km s}^{-1}, \quad (6.5)$$

where we used for the present neutrino temperature  $T_\nu^0 \simeq (4/11)^{1/3} T_Y^0$  and  $T_Y^0 \simeq 2.726 \text{ K}$ . This gives for the free-streaming wavelength and wavenumber during matter or  $\Lambda$  domination

$$k_{\text{FS}}(t) = 0.8 \frac{\sqrt{\Omega_\Lambda + \Omega_m(1+z)^3}}{(1+z)^2} \left( \frac{m}{1 \text{ eV}} \right) h \text{ Mpc}^{-1}, \quad (6.6)$$

$$\lambda_{\text{FS}}(t) = 8 \frac{1+z}{\sqrt{\Omega_\Lambda + \Omega_m(1+z)^3}} \left( \frac{1 \text{ eV}}{m} \right) h^{-1} \text{ Mpc},$$

where  $\Omega_\Lambda$  and  $\Omega_m$  are the cosmological constant and matter density fractions, respectively, evaluated today. After the nonrelativistic transition and during matter domination, the free-streaming length continues to increase, but only like  $(aH)^{-1} \propto t^{1/3}$ , that is, more slowly than the scale factor  $a \propto t^{2/3}$ . Therefore, the comoving free-streaming length  $\lambda_{\text{FS}}/a$  actually decreases like  $(a^2 H)^{-1} \propto t^{-1/3}$ . As a consequence, for neutrinos becoming nonrelativistic during matter domination, the comoving free-streaming wavenumber passes through a minimum  $k_{\text{nr}}$  at the time of the transition, that is, when  $m = \langle p \rangle = 3.15 T_\nu$  and  $a_0/a = (1+z) = 2.0 \times 10^3 (m/1 \text{ eV})$ . This minimum value is found to be

$$k_{\text{nr}} \simeq 0.018 \Omega_m^{1/2} \left( \frac{m}{1 \text{ eV}} \right)^{1/2} h \text{ Mpc}^{-1}. \quad (6.7)$$

The physical effect of free streaming is to damp small-scale neutrino density fluctuations: neutrinos cannot be confined into (or kept outside of) regions smaller than the free-streaming length, because their velocity is greater than the escape velocity from gravitational potential wells on those scales. Instead, on scales much larger than the free-streaming scale, the neutrino velocity can be effectively considered as vanishing, and after the nonrelativistic transition the neutrino perturbations behave like CDM perturbations. In particular, modes

with  $k < k_{\text{nr}}$  are never affected by free streaming and evolve like being in a pure  $\Lambda$ CDM model.

### 6.3. Impact of Massive Neutrinos on the Matter Power Spectrum

The small initial cosmological perturbations evolve within the linear regime at early times. During matter domination, the smallest cosmological scales start evolving nonlinearly, leading to the formation of the structures we see today. In the recent universe, the largest observable scales are still related to the linear evolution, while other scales can only be understood using nonlinear N-body simulations. We will not review here all the details of this complicated evolution (see [2, 7, 8] and references therein), but we will emphasize the main effects caused by massive neutrinos on linear scales in the framework of the standard cosmological scenario: a  $\Lambda$  Mixed Dark Matter ( $\Lambda$ MDM) model, where mixed refers to the inclusion of some HDM component.

On large scales (that is, on wave numbers smaller than the value  $k_{\text{nr}}$  defined in the previous subsection), neutrino free streaming can be ignored, and neutrino perturbations are indistinguishable from CDM perturbations. On those scales, the matter power spectrum  $P(k, z)$  can be shown to depend only on the matter density fraction today (including neutrinos),  $\Omega_m$ , and on the primordial perturbation spectrum. If the neutrino mass is varied with  $\Omega_m$  fixed, the large-scale power spectrum remains invariant.

On small scales such that  $k > k_{\text{nr}}$ , the matter power spectrum is affected by neutrino masses for essentially the three following reasons.

(1) Massive neutrinos do not cluster on those scales. The matter power spectrum can be expanded as a function of the three nonrelativistic species,

$$P(k, z) = \left\langle \left| \frac{\delta\rho_{\text{cdm}} + \delta\rho_b + \delta\rho_\nu}{\rho_{\text{cdm}} + \rho_b + \rho_\nu} \right|^2 \right\rangle = \Omega_m^{-2} \left\langle |\Omega_{\text{cdm}}\delta_{\text{cdm}} + \Omega_b\delta_b + \Omega_\nu\delta_\nu|^2 \right\rangle. \quad (6.8)$$

On scales of interest and in the recent universe, baryon and CDM fluctuations are equal to each other, while  $\delta_\nu \ll \delta_{\text{cdm}}$ . Hence, even if the evolution of  $\delta_{\text{cdm}}$  was not affected by neutrino masses (which is not the case, see the remaining two points below), the power spectrum would be reduced by a factor  $(1 - f_\nu)^2$  with

$$f_\nu \equiv \frac{\Omega_\nu}{\Omega_m}. \quad (6.9)$$

(2) The redshift of radiation-to-matter equality  $z_{\text{eq}}$  or the baryon-to-CDM ratio  $\omega_b/\omega_{\text{cdm}}$  might be slightly affected by neutrino masses, with a potential impact on the small-scale matter power spectrum. This depends very much on which other parameters are kept fixed when the neutrino mass varies. If neutrino masses are smaller than roughly 0.5 eV, they are still relativistic at the time of radiation-to-matter equality, and the redshift of equality depends on  $(\omega_b + \omega_{\text{cdm}})$ , not on  $\omega_m$ . It is possible to increase  $M_\nu$  and  $\omega_m$  with fixed parameters  $\Omega_m, \omega_b, \omega_{\text{cdm}}$  (provided that the Hubble parameter also increases like the square root of  $\omega_m$ ). In that case, there is no significant impact of massive neutrinos on the matter power spectrum through background effects, that is, through a change in the homogeneous cosmological evolution. However, there are some important perturbation effects that we will now summarize.



(3) The growth rate of cold dark matter perturbations is reduced through an absence of gravitational back-reaction effects from free-streaming neutrinos. This growth rate is set by an equation of the type

$$\delta''_{\text{cdm}} + \frac{a'}{a} \delta_{\text{cdm}} = -k^2 \psi, \quad (6.10)$$

where  $\delta_{\text{cdm}}$  stands for the CDM relative density perturbation in Fourier space and  $\psi$  for the metric perturbation playing the role of the Newtonian potential inside the Hubble radius. There is a similar equation for decoupled baryons, and very soon after baryon decoupling we can identify  $\delta_{\text{b}} = \delta_{\text{cdm}}$  on scales of interest. On the right-hand side, we neglected time derivatives of metric fluctuations playing only a minor role. The right-hand side represents gravitational clustering and is given by the Poisson equation as a function of the total density fluctuation. The second term on the left-hand side represents Hubble friction, that is, the fact that the cosmological expansion enhances distances, reduces gravitational forces, and slows down gravitational clustering. The coefficient  $a'/a$  is given by the Friedmann equation as a function of the total background density. In a universe such that all species present in the Friedmann equation do cluster, as it is the case in a matter-dominated universe with  $\delta\rho_{\text{total}} \simeq \delta\rho_{\text{cdm}} + \delta\rho_{\text{b}}$  and  $\bar{\rho}_{\text{total}} = \bar{\rho}_{\text{cdm}} + \bar{\rho}_{\text{b}}$ , the solution is simply given by  $\delta_{\text{cdm}} \propto a$ : the so-called linear growth factor is proportional to the scale factor. But whenever one of the species contributing to the background expansion does not cluster efficiently, it can be neglected in the Poisson equation. In that case, the term on the right-hand side becomes smaller with respect to the Hubble friction term, and CDM (as well as baryons) clusters at a slower rate. This is the case in presence of massive neutrinos and for  $k \gg k_{\text{nr}}$ : the linear growth rate during matter domination is then equal to  $a^{1-3/5f_{\nu}}$ . During  $\Lambda$  domination, this effect sums up with that of the cosmological constant (or of any nonclustering dark energy), which also tends to reduce the growth rate for the very same reason.

In summary, the small-scale matter power spectrum  $P(k \geq k_{\text{nr}})$  is reduced in presence of massive neutrinos for at least two reasons: by the absence of neutrino perturbations in the total matter power spectrum and by a slower growth rate of CDM/baryon perturbations at late times. The third effect has the largest amplitude. At low redshift  $z \simeq 0$ , the step-like suppression of  $P(k)$  starts at  $k \geq k_{\text{nr}}$  and saturates at  $k \sim 1h/\text{Mpc}$  with a constant amplitude  $\Delta P(k)/P(k) \simeq -8f_{\nu}$ . This result was obtained by fitting numerical simulations [53], but a more accurate approximation can be derived analytically [2, 8]. As mentioned in the second item above, neutrino masses can have additional indirect effects through a change in the background evolution, depending on which cosmological parameters are kept fixed when  $M_{\nu}$  varies.

When fitting data, one can use analytical approximations to the full MDM or  $\Lambda$ MDM matter power spectrum, valid for arbitrary scales and redshifts, as listed in [8]. However, nowadays the analyses are performed using the matter power spectra calculated by Boltzmann codes such as CAMB [54] or CLASS [55] that solve numerically the evolution of the cosmological perturbations. The step-like suppression of the matter power spectrum induced by various values of  $f_{\nu}$  is shown in Figure 7.

Is it possible to mimic the effect of massive neutrinos on the matter power spectrum with some combination of other cosmological parameters? If so, one would say that a parameter degeneracy exists, reducing the sensitivity to neutrino masses. This possibility depends on the intervals  $[k_{\text{min}}, k_{\text{max}}]$  and  $[z_{\text{min}}, z_{\text{max}}]$  in which  $P(k, z)$  can be accurately measured. Ideally, if we could have  $k_{\text{min}} \leq 10^{-2}h \text{ Mpc}^{-1}$  and  $k_{\text{max}} \geq 1h \text{ Mpc}^{-1}$ , the effect

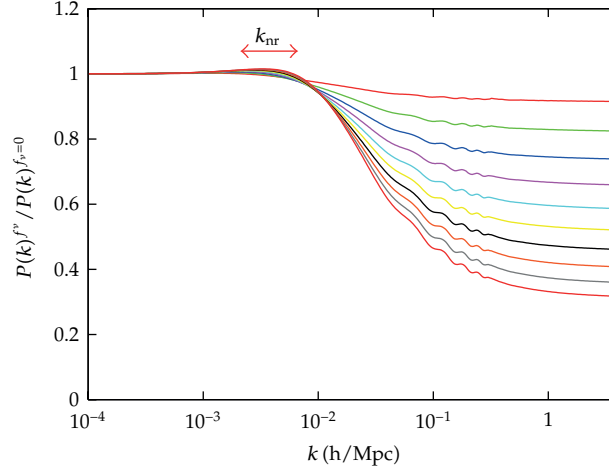


**Figure 7:** Ratio of the matter power spectrum including three degenerate massive neutrinos with density fraction  $f_\nu$  to that with three massless neutrinos. The parameters  $(\omega_m, \Omega_\Lambda) = (0.147, 0.70)$  are kept fixed, and from top to bottom the curves correspond to  $f_\nu = 0.01, 0.02, 0.03, \dots, 0.10$ . The individual masses  $m_\nu$  range from 0.046 to 0.46 eV, and the scale  $k_{nr}$  from  $2.1 \times 10^{-3} h \text{ Mpc}^{-1}$  to  $6.7 \times 10^{-3} h \text{ Mpc}^{-1}$  as shown on the top of the figure, from [8].

of the neutrino mass would be nondegenerate, because of its very characteristic step-like effect. Moreover, because neutrinos render the linear growth factor scale dependent, with  $\delta_m(k, z)$  proportional to  $a$  (resp., or  $a^{1-3/5f_\nu}$ ) for  $k < k_{nr}$  (resp.,  $k \gg k_{nr}$ ), the amplitude of the step-like suppression is redshift dependent. Using for example, weak lensing techniques or Lyman- $\alpha$  forest data, one could get accurate measurements of the matter spectrum at several redshifts in the range  $0 < z < 3$ . This will offer an opportunity to test the “time dependence” of the neutrino mass effect, and to distinguish it, for instance, from an equivalent step-like suppression in the primordial spectrum that would still imply a scale-independent growth factor.

The problem is that usually the matter power spectrum can only be accurately measured in the intermediate region where the mass effect is neither null nor maximal: in other words, many experiments only have access to the transition region in the step-like transfer function. In this region, the neutrino mass affects the slope of the matter power spectrum in a way which can be easily confused with the effect of other cosmological parameters. Because of these parameter degeneracies, the current LSS data alone cannot provide significant constraints on the neutrino mass, and it is necessary to combine them with other cosmological data, in particular the CMB anisotropy spectrum, which could lift most of the degeneracies. Still, for exotic models with for example, extrarelativistic degrees of freedom, a constant equation-of-state parameter of the dark energy different from  $-1$ , or a nonpower-law primordial spectrum, the neutrino mass bound can become significantly weaker.

The value of  $k_{\max}$  is not limited by observational sensitivities but by the range in which we trust predictions from linear theory. Beyond the scale of nonlinearity (of the order of  $k_{\max} = 0.15 h \text{ Mpc}^{-1}$  at  $z = 0$ ), the data is only useful provided that one is able to make accurate predictions not only for the nonlinear power spectrum, but also for redshift-space distortions (coming from the fact that we observe the redshift of objects, not their distance away from us) and finally for the scale dependence of the light-to-mass bias (relating the

power spectrum of a given category of observed compact objects to the underlying total matter power spectrum). Spectacular progresses are being carried on these three fronts, thanks to better N-body simulations and analytical techniques. Including massive neutrinos in such calculations is particularly difficult, but successful attempts were presented for example, in [56–58]. The neutrino mass impact on the nonlinear matter power spectrum is now modeled with rather good precision, at least within one decade above  $k_{\text{max}}$  in wave-number space. It appears that the step-like suppression is enhanced by nonlinear effects up to roughly  $\Delta P(k)/P(k) \simeq -10f_\nu$  (at redshift zero and  $k \sim 1h \text{ Mpc}^{-1}$ ) and is reduced above this scale. Hence, nonlinear corrections render the neutrino mass effect even more characteristic than in the linear theory and may help to increase the sensitivity of future experiments.

Until this point, we reduced the neutrino mass effect to that of the parameter  $f_\nu$  or  $M_\nu$ . In principle, the mass splitting between the three different families for a common total mass is visible in the matter power spectrum. The time at which each species becomes nonrelativistic depends on individual masses  $m_i$ . Hence, both the scale of the step-like suppression induced by *each* neutrino and the amount of suppression in the small-scale power spectrum have a small dependence on individual masses. The differences between the power spectrum of various models with the same total mass and different mass splittings were computed numerically in [59] for the linear spectrum and [58] for the nonlinear spectrum. At the moment, it seems that even the most ambitious future surveys will not be able to distinguish these mass splitting effects with a reasonable significance [60, 61].

#### 6.4. Impact of Massive Neutrinos on the CMB Anisotropy Spectrum

For neutrino masses of the order of 1 eV (about  $f_\nu \leq 0.1$ ) the three neutrino species are still relativistic at the time of photon decoupling, and the direct effect of free-streaming neutrinos on the evolution of the baryon-photon acoustic oscillations is the same in the  $\Lambda$ CDM and  $\Lambda$ MDM cases. Therefore, the effect of the mass can only appear at two levels that of the background evolution and that of secondary CMB anisotropies, related to the behavior of photon perturbations after decoupling. Both levels are potentially affected by the evolution of neutrinos after the time of their nonrelativistic transition. If neutrinos were heavier than a few eV, they would already be nonrelativistic at decoupling, and they could trigger more direct effects in the CMB, as described in [62]. However, we will see later that this situation is disfavoured by current upper bounds on the neutrino mass.

Let us first review the background effects of massive neutrinos on the CMB. Because the temperature and polarization spectrum shape are the result of several intricate effects, one cannot discuss the neutrino mass impact without specifying which other parameters are kept fixed. Neutrinos with a mass in the range from  $10^{-3} \text{ eV}$  to 1 eV should be counted as radiation at the time of equality and as nonrelativistic matter today: the total nonrelativistic density, parametrized by  $\omega_m = \Omega_m h^2$ , depends on the total neutrino mass  $M_\nu = \sum_i m_i$ . Hence, when  $M_\nu$  is varied, there must be a variation either in the redshift of matter-to-radiation equality  $z_{\text{eq}}$  or in the matter density today  $\omega_m$ .

This can potentially impact the CMB in three ways. A shift in the redshift of equality affects the position and amplitude of the peaks. A change in the nonrelativistic matter density at late times can impact both the angular diameter distance to the last scattering surface  $d_A(z_{\text{dec}})$ , controlling the overall position of CMB spectrum features in multipole space, and the slope of the low- $l$  tail of the CMB spectrum, due to the late Integrated Sachs-Wolfe (ISW) effect. Out of these three effects (changes in  $z_{\text{eq}}$ , in  $d_A$  and in the late ISW), only two

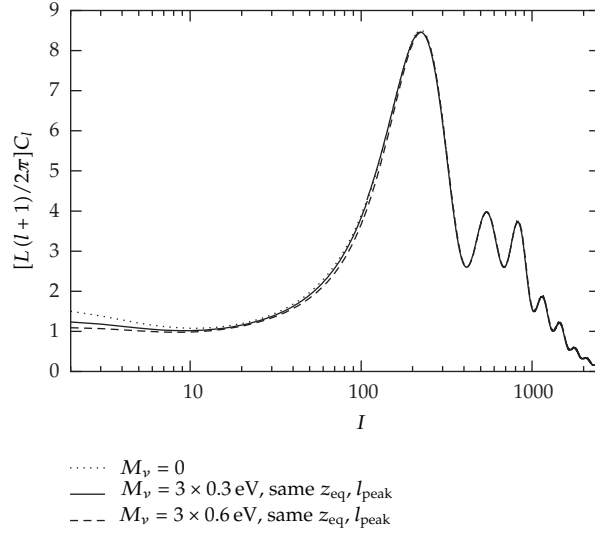


**Figure 8:** CMB temperature spectrum with different neutrino masses. Some of the parameters of the  $\Lambda$ MDM model have been varied together with  $M_\nu$  in order to keep fixed the redshift of equality and the angular diameter distance to last scattering.

can be cancelled by a simultaneous variation of the total neutrino mass and of other free parameters in the  $\Lambda$ MDM model. Hence, the CMB spectrum is sensitive to the background effect of the total neutrino mass. In practice, however, the late ISW effect is difficult to measure due to cosmic variance and CMB data alone cannot provide a useful information on sub-eV neutrino masses. If one considers extensions of the  $\Lambda$ MDM, this becomes even more clear: by playing with the spatial curvature, one can neutralize all three effects simultaneously. But as soon as CMB data is used in combination with other background cosmology observations (constraining for instance the Hubble parameter, the cosmological constant value, or the BAO scale), some bounds can be derived on  $M_\nu$ .

There exists another effect of massive neutrinos on the CMB at the level of secondary anisotropies: when neutrinos become nonrelativistic, they reduce the time variation of the gravitational potential inside the Hubble radius. This affects the photon temperature through the early ISW effect and leads to a depletion in the temperature spectrum of the order of  $(\Delta C_l/C_l) \sim -(M_\nu/0.1 \text{ eV})\%$  on multipoles  $20 < l < 500$ , with a dependence of the maximum depletion scale on individual masses  $m_i$ . This effect is roughly ten times smaller than the depletion in the small-scale matter power spectrum,  $\Delta P(k)/P(k) \sim -(M_\nu/0.01 \text{ eV})\%$ .

We show in Figure 8 the effect on the CMB temperature spectrum of increasing the neutrino mass while keeping  $z_{\text{eq}}$  and  $d_A$  fixed: the only observed differences are then for  $2 < l < 50$  (late ISW effect due to neutrino background evolution) and for  $50 < l < 200$  (early ISW effect due to neutrino perturbations).

We conclude that the CMB alone is not a very powerful tool for constraining sub-eV neutrino masses and should be used in combination with homogeneous cosmology constraints and/or measurements of the LSS power spectrum, for instance from galaxy clustering, galaxy lensing, or CMB lensing (see Section 8).

## 7. Current Bounds on Neutrino Masses

In this section we review how the available cosmological data are used to get information on the absolute scale of neutrino masses, complementary to laboratory experiments. Note that the bounds in the next subsections are all based on the Bayesian inference method, and the upper bounds on the sum of neutrino masses are given at 95% C.L. after marginalization over all free cosmological parameters. We refer the reader to Section 5.1 of [8] for a detailed discussion on this statistical method, as well as for most of the references for the experimental data or parameter analysis.

### 7.1. CMB Anisotropy Bounds

The experimental situation of the measurement of the CMB anisotropies is dominated by the seven-year release of WMAP data [17], which improved the already precise TT and TE angular power spectra of the previous releases and included a detection of the E-polarization self-correlation spectrum (EE). On similar or smaller angular scales than WMAP, we have results from experiments that are either ground based or balloon borne (ACT, SPT, etc.).

We saw in the previous section that the CMB spectrum has a small sensitivity to neutrino masses even when each mass is below 0.5 eV, and all nonrelativistic transitions take place after photon decoupling [63]. This sensitivity is due to background effects (mainly the late ISW effect if all other  $\Lambda$ CDM parameters are left free) plus perturbation effects (mainly the early ISW effect). Therefore, it is possible to constrain neutrino masses using CMB experiments only, down to the level at which these small effects are masked by instrumental noise, by cosmic variance, or by parameter degeneracies in the case of some cosmological models beyond the minimal  $\Lambda$  Mixed Dark matter framework. WMAP alone is able to set a limit  $M_\nu < 1.3\text{--}1.4\text{ eV}$  depending on whether the dark energy component is a cosmological constant or not [17]. Because the neutrino mass effects in the CMB are visible mainly at  $l < 500$ , combining WMAP data with other CMB datasets (from e.g., ACT or SPT) does not improve this bound. On the contrary, adding more information to the background cosmological evolution is very useful, because it helps removing degeneracies between the various parameters: in that case, the CMB data can better probe neutrino masses through their background effects. For instance, the bound from WMAP combined with BAO scale measurements and a direct determination of  $H_0$  by the Hubble space telescope Key Project [64] is significantly stronger:  $M_\nu < 0.58\text{ eV}$  (95% CL) [17], while the combination of WMAP with a different  $H_0$  determination at various redshift from early-type galaxy evolution gives  $M_\nu < 0.48\text{ eV}$  (95% CL) [65]. These are important results, because they do not depend on the uncertainties from LSS data discussed next.

### 7.2. Large-Scale Structure Observations

The matter power spectrum can be probed with various methods on different scales and redshifts. Let us review here the major techniques which have led so far to relevant neutrino mass bounds.



### 7.2.1. Galaxy Power Spectrum

Galaxy maps (or, similarly, cluster maps) can be smoothed over small scales and Fourier transformed in order to provide a power spectrum. Relating such a spectrum to the total matter power spectrum is a tricky exercise, especially on small scales (corresponding to wave-numbers  $k > 0.1h \text{ Mpc}^{-1}$ ), because it is difficult to make accurate predictions for nonlinear corrections, redshift-space distortions, and the light-to-mass bias. Current bounds are based on the analysis of linear scales only, for which the assumption of a scale-independent bias is well motivated. This bias is, however, left as a free parameter, in such way that galaxy spectrum data give indications on the shape but not on the global amplitude of  $P(k, z)$ . In the next subsection, we will report constraints from the halo power spectrum of Large Red Galaxies (denoted later as Gal-LRG), measured by [66], the spectrum of the MegaZ catalogue (Gal-MegaZ), used by [67], and the WiggleZ Dark Energy Survey (Gal-WiggleZ), used by [68]. The first two data sets are actually extracted from the same big survey, the Sloan Digital Sky Survey (SDSS).

For sufficiently deep galaxy surveys, it is possible to separate galaxies into redshift bins and compute different correlation functions at different redshifts. This technique, called tomography, can be very useful for constraining the scale-dependent growth factor induced by neutrino masses. In that case, the data can be reduced to a set of two-dimension power spectra in different shells, each of them related to  $P(k, z)$  in a narrow redshift range. Recently, such a tomographic analysis was used by [69] for constraining neutrinos, using galaxies from the Canada-France-Hawaii-Telescope Legacy Survey (CFHTLS), split in three redshift bins covering the ranges  $0.5 < z < 0.6$ ,  $0.6 < z < 0.8$  and  $0.8 < z < 1.0$  (this dataset will be denoted as Gal-CFHTLS).

### 7.2.2. Cluster Mass Function

Instead of probing directly the matter power spectrum  $P(k, z)$  from the spatial distribution of objects, it is possible to constrain integrated quantities of the type  $\int dk P(k)W(k)$ , where  $W(k)$  stands for a given window function. One such quantity is related to the histogram of cluster masses. If the mass of a significant number of galaxy clusters within a given redshift bin is known, this histogram gives an estimate of the so-called cluster mass function,  $dn(M, z)/dM$ , with  $dn$  being the number of clusters of redshift approximately equal to  $z$ , and with a mass in the range  $[M, M + dM]$ . This function is related to  $\sigma^2(M, z)$ , the variance of the density in spheres enclosing a mass  $M$ , itself derived from the convolution of the power spectrum  $P(k, z)$  with an appropriate window function. In the next subsection we will refer to bounds derived from cluster abundances probed by X-ray observations from the ROSAT survey, presented by [70] (denoted later as Clus-ROSAT) and by optical observations from the MaxBCG catalogue, presented by [71] (denoted later as Clus-MaxBCG).

### 7.2.3. Galaxy Weak Lensing

The image of observed galaxies is distorted by gravitational lensing effects, caused by density fluctuations along the line of sight. One of these effects is called cosmic shear. It corresponds to the squeezing of an image in one direction in the sky and its stretching in the orthogonal direction. Because such distortions are coherent over the angular size of the lensing potential wells responsible for lensing, they tend to align slightly the apparent major axis of galaxies in

a given patch of the sky. Hence the average cosmic shear in a given direction can be estimated statistically by averaging over major axis orientations. The analysis of a catalogue of images leads to a map of the lensing potential, itself related to the matter power spectrum  $P(k, z)$  through the Poisson equation. If the number of source galaxies is sufficient, it is possible to split the catalogue in several redshift bins and to obtain a three-dimensional reconstruction of the gravitational potential in our past-line cone and of  $P(k, z)$  at various redshifts. Cosmic shear tomography is particularly useful for measuring neutrino masses, because it can probe the scale-dependent growth factor induced by neutrino masses over an extended range of redshifts. Current cosmic shear surveys already allow to put bounds on neutrino parameters: we will refer later to results from the CFHTLS presented by [72] and denoted as WL-CFHTLS.

#### 7.2.4. Lyman Alpha Forests

The most luminous and distant compact objects that we can observe are quasars. Some of the photons emitted by quasars interact along the line-of-sight. In particular, a fraction of photons are absorbed at the Lyman alpha wavelength by hydrogen atoms located in the Interstellar Galactic Medium (IGM). The absorbed fraction in a given point of the photon trajectory is proportional to the local density of neutral hydrogen. Because photons are continuously redshifted, absorption in a given point is seen by the observer as a depletion of the spectrum at a given frequency. Hence, inside a limited range called the *Lyman alpha forest*, the frequency dependence of quasar spectra is a tracer of the spatial fluctuations of the hydrogen density along the line of sight. Lyman alpha forests in quasar spectra offer an opportunity to reconstruct the hydrogen density fluctuation along several line-of-sights in a given redshift range. After Fourier expanding each spectrum and averaging over many spectra, one gets an estimate of the so-called flux power spectrum  $P_F(z, k)$  that can be related to the total matter power spectrum  $P(k, z)$ . Unfortunately, the flux power spectrum does not probe linear scales but mildly nonlinear scales. In order to relate  $P_F(z, k)$  to  $P(k)$ , it is necessary to perform N-body simulations with a hydrodynamical treatment of baryons, accounting for the complicated thermodynamical evolution of the IGM (which depends on star formation). Also, a limitation of this technique comes from the fact that the emitted quasar spectra already have a nontrivial frequency dependence and that photons are affected by several other effects than Lyman alpha absorption along the line-of-sight. Nevertheless, a careful modeling of all relevant effects allows to obtain interesting constraints. The fact that Lyman alpha forests probe mildly nonlinear scales rather than strongly nonlinear ones is of course crucial for keeping systematic errors under control. Lyman alpha observations typically constrain the matter power spectrum in the wavenumber range  $0.3 < k < 3h/\text{Mpc}$  and in the redshift range  $2 < z < 5$ . We mention below some neutrino mass bounds inferred from quasar spectra obtained by the SDSS and presented in [73], denoted as Ly- $\alpha$ -SDSS.

### 7.3. Large-Scale Structure Bounds

Using LSS observations in combination with CMB data offers an opportunity to observe (or to bound) the step-like suppression of the matter power spectrum in presence of neutrino masses, as explained in Section 6.3 and illustrated in Figure 7. The use of CMB data is crucial in order to constrain parameters like the baryon density, the primordial spectrum amplitude, the tilt, and a combination of  $\omega_M$  and  $h$ . Without such constraints, there would be too much

**Table 1:** 95% CL upper bounds on the total neutrino mass  $M_\nu$  in eV, for various combinations of CMB, homogeneous cosmology, and LSS data sets. The first seven lines refer to galaxy power spectrum measurements, the next two lines to cluster mass function measurements, the last line to a weak lensing survey. WMAP5 or 7 stands for WMAP 5 or 7-year data.  $H_0$  refers to the direct measurement by the HST Key Project [64] and BAO to estimates of the scale of Baryon Acoustic Oscillations at various redshifts. Other acronyms refer to various Large-Scale Structure dataset referred in Section 7.2. In the last column, the cosmological constant was replaced by a Dark Energy component with arbitrary equation-of-state parameter  $w$ .

Cosmological data	Reference	$w = -1$	$w \neq -1$
WMAP7 + Gal-LRG + $H_0$	[17]	0.44	0.76
WMAP5 + Gal-MegaZ + BAO + SNIa	[67]	0.325	0.491
WMAP5 + Gal-MegaZ + BAO + SNIa + $H_0$	[67]	0.281	0.471
WMAP7 + Gal-WiggleZ	[68]	0.60	—
WMAP7 + Gal-WiggleZ + BAO + $H_0$	[68]	0.29	—
WMAP7 + Gal-CFHTLS	[69]	0.64 (0.44)	—
WMAP7 + Gal-CFHTLS + $H_0$	[69]	0.41 (0.29)	—
WMAP5 + BAO + SNIa + Clus-ROSAT	[70]	0.33	0.43
WMAP5 + $H_0$ + Clus-MaxBCG	[71]	0.40	0.47
WMAP5 + BAO + SNIa + WL-CFHTLS	[72]	0.53	—

freedom in the matter power spectrum fitted to LSS data for identifying a smooth step-like suppression.

We summarize in Table 1 the main constraints on  $M_\nu$ , available at the time of writing, obtained from combinations of CMB plus homogeneous cosmology data, galaxy power spectrum data, and cluster abundance data. Current data set are far from reaching the sensitivity required to probe the mass splitting of the total mass  $M_\nu = \sum_i m_{\nu_i}$  between different species. The constraints mentioned below have been derived in the case of three degenerate neutrinos with mass  $m_\nu = M_\nu/3$ , but they roughly apply to the total mass of any scenario. Also, the bounds shown in the first column of Table 1 have been obtained under the assumption of a minimal  $\Lambda$ CDM model with massive neutrinos, featuring seven free parameters. More conservative bounds are sometimes derived for basic extensions of this model, with one or two more parameters. The constraints do not change significantly when assuming, for instance, a primordial spectrum with a running of the tilt [ $d \ln n_s / d \ln k$ ] or a significant contribution to the CMB of primordial gravitational waves [71]. Parameters known to be slightly degenerate with neutrino masses and leading to weaker bounds are  $w$ , the equation-of-state parameter of a Dark Energy component (substituting the cosmological constant), and  $N_{\text{eff}}$ , the effective number of neutrinos discussed in Section 3. The degeneracy with  $w$ , explained in [74], is illustrated by the last column in Table 1. We did not include in this table current limits from Lyman alpha forest data: this is a delicate matter for the reasons mentioned previously, and a careful modeling of all systematic effects leads to rather weak neutrino mass bounds. The conservative analysis of [73], based on Ly- $\alpha$ -SDSS, gives a bound  $M_\nu < 0.9$  eV (95% CL) from Ly- $\alpha$ -SDSS data alone.

In conclusion, the combination of available data sets consistently indicates that the total neutrino mass is below 0.3 eV at the 95% CL (0.5 eV if we allow for Dark Energy with arbitrary  $w$ ). This means that the “degenerate scenario” in which all neutrinos share roughly the same mass is almost excluded. The data is about to probe the region in which masses are different from each other and are ranked according to the NH or IH scenario. Other recent summaries of existing bounds have been recently presented in [6, 17, 50, 71, 75].

## 8. Future Sensitivities on Neutrino Masses from Cosmology

Future CMB observations will have increasing sensitivity to neutrino masses, not only thanks to smaller error bars on the temperature and polarization spectra. They will make it possible to probe the large-scale structure of the universe with a new technique: CMB lensing extraction. The weak lensing of the last scattering surface by nearby galaxy clusters induces specific non-Gaussian patterns in CMB maps that can be extracted using some nonlinear estimators. This method allows to measure the lensing potential up to  $z \sim 3$  and to infer constraints on  $P(k, z)$  at such high redshifts.

In the very close future, significant improvements on the neutrino mass bounds will be triggered by the Planck CMB satellite. The forecasts presented in [76] predict a neutrino mass sensitivity of  $\sigma(M_\nu) \sim 0.1$  eV from Planck alone, using the lensing extraction technique of [77]. This would be twice better than without lensing extraction.

Several galaxy surveys with better sensitivity and larger volume are about to release data or have been planned over the next decades, including the Baryon Oscillation Spectroscopic Survey (<http://cosmology.lbl.gov/BOSS/>) (BOSS), the Dark Energy Survey (<http://www.darkenergysurvey.org/>) (DES), the Large Synoptic Survey Telescope (<http://www.lsst.org/>) (LSST), or the Euclid satellite (<http://sci.esa.int/euclid>). Also, in [78] it was pointed out that in the future accurate measurements could be inferred from cluster surveys. Because clusters are more luminous than galaxies, they can be mapped up to higher redshift. Concerning cosmic shear surveys, spectacular improvements are expected from Pan-STARRS (<http://pan-starrs.ifa.hawaii.edu/>) or the DES, LSST, and the Euclid surveys already mentioned above.

In a near future, the prediction of [79] is that the combination of Planck (with lensing extraction) with BAO scale information from BOSS could lower the error down to  $\sigma(M_\nu) \sim 0.06$  eV. In addition, the authors of [80] find that adding Lyman alpha data from BOSS should lead to comparable sensitivities, and even better results might be expected from the addition of galaxy power spectrum data from the same survey.

With better tomographic data (for either galaxy clustering or cosmic shear), it will become possible to probe the scale dependence of the growth factor induced by neutrino masses (or in other words, the fact that the step-like suppression has an amplitude increasing with time) and to reach spectacular sensitivities. We present below the typical sensitivities expected for a collection of planned surveys (not all approved). These numbers should be taken with care because forecasts are based on an idealization of each experiment, as well as on several assumptions like the underlying cosmological model or even the fiducial value of the neutrino mass itself.

In [81] it was found that the measurement of the galaxy harmonic power spectrum in seven redshift bins by the DES should lead to a sensitivity of  $\sigma(M_\nu) \sim 0.06$  eV when combined with Planck data (without lensing extraction). Similar bounds were derived in [82] for another combination of comparable experiments. This shows that at the horizon of 2014 or 2015, a total neutrino mass close to  $M_\nu \simeq 0.1$  eV could be marginally detected at the  $2\text{-}\sigma$  level by cosmological observations. Because this value coincides with the lowest possible total mass in the inverted hierarchy scenario, the latter could start to be marginally ruled out in case the data still prefers  $M_\nu = 0$ .

The sensitivity of cosmic shear data from a satellite experiment comparable to Euclid was calculated in [83], where it was found that it would shrink to  $\sigma(M_\nu) \sim 0.03$  eV in combination with Planck data (without lensing extraction). The forecast of [84] based on galaxy clustering data also from Euclid (completed at small redshift by similar data from

BOSS) gives comparable numbers. Constraints based on the ground-based Large Synoptic Survey Telescope should be slightly weaker [85]. Hence, in the early 2020's, we expect that a combination of cosmological data sets could detect the total neutrino mass of the normal hierarchy scenario,  $M_\nu \simeq 0.05$  eV, at the  $2\text{-}\sigma$  level. If the total mass is instead close to  $M_\nu \simeq 0.1$  eV, it will be detected at the  $4\text{-}\sigma$  level. However, in that case, available experiments would not have enough sensitivity for making the difference between an inverted and normal hierarchy scenario with the same  $M_\nu$ .

Even more progress could be provided by the promising technique of 21-cm surveys. Instead of mapping the distribution of hydrogen atoms through the absorption rate of photons traveling from quasars, it should be possible to observe directly the photons emitted by these atoms at a wavelength  $\lambda \simeq 21$  cm from the transition from one hyperfine level to the other. While travelling towards the observer, these photons are redshifted, and seen with a wavelength indicating the position of the emitting atoms in redshift space. Recent theoretical progresses in this field show that using this technique, future dedicated experiments should be able to map hydrogen and hence baryonic fluctuations at very high redshift (typically  $6 < z < 12$ ) and to probe the matter power spectrum deep inside the matter-dominated regime on linear scales [86]. This field is still in its infancy, and the forecasts presented so far have to be taken with care, due to the difficulty to make a realistic estimate of systematic errors in future data sets. A sensitivity of  $\sigma(M_\nu) \sim 0.075$  eV for the combination of Planck with the Square Kilometer Array (SKA) project, or  $\sigma(M_\nu) \sim 0.0075$  eV with the Fast Fourier Transform Telescope (FFTT), was found in [61]. However, the authors show that such impressive experiments would still fail in discriminating between the NH and IH scenario.

An eventual post-Planck CMB satellite or post-Euclid survey would also have a great potential. The forecast analysis in [87] shows that for a CMB satellite of next generation one could get  $\sigma(M_\nu) \sim 0.03$  eV alone, thanks to a very precise reconstruction of the CMB lensing potential, while [78] discusses the potential of cluster surveys. Finally, the authors of [60] show how far the characteristics of an hypothetical galaxy or cosmic shear survey should be pushed in order to discriminate between two allowed NH and IH scenarios with the same total mass.

## 9. Conclusions

Neutrinos, despite the weakness of their interactions and their small masses, can play an important role in cosmology that we have reviewed in this contribution. In addition, cosmological data can be used to constrain neutrino properties, providing information on these elusive particles that complements the efforts of laboratory experiments. In particular, the data on cosmological observables have been used to bound the radiation content of the Universe via the effective number of neutrinos, including a potential extra contribution from other relativistic particles.

But probably the most important contribution of Cosmology to our knowledge of neutrino properties is the information it can provide on the absolute scale of neutrino masses. We have seen that the analysis of cosmological data can lead to either a bound or a measurement of the sum of neutrino masses, an important result complementary to terrestrial experiments such as tritium-beta decay and neutrinoless double-beta decay experiments. In the next future, thanks to the data from new cosmological experiments we could even hope to test the minimal values of neutrino masses guaranteed by the present evidences for flavour



neutrino oscillations. For this and many other reasons, we expect that neutrino cosmology will remain an active research field in the next years.

## Acknowledgments

S. Pastor was supported by the Spanish Grants FPA2011-22975, Multidark Consolider CSD2009-00064 (MINECO), and PROMETEO/2009/091 (Generalitat Valenciana), as well as by the EC Contract UNILHC PITN-GA-2009-237920. He thanks the Galileo Galilei Institute for Theoretical Physics for the hospitality and the INFN for partial support during the completion of this work.

## References

- [1] A. D. Dolgov, "Neutrinos in cosmology," *Physics Reports*, vol. 370, no. 4-5, pp. 333–535, 2002.
- [2] J. Lesgourgues, G. Mangano, G. Miele, and S. Pastor, *Neutrino Cosmology*, Cambridge University Press, Cambridge, UK, 2013.
- [3] G. Steigman, "Neutrinos and big bang nucleosynthesis," *Advances in High Energy Physics*. In press.
- [4] E. Nardi, A. Riotto, and C. S. Fong, *Leptogenesis in the Universe*, Contribution to this Special issue.
- [5] S. Hannestad, "Primordial neutrinos," *Annual Review of Nuclear and Particle Science*, vol. 56, pp. 137–161, 2006.
- [6] S. Hannestad, "Neutrino physics from precision cosmology," *Progress in Particle and Nuclear Physics*, vol. 65, no. 2, pp. 185–208, 2010.
- [7] Y. Y. Y. Wong, "Neutrino mass in cosmology: status and prospects," *Annual Review of Nuclear and Particle Science*, vol. 61, pp. 69–98, 2011.
- [8] J. Lesgourgues and S. Pastor, "Massive neutrinos and cosmology," *Physics Reports*, vol. 429, no. 6, pp. 307–379, 2006.
- [9] M. Kamionkowski and A. Kosowsky, "The cosmic microwave background and particle physics," *Annual Review of Nuclear and Particle Science*, vol. 49, no. 1, pp. 77–123, 1999.
- [10] E. W. Kolb and M. S. Turner, *The Early Universe*, Addison-Wesley, Reading, Mass, USA, 1990.
- [11] S. Dodelson, *Modern Cosmology*, Academic Press, New York, NY, USA, 2003.
- [12] G. Mangano, G. Miele, S. Pastor, T. Pinto, O. Pisanti, and P. D. Serpico, "Relic neutrino decoupling including flavour oscillations," *Nuclear Physics B*, vol. 729, no. 1-2, pp. 221–234, 2005.
- [13] F. Iocco, G. Mangano, G. Miele, O. Pisanti, and P. D. Serpico, "Primordial nucleosynthesis: from precision cosmology to fundamental physics," *Physics Reports*, vol. 472, no. 1–6, pp. 1–76, 2009.
- [14] Particle Data Group Collaboration, "Review of particle physics," *Journal of Physics G*, vol. 37, no. 7, Article ID 075021, 2010.
- [15] S. Sarkar, "Big bang nucleosynthesis and physics beyond the standard model," *Reports on Progress in Physics*, vol. 59, no. 12, pp. 1493–1609, 1996.
- [16] G. Mangano and P. D. Serpico, "A robust upper limit on  $N_{\text{eff}}$  from BBN, circa 2011," *Physics Letters B*, vol. 701, no. 3, pp. 296–299, 2011.
- [17] E. Komatsu, K. M. Smith, J. Dunkley et al., "Seven-year Wilkinson Microwave Anisotropy Probe (WMAP) observations: cosmological interpretation," *Astrophysical Journal*, vol. 192, supplement 2, p. 18, 2011.
- [18] J. Dunkley, R. Hlozek, J. Sievers et al., "The Atacama Cosmology Telescope: cosmological parameters from the 2008 power spectra," *The Astrophysical Journal*, vol. 739, no. 1, p. 52, 2011.
- [19] R. Keisler, C. L. Reichard, K. A. Aird et al., "A measurement of the damping tail of the cosmic microwave background power spectrum with the South Pole telescope," *The Astrophysical Journal*, vol. 743, no. 1, p. 28, 2011.
- [20] J. Hamann, "Evidence for extra radiation? Profile likelihood versus Bayesian posterior," *Journal of Cosmology and Astroparticle Physics*, vol. 1203, p. 021, 2012.
- [21] G. L. Fogli, E. Lisi, A. Marrone, and A. Palazzo, "Global analysis of three-flavor neutrino masses and mixings," *Progress in Particle and Nuclear Physics*, vol. 57, no. 2, pp. 742–795, 2006.
- [22] M. C. González-García and M. Maltoni, "Phenomenology with massive neutrinos," *Physics Reports*, vol. 460, no. 1–3, pp. 1–129, 2008.

- [23] T. Schwetz, M. Tórtola, and J. W. F. Valle, "Global neutrino data and recent reactor fluxes: the status of three-flavour oscillation parameters," *New Journal of Physics*, vol. 13, Article ID 063004, 2011.
- [24] H.-S. Kang and G. Steigman, "Cosmological constraints on neutrino degeneracy," *Nuclear Physics B*, vol. 372, no. 1-2, pp. 494–520, 1992.
- [25] S. H. Hansen, G. Mangano, A. Melchiorri, G. Miele, and O. Pisanti, "Constraining neutrino physics with BBN and CMBR," *Physical Review D*, vol. 65, p. 023511, 2002.
- [26] A. D. Dolgov, S. H. Hansen, S. Pastor, S. T. Petcov, G. G. Raffelt, and D. V. Semikoz, "Cosmological bounds on neutrino degeneracy improved by flavor oscillations," *Nuclear Physics B*, vol. 632, no. 1–3, pp. 363–382, 2002.
- [27] Y. Y. Y. Wong, "Analytical treatment of neutrino asymmetry equilibration from flavor oscillations in the early universe," *Physical Review D*, vol. 66, no. 2, Article ID 025015, 2002.
- [28] K. N. Abazajian, J. F. Beacom, and N. F. Bell, "Stringent constraints on cosmological neutrino-antineutrino asymmetries from synchronized flavor transformation," *Physical Review D*, vol. 66, no. 1, Article ID 013008, 2002.
- [29] P. D. Serpico and G. G. Raffelt, "Lepton asymmetry and primordial nucleosynthesis in the era of precision cosmology," *Physical Review D*, vol. 71, no. 12, Article ID 127301, 2005.
- [30] S. Pastor, T. Pinto, and G. G. Raffelt, "Relic density of neutrinos with primordial asymmetries," *Physical Review Letters*, vol. 102, no. 24, Article ID 241302, 2009.
- [31] G. Mangano, G. Miele, S. Pastor, O. Pisanti, and S. Sarikas, "Constraining the cosmic radiation density due to lepton number with Big Bang Nucleosynthesis," *Journal of Cosmology and Astroparticle Physics*, vol. 1103, no. 3, Article ID 035, 2011.
- [32] G. Mangano, G. Miele, S. Pastor, O. Pisanti, and S. Sarikas, "Updated BBN bounds on the cosmological lepton asymmetry for non-zero  $\theta_{13}$ ," *Physics Letters B*, vol. 708, no. 1-2, pp. 1–5, 2012.
- [33] E. Castorina, U. Franca, M. Lattanzi et al., "Cosmological lepton asymmetry with a nonzero mixing angle  $13^\circ$ ," *Physical Review D*, vol. 86, no. 2, Article ID 023517, 11 pages, 2012.
- [34] K. N. Abazajian, M. A. Acero, S. K. Agarwalla et al., "Light sterile neutrinos: a white paper," In press, <http://arxiv.org/abs/1204.5379>.
- [35] D. Kirilova and M. Panayotova, "Relaxed big bang nucleosynthesis constraints on neutrino oscillation parameters," *Journal of Cosmology and Astroparticle Physics*, no. 12, Article ID 014, 2006.
- [36] R. Barbieri and A. Dolgov, "Bounds on sterile neutrinos from nucleosynthesis," *Physics Letters B*, vol. 237, no. 3-4, pp. 440–445, 1990.
- [37] S. Hannestad, I. Tamborra, and T. Tram, "Thermalisation of light sterile neutrinos in the early universe," *Journal of Cosmology and Astroparticle Physics*, vol. 1207, p. 025, 2012.
- [38] A. D. Dolgov and F. L. Villante, "BBN bounds on active-sterile neutrino mixing," *Nuclear Physics B*, vol. 679, no. 1-2, pp. 261–298, 2004.
- [39] M. Cirelli, G. Marandella, A. Strumia, and F. Vissani, "Probing oscillations into sterile neutrinos with cosmology, astrophysics and experiments," *Nuclear Physics B*, vol. 708, no. 1–3, pp. 215–267, 2005.
- [40] A. Mirizzi, N. Saviano, G. Miele, and P. D. Serpico, "Light sterile neutrino production in the early universe with dynamical neutrino asymmetries," *Physical Review D*, vol. 86, no. 5, Article ID 053009, 2012.
- [41] C. Giunti and M. Laveder, "Implications of 3+1 short-baseline neutrino oscillations," *Physics Letters B*, vol. 706, no. 2-3, pp. 200–207, 2011.
- [42] R. Foot and R. R. Volkas, "Reconciling sterile neutrinos with big bang nucleosynthesis," *Physical Review Letters*, vol. 75, no. 24, pp. 4350–4353, 1995.
- [43] C. T. Kishimoto and G. M. Fuller, "Lepton-number-driven sterile neutrino production in the early universe," *Physical Review D*, vol. 78, no. 2, Article ID 023524, 2008.
- [44] D. V. Forero, M. A. Tortola, and J. W. F. Valle, "Global status of neutrino oscillation parameters after Neutrino-2012," *Physical Review D*, vol. 86, no. 7, Article ID 073012, 2012.
- [45] G. L. Fogli, E. Lisi, A. Marrone, D. Montanino, and A. M. Palazzo, "Global analysis of neutrino masses, mixings and phases: entering the era of leptonic CP violation searches," *Physical Review D*, vol. 86, no. 1, Article ID 013012, 2012.
- [46] M. C. González-García, M. Maltoni, J. Salvado, and T. Schwetz, "Global fit to three neutrino mixing: critical look at present precision," In press, <http://arxiv.org/abs/1209.3023>.
- [47] A. Giuliani and A. Poves, "Neutrinoless double beta decay," *Advances in High Energy Physics*. In press.
- [48] G. Drexlin, V. Hannen, S. Mertens, and C. Weinheimer, "Current direct neutrino mass measurements," *Advances in High Energy Physics*. In press.

- [49] G. L. Fogli, E. Lisi, A. Marrone et al., "Observables sensitive to absolute neutrino masses. II," *Physical Review D*, vol. 78, no. 3, Article ID 033010, 2008.
- [50] M. C. González-García, M. Maltoni, and J. Salvado, "Robust cosmological bounds on neutrinos and their combination with oscillation results," *Journal of High Energy Physics*, vol. 1008, p. 117, 2010.
- [51] J. R. Primack, "Whatever happened to hot dark matter?" *SLAC Beam Line*, vol. 31N3, pp. 50–57, 2001.
- [52] A. Boyarsky, O. Ruchayskiy, and M. Shaposhnikov, "The role of sterile neutinos in cosmology and astrophysics," *Annual Review of Nuclear and Particle Science*, vol. 59, pp. 191–214, 2009.
- [53] W. Hu, D. J. Eisenstein, and M. Tegmark, "Weighing neutrinos with galaxy surveys," *Physical Review Letters*, vol. 80, no. 24, pp. 5255–5258, 1998.
- [54] A. Lewis, A. Challinor, and A. Lasenby, "Efficient computation of CMB anisotropies in closed FRW models," *The Astrophysical Journal*, vol. 538, no. 2, p. 473, 2000.
- [55] J. Lesgourgues and T. Tram, "The cosmic linear anisotropy solving system (CLASS) IV: efficient implementation of non-cold relics," *Journal of Cosmology and Astroparticle Physics*, vol. 1109, Article ID 032, 2011.
- [56] J. Brandbyge and S. Hannestad, "Resolving cosmic neutrino structure: a hybrid neutrino N-body scheme," *Journal of Cosmology and Astroparticle Physics*, vol. 1001, no. 1, Article ID 021, 2010.
- [57] S. Bird, M. Viel, and M. G. Haehnelt, "Massive neutrinos and the non-linear matter power spectrum," *Monthly Notices of the Royal Astronomical Society*, vol. 420, no. 3, Article ID 2551, 2012.
- [58] C. Wagner, L. Verde, and R. Jimenez, "Effects of the neutrino mass splitting on the non-linear matter power spectrum," *The Astrophysical Journal Letters*, vol. 752, no. 2, p. L31, 2012.
- [59] J. Lesgourgues, S. Pastor, and L. Perotto, "Probing neutrino masses with future galaxy redshift surveys," *Physical Review D*, vol. 70, no. 4, Article ID 045016, 2004.
- [60] R. Jimenez, T. Kitching, C. Peña-Garay, and L. Verde, "Can we measure the neutrino mass hierarchy in the sky?" *Journal of Cosmology and Astroparticle Physics*, vol. 1005, no. 5, Article ID 035, 2010.
- [61] J. R. Pritchard and E. Pierpaoli, "Constraining massive neutrinos using cosmological 21 cm observations," *Physical Review D*, vol. 78, no. 6, Article ID 065009, 2008.
- [62] S. Dodelson, E. Gates, and A. Stebbins, "Cold + hot dark matter and the cosmic microwave background scott dodelson," *Astrophysical Journal Letters*, vol. 467, no. 1, pp. 10–18, 1996.
- [63] K. Ichikawa, M. Fukugita, and M. Kawasaki, "Constraining neutrino masses by CMB experiments alone," *Physical Review D*, vol. 71, no. 4, Article ID 043001, 2005.
- [64] W. L. Freedman, B. F. Madore, B. K. Gibson et al., "Final results from the Hubble Space Telescope key project to measure the Hubble constant," *Astrophysical Journal Letters*, vol. 553, no. 1, pp. 47–72, 2001.
- [65] M. Moresco, "New constraints on cosmological parameters and neutrino properties using the expansion rate of the Universe to  $z \sim 1.75$ ," *Journal of Cosmology and Astroparticle Physics*, vol. 1207, Article ID 053, 2012.
- [66] B. A. Reid, J. N. Chengalur, A. Begum, and I. D. Karachentsev, "Cosmological constraints from the clustering of the Sloan digital sky survey DR7 luminous red galaxies," *Monthly Notices of the Royal Astronomical Society*, vol. 404, no. 1, pp. 60–63, 2010.
- [67] S. A. Thomas, F. B. Abdalla, and O. Lahav, "Upper bound of 0.28 eV on neutrino masses from the largest photometric redshift survey," *Physical Review Letters*, vol. 105, no. 3, Article ID 031301, 2010.
- [68] S. Riemer-Sørensen, C. Blake, D. Parkinson et al., "WiggleZ Dark energy survey: cosmological neutrino mass constraint from blue high-redshift galaxies," *Physical Review D*, vol. 85, no. 8, Article ID 081101, 2012.
- [69] J.-Q. Xia, B. R. Granett, M. Viel et al., "Constraints on massive neutrinos from the CFHTLS angular power spectrum," *Journal of Cosmology and Astroparticle Physics*, vol. 1206, Article ID 010, 2012.
- [70] A. Mantz, S. W. Allen, D. Rapetti, and H. Ebeling, "The observed growth of massive galaxy clusters-I. Statistical methods and cosmological constraints," *Monthly Notices of the Royal Astronomical Society*, vol. 406, no. 3, pp. 1759–1772, 2010.
- [71] B. A. Reid, L. Verde, R. Jimenez, and O. Mena, "Robust neutrino constraints by combining low redshift observations with the CMB," *Journal of Cosmology and Astroparticle Physics*, vol. 1001, no. 1, Article ID 003, 2010.
- [72] I. Tereno, C. Schmid, J. P. Uzan, M. Kilbinger, F. H. Vincent, and L. Fu, "CFHTLS weak-lensing constraints on the neutrino masses," *Astronomy and Astrophysics*, vol. 500, no. 2, pp. 657–665, 2009.
- [73] M. Viel, M. G. Haehnelt, and V. Springel, "The effect of neutrinos on the matter distribution as probed by the intergalactic medium," *Journal of Cosmology and Astroparticle Physics*, vol. 2010, no. 6, Article ID 015, 2010.

- [74] S. Hannestad, "Neutrino masses and the dark energy equation of state:Relaxing the cosmological neutrino mass bound," *Physical Review Letters*, vol. 95, no. 22, Article ID 221301, 2005.
- [75] K. N. Abazajian, E. Calabrese, A. Cooray et al., "Cosmological and astrophysical neutrino mass measurements," *Astroparticle Physics*, vol. 35, no. 4, pp. 177–184, 2011.
- [76] L. Perotto, J. Lesgourgues, S. Hannestad, H. Tu, and Y. Y. Y. Wong, "Probing cosmological parameters with the CMB: forecasts from Monte Carlo simulations," *Journal of Cosmology and Astroparticle Physics*, vol. 0610, no. 10, Article ID 013, 2006.
- [77] T. Okamoto and W. Hu, "CMB lensing reconstruction on the full sky," *Physical Review D*, vol. 67, Article ID 083002, 2003.
- [78] S. Wang, Z. Haiman, W. Hu, J. Khoury, and M. May, "Weighing neutrinos with galaxy cluster surveys," *Physical Review Letters*, vol. 95, no. 1, Article ID 011302, 2005.
- [79] T. Sekiguchi, K. Ichikawa, T. Takahashi, and L. Greenhill, "Neutrino mass from cosmology: impact of high-accuracy measurement of the Hubble constant," *Journal of Cosmology and Astroparticle Physics*, vol. 1003, no. 3, Article ID 015, 2010.
- [80] S. Gratton, A. Lewis, and G. Efstathiou, "Prospects for constraining neutrino mass using Planck and Lyman- $\alpha$  forest data," *Physical Review D*, vol. 77, no. 8, Article ID 083507, 2008.
- [81] O. Lahav, A. Kiakotou, F. B. Abdalla, and C. Blake, "Forecasting neutrino masses from galaxy clustering in the Dark Energy Survey combined with the Planck measurements," *Monthly Notices of the Royal Astronomical Society*, vol. 405, no. 1, pp. 168–176, 2010.
- [82] T. Namikawa, S. Saito, and A. Taruya, "Probing dark energy and neutrino mass from upcoming lensing experiments of CMB and galaxies," *Journal of Cosmology and Astroparticle Physics*, vol. 1012, no. 12, Article ID 027, 2010.
- [83] T. D. Kitching, A. F. Heavens, L. Verde, P. Serra, and A. Melchiorri, "Finding evidence for massive neutrinos using 3D weak lensing," *Physical Review D*, vol. 77, no. 10, Article ID 103008, 2008.
- [84] C. Carbone, L. Verde, Y. Wang, and A. Cimatti, "Neutrino constraints from future nearly all-sky spectroscopic galaxy surveys," *Journal of Cosmology and Astroparticle Physics*, vol. 1103, no. 3, Article ID 030, 2011.
- [85] S. Hannestad, H. Tu, and Y. Y. Y. Wong, "Measuring neutrino masses and dark energy with weak lensing tomography," *Journal of Cosmology and Astroparticle Physics*, no. 6, Article ID 025, 2006.
- [86] J. R. Pritchard and A. Loeb, "21 cm cosmology," *Reports on Progress in Physics*, vol. 75, Article ID 086901, 2012.
- [87] J. Lesgourgues, L. Perotto, S. Pastor, and M. Piat, "Probing neutrino masses with CMB lensing extraction," *Physical Review D*, vol. 73, no. 4, Article ID 045021, 2006.

## Review Article

# Neutrinoless Double-Beta Decay

**Andrea Giuliani<sup>1</sup> and Alfredo Poves<sup>2</sup>**

<sup>1</sup> CNRS, Centre de Spectroscopie Nucléaire et de Spectroscopie de Masse, Bâtiment 108, Campus d'Orsay, 91405 Orsay, France

<sup>2</sup> Departamento de Física Teórica, IFT-UAM/CSIC, Universidad Autónoma de Madrid, Cantoblanco, 28049 Madrid, Spain

Correspondence should be addressed to Andrea Giuliani, [andrea.giuliani@mib.infn.it](mailto:andrea.giuliani@mib.infn.it)

Received 2 August 2012; Accepted 9 October 2012

Academic Editor: Arthur B. McDonald

Copyright © 2012 A. Giuliani and A. Poves. This is an open access article distributed under the Creative Commons Attribution License, which permits unrestricted use, distribution, and reproduction in any medium, provided the original work is properly cited.

This paper introduces the neutrinoless double-beta decay (the rarest nuclear weak process) and describes the status of the research for this transition, both from the point of view of theoretical nuclear physics and in terms of the present and future experimental scenarios. Implications of this phenomenon on crucial aspects of particle physics are briefly discussed. The calculations of the nuclear matrix elements in case of mass mechanisms are reviewed, and a range for these quantities is proposed for the most appealing candidates. After introducing general experimental concepts—such as the choice of the best candidates, the different proposed technological approaches, and the sensitivity—we make the point on the experimental situation. Searches running or in preparation are described, providing an organic presentation which picks up similarities and differences. A critical comparison of the adopted technologies and of their physics reach (in terms of sensitivity to the effective Majorana neutrino mass) is performed. As a conclusion, we try to envisage what we expect round the corner and at a longer time scale.

## 1. Introduction

The double-beta decay is the rarest nuclear weak process. It takes place between two even-even isobars, when the decay to the intermediate nucleus is energetically forbidden due to the pairing interaction, which shifts the even-even and the odd-odd mass parabolas in a given isobaric chain; therefore, only due to the pairing interaction can the double-beta decay be observed. This is seen clearly in Figure 1. The two-neutrino decay conserves the lepton number and was originally proposed by Goeppert-Mayer in 1935 [1]. It is a second-order weak process, this is the reason of its low rate, and the first direct laboratory detection was only achieved as recently as 1987 [2]. Since then, it has been measured for a dozen of



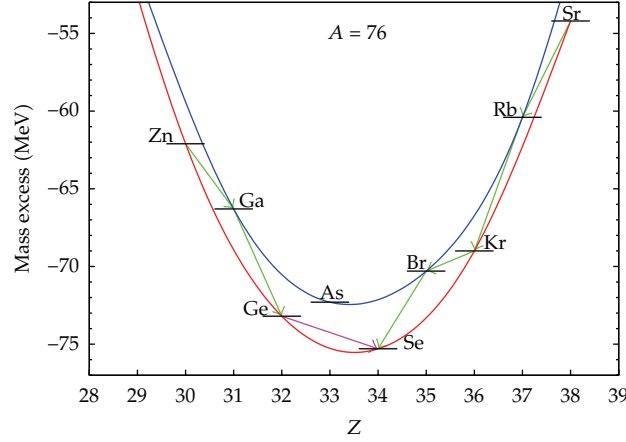


**Figure 1:** Representation of the energies of the  $A = 76$  isobars. The single-beta decay ( $\beta$ )—green arrows—between  $^{76}\text{Ge}$  and  $^{76}\text{Se}$  is energetically forbidden, hence leaving double beta ( $\beta\beta$ )—pink arrow—as the only decay channel. The two mass parabolas exist because of the pairing interaction that lowers the energy of even  $Z$ —even  $N$  nuclei with respect to odd  $Z$ —odd  $N$  nuclei. For odd  $A$  nuclei there is a single mass parabola, and all single-beta transitions are energetically allowed (taken from J. Menendez’s PhD thesis).

nuclei [3], with lifetimes in the range  $10^{18}$ – $10^{22}$  y. The alternative is the neutrinoless double-beta decay ( $0\nu\beta\beta$ ), proposed by Furry [4] after the Majorana theory of the neutrino [5]. The neutrinoless decay  $0\nu\beta\beta$  can only take place if the neutrino is a massive Majorana particle and demands an extension of the standard model of the electroweak interactions, because it violates the lepton number conservation. Therefore, the observation of the double-beta decay without emission of neutrinos will sign the Majorana character of the neutrino. The corresponding nuclear reactions are the following:

$$\begin{aligned} {}^A_Z X_N &\longrightarrow {}^A_{Z+2} X_{N-2} + 2e^- + 2\bar{\nu}_e, \\ {}^A_Z X_N &\longrightarrow {}^A_{Z+2} X_{N-2} + 2e^-. \end{aligned} \quad (1.1)$$

Currently, there is a number of experiments either taking place or expected for the near future—see, for example, [6, 7] and Section 7.3.—devoted to detect this process and to set up firmly the nature of neutrinos. Most stringent limits on the lifetime are of the order of  $10^{25}$  y. A discussed claim for the existence of  $0\nu\beta\beta$  decay in the isotope  $^{76}\text{Ge}$  (see Section 7.1) declares that the half-life is about  $2.2 \times 10^{25}$  y [8]. Furthermore, the  $0\nu\beta\beta$  decay is also sensitive to the absolute scale of the neutrino masses (if the process is mediated by the so-called mass mechanism), and hence to the mass hierarchy (see Section 2). Since the half-life of the decay is determined, together with the effective Majorana neutrino mass (defined later in Section 2), by the nuclear matrix elements for the process NME, its knowledge is essential to predict the most favorable decays and, once detection is achieved, to settle the neutrino mass scale and hierarchy.

Another process of interest is the resonant double-electron capture which could have lifetimes competitive with the neutrinoless double-beta decay ones only if there is a degeneracy of the atomic mass of the initial and final states at the eV level [9]. For the moment, high-precision mass measurements have discarded all the proposed candidates (see [10] for a recent update of the subject). As in the neutrinoless double-beta decay,

the decay rate depends on the effective Majorana neutrino mass and the NME defined in Section 3.

## 2. Neutrinoless Double-Beta Decay and New Physics

The main feature of  $0\nu\beta\beta$  decay is just the violation of the lepton number. In the modern (standard model) perspective, this is as important as the violation of the baryon number. In a very general context, we can imagine this process as a mechanism capable to *create* electrons in a nuclear transition. It is pretty evident and well known that this transition is not necessarily due the exchange of Majorana neutrinos (mass mechanism) as a leading contribution, although its observation would prove that neutrinos are self-conjugate particles [11]. Many extensions of the standard model generate Majorana neutrino masses and offer a plethora of  $0\nu\beta\beta$  decay mechanisms, like the exchange of right-handed W-bosons, SUSY superpartners with R-parity violating, leptoquarks, or Kaluza-Klein excitations, among others, which have been discussed in the literature. Possibilities to disentangle at least some of the possible mechanisms (e.g., that related to the existence of right-handed currents) rely on the analysis of angular correlations between the emitted electrons (possible only in one of the future proposed searches), the study of the branching ratios of  $0\nu\beta\beta$  decays to ground and excited states, a comparative study of the  $0\nu\beta\beta$  decay and neutrinoless electron capture with the emission of a positron, and analysis of possible links with other lepton-flavor violating processes.

However, after the discovery of neutrino flavor oscillations (which prove that neutrinos are massive particles), the mass mechanism occupies a special place. It relates neatly the  $0\nu\beta\beta$  decay to important parameters of the neutrino physics, fixes clear experimental targets, and provides a clue to compare on equal footing experiments which present considerable differences from the methodological and technological points of view. In fact, as extensively discussed in Section 3, the lifetime of the  $0\nu\beta\beta$  decay is related to the so-called effective Majorana neutrino mass, defined by the following equation:

$$\langle m_\nu \rangle = \left| \sum_k U_{ek}^2 m_k \right| = \left| \sum_k |U_{ek}|^2 m_k e^{i\alpha_k} \right|. \quad (2.1)$$

This crucial parameter contains the three neutrino masses  $m_k$ , the elements of the first row of the neutrino mixing matrix  $U_{ek}$ , and the unknown CP-violating Majorana phases  $\alpha_k$  (only two of them have a physical meaning), which make cancellation of terms possible:  $\langle m_\nu \rangle$  could be smaller than any of the  $m_k$ . Thanks to the information we have from oscillations, it is useful to express  $\langle m_\nu \rangle$  in terms of three unknown quantities: the mass scale, represented by the mass of the lightest neutrino  $m_{\min}$ , and the two Majorana phases. It is then common to distinguish three mass patterns: normal hierarchy, where  $m_1 < m_2 < m_3$ , inverted hierarchy, where  $m_3 < m_1 < m_2$ , and the quasidegenerate spectrum, where the differences between the masses are small with respect to their absolute values. We ignore Nature's choice about the neutrino mass ordering at the moment, and the  $0\nu\beta\beta$  decay has the potential to provide this essential information. In fact, if it can be experimentally established that  $\langle m_\nu \rangle \geq 50$  meV, one can conclude that the quasidegenerate pattern is the correct one and extract an allowed range of  $m_{\min}$  values. On the other hand, if  $\langle m_\nu \rangle$  lies in the range 20–50 meV, the pattern is likely inverted hierarchy, although the normal hierarchy cannot be excluded if the lightest neutrino mass sits on the far right of the allowed band. Eventually, if one could determine that

$\langle m_\nu \rangle < 20$  meV but nonvanishing, the conclusion would be that the normal-hierarchy pattern holds. It turns out therefore that  $0\nu\beta\beta$  is important over two fronts: the comprehension of fundamental aspects of elementary particle physics and the contribution to the solution of hot astroparticle and cosmological problems, related to the neutrino mass scale and nature.

### 3. Formalism

The starting point for the description of the  $0\nu\beta\beta$  decay in the mass mode is the weak Hamiltonian:

$$H_W = \frac{G}{\sqrt{2}} (j_{L\mu} J_L^{\mu\dagger}) + \text{h.c.}, \quad (3.1)$$

where  $j_{L\mu}$  is the leptonic current, and the hadronic—nuclear—counterpart is given in the impulse approximation by

$$J_L^{\mu\dagger} = \bar{\Psi} \tau^+ \left( g_V(q^2) \gamma^\mu - i g_M(q^2) \frac{\sigma^{\mu\nu}}{2M_p} - g_A(q^2) \gamma^\mu \gamma_5 + g_P(q^2) q^\mu \gamma_5 \right) \Psi, \quad (3.2)$$

with  $q^\mu$  the momentum transferred from hadrons to leptons, this is,  $q^\mu = p_{\text{neutron}}^\mu - p_{\text{proton}}^\mu$ .

In the nonrelativistic case, and discarding energy transfers between nucleons, we have

$$J_L^{\mu\dagger}(\mathbf{x}) = \sum_{n=1}^A \tau_n^- \left( g^{\mu 0} J^0(q^2) + g^{\mu k} J_n^k(q^2) \right) \delta(\mathbf{x} - \mathbf{r}_n), \quad (3.3)$$

where

$$\begin{aligned} J^0(q^2) &= g_V(q^2), \\ J_n(q^2) &= i g_M(q^2) \frac{\sigma_n \times \mathbf{q}}{2M_p} + g_A(q^2) \sigma_n - g_P(q^2) \frac{\mathbf{q}(\mathbf{q} \cdot \sigma_n)}{2M_p}. \end{aligned} \quad (3.4)$$

The parameterization of the couplings by the standard dipole form factor—to take into account the finite nuclear size (FNS)—and the use of the CVC and PCAC hypotheses—for the magnetic and pseudoscalar couplings  $g_M$  and  $g_P$ —are those described in [12]. We take as values of the bare couplings  $g_V(0) = 1$  and  $g_A(0) = 1.25$ .

Due to the high momentum of the virtual neutrino in the nucleus— $\approx 100$  MeV—we can replace the intermediate state energy by an average value and then use the closure relation to sum over all the intermediate states. This approximation is correct to better than 90% [13]. We also limit our study to transitions to  $0^+$  final states and assume electrons to be emitted in  $s$  wave. Corrections to these approximations are of the order of 1% at most, due to the fact that in the other cases effective nuclear operators of higher orders are needed to couple the initial

and final states. With these considerations, the expression for the half-life of the  $0\nu\beta\beta$  decay can be written as [14, 15]

$$\left(T_{1/2}^{0\nu\beta\beta}(0^+ \rightarrow 0^+)\right)^{-1} = G_{01} \left|M^{0\nu\beta\beta}\right|^2 \left(\frac{\langle m_\nu \rangle}{m_e}\right)^2, \quad (3.5)$$

where  $\langle m_\nu \rangle$ , the effective Majorana neutrino mass, was introduced in (2.1), and  $G_{01}$  is a kinematic factor (known also as phase-space factor)—dependent on the charge, mass, and available energy of the process, in the following denoted also as  $Q$ -value or simply  $Q$ .  $M^{0\nu\beta\beta}$  is the NME object of study in this section. As already discussed, the neutrino mass scale is directly related to the decay rate. The kinematic factor  $G_{01}$  depends on the value of the coupling constant  $g_A$ . Therefore, the NMEs obtained with different  $g_A$  values cannot be directly compared. If we redefine the NME as:

$$M'^{0\nu\beta\beta} = \left(\frac{g_A}{1.25}\right)^2 M^{0\nu\beta\beta}, \quad (3.6)$$

the new NMEs  $M'^{0\nu\beta\beta}$ 's are directly comparable no matter which was the value of  $g_A$  employed in their calculation, since they share a common  $G_{01}$  factor—the one calculated with  $g_A = 1.25$ . In this sense, the translation of  $M'^{0\nu\beta\beta}$ 's into half-lives is transparent.

The NME is obtained from the effective transition operator resulting of the product of the nuclear currents:

$$\Omega(q) = -h^F(q) + h^{GT}(q)\sigma_n\sigma_m - h^T(q)\mathbf{S}_{nm}^q, \quad (3.7)$$

where  $\mathbf{S}_{nm}^q = 3(\hat{\mathbf{q}}\sigma_n\hat{\mathbf{q}}\sigma_m) - \sigma_n\sigma_m$  is the tensor operator. The functions  $h(q)$  can be labeled according to the current terms from which they come:

$$\begin{aligned} h^F(q) &= h_{vv}^F(q), \\ h^{GT}(q) &= h_{aa}^{GT}(q) + h_{ap}^{GT}(q) + h_{pp}^{GT}(q) + h_{mm}^{GT}(q), \\ h^T(q) &= h_{ap}^T(q) + h_{pp}^T(q) + h_{mm}^T(q), \end{aligned} \quad (3.8)$$

whose explicit form can be found in [12].

Till recently, only  $h_{aa}$  and  $h_{vv}$  terms were considered. However, rough estimates of the value of these terms taking  $q \approx 100$  MeV give  $h_{aa} \approx h_{vv} \approx 1$ ,  $h_{ap} \approx 0.20$ ,  $h_{pp} \approx 0.04$ , and  $h_{mm} \approx 0.02$ . Therefore, according to the figures, certainly  $h_{ap}$  cannot be neglected. Since the Gamow-Teller contribution will be the dominant one, and both the  $h_{pp}$  and  $h_{mm}$  have the same sign and opposite to  $h_{ap}$ , it seems sensible to keep all these terms in the calculation.

Integrating over  $\mathbf{q}$ , we get the corresponding operators in position space, which are called the neutrino potentials. Before radial integration, they look like

$$\begin{aligned} V_x^{F/GT}(r) &= \frac{2}{\pi} \frac{R}{g_A^2(0)} \int_0^\infty j_0(qr) \frac{h_x^{F/GT}(q)}{(q + \mu)} q dq, \\ V_x^T(r) &= \frac{2}{\pi} \frac{R}{g_A^2(0)} \int_0^\infty -j_2(qr) \frac{h_x^T(q)}{(q + \mu)} q dq, \end{aligned} \quad (3.9)$$

where  $j_n(x)$  are the spherical Bessel functions,  $r$  is the distance between nucleons, and  $R$ , which makes the result dimensionless, is taken as  $R = r_0 A^{1/3}$ , with  $r_0 = 1.2$  fm.

Finally, the NME reads

$$\begin{aligned} M^{0\nu\beta\beta} &= - \left( \frac{g_V(0)}{g_A(0)} \right)^2 M^F + M^{GT} - M^T \\ &= \left\langle 0_f^+ \left| \sum_{n,m} \tau_n^- \tau_m^- \left( -V^F(r) + V^{GT}(r) \sigma_n \sigma_m - V^T(r) \mathbf{S}_{nm}^T \right) \right| 0_i^+ \right\rangle. \end{aligned} \quad (3.10)$$

Until very recently, the short-range correlations were taken into account in the calculation of the NME using the Jastrow prescription of [16, 17] as follows:

$$\begin{aligned} \langle 0_f^+ | V(r) | 0_i^+ \rangle_{\text{src}} &= \langle 0_f^+ f(r) | V(r) | f(r) 0_i^+ \rangle \\ &= \left\langle 0_f^+ \left| f(r)^2 V(r) \right| 0_i^+ \right\rangle, \end{aligned} \quad (3.11)$$

with  $f(r) = 1 - e^{-ar^2}(1 - br^2)$ , where  $a = 1.1 \text{ fm}^{-2}$  and  $b = 0.68 \text{ fm}^{-2}$ .

However, there has been recent proposals [18] suggesting to use a more microscopic method—namely, the unitary correlation operator method (UCOM) [19]—to estimate the SRC, which leads to a much softer correction. A fully consistent calculation of the short-range effects made in [20], which regularizes the  $0\nu\beta\beta$  operator using the same prescription as that for the bare interaction, concludes that the effect of the short-range correlations is negligible if the nucleon dipole form factors are taken into account properly.

In summary, there is a broad consensus in the community about the form of the transition operator in the mass mode, which must include the higher-order terms in the nuclear current that we have discussed, and the proper nucleon form factors. The consensus extends to the validity of the closure approximation for the calculation of the NMEs and to the use of soft (or no) short-range corrections. The situation is less clear concerning the use of bare or quenched values of  $g_A$ , and we will discuss this specific point later on.

#### 4. The Nuclear Part of the NMEs

Once the main issues related to the transition operator are settled, we are left with the purely nuclear ingredient of the neutrinoless double-beta decay NMEs, the wave functions of the initial and final states of the process. Two different methods were traditionally used



to calculate the NMEs for  $0\nu\beta\beta$  decays, the quasiparticle random-phase approximation, and the shell model in large valence spaces (ISM). The QRPA has produced results for most of the possible emitters since long [21–23]. In this method, the pairing correlations are treated in the BCS approximation and the multipole ones at the RPA level. This is an important aspect because as we will show in what follows the pairing structure of the nuclear wave functions plays a prominent role in the size of the NMEs. The ISM, that was applied only to a few cases till recently, can nowadays describe (or will do it shortly) all the experimentally relevant decays but one, the decay of  $^{150}\text{Nd}$  [24]. Other approaches sharing a common prescription for the transition operator (including higher order corrections to the nuclear current), for the treatment of the short-range correlations (SRCs) and the finite size effects, are the Interacting Boson Model [25], the Generator Coordinate Method with the Gogny force [26], and the Projected Hartree-Fock-Bogoliubov method [27].

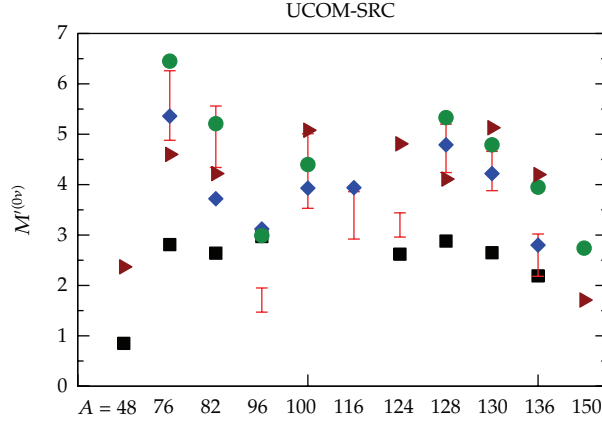
The ISM calculations are performed in different valence spaces and utilize well-tuned effective interactions which make it possible to describe with great accuracy many different observables in many different nuclei. All the details of the modern ISM approach can be found in the review of [28]. For instance, in the decay of  $^{48}\text{Ca}$ , we employ the KB3 interaction in the  $pf$  major shell. For the case of  $^{76}\text{Ge}$  and  $^{82}\text{Se}$ , the valence space consists of the  $1p_{3/2}$ ,  $0f_{5/2}$ ,  $1p_{1/2}$ , and  $0g_{9/2}$  orbits, and the interaction is the GCN28.50. Finally the  $0g_{7/2}$ ,  $1d_{3/2}$ ,  $1d_{5/2}$ ,  $2s_{1/2}$ , and  $0h_{11/2}$  valence space and the GCN50.82 interaction are used in the decays of  $^{124}\text{Sn}$ ,  $^{128}\text{Te}$ ,  $^{130}\text{Te}$ , and  $^{136}\text{Xe}$ . Notice that in these calculations, all the possible states of the valence particles in the valence states are taken into account, which leads to basis containing up to  $O(10^{10})$   $M = 0$  Slater determinants. QRPA valence spaces comprise typically two major oscillator shells. But only a minor fraction of the possible configurations are taken into account. The effect of the orbits excluded in the ISM calculations in comparison with the QRPA spaces was evaluated in [29], in the particular cases of  $A = 82$  and  $A = 136$ , and the effect was to increase the NMEs by less than 25%.

Figure 2 shows the most recent results of the different methods. We can see that in most cases the results of the ISM calculations are the smallest ones, while the largest ones may come from the IBM, QRPA, or GCM.

The difficulty is to decide upon the merit of the different approaches because of our limited understanding of the physical content of the two-body transition operator (and, indeed, the absence of any experimental anchorage). The situation is very different in the  $2\nu$  mode; the decay proceeds via the sum of virtual Gamow-Teller transitions from the initial nucleus to the  $1^+$  states of the intermediate odd-odd nucleus followed by another one to the final one. The matrix element is the sum over all the intermediate states of the products of the two Gamow-Teller amplitudes with an energy denominator (see (4.1) below):

$$M^{2\nu} = \sum_m \frac{\langle 0_f^+ | \vec{\sigma} t^- | m \rangle \langle m | \vec{\sigma} t^+ | 0_i^- \rangle}{E_m - (M_i + M_f)/2}. \quad (4.1)$$

Even without any experimental result, one could judge the validity of the predictions of the different nuclear models comparing their predictions for the  $\beta^-/\beta^+$  strength functions as measured in charge exchange reactions [32], the excitation energies of the  $1^+$  states of the intermediate nucleus, and so forth. Indeed, the ISM predictions of these observables are quite successful (see [33]) and we will come back to this issue later. In the  $0\nu$  decay, we lack of direct referents of this sort and the evaluation of the adequacy of the different methods is inevitably more ambiguous. A key point is therefore to understand better the peculiarities of



**Figure 2:** The neutrinoless double-beta decay; “state-of-the-art” NMEs: QRPA [30] (red bars) and [21, 22] (diamonds), ISM [31] (squares), IBM [25] (circles), and GCM [26] (triangles).

the  $0\nu$  operator to learn which are the properties of the initial and final nuclei to which it is more sensitive.

#### 4.1. The Role of the Pair Structure of Wave Functions in the NMEs

The two-body decay operator can be written in the Fock space representation as follows:

$$\widehat{M}^{(0\nu)} = \sum_J \left( \sum_{i,j,k,l} M_{i,j,k,l}^J \left( (a_i^\dagger a_j^\dagger)^J (a_k a_l)^J \right)^0 \right), \quad (4.2)$$

where the indices  $i, j, k$ , and  $l$  run over the single-particle orbits of the spherical nuclear mean field. Applying the techniques of [34], we can factorize the operators as follows:

$$\widehat{M}^{(0\nu)} = \sum_{J^\pi} \widehat{P}_{J^\pi}^\dagger \widehat{P}_{J^\pi}. \quad (4.3)$$

The operators  $\widehat{P}_{J^\pi}$  annihilate pairs of neutrons coupled to  $J^\pi$  in the parent nucleus, and the operators  $\widehat{P}_{J^\pi}^\dagger$  substitute them by pairs of protons coupled to the same  $J^\pi$ . The overlap of the resulting state with the ground state of the grand daughter nucleus gives the  $J^\pi$ -contribution to the NME. The—a priori complicated—internal structure of these exchanged pairs is dictated by the double-beta decay operators.

In order to explore the structure of the  $0\nu\beta\beta$  two-body transition operators, we have plotted in Figure 3 the contributions to the  $0\nu$  GT matrix element as a function of the  $J^\pi$  of the decaying pair in the  $A = 82$  and  $A = 130$  cases. The results are very suggestive, because the dominant contribution corresponds to the decay of  $J = 0$  pairs, whereas the contributions of the pairs with  $J > 0$  are either negligible or have opposite sign to the leading one. This behavior is common to all the cases that we have studied and is also present in the QRPA calculations, in whose context they had been discussed in [23, 35]. To grasp better this mechanism, we shall work in a basis of generalized seniority  $s$  ( $s$  counts the number of

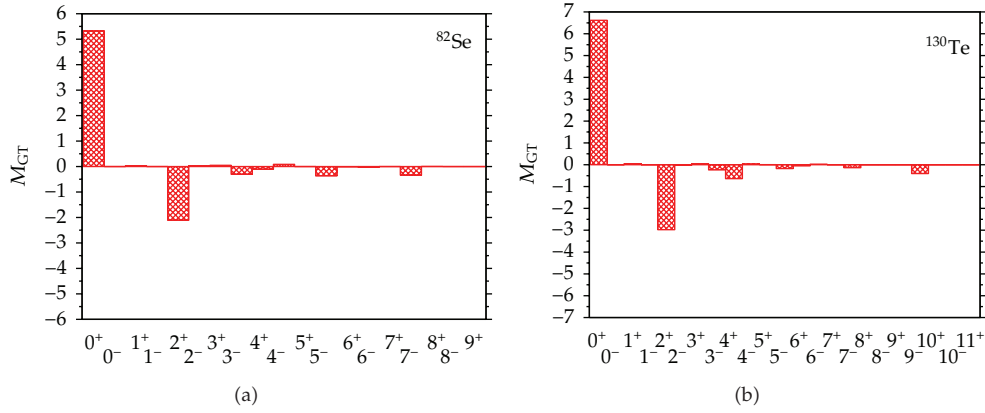


**Figure 3:** (Color online) Contributions to the Gamow-Teller matrix element of the  $^{82}\text{Se} \rightarrow ^{82}\text{Kr}$  and  $^{130}\text{Te} \rightarrow ^{130}\text{Xe}$  decays as a function of the  $J^\pi$  of the transformed pair.

**Table 1:** Decomposition of the wave function of the ground state of  $^{66}\text{Ge}$  according to its seniority components, in percentage, for different values of the deformation  $\beta$ .

$\beta$	$s = 0$	$s = 4$	$s = 6$	$s = 8$	$s = 10$
0.15	78	20	1	1	0
0.20	39	43	7	10	1
0.25	20	43	14	20	3
0.30	6	32	21	31	10

unpaired nucleons in the nucleus). If the two nuclei in the process had generalized seniority zero, only the  $J = 0$  pairs would contribute to the NME, which therefore would have a large value. This is better seen in Figure 4 where we plot the evolution of the values of the NMEs as a function of the maximum seniority which we allow in the wave functions of the decaying and stable nuclei.

It is clearly seen that truncations in seniority tend to overestimate the value of the NMEs. And this can give us a handle to evaluate the different descriptions in terms of their ability to describe properly the correlations which tend to break the nuclear Cooper pairs. High-seniority components are strongly connected to quadrupole correlations and indeed to nuclear deformation. As an example, we show in Table 1 the decomposition of the wave function of the nucleus  $^{66}\text{Ge}$ —that would exhibit a fictitious  $0\nu\beta\beta$  decay to its mirror  $^{66}\text{Se}$ —for different deformations, obtained by adding a variable extra quadrupole-quadrupole term to the interaction. It so happens that as the nucleus becomes more deformed, the high-seniority components become more important.

The next finding of this exercise is even more interesting because it gives us another clue on what is relevant in the nuclear wave functions from the NMEs point of view. We have plotted in Figure 5 the value of the NME as a function of the difference in deformation that we induce by adding the extra quadrupole-quadrupole term to the interaction only for the final nucleus  $^{66}\text{Se}$ . Notice in the first place that with the initial interaction both nuclei are mildly deformed (and their wave functions are identical after the exchange of neutrons and protons) with  $\beta \sim 0.2$ . In spite of that, the NME is a factor of two larger than the values obtained for the  $A = 76$  and  $A = 82$  decays in the same valence space and with the same

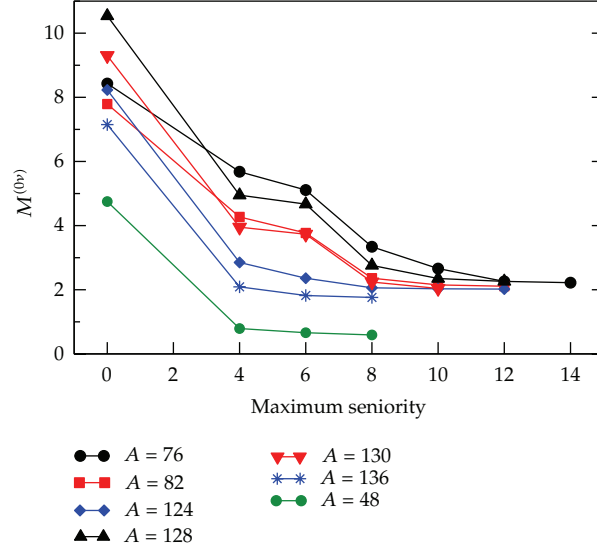


**Figure 4:** (Color online) The neutrinoless double-beta decay NMEs as a function of the maximum seniority allowed in the wave functions.

interaction. Hence, even if the two  $A = 66$  partners are deformed, the fact that their wave functions are identical enhances the decay (the fact that they are mirror nuclei also contributes to this enhancement mainly because of the Fermi contribution, which is enhanced due to the isospin selection rules). Nevertheless, the NME is still far from its expected value in the superfluid limit (NME $\sim$ 7). The figure shows that the reduction of the NME as the difference in deformation increases is very pronounced, and for  $\Delta\beta = 0.1$ , the NME is one-third of the initial one. If we increase the deformation of the two mirror nuclei by the same amount, the NME decreases as well, but less rapidly, for instance, if we deform both nuclei till  $\beta = 0.3$ , the value of the NME is reduced just by 25%.

This behavior of the NMEs with respect to the difference of deformation between parent and grand daughter is common to all the transitions between mirror nuclei that we have studied ( $A = 50$ ,  $A = 110$ ) and to more realistic cases like the  $A = 82$  decay that we have examined in detail in [36]. Therefore, we can submit that this is a robust result, that can be of importance for the only case which is for the moment out of reach of the ISM description; the decay of  $^{150}\text{Nd}$  that SNO+ will try to measure soon, because  $^{150}\text{Sm}$  is much more deformed than  $^{150}\text{Nd}$ . We have also shown in [36] that the reason for this quenching of the NME is the mismatch in seniority between the initial and final nuclei. Therefore, all the models which tend to smooth these differences and/or to overestimate the low-seniority components of the wave functions are bound to predict too large NMEs.

In Figure 6, the QRPA NMEs are compared with the ISM ones without truncation and truncated at seniority  $s = 4$ . The comparison is very telling, because the agreement of the truncated ISM results with the QRPA is surprisingly good. Hence, it is apparent that the QRPA results (and the IBM and GCM ones) fall short in capturing in full the multipole correlations in the cases where they are important, and because of this, they produce NMEs which are larger than the ISM ones.

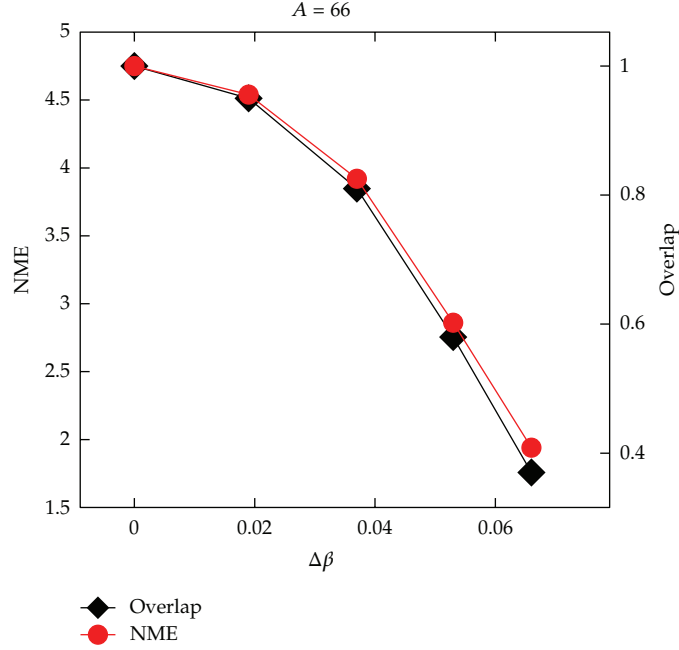


**Figure 5:**  $^{66}\text{Ge} \rightarrow ^{66}\text{Se}$  NME,  $M'^{0\nu}$ , as a function of the difference in deformation induced by an extra quadrupole interaction added to  $^{66}\text{Se}$ .

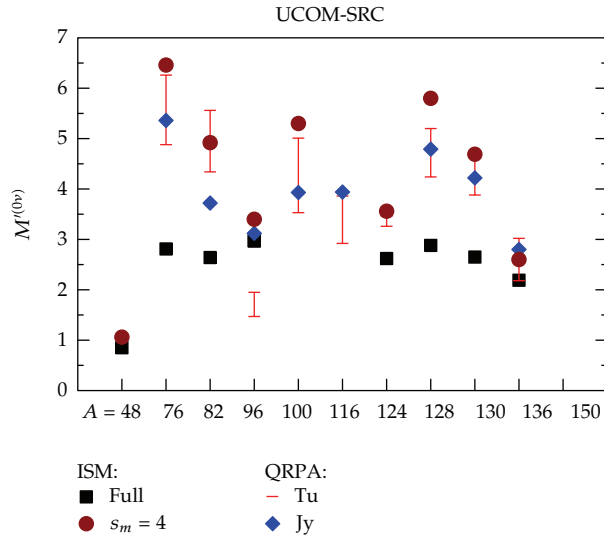


**Figure 6:** The QRPA results of Figure 2 compared with the ISM ones truncated at seniority  $s = 4$

#### 4.2. Other Benchmarks of the Nuclear Wave Functions

Even if we do not have access to observables that are unambiguously related to the neutrinoless NME, there is a plethora of experimental data which can be used to benchmark the wave functions of the participant nuclei, produced by the different nuclear models. We



**Table 2:** The GT NMEs of the  $A = 48$  decay in the generalized seniority basis.

$^{48}\text{Ti}$	$s = 0$ (59%)	$s = 4$ (36%)	$s = 6$ (4%)	$s = 8$ (1%)
$^{48}\text{Ca } s = 0$ (97%)	3.95	-3.68	—	—
$^{48}\text{Ca } s = 4$ (3%)	0.00	-0.26	0.08	-0.02

shall discuss the single  $\beta$  decays (and charge exchange data) together with the  $2\nu$  results in the context of the value of  $g_A$  which should be used in the calculations in the next section. We are aware of the fact that the different benchmarks are not independent.

(i) Shell and subshell closures: these are very prominent properties in the nuclear dynamics which should manifest in the NMEs. Indeed they do, because in this case the variations in the seniority structure between the initial and final nuclei are very abrupt, leading to very large cancellations of their NME. This is particularly acute in the decay of  $^{48}\text{Ca}$ , which is the only doubly magic nucleus candidate to neutrinoless double-beta decay and the one which has the smallest NME.

In Table 2, we show the seniority structures of  $^{48}\text{Ca}$  and  $^{48}\text{Ti}$ , and we can see that they are very different. We then compute the matrix elements  $\langle \nu_f(\beta) | O_{\text{GT}} | \nu_i(\alpha) \rangle$ , and we find the values listed in the same table. There are only two large matrix elements; one diagonal and another off-diagonal ( $\Delta s = 4$ ) of the same size and opposite sign. If the two nuclei were dominated by the seniority zero components, one should obtain  $M_{\text{GT}} \sim 4$ . If  $^{48}\text{Ti}$  were a bit more deformed,  $M_{\text{GT}}$  will be essentially zero. The value produced by the KB3 interaction is 0.75, which represents more than a factor five reduction with respect to the seniority zero limit. Earlier work on double-beta decays in a basis of generalized seniority (limited to  $s = 0$  and  $s = 4$  components) showing also this kind of cancellations can be found in [35].

Among the favored potential emitters, we have also a few cases of semimagic nuclei in which these effects are less dramatic; however, one should be aware of the fact that if a calculation overemphasizes a subshell closure, its NMEs are bound to be too small. This is possibly the situation in some calculations of the decay of  $^{96}\text{Zr}$ . Thus, all these spectroscopic issues should be verified with extreme care before trusting a NME.

(ii) Occupation numbers: another piece of information which is very relevant is provided by the analysis of the experimental spectroscopic factors of stripping and pick-up reactions that lead to the extraction of the occupation numbers of the orbits close to the Fermi level. This has been recently done for neutrons and protons in  $^{76}\text{Ge}$  and  $^{76}\text{Se}$  in a series of very careful experiments in [37, 38]. Its impact on the different calculations has been uneven; the experimental occupancies were in reasonable agreement with the ISM ones [39], while completely at odds with the QRPA ones [40, 41]. When the QRPA calculations were modified to reproduce these data, their NMEs came closer to the ISM one. There are experiments in progress for  $^{130}\text{Te}$  and  $^{130}\text{Xe}$ , but for the moment the information is limited to the neutron occupancies [42] (which by the way are not very different from the ISM ones).

(iii) Pair transfer amplitudes: in view of the important cancellations between the contributions to the NMEs coming from the transmutation of pairs of neutrons with  $J = 0^+$  and  $J \neq 0^+$ , the knowledge of the pair transfer amplitudes from and to the neighboring nuclei can be a very strict test of the nuclear wave functions. Reference [42] contains a review of the subject and a list of planned experiments.

(iv) Energy spectra and electromagnetic transitions: these are data which are traditionally the labels of the nuclear shapes and reflect the degree of multipole collectivity, superfluidity, shell closures, and so forth. We have seen that the difference in structure

between the initial and final nuclei is the major reason for the depletion of the NMEs and thus the importance of describing these properties accurately.

### 4.3. The Gamow-Teller Operator: To Quench or Not to Quench

It is a well-known fact that in order to explain the experimental transition probabilities of the Gamow-Teller decays, the predictions of any model which does not take into account explicitly the short-range correlations must be affected by a reduction factor. Quenching factors of 0.77 in the *sd*-shell, [43] and 0.74 in the *pf*-shell [44] have been extracted from fits to the experimental data in the ISM framework. The value tends asymptotically to 0.7. These results are consistent with those of a large series of charge exchange reactions, in which only about one half of the strength predicted by the Ikeda sum rule  $S_-(\text{GT}) - S_+(\text{GT}) = 3(N - Z)$  [45] was actually measured. The quenching factor can be interpreted as a kind of effective charge for the Gamow-Teller operator  $\tilde{\sigma}t^{\pm}$  due to the highly repulsive core of the nucleon-nucleon bare interaction [46]. In principle, "ab initio" calculations should be free of these limitations, but the results of the first attempts are not conclusive yet [47]. All the nuclear models that we are discussing in this paper share the need of using an effective Gamow-Teller operator for the description of the single  $\beta$  decays. And, once taken into account, they should be able to reproduce the experimental data, which so provide another important benchmark. Indeed, the ISM calculations perform quite well in this respect.

The main QRPA practitioners have had their Scylla and Charybdis with this issue, because when adjusting one of the key parameters in their calculations, the strength of the interaction in the particle-particle channel,  $g_{pp}$ , they had to sacrifice either the reproduction of the single-beta decays or the two neutrino double-beta decay transition probabilities. Finally, they have given up the single-beta decays and fixed their  $g_{pp}$ 's to the experimental half-lives of the  $2\nu$  decays. In some cases, the calculations were made both with quenched and with bare operators. In our opinion, the only consistent way of doing it is with the effective operator. In any case, as they fix the interaction case by case to the experimental data of the  $2\nu$  decays, we cannot judge on the merit of their approach in this respect.

The ISM description of the two neutrino double-beta mode started with the  $^{48}\text{Ca}$  decay in the full *pf*-shell, several years in advance of the experimental measure [48]. The prediction turned out to be quite accurate. For the other decays the situation is less favorable, because the ISM valence spaces are not complete in the sense of comprising all the spin orbit partners. In these spaces, we have made local fits to the single-beta decays, extracted the local quenching factors, and used them in the calculation of the  $2\nu$  decays, with rather satisfactory results. We have gathered all our results recently in [33].

The important question is what to do in the neutrinoless case. Contrary to the  $2\nu$ , all the multipoles contribute now to the NME, and, in fact, the channel with the Gamow-Teller quantum numbers is never dominant and quite often has opposite sign to the others. It is therefore not guaranteed that the right choice would be to affect all the channels of the quenching derived in the pure Gamow-Teller decays in the long wavelength limit. A very interesting effort to disentangle this problem was made by Hagen and Engel who went on renormalizing the two-body transition operator of the neutrinoless double-beta decay in the closure approximation in parallel to the renormalization of the bare nucleon nucleon interaction [49]. Their preliminary conclusion was that no renormalization was necessary. Another attempt along similar lines using chiral perturbation theory [47] has neither given a definite answer to this question, which is probably the major remaining source of uncertainty of the NMEs of the neutrinoless double-beta decays.

## 5. A Modest Proposal for the Ranges of Values of the NMEs

The question often posed to theorists working in this field is, what are the error bars of your NMEs? Obviously the error bar cannot be of statistical origin because we do not produce models at random. And if we could control the systematic errors, we should have done it already, hence improving our descriptions. That is why we speak of range of values in a very very loose sense. What would be nonsensical is to average the results of the different approaches blindly, without analyzing their respective merits or trends. Each one of the major methods has some advantages and drawbacks, whose effect in the values of the NME can be sometimes explored. The clear advantage of the ISM calculations is their full treatment of the nuclear correlations, while their drawback is that they may underestimate the NMEs due to the limited number of orbits in the affordable valence spaces. It has been estimated [29] that the effect can be of the order of 25%. On the contrary, the QRPA variants, the GCM in its present form, and the IBM are bound to underestimate the multipole correlations in one or another way. As it is well established that the action of the correlations is to diminish the NMEs, these methods should tend to overestimate their value. With these considerations in mind, we propose here an educated range of NME values which somehow take into account the limitations of the different approaches, very much in the mood of [50]. In what follows, we select the results of the major nuclear structure approaches which share the following common ingredients: (a) nucleon form factors of dipole shape; (b) soft short-range correlations computed with the UCOM method; (c) unquenched axial coupling constant  $g_A$ ; (d) higher-order corrections to the nuclear current; (e) nuclear radius  $R = r_0 A^{1/3}$ , with  $r_0 = 1.2$  fm. The IBM results are multiplied by 1.18 to account for the difference between Jastrow and UCOM, and the RQRPA ones are multiplied by 1.1/1.2 so as to line them up with the others in their choice of  $r_0 = 1.2$  fm. Therefore, the remaining discrepancies between the diverse approaches are solely due to the different nuclear wave functions which they employ.

Lets start with the  $^{150}\text{Nd}$  case, for which no ISM value is available. The GCM calculation [26] is clearly the most sophisticated in the market from the point of view of the nuclear structure, and gives the smallest NME. The two other approaches, QRPA [51] and IBM [25], give larger and similar results; therefore, we weight more the GCM value to propose a range [2.03–2.63] even if, in view of the precedent discussion on the effect of the missing correlations in these approaches, we could somehow overestimate it. For  $^{136}\text{Xe}$ , we have the ISM value which defines the lower end of the range, but we shall increase it by 25% to account for the limitations in the valence space (we shall apply this correction to all the ISM NMEs except the  $^{48}\text{Ca}$  one in which the ISM calculation include a full harmonic oscillator major shell). For the upper one, we average the NMEs from the RQRPA calculation of the Tubingen group [30], the GCM, the IBM, and the more recent pnQRPA result from the Jyvaskyla La Plata collaboration [40]. The resulting interval is [2.74–3.45]. With the same ingredients, we obtain a range [3.31–4.61] for  $^{130}\text{Te}$  and [3.60–4.69] for  $^{128}\text{Te}$ . For  $^{100}\text{Mo}$ , the ISM results are still preliminary, and we do not dare to offer an interval, so we propose only an upper bound of 4.23. In the  $^{96}\text{Zr}$  case, the NME depends critically on the degree of subshell neutron closure given by the calculation. The anomalously low value proposed by the QRPA calculation of the Tubingen group is surely due to this overclosure (we have checked this effect in our ISM calculation). Discarding this value, the range is [3.06–3.71] (but this time the ISM value is larger than the average of the QRPA and IBM). For  $^{82}\text{Se}$ , the interval is [3.30–4.54] using the latest SRQRPA [41]. In the case of the NME of the  $^{76}\text{Ge}$  decay, we can use an extra filter, namely, to demand that the calculations be consistent with the occupation numbers

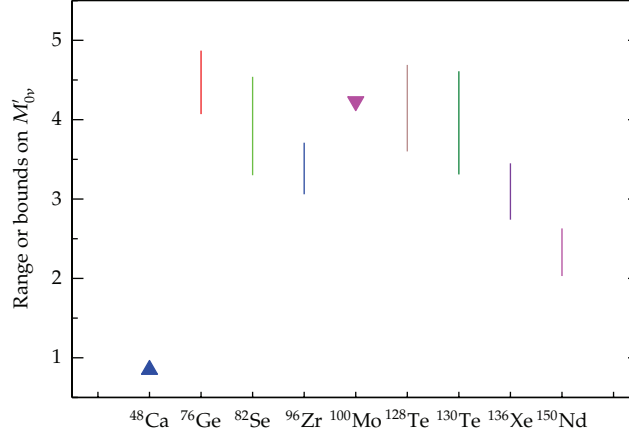


**Figure 7:** Proposed ranges of the NME values for some selected decays (see text).

measured by Schiffer and collaborators [37, 38]. This leaves us with the ISM [39], SRQRPA, and the pnQRPA. Averaging again the two QRPA values, we obtain the interval [4.07–4.87]. Finally, for the decay of  $^{48}\text{Ca}$ , we trust fully the ISM value. The GCM description of double magic nuclei is known to have serious drawbacks. Therefore, we keep the ISM value, 0.85, which can be taken as a lower bound not far from the exact value. We have gathered all these values in Figure 7. It is evident that there are two cases where the NMEs are clearly smaller than the average,  $^{48}\text{Ca}$  and  $^{150}\text{Nd}$ . For the rest of the decays, the differences in NMEs are within the uncertainty of the calculated values.

## 6. Experimental Challenge and Strategies

In the standard interpretation of neutrinoless double-beta decay in terms of mass mechanism, experimentalists designing a neutrinoless double-beta decay experiment have three hurdles to leap over in front of them. The first consists in scrutinizing the much debated  $^{76}\text{Ge}$  claim [8]: recent experimental results and present developments are very close to accomplish this task. The second one consists in approaching and then covering the inverted hierarchy region of the neutrino mass pattern. The third and ultimate goal is to explore the direct hierarchy region. In this section, we discuss the main guidelines to achieve these targets.

### 6.1. Size of the Challenge

First, we have to quantify in terms of signal and background rates the challenges that the experimentalists have to cope with. Since we do not want to be precise here, but just to assess orders of magnitude, we will make crude approximations in the formula of (3.5) which gives the rate. We will take  $M_{0\nu} \approx 3.5$  for the nuclear matrix elements (this choice is motivated by the results discussed in Section 5 and shown in Figure 7). We observe then that for most of the experimentally relevant isotopes the phase space term  $G_{01}$  (including the factor  $g_A^4$  with the axial coupling constant  $g_A$  set equal to 1.25) is in the range  $2 \times 10^{-13} - 5 \times 10^{-14} \text{ y}^{-1}$  (with significant exceptions discussed in Section 6.2). We will consider therefore a sort of “average” candidate isotope with  $M_{0\nu} = 3.5$  and  $G_{01} = 4 \times 10^{-14} \text{ y}^{-1}$ . In Table 3, we report the rates for

**Table 3:** Signal rates for an “average” double-beta decay candidate.

$\langle m_\nu \rangle$ (meV)	Signal rate (counts/(y kmol))	Significance of $\langle m_\nu \rangle$ value
300	$\sim 70$	$^{76}\text{Ge}$ claim in the Heidelberg-Moscow experiment
50	$\sim 2$	Higher bound of the inverted hierarchy region
20	$\sim 0.2$	Lower bound of the inverted hierarchy region
3	$\sim 7 \times 10^{-3}$	Center of the direct hierarchy region

1 kmol of isotope for this standard candidate in correspondence with the reference values of  $\langle m_\nu \rangle$ .

Considering that 1 kmol corresponds typically to several tens—one hundred kilograms of isotope mass, and that it is meaningful to operate a well designed  $0\nu\beta\beta$  experiment for  $\sim 5$  y, we immediately see that while scrutinizing the  $^{76}\text{Ge}$  claim may be done in principle with only  $\sim 10$  kg isotope, we need typically 1 ton of isotope mass in order to explore the inverted hierarchy region, just to accumulate a few signal counts. The direct hierarchy region seems for the moment out of the reach of the present technologies, since one would need sources of the order of 1 Mmol (typically 100 tons).

In addition, in order to appreciate such tiny signal rates, the background needs to be extremely low. The experimentalists are obliged to operate in conditions of almost zero background, given the constraints imposed by the size of the source. Acceptable background rates are of the order of 1–10 counts/(y kmol) if the goal is just to approach or touch the inverted hierarchy region, whereas one needs at least one order of magnitude lower values to explore it fully, around or even less than 1 count/(y ton).

## 6.2. Choice of the Double-Beta Decay Isotope

Which are the best isotopes to search for neutrinoless double-beta decay? Experimental practice shows that the following three factors weight the most in the design of an experiment:

- (i) the  $Q$ -value,
- (ii) the isotopic abundance together with the ease of enrichment,
- (iii) the compatibility with an appropriate detection technique.

The  $Q$ -value is probably the most important criterion. It influences both the phase space and the background. It is essentially a  $Q$ -value-based selection which determines the fact that at the moment there are only 9 experimentally relevant isotopes (listed in Table 4, which reports also other parameters and notes relevant for the discussion in the present section). The  $Q$ -values of all these isotopes are larger than 2.4 MeV, with the important exception of  $^{76}\text{Ge}$  ( $Q$ -value = 2.039 MeV) which remains in the elite mainly thanks to factor (iii). One can get a grasp of the  $Q$ -value situation in Figure 8, where all the 35 double-beta unstable nuclei are reported with their energy transition. The “magnificent nine” are highlighted. Two markers indicate two important energy limits in terms of background: the 2615 keV line represents the end-point of the natural gamma radioactivity; the 3270 keV line represents the  $Q$ -value of the  $^{214}\text{Bi}$  beta decay, which, among the  $^{222}\text{Rn}$  daughters, is the one releasing the highest-energy betas and gammas. The 9 candidates are divided by these two markers in three groups of three isotopes. The first group ( $^{76}\text{Ge}$ ,  $^{130}\text{Te}$ , and  $^{136}\text{Xe}$ ) has to cope



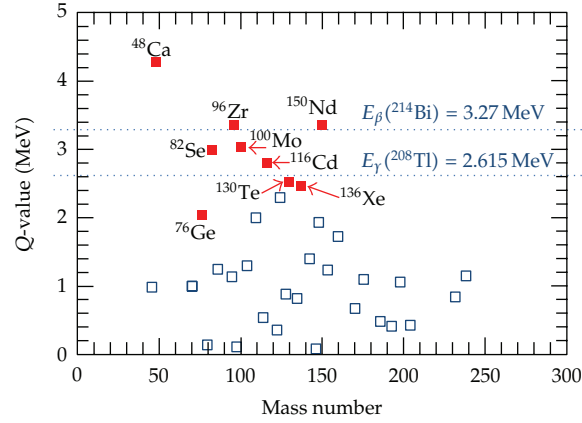


**Figure 8:** Double-beta decay candidates and their  $Q$ -values (adapted from [52]). The “magnificent nine” are highlighted and two background-relevant energy markers are indicated (see text).

**Table 4:** Relevant parameters and features of the “magnificent nine” double-beta decay candidates.

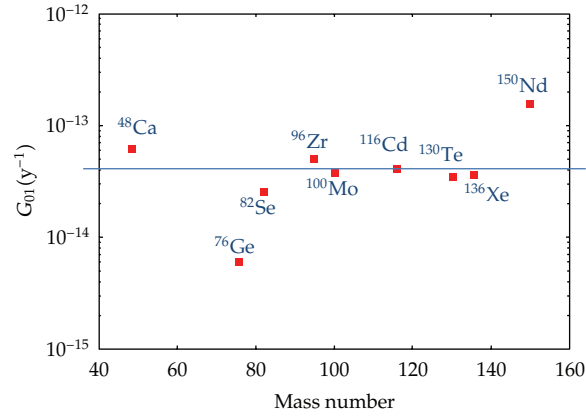
Double-beta candidate	$Q$ -value (MeV)	Phase space $G_{01}(\text{y}^{-1})$	Isotopic abundance (%)	Enrichable by centrifugation	Indicative cost normalized to Ge
$^{48}\text{Ca}$	4.27226 (404)	$6.05 \times 10^{-14}$	0.187	No	—
$^{76}\text{Ge}$	2.03904 (16)	$5.77 \times 10^{-15}$	7.8	Yes	1
$^{82}\text{Se}$	2.99512 (201)	$2.48 \times 10^{-14}$	9.2	Yes	1
$^{96}\text{Zr}$	3.35037 (289)	$5.02 \times 10^{-14}$	2.8	No	—
$^{100}\text{Mo}$	3.03440 (17)	$3.89 \times 10^{-14}$	9.6	Yes	1
$^{116}\text{Cd}$	2.81350 (13)	$4.08 \times 10^{-14}$	7.5	Yes	3
$^{130}\text{Te}$	2.52697 (23)	$3.47 \times 10^{-14}$	33.8	Yes	0.2
$^{136}\text{Xe}$	2.45783 (37)	$3.56 \times 10^{-14}$	8.9	Yes	0.1
$^{150}\text{Nd}$	3.37138 (20)	$1.54 \times 10^{-13}$	5.6	No	—

with some gamma background and with the Radon-induced one; the second group ( $^{82}\text{Se}$ ,  $^{100}\text{Mo}$ , and  $^{116}\text{Cd}$ ) is out of the reach of the bulk of the gamma environmental background but Radon may be a problem; the candidates of the third group ( $^{48}\text{Ca}$ ,  $^{96}\text{Zr}$ , and  $^{150}\text{Nd}$ ) are in the best position to realize a background-free experiment. As for the phase space, the situation is depicted in Figure 9. No great differences are observable among the various candidates, with the significant exceptions of  $^{76}\text{Ge}$ , which presents a small value of only  $\sim 6 \times 10^{-15} \text{y}^{-1}$  due to its low  $Q$  and, on the other side of  $^{150}\text{Nd}$ , characterized by a particularly high value of  $\sim 1.5 \times 10^{-13} \text{y}^{-1}$ .

As for the second criterion, natural isotopic abundances are reported in Table 4. Most of the abundances are in the few % range, with two significant exceptions: the positive case of  $^{130}\text{Te}$  that with its 33.8% value can be studied with high sensitivities even with natural samples; the negative case of  $^{48}\text{Ca}$ , well below 1%. Given the considerations exposed in Section 6.1, an ambitious experiment (aiming at exploring the inverted hierarchy region of the neutrino mass pattern) needs at least 100 kg of isotope mass. In order to keep the detector size reasonable (and recalling that the background scales roughly as the total *source*, and not *isotope*, mass), it is clear that isotopic enrichment is a necessary task for almost all high-sensitivity searches. The generally available enrichment techniques are reported in Table 5.

**Table 5:** Existing methods for isotope separation. The technologies relevant for neutrinoless double-beta decay are indicated in the fourth and in the three last lines.

Method of separation	Energy (eV/atom)	Status	Production capacity	Scale of price	Special requirements
Electromagnetic	$10^6$ – $10^7$	Commercial	~100 g/y	High	—
Gas diffusion	$3 \times 10^6$	Industrial	>tons/y	Medium	Gas compound
Gas nozzle	$10^6$	Industrial	>tons/y	Medium	Gas compound
Gas centrifuge	$3 \times 10^5$	Industrial	>tons/y	Low	Gas compound
Rectification	$10^2$	Industrial	>tons/y	Low	Light elements
Isotope exchange	$10^2$	Industrial	>tons/y	Low	Light elements
Ion cyclotron resonance	$10^3$	R&D	~100 kg/y	Medium	—
Atomic vapor laser I.S.	$10^2$	R&D	>100 kg/y	Medium	—
Molecular laser I.S.	$10^2$	R&D	>100 kg/y	Medium	—

**Figure 9:** Phase space of the nine more favourable double-beta decay isotopes (values taken from [53] and multiplied by  $g_A^4$  with the axial coupling constant  $g_A$  set at 1.25). The line refers to the “average” candidate considered in Section 6.1.

For cost, element-mass, and production-capacity reasons, the only technique extensively used so far for double-beta decay experiments is the gas-centrifuge one. Unfortunately, it can be applied only to gases. Therefore, only those elements which admit a stable gas compound can be enriched in this way. This is the case for  $^{76}\text{Ge}$ ,  $^{130}\text{Te}$ ,  $^{82}\text{Se}$ ,  $^{100}\text{Mo}$ , and  $^{116}\text{Cd}$  (normally the gas compound is a fluoride). Of course,  $^{136}\text{Xe}$  is a gas by itself. The enrichment cost is of the order of 50–100\$/g for germanium. For the other nuclides, the approximate scaling factor is reported in Table 4. For a sort of conspiracy of Nature, the three golden-plated isotopes  $^{48}\text{Ca}$ ,  $^{96}\text{Zr}$ , and  $^{150}\text{Nd}$  are not on this list. For these nuclides, other technologies have to be used, such as ion cyclotron resonance (ICR), molecular laser isotope separation (MLIS), and atomic vapor laser isotope separation (AVLIS), that, unlike gas centrifugation, are not exploited at the industrial level. Since several years, the last one is at the center of a project in France aiming at the reconversion of a facility designed to enrich uranium to the production of

$\sim 100$  kg of  $^{150}\text{Nd}$ . Recently [54], a possibility showed up to enrich Nd with centrifugation. This requires however to design special centrifuges operating at high temperatures at which a gaseous compound of neodymium is available.

The role of the third criterion will become more clear in the following sections, where specific detection technologies will be described. We would like however to discuss here three special emblematic cases in which the detector principle matches favorably with the isotope to study.

- (i)  $^{76}\text{Ge}$  large volume, high-purity, and high-energy resolution Ge-diodes are currently employed in gamma spectroscopy. A detector of this type containing germanium enriched in  $^{76}\text{Ge}$  is almost ideal for double-beta decay search. This explains why past (Heidelberg-Moscow and IGEX) and present (GERDA and Majorana) experiments were and are at the forefront in the field, in spite of the relatively low  $Q$  of this isotope.
- (ii)  $^{130}\text{Te}$  large crystals (up to 1 kg) of the compound  $\text{TeO}_2$  can be grown with high radiopurity. They can be used for the realization of bolometers with excellent performance. Given also the high natural isotopic abundance of  $^{130}\text{Te}$ , it is understandable why a past experiment like Cuoricino has been leading the field for several years, and why CUORE is one of the most promising future searches (both are based on arrays of  $\text{TeO}_2$  bolometers).
- (iii)  $^{136}\text{Xe}$  liquid and gaseous xenon is an ideal medium for particle detection. It can be used to equip TPCs with tracking/topology capability. Scintillation and ionization can provide reasonable energy resolution. This approach is exploited in experiments like EXO (now leading the field) and NEXT. In addition, xenon can be easily dissolved in organic liquid scintillators, allowing to reach very large masses exploiting existing facilities (this is the case of KamLAND-Zen). Last but not least, xenon is the element that can be isotopically enriched at the lowest prices and with the highest production capacity.

For the usual conspiracy of Nature, the three mentioned isotopes are the less favorable among the “magnificent nine” in terms of  $Q$ -value, but nevertheless they provide at the moment the most stringent limits on neutrinoless double-beta decay. This fact explains better than any digression how the detection technique remains a crucial factor for a highly sensitive search.

### 6.3. Experimental Approaches and Methods

From the experimental point of view, the shape of the two-electron sum energy spectrum enables to distinguish among the two discussed decay modes. In case of  $2\nu\beta\beta$ , this spectrum is expected to be a continuum between 0 and  $Q$  with a maximum around  $1/3 \cdot Q$ . For  $0\nu\beta\beta$ , the spectrum is just a peak at the energy  $Q$ , enlarged only by the finite energy resolution of the detector. The two distinctive energy distributions are shown in Figure 10(a). Additional signatures for the various processes are the single-electron energy distribution and the angular correlation between the two emitted electrons. As we have previously discussed,  $Q$  ranges from 2 to 3 MeV for the most promising candidates.

The experimental strategy pursued to investigate the  $0\nu\beta\beta$  decay consists of the development of a proper nuclear detector, with the purpose to reveal the two emitted electrons in real time and to collect their sum energy spectrum as a minimal information. Additional pieces of information can be provided in some cases, like single-electron energy

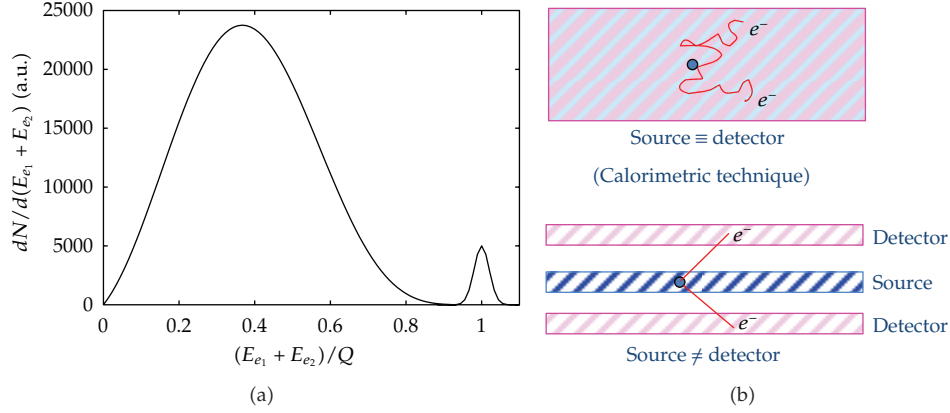


**Figure 10:** (a) Distribution of the sum of the two electron energies for  $0\nu\beta\beta$  and  $2\nu\beta\beta$ , obtained assuming that the  $2\nu\beta\beta$  rate is 100 times faster than the  $0\nu\beta\beta$ , and the FWHM detector energy resolution is 5%. (b) Schematic representation of the calorimetric technique and of the external source approach.

and initial momentum, or, in one proposed approach, the species of the daughter nucleus. The desirable features of this nuclear detector are as follows.

- (i) High-energy resolution, since a peak must be identified over an almost flat background in case of  $0\nu\beta\beta$ . In particular, this feature is very useful to keep under control the background induced by the tail of the  $2\nu\beta\beta$  spectrum. It can be shown that the ratio  $R_{0\nu/2\nu}$  of counts due to  $0\nu\beta\beta$  decay over those due to  $2\nu\beta\beta$  in a narrow window around the  $Q$ -value (of the order of the detector energy resolution) is given by the following expression [55]:

$$R_{0\nu/2\nu} = \frac{m_e}{7Q\delta^6} \frac{T_{1/2}^{2\nu\beta\beta}}{T_{1/2}^{0\nu\beta\beta}}, \quad (6.1)$$

where  $\delta = \Delta E_{\text{FWHM}}/Q$  is the fractional energy resolution at the  $Q$ -value. It is worth to note the strong dependence on the energy resolution of this expression. Candidates with a slow  $2\nu\beta\beta$  decay rate (like  $^{136}\text{Xe}$ , for which  $T_{1/2}^{2\nu\beta\beta} = 2.2 \times 10^{21}$  y) are of course more favorable than those with a fast  $2\nu$  process (like  $^{100}\text{Mo}$ , for which  $T_{1/2}^{2\nu\beta\beta} = 7.1 \times 10^{18}$  y). For the latter ones, an excellent energy resolution ( $<1\%$ ) is mandatory.

- (ii) Low background, which requires underground detector operation (to shield cosmic rays), very radiopure materials (the competing natural radioactivity decays have typical lifetimes of the order of  $10^9$ ,  $10^{10}$  years versus lifetimes longer than  $10^{25}$  years for  $0\nu\beta\beta$ ), and well-designed passive and/or active shielding against local environmental radioactivity.
- (iii) Large source, in order to monitor many candidate nuclides. Present sources are of the order of 10–100 kg in the most sensitive detectors, while experiments capable to cover the inverted hierarchy region need sources in the 100–1000 kg scale.

- (iv) Tracking and topology capability for the nuclear events, useful to reject background and to provide additional kinematical information on the emitted electrons.

Normally, the listed features cannot be met simultaneously in a single detection method. It is up to the experimentalist to choose the philosophy of the experiment and to select consequently the detector characteristics, privileging some properties with respect to others, having in mind of course the final sensitivity of the setup to half-life and to  $\langle m_\nu \rangle$ .

The searches for  $0\nu\beta\beta$  can be further classified into two main categories: the so-called calorimetric technique, in which the source is embedded in the detector itself, and the external-source approach, in which source and detector are two separate systems.

The calorimetric technique has been proposed and implemented with various types of detectors, such as scintillators, bolometers [56], solid-state devices [57], and gaseous chambers. There are advantages and limitations in this technique, which are here summarized:

- (i) due to the intrinsically high efficiency of the method, large source masses are possible:  $\sim 100$  kg has been demonstrated;  $\sim 1000$  kg is possible;
- (ii) with a proper choice of the detector type, a very high energy resolution (of the order of 0.1%) is achievable, as in Ge-diodes or in bolometers;
- (iii) there are severe constraints on detector material and therefore on the nuclides that can be investigated;
- (iv) it is difficult to reconstruct event topology, with the exception of liquid or gaseous Xe TPC, but at the price of a lower energy resolution.

For the external-source approach, many different detection techniques have been experimented as well: scintillation, gaseous TPCs, gaseous drift chambers, magnetic field for momentum and charge sign measurement, and time of flight. These are the main features, with positive and negative valence:

- (i) A neat event reconstruction is possible, making easier the achievement of a virtual zero background: however,  $0\nu\beta\beta$  cannot be distinguished by  $2\nu\beta\beta$  event by event if the total electron energy is around  $Q$ ; therefore, because of the low energy resolution,  $2\nu\beta\beta$  constitutes a severe background source for  $0\nu\beta\beta$ .
- (ii) Large source masses are not easy to achieve because of self-absorption in the source, so that the present limit is around 10 kg; 100 kg is possible with an extraordinary effort, while 1000 kg looks out of the reach of this approach.
- (iii) Normally the energy resolution is low (of the order of 10%), intrinsically limited by the fluctuations of the energy that the electrons deposit in the source itself.
- (iv) Efficiency is also low (in prospect of the order of 30%).

#### **6.4. The Experimental Sensitivity**

In order to compare different experiments, it is useful to give an expression providing the sensitivity of an experimental setup to the  $0\nu\beta\beta$  lifetime of the investigated candidate, and hence to determine the sensitivity to  $\langle m_\nu \rangle$  in case of mass mechanism. The first step involves only detector and setup parameters, while for the second step one needs reliable calculations of the NMEs, extensively discussed in Section 4. The sensitivity to lifetime  $F$  can be defined as the lifetime corresponding to the minimum detectable number of events over background



at a  $1\sigma$  confidence level. For the case of a source embedded in the detector and nonzero background, it holds

$$F = \frac{N_A \cdot \varepsilon \cdot \eta}{A} \cdot \left( \frac{M \cdot T}{b \cdot \Delta E} \right)^{1/2}, \quad (6.2)$$

where  $N_A$  is the Avogadro number,  $M$  is the detector mass (or source mass, in case of external-source approach),  $\varepsilon$  is the detector efficiency,  $\eta$  is the ratio between the total mass of the candidate nuclides and the detector (source) mass,  $\Delta E$  is the energy resolution, and  $b$  is the specific background, for example, the number of spurious counts per mass, time, and energy unit.

From this formula, one can see that in order to improve the performance of a given set-up, one can use either brute force (e.g., increasing the exposition  $M \cdot T$ ) or better technology, improving detector performance ( $\Delta E$ ) and background control ( $b$ ). Next-generation experiments require to work on both fronts.

In order to derive the sensitivity to  $\langle m_\nu \rangle$ , indicated as  $F_{\langle m_\nu \rangle}$ , one must combine (6.2) with (3.5), obtaining

$$F_{\langle m_\nu \rangle} \propto \frac{1}{(G_{01}(Q, Z))^{1/2} |M^{0\nu}|} \cdot \left( \frac{b \cdot \Delta E}{M \cdot T} \right)^{1/4}, \quad (6.3)$$

which shows how the nuclide choice is more relevant than the set-up parameters, on which the sensitivity depends quite weakly. The weak dependence on the exposure  $M \cdot T$  causes a rather fast saturation of the sensitivity. If an experiment has been run for 5 years and has established a given limit on  $\langle m_\nu \rangle$ , it must be run for further 75 years in order to improve it by a factor 2.

The formula reported in (6.2) assumes a Gaussian approximation for the distribution of the number of observed background counts. For small number of counts ( $<24$ ), the sensitivity should be computed by assuming a Poisson distribution of the background counts. However, (6.2) is extremely useful in evaluating the expected performances of prospective experiments, as it analytically links the experimental sensitivity with the detector parameters. It is a sort of “factor of merit” extensively used within the  $\beta\beta$  decay experimental community.

Nowadays, several experimental techniques promise to realize zero background investigations in the close future. In this circumstance, (6.2) and (6.3) do not hold anymore. The observation of 0 counts excludes  $N_b$  counts at a given confidence level. For instance,  $N_b = 3$  is excluded at the 95% c.l. in a Poisson statistics. Therefore, the sensitivity  $F_0$  for a 0 background experiment is given by

$$F_0 = \frac{N_A \cdot \varepsilon \cdot \eta}{A} \cdot \frac{M \cdot T}{N_b}, \quad (6.4)$$

and (6.3) modifies accordingly.

Uncertainties coming from NMEs prevent from determining precise  $\langle m_\nu \rangle$  values in correspondence to a given lifetime: normally a range is indicated, which takes into account the different models for the calculation of the NMEs.

## 7. Experimental Situation

We are now (July 2012) at a turning point in the experimental search for  $0\nu\beta\beta$  decay. In the last decade, two experiments (Cuoricino and NEMO3), now stopped, have reached an  $\langle m_\nu \rangle$  sensitivity close to the value claimed by a part of the Heidelberg-Moscow collaboration, in the range 0.2–1 eV. However, they were not able to confirm or disproof this claim, in part as a consequence of the uncertainties related to NMEs. In the meantime, several groups were preparing more ambitious searches capable to go well beyond the Heidelberg-Moscow sensitivity. In the last year, some of these searches (EXO-200, KamLAND-Zen, and GERDA) have started to take data and have released the first results, while others are in an advanced construction phase. In this section, we will review the past experiments and will describe the present experimental scenario, which is exciting and fast moving.

### 7.1. Past Experiments

In the nineties of the last century, the double-beta decay scene was dominated by the Heidelberg-Moscow (HM) experiment [58]. This search was based on a set of five Ge-diodes, enriched in the candidate isotope  $^{76}\text{Ge}$  at 86%, and operated underground with high energy resolution (typically, 4 keV FWHM) in the Laboratori Nazionali del Gran Sasso (LNGS), Italy. This search can be considered, even from the historical point of view, as the paradigm of the calorimetric approach discussed in Section 6.3. The total mass of the detectors was 10.9 kg, corresponding to a source strength of  $7.6 \times 10^{25}$   $^{76}\text{Ge}$  nuclei. The raw background, impressively low, is 0.17 counts/(keV kg y) around  $Q$  (2039 keV). It can be reduced by a further factor 5 using pulse shape analysis to reject multisite events. The limits on half-life and  $\langle m_\nu \rangle$  are, respectively,  $1.9 \times 10^{25}$  y and 0.3–0.6 eV (depending on the NMEs chosen for the analysis). A subset of the HM collaboration has however claimed the discovery of  $0\nu2\beta$  decay in 2001, with a half-life best value of  $1.5 \times 10^{25}$  y ( $(0.8 - 18.3) \times 10^{25}$  y at 95% c.l.), corresponding to a best value for  $\langle m_\nu \rangle$  of 0.39 eV (0.05 – 0.84 eV at 95% c.l. including nuclear matrix element uncertainty) [59]. This claim is based on the identification of tiny peaks in the region of the  $0\nu2\beta$  decay, one of which occurs at the  $^{76}\text{Ge}$   $Q$ -value. However, this announcement raised skepticism in the double-beta decay community [60], including a part of the HM collaboration itself [61], due to the fact that not all the claimed peaks could be identified and that the statistical significance of the peak looked weaker than the claimed  $2.2\sigma$  and dependent on the spectral window chosen for the analysis [62, 63]. However, new papers [8, 64] published later gave more convincing supports to the claim. The quality of the data treatment improved, and the exposure increased to 71.7 kg·y. In addition, a detailed analysis based on pulse shape analysis suggests that the peak at the  $^{76}\text{Ge}$   $Q$ -value is mainly formed by single-site events, as expected in case of double-beta decay, while the nearby recognized  $\gamma$  peaks are compatible with multisite events, as expected from  $\gamma$  interaction in that energy region and for detectors of that volume. A  $4.2\sigma$  effect is claimed. The half-life value claimed in the last paper is  $2.3 \times 10^{25}$  y [8]. The HM experiment is now over, and the final word on this crucial result will be given by other searches.

The top level of the external-source technique was reached nowadays by the NEMO3 experiment [65]. The NEMO3 detector, installed underground in the Laboratoire Souterrain de Modane (LSM), in France, is based on well-established technologies in experimental particle physics: the electrons emitted by the sources cross a magnetized tracking volume instrumented with Geiger cells and deliver their energy to a calorimeter based on plastic scintillators. Thanks to the division in 20 sectors of the set-up, many

nuclides can be studied simultaneously, such as  $^{100}\text{Mo}$ ,  $^{82}\text{Se}$ ,  $^{150}\text{Nd}$ ,  $^{116}\text{Cd}$ ,  $^{130}\text{Te}$ ,  $^{96}\text{Zr}$ , and  $^{48}\text{Ca}$ . The strongest source was  $^{100}\text{Mo}$  with  $4.1 \times 10^{25}$  nuclei. The energy resolution ranged from 11% to 14.5%. Results achieved with  $^{100}\text{Mo}$  fix the half-life limit to  $1 \times 10^{24}$  y, corresponding to limits of 0.8–1.3 eV on  $\langle m_\nu \rangle$ . In NEMO3 experiment, all the bonuses and all the limits of the external-source approach show off. From one side, the NEMO3 detector produces beautiful reconstruction of the sum and single-electron energy spectrum, and precious information about the angular distribution. Double-beta decay events can be neatly reconstructed with excellent background rejection. Thanks to the multisource approach,  $2\nu 2\beta$  decay has been detected in all the seven candidates under observation, a superb physical and technical achievement which makes the NEMO3 set-up a real “double-beta factory.” On the other hand, the low energy resolution and the unavoidable “bidimensional” structure of the sources make a further improvement of the sensitivity to  $0\nu 2\beta$  quite difficult, because of the background from  $2\nu 2\beta$  and the intrinsic limits in the source strength.

Bolometric detection of particles [66] is a technique particularly suitable to  $0\nu 2\beta$  search, providing high energy resolution and large flexibility in the choice of the sensitive material [56]. It can be considered the most advanced and promising application of the calorimetric technique in its high-energy resolution approach. In bolometers, the energy deposited in the detector by a nuclear event is measured by recording the temperature increase of the detector as a whole. In order to make this tiny heating appreciable and to reduce all the intrinsic noise sources, the detector must be operated at very low temperatures, of the order of 10 mK for large masses. Several interesting bolometric candidates were proposed and tested. The choice has fallen on natural  $\text{TeO}_2$  (tellurite) that has reasonable mechanical and thermal properties together with a very large (27% in mass) content of the  $2\beta$ -candidate  $^{130}\text{Te}$ . A large international collaboration has been running an experiment for five years, named Cuoricino (which means “small CUORE—heart—” in Italian), now stopped, which was based on this approach and was installed underground in the Laboratori Nazionali del Gran Sasso [67]. Cuoricino consisted of a tower of 13 modules, containing 62  $\text{TeO}_2$  crystals for a total mass of  $\sim 41$  kg, corresponding to a source strength of  $5.0 \times 10^{25}$   $^{130}\text{Te}$  nuclei. Cuoricino results are at the level of the HM experiment in terms of sensitivity to  $\langle m_\nu \rangle$ , covering a range of limits of 0.2–0.7 eV, depending on the choice of the nuclear matrix elements. A very low background (of the order of 0.18 counts/(keV kg y)) was obtained in the  $0\nu 2\beta$  decay region, similar to the one achieved in the HM set-up. The energy resolution is about 8 keV FWHM, quite reproducible in all the crystals. Unfortunately, Cuoricino, despite a sensitivity comparable to that of the HM experiment, cannot disprove the  $^{76}\text{Ge}$  claim due to the discrepancies in the nuclear matrix element calculations.

## 7.2. Features of the Present Generation Searches

In Section 6.1, we have seen that the background target for highly sensitive searches is around or even less than 1 count/(y ton), with the purpose to scrutinize without ambiguity the  $^{76}\text{Ge}$  claim and then to attack the inverted hierarchy region. In a high energy resolution experiment (with  $\Delta E_{\text{FWHM}} \sim 1$  keV), this request translates into a specific background coefficient  $b$  of the order of 1 count/(keV y ton), while the target is even more ambitious for low energy-resolution search, where however the most critical role is played by  $2\nu 2\beta$  decay. When designing a modern double-beta decay experiment and selecting a detector technology for it, the experimentalist should therefore ask himself or herself

three basic questions, the answer to which must be “yes” if that technology is viable and timely:

- (1) is the selected technology able to deal with 100 kg or better 1 ton of isotope, at least in prospect?
- (2) is the choice of the detector and of the related materials compatible with a background of the order of at most 1 count/(y ton) in the region of interest?
- (3) can the experiment be designed and constructed in a few years, and can the chosen technique provide at least 80% live time for several years?

The first question needs to be considered also from the economical point of view. As Table 4 shows, practically all the nuclei of interest, with the significant exception of  $^{130}\text{Te}$ , require isotopic enrichment. The cost of this process, when technically feasible, is in the range 10–300 \$/g. Therefore, a next-generation  $0\nu 2\beta$  experiment has a cost in the range of several tens of millions of dollars, just to get the basic material. Let us see now which solutions are under test worldwide to get a positive answer to the three questions listed above.

### 7.3. Classification and Overview of the Experiments

As already discussed in Section 6.3, two approaches are normally followed in  $0\nu 2\beta$  decay experiments (calorimetric technique and external source), and two classes of searches can be singled out depending on which experimental parameter is mostly emphasized: high energy resolution or tracking/topology capability. We will schematically review ten projects, grouped in five categories in relation with the approaches and the performance mentioned above (see Figure 11). For the half-life sensitivity, we will use the values declared by the authors, and we will translate this in a range of limits on  $\langle m_\nu \rangle$  using the results exposed in Section 5 and exposed in Figure 7. For the phase space factor, we have used the values reported in Table 4. The limits on the effective Majorana neutrino mass may therefore differ from those reported by the various collaborations, since we tried to estimate an educated guess of the NME range rather than taking indiscriminately the available calculations.

This list of ten projects do not cover the full range of existing  $0\nu\beta\beta$  searches but, according to our judgment, include the experiments with the highest chances to give important contributions to the field under discussion. Among these projects, more space will be given to those searches and techniques which have a special relevance, either for the results that they are providing at the moment or for the excellent prospects offered by the related technology.

The first category is characterized by a calorimetric approach with high energy resolution, with four planned projects.

GERDA [68] is an array of enriched Ge diodes immersed in liquid argon (rather than cooled down in a conventional cryostat) and investigating the isotope  $^{76}\text{Ge}$ . The experiment is located in LNGS, Italy. The proved energy resolution is 0.25% FWHM. The first phase (data taken from November 2011) consists of 14.6 kg of isotope mass. The second phase foresees 35 kg. As for the first phase, the predicted 1 y sensitivity to the  $0\nu\beta\beta$  half-life is  $3 \times 10^{25}$  y at 95% C.L., corresponding to a limit range on  $\langle m_\nu \rangle$  of 252–302 meV. The first phase will allow therefore to scrutinize the  $^{76}\text{Ge}$  claim. The second-phase sensitivity is  $2 \times 10^{26}$  after an exposure of 100 kg y, which gives 98–117 meV when translated in limits on the Majorana mass. The target background for the first phase was  $10^{-1}$  counts/(keV kg y). The experimental results showed a background higher by a factor two with respect to the expectations. The

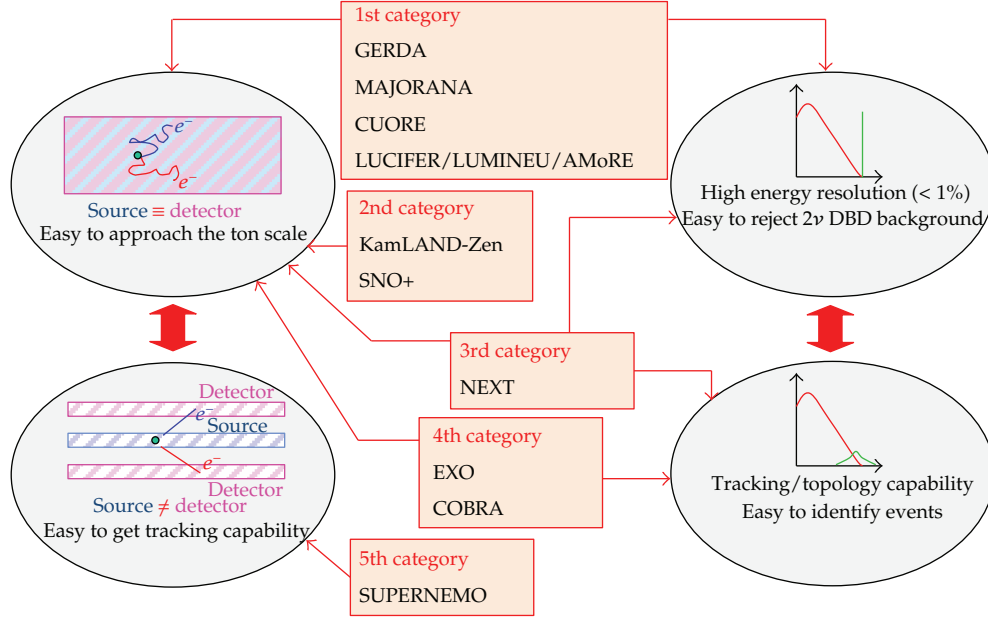


**Figure 11:** Experiments reviewed in the text are divided into five categories, according to the experimental approach and the main features of the detector performance. Running experiments are written in boldface fonts.

philosophy of the experiment is to work always in the zero background regime. Therefore, the background goal for the second phase is  $10^{-2}$  counts/(keV kg y), one order of magnitude lower than in the first phase given that the exposure will be higher by the same factor.

MAJORANA [69] is an array of enriched Ge diodes operated in conventional Cu cryostats and investigating the isotope  $^{76}\text{Ge}$ . Located in the SURF underground facility in the US, it has a modular structure, and the first step envisages the construction of a demonstrator containing 40 kg of germanium: up to 30 kg will be enriched at 86%. The proved energy resolution is 0.16% FWHM. The scope of the demonstrator is to show that a specific background level better than  $10^{-3}$  counts/(keV kg y) can be reached in 1 ton experiment. Merging with GERDA is foreseen in view of a 1 ton set-up. This corresponds to the so-called third phase of GERDA.

CUORE [70], a natural expansion of Cuoricino, will be an array of 988 natural  $\text{TeO}_2$  bolometers arranged in 19 towers and operated at 10 mK in a specially designed dilution cryostat. The total sensitive mass will be 741 kg, while the source will correspond to 200 kg of the isotope  $^{130}\text{Te}$ . CUORE will take advantage of the Cuoricino experience and will be located in LNGS, Italy. The proved energy resolution is 0.25% FWHM. The 90% C.L. 5 y sensitivity to the  $0\nu\beta\beta$  half-life is  $9.7 \times 10^{25}$  y, corresponding to a limit range on  $\langle m_\nu \rangle$  of 60–84 meV. CUORE is in the construction phase, and data taking is foreseen to start in 2014. A general test of the CUORE detector, comprising a single tower and named CUORE-0, will take data in fall 2012.

LUCIFER [71] will consist of an array of ZnSe scintillating bolometers operated at 20 mK, for the study of the isotope  $^{82}\text{Se}$ . The proof of principle with  $\sim 10$  kg enriched Se is foreseen in 2014. The proved energy resolution is better than 1% FWHM. LUCIFER is in the R&D phase, but it has however a considerable sensitivity by itself (of the order of  $\sim 100$  meV



for the effective Majorana mass). Given the high potential of the scintillating bolometers, capable to reject the harmful alpha background, other searches following this approach have recently started. In France, a project named LUMINEU will operate scintillating bolometers of the compound  $\text{ZnMoO}_4$ , for the study of the isotope  $^{100}\text{Mo}$ . In preliminary tests on this compound, resolutions better than 0.5% FWHM look feasible, and an excellent alpha discrimination power was demonstrated [72–74]. The first step of the project, that has the purpose to test the concept and measure the ultimate background, will consist of a pilot experiment consisting of an array of four crystals and containing 0.6 kg of  $^{100}\text{Mo}$ . Thanks to the foreseen zero background, this small set-up has however a remarkable sensitivity of  $5.3 \times 10^{24}$  y at 90% C.L. on the half-life of  $^{100}\text{Mo}$  [72]. It was also shown that the relatively short lifetime of  $2\nu\beta\beta$  decay of  $^{100}\text{Mo}$  does not produce dangerous background in this context [75]. In Korea, an experiment named AMoRE is developing scintillating bolometers of  $\text{CaMoO}_4$ , investigating once again the isotope  $^{100}\text{Mo}$  [76]. The AMoRE collaboration will employ crystals depleted in  $^{48}\text{Ca}$  (a source of background in this case), and enriched in  $^{100}\text{Mo}$ .

Even though these experiments do not have tracking capability, some spatial information and other tools help in reducing the background. An important asset is granularity, which is a major point for CUORE (array of 988 closely packed individual bolometers), MAJORANA (in prospect a set of modules with 57 closely packed individual Ge diodes per module), and the lower energy resolution experiment COBRA [77], discussed later (in the final design, 64000 individual semiconductor detectors). Closed packed arrays are foreseen also in the final stage of experiments based on scintillating bolometers. Granularity provides a substantial background suppression thanks to the rejection of simultaneous events in different detector elements, which cannot be ascribed to a  $0\nu\beta\beta$  process.

Another tool which can improve the sensitivity of Ge-based calorimetric searches is pulse shape analysis, already used in the HM experiment with remarkable results. It is well known that in ionization detectors one can achieve spatial information looking at the pulse shape of the current pulse. In particular, this fact will be exploited in GERDA using the so-called BEGe detectors [78], consisting of  $p$ -type HPGe devices with an  $n$ + contact covering the whole outer surface and a small  $p$ + contact located on the bottom. These detectors exhibit enhanced pulse shape discrimination properties, which can be exploited for background reduction purposes.

Other techniques to suppress background in calorimetric detectors are sophisticated forms of active shielding. For instance, the operation of the GERDA Ge diodes in liquid argon opens the way, in the second phase of the experiment, to the use of the cryogenic liquid as a scintillating active shield. In bolometers, it was clearly shown that additional bolometric elements thermally connected to the main detector in the form of thin slabs can identify events due to surface contamination [79, 80]. This is a particularly dangerous background source, presently the most limiting factor in the CUORE-predicted performance, since surface  $\alpha$ 's, degraded in energy, populate the spectral region of interest for  $0\nu\beta\beta$  decay. This shows that several refinements are possible in the high energy resolution calorimetric experiments, and that an important R&D activity is mandatory to improve the sensitivity of next-generation experiments.

A very promising development of the calorimetric approach realized by means of low-temperature detectors consists in the realization of scintillating bolometers [81], at the basis of the LUCIFER, LUMINEU, and AMoRE projects. The simultaneous detection of heat and scintillation light for the same event allows to reject  $\alpha$  particles with efficiency close to 100%, since the ratio between the photon and phonon yield is different for  $\alpha$  and for  $\gamma/\beta$

interactions. In addition, rejection by pulse shape analysis looks possible in some cases both in the heat and light channel. The  $\alpha$  rejection capability becomes formidably promising when applied to candidates with a  $Q$ -value higher than 2.6 MeV, that is, outside the natural  $\gamma$  radioactivity range, since in this case  $\alpha$ 's are the only really disturbing background source. This is the case for  $^{82}\text{Se}$  and  $^{100}\text{Mo}$ , which are the isotopes investigated in the present searches. A complete elimination of  $\alpha$ 's for these candidates could lead to specific background levels of the order of  $10^{-4}$  counts/keV/kg/y [72]. A research program in this field, partially already accomplished, has identified promising scintillating compounds of  $^{48}\text{Ca}$ ,  $^{100}\text{Mo}$ ,  $^{116}\text{Cd}$ , and  $^{82}\text{Se}$ , such as  $\text{PbMoO}_4$ ,  $\text{CdWO}_4$ ,  $\text{CaMoO}_4$ ,  $\text{SrMoO}_4$ ,  $\text{ZnMoO}_4$ ,  $\text{CaF}_2$ , and  $\text{ZnSe}$ . The choice of LUCIFER has fallen on  $\text{ZnSe}$ , because of the favorable mass fraction of the candidate, the availability of large radio-pure crystals, and the well-established enrichment/purification technology for Se. The compounds  $\text{ZnMoO}_4$  and  $\text{CaMoO}_4$  are equally promising, and this explains their use in the LUMINEU and AMoRE experiments. In nonscintillating materials like  $^{130}\text{Te}$  employed in CUORE, the  $\alpha$  rejection can be achieved exploiting the much weaker Cerenkov light (the two electrons emitted in the  $0\nu\beta\beta$  are above threshold and produce a flash of light with a total energy of approximately 140 eV). On the contrary,  $\alpha$  particles are by far below threshold and give rise to dark events. The detection of the Cerenkov light would improve dramatically the sensitivity of CUORE, providing the possibility to bring the specific background from the present  $10^{-2}$  counts/(keV kg y) to  $10^{-3}$  counts/(keV kg y). The detection of the Cerenkov light in a bolometric context, with a sensitivity allowing to fully reject  $\alpha$  events, requires exceptionally sensitive light detectors, which however look like being within the reach of recently developed technologies.

The second category of future experiments (calorimetric search with low energy resolution and no tracking capability) is represented by two samples which exploit different techniques and solve the low-energy-resolution problem with diverse measures.

KamLAND-Zen [82] is a followup of the KamLAND experiment, used for the detection of reactor neutrinos and located in the Kamioka mine in Japan. It was converted into an apparatus capable to study  $0\nu\beta\beta$  decay by dissolving Xe gas in an organic liquid scintillator contained in a nylon balloon, which, being immersed in the KamLAND set-up, is surrounded by 1 kton of liquid scintillator. The mass of the Xe-loaded scintillator is 13 tons, and the Xe weight fraction is about 2.5%, resulting in 300 kg of enriched  $^{136}\text{Xe}$ . The external scintillator works as a powerful active shield. A reasonable space resolution for interaction vertices allows to define a fiducial volume in the Xe-loaded scintillator, corresponding to 129 kg of  $^{136}\text{Xe}$ . The energy resolution at the  $Q$ -value is 10% FWHM. The purpose of the experiment was to scrutinize the  $^{76}\text{Ge}$  claim. After an exposure of  $10^4$  kg day, the experimental data showed an unexpected bump in the background structure rather close to the region of interest of  $0\nu\beta\beta$  that prevented to achieve the primary goal of the experiment. The background level was of the order of 10 counts/(50 keV) in 77.6 days, about 30 times worse than what was initially expected. Some interpretations were proposed for this peak. The most accredited one refers to a contamination of the isotope  $^{110m}\text{Ag}$ , whose decay releases a total energy of about 200 keV higher than the  $Q$ -value of  $^{136}\text{Xe}$ . This isotope could be of cosmogenic origin and could be present either in the balloon walls or in the Xe itself. In the latter case, Xe purification should reduce this background contribution, restoring the initially foreseen sensitivity of the experiment that was  $9.8 \times 10^{25}$  y at 90% C.L. in 5 y of data taking. The  $^{110m}\text{Ag}$  affair is a good example of the limitation of the low energy resolution experiments. In spite of this unexpected background source, the collaboration was able to set a significant limit on the half-life of the  $0\nu\beta\beta$  process, equal to  $5.7 \times 10^{24}$  y at 90% C.L. (corresponding to 329–414 meV for the effective Majorana mass). This result

however is obtained through a fit of the background spectrum without a really convincing background model. KamLAND-Zen has provided a superb measurement of the  $2\nu\beta\beta$  half-life of  $^{136}\text{Xe}$ , set at  $2.38 \pm 0.02(\text{stat}) \pm 0.14(\text{syst}) \times 10^{21} \text{ y}$  [82]. This was before the only missing  $2\nu\beta\beta$  measurement among the “magnificent nine.” The measured value is about 5 times shorter than a previous experimental limit on this process [83] and has confirmed a fully compatible result obtained by the EXO-200 experiment several months before [84] (see below).

SNO+ [85] is an upgrade of the solar neutrino experiment SNO, located at SNOLAB in Canada. The basic idea consists in filling the SNO detector (which contained heavy water in the solar-neutrino mode) with Nd-loaded liquid scintillator to investigate the isotope  $^{150}\text{Nd}$ . A crucial point is of course the possibility to enrich neodymium, discussed in Section 6.2. The SNO+ plan is to use 780 tons of liquid scintillator loaded with natural neodymium. If the Nd fraction is 0.1% w/w, as quoted in [85], the  $2\beta$  source results in 43.7 kg of  $^{150}\text{Nd}$ . The expected energy resolution in this configuration is 6.4% FWHM at the  $Q$ -value of  $^{150}\text{Nd}$ . There are however recent plans to increase the Nd concentration [86] up to 0.3% w/w, which gives slightly poorer energy resolution but better sensitivity. For the background rate, about 100 background events per kton of liquid scintillator and per year are expected via simulations in a 200 keV energy window around  $Q$ . The foreseen 3 y sensitivity on the half-life is  $1.3 \times 10^{25} \text{ y C.L.}$  [87], corresponding to a limit of 137–178 meV on the effective Majorana mass. Data taking with Nd-loaded scintillator is foreseen in 2014.

The third category includes an ambitious calorimetric experiment aiming at joining high energy resolution with tracking/topology capability.

NEXT [88] is a proposed 10 bar gaseous-xenon TPC, to be located in the Canfranc, Spain, and containing 89 kg of the isotope  $^{136}\text{Xe}$ . Clear two-track signature is achievable, thanks to the use of gaseous rather than liquid Xe. The estimated energy resolution is of the order of 1% FWHM, achieved thanks to the electroluminescence signal associated to the ionization electrons produced by the  $0\nu\beta\beta$  events. This is the only calorimetric experiment which is in principle capable to get reasonably high energy resolution in addition to topology capability. The experiment is in the R&D phase. Recent results on small prototypes have shown that the high-resolution target is indeed possible. The expected sensitivity, based on a simulation which foresees a specific background at the order of  $8 \times 10^{-4} \text{ counts}/(\text{keV kg y})$ , is of  $5.9 \times 10^{25} \text{ y}$  at 90% C.L., corresponding to the range 102–129 meV for the limits on  $\langle m_\nu \rangle$ .

The fourth category comprises calorimetric experiments based on detectors which compensate the low energy resolution with tracking or some form of event-topology capability. There are two samples in this group.

EXO [89] is a Xe TPC experiment which envisages a first phase known as EXO-200, which is now taking data. The second phase foresees a much higher isotope mass, in the 1–10 ton range. There is a unique case in direct-detection  $0\nu\beta\beta$  experiments; the second phase considers the possibility of tagging the Barium single ion—the  $\beta\beta$  decay daughter—by means of optical spectroscopy methods, in particular through laser fluorescence. The final state of the decay would be totally identified. If successful, this approach would eliminate any form of background, with the exception of that due to the  $2\nu\beta\beta$  decay. The EXO-200 TPC contains 200 kg of enriched liquid xenon and is located in the WIPP facility in the USA. The detector measures both the scintillation light (which provides the start signal for the TPC) and the ionization. The apparatus is capable to get topology information and to distinguish between single-site events (potential signal) and multisite events (certain background). The simultaneous exploitation of the correlated scintillation and charge signal allows to improve the energy resolution, which is 3.9% FWHM in the region of interest.

No signal was observed after an exposure of 32.5 kg yr, with a background of  $1.5 \times 10^{-3}$  counts/(keV kg yr) in the region of interest. This sets a lower limit on the half-life of the  $0\nu\beta\beta$  decay of  $^{136}\text{Xe}$  of  $1.6 \times 10^{25}$  y at 90% C.L. [90], corresponding to effective Majorana masses of less than 196–247 meV, depending on the matrix element calculation. Even if obtained with another isotope, this limit is so stringent to be in considerable tension with the  $^{76}\text{Ge}$  claim. EXO-200 has provided also the first remarkable measurement of the  $2\nu\beta\beta$  half-life of  $^{136}\text{Xe}$  [84], which resulted to be  $2.11 \pm 0.04(\text{stat}) \pm 0.21(\text{syst}) \times 10^{21}$  y, in excellent agreement with the result of KamLAND-Zen [82]. Possible improvements in the radon-induced background and in the data analysis could lead the EXO-200 sensitivity up to  $\sim 5 \times 10^{25}$  y at 90% C.L. in 4 y live time. A practical realization of the second phase, which is under study, consists in scaling up the successful EXO-200 set-up, with a sensitive mass of 4 tons of enriched xenon. This project is called nEXO [91], which could reach in a few years a sensitivity of the order of  $10^{27}$  y, allowing to explore deeply the inverted hierarchy region.

COBRA [77] is a proposed array of  $^{116}\text{Cd}$ -enriched CdZnTe semiconductor detectors at room temperature. Nine  $\beta\beta$  isotopes are under test in principle, but  $^{116}\text{Cd}$  is the only competing candidate. The final aim of the project is to deploy 117 kg of  $^{116}\text{Cd}$  with high granularity. Small-scale prototypes have been realized at LNGS, Italy. The proved energy resolution is 1.9% FWHM. The project is in R&D phase. Recent results on pixelization show that the COBRA approach may allow an excellent tracking capability, making possible, for example, a quite effective  $\alpha/\beta$  rejection.

The fifth category is represented by setups with external source (which necessarily leads to low energy resolution) and sophisticated tracking capability, allowing to reach virtually zero background in the relevant energy region (with the exception of the contribution from the  $2\nu\beta\beta$  tail). We will discuss one project belonging to this class.

SuperNEMO [92] is a proposed set-up composed by several modules containing source foils, tracking (drift chamber in Geiger mode), and calorimetric (low Z scintillator) sections. A magnetic field is present for charge sign identification. SuperNEMO will take advantage of the NEMO3 experience and will investigate  $^{82}\text{Se}$ , but the use of the golden-plated isotopes  $^{150}\text{Nd}$ ,  $^{96}\text{Zr}$ , and  $^{48}\text{Ca}$  is not excluded, if enrichment is technically feasible. As for NEMO3, SuperNEMO is the only experiment of the next generation having access to the energy distribution of the single electron and to the two-electron angular distribution. This information can lead to the identification of the leading  $0\nu\beta\beta$  mechanism (see Section 2), if the process is observed with high enough statistic. Important improvements are foreseen with respect to NEMO3, among which we mention the much larger source, the better energy resolution (from 10.5% to 7.5% FWHM), the higher efficiency (from 18% to 30%), and the much better radiopurity of the source ( $^{208}\text{Tl}$  and  $^{214}\text{Bi}$  contaminations to be improved by a factor 10 and a factor 30, resp.). The use of  $^{82}\text{Se}$ , whose  $2\nu\beta\beta$  half-life is a factor 10 slower than in  $^{100}\text{Mo}$ , reduces proportionally the contribution to the background. The radiopurity of the source is chosen so as to keep the background due to  $2\nu\beta\beta$  equal to that coming from the residual radioactive contamination: both are anticipated to be of the order of 1 counts/(100 kg y). A possible configuration foresees 20 modules with 5 kg source for each module, providing 100 kg of isotope mass. The predicted 5 y sensitivity at 90% C.L. is  $10^{26}$  y for  $^{82}\text{Se}$ , corresponding to a limit range of 71–98 meV on  $\langle m_\nu \rangle$ . The project is in an advanced R&D phase: the first module, operating as a demonstrator containing 7 kg of  $^{82}\text{Se}$ , will take data in 2013.

#### 7.4. The Technology and the Physics Race

As it is clear from the above discussion and from the experiment description, the three essential ingredients for a sensitive  $0\nu\beta\beta$  experiment are (i) a low background level in the region of interest, (ii) a corresponding high number of nuclides under observation, and (iii) the use of an intrinsically favorable candidate. We will focus now on the first point, referring in particular to (6.2), in which the expression  $b \cdot \Delta E$  appears. This combination is also crucial to define a zero-background experiment (for which  $b \cdot \Delta E \cdot T \cdot M \ll 1$ , being  $T$  the experiment duration and  $M$  the detector/source mass), whose sensitivity is given by (6.4). The two parameters  $b$  and  $\Delta E$  never appear separated, and their product is a sensible figure of merit for a given technology in terms of total background. However, if we want to use this figure of merit to compare coherently different experiments, we should express the specific background in terms of unit of number of candidate nuclides (or equivalently of a multiple of the number of moles) rather than of detector mass. We will redefine then the specific background as  $b' = N_{\text{back}} / [(E_{\text{max}} - E_{\text{min}}) \cdot T_{\text{back}} \cdot N_{\text{mol}}]$  (measured for instance in counts/(keV kmol y)), where  $[E_{\text{min}}, E_{\text{max}}]$  is the energy interval, containing the region of interest, over which a constant background can be assumed,  $T_{\text{back}}$  is the duration of the experiment aiming at fixing the background level, and  $N_{\text{mol}}$  is the number of moles of the candidate isotope which can potentially give a signal in the observed spectrum.

Figure 12 shows the plot of  $\Delta E$  (FWHM) versus  $b'$ . The diagonal lines correspond to constant values of this product. The technologies exploited by the experiments examined in Section 7.3 are represented as points on this plot, and the position of these points with respect to the diagonal lines allows a direct comparison between the various figures of merit. We have to stress that there are two types of experiments in this comparison: on one hand, past and running experiments, for which the background has already been measured; on the other hand, future searches, for which only projections and simulations are available. When possible, we have used the evaluation of the background provided by the collaborations themselves. We have to notice however that an experiment named CUORE-2 with a well-defined structure does not exist officially yet. We have hypothesized here that the background level for CUORE-2 is  $10^{-3}$  counts/(keV kg y), possible if the R&D activities ongoing to suppress the alpha background are successful. We have also assumed that CUORE-2 will be enriched. As for LUCIFER, since a precise quantitative evaluation of the background does not exist in the literature for the moment, we have used the results of simulations made for the very similar scintillating bolometers of  $\text{ZnMoO}_4$ , where a background level of  $3 \times 10^{-4}$  counts/(keV kg y) looks within the reach of this technology. For KamLAND-Zen, we have used the observed background level rather than that anticipated before running the experiment.

The points in Figure 12 are distributed in two clusters: we have a group of experiments with energy resolutions below 10 keV FWHM and another one with resolutions in the 100–300 keV range. The experiment NEXT is in between. The lowest background level was achieved by NEMO3, although EXO-200 is now challenging this primacy. Recalling the considerations made in Section 6.1, one immediately sees that many experiments use technologies capable to attain the background level (10–100 counts/(y kmol)) required to scrutinize the  $^{76}\text{Ge}$  claim (in fact, this task has been almost accomplished by EXO-200, and it will be accomplished soon by GERDA-1). In order to fully cover the quasidegenerate pattern of the neutrino mass and start to attack the inverted hierarchy region, we see that evolved forms of the calorimetric approach seem to be in the best position, even though NEXT and SuperNEMO are in the game.



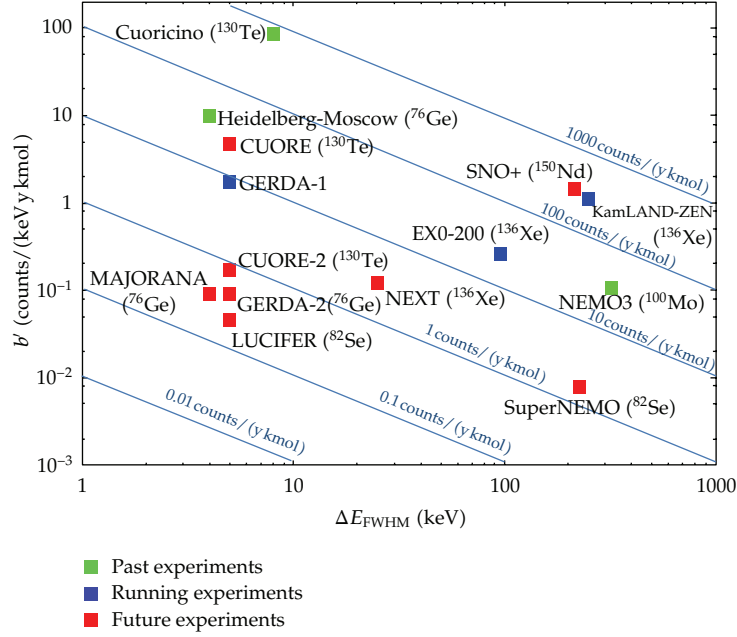


**Figure 12:** Comparison of technologies/experiments on the basis of the absolute background level they have achieved (green and blue points) or promise to achieve (red points), disentangling the role of the energy resolution  $\Delta E_{FWHM}$  from that of the specific background  $b'$  (related to the number of candidate nuclei rather than to the detector (or source) mass).

Of course, referring only to the specific background, the plot in Figure 12, while instructive, misses crucial aspects. The role played by the phase space of a given isotope does not appear. That is why, for example,  $^{76}\text{Ge}$ -based are not at all better than  $^{130}\text{Te}$ -based experiments in terms of sensitivity. Another crucial point that does not emerge is the scalability of the technique. Lower energy resolution approaches, like the ones pursued by the Xe-based experiments or searches making use of hundreds of tons of liquid scintillators as isotope solvent (KamLAND-Zen and SNO+), are much more suitable for ton or even multiton experiments.

Every approach has its good reasons, as one can see in Figure 13. Here, one can clearly see that the sensitivity reached by presently running experiments (in blue) is in the range 200–400 meV, barely at the level to scrutinize the  $^{76}\text{Ge}$  claim. Some important margins of improvement are expected for EXO-200, which is continuing data taking, and KamLAND-Zen, if the purification of Xe is successful and if other unexpected background sources do not appear. Several future searches, using a variety of technologies, should be able to cover fully the range of the claim and to approach the inverted hierarchy region.

## 8. Looking into the Crystal Ball

We discuss here the future prospects for  $0\nu\beta\beta$  search, concentrating on the very few projects that seem to be now in the position to impact substantially in the fields: GERDA (and MAJORANA), CUORE (and scintillating bolometers), EXO-200, SNO+, KamLAND-Zen, SuperNEMO, and possibly NEXT, if the achievements of the R&D phase will be confirmed also for the final detector. However, it is not possible to exclude rapid developments of the

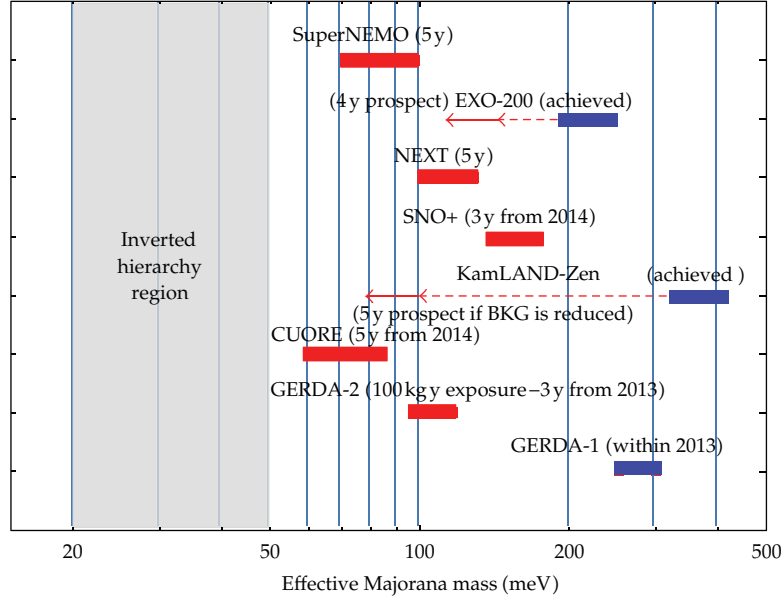


**Figure 13:** Sensitivity range to the effective Majorana neutrino mass for a set of relevant  $0\nu\beta\beta$  experiments. In blue, running experiments; in red, experiments in construction or requiring upgrades. We have used the NMEs proposed in Section 5.

present R&D programs towards real experiments. The continuation of the R&D activity is crucial, since the future of the search depends critically on the richness and variety of the technologies under development, which can lead to further increases of the sensitivities and to the possibility to study many isotopes with different approaches, essential elements in the medium long-term prospects for  $0\nu\beta\beta$  decay.

The future scenario of  $0\nu\beta\beta$  decay depends on the choice made by Nature on the neutrino mass pattern. In case of quasidegenerate pattern, that is,  $\langle m_\nu \rangle$  in the range 100–500 meV (this would be in agreement with the  $^{76}\text{Ge}$  claim), we expect the following developments.

- (i) GERDA will detect  $0\nu\beta\beta$  decay in  $^{76}\text{Ge}$ , marginally in the first phase and with high statistics in the second one.
- (ii) EXO-200 will detect  $0\nu2\beta$  decay in  $^{136}\text{Xe}$  and so would do KamLAND-Zen, if the background problems are solved. NEXT has also the chance to see it in the same isotope. These three  $^{136}\text{Xe}$  experiments could cross-check each other.
- (iii) CUORE will detect  $0\nu\beta\beta$  in  $^{130}\text{Te}$ .
- (iv) SNO+ will detect  $0\nu2\beta$  decay in  $^{150}\text{Nd}$ .
- (v) LUCIFER could detect  $0\nu2\beta$  decay in  $^{82}\text{Se}$  if the present R&D phase leads to a significant pilot experiment, and a major role could be played also by  $^{100}\text{Mo}$ -based scintillating bolometers.
- (vi) SuperNEMO may investigate the mechanism looking at the single-electron energy spectrum and at the electron angular distribution in  $^{82}\text{Se}$  or in  $^{150}\text{Nd}$ .

The redundancy of the candidates with positive observation will help in reducing the uncertainties coming from nuclear matrix element calculation: we would enter the precision

measurement era for  $0\nu 2\beta$  decay! We have however to stress that this optimistic scenario is already in tension with the present EXO-200 results.

In case of inverted hierarchy pattern, that is,  $\langle m_\nu \rangle$  in the range 20–50 meV, detection is still possible in the middle term, under the condition that the projects under development achieve the planned sensitivity in their “aggressive” version or with substantial upgrades.

- (i) CUORE could detect  $0\nu\beta\beta$  decay, more likely if enriched in  $^{130}\text{Te}$  and equipped with some method to get rid of the alpha background, or if upgraded in scintillating-bolometer mode.
- (ii) nEXO, the extension of EXO-200 under discussion, could detect  $0\nu\beta\beta$  decay in  $^{136}\text{Xe}$ .
- (iii) Extensions of KamLAND-Zen, of course after the solution of the present background problems, and of NEXT, if the first phase is successful, can also have the chance to observe  $0\nu\beta\beta$  decay in  $^{136}\text{Xe}$ .
- (iv) GERDA phase III, after merging with MAJORANA, could detect it in  $^{76}\text{Ge}$ .
- (v) SuperNEMO could marginally detect it if  $^{150}\text{Nd}$  mode will result at the end possible.
- (vi) SNO+ could detect it in  $^{150}\text{Nd}$  if Nd enrichment is viable.

The discovery in 3 or 4 isotopes is necessary for a convincing evidence, and it would be still possible thanks to the variety of projects and techniques under development. A nonobservation could be very important for neutrino physics as well. In fact, if  $0\nu\beta\beta$  experiments were able to exclude completely the inverted hierarchy region (putting say a limit on the effective Majorana mass at a level of 10–15 meV), and in the meantime future long baseline neutrino oscillation experiments discovered that the hierarchy is indeed inverted; this would be a strong indication towards a Dirac nature of neutrino.

In case of direct hierarchy pattern, that is,  $\langle m_\nu \rangle$  in the range 2–5 meV, new strategies have to be developed. At the moment, no viable solution is conceivable. However, given the importance of the subject, educated speculations on experiments with such a sensitivity are useful, and the running searches along with the R&D activities are very important to stimulate new ideas in view of this extreme challenge.

## Acknowledgments

This work was partially supported by the MICINN (Spain) (FPA2011-29854); by the Comunidad de Madrid (Spain) (HEPHACOS S2009-ESP-1473); by the Spanish Consolidated Ingenio 2010 Program, CPAN (CSD2007-00042).

## References

- [1] M. Goeppert-Mayer, “Double beta-disintegration,” *Physical Review*, vol. 48, no. 6, pp. 512–516, 1935.
- [2] S. R. Elliott, A. A. Hahn, and M. K. Moe, “Direct evidence for two-neutrino double-beta decay in  $^{82}\text{Se}$ ,” *Physical Review Letters*, vol. 59, no. 18, pp. 2020–2023, 1987.
- [3] A. S. Barabash, “Precise half-life values for two-neutrino double- $\beta$  decay,” *Physical Review C*, vol. 81, no. 3, Article ID 035501, 2010.
- [4] W. H. Furry, “On transition probabilities in double beta-disintegration,” *Physical Review*, vol. 56, no. 12, pp. 1184–1193, 1939.
- [5] E. Majorana, “Teoria simmetrica dell’elettrone e del positrone,” *Il Nuovo Cimento*, vol. 14, no. 4, pp. 171–184, 1937.
- [6] F. T. Avignone III, S. R. Elliott, and J. Engel, “Double beta decay, Majorana neutrinos, and neutrino mass,” *Reviews of Modern Physics*, vol. 80, no. 2, pp. 481–516, 2008.

- [7] J. J. Gómez-Cadenas, J. Martín-Albo, M. Mezzetto, F. Monrabal, and M. Sorel, "The search for neutrinoless double beta decay," *Rivista del Nuovo Cimento*, vol. 35, pp. 29–98, 2012.
- [8] H. V. Klapdor-Kleingrothaus and I. V. Krivosheina, "The evidence for the observation of  $0\nu\beta\beta$  decay: the identification of  $0\nu\beta\beta$  events from the full spectra," *Modern Physics Letters A*, vol. 21, no. 20, pp. 1547–1566, 2006.
- [9] J. Bernabeu, A. De Rujula, and C. Jarlskog, "Neutrinoless double electron capture as a tool to measure the electron neutrino mass," *Nuclear Physics, Section B*, vol. 223, no. 1, pp. 15–28, 1983.
- [10] M. I. Krivoruchenko, F. Šimkovic, D. Frekers, and A. Faessler, "Resonance enhancement of neutrinoless double electron capture," *Nuclear Physics A*, vol. 859, no. 1, pp. 140–171, 2011.
- [11] J. Schechter and J. W. F. Valle, "Neutrinoless double-decay in  $SU(2)\times U(1)$  theories," *Physical Review D*, vol. 25, no. 11, pp. 2951–2954, 1982.
- [12] F. Šimkovic, G. Pantis, J. D. Vergados, and A. Faessler, "Additional nucleon current contributions to neutrinoless double  $\beta$  decay," *Physical Review C*, vol. 60, no. 5, Article ID 055502, 1999.
- [13] K. Muto, "Neutrinoless double beta decay beyond closure approximation," *Nuclear Physics Section A*, vol. 577, no. 1-2, pp. 415–420, 1994.
- [14] M. Doi, T. Totani, H. Nishiura, K. Okuda, and E. Takasugi, "Neutrino masses and the double  $\beta$  decay," *Physics Letters B*, vol. 103, pp. 219–224, 1981.
- [15] M. Doi, T. Kotani, and E. Takasugi, "Double  $\beta$  decay and Majorana neutrino," *Progress of Theoretical Physics*, vol. 83, p. 1, 1985.
- [16] H. F. Wu, H. Q. Song, T. T. S. Kuo, W. K. Cheng, and D. Strottman, "Majorana neutrino and Lepton-Number non-conservation in  $^{48}\text{Ca}$  nuclear double beta decay," *Physics Letters B*, vol. 162, no. 4-6, pp. 227–232, 1985.
- [17] G. A. Miller and J. E. Spencer, "A survey of pion charge-exchange reactions with nuclei," *Annals of Physics*, vol. 100, no. 1-2, pp. 562–606, 1976.
- [18] M. Kortelainen, O. Civitarese, J. Suhonen, and J. Toivanen, "Short-range correlations and neutrinoless double beta decay," *Physics Letters Section B*, vol. 647, no. 2-3, pp. 128–132, 2007.
- [19] H. Feldmeier, T. Neff, R. Roth, and J. Schnack, "A unitary correlation operator method," *Nuclear Physics A*, vol. 632, no. 1, pp. 61–95, 1998.
- [20] F. Šimkovic, A. Faessler, H. Muther, V. Rodin, and M. Stauf, "The neutrinoless double beta decay matrix elements with selfconsistent short range correlations," *Physical Review C*, vol. 79, Article ID 055501, 2009.
- [21] M. Kortelainen and J. Suhonen, "Improved short-range correlations and the  $0\nu\beta\beta$  nuclear matrix elements of  $^{76}\text{Ge}$  and  $^{82}\text{Se}$ ," *Physical Review C*, vol. 75, Article ID 051303, 2007.
- [22] M. Kortelainen and J. Suhonen, "Nuclear matrix elements of neutrinoless double beta decay with improved short-range correlations," *Physical Review C*, vol. 76, Article ID 024315, 2007.
- [23] V. A. Rodin, A. Faessler, F. Šimkovic, and P. Vogel, "Assessment of uncertainties in QRPA  $0\nu\beta\beta$ -decay nuclear matrix elements," *Nuclear Physics A*, vol. 793, p. 213, 2007.
- [24] E. Caurier, J. Menéndez, F. Nowacki, and A. Poves, "Influence of pairing on the nuclear matrix elements of the neutrinoless  $\beta\beta$  decays," *Physical Review Letters*, vol. 100, no. 5, Article ID 052503, 2008.
- [25] J. Barea and F. Iachello, "Neutrinoless double- $\beta$  decay in the microscopic interacting boson model," *Physical Review C*, vol. 79, no. 4, Article ID 044301, 2009.
- [26] T. R. Rodríguez and G. Martínez-Pinedo, "Energy density functional study of nuclear matrix elements for neutrinoless  $\beta\beta$  decay," *Physical Review Letters*, vol. 105, Article ID 252503, 2010.
- [27] R. Chandra, K. Chaturvedi, P. K. Rath, P. K. Raina, and J. G. Hirsch, "Multipolar correlations and deformation effect on nuclear transition matrix elements of double- $\beta$  decay," *Europhysics Letters*, vol. 86, no. 3, Article ID 32001, 2009.
- [28] E. Caurier, G. Martínez-Pinedo, A. Poves, and A. P. Zuker, "The shell model as unified view of the nuclear structure," *Reviews of Modern Physics*, vol. 77, p. 425, 2005.
- [29] E. Caurier, F. Nowacki, and A. Poves, "Nuclear-structure aspects of the neutrinoless  $\beta\beta$  -decays," *European Physical Journal A*, vol. 36, no. 2, pp. 195–200, 2008.
- [30] F. Šimkovic, A. Faessler, V. Rodin, P. Vogel, and J. Engel, "Anatomy of the nuclear matrix elements of the neutrinoless  $\beta\beta$  decay," *Physical Review C*, vol. 77, Article ID 045503, 2008.
- [31] J. Menéndez, A. Poves, E. Caurier, and F. Nowacki, "Disassembling the nuclear matrix elements of the neutrinoless  $\beta\beta$  decay," *Nuclear Physics A*, vol. 818, no. 3-4, pp. 139–151, 2009.
- [32] P. Puppe, "High-resolution ( $^3\text{He},t$ ) reaction on the double- $\beta$  decaying nucleus  $^{136}\text{Xe}$ ," *Physical Review C*, vol. 84, Article ID 051305, 2011.

- [33] E. Caurier, F. Nowacki, A. Poves, and J. Retamosa, "Shell model studies of the double beta decays of  $^{136}\text{Xe}$ ," *Physics Letters B*, vol. 711, p. 62, 2012.
- [34] M. Dufour and A. P. Zuker, "Realistic collective nuclear Hamiltonian," *Physical Review C*, vol. 54, no. 4, pp. 1641–1660, 1996.
- [35] J. Engel, P. Vogel, X. Ji, and S. Pittel, "Double beta decay in the generalized-seniority scheme," *Physics Letters B*, vol. 225, no. 1-2, pp. 5–9, 1989.
- [36] J. Menéndez, "Deformation and the nuclear matrix elements of the neutrinoless  $\beta\beta$  decay," in *Proceedings of the International School Enrico Fermi, Course 170*, F. Ferroni, F. Vissani, and C. Brofferio, Eds., p. 163, IOS press, 2009.
- [37] J. P. Schiffer, S. J. Freeman, J. A. Clark et al., "Nuclear structure relevant to neutrinoless double  $\beta$  decay:  $^{76}\text{Ge}$  and  $^{76}\text{Se}$ ," *Physical Review Letters*, vol. 100, no. 11, Article ID 112501, 2008.
- [38] B. P. Kay, J. P. Schiffer, S. J. Freeman et al., "Nuclear structure relevant to neutrinoless double  $\beta$  decay: the valence protons in  $^{76}\text{Ge}$  and  $^{76}\text{Se}$ ," *Physical Review C*, vol. 79, no. 2, Article ID 021301, 2009.
- [39] J. Menéndez, A. Poves, E. Caurier, and F. Nowacki, "Occupancies of individual orbits, and the nuclear matrix element of the  $^{76}\text{Ge}$  neutrinoless  $\beta\beta$  decay," *Physical Review C*, vol. 80, no. 4, Article ID 048501, 2009.
- [40] J. Suhonen and O. Civitarese, "Effects of orbital occupancies on the neutrinoless  $\beta\beta$  matrix element of  $^{76}\text{Ge}$ ," *Physics Letters Section B*, vol. 668, no. 4, pp. 277–281, 2008.
- [41] F. Simkovic, A. Faessler, and P. Vogel, "The neutrinoless  $\beta\beta$  nuclear matrix elements and the occupancies of the individual orbits," *Physical Review C*, vol. 79, Article ID 015502, 2009.
- [42] S. J. Freeman and J. P. Schiffer, "Constraining the  $0\nu2\beta$  matrix elements by nuclear structure observables," *Journal of Physics G*, vol. 39, Article ID 124004, 2012.
- [43] B. H. Wildenthal, M. S. Curtin, and B. A. Brown, "Predicted features of the beta decay of neutron-rich sd-shell nuclei," *Physical Review C*, vol. 28, no. 3, pp. 1343–1366, 1983.
- [44] G. Martinez-Pinedo, A. Poves, E. Caurier, and A. P. Zuker, "The effective  $g_A$  in the pf shell," *Physical Review C*, vol. 53, Article ID R2602, 1996.
- [45] K. Ikeda, S. Fujii, and J. I. Fujita, "The (p,n) reactions and beta decays," *Physics Letters*, vol. 3, no. 6, pp. 271–272, 1963.
- [46] V. R. Pandharipande, I. Sick, and P. K. A. DeWitt Huberts, "Independent particle motion and correlations in fermion systems," *Reviews of Modern Physics*, vol. 69, no. 3, pp. 981–992, 1997.
- [47] J. Menéndez, D. Gazit, and A. Schwenk, "Chiral two-body currents in nuclei: Gamow-Teller transitions and neutrinoless double-beta decay," *Physical Review Letters*, vol. 107, no. 6, Article ID 062501, 2011.
- [48] E. Caurier, A. Poves, and A. P. Zuker, "A full  $0\hbar\omega$  description of the  $2\nu\beta\beta$  decay of  $^{48}\text{Ca}$ ," *Physics Letters*, vol. 252, p. 13, 1990.
- [49] J. Engel and G. Hagen, "Corrections to the neutrinoless double- $\beta$ -decay operator in the shell model," *Physical Review C*, vol. 79, no. 6, Article ID 064317, 2009.
- [50] J. J. Gomez-Cadenas, "Sense and sensitivity of double beta decay experiments," *Journal of Cosmology and Astroparticle Physics*, vol. 06, article 007, 2011.
- [51] D. -L. Fang, A. Faessler, V. Rodin, and F. Simkovic, "The neutrinoless  $\beta\beta$  decay of  $^{150}\text{Nd}$  with account for deformation," *Physical Review C*, vol. 82, Article ID 051301, 2010.
- [52] F. Šimkovic, "Double beta decay: a problem of particle, nuclear and atomic physics," *Progress in Particle and Nuclear Physics*, vol. 64, no. 2, pp. 219–227, 2010.
- [53] J. Kotila and F. Iachello, "Phase-space factors for double- $\beta$  decay," *Physical Review C*, vol. 85, Article ID 034316, 2012.
- [54] F. Piquemal, Private communication.
- [55] S. R. Elliot and P. Vogel, "Double Beta decay," *Annual Review of Nuclear and Particle Science*, vol. 52, pp. 115–151, 2002.
- [56] E. Fiorini and T. O. Niinikoski, "Low temperature calorimetry for rare decays," *Nuclear Instruments and Methods in Physics Research A*, vol. 224, p. 83, 1984.
- [57] G. F. Dell'Antonio and E. Fiorini, "Experimental and theoretical remarks on the double  $\beta$ -decay," *Il Nuovo Cimento*, vol. 17, no. 1, pp. 132–193, 1960.
- [58] H. V. Klapdor-Kleingrothaus, A. Dietz, L. Baudis et al., "Latest results from the HEIDELBERG-MOSCOW double beta decay experiment," *European Physical Journal A*, vol. 12, no. 2, pp. 147–154, 2001.
- [59] H. V. Klapdor-Kleingrothaus, A. Dietz, H. L. Harney, and I. V. Krivosheina, "Evidence for neutrinoless double beta decay," *Modern Physics Letters A*, vol. 16, no. 37, pp. 2409–2420, 2001.



- [60] C. E. Aalseth, A. S. Barabash, F. Böhm et al., "Comments on "Evidence for Neutrinoless Double Beta Decay"," *Modern Physics Letters A*, vol. 17, p. 1475, 2002.
- [61] A. M. Bakalyarov, A. Y. Balysh, S. T. Belyaev, V. I. Lebedev, and S. V. Zhukov, "Results of the experiment on investigation of Germanium-76 double beta decay," in *Proceedings of the NANP*, Dubna, Russia, 2003.
- [62] F. Feruglio, A. Strumia, and F. Vissani, "Neutrino oscillations and signals in  $\beta$  and  $0\nu 2\beta$  experiments," *Nuclear Physics B*, vol. 637, no. 1–3, pp. 345–377, 2002.
- [63] Y. G. Zdesenko, F. A. Danevich, and V. I. Tretyak, "Has neutrinoless double  $\beta$  decay of  $^{76}\text{Ge}$  been really observed?" *Physics Letters Section B*, vol. 546, no. 3–4, pp. 206–215, 2002.
- [64] H. V. Klapdor-Kleingrothaus, I. V. Krivosheina, A. Dietz, and O. Chkvorets, "Search for neutrinoless double beta decay with enriched  $^{76}\text{Ge}$  in Gran Sasso 1990–2003," *Physics Letters Section B*, vol. 586, no. 3–4, pp. 198–212, 2004.
- [65] A. S. Barabash and The Nemo Collaboration, "NEMO 3 double beta decay experiment: latest results," *Journal of Physics*, vol. 173, Article ID 012008, 2009.
- [66] A. Giuliani, "Particle and radiation detection with low-temperature devices," *Physica B*, vol. 280, no. 1–4, pp. 501–508, 2000.
- [67] C. Arnaboldi, "Results from a search for the  $0\nu\beta\beta$ -decay of  $^{130}\text{Te}$ ," *Physical Review C*, vol. 78, Article ID 035502, 2008.
- [68] S. Schönert, I. Abt, M. Altmann et al., "The GERmanium DETECTOR ARRAY (GERDA) for the search of neutrinoless  $\beta\beta$  decays of Ge-76 at LNGS," *Nuclear Physics B*, vol. 145, p. 242, 2005.
- [69] V. Giuseppe and (Majorana Collaboration), "The Majorana experiment," *Nuclear Physics B*, vol. 217, p. 44, 2011.
- [70] C. Arnaboldi, F. T. Avignone, J. Beeman et al., "Physics potential and prospects for the Cuoricino and CUORE experiments," *Astroparticle Physics*, vol. 20, p. 91, 2003.
- [71] A. Giuliani, I. Dafinei, F. Ferroni et al., "LUCIFER: an experimental breakthrough in the search for neutrinoless double beta decay," in *Proceedings of the BEYOND*, Cape Town, South Africa, 2010.
- [72] J. W. Beeman, F. A. Danevich, V. Y. Degoda et al., "A next-generation neutrinoless double beta decay experiment based on  $\text{ZnMoO}_4$  scintillating bolometers," *Physics Letters B*, vol. 710, p. 318, 2012.
- [73] J. W. Beeman, F. Bellini, S. Capelli et al., " $\text{ZnMoO}_4$ : a promising bolometer for neutrinoless double beta decay searches," *Astroparticle Physics*, vol. 35, p. 813, 2012.
- [74] J. W. Beeman, F. Bellini, C. Brofferio et al., "Performances of a large mass  $\text{ZnMoO}_4$  scintillating bolometer for a next generation neutrinoless double beta decay experiment," *European Physical Journal C*, vol. 72, no. 9, p. 2142, 2012.
- [75] D. M. Chernyak, F. A. Danevich, A. Giuliani, E. Olivieri, M. Tenconi, and V. I. Tretyak, "Random coincidence of  $2\nu 2\beta$  decay events as a background source in bolometric  $0\nu 2\beta$  decay experiments," *The European Physical Journal C*, vol. 72, article 1989, 2012.
- [76] S. J. Lee, J. H. Choi, F. A. Danevich et al., "The development of a cryogenic detector with  $\text{CaMoO}_4$  crystals for neutrinoless double beta decay search," *Astroparticle Physics*, vol. 34, pp. 732–737, 2011.
- [77] K. Zuber, "COBRA—double beta decay searches using CdTe detectors," *Physics Letters Section B*, vol. 519, no. 1–2, pp. 1–7, 2001.
- [78] M. Agostini, E. Bellotti, R. Brugnera et al., "Characterization of a broad energy germanium detector and application to neutrinoless double beta decay search in  $^{76}\text{Ge}$ ," *Journal of Instrumentation*, vol. 6, no. 4, Article ID P04005, 2011.
- [79] L. Foggetta, A. Giuliani, C. Nones, M. Pedretti, and S. Sangiorgio, "Surface-sensitive macrobolometers for the identification of external charged particles," *Applied Physics Letters*, vol. 86, no. 13, Article ID 134106, pp. 1–3, 2005.
- [80] L. Foggetta, A. Giuliani, C. Nones, M. Pedretti, C. Salvioni, and S. Sangiorgio, "Composite macro-bolometers for the rejection of surface radioactive background in rare-event experiments," *Astroparticle Physics*, vol. 34, no. 11, pp. 809–821, 2011.
- [81] S. Pirro, J. W. Beeman, S. Capelli, M. Pavan, E. Previtali, and P. Gorla, "Scintillating double-beta-decay bolometers," *Physics of Atomic Nuclei*, vol. 69, no. 12, pp. 2109–2116, 2006.
- [82] A. Gando and KamLAND-Zen Collaboration, "Measurement of the double- $\beta$  decay half-life of  $^{136}\text{Xe}$  with the KamLAND-Zen experiment," *Physical Review C*, vol. 85, 2012.
- [83] R. Bernabei, P. Belli, F. Cappella et al., "Investigation of  $\beta\beta$  decay modes in  $^{134}\text{Xe}$  and  $^{136}\text{Xe}$ ," *Physics Letters Section B*, vol. 546, no. 1–2, pp. 23–28, 2002.
- [84] N. Ackermanm and EXO Collaboration, "Observation of two-neutrino double-beta decay in  $^{136}\text{Xe}$  with the EXO-200 detector," *Physical Review Letters*, vol. 107, Article ID 212501, 2011.

- [85] C. Kraus and S. J. M. Peeters, "The rich neutrino programme of the SNO+ experiment," *Progress in Particle and Nuclear Physics*, vol. 64, no. 2, pp. 273–277, 2010.
- [86] B. V. Krosigk and SNO+ Collaboration, "Status of the SNO+ experiment," in *Proceedings of The 11th International Conference on Heavy Quarks and Leptons*, Prague, Czech Republic, 2012.
- [87] N. Fatemi-Ghomi and SNO+ Collaboration, private communication, 2012.
- [88] V. Alvarez and NEXT Collaboration, "The NEXT-100 experiment for neutrinoless double beta decay searches (Conceptual Design Report)," <http://arxiv.org/abs/1106.3630>.
- [89] M. Danilov, R. DeVoe, A. Dolgolenko et al., "Detection of very small neutrino masses in double-beta decay using laser tagging," *Physics Letters Section B*, vol. 480, no. 1-2, pp. 12–18, 2000.
- [90] M. Auger, D. J. Auty, P. S. Barbeau et al., "Search for neutrinoless double-beta decay in  $^{136}\text{Xe}$  with EXO-200," *Physica Scripta Review Letters*, vol. 109, no. 3, Article ID 032505, 2012.
- [91] A. Piepke and E. X. O. collaboration, "Double beta decay: EXO-200 and beyond," in *Fundamental Symmetries and Neutrinos Meeting*, Chicago, Ill, USA, 2012.
- [92] Y. Shitov and SuperNEMO Collaboration, "A search for neutrinoless double beta decay: from NEMO-3 to SuperNEMO," <http://arxiv.org/abs/1006.4775>.

## Research Article

# A Quantum Sensor for Neutrino Mass Measurements

**Juan Manuel Cornejo and Daniel Rodríguez**

*Departamento de Física Atómica Molecular y Nuclear, Universidad de Granada, 18071 Granada, Spain*

Correspondence should be addressed to Daniel Rodríguez, [danielrodriguez@ugr.es](mailto:danielrodriguez@ugr.es)

Received 6 July 2012; Accepted 7 September 2012

Academic Editor: Jose Bernabeu

Copyright © 2012 J. M. Cornejo and D. Rodríguez. This is an open access article distributed under the Creative Commons Attribution License, which permits unrestricted use, distribution, and reproduction in any medium, provided the original work is properly cited.

There are few experiments aiming at determining directly the mass of the electron antineutrino with a sensitivity of 0.2 eV by analyzing the end of the  $\beta$ -decay spectrum of specific nuclei. This sensitivity can be only reached if the uncertainties arising from systematic effects are very small and very well determined. The same holds for experiments aiming at improving the sensitivity in the determination of the mass of the electron neutrino using electron-capture ( $\epsilon$ )-decaying nuclei. One important input in these cases is an accurate  $Q$ -value of the decay which can be unambiguously determined from the difference of the mass of the mother and the daughter nuclei by means of Penning traps. In order to reach the required sensitivity, a novel device called *Quantum Sensor* is under construction at the University of Granada (Spain). The device will allow measuring atomic masses, and therefore  $Q$ -values from decays with unprecedented accuracy and sensitivity, using fluorescence photons from a laser-cooled ion instead of electronic detection. This paper will give an overview on  $Q$ -value measurements performed with Penning traps, relevant for neutrino mass spectrometry, describing the Quantum Sensor and the facility under construction. It will end by presenting the status of the project.

## 1. Introduction

Experimental results from atmospheric, solar, and reactor neutrino sources identified neutrino oscillations and established that neutrinos have rest masses [1–4]. However, neutrino oscillations are only sensitive to the differences of squared masses of different neutrino mass eigenstates. Absolute masses can be determined either by studying weak decays, that is, by determining the shape of the  $\beta$ -decay or, X-ray spectrum after electron capture ( $\epsilon$ -decay), near the endpoint with good statistics and without systematic uncertainties and fit it with the neutrino mass as free parameter [5, 6], or being able to measure the half-life of nuclei undergoing double  $\beta$ -decay transformations [7, 8]. The latter is a second-order weak process which has a very small transition probability. While the fit of the  $\beta$ -decay spectrum, or X-ray spectrum from  $\epsilon$ -decay, allows for determining the mass

independently whether the neutrino is a Dirac or Majorana particle, a successful half-life measurement from neutrinoless double  $\beta$ -decay ( $0\nu\beta\beta$ ) or double electron-capture ( $0\nu ee$ ) experiments would allow determining the Majorana neutrino mass, thus establishing the nature of the neutrino.

Either for single or double  $\beta(\epsilon)$  decay transformations, a precise and unambiguous measurement of the  $Q$ -value of the transition, is of significant importance and can be provided only using Penning traps. These devices can provide the highest accuracy in the determination of the mass of atomic nuclei [9, 10] and, since the  $Q$ -value from  $\beta$ , double  $\beta$ ,  $\epsilon$ , or double  $\epsilon$  decay can be determined from the difference of the masses of the mother and the daughter nuclei, Penning traps provide the highest accuracy in the determination of this energy. The role of the  $Q$ -value in neutrino physics varies depending on the experimental goal. The use of the  $Q$ -value obtained from Penning-trap measurements to fit accurately the energy window to search events from ( $0\nu\beta\beta$ )-decay on any of the eleven identified nuclides [11], or to conclude whether the predicted resonance enhancement for ( $0\nu ee$ )-decay for some specific nuclides exists [7], requires a relative mass uncertainty ( $\delta m/m$ ) ranging from  $10^{-8}$  to  $10^{-9}$ , which is in reach with several Penning-trap facilities (see, e.g., [12, 13]). For the determination of the mass of the electron (anti)neutrino from  $\beta$  or  $\epsilon$ -decay, the candidates more suitable are those with small  $Q$ -values. Since a large number of possible sources of systematic errors exist, any additional information or constraint is highly wanted. For the determination of  $m_{\bar{\nu}_e}$  from  $\beta$ -decay, a very important constraint is the endpoint energy  $E_0(m_{\bar{\nu}_e} = 0)$  for vanishing antineutrino mass as obtained by a measurement of the  $Q$ -value using high-accuracy mass spectrometry. The difference  $E = E_0(m_{\bar{\nu}_e} = 0) - E_0(m_{\bar{\nu}_e} \neq 0)$  must equal the mass of the electron antineutrino  $m_{\bar{\nu}_e}$ . From  $\epsilon$ -decay,  $m_{\bar{\nu}_e}$  can be obtained from the difference between the  $Q$ -value and the endpoint energy of the X-ray spectrum that originated from the decay of the daughter nucleus to the ground state. Either for  $\beta$  or  $\epsilon$ -decay, the  $Q$ -value must be very accurately measured requesting in some cases relative mass uncertainties better than  $10^{-11}$ .

There are two experiments in the world under construction by large international collaborations which envisage to measure the mass of the electron antineutrino with a sensitivity of 0.2 eV from single  $\beta$ -decay: the KARlsruhe TRItium Neutrino experiment (KATRIN) [14] and the Micro-calorimeter Array for a Rhenium Experiment (MARE) [15]. This sensitivity is one order of magnitude better compared to the present limit ( $m_{\bar{\nu}_e} < 2$  eV at 95% C. L.) [5], achieved by use of electrostatic retardation spectrometers at Troitsk [16] and Mainz [17], measuring the end of the  $\beta$ -decay spectrum of tritium ( $T_{1/2} = 12.3$  years)

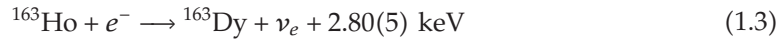
$$T_2 \longrightarrow \left({}^3\text{HeT}\right)^+ + e^- + \bar{\nu}_e + 18.5898(12) \text{ keV} \quad (1.1)$$

(see [18]). The KATRIN collaboration will also measure the  $\beta$ -decay spectrum of tritium, but with an spectrometer scaled up in diameter by a factor of 10 compared to the one in Mainz. The main spectrometer vessel has a diameter of 10 m and a length of 24 m, making it the largest mass spectrometer in the world. The MARE collaboration uses a totally different approach based on bolometers to measure the end of the  $\beta$ -decay spectrum of rhenium ( $T_{1/2} = 43.2 \times 10^9$  years)

$${}^{187}\text{Re} \longrightarrow {}^{187}\text{Os} + e^- + \bar{\nu}_e + 2.4653(17) \text{ keV} \quad (1.2)$$

(see [19]). There are two experiments from the same collaboration preceding MARE, called MANU [20] and MIBETA [19]. Measurements with MANU have yielded an upper limit for  $m_{\bar{\nu}_e}$  of 26 eV using a crystal of 1.5 mg of metallic rhenium cooled down to 60 mK with an activity of 1 Bq. The results with the MIBETA detector constrained further the upper limit down to 15 eV. MIBETA is comprised of 10 AgReO<sub>4</sub> crystals, 300  $\mu$ g each. The MARE collaboration has also as final goal the measurement of the mass of the electron antineutrino with a sensitivity of 0.2 eV [15, 21], but it will develop in two steps, that is, MARE I aiming at reaching 2 eV and MARE II aiming at improving this sensitivity by a factor of 10.

The MARE collaboration also plans to utilize the same technique, based on bolometers, to determine the mass of the electron neutrino with high sensitivity by measuring the  $\epsilon$ -decay from  $^{163}\text{Ho}$  ( $T_{1/2} = 4.5 \times 10^3$  years)



(see [6]). Though the  $Q$ -value is close to the one from the decay of  $^{187}\text{Re}$ , the half-life is seven orders of magnitude shorter. The main difficulty seems to be the implantation of pure  $^{163}\text{Ho}$  on the detector, as this radioisotope is produced in reactions with strong isobaric contamination [6]. Very recently, a group at the Kirchhoff-Institute for Physics in Heidelberg (Germany) has presented the use of low-temperature metallic magnetic calorimeters to measure the spectra following the  $\epsilon$ -decay of  $^{163}\text{Ho}$  (as well as the  $\beta$ -decay of  $^{187}\text{Re}$ ) [22]. The group succeeded to implant the  $^{163}\text{Ho}$  into the absorber of the detector. The experiment yielded a  $Q$ -value of 2.80(8) keV. Though some technical problems arising from the isobaric contamination of the sample have to be solved, the results are already very promising. The group at the Kirchhoff-Institute for Physics together with other groups has gathered in the ECHO (Electron Capture HOLmium experiment) Collaboration aiming at reaching in a short time scale a sensitivity on  $m_{\nu_e}$  of a few eV.

The  $Q$ -value given in (1.1) with  $\delta Q = 1.2$  eV has been determined from the difference of the masses of  $^3\text{H}$  ( $\delta m/m = 8.3 \times 10^{-10}$ ) and  $^3\text{He}$  ( $\delta m/m = 8.6 \times 10^{-10}$ ) using the SMILETRAP facility [18, 23]. A dedicated Penning-trap experiment is in operation at the Max-Planck Institute for Nuclear Physics (MPIK) in Heidelberg in the group of K. Blaum in order to reach an uncertainty in the determination of the  $Q$ -value of 0.1 eV [24], which corresponds to a relative mass uncertainty of a few times  $10^{-11}$ . Besides the group at the MPIK, the group of E.G. Myers at Florida State University is also preparing an experiment to measure the  $Q$ -value of the tritium decay using a Penning trap [25].

The  $Q$ -value given in (1.2) with  $\delta Q = 1.7$  eV has been obtained from the same experiment as the upper limit for the mass of the electron antineutrino [19]. Similarly, the  $Q$ -value given in (1.3) with  $\delta Q = 50$  eV has been obtained from the measurements performed with a bolometer setup [26]. In both cases, a different approach should be used, in order to obtain a result independent of systematic sources arising from the detectors. However, the masses of the nuclei involved in the rhenium and holmium decay are a factor of 60 and 54, respectively, larger compared to the masses of  $^3\text{H}$  and  $^3\text{He}$ . In the case of  $^{187}\text{Re}$ , this forces the determination of the mass with  $\delta m/m \sim 1.0 \times 10^{-11}$  to use the  $Q$ -value in combination with the outcomes from the MARE I campaign, and  $\delta m/m \sim 1.0 \times 10^{-12}$  in order to complement the results obtained in the second campaign (MARE II). A relative mass uncertainty of  $10^{-11}$  is within the present limit of Penning trap mass spectrometry and only demonstrated for low or medium mass-to-charge ratios [10]. A relative mass uncertainty of  $1.0 \times 10^{-12}$  is not in reach. Note that almost the same applies for the decay of  $^{163}\text{Ho}$ .



With the aim to improve the current performance, a novel device called *Quantum Sensor* is under development at the University of Granada using laser cooling in combination with the Penning trap [27]. The measurement of the atomic mass will be carried out using a system comprising two Penning traps with a common endcap, one for the ion under investigation and the other to confine a  $^{40}\text{Ca}^+$  ion which is laser-cooled to mK temperatures and will act as *sensor*. Since the ions are coupled via their axial oscillation frequencies, it is possible to exchange their motional energies. The cyclotron motion of the ion under investigation is transformed into axial motion along the magnetic field lines of the Penning trap and coupled to the sensor ion by the image current induced in the common endcap. The axial motion of the sensor ion in turn is monitored spatially resolved by its fluorescence light. In this way the detection of phonons is upgraded to a detection of photons.

## 2. The Penning Trap and the *Quantum Sensor*

In a Penning trap, charged particles are stored by the combination of a strong homogeneous magnetic field ( $\vec{B}$ ) and a nearly perfect quadrupole electrostatic field [28, 29]. The magnetic field is generated by a superconducting solenoid while the quadrupole field is performed by applying DC potentials to a set of electrodes with hyperbolical shapes as shown in the left side of Figure 1. In order to confine particles with positive polarity, the DC potential is applied either to the endcaps with respect to the ring electrode at ground (positive polarity) or to the ring with respect to the endcaps at ground (negative polarity). The right side of Figure 1 shows the electronic representation of a single ion with mass  $m$  and electronic charge  $q$  oscillating in the trap with a frequency  $\omega$  [30].

The motion of any ion with mass-to-charge ratio  $m/q$  stored in an ideal Penning trap can be described as the superposition of three independent motions, one in the direction of the magnetic field lines, called axial motion, with a characteristic oscillation frequency

$$\nu_z = \frac{1}{2\pi} \sqrt{\frac{qU}{md^2}}, \quad (2.1)$$

where  $d$  is a parameter related to the characteristics dimensions of the trap by

$$d = \sqrt{\frac{z_0^2}{2} + \frac{r_0^2}{4}}, \quad (2.2)$$

and two motions in the radial plane, which are named modified cyclotron and magnetron. Their characteristic frequencies are

$$\nu_{\pm} = \frac{\nu_c}{2} \pm \sqrt{\frac{\nu_c^2}{4} - \frac{\nu_z^2}{2}}, \quad (2.3)$$

where

$$\nu_c = \frac{1}{2\pi} \cdot \frac{q}{m} \cdot B \quad (2.4)$$

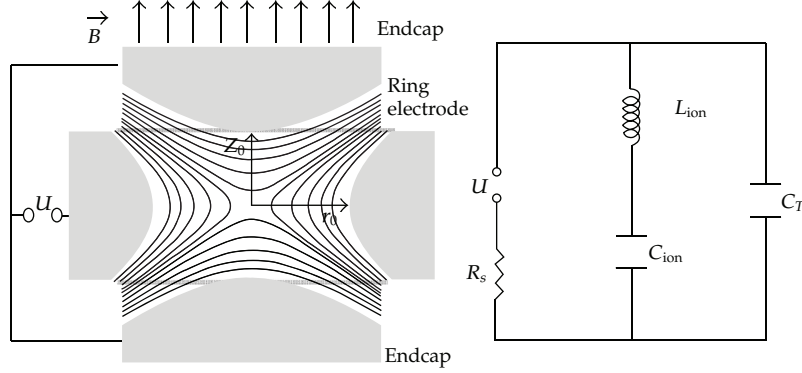


**Figure 1:** (right) Longitudinal projection of a hyperbolic Penning trap with cylindrical symmetry along the  $z$ -axis.  $U$  is the DC potential applied to the endcaps with respect to the ring. Due to the shape of the electrodes, the equipotential lines are hyperboloids of revolution.  $r_0$  and  $z_0$  give the characteristics dimensions of the Penning trap and are related by  $r_0 = \sqrt{2}z_0$ . (left) Equivalent circuit of the Penning trap with one stored ion. The ion can be described as an inductance ( $L_{\text{ion}} = m(2z_0)^2/q^2$ ) in series with a capacitor ( $C_{\text{ion}} = 1/(\omega^2 L_{\text{ion}})$ ).  $C_T$  gathers all the capacitances between the trap electrodes or between the electrodes and ground.  $R_s$  is the internal resistance of the power supply.

is the cyclotron frequency of the ion moving in a magnetic field in the absence of any electric field.

Each of the motions has associated an oscillation amplitude ( $\rho_+$ ,  $\rho_z$ , and  $\rho_-$ , resp.). The reduction of these amplitudes, normally referred to as cooling, is important, especially to perform precision experiments, since when the ions move close to the center of the trap, they are less sensitive to inhomogeneities of the magnetic field or to imperfections of the quadrupole potential created by unavoidable deviations of the trap electrodes from the ideal hyperboloidal geometry. Any cooling mechanism should provide a nonconservative force acting in the direction of the motions so as to reduce the ion energy. Cooling to very low temperatures improves also the sensitivity of the detection by reducing the thermal-noise level, which is important for some detection techniques in Penning-trap mass spectrometry. There are several mechanisms to cool the ions in a trap.

- (i) Cooling by collisions with buffer gas atoms or molecules [31] which is very general and applied in all Penning trap mass spectrometers installed at radioactive ion beam facilities.
- (ii) Resistive cooling by connecting the endcaps of the Penning trap, which has a capacitance  $C$ , with an outer inductance  $L$ , such that the oscillation frequency of the ion equals that of the  $LC$ -circuit [30].
- (iii) Laser cooling, provided the ionic level scheme of the ion allows for optical excitation [32]. This cooling method can provide the by far lowest temperatures.
- (iv) Sympathetic cooling. Here the cooling of the ion of interest is due to Coulomb interaction with an ion which can be cooled directly. For example, in [33],  $\text{Hg}^+$  ions were cooled by Coulomb interaction with laser-cooled  $\text{Be}^+$  ions.
- (v) Evaporative cooling. This cooling technique starts off with a cloud of ions. The hottest ions are forced to leave the trap until a single ion is left over which is the coldest one.

In a Penning trap, after cooling, the mass-to-charge ratio of the ion of interest is determined from its cyclotron frequency provided the magnetic field strength is known. The magnetic field strength  $B$  can be obtained from the cyclotron frequency measurement of an ion with well-known mass stored in the trap. The mass of the ion of interest  $(m/q)^{\text{ion}}$  can be written as

$$\left(\frac{m}{q}\right)^{\text{ion}} = \left(\frac{m}{q}\right)^{\text{ref}} \cdot \frac{\nu_c^{\text{ref}}}{\nu_c^{\text{ion}}}, \quad (2.5)$$

where the superscript ref represents the reference ion. The atomic mass can then be obtained by

$$m_{\text{atomic}} = \frac{\nu_c^{\text{ref}}}{\nu_c^{\text{ion}}} \cdot (m_{\text{ref}} - m_e - B_e) + m_e, \quad (2.6)$$

where  $B_e$  is the binding energy of the outer electron which is very accurately known and  $m_e$  is the mass of the electron measured with an uncertainty of about 10 meV. The cyclotron frequency can be measured using either the relationship

$$\nu_c = \nu_+ + \nu_-, \quad (2.7)$$

which only holds in the case of an ideal Penning trap [34], or the relationship

$$\nu_c^2 = \nu_+^2 + \nu_z^2 + \nu_-^2, \quad (2.8)$$

which is known as the invariance theorem and holds for the real Penning trap [28, 34]. Currently, there are two techniques which are used for the determination of  $\nu_c$ , namely, the time-of-flight (tof) resonance technique [35] used at the Penning-trap systems coupled to Radioactive Ion Beams (RIB) [29, 36] and the Induced-Image-Current (IIC) resonance technique applied to atomic ions from stable isotopes, molecular ions, or subatomic particles and antiparticles [9, 10, 37, 38]. A third technique referred to as *Quantum Sensor* (QS) is under development to push the present performance in Penning-trap mass spectrometry [27].

### 2.1. The TOF Resonance Technique

It is based on the coupling of the modified-cyclotron and magnetron motions by applying an external radiofrequency (RF) quadrupole field [35]. After probing the ions with the RF field, the cyclotron frequency is obtained from the time-of-flight spectra of the ions ejected from the trap and registered with a microchannel plate detector located outside the magnetic field lines. The time-of-flight spectrum is measured for different RF frequencies ( $\nu_{\text{RF}}$ ) around  $\nu_c$ . The mean time-of-flight of the distribution is plot versus  $\nu_{\text{RF}}$  and will be minimum for  $\nu_{\text{RF}} = \nu_c$  (resonance). There are variants of this technique which allows reaching a better relative mass uncertainty: the use of spatially separated quadrupole fields [39] for probing the ions or the use of higher-order multipolar fields [40, 41]. The determination of the cyclotron frequency using the tof technique requires several tens of ions, and, with sufficient statistics, it is possible

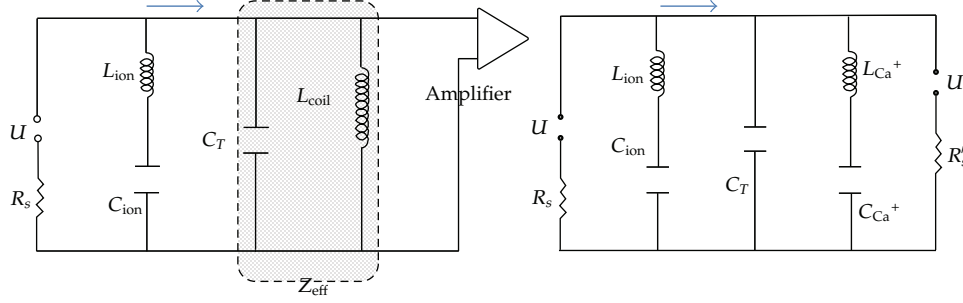


**Figure 2:** (right) Electronic equivalent of the ion in the trap attached to an external coil to apply the IIC technique. The inductance of the coil is taken so that the axial oscillation frequency of the ions in the trap is equal to the resonance frequency of the  $L_{\text{coil}}C_T$ -circuit. In this way, the circuit provides an effective impedance for the induced current (arrow in the top) before further amplification. The system must be operated at cryogenic temperature so that the electronic noise is minimum. (left) Electronic representation of the two ions connected via a common endcap. The energy is transferred from the ion of interest to the sensor ion within a time according to (2.9). The laser-cooled ion is at mK temperature and therefore more sensitive to the motion of the ion of interest. Since this is oscillating at very low energy (equivalent to mK temperature), any small transfer of energy will be already observed.

to attain a relative mass uncertainty ( $\delta m/m$ ) in the order of  $10^{-9}$ , provided a careful study of the different sources of systematic uncertainties has been performed.

## 2.2. The IIC Technique

It is based on the resonant amplification of the current a charged particle induces on the endcap electrodes while it is oscillating in the trap at cryogenic temperature [42]. In order to detect such a minute current, an effective impedance is created with an external  $LC$ -circuit (see, e.g., [43]) or a tuned Superconducting Quantum Interference Device (SQUID) [42], in resonance with the axial oscillation of the ion, such that  $\nu_z = 1/(2\pi\sqrt{LC})$ . Figure 2 shows, in the left side, the electronic representation. The axial oscillation frequency will be unfolded by applying a Fourier transformation to the current induced by the ion after flowing through the effective impedance ( $Z_{\text{eff}}$ ). Since  $\nu_c$  is determined from (2.8), one has to measure  $\nu_+$ ,  $\nu_z$ , and  $\nu_-$  only by observing the axial frequency of the ion in resonance with the  $LC$ -circuit. This is done either by coupling the motions with an external pulse at  $\nu_z \pm \nu_+$  or  $\nu_z \pm \nu_-$ , after probing the ion motion with an RF field around the corresponding radial frequency, transferring in this way the energy from one radial motion to the axial motion and looking for the time to damp the amplitude of the axial signal [44–46], or by looking to a shift in the axial frequency which depends on the modified-cyclotron orbit [10]. This technique allows one to reach relative mass uncertainties in the order of  $10^{-11}$  either by measuring the ion of interest and the reference ion sequentially in an ultrahigh stable magnetic field [10] or by storing both simultaneously in the trap [9].

## 2.3. The QS Technique

It is a novel technique for cooling, detection, and mass spectrometry of a single ion using a sensor ion ( $^{40}\text{Ca}^+$ ) which is laser-cooled to mK temperatures [27]. It is based on the axial coupling of two ions in different traps connected by a common endcap [47]. The electrical

representation is shown in the right side of Figure 2. The ion of interest is probed by applying an external RF field in a similar way as with the IIC technique. After conversion to axial motion by applying an external pulse, the ion of interest transfers its energy to the sensor ion by making equal their axial oscillation frequencies. After the motional amplitudes between the ion of interest and the sensor ion are exchanged, the laser is ON and the fluorescence of the sensor ion is monitored with a CCD camera. The electronic detection of image charges is replaced by laser spectroscopic detection [27]. The circuit sketched in the right side of Figure 2 indicates that the transfer of the energy between the ions can be described from the coupling of the two circuits within a time called  $t_{\text{ex}}$  and given by [47]

$$t_{\text{ex}} = 2\pi^2 \nu_z C \sqrt{L_{\text{ion}} L_{\text{Ca}^+}}. \quad (2.9)$$

In order to maintain the coupling and to transfer the energy, the oscillation frequencies of the two ions must be equal within

$$\Delta \nu_z = \frac{1}{2t_{\text{ex}}}. \quad (2.10)$$

The QS technique has the following advantages [27].

- (1) It is universal, independent of charge, and mass opposite to the IIC technique, not yet demonstrated for ions with mass-to-charge ratios above the one of  $^{133}\text{Cs}^{2+}$  [48].
- (2) A high signal-to-noise ratio can be realized for very small oscillation amplitudes compared to the IIC technique.
- (3) The ion under investigation and the sensor ion are well separated and can be individually manipulated.
- (4) The coupling of the two ions is well under control and can be changed easily in strength.
- (5) The ion under investigation and the sensor ion can be in different charge states. Both should have such a charge-over-mass ratio that the axial frequencies can be tuned equal or to harmonics.
- (6) The nonlinear Coulomb interaction of two ions stored in the same trap is avoided.
- (7) Fluctuations of the magnetic field of the superconductor are cancelled in first approximation by a measurement of the cyclotron frequency of the sensor ion.

Items 1, 2, and 6 are the current factors limiting the most precise measurement by Penning traps [9]. The following section will show the measurements carried out using Penning traps which are related to neutrino physics and will also briefly underline the advantages of the QS technique compared to the IIC technique for applications to the measurement of the mass of the electron antineutrino.

### 3. The Role of Penning Traps in Neutrino Physics

Penning traps are devices which have been proven to contribute to the determination of the mass of the electron (anti)neutrino or to determine its nature (whether it is a Dirac or a Majorana particle) envisaged by several international collaborations, by



performing extremely high-sensitive double- $\beta$ -decay experiments to search the signature for a neutrinoless process, by studying the end of the single  $\beta$ -decay spectrum from weak transitions following the idea by E. Fermi, or by measuring the X-ray spectrum following electron capture processes. While the signature to establish the nature of the neutrino has not been observed unambiguously yet [11], the study of the  $\beta$ -decay spectrum has already permitted to set an upper limit for the mass of the electron antineutrino [5]. A recent experiment following  $\epsilon$ -decay for the determination of the mass of the electron neutrino seems very promising [22]. The role of Penning traps lies on the accurate and unambiguous determination of the  $Q$ -value of any  $\beta(\epsilon)$  transformation (single or double) from the difference of the masses of the mother and the daughter nuclei. This determination does not suffer from systematic sources associated to detectors like intrinsic resolution, pile-up effects, electronic noise. In addition, only a few ions from the daughter and the mother nuclei are needed. Furthermore, in the case of a double  $\beta$  transformation, the Penning-trap  $Q$ -value determination can be performed in an infinitely shorter time scale compared to the expected half-lives of the mother nuclei, and if new candidates arise from theoretical predictions, the feasibility for the double decay can be easily cross-checked.

### 3.1. Neutrinoless Processes in $\beta$ Transformations

All the experiments in the world searching for a neutrinoless process concentrate on double  $\beta^-$  decay ( $0\nu\beta\beta$ ), a process predicted for the first time in 1939 [49] and described by

$$(A, Z) \longrightarrow (A, Z + 2) + 2e^- + Q_{\beta\beta}. \quad (3.1)$$

$Q_{\beta\beta}$  is calculated from the mass excess  $D$ , which is defined as

$$D(A, Z) = M(A, Z)c^2 - A \cdot u - (Z - N)m_e c^2, \quad (3.2)$$

using the relationship

$$Q_{\beta\beta} = D(A, Z) - D(A, Z + 2). \quad (3.3)$$

The parameter  $u$  in (3.2) is the atomic mass unit in keV, and  $E$  is the number of atomic electrons which appears from the fact that the mass excess is defined for neutral atoms. The probability for this transition is predicted to be higher compared, for example, to that of a neutrinoless double electron capture ( $0\nu\epsilon\epsilon$ ) process pointed out for the first time in 1955 [50] and described by

$$(A, Z) + 2e^- \longrightarrow (A, Z - 2) + Q_{\epsilon\epsilon}. \quad (3.4)$$

$Q_{\epsilon\epsilon}$  can be also calculated from the mass excess  $D$  using the relationship:

$$Q_{\epsilon\epsilon} = D(A, Z) - D(A, Z - 2). \quad (3.5)$$

The measurement of the well-defined energy  $Q_{\beta\beta}$  or  $Q_{\epsilon\epsilon}$  would imply the neutrino is a Majorana particle [51]. Table 1 shows in the last column the  $Q$ -values obtained by means of

Penning traps using different facilities worldwide, SMILETRAP in Sweden [23], JYFLTRAP in Finland [52], SHIPTRAP in Germany [53], ISOLTRAP at CERN [54], or the MIT trap now relocated at Florida State University (FSU) [55]. Save the MIT trap at FSU, where the IIC technique is used, all the other facilities employ a variant of the tof technique [39–41]. The relative mass uncertainties from these measurements are always better than  $1 \times 10^{-8}$ . The column  $\delta\bar{r}/\bar{r}$  in the table shows the relative uncertainty of the ratio between the cyclotron frequencies of the mother and the daughter nuclei. The resulting uncertainty in the  $Q$ -value is plotted also in Figure 3 (filled squares). Besides fixing accurately the energy window for observation of the events from running  $(0\nu\beta\beta)$ -decay experiments [55], the  $Q$ -value can be used to (re)evaluate very accurately the half-life of the parent nuclei as already addressed in [56]. For a  $(0\nu\beta\beta)$ -decay,  $T_{1/2}$  can be given by

$$\left[T_{1/2}^{0\nu}\right]^{-1} = G^{0\nu}(Q_{\beta\beta}, Z) g_A^4 \left(M^{0\nu}\right)^2 \frac{\langle m_\nu \rangle^2}{m_e^2}, \quad (3.6)$$

where  $G^{0\nu}$  is a precisely calculated phase-space factor which depends on the  $Q$ -value of the transition,  $g_A$  is the axial-vector coupling constant, and  $M^{0\nu}$  is the nuclear matrix element, which depends on the nuclear structure of the particular isotopes  $(A, Z)$ ,  $(A, Z + 1)$ , and  $(A, Z + 2)$  under study. Details about these calculations and the models employed can be found elsewhere [8, 57]. The probabilities for the  $(0\nu\beta\beta)$ -transitions are smaller compared to the cases where  $2\nu$  are emitted. The latter is then more sensitive to be observed with the same experimental arrangement. Though  $(0\nu\beta\beta)$ -transitions are expected with higher probability compared to  $(0\nu\epsilon\epsilon)$ -decays, a possible resonance enhancement of this process might occur if the initial and final states of the transition are degenerate in energy as proposed in [7]. The process can be written as

$$(A, Z) + 2e^- \longrightarrow (A, Z - 2)^* + Q \longrightarrow (A, Z - 2) + (Q_{\epsilon\epsilon} - E), \quad (3.7)$$

where  $(A, Z - 2)^*$  denotes the excited state of the daughter nucleus,  $Q$  is the energy released in such a decay which must be very small for resonance, and  $E$  is the decay energy from the excited state to the ground state of the daughter nucleus. The excited state has a width  $\Gamma$ . In this process, the half-life reads

$$\left[T_{1/2}^{0\nu}\right]^{-1} = \frac{(\Delta M)^2}{(Q_{\epsilon\epsilon} - E)^2 + \Gamma^2/4} \Gamma, \quad (3.8)$$

where  $\Delta M$  is the atom-mixing amplitude which is a function of several parameters, and  $Q$  is the mass difference between the ground-state atoms  $M(Z, A)$  and  $M(Z - 2, A)$ . Using this formalism, the atom mixing amplitude is proportional to the effective neutrino mass. The process is enhanced if the difference  $(Q_{\epsilon\epsilon} - E)$  is closer to zero. Several candidates were presented in [7] and some of them have been recently studied with Penning traps yielding in most of the cases a value for the half-life of the expected decay. All the  $Q_{\epsilon\epsilon}$ -values from Penning-trap mass spectrometry are also listed in Table 1. Table 2 shows other double decays and the expected half-lives according to [58]. The  $Q$ -values are obtained from the latest Atomic Mass Evaluation [59] and the uncertainties are also shown in Figure 3 (filled circles).

**Table 1:**  $Q$ -values for double  $\beta$  transformations determined from Penning-trap mass measurements on the mother and the daughter nuclei. In case where the measurement was performed at two different Penning-trap facilities, only the value with smaller relative mass uncertainty is shown.

Double decay	Decay type	$T_{1/2}$ (double decay) (years)	N.A. (mother) (%)	$\delta\bar{r}/\bar{r}$	$Q$ -value (keV)
$^{76}\text{Ge}$ - $^{76}\text{Se}^{(a)}$	$0\nu\beta\beta$	$>7.2 \times 10^{20}$ [11]	7.73	$7.8 \times 10^{-10**}$	2039.006 (50) [60]
$^{74}\text{Se}$ - $^{74}\text{Ge}^{(b)}$	$0\nu\epsilon\epsilon$	$\sim 5.0 \times 10^{43}$ [61]*	0.89	$7.4 \times 10^{-10}$	1209.169 (49) [61]
$^{96}\text{Ru}$ - $^{96}\text{Mo}^{(c)}$	$0\nu\epsilon\epsilon$	—	5.54	$1.4 \times 10^{-9}$	2714.51 (13) [62]
$^{100}\text{Mo}$ - $^{100}\text{Ru}^{(b)}$	$0\nu\beta\beta$	$>2.7 \times 10^{22}$ [11]	9.82	$1.8 \times 10^{-9}$	3034.40 (17) [63]
$^{110}\text{Pd}$ - $^{110}\text{Cd}^{(d)}$	$0\nu\beta\beta$	$6.8 \times 10^{23}$ [56]	11.72	$6.38 \times 10^{-9}$	2017.85 (64) [56]
$^{112}\text{Sn}$ - $^{112}\text{Cd}^{(b)}$	$0\nu\epsilon\epsilon$	$5.9 \times 10^{29}$ [12]*	0.97	$1.5 \times 10^{-9}$	1919.82 (16) [12]
$^{116}\text{Cd}$ - $^{116}\text{Sn}^{(b)}$	$0\nu\beta\beta$	$>8 \times 10^{21}$ [11]	7.49	$2.0 \times 10^{-9}$	2813.50 (13) [64]
$^{130}\text{Te}$ - $^{130}\text{Xe}^{(e)}$	$0\nu\beta\beta$	$>2.2 \times 10^{21}$ [11]	34.08	$9.8 \times 10^{-11}$	2527.518 (13) [65]
$^{136}\text{Xe}$ - $^{136}\text{Ba}^{(e)}$	$0\nu\beta\beta$	$>1.6 \times 10^{22}$ [11]	8.8573	$7.9 \times 10^{-11**}$	2457.83 (37) [55]
$^{136}\text{Ce}$ - $^{136}\text{Ba}^{(b)}$	$0\nu\epsilon\epsilon$	$>3.2 \times 10^{32}$ [66]*	0.185	$3.8 \times 10^{-9}$	2378.53 (27) [66]
$^{150}\text{Nd}$ - $^{150}\text{Sm}^{(b)}$	$0\nu\beta\beta$	$>1.5 \times 10^{21}$ [11]	5.638	$1.4 \times 10^{-9}$	3371.38 (20) [67]
$^{152}\text{Gd}$ - $^{152}\text{Sm}^{(c)}$	$0\nu\epsilon\epsilon$	$\sim 1.0 \times 10^{26}$ [13]*	0.20	$1.3 \times 10^{-9}$	55.70 (18) [13]
$^{156}\text{Dy}$ - $^{156}\text{Gd}^{(c)}$	$0\nu\epsilon\epsilon$	$6.0 \times 10^{28}$ [68]**	0.053	$7.0 \times 10^{-10}$	2005.95 (10) [68]
$^{162}\text{Er}$ - $^{162}\text{Dy}^{(c)}$	$0\nu\epsilon\epsilon$	—	0.139	$2.0 \times 10^{-9}$	1846.95 (30) [62]
$^{164}\text{Er}$ - $^{164}\text{Dy}^{(c)}$	$0\nu\epsilon\epsilon$	$\sim 1.0 \times 10^{30}$ [69]*	1.601	$7.6 \times 10^{-10}$	25.07 (12) [69]
$^{168}\text{Yb}$ - $^{168}\text{Er}^{(c)}$	$0\nu\epsilon\epsilon$	—	0.123	$1.6 \times 10^{-9}$	1409.27 (25) [62]
$^{180}\text{W}$ - $^{180}\text{Hf}^{(c)}$	$0\nu\epsilon\epsilon$	$\sim 5.0 \times 10^{27}$ [70]*	0.12	$1.6 \times 10^{-9}$	143.20 (27) [70]

The superscript besides the nuclides in the column “Double decay” serves to indicate the facility where the measurements were performed: <sup>(a)</sup>SMILETRAP, <sup>(b)</sup>JYFLTRAP, <sup>(c)</sup>SHIPTRAP, <sup>(d)</sup>ISOLTRAP, and <sup>(e)</sup>MIT trap at FSU. The natural abundances of the daughter nuclei are in general higher compared to those of the mother. (\*) Assuming  $m_{\nu_e} = 1$  eV. (\*\*) Partial half-life. (\*\*\*) Individual ratios are given with respect to a molecular ion.

**Table 2:** Expected half-lives for double  $\beta$ -transformations from [58]. The  $Q$ -values listed in the last column have been obtained using either (3.3) or (3.5) with the mass excess values and uncertainties quoted in the latest published volume of the Atomic Mass Evaluation [59]. One can observe that the uncertainties in the  $Q$ -values are one order of magnitude larger compared to those listed in Table 1.

Double Decay	Decay Type	$T_{1/2}$ (double decay) (years)	N.A. (mother) (%)	$\delta M_{\text{daughter}}/M_{\text{daughter}}$	$Q$ -value (keV)
$^{48}\text{Ca}$ - $^{48}\text{Ti}$	$0\nu\beta\beta$	$>5.8 \times 10^{22}$ [11]	0.187	$8.3 \times 10^{-8}$	4273.7 (4.1)
$^{78}\text{Kr}$ - $^{78}\text{Se}$	$0\nu\epsilon\epsilon$	$>1.5 \times 10^{21}$ [11]	0.375	$1.5 \times 10^{-8}$	2846.4 (2.0)
$^{82}\text{Se}$ - $^{82}\text{Kr}$	$0\nu\beta\beta$	$>3.6 \times 10^{23}$ [11]	8.73	$2.7 \times 10^{-8}$	2995.5 (2.7)
$^{96}\text{Zr}$ - $^{96}\text{Mo}$	$0\nu\beta\beta$	$>9.2 \times 10^{21}$ [11]	2.80	$2.6 \times 10^{-7}$	3347.7 (3.4)
$^{102}\text{Pd}$ - $^{102}\text{Ru}$	$0\nu\epsilon\epsilon$	—	1.02	$2.9 \times 10^{-8}$	1172.9 (3.2)
$^{106}\text{Cd}$ - $^{106}\text{Pd}$	$0\nu\epsilon\epsilon$	$>0.9 \times 10^{19}$ [58]	1.25	$5.7 \times 10^{-8}$	2770 (7)
$^{128}\text{Te}$ - $^{128}\text{Xe}$	$0\nu\beta\beta$	$>1.6 \times 10^{24}$ [11]	31.74	$1.5 \times 10^{-8}$	867.9 (2.2)
$^{130}\text{Ba}$ - $^{130}\text{Xe}$	$0\nu\epsilon\epsilon$	$>4 \times 10^{21}$ [58]	0.106	$2.3 \times 10^{-8}$	2620.1 (2.9)
$^{132}\text{Ba}$ - $^{132}\text{Xe}$	$0\nu\epsilon\epsilon$	$>3 \times 10^{20}$ [58]	0.101	$8.3 \times 10^{-9}$	845.7 (1.5)

### 3.2. Measurement of the Mass of the Electron Antineutrino from $\beta$ -Decay

A single  $\beta$ -decay process is described by

$$(A, Z) \longrightarrow (A, Z + 1) + e + \bar{\nu}_e + Q_\beta, \quad (3.9)$$

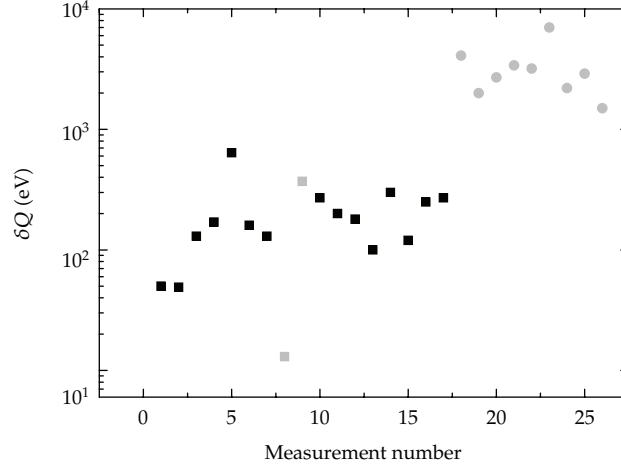


**Figure 3:** Uncertainty in the  $Q$ -values measured with Penning traps (filled squares) and from the latest published version of the Atomic Mass Evaluation (AME) [59] (filled circles). The squares in black and grey represent the results obtained using the *tof* and the *IIC* technique, respectively. The characteristics for the decays with the  $Q$ -values represented by filled circles are listed in Table 2.

where  $Q_\beta$  is the energy released in the decay shared by the electron and the antineutrino, given by

$$Q_\beta = [M(A, Z) - M(A, Z + 1) - m_e - m_{\bar{\nu}_e}]c^2, \quad (3.10)$$

or, in terms of the mass excess, by

$$Q_\beta = D(A, Z) - D(A, Z + 1) - m_{\bar{\nu}_e}c^2. \quad (3.11)$$

We will follow the notation  $Q_\beta(m_{\bar{\nu}_e} = 0) = E_0$ . In 1934 Enrico Fermi proposed the theory for  $\beta$ -decay. Within this theory and neglecting the energy of the recoil nucleus, the energy spectrum of electrons from the decay can be written as [15]

$$N_e(Z, E_e, m_{\nu_e}) = p_e E_e (E_0 - E_e) \sqrt{(E_0 - E_e)^2 - m_{\nu_e}^2 c^4} F(Z, E_e) S(E_e) [1 + \delta_R(Z, E_e)], \quad (3.12)$$

where  $p_e$  stands for the momentum of the electron,  $F(Z, E_e)$  is called the Fermi function to account for the nuclear charge,  $S(E_e)$  is the form factor of the  $\beta$  spectrum, containing the nuclear matrix element, and  $\delta_R(Z, E_e)$  is the radiative electromagnetic correction. One can study the spectrum using a transformation  $K(E_e)$  such that

$$K(E_e) = (E_0 - E_e) \left( 1 - \frac{m_{\nu_e}^2 c^4}{(E_0 - E_e)^2} \right)^{1/4}. \quad (3.13)$$

The representation of  $K(E_e)$  versus  $E_e$  is known as Kurie plot. By a detailed analysis of the shape of the end of the spectrum, the electron-neutrino mass can be unfolded. However, the

information on the neutrino mass is only in the final part of the spectrum within an energy interval  $\delta E$  containing a minute fraction of the total number of events

$$F(\delta E) \approx 2 \left( \frac{\delta E}{E_0} \right)^3. \quad (3.14)$$

For  $\delta E = 5 \text{ eV}$ , the fraction of events is  $3.9 \times 10^{-11}$  for KATRIN (1.1) and  $1.6 \times 10^{-8}$  for MARE (1.2). This is very small and therefore requires a very careful measurement including an extensive study of the systematics effects, which in the case of MARE (the bolometer approach) are

- (i) the response function of the detector,
- (ii) the decay to excited states of the daughter nucleus,
- (iii) the background due to cosmic rays and environmental radioactivity,
- (iv) pile-up effects.

There is a paper devoted to KATRIN in this issue [71], and therefore only the experiment devoted to the  $Q$ -value measurement from mass difference of the pair  ${}^3\text{H}-{}^3\text{He}$  using the UW-PTMS now in operation at the MPIK in Heidelberg in the division of Blaum [24] will be underlined to compare the method with the *Quantum Sensor* [27]. MARE, as KATRIN, aims at reaching finally a sensitivity of  $0.2 \text{ eV}/c^2$  in the measurement of the mass of the electron antineutrino. The first limit quoted by a group of the MARE collaboration for the mass of the electron antineutrino was  $26 \text{ eV}$  using the MANU detector [20]. The energy resolution was varied between 30 and 50 eV in the energy interval used for the fit, and the authors reported a  $Q$ -value of  $2470 \pm 1 \text{ (stat)} \pm 4 \text{ (syst)} \text{ eV}$  where the systematic uncertainty was due to the influence of the nonlinearity of the energy together with the choice of the energy interval for the analysis. Furthermore, they stated a dependence of the endpoint energy on the energy resolution; a variation of 5 eV in  $\sigma$  resulted in a variation of 1 eV.

The lowest limit quoted up to date from the decay of  ${}^{187}\text{Re}$ , measured by another group of the MARE collaboration, is  $15 \text{ eV}$  (90% C. L.) using the MIBETA detector [19]. In this paper, the authors quoted a  $Q$ -value of  $2465.3 \pm 0.5 \text{ (stat)} \pm 1.6 \text{ (syst)} \text{ eV}$ , where the systematic uncertainty was determined from the uncertainties in the energy resolution (28.5 eV at 2.46 keV), in the response function of the detector, and in the shape of the background of the  $\beta$ -spectrum. Still, the limit for the mass of the electron antineutrino is above the aimed value. According to the MARE proposal [15], the final value will be reached in two steps: MARE I aiming at  $m_{\bar{\nu}_e} < 2/c^2$  and MARE II aiming at  $m_{\bar{\nu}_e} < 0.2/c^2$ . In a very recent publication [72], a sensitivity of 4.5 eV at 90% C. L. is claimed to be possible using eight arrays of detectors based on silicon-implanted thermistors in combination with  $\text{AgReO}_4$  crystals after three years of data taking. This is a continuation of the work carried out with the MIBETA detector (energy resolution below 30 eV). However, the goal to be pursued in the MARE II phase will need novel technology, based on the so-called kinetic inductance detectors. An arrangement of  $10^5$  detectors 20 mg each is needed according to [72].

Many factors and many preceding results have been taken into account in order to get an accurate limit for the mass of the electron antineutrino. However, a different approach to reach a  $Q$ -value ( $E_0$ ) with a better accuracy and more important not subject to detector resolution, background sources, or pile-up effect is highly desirable. For this purpose, there is currently one Penning trap in operation at the MPIK in Heidelberg to measure the mass



difference of the pair  ${}^3\text{H}-{}^3\text{He}$  for KATRIN [24]. The device has been proven to work at the University of Washington in Seattle, where the mass for  ${}^4\text{He}^{2+}$  was measured with a relative mass uncertainty of  $1.5 \times 10^{-11}$  [10]. This corresponds to an uncertainty in the mass excess  $D$  of 0.06 eV, showing the feasibility to reach the accuracy required for KATRIN for the masses of  ${}^3\text{H}$  and  ${}^3\text{He}$  with the present performance of the spectrometer. In the case of MARE however, due to the higher masses of the daughter and the mother nuclei (a factor of 60 higher!), the uncertainty to be reached must be better and the new technique is needed. (In the case of the MARE project, the  $Q$ -value obtained from the mass difference as proposed in this paper, will differ slightly with the  $Q$ -value of the decay within the crystal. However, it can be corrected using an analytical expression given in the MARE proposal [15]. All the parameters involved are very accurately known.)

The setup at the MPIK uses the IIC technique to measure the shift in the axial frequency from the following relationship:

$$\frac{\delta\nu_z}{\nu_z} = \left[ \frac{B_2 d^2}{B_0} - 3C_4 \left( \frac{\nu_z}{\nu_+} \right)^2 \right] \frac{E_+}{qV_0}, \quad (3.15)$$

where the term  $B_2 d^2 / B_0$  is smaller compared to  $3C_4 (\nu_z / \nu_+)^2$ , so that

$$\frac{\delta\nu_z}{\nu_z} \approx 3C_4 \left( \frac{\nu_z}{\nu_+} \right)^2 \frac{E_+}{qV_0}. \quad (3.16)$$

$C_4$  is a term defined elsewhere which can be below  $10^{-4}$  in a so-called compensated Penning trap or in the order of  $10^{-2}$  for an uncompensated one [73]. An external RF field serves to probe the modified-cyclotron motion. The radial energy  $E_+$  in (3.15) is maximum when  $\nu_{\text{RF}} = \nu_+$ . Since the frequency  $\nu_+$  is constant, an increase in energy is caused by the increase of the oscillation amplitude  $\rho_+$ . We use here (3.16) to illustrate the advantage of using the QS technique versus the ICC technique. Figure 4 shows the relative variation of the axial oscillation frequency versus the oscillation amplitude  $\rho_+$  for several values of  $C_4$ . The vertical dotted lines mark the requested ion's modified-cyclotron radius ( $\rho_+$ ) in order to observe the induced current (IIC technique) [10] and the fluorescence (QS technique) [27]. As can be observed in the figure, the shift due to anharmonicities of the quadrupole field (following (3.16)) can be substantially reduced and one can aim at improving precision for the mass of the pairs  ${}^{187}\text{Re}^+ - {}^{187}\text{Os}^+$ . The QS technique, if successful, can be used therefore to contribute to the measurement pursued by the MARE collaboration, but can of course be applied to measure masses of  $\epsilon$ -decaying nuclei and contribute to the measurement of the mass of the electron neutrino.

### 3.3. Measurement of the Mass of the Electron Neutrino from $\epsilon$ -Decay

A single electron capture process is given by

$$(A, Z) + e^- \longrightarrow (A, Z - 1)^* + Q_\nu, \quad (3.17)$$

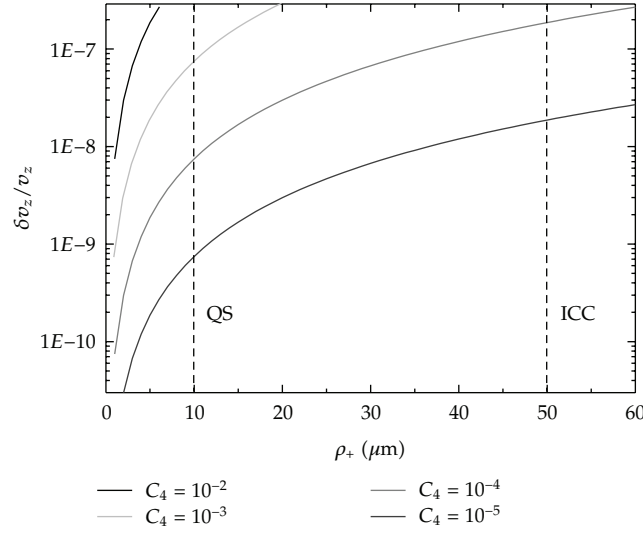


**Figure 4:** Relative variation of the axial frequency versus the modified-cyclotron radius of an ion with mass-to-charge ratio of 187. The  $y$ -axis is plotted up to  $\delta\nu_z/\nu_z = 2.9 \times 10^{-7}$ , which is the limit to maintain the coupling between the ion of interest and the sensor ion [27]. Using (2.9) and (2.10), the pairs  $^{187}\text{Re}^+ - ^{40}\text{Ca}^+$  and  $^{187}\text{Os}^+ - ^{40}\text{Ca}^+$  are coupled if their oscillation frequencies (we consider  $\nu_z = 100$  kHz) are equal within 29 mHz [27]. The ions are moving in a 7 T magnetic field, so that  $\nu_+(^{187}\text{Re}^+) = 565282.43$  Hz.

where  $Q_\nu$  comprises the energy and the rest mass of the emitted neutrino or by

$$(A, Z) + e^- \longrightarrow (A, Z - 1) + Q_e. \quad (3.18)$$

with

$$Q_e = Q_\nu + B. \quad (3.19)$$

$B$  stands here for the total energy that originated from the decay of the excited state of the daughter nucleus. This energy is emitted in the form of X-rays and can be measured with calorimeters. Suitable candidates are those with very low  $Q_e$ -values and very small  $Q_\nu$ . As in  $\beta$ -decay, the end of the emission spectrum must be fitted in order to obtain the mass of the electron neutrino. For the analytical form see, for example, [6]. There are two collaborations aiming at measuring the mass of the electron neutrino with a sensitivity firstly of a few eV using the  $e$ -decay of  $^{163}\text{Ho}$ , MARE [6], and ECHO [22]. In the framework of the second collaboration, a Penning trap is under development in order to perform very accurate mass measurements on the parent and the daughter nuclei [74]. The discussion on accuracy is similar to the previous section.

Other candidates with low  $Q_e$ -values have been pointed out for the same kind of experiment:  $^{100}\text{Pd}$  ( $T_{1/2} = 3.63$  d),  $^{101}\text{Rh}$  ( $T_{1/2} = 3.3$  y),  $^{131}\text{Cs}$  ( $T_{1/2} = 9,69$  d),  $^{134}\text{Ce}$  ( $T_{1/2} = 3.16$  d),  $^{57}\text{Tb}$  ( $T_{1/2} = 71$  y),  $^{159}\text{Dy}$  ( $T_{1/2} = 144,4$  d),  $^{161}\text{Ho}$  ( $T_{1/2} = 2,48$  h),  $^{163}\text{Ho}$  ( $T_{1/2} = 4570$  y),  $^{175}\text{Hf}$  ( $T_{1/2} = 70$  d),  $^{183}\text{Re}$  ( $T_{1/2} = 70$  d),  $^{194}\text{Hg}$  ( $T_{1/2} = 444$  y), or  $^{201}\text{Tl}$  ( $T_{1/2} = 3.04$  d) [75]. Though they are not natural abundant isotopes, those with long half-life can still be practicable in the proposed system, provided we can get the source.

#### 4. The Project TRAPSENSOR: Status

The *Quantum Sensor* will be developed within the project TRAPSENSOR at the University of Granada (Spain). The project will be run in two steps. In the first one, two independent setups will be built:

- (1) a commercial laser-desorption ion source, which is in operation at the University of Granada since July 2011, will be coupled to the Penning-trap beamline shown in Figure 6, which can allow for determination of  $Q$ -values using the *tof* technique to study, for instance, some of the cases listed in Table 2,
- (2) a radiofrequency trap with a laser system to cool  $^{40}\text{Ca}^+$  to mK temperatures (Doppler cooling), comprising a set of diode lasers and associated equipment, which will serve to define the final geometry of the *Quantum Sensor* using the setup shown in Figure 7.

During the second stage of the project, the *Quantum Sensor* will substitute the precision Penning trap in Figure 6. The elements will be presented in the following.

##### 4.1. The Laser Desorption Ion Source

The laser-desorption ion source is a commercial MALDI-*tof* system (model REFLEX III from Bruker). The acronym MALDI-*tof* stands for Matrix Assisted Laser Desorption Ionization Time Of Flight. In such device, a laser pulse on the sample produces the ions and serves as a trigger to measure the time the ions are registered in a microchannel plate detector at the end of a time-of-flight section. In July 2011 the production of  $\text{Re}^+$  and  $\text{Os}^+$  ions from naturally abundant isotopes at kinetic energies ranging from 20 keV down to a few tens of eV was accomplished. The laser utilized in these experiments is a doubled-frequency Nd:YAG laser (model Brilliant from Quantel) with  $\lambda = 532$  nm, a pulse width of  $\approx 4$  ns, and a repetition rate of 10 Hz. Figure 5 shows the time-of-flight (*tof*) signal of  $\text{Re}^+$  ions at 20 keV (normal operation of the system), and 1 keV, which is the lower energy required to transport the ions through the transfer section and to inject them into the Penning traps (Figure 6). A rhenium foil was glued in the target plate of the MALDI apparatus and the laser energy was fixed to around  $800 \text{ mJ/cm}^2$ . Systematic investigations have been carried out varying the laser power, the ion energy, and the sample preparation, especially for osmium since it is supplied in small grains. The results together with the mechanical coupling to the Penning-trap beamline will be presented elsewhere [76].

##### 4.2. The Penning-Trap Beamline

The layout of the Penning-trap beamline is shown in Figure 6. The system is comprised of a transfer section and two Penning traps housed in the same superconducting solenoid which has two homogeneous magnetic field regions separated by 20 cm. The first region has a homogeneity of  $1 \text{ ppm/cm}^3$  while the second reaches  $0.1 \text{ ppm/cm}^3$ . The superconducting magnet is similar to the one at SHIPTRAP [53], JYFLTRAP [52], and TRIGATRAP [77] and will be available at the University of Granada from October 2012. The magnetic field strength is 7 T in the region where the traps are located.

The first Penning trap in the beamline is made of a stack of cylinders in a similar way to the one conceptually designed for the preparation of the ions at MATS (precise

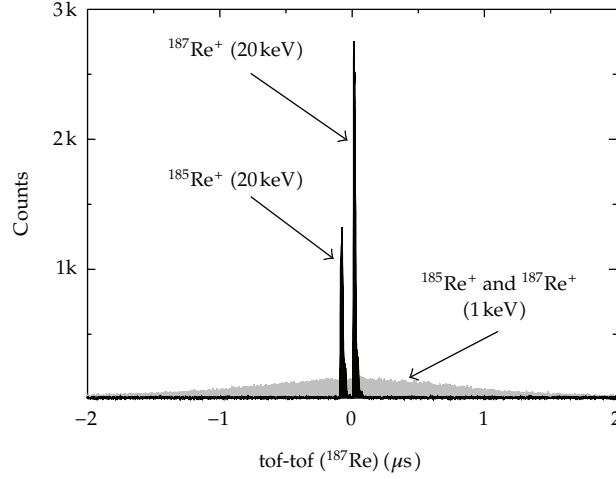


**Figure 5:** Time-of-flight (tof) signal of  $\text{Re}^+$  ions produced with the laser desorption ion source at two different kinetic energies: 20 keV (black) and 1 keV (grey). Both distributions result from the accumulation of 200 cycles. In order to observe them in the same panel, the tof at 20 keV is given with respect to the tof of the  $^{187}\text{Re}^+$  ions ( $18\ \mu\text{s}$ ), and the one at 1 keV with respect to the tof of the  $\text{Re}^+$  ions distribution ( $83\ \mu\text{s}$ ). The rhenium foil with natural abundance of 37.4% for  $^{185}\text{Re}$  and 62.6% for  $^{187}\text{Re}$ , as can be observed from the peak distribution at 20 keV, was prepared in the target lab of GSI-Darmstadt (Germany).

measurements on very short-lived nuclei using an Advanced Trapping System) to be built at the future facility for Antiprotons and Ion Research (FAIR) in Darmstadt [36]. This Penning trap will serve to prepare the ion beam coming from the laser-desorption ion source using the buffer-gas cooling technique [31], before injection into the precision Penning trap where measurements will take place. This trap allows for isobaric separation which will be important if finally rhenium and osmium ions are extracted simultaneously from the same sample. The measurement trap is hyperbolical and identical to the precision Penning trap at TRIGATRAP [77]. This trap will allow for high-precision mass measurements using the tof technique during the first stage of the project and will be replaced in the second stage by the *Quantum Sensor* developed in Granada. The precision Penning trap will be operated at liquid helium temperature (4 K) by means of a cryocooler. The two-stage pulsed-tube cold head is located in a vacuum cross in front of the superconducting magnet to cool down the traps by thermal contact. The transfer section comprises electrostatic lenses and quadrupole deflectors and is identical to the transfer section at SHIPTRAP [53, 78]. All the beamline is housed in CF160 vacuum chambers and will be operated in high vacuum by means of three turbo molecular pumps, two of them with a pumping speed of  $800\ \text{l/s}$  backed by roughing pumps with pumping speeds of  $35\ \text{m}^3/\text{h}$  located at both sides of the superconducting magnet. The third turbo pump, has a pumping speed of  $335\ \text{l/s}$  and is backed by a primary pump with  $3.8\ \text{m}^3/\text{h}$ .

#### 4.3. The Laser System for $^{40}\text{Ca}^+$

The principle of laser cooling was briefly underlined in a previous section. Since in this experiment the electronic detection will be exchanged by photon counting, it is important to show the setup to test the laser cooling of  $^{40}\text{Ca}^+$  in the way described previously in [27] and based on references therein. The layout of this setup is shown in Figure 7. This ion species

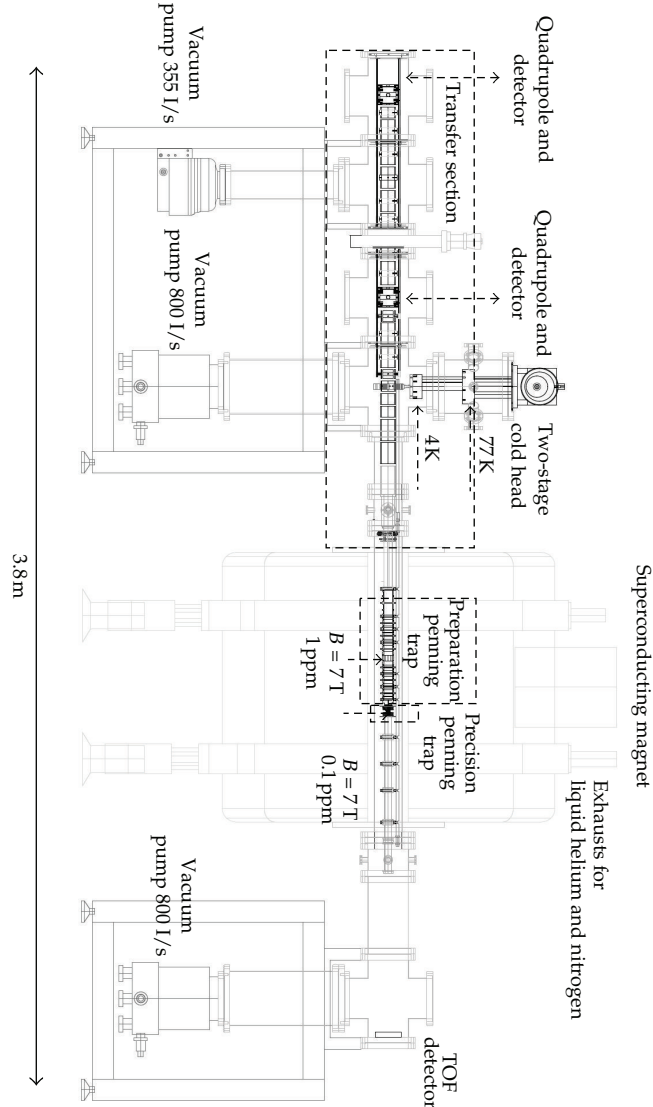


**Figure 6:** Layout of the Penning-trap beamline to perform high-precision mass measurements. The beamline will be coupled to an existing laser-desorption ion source.

has a transition at  $\lambda = 397 \text{ nm}$  for Doppler cooling ( $4^2S_{1/2} \rightarrow 4^2P_{1/2}$ ) which can be addressed using a diode laser. Another diode laser at  $\lambda = 866 \text{ nm}$  ( $4^2P_{1/2} \rightarrow 3^2D_{3/2}$ ) is required in order to repump the ion when it decays to the dark state  $3^2D_{3/2}$  with a branching ratio of 7%. Thus, only a couple of lasers would be needed to cool the sensor ion. However, since the ion has to be stored finally in a 7 T magnetic field, the  $S_{1/2}$  and  $P_{1/2}$  levels are split in two and the  $D_{3/2}$  level in four due to the Zeeman effect, requesting two lasers at 397 nm and four lasers at 866 nm. The other two lasers at 854 nm shown in the figure will serve to repump from the state  $3^2D_{5/2}$  to the state  $4^2P_{1/2}$ . This spontaneous decay has been observed with a branching ratio relative to the main decay of  $4.2 \times 10^{-7} B^2$  ( $B$  given in Tesla) by a group in London [79].



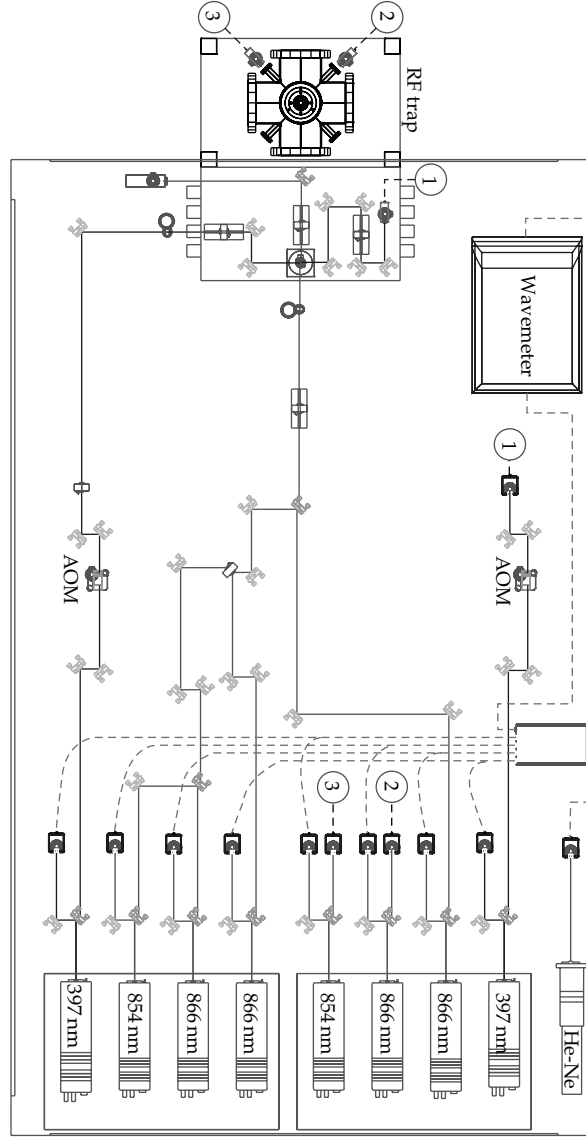


**Figure 7:** Optical table with the laser system and associated elements to perform laser cooling of  $^{40}\text{Ca}^+$ . For details see text.

As shown in Figure 7, two independent laser systems, each of them comprising four lasers, have been set up. The frequency of the lasers is locked using a very accurate wavemeter ( $3\sigma = 10 \text{ MHz}$ ) and a HeNe laser at  $\lambda = 632 \text{ nm}$  as a reference. The optics for one of the laser systems consists of mirrors and lenses to combine the different wavelengths in one line and to obtain a very strong focus ( $\Delta r_{\text{FWHM}} < 10 \mu\text{m}$ ) in the center of the CF100 vacuum cross, with several view ports, where an RF trap is located. The different wavelengths for the second laser system will be transported through optical fibers directed into the chamber (see 1, 2, and 3 in Figure 7). Finally, an AOM (Acoustic Optical Modulator) will be placed in the 397 nm laser line to switch ON and OFF the laser in very short times to follow the detection scheme

presented in [27]. The fluorescence will be monitored with a CCD camera located on top of the vacuum cross.

## 5. Perspectives

In this paper we have presented a new concept to improve the performance in mass spectrometry in terms of accuracy and sensitivity focusing on the application to neutrino mass spectrometry. With the setup presented, the authors envisage to yield a very accurate  $Q$ -value in the  $\beta$ -decay from  $^{187}\text{Re}$  to  $^{187}\text{Os}$  to contribute to the measurements to be pursued by the international MARE collaboration. The system can be also used for the determination of the  $Q$ -value in the  $\epsilon$ -decay from  $^{163}\text{Ho}$  to  $^{163}\text{Dy}$  provided the source is available. During the development of the system the project is structured in a way where also measurements relevant for neutrinoless double beta decay or double electron capture decay might be possible on candidates not measured yet with Penning traps. Production of any ion from solid samples can be accomplished with our universal laser desorption ion source. Ions from gas atoms can be also easily created within the preparation Penning trap.

The project officially started in November 2011, when the main equipment was ordered. The laboratory was prepared in the basement of the Faculty of Sciences and the first instruments were placed in March 2012. The beamline in Figure 6 is currently under completion. The superconducting magnet will be delivered in October 2012 and the design of the Penning-trap system has been finished and the control system of all the elements, power supplies, RF generators, and FPGA cards for pulse generation and data taking is already implemented. The coupling of the laser desorption ion source to the transfer section is currently ongoing [76]. Save for the AOM, recently ordered, the system shown in Figure 7 is completed so as to start the laser-cooling experiment. By the end of the year 2012, both setups should be in operation, so that we can start developing the *Quantum Sensor* within a time period of two years. For this purpose a third independent setup will be built to test the electronic coupling while mass measurements using the *tof* technique can be accomplished in the beamline and cooling experiments to optimize the laser system can take place in the optical table. The implementation of the device in the beamline is expected for 2015. Then, the system will be first fully devoted to the measurement of the  $Q$ -value of the decay  $^{187}\text{Re}$  to  $^{187}\text{Os}$ . We hope to match the time schedule of the MARE collaboration.

## Acknowledgments

The construction of the device described in this paper has been recently started and it is funded by the European Research Council within the ERC-2011-StG call (contract no. 268648-TRAPSENSOR). Besides the applications for neutrino mass spectrometry, the device has been also conceived for applications in the field of nuclear physics. During the conception of the project, D. Rodríguez acknowledges funding from the Spanish Ministry of Science and Innovation (now integrated in the Ministry for Economy and Competitiveness) through the projects FPA2009-14091-C02-02 and FPA2010-14803. D. Rodríguez would like to thank especially H.-Jürgen Kluge for discussions on the concept of the *Quantum Sensor*, and Richard Thompson and Danny Segal for showing their laser labs in London and for many discussions which helped to start setting up the laser system in Granada. D. Rodríguez would like to thank also Reiner Blatt, Markus Heinrich and Michael Brownnut for showing the laser labs in Innsbruck. The authors warmly thank Rodolfo Sánchez who has set up the laser optics and the locking-frequency system with the wavemeter, Michael Block who provided

the blueprints for many components in the beamline, and Dennis Renisch for his active participation in the measurements carried out with the MALDI in July 2011, which will be reported in a separated paper. J. M. Cornejo wants to thank the Centre for Particles, Astroparticles and Nuclear Physics in Spain for his contract. The authors would like to thank the target lab at GSI-Darmstadt for the preparation of the rhenium foil. The MALDI apparatus is a long-term loan from the University of Mainz. Klaus Wendt and Norbert Trautmann, are especially acknowledged for taking care of this in Mainz. Ignacio Porras is also especially acknowledged for providing a data acquisition module for the MALDI apparatus funded by the GREIB (Granada Research Initiative in Bio-Health) project at the University of Granada to the FQM220 group. Finally, the authors would like to thank the Vice-Rectorate for Infrastructure, the Office for International Projects, and the Department of Atomic Molecular and Nuclear Physics at the University of Granada for their contributions to the construction of the laboratory.

## References

- [1] Q. R. Ahmad, R. C. Allen, T. C. Andersen et al., "Direct evidence for neutrino flavor transformation from neutral-current interactions in the Sudbury Neutrino Observatory," *Physical Review Letters*, vol. 89, no. 1, Article ID 011301, 6 pages, 2002.
- [2] M. Maltoni, T. Schwetz, M. Tórtola, and J. W. F. Valle, "Status of global fits to neutrino oscillations," *New Journal of Physics*, vol. 6, pp. 1–37, 2004.
- [3] T. Schwetz, M. Tórtola, and J. W. F. Valle, "Three-flavour neutrino oscillation update," *New Journal of Physics*, vol. 10, Article ID 113011, 2008.
- [4] H. Nunokawa, S. Parke, and J. W. F. Valle, "CP violation and neutrino oscillations," *Progress in Particle and Nuclear Physics*, vol. 60, no. 2, pp. 338–402, 2008.
- [5] E. W. Otten and C. Weinheimer, "Neutrino mass limit from tritium  $\beta$ -decay," *Reports on Progress in Physics*, vol. 71, no. 8, Article ID 086201, 2008.
- [6] F. Gatti, M. Ribeiro Gomes, R. Vaccarone, G. Gallinaro, L. Ferrari, and D. Bagliani, "Study of sensitivity improvement for MARE-1 in Genoa," *Journal of Low Temperature Physics*, vol. 151, no. 3-4, pp. 603–606, 2008.
- [7] J. Bernabeu, A. De Rújula, and C. Jarlskog, "Neutrinoless double electron capture as a tool to measure the electron neutrino mass," *Nuclear Physics, Section B*, vol. 223, no. 1, pp. 15–28, 1983.
- [8] F. Šimkovic, A. Faessler, H. Mütter, V. Rodin, and M. Stauf, " $0\nu\beta\beta$ -decay nuclear matrix elements with self-consistent short-range correlations," *Physical Review C*, vol. 79, no. 5, Article ID 055501, 10 pages, 2009.
- [9] S. Rainville, J. K. Thompson, and D. E. Pritchard, "An ion balance for ultra-high-precision atomic mass measurements," *Science*, vol. 303, no. 5656, pp. 334–338, 2004.
- [10] R. S. Van Dyck Jr., D. B. Pinegar, S. Van Liew, and S. L. Zafonte, "The UW-PTMS: systematic studies, measurement progress, and future improvements," *International Journal of Mass Spectrometry*, vol. 251, no. 2-3, pp. 231–242, 2006.
- [11] A. S. Barabash, "Double  $\beta$ -decay: historical review of 75 years of research," *Physics of Atomic Nuclei*, vol. 74, no. 4, pp. 603–613, 2011.
- [12] S. Rahaman, V.-V. Elomaa, T. Eronen et al., "Accurate Q-value for the  $^{112}\text{Sn}$  double- $\beta$ -decay and its implication for the search of the neutrino mass," *Physical Review Letters*, vol. 103, no. 4, Article ID 042501, 4 pages, 2009.
- [13] S. Eliseev, C. Roux, K. Blaum et al., "Resonant enhancement of neutrinoless double-electron capture in  $^{152}\text{Gd}$ ," *Physical Review Letters*, vol. 106, no. 5, Article ID 052504, 4 pages, 2011.
- [14] J. Angrik et al., "KATRIN design report," Wissenschaftliche Berichte FZKA 7090, 2005.
- [15] F. Gatti et al., "MARE Technical Design Report," 2006, <http://mare.dfm.uninsubria.it/frontend/exec.php>.
- [16] V. M. Lobashev, "Study of the tritium beta-spectrum in experiment 'Troitsk  $\nu$ -mass'," *Progress in Particle and Nuclear Physics*, vol. 48, no. 1, pp. 123–131, 2002.
- [17] Ch. Kraus, B. Bornschein, L. Bornschein et al., "Final results from phase II of the Mainz neutrino mass search in tritium  $\beta$ -decay," *European Physical Journal C*, vol. 40, no. 4, pp. 447–468, 2005.

- [18] Sz. Nagy, T. Fritioff, M. Björkhage, I. Bergström, and R. Schuch, "On the Q-value of the tritium  $\beta$ -decay," *Europhysics Letters*, vol. 74, no. 3, pp. 404–410, 2006.
- [19] M. Sisti, C. Arnaboldi, C. Brofferio et al., "New limits from the Milano neutrino mass experiment with thermal microcalorimeters," *Nuclear Instruments and Methods in Physics Research, Section A*, vol. 520, no. 1–3, pp. 125–131, 2004.
- [20] M. Galeazzi, F. Fontanelli, F. Gatti, and S. Vitale, "End-point energy and half-life of the  $^{187}\text{Re}$   $\beta$ -decay," *Physical Review C*, vol. 63, no. 1, Article ID 014302, 7 pages, 2001.
- [21] A. Monfardini, C. Arnaboldi, C. Brofferio et al., "The microcalorimeter arrays for a rhenium experiment (MARE): a next-generation calorimetric neutrino mass experiment," *Nuclear Instruments and Methods in Physics Research, Section A*, vol. 559, no. 2, pp. 346–348, 2006.
- [22] P. C.-O. Ranitzsch, J.-P. Porst, S. Kempf et al., "Development of metallic magnetic calorimeters for high precision measurements of calorimetric  $^{187}\text{Re}$  and  $^{163}\text{Ho}$  Spectra," *Journal of Low Temperature Physics*, vol. 167, no. 5–6, pp. 1004–1014, 2012.
- [23] I. Bergström, C. Carlberg, T. Fritioff, G. Douysset, J. Schönfelder, and R. Schuch, "SMILETRAP—a Penning trap facility for precision mass measurements using highly charged ions," *Nuclear Instruments and Methods in Physics Research, Section A*, vol. 487, no. 3, pp. 618–651, 2002.
- [24] C. Diehl, K. Blaum, M. Höcker et al., "Progress with the MPIK/UW-PTMS in Heidelberg," *Hyperfine Interactions*, vol. 199, pp. 291–300, 2011.
- [25] <http://www.physics.fsu.edu/research/atomic.html#penning>.
- [26] F. Gatti, P. Meunier, C. Salvo, and S. Vitale, "Calorimetric measurement of the  $^{163}\text{Ho}$  spectrum by means of a cryogenic detector," *Physics Letters, Section B*, vol. 398, no. 3–4, pp. 415–419, 1997.
- [27] D. Rodríguez, "A quantum sensor for high-performance mass spectrometry," *Applied Physics B*, vol. 107, no. 4, pp. 1031–1042, 2011.
- [28] L. S. Brown and G. Gabrielse, "Geonium theory: physics of a single electron or ion in a Penning trap," *Reviews of Modern Physics*, vol. 58, no. 1, pp. 233–311, 1986.
- [29] K. Blaum, "High-accuracy mass spectrometry with stored ions," *Physics Reports*, vol. 425, no. 1, pp. 1–78, 2006.
- [30] D. J. Wineland and H. G. Dehmelt, "Principles of the stored ion calorimeter," *Journal of Applied Physics*, vol. 46, no. 2, pp. 919–930, 1975.
- [31] G. Savard, S. Becker, G. Bollen et al., "A new cooling technique for heavy ions in a Penning trap," *Physics Letters A*, vol. 158, no. 5, pp. 247–252, 1991.
- [32] W. M. Itano and D. J. Wineland, "Laser cooling of ions stored in harmonic and Penning traps," *Physical Review A*, vol. 25, no. 1, pp. 35–54, 1982.
- [33] D. J. Larson, J. C. Bergquist, J. J. Bollinger, W. M. Itano, and D. J. Wineland, "Sympathetic cooling of trapped ions: a laser-cooled two-species nonneutral ion plasma," *Physical Review Letters*, vol. 57, no. 1, pp. 70–73, 1986.
- [34] G. Gabrielse, "The true cyclotron frequency for particles and ions in a Penning trap," *International Journal of Mass Spectrometry*, vol. 279, no. 2–3, pp. 107–112, 2009.
- [35] M. König, G. Bollen, H. J. Kluge, T. Otto, and J. Szerypo, "Quadrupole excitation of stored ion motion at the true cyclotron frequency," *International Journal of Mass Spectrometry and Ion Processes*, vol. 142, no. 1–2, pp. 95–116, 1995.
- [36] D. Rodríguez, K. Blaum, W. Nörtershäuser et al., "MATS and LaSpec: high-precision experiments using ion traps and lasers at FAIR," *European Physical Journal*, vol. 183, no. 1, pp. 1–123, 2010.
- [37] D. L. Farnham, R. S. Van Dyck, and P. B. Schwinberg, "Determination of the electron's atomic mass and the proton/electron mass ratio via penning trap mass spectroscopy," *Physical Review Letters*, vol. 75, no. 20, pp. 3598–3601, 1995.
- [38] G. Gabrielse, A. Khabbaz, D. S. Hall, C. Heimann, H. Kalinowsky, and W. Jhe, "Precision mass spectroscopy of the antiproton and proton using simultaneously trapped particles," *Physical Review Letters*, vol. 82, no. 16, pp. 3198–3201, 1999.
- [39] S. George, S. Baruah, B. Blank et al., "Ramsey method of separated oscillatory fields for high-precision penning trap mass spectrometry," *Physical Review Letters*, vol. 98, no. 16, Article ID 162501, 2007.
- [40] R. Ringle, G. Bollen, P. Schury, S. Schwarz, and T. Sun, "Octupolar excitation of ion motion in a Penning trap—A study performed at LEBIT," *International Journal of Mass Spectrometry*, vol. 262, no. 1–2, pp. 33–44, 2007.
- [41] S. Eliseev, M. Block, A. Chaudhuri et al., "Octupolar excitation of ions stored in a Penning trap mass spectrometer—A study performed at SHIPTRAP," *International Journal of Mass Spectrometry*, vol. 262, no. 1–2, pp. 45–50, 2007.

- [42] R. M. Weisskoff, G. P. Lafyatis, K. R. Boyce, E. A. Cornell, R. W. Flanagan, and D. E. Pritchard, “rf SQUID detector for single-ion trapping experiments,” *Journal of Applied Physics*, vol. 63, no. 9, pp. 4599–4604, 1988.
- [43] J. Ketelaer, K. Blaum, M. Block et al., “Recent developments in ion detection techniques for Penning trap mass spectrometry at TRIGA-TRAP,” *European Physical Journal A*, vol. 42, no. 3, pp. 311–317, 2009.
- [44] E. A. Cornell, R. M. Weisskoff, K. R. Boyce, R. W. Flanagan, G. P. Lafyatis, and D. E. Pritchard, “Single-ion cyclotron resonance measurement of  $M(\text{CO}^+)/M(\text{N}_2^+)$ ,” *Physical Review Letters*, vol. 63, no. 16, pp. 1674–1677, 1989.
- [45] E. A. Cornell, R. M. Weisskoff, K. R. Boyce, and D. E. Pritchard, “Mode coupling in a Penning trap:  $\pi$  pulses and a classical avoided crossing,” *Physical Review A*, vol. 41, no. 1, pp. 312–315, 1990.
- [46] E. A. Cornell, *Mass spectroscopy using single ion cyclotron resonance [Ph.D. thesis]*, Massachusetts Institute of Technology, 1990.
- [47] D. J. Heinzen and D. J. Wineland, “Quantum-limited cooling and detection of radio-frequency oscillations by laser-cooled ions,” *Physical Review A*, vol. 42, no. 5, pp. 2977–2994, 1990.
- [48] M. P. Bradley, J. V. Porto, S. Rainville, J. K. Thompson, and D. E. Pritchard, “Penning trap measurements of the masses of  $^{133}\text{Cs}$ ,  $^{87,85}\text{Rb}$ , and  $^{23}\text{Na}$  with uncertainties  $\leq 0.2$  ppb,” *Physical Review Letters*, vol. 83, no. 22, pp. 4510–4513, 1999.
- [49] W. H. Furry, “On transition probabilities in double beta-disintegration,” *Physical Review*, vol. 56, no. 12, pp. 1184–1193, 1939.
- [50] R. G. Winter, “Double K capture and single K capture with positron emission,” *Physical Review*, vol. 100, no. 1, pp. 142–144, 1955.
- [51] E. Majorana, “Teoria simmetrica dell’elettrone e del positrone,” *Il Nuovo Cimento*, vol. 14, no. 4, pp. 171–184, 1937.
- [52] V. S. Kolhinen, S. Kopecky, T. Eronen et al., “JYFLTRAP: a cylindrical Penning trap for isobaric beam purification at IGISOL,” *Nuclear Instruments and Methods in Physics Research, Section A*, vol. 528, no. 3, pp. 776–787, 2004.
- [53] S. Rahaman, M. Block, D. Ackermann et al., “On-line commissioning of SHIPTRAP,” *International Journal of Mass Spectrometry*, vol. 251, no. 2-3, pp. 146–151, 2006.
- [54] M. Mukherjee, D. Beck, K. Blaum et al., “ISOLTRAP: an on-line Penning trap for mass spectrometry on short-lived nuclides,” *The European Physical Journal A*, vol. 35, no. 1, pp. 1–29, 2008.
- [55] M. Redshaw, E. Wingfield, J. McDaniel, and E. G. Myers, “Mass and double  $\beta$ -decay  $Q$ -value of  $^{136}\text{Xe}$ ,” *Physical Review Letters*, vol. 98, no. 5, Article ID 053003, 4 pages, 2007.
- [56] D. Fink, J. Barea, D. Beck et al., “ $Q$ -value and half-lives for the double- $\beta$ -decay nuclide  $^{110}\text{Pd}$ ,” *Physical Review Letters*, vol. 108, no. 6, Article ID 062502, 4 pages, 2012.
- [57] J. Suhonen and O. Civitarese, “Weak-interaction and nuclear-structure aspects of nuclear double  $\beta$ -decay,” *Physics Report*, vol. 300, no. 3-4, pp. 123–214, 1998.
- [58] A. S. Barabash, “Double  $\beta$ -decay: present status,” *Physics of Atomic Nuclei*, vol. 73, no. 1, pp. 162–178, 2010.
- [59] G. Audi, A. H. Wapstra, and C. Thibault, “The Ame2003 atomic mass evaluation—(II). Tables, graphs and references,” *Nuclear Physics A*, vol. 729, no. 1, pp. 337–676, 2003.
- [60] G. Douysset, T. Fritioff, C. Carlberg, I. Bergström, and M. Björkhage, “Determination of the  $^{76}\text{Ge}$  double  $\beta$ -decay  $Q$ -value,” *Physical Review Letters*, vol. 86, no. 19, pp. 4259–4262, 2001.
- [61] V. S. Kolhinen, V. V. Elomaa, T. Eronen et al., “Accurate  $Q$ -value for the  $^{74}\text{Se}$  double-electron-capture decay,” *Physics Letters, Section B*, vol. 684, no. 1, pp. 17–21, 2010.
- [62] S. Eliseev, D. Nesterenko, K. Blaum et al., “ $Q$ -values for neutrinoless double-electron capture in  $^{96}\text{Ru}$ ,  $^{162}\text{Er}$ , and  $^{168}\text{Yb}$ ,” *Physical Review C*, vol. 83, no. 3, Article ID 038501, 3 pages, 2011.
- [63] S. Rahaman, V. V. Elomaa, T. Eronen et al., “ $Q$ -values of the  $^{76}\text{Ge}$  and  $^{100}\text{Mo}$  double  $\beta$ -decays,” *Physics Letters, Section B*, vol. 662, no. 2, pp. 111–116, 2008.
- [64] S. Rahaman, V. V. Elomaa, T. Eronen et al., “Double  $\beta$ -decay  $Q$ -values of  $^{116}\text{Cd}$  and  $^{130}\text{Te}$ ,” *Physics Letters, Section B*, vol. 703, no. 4, pp. 412–416, 2011.
- [65] M. Redshaw, B. J. Mount, E. G. Myers, and F. T. Avignone II, “Masses of  $^{130}\text{Te}$  and  $^{130}\text{Xe}$  and double- $\beta$ -decay  $Q$ -value of  $^{130}\text{Te}$ ,” *Physical Review Letters*, vol. 102, no. 21, Article ID 212502, 4 pages, 2009.
- [66] V. S. Kolhinen, T. Eronen, D. Gorelov et al., “On the resonant neutrinoless double-electron-capture decay of  $^{136}\text{Ce}$ ,” *Physics Letters, Section B*, vol. 697, no. 2, pp. 116–120, 2011.
- [67] V. S. Kolhinen et al., “Double- $\beta$ -decay  $Q$ -value of  $^{150}\text{Nd}$ ,” *Physical Review C*, vol. 82, Article ID 022501, 4 pages, 2010.
- [68] S. Eliseev, M. Goncharov, K. Blaum et al., “Multiple-resonance phenomenon in neutrinoless double-electron capture,” *Physical Review C*, vol. 84, no. 1, Article ID 012501, 4 pages, 2011.



- [69] S. Eliseev, C. Roux, K. Blaum et al., “Octupolar-excitation Penning-trap mass spectrometry for Q-value measurement of double-electron capture in  $^{164}\text{Er}$ ,” *Physical Review Letters*, vol. 107, no. 15, Article ID 152501, 5 pages, 2011.
- [70] C. Droese, K. Blaum, M. Block et al., “Probing the nuclide  $^{180}\text{W}$  for neutrinoless double-electron capture exploration,” *Nuclear Physics A*, vol. 875, pp. 1–7, 2012.
- [71] G. Drexlin et al., “Absolute Neutrino Mass,” This issue.
- [72] A. Nucciotti et al., “The first phase of the MARE project in Milano,” *Nuclear Instruments and Methods A*, vol. 617, pp. 509–510, 2010.
- [73] G. Gabrielse, “Relaxation calculation of the electrostatic properties of compensated Penning traps with hyperbolic electrodes,” *Physical Review A*, vol. 27, no. 5, pp. 2277–2290, 1983.
- [74] K. Blaum, Y. N. Novikov, and G. Werth, “Penning traps as a versatile tool for precise experiments in fundamental physics,” *Contemporary Physics*, vol. 51, no. 2, pp. 149–175, 2010.
- [75] Yu. N. Novikov, private communication.
- [76] A. Lorenzo et al., “Adapting a laser desorption ion source to perform precision experiments in Penning traps,” in preparation.
- [77] J. Ketelaer, J. Krämer, D. Beck et al., “TRIGA-SPEC: a setup for mass spectrometry and laser spectroscopy at the research reactor TRIGA Mainz,” *Nuclear Instruments and Methods in Physics Research, Section A*, vol. 594, no. 2, pp. 162–177, 2008.
- [78] M. Block, private communication.
- [79] D. R. Crick, S. Donnellan, D. M. Segal, and R. C. Thompson, “Magnetically induced electron shelving in a trapped  $\text{Ca}^+$  ion,” *Physical Review A*, vol. 81, no. 5, Article ID 052503, 4 pages, 2010.

## Research Article

# Solar Neutrino Observables Sensitive to Matter Effects

H. Minakata<sup>1</sup> and C. Peña-Garay<sup>2</sup>

<sup>1</sup> Department of Physics, Tokyo Metropolitan University, Hachioji, Tokyo 192-0397, Japan

<sup>2</sup> Institut de Física Corpuscular, CSIC, Universitat de València, Apartado de Correos 22085, E 46071 València, Spain

Correspondence should be addressed to H. Minakata, hisakazu.minakata@gmail.com

Received 25 July 2012; Accepted 1 October 2012

Academic Editor: Arthur B. McDonald

Copyright © 2012 H. Minakata and C. Peña-Garay. This is an open access article distributed under the Creative Commons Attribution License, which permits unrestricted use, distribution, and reproduction in any medium, provided the original work is properly cited.

We discuss constraints on the coefficient  $A_{\text{MSW}}$  which is introduced to simulate the effect of weaker or stronger matter potential for electron neutrinos with the current and future solar neutrino data. The currently available solar neutrino data leads to a bound  $A_{\text{MSW}} = 1.47_{+0.54}^{-0.42} (-0.82_{+1.88})$  at  $1\sigma$  ( $3\sigma$ ) CL, which is consistent with the Standard Model prediction  $A_{\text{MSW}} = 1$ . For weaker matter potential ( $A_{\text{MSW}} < 1$ ), the constraint which comes from the flat  ${}^8\text{B}$  neutrino spectrum is already very tight, indicating the evidence for matter effects. However for stronger matter potential ( $A_{\text{MSW}} > 1$ ), the bound is milder and is dominated by the day-night asymmetry of  ${}^8\text{B}$  neutrino flux recently observed by Super-Kamiokande. Among the list of observables of ongoing and future solar neutrino experiments, we find that (1) an improved precision of the day-night asymmetry of  ${}^8\text{B}$  neutrinos, (2) precision measurements of the low-energy quasi-monoenergetic neutrinos, and (3) the detection of the upturn of the  ${}^8\text{B}$  neutrino spectrum at low energies are the best choices to improve the bound on  $A_{\text{MSW}}$ .

## 1. Introduction

Neutrino propagation in matter is described by the Mikheyev-Smirnov-Wolfenstein (MSW) theory [1–4]. It was successfully applied to solve the solar neutrino problem [5], the discrepancy between the data [6–15], and the theoretical prediction of solar neutrino flux [16], which blossomed into the solution of the puzzle, the large-mixing-angle (LMA) MSW solution. The solution is in perfect agreement with the result obtained by KamLAND [17] detector which measured antineutrinos from nuclear reactors, where the flavor conversion corresponds to vacuum oscillations with subpercent corrections due to matter effects.

The MSW theory relies on neutrino interaction with matter dictated by the standard electroweak theory and the standard treatment of refraction which is well-founded in

the theory of refraction of light. Therefore, it is believed to be on a firm basis. On the observational side it predicts a severer reduction of the solar neutrino flux at high energies due to the adiabatic flavor transition in matter than at low energies where the vacuum oscillation effect dominates. Globally, the behavior is indeed seen in the experiments observing  $^8\text{B}$  solar neutrinos at high energies [11–14] and in radiochemical experiments detecting low-energy pp and  $^7\text{Be}$  neutrinos [6–10] and more recently by the direct measurement of  $^7\text{Be}$  neutrinos by Borexino [15]. For a summary plot of the current status of high- and low-energy solar neutrinos, see the review of solar neutrinos in this series. Therefore, one can say that the MSW theory is successfully confronted with the available experimental data.

Nevertheless, we believe that further test of the MSW theory is worth pursuing. First of all, it is testing the charged current (CC) contribution to the index of refraction of neutrinos of the Standard Model (SM), which could not be tested anywhere else. Furthermore, in analyses of future experiments to determine  $\delta$  and the mass hierarchy, the MSW theory is usually assumed to disentangle the genuine effect of CP phase  $\delta$  from the matter effect. Therefore, to prove it to the accuracy required by measurement of  $\delta$  is highly desirable to make discovery of CP violation robust in such experiments that could have matter effect contamination. This reasoning was spelled out in [18]. Since the survival probability  $P_{ee}$  does not depend on  $\delta$  solar neutrinos provide us with a clean environment for testing the theory of neutrino propagation in matter.

We notice that in solar neutrinos, the transition from low- to high-energy behaviors mentioned above has not been clearly seen in a single experiment in a solar-model-independent manner. The Borexino and KamLAND experiments tried to fill the gap by observing  $^8\text{B}$  neutrinos at relatively low energies [19, 20]. SNO published the results of analyses with lower threshold energy of 3.5 MeV [21, 22], and the similar challenge is being undertaken by the Super-Kamiokande (SK) group [23]. In addition to  $^7\text{Be}$ , a new low-energy neutrino line, pep neutrinos, was observed by Borexino [24]. Recently, the SK group announced their first detection of the day-night asymmetry of  $^8\text{B}$  neutrinos [23]. As we will see in Section 3 it gives a significant impact on our discussions. With these new experimental inputs, as well as all the aforementioned ones, it is now quite timely to revisit the question of how large deviation from the MSW theory is allowed by data.

In this paper, we perform such a test of the theory of neutrino propagation in the environments of solar and earth matter. For this purpose, we need to specify the framework of how deviation from the MSW theory is parametrized. We introduce, following [25, 26], the parameter  $A_{\text{MSW}}$  defined as the ratio of the effective coupling of weak interactions measured with coherent neutrino matter interactions in the forward direction to the Fermi coupling constant  $G_F$ . We first analyze the currently available solar neutrino data to obtain the constraints on  $A_{\text{MSW}}$  and find that the features of the constraints differ depending upon  $A_{\text{MSW}} < 1$  or  $A_{\text{MSW}} > 1$ . We will discuss interpretations of the obtained constraints including this feature and provide a simple qualitative model to explain the bound at  $A_{\text{MSW}} > 1$ , more nontrivial one. We then discuss the question of to what extent the constraints on  $A_{\text{MSW}}$  can be made stringent by various future solar neutrino observables.

Our framework of testing the theory of neutrino propagation in matter requires comments. It actually involves the three different ingredients: (1) non-SM weak interactions in the forward direction parametrized as  $A_{\text{MSW}}G_F$ , (2) refraction theory of neutrino propagation in matter which includes the resonant enhancement of neutrino flavor conversion [1–4] and (3) electron number densities in the sun and in the earth. However, on ground of well-founded refraction theory and because no problem can be arguably raised in the formulation of the MSW mechanism we do not question the validity of (2). We also note

that the electron number density in the sun is reliably calculated by the standard solar model (SSM), and the result is cross-checked by helioseismology to an accuracy much better than the one discussed here. We can also take the earth matter density and chemical compositions calculated by the preliminary reference earth model (PREM) [27] as granted. It is the case because the earth matter-dependent observable, the day-night variation of solar neutrino flux, is insensitive to the precise profile of the earth matter density. Therefore, we assume that our test primarily examines the aspect (1), namely, whether neutrino matter coupling in the forward direction receives additional contribution beyond those of SM.

Are non-SM weak interactions parametrized as  $A_{\text{MSW}}G_F$  general enough? Most probably not because in many models with new non-SM interactions they have flavor structure. Flavor-dependent new neutral current interactions have been discussed in the framework of nonstandard interactions (NSI) of neutrinos [28–33], and constraints on effective neutrino matter coupling were obtained with this setting, for example, in [34, 35]. With solar neutrinos see [36] for discussion of NSI. If we denote the elements of NSI as  $\varepsilon_{\alpha\beta}$  ( $\alpha\beta = e, \mu, \tau$ ), our  $A_{\text{MSW}}$  may be interpreted as  $A_{\text{MSW}} = 1 + \varepsilon_{ee}$ , assuming that  $\varepsilon_{\alpha\beta} \ll \varepsilon_{ee}$  for  $\alpha \neq e, \beta \neq e$ . To deal with the fully generic case, however, we probably have to enlarge the framework of constraining the NSI parameters by including other neutrino sources, in particular, the accelerator and atmospheric neutrinos. See Section 4 for more comments.

## 2. Simple Analytic Treatment of Matter Effect Dependences

In this section, we give a simple analytic description of how various solar neutrino observables depend upon the matter effect. It should serve for intuitive understanding of the characteristic features which we will see in the later sections. The reader will find a physics discussion in the flavor conversion review of this series. In the following, we denote the matter densities inside the sun and in the earth as  $\rho_S$  and  $\rho_E$ , respectively. Solar neutrino survival or appearance probabilities depend on three oscillation parameters: the solar oscillation parameters ( $\theta_{12}, \Delta m_{21}^2 \equiv m_2^2 - m_1^2$ ) and  $\theta_{13}$ . Smallness of the recently measured value of  $\theta_{13}$  [37–41] and its small error greatly restrict the uncertainty introduced by this parameter on the determination of matter effects.

To quantify possible deviation from the MSW theory, we introduce the parameter  $A_{\text{MSW}}$  by replacing the Fermi coupling constant  $G_F$  by  $A_{\text{MSW}}G_F$  [25, 26]. The underlying assumption behind such simplified framework is that the deviation from the Fermi coupling constant is universal over fermions, in particular up and down quarks.

The survival probability in the absence of the earth matter effect, that is, during the day, is well described by [42–44]:

$$P_{ee}^D = \cos^4\theta_{13} \left( \frac{1}{2} + \frac{1}{2} \cdot \cos 2\theta_S \cdot \cos 2\theta_{12} \right) + \sin^4\theta_{13}. \quad (2.1)$$

Here  $\theta_S$  is the mixing angle at the production point inside the sun:

$$\cos 2\theta_S \equiv \cos 2\theta_m(\rho_S), \quad (2.2)$$

**Table 1:** Average electron density at the neutrino production region and energy of the relevant pp solar neutrinos fluxes. Last column shows the ratio of the electron neutrino elastic scattering with electrons cross-section to the  $\mu$  (or  $\tau$ ) neutrino one. For this calculation, we have assumed a measured electron kinetic energy range of [0.05, 0.4], [1, 1.4], [0, 0.8], and [5, 16] MeV for the pp, pep,  $^7\text{Be}$ , and  $^8\text{B}$ , respectively.

Source	$\rho_S Y_e (\text{g cm}^{-3})$	Energy (MeV)	$\sigma_\mu/\sigma_e$
pp	67.9	$\leq 0.42$	0.284
pep	73.8	1.44	0.203
$^7\text{Be}$	86.5	0.86	0.221
$^8\text{B}$	92.5	$\leq 16$	0.155

where  $\theta_m(\rho)$  is the mixing angle in matter of density  $\rho_S$ ,

$$\cos 2\theta_S = \frac{\cos 2\theta_{12} - \xi_S}{(1 - 2\xi_S \cos 2\theta_{12} + \xi_S^2)^{1/2}}. \quad (2.3)$$

In (2.4),  $\xi_S$  is defined as the ratio of the neutrino oscillation length in vacuum,  $l_\nu$ , to the refraction length in matter,  $l_0$ :

$$\begin{aligned} \xi_S \equiv \frac{l_\nu}{l_0} &= \frac{2\sqrt{2}A_{\text{MSW}}G_F\rho_S Y_e \cos^2\theta_{13}}{m_N} \frac{E}{\Delta m^2} \\ &= 0.203 \times A_{\text{MSW}} \cos^2\theta_{13} \left( \frac{E}{1 \text{ MeV}} \right) \left( \frac{\rho_S Y_e}{100 \text{ g cm}^{-3}} \right), \end{aligned} \quad (2.4)$$

where

$$l_\nu \equiv \frac{4\pi E}{\Delta m^2}, \quad l_0 \equiv \frac{2\pi m_N}{\sqrt{2}A_{\text{MSW}}G_F\rho_S Y_e \cos^2\theta_{13}}. \quad (2.5)$$

In (2.4) and (2.5),  $\rho_S$  is the matter density,  $Y_e$  is the number of electrons per nucleon, and  $m_N$  is the nucleon mass. In the last term we have used the best fit of the global analysis  $\Delta m_{21}^2 = 7.5 \times 10^{-5} \text{ eV}^2$ . The average electron number densities  $\rho_S Y_e$  at the production point of various solar neutrino fluxes are tabulated in Table 1. These numbers serve to show the differences in solar densities probed by the different sources of neutrinos, but the precise calculations are correctly done by averaging the survival probability with the production point distribution of the corresponding source [5, 16, 45].

We observe that  $P_{ee}^D$  in (2.1) depends on neutrino energy  $E$  and  $A_{\text{MSW}}$  in the particular combination  $A_{\text{MSW}}E$ . The property may have the following implications to constraints on  $A_{\text{MSW}}$ : (1) since shifting  $A_{\text{MSW}}$  is equivalent to shifting  $E$  our analysis which calculates  $\chi^2$  as a function of  $A_{\text{MSW}}$  is inevitably affected by the whole spectrum. (2) Nonetheless, we generically expect that the constraint at  $A_{\text{MSW}} < 1$  ( $A_{\text{MSW}} > 1$ ) principally comes from neutrino spectrum at high (low) energies. It appears that the apparently contradictory remarks are both true in view of the results in Section 3.



## 2.1. Energy Spectrum

Solar neutrino observables taken in a single experiment have not shown an energy dependence yet. The neutrino oscillation parameters are such that we cannot expect strong energy dependences. At low neutrino energies, small  $\xi_S$ , (2.1) can be approximated by

$$P_{ee}^D = \cos^4\theta_{13} \left[ 1 - \frac{1}{2} \sin^2 2\theta_{12} (1 + \cos 2\theta_{12} \xi_S) \right] + \sin^4\theta_{13}, \quad (2.6)$$

whereas at high energies, small  $1/\xi_S$ , the oscillation probability (2.1) can be approximated, keeping only the first energy-dependent term as

$$P_{ee}^D = \cos^4\theta_{13} \left[ \sin^2\theta_{12} + \frac{1}{4} \sin^2 2\theta_{12} \cos 2\theta_{12} \left( \frac{1}{\xi_S} \right)^2 \right] + \sin^4\theta_{13}. \quad (2.7)$$

Notice that the correction to the asymptotic behavior is linear in  $A_{\text{MSW}}$  at low energies while it is quadratic in  $A_{\text{MSW}}^{-1}$  at high energies. It may mean that the energy spectrum at low energies could be more advantageous in tightening up the constraint on  $A_{\text{MSW}}$  provided that these formulas with leading order corrections are valid.

It is well known that, in the LMA MSW mechanism,  $^8\text{B}$  neutrino spectrum must show an upturn from the asymptotic high energy ( $E \gg 10 \text{ MeV}$ ) to lower energies. The behavior is described by the correction term in (2.7) but only at a qualitative level. It indicates that the upturn component in the spectrum is a decreasing function of  $A_{\text{MSW}}$ . On the other hand, at low energies populated by pp,  $^7\text{Be}$ , and pep neutrinos, the solar neutrino energy spectrum displays vacuum-averaged oscillations or decoherence, (2.6). The deviation from this asymptotic low energy limit can be described by the correction term in (2.6) again at the (better) qualitative level. The term depends upon  $A_{\text{MSW}}$  linearly so that the correction term is an increasing function of  $A_{\text{MSW}}$ . Because of the negative sign in the correction term in (2.6), larger values of  $A_{\text{MSW}}$  lead to smaller absolute values of  $P_{ee}$  in both low- and high-energy regions. (The simpler way to reach the same conclusion is to use the property  $P_{ee}^D(E, sA_{\text{MSW}}) = P_{ee}^D(sE, A_{\text{MSW}})$  mentioned earlier. Then, for larger  $A_{\text{MSW}}$  ( $s > 1$ )  $P_{ee}^D$  corresponds to the one at higher energy. Since  $P_{ee}^D$  is a monotonically decreasing function of  $E$ , larger the  $A_{\text{MSW}}$ , smaller the  $P_{ee}^D$ .)

To see how accurate is the behavior predicted by the above approximate analytic expressions, we have computed numerically (using the PREM profile) the average  $\langle [(1 - r_{\mu/e})P_{ee} + r_{\mu/e}](E_{e,i}) \rangle$  as a function of electron energy. Here,  $\langle O \rangle$  means taking average of  $P_{ee}$  over neutrino energies with neutrino fluxes times the differential cross-sections integrated over the true electron energy with response function. In the above expression,  $r_{\mu/e} \equiv \sigma_{\mu}/\sigma_e$  with  $\sigma_e$  and  $\sigma_{\mu}$  being the cross-sections of  $\nu_e e$  and  $\nu_{\mu} e$  scattering, respectively. The computed results confirm qualitatively the behavior discussed above based on our analytic approximations. Thus, the energy spectrum of solar neutrinos at low and high energies can constrain  $A_{\text{MSW}}$  in this way, as will be shown quantitatively in Section 3.

## 2.2. Day-Night Variation

The  $\nu_e$  survival probability at night during which solar neutrinos pass through the earth can be written, assuming adiabaticity, as [46, 47]

$$P_{ee}^N = P_{ee}^D - \cos 2\theta_S \cos^2 \theta_{13} \langle f_{\text{reg}} \rangle_{\text{zenith}}, \quad (2.8)$$

where  $P_{ee}^D$  is the one given in (2.1).  $f_{\text{reg}}$  denotes the regeneration effect in the earth and is given as  $f_{\text{reg}} = P_{2e} - \sin^2 \theta_{12} \cos^2 \theta_{13}$ , where  $P_{2e}$  is the transition probability of second mass eigenstate to  $\nu_e$ . Under the constant density approximation in the earth,  $f_{\text{reg}}$  is given by [46, 47]

$$f_{\text{reg}} = \xi_E \cos^2 \theta_{13} \sin^2 2\theta_E \sin^2 \left[ A_{\text{MSW}} a_E \cos^2 \theta_{13} \left( 1 - 2\xi_E^{-1} \cos^2 \theta_{12} + \xi_E^{-2} \right)^{1/2} \left( \frac{L}{2} \right) \right] \quad (2.9)$$

for passage of distance  $L$ , where we have introduced  $a_E \equiv \sqrt{2} G_F N_e^{\text{earth}} = \sqrt{2} G_F \rho_E Y_{eE} / m_N$ . In (2.9),  $\theta_E$  and  $\xi_E$  stand for the mixing angle and the  $\xi$  parameter (see (2.4)) with matter density  $\rho_E$  in the earth. Within the range of neutrino parameters allowed by the solar neutrino data, the oscillatory term averages to  $1/2$  in good approximation when integrated over zenith angle. Then, the equation simplifies to

$$\langle f_{\text{reg}} \rangle_{\text{zenith}} = \frac{1}{2} \cos^2 \theta_{13} \xi_E \sin^2 2\theta_E. \quad (2.10)$$

At  $E = 7$  MeV, which is a typical energy for  $^8\text{B}$  neutrinos,  $\xi_E = 3.98 \times 10^{-2}$  and  $\sin 2\theta_E = 0.940$  for the average density  $\bar{\rho}_E = 5.6 \text{ g/cm}^3$  and the electron fraction  $Y_{eE} = 0.5$  in the earth. Then,  $\langle f_{\text{reg}} \rangle_{\text{zenith}}$  is given as  $\langle f_{\text{reg}} \rangle_{\text{zenith}} = 1.72 \times 10^{-2}$  for  $A_{\text{MSW}} = 1$  and  $\sin^2 2\theta_{13} = 0.089$ . This result is in reasonable agreement with more detailed estimate using the PREM profile [27] for the earth matter density.

We now give a simple estimate of the day-night asymmetry  $A_{DN}$  assuming constant matter density approximation in the earth and its  $A_{\text{MSW}}$  dependence. Under the approximation of small regeneration effect  $f_{\text{reg}} \ll 1$ , the day-night asymmetry  $A_{DN}$  for the CC number of counts  $N_{\text{CC}}$  measurement is approximately given by

$$A_{DN}^{\text{CC}} \equiv \frac{N_{\text{CC}}^N - N_{\text{CC}}^D}{(1/2)[N_{\text{CC}}^N + N_{\text{CC}}^D]} \approx -\frac{2 \cos 2\theta_S}{1 + \cos 2\theta_{12} \cos 2\theta_S} \langle f_{\text{reg}} \rangle_{\text{zenith}}, \quad (2.11)$$

where in the right-hand side we have approximated  $A_{DN}^{\text{CC}}$  by the asymmetry of survival probabilities in day and in night at an appropriate neutrino energy and ignored the terms of order  $\langle f_{\text{reg}} \rangle_{\text{zenith}}^2$ . Notice that the effects of the solar and the earth matter densities are contained only in  $\cos 2\theta_S$  and  $\langle f_{\text{reg}} \rangle_{\text{zenith}}$ , respectively.

At  $E = 7$  MeV,  $\xi_S = 1.31$ ,  $\cos 2\theta_{12} = 0.377$ ,  $\cos 2\theta_S = -0.710$ , and hence  $A_{DN}^{\text{CC}} = 3.41 \times 10^{-2} A_{\text{MSW}} \cos^4 \theta_{13}$ , about 3% day-night asymmetry for  $A_{\text{MSW}} = 1$ . Note that  $\cos^4 \theta_{13} = 0.95$  for  $\sin^2 2\theta_{13} = 0.1$ , so that the impact of  $\theta_{13}$  on  $A_{DN}^{\text{CC}}$  gives only a minor modification. Though based on crude approximations, the value of  $A_{DN}^{\text{CC}}$  at  $A_{\text{MSW}} = 1$  obtained above is in excellent agreement with the one evaluated numerically for SNO CC measurement.

**Table 2:** The  $\Delta\chi^2$  minimum of  $A_{\text{MSW}}$ , the allowed regions of  $A_{\text{MSW}}$  at  $1\sigma$ , and  $3\sigma$  CL are shown in the first, second, and third columns, respectively, for the analyses with the currently available data (first row), the one with spectrum upturn of  $^8\text{B}$  neutrinos at  $3\sigma$  added to the current data (second row), the one with  $^7\text{Be}$  and pep neutrinos with 5% and 3% accuracies, respectively, added to the current data (third row), the one with the new spectral information in the second and the third rows added to the current data (fourth row), and the one with day-night asymmetry of  $^8\text{B}$  neutrinos at  $3\sigma$  added to the current data (fifth row). The last row presents results of global analysis with all the above data. The numbers in parentheses imply the ones obtained with improved knowledge of  $\theta_{12}$ ; see text for details.

Analysis	$\Delta\chi^2$ minimum	Allowed region ( $1\sigma$ )	Allowed region ( $3\sigma$ )
present data	$A_{\text{MSW}} = 1.47$	1.05–2.01 (1.05–2.00)	0.65–3.35 (0.65–3.27)
+upturn ( $3\sigma$ )	1.34	1.02–1.79 (1.02–1.76)	0.65–3.00 (0.66–2.88)
+ $^7\text{Be}$ (5%), pep (3%)	1.25	0.97–1.53 (0.97–1.52)	0.65–2.34 (0.65–2.31)
+spectral shape	1.22	0.97–1.49 (0.97–1.46)	0.65–2.23 (0.65–2.12)
+ $A_{\text{DN}}$ ( $3\sigma$ )	1.17	0.96–1.43 (0.96–1.42)	0.66–1.98 (0.66–1.97)
+all	1.12	0.95–1.33 (0.95–1.32)	0.67–1.78 (0.67–1.73)

SNO and SK observe the day-night asymmetry by measurement of CC reactions and elastic scattering (CC + NC), respectively. We have computed  $A_{\text{DN}}$  as a function of  $A_{\text{MSW}}$  numerically (with PREM profile) without using analytic approximation. The result of  $A_{\text{DN}}$  scales linearly with  $A_{\text{MSW}}$  in a good approximation,  $A_{\text{DN}}^{\text{CC}} \approx 0.044A_{\text{MSW}}$ . Similarly, the day-night asymmetry for elastic scattering measurement can be easily computed. Its relationship to the  $A_{\text{DN}}^{\text{CC}}$  can be estimated in the similar manner as in (2.11),

$$A_{\text{DN}}^{\text{ES}} \equiv \frac{N_{\text{ES}}^{\text{N}} - N_{\text{ES}}^{\text{D}}}{(1/2)[N_{\text{ES}}^{\text{N}} + N_{\text{ES}}^{\text{D}}]} \approx A_{\text{DN}}^{\text{CC}} \times \left[ 1 + \frac{2r_{\mu/e}}{(1 - r_{\mu/e})[P_{\text{ee}}^{\text{N}} + P_{\text{ee}}^{\text{D}}]} \right]^{-1}, \quad (2.12)$$

taking into account the modification due to NC scattering. Using approximate values,  $r_{\mu/e} = 1/6$  and  $(1/2)[P_{\text{ee}}^{\text{N}} + P_{\text{ee}}^{\text{D}}] = 1/3$ , the factor in the square bracket can be estimated to be  $5/8$ , giving a reasonable approximation for the ratio of  $A_{\text{DN}}^{\text{ES}}$  to  $A_{\text{DN}}^{\text{CC}}$ . A better approximation to the computed results of the  $A_{\text{MSW}}$  dependence of the asymmetry is given by  $A_{\text{DN}}^{\text{ES}} = 0.02A_{\text{MSW}}$ .

### 3. Constraints on $A_{\text{MSW}}$ by Solar Neutrino Observables

In this section we investigate quantitatively to what extent  $A_{\text{MSW}}$  can be constrained by the current and the future solar neutrino data. The results of our calculations are presented in Figure 1, supplemented with the relevant numbers in Table 2. We will discuss the results and their implications to some details in a step-by-step manner. We first discuss the constraints by the data currently available (Section 3.1). Then, we address the question of how the constraint on  $A_{\text{MSW}}$  can be tightened with the future solar neutrino data, the spectral upturn of  $^8\text{B}$  neutrinos (Section 3.2), the low-energy  $^7\text{Be}$  and pep neutrinos (Section 3.3), and finally the day-night asymmetry of the solar neutrino flux (Section 3.4). We pay special attention to the question of how the constraints on  $A_{\text{MSW}}$  depend upon the significance of these measurements.

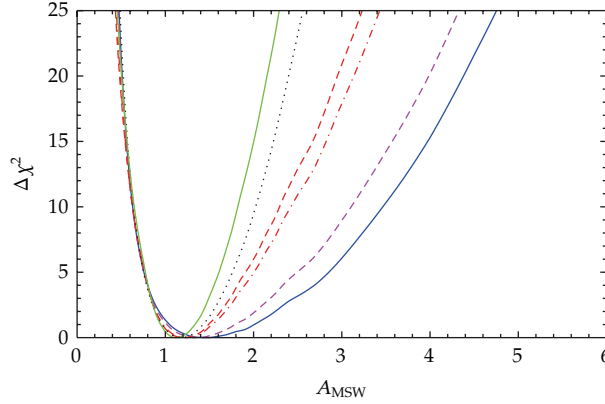


**Figure 1:**  $\Delta\chi^2$  as a function of  $A_{\text{MSW}}$  for the currently available solar neutrino data (shown in blue solid line) and the various solar neutrino observables expected in the near future (by color lines specified in the following). The current data include the one from SNO lower energy threshold analysis and SK I–IV. In addition to the current constraints on  $A_{\text{MSW}}$ , we show the improved constraints when future solar neutrino data are added one by one:  $3\sigma$  detection of the SK spectral upturn (magenta dashed line), low-energy solar neutrino flux measurements of  ${}^7\text{Be}$  at 5% and pep at 3% (red dash-dotted line), and  $3\sigma$  detection of the SK day-night asymmetry (black dotted line). The red dashed line shows the improved constraints by adding future spectral information at high and low energies. Finally, the global analysis by adding all the spectral information data and the day-night data produces the solid green line.

### 3.1. Current Constraint on $A_{\text{MSW}}$

We include in our global analyses the KamLAND and all the available solar neutrino data [6–15, 17, 19–23]. To obtain all the results quoted in this paper we marginalize over the mixing angles  $\theta_{12}$  and  $\theta_{13}$ , the small mass squared difference  $\Delta m_{21}^2$ , and the solar neutrino fluxes  $f_i$  [16, 48] imposing the luminosity constraint [49, 50]. We include in the analysis the  $\theta_{13}$  dependence derived from the analysis of the atmospheric, accelerator, and reactor data included in [51] as well as the recent measurement of  $\theta_{13}$  by [37–41]. The  $\chi^2$  used is defined by

$$\chi_{\text{global}}^2(A_{\text{MSW}}) = \text{Marg} \left[ \chi_{\text{solar}}^2 \left( \Delta m_{21}^2, \theta_{12}, \theta_{13}, A_{\text{MSW}}, f_{\text{B}}, f_{\text{Be}}, f_{\text{pp}}, f_{\text{CNO}} \right) + \chi_{\text{KamLAND}}^2 \left( \Delta m_{21}^2, \theta_{12}, \theta_{13} \right) + \chi_{\text{REACTOR+ATM+ACC}}^2(\theta_{13}) \right], \quad (3.1)$$

where Marg implies to marginalize over the parameters shown but not over  $A_{\text{MSW}}$ . Further details of the analysis methods can be found in [48].

The currently available neutrino data (blue solid line), which include SNO lower-energy threshold data [21, 22] and SK IV [23], do not allow a very precise determination of the  $A_{\text{MSW}}$  parameter. A distinctive feature of the  $\Delta\chi^2$  parabola shown in Figure 1 is the asymmetry between the small and large  $A_{\text{MSW}}$  regions. At  $A_{\text{MSW}} < 1$  the parabola is already fairly steep, and the “wall” is so stiff that can barely be changed by including the future data. While at  $A_{\text{MSW}} > 1$  the slope is relatively gentle. More quantitatively,  $A_{\text{MSW}} = 1.47_{-0.42}^{+0.54} ({}_{-0.82}^{+1.88})$  at  $1\sigma$  ( $3\sigma$ ) CL. The best fit point with the present data is significantly larger than unity,  $A_{\text{MSW}} = 1.47$ . It was 1.32 before and has driven to the larger value mostly by the new SK data which indicates a stronger matter effect than those expected by the MSW LMA region

preferred by the KamLAND data. The larger best fit value could also partly be due to an artifact of the weakness of the constraint in  $A_{\text{MSW}} > 1$  region. Notice that the Standard Model MSW theory value  $A_{\text{MSW}} = 1$  is off from the  $1\sigma$  region but only by a tiny amount, as seen in Table 2. Let us understand these characteristics.

The lower bound on  $A_{\text{MSW}}$  mostly comes from the SK and the SNO data which shows that  $^8\text{B}$  neutrino spectrum at high energies is well described by the adiabatic LMA MSW solution ( $A_{\text{MSW}} = 1$ ). The energy spectrum is very close to a flat one with  $P_{ee}$  which can be approximated by  $\sin^2\theta$  with corrections due to the contribution of the energy-dependent term (see (2.7)). The value is inconsistent with the vacuum oscillation, and hence the point  $A_{\text{MSW}} = 0$  is highly disfavored, showing the evidence for the matter effect.

One would think that the upper bound on  $A_{\text{MSW}}$  should come from either the low energy solar neutrino data or the deviation from the flat spectra at high energies. But, we still lack precise information on low-energy solar neutrinos, and the spectral upturn of  $^8\text{B}$  neutrinos has not been observed beyond the level in [19, 20]. Then, what is the origin of the upper bound  $A_{\text{MSW}} < 2$  at about  $1\sigma$  CL? We argue that it mainly comes from the day-night asymmetry of  $^8\text{B}$  neutrino flux which is contained in the binned data of SK and SNO. Recently, the SK collaboration reported a positive indication of the day-night asymmetry though the data is still consistent with no asymmetry at  $2.3\sigma$  CL [23].

To show the point, we construct a very simple model for  $\Delta\chi^2$  for the day-night asymmetry  $A_{\text{DN}}^{\text{ES}}$ . It is made possible by the approximate linearity of  $A_{\text{DN}}^{\text{ES}}$  to  $A_{\text{MSW}}$ . Let us start from the data of day-night asymmetry at SK I-IV obtained with the D/N amplitude method [23]:  $A_{\text{DN}}^{\text{ES}} = (2.8 \pm 1.1 \pm 0.5)\%$ , giving the total error 1.2% if added in quadrature. The expectation of  $A_{\text{DN}}^{\text{ES}}$  by the LMA solution is  $A_{\text{DN}}^{\text{ES}} = A_{\text{MSW}} \times 2.1\%$  for  $\Delta m_{21}^2 = 7.6 \times 10^{-5} \text{ eV}^2$ . Then, one can create an approximate model  $\Delta\chi^2$  as  $\Delta\chi^2 = [(A_{\text{DN}} - 2.8\%)/1.2\%]^2 = 3.1(A_{\text{MSW}} - 1.3)^2$ .

Despite admittedly crude nature it seems to capture the qualitative features of  $\Delta\chi^2$  with the current data (blue solid line) in Figure 1 in region  $A_{\text{MSW}} > 1$ . It is true that it predicts a little too steep rise of  $\Delta\chi^2$  and leads to  $\Delta\chi^2 \simeq 22$  at  $A_{\text{MSW}} = 4$ , whereas  $\Delta\chi^2 \simeq 15$  in Figure 1. In the actual numerical analysis for Figure 1, however,  $\Delta\chi^2$  parabola can naturally become less steep because various other parameters are varied to accommodate such a large values of  $A_{\text{MSW}}$ . Therefore, we find that about  $2\sigma$  evidence of  $A_{\text{DN}}^{\text{ES}}$  in the SK data is most likely the main cause of the sensitivity to  $A_{\text{MSW}}$  in the region  $A_{\text{MSW}} > 1$ . The simple model cannot explain the behavior of  $\Delta\chi^2$  in region  $A_{\text{MSW}} < 1$  in Figure 1, because the other more powerful mechanism is at work to lead to stronger bound on  $A_{\text{MSW}}$ , as discussed above.

To what extent an improved knowledge of  $\theta_{12}$  affects  $A_{\text{MSW}}$ ? It was suggested that a dedicated reactor neutrino experiment can measure  $\sin^2\theta_{12}$  to  $\simeq 2\%$  accuracy [52, 53]. It is also expected that precision measurement of pp spectrum could improve the accuracy of  $\theta_{12}$  determination to a similar extent [48]. Therefore, it is interesting to examine to what extent an improved knowledge of  $\theta_{12}$  affects the constraint on  $A_{\text{MSW}}$ . Therefore, we recompute the  $\Delta\chi^2$  curves presented in Figure 1 by adding the artificial term  $(\sin^2\theta_{12} - \text{BEST})^2/0.02$  in the  $\Delta\chi^2$  assuming 2% accuracy in  $\sin^2\theta_{12}$  determination. The result of this computation is given in Table 2 in parentheses. As we see, size of the effect of improved  $\theta_{12}$  knowledge is not very significant.

### 3.2. Spectrum of Solar Neutrinos at High Energies

Evidence for the upturn of  $^8\text{B}$  neutrino spectrum must contribute to constrain the larger values of  $A_{\text{MSW}}$  because  $A_{\text{MSW}}$  could be very large without upturn, if day-night asymmetry



is ignored. We discuss the impact on  $A_{\text{MSW}}$  of seeing the upturn in recoil electron energy spectrum with  $3\sigma$  significance, which we assume to be in the region  $E_e \geq 3.5$  MeV. To calculate  $\Delta\chi^2$  we assume the errors estimated by the SK collaboration [23]. Adding the simulated data to the currently available dataset produces the magenta dashed line in Figure 1. We find a 25% reduction of the  $3\sigma$  allowed range,  $A_{\text{MSW}} = 1.34_{+0.45}^{-0.32}({}_{+1.66}^{-0.69})$  at  $1\sigma$  ( $3\sigma$ ) CL. We can see that it does improve the upper bound on  $A_{\text{MSW}}$ , for which the current constraint (blue solid line) is rather weak, but the improvement in the precision of  $A_{\text{MSW}}$  is still moderate.

Some remarks are in order about the minimum point of  $\Delta\chi^2$ . The best fit point with the present data is at  $A_{\text{MSW}} > 1$  as we saw above. For the analysis with future data discussed in this and the subsequent subsections, we assume that the  $\Delta\chi^2$  minimum is always at  $A_{\text{MSW}} = 1$  for simulated data. Therefore, the analysis with the present plus simulated data tends to pull the  $\Delta\chi^2$  minimum toward smaller values of  $A_{\text{MSW}}$ , and at the same time make the  $\Delta\chi^2$  parabola narrower around the minimum. By conspiracy between these two features the current constraint (blue solid line) is almost degenerate to the other lines at  $A_{\text{MSW}} < 1$ , the ones with spectral upturn (magenta dashed line) and low-energy neutrinos (red dash-dotted line). These features can be observed in Figure 1 and in Table 2.

### 3.3. Spectrum of Solar Neutrinos at Low Energies

Now, let us turn to the low-energy solar neutrinos,  ${}^7\text{Be}$  and pep lines. The Borexino collaboration has already measured the  ${}^7\text{Be}$  neutrino-electron scattering rate to an accuracy of  $\approx \pm 5\%$  [15], which we assume throughout this section. For pep neutrinos we assume measurement with 3% precision in the future. See [24] for the first observation of pep neutrinos and its current status of the uncertainties.

The measurement of the pep flux has two important advantages, when compared to the  ${}^7\text{Be}$  flux, in determining  $A_{\text{MSW}}$ : (a) the neutrino energy is higher, 1.44 MeV, so the importance of the solar matter effects is larger and (b) the uncertainty in the theoretical estimate is much smaller. Firstly, the ratio of the pep to the pp neutrino flux is robustly determined by the SSM calculations, so it can be determined more accurately than the individual fluxes because the ratio depends only weakly on the solar astrophysical inputs. Secondly, a very precise measurement of the  ${}^7\text{Be}$  flux, with all the other solar data and assuming energy conservation (luminosity constraint) leads to a very precise determination of the pp and pep flux, at the level of  $\sim 1\%$  accuracy [48]. On the other hand, to determine  ${}^7\text{Be}$  flux experimentally, we have to use the SSM flux to determine the neutrino survival probability, and therefore, the uncertainties in the theoretical estimate [16] limit the precision of the  ${}^7\text{Be}$  flux measurement.

The red dash-dotted line in Figure 1 shows the result of the combined analysis of future low energy data, an improved  ${}^7\text{Be}$  measurement with 5% precision, and a future pep measurement with 3% precision, added to the current data. The obtained constraint on  $A_{\text{MSW}}$  is  $A_{\text{MSW}} = 1.25 \pm 0.28({}_{+1.09}^{-0.60})$  at  $1\sigma$  ( $3\sigma$ ) CL. The resultant constraint on  $A_{\text{MSW}}$  from above is much more powerful than the one obtained with spectrum upturn of high-energy  ${}^8\text{B}$  neutrinos at  $3\sigma$ .

By having solar neutrino spectrum information both at high and low energies it is tempting to ask how tight the constraint becomes if we combine them. The result of this exercise is plotted by the red dashed line in Figure 1 and is also given in Table 2. The resultant constraint on  $A_{\text{MSW}}$  is  $A_{\text{MSW}} = 1.22_{+0.27}^{-0.25}({}_{+1.01}^{-0.57})$  at  $1\sigma$  ( $3\sigma$ ) CL.

### 3.4. Day-Night Asymmetry

To have a feeling on to what extent constraint on  $A_{\text{MSW}}$  can be tightened by possible future measurement, we extend the simple-minded model discussed in Section 3.1, but with further simplification of assuming  $A_{\text{MSW}} = 1$  as the best fit. Let us assume that the day-night asymmetry  $A_{\text{DN}}^{\text{ES}}$  can be determined with  $(2/N)\%$  accuracy, an evidence for the day-night asymmetry at  $N\sigma$  CL. Then, the appropriate model  $\Delta\chi^2$  is given under the same approximations as in Section 3.1 as  $\Delta\chi^2 = N^2(A_{\text{MSW}} - 1)^2$ . We boldly assume that the day-night asymmetry at  $3\sigma$  CL would be a practical goal in SK. It predicts  $\Delta\chi^2 = 9(A_{\text{MSW}} - 1)^2$ , which means that  $A_{\text{MSW}}$  can be constrained to the accuracy of 33% uncertainty at  $1\sigma$  CL.

Now, we give the result based on the real simulation of data. The black dotted line in Figure 1 shows the constraint on  $A_{\text{MSW}}$  obtained by future  $3\sigma$  CL measurement of the day-night asymmetry, which is added to the present solar neutrino data. As we see, the day-night asymmetry is very sensitive to the matter potential despite our modest assumption of  $3\sigma$  CL measurement of  $A_{\text{DN}}^{\text{ES}}$ . (Given the powerfulness of the day-night asymmetry for constraining  $A_{\text{MSW}}$ , it is highly desirable to measure it at higher CL in the future. Of course, it would be a challenging task and probably requires a megaton class water Cherenkov or large volume liquid scintillator detectors with solar neutrino detection capability. They include, e.g., Hyper-Kamiokande [54], UNO [55], or the ones described in [56]). The obtained constraint on  $A_{\text{MSW}}$  is  $A_{\text{MSW}} = 1.17_{-0.21}^{+0.26}({}_{-0.51}^{+0.81})$  at  $1\sigma$  ( $3\sigma$ ) CL. The obtained upper bound on  $A_{\text{MSW}}$  is actually stronger than the one expected by our simple-minded model  $\Delta\chi^2$ . Apart from the shift of the best fit to a larger value of  $A_{\text{MSW}}$ , the behavior of  $\Delta\chi^2$  is more like  $\Delta\chi^2 \approx 14(A_{\text{MSW}} - 1)^2$  in the region  $A_{\text{MSW}} > 1$ . It can also be seen in Figure 1 that the upper bound on  $A_{\text{MSW}}$  due to the day-night asymmetry at  $3\sigma$  CL (black dotted line) is stronger than the one from combined analysis of all the expected measurements of the shape of the spectrum (red dashed line) discussed at the end of Section 3.3.

### 3.5. Global Analysis

We now discuss to what extent the constraint on  $A_{\text{MSW}}$  can become stringent when all the data of various observable are combined. The solid green line in Figure 1 shows the constraint on  $A_{\text{MSW}}$  obtained by the global analysis combining all the datasets considered in our analysis. The obtained sensitivity reads  $A_{\text{MSW}} = 1.12_{-0.21}^{+0.17}({}_{-0.45}^{+0.66})$  at  $1\sigma$  ( $3\sigma$ ) CL. Therefore, the present and the future solar neutrino data, under the assumptions of the accuracies of measurement stated before, can constrain  $A_{\text{MSW}}$  to  $\approx 15\%$  ( $40\%$ ) at  $1\sigma$  ( $3\sigma$ ) CL from below and to  $\approx 20\%$  ( $60\%$ ) at  $1\sigma$  ( $3\sigma$ ) CL from above. If we compare this to the current constraint  $A_{\text{MSW}} = 1.47_{-0.54}^{+0.42}({}_{-0.82}^{+1.88})$  the improvement of the errors for  $A_{\text{MSW}}$  over the current precision is, very roughly speaking, a factor of  $\approx 1.5$ – $2$  in region  $A_{\text{MSW}} < 1$ , and it is a factor of  $\approx 2$  at  $A_{\text{MSW}} > 1$ . Noticing that the efficiency of adding more data to have tighter constraint at  $A_{\text{MSW}} < 1$  is weakened by shift of the minimum of  $\Delta\chi^2$ , improvement of the constraint on  $A_{\text{MSW}}$  is more significant at  $A_{\text{MSW}} > 1$ .

## 4. Summary

In this paper, we have discussed the question of to what extent tests of the MSW theory can be made stringent by various solar neutrino observables. First, we have updated the constraint on  $A_{\text{MSW}}$ , the ratio of the effective coupling constant of neutrinos to  $G_F$ , the Fermi coupling constant with the new data including SNO  $^8\text{B}$  spectrum and SK day-night asymmetry. Then,

we have discussed in detail how and to what extent the solar neutrino observable in the future tightens the constraint on  $A_{\text{MSW}}$ .

The features of the obtained constraints can be summarized as follows.

- (i) Interpretation of solar neutrino data at high energies by the vacuum oscillation is severely excluded by the SNO and SK experiments, which leads to a strong and robust lower bound on  $A_{\text{MSW}}$ . On the other hand, the day-night asymmetry at  $\approx 2\sigma$  level observed by SK dominates the bound at high  $A_{\text{MSW}}$  side. We find that present data lead to  $A_{\text{MSW}} = 1.47^{+0.54}_{-0.42} ({}^{+1.88}_{-0.82})$  at  $1\sigma$  ( $3\sigma$ ) CL. The Standard Model prediction  $A_{\text{MSW}} = 1$  is outside the  $1\sigma$  CL range but only by tiny amount.
- (ii) We have explored the improvements that could be achieved by solar neutrinos experiments, ongoing and in construction. We discussed three observables that are sensitive enough to significantly improve the limits on  $A_{\text{MSW}}$ , particularly in the region  $A_{\text{MSW}} > 1$ : (a) upturn of the  ${}^8\text{B}$  solar neutrino spectra at low energies at  $3\sigma$  CL, (b) high precision measurement of monoenergetic low-energy solar neutrinos,  ${}^7\text{Be}$  (5% precision), and pep (3% precision) neutrinos, and (c) day-night asymmetry of the  ${}^8\text{B}$  solar neutrino flux at  $3\sigma$  CL. They lead to the improvement of the bound as follows:

- (a)  $A_{\text{MSW}} = 1.34^{+0.45}_{-0.32} ({}^{+1.66}_{-0.69})$  at  $1\sigma$  ( $3\sigma$ ) CL,
- (b)  $A_{\text{MSW}} = 1.25 \pm 0.28 ({}^{+0.60}_{-1.09})$  at  $1\sigma$  ( $3\sigma$ ) CL,
- (c)  $A_{\text{MSW}} = 1.17^{+0.26}_{-0.21} ({}^{+0.81}_{-0.51})$  at  $1\sigma$  ( $3\sigma$ ) CL.

It could be expected that future measurement by SNO+ [57, 58] and KamLAND [59] may detect spectrum modulation of B neutrinos at low energies at CL higher than  $3\sigma$ .

Finally, by combining all the datasets we have considered we obtain  $A_{\text{MSW}} = 1.12^{+0.21}_{-0.17} ({}^{+0.66}_{-0.45})$  at  $1\sigma$  ( $3\sigma$ ) CL.

- (iii) As mentioned in Section 1, the issue of effective neutrino matter coupling in a wider context may be better treated in the framework of NSI. If we think about the extended setting together with accelerator and atmospheric neutrino measurement to look for effects of NSI, the off-diagonal elements  $\varepsilon_{\alpha\beta}$  ( $\alpha \neq \beta$ ) can be better constrained by long-baseline experiments. In fact, in a perturbative treatment with small parameter  $\epsilon \equiv \Delta m_{21}^2 / \Delta m_{31}^2$  with the assumption  $\varepsilon_{\alpha\beta} \sim \epsilon$ , the terms with  $\varepsilon_{e\mu}$  and  $\varepsilon_{e\tau}$  are of second order in  $\epsilon$ , while  $\varepsilon_{ee}$  comes only at third order in  $\epsilon$  [60]. The analyses show that the sensitivity to  $\varepsilon_{ee}$  is indeed lower at least by an order of magnitude compared to the ones to  $\varepsilon_{e\mu}$  or  $\varepsilon_{e\tau}$ . See the analysis in [61] and the references cited therein. It is also known that  $\varepsilon_{\mu\tau}$  can be severely constrained by atmospheric neutrinos [62]. Hence, we feel that the solar neutrinos are still a powerful and complementary probe for  $\varepsilon_{ee}$  in such extended setting.

In conclusion, testing the theory of neutrino propagation in matter deserves further endeavor. The lack of an accurate measurement of the matter potential felt by solar neutrinos reflects the fact that solar neutrino data only do not precisely determine the mass square splitting. The good match of the independently determined mass square splitting by solar neutrino data and by reactor antineutrino data will confirm the Standard Model prediction of the relative index of refraction of electron neutrinos to the other flavor neutrinos. The lack of match of both measurements would point to new physics like the one tested here.

## Acknowledgments

We thank the Galileo Galilei Institute for Theoretical Physics and the organizers of the workshop “What is  $\nu$ ?” for warm hospitality. C. Peña-Garay is supported in part by the Spanish MICINN Grants FPA-2007-60323 and FPA2011-29678, the Generalitat Valenciana Grant PROMETEO/2009/116, and the ITN INVISIBLES (Marie Curie Actions, PITN-GA-2011-289442). H. Minakata is supported in part by KAKENHI, Grant-in-Aid for Scientific Research No. 23540315, Japan Society for the Promotion of Science.

## References

- [1] L. Wolfenstein, “Neutrino oscillations in matter,” *Physical Review D*, vol. 17, no. 9, pp. 2369–2374, 1978.
- [2] S. P. Mikheev and A. Y. Smirnov, “Resonance enhancement of oscillations in matter and solar neutrino spectroscopy,” *Soviet Journal of Nuclear Physics*, vol. 42, pp. 913–917, 1985.
- [3] S. P. Mikheev and A. Y. Smirnov, “Resonance enhancement of oscillations in matter and solar neutrino spectroscopy,” *Yadernaya Fizika*, vol. 42, pp. 1441–1448, 1985.
- [4] S. P. Mikheev and A. Y. Smirnov, “Resonant amplification of  $\nu$  oscillations in matter and solar-neutrino spectroscopy,” *Il Nuovo Cimento C*, vol. 9, no. 1, pp. 17–26, 1986.
- [5] J. N. Bahcall, *Neutrino Astrophysics*, Cambridge University Press, Cambridge, UK, 1989.
- [6] B. T. Cleveland et al., “Measurement of the solar electron neutrino flux with the homestake chlorine detector,” *The Astrophysical Journal*, vol. 496, no. 1, p. 505, 1998.
- [7] J. N. Abdurashitov, E. P. Veretenkin, V. M. Vermul et al., “Solar neutrino flux measurements by the Soviet-American gallium experiment (SAGE) for half the 22-year solar cycle,” *Journal of Experimental and Theoretical Physics*, vol. 95, no. 2, pp. 181–193, 2002.
- [8] J. N. Abdurashitov, E. P. Veretenkin, V. M. Vermul et al., “Solar neutrino flux measurements by the Soviet-American gallium experiment (SAGE) for half the 22-year solar cycle,” *Zhurnal Éksperimental’no i Teoreticheskoy Fiziki*, vol. 122, no. 2, pp. 211–226, 2002.
- [9] W. Hampel, J. Handta, G. Heusser et al., “GALLEX solar neutrino observations: results for GALLEX IV,” *Physics Letters B*, vol. 447, no. 1-2, pp. 127–133, 1999.
- [10] M. Altmanna, M. Balatab, P. Belli et al., “Complete results for five years of GNO solar neutrino observations,” *Physics Letters B*, vol. 616, no. 3-4, pp. 174–190, 2005.
- [11] J. Hosaka, K. Ishihara, J. Kameda, Y. Koshio et al., “Solar neutrino measurements in Super-Kamiokande-I,” *Physical Review D*, vol. 73, no. 11, Article ID 112001, 33 pages, 2006.
- [12] K. Abe, Y. Hayato, T. Iida et al., “Solar neutrino results in Super-Kamiokande-III,” *Physical Review D*, vol. 83, Article ID 052010, 19 pages, 2011.
- [13] B. Aharmim, Q. R. Ahmad, S. N. Ahmed et al., “Determination of the  $\nu_e$  and total  $^8\text{B}$  solar neutrino fluxes using the Sudbury Neutrino Observatory Phase I data set,” *Physical Review C*, vol. 75, no. 4, Article ID 045502, 69 pages, 2007.
- [14] B. Aharmim, S. N. Ahmed, A. E. Anthony et al., “Electron energy spectra, fluxes, and day-night asymmetries of  $^8\text{B}$  solar neutrinos from the 391-day salt phase SNO data set,” *Physical Review C*, vol. 72, no. 5, Article ID 055502, 47 pages, 2005.
- [15] G. Bellini, J. Benziger, D. Bick et al. et al., “Precision measurement of the  $^7\text{Be}$  solar neutrino interaction rate in borexino,” *Physics Review Letters*, vol. 107, no. 14, Article ID 141302, 5 pages, 2011.
- [16] A. M. Serenelli, W. C. Haxton, and C. Peña-Garay, “Solar models with accretion. I. Application to the solar abundance problem,” *Astrophys. J.*, vol. 743, no. 1, article 24, 2011.
- [17] A. Gando, Y. Gando, K. Ichimura et al., “Constraints on  $\theta_{13}$  from a three-flavor oscillation analysis of reactor antineutrinos at kamLAND,” *Physical Review D*, vol. 83, no. 5, Article ID 052002, 11 pages, 2011.
- [18] H. Minakata, “Measuring earth matter density and testing the MSW theory,” <http://arxiv.org/abs/0705.1009>.
- [19] G. Bellini, J. Benziger, S. Bonetti et al., “Measurement of the solar  $^8\text{B}$  neutrino rate with a liquid scintillator target and 3 MeV energy threshold in the Borexino detector,” *Physical Review D*, vol. 82, no. 3, Article ID 033006, 10 pages, 2010.
- [20] S. Abe, K. Furuno, A. Gando et al., “Measurement of the  $^8\text{B}$  solar neutrino flux with the kamLAND liquid scintillator detector,” *Physical Review C*, vol. 84, no. 3, Article ID 035804, 6 pages, 2011.
- [21] B. Aharmim, S. N. Ahmed, A. E. Anthony et al., “Low energy threshold analysis of the phase I and phase II data sets of the sudbury neutrino observatory,” *Physical Review C*, vol. 81, no. 5, Article ID 055504, 49 pages, 2010.

- [22] B. Aharmim et al., "Combined analysis of all three Phases of solar neutrino data from the sudbury neutrino observatory," <http://arxiv.org/abs/1109.0763>.
- [23] M. Smy, "Talk at XXIV international conference on neutrino physics and astrophysics (Neutrino 2012)," in *Proceedings of the 25th International Conference on Neutrino Physics and Astrophysics (Neutrino '12)*, Kyoto, Japan, June 2012.
- [24] G. Bellini, J. Benziger, D. Bick et al., "First evidence of pep solar neutrinos by direct detection in Borexino," *Physical Review Letters*, vol. 108, no. 5, Article ID 051302, 6 pages, 2012.
- [25] G. Fogli and E. Lisi, "Evidence for the MSW effect," *New Journal of Physics*, vol. 6, p. 139, 2004.
- [26] G. L. Fogli, E. Lisi, A. Palazzo, and A. M. Rotunno, "Solar neutrino oscillations and indications of matter effects in the Sun," *Physical Review D*, vol. 67, no. 7, Article ID 073001, 2003.
- [27] A. M. Dziewonski and D. L. Anderson, "Preliminary reference Earth model," *Physics of the Earth and Planetary Interiors*, vol. 25, no. 4, pp. 297–356, 1981.
- [28] L. Wolfenstein, "Neutrino oscillations in matter," *Physical Review D*, vol. 17, no. 9, pp. 2369–2374, 1978.
- [29] J. W. F. Valle, "Resonant oscillations of massless neutrinos in matter," *Physics Letters B*, vol. 199, no. 3, pp. 432–436, 1987.
- [30] M. M. Guzzo, A. Masiero, and S. T. Petcov, "On the MSW effect with massless neutrinos and no mixing in the vacuum," *Physics Letters B*, vol. 260, no. 1-2, pp. 154–160, 1991.
- [31] E. Roulet, "Mikheyev-Smirnov-Wolfenstein effect with flavor-changing neutrino interactions," *Physical Review D*, vol. 44, no. 4, pp. R935–R938, 1991.
- [32] Y. Grossman, "Non-standard neutrino interactions and neutrino oscillation experiments," *Physical Letters B*, vol. 359, no. 1-2, pp. 141–147, 1995.
- [33] Z. Berezhiani and A. Rossi, "Limits on the non-standard interactions of neutrinos from  $e^+e^-$  colliders," *Physical Letters B*, vol. 535, no. 1-4, Article ID 011113, pp. 207–218, 2002.
- [34] S. Davidson, C. Pena-Garay, N. Rius, and A. Santamaria, "Present and future bounds on non-standard neutrino interactions," *Journal of High Energy Physics*, vol. 2003, no. 03, article 011, 2003.
- [35] C. Biggio, M. Blennow, and E. Fernandez-Martinez, "General bounds on non-standard neutrino interactions," *Journal of High Energy Physics*, vol. 2009, no. 08, article 090, 2009.
- [36] A. Friedland, C. Lunardini, and C. Pena-Garay, "Solar neutrinos as probes of neutrino-matter interactions," *Physics Letters B*, vol. 594, no. 3-4, pp. 347–354, 2004.
- [37] K. Abe, N. Abgrall, Y. Ajima et al., "Indication of electron neutrino appearance from an accelerator-produced off-axis muon neutrino Beam," *Physical Review Letters*, vol. 107, no. 4, Article ID 041801, 8 pages, For more recent update, see: T. Nakaya, Talk at XXIV International Conference on Neutrino Physics and Astrophysics (Neutrino 2012), Kyoto, Japan, June, 2012.
- [38] P. Adamson, D. J. Auty, D. S. Ayres et al., "Improved search for muon-neutrino to electron-neutrino oscillations in MINOS," *Physical Review Letters*, vol. 107, no. 18, Article ID 181802, 6 pages, 2011.
- [39] Y. Abe, C. Aberle, T. Akiri et al., "Indication of reactor  $\bar{\nu}_e$  disappearance in the double chooz," *Physical Review Letters*, vol. 108, no. 13, Article ID 131801, 7 pages, 2012, For update, see: M. Ishitsuka, Talk at Neutrino 2012.
- [40] F. P. An, J. Z. Bai, A. B. Balantekin et al., "Observation of electron-antineutrino disappearance at Daya Bay," *Physical Review Letters*, vol. 108, no. 17, Article ID 171803, 7 pages, 2012.
- [41] J. K. Ahn, S. Chebotaryov, J. H. Choi et al., "Observation of reactor electron antineutrino disappearance in the RENO experiment," *Physical Review Letters*, vol. 108, no. 19, Article ID 191802, 6 pages, 2012.
- [42] S. J. Parke, "Nonadiabatic level crossing in resonant neutrino oscillations," *Physical Review Letters*, vol. 57, no. 10, pp. 1275–1278, 1986.
- [43] C.-S. Lim, Brookhaven National Laboratory Report BNL-39675-mc, BNL Neutrino, 1987.
- [44] X. Shi and D. N. Schramm, "An update on the solar neutrino problem and the three-family MSW effect allowing for astrophysical uncertainties," *Physics Letters B*, vol. 283, no. 3-4, pp. 305–312, 1992.
- [45] P. C. de Holanda, W. Liao, and A. Y. Smirnov, "Toward precision measurements in solar neutrinos," *Nuclear Physics B*, vol. 702, no. 1-2, pp. 307–332, 2004.
- [46] M. C. Gonzalez-Garcia, C. Pena-Garay, Y. Nir, and A. Y. Smirnov, "Phenomenology of maximal and near-maximal lepton mixing," *Physical Review D*, vol. 63, no. 1, Article ID 013007, 23 pages, 2001.
- [47] M. C. Gonzalez-Garcia, C. Pena-Garay, and A. Y. Smirnov, "Zenith angle distributions at Super-Kamiokande and SNO and the solution of the solar neutrino problem," *Physical Review D*, vol. 63, no. 11, Article ID 113004001231, 18 pages, 2001.
- [48] J. N. Bahcall and C. Pena-Garay, "A road map to solar neutrino fluxes, neutrino oscillation parameters, and tests for new physics," *Journal of High Energy Physics*, vol. 2003, no. 11, article 004, 2003.



- [49] M. Spiro and D. Vignaud, "Solar model independent neutrino oscillation signals in the forthcoming solar neutrino experiments?" *Physics Letters B*, vol. 242, no. 2, pp. 279–284, 1990.
- [50] J. N. Bahcall, "The luminosity constraint on solar neutrino fluxes," *Physical Review C*, vol. 65, no. 2, Article ID 025801, 5 pages, 2002.
- [51] M. C. Gonzalez-Garcia, M. Maltoni, and J. Salvado, "Updated global fit to three neutrino mixing: status of the hints of  $\theta_{13} > 0$ ," *Journal of High Energy Physics*, vol. 2010, no. 4, article 56, 2010.
- [52] H. Minakata, H. Nunokawa, W. J. C. Teves, and R. Zukanovich Funchal, "Reactor measurement of  $\theta_{12}$ : principles, accuracies, and physics potentials," *Physical Review D*, vol. 71, no. 1, Article ID 013005, 17 pages, 2005.
- [53] A. Bandyopadhyay, S. Choubey, S. Goswami, and S. T. Petcov, "High precision measurements of  $\theta_{\odot}$  in the solar and reactor neutrino experiments," *Physical Review D*, vol. 72, no. 3, Article ID 033013, 21 pages, 2005.
- [54] K. Abe, T. Abe, H. Aihara et al., "Letter of intent: the hyper-kamiokande experiment—detector design and physics potential," <http://arxiv.org/abs/1109.3262>.
- [55] C. K. Jung, "Feasibility of a next generation underground water Cherenkov detector: UNO," in *Next Generation Nucleon Decay And Neutrino Detector (NNN '99)*, vol. 533 of *AIP Conference Proceedings*, pp. 29–34, Stony Brook, NY, USA, September 1999.
- [56] A. Rubbia, "The LAGUNA Design Study—towards giant liquid based underground detectors for neutrino physics and astrophysics and proton decay searches," *Acta Physica Polonica B*, vol. 41, no. 7, p. 1727, 2010.
- [57] M. C. Chen, "SNO and SNO+," in *Proceedings of the Next Generation Nucleon Decay and Neutrino Detector (NNN '99)*, vol. 944 of *AIP Conference Proceedings*, pp. 25–30, 2007.
- [58] A. B. McDonald, "Talk at XXIV International Conference on Neutrino Physics and Astrophysics (Neutrino 2012)," in *Proceedings of the 25th International Conference on Neutrino Physics and Astrophysics (Neutrino '12)*, Kyoto, Japan, June 2012.
- [59] K. Inoue, private communications.
- [60] T. Kikuchi, H. Minakata, and S. Uchinami, "Perturbation theory of neutrino oscillation with nonstandard neutrino interactions," *Journal of High Energy Physics*, vol. 2009, no. 03, article 114, 2009.
- [61] P. Coloma, A. Donini, J. Lopez-Pavon, and H. Minakata, "Non-standard interactions at a neutrino factory: correlations and CP violation," *Journal of High Energy Physics*, vol. 2011, no. 08, article 036, 2011.
- [62] N. Fornengo, M. Maltoni, R. Tomas, and J. W. F. Valle, "Probing neutrino non-standard interactions with atmospheric neutrino data," *Physical Review D*, vol. 65, no. 1, Article ID 013010, 11 pages, 2002.

## Review Article

# Atmospheric Neutrinos

**Takaaki Kajita**

*Institute for Cosmic Ray Research and Kavli-IPMU, The University of Tokyo, Kashiwa-no-ha 5-1-5, Kashiwa, Chiba 277-8582, Japan*

Correspondence should be addressed to Takaaki Kajita, [kajita@icrr.u-tokyo.ac.jp](mailto:kajita@icrr.u-tokyo.ac.jp)

Received 8 July 2012; Accepted 11 September 2012

Academic Editor: Koichiro Nishikawa

Copyright © 2012 Takaaki Kajita. This is an open access article distributed under the Creative Commons Attribution License, which permits unrestricted use, distribution, and reproduction in any medium, provided the original work is properly cited.

Atmospheric neutrinos are produced as decay products in hadronic showers resulting from collisions of cosmic rays with nuclei in the atmosphere. Electron-neutrinos and muon-neutrinos are produced mainly by the decay chain of charged pions to muons to electrons. Atmospheric neutrino experiments observed zenith angle and energy-dependent deficit of muon-neutrino events. It was found that neutrino oscillations between muon-neutrinos and tau-neutrinos explain these data well. This paper discusses atmospheric neutrino experiments and the neutrino oscillation studies with these neutrinos.

## 1. Introduction

Neutrinos are produced in various places such as in the Sun, the Earth, the atmosphere, and during the core collapse of a massive star. In addition neutrinos are produced in nuclear power plants and with beams of high energy protons. These neutrinos have been studied by various neutrino experiments. One of these experiments is called atmospheric neutrino experiments. These experiments study neutrinos produced by cosmic ray interactions in the atmosphere.

It has been recognized that the small but finite neutrino masses can be understood naturally by the Seesaw mechanism [1–3] by introducing super-heavy neutral particles. Therefore, it is widely understood that the experimental study of neutrino masses and mixing angles are one of the few ways to explore the physics beyond the standard model.

One of the most sensitive methods to observe small neutrino masses is to study neutrino flavor oscillations [4, 5]. If neutrinos have finite masses, each flavor eigenstate (e.g.,  $\nu_\mu$ ) can be expressed by a combination of mass eigenstates ( $\nu_1$ ,  $\nu_2$ , and  $\nu_3$ ). The relation

between the mass eigenstates ( $\nu_1$ ,  $\nu_2$ , and  $\nu_3$ ) and the flavor eigenstates ( $\nu_e$ ,  $\nu_\mu$ , and  $\nu_\tau$ ) can be expressed by

$$\begin{pmatrix} \nu_e \\ \nu_\mu \\ \nu_\tau \end{pmatrix} = U \begin{pmatrix} \nu_1 \\ \nu_2 \\ \nu_3 \end{pmatrix}, \quad (1.1)$$

where  $U$  is the mixing matrix. The mixing matrix  $U$  is expressed by

$$U = \begin{pmatrix} c_{12}c_{13} & s_{12}c_{13} & s_{13}e^{-i\delta} \\ -s_{12}c_{23} - c_{12}s_{23}s_{13}e^{i\delta} & c_{12}c_{23} - s_{12}s_{23}s_{13}e^{i\delta} & s_{23}c_{13} \\ s_{12}s_{23} - c_{12}c_{23}s_{13}e^{i\delta} & -c_{12}s_{23} - s_{12}c_{23}s_{13}e^{i\delta} & c_{23}c_{13} \end{pmatrix}, \quad (1.2)$$

where  $c_{ij}$  and  $s_{ij}$  represent  $\cos \theta_{ij}$  and  $\sin \theta_{ij}$ , respectively.

For simplicity, let us discuss two flavor neutrino oscillations. The probability for a neutrino produced in a flavor state  $\nu_\mu$  to be observed in a flavor state  $\nu_\tau$  after traveling a distance  $L$  through the vacuum is

$$P(\nu_\mu \rightarrow \nu_\tau) = \sin^2 2\theta_{23} \sin^2 \left( \frac{1.27 \Delta m_{23}^2 (\text{eV}^2) L (\text{km})}{E_\nu (\text{GeV})} \right), \quad (1.3)$$

where  $E_\nu$  is the neutrino energy,  $\theta_{23}$  is the mixing angle between the flavor eigenstates and the mass eigenstates, and  $\Delta m_{23}^2$  is the mass-squared difference of the neutrino mass eigenstates ( $\equiv |m_2^2 - m_3^2|$ ).

It can be immediately noticed that, in order to study small neutrino masses, one has to study neutrino oscillations with a long neutrino flight length or with a low energy neutrino beam. Atmospheric neutrinos are unique, because they travel very long distances of up to 12,800 km, that is, the diameter of the Earth. The typical energy of these neutrinos is 1 GeV. Therefore, one expects that it should be possible to study neutrino oscillations with atmospheric neutrinos if  $\Delta m_{23}^2$  is  $\sim 10^{-4} \text{ eV}^2$  or larger.

The above 2-flavor oscillation formula has to be generalized to three-flavor oscillations. In the three-flavor oscillation framework, neutrino oscillations are parametrized by three mixing angles ( $\theta_{12}$ ,  $\theta_{23}$ , and  $\theta_{13}$ ), three mass squared differences ( $\Delta m_{12}^2$ ,  $\Delta m_{23}^2$ , and  $\Delta m_{13}^2$ ; among the three  $\Delta m^2$ 's, only two are independent), and one CP phase ( $\delta$ ). As we will discuss later  $\theta_{23}$  and  $\Delta m_{23}^2$  are most relevant to present atmospheric neutrino experiments.  $\theta_{12}$  and  $\Delta m_{12}^2$  are most relevant to solar and long baseline reactor neutrino experiments.  $\theta_{13}$  was most recently measured by accelerator-based long baseline and reactor neutrino oscillation experiments.

Due to the hierarchies,  $\Delta m_{12}^2 \ll \Delta m_{23}^2$  and  $\theta_{13} \ll (\theta_{12}, \theta_{23})$ , it is approximately correct to assume two-flavor oscillations for analyses of many existing neutrino oscillation data. Therefore, in this paper, first, we discuss the atmospheric neutrino data in terms of two-flavor neutrino oscillations assuming two significantly different  $\Delta m^2$ 's. Later we extend our discussions to full three-flavor oscillations.

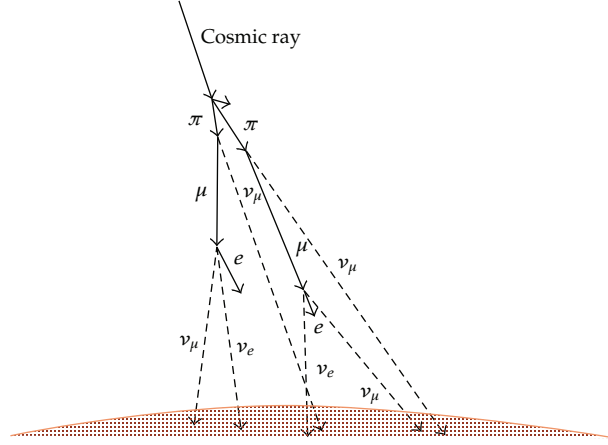


Figure 1: Schematic drawing of the production of atmospheric neutrinos.

## 2. Atmospheric Neutrino Flux

The study of  $\nu$  oscillations implies the comparison of the data with theoretical predictions calculated with and without the presence of oscillations.

Cosmic rays are high energy particles arriving at the Earth from the Universe. The cosmic ray flux at the Earth is measured experimentally. In the GeV/nucleon energy region, these cosmic-ray particles are mostly protons, about 5% are Helium nuclei, and a still smaller fraction are heavier nuclei. The energy spectrum of these particles extends to very high energies, although the flux of these particles decreases rapidly with the increasing energy. These particles, once enter into the Earth's atmosphere, interact with the nuclei in the high altitude atmosphere. Typically, in these high energy cosmic ray interactions with the air nuclei, many pions, and less abundantly  $K$  mesons, are produced. These mesons decay to other particles: for example, a  $\pi^+$  decays to a muon ( $\mu^+$ ) and a  $\nu_\mu$ . The produced muon ( $\mu^+$ ) is also unstable and decays to a positron ( $e^+$ ), a  $\bar{\nu}_\mu$  and a  $\nu_e$ . The charge conjugate decay chain occurs for  $\pi^-$ :

$$\begin{array}{ll}
 \pi^+ \longrightarrow \mu^+ + \nu_\mu & \pi^- \longrightarrow \mu^- + \bar{\nu}_\mu \\
 \downarrow & \downarrow \\
 e^+ + \nu_e + \bar{\nu}_\mu & e^- + \bar{\nu}_e + \nu_\mu.
 \end{array} \quad (2.1)$$

In this manner, neutrinos are produced when a cosmic-ray particle enters into the atmosphere. Smaller contributions come from the kaon decays. Figure 1 shows schematically the production of neutrinos in the atmosphere. These neutrinos are called atmospheric neutrinos.

Equation (2.1) indicates that the fluxes of  $\nu_e$ ,  $\nu_\mu$ 's and antineutrinos are strictly related to each other, and in particular that, if all the muons decay, one has

$$\phi(\nu_\mu + \bar{\nu}_\mu) \simeq 2\phi(\nu_e + \bar{\nu}_e), \quad (2.2)$$

where  $\phi$  represents the neutrino flux. In the energy range where some of the muons do not decay before reaching the ground, that is, above a few GeV neutrino energy,  $\phi(\nu_\mu + \bar{\nu}_\mu) > \phi(\nu_e + \bar{\nu}_e)$ . However, even in this energy range, the flux ratio  $\phi(\nu_\mu + \bar{\nu}_\mu)$  over  $\phi(\nu_e + \bar{\nu}_e)$  is still

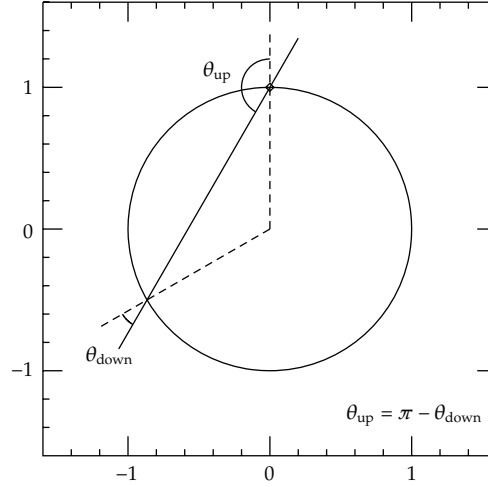


**Figure 2:** A neutrino trajectory that enters a spherical Earth with zenith angle  $\theta_{\text{down}}$  will exit with a new zenith angle  $\theta_{\text{up}} = \pi - \theta_{\text{down}}$ . Assuming that the primary fluxes are equal at the entry and exit points (isotropy) one can deduce the updown symmetry of the fluxes [54].

calculated accurately, because the fraction of muons that decay before reaching the ground can be accurately estimated.

Equation (2.1) also indicates

$$\phi(\nu_\mu) \simeq \phi(\bar{\nu}_\mu), \quad (2.3)$$

because both the  $\pi^+$  and  $\pi^-$  decay chains produce a  $\nu_\mu$  and a  $\bar{\nu}_\mu$ . Finally, (2.1) indicates that a  $\nu_e$  ( $\bar{\nu}_e$ ) is produced by a  $\pi^+$  ( $\pi^-$ ) decay chain. Thus the  $\nu_e$  over  $\bar{\nu}_e$  flux ratio is approximately equal to the  $\pi^+$  over  $\pi^-$  production ratio. The  $\pi^+/\pi^-$  production ratio can be estimated by measuring the  $\mu^+/\mu^-$  flux ratio, which is accurately measured. These considerations suggest that, in general, the  $\bar{\nu}_\mu$  over  $\nu_\mu$  and  $\bar{\nu}_e$  over  $\nu_e$  flux ratios are also predicted accurately.

Another very robust result of the atmospheric neutrino flux calculation is the prediction that, in the absence of neutrino oscillations, the neutrino fluxes are to a very good approximation updown symmetric for every neutrino type:

$$\phi_{\nu_\alpha}(E, \cos \theta) = \phi_{\nu_\alpha}(E, -\cos \theta), \quad (2.4)$$

where  $\theta$  is the zenith angle of the neutrino direction. Equation (2.4) can be derived by a geometric argument (see Figure 2), from the assumptions of the isotropy of the cosmic ray flux, and the sphericity of the Earth. However, it should be noted that the updown symmetry is not exact in the neutrino energy range of 1 GeV or less, due to geomagnetic field effects, as discussed later.

The primary cosmic-ray flux decreases rapidly with the energy, approximately  $E^{-2.7}$  in the 10 GeV to TeV energy region. Therefore, the calculated neutrino flux rapidly decreases with the increasing energy. Figure 3 shows the calculated energy spectrum of atmospheric neutrinos at the Kamioka and the Soudan-2 sites [6].



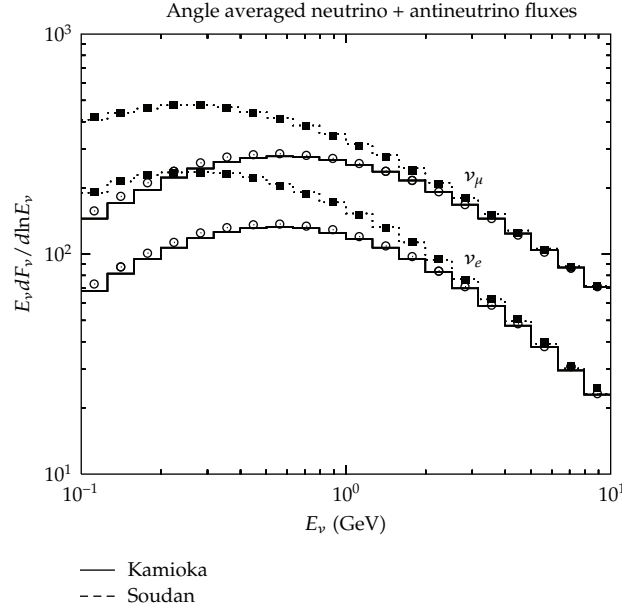


**Figure 3:** The atmospheric neutrino energy spectrum calculated for the Kamioka and Soudan-2 sites [6]. The  $(\nu_\mu + \bar{\nu}_\mu)$  and  $(\nu_e + \bar{\nu}_e)$  fluxes are plotted for the three-dimensional (points) and one-dimensional (histograms) calculations. The solid histograms are for the Kamioka site and the dashed histograms are for the Soudan-2 site.

The difficulties and the uncertainties in the calculation of atmospheric neutrino fluxes differ between high and low energies. For low energy neutrinos with energies of about 1 GeV, the primary fluxes of cosmic ray components are relatively well known. On the other hand, the low energy cosmic ray fluxes of less than about 10 GeV are modulated by solar activity and are affected by the geomagnetic field through a rigidity ( $\equiv$  momentum/charge) cutoff. The cutoff is lower near the poles, and therefore the low energy flux is higher for detectors located near the poles than those near the equator. Note that the cosmic ray fluxes in interstellar space are to a very good approximation constant in time and isotropic in direction.

For neutrinos with energy higher than about 100 GeV, primary cosmic rays with energies higher than 1000 GeV are relevant. At these energies, solar activity and the rigidity cutoff do not affect the cosmic rays, but the measurement of the higher energy primary cosmic ray flux is less accurate. In addition, in this energy range, the fraction of  $K$  production is a very important factor for the neutrino flux calculation. However, the  $K$  production cross-section is not known accurately.

In recent years, the flux calculations have been improved substantially. Results from the most recent work are described below [7, 8]. Figure 4 shows the estimated uncertainty of absolute atmospheric neutrino flux [8]. Practically, the flux calculation can be calibrated by measuring the primary cosmic ray and the secondary muon fluxes. Therefore, in the energy range of 1 to 10 GeV, the estimated uncertainty is less than 10%. Below and above this energy range, the uncertainty gets larger: The uncertainty below 1 GeV is larger due to the limited available data of the secondary muon flux in the GeV energy range at the balloon altitude. Due to the energy loss of the muons in the atmosphere, the muon flux measurement on the ground does not help much in this energy range. In the energy range above 10 GeV,

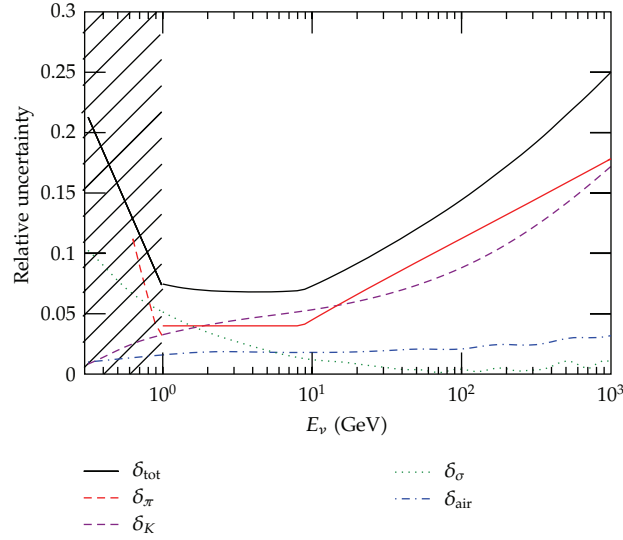


**Figure 4:** Estimated uncertainty of absolute atmospheric neutrino flux as a function of the neutrinos energy [8]. With the updated flux calculation, the uncertainty below 1 GeV is slightly improved to ~15% at 0.3 GeV [7].

the uncertainty is larger due mainly to the increasing uncertainty of the muon flux and the uncertainty in the  $K$  production.

Figure 5 shows the calculated  $\nu_\mu + \bar{\nu}_\mu$  over  $\nu_e + \bar{\nu}_e$ ,  $\nu_\mu$  over  $\bar{\nu}_\mu$  and  $\nu_e$  over  $\bar{\nu}_e$  flux ratios as a function of the neutrino energy, integrated over solid angle. These ratios are essentially independent of the primary cosmic ray spectrum and the details of the calculation. In the energy region of less than about 10 GeV, most of the neutrinos are produced by the decay chain of pions and the expected uncertainty of the  $\nu_\mu + \bar{\nu}_\mu$  over  $\nu_e + \bar{\nu}_e$  ratio is about 2 to 3%. In the higher energy region ( $>10$  GeV), the contribution of  $K$  decay in the neutrino production is more important. There, the ratio depends more on the  $K$  production cross-sections and the uncertainty of the ratio is expected to be larger. We also notice that the  $\nu_\mu$  over  $\bar{\nu}_\mu$  flux ratio agrees well among the calculations below a few GeV neutrino energies. Above this energy range, the uncertainties get slightly larger.

Figure 6 shows the zenith angle dependence of the atmospheric neutrino fluxes for several neutrino energies at Kamioka. At low energies, the fluxes of downward-going neutrinos are lower than those of upward-going neutrinos. This is due to the cutoff of primary cosmic rays by the geomagnetic field (rigidity cutoff). For neutrino energies higher than a few GeV, the calculated fluxes are essentially updown symmetric, because the primary particles are more energetic than the rigidity cutoff. The enhancement of the flux near horizon for low energy neutrinos is a feature characteristic of full three-dimensional flux calculations [9, 10]. The 3-dimensional effect is only important below about 1 GeV. However, the horizontal enhancement cannot be seen in the lepton zenith angle distribution, due to the relatively poor angular correlation between neutrinos and leptons below 1 GeV.

The uncertainties in the lepton (not the neutrino) updown and vertical-horizontal ratios can be estimated by comparing the predicted ratios by various flux models by a Monte Carlo simulation. These uncertainties generally depend on the energy and the neutrino flavor. The uncertainty in the updown event ratio is about 1% level in the energy region below 1 GeV

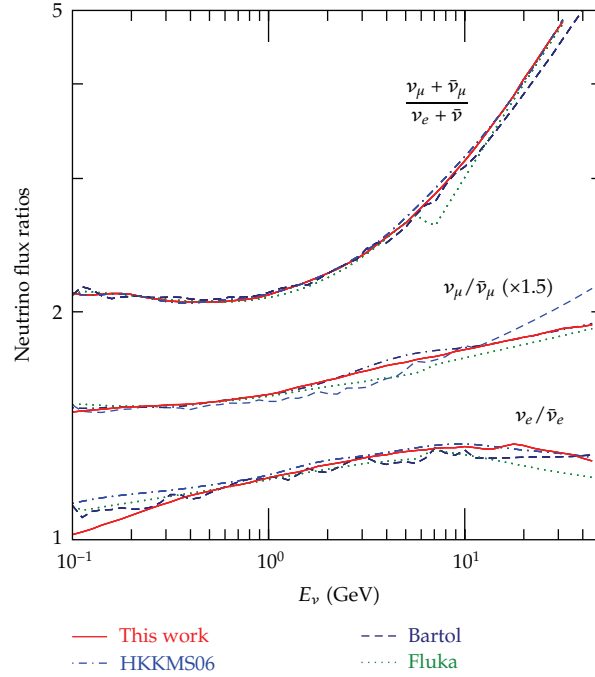


**Figure 5:** Comparison of the calculated flux ratios for Kamioka by the Bartol group [6], the Fluka group [10], HKKM06 [8] and HKKM11 (“This Work” in the figure) [7].

and is less than 1% above 1 GeV. The main source of the uncertainty in the vertical-horizontal ratio around a GeV is the size of the horizontal enhancement of the flux due to the three-dimensional effect; the uncertainty is estimated to be a few percent or less. In the higher energy region, where upward through-going muons are relevant, the largest source of the uncertainty in the vertical-horizontal ratio is the  $K$  production cross-section, and the vertical-horizontal uncertainty is estimated to be 3% [11].

Finally, for the prediction of the observable event rate, one has to include a description of the neutrino cross-sections in the energy range of relevance. For typical atmospheric neutrino experiments, the energy range that needs to be considered is approximately from 0.1 GeV to more than 1 TeV. We refer the details of the neutrino interactions in [12].

### 3. Brief History

Atmospheric neutrino experiments started in the 1960s. One experiment was carried out in the Kolar Gold Field in India [13]. Another experiment was carried out at the East Rand Proprietary Mine in South Africa [14]. In these experiments, neutrino interactions occurring in the rock surrounding a neutrino detector were measured. Since the experiments were carried out in extremely deep underground (about 8000 meters water equivalent (m.w.e.)), charged particles traversing the detectors almost horizontally were essentially of atmospheric neutrino origin. Also, since it was required that the particle should penetrate through the rock and the detector, most of these neutrino events should have been charged current (CC)  $\nu_\mu$  interactions.

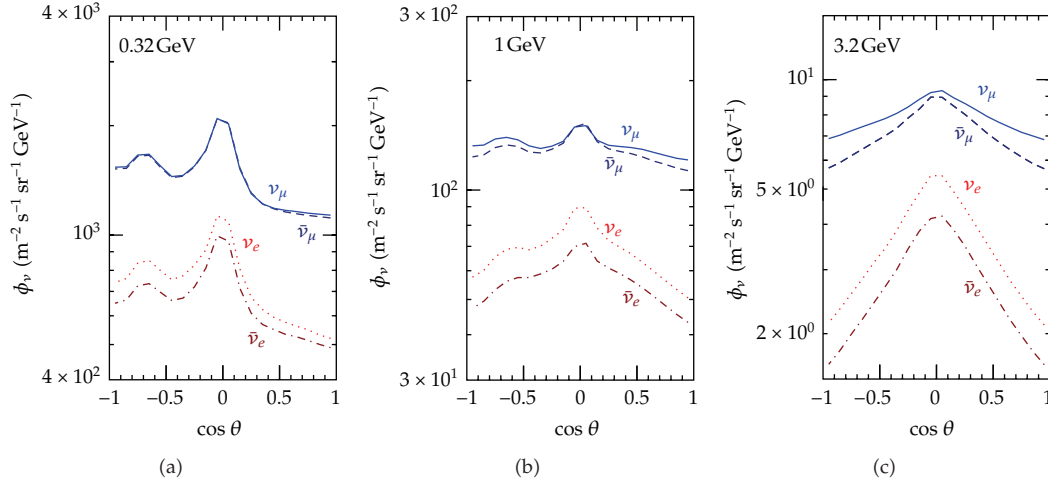


**Figure 6:** The zenith angle dependence of atmospheric neutrino flux averaged over all azimuthal angles calculated for Kamioka. Here  $\theta$  is the arrival direction of the neutrino, with  $\cos \theta = 1$  ( $-1$ ) for vertically downward- (upward-) going neutrinos [7].

In the early 1980s, the first massive underground detectors (of the order 1 kton) were constructed, primarily to search for proton decay as predicted by early Grand Unified Theories [15, 16]. The most serious background for proton decay searches was atmospheric neutrino events, at a rate of approximately  $10^2$  events/kt/yr. Therefore, these experiments were required to study atmospheric neutrino events in order to understand the proton decay background. One of these experiments was Kamiokande. It was a 3-kton water Cherenkov detector. Kamiokande measured the number of single Cherenkov-ring  $e$ -like and  $\mu$ -like events, which were mostly CC  $\nu_e$  and  $\nu_\mu$  interactions, respectively. In 1988, they found that the number of  $\mu$ -like events had a significant deficit compared with the Monte Carlo prediction, while the number of  $e$ -like events had that in agreement with the prediction within the statistical and systematic errors [17]. As already discussed, the flavor ratio of the atmospheric neutrino flux,  $(\nu_\mu + \bar{\nu}_\mu)/(\nu_e + \bar{\nu}_e)$ , has been calculated accurately. This can be explained by the deficit of CC  $\nu_\mu$  events. Consistent results were reported from the IMB water Cherenkov experiment in 1991 [18] and from the Soudan-2 experiment in 1997 [19], as well as from the updated analysis of the Kamiokande data in 1992 [20].

Another important hint toward the understanding of the atmospheric neutrino problem was given in the mid 1990s [21]. Zenith angle distributions for multi-GeV fully contained events and partially contained events were studied in Kamiokande. For detectors near the surface of the Earth, the neutrino flight distance, and thus the neutrino oscillation probability, is a function of the zenith angle of the neutrino direction. Vertically downward-going neutrinos travel about 15 km while vertically upward-going neutrinos travel about 12,800 km before interacting in the detector. The Kamiokande data showed that the deficit of  $\mu$ -like events depended on the zenith angle, and thus on the neutrino flight length. However, due to the relatively poor event statistics, the statistical significance of the updown asymmetry in the Kamiokande data was 2.9 standard deviations, and therefore the data were not conclusive.

In 1996, a much larger detector, Super-Kamiokande, started taking data. Super-Kamiokande (Super-K) is a 50-kton water Cherenkov detector with approximately 11,000 and 1,900 inner and outer detector PMTs. Figure 7 shows the schematic drawing of the

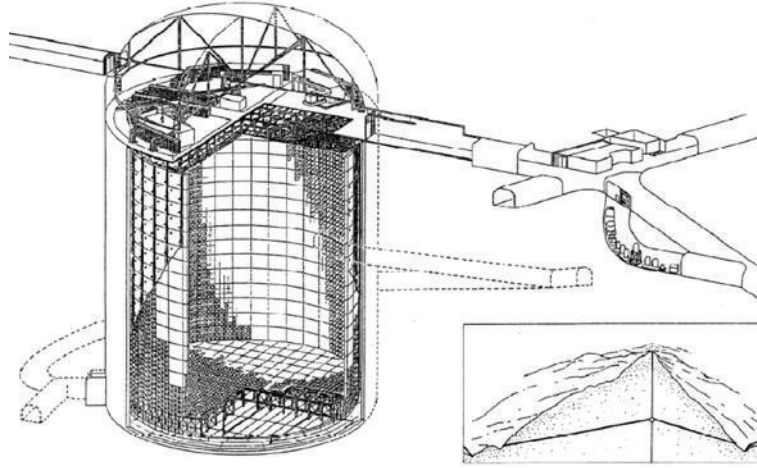


**Figure 7:** The Super-Kamiokande detector. It is a 50 kton water Cherenkov detector with approximately 11,000 and 1,900 inner and outer detector PMTs. It is located 1-km deep underground.

Super-Kamiokande detector. In 1998, the Super-K experiment, with substantially larger data statistics than those in the previous experiments, concluded that the atmospheric neutrino data gave evidence for neutrinos oscillations [22, 23]. The data clearly showed the deficit of upward-going  $\nu_\mu$  events in the multi-GeV energy range, as well as the smaller  $\mu$ -like/ $e$ -like event ratio than what was expected, the smaller upward-going stopping/through-going muon ratio than what was expected, and the distortion of the zenith angle distribution for the upward through-going muons. In addition, the MACRO [24] and Soudan-2 [25] experiments observed similar distributions with the analyses of upward-going muon data and the contained neutrino data, respectively. Since then, the atmospheric neutrino experiments have been contributing substantially to our understanding of neutrino masses and mixing angles.

#### 4. Present Atmospheric Neutrino Experiments

Atmospheric neutrinos can be detected by underground neutrino detectors. Interactions of low energy neutrinos, around 1 GeV, have all of the final state particles “fully contained (FC)” in the detector. Higher energy charged current  $\nu_\mu$  interactions may result in the muon exiting the detector; these are referred to as “partially contained (PC).” In order to reject background from cosmic-ray particles, as well as to cleanly reconstruct the details of the event, the vertex position of the interaction is typically defined to be within some fiducial volume. In addition, some of the detectors are equipped with outer detectors (also referred to as veto- or antineutrino detectors) to easily identify penetrating particles.

There is a third category of charged current  $\nu_\mu$  events, where the interaction occurs outside the detector, and the muon enters and either passes through the detector or stops in the detector. These are referred to as “upward-going muons” because one generally requires they originate from below the horizon to ensure that a sufficient amount of rock absorbs ordinary cosmic ray muons. The fully contained, partially contained, and upward-going muon event samples have a certain range of parent neutrino energies. As an example, Figure 8 shows the distribution of parent neutrino energies for each category of event samples for the Super-Kamiokande experiment [26]. The energies of atmospheric neutrinos observed



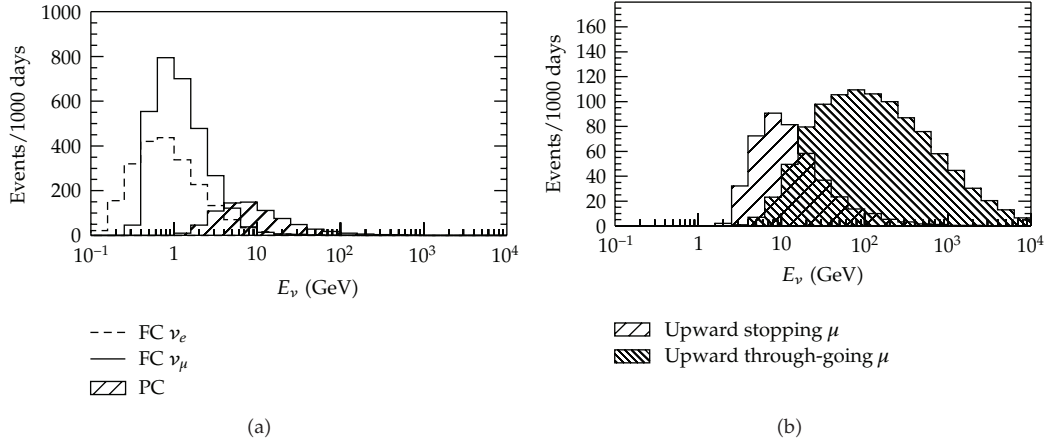


**Figure 8:** The parent neutrino energy distributions for several different classifications of atmospheric neutrino events for the Super-Kamiokande analysis [26]; for other detectors they will be similar but different depending on detector size, which controls the maximum energy of a fully contained event and the minimum energy of a through-going muon.

in underground detectors range from about 100 MeV to higher than 10 TeV. Depending on the type of experiment, these types of events are studied.

As of this writing, there are four experiments that are presently studying atmospheric neutrinos: Super-K, MINOS, SNO, and IceCube.

SNO was a well-known solar neutrino detector. This experiment was able to measure muons as well, which were generated by high energy atmospheric neutrino interactions in the surrounding rock [27]. Since the SNO detector was located 2 km underground, near-horizontal downward-going muons are neutrino induced. The typical neutrino energy for these muons is 100 GeV. With the currently known  $\Delta m^2$  value, one can easily estimate that the effect of neutrino oscillation is negligibly small for neutrinos that generate these near-horizontal downward-going muons. Therefore, these muon data can be used to calibrate the calculated atmospheric neutrino flux. The measured downward-going muon flux [27] was  $1.22 \pm 0.09$ -times higher than the calculated one by the Bartol group [6]. This result suggests that the absolute flux normalization in the 100 GeV energy range should be improved by future flux calculations.

MINOS is mainly a detector for long baseline neutrino oscillation experiment. However, being located 2070 m.w.e. underground, it can also detect atmospheric neutrinos. It is the first magnetized tracking detector for atmospheric neutrinos. MINOS is able to get information on the track direction, the charge, and the momentum. In [28] the initial results from MINOS on the study of separated atmospheric  $\nu_\mu$  and  $\bar{\nu}_\mu$  events were presented. The data were consistent with the standard  $\nu_\mu \rightarrow \nu_\tau$  oscillations. The study was updated with significantly more data [29].

IceCube is a neutrino telescope whose main purpose is to study very high energy astrophysical neutrinos. The main background for the search for these astrophysical neutrinos are high energy atmospheric neutrinos. In [30] the atmospheric  $\nu_\mu$  energy spectrum from 100 GeV to 400 TeV was measured. In this energy range, the energy loss of a muon is approximately proportional to  $\log(E_\mu)$ . Thus the muon and the parent neutrino energy spectra can be estimated. The measured spectrum was consistent with the predictions within the errors.

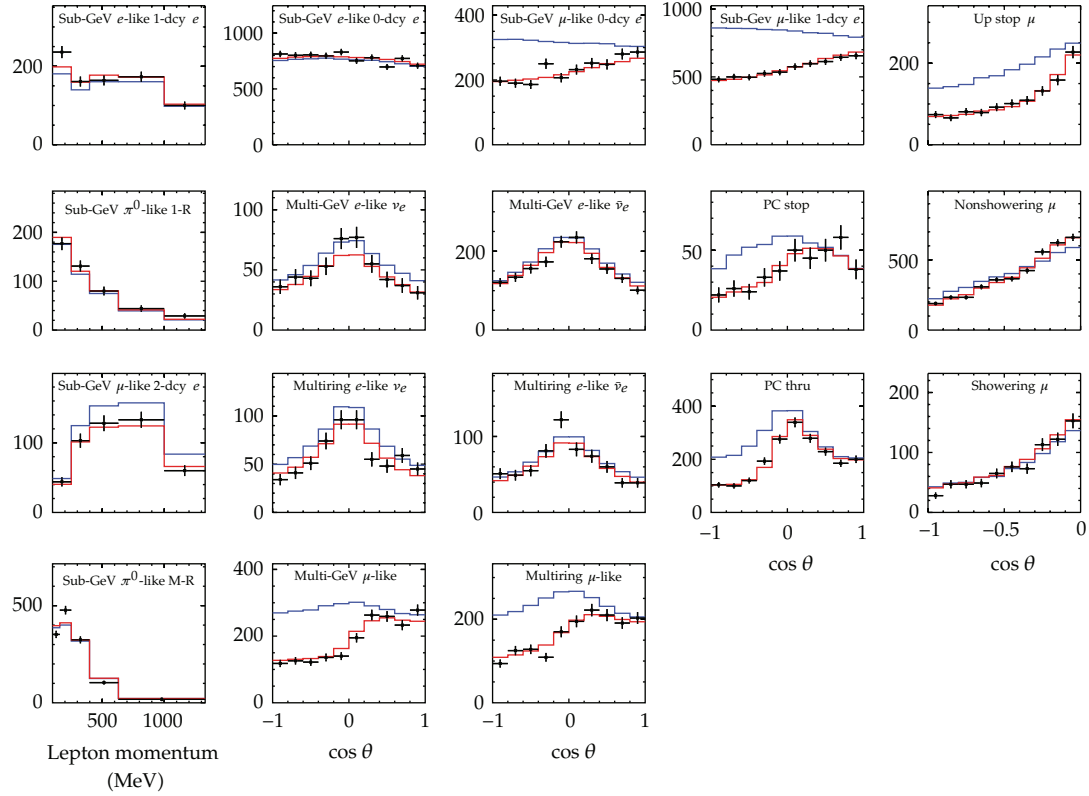


**Figure 9:** Zenith angle distributions observed in Super-K (240-kton · year exposure), except for 4 panels in the left (which show momentum distributions). The blue histograms show the Monte Carlo prediction without oscillations. The red histograms show the best fit  $\nu_\mu \leftrightarrow \nu_\tau$  expectation. Sub-GeV (multi-GeV) events are defined to have the visible energy less (greater) than 1.33 GeV. “PC stop” (“PC through”) means partially contained events with at least one particle exiting from the inner detector but stopping in the outer detector.

Recently, IceCube added 8 infill strings to the existing IceCube array (DeepCore). In this volume, lower energy (below 100 GeV) neutrinos can be observed. DeepCore observed the deficit of  $\nu_\mu$  interactions due to neutrino oscillations [31].

These experiments contribute to the studies of atmospheric neutrinos in various ways. However, as far as the neutrino oscillation studies are concerned, the statistics of the atmospheric neutrino events in the relevant energy region are dominated by the data from Super-K. Therefore, hereafter, we mainly discuss the atmospheric neutrino results from Super-K.

Super-K has several phases. Data from Super-K I to IV are used for many physics analyses. The total exposure of the detector for fully contained atmospheric neutrino analysis is 240-kton · yr as of June 2012 [32]. Figure 9 shows the zenith angle distributions for various subsamples from Super-K. Recently Super-K has made a new analysis of enriching the  $\nu_e$  and  $\bar{\nu}_e$  events separately by a maximum likelihood method based on information such as the number of electrons from (pion to) muon decays or the fraction of energy carried by hadrons. The separated distributions for  $\nu_e$  and  $\bar{\nu}_e$  enriched samples are also shown. By fitting the zenith angle distributions (see [26] for the analysis method and the results with less data statistics), the oscillation parameters are accurately measured.

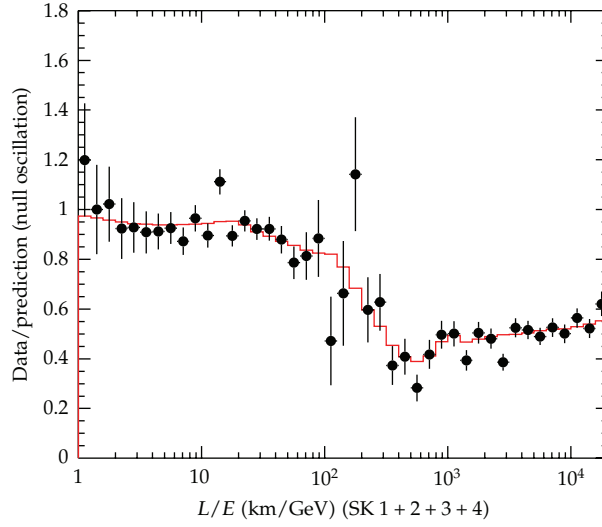


**Figure 10:**  $L/E$  distribution from Super-K (240-kton · year exposure). Data over no-oscillation Monte Carlo prediction are plotted as a function of  $L/E$ . Events that satisfy the  $L/E$  resolution cut (i.e.,  $\sigma(L/E) < 70\%$ ) [33] are used. The red histogram shows the best fit  $\nu_\mu \leftrightarrow \nu_\tau$  expectation.

Furthermore, Super-K updated the  $L/E$  analysis using only high  $L/E$  resolution  $\mu$ -like and PC events (see [33] for details of the analysis). Figure 10 shows the updated  $L/E$  plot from Super-K. One of the initial motivations for the  $L/E$  analysis was to test if the  $\nu_\mu$  disappearance probability obeys the sinusoidal function as predicted by neutrino oscillations. This analysis was also used to discriminate the oscillation and the alternative models that fit to the zenith angle distributions rather well. These models included neutrino decay [34, 35] and neutrino decoherence [36, 37] models. The  $L/E$  distribution shows a dip around  $L/E = 500$  km/GeV that corresponds to the first oscillation minimum. The distribution is used to compare the oscillation and other hypotheses and to constrain the other hypotheses: the decay and decoherence models are disfavored at 4.0 and 4.8 standard deviations, respectively. Due to the observation of the dip, the allowed region of the oscillation parameters, especially that of  $\Delta m_{23}^2$ , is accurately measured.

#### 4.1. Flavor Oscillation Analyses

Neutrino oscillation analyses were carried out using the observed data in various atmospheric neutrino experiments. In these analyses, the treatment of the systematic errors is very important, since, in some cases, the systematic errors have significant effects to the results of the analyses. Therefore, systematic errors are carefully studied and taken into account in the oscillation analyses. In the case of Super-Kamiokande, the number of the systematic error terms in the analyses are more than 100. Some of them are related to the flux, the neutrino interaction, and the detector.

Figure 11 shows the allowed regions of two-flavor  $\nu_\mu \leftrightarrow \nu_\tau$  oscillation parameters from the atmospheric neutrino and long baseline neutrino oscillation experiments. We find that the allowed regions overlap well, suggesting further that the standard neutrino oscillation scenario is valid. From this figure, we find that  $\Delta m_{23}^2$  is most accurately measured by the

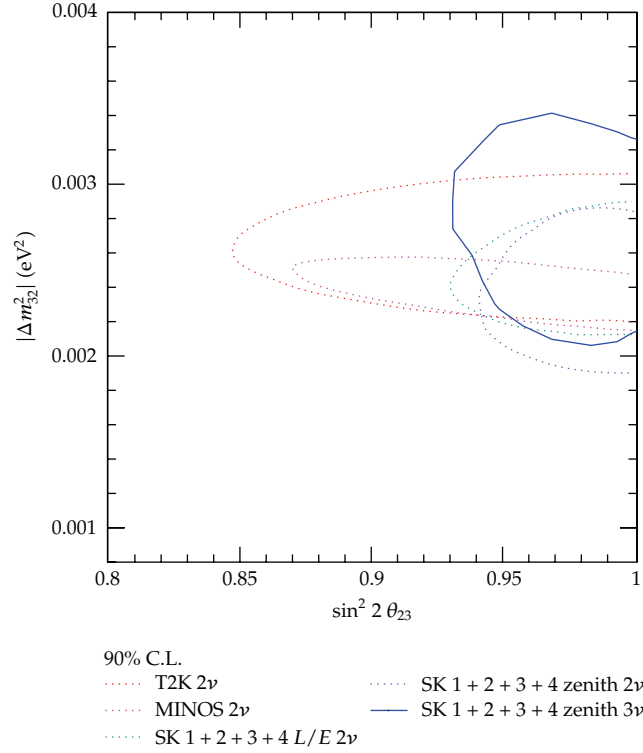


**Figure 11:** 90% C.L. allowed regions of  $\sin^2 2\theta_{23}$  and  $\Delta m_{23}^2$  oscillation parameters from atmospheric neutrino [32] and long baseline [38, 55] neutrino oscillation experiments with  $\nu_\mu \leftrightarrow \nu_\tau$  2-flavor oscillation assumption. For atmospheric neutrinos, results from the zenith angle and  $L/E$  analyses are plotted. Also shown is the allowed region on these parameters from the full 3-flavor analysis of the Super-K atmospheric neutrino data. For 3-flavor oscillations, normal mass hierarchy and the best fit  $\sin^2 \theta_{13}$  are assumed.

MINOS long baseline experiment [38], while the mixing parameter is still measured most accurately by the Super-K atmospheric neutrino experiment. The reason for the possibility to measure  $\sin^2 2\theta_{23}$  accurately in atmospheric neutrino experiments can be understood easily: one finds that  $1 - \sin^2 2\theta_{23} = \text{number of upgoing events} / \text{number of down going events}$  in the energy range where the neutrino and the lepton directions have good correlation (i.e., multi-GeV energy range). In addition, the flux is predicted to be updown symmetric to a very good approximation in the multi-GeV energy range. Finally, it should also be noted that  $\sin^2 2\theta_{23}$  is consistent with 1.0.

#### 4.2. Tau Appearance

About one CC  $\nu_\tau$  event per kiloton year exposure is expected to occur in an atmospheric neutrino detector for  $\nu_\mu \rightarrow \nu_\tau$  oscillations with the present best fit oscillation parameters. The low event rate is due to the soft energy spectrum of the atmospheric neutrino flux and the threshold effect, which requires a  $\nu_\tau$  energy of at least 3.5 GeV to produce a  $\tau$  lepton. These  $\tau$  typically decay to hadrons (the branching ratio is 64%) within 1 mm from the vertex point. These events should be upward-going but otherwise similar to energetic NC events. Hence

it is difficult to isolate  $\nu_\tau$  events with the event-by-event bases in the ongoing atmospheric neutrino experiments.

Super-K searched for CC  $\nu_\tau$  events in the multi-GeV FC events. First, it was required that the most energetic ring is  $e$ -like, in order to reduce the CC  $\nu_\mu$  background. Then, the candidate  $\nu_\tau$  events were selected by a neural-network method. Several variables of event reconstruction were used as the inputs to these analyses. Then, the zenith angle distribution as a function of the output parameter of the neural network is used to estimate the number of  $\nu_\tau$  events statistically. It is important to notice that the estimation is possible, because both the  $\nu_\tau$  signal and background events have accurately predicted zenith angle distributions. Figure 12 shows the output from the neural-network analysis and the zenith angle distributions from the tau analysis. The best fit number of  $\nu_\tau$  interactions that occurred in the fiducial volume of the detector during the  $173\text{-kton}\cdot\text{yr}$  exposure was  $180.1 \pm 44.3(\text{stat.})^{+17.8}_{-15.2}(\text{syst.})$  [39]. The expected number was  $120.2^{+34.2}_{-34.8}$ . The observed number of  $\nu_\tau$  interactions was consistent with the  $\nu_\mu \rightarrow \nu_\tau$  expectation. As of this writing, the  $\theta_{13}$  mixing angle has been determined accurately [40–44]. This has a significant impact on the systematic error of the tau appearance, since one of the largest systematic errors in the previous analysis [45] was due to the unknown value of  $\theta_{13}$ , that is, the unknown contribution of the electron appearance events in the upward-going direction in the tau-like sample. In the most updated analysis [39],  $\nu_\tau$  appearance is required to fit the atmospheric neutrino data with a significance at the 3.8 standard deviation level.

### 4.3. Flavor Oscillation Analyses

Recent data from the Daya Bay [40], RENO [41], and Double CHOOZ [42] reactor experiments as well as those from the T2K [43] and MINOS [44] long baseline experiments showed that  $\sin^2\theta_{13} = 0.0245^{+0.0034}_{-0.0031}$  for normal hierarchy [46]. For inverted hierarchy, the central value is 0.0246 [46]. Although the atmospheric neutrino data are well fit by 2-flavor  $\nu_\mu \leftrightarrow \nu_\tau$  oscillations, 3-flavor oscillation effects should be visible at some level. With the observation of nonzero  $\theta_{13}$ , it is interesting to ask if atmospheric neutrino experiments can determine the mass hierarchy or the CP phase in the neutrino mixing matrix.

Since the 3-flavor oscillations include  $\nu_e$ 's, let us write the oscillation effects as follows:

$$\begin{aligned} \left( \frac{F_{\nu_e}^{\text{osc}}}{F_{\nu_e}^0} \right) &= \Delta_1(\theta_{13}) \\ &+ \Delta_2(\Delta m_{12}^2, \theta_{12}) \\ &+ \Delta_3(\theta_{13}, \Delta m_{12}^2, \theta_{12}, \delta), \end{aligned} \quad (4.1)$$

where  $F_{\nu_e}^{\text{osc}}$  and  $F_{\nu_e}^0$  are the atmospheric  $\nu_e$  fluxes with and without oscillations, and  $\Delta_i$  are the  $\nu_e$  flux change due to oscillation in matter driven by the parameters listed in the parentheses. Figure 13 shows the oscillation probability ( $P(\nu_\mu \rightarrow \nu_e)$ ) as a function of the neutrino energy ( $E_\nu$ ) and zenith angle ( $\cos\Theta_z$ ). In this plot, normal mass hierarchy is assumed, and the oscillation probability is for neutrinos.

Atmospheric neutrino experiments are sensitive to all the  $\Delta_i$ 's in (4.1). Since the matter enhancement of oscillations is only effective for neutrinos and not for antineutrinos for



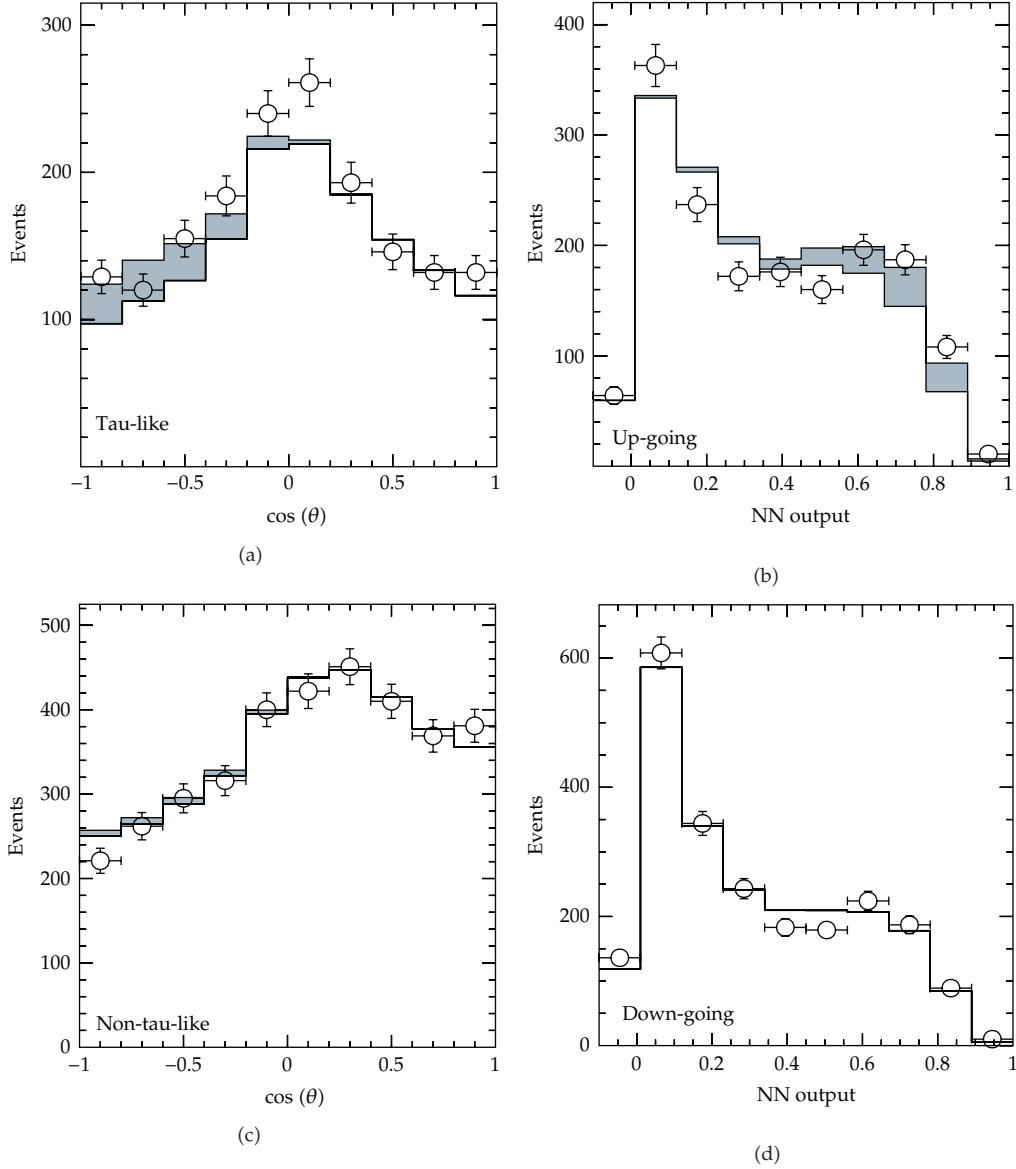


**Figure 12:** Left: zenith angle distribution for the tau-like and non-tau-like events observed in Super-K I to III (173-kton  $\cdot$  yr). The shaded region and solid histogram show the fitted tau neutrino contribution and the non-tau atmospheric neutrino interactions, respectively. Right: fit results showing the output of the neural-network analysis for upward-going and downward-going events. Events near NN output = 1 (0) are most tau-like (non-tau-like).

the normal mass hierarchy, and since there are several features that are different for neutrinos and antineutrino interactions, it might be possible to determine the mass hierarchy with atmospheric neutrino data. The interference term (CP violation term) may also play an important role in atmospheric neutrino oscillations. In fact, some authors (see, e.g., [47]) have indicated the potential importance of the full 3-flavor analysis in atmospheric neutrino experiments, even before the discovery of nonzero  $\theta_{13}$ .

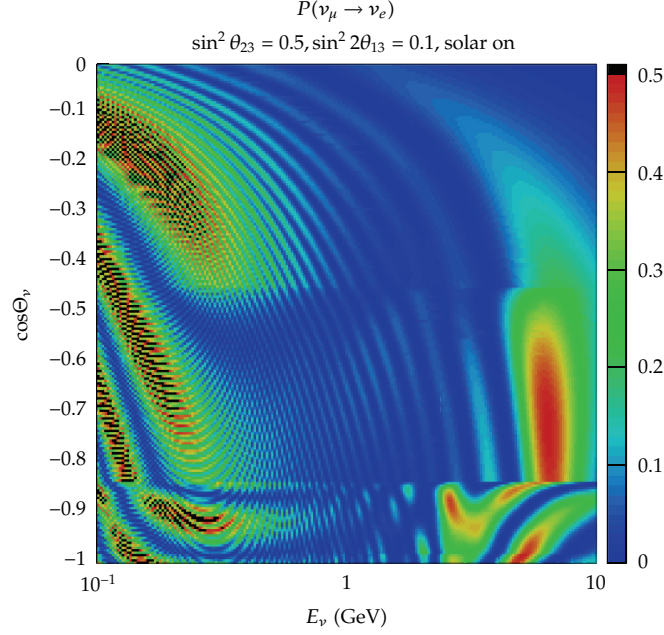


**Figure 13:**  $P(\nu_\mu \rightarrow \nu_e)$  is plotted as a function of the neutrino energy ( $E_\nu$ ) and the zenith angle ( $\Theta_z$ ). The oscillation probability is shown by the color. The large oscillation probability in the 5- to 10-GeV energy and for  $\cos\Theta_z < 0.5$  is due to  $\theta_{13}$  with the matter effects. Below about 300 MeV, the oscillation effects due to solar terms with the matter effects are seen. Between these two energy regions, there are effects due to the interference of these two effects (CP phase).

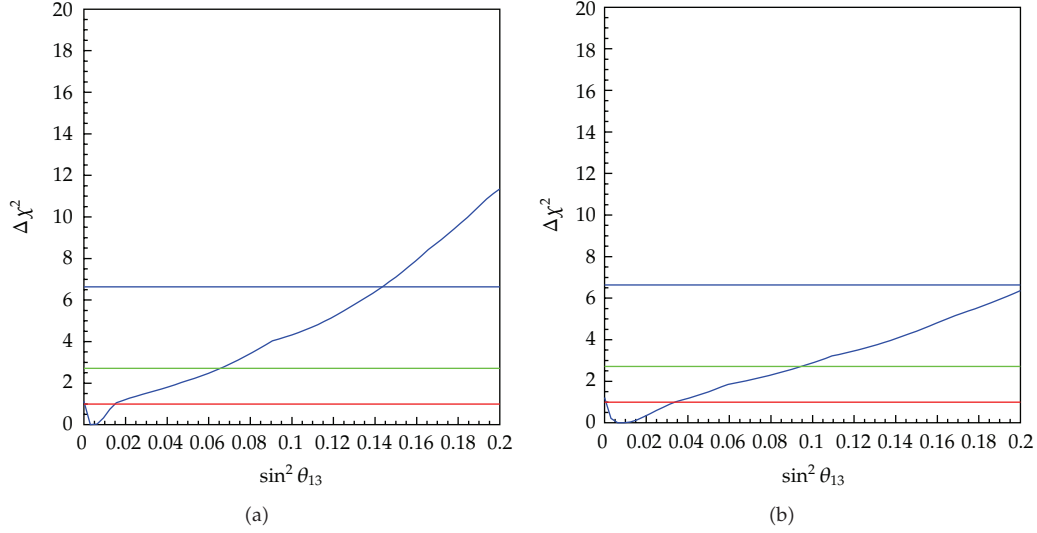
Super-Kamiokande carried out a full 3-flavor analysis [32]. Figure 14 shows the  $\chi^2 - \chi_{\min}^2$  distributions as a function of  $\sin^2\theta_{13}$  for normal and inverted hierarchy cases. At present, the data are consistent with the reactor and accelerator measurement on  $\sin^2\theta_{13}$ .

Figure 15 shows the  $\chi^2$  distributions as a function of  $\delta_{\text{CP}}$  for normal and inverted hierarchy cases. There is some difference in the  $\chi^2$  depending on the mass hierarchies and on  $\delta_{\text{CP}}$ : the  $\chi^2$  difference for the best fit  $\delta_{\text{CP}}$  point and the worst fit point is 2.5 for both normal and inverted mass hierarchies. The minimum  $\chi^2$  value for the inverted mass hierarchy is smaller than that of the normal mass hierarchy by 1.2. It is clear that the present data cannot determine the mass hierarchy. However, they suggest that the future atmospheric neutrino experiments with much higher statistics or with the  $\nu$  and  $\bar{\nu}$  separation might be able to determine the mass hierarchy.

Figure 16 shows the  $\chi^2 - \chi_{\min}^2$  distributions as a function of  $\sin^2\theta_{23}$  for normal and inverted hierarchy cases. If  $\theta_{13}$  is constrained to the present best fit value and the normal hierarchy is assumed, the best fit  $\sin^2\theta_{23}$  is less than 0.5. However, in the other cases, the best fit  $\sin^2\theta_{23}$  is larger than 0.5. In any case, all the curves suggest that the data are consistent with the maximal mixing, that is,  $\sin^2\theta_{23} = 0.5$ .

## 5. Future Directions

Present data from Super-K suggest that future atmospheric neutrino experiments might determine the mass hierarchy and constrain the CP phase. Sensitivity studies have been carried out with different detector technologies.



**Figure 14:**  $\chi^2 - \chi^2_{\min}$  distributions as a function of  $\sin^2\theta_{13}$  for normal (a) and inverted (b) hierarchies from a full 3-flavor oscillation analysis of the Super-K data. Red, green, and blue lines show 68, 90, and 99% C.L., respectively. The  $\chi^2_{\min}$  is independently calculated for each hierarchy.

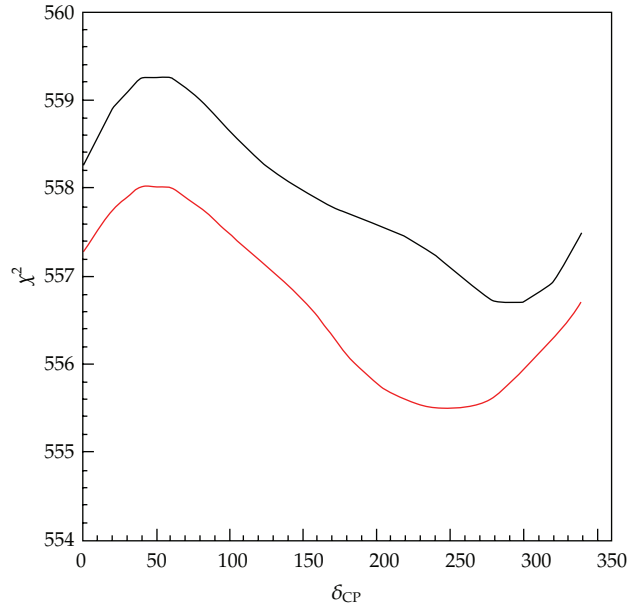


**Figure 15:**  $\chi^2$  distribution as a function of  $\delta_{CP}$  for normal (black line) and inverted (red line) hierarchies from a full 3-flavor oscillation analysis of the Super-K data.

Figure 17 shows the sensitivity to the mass hierarchy in a water Cherenkov detector (Hyper-Kamiokande) [48]. Hyper-Kamiokande will have 1-Mton total mass and 0.56-Mton fiducial mass. The sensitivity is defined as the  $\chi^2$  difference between the normal and inverted mass hierarchies as a function of the detector exposure. Assuming that  $\sin^2\theta_{23} = 0.5$  and

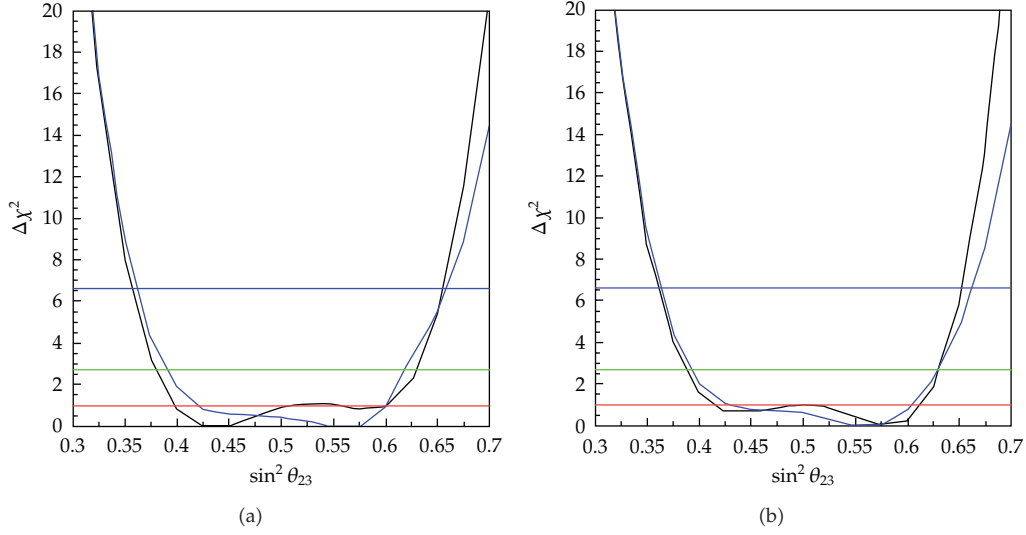


**Figure 16:**  $\chi^2 - \chi^2_{\min}$  distributions as a function of  $\sin^2\theta_{23}$  for normal (a) and inverted (b) hierarchies from the Super-K full 3-flavor oscillation analysis. Black and blue lines show the  $\chi^2$  distributions with and without the constraint of  $\sin^2\theta_{13}$ .

$\sin^2 2\theta_{13} = 0.1$ , the mass hierarchy can be determined at more than the 3-standard deviation level with 5 years of operation for both mass hierarchy cases.

The effects of  $\theta_{13}$  and mass hierarchy to the  $\nu_\mu$  flux are somewhat smaller. However, if the muon charge is measured, a detector will be sensitive to the mass hierarchy. Figure 18 shows the  $P_{\nu_\mu \rightarrow \nu_\mu}(\text{NH}) - P_{\nu_\mu \rightarrow \nu_\mu}(\text{IH})$  for  $\sin^2 2\theta_{13} = 0.1$  and for 2 different zenith angles [49]. One finds the difference for normal and inverted mass hierarchies. The INO project will utilize this feature. The ICAL detector at the INO site will be a 50-kton iron calorimeter detector with 1.5 Tesla magnetic field [50]. Figure 19 shows the schematic view of the ICAL detector, as a typical example of the iron calorimeter detector. Figure 20 shows the expected sensitivity to the mass hierarchy [49]. With the presently known  $\sin^2 2\theta_{13}$  it is possible for ICAL to determine the mass hierarchy, although it may take more than 10 years to reach 3-standard deviation level.

Another proposal is to install additional 20 strings to the existing IceCube's DeepCore detector at the South Pole (PINGU) [51, 52]. Due to its huge fiducial mass ( $O(10)$  Mton) and a lowered energy threshold compared with IceCube/DeepCore, PINGU will have sensitivity to the mass hierarchy. Figure 21 shows the estimated  $(N_\mu^{\text{IH}} - N_\mu^{\text{NH}})/\sqrt{N_\mu^{\text{NH}}}$  for an assumed energy and angular resolutions. Depending on the assumption, it could be possible to determine the mass hierarchy with 5-year data at the 4- to 22-standard deviation level [53].

In addition, it should be pointed out that water Cherenkov detectors are sensitive to the octant of  $\theta_{23}$  and CP phase due to the possibility of observing subleading effects in the sub-GeV to GeV energy region. Figure 22 shows the expected sensitivity to the octant determination in Hyper-K. Even if  $\sin^2 2\theta_{23} = 0.99$ , it will be possible to determine the octant of  $\theta_{23}$  at 90% C.L. for the presently known  $\sin^2 2\theta_{13}$ .

Future atmospheric neutrino experiments will have some sensitivity to the CP phase as shown in [48]. However, it is also true that the sensitivity is limited compared with the planned accelerator-based long baseline experiments. Probably, atmospheric neutrinos

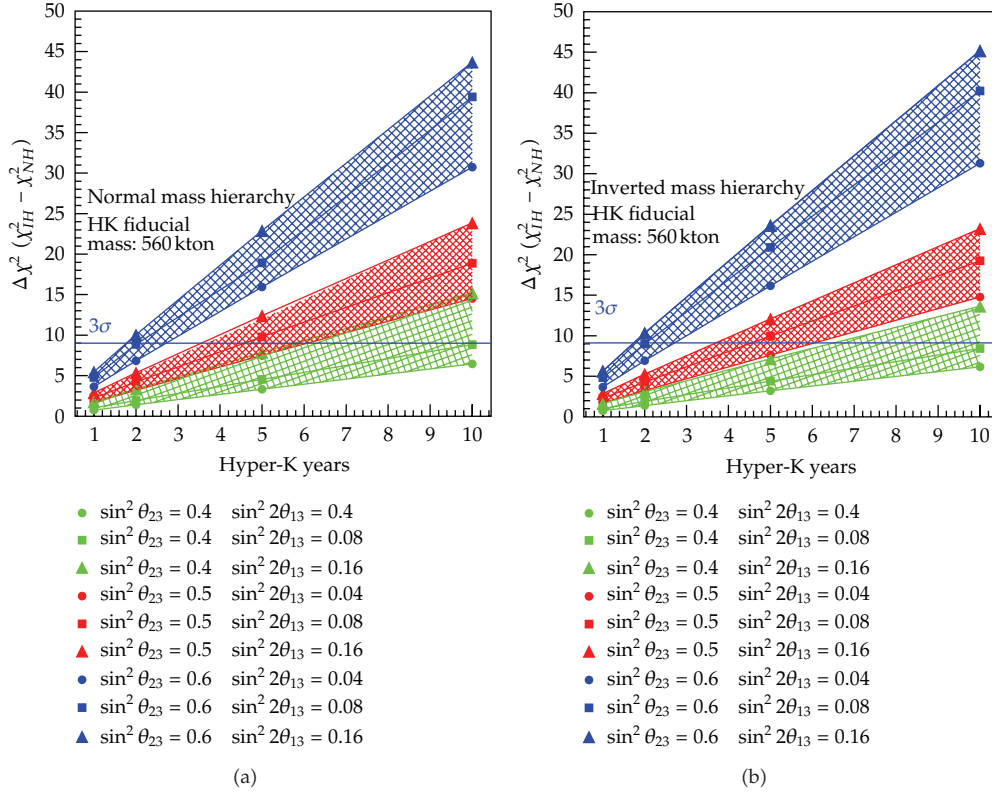


**Figure 17:** Estimated sensitivity for the determination of mass hierarchy as a function of the Hyper-Kamiokande exposure (years), and as a function of  $\sin^2 \theta_{23}$  and  $\sin^2 2\theta_{13}$ . (a) and (b) show the normal and inverted mass hierarchy cases, respectively. Green, red, and blue areas show the estimated  $\Delta\chi^2 (\equiv \chi^2_{\text{wrong}} - \chi^2_{\text{correct}})$  for  $\sin^2 \theta_{23} = 0.4, 0.5$ , and  $0.6$ , respectively. The sensitivity weekly depends on the value of  $\sin^2 2\theta_{13}$ .

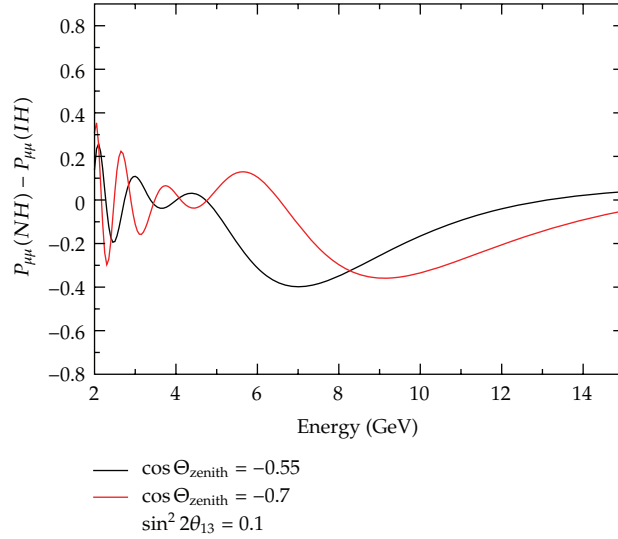


**Figure 18:**  $P_{\nu_\mu \rightarrow \nu_\mu}(\text{NH}) - P_{\nu_\mu \rightarrow \nu_\mu}(\text{IH})$  for  $\sin^2 2\theta_{13} = 0.1$  and for neutrinos propagating through the Earth. Red and black lines show  $P_{\nu_\mu \rightarrow \nu_\mu}(\text{NH}) - P_{\nu_\mu \rightarrow \nu_\mu}(\text{IH})$  for  $\cos \Theta_{\text{zenith}} = -0.7$  and  $-0.55$ , respectively.



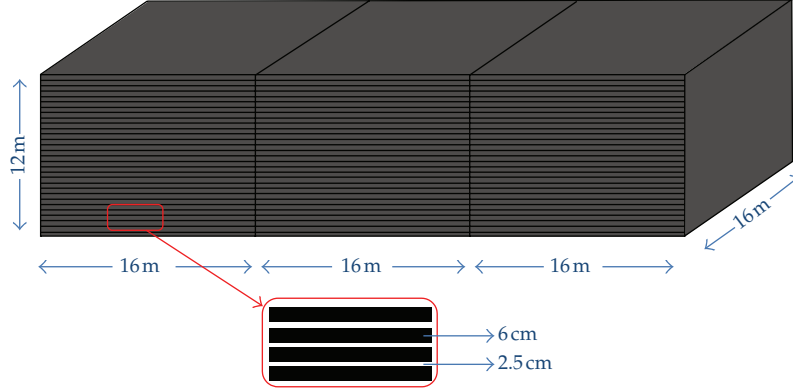


**Figure 19:** Schematic view of the 50-kton iron calorimeter detector ICAL at the INO site. The detector consists of 3 modules each having 140 layers of magnetized iron plates of 6 cm thickness. The 2.5 cm gaps between the plates house the RPCs.

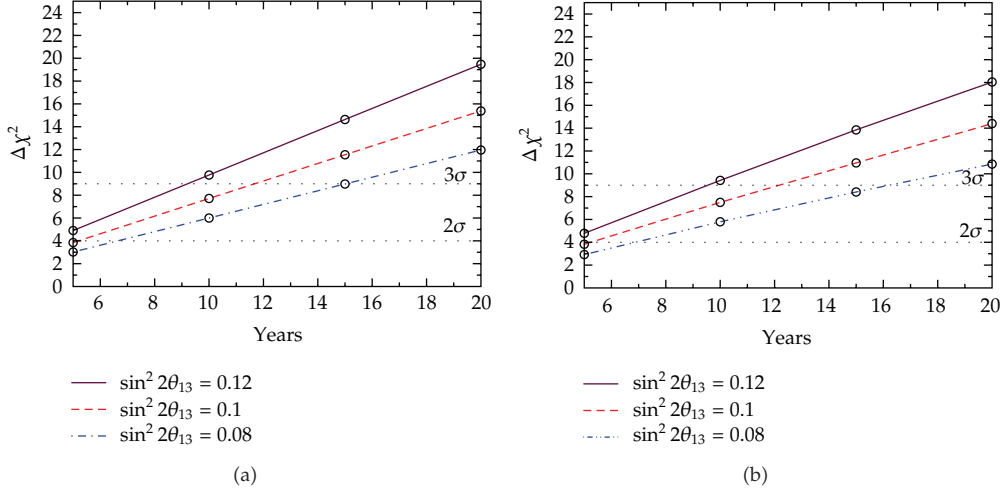


**Figure 20:** Estimated sensitivity for the mass hierarchy as a function of the ICAL exposure (years), and as a function of  $\sin^2 2\theta_{13}$  for normal (a) and inverted (b) hierarchies.

experiments can give independent confirmation of the accelerator results on CP violation. Finally, it should be pointed out that some of the planned long baseline experiments will not have long enough baseline length. Therefore these experiments may not be able to determine the mass hierarchy. If the mass hierarchy is not known, the CP phase cannot be uniquely determined. The determination of the mass hierarchy with future atmospheric neutrino experiments may contribute to eliminate the false CP solution. In this sense, future atmospheric neutrino and long baseline experiments will be complementary.

## 6. Summary

In this paper, the studies of the atmospheric neutrinos are described. The  $L/E$  range in atmospheric neutrinos is very wide, corresponding to the wide neutrino mass range to

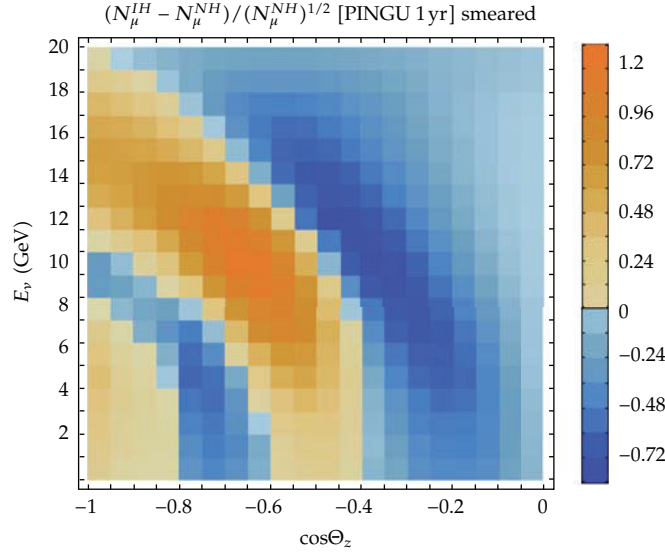


**Figure 21:** The distribution of  $(N_\mu^{IH} - N_\mu^{NH})/\sqrt{N_\mu^{NH}}$  in the  $(E_\nu$  versus  $\cos\Theta_z$ ) plane. This figure assumes  $\sigma_E = 0.3E_\nu$  and  $\sigma_\theta = \sqrt{m_p/E_\nu}$ .

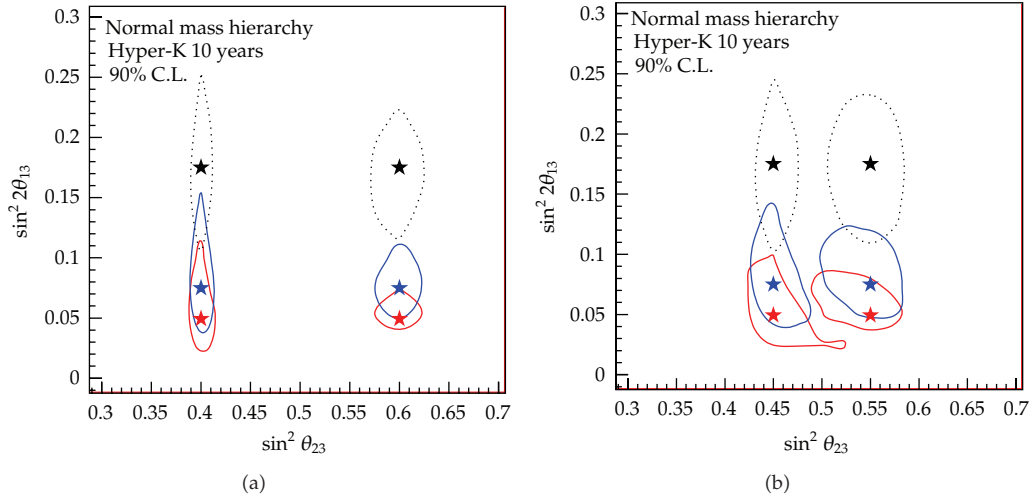


**Figure 22:** 90% C.L. sensitivity for the determination of octant of  $\theta_{23}$  as a function of  $\sin^2 2\theta_{13}$  after 10 years of the Hyper-Kamiokande operation. (a) shows the case of  $\sin^2 2\theta_{23} = 0.96$  ( $\sin^2 \theta_{23} = 0.4$  or  $0.6$ ). (b) shows the case of  $\sin^2 2\theta_{23} = 0.99$  ( $\sin^2 \theta_{23} = 0.45$  or  $0.55$ ). Normal mass hierarchy is assumed.

be studied by oscillation experiments. Therefore, in a sense, atmospheric neutrinos were a natural source to discover neutrino oscillations when the neutrino masses were unknown. It took about 10 years from the discovery of the atmospheric neutrino anomaly to the conclusion of neutrino oscillations in 1998. In the subsequent 14 years, the data and the understanding of the neutrino oscillations were improved substantially. These include the confirmation

of  $\nu_\mu \leftrightarrow \nu_\tau$  oscillations by accelerator based-long baseline experiments, discovery of solar neutrino oscillations, and the discovery of non-zero  $\sin^2\theta_{13}$ .

It is widely believed that the discovery of the neutrino masses opened a window to new physics beyond the standard model of particle physics. In particular, large mixing angles seem to be giving us some hint for our deeper understanding in the relation between quarks and leptons. The small but finite neutrino masses could also be the key to the understanding of the baryon and antibaryon asymmetry in the Universe. Largely motivated by these physics, new proposals and ideas for the future neutrino oscillation experiments have been discussed extensively. Atmospheric neutrino experiments are one of them. It is likely that atmospheric neutrino experiments will continue to contribute to the studies of neutrino oscillations.

## Acknowledgments

The authors gratefully acknowledge the Members of the Super-Kamiokande Collaboration for useful discussions and information. This work was partly supported by the Japanese Ministry of Education, Culture, Sports, Science and Technology and by the Japan Society for the Promotion of Science.

## References

- [1] P. Minkowski, " $\mu \rightarrow e\gamma$  at a rate of  $10^9$  muon decays?" *Physics Letters B*, vol. 67, p. 421, 1977.
- [2] T. Yanagida, "Horizontal gauge symmetry and masses of neutrinos," in *Proceedings of the Workshop on the Unified Theory and Baryon Number in the Universe*, O. Sawada and A. Sugamoto, Eds., pp. 95–98, 1979, (KEK report 79-18, 1979).
- [3] M. Gell-Mann, P. Ramond, and R. Slansky, "Complex spinors and unified theories," in *Supergravity*, P. van Nieuwenhuizen and D. Z. Freedman, Eds., pp. 315–321, North Holland, Amsterdam, 1979.
- [4] Z. Maki, M. Nakagawa, and S. Sakata, "Remarks on the unified model of elementary particles," *Progress of Theoretical Physics*, vol. 28, no. 5, pp. 870–880, 1962.
- [5] B. Pontecorvo, "Neutrino experiments and the problem of conservation of leptonic charge," *Soviet Physics*, vol. 26, pp. 984–988, 1968.
- [6] G. D. Barr, T. K. Gaisser, P. Lipari, S. Robbins, and T. Stanev, "Three-dimensional calculation of atmospheric neutrinos," *Physical Review D*, vol. 70, no. 2, Article ID 023006, 13 pages, 2004.
- [7] M. Honda, T. Kajita, K. Kasahara, and S. Midorikawa, "Improvement of low energy atmospheric neutrino flux calculation using the JAM nuclear interaction model," *Physical Review D*, vol. 83, no. 12, Article ID 123001, 2011.
- [8] M. Honda, T. Kajita, K. Kasahara, S. Midorikawa, and T. Sanuki, "Calculation of atmospheric neutrino flux using the interaction model calibrated with atmospheric muon data," *Physical Review D*, vol. 75, no. 4, Article ID 043006, 2007.
- [9] G. Battistoni, A. Ferrari, P. Lipari, T. Montaruli, P. R. Sala, and T. Rancati, "A three-dimensional calculation of atmospheric neutrino flux," *Astroparticle Physics*, vol. 12, no. 4, pp. 315–333, 2000.
- [10] G. Battistoni, A. Ferrari, T. Montaruli, and P. R. Sala, "The FLUKA atmospheric neutrino flux calculation," *Astroparticle Physics*, vol. 19, no. 2, pp. 269–290, 2003.
- [11] P. Lipari, "Review of sources of atmospheric neutrinos," *Nuclear Physics B*, vol. 91, no. 1–3, pp. 159–166, 2001.
- [12] J. Morfin, J. Nieves, and J. Sobczyk, "Neutrino-nucleus interaction," *Advances in High Energy Physics*. In press.
- [13] C. V. Achar, M. G. K. Menon, V. S. Narasimham, P. V. Ramana Murthy, and B. V. Sreekantan, "Detection of muons produced by cosmic ray neutrinos deep underground," *Physics Letters*, vol. 18, no. 2, pp. 196–199, 1965.
- [14] F. Reines, M. F. Crouch, T. L. Jenkins, W. R. Kropp, H. S. Gurr, and G. R. Smith, "Evidence for high-energy cosmic ray neutrino interactions," *Physical Review Letters*, vol. 15, no. 9, pp. 429–433, 1965.
- [15] J. C. Pati and A. Salam, "Is Baryon number conserved?" *Physical Review Letters*, vol. 31, no. 10, pp. 661–664, 1973.

- [16] H. Georgi and S. L. Galshow, "Unity of all elementary particle forces," *Physical Review Letters*, vol. 32, no. 8, pp. 438–441, 1974.
- [17] K. S. Hirata, T. Kajita, M. Koshiba et al., "Experimental study of the atmospheric neutrino flux," *Physics Letters B*, vol. 205, no. 2-3, pp. 416–420, 1988.
- [18] D. Casper, R. Becker-Szendy, C. B. Bratton et al., "Measurement of atmospheric neutrino composition with IMB-3," *Physical Review Letters*, vol. 66, pp. 2561–2564, 1991.
- [19] W. W. M. Allison, G. J. Alner, D. S. Ayres et al., "Measurement of the atmospheric neutrino flavor composition in Soudan-2," *Physics Letters B*, vol. 391, pp. 491–500, 1997.
- [20] K. S. Hirata, K. Inoue, T. Ishida et al., "Observation of a small atmospheric  $\nu_\mu/\nu_e$  ratio in Kamiokande," *Physics Letters B*, vol. 280, no. 1-2, pp. 146–152, 1992.
- [21] Y. Fukuda, T. Hayakawa, K. Inoue et al., "Atmospheric  $\nu_\mu/\nu_e$  ratio in the multi-GeV energy range," *Physics Letters B*, vol. 335, no. 2, pp. 237–245, 1994.
- [22] Y. Fukuda, T. Hayakawa, E. Ichihara et al., "Evidence for oscillation of atmospheric neutrinos," *Physical Review Letters*, vol. 81, no. 8, pp. 1562–1567, 1998.
- [23] T. Kajita, "Atmospheric neutrino results from Super-Kamiokande and Kamiokande—evidence for  $\nu\mu$  oscillations," *Nuclear Physics B*, vol. 77, no. 1–3, pp. 123–132, 1999.
- [24] M. Ambrosio, R. Antolínig, C. Aramo et al., "Measurement of the atmospheric neutrino induced upgoing muon flux using MACRO," *Physics Letters B*, vol. 434, pp. 451–457, 1998.
- [25] M. C. Sanchez, W. W. M. Allison, G. J. Alner et al., "Measurement of the L/E distributions of atmospheric neutrinos in Soudan 2 and their interpretation as neutrino oscillations," *Physical Review D*, vol. 68, no. 11, Article ID 113004, 14 pages, 2003.
- [26] Y. Ashie, J. Hosaka, K. Ishihara et al., "A measurement of atmospheric neutrino oscillation parameters by Super-Kamiokande I," *Physical Review D*, vol. 71, Article ID 112005, 2005.
- [27] B. Aharmim, S. Ahmed, T. Andersen et al., "Measurement of the cosmic ray and neutrino-induced muon flux at the sudbury neutrino observatory," *Physical Review D*, vol. 80, Article ID 012001, 2009.
- [28] P. Adamson, T. Alexopoulos, W. Allison et al., "First observations of separated atmospheric  $\nu_\mu$  and  $\bar{\nu}_\mu$  events in the MINOS detector," *Physical Review D*, vol. 73, no. 7, Article ID 072002, 2006.
- [29] B. Rebel and MINOS Collaboration, "Observation of atmospheric neutrinos and antineutrinos by the MINOS experiment," in *Proceedings of the 25th International Conference on Neutrino Physics and Astrophysics*, Kyoto, Japan, June 2012.
- [30] R. Abbasi, Y. Abdou, T. Abu-Zayyad et al., "Measurement of the atmospheric neutrino energy spectrum from 100 GeV to 400 TeV with IceCube," *Physical Review D*, vol. 83, Article ID 012001, 2011.
- [31] A. Gross and IceCube Collaboration, "Atmospheric neutrino oscillations with Ice-Cube/DeepCore," in *Proceedings of the 25th International Conference on Neutrino Physics and Astrophysics*, Kyoto, Japan, June 2012.
- [32] Y. Itow, "Atmospheric neutrinos—results from running experiments," in *Proceedings of the 25th International Conference on Neutrino Physics and Astrophysics*, Kyoto, Japan, June 2012.
- [33] Y. Ashie, J. Hosaka, K. Ishihara et al., "Evidence for an oscillatory signature in atmospheric neutrino oscillation," *Physical Review Letters*, vol. 93, no. 10, Article ID 101801, 6 pages, 2004.
- [34] V. D. Barger, J. G. Learned, S. Pakvasa, and T. J. Weiler, "Neutrino decay as an explanation of atmospheric neutrino observations," *Physical Review Letters*, vol. 82, no. 13, pp. 2640–2643, 1999.
- [35] V. D. Barger, J. G. Learned, P. Lipari, M. Lusignoli, S. Pakvasa, and T. J. Weiler, "Neutrino decay and atmospheric neutrinos," *Physics Letters B*, vol. 462, no. 1-2, pp. 109–114, 1999.
- [36] Y. Grossman and M. P. Worah, "Atmospheric  $\nu/\mu$  deficit from decoherence," <http://arxiv.org/abs/hep-ph/9807511>.
- [37] E. Lisi, A. Marrone, and D. Montanino, "Probing possible decoherence effects in atmospheric neutrino oscillations," *Physical Review Letters*, vol. 85, no. 6, pp. 1166–1169, 2000.
- [38] P. Adamson, C. Andreopoulos, R. Armstrong et al., "Measurement of the neutrino mass splitting and flavor mixing by MINOS," *Physical Review Letters*, vol. 106, Article ID 181801, 2011.
- [39] K. Abe, Y. Hayato, T. Iida et al., "A measurement of the appearance of atmospheric tau neutrinos by super-kamiokande," <http://arxiv.org/abs/1206.0328>.
- [40] F. P. An, J. Z. Bai, A. B. Balantekin et al., "Observation of electron-antineutrino disappearance at Daya Bay," *Physical Review Letters*, vol. 108, Article ID 171803, 7 pages, 2012.
- [41] J. K. Ahn, S. Chebotaryov, J. H. Choi et al., "Observation of reactor electron antineutrino disappearance in the RENO experiment," *Physical Review Letters*, vol. 108, Article ID 191802, 6 pages, 2012.
- [42] Y. Abe, C. Aberle, T. Akiri et al., "Indication for the disappearance of reactor electron antineutrinos in the Double Chooz experiment," *Physical Review Letters*, vol. 108, Article ID 131802, 2012.

- [43] K. Abe, N. Abgrall, Y. Ajima et al., "Indication of electron neutrino appearance from an accelerator-produced off-axis Muon Neutrino Beam," *Physical Review Letters*, vol. 107, Article ID 041801, 2011.
- [44] P. Adamson, D. J. Auty, D. S. Ayres et al., "Improved search for muon-neutrino to electronneutrino oscillations in MINOS," *Physical Review Letters*, vol. 107, Article ID 181802, 2011.
- [45] K. Abe, Y. Hayato, T. Iida et al., "A measurement of atmospheric neutrino flux consistent with tau neutrino appearance," *Physical Review Letters*, vol. 97, Article ID 171801, 2006.
- [46] G. L. Fogli, E. Lisi, A. Marrone, D. Montanino, A. Palazzo, and A. M. Rotunno, "Global analysis of neutrino masses, mixings and phases: entering the era of leptonic CP violation searches," *Physical Review D*, vol. 86, no. 1, Article ID 013012, 10 pages, 2012.
- [47] G. L. Fogli, E. Lisi, A. Marrone, and A. Palazzo, "Global analysis of three-flavor neutrino masses and mixings," *Progress in Particle and Nuclear Physics*, vol. 57, no. 2, pp. 742–795, 2006.
- [48] K. Abe, T. Abe, H. Aihara et al., "Letter of intent: the hyper-kamiokande experiment—detector design and physics potential," <http://arxiv.org/abs/1109.3262>.
- [49] S. Choubey, "Future of atmospheric neutrino measurements," in *Proceedings of the 25th International Conference on Neutrino Physics and Astrophysics*, Kyoto, Japan, June 2012.
- [50] M. S. Athar, INO Collaboration et al., "India-based Neutrino Observatory: Project Report," Volume I., INO-2006-01.
- [51] D. J. Koskinen, "IceCube-DeepCore-PINGU: fundamental neutrino and dark matter physics at the South Pole," *Modern Physics Letters A*, vol. 26, pp. 2899–2915, 2011.
- [52] D. R. Grant, "(IceCube/PINGU Collaboration), 'Extending IceCube-DeepCore with PINGU'," in *Proceedings of the 25th International Conference on Neutrino Physics and Astrophysics*, Kyoto, Japan, June 2012.
- [53] E. Kh. Akhmedov, S. Razzaque, and A. Yu. Smirnov, "Mass hierarchy, 2-3 mixing and CP-phase with huge atmospheric neutrino detectors," <http://arxiv.org/abs/1205.7071>.
- [54] T. Kajita and P. Lipari, "Atmospheric neutrinos and neutrino oscillations," *Comptes Rendus Physique*, vol. 6, no. 7, pp. 739–748, 2005.
- [55] K. Abe, N. Abgrall, Y. Ajima et al., "First Muon-Neutrino disappearance study with an off-axis beam," *Physical Review D*, vol. 85, Article ID 031103, 2012.



## Review Article

# Electromagnetic Properties of Neutrinos

**C. Brogini,<sup>1</sup> C. Giunti,<sup>2</sup> and A. Studenikin<sup>3,4</sup>**

<sup>1</sup> INFN, Sezione di Padova, Via F. Marzolo 8, 35131 Padova, Italy

<sup>2</sup> INFN, Sezione di Torino, Via P. Giuria 1, 10125 Torino, Italy

<sup>3</sup> Department of Theoretical Physics, Moscow State University, Moscow 119991, Russia

<sup>4</sup> Joint Institute for Nuclear Research, Dubna 141980, Moscow, Russia

Correspondence should be addressed to C. Giunti, giunti@to.infn.it

Received 2 July 2012; Accepted 7 August 2012

Academic Editor: Jose Bernabeu

Copyright © 2012 C. Brogini et al. This is an open access article distributed under the Creative Commons Attribution License, which permits unrestricted use, distribution, and reproduction in any medium, provided the original work is properly cited.

In this paper, we discuss the main theoretical aspects and experimental effects of neutrino electromagnetic properties. We start with a general description of the electromagnetic form factors of Dirac and Majorana neutrinos. Then, we discuss the theory and phenomenology of the magnetic and electric dipole moments, summarizing the experimental results and the theoretical predictions. We discuss also the phenomenology of a neutrino charge radius and radiative decay. Finally, we describe the theory of neutrino spin and spin-flavor precession in a transverse magnetic field and we summarize its phenomenological applications.

## 1. Introduction

The investigation of neutrino properties is one of the most active fields of research in current high-energy physics. Neutrinos are special particles, because they interact very weakly and their masses are much smaller than those of the other fundamental fermions (charged leptons and quarks). In the Standard Model neutrinos are massless and have only weak interactions. However, the observation of neutrino oscillations by many experiments (see [1–4]) imply that neutrinos are massive and mixed. Therefore, the Standard Model must be extended to account for neutrino masses. In many extensions of the Standard Model neutrinos acquire also electromagnetic properties through quantum loops effects. Hence, the theoretical and experimental study of neutrino electromagnetic interactions is a powerful tool in the search for the fundamental theory beyond the Standard Model. Moreover, the electromagnetic interactions of neutrinos can generate important effects, especially in astrophysical environments, where neutrinos propagate for long distances in magnetic fields both in vacuum and in matter.

In this paper, we review the theory and phenomenology of neutrino electromagnetic interactions. After a derivation of all the possible types of electromagnetic interactions of Dirac and Majorana neutrinos, we discuss their effects in terrestrial and astrophysical environments and the corresponding experimental results. In spite of many efforts in the search of neutrino electromagnetic interactions, up to now there is no positive experimental indication in favor of their existence. However, the existence of neutrino masses and mixing implies that nontrivial neutrino electromagnetic properties are plausible and experimentalists and theorists are eagerly looking for them.

In this review, we use the notation and conventions in [1]. When we consider neutrino mixing, we have the relation:

$$\nu_{\alpha L} = \sum_{k=1}^3 U_{\alpha k} \nu_{kL} \quad (\alpha = e, \mu, \tau) \quad (1.1)$$

between the left-handed components of the three flavor neutrino fields  $\nu_e, \nu_\mu, \nu_\tau$  and the left-handed components of three massive neutrino fields  $\nu_k$  with masses  $m_k$  ( $k = 1, 2, 3$ ). The  $3 \times 3$  mixing matrix  $U$  is unitary ( $U^\dagger = U^{-1}$ ).

Neutrino electromagnetic properties are discussed in [4–7], and in the previous reviews in [8–14].

The structure of this paper is as follows. In Section 2, we discuss the general form of the electromagnetic interaction of Dirac and Majorana neutrinos, which is expressed in terms of form factors, and the derivation of the form factors in gauge models. In Section 3, we discuss the phenomenology of the neutrino magnetic and electric dipole moments in laboratory experiments. These are the most studied electromagnetic properties of neutrinos, both experimentally and theoretically. In Section 4, we review the theory and experimental constraints on the neutrino charge radius. In Section 5, we discuss neutrino radiative decay and the astrophysical bounds on a neutrino magnetic moment obtained from the study of plasmon decay in stars. In Section 6 we discuss neutrino spin and spin-flavor precession. In conclusion, in Section 7, we summarize the status of our knowledge of neutrino electromagnetic properties and we discuss the prospects for future research.

## 2. Electromagnetic Form Factors

The importance of neutrino electromagnetic properties was first mentioned by Pauli in 1930, when he postulated the existence of this particle and discussed the possibility that the neutrino might have a magnetic moment. Systematic theoretical studies of neutrino electromagnetic properties started after it was shown that in the extended Standard Model with right-handed neutrinos the magnetic moment of a massive neutrino is, in general, nonvanishing and that its value is determined by the neutrino mass [15–23].

Neutrino electromagnetic properties are important because they are directly connected to fundamentals of particle physics. For example, neutrino electromagnetic properties can be used to distinguish Dirac and Majorana neutrinos (see [21, 22, 24–27]) and also as probes of new physics that might exist beyond the Standard Model (see [28–30]).

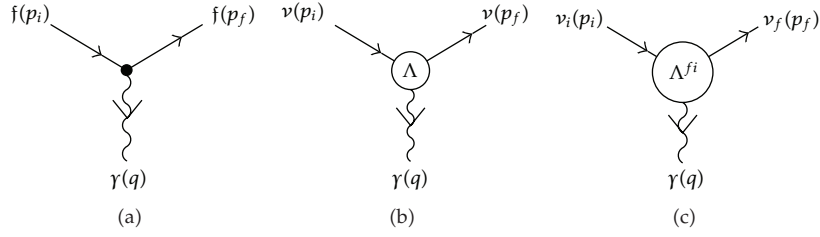


**Figure 1:** Tree-level coupling of a charged fermion  $f$  with a photon  $\gamma$  (a), effective coupling of a neutrino  $\nu$  with a photon (b), and effective coupling of neutrinos with a photon taking into account possible transitions between two different initial and final massive neutrinos  $\nu_i$  and  $\nu_f$  (c).

## 2.1. Dirac Neutrinos

In the Standard Model, the interaction of a fermionic field  $f(x)$  with the electromagnetic field  $A^\mu(x)$  is given by the interaction Hamiltonian:

$$\mathcal{H}_{\text{em}}(x) = j_\mu(x)A^\mu(x) = q_f \bar{f}(x)\gamma_\mu f(x)A^\mu(x), \quad (2.1)$$

where  $q_f$  is the charge of the fermion  $f$ . Figure 1(a) shows the corresponding tree-level Feynman diagram (the photon  $\gamma$  is the quantum of the electromagnetic field  $A^\mu(x)$ ).

For neutrinos, the electric charge is zero and there are no electromagnetic interactions at tree-level (however, in some theories beyond the Standard Model neutrinos can be millicharged particles (see [13])). However, such interactions can arise at the quantum level from loop diagrams at higher order of the perturbative expansion of the interaction. In the one-photon approximation, the electromagnetic interactions of a neutrino field  $\nu(x)$  can be described by the effective interaction Hamiltonian:

$$\mathcal{H}_{\text{eff}}(x) = j_\mu^{\text{eff}}(x)A^\mu(x) = \bar{\nu}(x)\Lambda_\mu \nu(x)A^\mu(x), \quad (2.2)$$

where  $j_\mu^{\text{eff}}(x)$  is the effective neutrino electromagnetic current four-vector and  $\Lambda_\mu$  is a  $4 \times 4$  matrix in spinor space which can contain space-time derivatives, such that  $j_\mu^{\text{eff}}(x)$  transforms as a four-vector. Since radiative corrections are generated by weak interactions which are not invariant under a parity transformation,  $j_\mu^{\text{eff}}(x)$  can be a sum of polar and axial parts. The corresponding diagram for the interaction of a neutrino with a photon is shown in Figure 1(b), where the blob represents the quantum loop contributions.

We are interested in the neutrino part of the amplitude corresponding to the diagram in Figure 1(b), which is given by the matrix element:

$$\langle \nu(p_f, h_f) | j_\mu^{\text{eff}}(x) | \nu(p_i, h_i) \rangle, \quad (2.3)$$

where  $p_i(p_f)$  and  $h_i(h_f)$  are the four-momentum and helicity of the initial (final) neutrino. Taking into account that

$$\partial^\mu j_\mu^{\text{eff}}(x) = i [\not{p}^\mu, j_\mu^{\text{eff}}(x)], \quad (2.4)$$

where  $\not{p}^\mu$  is the four-momentum operator which generate translations, the effective current can be written as

$$j_\mu^{\text{eff}}(x) = e^{i\not{p} \cdot x} j_\mu^{\text{eff}}(0) e^{-i\not{p} \cdot x}. \quad (2.5)$$

Since  $\not{p}^\mu |v(p)\rangle = p^\mu |v(p)\rangle$ , we have

$$\langle v(p_f) | j_\mu^{\text{eff}}(x) | v(p_i) \rangle = e^{i(p_f - p_i) \cdot x} \langle v(p_f) | j_\mu^{\text{eff}}(0) | v(p_i) \rangle, \quad (2.6)$$

where we suppressed for simplicity the helicity labels which are not of immediate relevance. Here we see that the unknown quantity which determines the neutrino-photon interaction is  $\langle v(p_f) | j_\mu^{\text{eff}}(0) | v(p_i) \rangle$ . Considering that the incoming and outgoing neutrinos are free particles which are described by free Dirac fields with the standard Fourier expansion in (2.139) of [1], we have

$$\langle v(p_f) | j_\mu^{\text{eff}}(0) | v(p_i) \rangle = \bar{u}(p_f) \Lambda_\mu(p_f, p_i) u(p_i). \quad (2.7)$$

The electromagnetic properties of neutrinos are embodied by  $\Lambda_\mu(p_f, p_i)$ , which is a matrix in spinor space and can be decomposed in terms of linearly independent products of Dirac  $\gamma$  matrices and the available kinematical four-vectors  $p_i$  and  $p_f$ . The most general decomposition can be written as (see [11])

$$\begin{aligned} \Lambda_\mu(p_f, p_i) = & f_1(q^2) q_\mu + f_2(q^2) q_\mu \gamma_5 + f_3(q^2) \gamma_\mu + f_4(q^2) \gamma_\mu \gamma_5 \\ & + f_5(q^2) \sigma_{\mu\nu} q^\nu + f_6(q^2) \epsilon_{\mu\nu\rho\gamma} q^\nu \sigma^{\rho\gamma}, \end{aligned} \quad (2.8)$$

where  $f_k(q^2)$  are six Lorentz-invariant form factors ( $k = 1, \dots, 6$ ) and  $q$  is the four-momentum of the photon, which is given by

$$q = p_i - p_f, \quad (2.9)$$

from energy-momentum conservation. Notice that the form factors depend only on  $q^2$ , which is the only available Lorentz-invariant kinematical quantity, since  $(p_i + p_f)^2 = 4m^2 - q^2$ . Therefore,  $\Lambda_\mu(p_f, p_i)$  depends only on  $q$  and from now on we will denote it as  $\Lambda_\mu(q)$ .

Since the Hamiltonian and the electromagnetic field are Hermitian ( $\mathcal{H}_{\text{eff}}^\dagger = \mathcal{H}_{\text{eff}}$  and  $A^{\mu\dagger} = A^\mu$ ), the effective current must be Hermitian,  $j_\mu^{\text{eff}\dagger} = j_\mu^{\text{eff}}$ . Hence, we have

$$\langle v(p_f) | j_\mu^{\text{eff}}(0) | v(p_i) \rangle = \langle v(p_i) | j_\mu^{\text{eff}}(0) | v(p_f) \rangle^*, \quad (2.10)$$

which leads to

$$\Lambda_\mu(q) = \gamma^0 \Lambda_\mu^\dagger(-q) \gamma^0. \quad (2.11)$$

This constraint implies that

$$f_2, f_3, f_4 \text{ are real,} \quad (2.12)$$

$$f_1, f_5, f_6 \text{ are imaginary.} \quad (2.13)$$

The number of independent form factors can be reduced by imposing current conservation,  $\partial^\mu j_\mu^{\text{eff}}(x) = 0$ , which is required by gauge invariance (i.e., invariance of  $\mathcal{L}_{\text{eff}}(x)$  under the transformation  $A^\mu(x) \rightarrow A^\mu(x) + \partial^\mu \varphi(x)$  for any  $\varphi(x)$ , which leaves invariant the electromagnetic tensor  $F^{\mu\nu} = \partial^\mu A^\nu - \partial^\nu A^\mu$ ). Using (2.4), current conservation implies that

$$\langle v(p_f) | [\rho^\mu, j_\mu^{\text{eff}}(0)] | v(p_i) \rangle = 0. \quad (2.14)$$

Hence, in momentum space, we have the constraint:

$$q^\mu \bar{u}(p_f) \Lambda_\mu(q) u(p_i) = 0, \quad (2.15)$$

which implies that

$$f_1(q^2)q^2 + f_2(q^2)q^2\gamma_5 + 2mf_4(q^2)\gamma_5 = 0. \quad (2.16)$$

Since  $\gamma_5$  and the unity matrix are linearly independent, we obtain the constraints:

$$f_1(q^2) = 0, \quad f_4(q^2) = -\frac{f_2(q^2)q^2}{2m}. \quad (2.17)$$

Therefore, in the most general case, consistent with Lorentz and electromagnetic gauge invariance, the vertex function is defined in terms of four form factors [25–27]:

$$\Lambda_\mu(q) = f_Q(q^2)\gamma_\mu - f_M(q^2)i\sigma_{\mu\nu}q^\nu + f_E(q^2)\sigma_{\mu\nu}q^\nu\gamma_5 + f_A(q^2)(q^2\gamma_\mu - q_\mu\gamma)\gamma_5. \quad (2.18)$$

where  $f_Q = f_3$ ,  $f_M = if_5$ ,  $f_E = -2if_6$ , and  $f_A = -f_2/2m$  are the real charge, dipole magnetic and electric, and anapole neutrino form factors. For the coupling with a real photon ( $q^2 = 0$ ),

$$f_Q(0) = q, \quad f_M(0) = \mu, \quad f_E(0) = \epsilon, \quad f_A(0) = a, \quad (2.19)$$

where  $q$ ,  $\mu$ ,  $\epsilon$ , and  $a$  are, respectively, the neutrino charge, magnetic moment, electric moment and anapole moment. Although above we stated that  $q = 0$ , here we did not enforce this equality because in some theories beyond the Standard Model neutrinos can be millicharged particles (see [13]).

Now, it is interesting to study the properties of  $\mathcal{L}_{\text{eff}}(x)$  under a CP transformation, in order to find which of the terms in (2.18) violate CP. Let us consider the active CP transformation:

$$U_{\text{CP}}\nu(x)U_{\text{CP}}^\dagger = \xi^{\text{CP}}\gamma^0 C\bar{\nu}^T(x_P), \quad (2.20)$$



where  $\xi^{\text{CP}}$  is a phase,  $\mathcal{C}$  is the charge-conjugation matrix (such that  $\mathcal{C}\gamma_\mu^T\mathcal{C}^{-1} = -\gamma_\mu$ ,  $\mathcal{C}^\dagger = \mathcal{C}^{-1}$  and  $\mathcal{C}^T = -\mathcal{C}$ ), and  $x_P^\mu = x_\mu$ . For the Standard Model electric current  $j_\mu(x)$  in (2.1), we have

$$j_\mu(x) \xrightarrow{\text{CP}} U_{\text{CP}} j_\mu(x) U_{\text{CP}}^\dagger = -j^\mu(x_P). \quad (2.21)$$

Hence, the Standard Model electromagnetic interaction Hamiltonian  $\mathcal{H}_{\text{em}}(x)$  is left invariant by (the transformation  $x \rightarrow x_P$  is irrelevant since all amplitudes are obtained by integrating over  $d^4x$ )

$$A_\mu(x) \xrightarrow{\text{CP}} -A^\mu(x_P). \quad (2.22)$$

CP is conserved in neutrino electromagnetic interactions (in the one-photon approximation) if  $j_\mu^{\text{eff}}(x)$  transforms as  $j_\mu(x)$ :

$$\text{CP} \Longleftrightarrow U_{\text{CP}} j_\mu^{\text{eff}}(x) U_{\text{CP}}^\dagger = -j_{\text{eff}}^\mu(x_P). \quad (2.23)$$

For the matrix element (2.7), we obtain

$$\text{CP} \Longleftrightarrow \Lambda_\mu(q) \xrightarrow{\text{CP}} -\Lambda^\mu(q). \quad (2.24)$$

One can find that under a CP transformation we have

$$\Lambda_\mu(q) \xrightarrow{\text{CP}} \gamma^0 \mathcal{C} \Lambda_\mu^T(q_P) \mathcal{C}^\dagger \gamma^0, \quad (2.25)$$

with  $q_P^\mu = q_\mu$ . Using the form factor expansion in (2.18), we obtain

$$\Lambda_\mu(q) \xrightarrow{\text{CP}} -\left[ f_Q(q^2) \gamma^\mu - f_M(q^2) i\sigma^{\mu\nu} q_\nu - f_E(q^2) \sigma^{\mu\nu} q_\nu \gamma_5 + f_A(q^2) (q^2 \gamma^\mu - q^\mu \not{q}) \gamma_5 \right]. \quad (2.26)$$

Therefore, only the electric dipole form factor violates CP:

$$\text{CP} \Longleftrightarrow f_E(q^2) = 0. \quad (2.27)$$

So far, we have considered only one massive neutrino field  $\nu(x)$ , but according to the mixing relation (1.1), the three flavor neutrino fields  $\nu_e, \nu_\mu, \nu_\tau$  are unitary linear combinations of three massive neutrinos  $\nu_k$  ( $k = 1, 2, 3$ ). Therefore, we must generalize the discussion to the case of more than one massive neutrino field. The effective electromagnetic interaction Hamiltonian in (2.2) is generalized to

$$\mathcal{H}_{\text{eff}}(x) = j_\mu^{\text{eff}}(x) A^\mu(x) = \sum_{k,j=1}^3 \bar{\nu}_k(x) \Lambda_\mu^{kj} \nu_j(x) A^\mu(x), \quad (2.28)$$

where we take into account possible transitions between different massive neutrinos. The physical effect of  $\mathcal{L}_{\text{eff}}$  is described by the effective electromagnetic vertex in Figure 1(c), with the neutrino matrix element:

$$\langle \nu_f(p_f) | j_\mu^{\text{eff}}(0) | \nu_i(p_i) \rangle = \overline{u}_f(p_f) \Lambda_\mu^{fi}(p_f, p_i) u_i(p_i). \quad (2.29)$$

As in the case of one massive neutrino field,  $\Lambda_\mu^{fi}(p_f, p_i)$  depends only on the four-momentum  $q$  transferred to the photon and can be expressed in terms of six Lorentz-invariant form factors:

$$\begin{aligned} \Lambda_\mu^{fi}(q) = & f_1^{fi}(q^2) q_\mu + f_2^{fi}(q^2) q_\mu \gamma_5 + f_3^{fi}(q^2) \gamma_\mu + f_4^{fi}(q^2) \gamma_\mu \gamma_5 \\ & + f_5^{fi}(q^2) \sigma_{\mu\nu} q^\nu + f_6^{fi}(q^2) \epsilon_{\mu\nu\rho\gamma} q^\nu \sigma^{\rho\gamma}. \end{aligned} \quad (2.30)$$

The Hermitian nature of  $j_\mu^{\text{eff}}$  implies that  $\langle \nu_f(p_f) | j_\mu^{\text{eff}}(0) | \nu_i(p_i) \rangle = \langle \nu_i(p_i) | j_\mu^{\text{eff}}(0) | \nu_f(p_f) \rangle^*$ , leading to the constraint:

$$\Lambda_\mu^{fi}(q) = \gamma^0 \left[ \Lambda_\mu^{if}(-q) \right]^\dagger \gamma^0. \quad (2.31)$$

Considering the  $3 \times 3$  form factor matrices  $f_k$  in the space of massive neutrinos with components  $f_k^{fi}$  for  $k = 1, \dots, 6$ , we find that

$$f_2, f_3, f_4 \quad \text{are Hermitian}, \quad (2.32)$$

$$f_1, f_5, f_6 \quad \text{are anti-Hermitian}. \quad (2.33)$$

Following the same method used in (2.4)–(2.16), one can find that current conservation implies the constraints:

$$f_1^{fi}(q^2) q^2 + f_3^{fi}(q^2) (m_f - m_i) = 0, \quad f_2^{fi}(q^2) q^2 + f_4^{fi}(q^2) (m_f + m_i) = 0. \quad (2.34)$$

Therefore, we obtain

$$\Lambda_\mu^{fi}(q) = \left( \gamma_\mu - q_\mu \frac{\not{q}}{q^2} \right) \left[ f_Q^{fi}(q^2) + f_A^{fi}(q^2) q^2 \gamma_5 \right] - i \sigma_{\mu\nu} q^\nu \left[ f_M^{fi}(q^2) + i f_E^{fi}(q^2) \gamma_5 \right], \quad (2.35)$$

where  $f_Q^{fi} = f_3^{fi}$ ,  $f_M^{fi} = i f_5^{fi}$ ,  $f_E^{fi} = -2i f_6^{fi}$  and  $f_A^{fi} = -f_2^{fi} / (m_f + m_i)$ , with

$$f_\Omega^{fi} = \left( f_\Omega^{if} \right)^* \quad (\Omega = Q, M, E, A). \quad (2.36)$$

Note that since  $\overline{u}_f(p_f) \not{q} u_i(p_i) = (m_f - m_i) \overline{u}_f(p_f) u_i(p_i)$ , if  $f = i$ , (2.35) correctly reduces to (2.18).

The form factors with  $f = i$  are called “diagonal,” whereas those with  $f \neq i$  are called “off-diagonal” or “transition form factors.” This terminology follows from the expression:

$$\Lambda_\mu(q) = \left( \gamma_\mu - q_\mu \frac{\not{q}}{q^2} \right) \left[ f_Q(q^2) + f_A(q^2) q^2 \gamma_5 \right] - i \sigma_{\mu\nu} q^\nu \left[ f_M(q^2) + i f_E(q^2) \gamma_5 \right], \quad (2.37)$$

in which  $\Lambda_\mu(q)$  is a  $3 \times 3$  matrix in the space of massive neutrinos expressed in terms of the four Hermitian  $3 \times 3$  matrices of form factors:

$$f_\Omega = f_\Omega^\dagger \quad (\Omega = Q, M, E, A). \quad (2.38)$$

For the coupling with a real photon ( $q^2 = 0$ ), we have

$$f_Q^{fi}(0) = q_{fi}, \quad f_M^{fi}(0) = \mu_{fi}, \quad f_E^{fi}(0) = e_{fi}, \quad f_A^{fi}(0) = a_{fi}, \quad (2.39)$$

where  $q_{fi}$ ,  $\mu_{fi}$ ,  $e_{fi}$ , and  $a_{fi}$  are, respectively, the neutrino charge, magnetic moment, electric moment, and anapole moment of diagonal ( $f = i$ ) and transition ( $f \neq i$ ) types.

Considering now CP invariance, the transformation (2.23) of  $j_\mu^{\text{eff}}(x)$  implies the constraint in (2.24) for the  $N \times N$  matrix  $\Lambda_\mu(q)$  in the space of massive neutrinos. Using (2.20), we obtain

$$\Lambda_\mu^{fi}(q) \xrightarrow{\text{CP}} \xi_f^{\text{CP}} \xi_i^{\text{CP}*} \gamma^0 \mathcal{C} \left[ \Lambda_\mu^{if}(q_P) \right]^T \mathcal{C}^\dagger \gamma^0, \quad (2.40)$$

where  $\xi_k^{\text{CP}}$  is the CP phase of  $\nu_k$ . Since the three massive neutrinos take part to standard charged-current weak interactions, their CP phases are equal if CP is conserved (see [1]). Hence, we have

$$\Lambda_\mu^{fi}(q) \xrightarrow{\text{CP}} \gamma^0 \mathcal{C} \left[ \Lambda_\mu^{if}(q_P) \right]^T \mathcal{C}^\dagger \gamma^0. \quad (2.41)$$

Using the form factor expansion in (2.35), we obtain

$$\Lambda_\mu^{fi}(q) \xrightarrow{\text{CP}} - \left\{ \left( \gamma^\mu - q^\mu \frac{\not{q}}{q^2} \right) \left[ f_Q^{if}(q^2) + f_A^{if}(q^2) q^2 \gamma_5 \right] - i \sigma^{\mu\nu} q_\nu \left[ f_M^{if}(q^2) - i f_E^{if}(q^2) \gamma_5 \right] \right\}. \quad (2.42)$$

Imposing the constraint in (2.24), for the form factors, we obtain

$$\text{CP} \Longleftrightarrow \begin{cases} f_\Omega^{fi} = f_\Omega^{if} = \left( f_\Omega^{fi} \right)^* & (\Omega = Q, M, A), \\ f_E^{fi} = -f_E^{if} = -\left( f_E^{fi} \right)^*, \end{cases} \quad (2.43)$$

where, in the last equalities, we took into account the constraints (2.36). For the Hermitian  $3 \times 3$  form factor matrices, we obtain that if CP is conserved  $f_Q$ ,  $f_M$  and  $f_A$ , are real and symmetric and  $f_E$  is imaginary and antisymmetric:

$$\text{CP} \iff \begin{cases} f_\Omega = f_\Omega^T = f_\Omega^* & (\Omega = Q, M, A), \\ f_E = -f_E^T = -f_E^*. \end{cases} \quad (2.44)$$

Let us now consider antineutrinos. Using for the massive neutrino fields, the Fourier expansion in (2.139) of [1], the effective antineutrino matrix element for  $\bar{\nu}_i(p_i) \rightarrow \bar{\nu}_f(p_f)$  transitions is given by

$$\langle \bar{\nu}_f(p_f) | j_\mu^{\text{eff}}(0) | \bar{\nu}_i(p_i) \rangle = -\bar{v}_i(p_i) \Lambda_\mu^{if}(q) v_f(p_f). \quad (2.45)$$

Using the relation:

$$u(p) = C \bar{v}^T(p), \quad (2.46)$$

we can write it as

$$\langle \bar{\nu}_f(p_f) | j_\mu^{\text{eff}}(0) | \bar{\nu}_i(p_i) \rangle = \bar{u}_f(p_f) C [\Lambda_\mu^{if}(q)]^T C^\dagger u_i(p_i), \quad (2.47)$$

where transposition operates in spinor space. Therefore, the effective form factor matrix in spinor space for antineutrinos is given by

$$\bar{\Lambda}_\mu^{fi}(q) = C [\Lambda_\mu^{if}(q)]^T C^\dagger. \quad (2.48)$$

Using the properties of the charge-conjugation matrix and the expression (2.35) for  $\Lambda_\mu^{if}(q)$ , we obtain the antineutrino form factors:

$$\bar{f}_\Omega^{fi} = -f_\Omega^{if} \quad (\Omega = Q, M, E), \quad (2.49)$$

$$\bar{f}_A^{fi} = f_A^{if}. \quad (2.50)$$

Therefore, in particular the diagonal magnetic and electric moments of neutrinos and antineutrinos have the same size with opposite signs, as the charge, if it exists. On the other hand, the diagonal neutrino and antineutrino anapole moments are equal.

## 2.2. Majorana Neutrinos

A massive Majorana neutrino is a neutral spin 1/2 particle which coincides with its antiparticle. The four degrees of freedom of a massive Dirac field (two helicities and two particle-antiparticle) are reduced to two (two helicities) by the Majorana constraint:

$$\nu_k = \nu_k^c = \mathcal{C}\overline{\nu_k}^T. \quad (2.51)$$

Since a Majorana field has half the degrees of freedom of a Dirac field, it is possible that its electromagnetic properties are reduced. From the relations (2.49) and (2.50) between neutrino and antineutrino form factors in the Dirac case, we can infer that in the Majorana case the charge, magnetic, and electric form factor matrices are antisymmetric and the anapole form factor matrix is symmetric. In order to confirm this deduction, let us calculate the neutrino matrix element corresponding to the effective electromagnetic vertex in Figure 1(c), with the effective interaction Hamiltonian in (2.28), which takes into account possible transitions between two different initial and final massive Majorana neutrinos  $\nu_i$  and  $\nu_f$ . Using the neutrino Majorana fields, the Fourier expansion in (6.99) of [1], we obtain

$$\langle \nu_f(p_f) | j_\mu^{\text{eff}}(0) | \nu_i(p_i) \rangle = \overline{u}_f(p_f) \Lambda_\mu^{fi}(p_f, p_i) u_i(p_i) - \overline{v}_i(p_i) \Lambda_\mu^{if}(p_f, p_i) v_f(p_f). \quad (2.52)$$

Using (2.46), we can write it as

$$\overline{u}_f(p_f) \left\{ \Lambda_\mu^{fi}(p_f, p_i) + \mathcal{C} \left[ \Lambda_\mu^{if}(p_f, p_i) \right]^T \mathcal{C}^\dagger \right\} u_i(p_i), \quad (2.53)$$

where transposition operates in spinor space. Therefore, the effective form factor matrix in spinor space for Majorana neutrinos is given by

$$\tilde{\Lambda}_\mu^{fi}(p_f, p_i) = \Lambda_\mu^{fi}(p_f, p_i) + \mathcal{C} \left[ \Lambda_\mu^{if}(p_f, p_i) \right]^T \mathcal{C}^\dagger. \quad (2.54)$$

As in the case of Dirac neutrinos,  $\Lambda_\mu^{fi}(p_f, p_i)$  depends only on  $q = p_f - p_i$  and can be expressed in terms of six Lorentz-invariant form factors according to (2.30). Hence, we can write the  $3 \times 3$  matrix  $\tilde{\Lambda}_\mu(p_f, p_i)$  in the space of massive Majorana neutrinos as

$$\begin{aligned} \tilde{\Lambda}_\mu(q) = & \tilde{f}_1(q^2) q_\mu + \tilde{f}_2(q^2) q_\mu \gamma_5 + \tilde{f}_3(q^2) \gamma_\mu + \tilde{f}_4(q^2) \gamma_\mu \gamma_5 \\ & + \tilde{f}_5(q^2) \sigma_{\mu\nu} q^\nu + \tilde{f}_6(q^2) \epsilon_{\mu\nu\rho\gamma} q^\nu \sigma^{\rho\gamma}, \end{aligned} \quad (2.55)$$

with

$$\begin{aligned} \tilde{f}_k &= f_k + f_k^T \implies \tilde{f}_k = \tilde{f}_k^T \quad \text{for } k = 1, 2, 4, \\ \tilde{f}_k &= f_k - f_k^T \implies \tilde{f}_k = -\tilde{f}_k^T \quad \text{for } k = 3, 5, 6. \end{aligned} \quad (2.56)$$



Now, we can follow the discussion in Section 2.1 for Dirac neutrinos taking into account the additional constraints (2.56) for Majorana neutrinos. The hermiticity of  $j_\mu^{\text{eff}}$  and current conservation lead to an expression similar to that in (2.37):

$$\tilde{\Lambda}_\mu(q) = \left( \gamma_\mu - q_\mu \frac{\not{q}}{q^2} \right) \left[ \tilde{f}_Q(q^2) + \tilde{f}_A(q^2) q^2 \gamma_5 \right] - i \sigma_{\mu\nu} q^\nu \left[ \tilde{f}_M(q^2) + i \tilde{f}_E(q^2) \gamma_5 \right], \quad (2.57)$$

with  $\tilde{f}_Q^{fi} = \tilde{f}_3^{fi}$ ,  $\tilde{f}_M^{fi} = i \tilde{f}_5^{fi}$ ,  $\tilde{f}_E^{fi} = -2i \tilde{f}_6^{fi}$ , and  $\tilde{f}_A^{fi} = -\tilde{f}_2^{fi} / (m_f + m_i)$ . For the Hermitian  $3 \times 3$  form factor matrices in the space of massive neutrinos,

$$\tilde{f}_\Omega = \tilde{f}_\Omega^\dagger \quad (\Omega = Q, M, E, A), \quad (2.58)$$

the Majorana constraints (2.56) imply that

$$\tilde{f}_\Omega = -\tilde{f}_\Omega^T \quad (\Omega = Q, M, E), \quad (2.59)$$

$$\tilde{f}_A = \tilde{f}_A^T. \quad (2.60)$$

These relations confirm the expectation discussed above that for Majorana neutrinos the charge, magnetic and electric form factor matrices are antisymmetric and the anapole form factor matrix is symmetric.

Since  $\tilde{f}_Q$ ,  $\tilde{f}_M$ , and  $\tilde{f}_E$  are antisymmetric, a Majorana neutrino does not have diagonal charge and dipole magnetic, and electric form factors. It can only have a diagonal anapole form factor. On the other hand, Majorana neutrinos can have as many off-diagonal (transition) form factors as Dirac neutrinos.

Since the form factor matrices are Hermitian as in the Dirac case,  $\tilde{f}_Q$ ,  $\tilde{f}_M$ , and  $\tilde{f}_E$  are imaginary, whereas  $\tilde{f}_A$  is real:

$$\tilde{f}_\Omega = -\tilde{f}_\Omega^* \quad (\Omega = Q, M, E), \quad (2.61)$$

$$\tilde{f}_A = \tilde{f}_A^*. \quad (2.62)$$

Considering now CP invariance, the case of Majorana neutrinos is rather different from that of Dirac neutrinos, because the CP phases of the massive Majorana fields  $\nu_k$  are constrained by the CP invariance of the Lagrangian Majorana mass term:

$$\mathcal{L}_M = \frac{1}{2} \sum_k m_k \nu_k^T C^\dagger \nu_k. \quad (2.63)$$

In order to prove this statement, let us first notice that since a massive Majorana neutrino field  $\nu_k$  is constrained by the Majorana relation in (2.51), only the parity transformation part is effective in a CP transformation:

$$U_{\text{CP}} \nu_k(x) U_{\text{CP}}^\dagger = \xi_k^{\text{CP}} \gamma^0 \nu_k(x_P). \quad (2.64)$$

Considering the mass term in (2.63), we have

$$U_{\text{CP}} \nu_k^T \mathcal{C}^\dagger \nu_k U_{\text{CP}}^\dagger = -\xi_k^{\text{CP}^2} \nu_k^T \mathcal{C}^\dagger \nu_k. \quad (2.65)$$

Therefore,

$$\text{CP} \iff \xi_k^{\text{CP}} = \eta_k i, \quad (2.66)$$

with  $\eta_k = \pm 1$ . These CP signs can be different for the different massive neutrinos, even if they all take part to the standard charged-current weak interactions through neutrino mixing, because they can be compensated by the Majorana CP phases in the mixing matrix (see [1]). Therefore, from (2.40), we have

$$\tilde{\Lambda}_\mu^{fi}(q) \xrightarrow{\text{CP}} \eta_f \eta_i \gamma^0 \mathcal{C} [\tilde{\Lambda}_\mu^{if}(q_P)]^T \mathcal{C}^\dagger \gamma^0. \quad (2.67)$$

Imposing a CP constraint analogous to that in (2.24), we obtain

$$\text{CP} \iff \begin{cases} f_\Omega^{fi} = \eta_f \eta_i f_\Omega^{if} = \eta_f \eta_i (f_\Omega^{fi})^*, \\ f_E^{fi} = -\eta_f \eta_i f_E^{if} = -\eta_f \eta_i (f_E^{fi})^*, \end{cases} \quad (2.68)$$

with  $\Omega = Q, M, A$ . Taking into account the constraints (2.61) and (2.62), we have two cases:

$$\text{CP}, \eta_f = \eta_i \iff f_Q^{fi} = f_M^{fi} = 0, \quad (2.69)$$

$$\text{CP}, \eta_f = -\eta_i \iff f_E^{fi} = f_A^{fi} = 0. \quad (2.70)$$

Therefore, if CP is conserved, two massive Majorana neutrinos can have either a transition electric form factor or a transition magnetic form factor, but not both, and the transition electric form factor can exist only together with a transition anapole form factor, whereas the transition magnetic form factor can exist only together with a transition charge form factor. In the diagonal case  $f = i$ , (2.69) does not give any constraint, because only diagonal anapole form factors are allowed for Majorana neutrinos.

### 2.3. Form Factors in Gauge Models

From the demand that the form factors at zero momentum transfer,  $q^2 = 0$ , are elements of the scattering matrix, it follows that in any consistent theoretical model the form factors in the matrix element (2.7) should be gauge independent and finite. Then, the form factors values at  $q^2 = 0$  determine the static electromagnetic properties of the neutrino that can be probed or measured in the direct interaction with external electromagnetic fields. This is the case for charge, dipole magnetic, and electric neutrino form factors in the minimally extended Standard Model.

In non-Abelian gauge theories, the form factors in the matrix element (2.7) at nonzero momentum transfer,  $q^2 \neq 0$ , can be noninvariant under gauge transformations. This happens

because in general the off-shell photon propagator is gauge dependent. Therefore, the one-photon approximation is not enough to get physical quantities. In this case, the form factors in the matrix element (2.7) cannot be directly measured in an experiment with an external electromagnetic field. However, they can contribute to higher-order diagrams describing some processes that are accessible for experimental observation (see [31]).

Note that there is an important difference between the electromagnetic vertex function of massive and massless neutrinos [32, 33]. For the case of a massless neutrino, the matrix element (2.7) of the electromagnetic current can be expressed in terms of only one Dirac form factor  $f_D(q^2)$  (see also [30]):

$$\bar{u}(p')\Lambda_\mu(q)u(p) = f_D(q^2)\bar{u}(p')\gamma_\mu(1 + \gamma_5)u(p). \quad (2.71)$$

It follows that the electric charge and anapole form factors for a massless neutrino are related to the Dirac form factor  $f_D(q^2)$ , and hence to each other:

$$f_Q(q^2) = f_D(q^2), \quad f_A(q^2) = \frac{f_D(q^2)}{q^2}. \quad (2.72)$$

In the case of a massive neutrino, there is no such simple relation between electric charge and anapole form factors since the  $q_\mu \not{q} \gamma_5$  term in the anapole part of the vertex function (2.18) cannot be neglected.

Moreover, a direct calculation of the massive neutrino electromagnetic vertex function, taking into account all the diagrams in Figures 15–17 of [13], reveals that each of the Feynman diagrams gives nonzero contribution to the term proportional to  $\gamma_\mu \gamma_5$  [32, 33]. These contributions are not vanishing even at  $q^2 = 0$ . Therefore, in addition to the usual four terms in (2.18) an extra term proportional to  $\gamma_\mu \gamma_5$  appears and a corresponding additional form factor  $f_5(q^2)$  must be introduced. This problem is related to the decomposition of the massive neutrino electromagnetic vertex function. The calculation of the contributions of the proper vertex diagrams (Figure 15 of [13]) and  $\gamma - Z$  self-energy diagrams (Figures 16 and 17 of [13]) for arbitrary gauge fixing parameter  $\alpha = 1/\xi$  in the general  $R_\xi$  gauge and arbitrary mass parameter  $a = m_l^2/m_W^2$  shows that at least in the zeroth and first orders of the expansion over the small neutrino mass parameter  $b = (m_\nu/m_W)^2$ , the corresponding “charge”  $f_5(q^2 = 0)$  is zero. The cancellation of contributions from the proper vertex and self-energy diagrams to the form factor  $f_5(q^2)$  at  $q^2 \neq 0$ ,

$$f_5(q^2) = f_5^{(\gamma-Z)}(q^2) + f_5^{(\text{prop.vert.})}(q^2) = 0, \quad (2.73)$$

was also shown [32, 33] for arbitrary mass parameters  $a$  and  $b$  in the 't Hooft-Feynman gauge  $\alpha = 1$ .

Hence, in the minimally extended Standard Model one can perform a direct calculation of the neutrino vertex function leading to the four terms in (2.18) with gauge-invariant electric charge, magnetic, electric, and anapole moments.

### 3. Magnetic and Electric Dipole Moments

The neutrino dipole magnetic and electric form factors (and the corresponding magnetic and electric dipole moments) are theoretically the most well-studied and understood among the form factors. They also attract a reasonable attention from experimentalists, although the neutrino magnetic moment predicted in the extended Standard Model with right-handed neutrinos is proportional to the neutrino mass and, therefore, it is many orders of magnitude smaller than the present experimental limits obtained in terrestrial experiments.

#### 3.1. Theoretical Predictions

The first calculations of the neutrino dipole moments within the minimal extension of the Standard Model with right-handed neutrinos were performed in [15–22]. The explicit evaluation of the one-loop contributions to the neutrino dipole moments in the leading approximation over the small parameters  $b_i = m_i^2/m_W^2$  (where  $m_i$  are the neutrino masses,  $i = 1, 2, 3$ ), that in addition exactly accounts for the dependence on the small parameters  $a_l = m_l^2/m_W^2$  (with  $l = e, \mu, \tau$ ), yields, for Dirac neutrinos [7, 18–23],

$$\left. \begin{array}{l} \mu_{ij}^D \\ e_{ij}^D \end{array} \right\} = \frac{eG_F}{8\sqrt{2}\pi^2} (m_i \pm m_j) \sum_{l=e,\mu,\tau} f(a_l) U_{li}^* U_{lj}, \quad (3.1)$$

where

$$f(a_l) = \frac{3}{4} \left[ 1 + \frac{1}{1-a_l} - \frac{2a_l}{(1-a_l)^2} - \frac{2a_l^2 \ln a_l}{(1-a_l)^3} \right]. \quad (3.2)$$

All the charged lepton parameters  $a_l$  are small. In the limit  $a_l \ll 1$ , one has

$$f(a_l) \simeq \frac{3}{2} \left( 1 - \frac{a_l}{2} \right). \quad (3.3)$$

From (3.1) and (3.3), the diagonal magnetic moments of Dirac neutrinos are given by

$$\mu_{ii}^D \simeq \frac{3eG_F m_i}{8\sqrt{2}\pi^2} \left( 1 - \frac{1}{2} \sum_{l=e,\mu,\tau} a_l |U_{li}|^2 \right). \quad (3.4)$$

This result exhibits the following important features. The magnetic moment of a Dirac neutrino is proportional to the neutrino mass and for a massless Dirac neutrino in the Standard Model (in the absence of right-handed charged currents), the magnetic moment is zero. The magnetic moment of a massive Dirac neutrino, at the leading order in  $a_l$ , is independent of the neutrino mixing matrix and of the values of the charged lepton masses. The numerical value of the Dirac neutrino magnetic moment is

$$\mu_{ii}^D \simeq 3.2 \times 10^{-19} \left( \frac{m_i}{\text{eV}} \right) \mu_B. \quad (3.5)$$

Taking into account the existing constraint of the order of 1 eV on the neutrino masses (see [1–4]), this value is several orders of magnitude smaller than the present experimental limits, which are discussed in Section 3.4.

From (3.1), it can be clearly seen that in the extended Standard Model with right-handed neutrinos the static (diagonal) electric dipole moment of a Dirac neutrino vanishes,  $\epsilon_{ii}^D = 0$ , in spite of possible CP violations generated by the Dirac phase in the mixing matrix (as shown in (2.27), Dirac neutrinos may have nonzero diagonal electric moments only in theories where CP invariance is violated). For a Majorana neutrino, both the diagonal magnetic and electric moments are zero,  $\mu_{ii}^M = \epsilon_{ii}^M = 0$ , as shown in Section 2.2.

Let us consider now the neutrino transition moments, which are given by (3.1) for  $i \neq j$ . Considering only the leading term  $f(a_l) \simeq 3/2$  in the expansion (3.3), one gets vanishing transition moments, because of the unitarity relation:

$$\sum_l U_{li}^* U_{lj} = \delta_{ij}. \quad (3.6)$$

Therefore, the first nonvanishing contribution comes from the second term in the expansion (3.3) of  $f(a_l)$ , which contains the additional small factor  $a_l = m_l^2/m_W^2$ :

$$\left. \begin{array}{l} \mu_{ij}^D \\ \epsilon_{ij}^D \end{array} \right\} \simeq -\frac{3eG_F}{32\sqrt{2}\pi^2} (m_i \pm m_j) \sum_{l=e,\mu,\tau} \left( \frac{m_l}{m_W} \right)^2 U_{li}^* U_{lj}, \quad (3.7)$$

for  $i \neq j$ . Thus, the transition moments are suppressed with respect to the diagonal magnetic moments in (3.4). This suppression is called “GIM mechanism,” in analogy with the suppression of flavor-changing neutral currents in hadronic processes discovered in [34]. Numerically, the Dirac transition moments are given by

$$\left. \begin{array}{l} \mu_{ij}^D \\ \epsilon_{ij}^D \end{array} \right\} \simeq -4 \times 10^{-23} \left( \frac{m_i \pm m_j}{\text{eV}} \right) f_{ij} \mu_B, \quad (3.8)$$

with

$$f_{ij} = \sum_{l=e,\mu,\tau} \left( \frac{m_l}{m_\tau} \right)^2 U_{li}^* U_{lj}. \quad (3.9)$$

Also, Majorana neutrinos can have nonvanishing transition magnetic and electric moments, as discussed in Section 2.2. Assuming CP conservation and neglecting model-dependent Feynman diagrams depending on the details of the scalar sector [7, 21, 22, 24], if  $\nu_i$  and  $\nu_j$  have the same CP phase,

$$\mu_{ij}^M = 0, \quad \epsilon_{ij}^M = 2\epsilon_{ij}^D, \quad (3.10)$$



whereas if  $\nu_i$  and  $\nu_j$  have opposite CP phases,

$$\mu_{ij}^M = 2\mu_{ij}^D, \quad \epsilon_{ij}^D = 0, \quad (3.11)$$

with  $\epsilon_{ij}^D$  and  $\mu_{ij}^D$  given by (3.1). Hence, although the nonvanishing Majorana transition moments are twice the Dirac ones, they are equally suppressed by the GIM mechanism. However, the model-dependent contributions of the scalar sector can enhance the Majorana transition moments (see [21, 35, 36]).

In recent studies, the value of the diagonal magnetic moment of a massive Dirac neutrino was calculated in the one-loop approximation in the extended Standard Model with right-handed neutrinos, accounting for the dependence on the neutrino mass parameter  $b_i = m_i^2/m_W^2$  [37] and accounting for the exact dependence on both mass parameters  $b_i$  and  $a_l = m_l^2/m_W^2$  [32, 33]. The calculations of the neutrino magnetic moment which take into account exactly the dependence on the masses of all particles can be useful in the case of a heavy neutrino with a mass comparable or even exceeding the values of the masses of other known particles. Note that the LEP data require that the number of light neutrinos coupled to the  $Z$  boson is three [38]. Therefore, any additional active neutrino must be heavier than  $m_Z/2$ . This possibility is not excluded by current data (see [39]).

For a heavy neutrino with mass  $m_i$ , much larger than the charged lepton masses but smaller than the  $W$ -boson mass ( $2 \text{ GeV} \ll m_i \ll 80 \text{ GeV}$ ), the authors of [32, 33] obtained the diagonal magnetic moment:

$$\mu_{ii} \simeq \frac{3eG_F}{8\pi^2\sqrt{2}} m_i \left( 1 + \frac{5}{18} b_i \right), \quad (3.12)$$

whereas for a heavy neutrino with mass  $m_i$  much larger than the  $W$ -boson mass, they got

$$\mu_{ii} \simeq \frac{eG_F}{8\pi^2\sqrt{2}} m_i. \quad (3.13)$$

Note that in both cases the Dirac neutrino magnetic moment is proportional to the neutrino mass. This is an expected result, because the calculations have been performed within the extended Standard Model with right-handed neutrinos.

At this point, a question arises: "Is a neutrino magnetic moment always proportional to the neutrino mass?" The answer is "No." For example, much larger values of the Dirac neutrino magnetic moment can be obtained in  $SU(2)_L \times SU(2)_R \times U(1)$  left-right symmetric models with direct right-handed neutrino interactions (see [15, 40–42]). The massive gauge bosons states  $W_1$  and  $W_2$  have, respectively, predominant left-handed and right-handed coupling, since

$$W_1 = W_L \cos \xi - W_R \sin \xi, \quad W_2 = W_L \sin \xi + W_R \cos \xi, \quad (3.14)$$

where  $\xi$  is a small mixing angle and the fields  $W_L$  and  $W_R$  have pure  $V \pm A$  interactions. The magnetic moment of a neutrino  $\nu_l$  calculated in this model, neglecting neutrino mixing, is

$$\mu_{\nu_l} = \frac{eG_F}{2\sqrt{2}\pi^2} \left[ m_l \left( 1 - \frac{m_{W_1}^2}{m_{W_2}^2} \right) \sin 2\xi + \frac{3}{4} m_{\nu_l} \left( 1 + \frac{m_{W_1}^2}{m_{W_2}^2} \right) \right], \quad (3.15)$$

where the term proportional to the charged lepton mass  $m_l$  is due to the left-right mixing. This term can exceed the second term in (3.15), which is proportional to the neutrino mass  $m_{\nu_l}$ .

### 3.2. Neutrino-Electron Elastic Scattering

The most sensitive and widely used method for the experimental investigation of the neutrino magnetic moment is provided by direct laboratory measurements of low-energy elastic scattering of neutrinos and antineutrinos with electrons in reactor, accelerator and solar experiments. Detailed descriptions of several experiments can be found in [12, 43].

Extensive experimental studies of the neutrino magnetic moment, performed during many years, are stimulated by the hope to observe a value much larger than the prediction in (3.5) of the minimally extended Standard Model with right-handed neutrinos. It would be a clear indication of new physics beyond the extended Standard Model. For example, the effective magnetic moment in  $\bar{\nu}_e$ - $e$  elastic scattering in a class of extradimension models can be as large as  $\sim 10^{-10} \mu_B$  [44]. Future higher precision reactor experiments can, therefore, be used to provide new constraints on large extradimensions.

The possibility for neutrino-electron elastic scattering due to neutrino magnetic moment was first considered in [45] and the cross-section of this process was calculated in [46, 47]. Discussions on the derivation of the cross-section and on the optimal conditions for bounding the neutrino magnetic moment, as well as a collection of cross-section formulas for elastic scattering of neutrinos (antineutrinos) on electrons, nucleons, and nuclei can be found in [48, 49].

Let us consider the elastic scattering:

$$\nu + e^- \longrightarrow \nu + e^- \quad (3.16)$$

of a neutrino with energy  $E_\nu$  with an electron at rest in the laboratory frame. There are two observables: the kinetic energy  $T$  of the recoil electron and the recoil angle  $\chi$  with respect to the neutrino beam, which are related by

$$\cos \chi = \frac{E_\nu + m_e}{E_\nu} \left[ \frac{T}{T + 2m_e} \right]^{1/2}. \quad (3.17)$$

The electron kinetic energy is constrained from the energy-momentum conservation by

$$T \leq \frac{2E_\nu^2}{2E_\nu + m_e}. \quad (3.18)$$

Since, in the ultrarelativistic limit, the neutrino magnetic moment interaction changes the neutrino helicity and the Standard Model weak interaction conserves the neutrino helicity, the two contributions add incoherently in the cross-section which can be written as [49]

$$\frac{d\sigma}{dT} = \left(\frac{d\sigma}{dT}\right)_{\text{SM}} + \left(\frac{d\sigma}{dT}\right)_{\mu}. \quad (3.19)$$

The small interference term due to neutrino masses has been derived in [50].

The weak-interaction cross-section is given by

$$\left(\frac{d\sigma}{dT}\right)_{\text{SM}} = \frac{G_F^2 m_e}{2\pi} \left[ (g_V + g_A)^2 + (g_V - g_A)^2 \left(1 - \frac{T}{E_\nu}\right)^2 + (g_A^2 - g_V^2) \frac{m_e T}{E_\nu^2} \right], \quad (3.20)$$

with the standard coupling constants  $g_V$  and  $g_A$  given by

$$g_V = \begin{cases} 2\sin^2\theta_W + \frac{1}{2} & \text{for } \nu_e, \\ 2\sin^2\theta_W - \frac{1}{2} & \text{for } \nu_\mu, \nu_\tau, \end{cases} \quad (3.21)$$

$$g_A = \begin{cases} \frac{1}{2} & \text{for } \nu_e, \\ -\frac{1}{2} & \text{for } \nu_\mu, \nu_\tau. \end{cases} \quad (3.22)$$

In antineutrino-electron elastic scattering, one must substitute  $g_A \rightarrow -g_A$ .

The neutrino magnetic-moment contribution to the cross section is given by [49]

$$\left(\frac{d\sigma}{dT}\right)_{\mu} = \frac{\pi\alpha^2}{m_e^2} \left(\frac{1}{T} - \frac{1}{E_\nu}\right) \left(\frac{\mu_\nu}{\mu_B}\right)^2, \quad (3.23)$$

where  $\mu_\nu$  is the effective magnetic moment discussed in Section 3.3.

The two terms  $(d\sigma/dT)_{\text{SM}}$  and  $(d\sigma/dT)_{\mu}$  exhibit quite different dependences on the experimentally observable electron kinetic energy  $T$ , as illustrated in Figure 2, where the values of the two terms averaged over the typical antineutrino reactor spectrum are plotted for six values of the neutrino magnetic moment,  $\mu_\nu^{(N)} = N \times 10^{-11} \mu_B$ , with  $N = 1, 2, 3, 4, 5, 6$  [43] (see also [49]). One can see that small values of the neutrino magnetic moment can be probed by lowering the electron recoil energy threshold. In fact, from (3.20) and (3.23), one can find that  $(d\sigma/dT)_{\mu}$  exceeds  $(d\sigma/dT)_{\text{SM}}$  for

$$T \lesssim \frac{\pi^2 \alpha^2}{G_F^2 m_e^3} \left(\frac{\mu_\nu}{\mu_B}\right)^2. \quad (3.24)$$

It was proposed in [51] that electron binding in atoms (the “atomic ionization” effect in neutrino interactions on Ge target) can significantly increase the electromagnetic contribution

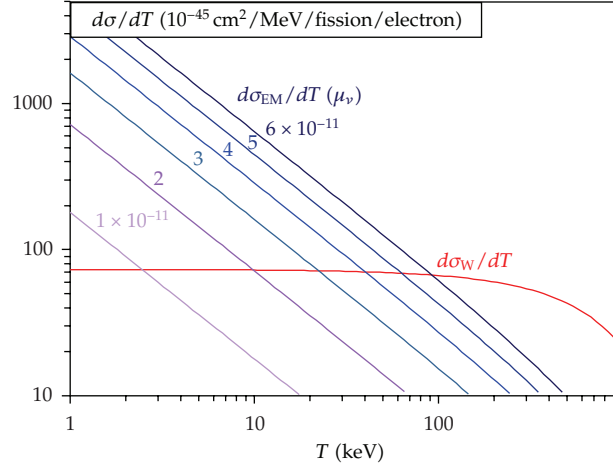


**Figure 2:** Standard Model weak (W) and magnetic moment electromagnetic (EM) contributions to the cross section for several values of the neutrino magnetic moment [43].

to the differential cross-section with respect to the free electron approximation. However, detailed considerations of the atomic ionization effect in (anti)neutrino atomic electron scattering experiments presented in [52–57] show that the effect is by far too small to have measurable consequences even in the case of the low energy threshold of 2.8 keV reached in the GEMMA experiment [58].

### 3.3. Effective Dipole Moments

In scattering experiments, the neutrino is created at some distance from the detector as a flavor neutrino, which is a superposition of massive neutrinos. Therefore, the magnetic moment that is measured in these experiment is not that of a massive neutrino, but it is an effective magnetic moment which takes into account neutrino mixing and the oscillations during the propagation between source and detector [50, 59]:

$$\mu_\nu^2(\nu_\alpha, L, E) = \sum_j \left| \sum_k U_{\alpha k}^* e^{-im_k^2 L/2E} (\mu_{jk} - i\epsilon_{jk}) \right|^2, \quad (3.25)$$

where we have written explicitly the dependence from the initial neutrino flavor  $\nu_\alpha$ , the distance  $L$ , and the energy  $E$ . In this expression of the effective  $\mu_\nu$ , one can see that in general both the magnetic and electric dipole moments contribute to the elastic scattering. Note that  $\mu_\nu(\nu_\alpha, L, E)$  depends only on the neutrino squared-mass differences: considering for simplicity only the magnetic moment contribution, we have

$$\mu_\nu^2(\nu_\alpha, L, E) = \sum_j \sum_{kk'} U_{\alpha k}^* U_{\alpha k'} e^{-i\Delta m_{kk'}^2 L/2E} \mu_{jk} \mu_{jk'}. \quad (3.26)$$

In the case of Majorana neutrinos, there are no diagonal magnetic and electric dipole moments and  $\mu_\nu^2$  receives contributions only from the transition dipole moments.

Furthermore, if CP is conserved, there are either only magnetic or electric transition dipole moments (see Section 2.2).

The general expression for  $\mu_\nu^2(\nu_\alpha, L, E)$  can be simplified in some cases [59]. For instance, for Dirac neutrinos with only diagonal magnetic moments  $\mu_{ij} = \mu_i \delta_{ij}$ , we have the effective flavor magnetic moment:

$$\mu_\nu^2(\nu_\alpha, L, E) \longrightarrow \left(\mu_\alpha^D\right)^2 = \sum_i |U_{\alpha i}|^2 \mu_i^2. \quad (3.27)$$

Since in this case there is no dependence on the distance  $L$  and the neutrino energy, the magnetic cross-section is characterized by the initial neutrino flavor rather than by the composition of mass states in the detector. In this case, measurements of all flavor magnetic moments and mixing parameters can allow the extraction of all the fundamental moments  $\mu_i$ .

### 3.4. Experimental Limits

The constraints on the neutrino magnetic moment in direct laboratory experiments have been obtained so far from the lack of any observable distortion of the recoil electron energy spectrum. Experiments of this type have started about 40 years ago. The strategy applied during all these years in reactor experiments is rather simple: minimize the threshold on the recoil energy for the detection of the scattered electron, keeping at the same time a reasonable background level. Since the region of interest coincides with the energy region dominated by radioactivity, low intrinsic radioactivity detectors have been employed together with active and passive shields. In addition, all the experiments were running inside laboratories with significant overburden of concrete, corresponding to several meters of water. This was enough to suppress the soft component of cosmic rays.

In all the experiments, with one exception only, the signal due to the antineutrinos from the reactor (about  $2 \times 10^{20} \text{ s}^{-1} \text{ GW thermal}^{-1}$ ) is obtained from the difference between the reactor-on and reactor-off rate. Clearly, this requires the same background with the reactor on as with the reactor off.

$\bar{\nu}_e$ - $e$  elastic scattering was first observed in the pioneering experiment [60] at the Savannah River Laboratory. The setup was made of a 15.9 kg plastic scintillator target divided into 16 optically isolated elements, totally enclosed inside a 300 kg NaI crystal shielded with lead and cadmium. Finally, the entire setup was immersed into 2200 liters of liquid scintillator. Both the NaI and the liquid scintillator detectors were working as veto against cosmics and gamma-rays from the laboratory. In the electron kinetic energy range from 1.5 MeV to 4.5 MeV, a reactor-on rate of  $47.5 \pm 1$  events/day was measured, to be compared with a reactor-off rate of  $40.4 \pm 0.9$  events/day. A revised analysis of the Savannah River Laboratory data [49] with an improved reactor neutrino spectrum and a more precise value of  $\sin^2 \theta_W$  gave hints for a neutrino magnetic moment on the order of  $(2-4) \times 10^{-10} \mu_B$ .

However, lower limits were then obtained by two experiments performed at nuclear reactors in Russia. The Krasnoyarsk experiment [61] had a 103 kg target of liquid organofluoric scintillator contained into seven scintillation chambers. The absence of hydrogen in the target was a significant improvement, since the  $\bar{\nu}_e$ - $p$  charged-current reaction, which has a much larger cross-section than  $\bar{\nu}_e$ - $e$ , had been an important background source in the Savannah River experiment. The active target was then surrounded by a passive shield of steel, copper, lead, and borated polyethylene. Finally, two layers of plastic



scintillators were vetoing the cosmic muons. With a count rate of  $8.3 \pm 0.3$  (reactor-on) and  $7.1 \pm 0.4$  (reactor-off) in the electron energy range 3.15–5.18 MeV, the Krasnoyarsk collaboration obtained the limit:

$$\mu_{\bar{\nu}_e} \leq 2.4 \times 10^{-10} \mu_B \quad (90\% \text{ C.L.}). \quad (3.28)$$

A completely different detector was built for the Rovno [62] experiment: 600 silicon detectors, for a total mass of 75 kg, with a passive shield of mercury, copper, cadmium absorber, and graphite. Finally, the setup was enclosed inside a veto made of plastic scintillators. With a rate of  $4963 \pm 12$  events/day (reactor-on) and  $4921 \pm 16$  events/day (reactor-off) in the electron recoil energy range 0.6–2 MeV, it has been possible to obtain a limit on the neutrino magnetic moment of

$$\mu_{\bar{\nu}_e} \leq 1.9 \times 10^{-10} \mu_B \quad (90\% \text{ C.L.}). \quad (3.29)$$

Finally, more stringent limits have been obtained in the two most recent experiments at reactors. TEXONO [63] has been performed at the Kuo-Sheng nuclear power station. The detector, a 1.06 kg high-purity germanium, was completely surrounded by NaI (Tl) and CsI (Tl) crystals working as anti-Compton. The whole setup was contained inside a shield made of copper, boron-loaded polyethylene, stainless steel, lead, and plastic scintillators. A background of about 1 event/keV·kg·day could be achieved above the threshold of 12 keV, giving the limit:

$$\mu_{\bar{\nu}_e} \leq 7.4 \times 10^{-11} \mu_B \quad (90\% \text{ C.L.}). \quad (3.30)$$

At the moment, the world best limit is coming from the GEMMA experiment at the Kalinin nuclear power plant. A 1.5 kg high-purity germanium detector is placed inside a cup-shaped NaI crystal and surrounded by copper, lead, and plastic scintillators. With an energy threshold as low as 2.8 keV, the GEMMA collaboration obtained [58]

$$\mu_{\bar{\nu}_e} \leq 2.9 \times 10^{-11} \mu_B \quad (90\% \text{ C.L.}). \quad (3.31)$$

The experiment which followed a strategy different from the study of the reactor-on and reactor-off rate was MUNU. As a matter of fact, the detector [64] was able to provide not only the energy but also the topology of events. As a consequence, the initial direction of an electron track could be measured and the electron scattering angle reconstructed. This allowed to look for the reactor signal by comparing forward electrons, having as reference the reactor to detector axis, with the backward ones. In this way, the background is measured online, which eliminates problems from detector instabilities, as well as from a possible time dependence of the background itself. The central component of the detector consisted of an acrylic vessel time-projected chamber (a cylinder 90 cm in diameter and 162 cm long) filled with  $\text{CF}_4$  at 3 bar pressure and immersed in a steel tank (2 m diameter and 3.8 m long) filled with  $10 \text{ m}^3$  liquid scintillator viewed by 48 photomultipliers. The total target mass of  $\text{CF}_4$  was 11.4 kg. Finally, the setup was surrounded by boron-loaded polyethylene and lead. With

a total rate of  $6.8 \pm 0.3$  events/day in the forward direction and a background of  $5.8 \pm 0.17$  events/day, the following upper bounds have been obtained [65]:

$$\mu_{\bar{\nu}_e} \leq 9 \times 10^{-11} \mu_B \quad (90\% \text{ C.L.}). \quad (3.32)$$

Several experiments at accelerators have searched for an effect due to the magnetic moment of  $\nu_\mu$  in  $\nu_\mu-e$  and  $\bar{\nu}_\mu-e$  elastic scattering (see [66]). The current best limit has been obtained in the LSND experiment [67]:

$$\mu_{\nu_\mu} \leq 6.8 \times 10^{-10} \mu_B \quad (90\% \text{ C.L.}). \quad (3.33)$$

The DONUT collaboration has investigated  $\nu_\tau-e$  and  $\bar{\nu}_\tau-e$  elastic scattering, finding the limit [68]:

$$\mu_{\nu_\tau} \leq 3.9 \times 10^{-7} \mu_B \quad (90\% \text{ C.L.}). \quad (3.34)$$

Solar neutrino experiments as Super-Kamiokande and Borexino can also search for a neutrino magnetic moment signal by studying the shape of the electron spectrum. Since the neutrino magnetic moment depends both on the mixing and on the propagation properties of the neutrino, then oscillations are here relevant.

The analysis of the recoil electron spectrum generated by solar neutrinos in the Super-Kamiokande experiment gave [69]

$$\mu_\nu \leq 1.1 \times 10^{-10} \mu_B \quad (90\% \text{ C.L.}), \quad (3.35)$$

where  $\mu_\nu$  is not the same as  $\mu_{\bar{\nu}_e}$  since it is given by a different combination of the magnetic moment of the neutrino mass eigenstates (see Section 3.3).

The limit

$$\mu_\nu \leq 5.4 \times 10^{-11} \mu_B \quad (90\% \text{ C.L.}) \quad (3.36)$$

has been recently obtained in the Borexino solar neutrino scattering experiment [70]. An upper limit on the neutrino magnetic moment  $\mu_\nu \leq 8.4 \times 10^{-11} \mu_B$  has been found in an independent analysis of the first release of the Borexino experiment data performed in [71]. It was also shown that with reasonable assumptions on the oscillation probability this limit translates into the conservative upper limits on the magnetic moments of  $\nu_\mu$  and  $\nu_\tau$ :

$$\mu_{\nu_\mu} \leq 1.5 \times 10^{-10} \mu_B, \quad \mu_{\nu_\tau} \leq 1.9 \times 10^{-10} \mu_B \quad (90\% \text{ C.L.}). \quad (3.37)$$

The limit on  $\mu_{\nu_\tau}$  is three order of magnitude stronger than the direct limit (3.34).

The global fit [72, 73] of the magnetic moment data from the reactor and solar neutrino experiments for the Majorana neutrinos produces limits on the neutrino transition moments:

$$\mu_{23}, \mu_{31}, \mu_{12} < 1.8 \times 10^{-10} \mu_B \quad (90\% \text{ C.L.}). \quad (3.38)$$

Finally, an interesting new possibility for providing more stringent constraints on the neutrino magnetic moment from  $\bar{\nu}_e$ - $e$  scattering experiments was discussed in [74] on the basis of an observation [75] that “dynamical zeros” appear in the Standard Model contribution to the scattering cross-section.

### 3.5. Theoretical Considerations

As it was already mentioned before, there is a gap of many orders of magnitude between the present experimental limits  $\sim 10^{-11} \mu_B$  on neutrino magnetic moments (discussed in Section 3.4) and the prediction (3.5) of the minimal extension of the Standard Model with right-handed neutrinos. At the same time, the experimental sensitivity of reactor  $\bar{\nu}_e$ - $e$  elastic scattering experiments has improved by only one order of magnitude during a period of about twenty years (see [49], where a sensitivity of  $\sim 10^{-10} \mu_B$  is discussed). However, the experimental studies of neutrino magnetic moments are stimulated by the hope that new physics beyond the minimally extended Standard Model with right-handed neutrinos might give much stronger contributions. One of the examples in which it is possible to avoid the neutrino magnetic moment being proportional to a (small) neutrino mass, that would in principle make a neutrino magnetic moment accessible for experimental observations, is realized in the left-right symmetric models considered at the end of Section 3.1.

Other interesting possibilities of obtaining neutrino magnetic moments larger than the prediction (3.5) of the minimal extension the Standard Model with right-handed neutrinos have been considered recently. In this concern, we note that it was proposed in [44] to probe a class of large extradimensions models with future reactors searches for neutrino magnetic moments. The results obtained within the Minimal Supersymmetric Standard Model with  $R$ -parity violating interactions [76, 77] show that the Majorana transition magnetic moment might be significantly above the scale of (3.5).

Considering the problem of large neutrino magnetic moments, one can write down a generic relation between the size of a neutrino magnetic moment  $\mu_\nu$  and the corresponding neutrino mass  $m_\nu$  [28, 29, 35, 78–80]. Suppose that a large neutrino magnetic moment is generated by physics beyond a minimal extension of the Standard Model at an energy scale characterized by  $\Lambda$ . For a generic diagram corresponding to this contribution to  $\mu_\nu$ , one can again use the Feynman graph in Figure 1(b); the shaded circle in this case denotes effects of new physics beyond the Standard Model. The contribution of this diagram to the magnetic moment is

$$\mu_\nu \sim \frac{eG}{\Lambda}, \quad (3.39)$$

where  $e$  is the electric charge and  $G$  is a combination of coupling constants and loop factors. The same diagram of Figure 1(b) but without the photon line gives a new physics contribution to the neutrino mass:

$$\delta m_\nu \sim G\Lambda. \quad (3.40)$$

Combining the estimates (3.39) and (3.40), one can get the relation:

$$\delta m_\nu \sim \frac{\Lambda^2}{2m_e} \frac{\mu_\nu}{\mu_B} = \frac{\mu_\nu}{10^{-18}\mu_B} \left( \frac{\Lambda}{1 \text{ TeV}} \right)^2 \text{ eV} \quad (3.41)$$

between the one-loop contribution to the neutrino mass and the neutrino magnetic moment.

It follows that, generally, in theoretical models that predict large values for the neutrino magnetic moment, simultaneously large contributions to the neutrino mass arise. Therefore, a particular fine tuning is needed to get a large value for the neutrino magnetic moment while keeping the neutrino mass within experimental bounds. One of the possibilities [78] is based on the idea of suppressing the ratio  $m_\nu/\mu_\nu$  with a symmetry: if a  $SU(2)_\nu$  symmetry is an exact symmetry of the Lagrangian of a model, because of different symmetry properties of the mass and magnetic moment even a massless neutrino can have a nonzero magnetic moment. If, as it happens in a realistic model, the  $SU(2)_\nu$  symmetry is broken and if this breaking is small, the ratio  $m_\nu/\mu_\nu$  is also small, giving a natural way to obtain a magnetic moment of the order of  $\sim 10^{-11}\mu_B$  without contradictions with the neutrino mass experimental constraints. Several possibilities based on the general idea of [78] were considered in [81–86].

Another idea of neutrino mass suppression without suppression of the neutrino magnetic moment was discussed in [35] within the Zee model [87], which is based on the Standard Model gauge group  $SU(2)_L \times U(1)_Y$  and contains at least three Higgs doublets and a charged field which is a singlet of  $SU(2)_L$ . For this kind of models, there is a suppression of the neutrino mass diagram, while the magnetic moment diagram is not suppressed.

It is possible to show with more general and rigorous considerations [28, 29, 80] that the  $\Lambda^2$  dependence in (3.41) arises from the quadratic divergence in the renormalization of the dimension-four neutrino mass operator. A general and model-independent upper bound on the Dirac neutrino magnetic moment, which can be generated by an effective theory beyond the Standard Model, has been derived [28, 29, 80] from the demand of absence of fine-tuning of effective operator coefficients and from the current experimental information on neutrino masses. A model with Dirac fermions, scalars, and gauge bosons that is valid below the scale  $\Lambda$  and respects the Standard Model  $SU(2)_L \times U(1)_Y$  symmetry was considered. Integrating out the physics above the scale  $\Lambda$ , the following effective Lagrangian that involves right-handed neutrinos  $\nu_R$ , lepton isodoublets and the Higgs doublet can be obtained:

$$\mathcal{L}_{\text{eff}} = \sum_{n,j} \frac{C_j^n(\mu)}{\Lambda^{n-4}} \mathcal{O}_j^{(n)}(\mu) + \text{H.c.}, \quad (3.42)$$

where  $\mu$  is the renormalization scale,  $n \geq 4$  denotes the operator dimension and  $j$  runs over independent operators of a given dimension. For  $n = 4$ , a neutrino mass arises from the operator  $\mathcal{O}_1^{(4)} = \bar{L}\tilde{\Phi}\nu_R$ , where  $\tilde{\Phi} = i\sigma_2\Phi^*$ . In addition, if the scale  $\Lambda$  is not extremely large with respect to the electroweak scale, an important contribution to the neutrino mass can arise also from higher dimension operators. At this point, it is important to note that the combination of the  $n = 6$  operators appearing in the Lagrangian (3.42) contains the magnetic moment operator  $\bar{\nu}\sigma_{\mu\nu}\nu F^{\mu\nu}$  and also generates a contribution  $\delta m_\nu$  to the neutrino mass [28, 29, 80]. Solving the renormalization group equation from the scale  $\Lambda$  to the electroweak scale, one

finds that the contributions to the neutrino magnetic moment and to the neutrino mass are connected to each other by

$$|\mu_\nu^D| = \frac{16\sqrt{2}G_F m_e \delta m_\nu \sin^4 \theta_W}{9\alpha^2 |f| \ln(\Lambda/v)} \mu_B, \quad (3.43)$$

where  $\alpha$  is the fine structure constant,  $v$  is the vacuum expectation value of the Higgs doublet,

$$f = 1 - r - \frac{2}{3} \tan^2 \theta_W - \frac{1}{3} (1 + r) \tan^4 \theta_W, \quad (3.44)$$

and  $r$  is a ratio of effective operator coefficients defined at the scale  $\Lambda$  which is of order unity without fine tuning. If the neutrino magnetic moment is generated by new physics at a scale  $\Lambda \sim 1$  TeV and the corresponding contribution to the neutrino mass is  $\delta m_\nu \lesssim 1$  eV, then the bound  $\mu_\nu \lesssim 10^{-14} \mu_B$  can be obtained. This bound is some orders of magnitude stronger than the constraints from reactor and solar neutrino scattering experiments discussed before.

The model-independent limit on a Majorana neutrino transition magnetic moment  $\mu_\nu^M$  was also discussed in [28, 29, 80]. However, the limit in the Majorana case is much weaker than that in the Dirac case, because for a Majorana neutrino, the magnetic moment contribution to the mass is Yukawa suppressed. The limit on  $\mu_\nu^M$  is also weaker than the present experimental limits if  $\mu_\nu^M$  is generated by new physics at the scale  $\Lambda \sim 1$  TeV. An important conclusion of [28, 29, 80], based on model-independent considerations of the contributions to  $\mu_\nu$ , is that if a neutrino magnetic moment of order  $\mu_\nu \geq 10^{-15} \mu_B$  were observed in an experiment, it would give a proof that neutrinos are Majorana rather than Dirac particles.

#### 4. Neutrino Charge Radius

Even if the electric charge of a neutrino is vanishing, the electric form factor  $f_Q(q^2)$  can still contain nontrivial information about neutrino electromagnetic properties. Considering  $f_Q(0) = 0$ , in the static limit ( $q^2 \rightarrow 0$ ), the electric form factor is given by

$$f_Q(q^2) = q^2 \left. \frac{df_Q(q^2)}{dq^2} \right|_{q^2=0} + \dots \quad (4.1)$$

The leading contribution can be expressed in terms of a neutrino charge radius considering a static spherically symmetric charge distribution of density  $\rho(r)$  (with  $r = |\vec{x}|$ ) in the so-called “Breit frame,” where  $q_0 = 0$ . In this approximation, we have

$$f_Q(q^2) = \int \rho(r) e^{i\vec{q}\cdot\vec{x}} d^3x = 4\pi \int \rho(r) \frac{\sin(qr)}{qr} r^2 dr, \quad (4.2)$$



where  $q = |\vec{q}|$ . Since  $df_Q/dq^2|_{q^2=0} = -\langle r^2 \rangle/6$ , with  $\langle r^2 \rangle = \int r^2 \rho(r) dr$ , the neutrino charge radius is defined by

$$\langle r_v^2 \rangle = -6 \frac{df_Q(q^2)}{dq^2} \Big|_{q^2=0}. \quad (4.3)$$

Note that  $\langle r_v^2 \rangle$  can be negative, because the charge density  $\rho(r)$  is not a positively defined function of  $r$ .

In one of the first studies [31], it was claimed that in the Standard Model and in the unitary gauge, the neutrino charge radius is ultraviolet-divergent and so it is not a physical quantity. A direct one-loop calculation [32, 33] of proper vertices and  $\gamma - Z$  self-energy (Figures 15 and 16 of [13]) contributions to the neutrino charge radius performed in a general  $R_\xi$  gauge for a massive Dirac neutrino gave also a divergent result. However, it was shown [88], using the unitary gauge, that, by including in addition to the usual terms also contributions from diagrams of the neutrino-lepton neutral current scattering ( $Z$  boson diagrams), it is possible to obtain for the neutrino charge radius a gauge-dependent but finite quantity. Later on, it was also shown [16] that in order to define the neutrino charge radius as a physical quantity, one has also to consider box diagrams (see Figure 18 of [13]), which contribute to the scattering process  $\nu + \ell \rightarrow \nu + \ell$ , and that in combination with contributions from the proper diagrams it is possible to obtain a finite and gauge-independent value for the neutrino charge radius. In this way, the neutrino electroweak radius was defined [89, 90] and an additional set of diagrams that give contribution to its value was discussed in [91]. Finally, in a series of papers [92–94] the neutrino electroweak radius as a physical observable has been introduced. In the corresponding calculations, performed in the one-loop approximation including additional terms from the  $\gamma - Z$  boson mixing and the box diagrams involving  $W$  and  $Z$  bosons, the following gauge-invariant result for the neutrino charge radius has been obtained:

$$\langle r_{\nu_\alpha}^2 \rangle = \frac{G_F}{4\sqrt{2}\pi^2} \left[ 3 - 2 \log \left( \frac{m_\alpha^2}{m_W^2} \right) \right], \quad (4.4)$$

where  $m_W$  and  $m_\alpha$  are the  $W$  boson and lepton masses ( $\alpha = e, \mu, \tau$ ). This result, however, revived the discussion [95–98] on the definition of the neutrino charge radius. Numerically, for the electron neutrino electroweak radius, it yields [92–94]

$$\langle r_{\nu_e}^2 \rangle = 4 \times 10^{-33} \text{ cm}^2, \quad (4.5)$$

which is very close to the numerical estimations obtained much earlier in [89, 90].

Note that the neutrino charge radius can be considered as an effective scale of the particle's "size," which should influence physical processes such as, for instance, neutrino scattering off electron. To incorporate the neutrino charge radius contribution in the cross-section (3.20), the following substitution [49, 99, 100] can be used:

$$g_V \longrightarrow \frac{1}{2} + 2\sin^2\theta_W + \frac{2}{3}m_W^2 \langle r_{\nu_e}^2 \rangle \sin^2\theta_W. \quad (4.6)$$

Using this method, the TEXONO collaboration obtained [101]

$$-2.1 \times 10^{-32} \text{ cm}^2 < \langle r_{\bar{\nu}_e}^2 \rangle < 3.3 \times 10^{-32} \text{ cm}^2 \quad (90\% \text{ C.L.}). \quad (4.7)$$

Other available bounds on the electron neutrino charge radius are from primordial nucleosynthesis [102]

$$\langle r_{\nu_e}^2 \rangle \lesssim 7 \times 10^{-33} \text{ cm}^2, \quad (4.8)$$

from SN 1987A [103]

$$\langle r_{\bar{\nu}_e}^2 \rangle \lesssim 2 \times 10^{-33} \text{ cm}^2, \quad (4.9)$$

from neutrino neutral-current reactions [104]

$$-2.74 \times 10^{-32} \text{ cm}^2 < \langle r_{\nu_e}^2 \rangle < 4.88 \times 10^{-32} \text{ cm}^2 \quad (90\% \text{ C.L.}), \quad (4.10)$$

from solar experiments (Kamiokande II and Homestake) [105, 106]

$$\langle r_{\nu_e}^2 \rangle < 2.3 \times 10^{-32} \text{ cm}^2 \quad (95\% \text{ C.L.}), \quad (4.11)$$

from an evaluation of the weak mixing angle  $\sin^2\theta_W$  by a combined fit of all electron neutrino elastic scattering data [107]

$$-0.13 \times 10^{-32} \text{ cm}^2 < \langle r_{\nu_e}^2 \rangle < 3.32 \times 10^{-32} \text{ cm}^2 \quad (90\% \text{ C.L.}). \quad (4.12)$$

Comparing the theoretical value in (4.5) with the experimental limits in (4.7)–(4.12), one can see that they differ at most by one order of magnitude. Therefore, one may expect that the experimental accuracy will soon reach the value needed to probe the theoretical predictions for the neutrino effective charge radius.

The effects of new physics beyond the Standard Model can also contribute to the neutrino charge radius. Let us only mention that the anomalous  $WW\gamma$  vertex contribution to the neutrino effective charge radius has been studied in [30], and shown to correspond to a contribution  $\lesssim 10^{-34} \text{ cm}^2$  to  $|\langle r_{\nu_e}^2 \rangle|$ . Note that this is only one order of magnitude lower than the expected value of the charge radius in the Standard Model.

A detailed discussion on the possibilities to constrain the  $\nu_\tau$  and  $\nu_\mu$  charge radii from astrophysical and cosmological observations and from terrestrial experiments can be found in [108].

## 5. Radiative Decay and Plasmon Decay

If the masses of neutrinos are nondegenerate, the radiative decay of a heavier neutrino  $\nu_i$  into a lighter neutrino  $\nu_f$  (with  $m_i > m_f$ ) with emission of a photon,

$$\nu_i \longrightarrow \nu_f + \gamma, \quad (5.1)$$

may proceed in vacuum [15, 16, 18–21, 23, 109, 110]. Early discussions of the possible role of neutrino radiative decay in different astrophysical and cosmological settings can be found in [111–116].

For the case of a Dirac neutrino, the decay rate in the minimal extension of the Standard Model with right-handed neutrinos is [15, 16, 18–21, 23, 109, 110]

$$\Gamma_{\nu_i^D \rightarrow \nu_j^D + \gamma} = \frac{\alpha G_F^2}{128\pi^4} \left( \frac{m_i^2 - m_j^2}{m_j} \right)^3 (m_i^2 + m_j^2) \left| \sum_{l=e,\mu,\tau} f(a_l) U_{lj} U_{li}^* \right|^2, \quad (5.2)$$

where  $f(a_l)$  is given by (3.2). Recalling the results for the Dirac neutrino magnetic and electric transition moments  $\mu_{ij}$  and  $\epsilon_{ij}$ , given in (3.1), one can rewrite (5.2) as (see [117, 118])

$$\Gamma_{\nu_i \rightarrow \nu_j + \gamma} = \frac{|\mu_{ij}|^2 + |\epsilon_{ij}^2|}{8\pi} \left( \frac{m_i^2 - m_j^2}{m_j} \right)^3. \quad (5.3)$$

For degenerate neutrino masses ( $m_i = m_j$ ), the process is kinematically forbidden in vacuum.

Note that there are models (see for instance [119]) in which the neutrino radiative decay rates (as well as the magnetic moment discussed above) of a nonstandard Dirac neutrinos are much larger than those predicted in the minimally extended Standard Model.

For Majorana neutrinos, if CP is violated, the decay rate is given by (5.3). If CP is conserved, we have two cases: if the Majorana neutrinos  $\nu_i$  and  $\nu_j$  have the same CP eigenvalues, (2.69) and (3.10) imply that the decay process is induced purely by the neutrino electric transition dipole moment, because  $\mu_{ij} = 0$ ; on the other hand, if the two Majorana neutrinos have opposite CP eigenvalues, from (2.70) and (3.11), one can see that the transition is purely of magnetic dipole type ( $\epsilon_{ij} = 0$ ).

For numerical estimations, it is convenient to express (5.3) in the following form:

$$\Gamma_{\nu_i \rightarrow \nu_j + \gamma} = 5.3 \left( \frac{\mu_{\text{eff}}}{\mu_B} \right)^2 \left( \frac{m_i^2 - m_j^2}{m_j^2} \right)^3 \left( \frac{m_i}{1 \text{ eV}} \right)^3 s^{-1}, \quad (5.4)$$

with the effective neutrino magnetic moment  $\mu_{\text{eff}} = \sqrt{|\mu_{ij}|^2 + |\epsilon_{ij}^2|}$ .

The neutrino radiative decay can be constrained by the absence of decay photons in reactor  $\bar{\nu}_e$  and solar  $\nu_e$  fluxes. The limits on  $\mu_{\text{eff}}$  that have been obtained from these considerations are much weaker than those obtained from neutrino scattering terrestrial experiments. Stronger constraints on  $\mu_{\text{eff}}$  (though still weaker than the terrestrial ones) have been obtained from the neutrino decay limit set by SN 1987A and from the limits on the

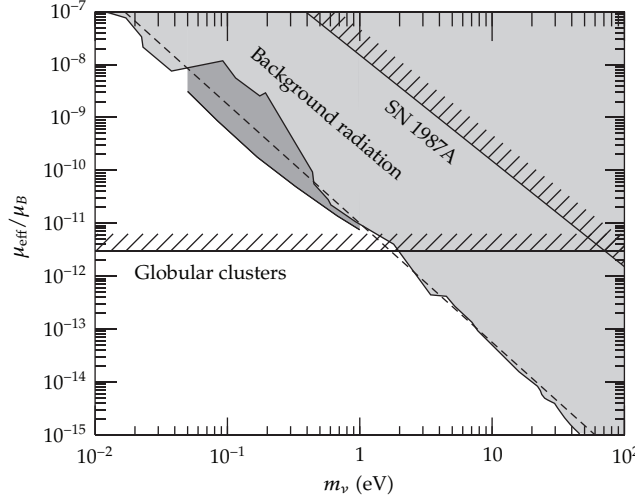


**Figure 3:** Astrophysical limits on neutrino transition moments [117, 118].

distortion of the Cosmic Microwave Background Radiation (CMBR). These limits can be expressed as (see [117, 118] and references therein)

$$\frac{\mu_{\text{eff}}}{\mu_B} < \begin{cases} 0.9 \times 10^{-1} \left( \frac{\text{eV}}{m_\nu} \right)^2 & \text{Reactor } (\bar{\nu}_e), \\ 0.5 \times 10^{-5} \left( \frac{\text{eV}}{m_\nu} \right)^2 & \text{Sun } (\nu_e), \\ 1.5 \times 10^{-8} \left( \frac{\text{eV}}{m_\nu} \right)^2 & \text{SN1987A (all flavors),} \\ 1.0 \times 10^{-11} \left( \frac{\text{eV}}{m_\nu} \right)^{9/4} & \text{CMBR (all flavors).} \end{cases} \quad (5.5)$$

Detailed discussions (and corresponding references) on the astrophysical constraints on the neutrino magnetic and electric transition moments, summarized in Figure 3, can be found in [117, 118].

For completeness, we would like to mention that other processes characterized by the same signature of (5.1) have been considered (for a review of the literature see [120–124]).

- (i) The photon radiation by a massless neutrino ( $\nu_i \rightarrow \nu_j + \gamma, i = j$ ) due to the vacuum polarization loop diagram in the presence of an external magnetic field [125].
- (ii) The photon radiation by a massive neutrino with nonvanishing magnetic moment in constant magnetic and electromagnetic wave fields [126–129].
- (iii) The Cherenkov radiation due to the nonvanishing neutrino magnetic moment in an homogeneous and infinitely extended medium, which is only possible if the speed of the neutrino is larger than the speed of light in the medium [130, 131].
- (iv) The transition radiation due to a nonvanishing neutrino magnetic moment which would be produced when the neutrino crosses the interface of two media with different refractive indices [132–134].

- (v) The Cherenkov radiation of a massless neutrino due to its induced charge in a medium [135, 136]. (Note that the neutrino electromagnetic properties are in general affected by the external environment. In particular, a neutrino can acquire an electric charge in magnetized matter [135, 136] and the neutrino magnetic moment depends on the strength of external electromagnetic fields [127, 137, 138]. A recent study of the neutrino electromagnetic vertex in magnetized matter can be found in [139]. See also [122, 123] for a review of neutrino interactions in external electromagnetic fields.)
- (vi) The Cherenkov radiation of massive and massless neutrinos in a magnetized medium [120, 140].
- (vii) The neutrino radiative decay ( $\nu_i \rightarrow \nu_j + \gamma, i \neq j$ ) in external fields and media (see [141–146] and references therein).
- (viii) The spin light of neutrino in matter ( $SL\nu$ ) that is a mechanism of electromagnetic radiation due to the precession or transition of magnetic or electric (transition) moments of massive neutrinos when they propagate in background matter [121, 147–151].

A very interesting process, for the purpose of constraining neutrino electromagnetic properties, is the photon (plasmon) decay into a neutrino-antineutrino pair:

$$\gamma^* \longrightarrow \nu + \bar{\nu}. \quad (5.6)$$

This process becomes kinematically allowed in media, because a photon with the dispersion relation  $\omega_\gamma^2 + \vec{k}_\gamma^2 > 0$  roughly behaves as a particle with an effective mass.

Plasmon decay generated by the neutrino coupling to photons due to a magnetic moment  $\mu_\nu$  (and/or to a neutrino electric millicharge  $q_\nu$ ) was first considered in [152] as a possible source of energy loss of the Sun. The requirement that the energy loss does not exceed the solar luminosity gave [117, 118]

$$\mu_\nu \lesssim 4 \times 10^{-10} \mu_B, \quad (5.7)$$

and  $q_\nu \lesssim 6 \times 10^{-14} e$ .

The tightest astrophysical bound on a neutrino magnetic moment is provided by the observed properties of globular cluster stars. The plasmon decay (5.6) inside the star liberates the energy  $\omega_\gamma$  in the form of neutrinos that freely escape the stellar environment. This nonstandard energy loss cools a red giant star so fast that it can delay helium ignition. From the lack of observational evidence of this effect, the following limit has been found [153]:

$$\mu_\nu \leq 3 \times 10^{-12} \mu_B, \quad (5.8)$$

and  $q_\nu \lesssim 2 \times 10^{-14} e$ . This is the most stringent astrophysical constraint on a neutrino magnetic moment, applicable to both Dirac and Majorana neutrinos. The same limit applies for the neutrino magnetic transition moments as well as for the electric (transition) moments.

Recently, it has been shown that the additional cooling due to neutrino magnetic moments generates qualitative changes to the structure and evolution of stars with masses



between 7 and 18 solar masses, rather than simply changing the time scales of their burning [154]. The resulting sensitivity to the neutrino magnetic moment has been estimated to be at the level of  $(2 - 4) \times 10^{-11} \mu_B$ .

## 6. Spin-Flavor Precession

If neutrinos have magnetic moments, the spin can precess in a transverse magnetic field [155–157].

Let us first consider the spin precession of a Dirac neutrino generated by its diagonal magnetic moment  $\mu$ . The spatial evolution of the left-handed and right-handed helicity amplitudes  $\varphi_L(x)$  and  $\varphi_R(x)$  in a transverse magnetic field  $B_\perp(x)$  is given by

$$i \frac{d}{dx} \begin{pmatrix} \varphi_L(x) \\ \varphi_R(x) \end{pmatrix} = \begin{pmatrix} 0 & \mu B_\perp(x) \\ \mu B_\perp(x) & 0 \end{pmatrix} \begin{pmatrix} \varphi_L(x) \\ \varphi_R(x) \end{pmatrix}. \quad (6.1)$$

The differential equation (6.1) can be solved through the transformation:

$$\begin{pmatrix} \varphi_L(x) \\ \varphi_R(x) \end{pmatrix} = \frac{1}{\sqrt{2}} \begin{pmatrix} 1 & 1 \\ -1 & 1 \end{pmatrix} \begin{pmatrix} \varphi_-(x) \\ \varphi_+(x) \end{pmatrix}. \quad (6.2)$$

The new amplitudes  $\varphi_-(x)$  and  $\varphi_+(x)$  satisfy decoupled differential equations, whose solutions are

$$\varphi_\mp(x) = \exp \left[ \pm i \int_0^x dx' \mu B_\perp(x') \right] \varphi_\mp(0). \quad (6.3)$$

If we consider an initial left-handed neutrino, we have

$$\begin{pmatrix} \varphi_L(0) \\ \varphi_R(0) \end{pmatrix} = \begin{pmatrix} 1 \\ 0 \end{pmatrix} \Rightarrow \begin{pmatrix} \varphi_-(0) \\ \varphi_+(0) \end{pmatrix} = \frac{1}{\sqrt{2}} \begin{pmatrix} 1 \\ 1 \end{pmatrix}. \quad (6.4)$$

Then, the probability of  $\nu_L \rightarrow \nu_R$  transitions is given by

$$P_{\nu_L \rightarrow \nu_R}(x) = |\varphi_R(x)|^2 = \sin^2 \left( \int_0^x dx' \mu B_\perp(x') \right). \quad (6.5)$$

Note that the transition probability is independent from the neutrino energy (contrary to the case of flavor oscillations) and the amplitude of the oscillating probability is unity. Hence, when the argument of the sine is equal to  $\pi/2$ , there is complete  $\nu_L \rightarrow \nu_R$  conversion.

The precession  $\nu_{eL} \rightarrow \nu_{eR}$  in the magnetic field of the Sun was considered in 1971 [155] as a possible solution of the solar neutrino problem. If neutrinos are Dirac particles, right-handed neutrinos are sterile and a  $\nu_{eL} \rightarrow \nu_{eR}$  conversion could explain the disappearance of active solar  $\nu_{eL}$ 's.

In 1986, it was realized [156, 157] that the matter effect during neutrino propagation inside of the Sun suppresses  $\nu_{eL} \rightarrow \nu_{eR}$  transition by lifting the degeneracy of  $\nu_{eL}$  and  $\nu_{eR}$ .

Indeed, taking into account matter effects, the evolution equation (6.1) for a Dirac neutrino becomes

$$i \frac{d}{dx} \begin{pmatrix} \varphi_L(x) \\ \varphi_R(x) \end{pmatrix} = \begin{pmatrix} V(x) & \mu B_\perp(x) \\ \mu B_\perp(x) & 0 \end{pmatrix} \begin{pmatrix} \varphi_L(x) \\ \varphi_R(x) \end{pmatrix}, \quad (6.6)$$

with the appropriate potential  $V(x)$  which depends on the neutrino flavor:

$$V_\alpha(x) = V_{CC}(x) \delta_{\alpha e} + V_{NC}(x). \quad (6.7)$$

Here,  $V_{CC}$  and  $V_{NC}$  are the charged-current and neutral-current potentials given by

$$V_{CC}(x) = \sqrt{2} G_F N_e(x), \quad V_{NC}(x) = -\frac{1}{2} \sqrt{2} G_F N_n(x), \quad (6.8)$$

where  $N_e(x)$  and  $N_n(x)$  are the electron and neutron number densities in the medium. For antineutrinos,  $\bar{V}_\alpha(x) = -V_\alpha(x)$ .

In the case of a constant matter density, the differential equation (6.6) can be solved analytically with the orthogonal transformation:

$$\begin{pmatrix} \varphi_L(x) \\ \varphi_R(x) \end{pmatrix} = \begin{pmatrix} \cos \xi & \sin \xi \\ -\sin \xi & \cos \xi \end{pmatrix} \begin{pmatrix} \varphi_-(x) \\ \varphi_+(x) \end{pmatrix}. \quad (6.9)$$

The angle  $\xi$  is chosen in order to diagonalize the matrix operator in (6.6):

$$\sin 2\xi = \frac{2\mu B_\perp}{\Delta E_M}, \quad (6.10)$$

with the effective energy splitting in matter

$$\Delta E_M = \sqrt{V^2 + (2\mu B_\perp)^2}. \quad (6.11)$$

The decoupled evolution of  $\varphi_\mp(x)$  is given by:

$$\varphi_\mp(x) = \exp \left[ -\frac{i}{2} (V \mp \Delta E_M) x \right] \varphi_\mp(0). \quad (6.12)$$

For an initial left-handed neutrino,

$$\begin{pmatrix} \varphi_-(0) \\ \varphi_+(0) \end{pmatrix} = \begin{pmatrix} \cos \xi \\ \sin \xi \end{pmatrix}, \quad (6.13)$$

leading to the oscillatory transition probability:

$$P_{\nu_L \rightarrow \nu_R}(x) = |\varphi_R(x)|^2 = \sin^2 2\xi \sin^2 \left( \frac{1}{2} \Delta E_M x \right). \quad (6.14)$$

Since in matter  $\Delta E_M > 2\mu B_\perp$ , the matter effect suppresses the amplitude of  $\nu_L \rightarrow \nu_R$  transitions. However, these transitions are still independent from the neutrino energy, which does not enter in the evolution equation (6.6).

When it was known, in 1986 [156, 157], that the matter potential has the effect of suppressing  $\nu_L \rightarrow \nu_R$  transitions because it breaks the degeneracy of left-handed and right-handed states, it did not take long to realize, in 1988 [158, 159], that the matter potentials can cause resonant spin-flavor precession if different flavor neutrinos have transition magnetic moments (spin-flavor precession in vacuum was previously discussed in [24]).

Let us denote with  $\varphi_{ah}(x)$  the flavor and helicity amplitudes (with  $\alpha = e, \mu, \tau$  and  $h = \pm 1$ ), that is,  $\varphi_{\alpha-1}(x) \equiv \varphi_{\alpha L}(x)$  and  $\varphi_{\alpha+1}(x) \equiv \varphi_{\alpha R}(x)$ . Considering neutrino mixing, the evolution of the flavor and helicity amplitudes is given by

$$i \frac{d\varphi_{ah}(x)}{dx} = \sum_{\beta} \sum_{h'=\pm 1} \left[ \left( \sum_k U_{ak} \frac{m_k^2}{2E} U_{\beta k}^* + V_{\alpha}(x) \delta_{\alpha\beta} \right) \delta_{hh'} + \mu_{\alpha\beta} B_{\perp}(x) \delta_{-hh'} \right] \varphi_{\beta h'}(x), \quad (6.15)$$

with the effective magnetic moments in the flavor basis:

$$\mu_{\alpha\beta} = \sum_{k,j} U_{\alpha k} \mu_{kj} U_{\beta j}^*. \quad (6.16)$$

For a Dirac neutrino, from (2.36), we have

$$\mu_{jk} = \mu_{kj}^* \implies \mu_{\beta\alpha} = \mu_{\alpha\beta}^*. \quad (6.17)$$

If CP is conserved, from (2.43), and the reality of the mixing matrix, for a Dirac neutrino, we obtain

$$\text{CP} \implies \mu_{jk} = \mu_{kj} \implies \mu_{\beta\alpha} = \mu_{\alpha\beta}. \quad (6.18)$$

For a Majorana neutrino, from (2.59) and (2.61), we have

$$\mu_{jk} = -\mu_{kj}, \quad \mu_{kj} = -\mu_{jk}^*. \quad (6.19)$$

Hence, in the mass basis of Majorana neutrinos, there are no diagonal magnetic moments and the transition magnetic moments are imaginary. If CP is not conserved, the mixing matrix is not real and the constraints (6.19) do not imply similar relations between the effective magnetic moments in the flavor basis, for which we have only the relation in (6.17) as for Dirac neutrinos. In particular, Majorana neutrinos can have diagonal effective magnetic moments in the flavor basis if CP is not conserved. Let us emphasize that both Dirac and Majorana phases contribute to this effect. Therefore, it occurs also in the case of two-neutrino mixing, in which there is one Majorana phase.

On the other hand, if CP is conserved, there is no additional constraint on the magnetic moments of Majorana neutrinos in the mass basis, as we have seen in Section 2.2. However, in this case, the mixing matrix is real and we have

$$\text{CP} \implies \mu_{\beta\alpha} = -\mu_{\alpha\beta}, \quad \mu_{\alpha\beta} = -\mu_{\alpha\beta}^*. \quad (6.20)$$

Hence, only if CP is conserved, there are no diagonal magnetic moments of Majorana neutrinos in the flavor basis as in the mass basis.

In the following, we discuss the spin-flavor evolution equation in the two-neutrino mixing approximation, which is interesting for understanding the relevant features of neutrino spin-flavor precession.

Considering Dirac neutrinos, from (6.15), it follows that the generalization of (6.1) to two-neutrino  $\nu_e - \nu_\mu$  mixing is, using an analogous notation,

$$i \frac{d}{dx} \begin{pmatrix} \varphi_{eL}(x) \\ \varphi_{\mu L}(x) \\ \varphi_{eR}(x) \\ \varphi_{\mu R}(x) \end{pmatrix} = H \begin{pmatrix} \varphi_{eL}(x) \\ \varphi_{\mu L}(x) \\ \varphi_{eR}(x) \\ \varphi_{\mu R}(x) \end{pmatrix}, \quad (6.21)$$

with the effective Hamiltonian matrix:

$$H = \begin{pmatrix} -\frac{\Delta m^2}{4E} \cos 2\vartheta + V_e & \frac{\Delta m^2}{4E} \sin 2\vartheta & \mu_{ee} B_\perp(x) & \mu_{e\mu} B_\perp(x) \\ \frac{\Delta m^2}{4E} \sin 2\vartheta & \frac{\Delta m^2}{4E} \cos 2\vartheta + V_\mu & \mu_{e\mu}^* B_\perp(x) & \mu_{\mu\mu} B_\perp(x) \\ \mu_{ee} B_\perp(x) & \mu_{e\mu} B_\perp(x) & -\frac{\Delta m^2}{4E} \cos 2\vartheta & \frac{\Delta m^2}{4E} \sin 2\vartheta \\ \mu_{e\mu}^* B_\perp(x) & \mu_{\mu\mu} B_\perp(x) & \frac{\Delta m^2}{4E} \sin 2\vartheta & \frac{\Delta m^2}{4E} \cos 2\vartheta \end{pmatrix}, \quad (6.22)$$

where we have used the constraint (6.17) for the transition magnetic moments. The matter potential can generate resonances, which occur when two diagonal elements of  $H$  become equal. Besides the standard MSW resonance in the  $\nu_{eL} \rightleftharpoons \nu_{\mu L}$  channel for  $V_{CC} = \Delta m^2 \cos 2\vartheta / 2E$  (see [1–4]), there are two possibilities

- (1) There is a resonance in the  $\nu_{eL} \rightleftharpoons \nu_{\mu R}$  channel for

$$V_e = \frac{\Delta m^2}{2E} \cos 2\vartheta. \quad (6.23)$$

The density at which this resonance occurs is not the same as that of the MSW resonance, because of the neutral-current contribution to  $V_e = V_{CC} + V_{NC}$ . The location of this resonance depends on both  $N_e$  and  $N_n$ .

- (2) There is a resonance in the  $\nu_{\mu L} \rightleftharpoons \nu_{eR}$  channel for

$$V_\mu = -\frac{\Delta m^2}{2E} \cos 2\vartheta. \quad (6.24)$$

If  $\cos 2\vartheta > 0$ , this resonance is possible in normal matter, since the sign of  $V_\mu = V_{NC}$  is negative, as one can see from (6.8).

In practice, the effect of these resonances could be the disappearance of active  $\nu_{eL}$  or  $\nu_{\mu L}$  into sterile right-handed states.

Let us consider now the more interesting case of Majorana neutrinos, which presents two fundamental differences with respect to the Dirac case.

- (A) If CP is conserved, Majorana neutrinos can have only a transition magnetic moment  $\mu_{e\mu} = -\mu_{\mu e} = -\mu_{e\mu}^*$  in the flavor basis.
- (B) The right-handed states are not sterile, but they interact as right-handed Dirac antineutrinos.

Assuming CP conservation, the evolution equation of the amplitudes is given by (6.21) with the effective Hamiltonian matrix:

$$H = \begin{pmatrix} -\frac{\Delta m^2}{4E} \cos 2\vartheta + V_e & \frac{\Delta m^2}{4E} \sin 2\vartheta & 0 & \mu_{e\mu} B_{\perp}(x) \\ \frac{\Delta m^2}{4E} \sin 2\vartheta & \frac{\Delta m^2}{4E} \cos 2\vartheta + V_{\mu} & -\mu_{e\mu} B_{\perp}(x) & 0 \\ 0 & \mu_{e\mu} B_{\perp}(x) & -\frac{\Delta m^2}{4E} \cos 2\vartheta - V_e & \frac{\Delta m^2}{4E} \sin 2\vartheta \\ -\mu_{e\mu} B_{\perp}(x) & 0 & \frac{\Delta m^2}{4E} \sin 2\vartheta & \frac{\Delta m^2}{4E} \cos 2\vartheta - V_{\mu} \end{pmatrix}. \quad (6.25)$$

Again, besides the standard MSW resonance in the  $\nu_{eL} \rightleftharpoons \nu_{\mu L}$  channel, there are two possible resonances

- (1) There is a resonance in the  $\nu_{eL} \rightleftharpoons \nu_{\mu R}$  channel for

$$V_{CC} + 2V_{NC} = \frac{\Delta m^2}{2E} \cos 2\vartheta. \quad (6.26)$$

- (2) There is a resonance in the  $\nu_{\mu L} \rightleftharpoons \nu_{eR}$  channel for

$$V_{CC} + 2V_{NC} = -\frac{\Delta m^2}{2E} \cos 2\vartheta. \quad (6.27)$$

The location of both resonances depend on both  $N_e$  and  $N_n$ . If  $\cos 2\vartheta > 0$ , only the first resonance can occur in normal matter, where  $N_n \simeq N_e/6$ . A realization of the second resonance requires a large neutron number density, as that in a neutron star.

The neutrino spin oscillations in a transverse magnetic field with a possible rotation of the field-strength vector in a plane orthogonal to the neutrino-propagation direction (such rotating fields may exist in the convective zone of the Sun) have been considered in [160–163]. The effect of the magnetic-field rotation may substantially shift the resonance point of neutrino oscillations. Neutrino spin oscillations in electromagnetic fields with other different configurations, including a longitudinal magnetic field and the field of an electromagnetic wave, were examined in [164–169].

It is possible to formulate a criterion [163] for finding out if the neutrino spin and spin-flavor precession is significant for given neutrino and background medium properties. The



probability of oscillatory transitions between two neutrino states  $\nu_{\alpha L} \leftrightarrow \nu_{\beta R}$  can be expressed in terms of the elements of the effective Hamiltonian matrices (6.22) and (6.25) as

$$P_{\nu_{\alpha L} \leftrightarrow \nu_{\beta R}} = \sin^2 \vartheta_{\text{eff}} \sin^2 \frac{x\pi}{L_{\text{eff}}}, \quad (6.28)$$

where

$$\sin^2 \vartheta_{\text{eff}} = \frac{4H_{\alpha\beta}^2}{4H_{\alpha\beta}^2 + (H_{\beta\beta} - H_{\alpha\alpha})^2}, \quad L_{\text{eff}} = \frac{2\pi}{\sqrt{4H_{\alpha\beta}^2 + (H_{\beta\beta} - H_{\alpha\alpha})^2}}. \quad (6.29)$$

The transition probability can be of order unity if the following two conditions hold simultaneously: (1) the amplitude of the transition probability must be sizable (at least  $\sin^2 \vartheta_{\text{eff}} \gtrsim 1/2$ ); (2) the neutrino path length in a medium with a magnetic field should be longer than half the effective length of oscillations  $L_{\text{eff}}$ . In accordance with this criterion, it is possible to introduce the critical strength of a magnetic field  $B_{\text{cr}}$  which determines the region of field values  $B_{\perp} > B_{\text{cr}}$  at which the probability amplitude is not small ( $\sin^2 \vartheta_{\text{eff}} > 1/2$ ):

$$B_{\text{cr}} = \frac{1}{2\tilde{\mu}} \sqrt{(H_{\beta\beta} - H_{\alpha\alpha})^2}, \quad (6.30)$$

where  $\tilde{\mu}$  is  $\mu_{ee}$ ,  $\mu_{\mu\mu}$ ,  $\mu_{e\mu}$ , or  $\mu_{\mu e}$  depending on the type of neutrino transition process in question.

Consider, for instance, the case of  $\nu_{eL} \leftrightarrow \nu_{\mu R}$  transitions of Majorana neutrinos. From (6.25) and (6.30), it follows [163] that

$$B_{\text{cr}} = \left| \frac{1}{2\tilde{\mu}} \left( \frac{\Delta m^2 \cos 2\vartheta}{2E} - \sqrt{2} G_{\text{F}} N_{\text{eff}} \right) \right|, \quad (6.31)$$

where  $N_{\text{eff}} = N_e - N_n$ . For getting numerical estimates of  $B_{\text{cr}}$ , it is convenient to rewrite (6.31) in the following form:

$$B_{\text{cr}} \approx 43 \frac{\mu_B}{\tilde{\mu}} \left| \cos 2\vartheta \left( \frac{\Delta m^2}{\text{eV}^2} \right) \left( \frac{\text{MeV}}{E} \right) - 2.5 \times 10^{-31} \left( \frac{N_{\text{eff}}}{\text{cm}^{-3}} \right) \right| \text{Gauss}. \quad (6.32)$$

An interesting feature of the evolution equation (6.21) in the case of Majorana neutrinos is that the interplay of spin precession and flavor oscillations can generate  $\nu_{eL} \rightarrow \nu_{eR}$  transitions [170]. Since  $\nu_{eR}$  interacts as right-handed Dirac antineutrinos, it is often denoted by  $\bar{\nu}_{eR}$ , or only  $\bar{\nu}_e$ , and called “electron antineutrino.” This state can be detected through the inverse  $\beta$ -decay reaction:

$$\bar{\nu}_e + p \longrightarrow n + e^+, \quad (6.33)$$

having a threshold  $E_{\text{th}} = 1.8 \text{ MeV}$ .

The possibility of  $\nu_e \rightarrow \bar{\nu}_e$  transitions generated by spin-flavor precession of Majorana neutrinos is particularly interesting for solar neutrinos, which experience matter effects in the interior of the Sun in the presence of the solar magnetic field (see [10, 171]). Taking into account the dominant  $\nu_e \rightarrow \nu_a$  transitions due to neutrino oscillations (see [1–4]), with  $\nu_a = \cos \vartheta_{23} \nu_\mu - \sin \vartheta_{23} \nu_\tau$  and  $\sin^2 2\vartheta_{23} > 0.95$  (90% C.L.) [66], the probability of solar  $\nu_e \rightarrow \bar{\nu}_e$  transitions is given by [172]

$$P_{\nu_e \rightarrow \bar{\nu}_e} \simeq 1.8 \times 10^{-10} \sin^2 2\vartheta_{12} \left( \frac{\mu_{ea}}{10^{-12} \mu_B} \frac{B_\perp(0.05R_\odot)}{10 \text{ kG}} \right)^2, \quad (6.34)$$

where  $\mu_{ea}$  is the transition magnetic moment between  $\nu_e$  and  $\nu_a$ ,  $\sin^2 2\vartheta_{12} = 0.857^{+0.023}_{-0.025}$  [66] and  $R_\odot$  is the radius of the Sun.

It is also possible that spin-flavor precession occurs in the convective zone of the Sun, where there can be random turbulent magnetic fields [173–175]. In this case [176],

$$P_{\nu_e \rightarrow \bar{\nu}_e} \approx 10^{-7} S^2 \left( \frac{\mu_{ea}}{10^{-12} \mu_B} \right)^2 \left( \frac{B}{20 \text{ kG}} \right)^2 \left( \frac{3 \times 10^4 \text{ km}}{L_{\max}} \right)^{p-1} \times \left( \frac{8 \times 10^{-5} \text{ eV}^2}{\Delta m_{21}^2} \right)^p \left( \frac{E}{10 \text{ MeV}} \right)^p \left( \frac{\cos^2 \vartheta_{12}}{0.7} \right)^p, \quad (6.35)$$

where  $S$  is a factor of order unity depending on the spatial configuration of the magnetic field,  $B$  is the average strength of the magnetic field at the spatial scale  $L_{\max}$ , which is the largest scale of the turbulence,  $p$  is the power of the turbulence scaling,  $\Delta m_{21}^2 = 7.50^{+0.19}_{-0.20} \times 10^{-5} \text{ eV}^2$  [66], and  $E$  is the neutrino energy. A possible value of  $p$  is 5/3 [173–175], corresponding to Kolmogorov turbulence. Conservative values for the other parameters are  $B = 20 \text{ kG}$  and  $L_{\max} = 3 \times 10^4 \text{ km}$ .

In 2002, the Super-Kamiokande Collaboration established for the flux of solar  $\bar{\nu}_e$ 's a 90% C.L. an upper limit of 0.8% of the Standard Solar Model (SSM) neutrino flux in the range of energy from 8 to 20 MeV [177] by taking as a reference the BP00 SSM prediction  $\phi_{\text{sB}}^{\text{BP00}} = 5.05 \times 10^6 \text{ cm}^{-2} \text{ s}^{-1}$  for the solar  $^8\text{B}$  flux [178] and assuming an undistorted  $^8\text{B}$  spectrum for the  $\bar{\nu}_e$ 's. This limit was improved in 2003 by the KamLAND Collaboration [179] to  $2.8 \times 10^{-4}$  of the BP00 SSM prediction at 90% C.L. by measuring  $\phi_{\bar{\nu}_e} < 370 \text{ cm}^{-2} \text{ s}^{-1}$  (90% C.L.) in the energy range 8.3–14.8 MeV, which corresponds to  $\phi_{\bar{\nu}_e} < 1250 \text{ cm}^{-2} \text{ s}^{-1}$  (90% C.L.) in the entire  $^8\text{B}$  energy range assuming an undistorted spectrum.

Recently, the Borexino collaboration established the best limit on the probability of solar  $\nu_e \rightarrow \bar{\nu}_e$  transitions [180]:

$$P_{\nu_e \rightarrow \bar{\nu}_e} < 1.3 \times 10^{-4} \quad (90\% \text{ C.L.}), \quad (6.36)$$

by taking as a reference  $\phi_{\text{sB}}^{\text{SSM}} = 5.88 \times 10^6 \text{ cm}^{-2} \text{ s}^{-1}$  [181] and assuming an undistorted  $^8\text{B}$  spectrum for the  $\bar{\nu}_e$ 's. They measured  $\phi_{\bar{\nu}_e} < 320 \text{ cm}^{-2} \text{ s}^{-1}$  (90% C.L.) for  $E_{\bar{\nu}_e} > 7.3 \text{ MeV}$ , which corresponds to  $\phi_{\bar{\nu}_e} < 760 \text{ cm}^{-2} \text{ s}^{-1}$  (90% C.L.) in the entire  $^8\text{B}$  energy range assuming an undistorted spectrum.

The implications of the limits on the flux of solar  $\bar{\nu}_e$ 's on Earth for the spin-flavor precession of solar neutrinos have been studied in several papers [172–175, 182–185], taking

into account the dominant  $\nu_e \rightarrow \nu_\mu, \nu_\tau$  transitions due to neutrino oscillations (see [1–4]). Using (6.34) and (6.36), we obtain

$$\mu_{ea} \lesssim 1.3 \times 10^{-12} \frac{7 \text{ MG}}{B_\perp(0.05R_\odot)} \mu_B, \quad (6.37)$$

with  $600 \text{ G} \lesssim B_\perp(0.05R_\odot) \lesssim 7 \text{ MG}$  [180]. In the case of spin-flavor precession in the convective zone of the Sun with random turbulent magnetic fields, (6.35) and (6.36) give, assuming  $p = 5/3$ ,

$$\mu_{ea} \lesssim 4 \times 10^{-11} \text{ S}^{-1} \frac{20 \text{ kG}}{B} \left( \frac{L_{\max}}{3 \times 10^4 \text{ km}} \right)^{1/3} \mu_B. \quad (6.38)$$

The spin-flavor mechanism was also considered [186] in order to describe time variations of solar-neutrino fluxes in Gallium experiments. The effect of a nonzero neutrino magnetic moment is also of interest in connection with the analysis of helioseismological observations [187].

The idea that the neutrino magnetic moment may solve the supernova problem, that is, that the neutrino spin-flip transitions in a magnetic field provide an efficient mechanism of energy transfer from a protoneutron star, was first discussed in [188] and then investigated in some detail in [189–191]. The possibility of a loss of up to half of the active left-handed neutrinos because of their transition to sterile right-handed neutrinos in strong magnetic fields at the boundary of the neutron star (the so-called boundary effect) was considered in [163].

## 7. Summary and Perspectives

In this review, we have considered the electromagnetic properties of neutrinos with focus on the most important issues related to the problem. The main results discussed in the paper can be summed up as follows.

In the most general case, the neutrino electromagnetic vertex function is defined in terms of four form factors: the charge, dipole magnetic, and electric and anapole form factors. This decomposition is consistent with Lorentz and electromagnetic gauge invariance. The four form factors at zero momentum transfer  $q^2 = 0$  are, respectively, the neutrino charge, magnetic moment, electric moment, and anapole moment. These quantities contribute to elements of the scattering matrix and describe neutrino interactions with real photons.

An important characteristic of neutrino electromagnetic properties is that they are different for Dirac and Majorana neutrinos. In particular, Majorana neutrinos cannot have diagonal magnetic or electric moments. Thus, studies of neutrino electromagnetic interactions can be used as a procedure to distinguish whether a neutrino is a Dirac or Majorana particle.

Moreover, CP invariance in the lepton sector puts additional constraints on the neutrino form factors and can be tested with experimental probes of neutrino electromagnetic interactions.

Up to now, no effect of neutrino electromagnetic properties has been found in terrestrial laboratory experiments and in the analyses of astrophysical and cosmological data. However, massive neutrinos have nontrivial electromagnetic properties in a wide set

of theoretical frameworks, including the simplest extension of the Standard Model with inclusion of singlet right-handed neutrinos. Therefore, the search for nonvanishing neutrino electromagnetic properties is of great interest for experimentalist and theorists.

The neutrino dipole magnetic (and also electric) moment is theoretically the most well studied and understood among the neutrino electromagnetic moments. In models which extend the Standard Model with the addition of singlet right-handed neutrinos, a Dirac neutrino has a nonzero magnetic moment proportional to the neutrino mass, which yields a very small value for the magnetic moment, less than about  $3 \times 10^{-19} \mu_B$  for a neutrino mass smaller than 1 eV (3.5). Extra terms contributing to the magnetic moment of the neutrino that are not proportional to the neutrino mass may exist, for example, in the framework of left-right symmetric models. In this type of models, as well as in other generalizations of the Standard Model, as, for instance, in supersymmetric and extradimension models, values of the neutrino magnetic moment much larger than  $10^{-19} \mu_B$  can be obtained.

The most severe terrestrial experimental upper bound for the effective electron antineutrino magnetic moment,  $\mu_{\bar{\nu}_e} \leq 2.9 \times 10^{-11} \mu_B$  at 90% C.L. (3.31), has been recently obtained in the direct antineutrino-electron scattering experiment performed by the GEMMA collaboration [58]. This value is still about an order of magnitude weaker than the upper bound  $\mu_\nu \lesssim 3 \times 10^{-12} \mu_B$  (5.8) obtained from astrophysics (considering the cooling of red giant stars) [153].

There is a gap of some orders of magnitude between the present experimental limits  $\sim 10^{-11} \div 10^{-12} \mu_B$  on neutrino magnetic moments and the predictions of different extensions of the Standard Model which hint at a range  $\sim 10^{-14} \div 10^{-15} \mu_B$  [28, 29, 80] (see Section (3.5)). The terrestrial experimental constraints have been improved by only one order of magnitude during a period of about twenty years. Further improvements are very important, but unfortunately at the moment there is no new idea which could lead to fast improvements in the near future. On the other hand, astrophysical studies could allow significant improvements of the sensitivity to nontrivial neutrino electromagnetic properties and maybe find a positive indication in their favor. In particular, neutrino flows in extreme astrophysical environments with very strong magnetic fields are sensitive to small values of the neutrino electromagnetic moments. An example is the modelling of neutrinos propagation during core-collapse supernovae (see [192] and references therein) where very strong magnetic fields are believed to exist and in which the influence of neutrino electromagnetic properties has not yet been taken into account.

## Acknowledgments

The work of A. Studenikin on this paper has been partially supported by the Russian Foundation for Basic Research (Grants no. 11-02-01509 and no. 12-02-06833) and the Ministry of Education and Science of Russia (State Contract no. 12.741.11.0180 and Projects no. 2012-1.2.1-12-000-1012-1958 and no. 2012-1.1-12-000-1011-6097). C. Giunti would like to thank the Department of Physics of the University of Torino for hospitality and support.

## References

- [1] C. Giunti and C. W. Kim, *Fundamentals of Neutrino Physics and Astrophysics*, Oxford University Press, Oxford, UK, 2007.
- [2] M. C. Gonzalez-Garcia and M. Maltoni, "Phenomenology with massive neutrinos," *Physics Reports*, vol. 460, no. 1–3, pp. 1–129, 2008.

- [3] S. Bilenky, *Introduction to the Physics of Massive and Mixed Neutrinos*, vol. 817 of *Lecture Notes in Physics*, Springer, New York, NY, USA, 2010.
- [4] Z. Z. Xing and S. Zhou, *Neutrinos in Particle Physics, Astronomy and Cosmology*, Zhejiang University Press, 2011.
- [5] C. W. Kim and A. Pevsner, *Neutrinos in Physics and Astrophysics*, vol. 8 of *Contemporary Concepts in Physics*, Harwood Academic Press, 1993.
- [6] M. Fukugita and T. Yanagida, *Physics of Neutrinos and Applications to Astrophysics*, Springer, New York, NY, USA, 2003.
- [7] R. N. Mohapatra and P. B. Pal, *Massive Neutrinos in Physics and Astrophysics*, vol. 72 of *Lecture Notes in Physics*, World Scientific, River Edge, NJ, USA, 3rd edition, 2004.
- [8] G. G. Raffelt, "Astrophysical methods to constrain axions and other novel particle phenomena," *Physics Reports*, vol. 198, no. 1-2, pp. 1–113, 1990.
- [9] G. G. Raffelt, "Astrophysics probes of particle physics," *Physics Reports*, vol. 333-334, pp. 593–618, 2000.
- [10] J. Pulido, "The solar neutrino problem and the neutrino magnetic moment," *Physics Reports*, vol. 211, no. 4, pp. 167–199, 1992.
- [11] M. Nowakowski, E. A. Paschos, and J. M. Rodríguez, "All electromagnetic form factors," *European Journal of Physics*, vol. 26, no. 4, pp. 545–560, 2005.
- [12] H. T. Wong and H. B. Li, "Neutrino magnetic moment," *Modern Physics Letters A*, vol. 20, no. 15, article 1103, 2005.
- [13] C. Giunti and A. Studenikin, "Neutrino electromagnetic properties," *Physics of Atomic Nuclei*, vol. 72, no. 12, pp. 2089–2125, 2009.
- [14] A. Studenikin, "Neutrino magnetic moment: a window to new physics," *Nuclear Physics B*, vol. 188, pp. 220–222, 2009, Proceedings of the Neutrino Oscillation Workshop, Otranto, Italy, September 2008.
- [15] W. J. Marciano and A. I. Sanda, "Exotic decays of the muon and heavy leptons in gauge theories," *Physics Letters B*, vol. 67, no. 3, pp. 303–305, 1977.
- [16] B. W. Lee and R. E. Shrock, "Natural suppression of symmetry violation in gauge theories: muon- and electron-lepton-number nonconservation," *Physical Review D*, vol. 16, no. 5, pp. 1444–1473, 1977.
- [17] K. Fujikawa and R. Shrock, "Magnetic moment of a massive neutrino and neutrino-spin rotation," *Physical Review Letters*, vol. 45, no. 12, pp. 963–966, 1980.
- [18] S. Petcov, "Neutrino gamma in the Weinberg-Salam Model with Neutrino Mixing," *Soviet Journal of Nuclear Physics*, vol. 25, p. 340, 1977.
- [19] S. Petcov, "Neutrino gamma in the Weinberg-Salam Model with Neutrino Mixing," *Soviet Journal of Nuclear Physics*, vol. 25, p. 698, 1977.
- [20] S. Petcov, "Neutrino gamma in the Weinberg-Salam Model with Neutrino Mixing," *Soviet Journal of Nuclear Physics*, vol. 25, p. 1336, 1977.
- [21] P. B. Pal and L. Wolfenstein, "Radiative decays of massive neutrinos," *Physical Review D*, vol. 25, no. 3, pp. 766–773, 1982.
- [22] R. E. Shrock, "Electromagnetic properties and decays of Dirac and Majorana neutrinos in a general class of gauge theories," *Nuclear Physics B*, vol. 206, no. 3, pp. 359–379, 1982.
- [23] S. M. Bilenky and S. T. Petcov, "Massive neutrinos and neutrino oscillations," *Reviews of Modern Physics*, vol. 59, no. 3, pp. 671–754, 1987.
- [24] J. Schechter and J. W. F. Valle, "Majorana neutrinos and magnetic fields," *Physical Review D*, vol. 24, no. 7, pp. 1883–1889, 1981.
- [25] J. F. Nieves, "Electromagnetic properties of Majorana neutrinos," *Physical Review D*, vol. 26, no. 11, pp. 3152–3158, 1982.
- [26] B. Kayser, "Majorana neutrinos and their electromagnetic properties," *Physical Review D*, vol. 26, no. 7, pp. 1662–1670, 1982.
- [27] B. Kayser, "CPT, CP, and C phases, and their effects, in Majorana-particle processes," *Physical Review D*, vol. 30, no. 5, pp. 1023–1033, 1984.
- [28] N. F. Bell, V. Cirigliano, M. J. Ramsey-Musolf et al., "How magnetic is the Dirac neutrino?" *Physical Review Letters*, vol. 95, no. 15, Article ID 151802, 4 pages, 2005.
- [29] N. F. Bell, M. Gorchtein, M. J. Ramsey-Musolf, P. Vogel, and P. Wang, "Model independent bounds on magnetic moments of Majorana neutrinos," *Physics Letters B*, vol. 642, no. 4, pp. 377–383, 2006.
- [30] H. Novales-Sanchez, A. Rosado, V. Santiago-Olan, and J. Toscano, "Effects of physics beyond the standard model on the neutrino charge radius: an effective Lagrangian approach," *Physical Review D*, vol. 78, no. 7, Article ID 073014, 8 pages, 2008.



- [31] W. A. Bardeen, R. Gastmans, and B. Lautrup, "Static quantities in Weinberg's model of weak and electromagnetic interactions," *Nuclear Physics B*, vol. 46, no. 1, pp. 319–331, 1972.
- [32] M. Dvornikov and A. Studenikin, "Electric charge and magnetic moment of a massive neutrino," *Physical Review D*, vol. 69, no. 7, Article ID 073001, 21 pages, 2004.
- [33] M. Dvornikov and A. Studenikin, "Electromagnetic form factors of a massive neutrino," *Journal of Experimental and Theoretical Physics*, vol. 99, no. 2, pp. 254–269, 2004.
- [34] S. L. Glashow, J. Iliopoulos, and L. Maiani, "Weak interactions with lepton-hadron symmetry," *Physical Review D*, vol. 2, no. 7, pp. 1285–1292, 1970.
- [35] S. M. Barr, E. Freire, and A. Zee, "Mechanism for large neutrino magnetic moments," *Physical Review Letters*, vol. 65, no. 12, pp. 2626–2629, 1990.
- [36] B. Pal, "Zee model on Majorana neutrino mass and magnetic moment," *Physical Review D*, vol. 44, no. 8, pp. 2261–2264, 1991.
- [37] L. G. Cabral-Rosetti, J. Bernabeu, J. Vidal, and A. Zepeda, "Charge and magnetic moment of the neutrino in the background field method and in the linear  $R_{\xi}^L$  gauge," *The European Physical Journal C*, vol. 12, pp. 633–642, 2000, <http://arxiv.org/abs/hep-ph/9907249>.
- [38] The ALEPH Collaboration, The DELPHI Collaboration, The L3 Collaboration et al., "Precision electroweak measurements on the Z resonance," *Physics Reports*, vol. 427, no. 5-6, pp. 257–454, 2006.
- [39] S. A. Cetin, G. W. S. Hou, V. E. Ozcan, A. N. Rozanov, and S. Sultansoy, "Status of the fourth generation—a brief summary of B3SM-III workshop in four parts," in *Proceedings of the B3SM-III*, Bogazici University, Istanbul, Turkey, October 2011, <http://arxiv.org/abs/1112.2907>.
- [40] J. E. Kim, "Neutrino magnetic moment," *Physical Review D*, vol. 14, no. 11, pp. 3000–3002, 1976.
- [41] M. Czakon, J. Gluza, and M. Zralek, "Neutrino magnetic moments in left-right symmetric models," *Physical Review D*, vol. 59, no. 1, Article ID 013010, 6 pages, 1999.
- [42] M. A. B. Beg, W. J. Marciano, and M. Ruderman, "Properties of neutrinos in a class of gauge theories," *Physical Review D*, vol. 17, no. 5, pp. 1395–1401, 1978.
- [43] A. G. Beda, V. B. Brudanin, E. V. Demidova et al., "First result for the neutrino magnetic moment from measurements with the GEMMA spectrometer," *Physics of Atomic Nuclei*, vol. 70, no. 11, pp. 1873–1884, 2007.
- [44] R. N. Mohapatra, S. P. Ng, and H. Yu, "Reactor searches for neutrino magnetic moment as a probe of extra dimensions," *Physical Review D*, vol. 70, no. 5, Article ID 057301, 4 pages, 2004.
- [45] J. F. Carlson and J. R. Oppenheimer, "The impacts of fast electrons and magnetic neutrons," *Physical Review*, vol. 41, no. 6, pp. 763–792, 1932.
- [46] H. Bethe, "Ionization power of a neutrino with magnetic moment," *Mathematical Proceedings of the Cambridge Philosophical Society*, vol. 31, no. 1, pp. 108–115, 1935.
- [47] G. Domogatsky and D. Nadezhin, "Modern theory of star evolution and experiments of F. Reines on anti  $\nu$  e-scattering detection," *Yadernaya Fizika*, vol. 12, p. 1233, 1970.
- [48] A. V. Kyulldjiev, "Searching for effects of neutrino magnetic moments at reactors and accelerators," *Nuclear Physics B*, vol. 243, no. 3, pp. 387–397, 1984.
- [49] P. Vogel and J. Engel, "Neutrino electromagnetic form factors," *Physical Review D*, vol. 39, no. 11, pp. 3378–3383, 1989.
- [50] W. Grimus and P. Stockinger, "Effects of neutrino oscillations and neutrino magnetic moments on elastic neutrino-electron scattering," *Physical Review D*, vol. 57, no. 3, pp. 1762–1768, 1998.
- [51] H. T. Wong, H. B. Li, and S. T. Lin, "Enhanced sensitivities for the searches of neutrino magnetic moments through atomic ionization," *Physical Review Letters*, vol. 105, no. 6, Article ID 061801, 4 pages, 2010.
- [52] M. Voloshin, "Neutrino scattering on atomic electrons in searches for the neutrino magnetic moment," *Physical Review Letters*, vol. 105, no. 20, Article ID 201801, 4 pages, 2010.
- [53] K. A. Kouzakov and A. I. Studenikin, "Magnetic neutrino scattering on atomic electrons revisited," *Physics Letters B*, vol. 696, no. 3, pp. 252–256, 2011.
- [54] K. A. Kouzakov and A. I. Studenikin, "Electromagnetic neutrino-atom collisions: the role of electron binding," *Nuclear Physics B*, vol. 217, no. 1, pp. 353–356, 2011.
- [55] K. A. Kouzakov, A. I. Studenikin, and M. B. Voloshin, "Testing neutrino magnetic moment in ionization of atoms by neutrino impact," *JETP Letters*, vol. 93, pp. 699–703, 2011, <http://arxiv.org/abs/1105.5543>.
- [56] K. A. Kouzakov, A. I. Studenikin, and M. B. Voloshin, "Neutrino-impact ionization of atoms in searches for neutrino magnetic moment," *Physical Review D*, vol. 83, no. 11, Article ID 113001, 11 pages, 2011.

- [57] K. A. Kouzakov, A. I. Studenikin, and M. B. Voloshin, "On neutrino-atom scattering in searches for neutrino magnetic moments," in *Proceedings of the 24th International Conference on Neutrino Physics and Astrophysics*, Athens, Greece, June 2010, <http://arxiv.org/abs/1102.0643>.
- [58] A. G. Beda, V. B. Brudanin, V. G. Egorov et al., "The results of search for the neutrino magnetic moment in GEMMA experiment," *Advances in High Energy Physics*, vol. 2012, Article ID 350150, 12 pages, 2012.
- [59] J. F. Beacom and P. Vogel, "Neutrino magnetic moments, flavor mixing, and the super-kamiokande solar data," *Physical Review Letters*, vol. 83, no. 25, pp. 5222–5225, 1999.
- [60] F. Reines, H. Gurr, and H. Sobel, "Detection of  $\bar{\nu}_e$ -e scattering," *Physical Review Letters*, vol. 37, no. 6, pp. 315–318, 1976.
- [61] G. S. Vidyakin, V. N. Vyrodov, I. I. Gurevich et al., "Limitations on the magnetic moment and charge radius of the electron antineutrino," *JETP Letters*, vol. 55, no. 4, article 206, 1992.
- [62] A. I. Derbin, A. V. Chernyi, L. A. Popeko, V. N. Muratova, G. A. Shishkina, and S. I. Bakhlanov, "Experiment on antineutrino scattering by electrons at a reactor of the Rovno nuclear power plant," *JETP Letters*, vol. 57, no. 12, article 768, 1993.
- [63] H. T. Wong, H. B. Li, S. T. Lin et al., "Search of neutrino magnetic moments with a high-purity germanium detector at the Kuo-Sheng nuclear power station," *Physical Review D*, vol. 75, no. 1, Article ID 012001, 16 pages, 2007.
- [64] C. Amsler, M. Avenier, G. Bagieu et al., "The MUNU experiment, general description," *Nuclear Instruments and Methods in Physics Research A*, vol. 396, no. 1-2, pp. 115–129, 1997.
- [65] Z. Daraktchieva, C. Amsler, M. Avenier et al., "Final results on the neutrino magnetic moment from the MUNU experiment," *Physics Letters B*, vol. 615, no. 3-4, pp. 153–159, 2005.
- [66] J. Beringer, J. F. Arguin, R. M. Barnett et al., "Review of particle physics," *Physical Review D*, vol. 86, no. 1, Article ID 010001, 1528 pages, 2012.
- [67] L. B. Auerbach, R. L. Burman, D. O. Caldwell et al., "Measurement of electron-neutrino electron elastic scattering," *Physical Review D*, vol. 63, no. 11, 11 pages, 2001.
- [68] R. Schwienhorst, D. Ciampa, C. Erickson et al., "A new upper limit for the tau-neutrino magnetic moment," *Physics Letters B*, vol. 513, no. 1-2, pp. 23–29, 2001.
- [69] D. W. Liu, Y. Ashie, S. Fukuda et al., "Limits on the neutrino magnetic moment using 1496 days of Super-Kamiokande-I solar neutrino data," *Physical Review Letters*, vol. 93, no. 2, Article ID 021802, 5 pages, 2004.
- [70] C. Arpesella, H. O. Back, M. Balata et al., "Direct measurement of the  $^7\text{Be}$  solar neutrino flux with 192 days of Borexino data," *Physical Review Letters*, vol. 101, no. 9, Article ID 091302, 6 pages, 2008.
- [71] D. Montanino, M. Picariello, and J. Pulido, "Probing neutrino magnetic moment and unparticle interactions with Borexino," *Physical Review D*, vol. 77, no. 9, Article ID 093011, 9 pages, 2008.
- [72] W. Grimus, M. Maltoni, T. Schwetz, M. A. Tortola, and J. W. F. Valle, "Constraining Majorana neutrino electromagnetic properties from the LMA-MSW solution of the solar neutrino problem," *Nuclear Physics B*, vol. 648, no. 1-2, pp. 376–396, 2003.
- [73] M. A. Tortola, "Constraining neutrino magnetic moment with solar and reactor neutrino data," in *Proceedings of the International Workshop on Astroparticle and High Energy Physics (AHEP-2003)*, Valencia, Spain, October 2003, <http://arxiv.org/abs/hep-ph/0401135>.
- [74] J. Bernabeu, J. Papavassiliou, and M. Passera, "Dynamical zero in  $\bar{\nu}_e$ -e $^-$  scattering and the neutrino magnetic moment," *Physics Letters B*, vol. 613, no. 3-4, pp. 162–169, 2005.
- [75] J. Segura, J. Bernabeu, F. Botella, and J. Penarrocha, "Dynamical zeros in neutrino-electron elastic scattering at leading order," *Physical Review D*, vol. 49, no. 3, pp. 1633–1636, 1994.
- [76] M. Goźdz, W. A. Kaminski, F. Simkovic, and A. Faessler, "Transition magnetic moments of Majorana neutrinos in supersymmetry without R-parity in light of neutrino oscillations," *Physical Review D*, vol. 74, no. 5, Article ID 055007, 11 pages, 2006.
- [77] M. Goźdz, W. A. Kaminski, and F. Simkovic, "Majorana neutrino magnetic moments," *International Journal of Modern Physics E*, vol. 15, no. 2, article 441, 2006.
- [78] M. Voloshin, "On compatibility of small mass with large magnetic moment of neutrino," *Soviet Journal of Nuclear Physics*, vol. 48, p. 512, 1988.
- [79] P. B. Pal, "Particle physics confronts the solar neutrino problem," *International Journal of Modern Physics A*, vol. 7, no. 22, article 5387, 1992.
- [80] N. F. Bell, "How magnetic is the neutrino?" *International Journal of Modern Physics A*, vol. 22, no. 27, article 4891, 2007, Festschrift in honour of B. H. J. McKellar and G. C. Joshi.
- [81] M. Leurer and N. Marcus, "A model for a large neutrino magnetic transition moment and naturally small mass," *Physics Letters B*, vol. 237, no. 1, pp. 81–87, 1990.

- [82] K. Babu and R. N. Mohapatra, "Large transition magnetic moment of the neutrino from horizontal symmetry," *Physical Review D*, vol. 42, no. 11, pp. 3778–3793, 1990.
- [83] H. Georgi and L. Randall, "Charge conjugation and neutrino magnetic moments," *Physics Letters B*, vol. 244, no. 2, pp. 196–202, 1990.
- [84] G. Ecker, W. Grimus, and H. Neufeld, "A light Zeldovich-Konopinski-Mahmoud neutrino with a large magnetic moment," *Physics Letters B*, vol. 232, no. 2, pp. 217–221, 1989.
- [85] D. Chang, W. Y. Keung, S. Lipovaca, and G. Senjanovic, "Neutrino magnetic moment and the dicyclic group," *Physical Review Letters*, vol. 67, no. 8, pp. 953–956, 1991.
- [86] R. Barbieri and R. N. Mohapatra, "A neutrino with a large magnetic moment and a naturally small mass," *Physics Letters B*, vol. 218, no. 2, pp. 225–229, 1989.
- [87] A. Zee, "A theory of lepton number violation and neutrino Majorana masses," *Physics Letters B*, vol. 93, no. 4, pp. 389–393, 1980.
- [88] S. Lee, "Higher-order corrections to leptonic processes and the renormalization of Weinberg's theory of weak interactions in the unitary gauge," *Physical Review D*, vol. 6, no. 6, pp. 1701–1717, 1972.
- [89] J. Lucio, A. Rosado, and A. Zepeda, "Neutrino charge in the linear  $R_\xi$  gauge," *Physical Review D*, vol. 29, no. 7, pp. 1539–1541, 1984.
- [90] J. Lucio, A. Rosado, and A. Zepeda, "Characteristic size for the neutrino," *Physical Review D*, vol. 31, no. 5, pp. 1091–1096, 1985.
- [91] G. Degrossi, A. Sirlin, and W. J. Marciano, "Effective electromagnetic form factor of the neutrino," *Physical Review D*, vol. 39, no. 1, pp. 287–294, 1989.
- [92] J. Bernabeu, L. G. Cabral-Rosetti, J. Papavassiliou, and J. Vidal, "Charge radius of the neutrino," *Physical Review D*, vol. 62, no. 11, Article ID 113012, 19 pages, 2000.
- [93] J. Bernabeu, J. Papavassiliou, and J. Vidal, "Observability of the Neutrino Charge Radius," *Physical Review Letters*, vol. 89, no. 10, Article ID 101802, 4 pages, 2002.
- [94] J. Bernabeu, J. Papavassiliou, and J. Vidal, "The neutrino charge radius as a physical observable," *Nuclear Physics B*, vol. 680, no. 1–3, pp. 450–478, 2004.
- [95] K. Fujikawa and R. Shrock, "Comment on 'observability of the neutrino charge Radius'," in press, <http://arxiv.org/abs/hep-ph/0303188>.
- [96] K. Fujikawa and R. Shrock, "Neutrino electroweak radius," *Physical Review D*, vol. 69, no. 1, Article ID 013007, 8 pages, 2004.
- [97] J. Papavassiliou, J. Bernabeu, D. Binosi, and J. Vidal, "The effective neutrino charge radius," *The European Physical Journal C*, vol. 33, supplement 1, pp. S865–S867, 2004, Proceedings of the EPS 2003, Aachen, Germany.
- [98] J. Bernabeu, D. Binosi, and J. Papavassiliou, "The effective neutrino charge radius in the presence of fermion masses," *Nuclear Physics B*, vol. 716, no. 1–2, pp. 352–372, 2005.
- [99] A. Grau and J. Grifols, "Neutrino charge radius and substructure," *Physics Letters B*, vol. 166, no. 2, pp. 233–237, 1986.
- [100] K. Hagiwara, S. Matsumoto, D. Haidt, and C. Kim, "A novel approach to confront electroweak data and theory," *Zeitschrift Für Physik C*, vol. 64, no. 4, pp. 559–620, 1994.
- [101] M. Deniz, S. T. Lin, V. Singh et al., "Measurement of  $\bar{\nu}_e$ -electron scattering cross section with a CsI(Tl) scintillating crystal array at the Kuo-Sheng nuclear power reactor," *Physical Review D*, vol. 81, no. 7, Article ID 072001, 17 pages, 2001.
- [102] J. Grifols and E. Masso, "Bound on the neutrino charge radius from primordial nucleosynthesis," *Modern Physics Letters A*, vol. 2, no. 3, article 205, 1987.
- [103] J. A. Grifols and E. Masso, "Charge radius of the neutrino: a limit from SN 1987 A," *Physical Review D*, vol. 40, no. 12, pp. 3819–3820, 1989.
- [104] R. Allen, H. H. Chen, P. J. Doe et al., "Experimental bound on the charge radius of the electron neutrino," *Physical Review D*, vol. 43, no. 1, pp. R1–R3, 1991.
- [105] A. M. Mourao, J. Pulido, and J. P. Ralston, "The neutrino electromagnetic moments and charge radius confront Kamiokande II and Homestake experimental results," *Physics Letters B*, vol. 285, no. 4, pp. 364–370, 1992.
- [106] A. M. Mourao, J. Pulido, and J. P. Ralston, "Erratum: the neutrino electromagnetic moments and charge radius confront Kamiokande II and Homestake experimental results," *Physics Letters B*, vol. 288, no. 3–4, p. 421, 1992.
- [107] J. Barranco, O. G. Miranda, and T. I. Rashba, "Improved limit on electron neutrino charge radius through a new evaluation of the weak mixing angle," *Physics Letters B*, vol. 662, no. 5, pp. 431–435, 2008.

- [108] M. Hirsch, E. Nardi, and D. Restrepo, "Bounds on the tau and muon neutrino vector and axial vector charge radius," *Physical Review D*, vol. 67, no. 3, Article ID 033005, 10 pages, 2003.
- [109] T. Goldman and G. J. Stephenson Jr., "Limits on the mass of the muon neutrino in the absence of muon-lepton-number conservation," *Physical Review D*, vol. 16, no. 7, pp. 2256–2259, 1977.
- [110] G. T. Zatsepin and A. Y. Smirnov, "Neutrino decay in gauge theories," *Yadernaya Fizika*, vol. 28, p. 1569, 1978.
- [111] D. A. Dicus, E. W. Kolb, and V. L. Teplitz, "Cosmological upper bound on heavy-neutrino lifetimes," *Physical Review Letters*, vol. 39, no. 4, pp. 168–171, 1977.
- [112] K. Sato and M. Kobayashi, "Cosmological constraints on the mass and the number of heavy Lepton neutrinos," *Progress of Theoretical Physics*, vol. 58, no. 6, pp. 1775–1789, 1977.
- [113] F. Stecker, "Have massive cosmological neutrinos already been detected?" *Physical Review Letters*, vol. 45, no. 17, pp. 1460–1462, 1980.
- [114] R. Kimble, S. Bowyer, and P. Jakobsen, "Astrophysical constraints on the radiative lifetime of neutrinos with mass between 10 and 100 eV/c<sup>2</sup>," *Physical Review Letters*, vol. 46, no. 2, pp. 80–83, 1981.
- [115] A. Melott and D. Sciama, "Neutrino-lifetime constraints from neutral hydrogen in the galactic halo," *Physical Review Letters*, vol. 46, no. 21, pp. 1369–1372, 1981.
- [116] A. De Rújula and S. Glashow, "Galactic neutrinos and uv astronomy," *Physical Review Letters*, vol. 45, no. 11, pp. 942–944, 1980.
- [117] G. Raffelt, *Stars As Laboratories for Fundamental Physics: The Astrophysics of Neutrinos, Axions, and Other Weakly Interacting Particles*, University of Chicago Press, Chicago, Ill, USA, 1996.
- [118] G. G. Raffelt, "Limits on neutrino electromagnetic properties—an update," *Physics Reports*, vol. 320, no. 1–6, pp. 319–327, 1999.
- [119] S. Petcov, "Remarks on the Zee model of neutrino mixing ( $\mu \rightarrow e + \gamma, \nu_H \rightarrow \nu_L + \gamma$ , etc.)," *Physics Letters B*, vol. 115, no. 5, pp. 401–406, 1982.
- [120] A. N. Ioannisian and G. G. Raffelt, "Cherenkov radiation by massless neutrinos in a magnetic field," *Physical Review D*, vol. 55, no. 11, pp. 7038–7043, 1997.
- [121] A. Lobanov and A. Studenikin, *Physics Letters B*, vol. 564, no. 1-2, pp. 27–34, 2003.
- [122] A. I. Studenikin, "Neutrinos in electromagnetic fields and moving media," *Physics of Atomic Nuclei*, vol. 67, no. 5, pp. 993–1002, 2004.
- [123] A. I. Studenikin, "Neutrinos in matter and external fields," *Physics of Atomic Nuclei*, vol. 70, no. 7, pp. 1275–1287, 2007.
- [124] A. Studenikin, "Neutrinos and electrons in background matter: a new approach," *Annales de la Fondation Louis de Broglie*, vol. 31, no. 2-3, pp. 286–316, 2006.
- [125] D. V. Galtsov and N. S. Nikitina, "Photoneutrino processes in a strong field," *Soviet Physics, JETP*, vol. 35, p. 1047, 1972.
- [126] A. Borisov, V. C. Zhukovsky, and A. Ternov, "Electromagnetic properties of the massive dirac neutrino in an external electromagnetic field," *Soviet Physics Journal*, vol. 31, no. 3, pp. 228–233, 1988.
- [127] A. Borisov, V. C. Zhukovsky, and A. Ternov, "Electromagnetic properties of massive neutrinos," *Soviet Physics, Doklady*, vol. 34, p. 884, 1989.
- [128] V. Skobelev, "Reaction whereby a photon decays into a neutrino-antineutrino pair and a neutrino decays into a photon-neutrino pair in a strong magnetic field," *Zhurnal Èksperimental'noi i Teoreticheskoi Fiziki*, vol. 71, pp. 1263–1267, 1976.
- [129] V. Skobelev, "Interaction between a massive neutrino and a plane wave field," *Soviet Physics, JETP*, vol. 73, p. 40, 1991.
- [130] M. Radomski, "Neutrino magnetic moment, plasmon Čerenkov radiation, and the solar-neutrino problem," *Physical Review D*, vol. 12, no. 8, pp. 2208–2211, 1975.
- [131] W. Grimus and H. Neufeld, "Cherenkov radiation of neutrinos," *Physics Letters B*, vol. 315, no. 1-2, pp. 129–133, 1993.
- [132] M. Sakuda, "Proposed method to measure the neutrino magnetic moment," *Physical Review Letters*, vol. 72, no. 6, pp. 804–807, 1994.
- [133] M. Sakuda and Y. Kurihara, "Transition radiation of the neutrino magnetic moment," *Physical Review Letters*, vol. 74, no. 8, pp. 1284–1287, 1995.
- [134] W. Grimus and H. Neufeld, "Transition radiation of ultrarelativistic neutral particles," *Physics Letters B*, vol. 344, no. 1-4, pp. 252–258, 1995.
- [135] V. Oraevsky, V. Semikoz, and Y. Smorodinsky, "Polarization loss and induced electric charge of neutrinos in plasmas," *JETP Letters*, vol. 43, no. 12, article 709, 1986.



- [136] J. C. D'Olivo, J. F. Nieves, and P. B. Pal, "Cherenkov radiation by massless neutrinos," *Physics Letters B*, vol. 365, no. 1–4, pp. 178–184, 1996.
- [137] A. Borisov, V. C. Zhukovsky, A. Kurilin, and A. Ternov, "Radiative corrections to neutrino mass in external electromagnetic field," *Yadernaya Fizika*, vol. 41, p. 743, 1985.
- [138] S. S. Masood, A. Perez Martinez, H. Perez-Rojas, R. Gaitan, and S. Rodriguez-Romo, "Effective magnetic moment of neutrinos in strong magnetic fields," *Revista Mexicana de Fisica*, vol. 48, no. 006, p. 501, 2002.
- [139] J. F. Nieves, "Electromagnetic vertex of neutrinos in an electron background and a magnetic field," *Physical Review D*, vol. 68, no. 11, Article ID 113003, 13 pages, 2003.
- [140] S. Mohanty and M. K. Samal, "Cherenkov radiation by neutrinos in a supernova core," *Physical Review Letters*, vol. 77, no. 5, pp. 806–809, 1996.
- [141] C. Giunti, C. Kim, and W. Lam, "Radiative decay and magnetic moment of neutrinos in matter," *Physical Review D*, vol. 43, no. 1, pp. 164–169, 1991.
- [142] A. Gvozdev, N. Mikheev, and L. Vasilevskaya, "The magnetic catalysis of the radiative decay of a massive neutrino in the standard model with lepton mixing," *Physics Letters B*, vol. 289, no. 1–2, pp. 103–108, 1992.
- [143] V. Skobelev, "Decay of massive neutrinos in a strong magnetic field," *Journal of Experimental and Theoretical Physics*, vol. 81, p. 1, 1995.
- [144] V. C. Zhukovsky, P. Eminov, and A. Grigoruk, "Radiative decay of a massive neutrino in the Weinberg-Salam model with mixing in a constant uniform magnetic field," *Modern Physics Letters A*, vol. 11, no. 39–40, pp. 3119–3126, 1996.
- [145] M. Kachelriess and G. Wunner, "Radiative neutrino decays in very strong magnetic fields," *Physics Letters B*, vol. 390, no. 1–4, pp. 263–267, 1997.
- [146] A. Ternov and P. Eminov, "Radiative decay of the massive neutrino in magnetized plasma," *Journal of Physics G*, vol. 29, no. 2, article 357, 2003.
- [147] A. Lobanov and A. Studenikin, "Neutrino self-polarization effect in matter," *Physics Letters B*, vol. 601, no. 3–4, pp. 171–175, 2004.
- [148] A. Grigoriev, M. Dvornikov, and A. Studenikin, "Spin light of neutrino in gravitational fields," *International Journal of Modern Physics D*, vol. 14, no. 2, article 309, 2005.
- [149] A. Studenikin and A. Ternov, "Neutrino quantum states and spin light in matter," *Physics Letters B*, vol. 608, no. 1–2, pp. 107–114, 2005.
- [150] A. Grigorev, A. Studenikin, and A. Ternov, "Quantum theory of neutrino spin light in dense matter," *Physics Letters B*, vol. 622, no. 3–4, pp. 199–206, 2005.
- [151] A. Lobanov, "High energy neutrino spin light," *Physics Letters B*, vol. 619, no. 1–2, pp. 136–144, 2005.
- [152] J. Bernstein, M. Ruderman, and G. Feinberg, "Electromagnetic properties of the neutrino," *Physical Review*, vol. 132, no. 3, pp. 1227–1233, 1963.
- [153] G. Raffelt, "New bound on neutrino dipole moments from globular-cluster stars," *Physical Review Letters*, vol. 64, no. 24, pp. 2856–2858, 1990.
- [154] A. Heger, A. Friedland, M. Giannotti, and V. Cirigliano, "The impact of neutrino magnetic moments on the evolution of massive stars," *The Astrophysical Journal*, vol. 696, no. 1, article 608, 2009.
- [155] A. Cisneros, "Effect of neutrino magnetic moment on solar neutrino observations," *Astrophysics and Space Science*, vol. 10, no. 1, pp. 87–92, 1971.
- [156] M. B. Voloshin and M. I. Vysotsky, "Neutrino magnetic moment and time variation of solar neutrino flux," *Soviet Journal of Nuclear Physics*, vol. 44, article 544, 1986.
- [157] L. B. Okun, M. B. Voloshin, and M. I. Vysotsky, "Neutrino electrodynamics and possible consequences for solar neutrinos," *Soviet Physics, JETP*, vol. 64, p. 446, 1986.
- [158] E. K. Akhmedov, "Resonance enhancement of the neutrino spin precession in matter and the solar neutrino problem," *Soviet Journal of Nuclear Physics*, vol. 48, p. 382, 1988.
- [159] C. S. Lim and W. J. Marciano, "Resonant spin-flavor precession of solar and supernova neutrinos," *Physical Review D*, vol. 37, no. 6, pp. 1368–1373, 1988.
- [160] J. Vidal and J. Wudka, "Non-dynamical contributions to left-right transitions in the solar neutrino problem," *Physics Letters B*, vol. 249, no. 3–4, pp. 473–477, 1990.
- [161] A. Smirnov, "The geometrical phase in neutrino spin precession and the solar neutrino problem," *Physics Letters B*, vol. 260, no. 1–2, pp. 161–164, 1991.



- [162] E. K. Akhmedov, S. Petcov, and A. Smirnov, "Neutrinos with mixing in twisting magnetic fields," *Physical Review D*, vol. 48, no. 5, pp. 2167–2181, 1993.
- [163] G. Likhachev and A. Studenikin, "Neutrino oscillations in the magnetic field of the sun, supernovae, and neutron stars," *Journal of Experimental and Theoretical Physics*, vol. 81, pp. 419–425, 1995.
- [164] E. K. Akhmedov and M. Y. Khlopov, "Resonant amplification of neutrino oscillations in longitudinal magnetic field," *Modern Physics Letters A*, vol. 3, no. 5, pp. 451–457, 1988.
- [165] E. K. Akhmedov and M. Khlopov, "Resonant Enhancement of Neutrino Oscillations in Longitudinal Magnetic Field," *Soviet Journal of Nuclear Physics*, vol. 47, p. 689, 1988.
- [166] A. Egorov, A. Lobanov, and A. Studenikin, "Neutrino oscillations in electromagnetic fields," *Physics Letters B*, vol. 491, no. 1-2, pp. 137–142, 2000.
- [167] A. Lobanov and A. Studenikin, "Neutrino oscillations in moving and polarized matter under the influence of electromagnetic field," *Physics Letters B*, vol. 515, no. 1-2, pp. 94–98, 2001.
- [168] M. S. Dvornikov and A. I. Studenikin, "Neutrino oscillations in the field of a linearly polarized electromagnetic wave," *Physics of Atomic Nuclei*, vol. 64, no. 9, pp. 1624–1627, 2001.
- [169] M. S. Dvornikov and A. I. Studenikin, "Parametric resonance in neutrino oscillations in periodically varying electromagnetic fields," *Physics of Atomic Nuclei*, vol. 67, no. 4, pp. 719–725, 2004.
- [170] E. K. Akhmedov, "Antineutrinos from the sun," *Physics Letters B*, vol. 255, no. 1, pp. 84–88, 1991.
- [171] X. Shi, D. Schramm, R. Rosner, and D. Dearborn, "On using a neutrino magnetic moment to attack the solar neutrino problem," *Comments on Nuclear and Particle Physics*, vol. 21, pp. 151–182, 1993.
- [172] E. K. Akhmedov and J. Pulido, "Solar neutrino oscillations and bounds on neutrino magnetic moment and solar magnetic field," *Physics Letters B*, vol. 553, no. 1-2, pp. 7–17, 2003.
- [173] O. G. Miranda, T. I. Rashba, A. I. Rez, and J. W. F. Valle, "Constraining the neutrino magnetic moment with anti-neutrinos from the sun," *Physical Review Letters*, vol. 93, no. 5, Article ID 051304, 4 pages, 2004.
- [174] O. G. Miranda, T. I. Rashba, A. I. Rez, and J. W. F. Valle, "Enhanced solar anti-neutrino flux in random magnetic fields," *Physical Review D*, vol. 70, no. 11, Article ID 113002, 11 pages, 2004.
- [175] A. Friedland, "Do solar neutrinos constrain the electromagnetic properties of the neutrino?" in press, <http://arxiv.org/abs/hep-ph/0505165>.
- [176] G. Raffelt and T. Rashba, "Mimicking diffuse supernova antineutrinos with the sun as a source," *Physics of Atomic Nuclei*, vol. 73, no. 4, pp. 609–613, 2010.
- [177] Y. Gando, S. Fukuda, Y. Fukuda et al., "Search for  $\bar{\nu}_e$  from the sun at Super-Kamiokande-I," *Physical Review Letters*, vol. 90, no. 17, Article ID 171302, 5 pages, 2003.
- [178] J. N. Bahcall, M. H. Pinsonneault, and S. Basu, "Solar models: current epoch and time dependences, neutrinos, and helioseismological properties," *The Astrophysical Journal*, vol. 555, no. 2, article 990, 2001.
- [179] K. Eguchi, S. Enomoto, K. Furuno et al., "High sensitivity search for  $\bar{\nu}_e$ 's from the sun and other sources at KamLAND," *Physical Review Letters*, vol. 92, no. 7, Article ID 071301, 5 pages, 2004.
- [180] G. Bellini, J. Benziger, S. Bonetti et al., "Study of solar and other unknown anti-neutrino fluxes with Borexino at LNGS," *Physics Letters B*, vol. 696, no. 3, pp. 191–196, 2011.
- [181] A. Serenelli, S. Basu, J. W. Ferguson, and M. Asplund, "New solar composition: the problem with solar models revisited," *The Astrophysical Journal*, vol. 705, no. 2, article L123, 2009.
- [182] B. C. Chauhan, J. Pulido, and E. Torrente-Lujan, "KamLAND, solar antineutrinos and the solar magnetic field," *Physical Review D*, vol. 68, no. 3, Article ID 033015, 6 pages, 2003.
- [183] A. B. Balantekin and C. Volpe, "Does the neutrino magnetic moment have an impact on solar neutrino physics?" *Physical Review D*, vol. 72, no. 3, Article ID 033008, 7 pages, 2005.
- [184] M. M. Guzzo, P. C. de Holanda, and O. L. G. Peres, "Random magnetic fields inducing solar neutrino spin-flavor precession in a three generation context," *Physical Review D*, vol. 72, no. 7, Article ID 073004, 10 pages, 2005.
- [185] D. Yilmaz, "Joint analysis of solar neutrino and new KamLAND data in the RSFP framework," in press, <http://arxiv.org/abs/0810.1037>.
- [186] J. Pulido, B. C. Chauhan, and R. S. Raghavan, "Solar neutrinos: spin flavour precession and LMA," in *Proceedings of the 12th Lomonosov Conference in Elementary Particle Physics*, Moscow, Russia, August 2005, <http://arxiv.org/abs/hep-ph/0511341>.
- [187] S. Couvidat, S. Turck-Chièze, and A. G. Kosovichev, "Solar seismic models and the neutrino predictions," *Astrophysical Journal*, vol. 599, no. 2 I, pp. 1434–1448, 2003.
- [188] A. Dar, Print-87-0178 IAS, Princeton, NJ, USA, 1987.
- [189] S. Nussinov and Y. Rephaeli, "Magnetic moments of neutrinos: particle and astrophysical aspects," *Physical Review D*, vol. 36, no. 8, pp. 2278–2282, 1987.

- [190] I. Goldman, Y. Aharonov, G. Alexander, and S. Nussinov, "Implications of the supernova SN1987A neutrino signals," *Physical Review Letters*, vol. 60, no. 18, pp. 1789–1792, 1988.
- [191] J. M. Lattimer and J. Cooperstein, "Limits on the neutrino magnetic moment from SN1987A," *Physical Review Letters*, vol. 61, no. 1, pp. 23–26, 1988.
- [192] Y. Pehlivan, A. B. Balantekin, T. Kajino, and T. Yoshida, "Invariants of collective neutrino oscillations," *Physical Review D*, vol. 84, no. 6, Article ID 065008, 19 pages, 2011.

## Research Article

# The Results of Search for the Neutrino Magnetic Moment in GEMMA Experiment

**A. G. Beda,<sup>1</sup> V. B. Brudanin,<sup>2</sup> V. G. Egorov,<sup>2</sup> D. V. Medvedev,<sup>2</sup>  
V. S. Pogosov,<sup>2,3</sup> M. V. Shirchenko,<sup>2</sup> and A. S. Starostin<sup>1</sup>**

<sup>1</sup> State Science Center, Institute for Theoretical and Experimental Physics (ITEP), 117218 Moscow, Russia

<sup>2</sup> Laboratory of Nuclear Problems (LNP), Joint Institute for Nuclear Research (JINR), 141980 Dubna, Russia

<sup>3</sup> Alikhanyan National Laboratory (ANL), Yerevan Physics Institute (YerPhI), 375036 Yerevan, Armenia

Correspondence should be addressed to D. V. Medvedev, chess1984@mail.ru

Received 27 December 2011; Revised 16 March 2012; Accepted 2 April 2012

Academic Editor: Arthur B. McDonald

Copyright © 2012 A. G. Beda et al. This is an open access article distributed under the Creative Commons Attribution License, which permits unrestricted use, distribution, and reproduction in any medium, provided the original work is properly cited.

The result of the neutrino magnetic moment measurement at the Kalinin Nuclear Power Plant (KNPP) with GEMMA spectrometer is presented. The antineutrino-electron scattering is investigated. A high-purity germanium detector with a mass of 1.5 kg placed at a distance of 13.9 m from the 3 GW<sub>th</sub> reactor core is exposed to the antineutrino flux of  $2.7 \times 10^{13}$  1/cm<sup>2</sup>/s. The recoil electron spectra taken in 18134 and 4487 hours for the reactor ON and OFF periods are compared. The upper limit for the neutrino magnetic moment  $\mu_\nu < 2.9 \times 10^{-11} \mu_B$  at 90% C.L. is derived from the data processing.

## 1. Introduction

The Minimally Extended Standard Model (MSM) predicts a very small magnetic moment value for the massive neutrino ( $\mu_\nu \sim 10^{-19} \mu_B$ ) that cannot be observed in experiment at present. However, there are a number of theory extensions beyond the MSM where NMM could be at the level of  $10^{-(10 \div 12)} \mu_B$  [1–5] for Majorana neutrino. At the same time, it follows from general considerations [6, 7] that the Dirac NMM cannot exceed  $10^{-14} \mu_B$ . Therefore, the observation of NMM value higher than  $10^{-14} \mu_B$  would be an evidence of new physics and indicate undoubtedly [8–10] that neutrino is a Majorana particle. Furthermore, according to [11] new lepton number violating physics responsible for the generation of NMM arises at the scale  $\Lambda$  which is well below the see-saw scale. For example, for  $\mu_\nu = 1.0 \times 10^{-11} \mu_B$  and the neutrino mass  $m_\nu = 0.3$  eV, we can find that  $\Lambda \leq 100$  TeV.

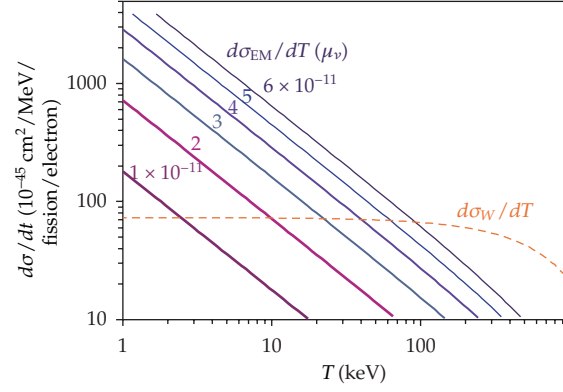


Figure 1: Weak ( $W$ ) and electromagnetic ( $EM$ ) cross-sections calculated for several NMM values.

It is rather important to make laboratory NMM measurements sensitive enough to reach the  $\sim 10^{-11} \mu_B$  region. The Savanna River experiment by Reines' group can be considered as the beginning of such measurements. Over a period of thirty years, the sensitivity of reactor experiments has been improved by only a factor of three: from  $[2 - 4] \times 10^{-10} \mu_B$  [12, 13] to  $[6 - 7] \times 10^{-11} \mu_B$  [14, 15]. Similar limits were obtained for solar neutrinos [16, 17], but, due to the MSW effect (as well as matter-enhanced oscillations in the Sun), their flavor composition changes and therefore the solar NMM results could differ from the reactor ones. In this paper, the result of NMM measurement by the collaboration of ITEP (Moscow) and JINR (Dubna) is presented. The measurements are carried out with the GEMMA spectrometer [15, 18, 19] at the 3 GW<sub>th</sub> reactor of the KNPP.

## 2. Experimental Approach

A laboratory measurement of the NMM is based on its contribution to the  $\nu - e$  scattering. For nonzero NMM, the  $\nu - e$  differential cross-section is [8] a sum of weak interaction cross-section ( $d\sigma^W/dT$ ) and electromagnetic one ( $d\sigma^{EM}/dT$ ):

$$\frac{d\sigma^W}{dT} = G_F^2 \cdot \left(\frac{m}{2\pi}\right) \cdot \left[ 4x^4 + (1 + 2x^2)^2 \cdot \left(1 - \frac{T}{E}\right)^2 - \frac{2x^2(1 + x^2)mT}{E^2} \right], \quad (2.1)$$

$$\frac{d\sigma^{EM}}{dT} = \pi r_0^2 \left(\frac{\mu_\nu}{\mu_B}\right)^2 \left(\frac{1}{T} - \frac{1}{E}\right), \quad (2.2)$$

where  $E$  is the incident neutrino energy,  $T$  is the electron recoil energy,  $x^2 = \sin^2 \theta_W = 0.232$  is a Weinberg parameter, and  $r_0$  is a classical electron radius ( $\pi r_0^2 = 2.495 \times 10^{-25} \text{ cm}^2$ ).

Figure 1 shows differential cross-sections (2.1) and (2.2) averaged over the typical antineutrino reactor spectrum versus the electron recoil energy. One can see that, at low recoil energy ( $T \ll E_\nu$ ), the value of  $d\sigma^W/dT$  becomes almost constant while  $d\sigma^{EM}/dT$  increases as  $T^{-1}$ . It becomes evident that the lower the detector threshold is, the more considerable increase in the NMM effect with respect to the weak unremovable contribution we can obtain.

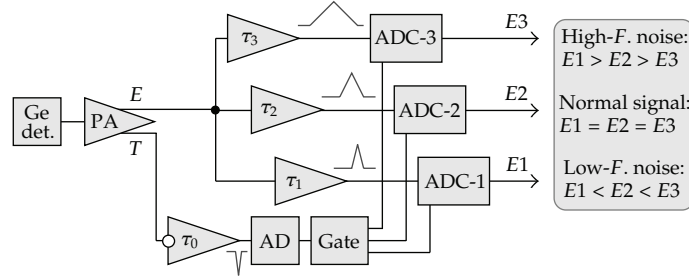


Figure 2: Signal processing scheme.

To realize this useful feature in our GEMMA spectrometer [15], we use a 1.5 kg HPGe detector with the energy threshold as low as 2.8 keV. To be sure that there is no efficiency cut at this energy, the “hard” trigger threshold is set twice lower (1.5 keV).

The background suppression is realized by means of various methods. The detector (Figure 3) is placed inside a cup-shaped NaI crystal with 14 cm thick walls and surrounded by 5 cm of electrolytic copper and 15 cm of lead. This active and passive shielding reduces the external  $\gamma$ -background in the ROI (the region of interest (ROI) in our analysis includes two fragments from 2.8 to 9.4 and from 11.2 to 55 keV, i.e., the low-energy part of the continuous spectrum without peaks which could depend on the reactor operation) to the level of  $\sim 2$  counts/keV/kg/day. Being located just under the reactor number 2 of KNPP (at the distance of 13.9 m from the reactor core center), the detector is well shielded against the hadronic component of cosmic rays by the reactor body and technologic equipment (overburden  $\sim 70$  m w.e.). The muon component is reduced by a factor of 10 at  $\pm 20^\circ$  with respect to vertical line and 3 at  $70^\circ \div 80^\circ$ . Nevertheless, a part of residual muons is captured in the massive shielding and produce neutrons that scatter elastically in Ge detector and raise the low-energy background. To suppress this effect, the spectrometer is covered with additional plastic scintillator plates which produce relatively long  $\mu$ -veto signals. In order to reduce nonphysical low-amplitude circuit noise (afterpulses, radio frequency interference, microphonism, etc.), the detector signal is processed by three parallel independent electronic channels with different shaping time (Figure 2). This allows us to apply a primitive Fourier analysis [20] and thus discriminate the artefact signals.

### 3. Data Taking and Processing

In order to get a recoil electron spectrum, we use a differential method comparing the spectra measured at the reactor operation (ON) and shut down (OFF) periods. Our experiment is divided into 3 phases. For Phase-I, we have 5184 and 1853 hours for the reactor ON and OFF periods, respectively. 6798 ON-hours and 1021 OFF-hours of live time statistics have been found to be available for analysis in Phase-II. Today, we can add Phase-III results. They contain 6152 ON-hours and 1613 OFF-hours of live time statistics.

During the measurement, the signals of the HPGe detector, anticompton NaI shielding, and outer antic cosmic plastic counters as well as dead time information are collected on the event by event basis. The detection efficiency just above the threshold is checked with a pulser. The neutrino flux during the ON period is estimated via the reactor thermal power measured with accuracy of 0.7%.



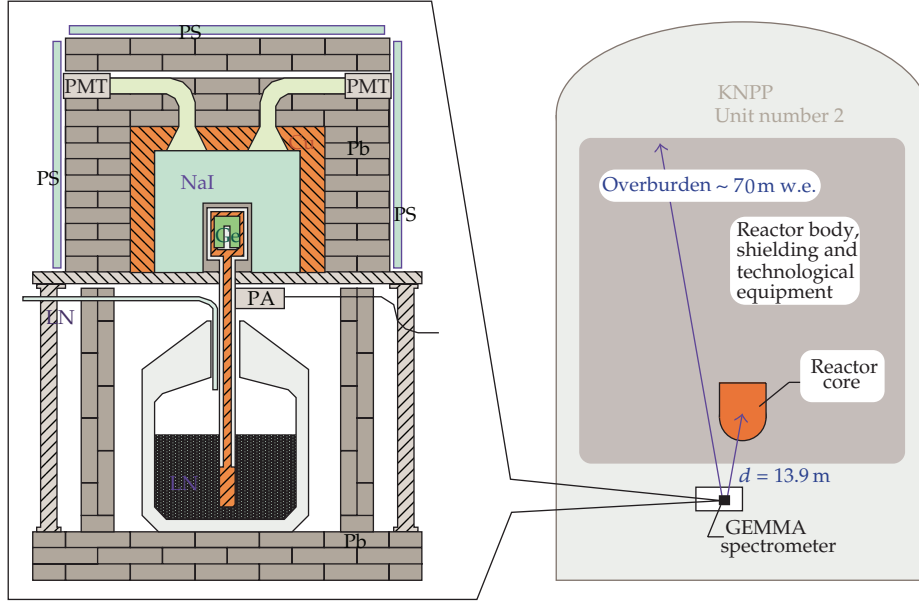


**Figure 3:** Ge detector inside the active (NaI, PS) and passive (Cu, Pb) shielding.

At the beginning of the experiment, the background was measured with and without shielding. On Figure 4, one can see the background suppression due to passive and active shielding.

The collected data are processed in several steps. The first step involves different selections aimed to suppress nonphysical and physical backgrounds.

- (1) *Bad run* rejection. We reject those hour-long runs which correspond to the periods of liquid nitrogen filling and any mechanical or electrical work at the detector site as it could produce noise.
- (2) *Radioactive noble gas* rejection. Unfortunately, the detector shielding turned out to be not tight enough against radioactive noble gases. To smooth away this design defect, we analyze energy spectra measured during each several hours and check the stability of the  $\gamma$ -background. If any visible excess of 81 keV ( $^{133}\text{Xe}$ ), 250 keV ( $^{135}\text{Xe}$ ) or 1294 keV ( $^{41}\text{Ar}$ )  $\gamma$ -line occurs, the corresponding runs are removed. (In fact these files are used later for the “noble gas” correction for the rest of the data.)
- (3) *Detector noise* rejection. For some obscure reasons, our Ge detector happened to become noisy from time to time. In order to reject these noisy periods, the low-amplitude count rate is checked second by second and those seconds that contain more than 5 events with  $E > 2$  keV are rejected.
- (4) *Audio-frequency* rejection. We reject those events which are separated by a time interval shorter than 80 ms or equal to  $[n \cdot (20.0 \pm 0.1)]$  ms. In this way, we suppress the noise caused by mechanical vibrations (ringing) and the 50 Hz power line frequency.
- (5) *Fourier* rejection. As it has already been mentioned, the real and the artefact signals have different Fourier spectra. To exploit this difference, we build three plots similar to that shown in Figure 5: ( $E_2$  versus  $E_1$ ), ( $E_3$  versus  $E_2$ ), and ( $E_1$  versus  $E_3$ ).

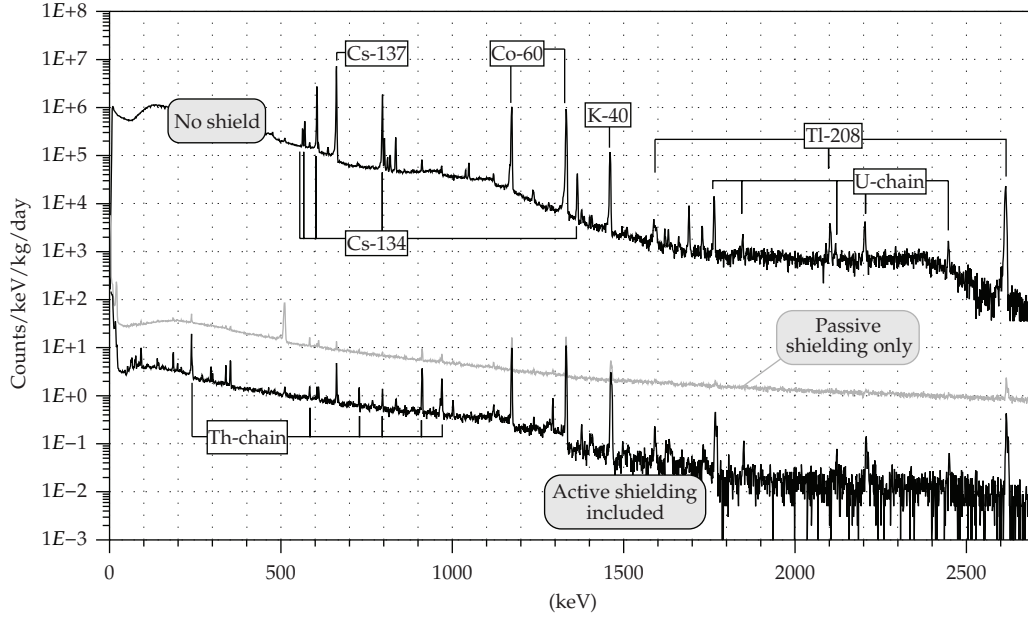


**Figure 4:** Gamma spectra measured at the detector site under different shielding conditions. ON and OFF reactor periods do not demonstrate any visible difference.

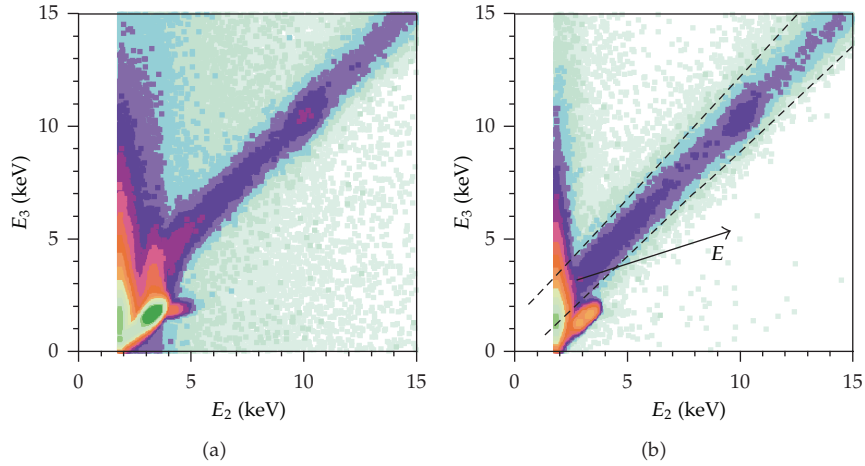


**Figure 5:** Example of the Fourier analysis made with different shaping times: ADC-2 operates with  $4\ \mu\text{s}$  pulses, and ADC-3 operates with  $12\ \mu\text{s}$  pulses. Plot (a) is made *before* and (b) *after* the “audio-frequency” rejection; one can see that most of the rejected events are nondiagonal. (The color intensity scale is logarithmic.)

The real signal falls into diagonals ( $E_1 \approx E_2 \approx E_3$ ) within the energy resolution, whereas any nonphysical artefact shows a different pattern. We select only diagonal events and thus additionally reject low- and high-frequency noise. To ensure the best cutoff, we replace  $E_1, E_2$ , and  $E_3$  by their linear combination  $E$ :

$$E = aE_1 + bE_2 + cE_3, \quad (3.1)$$

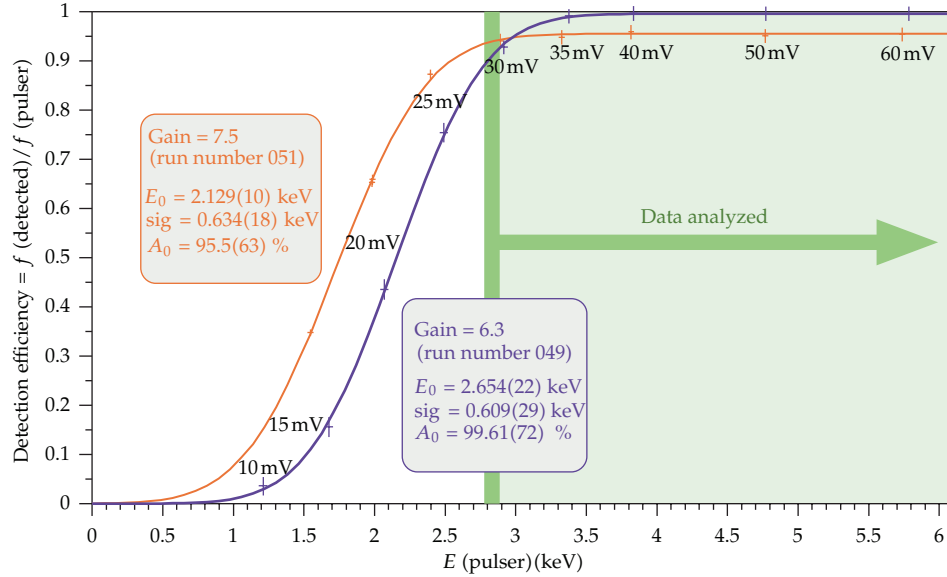


**Figure 6:** Low-energy threshold function measured with 50 Hz pulser at several amplitudes. Decreasing of the “hard” threshold minimizes the correction value but also decreases total detection efficiency (because of higher load and therefore higher dead time).

where the weights  $a, b, c$  are chosen (subjectively) so as to make the vector be antiparallel to the noise gradient (Figure 5(b)).

After the above rejections, we construct energy spectra for the ON and OFF periods and correct them in the following two steps (the corrections do not give a significant error to the final result as they affect ON and OFF spectra in the same way):

- (1) *Noble gas* correction. As our spectrometer is not located in a special laboratory but in the technological room sometimes, there are short operational periods when the concentration of  $^{41}\text{Ar}$ ,  $^{133}\text{Xe}$ , and  $^{135}\text{Xe}$  in this room becomes higher than usual. Spectra measured under these conditions are used to evaluate the contribution of each radioactive gas to the low-energy part of the background. These contributions normalized to the intensities of the corresponding  $\gamma$ -lines are then subtracted from those few ON and OFF spectra where small traces of these lines are still present. In this case, the value of such correction in the ROI does not exceed 1-2%.
- (2) *Low-energy* threshold correction. The detection efficiency  $\eta$  just above the threshold  $E_0$  is measured with a pulser and is fitted with the function

$$\eta(E) = \int_{-\infty}^E \frac{1}{\sqrt{2\pi}\sigma} e^{-(x-E_0)^2/2\sigma^2} dx, \quad (3.2)$$

where  $\sigma$  stands for the detector energy resolution. Experimental spectra are then corrected by the function (3.2) which becomes significant at energies below 2.8 keV in our case (Figure 6).

During the long-term measurements, it is crucial to establish the long-term stability as well. In our case, this problem is divided into two main parts: the background constancy

and the hardware stability. The main source of background instability is the presence of noble gases (see “noble gas correction”). One of the best ways to check the hardware is to control the position of some energy peak because almost any changes in the hardware result in its shift. But, in the low background measurements, this method could not be applied due to insufficient statistics. That is why we have used the following procedure. First, we have made the binning of overall data. The idea of this binning consists in obtaining enough data in some devoted spectrum lines. The next step is to check if those peaks have some additional broadening because of possible amplification changes during the bin time. If this broadening appears to be large enough (10% or more), we perform the rebinning to find the exact time of the shift and possibly distinguish its origin. Then, the data divided in this way are transferred to the uniform energy scale (0.1 keV/channel) and only after that are summed up. Thus, we automatically reduce the influence of the hardware instability to the negligible level.

As a result, we obtain energy spectra  $S$  for the ON and OFF periods which must be normalized by the corresponding active times  $T_{\text{ON}}$  and  $T_{\text{OFF}}$  and then compare them to each other taking into account the additional neutrino dependent term:

$$\frac{S_{\text{ON}}}{T_{\text{ON}}} = \frac{S_{\text{OFF}}}{T_{\text{OFF}}} + m_d \Phi_\nu (W + X * \text{EM}). \quad (3.3)$$

The last term includes the fiducial detector mass  $m_d$  and the antineutrino flux  $\Phi_\nu$  (known with an accuracy of 1.7% and 3.5%, resp.) multiplied by the sum of two neutrino contributions: the weak one ( $W$ ) which can be calculated easily using formula (2.1) and is completely negligible in our case and the electromagnetic one (EM) which is proportional to the squared NMM value:

$$X \equiv \left( \frac{\mu_\nu}{10^{-11} \mu_B} \right)^2. \quad (3.4)$$

Unfortunately, the exposition times of ON and OFF periods are not equal. A usual OFF period is much shorter, and therefore the final sensitivity is limited by the background uncertainties. However, today after four years of data taking, we know the ROI background structure with good confidence (280 kg\*day of OFF statistics). It gives us the right to introduce additional information in our analysis, namely, to state that our background is a *smooth curve*.

To implement this conventional idea, we fit the background OFF spectrum in the ROI from 2.8 keV to 55 keV with a parametrized smooth function (e.g., a sum of Gaussian, exponential, and linear functions). We can also use splines for this procedure. All these fits produce slightly different results, and their spread is taken into account in the final systematic error.

Then, we compare the ON spectrum channel by channel with the obtained background curve and extract the  $X$ -value (or its upper limit) from (3.3). This evaluation is more complicated than expected because it is very difficult to count active times  $T_{\text{ON}}$  and  $T_{\text{OFF}}$  precisely in a proper way (especially after numerous selections of the events). To avoid possible errors caused by this procedure, we divide the active time normalization into two parts: absolute ( $T_{\text{ON}}$ ) and relative ( $\tau \equiv T_{\text{ON}}/T_{\text{OFF}}$ ).

Roughly, both the  $T_{\text{ON}}$  and  $T_{\text{OFF}}$  active times are estimated using several background  $\gamma$ -lines: the 238 keV line of  $^{212}\text{Pb}$ , the 1173 keV and 1333 keV lines of  $^{60}\text{Co}$ , and the 1461 keV line

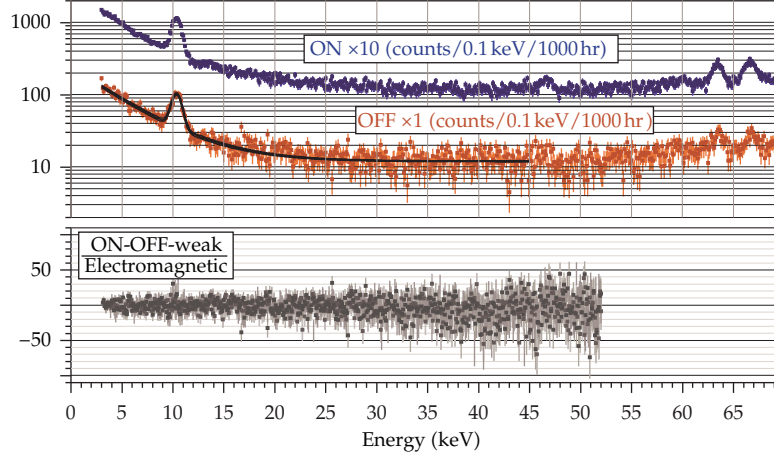


**Figure 7:** Fragments of the experimental ON and OFF spectra (top) and their difference normalized by the electromagnetic cross-section (bottom).

of  $^{40}\text{K}$ . This radiation originates from the pollution of the internal parts of the spectrometer and is therefore stable in time and does not depend on the reactor operation. Comparing the intensities of the above lines measured *with* and *without* any selections, we get the estimates  $T'_{\text{ON}}$  and  $T'_{\text{OFF}}$  with an accuracy of 0.9% and 1.9%, respectively. However, this is not enough to evaluate the  $\tau$  value with the required precision. We resolve this problem in the following way.

The relative ON/OFF time factor  $\tau$  is represented as a product of its estimate  $\tau' = T'_{\text{ON}}/T'_{\text{OFF}}$  (which is a constant known with an accuracy of 2.1%) and a correction factor  $K$  (which should be not far from 1.0):  $\tau = K\tau'$ . Then, (3.3) can be transformed to

$$W + X * \text{EM} = (S_{\text{ON}} - K\tau'S_{\text{OFF}}) * (T_{\text{ON}}m_d\Phi_v)^{-1}. \quad (3.5)$$

As one can see, the absolute time normalization  $T_{\text{ON}}$  contributes to the final result in the same way as  $\Phi_v$  or  $m_d$  (i.e., simply as a *factor*), and therefore we can replace  $T_{\text{ON}}$  by its estimate  $T'_{\text{ON}}$ . Standard systematic deviation  $\delta X$  caused by this factor is not significant:

$$\frac{\delta X}{X} = \frac{\delta(T_{\text{ON}}m_d\Phi_v)}{T_{\text{ON}}m_d\Phi_v} = \sqrt{(0.9\%)^2 + (1.7\%)^2 + (3.5\%)^2} \approx 4.0\%. \quad (3.6)$$

Preliminary time normalization can be performed not only with the background  $\gamma$ -lines but also with a part of the continuous spectrum (e.g., from 20 to 55 keV). Both methods give very similar results, but the second one provides better precision due to higher statistics. Comparison of  $\gamma$ -lines as well as integrals of continuous parts between ON and OFF spectra remaining after application of selection procedure allows us to extract  $K$ -value with accuracy better than 1%.

Figure 7 illustrates good background knowledge. Furthermore, its bottom part shows that there is no visible deviation of  $X$ -value from zero within statistical errors. This demonstrates that our way of data processing is adequate and does not bring in an additional systematic error.



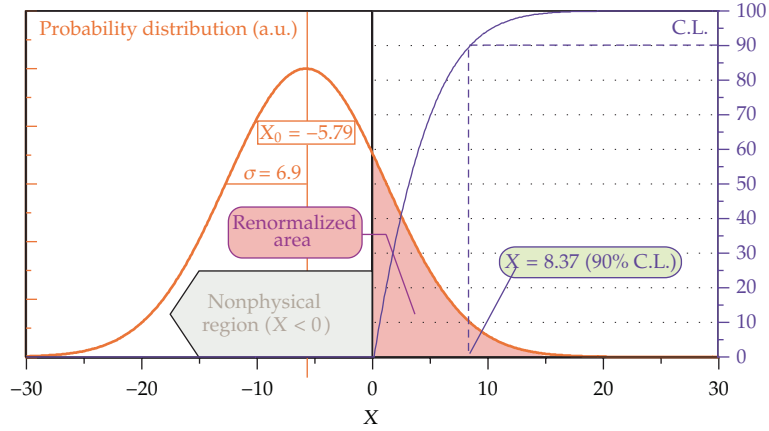


Figure 8: Final probability distribution of  $X$ .

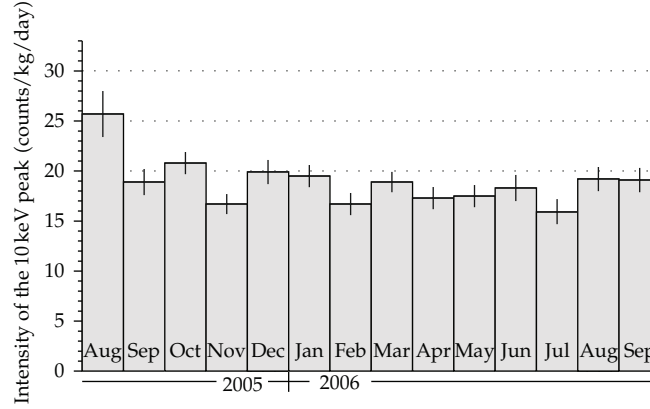


Figure 9: Variation of 10 keV peak intensity in time.

To extract the NMM value, we compare ON spectrum with the obtained curve channel by channel (to be more precise, with a narrow corridor with the width given by the fitting uncertainty). Applying this procedure to the total statistics of Phases I + II + III, we get the final distribution for  $X$  (Figure 8).

After a conventional renormalization recommended by the Particle Data Group [21] and described in our previous work [19], we extract the upper limit for the  $X$  parameter and thus get the following NMM limit:

$$\mu_\nu < 2.9 * 10^{-11} \mu_B. \quad (3.7)$$

The data is processed in the energy region of interest (ROI) from 2.8 keV to 55 keV with a step of 0.1 keV. The region from 9.4 keV to 11.2 keV is excluded as the corresponding peak could vary in time. The time dependence of the peak intensity is traced (Figure 9). As one can see after two months of data taking, it became almost constant. This peak has an internal origin, so it is always observed as complete absorption peak without low-energy compton

tail. Taking additionally into account that the intensity is rather small, we can state that the affection of this peak to the region below 9.4 keV due to finite energy resolution is negligible.

There are two kinds of possible systematic errors in the procedure of  $X$ -value extraction from experimental data. The first one arises from the uncertainties in knowledge of the neutrino energy spectrum and initial intensity as well as its distortions caused by possible short-baseline neutrino oscillations [22]. It includes also the uncertainty of the reactor thermal power, detector fiducial volume, and effective measurement time. Each of these terms enters the final result as a *factor* so that a sum of their relative errors gives a small rise only to the  $X$ -distribution width ( $\sim 10\%$ ) but not the central value. That is why it is not very important for the case of upper limit estimation. The second source of systematic error originates from the background estimation. As it was mentioned, the idea of the experiment is to compare low-energy background measured for the reactor ON and OFF periods *ceteris paribus*. Nonequivalence of the conditions could either shift the mean value to the unphysical (negative) region or mimic the nonzero NMM value. It could be caused by the incorrect normalization of the measurement times  $T_{\text{ON}}/T_{\text{OFF}}$  as well as by presence of any unrecorded background component correlated with the reactor operation. The absence of the above effects is demonstrated in Figure 8. One can see the deviation of central value  $X_0$  from zero to be comparable with the dispersion  $\sigma$ . That proves the validity of our assumptions and the propriety of the chosen method for estimation of the upper limit on  $X$ -value.

#### 4. Future Plans

At present time, we prepare experiment GEMMA-II. The experimental setup is being placed under the reactor number 3 where the distance from the centre of the core is 10 m. In this way, we double the antineutrino flux up to  $5.4 \times 10^{13}$  1/cm<sup>2</sup>/s. The  $\gamma$ -background conditions in the new room are much better (by an order of magnitude), and the climate conditions are more stable. Furthermore, being equipped with a special lifting mechanism, the spectrometer will be moveable. It gives us an opportunity to vary on-line the antineutrino flux significantly and thus suppress the main systematic errors caused by the possible long-term instability and uncertainties of background knowledge. The mass of the detector is increased by a factor of 4 (two detectors with a mass of 3 kg each). To avoid the “Xe-problems,” the internal part of the detector shielding will be gas tight. A special U-type low-background cryostat is used in order to improve the passive shielding and thus reduce the external background in the ROI down to  $\sim 0.5\text{--}1.0$  (keV\*kg\*day)<sup>-1</sup>. A special care is taken to improve antimicrophonic and electric shielding. We also plan to reduce the effective threshold from 2.8 to 1.5 keV. The neutrino flux monitoring will be available by means of special detector (project DANSS, to be published). As a result of all the improvements we will be able to suppress the systematic errors and expect the experimental sensitivity to be at the level of  $1 \times 10^{-11} \mu_B$  and thus to reach the region of astrophysical interest.

#### 5. Conclusion

The experimental NMM search with GEMMA spectrometer has been going on at KNNP (Russia) since 2005. The HPGe detector of 1.5 kg placed 13.9 m under the core of the 3 GW<sub>th</sub> water moderated reactor has been exposed to the antineutrino flux of  $2.7 \times 10^{13}$  1/cm<sup>2</sup>/s. As a result of the measurement (about 18000 ON-hours and 4500 OFF-hours of live time) the world best upper limit of  $2.9 \times 10^{-11} \mu_B$  at 90% C.L. was set for the NMM.

The analysis of data indicates that the sensitivity limit of the setup is almost reached. To improve it we prepare significant upgrading of the spectrometer (GEMMA-II). Within the framework of this project we plan to use the antineutrino flux of  $5.4 \times 10^{13} \text{ 1/cm}^2/\text{s}$ , increase the mass of the germanium detector by a factor of four, and decrease the level of the background. These measures will provide us the possibility of achieving the NMM limit at the level of  $1.0 \times 10^{-11} \mu_B$ .

## Acknowledgments

The authors are grateful to the Directorates of ITEP and JINR for constant support of this work and especially to M. V. Danilov for his important comments. The authors appreciate the administration of the KNPP and the staff of the KNPP Radiation Safety Department for permanent assistance in the experiment. This work is supported by the Russian State Corporation ROSATOM and by the Russian Foundation for Basic Research, Projects 09-02-00449 and 09-02-12363.

## References

- [1] M. B. Voloshin, M. I. Vysotsky, and L. B. Okun, "Neutrino electrodynamics and possible effects for solar neutrinos," *Journal of Experimental and Theoretical Physics*, vol. 64, pp. 446–452, 1986.
- [2] M. Fukugita and T. Yanagida, "Particle-physics model for voloshin-vysotsky-okun solution to the solar-neutrino problem," *Physical Review Letters*, vol. 58, no. 18, pp. 1807–1809, 1987.
- [3] S. Pakvasa and J. W. F. Valle, "Neutrino properties before and after KamLAND," *Proceedings of the Indian National Science Academy A*, vol. 70A, pp. 189–222, 2004.
- [4] M. Gorchtein, N. F. Bell, M. J. Ramsey-Musolf, P. Vogel, and P. Wang, "Model independent naturalness bounds on magnetic moments of majorana neutrinos," in *Proceedings of the 14th International Conference on Supersymmetry and the Unification of Fundamental Interactions (SUSY '06)*, vol. 903 of AIP Conference Proceedings, pp. 287–290, June 2006.
- [5] N. F. Bell, M. Gorchtein, M. J. Ramsey-Musolf, P. Vogel, and P. Wang, "Model independent bounds on magnetic moments of majorana neutrinos," *Physics Letters B*, vol. 642, no. 4, pp. 377–383, 2006.
- [6] N. F. Bell, V. Cirigliano, M. J. Ramsey-Musolf, P. Vogel, and M. B. Wise, "How magnetic is the dirac neutrino?" *Physical Review Letters*, vol. 95, no. 15, Article ID 151802, 4 pages, 2005.
- [7] N. F. Bell, V. Cirigliano, M. J. Ramsey-Musolf, P. Vogel, and M. B. Wise, "Magnetic moments of dirac neutrinos," in *Proceedings of the 17th International Conference on Particles and Nuclei*, vol. 842 of AIP Conference Proceedings, pp. 874–876, Santa Fe, NM, USA, October 2005.
- [8] B. Kayser, "Neutrino properties," in *Proceedings of the Neutrino*, Christchurch, New Zealand, May 2008.
- [9] C. Giunti and A. Studenikin, "Neutrino electromagnetic properties," *Physics of Atomic Nuclei*, vol. 72, no. 12, pp. 2089–2125, 2009.
- [10] A. Studenikin, "Neutrino magnetic moment: a window to new physics," *Nuclear Physics B*, vol. 188, pp. 220–222, 2009.
- [11] N. F. Bell, "How magnetic is the neutrino?" *International Journal of Modern Physics A*, vol. 22, no. 27, pp. 4891–4899, 2007.
- [12] F. Reines, H. S. Gurr, and H. W. Sobel, "Detection of  $\bar{\nu}_e - e$  scattering," *Physical Review Letters*, vol. 37, no. 6, pp. 315–318, 1976.
- [13] P. Vogel and J. Engel, "Neutrino electromagnetic form factors," *Physical Review D*, vol. 39, no. 11, pp. 3378–3383, 1989.
- [14] T. H. Wong et al., "Search of neutrino magnetic moments with a high-purity germanium detector at the Kuo-Sheng nuclear power station," *Physical Review D*, vol. 75, no. 1, Article ID 012001, 16 pages, 2007.
- [15] A. G. Beda, V. B. Brudanin, E. V. Demidova et al., "First result for the neutrino magnetic moment from measurements with the GEMMA spectrometer," *Physics of Atomic Nuclei*, vol. 70, no. 11, pp. 1873–1884, 2007.

- [16] D. W. Liu et al., "Limits on the neutrino magnetic moment using super-kamiokande solar neutrino data," *International Journal of Modern Physics A*, vol. 20, no. 14, pp. 3110–3112, 2005.
- [17] C. Arpesella and The Borexino Collaboration, "Direct measurement of the  $^7\text{Be}$  solar neutrino flux with 192 days of borexino data," *Physical Review Letters*, vol. 101, no. 9, 6 pages, 2008.
- [18] A. G. Beda, E. V. Demidova, A. S. Starostin, and M. B. Voloshin, "Low-background Ge-NaI spectrometer for measurement of the neutrino magnetic moment," *Physics of Atomic Nuclei*, vol. 61, no. 1, pp. 66–73, 1998.
- [19] A. G. Beda, V. B. Brudanin, E. V. Demidova et al., "Status of the experiment on the measurement of the neutrino magnetic moment with the spectrometer GEMMA," *Physics of Atomic Nuclei*, vol. 67, pp. 1948–1952, 2004.
- [20] E. Garcia, F. T. Avignone III, R. L. Brodzinski et al., "Dark matter searches with a germanium detector at the canfranc tunnel," *Nuclear Physics B*, vol. 28, no. 1, pp. 286–292, 1992.
- [21] W.-M. Yao et al., "Review of Particle Physics," *Journal of Physics G*, vol. 33, no. 1, 2006.
- [22] G. Mention, M. Fechner, T. H. Lasserre et al., "The reactor antineutrino anomaly," *Physical Review D*, vol. 83, no. 7, 20 pages, 2011.